A. Maeder

Physics, Formation and Evolution of Rotating Stars

A&A
LIBRARY

Springer

ASTRONOMY AND ASTROPHYSICS LIBRARY

André Maeder

Physics, Formation and Evolution of Rotating Stars

 Springer

André Maeder
Université Genève
Observatoire de Genève
1290 Sauverny
Switzerland
andre.maeder@unige.ch

Preface

Rotation is often considered as a side effect in stellar evolution, a point not deserving more than a section at the end of a book. However, at each step from star formation to the final stages of evolution, rotation is present and in some cases even dominates the course of evolution, the timescales and the nucleosynthesis. This is in particular the case in star formation, where the initial angular momentum has to be reduced by a factor of 10^5 at least. Also during nuclear evolution the rotational instabilities drive internal mixing of the elements and rotation may enhance the mass loss rates. Recent works (see Chap. 29) even suggest that rotation is a dominant effect in the evolution and element synthesis of the first stars at zero and very low metallicities. Also, stellar rotation is an essential ingredient for the occurrence of gamma-ray bursts (GRBs). This is why here we thoroughly examine the basic mechanical and thermal effects of rotation during evolution, their influence on stellar winds, the effects of differential rotation and associated instabilities and the possible dynamos generated in rotating stars. Also, the observational signatures of rotational effects are numerous, first from spectroscopy and now also from interferometric observations, from chemical abundance determinations, from helioseismology and asteroseismology, etc.

To be useful at an introductory level, this book presents in a didactical way the basic concepts of stellar structure and evolution in chapters indicated by a star ($\star$). These chapters form a basic course, while the other more specialized chapters form an advanced course. In general, I have given the step-by-step derivations of the analytical developments for the reader's comfort.

Three centuries ago, there were books covering all scientific domains, with even a touch of theology in addition. Then, science became more specialized. Half a century ago, there were still books, like the one by Pecker and Schatzman, able to present the whole astronomy at a specialized level. Nowadays, due to the explosion of scientific knowledge, it is becoming a considerable task to cover fields like stellar formation and evolution. Thus, despite the many subjects studied in this book, there are still many topics not treated here, in particular the properties of stellar remnants, which deserve full books (see for example [83] and [281]). The same applies to the evolution of binary stars, the fact they are not treated here does not mean that they have not a certain importance. Indeed, most effects studied here also find an application in binaries, however with a higher degree of complexity due to the interaction

with tidal mixing, tidal generation of gravity waves, transport of angular momentum and mass transfer.

As a consequence of the extraordinary vitality of astrophysics, the numerical models and observational results tend soon to become obsolete, being superseded by new results from more detailed computations and modern techniques. Therefore, I usually tried to emphasize the analytical results, which express the fundamental physics of the problem and fortunately are not aging in the same way. Numerical models, whenever presented, are given mainly for providing illustrations of the general properties. For specific applications, the last (and hopefully best) precise values are always recommended.

I want to quote and express my gratitude, when possible, to eminent scientists, colleagues and friends for their major help in the course of my career: Profs. P. Bouvier, G. Burki, P. Conti, A.N. Cox, M. Golay, B. Hauck, R. Kippenhahn, J. Lequeux, M. Mayor, G. Meynet, F. Rufener, E. Schatzman, M. Schwarzschild, L. Smith, G. Tammann, J.P. Zahn. I kindly ask the readers to consider that this book is not aiming at giving a historical perspective, nor to give quotations in proportion to author achievements. For that, it is better to consult the ADS databases. I also thank very much many colleagues for fruitful collaborations and for participating in the manuscript correction: C. Charbonnel, P. Eggenberger, S. Ekström, C. Georgy, R. Hirschi, S. Mathis, G. Meynet, N. Mowlavi. I apologize for the unavoidable remaining mistakes, which are evidently my responsibility. I also thank Prof. C. Chiosi for most helpful remarks on the manuscript and Dr. Ramon Khanna of Springer for fruitful and constructive interactions. Last but not least, I express my deep gratitude to my wife Elisabeth for her inalterable kindness and support.

Finally, I wish to the students in astrophysics and readers as much joy and fun in their attempts to discover and understand the processes which rule the stars as I have myself, whether it concerns astrophysics or all the other marvels of Nature.

Geneva Observatory, Switzerland,   *André Maeder*
                                                                                          May 2008

Contents

Part II   Physical Properties of Stellar Matter

Part I
Stellar Equilibrium With and Without Rotation

Chapter 1
The Mechanical Equilibrium of Stars[*]

If the stars would not be in equilibrium during most of their life, stable conditions permitting life would not have been present on the Earth. Mechanical equilibrium is a necessary condition for stable luminosity and temperature over long periods of time. It is a fundamental property of stars, implying the exact balance between the gravity force which attracts the matter toward the center and the force due to the thermal pressure, which resists gravity. Any departure from this equilibrium will immediately lead to a strong reaction for restoring the equilibrium state. Let us suppose, for example, that the Sun is arbitrarily compressed to a smaller radius. The gas becomes hotter rising the internal pressure. The higher pressure provokes an expansion re-settling the star to its equilibrium state. Conversely, an arbitrary extension of the radius would decrease the internal temperature and pressure, the Sun would then contract again. Such re-adjustments are very fast, they would occur at the dynamical timescale of the order of half an hour for the Sun, which is almost instantaneous with respect to solar evolution.

The mechanical equilibrium of a star governs all its properties. It is always satisfied except in very short phases, such as the initial collapse of interstellar clouds or in supernova explosions.

1.1 Momentum and Continuity Equations

1.1.1 Hydrodynamical Equations

The basic equations of hydrodynamics determining the mechanical equilibrium of a star are the equation of continuity, which expresses mass conservation, and the equation of Navier–Stokes, which is the equation of motion. They are derived in Appendix B.1. For a medium of density ϱ and velocity $\boldsymbol{v}$, the equation of continuity is

$$\frac{\partial \varrho}{\partial t} + \operatorname{div}(\varrho \, \boldsymbol{v}) = 0 \,, \tag{1.1}$$

[*]This chapter may form the matter of a basic introductory course.

and the equation of Navier–Stokes

$$\frac{d\mathbf{v}}{dt} = \frac{\partial \mathbf{v}}{\partial t} + (\mathbf{v} \cdot \nabla)\,\mathbf{v} = \mathbf{a} - \frac{1}{\varrho}\,\nabla P + \nu \nabla^2 \mathbf{v}\,, \tag{1.2}$$

where $\mathbf{a}$ is the acceleration due to external forces, P the pressure and ν the kinematic coefficient of viscosity (B.50). Let us consider a spherical star, where r is the distance to the center and assume that the viscous effects are negligible. First, we do not suppose hydrostatic equilibrium, letting open the possibility of internal motions. The spherical components of the Navier–Stokes equation (1.2) become

$$\frac{d\mathbf{v}}{dt} = (\ddot{r}, 0, 0)\,, \quad \nabla P = \left(\frac{\partial P}{\partial r}, 0, 0\right), \quad \mathbf{a} = \mathbf{g} = (-g, 0, 0)\,, \tag{1.3}$$

where $\mathbf{g}$ is the vector of gravity directed toward the stellar interior. Its modulus is $g = GM_r/r^2$, with G the constant of gravitation and M_r the mass interior to radius r (Fig. 1.1). Thus the Navier–Stokes equation leads to

$$\ddot{r} = -\frac{1}{\varrho}\frac{\partial P}{\partial r} - \frac{GM_r}{r^2}\,. \tag{1.4}$$

This is the momentum equation of hydrodynamic models. It expresses that the acceleration is the sum of two contributions:

– the acceleration due to the pressure gradient which is directed toward the exterior, since $\partial P/\partial r < 0$,
– the gravity $\mathbf{g}$ directed toward the stellar interior.

Depending on the kind of motion, $\ddot{r}$ may be positive or negative. For example in a pulsating star, $\ddot{r}$ changes sign during a pulsation cycle. In some stages, such as the collapse of an interstellar cloud (Sect. 18.2.4), the internal pressure forces are negligible, so that one is just left with the equation of free fall (18.20).
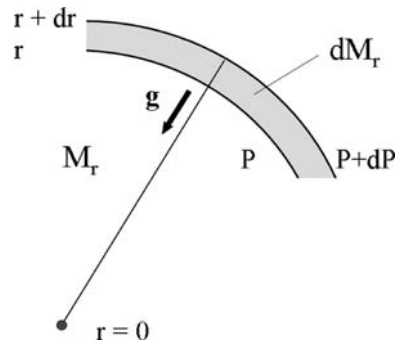
Fig. 1.1 Some definitions. dP is the difference of pressure between the levels in r and $r+dr$. M_r is the mass interior to level r, dM_r is the mass between r and $r+dr$

1.1.2 Hydrostatic Equilibrium

If there is no fast radial motions, we have a situation of hydrostatic equilibrium. This is the general situation of most stars. The internal pressure gradient is balancing the gravity everywhere in the star. The equations in vectorial and scalar forms are

$$\nabla P = \varrho\, \boldsymbol{g} \quad \text{and} \quad \frac{1}{\varrho}\frac{dP}{dr} = -\frac{GM_r}{r^2}, \tag{1.5}$$

consistently with definitions (1.3). This equation says that at any level in a star in equilibrium the gradient of pressure sustains the matter against the gravity force by volume unity. Equation (1.4) is to be taken rather than (1.5) if the ratio $|\ddot{r}/g|$ is not negligible. In practice, this applies only to stellar pulsations, early stages of star formation and advanced phases of evolution. The above equation of hydrostatic equilibrium (1.5) may also be found very simply by considering a thin shell between radius r and $r+dr$, with pressures P and $P+dP$, respectively. Let M_r be the mass inside radius r (Fig. 1.1). The difference of pressure dP is

$$dP = -\varrho\, g\, dr = -\varrho\, \frac{GM_r}{r^2}\, dr, \tag{1.6}$$

which just gives (1.5).

1.1.3 Mass Conservation and Continuity Equation

In spherical symmetry, the change of the mass $M_r(t)$ in a sphere of radius r can be written as

$$dM_r(r,t) = 4\pi r^2 \varrho\, dr - 4\pi r^2 \varrho\, v\, dt. \tag{1.7}$$

The first term on the right represents the change of mass due to a variation of radius r at a given time t, the second term expresses the flux of mass out of the sphere of constant r due to an outward motion with velocity $v > 0$. The differential $dM_r(r,t)$ can also be written as

$$dM_r(r,t) = \left(\frac{\partial M_r}{\partial r}\right)_t dr + \left(\frac{\partial M_r}{\partial t}\right)_r dt. \tag{1.8}$$

Comparing with (1.7), we make the identifications,

$$\left(\frac{\partial M_r}{\partial r}\right)_t = 4\pi r^2 \varrho \quad \text{and} \quad \left(\frac{\partial M_r}{\partial t}\right)_r = -4\pi r^2 \varrho\, v. \tag{1.9}$$

- The first expression is the definition of the local density $\varrho(r)$. It also allows us to move from variable r to M_r and reciprocally at a given time.

– The second equation expresses the change of mass in a sphere due to the motion of matter which goes through its surface. At the stellar surface, this equation gives the mass loss rate (or gain) $\dot{M}$ as a function of the wind velocity $v > 0$ for an outward stellar wind or $v < 0$ for an accretion of matter. As dM_r is an exact differential, one has

$$\left(\frac{\partial}{\partial t}\left(\frac{\partial M_r}{\partial r}\right)_t\right)_r = \left(\frac{\partial}{\partial r}\left(\frac{\partial M_r}{\partial t}\right)_{r}\right)_t, \tag{1.10}$$

which gives

$$4\pi r^2 \frac{\partial \varrho}{\partial t} = -4\pi \frac{\partial}{\partial r}(r^2 \varrho v) \quad \text{or} \quad \frac{\partial \varrho}{\partial t} + \frac{1}{r^2}\frac{\partial}{\partial r}(r^2 \varrho v) = 0. \tag{1.11}$$

This is just the spherical form of the continuity equation (1.1). Thus, (1.7) also expresses the continuity equation.

In a static situation, the velocity v is zero, the derivative $(\partial M_r / \partial t)_r = 0$ and we are left with the first of the two equations (1.9). Expression (1.7) and the continuity equation become,

$$\frac{dM_r}{dr} = 4\pi r^2 \varrho. \tag{1.12}$$

There is no partial derivative: in a static case, there is only one variable r.

1.1.4 Lagrangian and Eulerian Variables

In stellar evolution, the coordinate r is not always convenient as an independent variable. Except for particular cases of heavy mass loss, the stellar mass remains almost constant, while the stellar radius may rapidly change. It is thus more appropriate (and simpler) to choose the mass M_r or the mass fraction (M_r/M) as an independent variable. This choice is usually done in model computations. The transition between variables (r,t) and (M_r,t) is made with the help of the first of equations (1.9):

$$\left(\frac{\partial}{\partial M_r}\right)_t = \left(\frac{\partial r}{\partial M_r}\right)_t \frac{\partial}{\partial r} = \frac{1}{4\pi r^2 \varrho}\frac{\partial}{\partial r}. \tag{1.13}$$

We may express the equation of motion (1.4) in the hydrodynamical case as

$$\frac{\ddot{r}}{4\pi r^2} = -\frac{\partial P}{\partial M_r} - \frac{GM_r}{4\pi r^4}. \tag{1.14}$$

Equations (1.6) and (1.12) for hydrostatic equilibrium are

$$\frac{dP}{dM_r} = -\frac{GM_r}{4\pi r^4} \quad \text{and} \quad \frac{dr}{dM_r} = \frac{1}{4\pi r^2 \varrho}, \tag{1.15}$$

the time t being absent in these equations.

The equations written as a function of (M_r, t) in the hydrodynamic case, or of M_r in the hydrostatic case, are in Lagrangian variables. In this case, one follows the mass elements during evolution. The equations written as a function of (r, t) or of (r) are in Eulerian variables. One has the following relation between the time derivatives of a function f in the Lagrangian and Eulerian cases,

$$\frac{df}{dt} = \frac{\partial f}{\partial r}\left(\frac{\partial r}{\partial t}\right)_{M_r} + \left(\frac{\partial f}{\partial t}\right)_r \tag{1.16}$$

or more generally

$$\frac{df}{dt} = \boldsymbol{u} \cdot \boldsymbol{\nabla} f + \left(\frac{\partial f}{\partial t}\right)_r . \tag{1.17}$$

On the left side, one follows a given mass element in time, the first term on the right expresses the change due to the motion of the matter with a velocity $\boldsymbol{u}$. The second term on the right expresses the time derivative at a given location in space. The following expressions for the derivative attached to a given mass element are generally equivalent

$$\frac{d}{dt} \equiv \left(\frac{\partial}{\partial t}\right)_{M_r} \equiv \frac{D}{Dt} . \tag{1.18}$$

These are sometimes called the hydrodynamical derivatives.

1.1.5   Estimates of Pressure, Temperature and Timescales

1.1.5.1   Internal Pressure

The equation of hydrostatic equilibrium (1.6) leads to an estimate of the order of magnitude of the internal pressure P in terms of the stellar mass M and radius R. By taking rough average values of the quantities in (1.5), $|dP/dr| \sim P_c/R$ with P_c the central pressure, $M_r \sim M/2$, $r \sim R/2$, we get the following orders of magnitude:

$$\frac{P_c}{R} \sim 2\frac{GM}{R^2}\bar{\varrho} . \tag{1.19}$$

The average density $\bar{\varrho} = 3M/(4\pi R^3)$ leads to

$$P_c \sim \frac{3}{2\pi}\frac{GM^2}{R^4} . \tag{1.20}$$

This provides a rough order of magnitude of the central pressure, it can also be used as an estimate of the average pressure $\bar{P}$. For the Sun, we get a value of $P \sim 5.4 \times 10^{15}$ g s^{-2} cm^{-1}. However, the most useful result from (1.20) is the behavior of the pressure with stellar mass M and radius R.

1.1.5.2   Limits on Central Pressure

Some limits on the central pressure can also be obtained [111, 423]. Integration of the first equation of (1.15) gives

$$P_c - P = \frac{G}{4\pi} \int_0^r \frac{M_r \, dM_r}{r^4} \, , \tag{1.21}$$

where P_c is the central pressure. Using $\overline{\varrho}(r) = 3M_r/(4\pi r^3)$, one has $r^4 = [3M_r/(4\pi\overline{\varrho}(r))]^{\frac{4}{3}}$ and

$$P_c - P = \frac{G}{4\pi} \left(\frac{4}{3}\pi\right)^{\frac{4}{3}} \int_0^r \overline{\varrho}^{\frac{4}{3}}(r) M_r^{-\frac{1}{3}} \, dM_r \, . \tag{1.22}$$

As the average density $\overline{\varrho}(r)$ inside a given radius r does not increase outward, one has a lower bound for central pressure

$$P_c \geq \frac{G}{4\pi} \left(\frac{4}{3}\pi\right)^{\frac{4}{3}} \overline{\varrho}^{\frac{4}{3}}(r) \int_0^{M(R)} M_r^{-\frac{1}{3}} dM_r = \frac{1}{2} \left(\frac{4}{3}\pi\right)^{\frac{1}{3}} G\overline{\varrho}^{\frac{4}{3}} M^{\frac{2}{3}} \, , \tag{1.23}$$

where $\overline{\varrho}$ and M apply to the whole star. One assumes that the total pressure at the stellar surface is negligible. On the other side, $\overline{\varrho}(r)$ is always inferior to the central density ϱ_c, thus one also has

$$P_c \leq \frac{1}{2} \left(\frac{4}{3}\pi\right)^{\frac{1}{3}} G\varrho_c^{\frac{4}{3}} M^{\frac{2}{3}} \, . \tag{1.24}$$

Thus, one obtains an upper and a lower bound for the central pressure in a star. These bounds result from hydrostatic equilibrium and from the assumption that ϱ decreases outward. We use these limits in Sect. 3.6.1.

1.1.5.3   Interior Temperature

One can also make a simple estimate of the internal temperature T of a chemically homogeneous sphere obeying the law of perfect gases (7.31),

$$P_g = \frac{\mathcal{R}}{\mu} \varrho T = \frac{k}{\mu m_u} \varrho T \, , \tag{1.25}$$

where P_g is the perfect gas pressure, $\mathcal{R}$ the gas constant, k the Boltzmann constant, μ the mean molecular weight, m_u is the atomic mass unit, i.e., $(1/12)$ of the mass of the neutral ^{12}C atom, $m_u = 1.6605 \times 10^{-24}$ g (cf. Appendix A.1). If the pressure $\overline{P} \sim P_c$ (1.20), taking the average density $\overline{\varrho} \sim M/R^3$, we get an order of magnitude for the average internal temperature,

$$\overline{T} \sim \frac{\mu\, m_{\mathrm{u}}}{k} \frac{GM}{R}\,. \tag{1.26}$$

The interest of this expression is that it shows the functional dependence of $\overline{T}$ versus mass M and radius R. A better estimate is given below (cf. 1.51).

1.1.5.4   Dynamical Timescales

The dynamical timescale τ_{dyn} characterizes the departures from mechanical equilibrium. Let us suppose that the internal pressure gradient in a gravitationally bound configuration becomes negligible (a situation which occurs in cloud collapse or in the core collapse leading to supernova explosion). Then, (1.4) or (1.14) leads to the following scaling for a spherical object of mass M and radius R:

$$\frac{R}{\tau_{\mathrm{dyn}}^2} \sim \frac{GM}{R^2}\,, \tag{1.27}$$

$$\text{giving}\quad \tau_{\mathrm{dyn}} \sim \left(\frac{R^3}{GM}\right)^{\frac{1}{2}} \sim (G\overline{\varrho})^{-\frac{1}{2}}\,. \tag{1.28}$$

If the internal pressure is negligible, the star collapses under its own gravity and the dynamical timescale τ_{dyn} is essentially the free-fall timescale. The integration of (1.4) for the case of free fall is given in Sect. 18.2.4. For the Sun, $\tau_{\mathrm{dyn}} = 1.8 \times 10^3$ s, i.e., half an hour. For a red giant with $\overline{\varrho} \approx 10^{-6}$ g cm^{-3}, $\tau_{\mathrm{dyn}} \approx 40$ days. For a white dwarf with $\overline{\varrho} \approx 10^6$ g cm^{-3}, $\tau_{\mathrm{dyn}} \sim$ a few seconds. For any gravitational configuration, we may estimate the dynamical timescale. For the Universe as a whole, this time is of the order of the Hubble time, i.e., 10^{10} yr. The example of the Sun, where τ_{dyn} is very short with respect to the evolutionary timescale, shows that any departure from mechanical equilibrium leads to an immediate reaction. This implies that the mechanical equilibrium is always very quickly and closely adjusted, due to the fast mechanical response of the star.

 We have supposed above that the pressure becomes negligible, but we can also estimate τ_{dyn}, if the effect of the internal pressure becomes large with respect to gravity. In this case, the scaling of (1.4) leads to

$$\frac{R}{\tau_{\mathrm{dyn}}^2} \sim \frac{1}{\varrho} \frac{P}{R}\,, \tag{1.29}$$

which gives, with (1.20) and $\overline{\varrho} \sim M/R^3$,

$$\frac{R}{\tau_{\mathrm{dyn}}} \sim \left(\frac{P}{\overline{\varrho}}\right)^{\frac{1}{2}} \sim \left(\frac{GM}{R}\right)^{\frac{1}{2}}\,. \tag{1.30}$$

As above in (1.28), the dynamical timescale $\tau_{\mathrm{dyn}} \sim 1/\sqrt{G\overline{\varrho}}$, which is quite consistent. The sound speed in a gas is $c_{\mathrm{s}} = \sqrt{\Gamma_1 P/\varrho}$ (see 32.26), where Γ_1 is defined

in (7.57). For a perfect gas, $\Gamma_1 \rightarrow \gamma_g = c_P/c_V$, i.e., $5/3$ in a ionized medium. Thus, from (1.30), one has $\tau_{\text{dyn}} \sim R/\bar{c}_s$, which means that the dynamical timescale of a star is of the order of the time necessary for the sound speed to cross the stellar radius. This is not surprising since the sound velocity characterizes the pressure adjustments. For the same reason, the dynamical timescale is of the order of the fundamental period in a pulsating star. In a perfect gas $c_s \sim \sqrt{T}$, thus the outer stellar layers, which have lower T values, mainly determine the dynamical timescale as well as the stellar pulsations periods.

1.2   The Potential Energy

The mechanical equilibrium of a star implies that the gravitational energy, i.e., the potential energy, is of the same order as the thermal energy, which supports the star against gravitation.

Let us consider a non-rotating spherical star in the process of formation by addition of new mass elements. Let M_r be the mass already collected at the interior of radius r (Fig. 1.1). The work dW provided by the gravitational force $\boldsymbol{F}$ when it brings a new mass element δM_r from radius $r + dr$ to r is

$$dW = \boldsymbol{F} \cdot \boldsymbol{dr} = \frac{GM_r\,\delta M_r}{r^2}\,dr\,. \tag{1.31}$$

This is positive since $\boldsymbol{F}$ and $\boldsymbol{dr}$ have the same direction. The work δW to bring δM_r from the infinity to radius r is

$$\delta W = GM_r\,\delta M_r \int_{\infty}^{r} \frac{dr}{r^2} = -\frac{GM_r}{r}\,\delta M_r\,. \tag{1.32}$$

One defines the potential energy for a mass element as $\delta\Omega = \delta W$. The formation of an entire star of mass M represents a potential energy

$$\Omega = -G \int_0^M \frac{M_r\,dM_r}{r}\,. \tag{1.33}$$

This is the energy lost by the reservoir of gravitational energy during the formation of a star. The energy lost by the initial cloud is gained, for example, by the thermal energy of the gas. During the formation of a star, the potential energy becomes more and more negative. The potential energy of an interstellar cloud dispersed over a very extended region is zero, this is the maximum value. As a protostellar cloud contracts and forms a star, the potential energy of the configuration decreases, becoming negative.

Often, one writes the potential energy of a star in the simplified form

$$\Omega = -q\,\frac{GM^2}{R}\,, \tag{1.34}$$

where q is a numerical factor which depends on the internal density distribution of the star. For a star with a constant density, using $dM_r = 4\pi r^2 \varrho\, dr$ and $M_r = (4/3)\pi \varrho r^3$, one immediately obtains $\Omega = -(3/5)\, GM^2/R$, i.e., a factor $q = 3/5$. In Sect. 24.5, we shall see the values of q for some other density distributions. In particular, a factor $q = 3/2$ is more appropriate to the density distribution of Main Sequence (MS) stars.

1.2.1   Relation to the Potential and Poisson Equation

The components of $\boldsymbol{g}$ are $(-g, 0, 0)$. The gravity $\boldsymbol{g}$ is derived from the gravitational potential Φ by the relation

$$\boldsymbol{g} = -\boldsymbol{\nabla}\Phi \quad \text{with} \quad g = \frac{\partial \Phi}{\partial r}, \tag{1.35}$$

according to the definition (1.3) of $\boldsymbol{g}$. For spherical symmetry, one has

$$g = \frac{\partial \Phi}{\partial r} = \frac{GM_r}{r^2} \tag{1.36}$$

and the equation of hydrostatic equilibrium can be written as

$$\boldsymbol{\nabla}P = \varrho\, \boldsymbol{g} = -\varrho\, \boldsymbol{\nabla}\Phi. \tag{1.37}$$

Sometimes the potential is defined with a different sign. There is a relation between the potential energy Ω and the gravitational potential Φ. This relation is not immediately useful here, but it is needed in Sect. 24.5. In spherical symmetry, one has

$$\Phi(r) = \int_0^r \frac{GM_r}{r^2}\, dr + \text{const.}, \tag{1.38}$$

where the constant is chosen so that $\Phi(\infty) = 0$. One can write the potential energy Ω as follows

$$-\Omega = \frac{1}{2}\, G \int_0^M \frac{1}{r}\, dM_r^2 = \frac{1}{2}\frac{GM^2}{R} + \frac{1}{2} G \int_0^{R(M)} \frac{M_r^2\, dr}{r^2}. \tag{1.39}$$

With $d\Phi/dr = GM_r/r^2$, one gets

$$-\Omega = \frac{1}{2}\frac{GM^2}{R} + \frac{1}{2}\int_0^{\Phi(M)} M_r d\Phi$$

$$= \frac{1}{2}\frac{GM^2}{R} + \frac{1}{2}M\Phi(M) - \frac{1}{2}\int_0^M \Phi\, dM_r. \tag{1.40}$$

The sum of the first two terms is zero since $\Phi(M) = -GM/R$ for a sphere according to Newton's theorem. One has

$$\Omega = \frac{1}{2} \int_0^M \Phi \, dM_r \, . \qquad (1.41)$$

The potential energy of a spherical star is the half of the average potential weighted by the mass.

From the equation of hydrostatic equilibrium (1.6), one may write M_r as $M_r = -[r^2/(G\varrho)] \, (dP/dr)$. By inserting this expression into (1.12), we get

$$\frac{1}{r^2} \frac{d}{dr} \left(\frac{r^2}{\varrho} \frac{dP}{dr} \right) = -4 \pi G \varrho \, . \qquad (1.42)$$

We may express (dP/dr) with (1.37) and get

$$\frac{1}{r^2} \frac{d}{dr} \left(r^2 \frac{d\Phi}{dr} \right) = 4 \pi G \varrho \, . \qquad (1.43)$$

We recognize the radial component of the Poisson equation

$$\Delta \Phi = 4 \pi G \varrho \, . \qquad (1.44)$$

It is indeed quite consistent that our equations for stellar equilibrium imply the Poisson equation, which is the fundamental relation between the material content of space and the potential exerted by the matter.

1.2.2   The Potential Energy as a Function of Pressure

A useful expression of the potential energy Ω as a function of the internal pressure P can be derived for a star in hydrostatic equilibrium. From (1.33), one may also write

$$\Omega = -\frac{G}{2} \int_0^M \frac{dM_r^2}{r} \, . \qquad (1.45)$$

The equation of hydrostatic equilibrium (1.6) multiplied on the right side by $dM_r/(4\pi r^2 \varrho dr) = 1$ yields

$$\frac{dP}{dr} = -\frac{G}{8 \pi r^4} \frac{dM_r^2}{dr} \, , \qquad (1.46)$$

from which we may express dM_r^2 in (1.45) and get

$$\Omega = 4 \pi \int_0^{P(R)} r^3 \, dP = \left[4\pi r^3 P \right]_0^R - 12 \pi \int_0^R P r^2 dr \, . \qquad (1.47)$$

If $P(R)$ is the pressure at the surface of the configuration, we get

$$\Omega = 4\pi R^3 P(R) - 3 \int_0^R P \, dV .$$ (1.48)

In some cases, for example for a stellar core, one cannot take $P(R)$ equal to zero, since the pressure of the surrounding layers is not negligible. However, in most cases, for example for a star as a whole, one may consider that the pressure $P(R)$ at the surface is negligible and thus ignore the first term on the right-hand side of (1.48) and get

$$\Omega = -3 \int_0^R P \, dV .$$ (1.49)

This is an expression frequently used for the potential energy of a configuration in hydrostatic equilibrium.

1.2.3 The Internal Stellar Temperature

Let us estimate the potential energy of a star of perfect gas obeying the equation of state $P = [k/(\mu m_u)]\varrho T$ (1.25). From (1.49), one has

$$\Omega = -3\frac{k}{\mu m_u} \int_0^R \varrho T \, dV = -3\frac{k}{\mu m_u} \int_0^M T \, dM_r \equiv -3\frac{k}{\mu m_u} \overline{T} M ,$$ (1.50)

where $\overline{T}$, as defined above, is the internal temperature averaged over the stellar mass. With (1.34), one gets

$$\overline{T} = \frac{1}{3}\frac{\mu m_u}{k} q \frac{GM}{R} .$$ (1.51)

One finds the same functional dependence as above (1.26). For $q = 3/2$, we would get in the case of the Sun an average temperature $\overline{T} \approx 7 \times 10^6$ K, which is a satisfactory order of magnitude (see Fig. 25.8).

1.3 The Virial Theorem for Stars

The Virial theorem expresses a basic relation between the potential energy and the internal energy in a star at equilibrium. Evidently, these two energies must be of the same order in a star at equilibrium, but one can be more precise. The Virial theorem has wide applications and many important results of astrophysics for stars, clusters, galaxies, etc., can be derived to the first order from this theorem [137]. We start from a basic result of statistical mechanics (Appendix C.3), which states that the ratio of pressure P to the density of the kinetic energy u in a gaseous medium is limited by

$$\frac{1}{3} \leq \frac{P}{u} \leq \frac{2}{3} . \tag{1.52}$$

The upper limit applies to a non-relativistic medium. For a perfect gas we have $u = (3/2) [k/(\mu m_{\mathrm{u}})] \varrho T$ and the pressure is given by (7.31). The potential energy of any non-relativistic medium becomes with (1.49)

$$\Omega = -2 \int_0^R u \, dV = -2 E_{\mathrm{cin}} , \tag{1.53}$$

where E_{cin} is the total kinetic energy of particle translation in the configuration. The Virial theorem is thus

$$2 E_{\mathrm{cin}} + \Omega = 0 . \tag{1.54}$$

For a star in equilibrium, twice the kinetic energy of the particles is equal to the absolute value of the potential energy. The Virial theorem expresses the balance between the effects of gravitation and those of pressure which support the star against gravitation. The hypothesis of equilibrium enters with the use of (1.46) in the expression of the potential energy. The other possible internal motions (in addition to translation) are not accounted for, as well as the other energy sources, such as atomic excitation and ionization.

The lower limit in (1.52) applies to relativistic particles. For example, for the photons one has $u = a T^4$ and the radiation pressure is $P = (1/3) a T^4$. For relativistic particles with $P = (1/3) u$, we get with (1.49)

$$E_{\mathrm{cin}} + \Omega = 0 . \tag{1.55}$$

This is the Virial theorem for a star made of relativistic particles. There is no factor 2 as in (1.54). For a mono-atomic gas, the total energy of the star is $E = E_{\mathrm{cin}} + \Omega$, which is zero. This means that a star made of relativistic particles is unstable, since a negligible energy can spread it out.

1.3.1   Star with Perfect Gas Law

Let us first consider the Virial equilibrium for a star of perfect gas. The kinetic energy of an average particle is $(1/2) \mu m_{\mathrm{u}} \overline{v^2} = (3/2) k \overline{T}$, where $\overline{T}$ is the average temperature. For the ensemble N of particles in the star, the total kinetic energy is

$$E_{\mathrm{cin}} = \frac{3}{2} N k \overline{T} . \tag{1.56}$$

E_{cin} can be related to the internal energy, which for one particle is $U = c_{\mathrm{V}} \mu m_{\mathrm{u}} \overline{T}$. There, c_{V} is the specific heat at constant volume by unit of mass. For the N particles in a star, the internal energy is

$$U = c_V N \mu m_u \overline{T}. \tag{1.57}$$

The internal energy U contains all forms of internal energy: thermal energy, radiation, atomic excitation, ionization, electron degeneracy, etc. Eliminating $\overline{T}$ between (1.56) and (1.57), one gets $U = c_V \mu m_u 2 E_c / (3k)$. For a perfect gas, one has $c_P - c_V = k/(\mu m_u)$, where c_P is the specific heat at constant pressure per unit of mass. Thus, (1.57) becomes

$$U = \frac{2}{3} \frac{c_V}{c_P - c_V} E_{cin} = \frac{2}{3} \frac{1}{\gamma_g - 1} E_{cin}, \tag{1.58}$$

where γ_g is the ratio of the specific heats $\gamma_g = c_P/c_V$ for a perfect gas. Thus, one has $2E_c = 3(\gamma_g - 1)U$. One verifies that for a mono-atomic perfect gas with $\gamma_g = 5/3$ the internal energy U is equal to the kinetic energy E_c. The Virial theorem for a star of perfect gas becomes

$$3(\gamma_g - 1)U + \Omega = 0. \tag{1.59}$$

It expresses the equilibrium between the internal energy which supports the star and gravitation. The total energy $E = U + \Omega$ can be written as

$$E = -\frac{\Omega}{(3\gamma_g - 3)} + \Omega = \frac{(3\gamma_g - 4)}{(3\gamma_g - 3)} \Omega. \tag{1.60}$$

If $E > 0$, the star is unstable since it can do some work to spread its matter out in space. A negative E expresses the physical cohesion of a star. A necessary condition for stellar stability is $E < 0$. Since $\Omega < 0$, one must have

$$\gamma_g > \frac{4}{3} \quad \text{for stability}. \tag{1.61}$$

This shows that the thermodynamic properties of a medium are critical for stability. In the case of a perfect mono-atomic gas with $\gamma_g = 5/3$, this condition is satisfied. If it is not, the characteristic time of the departure from equilibrium is the dynamical timescale (1.28).

A value $\gamma_g < 4/3$ would imply, for example during a contraction, that the resulting increase of the gravity force is larger than the increase of the pressure gradient. Thus, contraction would go on unimpeded. This is clear from the meaning of γ_g, which is given by $\gamma_g = (\partial \ln P / \partial \ln \varrho)_{ad}$ (see Sect. 7.4.1). A simple scaling of gravity effects (Sect. 1.1.5) shows that $\overline{P} \sim M^2/R^4$ and $\overline{\varrho} \sim M/R^3$, so that at constant M, the changes of $\overline{P}$ and $\overline{\varrho}$ are related by $\Delta \overline{P} \sim (4/3)\Delta \overline{\varrho}$ for an equilibrium configuration. If $\gamma_g < 4/3$, the thermal pressure increase in a density change is not sufficient to maintain equilibrium, which leads to collapse. We also note that if $\gamma_g < 1$, stability is also formally present. However, starting from $\gamma \sim 3/5$, the limit $\gamma = 4/3$ is crossed first.

We may wonder about the effects of rotation on the Virial theorem. Models of rotating stars on the Main Sequence show that the energy of rotation is negligible with respect to the potential energy. At the critical velocity, the energy of rotation is a few percents of the potential energy.

1.3.2   Star with a General Equation of State

For a medium, which is not a perfect gas, what happens to the Virial theorem expressed in the form (1.59)? As stated above, a departure from the mechanical equilibrium is characterized by the dynamical timescale (1.28) which is very short and usually much smaller than the thermal timescale (1.73). This means that the perturbations of the mechanical equilibrium can be considered as adiabatic. The total change ΔE of energy due the perturbation is the sum of the changes of the internal and potential energies,

$$\Delta E = \Delta U + \Delta \Omega \tag{1.62}$$

with the total internal energy $U = \int_0^M u \, dM_r$, where u is the internal energy per mass unit. The First Principle of thermodynamics implies that

$$\Delta q = \Delta u - \frac{P}{\varrho^2} \Delta \varrho = 0 \,, \tag{1.63}$$

for an adiabatic change. Δq is the energy provided to the system by mass unit and $-(P/\varrho^2)\Delta\varrho$ is the work provided by the system to the exterior. One can define a generalized adiabatic exponent (see Sect. 7.4)

$$\Gamma_1 \equiv \left(\frac{\partial \ln P}{\partial \ln \varrho} \right)_{\text{ad}}, \quad \text{i.e.,} \quad \frac{\Delta P}{P} - \Gamma_1 \frac{\Delta \varrho}{\varrho} = 0 \,. \tag{1.64}$$

Let us express $\Delta\Omega$ from (1.49)

$$\Delta\Omega = -3\Delta \int_0^M \frac{P}{\varrho} \, dM_r = -3 \int_0^M \left(\frac{\Delta P}{\varrho} - \frac{P}{\varrho^2} \Delta\varrho \right) dM_r \,. \tag{1.65}$$

With (1.63) and (1.64), one has

$$\frac{\Delta P}{P} = \Gamma_1 \frac{\Delta \varrho}{\varrho} = \Gamma_1 \varrho \frac{\Delta u}{P}, \quad \text{i.e.,} \quad \frac{\Delta P}{\varrho} = \Gamma_1 \Delta u \,. \tag{1.66}$$

The change of potential energy $\Delta\Omega$ becomes with (1.66) and (1.63)

$$\Delta\Omega = -3 \int_0^M \left(\Gamma_1 \Delta u - \Delta u \right) dM_r = -3 \left(\overline{\Gamma_1} \Delta U - \Delta U \right) \,, \tag{1.67}$$

where $\overline{\Gamma_1}$ is an average value over the stellar mass with a weighting according to the density of internal energy. The generalized form of the Virial theorem is $\Delta\Omega + 3\Delta U(\overline{\Gamma_1} - 1) = 0$. After integration over the change Δ assuming the integration constant is zero and that $\overline{\Gamma_1}$ does not vary, one can write

$$\Omega + 3U(\overline{\Gamma_1} - 1) = 0. \tag{1.68}$$

This applies to a star in equilibrium for a general equation of state. The thermodynamic coefficient $\overline{\Gamma_1}$ is an average weighted by the density of internal energy. The hypothesis of equilibrium has been used in writing the expression $\Delta\Omega$ in (1.65). The above expression of the Virial theorem is similar to (1.59) with $\overline{\Gamma_1}$ instead of γ_g. As in (1.60), we can write the total energy in terms of $\overline{\Gamma_1}$ instead of γ_g and similarly one gets the condition

$$\overline{\Gamma_1} \geq \frac{4}{3}, \tag{1.69}$$

for stellar stability. In Main Sequence stars, ionization and radiation pressure are two effects reducing Γ_1. In practice, if Γ_1 becomes smaller than $4/3$ over some sufficient part of the star, some instabilities appear, either mildly or violently such as supernova explosion. The nature of the unstable event depends on where in the star and at what stage of the evolution Γ_1 becomes smaller than $4/3$. Many unstable or explosive events in stellar evolution occur because of Γ_1: stellar pulsations, pair instability supernovae, core collapse, neutron star formation, black-hole formation, etc. Thus, Γ_1 appears as a most fundamental physical parameter in stars.

1.3.3   Slow Contraction, the Kelvin–Helmholtz Timescale

Let us consider the slow contraction of a star. By "slow", we mean that the timescale of the contraction is much longer than the dynamical timescale (1.28). Thus, during contraction the Virial theorem is satisfied. This implies

a change   : $R \longrightarrow (R - \Delta R)$,
a decrease of the potential energy Ω : $\Delta\Omega < 0$,
an increase of the internal energy U : $U \to (U + \Delta U)$, with $\Delta U > 0$.

The Virial theorem relates the changes ΔU and $\Delta\Omega$. We may consider either the general case with Γ_1 or the case of a perfect gas with γ_g, which is appropriate for star formation. Let us write the theorem like

$$\Delta U = \frac{1}{3(\gamma_g - 1)}(-\Delta\Omega). \tag{1.70}$$

The radiated energy ΔE_{rad} is the difference between the energy produced by gravitation and what is converted into internal energy

$$\Delta E_{\text{rad}} = (-\Delta\Omega) - \Delta U = \frac{3\gamma_g - 4}{3\gamma_g - 3}(-\Delta\Omega). \quad (1.71)$$

We see that for a mono-atomic gas with $\gamma_g = 5/3$, the half of the energy liberated by the decrease of the potential energy is used to increase the internal energy, while the other half is radiated. For an average luminosity $\overline{L}$, we have with (1.34)

$$\Delta E_{\text{rad}} = \overline{L}t = \frac{3\gamma_g - 4}{3\gamma_g - 3}q\frac{GM^2}{R}. \quad (1.72)$$

From this expression, one can define a timescale t_{KH}, called the Kelvin–Helmholtz timescale, which for $\gamma_g = 5/3$ is

$$t_{\text{KH}} = \frac{q}{2}\frac{GM^2}{R\overline{L}} \sim \frac{GM^2}{R\overline{L}}. \quad (1.73)$$

For the present Sun, $q \approx 3/2$ (Sect. 24.5.1). In literature, the definition of t_{KH} is given with a variety of numerical coefficients $\frac{q}{2}$, $1/2$, $3/4$ or 1. Let us take a factor unity. According to its definition, t_{KH} is the timescale during which a star of mass M and radius R can produce an average luminosity $\overline{L}$ at the expense of the gravitational energy. For the present solar values, $t_{\text{KH}} = 3.1 \times 10^7$ yr. This timescale characterizes the pre-Main Sequence phase of stellar evolution and also the contraction phases which separate the phases of nuclear burning, in particular between the H- and He-burning phases. Below in Sect. 3.2.4, we shall see that the Kelvin–Helmholtz timescale is also the thermal timescale of a star, which characterizes the thermal adjustments of the star. This meaning is not immediately evident from the above definition.

One sees from the above simple developments that many major stellar properties arise from the mechanical equilibrium and its two main equations for hydrostatic equilibrium and continuity.

Chapter 2
The Mechanical Equilibrium of Rotating Stars

"Epur si muove" said Galileo Galilei when claiming that the Earth is rotating. Due to rotation, the equatorial radius of the Earth is about 21.4 km longer than its polar radius, so that the Mississippi from its source to the Gulf of Mexico is "raising" away from the Earth center. Of course, in terms of the equipotentials it is "descending" to the sea.

The same can also be said about the stars, where the effects of rotation are on the average much larger than on the Earth. In stars, the equatorial radius can be much bigger than the polar radius, up to about 1.5 times the polar radius. This shows the importance of the possible rotational effects. In addition, while the Earth rotates like a solid body, stars may have an internal differential rotation, with for example a core rotating faster than the outer envelope. Moreover, stellar rotation not only produces a flattening of the equilibrium configuration, but it drives internal circulation motions and various instabilities which transport both the chemical elements and the angular momentum.

2.1 Equilibrium Configurations

2.1.1 From Maclaurin Spheroids to the Roche Models

The stability of rotating configurations has been studied since long (see review in [315]), for example with Maclaurin spheroids, where the density ϱ is supposed constant or with the Roche model, which assumes an infinite central condensation. The complex reality lies between these two extreme cases.

In the case of the Maclaurin spheroids, the equilibrium configurations flatten for high rotation. For extremely high angular momentum, it tends toward an infinitely thin circular disk. The maximum value of the angular velocity Ω (supposed to be constant in the body) is $\Omega_{\max}^2 = 0.4494\,\pi\,G\,\varrho$. In reality, some instabilities would occur before this limit is reached.

In the case of the Roche model with constant Ω (this is not a necessary assumption), the equilibrium figure also flattens to reach a ratio of 2/3 between the polar

and the equatorial radii, with a maximum angular velocity $\Omega^2_{\max} = 0.7215\,\pi\,G\bar{\varrho}$, where $\bar{\varrho}$ is the mean density (see Sect. 4.4.2). Interestingly enough, for all stellar masses the rotational energy of the Roche model amounts to at most about 1% of the absolute value of the potential energy of the models considered with their real density distributions. Except for the academic case of stars with constant density or nearly constant density, the Roche approximation better corresponds to the stellar reality. Recent results from long-baseline interferometry [94, 465] support the application of the Roche model in the cases of Altair and Achernar, which both rotate very fast close to their break-up velocities (see Sect. 4.2.3). These new possibilities of observations open interesting perspectives.

Here, we consider models of real stars, with no a priori given density distributions and obeying a general equation of state. The properties of rotating stars depend on the distribution $\Omega(r)$ in the stellar interiors. The first models were applied to solid body rotation, i.e., $\Omega = $ const. throughout the stellar interior. More elaborate models consider differential rotation, in particular the case of the so-called shellular rotation [632], i.e., with a rotation law $\Omega(r)$ constant on isobaric shells and depending on the first order of the distance to the stellar center (see Sect. 2.2). The reason for such a rotation law rests on the strong horizontal turbulence in differentially rotating stars, which imposes a constancy of Ω on isobars [632]. In the vertical direction, the turbulence is weak due to the stable density stratification.

Interestingly enough, recent models with rotation and magnetic fields give rotation laws $\Omega(r)$ rather close to solid body rotation (Sect. 13.6), nevertheless with some significant deviations from constant Ω. Thus, whether or not magnetic fields play a role, it is necessary to account for rotation laws which are not constant in stellar interiors during evolution.

2.1.2 Hydrostatic Equilibrium for Solid Body Rotation

We first consider the angular velocity $\Omega = $ as constant throughout the star. Let us assume hydrostatic equilibrium and ignore viscous terms. The Navier–Stokes equation (1.2) becomes with account of the centrifugal acceleration

$$\frac{1}{\varrho}\boldsymbol{\nabla}P = -\boldsymbol{\nabla}\Phi + \frac{1}{2}\Omega^2\boldsymbol{\nabla}(r\sin\vartheta)^2\,, \qquad (2.1)$$

according to (B.24) and following remarks. $\varpi = r\sin\vartheta$ is the distance to the rotation axis (Fig. 2.1). The above expression of the centrifugal force gives a projection $\Omega^2\varpi\sin\vartheta$ along vector $\boldsymbol{r}$ and a projection $\Omega^2\varpi\cos\vartheta$ along vector $\boldsymbol{\vartheta}$. The quantity Φ is the gravitational potential, which is unmodified by rotation in the Roche approximation,

$$\boldsymbol{g} = -\boldsymbol{\nabla}\Phi = -\frac{GM_r}{r^2}\frac{\boldsymbol{r}}{r}\,. \qquad (2.2)$$
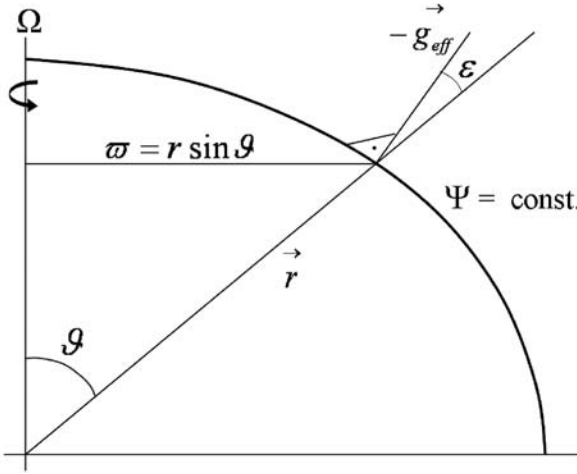
Fig. 2.1 Some geometrical parameters in a rotating star. The angle ε is the angle between the vector radius and the normal $-\boldsymbol{g}_{\text{eff}}$ to an equipotential

The components of $\boldsymbol{g}$ are $(-g, 0, 0)$ and $g = \frac{\partial \Phi}{\partial r}$ (cf. 1.35). If Ω is constant or has a cylindrical symmetry, the centrifugal acceleration can also be derived from a potential, say V. One has

$$- \nabla V = \Omega^2 \,\boldsymbol{\varpi} \quad \text{and thus} \quad V = -\frac{1}{2}\Omega^2 \varpi^2 \,. \tag{2.3}$$

The total potential Ψ is

$$\Psi = \Phi + V \,, \tag{2.4}$$

and with (1.44) one has

$$\nabla^2 \Psi = \nabla^2 \Phi + \nabla^2 V \quad \text{with} \quad \nabla^2 \Phi = 4\pi G \varrho \,. \tag{2.5}$$

In cylindrical coordinates, one can write

$$(\nabla^2 V)_\varpi = \frac{1}{\varpi} \frac{\partial}{\partial \varpi}\left(-\varpi^2 \Omega^2\right) = -2\,\Omega^2 \tag{2.6}$$

and thus the Poisson equation with rotation becomes

$$\nabla^2 \Psi = 4\pi G \varrho - 2\,\Omega^2 \,. \tag{2.7}$$

Barotropic star: the equation of hydrostatic equilibrium becomes

$$\frac{1}{\varrho}\nabla P = -\nabla \Psi = \boldsymbol{g}_{\text{eff}}. \tag{2.8}$$

The effective gravity $\boldsymbol{g}_{\text{eff}}$ results from both gravitation and centrifugal acceleration. Care must be given on how Φ and Ψ are defined, since one often finds expressions with a different sign. The above expression implies that the pressure is constant on an equipotential, i.e., one has $P = P(\Psi)$. Thus, the equipotentials and isobars coincide in this case and the star is said to be *barotropic*, otherwise it is said to be *baroclinic* (Sect. 2.2). With $\nabla P = (dP/d\Psi)\nabla\Psi$, (2.8) becomes $(1/\varrho)\,dP/d\Psi = -1$. Thus, the density is also a function $\varrho = \varrho(\Psi)$ of Ψ only. Through the equation of state $P = P(\varrho, T)$, one also has $T = T(\Psi)$. The quantities ϱ, P, T are constant on the equipotentials $\Psi = \text{const}$. The same conclusions are valid for Ω constant on cylindrical surfaces around the rotation axis.

2.1.3 Stellar Surface and Gravity

The stellar surface is an equipotential $\Psi = \text{const.}$, otherwise there would be "mountains" on the star and matter flowing from higher to lower levels. The total potential at a level r and at colatitude ϑ ($\vartheta = 0$ at the pole) in a star of constant angular velocity Ω can be written as

$$\Psi(r, \vartheta) = -\frac{GM_r}{r} - \frac{1}{2}\Omega^2 r^2 \sin^2\vartheta. \tag{2.9}$$

One assumes in the Roche model that the gravitational potential $\Phi = -GM_r/r$ of the mass M_r inside radius r is not distorted by rotation. The inner layers are considered as spherical, which gives the same external potential as if the whole mass is concentrated at the center.

Let us consider a star of total mass M and call $R(\vartheta)$ the stellar radius at colatitude ϑ. Since the centrifugal force is zero at the pole, the potential at the stellar pole is just GM/R_{p}, where R_{p} is the polar radius. This fixes the constant value of the equipotential at the stellar surface, which is given by

$$\frac{GM}{R} + \frac{1}{2}\Omega^2 R^2 \sin^2\vartheta = \frac{GM}{R_{\text{p}}}. \tag{2.10}$$

A more tractable form is given below (2.18). The shape of a Roche model is illustrated in Fig. 2.2 for different rotation velocities (the radii for non-rotating stars of different masses and metallicities Z are given in Fig. 25.7). Figure 2.3 illustrates the variation of the ratio of the equatorial radius to the polar radius for the Roche model as a function of the parameter $\omega = \Omega/\Omega_{\text{crit}}$. We see that up to $\omega = 0.7$, the increase of the equatorial radius is inferior to 10%. The increase of the equatorial radius essentially occurs in the high rotation domain.

The effective gravity resulting from the gravitational potential and from the centrifugal force is given by (2.8). If $\boldsymbol{e}_r$ and $\boldsymbol{e}_\vartheta$ are the unity vectors in the radial and latitudinal directions, the effective gravity vector at the stellar surface is
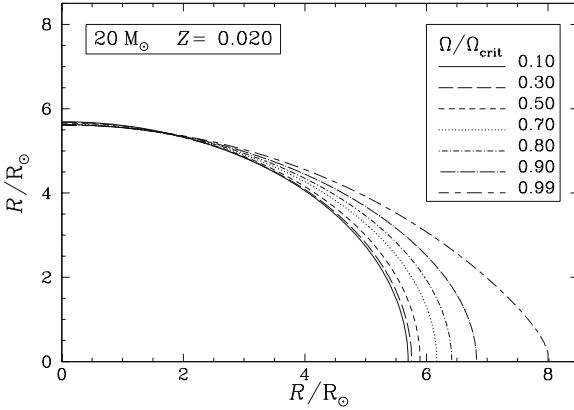
Fig. 2.2 The shape $R(\vartheta)$ of a rotating star in one quadrant. A $20\,M_\odot$ star with $Z = 0.02$ on the ZAMS is considered with various ratios $\omega = \Omega/\Omega_{\mathrm{crit}}$ of the angular velocity to the critical value at the surface. One barely notices the small decrease of the polar radii for higher rotation velocities (cf. Fig. 2.7). Courtesy of S. Ekström
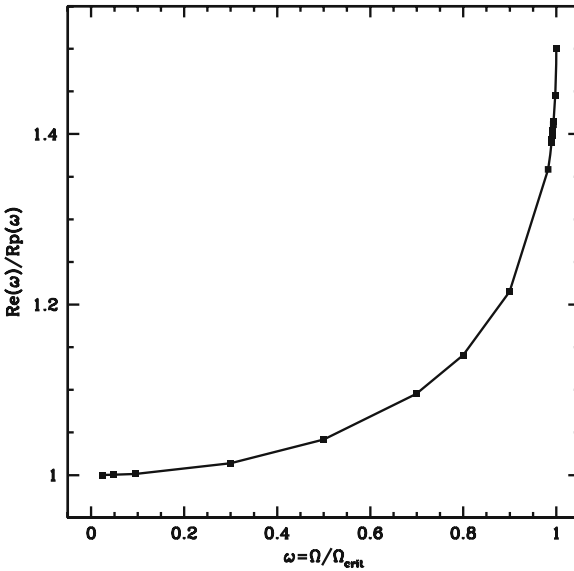
Fig. 2.3 The variation of the ratio $R_{\mathrm{e}}/R_{\mathrm{p}}$ of the equatorial to the polar radius as a function of the rotation parameter ω in the Roche model

$$\boldsymbol{g}_{\mathrm{eff}} = \left[-\frac{GM}{R^2(\vartheta)} + \Omega^2 R(\vartheta) \sin^2\vartheta \right] \boldsymbol{e}_r + \left[\Omega^2 R(\vartheta) \sin\vartheta \cos\vartheta \right] \boldsymbol{e}_\vartheta \ . \qquad (2.11)$$

The gravity vector is not parallel to the vector radius as shown in Fig. 2.1. The modulus $g_{\mathrm{eff}} = |\boldsymbol{g}_{\mathrm{eff}}|$ of the effective gravity is

$$g_{\text{eff}} = \left[\left(-\frac{GM}{R^2(\vartheta)} + \Omega^2 R(\vartheta) \sin^2 \vartheta \right)^2 + \Omega^4 R^2(\vartheta) \sin^2 \vartheta \cos^2 \vartheta \right]^{\frac{1}{2}} , \quad (2.12)$$

which can also be written as in (2.20).

2.1.4 Critical Velocities

The critical velocity, also called break-up velocity, is reached when the modulus of the centrifugal force becomes equal to the modulus of the gravitational attraction at the equator. The maximum angular velocity Ω_{crit}, which makes $g_{\text{eff}} = 0$ at the equator ($\vartheta = \pi/2$) is thus from (2.12)

$$\Omega_{\text{crit}}^2 = \frac{GM}{R_{\text{e,crit}}^3} , \quad (2.13)$$

where $R_{\text{e,crit}}$ is the equatorial radius at break-up. If one introduces this value of Ω_{crit} in the equation of the surface (2.10) at break-up, one gets for the ratio of the equatorial to the polar radius at critical velocity,

$$\frac{R_{\text{e,crit}}}{R_{\text{p,crit}}} = \frac{3}{2} . \quad (2.14)$$

At break-up, the equatorial radius is equal to 1.5 times the polar radius. The equatorial break-up velocity is thus

$$v_{\text{crit,1}}^2 = \Omega_{\text{crit}}^2 R_{\text{e,crit}}^2 = \frac{GM}{R_{\text{e,crit}}} = \frac{2 GM}{3 R_{\text{p,crit}}} . \quad (2.15)$$

This expression is the one quite generally used; however, formally it applies to solid body rotation. The index "1" indicates the classical critical velocity, to distinguish it from a second value $v_{\text{crit,2}}$ which applies to high mass stars with a high Eddington factor (see Sect. 4.4.2). If we now introduce a non-dimensional rotation parameter ω, defined as the ratio of the angular velocity to the angular velocity at break-up,

$$\omega = \frac{\Omega}{\Omega_{\text{crit}}} \quad \text{which gives} \quad \omega^2 = \frac{\Omega^2 R_{\text{e,crit}}^3}{GM} . \quad (2.16)$$

One can also write

$$\Omega^2 = \frac{8}{27} \frac{GM \omega^2}{R_{\text{p crit}}^3} , \quad (2.17)$$

and the equation of the surface (2.10) becomes with $x = R/R_{\text{p,crit}}$

$$\frac{1}{x} + \frac{4}{27} \omega^2 x^2 \sin^2 \vartheta = \frac{R_{\text{p,crit}}}{R_{\text{p}}(\omega)} . \quad (2.18)$$

If the polar radius does not change with ω (but see Fig. 2.7), the second member is equal to 1. Equation (2.18) is an algebraic equation of the third degree. Our experience suggests it is better solved by the Newton method rather than by the Cardan solutions of a third degree polynomial, because the Cardan solutions may diverge at the poles. Also depending on the value of $R_{\mathrm{p,crit}}/R_{\mathrm{p}}(\omega)$, for ω close to 1 the discriminant of the polynomial equation may change its sign implying another form for the solution. The comparison with the interferometric observations of stellar oblateness and gravity darkening is given in Sect. 4.2.3.

Figure 2.4 shows the critical velocities $v_{\mathrm{crit,1}}$ for stars of various masses and metallicities. The critical velocities grow with stellar masses, because the stellar radii increase only slowly with stellar masses. The critical velocities are very large for low metallicity stars, since their radii are much smaller as a result of their lower opacities. Comparison between observed and theoretical values of velocities is given in Table 4.1. The distribution of rotational velocities for about 500 B-type stars is shown in Fig. 27.1.

Figure 2.5 shows the ratio $v/v_{\mathrm{crit,1}}$ of the equatorial velocity to the critical equatorial velocity as a function of the parameter $\omega = \Omega/\Omega_{\mathrm{crit}}$ in the Roche model. For low rotation ($\omega < 0.5$), a linear approximation of v in terms of ω is valid

$$v^2 \;=\; \frac{8}{27}\frac{GM\omega^2}{R_{\mathrm{p,crit}}^3}R_{\mathrm{e}}^2 \approx \frac{8}{27}\frac{GM\omega^2}{R_{\mathrm{p,crit}}} \;=\; \frac{4}{9}\omega^2\, v_{\mathrm{crit,1}}^2 \;, \tag{2.19}$$

as illustrated in Fig. 2.5. The relation of $(v/v_{\mathrm{crit,1}})$ vs. ω would be independent of stellar mass M and metallicity Z if the polar radius would not vary with rotation. As R_{p} is a function of ω which slightly depends on M and Z (cf. Fig. 2.7), this also introduces some slight dependence on mass and metallicity, not accounted for in the relation illustrated by Fig. 2.5.
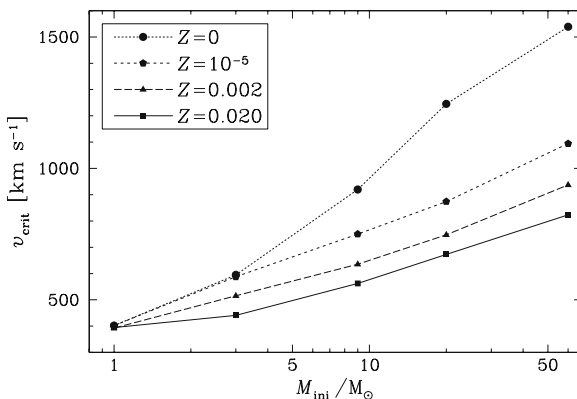
Fig. 2.4 The critical velocities $v_{\mathrm{crit,1}}$ as a function of stellar masses for different metallicities Z for stars on the ZAMS. The effect of the changes of the polar radius with rotation is accounted for. From S. Ekström et al. [176]
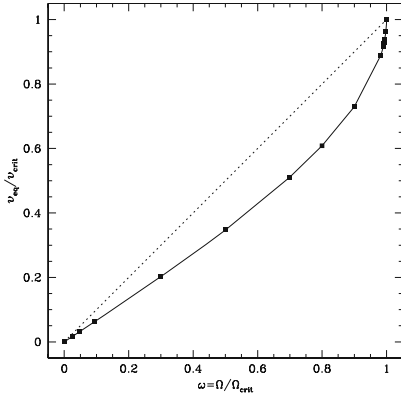
Fig. 2.5 The variation of the ratio $v/v_{\text{crit},1}$ of the equatorial velocity to the critical velocity as a function of the rotation parameter ω in the Roche model. The polar radius is assumed not to change with the stellar mass here. The *dotted line* connects the origin to the maximum value

The variations of the equatorial velocities v as a function of ω are illustrated for stars of different masses in Fig. 2.6. As the stellar radii change with M and Z, the relations of the velocities v with respect to ω are evidently different for the different masses and metallicities (in addition account is also given to the small effect of the change of the polar radius for the different M and Z, as mentioned above). The critical velocities for the most massive stars, where radiation pressure effects are large, are discussed in Sect. 4.4.

In terms of the parameters x and ω, the surface gravity at a colatitude ϑ on a rotating star can be expressed as

$$g_{\text{eff}} = \frac{GM}{R^2_{\text{p,crit}}} \left[\left(-\frac{1}{x^2} + \frac{8}{27}\,\omega^2 x \sin^2 \vartheta \right)^2 + \left(\frac{8}{27}\,\omega^2 x \sin \vartheta \cos \vartheta \right)^2 \right]^{\frac{1}{2}}, \qquad (2.20)$$

where $GM/R^2_{\text{p,crit}}$ is the gravity at the pole at break-up. This is the maximum value and the term in square bracket is always smaller than 1.0.

Angle between g_{eff} and r: On the surface of a rotating star, the normal to the surface does not coincide with the direction of the vector radius (it coincides only at the pole and equator). There is an angle ε, generally small, between the directions of r and of $-g_{\text{eff}}$ (see Fig. 2.1)

$$\cos \varepsilon = -\frac{g_{\text{eff}} \cdot r}{|g_{\text{eff}}| \cdot |r|}\,. \qquad (2.21)$$
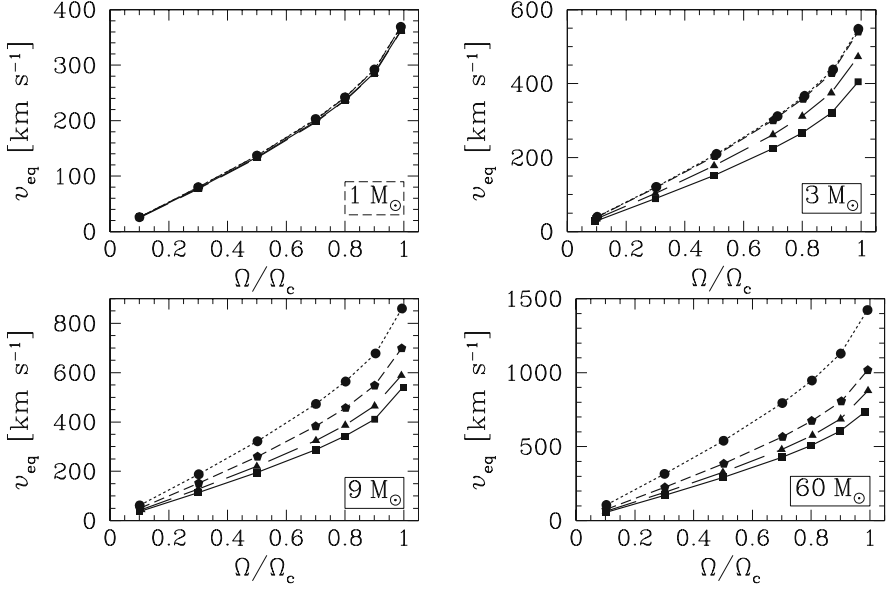
Fig. 2.6 Variations of the surface velocity v at the equator as a function of the rotation parameter $\omega = \Omega/\Omega_{\mathrm{crit}}$ for stars of different masses and metallicities Z with the same coding as in Fig. 2.4. From S. Ekström et al. [176]

By using (2.11), one gets for the angle ε in terms of x and ω,

$$\cos\varepsilon = \frac{\frac{1}{x^2} - \frac{8}{27}\omega^2 x\sin^2\vartheta}{\left[\left(-\frac{1}{x^2} + \frac{8}{27}\omega^2 x\sin^2\vartheta\right)^2 + \left(\frac{8}{27}\omega^2 x\sin\vartheta\cos\vartheta\right)^2\right]^{\frac{1}{2}}} . \tag{2.22}$$

The angle ε intervenes in the expression of the surface element $d\sigma$ on an equipotential of a rotating star

$$d\sigma = \frac{r^2\sin\vartheta\,d\varphi d\vartheta}{\cos\varepsilon} , \tag{2.23}$$

where φ is the longitude such that $\Omega = d\varphi/dt$. This means that the element of arc in ϑ along the real surface is slightly longer than the element of spherical arc (Fig. 2.1). The above expression is used in the calculation of the stellar surface and of the emergent flux from a rotating star.

2.1.5 Polar Radius as a Function of Rotation

In first approximation, one may consider that the polar radii are independent of rotation and use values such as given by Fig. 25.7. In reality the polar radii $R_{\mathrm{p}}(\omega)$ have

a slight dependence on ω, which results from the small changes of internal structure brought about by centrifugal force. The rate of change is given by the models of internal structure with rotation. While the equatorial radius strongly inflates, the polar radius decreases by a few percent in general (Fig. 2.7), mostly as a result of a slight decrease of the internal T due to the lower effective gravity. Below $40\,M_\odot$, the decrease of $R_p(\omega)$ at the critical velocity amounts to less than 2% [408]. Near $1\,M_\odot$, the decrease of $R_p(\omega)$ with rotation is larger.

Surprisingly, at $60\,M_\odot$ there is an increase of the polar radius with growing rotation (Fig. 2.7). This results from the fact that the radiation pressure is relatively important. As the temperature in the polar regions is much higher than at the equator as a result of von Zeipel's theorem (Sect. 4.2.2), the relative increase of the radiation pressure in the outer layers is much higher with a consequent inflation of the polar radius.

One may rather well represent the change of the polar radius as a function of ω by a form

$$R_p(\omega) = R_p(0)\left(1 - a\,\omega^2\right), \tag{2.24}$$

where a is a constant for models of a given mass [181]. Figure 2.8 provides information on the changes of polar radii at other Z values. It shows the changes of the polar radius at $\omega = 0.90$ for stars of different masses and metallicities. One again notices the general slight decrease of the polar radius at high rotation for most stellar masses, while the most massive stars in particular at the higher metallicities experience an increase.
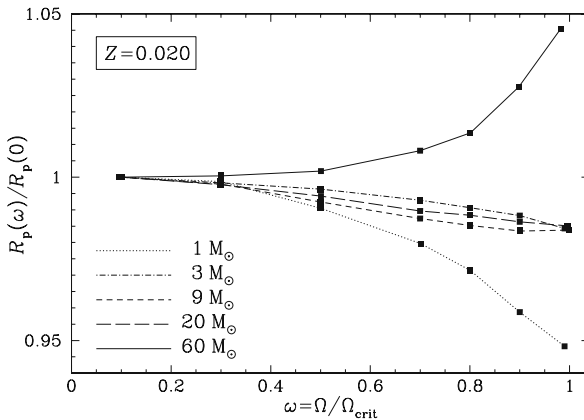
Fig. 2.7 Variations of the polar radius as a function of the rotation parameter ω normalized to the value without rotation for stars of different initial masses at $Z = 0.02$. From S. Ekström et al. [176]
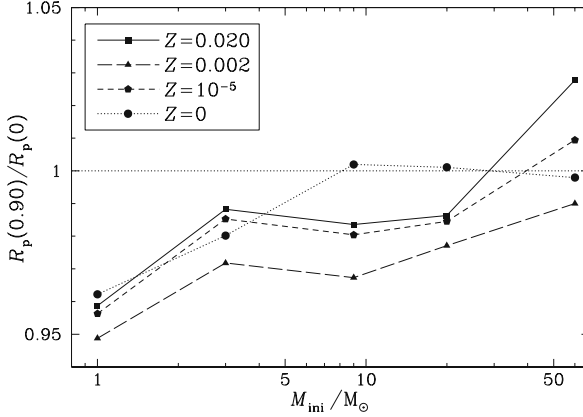
Fig. 2.8 Variations of the ratio of the polar radius at $\omega = 0.90$ to the value at zero rotation as a function of initial masses for different Z. Courtesy from S. Ekström

2.2 Equations of Stellar Structure for Shellular Rotation

Let us consider the interesting case of shellular rotation, where Ω is constant on isobars (i.e., surface of constant pressure), but varies according to the radial coordinate of the isobars. Rotation is shellular because differential rotation in radiative regions produces anisotropic turbulence [632], much stronger in the horizontal direction than in the vertical one due to stable stratification (Sect. 12.1). Since one has the relation $\nabla P = g_{\mathrm{eff}}$, the words "constant in the horizontal direction" mean constant on isobars, i.e., $\Omega = \Omega(P)$. One writes at a given point (r, ϑ) in spherical coordinates the angular velocity Ω

$$\Omega(r, \vartheta) = \overline{\Omega}(r) + \widehat{\Omega}(r, \vartheta) , \tag{2.25}$$

with $\widehat{\Omega} \ll \overline{\Omega}$ (the average $\overline{\Omega}$ on an isobar with radius r is taken according to (10.105) so as to satisfy the equation for the conservation of angular momentum [632]). The quantity $\widehat{\Omega}(r, \vartheta)$ can be developed in terms of the Legendre polynomials. The account of terms higher than the second order allows one to consider higher rotation velocities [386]. To the second order, one writes

$$\widehat{\Omega}(r, \vartheta) = \Omega_2(r) P_2(\cos \vartheta) . \tag{2.26}$$

This writing is sufficient for the approximation developed here. However, for the developments of $\Omega(r, \vartheta)$ used for the transport of angular momentum, one should rather write for consistency $\widehat{\Omega}(r, \vartheta) = \Omega_2(r) [P_2(\cos \vartheta) + (1/5)]$. This is demonstrated in Appendix B.6.1, see also [386]. For the present purpose, we do not need to specify the development of $\widehat{\Omega}(r, \vartheta)$. The different variables P, T, ϱ, etc. can be developed in Legendre polynomials (e.g., Sect. 11.1.1).

Let us emphasize that the isobars are not spherical surfaces. There is an angle ε (see Fig. 2.1) between the radial direction and the direction of gravity or between a spherical shell and an equipotential. As an example, in the Roche model at break-up rotation at a colatitude $\vartheta = 45°$ this angle is $13°$. For lower rotation, it rapidly decreases, behaving like Ω^2. Thus, if one writes the shellular rotation as $\Omega \approx \Omega(r)$, one should not consider the cases of extreme rotation velocities.

2.2.1 Properties of the Isobars

In the case of shellular rotation, the centrifugal force cannot be derived from a potential and thus (2.3) does not apply. Let us consider the surface of constant Ψ (2.9),

$$\Psi = \Phi - \frac{1}{2}\Omega^2 r^2 \sin^2\vartheta = \text{const.} \qquad (2.27)$$

As in Sect. 1.2.1, the gravitational potential is defined by $\partial\Phi/\partial r = GM_r/r^2$ and $\Phi = -GM_r/r$ in the Roche approximation. The components of the gradient of Ψ are in polar coordinates (r, ϑ)

$$\frac{\partial\Psi}{\partial r} = \frac{\partial\Phi}{\partial r} - \Omega^2 r \sin^2\vartheta - r^2\sin^2\vartheta\,\Omega\,\frac{\partial\Omega}{\partial r}, \qquad (2.28)$$

$$\frac{1}{r}\frac{\partial\Psi}{\partial\vartheta} = \frac{1}{r}\frac{\partial\Phi}{\partial\vartheta} - \Omega^2 r \sin\vartheta\cos\vartheta - r^2\sin^2\vartheta\,\Omega\,\frac{1}{r}\frac{\partial\Omega}{\partial\vartheta}, \qquad (2.29)$$

The first two components of the gravity $\boldsymbol{g}_{\text{eff}} = (-g_{\text{eff},r}, g_{\text{eff},\vartheta}, 0)$ are according to (2.11) in the Roche model,

$$g_{\text{eff},r} = \frac{\partial\Phi}{\partial r} - \Omega^2 r \sin^2\vartheta \quad \text{and}$$

$$g_{\text{eff},\vartheta} = \Omega^2 r \sin\vartheta\cos\vartheta \,. \qquad (2.30)$$

Thus, by comparing these terms and the derivatives of Ψ, one can write

$$\boldsymbol{g}_{\text{eff}} = -\boldsymbol{\nabla}\Psi - r^2\sin^2\vartheta\,\Omega\,\boldsymbol{\nabla}\Omega. \qquad (2.31)$$

The equation of hydrostatic equilibrium $\boldsymbol{\nabla}P = \varrho\,\boldsymbol{g}_{\text{eff}}$ is thus

$$\boldsymbol{\nabla}P = -\varrho\left(\boldsymbol{\nabla}\Psi + r^2\sin^2\vartheta\,\Omega\,\boldsymbol{\nabla}\Omega\right). \qquad (2.32)$$

Since Ω is constant on isobars, the vector $\boldsymbol{\nabla}\Omega$ is parallel to $\boldsymbol{\nabla}P$. The hydrostatic equation (2.32) implies the parallelism of $\boldsymbol{\nabla}P$ and $\boldsymbol{\nabla}\Psi$. Thus, in this non-conservative case the surfaces defined by $\Psi = \text{const.}$ (2.27) are isobaric surfaces [408], but they are not equipotential and the star is said to be *baroclinic*. In the case of solid body rotation, isobars and equipotentials coincide and the star is *barotropic*.

In literature, Ψ and Φ are often defined with different signs, care has to be given because this may lead to different expressions.

Thus, for shellular rotation one may choose to write the equations of the stellar structure on the isobars and use, with little changes, a method devised for the conservative case [283], with the advantage to keep the equations for stellar structure one-dimensional. The main change concerns the expression of the average density between isobars, as given below (cf. 2.47). Some further properties of baroclinic stars are studied in Sect. 10.5.3.

2.2.2   Hydrostatic Equilibrium

It is useful to write the equations of hydrostatic equilibrium and mass conservation in a form similar to that of the non-rotating case [283] in order to minimize the modifications necessary for calculating rotating stars with shellular rotation. One associates a radius r_P to an isobar, it is defined by

$$V_P \equiv \frac{4\pi}{3} r_P^3 , \tag{2.33}$$

where V_P is the volume inside the isobar. For any quantity q, which is not constant over an isobaric surface, a mean value is defined by

$$<q> \equiv \frac{1}{S_P} \oint_{\Psi=\mathrm{const}} q \, d\sigma , \tag{2.34}$$

where S_P is the total surface of the isobar and $d\sigma$ is an element of this surface defined by (2.23).

The effective gravity can no longer be defined as a gradient $\mathbf{g}_{\mathrm{eff}} = -\nabla\Psi$, since Ψ is not a potential. One uses the fact that $\nabla\Omega$ is parallel to $\nabla\Psi$,

$$\nabla\Omega = -\alpha\,\nabla\Psi \quad \mathrm{with} \quad \alpha = \left|\frac{d\Omega}{d\Psi}\right| . \tag{2.35}$$

Let us call dn the average distance between two neighboring isobaric surfaces, $(dn \cong dr_P)$. From (2.31), we get for the modulus of $\mathbf{g}_{\mathrm{eff}} = (-g_{\mathrm{eff},r},\, g_{\mathrm{eff},\vartheta},\, 0)$,

$$g_{\mathrm{eff}} = \left(1 - r^2 \sin^2\vartheta\,\Omega\,\alpha\right)\frac{d\Psi}{dn} . \tag{2.36}$$

The equation of hydrostatic equilibrium (2.32) becomes similarly

$$\frac{dP}{dn} = -\varrho\left(1 - r^2 \sin^2\vartheta\,\Omega\,\alpha\right)\frac{d\Psi}{dn} , \tag{2.37}$$

which shows the constancy of $\varrho\left(1 - r^2 \sin^2\vartheta\,\Omega\,\alpha\right)$ on isobars.

We want to use the mass M_P inside an isobar as the independent variable,

$$dM_P = \int_{\Psi=\text{const}} \varrho \, dn \, d\sigma = d\Psi \int_{\Psi=\text{const}} \varrho \, \frac{dn}{d\Psi} \, d\sigma$$

$$= d\Psi \int_{\Psi=\text{const}} \varrho \, \frac{\left(1 - r^2 \sin^2 \vartheta \, \Omega \, \alpha\right)}{g_{\text{eff}}} \, d\sigma \, . \tag{2.38}$$

The last equality is obtained by using (2.36). Since $\varrho \left(1 - r^2 \sin^2 \vartheta \, \Omega \, \alpha\right)$ is constant on isobars, we can easily integrate this equation by using also the definition (2.34)

$$\frac{d\Psi}{dM_P} = \frac{1}{\varrho \left(1 - r^2 \sin^2 \vartheta \, \Omega \, \alpha\right) < g_{\text{eff}}^{-1} > S_P} \, . \tag{2.39}$$

With (2.37), this becomes simply

$$\frac{dP}{dM_P} = \frac{-1}{< g_{\text{eff}}^{-1} > S_P} \, . \tag{2.40}$$

We define a quantity

$$f_P = \frac{4 \pi r_P^4}{G M_P S_P} \frac{1}{< g_{\text{eff}}^{-1} >} \, , \tag{2.41}$$

which is equal to 1.0 for a non-rotating star. With this definition the equation of hydrostatic equilibrium in Lagrangian coordinates finally becomes [408]

$$\frac{dP}{dM_P} = -\frac{G M_P}{4 \pi r_P^4} f_P \, . \tag{2.42}$$

Apart from the factor f_P, this equation keeps the same form as in the non-rotating case (cf. 1.15).

2.2.3 Continuity Equation

Similarly, we want an equation equivalent to (1.15) for shellular rotation. According to (2.33), the volume of a shell between two isobars is

$$dV_P = 4 \pi r_P^2 \, dr_P \, , \tag{2.43}$$

which can also be written as

$$dV_P = \int_{\Psi=\text{const}} dn \, d\sigma = d\Psi \int_{\Psi=\text{const}} \frac{dn}{d\Psi} \, d\sigma$$

$$= d\Psi \int_{\Psi=\text{const}} \frac{\left(1 - r^2 \sin^2 \vartheta \, \Omega \, \alpha\right)}{g_{\text{eff}}} \, d\sigma \, , \tag{2.44}$$

where we have used (2.36). By applying (2.34), we get

$$dV_P = d\Psi S_P \left[<g_{\text{eff}}^{-1}> - <g_{\text{eff}}^{-1} r^2 \sin^2 \vartheta> \Omega\, \alpha \right] . \tag{2.45}$$

This expression together with (2.43) and (2.39) leads to

$$\frac{dr_P}{dM_P} = \frac{1}{4\pi r_P^2 \bar\varrho} , \tag{2.46}$$

$$\text{with} \quad \bar\varrho = \frac{\varrho\left(1 - r^2 \sin^2 \vartheta\, \Omega\alpha\right) <g_{\text{eff}}^{-1}>}{<g_{\text{eff}}^{-1}> - <g_{\text{eff}}^{-1} r^2 \sin^2 \vartheta> \Omega\alpha} . \tag{2.47}$$

The quantity $\bar\varrho$ is not equal to $<\varrho>$. From the definition (2.34), $<\varrho>$ is the average density on an isobar, while from (2.46) we see that formally $\bar\varrho$ is the average density in the element volume between two isobars. When the mass steps are very small the difference between $<\varrho>$ and $\bar\varrho$ becomes negligible; however, it is preferable to strictly respect the above definitions.

The two Eqs. (2.42) and (2.46) are the basic equations for the hydrostatic equilibrium of stars with shellular rotation [408], replacing the corresponding Eq. (1.15) of the case without rotation.

2.2.4   Equation of the Surface for Shellular Rotation

In the case of shellular rotation, the isobars are defined by expression (2.27), which is identical to the expression of the equipotentials for solid body rotation. We may search the equation of the equipotential, in particular for the stellar surface. An equipotential is defined by the condition that a displacement ds on it neither requires nor produces energy,

$$g_{\text{eff}} \cdot ds = 0 . \tag{2.48}$$

The effective gravity is given by (2.31) and the above product becomes

$$\frac{\partial \Psi}{\partial r} dr + \frac{1}{r}\frac{\partial \Psi}{\partial \vartheta} r\, d\vartheta + r^2 \sin^2 \vartheta\, \Omega \frac{\partial \Omega}{\partial r} dr + r^2 \sin^2 \vartheta \frac{\Omega}{r}\frac{\partial \Omega}{\partial \vartheta} r\, d\vartheta = 0 . \tag{2.49}$$

For shellular rotation, this equation simplifies to

$$d\Psi + r^2 \sin^2 \vartheta\, \Omega \frac{d\Omega}{dr} dr = 0 . \tag{2.50}$$

This is a more general form of the equation of equipotentials (cf. 2.9). If $\Omega = \text{const.}$ it simplifies to $\Psi = \text{const.}$ and gives (2.10) again. Expression (2.50) can be integrated to give the equation of the stellar surface,

$$-\frac{GM}{R(\vartheta)} - \frac{1}{2}\Omega^2 R^2(\vartheta) \sin^2 \vartheta + \sin^2 \vartheta \int_{R_p}^{R(\vartheta)} r^2(\vartheta)\, \Omega \frac{d\Omega}{dr} dr = \frac{GM}{R_p} . \tag{2.51}$$

This equation gives the shape $R(\vartheta)$ of the star as a function of $\Omega(r)$ in the external regions. If $d\Omega/dr < 0$ in the external layers, the above expression indicates that the real oblateness of the star is slightly larger than the one which would be obtained by using the Ω value effectively observed at the equator. In general, in the outer stellar layers the gradient $d\Omega/dr$ is nearly flat, thus the difference with respect to the usual Roche surface should be small. We have assumed that the gravitational potential of the inner layers is still the potential of a spherical object, which is satisfactory for evolution in the H-burning phase, but maybe not in advanced stages where central rotation may become very high. Interferometric observations are reported in Sect. 4.2.3.

The above developments allow us to construct equilibrium models of rotating stars in one dimension, which is most useful in view of the calculation of grids of evolutionary models of rotating stars. Ignoring the effects of rotation on the structure equations leads to incomplete models. We emphasize that in general the main effects of rotation on the evolution are those due to the internal mixing of the chemical elements, to the transport of angular momentum and to the enhancement of the mass loss in massive stars. These effects are studied in further chapters.

Chapter 3
The Energetic Equilibrium of Stars*

If God on his (or her?) big computer would decide to switch off the nuclear reactions in the Sun, what would happen? The answer is "nothing" at first. Differences in the solar luminosity would only occur after millions of years. The reason is that the timescale for the thermal adjustment of a star is long (this timescale is called the Kelvin–Helmholtz timescale).

Let us consider a neutrino emitted in the solar center. As its cross section is very small, it does not interact with the solar matter and escapes from the solar surface about 2 s later. For a photon, the situation is completely different, because its cross section is large. As soon as it is emitted, it is absorbed by an atom, then it is re-emitted in a random direction, re-absorbed, re-emitted in another direction, etc. The mean free path between two successive interactions is very small, i.e., from about 0.01 cm in the center to 1 cm in the envelope. Thus, the photons even traveling at the velocity of light have a very long way to make before these random motions finally bring them to the stellar surface, a few 10 million years later.

The energetic equilibrium, i.e., the balance between the energy production and its transport out of the star, is another essential piece of the general stellar equilibrium. The energy production "needs" to adjust its rate to match the radiative losses at the surface. Let us suppose it would not do it. There would be more and more energy accumulating at the center and the star would inflate. This inflation would decrease the inner pressure and temperature and as a consequence slow down the nuclear reactor. Thus, a star like the Sun is a beautiful self-controlled nuclear reactor where the energy production rates adjust themselves to just supply the energy which is going out.

3.1 The Radiative Transfer

Radiative transfer, i.e., the transport of energy by photons, is the most important process of energy transport in stars. Convection also contributes to the transport of

---

*This chapter may form the matter of a basic introductory course.

energy and matter in stars; however, in general convection is present over limited regions, while radiative transfer is present everywhere. Conduction by electrons is important only in degenerate media. Some basic definitions and properties of radiation are given in Appendix C.1.

3.1.1 Equation of Radiative Transfer

Let us consider a radiation beam at frequency v in a given direction s in stellar medium as illustrated in Fig. C.1. The energy dU_v transmitted by an element of the medium in a direction perpendicular to the surface element $d\sigma$ centered on a solid angle $d\Omega$, during the time dt and in the frequency interval dv is

$$dU_v \equiv I_v \, d\sigma \, dv \, d\Omega \, dt \, . \tag{3.1}$$

Here, the surface element is perpendicular to the direction of the radiation beam, so that $\cos \vartheta = 1$ in Eq. (C.1). The above expression defines the specific intensity I_v in erg s^{-1} cm^{-2} steradian^{-1} Hz^{-1}. The energies emitted dU_v^{em} and absorbed dU_v^{abs} are

$$dU_v^{\text{em}} \equiv j_v \varrho \, d\sigma \, ds \, dv \, d\Omega \, dt \quad \text{and} \quad dU_v^{\text{abs}} \equiv \kappa_v I_v \varrho \, d\sigma \, ds \, dv \, d\Omega \, dt \, . \tag{3.2}$$

These define the emission coefficient j_v (erg s^{-1} g^{-1} steradian^{-1} Hz^{-1}) and the absorption or opacity coefficient κ_v (cm^2 g^{-1}). In a medium with emission and/or absorption over the length ds, there is a change of specific intensity dI_v and a corresponding change of the energy transmitted

$$dU_v^{\text{trans}} = dI_v \, d\sigma \, dv \, d\Omega \, dt \, . \tag{3.3}$$

The change of energy is equal to the difference between the energy emitted and the energy absorbed: $dU_v^{\text{trans}} = dU_v^{\text{em}} - dU_v^{\text{abs}}$. With (3.3), this leads to the equation of radiative transfer in the direction of the element of length ds,

$$\frac{dI_v}{ds} = j_v \varrho - \kappa_v \varrho I_v \, . \tag{3.4}$$

In a medium without emission, one has $dI_v = -\kappa_v I_v \varrho \, ds$. If $I_v(0)$ is the intensity in s_0, one has at a point s for constant density and absorption coefficient

$$I_v(s) = I_v(0) \, e^{-\kappa_v \varrho (s - s_0)} \, . \tag{3.5}$$

There is an exponential decrease of the intensity in the medium. A corresponding expression applies to the total intensity $I(s)$, if the opacity coefficient is independent of the frequencies. The "mean free path" of the photons is the length ℓ over which

Fig. 3.1 A pencil of light in spherical geometry. The angle $d\vartheta$ is negative since the angle $\vartheta + d\vartheta$ is smaller than ϑ
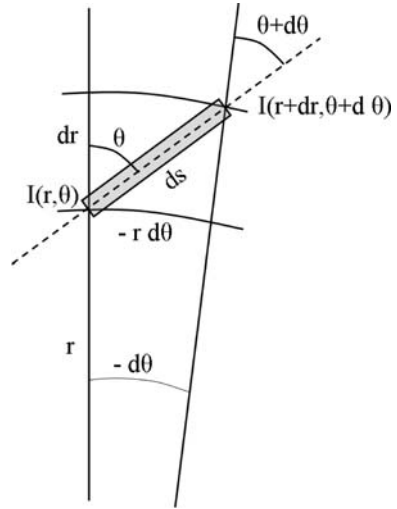
the intensity of the radiation decreases by a factor of e. It is (this may also be defined at a frequency ν)

$$\ell = \frac{1}{\kappa \varrho} . \tag{3.6}$$

For a spherical star, we may write the equation of transfer (3.4) as a function of (r, ϑ), the radial distance to the center and the co-latitude. As shown in Fig. 3.1, the projection of an element of length ds attached to a point (r, ϑ) on the radius is $dr = \cos \vartheta \, ds$, while the projection of ds onto the direction perpendicular to the radius is $-r \, d\vartheta = \sin \vartheta \, ds$. There is a negative sign, because the angle $\vartheta + d\vartheta$ is smaller than ϑ (Fig. 3.1), thus $d\vartheta$ is negative. The total derivative with respect to ds is

$$\frac{d}{ds} = \frac{\partial}{\partial r}\frac{dr}{ds} + \frac{\partial}{\partial \vartheta}\frac{d\vartheta}{ds} = \frac{\partial}{\partial r}\cos \vartheta - \frac{\sin \vartheta}{r}\frac{\partial}{\partial \vartheta} , \tag{3.7}$$

and the transfer equation (3.4) becomes

$$\frac{\partial I_\nu}{\partial r}\cos \vartheta - \frac{\sin \vartheta}{r}\frac{\partial I_\nu}{\partial \vartheta} = \varrho(j_\nu - \kappa_\nu I_\nu) . \tag{3.8}$$

This is the general form of the transfer equation in spherical geometry, it is applicable in the interior as well as in the atmospheres, even when thick.

3.1.2 Radiation Properties in Stellar Interiors

In stellar interiors, the radiation field is assumed to be that of a blackbody (C.13) characterized by the local value of temperature T. This situation is called local

thermodynamic equilibrium (LTE). The term "local" is important, because the full thermodynamic equilibrium would imply the same T throughout the whole star and thus no emergent radiation. The assumption of LTE rests on the following two properties:

1. The average T gradient in stars is very small. For example, for the Sun, it is

$$\left|\frac{dT}{dr}\right| \approx \frac{T_c}{R_\odot} \approx \frac{1.6 \times 10^7}{7 \times 10^{10}} \frac{K}{cm} \sim 2 \times 10^{-4} \; K\,cm^{-1}, \tag{3.9}$$

where T_c is the central temperature.

2. In stellar interiors, for an average value of the opacity coefficient $\kappa \sim 1\text{--}10^2$ $cm^2\,g^{-1}$ and a mean density of the order of $1\,g\,cm^{-3}$, we get a mean free path $\ell = 1/(\kappa \varrho) \sim 0.01\text{--}1$ cm (in the outer layers this may be larger since the density is very low). This implies that the relative change of T over a mean free path is about

$$\frac{\Delta T}{T} = \frac{\ell \left|\frac{dT}{dr}\right|}{T} \le \frac{10^{-4}}{10^7} \sim 10^{-11}. \tag{3.10}$$

Since over a mean free path ℓ, the relative variation of T is very small, the radiation field can be described by the Planck law $B_\nu(T)$ for the local temperature T. This justifies the LTE assumption. It also implies

$$I_\nu = B_\nu(T) \quad \text{and} \quad j_\nu = \kappa_\nu B_\nu(T). \tag{3.11}$$

This last expression (Kirchhoff's law) is obtained from (3.4) assuming local equilibrium $dI_\nu/ds \to 0$. The density u of radiation energy and the radiation pressure P_{rad} are thus in stellar interiors

$$u = aT^4 \quad \text{and} \quad P_{rad} = \frac{1}{3} aT^4. \tag{3.12}$$

In LTE, the isotropy is not complete, otherwise there would be no energy flux going out. The temperature T changes with the distance r to the stellar center, but locally the radiation properties can be described by Planck's law with the appropriate $T(r)$. In the stellar atmospheres, i.e., the region where the emergent spectrum is formed (a few 10^2 km in the Sun), the LTE assumption does not apply.

3.1.3 Transfer Equation

In the stellar interiors where LTE applies, the transfer equation (3.8) can be expressed in terms of u, F and P_{rad}, where F is the radiative flux at level r (C.5). For the moment, we ignore the index ν, meaning that the results may apply both to monochromatic and integrated quantities (but see Sect. 3.1.4). If one multiplies (3.8) by $\cos \vartheta$ and integrates over $d\Omega$ as given in Appendix C.1, one has

$$\int_{\Omega} \frac{\partial I}{\partial r} \cos^2 \vartheta \, d\Omega - \int_{\Omega} \frac{\partial I}{r \partial \vartheta} \cos \vartheta \sin \vartheta \, d\Omega =$$
$$\int_{\Omega} \varrho \, j \cos \vartheta \, d\Omega - \int_{\Omega} \varrho \, \kappa I \cos \vartheta \, d\Omega \,. \tag{3.13}$$

The first term on the left is equal to $c \, \partial P_{\text{rad}} / \partial r$ according to the definition (C.11). In the regions of a star where the LTE hypothesis is valid, the second term on the left is zero, since the intensity $I = B(T)$ varies only with radius r, therefore in this case $\partial I / \partial \vartheta = 0$. This is not true in distorted stars, but in most cases the horizontal gradient is negligible with respect to the vertical gradient. The integration of this second term leads to $(c/r)(3 P_{\text{rad}} - u)$. The atomic emission mechanisms are isotropic, thus the first term on the right is also equal to zero. The second term on the right is $-\varrho \kappa F$, i.e., the energy transmitted in all directions by units of volume and time. Therefore, in the general case (3.13) yields

$$\frac{\partial P_{\text{rad}}}{\partial r} + \frac{1}{r} (3 P_{\text{rad}} - u) + \frac{\varrho \kappa F}{c} = 0 \,. \tag{3.14}$$

In the quasi-isotropic case (Appendix C.1.1) , i.e., when the anisotropic component I_1 of the intensity is very small with respect to the isotropic one, $P_{\text{rad}} = (1/3) \, u$, thus (3.14) becomes

$$\frac{dP_{\text{rad}}}{dr} + \frac{\varrho \kappa F}{c} = 0 \,. \tag{3.15}$$

This basic equation relates the flux to the derivative of the radiation pressure. It can also be written for a specific frequency ν or a specific wavelength λ. In such cases one has, for example, for an interval of frequency $d\nu$,

$$\frac{dP_{\text{rad}, \nu}}{dr} d\nu + \frac{\varrho \kappa_\nu F_\nu}{c} d\nu = 0 \,, \tag{3.16}$$

or with λ instead of ν. The opacity κ_ν or κ_λ at the considered frequency or wavelength is considered. The flux at frequency ν is related to the total flux by (3.19) below.

We can now apply (3.15) in the case of LTE, with the expressions for the black body with a local T (Appendix C.1.1). As $P_{\text{rad}} = (1/3)aT^4$, one gets $dP_{\text{rad}}/dr = (4/3) \, aT^3 \, (dT/dr)$. In a star of luminosity L_r at level r, the radiative flux at level r is $F = L_r/(4 \pi r^2)$, thus (3.15) becomes

$$F = \frac{L_r}{4 \pi r^2} = -\frac{4 ac T^3}{3 \kappa \varrho} \frac{dT}{dr} \,. \tag{3.17}$$

This expression is fundamental for stellar structure, because radiation is generally the main process for the transport of energy in stars. It allows us to express the radiative equilibrium. The radiative flux has the form $F = -C_{\text{rad}} \, dT/dr$, it is proportional to the thermal gradient, with a coefficient of radiative conductivity $C_{\text{rad}} = 4 ac T^3 /(3 \kappa \varrho)$.

The expression of C_{rad} can also be obtained from the kinetic theory of gases. In this context, a coefficient of conductivity has the form $C_{\text{rad}} = (1/3)\varrho\, C_V\, \ell\, \bar{v}$ (cf. B.59), where $\bar{v}$ is the average velocity of the particles responsible for the transport, ℓ their mean free path, C_V the specific heat (by unit of mass) at constant volume. For transport by photons, $v = c$, $\ell = 1/(\kappa\varrho)$ and

$$\varrho\, C_V = \left(\frac{du}{dT}\right)_V = 4\,a\,T^3 \,. \tag{3.18}$$

With these terms, one also gets the above expression of C_{rad}.

3.1.4 The Rosseland Mean Opacity

Some care must be brought to the definition of the mean opacity κ in (3.17). In particular, it is to be noted that the mean opacity is not simply the integral of the monochromatic opacity, i.e., $\kappa \neq \int_0^\infty \kappa_\lambda\, d\lambda$. An appropriate definition has to be adopted to achieve consistency with the definition of the integrated flux over the frequencies or over the wavelengths,

$$F = \int_0^\infty F_\lambda\, d\lambda = \int_0^\infty F_\nu\, d\nu \,. \tag{3.19}$$

The radiation pressure is $P_{\text{rad}} = 4\pi I_0/(3c)$, with $I_0 = B(T)$ (cf. Appendix C.1). Thus, (3.15) becomes

$$\frac{4\pi}{3c}\frac{dB}{dr} = -\frac{\kappa\varrho F}{c} \quad \text{and} \quad \frac{4\pi}{3c}\frac{dB_\lambda}{dr} = -\frac{\kappa_\lambda\,\varrho\, F_\lambda}{c} \,. \tag{3.20}$$

The second form is obtained if instead of the quantities $B(T)$, F and P_{rad} integrated over the frequencies, one considers the monochromatic quantities expressed as a function of ν or of the wavelength λ. Let us express (3.19) with (3.20),

$$\frac{4\pi}{3}\frac{1}{\kappa}\frac{dB}{dr} = \frac{4\pi}{3}\int_0^\infty \frac{1}{\kappa_\lambda}\frac{dB_\lambda}{dr}\, d\lambda \,. \tag{3.21}$$

Both $B(T)$ and B_λ are functions of r through the temperature distribution $T(r)$ in the star, i.e., $dB/dr = (dB/dT)(dT/dr)$. This implies with (3.21) that the mean opacity κ in (3.17) must be defined as

$$\frac{1}{\kappa} = \frac{1}{dB/dT}\int_0^\infty \frac{1}{\kappa_\lambda}\frac{dB_\lambda}{dT}\, d\lambda \left(\text{or} \ = \frac{1}{dB/dT}\int_0^\infty \frac{1}{\kappa_\nu}\frac{dB_\nu}{dT}\, d\nu \right),$$

$$\text{with} \quad \frac{dB}{dT} = \int_0^\infty \frac{dB_\nu}{dT}\, d\nu = \frac{ac}{\pi}\,T^3 \,. \tag{3.22}$$

The opacity κ given by (3.22) is the "Rosseland mean opacity", which is used in the expression of the radiative flux in stellar interiors. This opacity gives a higher

weight to the higher frequencies. It can be shown that if the monochromatic opacity at wavelength λ behaves like $\kappa_\lambda \sim \lambda^\alpha$, the Rosseland mean opacity behaves like $\kappa \sim T^{-\alpha}$.

3.1.5   The Mass–Luminosity Relation

The mass–luminosity or *M–L* relation between stellar luminosities and masses is the most fundamental stellar property. It was first derived analytically by Eddington [168]. Nowadays, this relation is better established by numerical models, see for example Fig. 25.6 or Table 25.4. However, the expression of the radiative flux enables us to obtain a first estimate of this relation. Let us write (3.15) as follows:

$$\frac{d}{dr}\left(\frac{1}{3}aT^4\right) = -\frac{\kappa\varrho}{c}\frac{L_r}{4\pi r^2} \ .$$

(3.23)

Making the following estimates for a star of radius R and central temperature T_c: $-dT^4/dr \sim T_c^4/R$, $L_r \sim L$ and $r \sim R/2$, one gets

$$L \sim \frac{\pi\,a\,c}{3}R\,\frac{T_c^4}{\kappa\varrho} \ .$$

(3.24)

For the density, we take the average density $\bar{\varrho} = 3M/(4\pi R^3)$ and for the central temperature, we adopt the order of magnitude of the internal temperature (1.26) $\bar{T} \sim (\mu\,m_u/k)\,(GM/R)$, where μ is here the average mean molecular weight. We obtain for the luminosity

$$L \sim ac\left(\frac{Gm_u}{k}\right)^4\frac{\mu^4 M^3}{\kappa} \ ,$$

(3.25)

where we have skipped the numerical factors of the order of unity. This fundamental relation shows several remarkable properties:

– The luminosity grows with the third power of the mass, this is indeed a good average for stars from 1 to $100\,M_\odot$ in the hydrogen-burning phase. As an example, a star of $100\,M_\odot$ has a luminosity of about $10^6\,L_\odot$.
– A star with a higher mean molecular weight μ is overluminous with respect to a star of the same mass with a lower μ. Typical examples of such overluminous stars are Wolf–Rayet stars (Fig. 27.15), which are evolved bare cores left over from initially massive stars.
– In (3.25), there is nothing related to the nuclear energy production and it is a most striking result: *the luminosity L of a star does not depend on its nuclear reactions, but on its opacity*. This means that if the stellar opacity permits the photons to escape from the star, they do it. As a consequence, the star must produce in a

way or another the energy that is going out. This is done by stellar contraction and nuclear reactions. The nuclear reactions feed the stars in energy and allow them to shine for very long times, but the value of the luminosity is determined by the opacity.

We have derived the above result by considering that the transport of energy is done only by radiative transfer. There are other mechanisms of transport (e.g., convection, neutrino emission). However, radiative transfer is always present and during the main phases of evolution (H- and He-burning phases) it largely dominates, so the above relation is meaningful.

3.1.6   Photon Travel Times and *M–L* Relation

Among the various derivations of the *M–L* relation, the following one is conceptually enlightening. If $\ell \sim 1/(\kappa \varrho)$ is the mean free path of the photons, the total diffusion time of photons from the center to the surface is

$$\tau_{\text{tot}} \sim \frac{\ell}{c} N \,, \tag{3.26}$$

where N is the total number of interactions experienced by the photons during their random motions inside a star. Each time they are absorbed by a particle, they are emitted in a random direction, so a great number N of interactions is needed before they can get out of the star. The expression for N can easily be found as follows. The total diffusion time can be expressed as $\tau_{\text{tot}} \sim R^2/D$, where $D = (1/3)\ell c$ is the corresponding diffusion coefficient according to the kinetic theory of gases (Appendix B.4). The time between two consecutive interactions of a photon is $\tau \sim \ell/c$. Thus, we get

$$\tau_{\text{tot}} \sim \frac{3R^2}{\ell c} \sim \frac{3R^2}{\ell^2} \tau \,. \tag{3.27}$$

Thus, $N \equiv \tau_{\text{tot}}/\tau \sim 3 (R/\ell)^2$ and (3.26) becomes

$$\tau_{\text{tot}} \sim \frac{R^2}{c\ell} \sim \frac{R^2 \kappa \varrho}{c} \sim \frac{\kappa M}{cR} \,. \tag{3.28}$$

There we have taken $\varrho \sim M/R^3$. We again see that the opacity is the leading effect which determines the escape of photons and thus the luminosity L. In the Sun, $\kappa = 1\text{--}10^2 \text{ cm}^2 \text{ g}^{-1}$. A proper average of κ (weighted toward the high values of κ) should be made, this gives $\tau_{\text{tot}} \sim (1\text{--}3) \times 10^7$ yr. L is given by the ratio of the thermal energy content divided by the diffusion time τ_{tot},

$$L \sim \frac{a\overline{T}^4 \frac{4}{3}\pi R^3}{\tau_{\text{tot}}} \,. \tag{3.29}$$

With the average temperature given by (1.51), this gives

$$L \sim ac \left(\frac{Gm_\mathrm{u}}{k} \right)^4 \frac{\mu^4 M^3}{\kappa} , \qquad (3.30)$$

which is similar to (3.25), factors of the order of unity being skipped. The photons travel a few 10^7 yr with a velocity c in stochastic motions before reaching the stellar surface. This long time is the result of about 10^{24} interactions, which make the photons to randomly change their direction of propagation after each interaction. This is dramatically different from the case of neutrinos, which on average are out of the Sun about 2 s after their emission in the stellar center.

3.2 Energetic Equilibrium of a Star

3.2.1 Why Are Stars Stable Nuclear Reactors?

Why is the Sun so stable on the long term? Why does it not burn all its available nuclear fuel in a few hours? We shall see that it is essentially due to the law of perfect gases.

Let us suppose that there is an excess δq of energy production at the solar center with respect to what may go out. Since the specific heats are positive the temperature T increases. Now, due to the law of perfect gas $P = P(\varrho, T)$, the pressure P increases, which produces an expansion. The potential energy Ω becomes less negative and due to the Virial theorem, the internal energy U decreases, which means that there is a cooling. This cooling reduces the rate ε of nuclear energy generation (in erg g^{-1} s^{-1}) and thus there is less energy produced. The logical connections are

$$\delta q > 0 \Longrightarrow T \nearrow \ \Longrightarrow P \nearrow \qquad \text{due to } P = P(\varrho, T)$$
$$\Longrightarrow \text{expansion, thus } \Omega \nearrow \Longrightarrow U \searrow \quad \text{due to the Virial theorem}$$
$$\Longrightarrow T \searrow \Longrightarrow \varepsilon \searrow \Longrightarrow \delta q < 0 .$$

If there would be no $P(\varrho, T)$ relation, but just $P = P(\varrho)$ relation as in the case of the degenerate gases (cf. Sect. 7.7), this would work differently,

$$\delta q > 0 \Longrightarrow T \nearrow \Longrightarrow P \text{ unchanged}$$
$$\Longrightarrow \varepsilon \nearrow \Longrightarrow \delta q \gg 0 .$$

δq further increases leading to an explosion. This typically happens in the case of nuclear burning in a degenerate medium, as for example in the He flash

(Sect. 26.4.1). Further analyses of the nuclear stability and instabilities are made
in Sect. 3.5.

3.2.2 Energy Conservation

Energy is another fundamental property. Let us consider a certain volume V of gas
with a surface Σ and a mass M. Let dm be a small element of mass in this volume
and $d\sigma$ a small element of the surface Σ. Let q be the energy provided to the system
by units of mass and time. The energy conservation implies that the gain of energy
in the mass M per unit of time is equal to the energy produced minus the energy
which escapes through the surface Σ per unit of time,

$$\int_0^M \frac{dq}{dt} \, dm = \int_0^M \varepsilon \, dm - \oint_\Sigma \boldsymbol{F} \cdot \boldsymbol{d\sigma} \ . \tag{3.31}$$

ε is the energy produced per unit of time and mass, it is called the energy gener-
ation rate (in W kg^{-1} or in erg g^{-1} s^{-1}). The second term on the right is the flux
of energy through the surface, generally this is the radiative flux; however, some
mechanical energy may also be present in some stars. If ϱ is the average density in
the considered volume element, one has by Gauss theorem

$$\int_0^V \frac{dq}{dt} \varrho \, dV = \int_0^V \varrho \, \varepsilon \, dV - \int_0^V \boldsymbol{\nabla} \cdot \boldsymbol{F} \, dV \ . \tag{3.32}$$

This expression of energy conservation applies to any volume element, thus one has
locally

$$\frac{dq}{dt} = \varepsilon - \frac{1}{\varrho} \boldsymbol{\nabla} \cdot \boldsymbol{F} \ . \tag{3.33}$$

The rate of energy provided to the system dq/dt is given by the first principle of
thermodynamics $dq = dU + P \, dV$, U being the internal energy. The quantities q, U,
V are considered per unit of mass, thus $V = 1/\varrho$ and one has

$$\frac{dq}{dt} = \frac{dU}{dt} - \frac{P}{\varrho^2} \frac{d\varrho}{dt} = \varepsilon - \frac{1}{\varrho} \boldsymbol{\nabla} \cdot \boldsymbol{F} \ . \tag{3.34}$$

dq/dt is the energy provided to the system during a change of structure, typically
by an expansion or a contraction. We call

$$\varepsilon_{\text{grav}} \equiv -\frac{dq}{dt} \ . \tag{3.35}$$

Thus, $\varepsilon_{\text{grav}}$ is the energy produced by the system, since there is a negative sign.
If $\varepsilon_{\text{grav}} > 0$, some energy is provided by the system, typically in the case of stellar

contraction. If $\varepsilon_{grav} < 0$, there is some energy absorbed by the system, e.g., in stellar expansion. Thus, (3.34) becomes

$$\frac{1}{\varrho} \nabla \cdot F = \varepsilon + \varepsilon_{grav} . \tag{3.36}$$

ε is generally the sum of various nuclear processes. The nuclear energy production rate consists of $\varepsilon_{nucl,\gamma}$, the energy produced in the form of γ-rays, and of $\varepsilon_{nucl,\nu}$, the energy produced in the form of neutrinos. The γ-rays participate in the radiative transfer of energy since the medium is opaque for them, while in general the neutrinos escape immediately. Thus, the neutrino energy in general must not be counted in the radiative transfer. The neutrinos in stars are both the neutrinos emitted by nuclear reactions $\varepsilon_{nucl,\nu}$ and by various processes (photo-neutrinos, pair-neutrinos, plasma-neutrinos, etc.), which remove a lot of energy for central temperatures above 6×10^8 K. Thus, one has

$$\varepsilon = \underbrace{\varepsilon_{nucl,\gamma} + \varepsilon_{nucl,\nu}}_{\text{energy production}} - \underbrace{(\varepsilon_{nucl,\nu} + \varepsilon_{pair,photo,plasma,\nu})}_{\text{energy escape}} , \tag{3.37}$$

$$\text{which gives} \quad \varepsilon = \varepsilon_{nucl,\gamma} - \varepsilon_{pair,photo,plasma,\nu} . \tag{3.38}$$

Until the end of the helium-burning phase, the pair, photo, plasma ν can be ignored and thus $\varepsilon = \varepsilon_{nucl,\gamma}$.

For a spherical star, (3.36) takes a simpler form. The flux components in spherical coordinates are $F = \left(\frac{L_r}{4\pi r^2}, 0, 0 \right)$, so that the divergence becomes

$$\frac{1}{\varrho} \nabla \cdot F = \frac{1}{r^2} \frac{1}{\varrho} \frac{\partial}{\partial r} \left(r^2 \frac{L_r}{4\pi r^2} \right) = \frac{1}{4\pi r^2 \varrho} \frac{\partial}{\partial r} L_r = \frac{\partial L_r}{\partial M_r} . \tag{3.39}$$

The equation expressing the energetic equilibrium becomes with (3.36)

$$\frac{\partial L_r}{\partial M_r} = \varepsilon + \varepsilon_{grav} . \tag{3.40}$$

We could just have taken this expression as a definition of the energy production rate per unit of mass and time. Expressions (1.6), (1.12), (3.17) and (3.40) together with an appropriate expression for convective regions (cf. 5.57) form the basic set of equations for stellar structure (Sect. 24.1.1) .

3.2.3 Combined Equation of Conservation and Transfer

One may combine the equations of transfer and of energy production to get a more general equation expressing the energetic equilibrium. The energy dq provided to

the system can be written in terms of the specific entropy s (extensive quantities are per unit of mass) $dq = T\,ds$. The radiative flux is

$$F = -\chi \nabla T, \quad \text{with} \quad \chi = \frac{4\,ac\,T^3}{3\,\kappa\varrho} . \tag{3.41}$$

Thus, we have from (3.34)

$$\varrho\,\frac{dq}{dt} = \varrho T\,\frac{ds}{dt} = \varrho\,\varepsilon + \nabla \cdot (\chi\,\nabla T) . \tag{3.42}$$

With (1.17) we obtain a general form expressing the variation of entropy or the variation of heat content as a function of the nuclear energy production rate and of the radiative flux

$$\varrho T \left(\frac{\partial s}{\partial t} + \boldsymbol{u} \cdot \nabla s \right) = \varrho\,\varepsilon + \nabla \cdot (\chi\,\nabla T) . \tag{3.43}$$

This equation is the basic equation of energy conservation used in hydrodynamic problems, such as convection or meridional circulation.

3.2.4   Relation with the Heat Conduction

It is interesting to establish the connection between Eq. (3.43) and the usual equation of heat conduction in physics. Let us consider a small volume in the envelope of a star, there $\varepsilon = 0$ and (3.42) becomes

$$\varrho\,\frac{dq}{dt} = \nabla (\chi\,\nabla T) . \tag{3.44}$$

Let us suppose that $\chi = \text{const.}$ in the small volume considered. It is in pressure equilibrium and $dq = C_P\,dT$, thus (3.44) becomes

$$\frac{dT}{dt} = \frac{\chi}{\varrho\,C_P}\,\nabla^2 T \equiv K\nabla^2 T , \tag{3.45}$$

where K is the thermal diffusivity. This equation is analogous to the equation of heat conduction, where K plays the role of the coefficient of heat conduction in cm^2 s^{-1},

$$K = \frac{4\,ac\,T^3}{3\,\kappa\varrho^2 C_P}. \tag{3.46}$$

Warning: one notes C_P or C_V the specific heats for a general equation of state and c_P or c_V the values for a perfect gas. According to (3.45), the characteristic time of

thermal adjustment of a volume element of dimension ℓ is of the order

$$t_{\text{therm}} \sim \frac{\ell^2}{K} \, .$$ (3.47)

For the Sun, with $\ell = R_\odot$ one has $t_{\text{therm}} \sim 10^7$ yr and for a $10\,M_\odot$ star, it is of the order of 10^5 yr , see also Appendix B.5.3. Interestingly enough, this timescale for a star of mass M, radius R and luminosity L is of the same order as the Kelvin–Helmholtz timescale t_{KH} defined by (1.73).

$$t_{\text{therm}} \sim \frac{3 R^2 \kappa \varrho^2 C_{\text{P}}}{4 \, a c \, T^3} \sim \frac{R^2 \varrho \, C_{\text{P}}}{F} \left| \frac{dT}{dr} \right| \, ,$$ (3.48)

where we have used the expression of the radiative flux F (3.17). Now, we consider a perfect gas and one has $c_{\text{P}} = 5k/(2\mu m_{\text{u}})$ for a mono-atomic perfect gas. The flux is $F = L/(4\pi R^2)$. We approximate the temperature gradient by $\overline{T}/R$, since the central temperature is of the same order as the average internal temperature and get

$$t_{\text{therm}} \sim \frac{5}{2} R^2 \varrho \, \frac{k}{\mu m_{\text{u}}} \, \frac{4\pi R^2}{L} \, \frac{\overline{T}}{R} \, .$$ (3.49)

Taking for ϱ the average density, for the internal temperature the value given by (1.51) and skipping the numerical factors, one obtains

$$t_{\text{therm}} \sim \frac{G M^2}{R L} \, .$$ (3.50)

Thus the thermal timescale has the same order of magnitude as the Kelvin–Helmholtz timescale (1.73), i.e., $t_{\text{KH}} \sim t_{\text{therm}}$. One can understand this correspondence as follows. t_{KH} is the lifetime during which a star can produce a luminosity L from the gravitational energy Ω. According to the Virial theorem (1.3.2), Ω is of the same order of magnitude as the internal energy U. The ratio U/L gives the time that a star needs to radiate its internal energy, i.e., this is an estimate of the stellar thermal adjustment time t_{therm}.

3.3 Energy Generation Rate from Gravitational Contraction. Thermodynamic Expressions of dq

Gravitational contraction is a major source of stellar energy before hydrogen ignition and also between the subsequent nuclear phases. Conversely, an expansion of the star absorbs energy and thus reduces the stellar luminosity. Let us call dq the heat provided by the stellar medium or absorbed by it. Such a quantity is useful in various contexts where heat exchanges play a role, i.e., convection, hydrodynamical instabilities, stellar oscillations.

3.3.1 Contraction of a Star with Perfect Gas

Let us first examine the case of a mono-atomic perfect gas. From (3.35) and (3.34), one has

$$\varepsilon_{\text{grav}} = -\frac{dU}{dt} + \frac{P}{\varrho^2}\frac{d\varrho}{dt} = -\frac{3}{2}\frac{k}{\mu\, m_{\text{u}}}\frac{dT}{dt} + \frac{P}{\varrho^2}\frac{d\varrho}{dt}\,, \qquad (3.51)$$

where we have used the results of (1.57). We can now eliminate the temperature with the equation of perfect gases ((1.25) see also (7.31)),

$$\varepsilon_{\text{grav}} = -\frac{3}{2}\frac{dP}{\varrho\, dt} + \frac{5}{2}\frac{P\,d\varrho}{\varrho^2\, dt} = -\frac{3}{2}\varrho^{\frac{2}{3}}\frac{d}{dt}\left(\frac{P}{\varrho^{\frac{5}{3}}}\right). \qquad (3.52)$$

This expression gives the rate of gravitational energy production due to change of ϱ and P. It shows that in regions where $P \sim \varrho^{\frac{5}{3}}$, an expansion (or a contraction) demands (or produces) no energy. This applies for example to adiabatic convective zones.

3.3.2 Case of a General Equation of State

In stellar evolution, one needs an expression of $\varepsilon_{\text{grav}}$ applicable to a general equation of state and not only to the perfect gas. We start from the first principle of thermodynamics (1.63) and first take (ϱ, T) as the independent variables, ignoring the possible changes in composition. The various extensive quantities q, U, s and V are expressed by unit of mass.

$$dq = dU + P\,dV = \underbrace{\left(\frac{\partial U}{\partial T}\right)_{\varrho}}_{c_V} dT + \left[\left(\frac{\partial U}{\partial \varrho}\right)_{T} - \frac{P}{\varrho^2}\right] d\varrho\,, \qquad (3.53)$$

where the specific heat c_V is also expressed by unit of mass. We eliminate the terms containing U by using the properties of the specific entropy s,

$$ds = \frac{dq}{T} = \frac{1}{T}dU - \frac{P}{T\varrho^2}d\varrho$$

$$= \underbrace{\frac{1}{T}\left(\frac{\partial U}{\partial T}\right)_{\varrho}}_{\left(\frac{\partial s}{\partial T}\right)_{\varrho}} dT + \underbrace{\left(\frac{1}{T}\left(\frac{\partial U}{\partial \varrho}\right)_{T} - \frac{P}{T\varrho^2}\right)}_{\left(\frac{\partial s}{\partial \varrho}\right)_{T}} d\varrho\,. \qquad (3.54)$$

ds is an exact differential, thus one has

$$\left(\frac{\partial}{\partial \varrho} \left(\frac{\partial s}{\partial T} \right)_{\varrho} \right)_{T} = \left(\frac{\partial}{\partial T} \left(\frac{\partial s}{\partial \varrho} \right)_{T} \right)_{\varrho} , \tag{3.55}$$

which yields

$$\frac{1}{T} \frac{\partial^2 U}{\partial \varrho \partial T} = -\frac{1}{T^2} \left(\frac{\partial U}{\partial \varrho} \right)_{T} + \frac{1}{T} \frac{\partial^2 U}{\partial T \partial \varrho} + \frac{1}{T^2} \frac{P}{\varrho^2} - \frac{1}{T \varrho^2} \left(\frac{\partial P}{\partial T} \right)_{\varrho} . \tag{3.56}$$

After simplification, this becomes

$$\left(\frac{\partial U}{\partial \varrho} \right)_{T} - \frac{P}{\varrho^2} = -\frac{T}{\varrho^2} \left(\frac{\partial P}{\partial T} \right)_{\varrho} . \tag{3.57}$$

The term on the left-hand side is the term in square brackets in (3.53), thus

$$dq = C_V \, dT - \frac{T}{\varrho^2} \left(\frac{\partial P}{\partial T} \right)_{\varrho} d\varrho . \tag{3.58}$$

The terms containing U have disappeared from dq. As independent variables in stellar structure, one usually takes (P, T) rather than (ϱ, T) and thus we can eliminate ϱ by using the equation of state in its general form (7.63)

$$\frac{d\varrho}{\varrho} = \alpha \frac{dP}{P} - \delta \frac{dT}{T} + \varphi \frac{d\mu}{\mu} , \tag{3.59}$$

$$\text{with } \alpha = \left(\frac{\partial \ln \varrho}{\partial \ln P} \right)_{T,\mu} , \, \delta = -\left(\frac{\partial \ln \varrho}{\partial \ln T} \right)_{P,\mu} , \, \varphi = \left(\frac{\partial \ln \varrho}{\partial \ln \mu} \right)_{P,T} . \tag{3.60}$$

Let us first consider the case of a constant mean molecular weight μ. If μ is constant, the last term in (3.60) is absent,

$$dq = \left(C_V + \frac{T}{\varrho^2} \left(\frac{\partial P}{\partial T} \right)_{\varrho} \frac{\varrho \, \delta}{T} \right) dT - \frac{T}{\varrho^2} \left(\frac{\partial P}{\partial T} \right)_{\varrho} \frac{\varrho \, \alpha}{P} dP$$

$$= \underbrace{\left(C_V - \frac{T}{\varrho^2} \left(\frac{\partial P}{\partial T} \right)_{\varrho} \left(\frac{\partial \varrho}{\partial T} \right)_{P} \right)}_{C_P} dT - \frac{T}{\varrho^2} \left(\frac{\partial P}{\partial T} \right)_{\varrho} \left(\frac{\partial \varrho}{\partial P} \right)_{T} dP , \tag{3.61}$$

where we have used the expressions of α and δ. One can write

$$dq = C_P \, dT + \frac{T}{\varrho^2} \left(\frac{\partial \varrho}{\partial T} \right)_{P} dP , \tag{3.62}$$

since one has the Maxwell relation $(\partial P/\partial T)_{\varrho} = -(\partial \varrho/\partial T)_{P}/(\partial \varrho/\partial P)_{T}$. Such a relation is obtained by writing the derivatives of each of the variables (P, ϱ, T) as a

function of the other two, e.g., $dP = (\partial P/\partial \varrho)_T \, d\varrho + (\partial P/\partial T)_\varrho \, dT$ and in the same way for $dT = \cdots$ and $d\varrho = \cdots$. Then, putting dT and $d\varrho$ in the expression of dP, one gets the above relation. With the expression of δ, one has

$$dq = C_P \, dT - \frac{\delta}{\varrho} \, dP , \tag{3.63}$$

and $\varepsilon_{\mathrm{grav}}$ can be expressed as

$$\varepsilon_{\mathrm{grav}} = -\frac{dq}{dt} = -C_P \frac{dT}{dt} + \frac{\delta}{\varrho} \frac{dP}{dt} . \tag{3.64}$$

The rate of gravitational energy generation or absorption can be written as simple functions of the time derivative of pressure and temperature. This is most useful in the calculation of stellar models. Here, the heat change dq is expressed as a function $dq = dq(dT, dP)$. An expression of $dq = dq(dP, d\varrho)$ is useful in some cases, e.g., for stellar oscillations. It is derived in Appendix C.2.

3.3.3   The Entropy of Mixing

The mean molecular weight μ can change for different reasons. For example, the change of μ can result from a change in the ionization equilibrium. In this case, the elemental composition remains the same and the change of μ results from a change of temperature T and density ϱ. This kind of effect is already accounted for by the changes of α and δ.

Changes in μ may also result from transport processes by convection, meridional circulation, etc. In this case, the elemental composition is different and there is a direct contribution of the change of μ to the entropy and dq term. Expression (3.53) contains an additional term,

$$dq = C_V \, dT + \left[\left(\frac{\partial U}{\partial \varrho} \right)_{T,\mu} - \frac{P}{\varrho^2} \right] d\varrho + \left(\frac{\partial U}{\partial \mu} \right)_{\varrho,T} d\mu . \tag{3.65}$$

The equation of state (3.60) with the μ term gives instead of (3.61)

$$
\begin{aligned}
dq = C_P \, dT &- \frac{T}{\varrho^2} \left(\frac{\partial P}{\partial T} \right)_{\varrho,\mu} \left(\frac{\partial \varrho}{\partial P} \right)_{T,\mu} dP \\
&+ \underbrace{\left[\left(\frac{\partial U}{\partial \mu} \right)_{\varrho,T} + \frac{T}{\varrho^2} \left(\frac{\partial P}{\partial T} \right)_{\varrho,\mu} \frac{\varrho \varphi}{\mu} \right]}_{\mathcal{A}} d\mu ,
\end{aligned}
\tag{3.66}
$$

Thus, there is an additional term $A\,d\mu$. With the definitions of α and δ, the complete expression (3.62) can be written as

$$dq = C_P\,dT + \frac{T}{\varrho^2}\left(\frac{\partial\varrho}{\partial T}\right)_{P,\mu} dP + \underbrace{\left[\left(\frac{\partial U}{\partial\mu}\right)_{\varrho,T} - \frac{P\,\varphi\,\delta}{\varrho\,\alpha\,\mu}\right]}_{A} d\mu\,. \qquad (3.67)$$

This may be used to express $\varepsilon_{\mathrm{grav}}$ or the entropy $ds = dq/T$ in the general case with variable mean molecular weight.

In the case of a perfect mono-atomic gas with $U = (3/2)(\mathcal{R}T/\mu)$ and $\alpha = \delta = \varphi = 1$, the term A simplifies to

$$A = -\frac{5}{2}\frac{\mathcal{R}T}{\mu^2}\,. \qquad (3.68)$$

The expression of A in the case of a mixture of perfect gas and radiation is examined in Appendix C.4.4.

3.3.3.1   Effects of the Changes of μ in $\varepsilon_{\mathrm{grav}}$

One may estimate [284] the contribution of the term $A(d\mu/dt)$ in $\varepsilon_{\mathrm{grav}}$. From the expression (7.41) of the mean molecular weight as a function of the hydrogen content in mass fraction, one gets for a fully ionized medium,

$$\frac{d\mu}{dt} = -\frac{5}{4}\mu^2\frac{dX}{dt}\,. \qquad (3.69)$$

The change of H content is equal to the rate of nuclear energy production ε divided by the energy E produced per gram of transmuted hydrogen, $E \approx 6.3 \times 10^{18}$ erg g^{-1} (cf. Sect. 9.1),

$$\frac{dX}{dt} = -\frac{\varepsilon}{E}\,, \quad \text{thus} \quad A\frac{d\mu}{dt} = -\frac{25}{8}\frac{\mathcal{R}T}{E}\varepsilon\,. \qquad (3.70)$$

The estimates [284] show that the term $A\,d\mu/dt$ amounts to about $10^{-3} \times \varepsilon$ at a temperature of $T = 3 \times 10^7$ K, thus it is negligible in the MS phase. However, when convective dredge-up intervenes in more advanced evolutionary phases, this might be different.

3.3.4   The Difference of Specific Heats

Expression (3.61) allows us to express the difference $C_P - C_V$. We also use Maxwell's relation (see after 3.62) to express $(\partial P/\partial T)_\varrho$,

$$C_P - C_V = -\frac{T}{\varrho^2} \left(\frac{\partial P}{\partial T}\right)_\varrho \left(\frac{\partial \varrho}{\partial T}\right)_P = \frac{T}{\varrho^2} \frac{\left(\frac{\partial \varrho}{\partial T}\right)_P^2}{\left(\frac{\partial \varrho}{\partial P}\right)_T}, \tag{3.71}$$

and by expressing the derivatives in terms of α and δ, one obtains finally

$$C_P - C_V = \frac{P}{\varrho T} \frac{\delta^2}{\alpha}. \tag{3.72}$$

This is the most general expression of the difference of specific heats. In the case of a perfect gas, this becomes

$$c_P - c_V = \frac{P}{\varrho T} = \frac{k}{\mu\, m_{\rm u}} = \mathcal{R}/\mu \tag{3.73}$$

per unit of mass, a well-known expression in basic physics.

3.3.5   Adiabatic Gradient for Constant μ

The previous developments lead to some additional useful expressions. For an adiabatic transformation $dq = 0$ and from (3.63) one has

$$C_P\, dT = \frac{\delta}{\varrho}\, dP, \quad \text{or} \quad C_P \frac{T}{P} \left(\frac{\partial \ln T}{\partial \ln P}\right)_{\rm ad} = \frac{\delta}{\varrho}. \tag{3.74}$$

One usually considers the gradients of temperature with respect to pressure and define

$$\nabla \equiv \frac{\partial \ln T}{\partial \ln P}. \tag{3.75}$$

The adiabatic temperature gradient is according to (3.74)

$$\nabla_{\rm ad} = \frac{P\,\delta}{C_P \varrho T}. \tag{3.76}$$

For a perfect gas ($\alpha = \delta = 1$, cf. 3.60), one has

$$\nabla_{\rm ad} = \frac{P}{c_P \varrho T} = \frac{k}{c_P \mu\, m_{\rm u}} = \frac{c_P - c_V}{c_P} = \frac{\gamma - 1}{\gamma}. \tag{3.77}$$

If the gas is mono-atomic, $\gamma_{\rm g} = 5/3$, $\nabla_{\rm ad}$ is a constant with value $\nabla_{\rm ad} = 2/5$.

3.3.6 Adiabatic Gradient for Variable μ

For an adiabatic transformation with variable μ, we have from (3.67),

$$C_P \frac{dT}{dP} - \frac{\delta}{\varrho} + \mathcal{A}\frac{d\mu}{dP} = 0\,, \tag{3.78}$$

where $\mathcal{A}$ is given by (3.67). The adiabatic gradient becomes

$$\nabla_{\text{ad}} = \frac{P\delta}{C_P \varrho T} - \frac{\mathcal{A}\mu}{C_P T}\nabla_\mu \quad \text{with} \quad \nabla_\mu = \left(\frac{\partial \ln \mu}{\partial \ln P}\right). \tag{3.79}$$

This is the expression of the adiabatic gradient for a general equation of state with changes of μ. It contains an additional term with respect to (3.76). An expression of $\mathcal{A}$ for a medium of perfect gas with radiation pressure is given in (C.46). The first term on the right side is $(\partial \ln T/\partial \ln P)_{\text{ad},\mu} = P\delta/(C_P \varrho T)$, i.e., the adiabatic gradient for a fluid element which does not change the mean molecular weight μ during its lifetime. Let us consider the case of a perfect mono-atomic gas with $\mathcal{A}$ given by (3.68). One gets

$$\nabla_{\text{ad}} = \frac{P\delta}{c_P \varrho T} + \frac{5}{2}\frac{\mathcal{R}}{\mu\, c_P}\nabla_\mu\,. \tag{3.80}$$

We use (3.73) to eliminate $\mathcal{R}$ and get for $\gamma_{\text{g}} = c_P/c_V = 5/3$,

$$\nabla_{\text{ad}} = \frac{P\delta}{c_P \varrho T} + \nabla_\mu\,. \tag{3.81}$$

In the case of a perfect mono-atomic gas, the additional term is just equal to ∇_μ. One could expect that the above expressions have important consequences for the criteria of convective stability. This is however not the case, because even in a medium of variable μ, one follows the internal gradient of a fluid element in which μ does not vary (except possibly for ionization, but this is accounted for by α and δ). Thus, the adiabatic gradient is just that given by (3.76). There are however cases, in particular for meridional circulation, where the changes of μ have to be accounted for in the variations of entropy.

3.4   Changes of T and ϱ for Non-adiabatic Contraction

In case of non-adiabatic contraction (e.g., as it occurs in the pre-main sequence phase or between the H- and He-burning phases), there is a relation between the internal density and temperature. Let us consider a star which contracts from a radius R to R',

$$R' = R + \delta R = C_R R, \quad \text{thus} \quad C_R = 1 + \frac{\delta R}{R} . \tag{3.82}$$

For contraction, $C_R < 1$. We consider a homologous contraction, i.e., we assume a uniform contraction: at each level in the star, one has the same relation $r' = C_R r$ with the same value of C_R. The mass does not change, so that $\delta M_r = 0$ and $C_M = 1$. We have seen above that $P_c \sim GM^2/R^4$ ((1.20); see also Sect. 24.3), so that

$$1 + \frac{\delta P}{P} = \frac{1}{\left(1 + \frac{\delta r}{r}\right)^4} , \tag{3.83}$$

which gives in the linear approximation

$$\frac{\delta P}{P} = -4\frac{\delta r}{r} . \tag{3.84}$$

Similarly for the density, one has $C_\varrho = C_M/C_R^3$ and $\delta\varrho/\varrho = -3\delta r/r$. With (3.84) one has a relation between the variations of pressure and density

$$d\ln P = \frac{4}{3}d\ln\varrho . \tag{3.85}$$

With the general form of the equation of state (3.60) written here for a constant mean molecular weight μ, one gets

$$d\ln T = \frac{4\alpha - 3}{3\delta}d\ln\varrho . \tag{3.86}$$

This is an important expression relating the changes of temperature and density during a slow (non-adiabatic) contraction. This relation depends on the equation of state through the coefficients α and δ (3.60).

3.4.1 Major Consequences for Evolution

The above expression (3.86) has remarkable consequences both for star formation and evolution. For a perfect gas $\alpha = \delta = 1$, thus one has

$$d\ln T = \frac{1}{3}d\ln\varrho . \tag{3.87}$$

The slope is $1/3$ in the non-adiabatic case, i.e., the half of the slope in the adiabatic case (19.30, the slope $2/3$ applies only in very short phases, i.e., which occur with the dynamical timescale). The smaller slope here is understandable, since half of the energy from contraction is radiated away in the non-adiabatic case (Sect. 1.3.3).
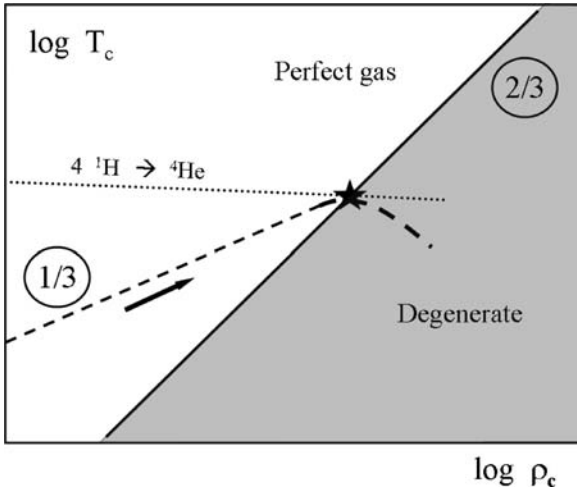
Fig. 3.2 Schematic representation of the central evolution of a star with indication of the perfect gas and degenerate domains separated by a slope of $2/3$ (*continuous line*). The track (*dashed line*) with an *arrow* indicates the path with slope $1/3$ followed by a contracting star. The *dotted line* indicates the T limit where H ignition occurs. The *star* marks the crossing of the *dotted* and *continuous lines*, which determines the brown dwarf upper limit

In the pre-main sequence phase, a slope of $\sim\!1/3$ applies when the evolution proceeds with the Kelvin–Helmholtz timescale (i.e., from point C in Fig. 19.4 until the star sets on the main sequence). It also approximately applies in the post-MS stages, when contraction supplies energy between the main phases of nuclear burning. Thus, the slope $1/3$ defines the main trend of stellar evolution in the diagram $\log T_c$ vs. $\log \varrho_c$, which represents the evolution of the central temperature as a function of the central density and is a fundamental diagram of stellar evolution (Fig. 3.2).

In the plane $\log T_c$ vs. $\log \varrho_c$, the separation between the domains of the perfect gas and of the degenerate electron gas has a slope $2/3$ (Fig. 3.2, see Sect. 7.8). The evolution of stellar centers proceeds with a flatter slope, implying that during evolution a star unavoidably moves toward the domain of degenerate gas. This is the basic reason why stars evolve to degenerate end points.

When the star enters the domain of complete electron degeneracy, the coefficients $\alpha \to \frac{3}{5}$ and $\delta \to 0$ (Sect. 7.8). This implies that at some stage during evolution α becomes smaller than $\frac{3}{4}$, while δ is not yet equal to zero. The ratio $(4\alpha - 3)/3\delta$ may thus become negative, meaning that for a star entering the degenerate domain, contraction does not produce a T increase.

The slope in the plane $\log T_c$ vs. $\log \varrho_c$ also intervenes for the lower mass limit of stars having hydrogen nuclear fusion. If a star enters the degenerate domain with a temperature below the limit for H burning of about 6×10^6 K, its further contraction does not produce an increase of T and H ignition will never occur (Fig. 3.2). The lower mass limit for H burning is about $0.08\,\mathrm{M}_\odot$ at solar metallicity. The objects

between about 0.01 and 0.08 $M_\odot$ resulting from the contraction–fragmentation process and below the limit for H ignition are the brown dwarfs.

3.5 Secular Stability of Nuclear Burning

We have seen above (Sect. 3.2.1) the main effects which allow stellar equilibrium to exist. Nuclear burning can exist in different conditions of state, it may occur in shell or in the presence of strong neutrino emissions. We now have the necessary basis to examine the conditions for the long-term (secular) stellar stability [608]. Let us consider a small sphere of radius r and mass M_r around the center and apply to it Eq. (3.40) of energetic equilibrium using (3.64) for the gravitational energy production,

$$\frac{L_r}{M_r} = \varepsilon - C_P \frac{dT}{dt} + \frac{\delta}{\varrho} \frac{dP}{dt} \, . \tag{3.88}$$

Let us suppose a small temperature perturbation T_1 around the equilibrium value T_0, so that the temperature can be written as $T = T_0 + T_1$. It results similarly in perturbations $P = P_0 + P_1$, $\varrho = \varrho_0 + \varrho_1$, $\varepsilon = \varepsilon_0 + \varepsilon_1$. The equilibrium values imply $\dot{T}_0 = 0$ and $\dot{P}_0 = 0$. We assume the perturbations to be fast enough so that the adiabatic approximation is valid, i.e., $L_{r1} = 0$. From (3.88), we get the relation between the changes of P, T and the perturbation of the nuclear energy production rate

$$\varepsilon_1 = C_P \dot{T}_1 - \frac{\delta}{\varrho_0} \dot{P}_1 \, . \tag{3.89}$$

From (3.86) and (3.85), we can relate the change of P and T,

$$d \ln P = \underbrace{\left(\frac{4\,\delta}{4\,\alpha - 3} \right)}_{\zeta} d \ln T \tag{3.90}$$

which also yields $P_1/P_0 = \zeta \, T_1/T_0$ and $\dot{P}_1/P_0 = \zeta \, \dot{T}_1/T_0$. Thus, we can express the perturbations of P in terms of those of T in (3.89) and get

$$\varepsilon_1 = C_P \dot{T}_1 - \frac{\delta}{\varrho_0} P_0 \, \zeta \, \frac{\dot{T}_1}{T_0} = C_P T_0 \left(1 - \nabla_{\mathrm{ad}} \, \zeta \right) \frac{\dot{T}_1}{T_0} \, , \tag{3.91}$$

where (3.76) is used. This relates the changes of input energy and temperature of the central regions. Now, we write the nuclear reaction rate in the simplified form $\varepsilon = \varepsilon_0 \, \varrho \, T^\nu$ (9.34). We also have

$$\frac{\varepsilon_1}{\varepsilon_0} = \nu \, \frac{T_1}{T_0} \, . \tag{3.92}$$

Finally, the relative perturbation of temperature is related to its time variation by

$$\frac{\dot{T}_1}{T_0} = A \frac{T_1}{T_0} \quad \text{with} \quad A = \frac{\varepsilon_0 \, v}{C_P T_0 \left(1 - \nabla_{\text{ad}} \zeta\right)} \; . \tag{3.93}$$

$A < 0$ implies stability and $A > 0$ instability since the perturbation will grow. This expression can be applied to several situations.

Nuclear reactions in MS stars: the law of perfect gas dominates with $\alpha = \delta = 1$, thus $\zeta = 4$. One has $\nabla_{\text{ad}} = 0.4$, thus $1 - \nabla_{\text{ad}} \zeta = -0.6$ and v is positive. Thus, A is negative and nuclear burning in MS stars is stable.

Neutrino losses: there one has negative ε (3.38). Thus, the conclusions are opposite to the above ones. Significant neutrino losses generally occur in degenerate conditions producing $\dot{T}_1 < 0$ and the star cools down, which reduces the neutrino emissions and leads to a stable situation. For a perfect gas, a strong (very hypothetical) neutrino emission would be destabilizing favoring central collapse.

Completely degenerate gas: in this case, $\alpha = 3/5$ and $\delta = 0$, which gives $\zeta = 0$. Thus, one gets $A > 0$ (the value of ∇_{ad} for complete non-relativistic degeneracy is also 0.4, cf. Schatzman [517]). Nuclear burning in a degenerate region is highly unstable. The additional energy ε_1 does not lead to an expansion, but the excess energy is stored thermally which increases T, which increases ε_1, etc. (Sect. 3.2.1). From (3.86), we get $3 \, \delta \, d\ln T_{\text{c}} = (4\alpha - 3) \, d\ln \varrho_{\text{c}}$. Since $\delta = 0$ and $(4\alpha - 3) \neq 0$, one gets $d\ln \varrho_{\text{c}} = 0$ and the star moves vertically in the $\log T_{\text{c}}$ vs. $\log \varrho_{\text{c}}$ diagram (Fig. 26.9) during the event, until either the degeneracy is lifted or the star is disrupted. In stars with $M < 2.2 \, M_\odot$ at standard Z, which ignite helium in degenerate conditions at the top of the red giant branch, this instability gives the "He flash". For stars in the mass range of 8–9 $M_\odot$, which ignites carbon in degenerate conditions (Sect. 26.4.1), this gives the "C detonation".

3.5.1 Shell Source Instability

Very thin nuclear-burning shells may also produce nuclear instabilities. Let us consider shell source burning at a distance r_0 from the center in a very thin shell of thickness $D \ll r_0$, as it occurs for example in the AGB stars. The mass in the shell is $m = 4\pi r_0^2 \varrho \, d$. If the shell extends, due to some perturbation keeping m and $r_0 \approx$ constant, the relative change of density in the shell is

$$\frac{d\varrho}{\varrho} = -\frac{dD}{D} = -\frac{r_0}{D} \frac{dr}{r_0} \; , \tag{3.94}$$

instead of $d\varrho/\varrho = -3 \, dr/r$ for a sphere. We can thus replace the geometry factor of 3 by r_0/D in the density variations and subsequent equations and one gets for ζ in (3.90)

$$\zeta = \frac{4\,\delta}{4\alpha - (r_0/D)} \, , \tag{3.95}$$

with all other conclusions being the same. This means that for a perfect gas, for $D \ll r_0$, we have $\zeta < 0$ and then $A > 0$. Thus the nuclear burning in very thin shell is unstable, one sees from (3.95) that for a perfect gas $A > 0$ for $D/r_0 < 5/12$. From (3.84) and (3.94), one gets

$$\frac{dP}{P} = 4\frac{D}{r_0}\frac{d\varrho}{\varrho} \, , \tag{3.96}$$

which means that a change of density in the shell makes almost no change of pressure, thus the equation of state (3.60) becomes

$$\frac{d\varrho}{\varrho} \approx -\delta\,\frac{dT}{T} \, . \tag{3.97}$$

Thus, a decrease of the shell density increases its temperature. The reason of this behavior is that a drop of the shell density does not change the pressure exerted by the outer layers on the shell, since the average shell radius changes very little. In a state of perfect gas, as the density decreases, T must increase to sustain the unchanged pressure. This instability is responsible for the thermal pulses in the advanced AGB phases (Sect. 26.6.1). It was originally found by Schwarzschild in numerical calculations and subsequently analytically explained [608]. The instability is lifted when the shell expands so much that the condition on its thinness is no longer satisfied.

3.6   The Role of Radiation Pressure in Stars

Radiation transports energy in stars and also acts as a pressure source. As pointed out by Eddington [168], "The outward flowing radiation may be compared to a wind blowing through the star and helping to distend it against gravity". The effects of radiation pressure on the thermodynamic properties are discussed with more details in Sect. 7.5. Here, one examines some first general effects of radiation pressure.

As before, we call P the total pressure. Here, it is the sum of the gas and radiation pressures $P = P_{gas} + P_{rad}$ and one defines β as the fraction of the gas pressure to the total pressure, one has

$$P_{gas} \equiv \beta P = \frac{k}{\mu\,m_u}\varrho T \, , \quad \text{and} \quad P_{rad} \equiv (1-\beta)P = \frac{1}{3}a T^4 \, , \tag{3.98}$$

according to (C.1). One can express T and write the total pressure P as

$$P = \frac{1}{3}a\frac{T^4}{1-\beta} = \frac{1}{3}\frac{a}{1-\beta}\frac{\beta^4 P^4}{\varrho^4}\left(\frac{\mu\,m_u}{k}\right)^4 \, . \tag{3.99}$$

One gets

$$P = \varrho^{\frac{4}{3}} \left[\frac{3}{a} \left(\frac{k}{\mu \, m_\mathrm{u}} \right)^4 \frac{1-\beta}{\beta^4} \right]^{\frac{1}{3}} . \tag{3.100}$$

This is a relation $P = P(\varrho,\beta)$, from which one concludes that the ratio $\beta = P_{\mathrm{gas}}/P$ cannot be constant inside a star. If this would be the case, one would have from (3.100) $P \sim \varrho^\gamma$ with $\gamma = 4/3$ and according to the Virial theorem (1.61) the star would be unstable.

Figure 3.3 shows the variation of β in the solar model. In most of the stellar interior, β is very close to 1.0. Near the stellar surface, β decreases slightly and then goes up again close to 1.000. In the very outer atmosphere of any star, β goes down to zero, since at the top of the atmosphere the gas pressure is zero and there is only the radiation pressure left. Figure 3.4 shows the variation of β in a $60\,\mathrm{M}_\odot$ star, we see a moderate increase from the center to the surface, before the decline to zero in the very outer layers.

In general the variations of β are limited over most of the stellar interior. Thus, in a first approximation one may consider that $P \sim \varrho^{4/3}$, although this is not exactly verified for the mentioned reasons. When the radiation pressure is negligible (e.g., for stars with a mass inferior to about $3\,\mathrm{M}_\odot$), one has approximately the ratio

$$\frac{\varrho}{T^3} \sim \mathrm{const} , \tag{3.101}$$

in the stellar interior. This property is used for minimizing the interpolations in the numerical tables of opacity data. Interestingly enough, this density distribution corresponds to an extremum of entropy (cf. Appendix C.4.2).
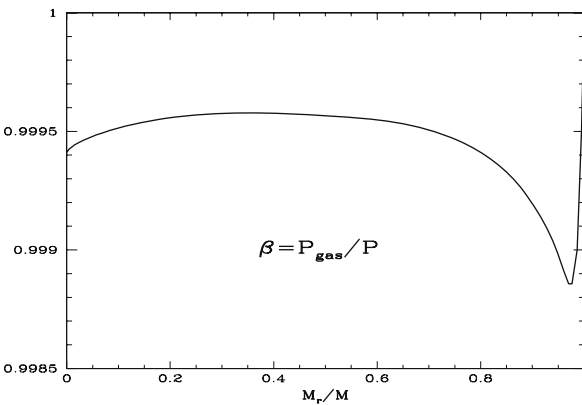
Fig. 3.3 Variation of the ratio β of the gas pressure to the total pressure as a function of the mass fraction in the Sun
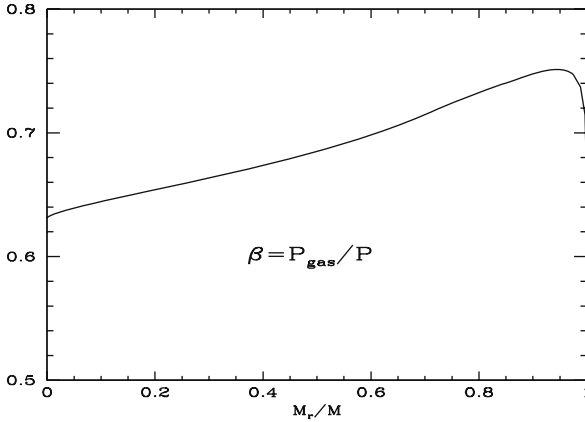
Fig. 3.4 Variation of the ratio β of the gas pressure to the total pressure as a function of the mass fraction in a $60\,M_\odot$ on the ZAMS

3.6.1 The Radiative Pressure as a Function of Mass

Let us examine the behavior of the radiation pressure with stellar masses by considering average values. The ratio P_{rad}/P_{gas} behaves like

$$\frac{P_{rad}}{P_{gas}} = \frac{1}{3}\frac{aT^3}{\varrho}\frac{\mu\,m_u}{k}\;.\tag{3.102}$$

We consider stars with a constant value of μ and we take for ϱ the average density $\overline{\varrho} = 3M/(4\pi R^3)$. Since $\beta P = [k/(\mu\,m_u)]\varrho T$, one gets for the average temperature $\overline{T}$ instead of (1.51)

$$\overline{T} \sim \frac{\beta}{3}\frac{\mu\,m_u}{k}\,q\,\frac{GM}{R}\;,\tag{3.103}$$

where q is a concentration factor (Sect. 1.2). The ratio of the two pressures becomes

$$\frac{P_{rad}}{P_{gas}} = \frac{4\pi}{3^5}\,a\left(\frac{m_u}{k}\right)^4 q^3\,G^3\,\beta^3\,\mu^4\,M^2\;.\tag{3.104}$$

Since $P_{rad}/P_{gas} = (1-\beta)/\beta$, one gets

$$\frac{\beta^4}{1-\beta}\,\mu^4\,M^2 \sim \frac{3^5}{4\pi a}\left(\frac{k}{m_u}\right)^4\frac{1}{G^3}\frac{1}{q^3}\;.\tag{3.105}$$

The second member depends only on the fundamental constants of physics. We can explicit the radiation-density constant $a = 4\sigma/c$ with $\sigma = (2\pi^5 k^4)/(15 h^3 c^2)$ and get

$$\left(\frac{\beta^4}{1-\beta} \right)^{\frac{1}{2}} \mu^2 M \sim \underbrace{0.344 \left(\frac{ch}{G} \right)^{\frac{3}{2}} \frac{1}{m_u^2}}_{10.09\,M_\odot} . \tag{3.106}$$

This means that for constant μ, one has

$$\frac{1-\beta}{\beta^4} \sim M^2 , \tag{3.107}$$

which for high radiation pressure ($\beta \ll 1$) leads to the behavior

$$\beta \sim M^{-1/2} . \tag{3.108}$$

Figure 3.5 shows the variations of the ratio β as function of the stellar masses. The values at the center and at the maximum of β are indicated. This figure also illustrates the limited variations of β in stellar interiors.

According to (3.106), stars in equilibrium supported by gas and radiation pressure have a natural mass scale based on the fundamental constants of physics, implying that M, μ and β are related by a simple relation. It is noticeable that without the effects of radiation pressure, we would not have this mass scale. Stars are gravitational-bound objects, where β is neither equal to 0 nor to 1, a point already emphasized by Eddington [168].
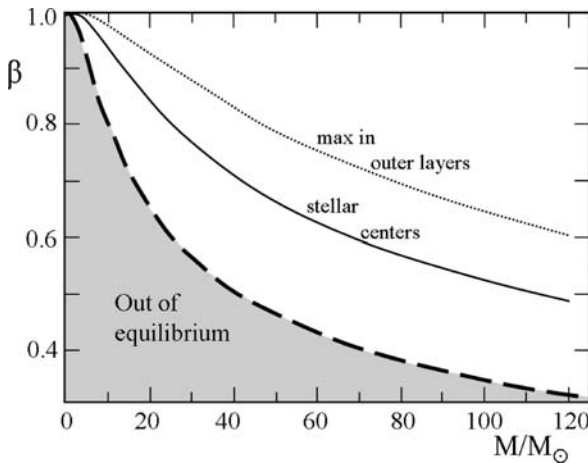
Fig. 3.5 Variation of the ratio $\beta = P_{gas}/P$ of the gas pressure to the total pressure as a function of the stellar masses on the ZAMS. The *continuous line* shows the value at the stellar center of models with $X = 0.705$ and $Z = 0.02$, the *dotted line* gives the maximum value of β inside these models. The *long-dashed line* indicates the minimum value of β permitted by relation (3.112) for a value of $\mu = 0.618$. Stars in the *gray region* have too high radiation pressure to be stable

3.6.1.1   Limits on Radiation Pressure

One may obtain some limits on radiation pressure in stellar centers by using the inequality (1.24) and expression (3.100), as shown by Chandrasekhar [111] (see also Mitalas [423]),

$$\left[\frac{3}{a}\left(\frac{k}{\mu\,m_u}\right)^4 \frac{1-\beta_c}{\beta_c^4}\right]^{\frac{1}{3}} \leq \frac{1}{2}\left(\frac{4}{3}\pi\right)^{\frac{1}{3}} GM_r^{\frac{2}{3}}. \tag{3.109}$$

Taking power 3 and expressing the radiation constant $a = 8\pi^5 k^4/(15\,c^3\,h^3)$, one gets after simplification in the center

$$\frac{135}{4\,\pi^6}\frac{c^3 h^3}{G^3}\frac{1}{m_u^4} \leq M^2\,\mu^4\,\frac{\beta_c^4}{1-\beta_c}, \tag{3.110}$$

which yields the condition

$$\underbrace{0.187\left(\frac{c\,h}{G}\right)^{\frac{3}{2}}\frac{1}{m_u^2}}_{5.48\ \mathrm{M}_\odot} \leq \mu^2 M\left(\frac{\beta_c^4}{1-\beta_c}\right)^{\frac{1}{2}}. \tag{3.111}$$

This inequality places an upper limit on the radiation pressure in the centers, i.e., on $(1-\beta_c)$, for a star of a given mass. This means that one must have $1-\beta_c \leq 1-\beta_*$. The maximum fraction of radiation pressure $(1-\beta_*)$ is uniquely determined by the mass M and the mean molecular weight μ by the equation

$$\mu^2 M = 5.48\left(\frac{1-\beta_*}{\beta_*^4}\right)^{\frac{1}{2}}, \tag{3.112}$$

where the mass M is expressed in units of the solar mass $\mathrm{M}_\odot$. The maximum values of the fraction $P_{\mathrm{rad}}/P = (1-\beta_*)$ are much higher than the current model values. Figure 3.5 compares the current stellar values to this limit.

The growth of radiation in massive stars is a destabilizing factor, as it leads to a decrease of the adiabatic exponents Γ_i (Sect. 7.5). Linear calculations [316] showed that instabilities rapidly develop and an upper mass limit of about $\mu^2 M \approx 22\ \mathrm{M}_\odot$ was suggested. Non-linear calculations show [12] that the instabilities lead to heavy mass loss, which then reduce the stellar mass. Further works [210] confirm the occurrence of instabilities for the most massive stars and that the stability boundary corresponds to about $120\,\mathrm{M}_\odot$ for Pop. I stars, which is about the initial mass of most luminous stars observed in the Galaxy.

3.6.2   The Eddington Luminosity

As radiation pressure opposes its force to gravity and becomes larger for more luminous stars, there is a luminosity limit, where the surface layers are no longer bound. This is the luminosity of Eddington [168], who noticed "The radiation observed to be emitted must work its way through the star, and if there were too much obstruction it would blow up the star".

Let us consider a particle submitted at level r to only the inward acceleration of gravity and outward acceleration of radiative pressure,

$$\boldsymbol{g} = -\frac{GM_r}{r^2}\frac{\boldsymbol{r}}{r} \quad \text{and} \quad \boldsymbol{g}_{\text{rad}} = -\frac{1}{\varrho}\frac{dP_{\text{rad}}}{dr}\frac{\boldsymbol{r}}{r}, \tag{3.113}$$

where $dP_{\text{rad}}/dr < 0$. One also has (3.15) and thus

$$\boldsymbol{g}_{\text{rad}} = \frac{\kappa F}{c}\frac{\boldsymbol{r}}{r} \quad \text{with} \quad F = \frac{L_r}{4\pi r^2}. \tag{3.114}$$

At a level r in the star, one has the sum of the two accelerations

$$\boldsymbol{g} + \boldsymbol{g}_{\text{rad}} = -\frac{GM_r}{r^2}\frac{\boldsymbol{r}}{r}\left[1 - \frac{\kappa L_r}{4\pi c\,GM_r}\right] = -\frac{GM_r}{r^2}\frac{\boldsymbol{r}}{r}\left[1 - \Gamma_r\right]. \tag{3.115}$$

Γ_r is the ratio of the luminosity to the maximum luminosity, i.e., the Eddington luminosity at level r. The Eddington limit is defined by the condition $\Gamma_r = 1$. At the stellar surface, the Eddington luminosity is

$$L_{\text{Edd}} = \frac{4\pi c\,GM}{\kappa}, \quad \text{numerically} \quad \frac{L_{\text{Edd}}}{L_\odot} = 1.30 \times 10^4\,\frac{1}{\kappa}\frac{M}{M_\odot}. \tag{3.116}$$

If the Eddington luminosity is reached at the surface, the upper layers are no longer bound and this favors heavy mass loss. For a star of mass M, L_{Edd} is an upper bound to the stellar luminosity. One defines a factor Γ as the ratio of the stellar to the Eddington luminosity,

$$\Gamma = \frac{\kappa L}{4\pi c\,GM}. \tag{3.117}$$

Already at luminosities well below L_{Edd}, massive stars lose mass by stellar winds driven by radiation pressure. The reason is that some ions have at certain frequencies very large opacities, sufficient to absorb enough momentum to accelerate them outward. By collision coupling, global stellar winds are generated (Chap. 14). The closer to the Eddington limit, the higher the stellar winds. Table 4.1 gives the Eddington ratios Γ calculated with electron scattering opacities for stars of 1–$120\,M_\odot$ at about the middle of their MS phase, when the central hydrogen content is 30% in mass. We see that Γ is significant only for the very massive stars.

The limit $\Gamma_r = 1$ can be reached or even be bypassed in some layers, particularly in the outer stellar envelope where opacity is large. If this happens, it produces convection in the considered stellar layers [309], see Sect. 5.5.1.

The Eddington luminosity is generally defined with κ the electron scattering opacity $\kappa_{es} = 0.2\,(1 + X)$ cm^2 g^{-1} (cf. Sect. 8.2), where X is the hydrogen mass fraction. This is justified for massive MS stars, where electron scattering is the dominant opacity source. However, in general it is meaningful to consider κ as the total opacity; in this case, one speaks sometimes of the "modified Eddington luminosity".

The condition $L < L_{Edd}$ can also be expressed by a condition on T_{eff}. By using the relation $L = 4\pi R^2 \sigma T_{eff}^4$, this condition becomes with (3.116)

$$T_{eff}^4 < \frac{c\,g}{\sigma\,\kappa}\,, \tag{3.118}$$

where g is the surface gravity. This shows that for a star of a given gravity, the effective temperature is limited.

3.6.2.1   The Upper Bound of Stellar Mass: First Approximation

The outward-directed radiation forces put an upper limit to the stellar masses. The Eddington luminosity grows linearly with mass. For a hydrogen mass fraction $X = 0.70$, one gets

$$\frac{L}{L_\odot} = 3.82 \times 10^4\,\frac{M}{M_\odot}\,. \tag{3.119}$$
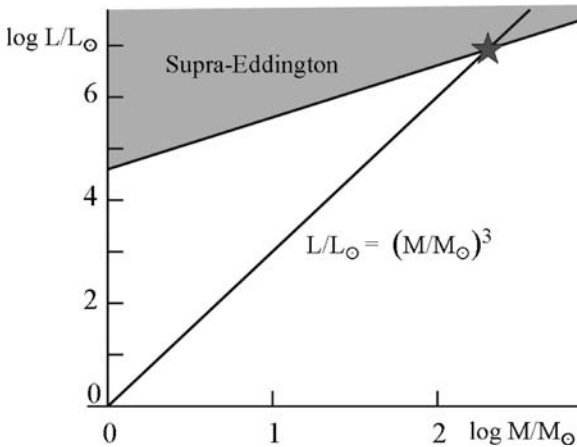
Fig. 3.6 The *steeper line* represents schematically the mass–luminosity relation, while the other line represents the Eddington luminosity as a function of mass for a value $X = 0.70$, which gives $\kappa_{es} = 0.34$ cm^2 g^{-1}. The star at the intersection of the two lines provides a first rough approximation of the maximum stellar mass

For MS stars, the mass–luminosity relation is of the form (3.25), one writes $L/L_\odot = (M/M_\odot)^3$. The luminosity grows steeply with mass and reaches the Eddington value at the intersection of the two curves (Fig. 3.6). This intersection is given by the equality of (3.119) with the $M-L$ relation. This gives $(M/M_\odot)^2 = 3.82 \times 10^4$, i.e., $M/M_\odot \approx 195$. This is a rough estimate (an overestimate) of the maximum stellar mass. With the above mass–luminosity relation, this corresponds to a maximum luminosity of $L/L_\odot = 7.4 \times 10^6$ or a bolometric luminosity of -12.45, according to the relation $M_{\mathrm{bol}} = -2.5\log(L/L_\odot) + 4.72$.

These values of the maximum mass and luminosity are higher than the estimates of the initial maximum mass of about $120\,M_\odot$ and a luminosity of about $10^{6.4}\,L_\odot$ as in the case of η Carinae for example [259]. The reason for the difference is that the maximum stellar mass is determined by the physical processes occurring during star formation (Chap. 22).

Chapter 4
The Energy Conservation and Radiative Equilibrium in Rotating Stars

We have seen that a star is a beautiful self-controlled nuclear reactor. If this reactor is rotating and severely distorted, how does it work? The density structure and energy transport are no longer the same at the equator and at the poles, the spherical symmetry is broken. The reactor fortunately keeps its global self-control (as everyone should do!), but the price to pay to maintain stability is to make some circulation of matter to compensate for the local deviations from the energetic equilibrium produced by rotation.

If a star rotates so fast that the centrifugal force at the surface is equal to gravity, the surface layers are no longer bound and may escape. However, at the stellar surface radiation pressure also tends to push the matter outside. How do these two forces, centrifugal and radiative, interact when the star is close to break-up?

4.1 Radiative Equilibrium for Rotating Stars

We examine what happens to the equations of the radiative flux (3.17) and of energetic equilibrium (3.40) in case of rotation, in order to provide the basic set of stellar structure equations for rotating stars, whether they are rotating as solid body or not.

4.1.1 The Equation of Radiative Transfer

As seen in Chap. 2, in a differentially rotating star the isobars obey to an equation similar to that of the equipotentials $\Psi = $ const. in the conservative case. The equations of stellar structure are written on these isobars (cf. Sect. 2.2.2). The equation of the vertical radiative transfer writes locally in a rotating star

$$F = -\frac{4acT^3}{3\kappa\varrho}\frac{dT}{dn} = -\frac{4acT^3}{3\kappa\varrho}\frac{dT}{dM_P}\varrho < g_{\text{eff}}^{-1} > S_P\, g_{\text{eff}}\,, \qquad (4.1)$$

where dn is the element of distance between two isobars and F is the radiative flux at a given point on the isobar. We have used the fact that $dT/dn = (dT/dM_P)(dM_P/d\Psi)(d\Psi/dn)$ and the expressions (2.36) for $(d\Psi/dn)$ and (2.39) for $dM_P/d\Psi$. S_P is the surface of the considered isobar. Integrating over it, one obtains

$$L_P = -\frac{4ac}{3} < g_{\text{eff}}^{-1} > S_P^2 < \frac{T^3 g_{\text{eff}}}{\kappa} \frac{dT}{dM_P} > , \tag{4.2}$$

which expresses the radiative transfer in rotating stars.

4.1.2 Conservation of Energy

The net energy outflow dL_P from a shell comprised between the isobars Ψ and $\Psi + d\Psi$ is equal to

$$dL_P = \int_{\Psi=\text{const}} \varepsilon \varrho \, dn \, d\sigma = d\Psi \int_{\Psi=\text{const}} \varepsilon \varrho \, \frac{dn}{d\Psi} \, d\sigma , \tag{4.3}$$

where ε is the net rate of energy production in the shell. Using (2.36) and the constancy of $\varrho(1 - r^2 \sin^2\theta \, \Omega \, \alpha)$ on an isobar, one can write

$$dL_P = d\Psi < \frac{\varepsilon}{g_{\text{eff}}} > S_{P\varrho} \left(1 - r^2 \sin^2\theta \, \Omega \, \alpha\right) . \tag{4.4}$$

With (2.39), one obtains by decomposing the energy generation rate into its nuclear, gravitational and neutrino components,

$$\frac{dL_P}{dM_P} = \frac{< \left(\varepsilon_{\text{nucl}} - \varepsilon_v + \varepsilon_{\text{grav}}\right) g_{\text{eff}}^{-1} >}{< g_{\text{eff}}^{-1} >} , \tag{4.5}$$

which is the equation for energy production in a rotating star in equilibrium.

4.1.3 Structure Equations for Rotating Stars

Because of the non-constancy of the density and temperature on isobars in the case of shellular rotation, the above equations are not as simple as in the conservative case. We shall now examine under which conditions, one can transform equations (2.42), (2.46), (4.2), (4.5) into a usable form as proposed by Kippenhahn & Thomas [283].

First, one sees that if, instead of ϱ, one considers the quantity $\bar{\varrho}$ (2.46) as a dependent variable, the continuity equation for the mass keeps its usual form. We shall consider also a mean temperature $\bar{T}$ obtained from the equation of state with as input

variables $\overline{\varrho}$, the isobaric P and the chemical composition. The chemical composition is supposed to be homogeneous on an isobaric surface due to the strong horizontal turbulence. The equations of energy conservation and energy transport are written with these mean values of density and temperature, in addition one makes the following approximations for energy conservation (4.5)

$$\frac{< (\varepsilon_{\mathrm{nucl}} - \varepsilon_v + \varepsilon_{\mathrm{grav}}) g_{\mathrm{eff}}^{-1} >}{< g_{\mathrm{eff}}^{-1} >} \approx \varepsilon_{\mathrm{nucl}}(\overline{\varrho}, \overline{T}) - \varepsilon_v(\overline{\varrho}, \overline{T}) + \varepsilon_{\mathrm{grav}}(\overline{\varrho}, \overline{T}), \qquad (4.6)$$

and for the radiative transfer (4.2),

$$< \frac{T^3 g_{\mathrm{eff}}}{\kappa} \frac{dT}{dM_P} > \approx \frac{\overline{T}^3 < g_{\mathrm{eff}} >}{\kappa(\overline{\varrho}, \overline{T})} \frac{d\overline{T}}{dM_P} . \qquad (4.7)$$

In convective regions, the temperature gradient is the adiabatic gradient (Sect. 5.3) and we approximate the average gradient there by

$$< \frac{d\ln T}{d\ln P} > = < \nabla_{\mathrm{ad}} > \approx \frac{d\ln \overline{T}}{d\ln P} . \qquad (4.8)$$

With these changes of variables and approximations we recover the set of stellar structure equations,

$$\frac{dP}{dM_P} = -\frac{GM_P}{4\pi r_P^4} f_P , \qquad \frac{dr_P}{dM_P} = \frac{1}{4\pi r_P^2 \overline{\varrho}} , \qquad (4.9)$$

$$\frac{dL_P}{dM_P} = \varepsilon_{\mathrm{nucl}} - \varepsilon_v + \varepsilon_{\mathrm{grav}} , \qquad (4.10)$$

$$\frac{d\ln T}{dM_P} = -\frac{GM_P}{4\pi r_P^4} f_P \min \left[\nabla_{\mathrm{ad}}, \nabla_{\mathrm{rad}} \frac{f_T}{f_P} \right] , \qquad (4.11)$$

$$\text{where} \quad f_P = \frac{4\pi r_P^4}{GM_P S_P} \frac{1}{< g_{\mathrm{eff}}^{-1} >} \qquad (4.12)$$

$$\text{and} \quad f_T = \left(\frac{4\pi r_P^2}{S_P} \right)^2 \frac{1}{< g_{\mathrm{eff}} >< g_{\mathrm{eff}}^{-1} >} . \qquad (4.13)$$

The simplifications (4.6)–(4.8) are not severe [408]. First, the equations describing the hydrostatic equilibrium and the conservation of mass are strictly valid (in the Roche model approximation) in the case of a "shellular rotation law", provided that $\overline{\varrho}$ is considered as the dependent variable for density. Moreover the strong horizontal turbulence homogenizes the chemical composition and reduces the ϱ and T contrasts on isobars.

The above equations are used in models of rotating stars in hydrostatic equilibrium instead of the basic equations we have derived above (1.15), (3.40) and (3.17), together with (5.57) in a convective region. On the whole, the above structural

changes have small consequences on the evolution with respect to the larger effects of mixing and mass loss induced by rotation, but they need to be included for the model consistency. However at the surface, rotation produces large distortions and enhances convection (Sects. 4.2.3, 6.5).

4.2   Radiative Transfer in Rotating Stars

Rotation deeply affects the radiative transfer in rotating stars, making the radiative flux non-constant on equipotential surfaces, even in the case of solid body rotation. At the stellar surface, this non-constancy leads to differences in the emergent luminosity and T_{eff} according to the latitude. A rotating star has effective gravity and temperature which vary according to the latitude. It is thus a kind of composite star, with an integrated spectrum being some mixture of stellar spectra of different gravities and T_{eff}. In addition, the Doppler effect broadens the spectral lines. In the stellar interior, the breakdown of radiative equilibrium on level surfaces leads to internal motions known as meridional circulation currents (Chap. 11). These are large-scale currents which mix the chemical elements and transport the angular momentum. Both effects deeply influence the evolution.

4.2.1   Breakdown of Radiative Equilibrium

The breakdown of radiative equilibrium on level surfaces can be shown in a simple way from the expression of the radiative flux (3.17). Let us consider the case of a star in solid body rotation. We have seen in Sect. 2.1.2 that the temperature T, pressure P and density ϱ are functions of only the total potential Ψ (gravity and rotation). The radiative flux at a level r

$$\boldsymbol{F} = -\frac{4\,ac\,T^3}{3\,\kappa\varrho}\boldsymbol{\nabla T} = \left(-\frac{4\,ac\,T^3}{3\,\kappa\varrho}\frac{dT}{d\Psi}\right)\boldsymbol{\nabla\Psi}\,, \tag{4.14}$$

since $T = T(\Psi)$ and the same for ϱ and P. The terms in the parentheses in the above expression are functions of Ψ only, since the opacity κ is a function of ϱ and T. Thus, we see that:

– the radiative flux is parallel to the gradient of Ψ,
– on an equipotential, the flux is proportional to $\nabla\Psi$ only, since the term in parentheses is constant on an equipotential.

This means that a change of T on a level surface will only change the average flux, without affecting the direction and the relative contributions to the flux according to the location on the level surface. Let us calculate the divergence of the radiative flux, which should be zero if there is no energy production or absorption (3.36),

$$\boldsymbol{\nabla} \cdot \boldsymbol{F} = \frac{d}{d\Psi}\left(-\frac{4\,ac\,T^3}{3\,\kappa\varrho}\frac{dT}{d\Psi}\right)(\nabla\Psi)^2 + \left(-\frac{4\,ac\,T^3}{3\,\kappa\varrho}\frac{dT}{d\Psi}\right)\nabla^2\Psi\,. \quad (4.15)$$

One also has (2.7), i.e., $\nabla^2\Psi = 4\pi G\varrho - 2\Omega^2$, where Ω is the (constant) angular velocity. Thus, in (4.15) everything is constant on an equipotential, except $\nabla\Psi$, because the equipotentials are differently spaced as a function of the colatitude ϑ. They are closer to each other in polar regions and more separated in equatorial regions. Therefore $\boldsymbol{\nabla} \cdot \boldsymbol{F}$ must vary on an equipotential: it cannot be zero at all values of ϑ, as it would be if the radiative equilibrium would be satisfied everywhere. Thus, there is locally a breakdown of radiative equilibrium. On the average on an equipotential, one has $< \boldsymbol{\nabla} \cdot \boldsymbol{F} >= 0$, since there is locally no energy produced or subtracted. From the pole to the equator, $\boldsymbol{\nabla} \cdot \boldsymbol{F}$ will be positive for some range of colatitudes and negative for other ones.

If locally $\boldsymbol{\nabla} \cdot \boldsymbol{F} > 0$, there is an excess of energy in the medium (cf. 3.36), which is heated and locally goes up. In the opposite case, it is cooler and goes down. The first term in the second member of (4.15), which behaves like $(\nabla\Psi)^2$ is larger at the pole than at the equator (more in the deep interior than in the external regions). This is the driving term of the circulation currents. It implies in the case of solid body rotation that in the deep radiative layers the circulation motion is rising at the pole and descending at the equator, in a reaction to the local departures from radiative equilibrium. This circulation is further studied in Chap. 11.

4.2.2 The Von Zeipel Theorem

The Von Zeipel theorem establishes a relation between the radiative flux at some colatitude ϑ on the surface of a rotating star and the local effective gravity $g_{\text{eff}}(\Omega, \vartheta)$, function of the angular velocity Ω and ϑ. Let us first consider the case of a uniformly rotating star. The flux is (3.17)

$$\boldsymbol{F}(\Omega, \vartheta) = -\chi\,\boldsymbol{\nabla}T(\Omega, \vartheta) \quad \text{with} \quad \chi = \frac{4\,ac\,T^3}{3\,\kappa\varrho}\,. \quad (4.16)$$

In a solid body rotating star, the equipotentials and isobars coincide (barotropic case), they are also surface of constant T and ϱ. Thus, one can write with the equation of hydrostatic equilibrium (2.8)

$$\boldsymbol{F}(\Omega, \vartheta) = -\chi\frac{dT}{dP}\boldsymbol{\nabla}P(\Omega, \vartheta) = -\varrho\,\chi\frac{dT}{dP}\boldsymbol{g}_{\text{eff}}(\Omega, \vartheta)\,. \quad (4.17)$$

The pressure gradient and effective gravity are parallel. We recall that according to our notations (Sect. 2.1.2; see (1.35)) the components of $\boldsymbol{g}$ are $(-g,\,0,\,0)$ and $g = \partial\Phi/\partial r$. The term $(\varrho\,\chi\,dT/dP)$ is constant on a given equipotential, thus the flux is proportional to the effective gravity on the equipotential. Let us estimate this coefficient of proportionality. For that we express the total luminosity $L(\Omega)$ on an

equipotential of surface Σ and use (2.8)

$$L(\Omega) = \int_\Sigma \boldsymbol{F}(\Omega, \vartheta) \cdot \boldsymbol{d\sigma} = + \left(\varrho \chi \frac{dT}{dP} \right) \int_\Sigma \boldsymbol{\nabla\Psi}(\Omega, \vartheta) \cdot \boldsymbol{d\sigma} . \qquad (4.18)$$

By Gauss theorem, this provides with the Laplacian of Ψ given by (2.7)

$$L(\Omega) = \left(\varrho \chi \frac{dT}{dP} \right) \int_V \nabla^2 \Psi dV = \left(\varrho \chi \frac{dT}{dP} \right) \int_V \left(4\pi G\varrho - 2\Omega^2 \right) dV . \qquad (4.19)$$

Thus, the proportionality coefficient is

$$\left(\varrho \chi \frac{dT}{dP} \right) = \frac{L(\Omega)}{4\pi G M_r \left(1 - \frac{\Omega^2}{2\pi G \overline{\varrho}_m} \right)} , \qquad (4.20)$$

where $\overline{\varrho}_m$ is the average density within the level surface considered. The above relation applies to any equipotential, but in general the von Zeipel theorem is considered at the surface of a star of total mass M and luminosity L. It writes

$$\boldsymbol{F}(\Omega, \vartheta) = -\frac{L}{4\pi G M^*} \, \boldsymbol{g}_{\text{eff}}(\Omega, \vartheta) \qquad (4.21)$$

$$\text{with} \qquad M^* = M \left(1 - \frac{\Omega^2}{2\pi G \overline{\varrho}_M} \right) , \qquad (4.22)$$

where $\overline{\varrho}_M$ is the average stellar density. Equation (4.21) is the von Zeipel theorem: it says that the radiative flux at the surface of a rotating star is proportional to the local effective gravity at the considered colatitude. Table 4.2 gives the relation between the rotation parameter $\omega = \Omega/\Omega_{\text{crit}}$ (2.16) and the ratio $\Omega^2/(2\pi G \overline{\varrho}_M)$ in (4.22).

From the local effective gravity (2.12) at a given colatitude ϑ, one may obtain the radiative flux locally and thus T_{eff} at this colatitude

$$T_{\text{eff}}(\Omega, \vartheta) = \left(\frac{L}{4\pi \sigma G M^*} \right)^{\frac{1}{4}} [g_{\text{eff}}(\Omega, \vartheta)]^{\frac{1}{4}} . \qquad (4.23)$$

Both g_{eff} and T_{eff} vary over the surface of a rotating star and influence the emergent spectrum. The equatorial regions are fainter and cooler than the polar ones, which are brighter and hotter. This effect is called the gravity-darkening. Figure 4.1 shows an example of the considerable variations of T_{eff} over the surface of a rotating star. The von Zeipel theorem in a differentially rotating star with shellular rotation shows only minor differences [350] with respect to (4.21). The differences, which essentially depend on the Ω gradient close to the surface, may slightly increase the contrast between the pole and the equator. Recently 2D models have tested the validity of the von Zeipel relation [330]. Depending on the rotation laws, there are some small differences.

Table 4.1 Initial masses, actual masses, log luminosities, log T_{eff}, radii, Eddington factor Γ, critical velocities $v_{\text{crit},1}$, spectral types and observed average rotational velocities for MS stars at the middle of MS evolution when the central H content $X_{\text{c}} = 0.30$. The masses, luminosities and radii are in solar units, the velocities in km s^{-1}. The average observed rotational velocities $\bar{v}$ are obtained from the observed $v \sin i$ [139, 463, 519] multipled by $4/\pi$ to correct for random orientation effects. See Table 14.2 for Γ at the end of the MS phase

Initial M	Actual M	LogL	LogT$_{\text{eff}}$	R	Γ	$v_{\text{crit},1}$	SP	$\bar{v}$
120	98.96	6.316	4.642	24.91	0.544	711	O3	–
85	77.61	6.114	4.603	23.63	0.436	646	O5	220
60	57.07	5.876	4.594	18.72	0.343	623	O6	220
40	38.74	5.551	4.571	14.32	0.239	586	O7.5	220
25	24.39	5.105	4.521	10.79	0.136	536	O9	220
20	19.60	4.867	4.490	9.46	0.098	513	B0	280
15	14.84	4.533	4.444	7.96	0.060	487	B0.5	290
12	11.95	4.252	4.402	6.99	0.039	466	B1	310
9	8.99	3.857	4.339	5.93	0.021	439	B2	255
7	7.00	3.485	4.277	5.14	1.14×10^{-2}	416	B3	240
5	5.00	2.956	4.184	4.29	4.70×10^{-3}	385	B5	290
4	4.00	2.588	4.117	3.82	2.52×10^{-3}	365	B7	320
3	3.00	2.090	4.026	3.28	1.06×10^{-3}	342	B9	260
2.5	2.50	1.759	3.968	2.92	5.98×10^{-4}	330	A1	–
2	2.00	1.353	3.897	2.54	2.93×10^{-4}	316	A7	160
1.7	1.70	1.055	3.846	2.28	1.74×10^{-4}	308	F1	110
1.5	1.50	0.825	3.821	1.96	1.16×10^{-4}	312	F3	75
1.25	1.25	0.488	3.795	1.50	6.41×10^{-5}	325	F7	35
1	1.00	−0.003	3.765	0.98	2.58×10^{-5}	360	G2	<10

Table 4.2 Relation between the rotation parameters $\omega = \Omega/\Omega_{\text{c}}$ and $\Omega^2/(2\pi G\bar{\varrho}_M)$ as defined by (2.16) and (4.35)

ω	$\Omega^2/(2\pi G\bar{\varrho}_M)$
0.00	0.000
0.20	0.009
0.40	0.035
0.50	0.057
0.60	0.085
0.70	0.120
0.80	0.165
0.90	0.223
0.95	0.259
0.99	0.292
1.00	0.361
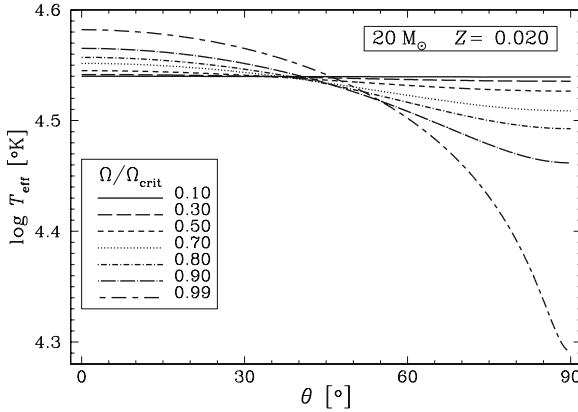
Fig. 4.1 Illustration of the von Zeipel theorem. The local T_{eff} as a function of the colatitude ϑ for models of 20 M$_\odot$ on the ZAMS with various ratios $\Omega/\Omega_{\mathrm{crit}}$ of the angular velocity to the critical value. The stellar shape is shown in Fig. 2.2. Courtesy G. Meynet

4.2.3 Interferometric Observations of Stellar Distortion and Gravity Darkening

Interferometric observations by Domiciano de Souza et al. [164] of the Be star Achernar (α Eri) with the VLTI indicate a ratio $R_{\mathrm{e}}/R_{\mathrm{p}} \approx 1.5$. After various claims, a recent analysis of the data by Carciofi et al. [94] confirms that the observations well agree with a rigidly rotating star at $\omega = 0.992$ in the Roche model, provided it is surrounded by a small disk.

VLTI observations [165] of the fast rotating star Altair ($M \approx 1.8$ M$_\odot$, A7IV-V) confirm a gravity darkening as predicted by the von Zeipel theorem. A successful fitting of the Roche model with a surface temperature following the von Zeipel gravity darkening law is also reported by Peterson et al. [465] for Altair, which rotates at 90% of its break-up angular velocity; this result is further confirmed [466].

The basic picture of gravity darkening is also supported by Monnier et al. [427], but instead of an exponent 0.25 as in (4.23), an exponent 0.19 is favored. Also, they notice an equatorial darkening stronger than predicted, which might result from faster equatorial rotation, of differences due to convection or opacity effects, etc. Let us note that an exponent as small as 0.08 is found by van Belle et al. [588] in the case of Alderamin (α Cep, type A7IV-V), which rotates at 83% of its break-up velocity. At this stage, we conclude that the possible deviations from von Zeipel theorem is a subject of further theoretical and observational investigations.

4.3 Interactions of Rotation and Radiation Effects

The total luminosity $L(\Omega)$ of a rotating star changes with rotation as a result of structural changes due to Eqs. (4.10), (4.11), (4.12), (4.13). Generally, the luminosity decreases with rotation because as a result of the expansion produced by rotation the star is a bit cooler and the opacity higher. Figure 4.2 shows the kind of variations of the luminosity with ω. As for the variations of polar radius (2.24), we can represent the variation of the luminosity by

$$L(\omega) = L(0)\left(1 - b\,\omega^2\right).\tag{4.24}$$

The models of Fig. 4.2 give $b = 0.23, 0.07, 0.065, 0.06, 0.05$ for stellar masses 1, 3, 9, 20 and 60 $M_\odot$.
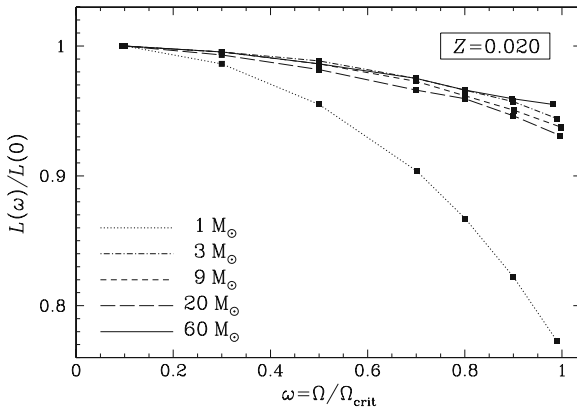
Fig. 4.2 Relative variations of the total stellar luminosity for models of various masses on the ZAMS at $Z = 0.02$ as a function of the rotation parameter $\omega = \Omega/\Omega_{\rm crit}$. From S. Ekström et al. [176]

4.3.1 The Γ, Ω and $\Omega\,\Gamma$ Limits

Not only the total luminosity is changing with rotation but also the local brightness changes over the stellar surface due to von Zeipel's theorem. This leads to differences of the radiation pressure over the surface of rotating stars, therefore the Eddington luminosity also varies on the surface [366].

For a rotating star, the total gravity is the sum of the gravitational, centrifugal and radiative accelerations,

$$\boldsymbol{g}_{\rm tot} = \boldsymbol{g}_{\rm eff} + \boldsymbol{g}_{\rm rad} = \boldsymbol{g}_{\rm grav} + \boldsymbol{g}_{\rm rot} + \boldsymbol{g}_{\rm rad}\,.\tag{4.25}$$

The centrifugal and radiative accelerations oppose their effects to the gravitational potential. The break–up limit $g_{\mathbf{tot}}=0$ can be reached in different ways and we may adopt different corresponding definitions:

- One usually speaks of the Eddington or Γ limit, when rotation effects can be neglected and $g_{\mathbf{rad}} + g_{\mathbf{grav}}=0$, which implies that $\Gamma = \kappa L/(4\pi cGM) = 1$ (cf. Sect. 3.6.2). The meaningful opacity κ is the total opacity, but often the Eddington limit is considered for the electron scattering opacity. Table 4.1 gives the Eddington factor for electron scattering opacity, as well as other parameters of stars at the middle of the main sequence.
- We may speak of the break-up or Ω limit for a star with an angular velocity Ω at the surface, when the effective gravity $g_{\mathbf{eff}}=g_{\mathbf{grav}} + g_{\mathbf{rot}}=0$ and when radiation pressure effects can be neglected. The reality of this limit has been discussed (cf. Sect. 4.4.2).
- We speak of the $\Omega\Gamma$ limit when the total gravity (4.25) $g_{\mathbf{tot}}=0$ with significant effects due to both rotation and radiation. This is the most general case, which should lead to the two previous cases in their respective limits.

4.3.2   The $\Omega\Gamma$ Limit: Combined Eddington and Rotation Limits

Let us examine the case of rotating stars close to the Eddington Limit, i.e., at the $\Omega\Gamma$ limit. The radiative acceleration is according to (3.114)

$$g_{\mathrm{rad}}(\Omega, \vartheta) = \frac{\kappa(\Omega, \vartheta)}{c} \, F(\Omega, \vartheta) \,. \tag{4.26}$$

The opacity in a rotating star may change according to the colatitude, since the temperature and gravity also change (for hot stars, the opacity is due to electron scattering and is constant over the stellar surface). With (4.21), we get for (4.25)

$$g_{\mathrm{tot}} = g_{\mathrm{eff}} \left[1 - \frac{\kappa(\Omega, \vartheta)L(P)}{4\pi c \, GM(1 - \frac{\Omega^2}{2\pi G \varrho_M})} \right] \,, \tag{4.27}$$

since due to von Zeipel's theorem, the radiative acceleration also depends on $g_{\mathbf{eff}}$. We neglect in the von Zeipel theorem the small correcting terms [350] which depend on the non-uniform rotation. In this expression, rotation is present both in $g_{\mathbf{eff}}$ and in the term in brackets.

To express the local Eddington factor, we must also consider the local limiting flux. It is defined by the condition $g_{\mathbf{tot}}=0$ locally. With the first of the relations (4.25) and with (4.26), one obtains

$$F_{\mathbf{lim}}(\Omega, \vartheta) = -\frac{c}{\kappa(\Omega, \vartheta)} g_{\mathbf{eff}}(\Omega, \vartheta) \,. \tag{4.28}$$

We may now define the ratio $\Gamma(\Omega, \vartheta)$ of the actual flux $F(\Omega, \vartheta)$ (4.21) to the limiting local flux (4.28) in a rotating star,

$$\Gamma(\Omega, \vartheta) = \frac{F(\Omega, \vartheta)}{F_{\lim}(\Omega, \vartheta)} = \frac{\kappa(\Omega, \vartheta) \, L(P)}{4\pi \, c \, GM \left(1 - \frac{\Omega^2}{2\pi G \bar{\varrho}_M}\right)} \, . \tag{4.29}$$

$\Gamma(\Omega, \vartheta)$ is the local Eddington ratio at the surface of a rotating star. It also depends on the rotation on the considered isobaric surface. For zero rotation $\Gamma(\Omega, \vartheta) = \Gamma$ and $L_{\mathrm{EDD}} = 4\pi c GM/\kappa$ as given by (3.116). κ is here the total opacity. Moreover, $L(P)$ also varies slightly with rotation, as indicated by the models of stellar interiors (Fig. 4.2).

One notes that the dependences of the flux $F(\Omega, \vartheta)$ and of the limiting flux $F_{\lim}(\Omega, \vartheta)$ with respect to g_{eff} cancel each other and that the only latitudinal effect occurs through the opacity $\kappa(\Omega, \vartheta)$. Thus, on the surface of a rotating star the local Eddington factor $\Gamma(\Omega, \vartheta)$ is the highest at the latitude where the opacity is the highest. In hot rotating stars, if electron scattering dominates everywhere, $\Gamma(\Omega, \vartheta)$ is in principle the same over the stellar surface. If the opacity increases with decreasing temperature, the opacity will be the highest at the equator and there the limit $\Gamma(\Omega, \vartheta) = 1$ is reached first. Thus, if matter escapes at the equator of a rotating star since the local Eddington limit is reached, it is formally not because the effective gravity is the lowest there, but because the opacity is the highest!

With the expression of $\Gamma(\Omega, \vartheta)$ in (4.29), the total gravity (4.27) can be written simply

$$\mathbf{g_{tot}} = \mathbf{g_{eff}} \left[1 - \Gamma(\Omega, \vartheta)\right] \, . \tag{4.30}$$

This shows that the expression for the total acceleration in a rotating star is similar to the usual one, except that Γ is replaced by the local value $\Gamma(\Omega, \vartheta)$. Sometimes, one finds in literature expressions such as $\mathbf{g_{tot}} = \mathbf{g_{eff}} \, (1 - \Gamma)$, this is not correct since this ignores the dependence of the local Eddington factor $\Gamma(\Omega, \vartheta)$ on (a) the angular velocity Ω and (b) the possible variations of opacity due to the change of local T_{eff} predicted by the von Zeipel theorem.

As defined in Sect. 4.3, the $\Omega\Gamma$ limit is reached, when the local Eddington ratio $\Gamma(\Omega, \vartheta) = 1$ at some colatitude ϑ. The condition $\Gamma(\Omega, \vartheta) = 1$ allows us to define a limiting luminosity $L_{\Omega\Gamma}$ at the $\Omega\Gamma$ limit. From (4.29) we have

$$L_{\Omega\Gamma} = \frac{4\pi c GM}{\kappa(\vartheta)} \left(1 - \frac{\Omega^2}{2\pi G \bar{\varrho}_M}\right) \, . \tag{4.31}$$

It means that for a certain angular velocity Ω on the stellar surface, the maximum permitted luminosity of a star is reduced by rotation [209, 366] with respect to the usual Eddington limit. In the above relation, $\kappa(\vartheta)$ is the largest value of the opacity on the surface of the rotating star. For the equation of the surface discussed above (Sect. 2.10), the maximum value of $\Omega^2/(2\pi G \bar{\varrho}_M) = 0.3607$, see also Table 4.2.

Let us emphasize that the above developments account for the reduction of the equatorial flux and of the possible opacity variations at the stellar surface. A higher equatorial opacity increases the T gradient and may drive convection in the equatorial regions. Thus, rotating massive stars close to the Eddington limit may show some convective envelope, particularly in the equatorial regions (see Sect. 5.5).

4.4   Critical Rotation Velocities

4.4.1   No Break-up Velocity for Differential Rotation ?

The concept of break-up velocity has been introduced above in the context of solid-body rotation. In this case, the critical velocity is given by (2.15). Table 4.1 gives the critical velocities for stars on the ZAMS with a standard composition with $Z = 0.02$ and $X = 0.70$. Figure 2.4 shows the values of the break-up velocities as a function of mass for stars of different contents in heavy elements Z. Low-Z stars have very high critical velocities, due to their smaller radii.

However, there are claims [566] that the concept of break-up velocity only applies for $\Omega = $ const. The argument is the following one. If at some stage during evolution of a differentially rotating star, the surface layers are spun up due for example to some contraction, there is a readjustment of the distribution of angular momentum and the star does never reach a stage with a critical velocity at its surface. Thus, it was concluded [566] that equatorial break-up is unlikely.

Indeed, whether a star in differential rotation can reach break-up or not is a matter of timescales. One has to know whether the timescale for the redistribution of the angular momentum is shorter than the timescale for the change of radius and surface velocity. According to recent models with rotation [367, 409], the transport of angular momentum is dominated by meridional circulation. In massive stars on the zero-age sequence, the redistribution of the angular momentum proceeds with timescales of the order of a few 10^4 yr. Even when this efficient redistribution of the angular momentum is accounted for, stellar models show that fast rotating stars, which have no large mass loss, may reach break-up during their MS evolution (Sect. 27.8). Thus, unless there is some other more efficient mechanism redistributing the angular momentum, I conclude that stars with shellular rotation do reach break-up (this is also the case for solid body rotation). This conclusion is supported by the existence of Be stars, currently considered [452] to be at break-up. Noticeably, the fraction of Be stars is even much larger in star clusters of lower metallicity Z than in the solar neighborhood [358]. These results tend to support the existence of critical velocities. These stars may experience mass loss and form equatorial disks, which then further dissipate by radiative effects from the central star.

4.4.2 Classical Expression of the Critical Velocity

We examine what happens to the break-up or critical velocity in a rotating star with a high radiation pressure. Often in literature [237], the critical or break-up velocity, where the centrifugal force just compensates Newtonian gravity, is written like

$$v_{\text{crit}}^2 = (GM/R)(1-\Gamma) , \qquad (4.32)$$

where Γ is the usual expression (3.116). This relation is only true for a uniform brightness over the surface of the rotating star, which contradicts the von Zeipel theorem.

The critical velocity is reached, when somewhere on the stellar surface the total gravity as given by (4.30) is zero, which implies

$$\boldsymbol{g}_{\text{eff}} \ [1-\Gamma_\Omega(\vartheta)]= \boldsymbol{0}. \qquad (4.33)$$

This equation has two roots which we call $v_{\text{crit},1}$ and $v_{\text{crit},2}$. At each rotation velocity, the lowest of the two roots is the significant one, since as soon as it is reached somewhere on the star, the matter is no longer bound.

The first root is given by the usual condition $\boldsymbol{g}_{\text{eff}} = \boldsymbol{0}$, obtained when radiation pressure is negligible. It implies the equality of the centrifugal acceleration and Newtonian gravity at the equator, i.e., $\Omega^2 R_{\text{e,crit}}^3/(GM) = 1$, where $R_{\text{e,crit}}$ is the equatorial radius at the critical velocity. This gives the classical expression of the critical velocity at the equator

$$v_{\text{crit},1} = \Omega\, R_{\text{e,crit}} = \left(\frac{2}{3}\frac{GM}{R_{\text{p,crit}}}\right)^{\frac{1}{2}} , \qquad (4.34)$$

with $R_{\text{p,crit}}$ ($= \frac{2}{3}R_{\text{e,crit}}$) the polar radius at the critical velocity. Interestingly enough, this critical velocity $v_{\text{crit},1}$ (which as shown below applies everywhere except to Γ values above 0.639) is independent of the Eddington factor. The reason for this independence is that, due to the von Zeipel theorem, the radiative flux (4.21) at the equator decreases the same way as the effective gravity, when rotation increases. Thus, for moderate rotation, the decrease of T_{eff} at the equator prevents significant radiation pressure effects. This is true as long as Γ is not too large.

Figure 2.4 illustrates the values of the critical velocities $v_{\text{crit},1}$ for stars of different masses and metallicities Z. The values of $v_{\text{crit},1}$ at the middle of the H-burning phase for stars in the range of 1–120 M$_\odot$ are compared in Table 4.1 with the average observed rotational velocities v at the corresponding spectral types. The critical values $v_{\text{crit},2}$ corresponding to the second root of (4.33) are discussed below in Sect. 4.4.4.

4.4.3 The Different Rotation Parameters

There are different rotation parameters Ω, ω, v, $v/v_{\mathrm{crit},1}$, $\Omega^2/(2\pi G\bar{\varrho}_M)$. Here we examine the relations between them in the Roche model. Let us express first the ratio $\Omega^2/(2\pi G\bar{\varrho}_M)$ which intervenes in the reduced mass, for example, in (4.29) and (4.31),

$$\frac{\Omega^2}{2\pi G\bar{\varrho}_M} = \frac{\Omega^2 V}{2\pi GM} = \frac{16}{81}\omega^2 V'(\omega)\,, \tag{4.35}$$

$$\text{with}\quad V'(\omega) = \frac{V(\omega)}{\frac{4}{3}\pi R_{\mathrm{p,crit}}^3}\quad\text{and}\quad \omega^2 = \frac{\Omega^2 R_{\mathrm{e,crit}}^3}{GM}\,, \tag{4.36}$$

according to (2.16). The rotation parameter $\omega = \Omega/\Omega_{\mathrm{crit}}$ is the fraction of the angular velocity at the classical break-up (2.16). The average density is $\bar{\varrho}_M(\omega) = M/V(\omega)$, where the total stellar volume $V(\omega)$ evidently depends on rotation. The quantity $V'(\omega)$ is the ratio of the actual volume of a star with rotation given by ω to the volume of a sphere of radius $R_{\mathrm{p,crit}}$. The volume $V'(\omega)$ is obtained by the numerical integration of the solutions of the surface equation (2.18). For low rotation velocities, one has $V' \approx 1$. At break-up velocity $v_{\mathrm{crit},1}$, the value of $V'(\omega) = 1.829$, which gives the maximum value of $\Omega^2/(2\pi G\bar{\varrho}_M) = 0.3607$ (see Table 4.2). One verifies easily that $\Omega^2/(2\pi G\bar{\varrho}_M)$ is also the ratio of centrifugal force to gravity along the average stellar radius (which corresponds to the radius R_{P_2} at the root $P_2(\cos\vartheta) = 0$ of the second Legendre polynomial, i.e., for $\sin^2\vartheta = 2/3$ which means a colatitude of $\sim 54^o$),

$$\frac{\Omega^2}{(2\pi G\bar{\varrho}_M)} = \frac{2}{3}\frac{\Omega^2 R_{P_2}^3}{GM}\,. \tag{4.37}$$

The correspondence between the rotation parameters $\omega = \Omega/\Omega_{\mathrm{crit}}$ and $\Omega^2/(2\pi G\bar{\varrho}_M)$ is given in Table 4.2. The ratio $\Omega^2/(2\pi G\bar{\varrho}_M)$ may also be expressed with the help of (4.34) and (4.36),

$$\frac{\Omega^2}{2\pi G\bar{\varrho}_M} = \frac{v^2 V}{2\pi GMR_{\mathrm{e}}^2} = \frac{2v^2 V}{6\pi R_{\mathrm{e}}^2 v_{\mathrm{crit},1}^2 R_{\mathrm{p,crit}}} = \frac{4}{9}\frac{v^2}{v_{\mathrm{crit},1}^2}\left[\frac{R_{\mathrm{p,crit}}^2}{R_{\mathrm{e}}^2}V'\right]\,. \tag{4.38}$$

The above expression (4.38) relates $\Omega^2/(2\pi G\bar{\varrho}_M)$ and $v/v_{\mathrm{crit},1}$. The term in brackets does not deviate much from unity. Thus, up to relatively large rotation velocity this ratio can be approximated by $(4/9)(v^2/v_{\mathrm{crit},1}^2)$ as illustrated by Fig. 4.3 (left).

The relation between $v/v_{\mathrm{crit},1}$ and ω is given by the expression (2.19) and Fig. 2.5 shows this relation. Expression (4.35) relates $\Omega^2/(2\pi G\bar{\varrho}_M)$ and ω; the corresponding numerical data are provided by Table 4.2. Some useful relations were also shown in Sect. 2.1.4; Fig. 2.4 shows $v_{\mathrm{crit},1}$ as a function of M for different metallicities Z and Fig. 2.6 shows v as a function of ω for different M and Z.
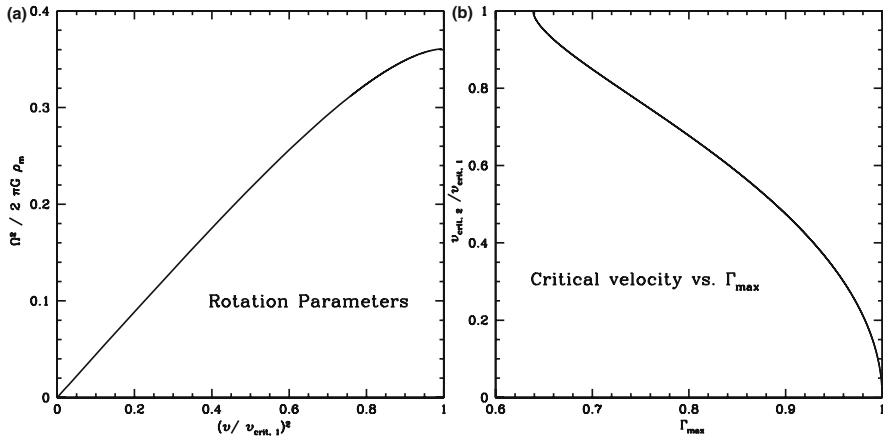
Fig. 4.3 *Left*: the relation between the rotation parameter $\Omega^2/2\pi G\bar{\varrho}_M$ and the ratio of the velocity v to the critical velocity $v_{\mathrm{crit},1}$. For low enough rotation velocities, one has the relation $\Omega^2/2\pi G\bar{\varrho}_M \approx \frac{4}{9}\frac{v^2}{v_{\mathrm{crit},1}^2}$. *Right*: the second root or critical velocity $v_{\mathrm{crit},2}$ expressed as a fraction of the usual critical velocity $v_{\mathrm{crit},1}$ as a function of the Eddington factor Γ for electron scattering (if the opacity varies over the surface, one has to to take the maximum value of Γ). When the Eddington factor tends towards 1.0, the break-up velocity goes to zero

4.4.4   Critical Velocity Near the Eddington Limit

Equation (4.33) has a second root given by the condition $\Gamma_\Omega(\vartheta) = 1$. As seen above, this condition is in general first met at the equator, due to the higher opacity there. From (4.29), this condition implies

$$\frac{\kappa(\Omega,\vartheta)L}{4\pi cGM} = 1 - \frac{\Omega^2}{2\pi G\bar{\varrho}_M} \ , \tag{4.39}$$

where L is the total luminosity at the rotation velocity considered. One takes the maximum Eddington ratio $\Gamma = \kappa(\Omega,\vartheta)L/(4\pi cGM)$ over the stellar surface, determined by the highest value of $\kappa(\Omega,\vartheta)$. For electron scattering opacity, Γ is the same over the whole stellar surface. Expression (4.39) can be written as

$$\frac{16}{81}\,\omega^2\,V'(\omega) = 1 - \Gamma \ . \tag{4.40}$$

For a star with a given maximum Γ ratio, this expression determines the value of the rotation parameter ω at which the break-up is reached. Thus, for a given value of Γ, one searches the value of ω which satisfies this equation. This is easily obtained by solving numerically the surface equation. Since the maximum value of $(16/81)\,\omega^2\,V'(\omega)$ (obtained for $\omega = 1$) is 0.3607, we see that if Γ is larger than 0.6393, the maximum value of ω is lower than 1.0. The corresponding critical velocity $v_{\mathrm{crit},2}$ is thus given by

$$v_{\mathrm{crit},2}^2 = \Omega^2 R_{\mathrm{e}}^2(\omega) = \frac{8}{27}\frac{GM}{R_{\mathrm{p,crit}}^3} R_{\mathrm{e}}^2(\omega)\,\omega^2\,, \tag{4.41}$$

where we use $\Omega^2 = \frac{8}{27}\frac{GM\omega^2}{R_{\mathrm{p,crit}}^3}$ (2.17). $R_{\mathrm{e}}(\omega)$ is the equatorial radius for a given value of the rotation parameter. Now, the maximum value of ω for a fixed value of Γ is given by (4.40) and the above expression becomes with (4.34),

$$v_{\mathrm{crit},2}^2 = \frac{3}{2}\frac{GM}{R_{\mathrm{p,crit}}^3} R_{\mathrm{e}}^2(\omega)\frac{1-\Gamma}{V'(\omega)} = \frac{9}{4}v_{\mathrm{crit},1}^2\frac{R_{\mathrm{e}}^2(\omega)}{R_{\mathrm{p,crit}}^2}\frac{1-\Gamma}{V'(\omega)}\,. \tag{4.42}$$

This gives the second root for a star with an Eddington factor Γ larger than 0.639. Figure 4.3 (right) illustrates the values of the critical velocity near the Eddington limit. For large Γ values, the critical velocity is much lower than the usual critical velocity $v_{\mathrm{crit},1}$. Thus, stars with a high Γ may reach the break-up velocities even for low rotation velocities. In the extreme case, for $\Gamma = 1$ even with $v = 0$ the surface is unbound. One may still formally write the first root, but the second is met first and thus is the only significant one for high enough Eddington factors ($\Gamma > 0.639$).

Physically, the reduction of the critical velocity given by the second root results from the reduction of the effective mass $M\left[1 - \Omega^2/(2\pi G\overline{\varrho}_M)\right]$ by rotation. This makes the critical Eddington limit to be reached earlier in evolution for a rotating star, conversely one could also say that it makes the critical velocity to be reached earlier for a star with a high Γ. The cases where the second root applies typically correspond to the $\Omega\Gamma$ limit as defined in Sect. 4.3. There, both rotation and radiation combine their effects to make a lower critical rotation limit.

The luminous blue variable (LBV) stars, such as η Carinae, are likely objects close to the $\Omega\Gamma$ limit (Fig. 27.23) and this proximity is certainly an essential reason for the occurrence of the LBV outbursts.

Chapter 5
Stellar Convection[*]

In most systems, whether stars, Earth or even humans, a heat excess may bring disorders. In stars, a heat excess (with respect to what radiation can transfer) drives turbulent chaotic convective motions. Convection, i.e., the turbulent turnover of matter in a medium heated from below, is a basic mechanism of energy transport in stars together with radiative transfer. In addition, it produces fast mixing of the chemical elements, generally leading to the chemical homogeneity of the convective regions, an effect which is rich of consequences. Convection transports the angular momentum, thus influencing the evolution of rotation. It also imposes a particular density structure characterized by a relatively low-density contrast (Sect. 24.5). It generates sonic waves observable in helioseismology and asteroseismology. Thus, convection is doing a lot in stellar physics and evolution!

All the necessary physics of convection is contained in the equations of continuity (1.1), momentum transport (B.19) and energy conservation (3.43), thus ideally the problem should be completely solved. However, the reality is far from ideal, because turbulent motions bring a great complexity in the properties of convection. The complete three-dimensional solution of these equations, all the way during stellar evolution, with sufficiently small steps in space and time will not be feasible before long. Thus, convection remains a weak point in the theory of stellar evolution.

For now, some numerical hydrodynamic models already enable us to test the simple phenomenological recipes currently used in stellar evolution. The answer is in general not so favorable to these simple recipes.

5.1 Gravity Waves and the Brunt–Väisälä Frequency

Let us consider a fluid element in a star at some level r_0 in equilibrium with the surrounding medium. If this cell is displaced vertically and the motion is adiabatic without viscous effects, the equation of motion is

$$\varrho_{\text{int}} \frac{d^2 r}{dt^2} + g\left(\varrho_{\text{int}} - \varrho_{\text{ext}}\right) = 0,\tag{5.1}$$

---

[*]This chapter may form the matter of a basic introductory course.

where $g > 0$ is the modulus of gravity, while ϱ_{int} and ϱ_{ext} are, respectively, the interior and exterior densities of the fluid element. For a small displacement $(r - r_0)$, one may develop to the first order

$$\varrho_{\text{int}}(r) = \varrho_{\text{int}}(r_0) + \frac{d\varrho_{\text{int}}}{dr}\bigg|_{r_0} (r - r_0),$$

$$\varrho_{\text{ext}}(r) = \varrho_{\text{ext}}(r_0) + \frac{d\varrho_{\text{ext}}}{dr}\bigg|_{r_0} (r - r_0). \tag{5.2}$$

The equation of motion becomes, since at r_0 one has $\varrho_{\text{int}}(0) = \varrho_{\text{ext}}(0)$,

$$\varrho_{\text{int}} \frac{d^2 r}{dt^2} + g \left(\frac{d\varrho_{\text{int}}}{dr} - \frac{d\varrho_{\text{ext}}}{dr} \right) (r - r_0) = 0. \tag{5.3}$$

This is the equation of harmonic motions without damping. The solution is of the form $(r - r_0) = A \exp(iNt)$, which yields

$$- \varrho_{\text{int}} A N^2 e^{iNt} + g \left(\frac{d\varrho_{\text{int}}}{dr} - \frac{d\varrho_{\text{ext}}}{dr} \right) A e^{iNt} = 0. \tag{5.4}$$

The oscillation frequency N of a fluid element displaced around its equilibrium position in a medium of gravity $\boldsymbol{g}$ is given by

$$N^2 = \frac{g}{\varrho} \left(\frac{d\varrho_{\text{int}}}{dr} - \frac{d\varrho_{\text{ext}}}{dr} \right). \tag{5.5}$$

N is the Brunt–Väisälä frequency. These oscillations are also known as gravity waves, since gravity is the restoring force (Sect. 17.1.1). The indices "int" or "ext" are absent from the density ϱ at the denominator, since at the equilibrium level the internal and external densities are the same. One has two possible situations:

- $(d\varrho_{\text{int}}/dr) > (d\varrho_{\text{ext}}/dr)$: $N^2 > 0$. N is real and the motion is oscillatory due to the recall force of gravity, it is neither amplified nor damped. The fluid element experiences a negligible displacement from the equilibrium level r_0. The medium is stable with respect to convection.
- $(d\varrho_{\text{int}}/dr) < (d\varrho_{\text{ext}}/dr)$: $N^2 < 0$. N is imaginary, so that

$$r - r_0 = A \exp \left[\pm \sqrt{\left(\frac{d\varrho_{\text{ext}}}{dr} - \frac{d\varrho_{\text{int}}}{dr} \right) t} \right]. \tag{5.6}$$

The sign $+$ concerns outward motions. The fluid element experiences a motion that removes it exponentially from the equilibrium level. The medium is unstable with respect to convection.

If one calls $\Delta\varrho = \varrho_{\text{int}} - \varrho_{\text{ext}}$, the Brunt–Väisälä frequency can be written

$$N^2 = \frac{g}{\varrho}\frac{d(\Delta\varrho)}{dr}\,, \qquad (5.7)$$

so that

$$\frac{d(\Delta\varrho)}{dr} > 0 \implies \text{stability}\,, \quad \frac{d(\Delta\varrho)}{dr} < 0 \implies \text{instability} \qquad (5.8)$$

with respect to convection. These conditions define whether the fluid element stays around the equilibrium level or deviates exponentially from it. They are used to define the criteria for convective instability in Sect. 5.1.2.

5.1.1 Relation with the Entropy Gradient

The Brunt–Väisälä frequency N is related to the entropy gradient in stellar interiors. Let us express the density as a function $\varrho = \varrho(s, P)$ of the specific entropy s and of pressure P, thus

$$d\varrho = \left(\frac{\partial\varrho}{\partial s}\right)_P ds + \left(\frac{\partial\varrho}{\partial P}\right)_s dP\,. \qquad (5.9)$$

For a fluid element in adiabatic motion and pressure equilibrium, one has $ds_{\text{int}} = 0$ and $dP_{\text{int}} = dP_{\text{ext}}$. Thus, the difference of the internal and external densities is

$$d\varrho_{\text{int}} - d\varrho_{\text{ext}} = \left(-\frac{\partial\varrho_{\text{ext}}}{\partial s}\right)_P ds_{\text{ext}}\,. \qquad (5.10)$$

The Brunt–Väisälä frequency becomes

$$N^2 = \frac{g}{\varrho}\frac{d(\Delta\varrho)}{dr} = -\frac{g}{\varrho}\left(\frac{\partial\varrho}{\partial s}\right)_P\frac{ds_{\text{ext}}}{dr}\,. \qquad (5.11)$$

Let us express the specific entropy ds as

$$ds = C_P\frac{dT}{T} + \left(\frac{\partial s}{\partial P}\right)_T dP\,, \qquad (5.12)$$

thus $d\varrho$ in (5.9) becomes

$$d\varrho = \left(\frac{\partial\varrho}{\partial s}\right)_P C_P\frac{dT}{T} + \left[\left(\frac{\partial\varrho}{\partial s}\right)_P\left(\frac{\partial s}{\partial P}\right)_T + \left(\frac{\partial\varrho}{\partial P}\right)_s\right]dP\,. \qquad (5.13)$$

The above expression implies

$$\left(\frac{\partial \varrho}{\partial T}\right)_P = \left(\frac{\partial \varrho}{\partial s}\right)_P \frac{C_P}{T} \ . \tag{5.14}$$

Thus, we can write the frequency N^2 (5.11) as follows

$$N^2 = -\frac{g}{\varrho}\frac{T}{C_P}\left(\frac{\partial \varrho}{\partial T}\right)_P \frac{ds_{\text{ext}}}{dr} = \frac{g}{C_P}\left(-\frac{\partial \ln \varrho}{\partial \ln T}\right)_P \frac{ds_{\text{ext}}}{dr} \ , \tag{5.15}$$

and with $\delta = -(\partial \ln \varrho / \partial \ln T)_P$,

$$N^2 = \frac{g\,\delta}{C_P}\frac{ds}{dr} \ , \tag{5.16}$$

where the index "ext" is now omitted. The condition for convection is

$$N^2 < 0 \quad \Longleftrightarrow \quad \frac{ds}{dr} < 0 \ . \tag{5.17}$$

There is convection in regions where the entropy decreases outward. Where it increases outward, there is no convection. Radiative transport and convection both evacuate the entropy excess which may exist in the interior. From star formation to the final remnants, the whole stellar evolution tends to remove entropy from the interior of stars to put it in the surrounding Universe (see also Sect. 26.4.2).

5.1.2   The Schwarzschild and Ledoux Criteria

We may express the Brunt–Väisälä frequency in terms of temperature gradients instead of density gradients. We use the equation of state in the general form (3.60), so that the gradient of the interior density is

$$\frac{d\ln \varrho_{\text{int}}}{dr} = \alpha\frac{d\ln P_{\text{int}}}{dr} - \delta\frac{d\ln T_{\text{int}}}{dr} \ . \tag{5.18}$$

We do not consider the possible variations of μ inside the moving cell, because it keeps the same composition. However, the mean molecular weight μ in the cell may change due, for example, to a difference in the ionization during the motion of the cell [285]. Such a change results from differences in P and T and is accounted for by the values of α and δ. In the ambient stellar medium, the composition may change and the density gradient is

$$\frac{d\ln \varrho_{\text{ext}}}{dr} = \alpha\frac{d\ln P_{\text{ext}}}{dr} - \delta\frac{d\ln T_{\text{ext}}}{dr} + \varphi\frac{d\ln \mu_{\text{ext}}}{dr} \ . \tag{5.19}$$

One considers $\alpha_{\text{ext}} = \alpha_{\text{int}}$, the same for δ. This is justified since α and δ are slowly varying functions and the differences between the internal and the external values of P and T are small. The density gradient becomes

$$\frac{1}{\varrho}\frac{d(\Delta\varrho)}{dr} = \delta\left(\frac{d\ln T_{\text{ext}}}{dr} - \frac{d\ln T_{\text{int}}}{dr}\right) - \varphi\frac{d\ln\mu_{\text{ext}}}{dr}\ . \tag{5.20}$$

In the first member, ϱ represents ϱ_{int} as well as ϱ_{ext}; accounting for a difference would introduce higher order terms, which are negligible. The pressure terms are neglected, because one considers fluid elements in pressure equilibrium with the surroundings. This is called the anelastic approximation. Since the perturbations of pressure move at the sound speed, the present developments are valid only if the motions of the fluid elements are subsonic. This is in general the case, however convection in red supergiants may be sonic, which makes the present development inapplicable (Sect. 5.5.3). The stability condition $d\Delta\varrho/dr > 0$ (5.8) implies

$$\frac{d\ln T_{\text{ext}}}{dr} > \frac{d\ln T_{\text{int}}}{dr} + \frac{\varphi}{\delta}\frac{d\ln\mu_{\text{ext}}}{dr}\ . \tag{5.21}$$

Following (3.75), one defines

$$\nabla \equiv \frac{d\ln T_{\text{ext}}}{d\ln P}, \quad \nabla_{\text{int}} \equiv \frac{d\ln T_{\text{int}}}{d\ln P}, \quad \nabla_{\mu} \equiv \frac{d\ln\mu_{\text{ext}}}{d\ln P}\ . \tag{5.22}$$

With these definitions, the Brunt–Väisälä frequency N (5.7) becomes

$$N^2 = \frac{g}{\varrho}\frac{d(\Delta\varrho)}{dr} = \frac{g\,\delta}{H_P}\left(\nabla_{\text{int}} - \nabla + \frac{\varphi}{\delta}\nabla_{\mu}\right)\ . \tag{5.23}$$

H_P is the pressure-scale height, defined as

$$H_P \equiv -\frac{dr}{dP}P\ . \tag{5.24}$$

If over some range of r, H_P would be constant, the integration of equation (5.24) would lead to $P(r) = P(r_0)\exp-(r-r_0)/H_P$. Thus, H_P is the height over which the pressure is changing by a factor of e. For the Earth, $H_P \approx 8$ km. Figure 5.1 shows the change of the pressure scale height H_P in the outer solar layers. It varies from about 200 km in the atmosphere to 0.1 $R_\odot$ in the deep interior. Often, the Brunt–Väisälä frequency is decomposed into two frequencies,

$$N^2 = N_T^2 + N_\mu^2, \quad \text{with } N_T^2 = \frac{g\,\delta}{H_P}(\nabla_{\text{int}} - \nabla) \quad \text{and } N_\mu^2 = \frac{g\,\varphi}{H_P}\nabla_\mu\ . \tag{5.25}$$

In stellar interiors, the Brunt–Väisälä frequency is generally written with ∇_{ad} instead of ∇_{int} because convection is adiabatic (Sect. 5.3). The condition of stability (5.21) becomes, taking into account that the internal and external pressure gradients are equal and that $d\ln P/dr < 0$,
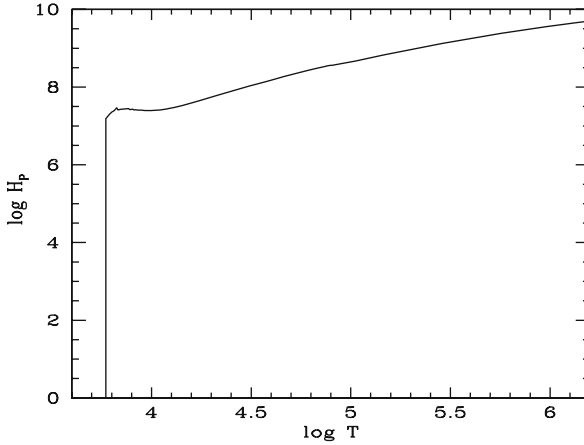
Fig. 5.1 The pressure scale height H_P in the outer solar layers. The value of $\log(H_P)$ is shown as a function of $\log T$, where H_P is expressed in cm. $T = 10^6$ K at $M_r/M_\odot = 0.995$, $R/R_\odot = 0.846$, see also Fig. 7.2

$$\nabla < \nabla_{\text{int}} + \frac{\varphi}{\delta} \nabla_\mu \ . \tag{5.26}$$

This is known as the Ledoux criterion for convection. In a chemically homogeneous medium, the stability criterion becomes

$$\nabla < \nabla_{\text{int}} \ , \tag{5.27}$$

which is known as the Schwarzschild criterion. A μ stratification favors convective stability, since $d\ln\mu/d\ln P > 0$ due to nuclear reactions producing heavier elements in stellar interiors. There are debates since more than 50 years as to whether the Ledoux or Schwarzschild criterion must be used in stellar evolution. We come back to this point in Sect. 6.2.

5.1.3   The Four T Gradients

We may consider four gradients:

1. ∇ the external gradient, where the index "ext" is omitted.
2. ∇_{int} the interior gradient in a moving fluid element.
3. One may also define an adiabatic gradient ∇_{ad}, which is the internal gradient when the moving cell does not exchange heat with the surrounding medium. According to Sect. 3.3.5, one has

$$\nabla_{\text{ad}} = \left(\frac{\partial \ln T}{\partial \ln P}\right)_{\text{ad}} = \frac{P\delta}{C_P \varrho T} \ . \tag{5.28}$$

The various ∇ are positive quantities since P and T grow simultaneously. ∇_{int} is larger than ∇_{ad}, i.e., the adiabatic gradient is flatter, because the temperature in an upward moving cell decreases faster due to heat losses than if the cell is adiabatic.

4. A radiative gradient ∇_{rad} can be defined. Let us first write the external T gradient as follows

$$\frac{dT}{dr} = \frac{T\,d\ln T}{d\ln P}\frac{d\ln P}{dr} = \frac{T\,\nabla}{-H_P} . \tag{5.29}$$

One can write the radiative flux (3.17) as

$$F_{\mathrm{rad}} = -\frac{4\,ac\,T^3}{3\,\kappa\varrho}\frac{dT}{dr} = \frac{4\,ac\,T^4}{3\,\kappa\varrho}\frac{\nabla}{H_P} . \tag{5.30}$$

The radiative gradient ∇_{rad} is defined as the thermal gradient which would be necessary to carry the sum $F_{\mathrm{tot}} = F_{\mathrm{conv}} + F_{\mathrm{rad}}$ of the radiative and convective fluxes by radiation only

$$F_{\mathrm{tot}} = F_{\mathrm{conv}} + F_{\mathrm{rad}} \equiv \frac{4\,ac\,T^4}{3\,\kappa\varrho}\frac{\nabla_{\mathrm{rad}}}{H_P} . \tag{5.31}$$

This is a fictitious, but calculable, gradient. In a convective zone, it is evidently larger than the other gradients, since in order to carry both the convective and the radiative energies by radiation only, one would need a steeper T gradient. From (5.31) and (C. 8), one has

$$\nabla_{\mathrm{rad}} = \frac{3\,\kappa\varrho\,H_P}{4\,ac\,T^4}\frac{L_r}{4\,\pi\,r^2} . \tag{5.32}$$

With H_P (5.24) and hydrostatic equilibrium (1.5), this can be written

$$\nabla_{\mathrm{rad}} = \frac{3}{16\,\pi\,acG}\frac{\kappa L_r P}{M_r T^4} . \tag{5.33}$$

In a convective zone, the following relations of order apply

$$\nabla_{\mathrm{rad}} > \nabla > \nabla_{\mathrm{int}} > \nabla_{\mathrm{ad}} . \tag{5.34}$$

The first inequality is just explained above, the second is the criterion (5.27) for convection and the third one expresses that the adiabatic gradient is flatter. Among these four gradients, two of them, ∇_{rad} (5.32) and ∇_{ad} (3.76) are easily calculated. The other two are discussed below, in stellar interiors (Sect. 5.3) and in the outer layers (Sect. 5.4).

5.1.3.1   Pressure- and Density-Scale Heights

The pressure scale height is defined by (5.24). In a similar way, one can define a density-scale height

$$H_\varrho \equiv -\frac{dr}{d\varrho}\,\varrho \,. \tag{5.35}$$

From the general equation of state (3.60), we have

$$-\frac{dP}{P} = -\frac{1}{\alpha}\frac{d\varrho}{\varrho} - \frac{\delta}{\alpha}\frac{dT}{T} + \frac{\varphi}{\alpha}\frac{d\mu}{\mu} \,. \tag{5.36}$$

With H_P defined by (5.24), we get

$$H_P^{-1} = \frac{H_\varrho^{-1}}{\alpha}\left(1 + \delta\frac{d\ln T}{d\ln\varrho} - \varphi\frac{d\ln\mu}{d\ln\varrho}\right) = \frac{H_\varrho^{-1}}{\alpha}\left(1 + \delta\frac{H_\varrho\nabla}{H_P} - \varphi\frac{\nabla_\mu H_\varrho}{H_P}\right), \tag{5.37}$$

with $\nabla = d\ln T/d\ln P$ and $\nabla_\mu = d\ln\mu/d\ln P$. We thus have

$$1 = \frac{H_P}{\alpha H_\varrho} + \frac{\delta\nabla}{\alpha} - \frac{\varphi\nabla_\mu}{\alpha} \quad \text{or} \quad H_P = H_\varrho\left(\alpha - \delta\nabla + \varphi\nabla_\mu\right) \,. \tag{5.38}$$

5.2   Mixing-Length Theory for the Convective Flux

The convective motions participate to the transport of energy, in addition to radiation which is always present. At a level r, the average flux results from the motions of the cells which have an average velocity $\overline{v}$ and an average T excess $\overline{\Delta T}$. Both the hotter upward moving fluid elements and the cooler downward moving elements contribute to the outward transport of energy. The convective flux is

$$F_{\text{conv}} = C_P\varrho\,\overline{v}\,\overline{\Delta T} \tag{5.39}$$

where C_P is the specific heat per unit of mass at constant pressure. One takes C_P because we consider subsonic convective motions, which implies that the cells are in pressure equilibrium with the surrounding medium. The product $C_P\Delta T$ is an energy per unit of mass, multiplied by ϱ and a vertical velocity, this is an energy per units of horizontal surface and time, i.e., a flux.

   Convection is essentially a non-local process: at a given level in the star the convective flux and other properties are determined by what happens in the surrounding levels. Fluid elements have a certain spectrum of sizes, velocities and temperatures and one assumes an average for each of these quantities. In most stellar models, a local formulation called the "mixing-length theory" (MLT) is used assuming that the properties of convection depend only on local conditions. This has great advantages for the computations, however it is a crude oversimplification from the point of view

of physics. Other theories have been developed (Chap. 6). The basic hypothesis of the MLT is that the fluid elements can be represented by an average cell, which moves over an average vertical distance ℓ called the mixing length, over which the cell keeps its identity before dissolving in the ambient medium and delivering its energy excess. Usually, the mixing-length ℓ is taken to be of the order of the pressure scale height H_P,

$$\ell = \alpha H_P , \tag{5.40}$$

with a coefficient α of the order of unity (this is not the α of the equation of state!). The reason for $\alpha \sim 1$ is, on one side, that it is unlikely that a convective cell keeps its identity over several scale heights, on the other side, if α would be $\ll 1$, there would be little significant fluid motions. The radius of the Sun and of red giants is sensitive to the value of α and current estimates lead to a value of $\alpha \approx 1.6$.

For a motion over the distance ℓ, the average velocity $\bar{v}$ and the T excess are estimated in $\ell/2$, for example, $\overline{\Delta T} \approx \Delta T(\ell/2)$,

$$\overline{\Delta T} \approx \left(\frac{dT_{\text{int}}}{dr} - \frac{dT}{dr} \right) \frac{\ell}{2} = (\nabla - \nabla_{\text{int}}) \frac{T}{H_P} \frac{\ell}{2} , \tag{5.41}$$

where one has used (5.29), ∇ is the external value. To get the velocity $\bar{v} = v(\ell/2)$, one needs first the density excess

$$\Delta\varrho(\ell/2) \approx \frac{d}{dr}(\Delta\varrho) \frac{\ell}{2} = -\varrho \, \delta \left(\frac{d \ln T_{\text{int}}}{dr} - \frac{d \ln T_{\text{ext}}}{dr} \right) \frac{\ell}{2}$$

$$= \varrho \, \delta \, (\nabla_{\text{int}} - \nabla) \frac{\ell}{2 H_P} . \tag{5.42}$$

One ignores the possible change of μ during the motion. The external and internal pressures are assumed the same, which is right for subsonic convection. The force $\mathcal{F}$ along the radial direction per unit volume is $-g\Delta\varrho$. The mean value is taken as half the value at the middle of ℓ (Fig. 5.2),

$$\overline{\mathcal{F}} \approx \frac{1}{2} \mathcal{F}(\ell/2) \approx -\frac{1}{2} g \Delta\varrho(\ell/2) = -\frac{1}{2} g \varrho \, \delta \, (\nabla_{\text{int}} - \nabla) \frac{\ell}{2 H_P} . \tag{5.43}$$

The buoyancy work up to the distance $\ell/2$ is $\overline{\mathcal{F}} \times (\ell/2)$. In the MLT, it is assumed that a fraction $1/2$ of this work is converted into the kinetic energy of the fluid element, i.e.,

$$\frac{1}{2} \left(\overline{\mathcal{F}} \frac{\ell}{2} \right) = \frac{1}{2} \varrho \, \bar{v}^2 . \tag{5.44}$$

The rest of the buoyancy work is assumed to be dissipated on the way. This gives for the average convective velocity
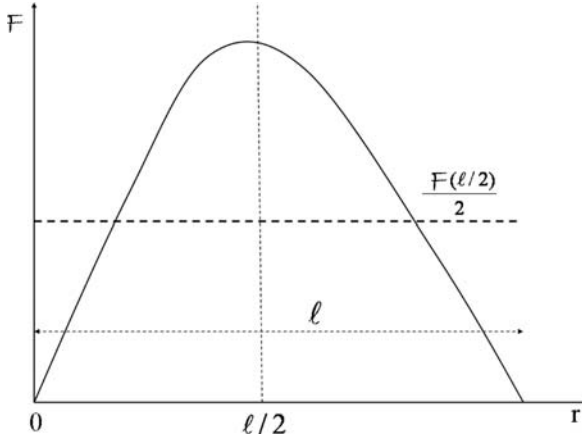
Fig. 5.2 Schematic representation of the force on a moving element

$$\bar{v}^2 = g\,\delta\,(\nabla - \nabla_{\text{int}})\,\frac{\ell^2}{8H_P}\,. \tag{5.45}$$

With the expressions of $\overline{\Delta T}$ and $\bar{v}$, the convective flux becomes

$$F_{\text{conv}} = C_P\varrho\,T\,(g\,\delta)^{\frac{1}{2}}\,(\nabla - \nabla_{\text{int}})^{\frac{3}{2}}\,\frac{\ell^2}{4\sqrt{2}H_P^{\frac{3}{2}}}\,. \tag{5.46}$$

This expression gives the convective flux as a function of the local variables. The various factors $1/2$, which enter at different places, are very uncertain, but even more critical is the averaging of the properties of the fluid.

5.2.1 Orders of Magnitude

5.2.1.1 In Stellar Interiors

We first examine the relevant orders of magnitude of convection in stellar interiors. To simplify, let us consider a point at $r = R_\odot/2$ and $M_r = M_\odot/2$ in the Sun. Let us assume that the whole flux is carried by convection and search the difference $(dT_{\text{int}}/dr) - (dT/dr)$ which would be necessary for that. From (5.46), we have

$$\left(\frac{dT_{\text{int}}}{dr} - \frac{dT}{dr}\right) = \left(\frac{F_{\text{conv}}\,\sqrt{2}\,4}{\varrho\,C_P\left(\frac{g\delta}{T}\right)^{\frac{1}{2}}\ell^2}\right)^{\frac{2}{3}}\,. \tag{5.47}$$

At the considered location, one has $F_{\text{conv}} \approx L_{\odot}/(\pi R_{\odot}^2) \approx 2.5 \times 10^{11}$ erg cm^{-2} s^{-1}, $g \approx 2\, GM_{\odot}/R_{\odot}^2 \approx 5.5 \times 10^4$ cm s^{-2} and we take $\varrho \approx 10^2$ g cm^{-3}, $T \approx 10^7$ K, $\delta = 1$, $\ell \approx 0.1\, R_{\odot} \approx 7 \times 10^9$ cm. This leads to a difference between the internal and the external T gradients $(dT_{\text{int}}/dr - dT/dr) = 5.1 \times 10^{-12}$ K cm^{-1}. This value is an overestimate, since all the energy would never be carried by convection only. The average T gradient in a star like the Sun is of the order of $dT/dr \sim T_c/R \sim 1.6 \times 10^7$ K$/(7 \times 10^{10}$ cm$) \sim 2.3 \times 10^{-4}$ K cm^{-1}. Thus, the difference of the internal and external T gradients is a fraction of the order of 10^{-8} of the average T gradient.

The average ΔT necessary to carry the flux would be

$$\overline{\Delta T} \approx \left(\frac{dT_{\text{int}}}{dr} - \frac{dT}{dr} \right) \frac{\ell}{2} = 5.1 \times 10^{-12} \frac{7 \times 10^9}{2} = 1.8 \cdot 10^{-2}\,\text{K}. \qquad (5.48)$$

Convective cells with an excess ΔT of only $\sim 10^{-2}$ K are able to carry the whole stellar flux in an ambient medium at $T \approx 10^7$ K! The values of ΔT are larger in more massive stars (Fig. 6.1), being up to a few degrees, but the conclusions are the same: the outgoing flux is a very small fraction of the thermal energy content of the star (a result in agreement with $I_1/I_0 \ll 1$ in Appendix C.1.1). The very small $\overline{\Delta T}$ is a major result which leads to great simplifications: convection is essentially adiabatic in stellar interiors.

One may also estimate the average velocity given by (5.45) and get $\bar{v} \approx 4.1 \times 10^2$ cm s^{-1}. Larger values are obtained in more massive stars (Fig. 6.1), up to a few 10^2 m s^{-1}. The "turnover time", i.e., the travel time of the cell over the distance ℓ is

$$t_{\text{turnover}} = \frac{\ell}{\bar{v}} \approx 1.7 \times 10^7 \text{ s} \approx 2 \times 10^2 \text{ days for the Sun}. \qquad (5.49)$$

This timescale is very short with respect to the MS lifetime. This implies that during most of evolution the convective mixing may be considered as instantaneous and that the convective zones are chemically homogeneous. This is however not true when the evolutionary timescales become of the same order as the convective timescale (Sect. 6.3).

5.2.1.2   External Layers

The same kind of estimate for $r = R_{\odot}$, $M_r = M_{\odot}$ and $L_r = L_{\odot}$, with a temperature $T \approx 10^4$ K, an average density of 10^{-6} g cm^{-3} and a mixing-length $\ell \approx H_P \approx 200$ km leads to

$$\left| \frac{dT_{\text{int}}}{dr} - \frac{dT}{dr} \right| \approx 10^{-4}\,\text{K cm}^{-1}, \qquad (5.50)$$

and $\Delta T \approx 10^3$ K. The average convective velocity is about 1 km s^{-1} and the turnover time of convective motions is about 5 min. Figure 5.3 illustrates the value of the
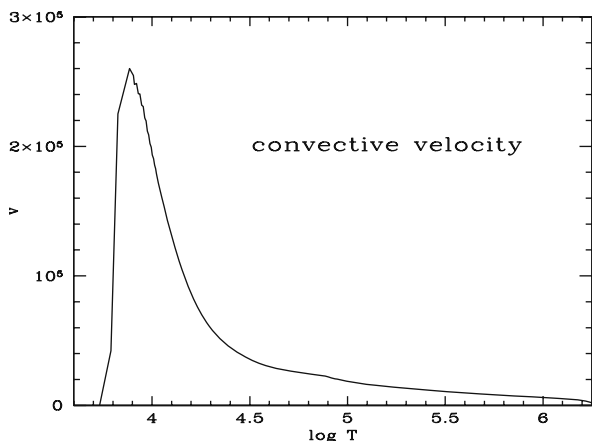
Fig. 5.3 Variation of the average velocity (in cm s^{-1}) of convective motions as a function of T in the outer solar layers. The velocity is maximum in the region of partial H ionization, where it reaches up to 30% of the sound velocity. See also Fig. 7.2

average convective velocity in the solar envelope. It peaks at 2.6 km s^{-1}. According to (5.45), the velocity reaches a maximum in the region, where the parameters δ and $\nabla - \nabla_{\text{int}}$ are the highest (cf. Figs. 5.5 and 7.5). This corresponds to the opacity peak, because a high opacity favors a large difference between T_{int} and T_{ext}, which in turn drives fast motions.

The excess ΔT is not negligible compared to the local T. Thus, convection in the outer layers is not adiabatic, which requires an appropriate treatment. The short turnover time determines the main frequencies observed in helioseismology. The reason for the difference in the convection properties between the stellar interior and exterior is due [147, 610] to the differences of density (factor of $\sim 10^8$), of H_P and T (factor of $\sim 10^3$).

5.3   Convection in Stellar Interiors

We have seen that the average temperature excess $\overline{\Delta T}$ of the convective fluid elements with respect to the surrounding medium is about 10^{-2} K in stellar interiors where the temperature is of the order of millions degrees. Thus, the radiative energy losses from the convective fluid elements are negligible and the convective motions are essentially adiabatic. What do we mean by stellar interiors? A convenient rule is to consider as interior the layers where H and He are fully ionized (cf. Fig. 7.2). The adiabatic convection in stellar interiors implies that the T gradient is equal to the adiabatic gradient,

$$\nabla_{\text{int}} = \nabla_{\text{ad}} . \tag{5.51}$$

In addition, from the previous section one has

$$\frac{\nabla - \nabla_{\mathrm{int}}}{\nabla} \approx 10^{-8} \,, \tag{5.52}$$

which means that at this level of approximation, the ambient gradient ∇ in the convective medium is equal to the internal gradient, which is itself equal to the adiabatic gradient. Thus, the three gradients are equal,

$$\nabla = \nabla_{\mathrm{int}} = \nabla_{\mathrm{ad}} \,. \tag{5.53}$$

In a convective zone, the inequalities (5.34) reduce to

$$\nabla_{\mathrm{rad}} > \nabla_{\mathrm{ad}} \,. \tag{5.54}$$

This is the Schwarzschild criterion in stellar interiors. Similarly the Ledoux criterion for convective instability in the stellar interior is

$$\nabla_{\mathrm{rad}} > \nabla_{\mathrm{ad}} + \frac{\varphi}{\delta} \nabla \mu \,. \tag{5.55}$$

In a radiative zone, one just has $\nabla_{\mathrm{rad}} = \nabla$ since the total flux, which depends on ∇_{rad}, is equal to the radiative flux, which depends on ∇. One also has $\nabla_{\mathrm{int}} = \nabla_{\mathrm{ad}}$ since the fluid motions are adiabatic. Thus, in a radiative zone, one has $\nabla_{\mathrm{rad}} < \nabla_{\mathrm{ad}}$. We have thus obtained the criteria for convection and for stability with respect to convection. The expression of ∇_{rad} is given by (5.32), ∇_{ad} is given by (3.76) in general and by (3.77) for a mono-atomic perfect gas. Figure 5.4 illustrates the typical course of ∇_{rad} and ∇_{ad} in a massive star. We notice the presence of a convective core and of an intermediate convective region in regions where $\nabla_{\mathrm{rad}} > \nabla_{\mathrm{ad}}$.

The equation expressing the temperature gradient in a convective zone is

$$\frac{d\ln T}{d\ln P} = \frac{P}{T}\frac{dT}{dP} = \nabla_{\mathrm{ad}} \quad \mathrm{thus} \quad \frac{dT}{dr} = \frac{T}{P}\frac{dP}{dr}\nabla_{\mathrm{ad}} \,. \tag{5.56}$$

In a medium of mono-atomic perfect gas, $\nabla_{\mathrm{ad}} = (\gamma_{\mathrm{g}} - 1)/\gamma_{\mathrm{g}}$, which gives $\nabla_{\mathrm{ad}} = 2/5$ for a perfect gas with $\gamma_{\mathrm{g}} = 5/3$. For a general equation of state $\nabla_{\mathrm{ad}} = P\delta/(C_P \varrho T)$ according to (7.57). One may write with account of (1.15)

$$\frac{dT}{dM_r} = -\frac{GM_r}{4\pi r^4}\frac{T}{P}\nabla \,, \tag{5.57}$$

with $\nabla = \nabla_{\mathrm{ad}}$ in a convective zone and $\nabla = \nabla_{\mathrm{rad}}$ in a radiative zone. We have obtained the T gradient in convective interiors without other developments. Difficulties come near the boundaries of convective zones, with the problem of overshooting (Sect. 6.1) and in semiconvective regions (Sect. 6.2).

In case of mono-atomic perfect gas with $\nabla_{\mathrm{ad}} = 2/5$, one has the following relation between structural variables in internal convective regions
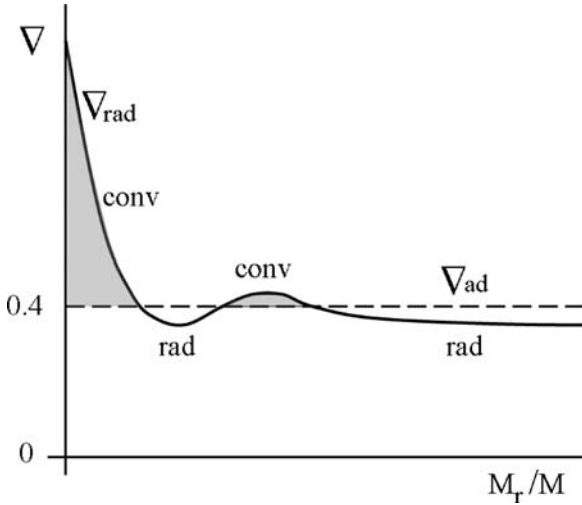
Fig. 5.4 Schematic representation of the course of ∇_{rad} and ∇_{ad} as a function of the mass coordinate in a massive star. Convection occurs in *gray areas*

$$P \sim T^{\frac{5}{2}} \;,\; \varrho \sim T^{\frac{3}{2}} \text{ and } P \sim \varrho^{\frac{5}{3}} \;. \tag{5.58}$$

These relations are typical of a polytrope of index $n = 3/2$ (Sect. 24.5). In this case, simple relations between the variables exist. This case corresponds to an extremum of entropy (Appendix C.4.2).

The Brunt–Väisälä frequency (5.23) becomes in the adiabatic interior

$$N_{\text{ad}}^2 = \frac{g\,\delta}{H_P}\left(\nabla_{\text{ad}} - \nabla + \frac{\varphi}{\delta}\nabla_\mu\right)\;. \tag{5.59}$$

with (to be compared to 5.25)

$$N_{\text{ad}}^2 = N_{T,\text{ad}}^2 + N_\mu^2\;,$$

$$\text{with } N_{T,\text{ad}}^2 = \frac{g\,\delta}{H_P}\left(\nabla_{\text{ad}} - \nabla\right), \quad \text{and} \quad N_\mu^2 = \frac{g\,\varphi}{H_P}\nabla_\mu\;, \tag{5.60}$$

N_μ^2 being unmodified. With $\Gamma_1 = (\partial \ln P / \partial \ln \varrho)_{\text{ad}}$ ((1.64) and (7.57)), we can also write directly from (5.7)

$$N_{\text{ad}}^2 = g\left(\frac{1}{\Gamma_1 P}\frac{dP}{dr} - \frac{1}{\varrho}\frac{d\varrho}{dr}\right)\;. \tag{5.61}$$

The first term on the right is the adiabatic internal density gradient, while the second is the external density gradient. In general, ∇ in (5.60) is just ∇_{rad}. However, the presence of shear, turbulence, semiconvection, etc... in the radiative zone may produce some small changes of the T gradient.

5.4   Non-adiabatic Convection

In convective stellar envelopes, the excess $\overline{\Delta T}$ is not negligible with respect to the local temperature and convection is no longer adiabatic. In practice, one generally considers that a non-adiabatic treatment is required in regions where the ionizations of H and He are incomplete.

5.4.1   Radiative Losses

Contrarily to (5.53), one has $\nabla \neq \nabla_{\text{int}} \neq \nabla_{\text{ad}}$ and the first two gradients need to be calculated explicitly. The energy lost by a turbulent eddy of diameter ℓ, temperature excess $\overline{\Delta T}$, surface Σ during its travel time $\Delta t = \ell / \overline{v}$ is from (3.17)

$$\Delta U_{\text{lost}} = \frac{4\,ac\,T^3}{3\,\kappa\varrho} \frac{\overline{\Delta T}}{\ell/2} \Delta t \, \Sigma \,. \tag{5.62}$$

The cell is assumed optically thick. The size of the convective element is taken equal to ℓ, the mixing length. This choice is rather arbitrary, however it avoids the introduction of several length scales. For $\overline{\Delta T}$ one takes (5.41). The energy lost by volume unity, with a ratio $\Sigma/V = 6/\ell$ for a sphere, is

$$\frac{\Delta U_{\text{lost}}}{V} = \frac{4\,ac\,T^3}{3\,\kappa\varrho} \left(\nabla - \nabla_{\text{int}} \right) \frac{T}{H_P} \frac{6}{\overline{v}} \,. \tag{5.63}$$

This loss of energy is made at the expense $\varrho\,\Delta q$ of the internal energy by volume unity, where Δq is given by (3.63)

$$\varrho\,\Delta q = \varrho\,C_P\,\Delta T + \frac{\varrho\,C_P T \nabla_{\text{ad}}}{P} \frac{dP}{dr} \Delta r = \varrho\,C_P T \left(\nabla_{\text{int}} - \nabla_{\text{ad}} \right) \frac{\ell}{H_P} \,, \tag{5.64}$$

where one uses (3.76) to express δ and (5.29) for the T gradient. From the equality of (5.63) and (5.64), one gets

$$\frac{3\varrho^2 C_P\,\kappa}{4\,ac\,T^3} \frac{\overline{v}\ell}{6} = \frac{\nabla - \nabla_{\text{int}}}{\nabla_{\text{int}} - \nabla_{\text{ad}}} \,. \tag{5.65}$$

The meaning of this ratio is interesting. It is the ratio, often called Γ (here it is not the Eddington factor!) of the thermal energy $C_P \varrho\,\Delta T_{\text{max}}V$ transported by the fluid elements to the radiative losses (5.62) on the way. ΔT_{max} is the T excess at the end of the path. One takes $\Delta T_{\text{max}} = 2\,\overline{\Delta T}$, thus

$$\Gamma = \frac{\text{energy transported}}{\text{energy lost}} = \frac{3\varrho^2 C_P\,\kappa}{4\,ac\,T^3} \frac{\overline{v}\ell}{6} = \frac{\overline{v}\ell}{6K} \,. \tag{5.66}$$

Γ is often called "the efficiency of convection", it is related to the Peclet number $\mathcal{P}e$ defined in Appendix B.5.3. From (5.66) and (5.65), one also derives an expression which is useful in several cases

$$\nabla_{\text{int}} - \nabla = \frac{\Gamma}{\Gamma + 1} \left(\nabla_{\text{ad}} - \nabla \right) . \tag{5.67}$$

With account of (5.25) and (5.60), we have

$$N_T^2 = \frac{\Gamma}{\Gamma + 1} N_{T,\text{ad}}^2 . \tag{5.68}$$

Let us note that a factor $2\ell/9$ is frequently used in convection theory, instead of $\ell/6$ for the ratio V/Σ given above. For consistency with classical references in literature such as [147], [610] or [285], we also adopt here the ratio $V/\Sigma = 2\ell/9$ in the treatment of non-adiabatic convection (the author is aware that this may continue for ever...). With this choice, (5.65) becomes

$$\frac{\varrho^2 C_P \kappa \bar{v} \ell}{6 a c T^3} = \frac{\nabla - \nabla_{\text{int}}}{\nabla_{\text{int}} - \nabla_{\text{ad}}} = \Gamma . \tag{5.69}$$

One expresses $\bar{v}$ with (5.45) and gets

$$\frac{1}{2U} = \frac{(\nabla - \nabla_{\text{int}})^{\frac{1}{2}}}{\nabla_{\text{int}} - \nabla_{\text{ad}}} , \tag{5.70}$$

$$\text{with} \quad U = \frac{3 a c T^3}{\varrho^2 C_P \kappa \ell^2} \left(\frac{8 H_P}{g \delta} \right)^{\frac{1}{2}} . \tag{5.71}$$

A second equation is obtained by expressing $F_{\text{conv}} = F_{\text{tot}} - F_{\text{rad}}$ with (5.46), (5.30) and (5.31)

$$\nabla_{\text{rad}} - \nabla = \frac{9}{8U} \left(\nabla - \nabla_{\text{int}} \right)^{\frac{3}{2}} . \tag{5.72}$$

Expressions (5.70) and (5.72) form a system of two equations with two unknown quantities ∇ and ∇_{int}, i.e., the structural gradient and the internal gradient of moving eddies. The solutions are given in Sect. 5.4.3.

5.4.2 Thermal Adjustment Timescale

The timescale t_{therm} for thermal adjustment is an important timescale. To estimate it, we consider a spherical bubble of volume V and diameter d with an average excess ΔT with respect to the surrounding. The timescale t_{therm} is given by the ratio of the excess of thermal energy content $C_P \Delta T_{\text{max}} \varrho V$ with respect to the radiative energy

loss per unit of time, where $\Delta T_{\max}$ is the temperature at the end of the path of the fluid element. We take $\Delta T_{\max} = 2\Delta T$

$$t_{\text{therm}} = \frac{C_P \, 2\Delta T \, \varrho \, V}{\frac{4acT^3}{3\kappa\varrho} \frac{\Delta T}{d/2} \, \Sigma} . \tag{5.73}$$

The ratio of the volume V to the surface Σ of a spherical bubble is $V/\Sigma = d/6$ and one has

$$t_{\text{therm}} = \frac{C_P \varrho^2 \kappa d^2}{8acT^3} = \frac{d^2}{6K} , \tag{5.74}$$

with K the thermal diffusivity (3.46). Γ as given above (5.66), with account of the spherical geometry of the fluid element, is related to the Peclet number $\mathcal{P}e$, which is usually defined as just the ratio $\mathcal{P}e = v\ell/K$, with no account of a particular geometry (see Appendix B.5.3).

5.4.3 Solutions for Non-adiabatic Convection

We follow here the developments by Hofmeister et al. [253] (see also [147, 285, 610]). Expression (5.70) is of the second degree in ∇_{int}, it can be written

$$\nabla_{\text{int}} = \nabla_{\text{ad}} - 2U^2 + 2U \sqrt{(\nabla - \nabla_{\text{ad}}) + U^2} . \tag{5.75}$$

With (5.70) again, it gives

$$(\nabla - \nabla_{\text{int}})^{\frac{1}{2}} = \sqrt{(\nabla - \nabla_{\text{ad}}) + U^2} - U , \tag{5.76}$$

and with (5.72)

$$\nabla_{\text{rad}} - \nabla = \frac{9}{8U} \left(\sqrt{(\nabla - \nabla_{\text{ad}}) + U^2} - U \right)^3 . \tag{5.77}$$

The desired solution ∇ is given by the solution of this equation in terms of U and $(\nabla_{\text{rad}} - \nabla_{\text{ad}})$, it can also be written

$$(\nabla - \nabla_{\text{ad}}) - (\nabla_{\text{rad}} - \nabla_{\text{ad}}) + \frac{9}{8U} \left(\sqrt{(\nabla - \nabla_{\text{ad}}) + U^2} - U \right)^3 = 0. \tag{5.78}$$

This cubic can also be expressed with $x = \sqrt{(\nabla - \nabla_{\text{ad}}) + U^2}$

$$x^3 - \frac{19}{9} U x^2 + 3U^2 x - \left(\frac{17}{9} U^3 + \frac{8}{9} U (\nabla_{\text{rad}} - \nabla_{\text{ad}}) \right) = 0 . \tag{5.79}$$

U is positive and there is only one real root x_1. The solution for ∇ is

$$\nabla = \nabla_{ad} + x_1^2 - U^2 \,, \tag{5.80}$$

with the following root x_1 for the above cubic equation [253]

$$x_1^2 = \frac{1}{W^2}\left(W^2 + \frac{19}{27}WU - \frac{E}{3}\right)^2 \quad \text{with} \quad W = \left(\frac{1}{2}A + \sqrt{D}\right)^{\frac{1}{3}}, \tag{5.81}$$

$$\frac{1}{2}A = \left\{\frac{4}{9}(\nabla_{rad} - \nabla_{ad}) + \left[\left(\frac{19}{27}\right)^3 - \frac{1}{9}\right]U^2\right\}U \,, \tag{5.82}$$

$$\text{and} \quad D = \left(\frac{A}{2}\right)^2 + \left(\frac{E}{3}\right)^3 \quad \text{and} \quad \frac{E}{3} = \frac{368}{729}U^2 \,. \tag{5.83}$$

This determines ∇ from (5.81) and then ∇_{int} is given by (5.75). These gradients allow us to express the velocity (5.45) and the convective flux (5.46), with the same expressions as before (Sect. 5.2).

5.4.4 Limiting Cases, Fraction Carried by Convection

Figure 5.5 shows the results of the application of the above development for the solar convective envelope. The gradients ∇ and ∇_{int} are higher than the adiabatic gradient in a very superficial zone corresponding to the velocity peak (Fig. 5.3) and to the partial ionization of hydrogen (Fig. 7.2). However, the various gradients converge rather rapidly as T increases. The value of ∇_{rad} is much higher, reaching values up to $\sim 2 \times 10^5$ due to the large opacity in the region of partial H and He ionizations (because of the large opacity, this T gradient needs to be very steep to carry the total flux).

5.4.4.1 Limits for $\Gamma \to \infty$ or 0

The full solution is applied to convection in stellar envelope. The solution admits two limiting cases:

– High convective efficiency with $\Gamma \to \infty$: from (5.69) this implies that $\nabla_{int} \to \nabla_{ad}$, from (5.70) one also has $U \to 0$. The radiative losses are negligible and convection is adiabatic. The high convective efficiency is favored by high densities in deep stellar interiors (5.69) and by the large ℓ, not compensated by the change of T in (5.69). In this limiting case, one is brought back to the simple solutions of Sect. 5.3, which are free from the MLT uncertainties.

   The case where the nuclear energy production is significant in convective eddies has been considered by [147, 610]. This energy production has generally a negligible effect since convection in the cores is adiabatic (the rate of energy
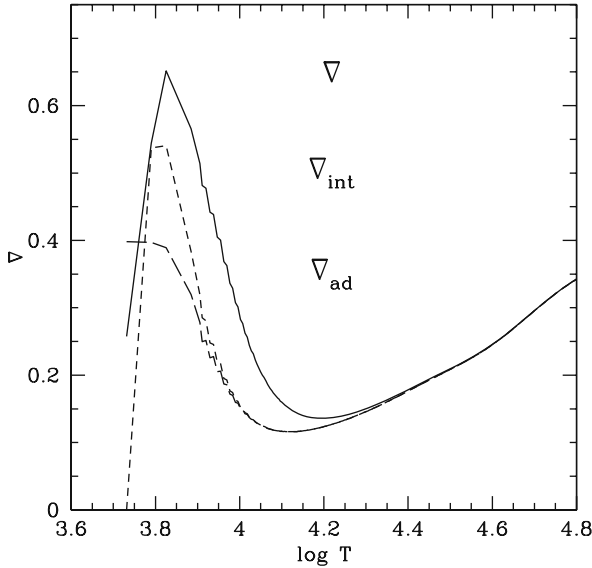
Fig. 5.5 Variations of ∇, ∇_{int}, ∇_{ad} in the outer part of the convective envelope of the Sun. ∇_{rad} is not represented here, it reaches a peak at 2×10^5 (!) for $\log T = 4.6$; at $\log T = 4.8$, it is 9×10^4 and it joins the common curve near $\log T = 6.2$. See also Fig. 7.2

production is very small compared to the thermal content). This does not affect the core limit, since near the edge of the convective cores, the energy production is in general very small.

– Zero convective efficiency, i.e., $\Gamma \to 0$: from (5.69) one has $\nabla_{\mathrm{int}} \to \nabla$, from (5.70) $U \to \infty$. From (5.72), one sees that $\nabla_{\mathrm{rad}} \to \nabla$, which implies that $F_{\mathrm{tot}} \to F_{\mathrm{rad}}$ according to (5.31) and (5.30). This means that convection transports a negligible energy, a situation favored by low densities. In this case, the above developments for non-adiabatic convection are necessary and they are affected by the uncertainties of the theory.

Figure 5.6 shows the variations of Γ in the outer solar layers. The convective efficiency tends toward zero at the surface. It is above unity between $T = 3 \times 10^4$ K and 1.5×10^5 K. One notes that Γ is rather small at the basis of the convective zone, which is located at about $\log T = 6.0$. The reason is the following one. The ratio ϱ/T^3 in (5.69) is about constant in a convective zone (cf. 5.58), ℓ increases by about 2 orders of a magnitude toward the interior, while $\bar{v}$ decreases by a bit less of this amount (Fig. 5.3). Thus, the variations of Γ mainly correspond to those of the opacity κ, and κ decreases by 2–3 orders of magnitude according to Fig. 8.4. The result is that the gradients ∇, ∇_{int} and ∇_{ad} are close to each other as typical in stellar interiors.
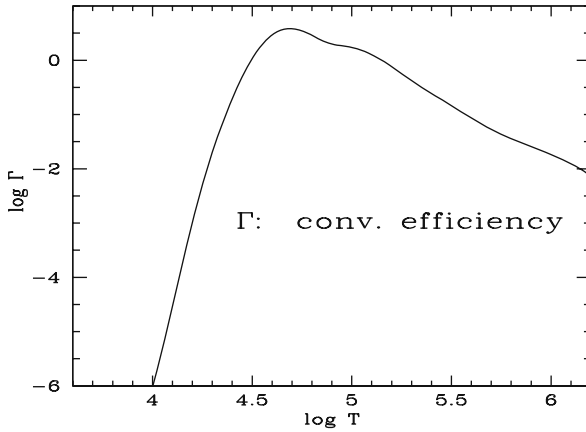
Fig. 5.6 Variation of the convective efficiency $\Gamma = \mathcal{P}e/6$ in the outer solar layers, calculated with (5.69)

5.4.4.2 Fraction Carried by the Convective Flux

It is often considered that adiabacy implies that most of the energy is carried by convection. This is not true! Adiabatic convection means that convection transports the maximum energy that it can do, i.e., without radiative losses. The ratio of the convective to the total flux is

$$\frac{F_{\text{conv}}}{F_{\text{tot}}} = \frac{F_{\text{tot}} - F_{\text{rad}}}{F_{\text{tot}}} = \frac{\nabla_{\text{rad}} - \nabla}{\nabla_{\text{rad}}} \; . \tag{5.84}$$

In the adiabatic case of the deep interior, one has (5.53), thus $F_{\text{conv}}/F_{\text{tot}} \approx (\nabla_{\text{rad}} - \nabla_{\text{ad}})/\nabla_{\text{rad}}$. This shows that the ratio of the convective to the total flux depends on the relative excess of ∇_{rad} with respect to ∇_{ad}. The convective flux represents a variable fraction of the total flux. In an example of non-local convection below (Fig. 6.1), we see that $F_{\text{conv}}/F_{\text{tot}}$ varies between 65% near the center and 0% at the edge of the core. Thus, adiabacy does not imply energy transport by convection only.

In the non-adiabatic case, it is only when Γ is extremely small, like at the solar surface or at the base of the convective envelope, that the convective transport tends to be negligible. This is well illustrated by the comparison of Figs. 5.6 and 5.7: although Γ is modest between $\log T = 5$ and 6, a high fraction of the energy is carried by the non-adiabatic convection. This is quite consistent with expression (5.84) and the fact that ∇_{rad} is enormously large with respect to ∇ or ∇_{ad} as illustrated in Fig. 5.5. Also, there is some transport of mechanical energy by convection in the outer solar layers, as well as in the extended envelopes of red-supergiant stars.
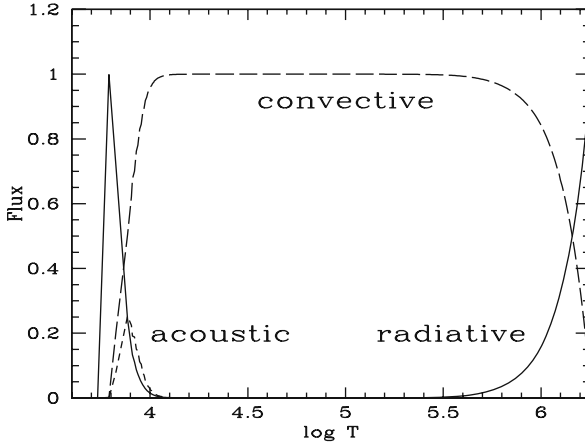
Fig. 5.7 Variation of the fraction of the radiative, convective and acoustic flux with respect to the total energy flux as a function of T in the outer solar layers

5.5 Convection in the Most Luminous Stars

In the most luminous stars, the large radiation pressure favors convection. In the cool red supergiants, in addition the large opacities lead to high convective velocities and thus large acoustic flux and pressure.

5.5.1 Convection Near the Eddington Limit

The Schwarzschild criterion for convection can also be expressed at a distance r from the center in terms of the Eddington ratio, noted here as $\Gamma_{\mathrm{Edd}}(r)$ to avoid confusion with the convective efficiency. ∇_{rad} as expressed by (5.33) becomes with the Eddington ratio $\Gamma_{\mathrm{Edd}}(r) = \kappa L_r/(4\pi c G M_r)$

$$\nabla_{\mathrm{rad}} = \frac{3}{16\pi a c G} \frac{\kappa L_r P}{M_r T^4} = \frac{\Gamma_{\mathrm{Edd}}(r)}{4(1-\beta)} \, , \tag{5.85}$$

where the various variables are at a level r, β is the ratio of the perfect gas to the total pressure. Thus, with ∇_{ad} given by (7.87) for the appropriate equation of state, the condition $\nabla_{\mathrm{rad}} > \nabla_{\mathrm{ad}}$ for convection becomes [309]

$$\Gamma_{\mathrm{Edd}}(r) > (1-\beta)\frac{32 - 24\beta}{32 - 24\beta - 3\beta^2} \, . \tag{5.86}$$

For positive β, which is always the case (see Fig. 3.5), the right-hand side of the above equation is always significantly lower than 1. Thus, if $\Gamma_{\mathrm{Edd}}(r) \to 1$,

convection appears in the concerned layers. Convection occurs in the layers reaching the Eddington limit or becoming supra-Eddington. Langer [309] emphasizes that $\Gamma_{\mathrm{Edd}}(r) \to 1$ does not imply another instability than convection in the stellar interiors. However, it does not precludes it either.

5.5.2 Density Inversion

Supra-Eddington layers do not occur in the deep interior because the opacity is not very high there. They occur in the outer convective envelope of very luminous stars, because of both the high opacity and the luminosity (Fig. 8.4). The supra-Eddington layers produce a density inversion as shown by numerical models. We can easily understand how an opacity peak generates supra-Eddington layers and a density inversion.

– First, a locally higher opacity joined to a very high radiative flux produces according to (3.15) a very negative gradient of radiation pressure dP_{rad}/dr.
– Since $g_{\mathrm{rad}} = -(1/\varrho)(dP_{\mathrm{rad}}/dr)$, g_{rad} is very large (positive) and the concerned layers become supra-Eddington, i.e., $g_{\mathrm{rad}} > g_{\mathrm{grav}}$.
– Now, the equation of hydrostatic equilibrium (1.6) can be written

$$\frac{dP_{\mathrm{gas}}}{dr} + \frac{dP_{\mathrm{rad}}}{dr} = -\varrho\, g_{\mathrm{grav}} \quad \text{or} \quad \frac{1}{\varrho}\frac{dP_{\mathrm{gas}}}{dr} = g_{\mathrm{rad}} - g_{\mathrm{grav}} \,. \tag{5.87}$$

– Since $g_{\mathrm{rad}} - g_{\mathrm{grav}} > 0$ in the supra-Eddington layers, one has $dP_{\mathrm{gas}}/dr > 0$, i.e., the gas pressure increases outward.
– The heat transfer in absence of energy sources implies that the temperature decreases outward, thus in order to have $dP_{\mathrm{gas}}/dr > 0$ one must also have $d\varrho/dr > 0$ according to the law of perfect gas. Thus, there is a density inversion over a certain mass range.

The density grows outward, before declining again in upper layers. The positive gas pressure makes an inward force opposed to the outward force of radiation in the supra-Eddington layers. Thus, hydrostatic equilibrium could in principle be maintained in the supra-Eddington layers, without an instability except convection [309]. However, the consequences of supra-Eddington layers have not been fully explored with hydrodynamic models. It is likely [48], if the density inversion is large enough in the case of very luminous stars, that an instability results with outward expansion motions.

5.5.3 Pressure and Flux of Turbulence

Turbulence contributes to the pressure support, as well to the transport of mechanical energy in stars. This particularly happens in red supergiants. The above

developments about convection suppose that the moving fluid elements are always in pressure equilibrium. This means that the timescale $t_{\text{dyn}} = \ell/c_s$ for establishing P equilibrium is much shorter than the turnover time $t_{\text{turnover}} = \ell/\bar{v}$, where c_s is the sound speed and $\bar{v}$ is the average convective velocity (5.45). This implies $\bar{v} \ll c_s$. If this not the case, convection is sonic, there are shocks and important dissipative effects in the medium.

The sound velocity is (Appendix C.26)

$$c_s \equiv \sqrt{\left(\frac{\partial P}{\partial \varrho}\right)_{\text{ad}}} = \sqrt{\frac{P}{\varrho}\left(\frac{\partial \ln P}{\partial \ln \varrho}\right)_{\text{ad}}} = \sqrt{\Gamma_1 \frac{P}{\varrho}} \,, \tag{5.88}$$

according to the definition of Γ_1 (7.57). For non-relativistic particles the ratio of the pressure P to the energy density u is equal to $2/3$ (Appendix B.3). Thus, the pressure of turbulent fluid elements is, assuming isotropy,

$$P_{\text{turb}} = \frac{2}{3} u_{\text{turb}} \approx \frac{2}{3} \frac{1}{2} \varrho \bar{v}^2 \,, \tag{5.89}$$

which is approximate, because an exact expression would need the knowledge of the spectrum of turbulence. With (5.88), P_{turb} becomes

$$P_{\text{turb}} = \frac{1}{3} \varrho c_s^2 \left(\frac{\bar{v}}{c_s}\right)^2 = \frac{1}{3} \Gamma_1 P \left(\frac{\bar{v}}{c_s}\right)^2 \,, \tag{5.90}$$

which means that the ratio of turbulent to total pressures behaves as

$$\frac{P_{\text{turb}}}{P} = \frac{1}{3} \Gamma_1 \mathcal{M}^2, \quad \text{with} \quad \mathcal{M} = \frac{\bar{v}}{c_s} \,, \tag{5.91}$$

where $\mathcal{M}$ is the Mach number of the convective motions. The typical values of the Mach number are $\sim 10^{-5}$ in convective cores and a few percents or less in convective envelopes, except at the peak of convective velocity (Fig. 5.3) where it reaches about 0.3. This implies that the turbulent pressure is negligible in convective cores, while P_{turb}/P is larger in convective envelopes. Figure 5.7 shows the various fluxes in the outer convective envelope of the Sun. The radiative flux dominates at the stellar surface and below the base of the convective envelope. The acoustic flux is significant only in a limited zone close to the surface, where the convective velocity is the highest (Fig. 5.3). In the envelopes of red supergiants, the acoustic flux is much more important; in this case the pressure of turbulence (5.90) needs to be accounted for in the mechanical equilibrium.

The gradient of the turbulent pressure produces an acceleration $\boldsymbol{g}_{\text{turb}}$

$$\boldsymbol{g}_{\text{turb}} = -\frac{1}{\varrho} \frac{dP_{\text{turb}}}{dr} \frac{\boldsymbol{r}}{r} \,. \tag{5.92}$$

If we ignore rotation, the total gravity g_{tot} is then (3.115)

$$g_{tot} = g_{grav} + g_{rad} + g_{turb} = -\frac{GM_r}{r^2}\frac{r}{r}[1 - \Gamma_r] + g_{turb}. \qquad (5.93)$$

The acceleration of turbulence can be related to the mechanical flux F_{turb} of energy due to turbulent motions,

$$F_{turb} = \vartheta \varrho \bar{v}^2 c_s, \qquad (5.94)$$

which is justified since the turbulent energy by volume unity $\varrho \bar{v}^2$ is carried at the speed of pressure perturbations (i.e., c_s), ϑ is a numerical factor which we take of the order of unity. One has

$$g_{turb} = -\frac{\alpha}{\varrho}\frac{d}{dr}\left(\varrho \bar{v}^2\right)\frac{r}{r} = -\frac{\alpha}{\vartheta \varrho}\frac{d}{dr}\left(\frac{F_{turb}}{c_s}\right)\frac{r}{r}. \qquad (5.95)$$

with $\alpha \approx 1/3$ according to (5.90). Near the stellar surface, the turbulent flux increases inward. Thus, the acceleration due to turbulence is directed outward. The limit of a zero gravity at the surface is reached for $g_{tot} = 0$, which gives
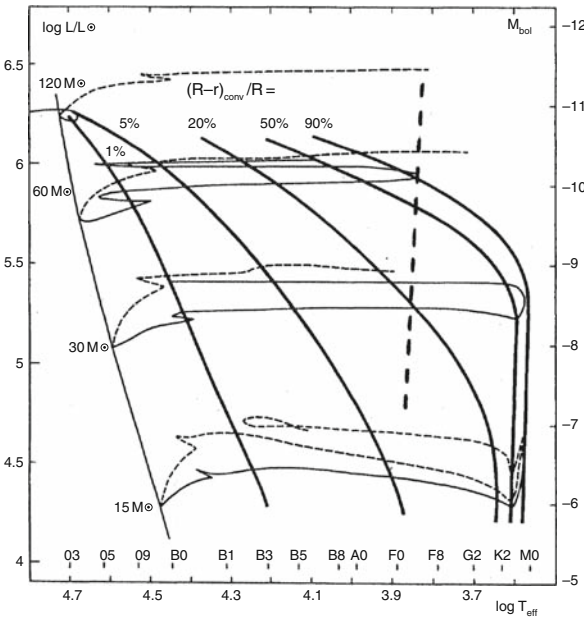
Fig. 5.8 The extent of the external convective envelope of stars in the upper part of the HR diagram, in percents of the stellar radius. Some evolutionary tracks with mass loss (*continuous lines*) and without mass loss (*broken lines*) are indicated. The heavy broken line near $\log T_{eff} = 3.85$ is the limit where cooler stars have convective velocities larger than the sound velocity. From the author [337]

$$\frac{GM_r}{r^2}\left(1-\Gamma_r\right)+\frac{\alpha}{\vartheta}\frac{d}{dr}\left(\frac{F_{\text{turb}}}{c_{\text{s}}}\right)=0 \,. \tag{5.96}$$

When the flux decreases outward, the last term is negative and is opposed to gravity. This limit may be called the "de Jager limit" [270], it says when the surface is no longer bound due to the account of the flux of turbulence and radiation pressure, while the Eddington limit is due to the radiation pressure only. When yellow- and red-supergiant stars approach this limit, their mass loss rates (due mainly to radiative effects on the dust) are strongly enhanced. One may suspect the de Jager limit to be the reason [270] why there are no red supergiants with $\log L/\text{L}_\odot \geq 5.5$, while the upper limit for early-type stars is $\log L/\text{L}_\odot \geq 6.5$. The upper observational limit of stars from the blue to the red side in the HR diagram is called the Humphreys–Davidson limit [260, 261], physically it results largely from the Eddington and de Jager limits.

Figure 5.8 shows the limit corresponding to a Mach number $\mathcal{M}=1$ for convective velocities. Cooler stars have a high turbulent pressure and a high flux of mechanical energy in their convective envelope. Figure 5.8 also shows that for massive stars, deep convective envelopes are not confined to cool stars, but are present up to spectral types B. This is due to the effect of the high radiation pressure, which lowers the adiabatic gradient (cf. Sect. 7.5), this effect is enhanced in rotating stars (Sect. 6.5). The presence of outer convective zones in massive stars may be a source of the observed clumping of the stellar winds.

Chapter 6
Overshoot, Semiconvection, Thermohaline Convection, Rotation and Solberg–Hoiland Criterion

The devil is often hidden in details or in what is looking at first as a detail and then reveals itself as a point of prime importance. Convection theory is full of such "details" able to critically change the results. We may mention the problem of overshooting, i.e., where is the exact edge of a convective zone, the role of the μ gradients, the heat losses by convective fluid elements, semiconvection and thermohaline mixing, the effects of rotation on convection, convection at sonic velocities, etc.

6.1 Convective Overshooting

The Schwarschild and Ledoux criteria for fixing the boundaries of convective regions give in fact the dynamical limit $r_{\Delta T}$ in the star, where the average temperature excess ΔT and thus the acceleration of the convective cells are zero. In reality, convective motions extend up to the kinematical limit r_v, where the velocity of the fluid elements is zero. The difference between the kinematical and the dynamical edges, r_v and $r_{\Delta T}$, is the distance of overshooting

$$d_{\mathrm{over}} = |r_v - r_{\Delta T}| \; . \tag{6.1}$$

The value of d_{over} is the average distance up to which convective mixing extends beyond the formal limit, defined by the Schwarzschild or Ledoux criteria. Overshooting may occur above convective cores or below convective envelopes. The overshooting from convective core determines the amount of nuclear fuel available for the star. The overshooting below the solar envelope is an "observable" parameter in helioseismology. We examine three different approaches to this problem.

6.1.1 Overshooting in an MLT Non-local Model

Overshooting is a non-local process, namely the extent of overshooting critically depends on the properties of the adjacent convective layers. Thus, it cannot be

treated in a local theory. Even in the mixing-length theory (MLT) a non-local approach is possible, where one follows the motion of an average fluid element from deep in the convective zone up to the place where its velocity is zero. The ratio of the total flux $F_{\text{tot}} = F_{\text{conv}} + F_{\text{rad}}$ to the conductive (here radiative) flux is equal to the Nusselt number $\mathcal{N}u$. The total flux is

$$F_{\text{tot}} = \frac{L_r}{4\pi r^2} = \mathcal{N}u F_{\text{rad}} = -\frac{4acT^3}{3\kappa\varrho}\mathcal{N}u\frac{dT}{dr}, \tag{6.2}$$

where the acoustic transport has been neglected. From (5.31), one has

$$\frac{dT}{dM_r} = \frac{GM_r}{4\pi r^4}\frac{T}{P}\frac{1}{\mathcal{N}u}\nabla_{\text{rad}}. \tag{6.3}$$

By comparison with (5.57), one has in an adiabatic convective zone

$$\frac{1}{Nu} \approx \frac{\nabla_{\text{ad}}}{\nabla_{\text{rad}}}. \tag{6.4}$$

Figure 6.1 shows the variations of $1/\mathcal{N}u$ in a 2 $M_\odot$ star.
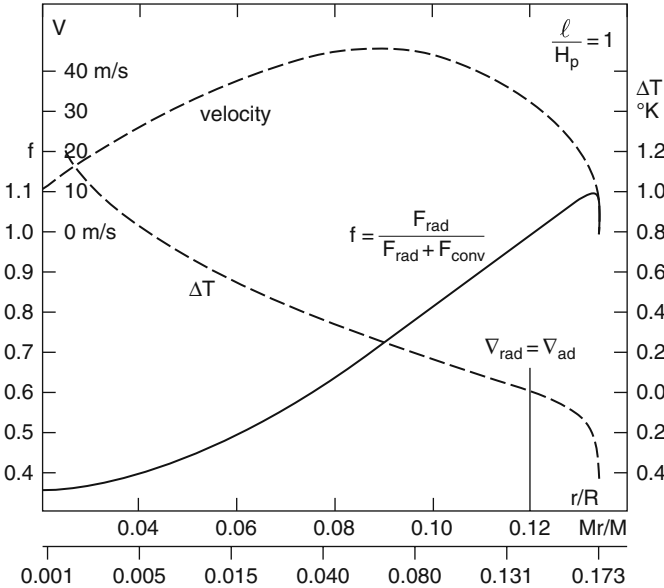
Fig. 6.1 The velocity v, excess ΔT and ratio $f = 1/\mathcal{N}u = F_{\text{rad}}/(F_{\text{rad}} + F_{\text{conv}})$ in the convective core of a 2 $M_\odot$ star on the ZAMS. From the author [335]

6.1.1.1   Critical Levels at the Edge of a Convective Core

Several critical levels at the edge of a convective core can be defined [354]. In addition to levels $r_{\Delta T}$ and r_v, one also has a level r_{Nu} where $Nu = 1$ and a level r_∇ where $\nabla_{ad} = \nabla_{rad}$. In the present approach, the levels r_{Nu} and $r_{\Delta T}$ coincide since $\Delta T = 0 \Rightarrow F_{conv} = 0$ and $Nu = 1$. The levels r_∇ and r_{Nu} do not coincide since (6.4) is not strictly realized, i.e., the real gradient ∇ differs from ∇_{ad} by about 10^{-8}. Due to this small difference, the distance between these two levels is negligible. Thus, at the external edge of a convective core, one has

$$r_\nabla \cong r_{Nu} = r_{\Delta T} < r_v \; . \tag{6.5}$$

In the non-local MLT [335, 527], the ballistic trajectory of an average fluid element is followed to study up to which level it goes. The T excess of a fluid element starting from a level r_i and moving to a level r is

$$\Delta T(r) = -\int_{r_i}^{r} \left[\left(\frac{dT}{dr} \right) - \left(\frac{dT}{dr} \right)_{ad} \right] dr \; . \tag{6.6}$$

In a stationary situation, the acceleration of the cell with a density excess $\Delta\varrho/\varrho = -\delta \Delta T/T$ is $v\,(dv/dr) = -g\,(\Delta\varrho/\varrho)$. In a non-local case, one has

$$\frac{v^2(r)}{2} = -\frac{1}{2} \int_{r_i}^{r} g\,\frac{\Delta\varrho}{\varrho}\,dr \; . \tag{6.7}$$

The factor $1/2$ in front of the integral means that the half of the work of buoyancy forces is dissipated by friction. The distance between the upper level r and the lower bound of integration r_i in (6.6) and (6.7) is limited by the mixing length. For consistency with local developments (Sect. 5.2), one takes $r - r_i \leq \ell/2$, where $\ell = \alpha H_P$. The relative density excess is expressed as a function of the T and μ excesses and the convective flux is given by (5.46).

Some results are illustrated in Fig. 6.1. The velocity reaches a maximum inside the core, then it decreases because the range of integration (from where the cell "remembers" acceleration) is limited. The value $v = 0$ is reached beyond the formal limit $\nabla_{rad} = \nabla_{ad}$. The excess ΔT decreases outward, it is zero at the formal limit $r_{\Delta T}$ and then negative, which decelerates the cell up to the dynamical limit r_v. A fraction of the energy is transported by radiation. At the formal limit, the convective flux is zero, the whole energy being carried by radiation. In the overshooting region, since $\Delta T < 0$ the convective flux is negative, the radiative flux must compensate for it making the Nusselt number smaller than 1. The relative departure from the adiabatic gradient is very small in the overshooting region as in the core ($\leq 10^{-7}$).

The overshooting distance is about 15% of the mixing-length ℓ, with little dependence on the ratio $\alpha = \ell/H_P$. The distance of overshooting is independent of the value of the fraction (e.g., $1/2$ or 1) of buoyancy forces which is converted to kinetic energy. However, a severe simplification of this approach is that no account is given to the spectrum of velocities and sizes of the convective elements.

6.1.2   The Roxburgh Criterion for Convective Overshoot

Another approach, in the form of an integral condition, has been proposed to estimate the distance of overshooting from convective core [500]. Let us express it in a simplified form. One starts from the energy equation (3.43) for a stationary situation and writes the radiative flux $\boldsymbol{F}_{\mathrm{rad}} = -\chi\,\boldsymbol{\nabla} T$,

$$\varrho\,\boldsymbol{u}\cdot\boldsymbol{\nabla} s = \frac{\varrho\,\varepsilon}{T} - \frac{1}{T}\boldsymbol{\nabla}\cdot\boldsymbol{F}_{\mathrm{rad}} + \frac{\Phi}{T}\,, \tag{6.8}$$

where the term Φ/T represents the rate of energy dissipation (in erg cm^{-3} s^{-1}), it is positive and contributes locally to the entropy increase. One has

$$\boldsymbol{\nabla}\cdot(\varrho\,\boldsymbol{u}\,s) = \varrho\,\boldsymbol{u}\cdot\boldsymbol{\nabla} s + s\,\boldsymbol{\nabla}\cdot(\varrho\,\boldsymbol{u})\,. \tag{6.9}$$

The second term on the right is zero according to the equation of continuity (B.3) in a stationary case. Thus,

$$\boldsymbol{\nabla}\cdot(\varrho\,\boldsymbol{u}\,s) = \frac{\varrho\,\varepsilon}{T} - \frac{1}{T}\boldsymbol{\nabla}\cdot\boldsymbol{F}_{\mathrm{rad}} + \frac{\Phi}{T}\,, \tag{6.10}$$

This equation is integrated over a sphere V which contains the convective core and the overshooting zone. Outside this volume the average velocity $\boldsymbol{u} = 0$ on a surface Σ and thus

$$\int_V \boldsymbol{\nabla}\cdot(\varrho\,\boldsymbol{u}\,s)\,dV = \int_\Sigma \varrho\,s\,\boldsymbol{u}\cdot d\boldsymbol{\sigma} = 0\,, \tag{6.11}$$

$$\int_V \frac{1}{T}\left(\boldsymbol{\nabla}\cdot\boldsymbol{F}_{\mathrm{rad}} - \varrho\,\varepsilon\right)dV - \int_V \frac{\Phi}{T}\,dV = 0\,. \tag{6.12}$$

The first two terms give with integration by parts

$$\int_V \frac{1}{T}\boldsymbol{\nabla}\cdot\boldsymbol{F}_{\mathrm{rad}}\,dV = \underbrace{\frac{1}{T}\int_\Sigma \boldsymbol{F}_{\mathrm{rad}}\cdot d\boldsymbol{\sigma}}_{L_{\mathrm{rad}}} - \int_V L_{\mathrm{rad}}\,d\left(\frac{1}{T}\right)\,, \tag{6.13}$$

$$\int_V \frac{1}{T}\varrho\,\varepsilon\,dV = \underbrace{\frac{1}{T}\int_V \varrho\,\varepsilon\,dV}_{L_{\mathrm{nuc}}} - \int_V L_{\mathrm{nuc}}\,d\left(\frac{1}{T}\right)\,. \tag{6.14}$$

Over the considered volume, the two luminosities L_{rad} and L_{nuc} must be equal (see below) and (6.12) becomes,

$$\int_V (L_{\mathrm{nucl}} - L_{\mathrm{rad}})\,d\left(\frac{1}{T}\right) = \int_V \frac{\Phi}{T}\,dV > 0\,. \tag{6.15}$$

If the dissipation rate $\Phi = 0$, we get the Roxburgh criterion,

$$\int_V (L_{\text{nucl}} - L_{\text{rad}}) \, d\left(\frac{1}{T}\right) = 0 \,. \tag{6.16}$$

The outer edge of the core with overshooting lies where this expression is satisfied (Fig. 6.2). Close to center, the nuclear (total) luminosity increases rapidly, then it tends toward a constant. In the core, the radiative luminosity is lower, because some flux is carried by convection (Fig. 6.1). At the edge of the core given by Schwarzschild's criterion the two luminosities are equal. In the overshooting region, the convective flux is negative since the T excess of the cells is negative, this implies that the radiative flux is larger than the total flux. Outside the overshooting zone, both fluxes are identical, since there is no other transport of energy. The criterion says that the integrals of the two luminosities as a function of $1/T$ are equal at the outer edge of the overshooting region (Fig. 6.2). In turn, this means that the integral of the positive convective flux (as a function of $1/T$) below the Schwarzschild limit must have the same size as the integral of the negative convective flux in the overshooting region.

The neglect of dissipation is not satisfactory [633]. Convection is highly turbulent and the turbulent viscosity, which is $\sim 10^{11}$ times larger than the molecular viscosity, has to be considered (Appendix B.4.1). Criterion (6.16) largely overestimates the overshooting distance, giving values at least twice as required by observational constraints (Sect. 6.1.4). Thus, although there is formally no free parameter, the uncertainty about dissipation is a problem for this criterion.
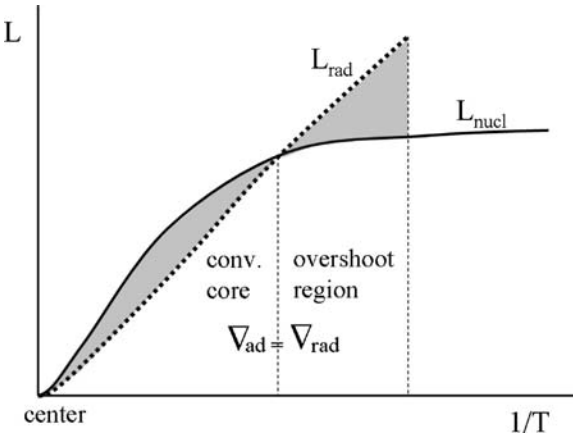
Fig. 6.2 Schematic representation of the Roxburgh criterion for convective overshooting. The various luminosities are represented as a function of $1/T$. The Schwarzschild limit is indicated. The overshooting distance is such that the two *gray* areas are equal. Adapted from [633]

6.1.3   Turbulence Modeling and Overshooting

The insufficiencies of the mixing-length theory are well known: it is local, it ignores the size and velocity distributions of the eddies and considers turbulence as incompressible. However, these properties are essential for a correct estimate of the amount of overshooting as shown by Canuto and Dubovikov [90]. Let us briefly give some insight into how the velocity and temperature fluctuations may influence the modeling of convective flux and overshooting.

Let w be the vertical velocity of fluid elements and $\theta\ (= \Delta T)$ the temperature fluctuations of the turbulent medium. The convective flux (5.46) is of the form $F_{\mathrm{conv}} = C_P \varrho\, \overline{w\,\theta}$. In the MLT, the flux is proportional to the T gradient,

$$\overline{w\,\theta} = -D_t \frac{\partial T}{\partial r} \; . \tag{6.17}$$

D_t is an appropriate turbulent diffusivity (see 6.24 below). However, in reality $\overline{w\,\theta}$ is not just depending on the T gradient, but also on the fluctuations of turbulence. The momentum and heat transport equations for the fluctuating vertical velocity w and for the temperature fluctuations θ are [91], consistently with Sects. 1.1 and 3.2,

$$\frac{\partial w}{\partial t} = g\,\alpha\,\theta - \frac{1}{\varrho}\frac{\partial P}{\partial r} \; , \tag{6.18}$$

$$\frac{\partial \theta}{\partial t} = -w\frac{\partial T}{\partial z} + K\frac{\partial^2 \theta}{\partial^2 z} \; , \tag{6.19}$$

where α is the volume expansion coefficient $\alpha = -\left(\frac{\partial \ln \varrho}{\partial T}\right)_P$, which is $1/T$ for a perfect gas and K is the thermal diffusivity (3.46). The first term in the second member of (6.19) represents the advection of T fluctuations, and the second term is the radiative heat conductivity (cf. 3.45). Multiplying (6.18) by θ and (6.19) by w and taking the averages, then by summing the two expressions one has

$$\frac{\partial}{\partial t}\,\overline{w\theta} = -\overline{w^2}\,\frac{\partial T}{\partial r} + g\,\alpha\,\overline{\theta^2} - \frac{\overline{\theta}\,\frac{\partial P}{\partial r}}{\varrho} + \dots. \tag{6.20}$$

Further equations for $\overline{w^2}$ and $\overline{\theta^2}$ can be established [91] from (6.18) and (6.19). The dots, here and below, represent terms not essential for our discussion. The term $\overline{(\theta/\varrho)\,\partial P/dr}$ can be written as

$$\frac{\overline{\theta}\,\frac{\partial P}{dr}}{\varrho} = \tau_{P\theta}^{-1}\overline{w\,\theta} + c_1\,g\,\alpha\overline{\theta^2} + \dots \; , \tag{6.21}$$

where c_1 is a constant. $\tau_{P\theta}$ is the timescale of the temperature–pressure correlation term $\overline{(\theta/\varrho)\,\partial P/dr}$, $\tau_{P\theta}$ being some function of the local thermal timescale (3.47) and of a dissipation timescale. Although (6.21) has some similarity with (6.19), its exact derivation is different (see [87] Eq. (43a); [88] Eq. (53)), it expresses that the

temperature–pressure correlations are related to both the velocity–T correlations and the T fluctuations. Introducing (6.21) into (6.20), one has

$$\frac{\partial}{\partial t}\,\overline{w\theta} = -\overline{w^2}\,\frac{\partial T}{\partial r} - \tau_{P\theta}^{-1}\overline{w\theta} + (1-c_1)\,g\,\alpha\,\overline{\theta^2} + \dots . \tag{6.22}$$

In a stationary state of turbulence, this becomes

$$\overline{w\theta} = -\tau_{P\theta}\,\overline{w^2}\,\frac{\partial T}{\partial r} + (1-c_1)\,g\,\alpha\,\tau_{P\theta}\,\overline{\theta^2} + \dots . \tag{6.23}$$

The comparison of this relation with (6.17) is interesting, one notes:

- The turbulent diffusivity D_t is given by

$$D_t = \tau_{P\theta}\,\overline{w^2}\,, \tag{6.24}$$

  which is to be compared to the MLT expression $D_t \approx (1/3)\,w\,\ell$ (Appendix B.4.1).
- The interesting point is the presence of other terms in addition to the above one. The convective flux contains in particular a contribution from the T fluctuations [91] (in some cases, this may give a positive convective flux, even if $\partial T/\partial r > 0$). The evaluation of the T fluctuations requires the solution of the equations of motion and energy conservation, with an account of the dissipation rate.
- The turbulent velocity $\overline{w^2}$ is determined by the equations of motions and its moments. The knowledge of $\tau_{P\theta}$ depends on the coupling of thermal and dynamical effects.

Equations such as (6.22) expressing the relations between the various fluctuations are important for the treatment of overshooting. Another expression for the flux F_w of kinetic energy $(1/2)\,\overline{w^3}$ may also be written [91]. When the convective flux becomes negative, kinetic energy from F_w may still be available to sustain convection (cf. Figs. 6.1 and 6.2). Thus an accurate description of the convective flux requires the knowledge of the velocity and T fluctuations and of their relations with the perturbations of pressure.

Various convection theories have been developed. In particular, Canuto and Mazzitelli [93] account for the spectrum of turbulence in velocities and sizes. A mixing-length, taken as equal to the distance to the top of the convective zone, is nevertheless adopted. Various improvements have been further made, in particular in a form which allows calculations of stellar structure [92]. Other non-local developments can be found in the literature [624].

The future in this field is coming from 2D and 3D numerical simulations, as illustrated in Fig. 6.3 (e.g., also [420]). After an initial transient situation, a stationary situation is reached with an input of kinetic energy which produces an extension of the convective core with respect to Schwarzschild's criterion [631]. Such models may provide indications on the appropriate treatment required for overshooting. Different approximations are often made in numerical simulations. For example, in the approximation of Boussinesq, the medium is considered as incompressible: the density variations are not considered, except when multiplied by gravity to give
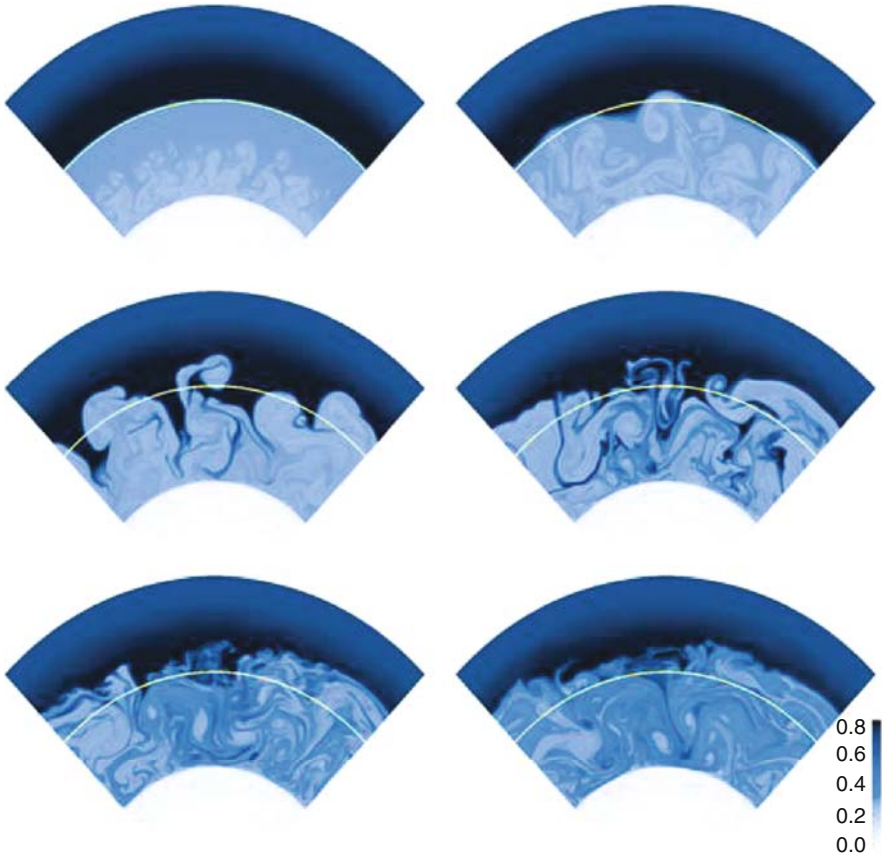
Fig. 6.3 2D numerical simulations of convection in the advanced phase of central O burning. Here, the mixed region (*cloudy*) overshoot by about 30% of the size of the convective region defined by Schwarzschild's criterion (*white curve*). Courtesy from Patrick Young [631]

a buoyancy force. (With the Boussinesq approximation, a system of five coupled differential equations for five variables can be established [91]: these are turbulent kinetic energy, average $\overline{\theta^2}$ of turbulent T fluctuations, turbulent pressure, convective flux and energy dissipation. The inclusion of the compressibility would require a system of 18 coupled differential equations.)

6.1.4 Observational Constraints

There are various constraints on the amount of overshooting from convective cores. The distance of the top of the MS (where central H content is zero) to the ZAMS in the HR diagram of open clusters is a sensitive test [360] about the real size of
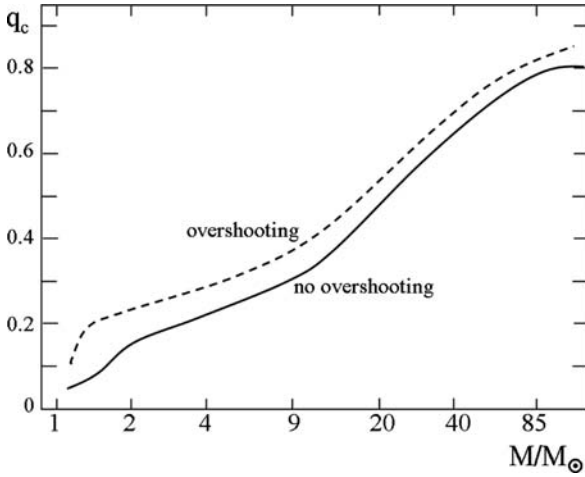
Fig. 6.4 The mass fraction of the convective cores without and with an overshooting $d_{over}/H_P = 0.25$. If the size r_c of the core is smaller than H_P, $d_{over} = 0.25\,r_c$. At 1.15 $M_\odot$, $d_{over}/H_P = 0.125$. From the author [363]

the convective cores, thus about overshooting. The core extension supported by observations corresponds to an overshooting distance $d_{over} = (0-0.10)\,H_P$ below 1.4 $M_\odot$, $d_{over} \approx 0.10\,H_P$ at about 1.5–2 $M_\odot$ and 0.3 H_P around 15 $M_\odot$ [159, 361]. This is in agreement with other determinations in this range of masses [158, 553], which suggest a value of d_{over} of about 0.2 H_P. This is comparable to the results of Sect. 6.1.1.

Figure 6.4 shows the size of the convective core as a function of stellar mass without overshooting and with an overshooting of 0.25 H_P. For small masses, the relative increase of the core size is large. As suggested above, the overshooting distances predicted by Roxburgh's criterion are too large. The value of 0.2 H_P found from cluster observations of various ages corresponds to about 50% of the distance predicted by Roxburgh's criterion [592]; for low masses of about 1.3 $M_\odot$ in the cluster M67, the observations support an overshooting distance equivalent to a fraction of 7% of the value predicted by Roxburgh's criterion (6.16). Helioseismic observations also support the existence of some overshooting below the external convective zone of the Sun, of about 7–10% of H_P. Asteroseismic observations will allow us to better estimate the overshooting from convective cores [163].

In this context, one may note that 1– other effects may extend the convective core, in particular rotational mixing (Chaps. 11 and 12); 2– the overshooting distance is usually referred to the core defined by Schwarzschild's criterion and 3– the use of the Ledoux criterion, the account for semiconvection (see Sect. 6.2) or of the Solberg–Hoiland criterion (Sect. 6.4) when rotation is present, could also influence what is defined as overshooting.

6.2 Semiconvection and Thermohaline Convection

Let us consider a zone in the stellar interior where the gradient ∇_{rad} is intermediate between the stability predicted by the Ledoux criterion (5.55) and the instability predicted by the Schwarzschild criterion (5.54)

$$\nabla_{\mathrm{int}} < \nabla < \nabla_{\mathrm{int}} + \frac{\varphi}{\delta}\nabla_\mu, \quad \text{with } \nabla_{\mathrm{int}} \approx \nabla_{\mathrm{ad}} \text{ and } \nabla \approx \nabla_{\mathrm{rad}}. \tag{6.25}$$

The instability occurring in this zone is called semiconvection. Formally, the result of a stability analysis (Sect. 5.1) indicates that there is no convection. This is true if convection is perfectly adiabatic. This is closely, but not exactly, the case even in the deep stellar interior.

Conditions (6.25) imply that an upward displaced convective eddy is denser (Ledoux criterion) than the surrounding medium, thus it is brought back by gravity. The eddy is also hotter (Schwarzschild's criterion) than the surrounding medium. Thus, it will radiate in the surrounding medium, this increases the internal density of the eddy. It thus goes down faster and its oscillations around the equilibrium position progressively become larger. The mixing produced by these growing oscillations is semiconvection (Fig. 6.5). Semiconvection occurs when ∇_μ is positive, i.e., when μ increases toward the interior, as is currently the case. Such a situation is sometimes called an overstability. The growth of the amplitudes of the oscillations is determined by the timescale of the thermal adjustment of a fluid element.

In some numerical models, the application of Schwarzshild's criterion may lead to a kind of "sandwich" of radiative and convective layers. The region above the core
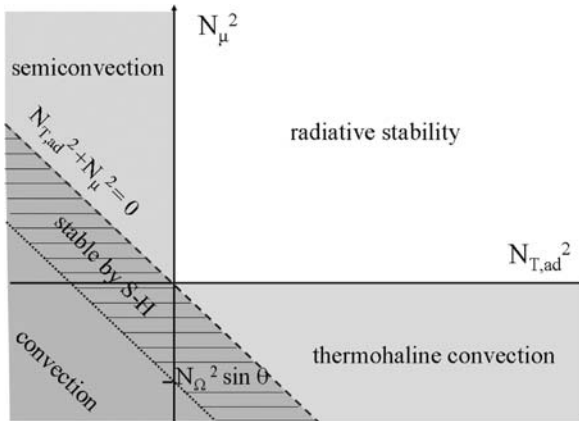
Fig. 6.5 Schematic illustration of the regions of convection, semiconvection, thermohaline convection and radiative stability in the plane showing the thermal and composition terms $N_{T,\mathrm{ad}}^2$ and N_μ^2 of the Brunt–Väisälä frequency as defined in (5.60). The hatched region schematically indicates where stabilization by rotation may occur due to the Solberg–Hoiland (SH) criterion (see Sect. 6.4.3)

breaks up into a series of shells where convective zones alternate with radiative ones. If there is a gradient of μ, this makes successive discontinuities of composition. The treatment of such zones with an appropriate diffusion coefficient describing the mixing, as suggested below, generally reduces or suppresses the stepwise chemical distribution.

It may also occur, more rarely, that the medium has a negative ∇_μ, i.e., with μ growing outward. This may result from accretion in a binary system. Such a situation remains stable as long as a bubble of fluid with a μ higher than the surroundings is hot enough to be lighter. However, radiative losses reduce T and at some point the bubble becomes denser than the surroundings and sinks. This is thermohaline convection. It occurs in the region indicated in Fig. 6.5. The occurrence of thermohaline motions depends on both the thermal diffusivity K and the particle diffusion ν, this is why such instabilities are called double diffusive. As the Prandtl number $\mathcal{P}r = \nu/K$ is very small in stars (cf. Appendix B.5.2), the thermal diffusion generally dominates and the bubbles of higher μ eventually descend in the medium. This is especially the case if the geometry of the unstable region favors the heat leakage by forming "salt fingers".

6.2.1   Various Approaches

Several methods have been applied to treat the semiconvective regions, let us briefly discuss some of them.

6.2.1.1   The Method of Schwarzschild and Härm

In the zone defined by (6.25) it is assumed [524] that matter is redistributed changing μ until $\nabla_{rad} = \nabla_{ad}$ is reached. This implies a large mixing. Later, it was proposed [505] that the matter redistribution rather leads to $\nabla_{rad} = \nabla_{ad} + (\varphi/\delta)\nabla\mu$, which implies less mixing. The consequences of these two assumptions were examined by Chiosi and Summa [128]. They showed that in the second case (Ledoux) the He-burning stage of massive stars (20 $M_\odot$) starts in the red, while in the first case (Schwarschild) it starts in the blue. This is quite consistent with the results of Sect. 27.3.6, where it is shown that more mixing leads to a longer blue evolution in the He-burning phase.

6.2.1.2   The Method of Langer, Sugimoto and Fricke

The growth rate of the overstable oscillatory motions has been calculated by Kato [278]. From this estimate, Langer et al. [313] have expressed a corresponding diffusion coefficient D_{SC} allowing them to treat semiconvection as a diffusion process

(Sect. 10.2). The oscillations are of the form $\delta f \sim \exp i(kx + st)$. The diffusion coefficient is expressed as $D_{SC} = (1/3)\ell v$, with $v = \ell s$ and $\ell = 2\pi/k$,

$$D_{SC} = \frac{\alpha K}{6} \frac{\nabla - \nabla_{ad}}{\nabla_{ad} - \nabla + \frac{\varphi}{\delta}\nabla_\mu} . \tag{6.26}$$

To be consistent with Kato's work, the numerical coefficient in (6.26) should rather be $(2\pi\alpha K)/6$. Here, K is the thermal diffusivity and α a numerical factor of the order of unity. Comparisons with observations [308] suggest that the above coefficient (6.26) should be multiplied by a factor of 0.01–0.04. If we account for the difference in the numerical factor mentioned above, the necessary reduction should reach a factor of 150–600! This is a problem for the above theory.

   The origin of the problem is likely that the above solution is not the general solution of the dispersion relation, but the solution for a Peclet number (Appendix B.5.3) $\mathcal{Pe} = t_{therm}/t_{dyn} \to \infty$, i.e., it assumes as perfectly adiabatic a process which is by essence non-adiabatic. This hypothesis leads to a large overestimate of the coefficient of semiconvective diffusion (see Sect. 6.2.3).

6.2.1.3   Stevenson's Method

The unstable oscillations drive resonance instabilities which feed the growth of smaller scale instabilities, which in turn break down and produces mixing on small scales. The diffusion coefficient [552] has an upper bound

$$D_{SC} \leq K \left(\frac{\nabla - \nabla_{ad}}{\nabla_\mu}\right)^2 \tag{6.27}$$

in the case of a perfect gas. The μ gradient being generally rather large in semiconvective region, this means that this coefficient is generally much smaller than the one by Langer et al.

6.2.1.4   Layered Convection

The assumption [544] is that layered convection takes place as is observed in the laboratory. The mixing is due to the overturn of cells in the medium separated by stable thin layers, across which transport proceeds by microscopic diffusion. The diffusion coefficient in a medium of perfect gas behaves like

$$D_{SC} \approx \sqrt{K K_{diff}} \frac{\nabla_{rad} - \nabla_{ad}}{\nabla_\mu} , \tag{6.28}$$

where K_{diff} is the coefficient of microscopic diffusion. As this coefficient is much smaller than K (e.g., by 10^{-8}), the predicted transport is very small. However, some numerical models of semiconvective zone do not support the layered structure and

show that it is rapidly destroyed [399] in a medium where the Prandtl number is small (ratio v/K of the viscosity to the thermal diffusivity), which is precisely the stellar case.

6.2.1.5   2D and 3D Simulations

Numerical 2D or 3D simulations of the kind shown in Fig. 6.3 are likely the best way to derive what happens exactly in a stellar semiconvective zone. Some 2D simulations of semiconvection were performed by Merryfield [399], they exhibit some qualitative similarities with the above picture by Langer et al. However, the numerical simulations were not performed on timescales and spatial extent large enough to allow tests of the various analytical coefficients. The non-linear effects limiting the amplitude of the overstable oscillations have also been studied [224]. In regions where ∇ is sufficiently different from ∇_{ad}, the solutions are also qualitatively similar to that of Langer et al. [313].

6.2.2   Kato Equation, Thermohaline Convection

Let us consider a blob of helium in equilibrium at some level in a radiative H-rich stellar layer. To be in equilibrium in a medium of lower mean molecular weight, the blob must be hotter than the surroundings. Progressively the blob cools, its density increases and it slowly moves down. The velocity, say v_μ, of the descending motion is determined by the heat leakage from the blob. A similar situation in laboratory experiments or in the sea is that of the "salt fingers" or thermohaline convection as seen above. The instability is slow and called a secular instability, it is governed by the thermal adjustment timescale.

6.2.2.1   Case of an Homogeneous Medium

Let us write the equation governing the change of the excess temperature DT (or ΔT) with time of a fluid element during its motion through an homogeneous medium. The change results from the thermal loss rate $-DT/t_{\mathrm{therm}}$ and from the difference between the internal and the external T during the vertical displacement over a distance Dr during a time Dt, $DT = (\nabla - \nabla_{\mathrm{int}})\,(T/H_P)\,Dr$ (5.41). However, since the heat losses are already explicitly accounted for, the difference to be considered during the motion is only the difference between the external and the adiabatic gradients. Thus, we write ∇_{ad} instead of ∇_{int} in this last expression,

$$\frac{1}{T}\frac{\partial}{\partial t}DT = \frac{v_\mu}{H_P}\left(\nabla - \nabla_{\mathrm{ad}}\right) - \frac{DT}{T\,t_{\mathrm{therm}}}\ . \tag{6.29}$$

This equation was first written by Kato (Eq. (7) in [278]), although with different notations and by Kippenhahn and Weigert (Eq. (6.27) in [285]). The thermal adjustment time t_{therm} is given in Appendix (B.5.3). Let us consider a stationary situation for a blob with $D\mu > 0$. The blob is in dynamical equilibrium with the medium, i.e., both DP and $D\varrho$ are zero. From the equation of state (3.60), one gets

$$\frac{DT}{T} = \frac{\varphi}{\delta} \frac{D\mu}{\mu} , \qquad (6.30)$$

where $D\mu/\mu$ is constant due to the homogeneity of the ambient medium. The first member of (6.29) is zero and one gets for the sinking velocity [285]

$$v_\mu = \frac{-H_P}{(\nabla_{\text{ad}} - \nabla) t_{\text{therm}}} \frac{\varphi}{\delta} \frac{D\mu}{\mu} . \qquad (6.31)$$

In a radiative medium $\nabla_{\text{ad}} > \nabla$, thus for $D\mu > 0$ one has $v_\mu < 0$ and the blob is sinking.

6.2.2.2   Case of an Inhomogeneous Medium

Let us now consider thermohaline instability in an ambient medium with a μ gradient ∇_μ, which is more appropriate in stars. In such a medium, the difference $D\mu$ varies with the location of the fluid element considered. The μ excess after a small trip over a distance Dr is

$$D\mu = \frac{\mu}{H_P} \nabla_\mu Dr . \qquad (6.32)$$

$D\mu$ is positive for $Dr > 0$. The first member of (6.29) is not equal to zero. The cell is in pressure equilibrium and (6.30) still applies. The change DT/T with time of the cell in equilibrium is thus

$$\frac{\partial}{\partial t} \left(\frac{DT}{T} \right) \approx \frac{\partial}{\partial t} \left(\frac{\varphi}{\delta} \frac{D\mu}{\mu} \right) \approx \frac{\partial}{\partial t} \left(\frac{\varphi}{\delta} \frac{\nabla_\mu}{H_P} Dr \right) \approx \frac{\varphi}{\delta} \frac{\nabla_\mu}{H_P} v_\mu \qquad (6.33)$$

By replacing in (6.29), one obtains

$$v_\mu = \frac{-H_P}{\left(\nabla_{\text{ad}} - \nabla + \frac{\varphi}{\delta} \nabla_\mu \right) t_{\text{therm}}} \frac{\varphi}{\delta} \frac{D\mu}{\mu} . \qquad (6.34)$$

This is a generalization of (6.31) and it gives the sinking velocity of a fluid element moving down as a result of cooling in a medium with a μ gradient [349]. The motions occur with the thermal timescale. This expression is more useful than (6.31) since salt fingers may occur in chemically inhomogeneous media. Not accounting for the ambient inhomogeneity gives wrong results. This velocity can be used to derive an appropriate diffusion coefficient.

6.2.3 Diffusion Coefficient for Semiconvection

Thermohaline and semiconvection are similar processes both involving N_μ^2 and N_T^2, but with a different sign of the μ gradient (Fig. 6.5). In order to analyze semiconvection at small scales, one considers a small displaced fluid element with both μ and T excesses with respect to the surroundings. Thus, locally this small fluid element is exactly in the situation of a thermohaline layer. This means that the above velocity v_μ is appropriate for both processes in their own context. The coefficient of semiconvection (6.26) was derived in the adiabatic limit, although semiconvection is a non-adiabatic effect. Here we derive this coefficient without making the adiabatic assumption.

6.2.3.1 From the "Sinking" Velocity

In a semiconvective zone (like in thermohaline convection), an upper fluid element is hotter and denser. The thermohaline velocity (or velocity excess in semiconvection) is determined by the heat losses (6.34). For a blob in equilibrium, one has (6.30), thus

$$v_\mu = \frac{-H_P}{\left(\nabla_{\text{ad}} - \nabla + \frac{\varphi}{\delta}\nabla_\mu\right)\tau_{\text{therm}}}\frac{DT}{T}. \tag{6.35}$$

The temperature difference between an eddy moving over a distance Dr and the medium is

$$\frac{DT}{T} = -\left(\nabla_{\text{int}} - \nabla\right)\frac{Dr}{H_P}, \tag{6.36}$$

for $Dr > 0$ one has $DT > 0$ as usual in a semiconvective region and v_μ is positive. The diffusion coefficient is $D_{\text{SC}} = (1/3)\left|v_\mu Dr\right|$ according to the definition (B.50). With the expression of the thermal time for a spherical blob $t_{\text{therm}} = d^2/(6K)$ from (B.66), one gets

$$D_{\text{SC}} = \frac{2K\left(\nabla - \nabla_{\text{int}}\right)}{\left(\nabla_{\text{ad}} - \nabla + \frac{\varphi}{\delta}\nabla_\mu\right)}, \tag{6.37}$$

which is positive. Eliminating ∇_{int} with (5.67) one gets

$$D_{\text{SC}} = \frac{2\Gamma}{\Gamma+1}\frac{K\left(\nabla - \nabla_{\text{ad}}\right)}{\left(\nabla_{\text{ad}} - \nabla + \frac{\varphi}{\delta}\nabla_\mu\right)}. \tag{6.38}$$

In the adiabatic limit, i.e., for $\Gamma \to \infty$, one finds again the coefficient by Langer et al. (6.26). For small values of Γ, the diffusion coefficient is much reduced, which brings a better agreement with observations. Typically, Γ is of the order of 10^{-2}–10^{-3} in stellar interiors (Fig. 5.6).

6.2.3.2   From Non-adiabatic Gravity Waves

The diffusion coefficient can be derived by taking into account the non-adiabatic effects in oscillatory motions at the Brunt–Väisälä frequency. The energy lost $DU_{\text{lost}} > 0$ by an eddy of diameter ℓ during a time Dt (5.62) leads to a decrease of T and thus an increase of ϱ

$$D\varrho = -\varrho\, \delta \frac{DT}{T} = -\frac{\delta}{C_P V T} (-DU_{\text{lost}}) = \frac{4ac T^3}{3 \kappa \varrho C_p} \frac{\delta DT}{T \ell} \frac{\Sigma}{V} Dt . \qquad (6.39)$$

For a sphere, the ratio of the surface to the volume is $\Sigma/V = 6/\ell$ and the excess of temperature is given by (6.36), thus we get

$$\frac{D\varrho}{\varrho} = \frac{6K \delta\, (\nabla - \nabla_{\text{int}})\, Dt}{H_P \ell} , \qquad (6.40)$$

where we have put $Dr = \ell$. This relative excess of density leads to a corresponding increase of the velocity of the gravity oscillation $Dv = g\,(d\varrho/\varrho) Dt$

$$Dv = \frac{6g K \delta\, (\nabla - \nabla_{\text{int}})\, Dt^2}{H_P \ell} , \qquad (6.41)$$

where the quantities are average over the interval of time Dt. The motions are oscillatory around an equilibrium position. The maximum of Dv is reached after $1/4$ of an oscillatory period $(2\pi/N_{\text{ad}})$. Let us consider that the average Dv is reached between 0 and the quarter of the period, say at $1/8$ of the period. Thus $Dt^2 = \pi^2/(16 N_{\text{ad}}^2)$ and Dv becomes with (5.59)

$$Dv = \frac{3\pi^2}{8} \frac{K\, (\nabla - \nabla_{\text{int}})}{\left(\nabla_{\text{ad}} - \nabla + \frac{\varphi}{\delta}\nabla_\mu\right) \ell} , \qquad (6.42)$$

Thus, the coefficient for semiconvective diffusion becomes with (5.67)

$$D_{\text{SC}} = \frac{1}{3} (Dv)\, \ell = \frac{\pi^2}{8} \frac{\Gamma}{\Gamma + 1} \frac{K\, (\nabla - \nabla_{\text{ad}})}{\left(\nabla_{\text{ad}} - \nabla + \frac{\varphi}{\delta}\nabla_\mu\right)} \qquad (6.43)$$

Apart from a small difference in the numerical factor (1.23 instead of 2), this is the same coefficient as that found above. The calculation of Γ as given by (5.66) is thus critical to determine the appropriate diffusion coefficient.

6.3   Time-Dependent Convection

During very fast evolution phases, mixing in the convective zone cannot be considered as instantaneous. This occurs when the nuclear timescales (9.9) are of the same

order of magnitude as the convection turnover time (5.49). If so, the nuclear species have the time to be partially transformed into other nuclear species during their convective transport over a mixing length. Thus, an appropriate treatment of this situation must be performed. This applies, for example, to the deuterium burning in the pre-main sequence phase and also to the fast nuclear burning in the convective cores of pre-supernovae.

For such cases, a diffusion treatment may be used with a diffusion equation of the form (10.29)

$$\varrho \frac{\partial X_i}{\partial t}\bigg|_{M_r} = \frac{1}{r^2} \frac{\partial}{\partial r} \left(\varrho \, r^2 \, D_{\mathrm{conv}} \frac{\partial X_i}{\partial r} \right) \,, \tag{6.44}$$

where D_{conv} is a diffusion coefficient appropriate to convection. The general form of a diffusion coefficient is given by (10.19), it is $D_{\mathrm{conv}} = \frac{1}{3} \overline{v} \, \ell$ (see also Appendix B.4.3). The velocity $\overline{v}$ is the average convective velocity given by (5.45). For the appropriate mixing-length ℓ, we may take the usual expression $\ell = \alpha \, H_P$ with α of the order of unity. The diffusion coefficients in convective zones are generally very large, of the order of 10^{15} or 10^{16} cm^2 s^{-1} consistently with the value of the convective velocities and the short turnover time.

The boundary conditions for (6.44) need some special care (see 10.31). In particular, if there is some mixing in the zone adjacent to the convective region, a good solution is to apply a diffusion scheme to both regions with their appropriate diffusion coefficients, this avoids the use of many boundary conditions. However, the interpolation of diffusion coefficients when they vary rapidly needs special care [414], see also Sect. 10.2.2.

6.4   Effects of Rotation on Convection

Stellar rotation influences the size and properties of the convective zone. In turn, convection produces some internal coupling of rotation. Many aspects of these interactions are still uncertain.

6.4.1   Oscillation Frequency in a Rotating Medium

The Brunt–Väisälä frequency, expressed by (5.23) or (5.59) and leading to the Schwarzschild and Ledoux criteria (see Sect. 5.1.2), was derived in the absence of rotation. However, a displaced element (Fig. 6.6) is also submitted to the change of centrifugal force which modifies the oscillation frequency N^2 and consequently the criterion for convective instability.
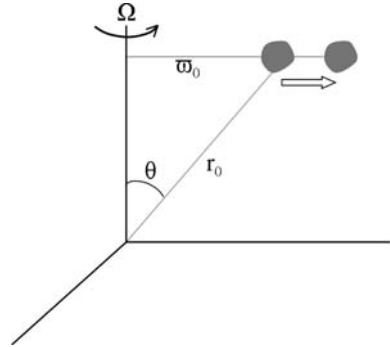
Let us write the equation of motion of a fluid element displaced from an equilibrium position at distance r_0 from the center to a nearby position r in a medium in rotation with an angular velocity Ω at r_0. Cylindrical symmetry is assumed. The equation is similar to (5.1), with a centrifugal acceleration in addition,

$$\frac{d^2 r}{dt^2} + \frac{g}{\varrho_{\text{int}}} (\varrho_{\text{int}} - \varrho_{\text{ext}}) - \varpi \left(\Omega_{\text{int}}^2 - \Omega_{\text{ext}}^2 \right) = 0 , \qquad (6.45)$$

where $\varpi_0 = r_0 \sin \vartheta$ is the distance to the rotation axis. Ω_{int} is the angular velocity of the displaced fluid element, while Ω_{ext} is the ambient angular velocity in the medium both being considered at point ϖ (in ϖ_0 one has $\Omega_{\text{int}} = \Omega_{\text{ext}}$). Let us call j the specific angular momentum $j = \varpi^2 \Omega$ with the appropriate index. One writes

$$\varpi \left(\Omega_{\text{int}}^2 - \Omega_{\text{ext}}^2 \right) = \frac{1}{\varpi^3} \left(j_{\text{int}}^2 - j_{\text{ext}}^2 \right) . \qquad (6.46)$$

One now assumes conservation of the specific angular momentum of the displaced fluid element. Thus j_{int} at the distance ϖ from the rotation axis is the same as at the distance ϖ_0 corresponding to the equilibrium position. This allows us to write, developing to the first order,

$$\frac{1}{\varpi^3} \left(j_{\text{int}}^2 - j_{\text{ext}}^2 \right) \approx -\frac{1}{\varpi^3} \frac{d\, j^2}{d\varpi} \Big|_0 (\varpi - \varpi_0) = -\frac{1}{\varpi^3} \frac{d \left(\Omega^2 \varpi^4 \right)}{d\varpi} \Big|_0 (\varpi - \varpi_0) . \qquad (6.47)$$

Developing the density as in (5.3), one has for (6.45)

$$\frac{d^2 r}{dt^2} + \left[\frac{g}{\varrho_{\text{int}}} \left(\frac{d\varrho_{\text{int}}}{dr} - \frac{d\varrho_{\text{ext}}}{dr} \right) + \frac{1}{\varpi^3} \frac{d \left(\Omega^2 \varpi^4 \right)}{d\varpi} \sin \vartheta \right] (r - r_0) = 0, \qquad (6.48)$$

the derivatives are taken in r_0. As in Sect. 5.1, we search a solution of the form $r - r_0 = A \exp(iNt)$ and get with (5.25) the oscillation frequency in a rotating medium

$$N^2 = N_T^2 + N_\mu^2 + N_\Omega^2 \sin \vartheta$$

$$= \frac{g\delta}{H_P} \left(\nabla_{\text{int}} - \nabla + \frac{\varphi}{\delta} \nabla_\mu \right) + \frac{1}{\varpi^3} \frac{d\left(\Omega^2 \varpi^4 \right)}{d\varpi} \sin \vartheta \,, \tag{6.49}$$

where ∇_{int} in deep stellar interiors is generally equal to ∇_{ad} (see Sect. 5.3). In 1D models, one may consider that the average situation corresponds to $P_2(\cos \vartheta) = 0$, i.e., $\cos^2 \vartheta = 1/3$ so that $\sin \vartheta = \sqrt{2/3}$. In general, the specific angular momentum increases outward, thus the oscillation frequency is higher in a rotating medium, consistently with an additional recall force acting on a displaced fluid element. It is to be noted that g is here the gravitational acceleration only, owing to (6.45).

6.4.2   The Rayleigh Criterion and Rayleigh–Taylor Instability

Let us clarify some definitions. The Rayleigh criterion is the criterion, which states the condition for a distribution of angular velocity to be stable (other stabilizing or destabilizing effects being ignored). It is expressed by the condition $N_\Omega^2 > 0$ (6.50) or by (6.51), the Rayleigh frequency in a rotating medium being the frequency N_Ω. The Rayleigh–Taylor instability occurs when a denser fluid is supported by a lighter one against a gravitational field or another acceleration. It can occur in very different contexts, for example, when a heavier gas is accreted onto a binary system or when a denser fluid is accelerated in a lighter one, as, for example, in galactic jets or supernova explosions. (Please note that the so-called Rayleigh instability or Plateau–Rayleigh instability concerns something very different, it occurs when surface tension breaks a jet into a stream of droplets.)

We consider the case of a medium of constant density, the sum $N_T^2 + N_\mu^2$ is zero and only the term with N_Ω^2 is left in (6.49). The stability condition requires in order that the oscillation motions do not grow exponentially

$$N_\Omega^2 = \frac{1}{\varpi^3} \frac{d\left(\Omega^2 \varpi^4 \right)}{d\varpi} > 0 \,, \tag{6.50}$$

since $\sin \vartheta$ is positive and equal to zero at the pole. If $N_\Omega^2 > 0$, the lower angular momentum of the upward displaced fluid element brings it back to the equilibrium position. In the opposite case, the higher angular momentum of the displaced element drives it farther. Condition (6.50) means that

– For stability, the specific angular momentum $j = \varpi^2 \Omega$ must increase outward.
– One also has from (6.50) for stability,

$$\frac{dj}{d\varpi} = \varpi \left(\varpi \frac{d\Omega}{d\varpi} + 2\Omega \right) > 0 \quad \text{or} \quad \frac{d\ln \Omega}{d\ln \varpi} > -2 \,. \tag{6.51}$$

This (or 6.50) expresses the Rayleigh criterion. Ω must not decrease too steeply outward, otherwise the angular momentum is higher in the inner layers and the

Rayleigh criterion is violated. If Ω is of the form $\Omega \sim r^{-\alpha}$, values of $\alpha > 2$ lead to instability by violation of the Rayleigh criterion.

– On the stellar surface, the angular momentum must also increase from pole to equator.

The characteristic timescale of the Rayleigh instability, if present, is the dynamical timescale $1/N_\Omega$ of the rotating system, i.e., of the order of $1/\Omega$. For the transport coefficient, an expression of the form

$$D = \frac{1}{3}\ell_\Omega^2 N_\Omega \, , \tag{6.52}$$

may be chosen according to Sect. 10.1.3, where ℓ_Ω is a characteristic length scale of the rotation motions, e.g., $\ell_\Omega \approx |\Omega\,(dr/d\Omega)|$.

6.4.3 The Solberg–Hoiland Criterion

In the presence of a density stratification, the stability condition is

$$N^2 = N_T^2 + N_\mu^2 + N_\Omega^2 \sin\vartheta > 0, \tag{6.53}$$

where ϑ is the colatitude (Fig. 6.4.1). This is the Solberg–Hoiland criterion for convective stability. As a matter of fact, it expresses a stability condition with respect to a form of the Rayleigh–Taylor instability. In the absence of rotation, the criterion is just the usual Ledoux criterion (5.26): $N_T^2 + N_\mu^2 > 0$. Condition (6.53) means that convective stability is favored by stellar rotation if the outward decrease of Ω is moderate according to condition (6.51). In this case, the extent of a convective region is slightly reduced by rotation, with a larger reduction at the equator than in polar regions. Figures 6.5 and 12.8 show the region where convective instability is prevented by rotation. In 1D models, an average value of $\sin\vartheta = \sqrt{2/3}$ may be taken. Criterion (6.53) also implies, if N_Ω^2 is negative enough, that a region which would have been radiatively stable could be unstable.

Since $N_T^2 = 0$ implies constant entropy (cf. Sect. 5.1.1), condition (6.53) also implies that on a μ constant isentropic surface, the angular velocity increases from pole to equator.

In the region just outside the convective core, both the μ and the Ω gradients can be very steep and highly dominating in (6.53). This is particularly the case in the advanced stages of nuclear burning. An equilibrium situation between the two gradients may possibly be reached for the following reasons. The high μ gradient in itself favors stability, but simultaneously the growth of central density, due to central condensation, leads to an increase of the Ω gradient. The steep Ω gradient may drive the instability. The resulting fast transport proceeds until stability is restored. Thus, an equilibrium situation is reached with

$$N_\mu^2 + \sqrt{\frac{2}{3}}N_\Omega^2 \approx 0 \tag{6.54}$$

in the region just outside the core in advanced evolutionary stages. This gives in terms of the μ and Ω gradients,

$$\frac{g}{\Omega^2}\frac{\varphi}{r}\frac{d\ln\mu}{d\ln r} \approx \sqrt{\frac{2}{3}}\left(2\frac{d\ln\Omega}{d\ln\varpi}+4\right). \qquad (6.55)$$

The steeper the μ gradient, the steeper the Ω gradient in such an equilibrium at the limit of the Solberg–Hoiland criterion.

6.4.4 Numerical Simulations

There are two extreme assumptions about rotation in a convective zone:

- Case A: it is generally assumed in 1D stellar evolution models that convective regions are rotating like a solid body. The argument is that the strong turbulent viscosity due to convective motions maintains a uniform distribution of angular velocity.
- Case B: an alternative possibility is that the distribution of the angular momentum is constant in convective regions. The argument is that large-scale motions dominate and conserve their angular momentum, thus establishing a uniform distribution of the specific angular momentum.

These two possibilities are very different. In the first case, one has a constant Ω, while in the second one has $\Omega \sim \varpi^{-2}$. In red giants, case B leads to more differential rotation, more shears and thus more mixing at the base of the convective envelope [455].

Between cases A and B, the reality is more complicated as suggested by 2D and 3D numerical simulations of convection, which have been applied to the solar convective envelope and to convective cores. Three-dimensional simulations of solar convection by Toomre and Brun [577] show that convection is time dependent with intricate flows, dominated by intermittent plumes of upflows and stronger downflows extending over much of the shell depth. Time-averaged angular velocity Ω distributions show the following features:

- In the equatorial regions, $\Omega(r)$ increases by 10–15% from radius $r/R_\odot = 0.71$ to the surface.
- Away from the equator, $\Omega(r)$ is lower with a smaller increase from the base of the convective zone to the top.
- In polar regions, $\Omega(r)$ is constant with depth, being about 30% lower than at the equator in surface.

Turbulent motions are coupled with several cells of meridional circulation in latitude and often two layers of cells in depth. These simulations [577] well reproduce the values $\Omega(r)$ obtained from helioseismology; however they do not support cases A or B above. One notes that solar rotation is very low and a different picture may apply to fast rotation, as well as to situations where the Mach number is high, like in red giants or supergiants.

6.4.4.1 Numerical Simulations of Convective Cores

Three-dimensional simulations of core convection in 2 $M_\odot$ stars of different rotation velocities have been made [71] in the anelastic approximation, i.e., for fluid elements in pressure equilibrium. Large-scale motions are dominant, with multicellular structures of meridional circulation, which are orders of magnitude faster than the classical meridional circulation in radiative envelopes. Hydrodynamic simulations [162] indicate faster convective velocities than estimated by the MLT. For moderate and rapid rotation, convective motions are mostly parallel [162] to the rotation axis, rather than vertical. Contrarily to the solar case, small-scale turbulent features are absent and there are no asymmetries between up and downflows. Convective plumes excite [71] gravity waves in the radiative envelope (cf. Fig. 6.3), where slow circulation is also noticed.

The convective cores rotate differentially. Some models [162] suggest that the variations of $\Omega(r)$ can be represented by $\Omega \sim \varpi^{-0.5}$, with a better agreement for fast than for slow rotation. In the slowly rotating models by Brun et al. [74], a central cylindrical region with slower rotation is present, with significant Ω gradients both in radius and in latitude. At the equator, $\Omega(r)$ increases with radius, while at higher latitude $\Omega(r)$ is almost flat. At the edge of the convective core, Ω at the equator is larger by 40% with respect to $\Omega(r)$ near the pole. As simulations evolve, the latitudinal differences are smaller. The convective core is prolate, i.e., elongated in the direction of the rotation axis. This feature is consistent with the prediction of the Solberg–Hoiland criterion (6.53). However, this formal core is surrounded by a region of overshooting, which is broader at the equator so that the overall region experiencing convective mixing is about spherical.

The numerical simulations indicate that the analytical approximations used in current stellar models are very rough and that their relative agreement with observational constraints likely results from the freedom offered by their adjustable parameters.

6.5 Convective Envelope in Rotating O-stars

Figure 5.8 indicates that massive O-stars have a small external convective envelope due to their high luminosity. Rotation amplifies these external convective regions. This occurs despite the inhibiting of the Solberg–Hoiland criterion, because another more important effect is present in envelopes: the rotational increase of the radiative gradient ∇_{rad} [357]. Let us write the Solberg–Hoiland criterion for stability in the case of a constant μ as is usual in envelopes

$$\nabla_{\mathrm{ad}} - \nabla_{\mathrm{rad}} + \nabla_\Omega \sin\vartheta > 0 \quad \text{with} \quad \nabla_\Omega = \frac{H_P}{g_{\mathrm{grav}}\delta} \frac{1}{\varpi^3} \frac{d(\Omega^2\varpi^4)}{d\varpi} , \qquad (6.56)$$

where $\varpi = r\sin\vartheta$ is the distance to the rotation axis and $\delta = -(\partial \ln\varrho / \partial \ln T)_P$. Here, we specify g_{grav} and g_{rad}. The local flux and the equation of hydrostatic

equilibrium are

$$\boldsymbol{F} = -\chi\boldsymbol{\nabla}T \quad \text{and} \quad \boldsymbol{\nabla}P = \varrho\,\boldsymbol{g}_{\text{eff}}\,, \quad \text{with } \chi = 4acT^3/(3\kappa\varrho). \tag{6.57}$$

Radiation pressure is included in P, the total pressure. With the von Zeipel theorem (4.21) and (4.22), the local radiative gradient becomes

$$\nabla_{\text{rad}} = \frac{dT}{dn}\frac{dn}{dP}\frac{P}{T} = \frac{3}{16\pi acG}\frac{\kappa L(P)P}{M_\star(r)T^4}\,, \tag{6.58}$$

where the derivatives are taken along a direction $\boldsymbol{n}$ perpendicular to the isobars. Except $L(P)$, the terms are local and thus have to be taken at the given (r, ϑ). With the Eddington factor Γ (3.117), we get

$$\nabla_{\text{rad}} = \frac{\Gamma}{4\left(1-\beta\right)\left(1-\frac{\Omega^2}{2\pi G\rho_{\text{m}}}\right)}\,, \tag{6.59}$$

where $\beta = P_{\text{g}}/P$ is the ratio of the gas to total pressure, thus $P/(aT^4) = 1/[3(1-\beta)]$. The adiabatic gradient ∇_{ad} is given by (7.87). As T varies with ϑ, β also varies with colatitude and we write $\beta(\vartheta)$. $\beta(\vartheta)$ is higher at the equator, which favors equatorial convection. The criterion (6.56) becomes

$$\frac{\Gamma(\vartheta)}{\left(1-\frac{\Omega^2}{2\pi G\rho_{\text{m}}}\right)} > 4\left[1-\beta(\vartheta)\right]\left(\nabla_{\text{ad}}+\nabla_\Omega\sin\vartheta\right)\,, \tag{6.60}$$

where the ϑ dependence of Γ comes only through $\kappa(\vartheta)$. In the absence of rotation, this expression is equivalent to (5.86). In a rotating star, the left-hand side of (6.60) is larger which favors convection, while ∇_Ω tends to inhibit convection.

The gradient ∇_Ω depends on the distribution of the specific angular momentum $j = \varpi^2\Omega$. As j decreases outward, ∇_Ω generally has a stabilizing effect. Let us consider the two extreme cases for $\Omega(r)$ already seen above.

– Constant specific angular momentum: a distribution $\Omega \sim r^{-2}$ may result from the Rayleigh–Taylor instability. This distribution is sometimes considered because plumes rapidly redistribute the angular momentum. If so, $\nabla_\Omega = 0$ and one is brought back to Schwarzschild's criterion.
– Constant angular velocity: this assumption is also used, with the argument that turbulent viscosity favors solid rotation. If so, one has

$$\nabla_\Omega = 4\frac{\Omega^2}{g_{\text{grav}}}\frac{H_P}{\delta} = \frac{4\Omega^2}{g_{\text{grav}}\,\varrho}\frac{P}{g_{\text{eff}}\delta}\,. \tag{6.61}$$

In the very outer layers, as long as $\kappa \approx \text{const.}$ and $g_{\text{eff}} \approx \text{const}$, at an optical depth τ one has $P \approx (g_{\text{eff}}/\kappa)\,\tau$ (cf. expr. 24.18). This gives

$$\nabla_\Omega \approx 4 \frac{\Omega^2}{g_{\text{grav}} \varrho \, \kappa \delta} \, \tau \approx 4 \left(\frac{\Omega^2 R^3}{GM} \right) \left[\frac{\tau}{\varrho \, \kappa R \delta} \right] . \tag{6.62}$$

The term in the first parenthesis is $\omega^2 = (\Omega/\Omega_c)^2$ at equator, while that in square brackets is the ratio $(R-r)/R$ (assuming $\delta = 1$), which is small in the envelope. Criterion (6.60) becomes in this approximation,

$$\frac{\Gamma}{\left(1 - \frac{\Omega^2}{2\pi G \rho_m} \right)} > 4\,(1-\beta) \left(\nabla_{\text{ad}} + \omega^2 \left[\frac{R-r}{R} \right] \sin \vartheta \right), \tag{6.63}$$

Table 6.1 Sizes of the external convective zones at the equator for 20 $M_\odot$ models at $Z = 0.02$ at the end of the MS phase. The sizes are given in terms of the radius at the top and bottom of the convective zone and in percentage of the radius. The mass fractions contained in the convective zones are indicated [357]

Model	$(r_{\text{top}}/R) - (r_{\text{bottom}})/R$	%	Mass fractions
$\Omega/\Omega_c = 0$	$\nabla_{\text{ad}} - \nabla_{\text{rad}} > 0$		
1st zone	0.992–0.999	0.7	2.6×10^{-9}
2nd zone	0.915–0.962	4.7	7.4×10^{-7}
$\Omega/\Omega_c = 0.94$	$\nabla_{\text{ad}} - \nabla_{\text{rad}} > 0$		
1st zone	0.958–0.988	3.0	1.3×10^{-8}
2nd zone	0.727–0.862	13.5	2.8×10^{-6}
$\Omega/\Omega_c = 0.94$	$\nabla_{\text{ad}} - \nabla_{\text{rad}} + \nabla_\Omega > 0$		
1st zone	0.960–0.988	2.8	1.2×10^{-8}
2nd zone	0.727–0.859	13.2	2.7×10^{-6}
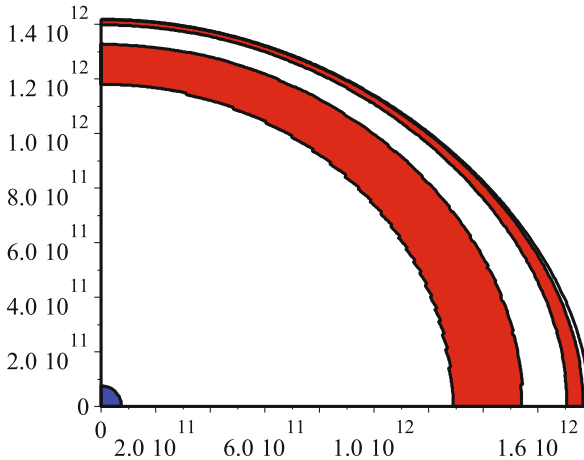
Fig. 6.7 Two-dimensional representation of the convective zones (*dark areas*) in a model of 20 $M_\odot$ with $X = 0.70$ and $Z = 0.020$ at the end of MS evolution with ($\Omega/\Omega_{\text{crit}} = 0.94$), with an account of only ∇_{rad} and ∇_{ad}. The axis units are cm. From the author, C. Georgy and G. Meynet [357]

where as above the various quantities are local ones. At low rotation, the Solberg–Hoiland term ∇_Ω is negligible with respect to the other terms. At high rotation for constant Ω, it is not negligible, but in general smaller than the other terms because the convective zone lies very close to the surface and the term $[(R-r)/R]$ is small.

Since the actual rotation laws are likely between the two extreme cases $\Omega(r) =$ const. and $\Omega \sim r^{-2}$, we conclude that the main effect of rotation on convection in stellar envelopes is not the inhibiting effect due to the Solberg–Hoiland criterion, but the effect of rotation on the thermal gradient ∇_{rad}, which enhances convection. Table 6.1 shows the dimensions of the external convective zone in 20 $M_\odot$ models with and without rotation, with and without the term ∇_Ω. One notices the increase in the size of the two convective zones with rotation. These zones occupy a significant fraction of the radius (Fig. 6.7); however, their masses are small.

The matter accelerated in the wind continuously crosses the convective zones in a dynamical process. Convection in the outer layers of O-type stars generates acoustic waves with periods of several hours to a few days. These waves propagate and are amplified in the winds, which have a lower density. They are likely to play a role in the origin of the clumping of stellar winds.

Part II
Physical Properties of Stellar Matter

Chapter 7
The Equation of State[*]

From the density of about 10^{-23} g cm^{-3} in the interstellar medium to a density of about 10^{15} g cm^{-3} in neutron stars the difference amounts to a factor 10^{38}. Over such different conditions, the physical state of the matter differs a lot. The physical state of a medium is described by an equation of state, which is a relation $P = P(\varrho, T)$ between the pressure P, density ϱ and temperature T for a given chemical composition. It is given either by an analytical expression, like the law of perfect gas, or by a table of numerical values. This equation plays an essential role in stellar evolution. An overview of the different physical states of matter is given in Fig. 7.8.

The study of the thermodynamic coefficients is generally not the beloved subject of students. However, a star is a thermodynamic machine, thus the thermodynamic parameters, such as the specific heats, the adiabatic exponents Γ_i, etc., determine most of the stellar properties. For example, they tell us how a star is heating when it contracts, whether the nuclear reactions are stable or not, when a stellar core collapses to make a supernova, etc.

7.1 Excitation and Ionization of Gases

The excitation and ionization of the stellar medium influences the matter properties, such as the mean molecular weight μ, the specific heats C_P and C_V as well as other thermodynamic properties. Partial ionization also increases the number of possible atomic transitions and thus the matter opacity.

7.1.1 Excitation

Let us consider a system of N atoms with energy states E_n, $E_{n'}$. We want to know the numbers N_n, $N_{n'}$ of atoms with energy states n, $n' \ldots$ as a function of T. These numbers determine the gas properties and the relative intensities of spectral lines. We

---

[*]This chapter may form the matter of a basic introductory course.

consider a situation of equilibrium for non-degenerate particles, i.e., for relatively low densities. The number of atoms with an electron in the level n is according to Boltzmann statistics (Appendix C.5)

$$N_n = g_n e^{\psi} e^{-E_n/(kT)}, \tag{7.1}$$

where g_n is the statistical weight of level n. The ratio of the numbers of electrons in levels n and n' is

$$\frac{N_{n'}}{N_n} = \frac{g_{n'}}{g_n} e^{-(E_{n'}-E_n)/(kT)} . \tag{7.2}$$

The total number is $N = \sum_n N_n$ with

$$\frac{N_n}{N_1} = \frac{g_n}{g_1} e^{-E_{n,1}/(kT)} \qquad E_{n,1} = E_n - E_1 , \tag{7.3}$$

$$\text{and } N = N_1 \sum_n \frac{N_n}{N_1} = \frac{N_1}{g_1} \underbrace{\sum_n g_n e^{-E_{n,1}/(kT)}}_{u(T)} . \tag{7.4}$$

$u(T)$ is the partition function, it can be regarded as the statistical weight of the whole system of atoms. The fraction of atoms in state n is

$$\frac{N_n}{N} = \frac{N_n}{N_1} \frac{N_1}{N} = \frac{g_n}{u(T)} e^{-(E_n-E_1)/(kT)} . \tag{7.5}$$

Function $u(T)$ tends toward infinity because $n \to \infty$ and the differences $E_{n,1}$ are finite. However, the interactions between ions lower the continuum level and limit the summation in (7.4). Thus, one can often take only the first terms in $u(T)$. Quantities $g_n, E_n, u(T)$ are tabulated for different elements (see http://vizier.u-strasbg.fr/OP.html).

7.1.1.1   Atomic Structure: The Case of Hydrogen

Each excitation state is characterized by three quantum numbers n, l, s. Number n is the principal quantum number; for hydrogen it is associated to the semi-major axis of the electron orbit. Number $n = 1$ refers to the first Bohr orbit. The n energy levels are divided into different orbital states l of angular momentum $l = 0, 1, 2, \ldots n-2,$ $n-1$. For each value of l, there are $2l+1$ states. For example, for $n = 3$ one has $l = 0, 1, 2$ and

$$\left. \begin{array}{ll} l = 0 & 2l+1 = 1 \\ l = 1 & 2l+1 = 3 \\ l = 2 & 2l+1 = 5 \end{array} \right\} = 9 . \tag{7.6}$$

An electron is noted $s, p, d, f, \ldots$ for $l = 0, 1, 2, 3, \ldots, n-1$, respectively. For each orbital state l, one has $2s + 1$ states of spin $s = \pm 1/2$, i.e., 2 states. The statistical weight g_n of the hydrogen atom is

$$g_n = 2 \sum_{K=1}^{n} \left(\underbrace{2(n-K)+1}_{l} \right) = 2n^2 , \tag{7.7}$$

which is easily demonstrated by recurrence. The energy of level n for hydrogen is $E_n = -13.6\,\text{eV}/n^2$ and

$$E_{n,1} = E_n - E_1 = -\frac{13.6}{n^2} + 13.6 = 13.6\,\frac{n^2 - 1}{n^2} , \tag{7.8}$$

$$u(T) \simeq g_1 e^{-E_{1,1}/(kT)} \simeq 2 , \tag{7.9}$$

$$\frac{N_n}{N} = n^2 e^{[(-13.6/(kT))\,(n^2-1)/n^2]} . \tag{7.10}$$

At different T, the ratios N_2/N are

$$
\begin{array}{ll}
T = 5 \times 10^3\,K & N_2/N = 2.1 \ \times 10^{-10} \\
 1 \times 10^4\,K & 2.9 \ \times 10^{-5} \\
 2 \times 10^4\,K & 1.08 \times 10^{-2} .
\end{array}
\tag{7.11}
$$

The population of upper levels increases rapidly with growing T.

7.1.2   Ionization of Gases: The Saha Equation

During ionization a bound electron is ejected into an unbound state. Ionization occurs when kT becomes of the order or larger than the ionization potential considered. The continuum begins at energy I_0. Each element has a series of ionization potentials I_i corresponding to the successive ionization states. The law of Saha expresses the relative concentrations of atoms in the successive ionization states. It is derived from Boltzmann formula (Appendix C.5) applied to the reaction
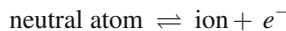
$$\text{neutral atom} \rightleftharpoons \text{ion} + e^-$$

Let n_{00}, n_{01} and n_e be the concentrations of neutral atoms, ions and electrons. The first index indicates the excitation level (0 for the fundamental level), the second indicates the ionization degree. The statistical weight g_e of a free electron with momentum $p = m_e v$ in the volume element dV is the ratio of the volume in the phase space to the size h^3 of a quantum cell with account of the spin number

$$g_e = 2\,\frac{d^3q\,d^3p}{h^3} = \frac{2\,dV\,4\pi\,p^2\,dp}{h^3} . \tag{7.12}$$

The statistical weight of the system ion plus electron is $g_e \times g_{01}$. In its ionized state, the system has the following energy relative to the fundamental level

$$E = I_0 + \frac{p^2}{2m_e} . \tag{7.13}$$

Boltzmann law applied to ionization gives

$$\frac{n_{01}}{n_{00}} = \frac{g_{01}\, g_e}{g_{00}}\, e^{-\left(I_0 + \frac{p^2}{2m_e}\right)/(kT)} . \tag{7.14}$$

In the second member, one should also have $\left(e^{\psi_{01}+\psi_e}/e^{\psi_{00}}\right)$, however, relation (C.60) implies

$$\psi_{01} + \psi_e - \psi_{00} = 0 , \tag{7.15}$$

so that the term containing ψ is equal to 1. Let us consider an ejected electron with a momentum in the interval $(p, p+\Delta p)$, it has a number $2\Delta V\, 4\pi p^2 \Delta p/h^3$ of quantum states. The volume occupied by the electron is $\Delta V = 1/n_e$, where n_e is the concentration. One has thus in the interval Δp

$$\frac{n_{01}}{n_{00}} = \frac{1}{n_e}\frac{g_{01}}{g_{00}}\frac{8\pi}{h^3}\, e^{-\left(I_0 + \frac{p^2}{2m_e}\right)/(kT)}\, p^2 \Delta p . \tag{7.16}$$

Integrating over the electron velocities gives

$$\int_0^\infty e^{\frac{-p^2}{2m_e kT}}\, p^2\, dp = \frac{\sqrt{\pi}}{4}\, (2m_e kT)^{3/2} , \tag{7.17}$$

because $\int_0^\infty t^2\, e^{-at^2}\, dt = (1/(4a))\sqrt{\pi/a}$. One obtains

$$\frac{n_{01}\, n_e}{n_{00}} = 2\frac{g_{01}}{g_{00}}\left(\frac{2\pi m_e kT}{h^2}\right)^{3/2}\, e^{-I_0/(kT)} . \tag{7.18}$$

This is Saha's equation, which gives the ratio of number of atoms ionized one time to those not ionized. The units are cm^{-3} on both sides.

7.1.3   The Saha–Boltzmann Equation

The above equation can be generalized for any other state of ionization

$$\frac{n_{0\,j+1}\, n_e}{n_{0\,j}} = 2\frac{g_{0\,j+1}}{g_{0\,j}}\left(\frac{2\pi m_e kT}{h^2}\right)^{3/2}\, e^{-I_j/(kT)} , \tag{7.19}$$

where I_j is the ionization potential from state j to $j+1$. Let E_{ij} be the excitation energy of level i of ion j relative to the fundamental level of this ion. The difference $(I_j - E_{ij})$ is the ionization potential from level (i, j) up to the fundamental level of the ionization state $j+1$. According to Boltzmann's law (Appendix C.5), one has $n_{ij}/n_{0j} = (g_{ij}/g_{0j})e^{-E_{ij}/(kT)}$ and this gives

$$\frac{n_{0\,j+1}\,n_e}{n_{ij}} = \frac{n_{0\,j+1}}{n_{0j}}\frac{n_{0j}}{n_{ij}}n_e = 2\frac{g_{0\,j+1}}{g_{ij}}\left(\frac{2\pi m_e kT}{h^2}\right)^{3/2} e^{-\left(\frac{I_j - E_{ij}}{kT}\right)}. \qquad (7.20)$$

One may search the expression giving the ratio n_{j+1}/n_j of atoms $j+1$ times ionized to those j times ionized, whatever the excitation state. One has $n_i/n = g_i/u(T)\,e^{-E_i/(kT)}$ which becomes for the (i, j) state

$$\frac{n_{ij}}{n_j} = \frac{g_{ij}}{u_j}\,e^{-E_{ij}/(kT)}, \qquad (7.21)$$

and for the state $(0, j+1)$ $\qquad \dfrac{n_{0\,j+1}}{n_{j+1}} = \dfrac{g_{0\,j+1}}{u_{j+1}}.$ $\qquad\qquad\qquad (7.22)$

By replacing in (7.20), one gets

$$\frac{n_{j+1}\,n_e}{n_j} = \frac{n_{ij}}{n_j}\frac{n_{0\,j+1}}{n_{ij}}n_e\frac{n_{j+1}}{n_{0\,j+1}} = 2\frac{u_{j+1}}{u_j}\left(\frac{2\pi m_e kT}{h^2}\right)^{3/2} e^{-I_j/(kT)}, \qquad (7.23)$$

which is the Saha–Boltzmann equation expressing the ratios of all atoms with ionization degree $j+1$ with respect to those of degree j.

Instead of the electronic concentration n_e, one uses sometimes the electronic pressure P_e

$$P_e = n_e\,kT \qquad (7.24)$$

and the Boltzmann–Saha equation becomes

$$\frac{n_{j+1}}{n_j} = 2\frac{u_{j+1}}{u_j}\left(\frac{2\pi m_e}{h^2}\right)^{3/2}\frac{(kT)^{5/2}}{P_e}e^{-I_j/(kT)}. \qquad (7.25)$$

Ionization is favored by a high temperature and a low electronic pressure. Thus, for the same value of T, the elements are more ionized in supergiant stars due to the low density in their external regions than in dwarfs. Of course, the elements with low ionization potential are ionized first.

If one has to estimate for example the ratio n_{20}/n_{tot} of the number of atoms in the Balmer series with respect to the total number of atoms (neutral and ionized), one writes the ratio as follows

$$\frac{n_{20}}{n_{tot}} = \frac{n_{20}}{n_0 + n_1} = \frac{n_{20}/n_0}{1 + \frac{n_1}{n_0}}, \qquad (7.26)$$

where n_{20}/n_0 is given by Boltzmann's law and n_1/n_0 by Saha's. The intensity of Balmer lines of hydrogen is maximum near 10^4 K.

7.1.4 Ionization Potentials and Negative Ions

The various atomic data are tabulated, see for example [10, 304] or the database under http://vizier.u-strasbg.fr/OP.html. The first ionization potentials of important elements are, expressed in eV,

1	H	13.60	11	Na	5.14	21	Sc	6.54
2	He	24.59	12	Mg	7.65	22	Ti	6.82
3	Li	5.39	13	Al	5.99	23	V	6.74
4	Be	9.32	14	Si	8.15	24	Cr	6.77
5	B	8.30	15	P	10.49	25	Mn	7.44
6	C	11.26	16	S	10.36	26	Fe	7.87
7	N	14.53	17	Cl	12.97	27	Co	7.86
8	O	13.62	18	Ar	15.76	28	Ni	7.64
9	F	17.42	19	K	4.34	29	Cu	7.73
10	Ne	21.56	20	Ca	6.11	30	Zn	9.39

The relatively abundant elements Na, Mg, Al, K, Ca, Si are easily ionized and are the main sources of free electrons in the solar atmosphere. The electrons liberated by these elements influence the ionization of H and He, the most abundant elements.

7.1.4.1   Negative Ions

A neutral atom may form a negative ion by capturing an additional electron. An important astrophysical case is

$$H + e^- \rightleftharpoons H^-. \tag{7.27}$$

The electric force of the atomic nucleus is not fully saturated by the bound electron and the proton may attach a second electron. Ion H^- is a strong opacity source (Sect. 8.3.1) in the outer solar layers for $\lambda < 16550$ Å with a maximum near 8000 Å. Saha equation gives

$$\frac{n_H}{n_{H^-}} P_e = \left(\frac{2\pi m_e}{h^2} \right)^{3/2} (kT)^{5/2} \, 2 \times \frac{2}{1} \, e^{\frac{-0.747\,eV}{kT}}. \tag{7.28}$$

The binding energy of the additional electron is weak, i.e., 0.747 eV, thus it is little bound. The abundance of H^- depends on the elements with a low ionization potentials. There are other negative ions, for example, O^- and C^-, which play a role in C-rich AGB stars. However, in general only H^- is a major opacity source.

7.2   **Perfect Gas and Mean Molecular Weights**

The model of an ideal gas assumes particles of negligible size, without interactions except the possibility of collisions. The pressure results from the particle collisions on the surroundings. The law of perfect gas relates the gas pressure P_g, the volume V and temperature T. It is often written for a mole, i.e., for the Avogadro number N_{AV} of gas particles,

$$P_g V_{\text{mole}} = \mathcal{R} T .$$

(7.29)

The gas constant $\mathcal{R} = k N_{AV}$, where k is the Boltzmann constant (Appendix A.1). If V is (here) the average volume occupied by one particle, the law becomes

$$P_g V = kT \quad \text{with} \quad V \equiv \frac{\mu \, m_u}{\varrho} ,$$

(7.30)

where $\mu \, m_u$ is the average mass of a particle and m_u the atomic mass unit (see Appendix A.1). It is also the inverse of the Avogadro Number $m_u = 1/N_{AV} = 1.66053$ 10^{-24} g; m_u slightly differs from the mass of the hydrogen atom. μ is the mean molecular weight. The law of perfect gas can be written as

$$P_g = \frac{\mathcal{R}}{\mu} \varrho T = \frac{k}{\mu \, m_u} \varrho T .$$

(7.31)

Ionization influences the mean molecular weight μ. Let us consider a medium with various elements j of atomic mass A_j. Let us call X_j the mass fraction of element j. The concentration n, i.e., the number of particles of any kinds by volume unity, is

$$n = \frac{\varrho}{\mu \, m_u} = \sum_j \varrho X_j \frac{N_{AV}}{A_j} (1 + E_j),$$

(7.32)

$$
\begin{aligned}
\varrho X_j \quad &: \text{partial density of element } j, \\
N_{AV}/A_j \quad &: \text{number of atoms } j \text{ per gram}, \\
1 + E_j \quad &: \text{number of particles } (1 \text{ ion} + E_j \text{ free electrons}) .
\end{aligned}
$$

(7.33)

The mean molecular weight is

$$\frac{1}{\mu} = \sum_j \frac{X_j}{A_j} (1 + E_j) .$$

(7.34)

The number of free electrons by volume unity is

$$n_e = \frac{\varrho}{m_u} \sum_j \frac{X_j}{A_j} E_j .$$

(7.35)

Let us define the mean molecular weight μ_e by free electron, i.e., the average number of mass units by free electron

$$n_e = \frac{\varrho}{\mu_e m_u}, \quad \text{thus} \quad \frac{1}{\mu_e} \equiv \sum_j \frac{X_j}{A_j} E_j . \tag{7.36}$$

The mean number of electrons per atom or ion is

$$E = \frac{\sum_j \frac{X_j}{A_j} E_j}{\sum_j \frac{X_j}{A_j}} . \tag{7.37}$$

For a neutral medium, $E_j = 0$ and the mean molecular weight is

$$\frac{1}{\mu_0} = \sum_j \frac{X_j}{A_j} . \tag{7.38}$$

For a fully ionized medium, one has $E_j = Z_j$ and the corresponding μ is

$$\frac{1}{\mu} = \sum_j \frac{X_j (1 + Z_j)}{A_j} . \tag{7.39}$$

The chemical abundances are often represented by X, Y, Z, which are the mass fractions of H, He and heavy elements (all except H and He). Many models and data concern a so-called standard composition, typically $X = 0.705, Y = 0.275, Z = 0.02$. Recent determinations of solar abundances yield $X = 0.7393$, $Y = 0.2485$, $Z = 0.0122$ according to Asplund, Grevesse and Sauval [20]. This has to be distinguished from the initial solar abundances because of microscopic diffusion of the elements during the evolution of the Sun. The initial solar abundances giving the best fit of helioseismic data, also accounting for the neon value from Cunha et al. [151], are $X = 0.720, Y = 0.266, Z = 0.014$ [169], see also Appendix A.3. As a function of X, Y, Z, the mean molecular weight of the fully ionized medium is

$$\frac{1}{\mu} \simeq 2X + \frac{3}{4}Y + \frac{Z}{2} . \tag{7.40}$$

With account of the fact that $X + Y + Z = 1$, one has

$$\frac{1}{\mu} \simeq \frac{5X + 3 - Z}{4} . \tag{7.41}$$

For pure ionized H, one has $\mu = 1/2$, and for ionized heavy elements $\mu \simeq 2$. The variation of μ in the outer solar layers is illustrated in Fig. 7.1. Below 8000 K, H and He are essentially neutral and $\mu \approx 1.296$ for the above standard mixture; for $T > 30\,000$ K, these elements are nearly fully ionized and the standard mixture gives $\mu = 0.615$ ($\mu = 0.6073$ for the best initial solar abundances).
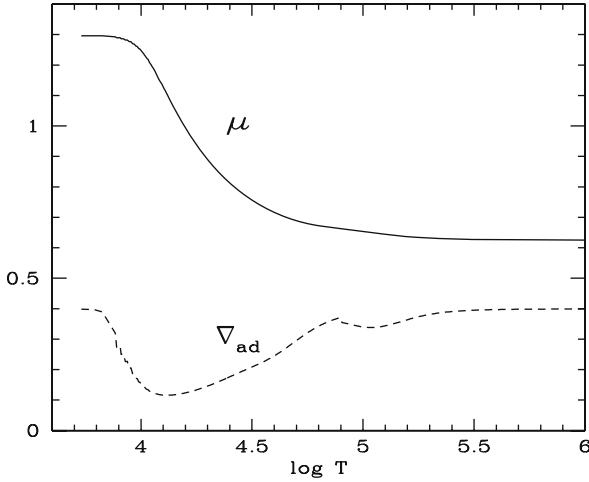
Fig. 7.1 Variations of the mean molecular weight μ and of the adiabatic gradient (see expression 7.57) as a function of temperature in the outer solar layers

The concentration of free electrons as a function of X, Y, Z is

$$n_e = \frac{\varrho}{m_u} \sum_j \frac{X_j}{A_j} Z_j \simeq \frac{\varrho}{2m_u} (1+X) \, . \tag{7.42}$$

$$\text{This implies} \quad \frac{1}{\mu_e} \simeq \frac{1}{2}(1+X), \tag{7.43}$$

an expression which is useful for electron scattering opacity (Sect. 8.2).

7.3   Partially Ionized Stellar Medium

Partially ionized media need to be treated with care because there is a coupling of the ionization of various elements. The free electrons from an element of low ionization potential influence the ionization equilibrium of other elements, due to the term n_e in (7.23). Let us call E the ratio of the numbers of free electrons and of atoms or ions. The pressure P_0 of both ions and neutral atoms and the pressure P_e of the electron gas are, respectively,

$$P_0 = \frac{k}{\mu_0 \, m_u} \varrho T = \frac{\mathcal{R}}{\mu_0} \varrho T \quad \text{and} \quad P_e = \frac{\mathcal{R}}{\mu_e} \varrho T \, . \tag{7.44}$$

μ_e is the mean mass by free electron $\mu_e = \mu_0/E$. The total pressure and mean molecular weight of the gas of neutral atoms, ions and free electron are

$$P_g = \frac{\mathcal{R}}{\mu_0} (1+E) \varrho T \quad \text{and} \quad \mu = \frac{\mu_0}{1+E} \, . \tag{7.45}$$

For a partially ionized medium, the mean number E must be determined. The ratio of the gas to the electronic pressure is $P_g/P_e = (1+E)/E$. The ratio $P_g/P_e \sim 2$ for a completely ionized H gas, while $P_e/P_g \to 0$ in cool stars.

7.3.1 Coupled Equations for a Medium Partially Ionized

Let us consider a medium of partially ionized H and He. The developments can be generalized for more elements [33]. One defines v_i as the fraction of atoms or ions of the element i with respect to the total number of atoms or ions, thus $\sum_i v_i = 1$. One defines X_i^s the fraction of atoms i in ionization stage s with respect to the total number of atoms or ions i. Thus, one has for the number E of free electrons per atom or ion

$$E = \sum_i v_i \sum_{s=0}^{Z_i} s X_i^s . \tag{7.46}$$

One also defines the number of atoms i in ionization states above s relative to the number of atoms or ions i,

$$Y_i^s = \sum_{r=s+1}^{Z_i} X_i^r . \tag{7.47}$$

Thus, the number E of free electrons is

$$E = \sum_i \sum_{s=0}^{Z_i-1} v_i Y_i^s . \tag{7.48}$$

For the mixture considered, element "1" is H and H^+, element "2" is He, He^+ and He^{++}. The above quantities are number ratios:

$$X_1^1 = \frac{H^+}{H+H^+} , \quad X_2^1 = \frac{He^+}{He+He^++He^{++}} , \quad X_2^2 = \frac{He^{++}}{He+He^++He^{++}} ,$$

$$Y_1^0 = X_1^1 , \qquad Y_2^0 = X_2^1 + X_2^2 , \qquad Y_2^1 = X_2^2 .$$

To simplify, we shall write the above quantities by X_1, X_2, X_3, Y_1, Y_2, Y_3. Thus, number E becomes

$$E = \sum_i v_i Y_i = v_1 X_1 + v_2(X_2 + X_3) + v_2 X_3 = v_1 X_1 + v_2 (X_2 + 2X_3) . \tag{7.49}$$

The Saha equation gives us the ratio

$$\frac{X_1 P_e}{(1-X_1)P_g} = K_1 \quad \text{with} \quad K_1 = \frac{(2\pi m_e)^{3/2} (kT)^{5/2}}{\beta P h^3} \omega_1 \, e^{-I_1/(kT)} , \tag{7.50}$$

where P is the total pressure and $\beta = P_g/P$ the ratio of the perfect gas pressure to total pressure (Sect. 3.6). The ratio of partition functions is $\omega_1 = 2u_H^+/u_H$. One has a total of four equations

$$
\left.
\begin{aligned}
\frac{X_1}{1-X_1}\frac{E}{1+E} &= K_1 \\[2mm]
\frac{X_2}{1-X_2-X_3}\frac{E}{1+E} &= K_2 \\[2mm]
\frac{X_3}{X_2}\frac{E}{1+E} &= K_3 \\[2mm]
v_1 X_1 + v_2(X_2 + 2X_3) &= E
\end{aligned}
\right\}
\begin{aligned}
&\text{four coupled equations with } X_1, X_2, X_3 \\
&\text{and } E \text{ as unknown quantities}
\end{aligned}
\quad (7.51)
$$

The K_i terms are defined in a similar way as for K_1 (7.50) with $I_1 = 13.598$ eV, $I_1 = 24.587$ eV and $I_2 = 54.416$ eV, and

$$
\omega_1 = 2\frac{u_H^+}{u_H} = 2\frac{1}{2} = 1, \quad \omega_2 = 2\frac{u_{He}^+}{u_{He}} = 2\frac{2}{1} = 4, \quad \omega_3 = 2\frac{u_{He}^{++}}{u_{He}^+} = 2\frac{1}{2} = 1.
$$

The four equations (7.51) are solved by an iterative process. In the first step, it is assumed that only H contributes to E, then He, etc. Such systems are solved for the most abundant elements and ionization degrees. These equations apply in a medium where the pressure is low, for example in the outer stellar layers or in the interstellar medium. Figure 7.2 shows the variations of the ionized fractions of H$^+$, He$^+$ and He^{++} in the outer solar layers. From 10^4 to 10^6 K, these fractions vary rapidly and produce changes of μ and of the various thermodynamic coefficients.
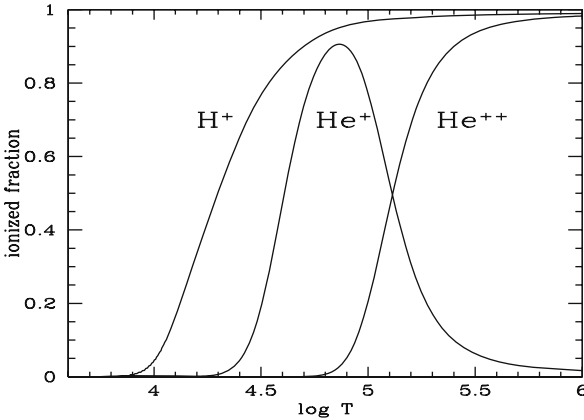
Fig. 7.2 Fractions of ionized hydrogen H$^+$ and of ionized helium He$^+$ and He^{++} as a function of the temperature in the outer solar layers of a solar model. $T = 10^6$ K at $M_r/M_\odot = 0.995$, $R/R_\odot = 0.846$

The Saha equation neglects the electrostatic interactions. In stellar depths, the elements are fully ionized although the above equations would not show it. The elements are ionized by pressure effects (Sect. 7.6.3). Another limitation is that we have used Boltzmann equation, thus thermodynamic equilibrium is assumed, which is correct when collisions dominate over radiative interactions. This is not the case for example in the solar corona.

7.3.2   Thermodynamic Coefficients for Partial Ionization

The calculation of the various thermodynamic functions demands the knowledge of $P(\varrho, T)$ and $U(P, T)$, the internal energy by mass unit. The internal energy is the sum of the kinetic energy of thermal agitation, the total ionization energy and the radiation energy (Appendix C.1.1),

$$
\begin{aligned}
U &= \frac{3}{2} \frac{kT}{\mu m_{\mathrm{u}}} + \frac{1}{\mu_0 m_{\mathrm{u}}} \sum_i \nu_i \sum_{s=0}^{Z_i-1} Y_i^s I_i^s + \frac{aT^4}{\varrho} \\
&= \frac{3}{2} \frac{\mathcal{R}T}{\mu} + \frac{R}{\mu_0 k} \sum_i \nu_i \sum_{s=0}^{Z_i-1} Y_i^s I_i^s + \frac{3(1-\beta)}{\beta} \frac{\mathcal{R}T}{\mu} \,, \\
U &= \frac{\mathcal{R}}{\mu_0} \left\{ \left[\frac{3}{2} + \frac{3(1-\beta)}{\beta} \right] (1+E) T + \frac{1}{k} \sum_i \nu_i \sum_{s=0}^{Z_i-1} Y_i^s I_i^s \right\} .
\end{aligned}
\tag{7.52}
$$

The thermodynamic functions of partially ionized gases have been calculated by Baker & Kippenhahn [33]. For example, with $U = U(P, T)$ one gets C_P and C_V by expressing

$$
C_P = \left(\frac{dQ}{dT} \right)_P = \left(\frac{\partial U}{\partial T} \right)_P - \frac{P}{\varrho^2} \left(\frac{\partial \varrho}{\partial T} \right)_P ,
\tag{7.53}
$$

$$
C_V = \left(\frac{dQ}{dT} \right)_\varrho = \left(\frac{\partial U}{\partial T} \right)_\varrho + \left(\frac{\partial U}{\partial P} \right)_T \left(\frac{\partial P}{\partial T} \right)_\varrho .
\tag{7.54}
$$

One designates by C_P and C_V the coefficients for a general equation of state and by c_P and c_V the coefficients for the perfect gas. For a neutral and for a fully ionized perfect gas, without radiation pressure effects, one has

$$
c_V = \frac{3}{2} \frac{\mathcal{R}}{\mu_0} \quad \text{and} \quad c_V = \frac{3}{2} \frac{\mathcal{R}}{\mu_0} (1+E) .
\tag{7.55}
$$

E is given by (7.37). In the case of hydrogen, the specific heat c_V is twice larger in the ionized than in the neutral medium. The above expressions allow one to find the various thermodynamic coefficients for a partially ionized medium [33]. The specific heats increase by an order of magnitude between 10^4 and 5×10^4 K due to
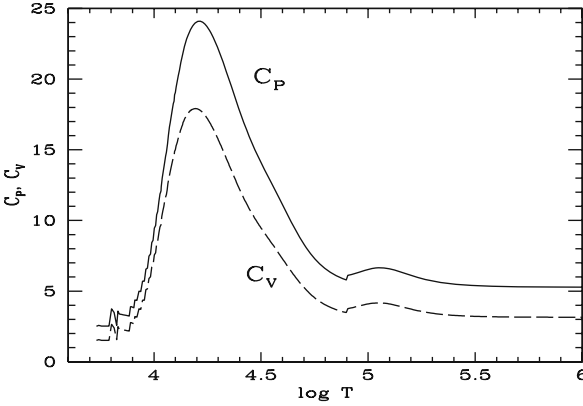
Fig. 7.3 Variations of the specific heats C_P and C_V as a function of T in the outer solar layers. The units of C_P and C_V are $\mathcal{R}/\mu_0$. The variations are due to the changes of partial ionization as in Fig. 7.2

partial ionization as illustrated by Fig. 7.3. The reason is that the heat brought to the system is used to increase the ionization fraction, while the temperature of the medium experiences only little changes during ionization.

7.4   Adiabatic Exponents and Thermodynamic Functions

These functions determine major events in stellar evolution, such as star formation, convection, pulsation, core collapse and supernova explosions. Let us examine some useful properties.

7.4.1   Definitions of the Adiabatic Exponents

For adiabatic transformations of a perfect gas, basic physics gives the following relations by unit of mass

$$P_g V^\gamma = \text{const.} \ , \quad \frac{P_g}{\varrho^\gamma} = \text{const.} \ , \quad \frac{T}{\varrho^{\gamma-1}} = \text{const.} \ , \quad P_g T^{\frac{\gamma}{1-\gamma}} = \text{const.}$$

This is easily demonstrated from (3.63) and (7.31). For adiabatic transformations in a medium with a general equation of state, one writes similarly

$$\frac{P}{\varrho^{\Gamma_1}} = \text{const.} \ , \qquad \frac{T}{\varrho^{\Gamma_3-1}} = \text{const.} \ , \qquad PT^{\frac{\Gamma_2}{1-\Gamma_2}} = \text{const.} \ , \qquad (7.56)$$

which imply the following definitions of the Γ_i

$$\Gamma_1 \equiv \left(\frac{d\ln P}{d\ln \varrho}\right)_{ad}, \quad \Gamma_3 - 1 \equiv \left(\frac{d\ln T}{d\ln \varrho}\right)_{ad},$$

$$\frac{\Gamma_2}{\Gamma_2 - 1} = \left(\frac{d\ln P}{d\ln T}\right)_{ad} \equiv \frac{1}{\nabla_{ad}}. \tag{7.57}$$

The quantity ∇_{ad} was given in Sect. 3.3.5. We may remark that only two of these Γ_i ($i = 1$–3) are independent, because of the identity

$$\frac{\Gamma_2}{\Gamma_2 - 1} = \frac{\Gamma_1}{\Gamma_3 - 1}. \tag{7.58}$$

Unlike the exponent γ in the case of perfect gas, the Γ_i are not equal to the ratio C_P/C_V. The Γ_i depend on the equation of state. Figure 7.4 illustrates the variations of the Γ_i in the outer solar layers. The Γ_i are equal to 5/3 for the neutral and fully ionized cases. In the domain of partial ionization (Fig. 7.2), the Γ_i become lower than 4/3, which is destabilizing according to the Virial theorem (Sect. 1.3.2), however not catastrophic since the low Γ_i occur only in a very small stellar mass fraction. Again, we may understand this behavior by noting, for example in the definition of $\Gamma_3 - 1$, that the variation of T is reduced by partial ionization when the density and pressure increase. Figure 7.1 shows the corresponding variations of $\nabla_{ad} = (\Gamma_2 - 1)/\Gamma_2$.
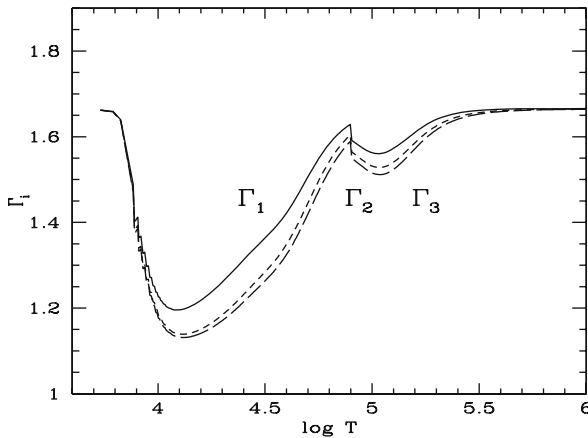
Fig. 7.4 The adiabatic exponents Γ_i as functions of temperature in the outer solar layers. In the neutral medium below 8000 K and in the fully ionized medium above $T = 3 \times 10^5$ K, the various Γ_i converge toward 5/3

7.4.2   Relation Between the Γ_i and Specific Heats

Let us consider the internal energy by unit of mass $U = U(T, \varrho)$. One has

$$dU = C_V\, dT + \left(\frac{\partial U}{\partial \varrho}\right)_T d\varrho \ . \tag{7.59}$$

Thus, the first law of thermodynamics gives

$$\delta q = dU + P\, dV = C_V dT + \left[\left(\frac{\partial U}{\partial \varrho}\right)_T - \frac{P}{\varrho^2}\right] d\varrho, \tag{7.60}$$

where δq is the heat provided to the system by unit of mass. For an adiabatic trans-
formation, $\delta q = 0$ gives for $\Gamma_3 - 1$ as defined above (7.57)

$$\Gamma_3 - 1 \equiv \left(\frac{d\ln T}{d\ln \varrho}\right)_{ad} = \frac{\frac{P}{\varrho} - \varrho\left(\frac{\partial U}{\partial \varrho}\right)_T}{C_V\, T}\ . \tag{7.61}$$

In addition, we have relation (3.57), which leads to

$$\Gamma_3 - 1 = \frac{1}{\varrho\, C_V}\left(\frac{\partial P}{\partial T}\right)_\varrho . \tag{7.62}$$

The equation of state is written in the general form (3.60). In the outer stellar layers,
one can ignore the variations of μ for the adiabatic coefficients. Of course, μ may
change locally due to ionization. However, these changes depend on T and ϱ and
are accounted for by α and δ. One has

$$d\ln\varrho = \alpha\, d\ln P - \delta\, d\ln T \ , \tag{7.63}$$

Figure 7.5 shows the variations of α and δ due to partial ionization in the outer solar
layers. The coefficient α experiences little change, while δ increases a lot. This is
due to the fact, as seen above, that in a zone of partial ionization T does not change
much. From (7.63) with $d\ln\varrho = 0$, one gets

$$\left(\frac{\partial \ln P}{\partial \ln T}\right)_\varrho = \frac{\delta}{\alpha}\ . \tag{7.64}$$

Thus, the adiabatic exponent $\Gamma_3 - 1$ becomes

$$\Gamma_3 - 1 = \frac{1}{\varrho\, C_V}\frac{P}{T}\frac{\delta}{\alpha}\ , \tag{7.65}$$

which provides a relation between $\Gamma_3 - 1$ and C_V. In order to obtain a relation
between Γ_1 and Γ_3, one uses (7.63), which directly gives

$$\Gamma_1 = \left(\frac{d\ln P}{d\ln \varrho}\right)_{ad} = \frac{1}{\alpha} + \frac{\delta}{\alpha}\left(\frac{d\ln T}{d\ln \varrho}\right)_{ad} \quad \text{and} \quad \Gamma_1 = \frac{1}{\alpha} + \frac{\delta}{\alpha}(\Gamma_3 - 1). \tag{7.66}$$
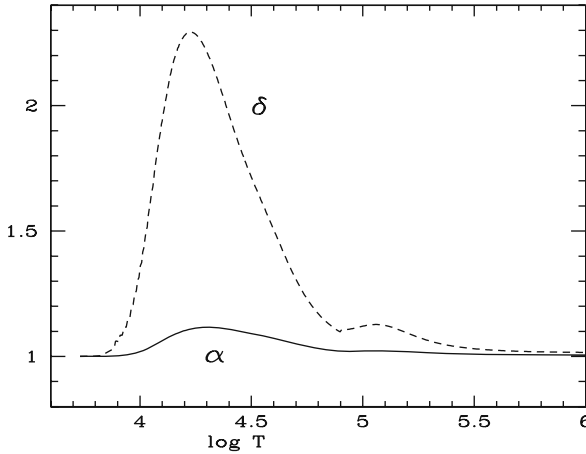
Fig. 7.5 The coefficients α and δ as a function of T in the outer stellar layers. The variations are due to the change of ionization shown in Fig. 7.2

The specific heat C_P at constant pressure is obtained from (3.76) and thus

$$\frac{\Gamma_2 - 1}{\Gamma_2} \equiv \nabla_{ad} \equiv \left(\frac{\partial \ln T}{\partial \ln P}\right)_{ad} = \frac{P\delta}{C_P \varrho T} \,. \tag{7.67}$$

This gives the expression of the specific heat C_P

$$C_P = \frac{P\delta}{\varrho T} \frac{\Gamma_2}{\Gamma_2 - 1} \,. \tag{7.68}$$

Taking the ratio of C_P (7.68) to C_V (7.65), one has

$$\frac{C_P}{C_V} = \frac{\Gamma_2}{\Gamma_2 - 1} \alpha\,(\Gamma_3 - 1) \,. \tag{7.69}$$

With (7.58), one gets finally for the ratio γ of the specific heats

$$\gamma \equiv \frac{C_P}{C_V} = \alpha \Gamma_1 \,. \tag{7.70}$$

One has to distinguish γ as defined here for a general equation of state from γ_g the ratio of the specific heats for a perfect gas. For $\delta = \alpha = 1$, one has

$$\Gamma_1 = \Gamma_3 = \Gamma_2 = \gamma_g \quad \text{for a perfect gas} \,. \tag{7.71}$$

The Γ_i are the generalizations for different equations of state of the usual ratio γ_g of the specific heats for a perfect gas.

7.4.2.1 Roadmap for Calculating Thermodynamic Functions

The steps to calculate the thermodynamic coefficients are better made in the following sequence for a medium with known $P = P(\varrho, T)$ and $U = U(\varrho, T)$, either analytically or numerically:

1. The first quantities to obtain are α and δ (3.60).
2. Then $C_V = \left(\frac{\partial U}{\partial T}\right)_\varrho$.
3. Expression (7.65) provides us with $\Gamma_3 - 1$.
4. Then expression (7.66) gives Γ_1.
5. With (7.58), one obtains $\Gamma_2/(\Gamma_2 - 1)$.

The specific heat C_P is provided by (7.68) and one may, if necessary, also obtain $\gamma = C_P/C_V$ (7.70). This method is quite useful and we now apply it for a mixture of perfect gas and radiation.

7.5 Thermodynamics of Mixture of Gas and Radiation

This mixture is appropriate for massive stars. One wants to obtain the various coefficients α, δ, C_V, $\Gamma_3 - 1$, Γ_1, $\Gamma_2/(\Gamma_2 - 1)$, C_P and γ. The total pressure P is the sum of the gas and radiation pressure

$$P = P_g + P_{rad} = \frac{k}{\mu\, m_u}\, \varrho\, T + \frac{1}{3}\, a\, T^4 . \tag{7.72}$$

The ratio β of gas to total pressure is $\beta = P_g/P$ (Sect. 3.6). The internal energy per mass unit is

$$U = \frac{a\, T^4}{\varrho} + C_V\, T = \frac{a\, T^4}{\varrho} + \frac{c_P - c_V}{\left(\frac{c_P - c_V}{c_V}\right)}\, T = \frac{a\, T^4}{\varrho} + \frac{k/(\mu\, m_u)}{\gamma_g - 1}\, T . \tag{7.73}$$

There the quantity γ_g is the ratio c_P/c_V for the perfect gas only. One can write $\varrho = \varrho(P, T)$ and derive the coefficients α and δ:

$$\varrho = \frac{P}{\left(\frac{kT}{\mu\, m_u}\right)} - \frac{1}{3}\frac{a\, T^3}{\left(\frac{k}{\mu\, m_u}\right)} , \tag{7.74}$$

$$\alpha = \left(\frac{\partial \ln \varrho}{\partial \ln P}\right)_T = \frac{P}{\varrho}\left(\frac{\partial \varrho}{\partial P}\right)_T = \frac{P}{\varrho}\frac{\mu\, m_u}{kT} = \frac{P}{P_g} = \frac{1}{\beta} , \tag{7.75}$$

$$\delta = -\left(\frac{\partial \ln \varrho}{\partial \ln T}\right)_P = -\frac{T}{\varrho}\left(\frac{\partial \varrho}{\partial T}\right)_P = \frac{T}{\varrho}\frac{P}{\left(\frac{kT^2}{\mu\, m_u}\right)} + \frac{T}{\varrho}\frac{a\, T^2}{\frac{k}{\mu\, m_u}}$$

$$= \frac{P}{P_g} + \frac{3\, P_{rad}}{P_g} = \frac{1}{\beta} + \frac{3\,(1 - \beta)}{\beta} = \frac{4}{\beta} - 3 . \tag{7.76}$$

Thus, one has for α and δ and their ratio

$$\alpha = \frac{1}{\beta}, \quad \delta = \frac{4}{\beta} - 3 \quad \text{and} \quad \frac{\delta}{\alpha} = 4 - 3\beta .$$ (7.77)

We express the coefficient φ of the equation of state (3.60) with $\mathcal{R} = k/m_{\mathrm{u}}$,

$$\varphi = \left(\frac{\partial \ln \varrho}{\partial \ln \mu}\right)_{P,T} = \frac{\mu}{\varrho}\left(\frac{\partial \varrho}{\partial \mu}\right)_{P,T} = \frac{\mu}{\varrho}\left[\frac{P}{\mathcal{R}T} - \frac{aT^3}{3\mathcal{R}T}\right]$$

$$= \frac{\mu}{\varrho}\left[\frac{\varrho}{\beta\mu} - \frac{(1-\beta)\varrho}{\beta\mu}\right] = 1 .$$ (7.78)

Thus, this coefficient is equal to 1, as for a perfect gas.

Let us now derive the expression of the specific heats. We write c_V, c_P the specific heats for the perfect gas and $\gamma_{\mathrm{g}} = c_P/c_V$. We call C_V and C_P the specific heats at constant volume and constant pressure for the mixture of ideal gas and radiation,

$$C_V = \left(\frac{\partial U}{\partial T}\right)_\varrho = \frac{4aT^3}{\varrho} + \frac{k/(\mu m_{\mathrm{u}})}{\gamma_{\mathrm{g}} - 1} = \frac{k/(\mu m_{\mathrm{u}})}{\gamma_{\mathrm{g}} - 1}\left(1 + (\gamma_{\mathrm{g}} - 1)\,12\frac{P_{\mathrm{rad}}}{P_{\mathrm{g}}}\right)$$

$$= \frac{k/(\mu m_{\mathrm{u}})}{\gamma_{\mathrm{g}} - 1}\left(\frac{\beta + 12(\gamma_{\mathrm{g}} - 1)(1-\beta)}{\beta}\right) .$$ (7.79)

For a mono-atomic gas, $\gamma_{\mathrm{g}} = 5/3$ and the specific heats c_V and C_V are

$$c_V = \frac{3}{2}\frac{k}{\mu m_{\mathrm{u}}} \quad \text{and} \quad C_V = c_V\frac{8 - 7\beta}{\beta} .$$ (7.80)

Then, we obtain $\Gamma_3 - 1$ with expression (7.65)

$$\Gamma_3 - 1 = \frac{P}{\varrho T}\frac{\delta/\alpha}{C_V} = \frac{(4 - 3\beta)(\gamma_{\mathrm{g}} - 1)}{\beta + 12(\gamma_{\mathrm{g}} - 1)(1-\beta)} .$$ (7.81)

For a mono-atomic gas, this simplifies to

$$\Gamma_3 - 1 = \frac{8 - 6\beta}{24 - 21\beta} .$$ (7.82)

With expression (7.66), one obtains for the general case

$$\Gamma_1 = \beta + \frac{(4 - 3\beta)^2(\gamma_{\mathrm{g}} - 1)}{\beta + 12(\gamma_{\mathrm{g}} - 1)(1-\beta)} ,$$ (7.83)

which for a mono-atomic gas simplifies to

$$\Gamma_1 = \frac{32 - 24\beta - 3\beta^2}{3(8 - 7\beta)} .$$ (7.84)

Then, we find $\Gamma_2/(\Gamma_2-1)=1/\nabla_{\mathrm{ad}}$ with the help of (7.58)

$$\frac{\Gamma_2}{\Gamma_2-1}=\frac{\Gamma_1}{\Gamma_3-1}=\frac{[\beta+12\,(\gamma_{\mathrm{g}}-1)\,(1-\beta)]\left[\beta+\frac{(4-3\beta)^2\,(\gamma_{\mathrm{g}}-1)}{\beta+12\,(\gamma_{\mathrm{g}}-1)\,(1-\beta)}\right]}{(4-3\beta)\,(\gamma_{\mathrm{g}}-1)}$$

$$=\frac{\beta^2+12\,\beta\,(\gamma_{\mathrm{g}}-1)\,(1-\beta)+(4-3\beta)^2\,(\gamma_{\mathrm{g}}-1)}{(4-3\beta)\,(\gamma_{\mathrm{g}}-1)}\ . \tag{7.85}$$

For a mono-atomic gas with $\gamma_{\mathrm{g}}=5/3$, one has

$$\frac{\Gamma_2}{\Gamma_2-1}=\frac{1}{\nabla_{\mathrm{ad}}}=\frac{-3\,\beta^2-24\,\beta+32}{2\,(4-3\beta)}\ . \tag{7.86}$$

For a perfect gas, i.e., when $\beta\to1$, Γ_1,Γ_2 and Γ_3 converge toward γ_{g}. For pure radiation, i.e., $\beta\to0$, the three adiabatic exponents converge toward $\Gamma_1=\Gamma_2=\Gamma_3=4/3$. According to Sect. 1.3.2, this is destabilizing. In general, Γ_i are between 5/3 and 1 (Fig. 7.4). The ratio $\gamma\equiv C_P/C_V$ of the mixture of perfect gas and radiation is given by (7.70)

$$\gamma=\alpha\,\Gamma_1=1+\frac{(4-3\beta)^2\,(\gamma_{\mathrm{g}}-1)}{\beta^2+12\,\beta\,(\gamma_{\mathrm{g}}-1)\,(1-\beta)}\ . \tag{7.87}$$

For a mono-atomic gas, this is

$$\gamma=\frac{32-24\,\beta-3\,\beta^2}{3\,\beta\,(8-7\beta)}\ . \tag{7.88}$$

Finally, the specific heat is provided by (7.70) which gives $C_P=\alpha\,\Gamma_1\,C_V$. One obtains after simplification

$$C_P=\frac{1}{\beta^2}\frac{k/(\mu\,m_{\mathrm{u}})}{\gamma_{\mathrm{g}}-1}\left[4\,(\beta^2+4\,\gamma_{\mathrm{g}}-4)-3\,\beta\,(-4+4\,\gamma_{\mathrm{g}}+\beta\,\gamma_{\mathrm{g}})\right]. \tag{7.89}$$

For $\gamma=\frac{5}{3}$, this becomes

$$C_P=\frac{k}{\beta^2\,\mu\,m_{\mathrm{u}}}\frac{3}{2}\left[\frac{32}{3}-8\,\beta-\beta^2\right]\ . \tag{7.90}$$

For a perfect gas ($\beta=1$), one has the usual value $c_P=(5/2)\,[k/(\mu\,m_{\mathrm{u}})]$. A relative increase of the radiation pressure makes the specific heats larger, while the adiabatic exponents $\Gamma_i\to4/3$, which is destabilizing.

7.6 Electrostatic Effects

For relatively high densities, like that of terrestrial matter, the electrical interactions between particles cannot be neglected because they modify all the properties of matter. The main effects are the following ones:

1. A pressure difference relative to the perfect gas (Sect. 7.6.2).
2. The energies of the atomic levels are influenced, in particular the ionization potential is lowered and the gas may be fully ionized by pressure effects (Sect. 7.6.3).
3. Crystallization may occur (Sect. 7.6.4).
4. The free electrons may contribute to the heat transport (Sect. 8.5).
5. The electron shielding lowers the electrostatic repulsions between nuclei and favors nuclear reactions (Sect. 9.4).

7.6.1 The Debye–Hückel Radius

Let us consider an ion of charge $+Ze$ with a cloud of electrons. The potential Φ obeys the Poisson equation

$$\nabla^2 \Phi = -4\pi \varrho_e \,, \tag{7.91}$$

where ϱ_e is the density of charges at the considered location. By comparing with Poisson's equation (1.44), one notes a sign minus in front of ϱ_e, where ϱ_e is the density of positive charges. This is consistent with the fact that the acceleration $a = \nabla \Phi$ is repulsive for another positive charge, while gravitation is attractive for two (positive) masses. The ion concentration n_i obeys Boltzmann's law, if the ions are considered as independent,

$$n_i = n_{0i}\, e^{-Z_i\, e\, \Phi/(kT)} \,, \tag{7.92}$$

where n_{0i} is the concentration in absence of the perturbations due to the other ions. Similarly, the electrons follow the same law for $Z = -1$:

$$n_e = n_{0e}\, e^{+e\Phi/(kT)} \,. \tag{7.93}$$

The electrons are attracted by the ions, thus $n_e > n_{0e}$ and $n_i < n_{0i}$. Developing these concentrations to the first order, one gets

$$n_i = n_{0i}\left(1 - \frac{Z_i\, e\, \Phi}{kT}\right) \quad \text{and} \quad n_e = n_{0e}\left(1 + \frac{e\Phi}{kT}\right). \tag{7.94}$$

The charge density is

$$\varrho_e = \sum_i n_i Z_i e - n_e e = \underbrace{\sum_i n_{0i} Z_i e - n_{0e} e}_{= 0 \text{ for neutrality}} - \sum_i \frac{n_{0i} Z_i^2 e^2 \, \Phi}{kT} - \frac{n_{0e} e^2 \, \Phi}{kT} . \qquad (7.95)$$

One can write

$$\varrho_e = \frac{-\Phi e^2}{kT} \chi n, \quad \text{with } n = \sum_i n_{0i} + n_{0e} \quad \text{and } \chi = \sum_i \frac{n_{0i}}{n} Z_i (Z_i + 1), \qquad (7.96)$$

where n is the total number of particles by volume unity without fluctuations and χ is the effective charge. One uses the fact that the unperturbed matter is neutral, i.e., $n_{0i} Z_i = n_{0e}$. One also has

$$n_{0i} = N_{AV} \frac{\varrho X_i}{A_i}, \; n = N_{AV} \frac{\varrho}{\mu} \quad \text{and } \chi = \mu \sum_i \frac{X_i}{A_i} Z_i (Z_i + 1) \equiv \mu \, \zeta . \qquad (7.97)$$

Let us introduce ϱ_e in the Poisson equation assuming spherical symmetry,

$$\frac{1}{r} \frac{d^2 (r\Phi)}{dr^2} = \frac{4\pi e^2}{kT} n \chi \, \Phi \equiv \frac{\Phi}{r_D^2}, \qquad (7.98)$$

with the Debye–Hückel radius (also called Debye length) defined by

$$r_D = \sqrt{\frac{kT}{4\pi e^2 n \chi}} . \qquad (7.99)$$

The above equation can also be written as

$$\frac{1}{2} \frac{d}{d(r\Phi)} \left[\frac{d(r\Phi)}{dr} \right]^2 = \frac{r\Phi}{r_D^2} \quad \text{since} \quad \frac{1}{2} 2 \frac{d(r\Phi)}{dr} \frac{d^2(r\Phi)}{d(r\Phi)dr} = \frac{r\Phi}{r_D^2}, \qquad (7.100)$$

and by integrating, one obtains

$$\frac{1}{2} d \left[\frac{d(r\Phi)}{dr} \right]^2 = \frac{r\Phi}{r_D^2} d(r\Phi) \quad \text{and} \quad \frac{d(r\Phi)}{dr} = \pm \frac{r\Phi}{r_D} + \text{const.} \qquad (7.101)$$

One chooses the sign minus and takes $\Phi = 0$ for $r \to \infty$, so that the constant is zero. We integrate the equation once more and get

$$\ln(r\Phi) = -\frac{r}{r_D} + \text{const}' \quad \text{or} \quad \Phi = \text{const}' \frac{e^{-r/r_D}}{r} . \qquad (7.102)$$

If $r_D \to \infty$, one must get the potential Ze/r of an isolated charge, this implies $\text{const}' = Ze$. The potential of the charge Ze with account of the screening effect

of the electrons is thus

$$\Phi = \frac{Ze}{r} e^{-r/r_{\mathrm{D}}}. \tag{7.103}$$

The potential with screening decreases faster than that of an isolated charge, because it is shielded by charges of the opposite sign. The Debye–Hückel radius is the radius for which the screening reduces the potential by a factor of e with respect to the potential of an isolated ion of charge Ze. In the E.S.U. system of units, $e^2 = 23.071 \times 10^{-20}$ cm erg. Contrarily to gravitation, the electric potential of a source is reduced by sources of the opposite sign.

7.6.2   Electrostatic Effects on the Gas Pressure

We examine the changes due to electrostatic effects on the law of perfect gas. We assume a weak density and a temperature sufficiently high so that Debye–Hückel theory is valid. The potential with screening is

$$\Phi = \frac{Ze}{r} e^{-\frac{r}{r_{\mathrm{D}}}} \simeq \frac{Ze}{r} - \frac{Ze}{r_{\mathrm{D}}} , \tag{7.104}$$

when $r_{\mathrm{D}} \gg r$. The second term expresses the potential near the ion of charge Ze due to the interaction with the other ions. Thus, the potential energy of the charge Ze due to the electrostatic interaction with other charges is

$$E_{\mathrm{ES}} = -\frac{Z^2 e^2}{r_{\mathrm{D}}} . \tag{7.105}$$

This electrostatic energy tends toward 0 when $T \to \infty$. The energy E_{ES} is negative whatever the sign of the charge Ze. As long as r_{D} is not infinite, the considered charge produces a surrounding cloud of radius r_{D} with an excess of charges of the opposite sign. The charge and the cloud form a system which is about neutral electrically, this system is bound and has a negative energy since one should provide some energy to separate it. This negative energy reduces the pressure in the medium.

If n_{i} is the concentration of the ions of type i with a charge $Z_{\mathrm{i}}e$, the total energy density of the electrostatic interaction is according to (7.105)

$$u_{ES} = -\frac{1}{2} \frac{e^2}{r_{\mathrm{D}}} \sum_i n_{\mathrm{i}} Z_i^2 . \tag{7.106}$$

This energy is negative for the same reason as above. The factor $1/2$ accounts for the fact that the energy of the electrostatic interaction of each particle is counted twice in the sum. The pressure due to the electrostatic interaction is (cf. B.47)

$$P_{ES} = \frac{1}{3} u_{ES} \tag{7.107}$$

because the electrostatic interaction propagates at the speed of light. Thus, one gets with (7.97)

$$P_{ES} = -\frac{1}{3}\frac{e^2\, e\,\sqrt{4\pi n\chi}}{(kT)^{1/2}\,2}\underbrace{\sum_i Z_i^2\, n_i}_{\simeq n\chi} = -\frac{1}{3}e^3\left(\frac{\pi}{kT}\right)^{1/2}(n\chi)^{3/2},\qquad(7.108)$$

with $$n\chi = \frac{\varrho}{\mu\, m_u}\,\mu\,\zeta = \frac{\varrho\,\zeta}{m_u},\qquad(7.109)$$

and the electrostatic pressure becomes

$$P_{ES} = -\frac{e^3}{3}\left(\frac{\pi}{kT}\right)^{1/2}\left(\frac{\zeta\varrho}{m_u}\right)^{3/2},\quad\text{where }\zeta = \sum_i\frac{X_i}{A_i}Z_i(Z_i+1).\qquad(7.110)$$

The electronic pressure is negative, because the electrostatic energy is negative (7.106). The pressure P_{ES} is to be added to the other sources of pressure, such as gas and radiation, $P_{tot} = P_g + P_{rad} + P_{ES} + \dots$.
  Numerically, one has

$$P_{ES} = -0.032\,\frac{\varrho^{1/2}}{T_6^{3/2}}\,\mu\,\zeta,\qquad(7.111)$$

with ϱ in g cm^{-3} and $T_6 = T/10^6\,K$. In the Sun, the ratio of the electrostatic to gas pressure is $P_{ES}/P_g \approx -0.015$. The ratio ϱ/T^3 does not vary much inside a star (cf. 3.101), thus the effect of the electrostatic corrections changes little with depth. For a standard composition, the formal equality

$$P_g = P_{ES}\quad\text{implies}\quad T = 1.37\times 10^5\varrho^{1/3}\quad K.\qquad(7.112)$$

This is shown in Fig. 7.8 with a dashed-dotted line. The above developments apply only for $(P_{ES})/P_g \ll 1$, thus for $T \gg 1.37\times 10^5\,\varrho^{1/3}$. The electrostatic pressure becomes relatively more important for lower mass stars. For very low-mass stars and brown dwarfs, a more detailed treatment of the equation of state is necessary.

7.6.3   Ionization by Pressure

The ion and its electronic cloud form a bound system. The energy of an electron in the cloud is $E_{ES} = -e^2/r_D$ (7.105). Thus, the energy of a "free" electron in the cloud (in the continuum) is below zero. Thus, the ionization potential is reduced with respect to that of an isolated atom.
  There is another effect: the energy levels of the bound states are also modified because the potential does not behave strictly as $1/r$. An electron bound to a nucleus of charge Ze is moving in a potential

$$V \simeq \frac{Ze}{r} - \frac{(Z-1)e}{r_{\mathrm{D}}}, \quad \text{for} \quad r \ll r_{\mathrm{D}}. \tag{7.113}$$

The second term is the potential resulting from the charge $Z-1$ of the ion and electron due to the interaction of this resulting charge with the other ones. The energy of the fundamental level is thus

$$E = -\frac{Ze^2}{r} + \frac{(Z-1)e^2}{r_{\mathrm{D}}}. \tag{7.114}$$

The energy of the bound state is shifted upward by an amount $(Z-1)e^2/r_{\mathrm{D}}$, while the energy of the continuum is lowered by $-e^2/r_{\mathrm{D}}$. As a result, the effective ionization potential becomes

$$I_{\mathrm{eff}} = I_0 - \frac{Ze^2}{r_{\mathrm{D}}}, \tag{7.115}$$

where I_0 is the theoretical value for an isolated atom. Ionization is favored when the gas becomes denser and electrostatic effects increase.

The excited atomic levels are also shifted toward higher energies, so that the highest levels lie in the continuum. This simplifies the calculation of the partition functions (Sect. 7.1.2). The summation no longer concerns an infinite series of levels, it can often be made with a limited number of terms. The changes of ionization potentials and energy levels also influence the calculation of radiative opacities.

For dense media, the Debye radius r_{D} is reduced and so does the effective ionization potential (7.115). Thus at a given temperature, there is a density value above which the medium is essentially ionized by pressure effect. Such a limit is shown for hydrogen in Fig. 7.8 by the dotted line which separates H^+ from H (close to the limit between the degenerate and non-degenerate domains). In practice, one often considers [285] that ionization is complete due to pressure effects, when Saha equation gives degrees of ionization which start decreasing toward the interior. The equation of state and the thermodynamic functions of fully ionized electron–ion plasmas have been established [107] for a wide range of physical conditions.

7.6.4 Crystallization

For high densities (e.g., $\varrho > 10^2$ g cm^{-3} at $T = 10^6$ K; see Fig. 7.8), the electrostatic forces between ions start dominating over the thermal energy. If the density still further increases, at some stage the ions are no longer subject to thermal motions, but are stuck to the nodes of a lattice determined by the repulsive forces between ions. The Coulomb plasma thus crystallizes.

Let us consider a medium of temperature T, electron and ion concentrations n_{e} and n_{i}, of charge Z and atomic mass number A. The Wigner–Seitz radii a_{e} and a_{i} are the mean inter-electron and inter-ion distances

$$a_e = \left(\frac{4}{3} \pi n_e\right)^{-\frac{1}{3}} \quad \text{and} \quad a_i = \left(\frac{4}{3} \pi n_i\right)^{-\frac{1}{3}}. \tag{7.116}$$

The condition of electric neutrality implies that $n_e = n_i Z$, thus,

$$a_i = a_e Z^{\frac{1}{3}}. \tag{7.117}$$

The Coulomb plasma is characterized by the ratios of the Coulomb energy to the thermal energy for the electrons and ions. These ratios are, respectively,

$$\Gamma_e \equiv \frac{e^2}{a_e k T} \quad \text{and} \quad \Gamma_i \equiv \frac{(Ze)^2}{a_i k T} = \Gamma_e Z^{\frac{5}{3}}. \tag{7.118}$$

Numerically, the value of Γ_e is

$$\Gamma_e = 2.693 \times 10^{-3} \frac{n_e^{\frac{1}{3}}}{T}. \tag{7.119}$$

with n_e given in cm^{-3} and T in K. The electron concentration is related to the density by (7.42), which may be expressed as $n_e = (\varrho/m_u)(<Z>/<A>)$, where $<Z>$ and $<A>$ are the average charge and mass numbers. From (7.117) and (7.119), one has the following relation between the temperature and density for a given value of Γ_i

$$T = \frac{2.27 \times 10^5}{\Gamma_i} Z^{\frac{5}{3}} \varrho^{\frac{1}{3}} \left(\frac{<Z>}{<A>}\right)^{\frac{1}{3}}, \tag{7.120}$$

with ϱ in g cm^{-3} and T in K. For $\Gamma_i = 1$, one has a gas where the electrostatic and thermal energies are of comparable importance (Fig. 7.8). For higher values, the medium progressively becomes a Coulomb liquid and for a value of $\Gamma_i \geq 175$, the liquid turns into a stable Coulomb crystal [475]. Thus, putting this value in (7.120) provides an approximate limit for crystallization for a medium of nuclei characterized by average Z and A values. An illustration of the location of this limit is shown in Fig. 7.8.

7.7 Degenerate Gases

The fermions, which are particles with spin $1/2, 3/2, \ldots$, obey the Fermi–Dirac statistics (Appendix C.5). The exclusion principle of Pauli tells us that the extension $\Delta^3 q_i \Delta^3 p_i$ in the phase space of position q_i and momentum p_i with $r = 1, 2, 3$ obeys the inequality

$$\Delta^3 q_i \Delta^3 p_i \geq h^3. \tag{7.121}$$

This already shows that if the density of a medium increases, i.e., if the space volume interval $\Delta^3 q_i$ decreases, the particles get a higher momentum. These high momenta are a source of pressure of quantum origin called the pressure of degeneracy and the gas (of electrons or neutrons) is said degenerate.

For an ionized medium with electrons of mass m_e and nuclei of mass m_N, one has energy equipartition. In the non-relativistic case, this implies

$$\frac{p_N^2}{2m_N} = \frac{p_e^2}{2m_e} , \tag{7.122}$$

where p_e and p_N are the corresponding momenta. Thus, one has the following ratio of momenta:

$$\frac{p_N}{p_e} = \left(\frac{m_N}{m_e}\right)^{1/2} = A^{1/2} \left(\frac{m_u}{m_e}\right)^{1/2}, \tag{7.123}$$

where A is the atomic mass of the nuclei considered. For a similar energy, the domain of the momenta of the nuclei is $A^{3/2} (m_u/m_e)^{3/2}$ times larger than the corresponding electron domain. This means that, for increasing densities, the electrons meet the limit set by Pauli's principle long before the nuclei. As the low-energy cells of the phase space are all occupied by two electrons, the further electrons to be squeezed into the phase space are shifted toward domains of higher momenta. This creates a new pressure source (Fig. 7.6). This is the process of electron degeneracy which intervenes at $\varrho \sim 1$ g cm^{-3} for $T < 10^5$ K. Thus, ordinary terrestrial matter is degenerate. At $\varrho \sim 10^4$ g cm^{-3}, degeneracy is present for $T < 3 \times 10^7$ K. The nuclei present in such media are not degenerate (perfect gas), only the electrons contribute to the pressure of degeneracy, which rapidly dominates for increasing densities. The neutron degeneracy appears at $\varrho \sim 10^{14}$ g cm^{-3} (Sect. 7.8).
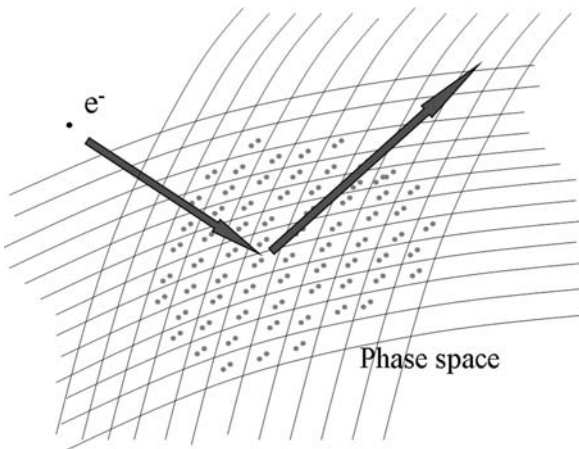
Fig. 7.6 Schematic representation of the phase space of electrons. A new electron is ejected toward cells of higher energy which creates the pressure of degeneracy

Let us consider N fermions with a total energy E, with numbers N_i of fermions with energy E_i such that

$$E = \sum_i N_i E_i \quad \text{and} \quad N = \sum_i N_i . \tag{7.124}$$

For particles with a half–integer spin, Fermi–Dirac statistics applies (Appendix C.5):

$$N_i = \frac{g_i}{e^{-\psi + \frac{E_i}{kT}} + 1} , \tag{7.125}$$

g_i is the statistical weight of particles with energy E_i in the phase domain $\Delta^3 p_i \Delta^3 q_i$. The electrons have two states of spin and

$$g_i = \frac{2}{h^3} \Delta^3 p_i \, \Delta^3 q_i . \tag{7.126}$$

For degenerate neutrinos, the numerical factor would be 1. For a continuous and isotropic distribution of kinetic energies, the concentration of particles becomes

$$n(p)\, d^3 p = \frac{8\pi\, p^2\, dp}{h^3} \underbrace{\left(\frac{1}{e^{-\psi + \frac{E}{kT}} + 1} \right)}_{q(\psi,\, E/(kT))}, \tag{7.127}$$

where $q(\psi,\, E/(kT))$ is the rate of occupation of the cells in the phase space, this function is illustrated in Fig. 7.7.

A non-degenerate gas is a gas where $q \ll 1$ for the considered value of $E/(kT)$. This means that $\psi \ll -1$, thus one has $q \simeq e^{\psi}\, e^{-E/(kT)}$ and the corresponding
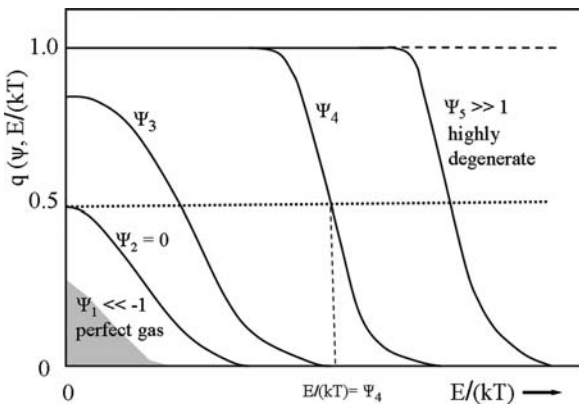
Fig. 7.7 Schematic representation of the occupation factor $q(\psi, E/(kT))$ as a function of the energy ratio $E/(kT)$ for different values of ψ. The distribution of a perfect gas is shown in grey: degeneracy is increasing from ψ_1 to ψ_5. The highly degenerate cases tend toward a step function with an edge at the Fermi energy

distribution is given by the Maxwell–Boltzmann law (Appendix C.6.2). A fully de-generate gas is a gas for which $\psi \to \infty$. Below a value of energy E_F, one has $q = 1$ and above it, one has $q = 0$. If all the cells in the phase space are occupied by two particles, one has just $n(p)\,d^3\,p = (8\pi\,p^2\,dp)/h^3$. For the energy $E/(kT) = \psi$, the occupation rate is $q = 1/2$ (Fig. 7.7). For a fully degenerate gas, the particles have non-zero velocities even at $T = 0$.

7.7.1 Partially Degenerate Gas

Between the state of perfect gas and full degeneracy, there is a continuous range of states with partial degeneracy. Let us express the pressure $P(\varrho,T)$ and the density of internal energy. First, the electronic concentration is

$$n_e = \int\int\int n(p)\,d^3\,p = \frac{8\pi}{h^3}\int_0^\infty \frac{p^2\,dp}{e^{-\psi+\frac{E}{kT}}+1}\,. \tag{7.128}$$

The density is $\varrho = \mu_e\,m_u\,n_e$ where μ_e is the mean molecular weight for free electrons. The pressure is according to (B.40)

$$P = \frac{1}{3}\int\int\int n(p)\,p\,v\,d^3\,p\,, \tag{7.129}$$

since $n(p)\,d^3\,p$ is the spatial concentration and thus

$$P = \frac{8\pi}{3h^3}\int_0^\infty \frac{v\,p^3\,dp}{e^{-\psi+\frac{E}{kT}}+1}\,. \tag{7.130}$$

The energy density

$$u = \int_0^\infty E\,n(p)\,d^3\,p = \frac{8\pi}{h^3}\int_0^\infty \frac{E\,p^2\,dp}{e^{-\psi+\frac{E}{kT}}+1}\,, \tag{7.131}$$

where E is the kinetic energy of translation. For increasing densities at a given tem-perature, the medium goes from the state of perfect gas to partial degeneracy, non-relativistic fully degeneracy, partially relativistic full degeneracy and relativistic full degeneracy.

7.7.2 Non-Relativistic Partial Degeneracy

This case is of interest in particular for the core of red giants. The energy of a par-ticle is $E = p^2/(2\,m_e)$, let us call $x = E/(kT) = p^2/(2m_ekT)$ and the concentration (7.128) becomes

$$n_e = \frac{8\pi}{h^3} \frac{(2m_e kT)^{3/2}}{2} \int_0^\infty \frac{x^{1/2}dx}{e^{-\psi+x}+1} = \frac{4\pi}{h^3}(2m_e kT)^{3/2} F_{1/2}(\psi). \qquad (7.132)$$

The function $F_{1/2}$ is the Fermi integral for $n = 1/2$, the Fermi integrals being defined by

$$F_n(\psi) = \int_0^\infty \frac{x^n\, dx}{e^{-\psi+x}+1}. \qquad (7.133)$$

Tables of the Fermi integrals for $n = 1/2, 3/2, 5/2$ as well as routines to calculate them for various cases are found in literature [174, 422]. The pressure (7.130) becomes with $v = p/m_e$

$$P = \frac{8\pi}{3h^3 m_e} \int_0^\infty \frac{p^4 dp}{e^{-\psi+E/(kT)}+1} = \frac{8\pi}{3h^3}kT(2m_e kT)^{3/2} \underbrace{\int_0^\infty \frac{x^{3/2}dx}{e^{-\psi+x}+1}}_{F_{3/2}(\psi)}. \qquad (7.134)$$

The equation of state is thus defined by the two parametric equations:

$$P = \frac{8\pi}{3\,h^3}(2m_e\, kT)^{3/2} kT\, F_{3/2}(\psi), \qquad (7.135)$$

$$\varrho = \frac{4\pi}{h^3}(2m_e\, kT)^{3/2} \mu_e m_u F_{1/2}(\psi). \qquad (7.136)$$

7.7.2.1   Case of Very Weak Degeneracy, $\psi \ll -1$

The functions of Fermi behave like $F_n(\psi) \longrightarrow e^\psi \int_0^\infty e^{-x}x^n\, dx$. One has the Γ function defined by

$$\int_0^\infty x^n e^{-ax}\, dx = \frac{\Gamma(n+1)}{a^{n+1}}, \qquad (7.137)$$

which has many properties, in particular $\Gamma(n+1) = n\Gamma(n)$, $\Gamma(1.5) = \sqrt{\pi}/2$ and $\Gamma(2.5) = (3/4)\sqrt{\pi}$. This gives

$$F_{1/2}(\psi) = \frac{\sqrt{\pi}\, e^\psi}{2} \quad \text{and} \quad F_{3/2}(\psi) = \frac{3}{4}\sqrt{\pi}\, e^\psi. \qquad (7.138)$$

The pressure and density become

$$P = \frac{8\pi}{3h^3}(2m_e kT)^{3/2}kT\frac{3}{4}\sqrt{\pi}e^\psi,$$

$$\varrho = \frac{4\pi}{h^3}(2m_e\, kT)^{3/2}\mu_e\, m_u \frac{\sqrt{\pi}}{2}e^\psi. \qquad (7.139)$$

If one eliminates ψ between these two equations, one gets the law of perfect gas for the electrons $P/\varrho = kT/(\mu_e m_u)$.

7.7.2.2   Case of Very Strong Degeneracy

The Fermi functions become

$$F_n(\psi) = \int_0^\psi x^n dx = \frac{\psi^{n+1}}{n+1} . \tag{7.140}$$

The integration is performed up to ψ, where the cells in the phase space are occupied. This allows us to express $F_{1/2}$ and $F_{3/2}$ in the parametric equations (7.135) and (7.136) and to eliminate ψ between them, we get

$$P = K_1 \left(\frac{\varrho}{\mu_e} \right)^{5/3} , \tag{7.141}$$

$$\text{with } K_1 = \frac{8\pi}{15h^3 m_e} \left(\frac{3h^3}{8\pi m_u} \right)^{5/3} = 9.99 \times 10^{12} \, \text{CGS}. \tag{7.142}$$

One can also obtain the density u of internal energy by (7.131), which is necessary for determining the thermodynamic parameters. One may verify that $u = (3/2)P$, which is expected for non-relativistic particles.

7.7.3   Completely Degenerate Gas

For higher densities, the gas becomes fully degenerate. First, it is non-relativistic with velocities $v \ll c$, then fully degenerate relativistic with $v \rightarrow c$.

7.7.3.1   Non-relativistic Fully Degenerate Medium

The occupation rate of the cells $q(\psi, E/(kT)) = 1$ up to a limiting momentum p_F, called the Fermi momentum, above which it is zero. The electronic concentration is thus from (7.128)

$$n_e = \frac{8\pi}{h^3} \int_0^{p_F} p^2 dp = \frac{8\pi}{3h^3} p_F^3 , \tag{7.143}$$

so that one has the following relation between p_F and the density ϱ

$$\frac{\varrho}{\mu_e} = \frac{8\pi}{3} \frac{m_u}{h^3} p_F^3 . \tag{7.144}$$

This allows us to define p_F as a function of density. The pressure becomes according to (7.130)

$$P = \frac{8\pi}{3h^3} \int_0^{p_F} \frac{p}{m_e} p^3 \, dp = \frac{8\pi}{15h^3} \frac{p_F^5}{m_e} . \tag{7.145}$$

One may also define the Fermi energy E_F as

$$E_F = \frac{p_F^2}{2m_e} = \frac{1}{2} \left(\frac{3}{8\pi} \right)^{\frac{2}{3}} \frac{h^2}{m_e \, (\mu_e \, m_u)^{\frac{2}{3}}} \varrho^{\frac{2}{3}} . \tag{7.146}$$

Numerically, this expression becomes

$$E_F = 4.1507 \times 10^{-11} \left(\frac{\varrho}{\mu_e} \right)^{\frac{2}{3}} \text{erg} = 2.5906 \times 10^{-5} \left(\frac{\varrho}{\mu_e} \right)^{\frac{2}{3}} \text{MeV}, \tag{7.147}$$

where the density is given in g cm^{-3}. From E_F, one can also define a Fermi temperature T_F with $T_F = 2E_F/k$. By eliminating p_F between (7.144) and (7.145), one obtains the equation of state

$$P = K_1 \left(\frac{\varrho}{\mu_e} \right)^{5/3} , \tag{7.148}$$

in agreement with (7.141), K_1 being defined by (7.142). The pressure is a function of density without any dependence on T. Thus, one has the same law at $T = 0$ K and at higher temperatures as long as $kT \ll E_F$. This is expected since the pressure does not arise from a thermal effect, but only from the quantum effect due to the exclusion principle.

7.7.3.2 Relativistic Fully Degenerate Medium

In this case, the electron velocities $v \to c$. The density is given by (7.144) with $p/m_e \to c$ in the expression of the pressure (7.145)

$$P = \frac{8\pi}{3h^3} \int_0^{p_F} cp^3 \, dp = \frac{2\pi c}{3h^3} p_F^4 . \tag{7.149}$$

By eliminating p_F, one gets

$$P = K_2 \left(\frac{\varrho}{\mu_e} \right)^{4/3} , \text{ with } K_2 = \frac{hc}{8m_u} \left(\frac{3}{\pi m_u} \right)^{1/3} = 1.243 \times 10^{15} \text{CGS}. \tag{7.150}$$

The pressure increases slowly with density (like $\varrho^{4/3}$) in the relativistic case than in the non-relativistic case (like $\varrho^{5/3}$). The reason is that in the non-relativistic regime an increase of the electron energy goes mainly to the velocity and thus to

the pressure. In the relativistic regime, the increase of the energy implies an increase of the particle mass and not of the velocity. The density of internal energy u is

$$u = \frac{8\pi}{h^3} \int_0^\infty E \, p^2 \, dp = \frac{8\pi c}{h^3} \frac{p_F^4}{4} \qquad \text{with } E = pc \,. \tag{7.151}$$

In this case, one consistently has $P = (1/3) \, u$.

7.7.3.3   Partially Relativistic Fully Degenerate Gas

The total energy of a relativistic particle is

$$E = \left[(m_0 c^2)^2 + (pc)^2\right]^{1/2} \,, \tag{7.152}$$

with m_0 the rest mass. The kinetic energy is $E_{\text{cin}} = (\gamma - 1) m_0 c^2$, with $\gamma = \left(1 - \frac{v^2}{c^2}\right)^{-1/2}$ and $p = \gamma m_0 v$. When $v \to c$, i.e., $\gamma \gg 1$, one has $E \to \gamma m_0 c^2$, $p \to \gamma m_0 c$ and $p = E/c$. One has quite generally

$$v = \frac{dE}{dp} = \frac{cp}{(p^2 + m_0^2 c^2)^{1/2}} = \frac{p/m_0}{\left[1 + \left(\frac{p}{m_0 c}\right)^2\right]^{1/2}} \,. \tag{7.153}$$

The pressure becomes according to (7.130)

$$P = \frac{8\pi}{3h^3} \int \frac{(p/m_0) \, p^3 \, dp}{\left[1 + \left(\frac{p}{m_0 c}\right)^2\right]^{1/2}} \qquad \text{with} \qquad q\left(\psi, \frac{E}{kT}\right) = 1 \,. \tag{7.154}$$

We use the substitution $\sinh \vartheta = p/(m_0 c)$ and get

$$P = \frac{8\pi}{3h^3} m_0^4 c^5 \int_0^{\vartheta_F} \frac{\sinh^4 \vartheta \, \underbrace{\cosh \vartheta \, d\vartheta}_{\cosh \vartheta}}{(1 + \sinh^2 \vartheta)^{1/2}} \,. \tag{7.155}$$

Integrating by parts, one has

$$\int_0^{\vartheta_F} \sinh^4 \vartheta \, d\vartheta = \frac{1}{4} \sinh^3 \vartheta_F \cosh \vartheta_F - \frac{3}{16} \sinh 2\vartheta_F + \frac{3}{8} \vartheta_F \,. \tag{7.156}$$

Setting $x = \sinh \vartheta_F = p_F / (m_0 c)$ gives

$$8 \int_0^{\vartheta_F} \sinh^4 \vartheta \, d\vartheta = x(x^2+1)^{1/2}(2x^2-3) + 3\ln(x+\sqrt{1+x^2}), \quad (7.157)$$

$$\text{and finally} \qquad P = \frac{\pi m_0^4 c^5}{3 h^3} f(x), \qquad\qquad (7.158)$$

$$\text{with} \quad f(x) = x(x^2+1)^{1/2}(2x^2-3) + 3\ln\underbrace{(x+\sqrt{1+x^2})}_{\sinh^{-1} x} . \; (7.159)$$

The density is written as (cf. 7.144)

$$\varrho = \frac{8\pi}{3} \mu_e m_u \left(\frac{m_0 c}{h}\right)^3 x^3 . \qquad\qquad (7.160)$$

These relations provide us with the parametric equations of partially relativistic fully degenerate gas. One finds again the two limiting cases. In the non-relativistic case with $x \ll 1$, the logarithmic term dominates, one has $f(x) \to \frac{8}{5}x^5$ and again

$$P = K_1 \left(\frac{\varrho}{\mu_e}\right)^{5/3} . \qquad\qquad (7.161)$$

In the relativistic case, with $x \gg 1$ one has $f(x) = 2x^4$ which leads to (7.150). This completes the different cases of degeneracy. The various corresponding thermodynamic coefficients can be found following the above method (7.4.2), see for example [147]. Analytical approximations of the Fermi integrals have been established by Eggleton [174] with an accuracy better than 0.1% . Expansions for quick and accurate computations of the thermodynamic functions in various conditions are provided by Blinnikov et al. [49].

7.7.4 Electrostatic Effects in a Degenerate Medium

When the density of a perfect gas increases, the electrostatic effects increase and the gas is less ideal. For a degenerate gas, the situation is inverse: the gas properties correspond more to Fermi's distribution when the density is higher. As shown by (7.147), the Fermi energy grows like $\varrho^{2/3}$, while the energy E_{ES} of the electrostatic interactions behaves like

$$E_{ES} \sim Ze^2/r_D \sim \sqrt{\varrho} , \qquad\qquad (7.162)$$

since $r_D \sim 1/\sqrt{\varrho}$ according to (7.99). E_F grows faster with density than E_{ES}, thus at higher densities, the electrostatic effects are relatively small. The corresponding equation of state and thermodynamic coefficients have been given in the form of analytic expressions by Chabrier and Pothekin [107].

7.7.5 A Note on the Consequences of Degeneracy and on White Dwarfs

Gas degeneracy has major consequences in stellar physics and evolution:

– While the contraction of a star in a state of perfect gas produces heating, this is no longer true for a degenerate gas (Sect. 3.4).
– While nuclear burning in a star of perfect gas is generally stable, nuclear reactions are unstable in a degenerate medium (Sect. 3.2.1): examples are the He flash in low-mass stars and C detonation for stars around $8\,M_\odot$.
– Degeneracy dramatically modifies the mass–radius relation, making the radius to decrease for larger masses, as in white dwarfs.
– Relativistic degeneracy, with a law of the form $P \sim \varrho^{4/3}$, is responsible for the Chandrasekhar and Oppenheimer–Volkoff masses, respectively, the maximum masses for white dwarfs and neutron stars.

We briefly discuss a few properties of white dwarfs (WD) directly related to electron degeneracy. The subject of the stellar remnants, i.e., of the WD, neutron stars and black holes is a very large subject deserving a full book in itself. See, for example, the books "Stellar Remnants" by Kawaler, Novikov and Srinivasan [281] and "Compact Objects in Astrophysics: White Dwarfs, Neutron Stars and Black Holes", edited by M. Camenzind [83].

Mass–radius relation: white dwarfs are made of fully degenerate electron gas, mostly non-relativistic. Let us express that the internal pressure (1.20) derived from hydrostatic equilibrium is of the order of (7.148) for the fully degenerate gas,

$$\frac{GM^2}{R^4} \approx K_1 \frac{M^{5/3}}{\mu_e^{5/3} R^5} \ . \tag{7.163}$$

After simplification, this gives

$$RM^{1/3} \approx \text{const.} \quad \text{num. [281]} \ \ \frac{R}{R_\odot} = 0.012 \left(\frac{M}{M_\odot}\right)^{-1/3} \left(\frac{\mu_e}{2}\right)^{-5/3}. \tag{7.164}$$

For WD, $\mu_e \approx 2$. The radius is smaller for higher masses! This beautifully shows that different equations of state lead to different relations between the stellar parameters. In the constant, there is K_1 which goes like the inverse of the mass of the degenerate particles (see 7.142), here the electrons. For a mass equal to $1\,M_\odot$, we get a radius of $\sim 10^{-2}\,R_\odot$, i.e., of the order of the Earth radius. The low luminosity ($\log(L/L_\odot) \approx -1.0$ to -4.5) of the white dwarfs is provided by the cooling of the non-degenerate gas of atomic nuclei. The characteristic cooling time of WD is $(1-2) \times 10^9$ yr. During their cooling they progressively become fainter and finally crystallize in their interior.

Neutrons are also fermions and to the first order the neutron stars also obey a $M - R$ relation of the above form. However, the neutron mass being 1839 times

larger than the mass of the electron, the corresponding K_1 would be reduced in the same proportion, thus the radius of a neutron star is much smaller than that of a white dwarf. The value depends on the exact equation of state at high densities (see also Sect. 7.8), current models give radii of 10–15 km.

Chandrasekhar's mass: for larger WD masses, R decreases down to a limit. For larger M, as R decreases the density grows fast and thus electron degeneracy also. The fully degenerate medium becomes more and more relativistic. Thus, P tends toward (7.150). If we do the same as for (7.163), we get

$$\frac{GM^2}{R^4} \approx \frac{K_2}{\mu_e} \frac{M^{4/3}}{R^4} . \tag{7.165}$$

The terms in R^4 disappear after simplification, implying that the mass is equal to a constant. Simplifying and expressing K_2 (7.150), we get

$$M \approx \left(\frac{K_2}{G}\right)^{3/2} \frac{1}{\mu_e^2} = \left(\frac{hc}{8m_u G}\right)^{3/2} \left(\frac{3}{\pi m_u}\right)^{1/2} \frac{1}{\mu_e^2} . \tag{7.166}$$

This can be written as

$$M_{Ch} \approx \left(\frac{c\hbar}{G m_u^2}\right)^{3/2} \frac{m_u}{\mu_e^2} , \tag{7.167}$$

where a factor π and other numerical factor are ignored. This is the order of magnitude of the Chandrasekhar mass [108], i.e., the upper mass limit of white dwarfs (corresponding to their minimum radius). The Chandrasekhar mass is a maximum mass because from (7.165) we see that gravitation (on the left) grows faster with M than the pressure of degeneracy (on the right). Moreover, since R is absent from (7.166), there is no possibility for a WD obeying this equation of state to change its radius. The ratio $\left(c\hbar/[G m_u^2]\right)^{3/2}$ is a dimensionless number equal to 2.25×10^{57}, function of the ratio of the quantum to the gravitation forces (which are the two opposed forces in a WD). The Chandrasekhar mass is thus of the order of this number times the mass unit $M_{Ch} \sim 2.25 \times 10^{57} \, (m_u/\mu_e^2)$, i.e., $\sim 1.88 \, M_\odot/\mu_e^2$. A more elaborate derivation gives [108, 281]

$$M_{Ch} = \frac{5.836 \, M_\odot}{\mu_e^2} . \tag{7.168}$$

For $\mu_e = 2$, this gives 1.46 $M_\odot$. The pressure of degeneracy acts on the electrons, while gravitation mainly acts on the nuclei which contain most of the stellar mass. With accurate models including the electric effects, a Chandrasekhar's mass of about 1.2 $M_\odot$ is found, in better agreement with the largest WD mass observed (cf. Fig. 26.21).

Neutron stars, for the same reasons as for WD, have a maximum mass, the Oppenheimer–Volkoff mass [450], which is of the order of 2–3 $M_\odot$. The exact value depends very much on the equation of state at very high densities.

7.8   Global View on the Equation of State

Detailed tables for the equation of state together with opacity tables (OPAL Library) are developed at the Lawrence Livermore National Laboratory (see description in Sect. 8.6.2). Various mixtures of elements are considered. The equation of state is tabulated on a temperature–density grid and interpolation codes are available. As of 2007, the web address for the OPAL tables is http://www-phys.llnl.gov/Research/OPAL/. Throughout this book, we are using the following general form of the equation of state [285]) (see also 3.60):

$$\frac{d\varrho}{\varrho} = \alpha \frac{dP}{P} - \delta \frac{dT}{T} + \varphi \frac{d\mu}{\mu} \,, \tag{7.169}$$

with $\alpha = \left(\dfrac{\partial \ln \varrho}{\partial \ln P} \right)_{T,\mu}$, $\delta = - \left(\dfrac{\partial \ln \varrho}{\partial \ln T} \right)_{P,\mu}$ and $\varphi = \left(\dfrac{\partial \ln \varrho}{\partial \ln \mu} \right)_{P,T}$.

$$\tag{7.170}$$

For a perfect gas, $\alpha = \delta = \varphi = 1$. For complete non-relativistic degeneracy one has $\alpha = 3/5$ and $\delta = 0$. Figure 7.8 shows a global view on different physical effects which dominate the equation of state in various parts of the plane $\log T$ vs. $\log \varrho$.
 – **Perfect gas.**

$$P_{\rm g} = \frac{k}{\mu \, m_{\rm u}} \varrho T \,.$$

The domain of the perfect gas P_g is the gray central area in Fig. 7.8. A thick dotted line shows the (ϱ, T) values for the Sun from the center to the surface. The Sun is well centered in the domain of perfect gas. The various limits for H^+, H and molecular H_2 are shown. At a given ϱ, for an increase of T the effects of radiation pressure become more important.
 – **Radiation pressure.**

$$P_{\rm rad} = \frac{1}{3} a T^4 \,.$$

The locus where $P_g = P_{\rm rad}$ is given by $[k/(\mu m_{\rm u})]\varrho T = (1/3)aT^4$, which yields

$$T = \left(\frac{3k}{\mu \, m_{\rm u} \, a} \right)^{1/3} \varrho^{1/3} \,. \tag{7.171}$$
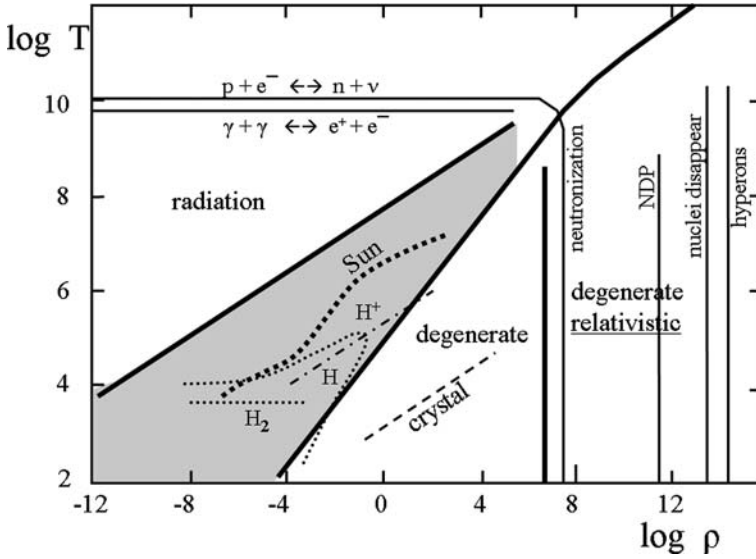
Fig. 7.8 The various domains with different equations of state in the plane $\log T$ vs. $\log \varrho$ are schematically shown. In the central gray domain, the law of perfect gas is dominating. The solar model lies in this area (*heavy dots*). The limits for ionized, neutral and molecular hydrogen are shown (*small dots*). The limits between the zones where the radiation pressure, perfect gas pressure, degenerate non-relativistic and degenerate relativistic pressures dominate are indicated by thick lines. The *dot–dashed line* is the locus where thermal and electrostatic pressure are equal (7.112). A limit for crystallization is shown by a thin dashed line (7.120)

– **Pair e^+e^- formation.**

   When the photon energy $E = h\nu = kT$ becomes higher than the threshold energy of electron of 0.51 Mev ($T \geq 5.9 \times 10^9$ K) one has an equilibrium

   $$\gamma + \gamma \rightleftharpoons e^+ + e^- . \tag{7.172}$$

   This reaction already starts at energies lower than the threshold energy, because of the Planck energy distribution. The above reaction reduces the specific heats and may also make the adiabatic exponents $\Gamma_i < 4/3$. The pair formation produces the pair instability supernovae (PISN).

– **Thermal neutronization.**

   If photons and electrons in thermal equilibrium have an energy higher than the energy difference between neutrons and protons, then one has an exchange reaction

   $$p + e^- \rightleftharpoons n + \nu \quad \text{for} \quad E \geq (m_N - m_P)\,c^2 = 1.29 \,\text{MeV} , \tag{7.173}$$

   which corresponds to $T \geq 1.5 \times 10^{10} K$.

– **Degenerate gas.**

$$P = K_2 \left(\frac{\varrho}{\mu_e} \right)^{\frac{5}{3}} .$$

When moving from the domain of perfect gases to higher densities, one enters the domain of degenerate gases. The locus, where the pressures of the perfect gas and of the fully degenerate gas are equal, is given by

$$\frac{k}{\mu\, m_u} \varrho\, T = K_1 \left(\frac{\varrho}{\mu_e} \right)^{5/3} , \quad \text{or} \quad T = K_1 \frac{\mu m_u}{k} \frac{\varrho^{2/3}}{\mu_e^{5/3}} . \qquad (7.174)$$

The slope of this limit in the diagram $\log T$ vs. $\log \varrho$ is $2/3$. This has major consequences for stellar evolution, since this slope is steeper than $\sim 1/3$, which is the slope followed by stars during evolution (Sect. 26.4).

– **Electrostatic effects and crystallization.**
The limit where electrostatic effects are of the same size as thermal effects is given by (7.120) for a parameter $\Gamma_i = 1$, as defined in (7.118). The limit where the Coulomb plasma crystallizes is given by the same expression for $\Gamma_i = 175$. Materials of our terrestrial environment often lie in the crystal domain.

– **Relativistic degeneracy.**

$$P = K_2 \left(\frac{\varrho}{\mu_e} \right)^{\frac{4}{3}} .$$

At very high densities, degeneracy becomes relativistic. The limit where the fully degenerate non-relativistic (7.148) and the fully degenerate relativistic pressure (7.150) are equal is

$$K_1 \left(\frac{\varrho}{\mu_e} \right)^{5/3} = K_2 \left(\frac{\varrho}{\mu_e} \right)^{4/3} . \qquad (7.175)$$

For $\mu_e = 2$, this limit is defined by $\log \varrho \simeq 6.59$.

– **Neutronization.**
When the Fermi energy E_F of the electrons is above the energy difference $(m_N - m_P)c^2 = 1.29$ MeV between the neutron and the proton, there is a shift of equilibrium

$$p + e^- \rightarrow n + \nu . \qquad (7.176)$$

It is the inverse reaction from the β decay $n \rightarrow p + e^- + \overline{\nu}$. The relativistic electron must have a momentum

$$p_F = \frac{1.29\,\text{MeV}}{c} = \frac{1.29 \times 1.602 \times 10^{-6}}{3 \times 10^{10}} = 6.89 \times 10^{-17}\, \text{CGS}, \quad (7.177)$$

$$\text{giving} \quad \varrho = \mu_e \frac{8\pi}{3} \frac{m_u}{h^3} p_F^3 = 3.13 \times 10^7 \text{g cm}^{-3} , \qquad (7.178)$$

for $\mu_e = 2$. Neutronization produces nuclei which are very rich in neutrons.
– **Toward higher densities.**

$$P \sim K\varrho^{\Gamma_1}, \tag{7.179}$$

with $\Gamma_1 \sim 1.4$ (see Figs. 21 and 22 by Srinivasan [281]). From densities of about 10^7 to 10^{15} g cm^{-3}, there are various processes, which occur in the structure of neutron stars [83, 86, 281].

– In the vacuum, the minimum of nuclear energy (i.e., the most bound nucleus) is reached for ^{56}Fe. At high density, the effects of degenerate electrons and of electrostatic interactions between nuclei displace the energy minimum toward higher values of the atomic mass number. Above $\varrho \approx 10^7$ g cm^{-3}, neutronization occurs. The electron energies are sufficient for them to be captured by protons in atomic nuclei. It is the inverse of the β-decay. Nuclei very rich in neutrons appear, which do not exist in the ordinary terrestrial conditions, such as elements with $Z \sim 50$ and A up to 10^3 or more. This forms a solid crystal due to the repulsive Coulomb forces of the nuclei.
– For $\varrho \geq 3 \times 10^{11}$ g cm^{-3}, the stability of nuclei with $N \gg Z$ decreases so much that they start to lose their neutrons. This is the so-called neutron drip point (NDP). The NDP occurs when the energy of a bound neutron in the heavy nucleus becomes larger than the energy of a free neutron in the medium. The nuclei still form a solid network.
– For $\varrho \geq 5 \times 10^{13}$ g cm^{-3}, the surviving nuclei dissolve to form a medium of degenerate neutrons with a few percents of electrons and protons. The free neutrons are stabilized by the degenerate electrons of very high Fermi energies.
– Above $\varrho = 3 \times 10^{14}$ g cm^{-3}, the equilibrium is shifted toward muons,

$$e^- \rightarrow \mu^- + \nu_e + \overline{\nu}_\mu , \tag{7.180}$$
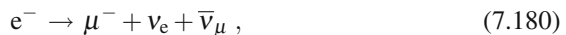
and then toward hyperons, for example,

$$n + e^- \rightarrow \Sigma^- + \nu_e . \tag{7.181}$$

In the very high density regime, the physical state very much depends on the shape of the nuclear potential at short ranges, which produces deviations from the ideal degenerate neutron gas. These effects determine the thermodynamic properties and the relevant coefficients.
– Between densities of 5×10^{13} and 7×10^{14} g cm^{-3}, superfluid "nn" pairs and supraconductor "pp" pairs may form. The spin numbers are integers and these particles are bosons. These pairs form when the densities are high enough for efficient attractive nuclear interactions. The equation of state in these regimes can be locally approximated by a polytrophic relation with $P = K\varrho^{\Gamma_1}$. The pressure tends toward $P \rightarrow \varrho c^2$ for densities above $\sim 10^{16}$ g cm^{-3}.

Chapter 8
The Opacities*

The opacity of stellar matter determines the speed at which a star spends its energy, i.e., at which rate the light goes out of a star. Thus, the luminosity of a star of a given mass is essentially determined by the opacity of the matter and *not by its nuclear reactions*. Opacity is thus a key factor in stellar properties. As an example, the first stars in the Universe (Chap. 29) which contained no heavy elements had much lower opacities and their properties were very different. The stellar opacities result from the many processes in atomic physics which affect the transfer of radiation.

Since a few decades, opacity data are provided as electronic data tables, such as the OPAL Opacity Tables by Forrest Rogers and Carlos Iglesias at Lawrence Livermore National Laboratory [493], or the "Opacity Project" (OP) developed by an international collaboration [525]. More details as well as the web sites are given in Sect. 8.6.2. Although most astrophysicists do not themselves calculate opacity data, they need to understand the main opacity mechanisms and their properties. Detailed developments are given by Rose [498] or by Cox & Giuli [147, 610]. Stellar opacities are mainly due to

- line absorption or bound–bound transition,
- electron scattering,
- photoionization or bound–free transitions, including H^- absorption,
- hyperbolic or free–free transitions.

8.1 Line Absorption, Electron Scattering, Rayleigh Diffusion

8.1.1 Recalls on the Atomic Oscillators

The simplest model describing the interaction of radiation with atoms is the harmonic oscillator. The atom is considered as a dipole oscillating under the effect of electromagnetic radiation [498]. The absorption coefficient per atom at frequency ν is given by

---

*This chapter may form the matter of a basic introductory course.

$$\kappa'_\nu \equiv \kappa_\nu \, \varrho \, , \tag{8.1}$$

where the opacity coefficient κ_ν in $cm^2 \, g^{-1}$ is defined in Sect. 3.1.1. The coefficient κ'_ν is the inverse of the mean free path ℓ (3.6). The oscillator model gives

$$\kappa'_\nu = \frac{\pi n e^2}{m_e c} \, \frac{4\gamma v^2}{4\pi^2 \, (v_0^2 - v^2)^2 + \gamma^2 v^2} \quad \text{with} \quad \gamma = \frac{2}{3} \frac{e^2 \, \omega^2}{m_e \, c^3} \, , \tag{8.2}$$

and the oscillation frequency $\omega = 2\pi \nu$, n is the number of atoms per volume unity. In the Gauss or E.S.U. system of units, one has $e^2 = 23.0708 \times 10^{-20}$ erg cm. Close to the resonance, one has $v_0^2 - v^2 \simeq 2v(v_0 - v)$ and thus the coefficient κ'_ν becomes

$$\kappa'_\nu \simeq \frac{\pi n e^2}{m_e \, c} \left[\frac{\gamma}{4\pi^2 \, (v_0 - v)^2 + \frac{\gamma^2}{4}} \right] . \tag{8.3}$$

The term in brackets is called the Lorentz profile. The quantum description of the atomic transitions leads to a modified expression

$$\kappa'_\nu = \frac{\pi e^2}{m_e c} \, n_{n'} \, f_{n'n} \left[\frac{\Gamma_n + \Gamma_{n'}}{4\pi^2 (v_0 - v)^2 + \frac{(\Gamma_n + \Gamma_{n'})^2}{4}} \right] . \tag{8.4}$$

Here, $n_{n'}$ is the number of the atoms considered on level n' by volume unity. $n_{n'} f_{n'n}$ is the effective number of electrons which can make the transition from level $n' \to n$. The f values are called the oscillator forces and are determined in laboratory for most atoms. Γ_n and $\Gamma_{n'}$ are the widths (in s^{-1}) of the two levels considered. $v_0 = (E_n - E'_n)/h$ is the frequency corresponding to the energy difference of the considered levels.

8.1.2   Spectral Lines or Bound–Bound Transitions

The absorption by spectral lines, due to bound–bound (bb) transitions between atomic levels, makes about 10% of the opacity in the solar center and about 50% in the outer layers, the bound–free transitions (Sect. 8.3) being more important in general. The difficulty to account for all spectral lines is a major source of uncertainty in the calculation of stellar opacities. All we know about the chemical abundances of stars is obtained from the study of spectral lines, which in addition provides information on the stellar gravity, temperature, motions, rotation, etc.

The coefficient κ'_ν for a given electronic transition can be written according to (8.4) in the following general form:

$$\kappa'_\nu = \frac{\pi e^2}{m_e c} \, n_{n'} \, f_{n'n} \, \phi_\nu, \tag{8.5}$$

where ϕ_ν is the broadening function, given by the term in square brackets in (8.4). $\phi_\nu d\nu$ expresses the probability of absorption between the frequencies ν and $\nu + d\nu$ and one has $\int_0^\infty \phi_\nu \, d\nu = 1$. The function ϕ_ν results from several effects which affect the absorption frequency: broadening by thermal Doppler effect which is the main effect in MS stars, collisions, turbulence, Stark and Zeeman effects, etc. The quantity

$$\sigma_\nu = \frac{\pi e^2}{m_e c} f_{n'n} \phi_\nu \tag{8.6}$$

is the cross-section, i.e., the effective surface of absorption, of the atom for the considered transition. At a given frequency, the bound–bound absorption coefficient is the sum over all transitions nn' and elements j:

$$\kappa_{\mathrm{bb}}(\nu, j) = \sum_j \sum_{nn'} \kappa_{nn'}(\nu, j) \,. \tag{8.7}$$

The elements of the Fe group, which are in significant amounts, have many bound electrons which largely contribute to the opacity in Pop. I stars. Various improvements in the calculation of atomic physics for the partially ionized Fe ions have led to an opacity increase by a factor of 3 for T equal to a few 10^5 K [492]. Amazingly, this increase was anticipated from comparisons between theoretical pulsation models and observations for β Cephei stars [551]. Other heavy elements have only a marginal impact [266]. The recent progresses in opacities mainly come from improvements in the calculations of bb transitions.

8.2   Electron Scattering

Free electrons cannot absorb photons, they only diffuse them according to conservation laws. Diffusion nevertheless produces an attenuation of the flux in the propagation direction. This is electron or Thomson scattering. From (8.2), one gets for $\left| \nu_0^2 - \nu^2 \right| \gg \gamma \nu$, i.e., for a range of frequencies much larger than the natural width,

$$\kappa_\nu' = \frac{8\,\pi}{3} \frac{n_e \, e^4}{m_e^2 c^4} \frac{1}{\left[\left(\frac{\nu_0}{\nu} \right)^2 - 1 \right]^2} \,. \tag{8.8}$$

n_e is the electron concentration. For free electrons, $\nu_0 \to 0$ and thus one has for frequencies $\nu \gg \nu_0$,

$$\kappa_\nu' = \frac{8\,\pi n_e \, e^4}{3\, m_e^2 \, c^4} = 0.66524 \times 10^{-24} \, n_e \,, \tag{8.9}$$

with n_e in cm^{-3} and κ_ν' in cm^{-1}. The ratio κ_ν'/n_e is the cross-section associated to the absorption by the considered particle

$$\kappa'_\nu = n_e\,\sigma \,, \tag{8.10}$$

and thus one has the Thomson cross-section for electron scattering:

$$\sigma_{es} = \frac{8\pi}{3}\left(\frac{e^2}{m_e c^2}\right)^2 = 0.66524\times 10^{-24}\ \text{cm}^2\,. \tag{8.11}$$

The electron scattering opacity κ_{es} is independent of ν and by (8.1)

$$\kappa_{es} = \frac{\kappa'}{\varrho} = \frac{n_e\,\sigma_{es}}{\varrho}\quad \text{with}\quad n_e \cong \frac{\varrho}{2\,m_u}(1+X)\,, \tag{8.12}$$

where the electron concentration n_e has been obtained in (7.42) under the hypothesis of a fully ionized medium. X is the hydrogen mass fraction. The opacity can be written as

$$\kappa_{es} \cong \frac{\sigma_{es}}{2\,m_u}(1+X) \cong 0.200\,(1+X)\ \text{cm}^2\ \text{g}^{-1}. \tag{8.13}$$

8.2.1 Electron Scattering at High Energies

As a result of photon diffusion by an electron, the wavelength of the photon is increased by $2\lambda_C \sin^2 \vartheta/2$, where $\lambda_C = h/(m_e c) = 2.426\times 10^{-10}$ cm is the Compton wavelength and ϑ the diffusion angle (the Compton wavelength for the electron is defined as the wavelength λ_C for which the energy hc/λ_C of the radiation is equal to the rest mass of the electron $m_e c^2$). The shift in wavelength is important only for high-enough energies, i.e., for non-negligible values of

$$\alpha = \frac{h\nu}{m_e c^2} = \frac{\lambda_C}{\lambda}\,. \tag{8.14}$$

This occurs for T such that $kT \sim h\nu$ is significant with respect to $m_e c^2$ (i.e., 0.511 MeV, i.e., $T \sim 5.93 \times 10^9$ K). In this T regime, the Klein–Nishina cross-section applies. One has for $\alpha \ll 1$ and $\alpha \gg 1$, respectively [610],

$$\sigma = \sigma_{es}\left(1 - 2\alpha + \frac{26}{5}\alpha^2 + \dots\right) \quad \text{and}\quad \sigma = \frac{3}{8\,\alpha}\sigma_{es}\left(\ln 2\alpha + \frac{1}{2}\right). \tag{8.15}$$

For $\alpha \ll 1$, degeneracy has no effect, since the change of the electron energy produced by the diffusion is negligible and it can stay in the same cell of the phase space. This is not true for $\alpha \gg 1$ and the cross-section is thus reduced.

8.2.2 Rayleigh Diffusion

Let us consider the case of low-energy photons interacting with a bound electron. One has $v \ll v_0$, frequency v_0 is high because electrons are strongly bound to atoms and molecules. From (8.8), one obtains

$$\kappa'_v = \frac{8\pi}{3} \frac{n_e e^4}{m_e^2 c^4} \left(\frac{v}{v_o}\right)^4 = n_e \sigma_{es} \left(\frac{\lambda_0}{\lambda}\right)^4. \tag{8.16}$$

Rayleigh scattering plays a role in the external regions of cool stars. In the terrestrial atmosphere, we are indebted to it for the blue sky.

8.3 Photoionization or Bound–Free Transitions

A bound electron in an atom is ejected by an incident photon and becomes a free electron (Fig. 8.1). Such a bound–free (bf) absorption process occurs only for photon energies higher than the ionization potential of the considered level n,

$$h v > I_n = \frac{2\pi^2 m e^4}{h^2} \frac{Z^2}{n^2} = R_\infty h c \frac{Z^2}{n^2}, \tag{8.17}$$

where $R_\infty = 2\pi^2 m_e e^4/(ch^3) = 1.09737 \times 10^5$ cm^{-1} is the Rydberg constant. This expression also defines an absorption edge, i.e., the lowest frequency v^* for bound–free absorption,

$$h v^* \sim 1/n^2. \tag{8.18}$$
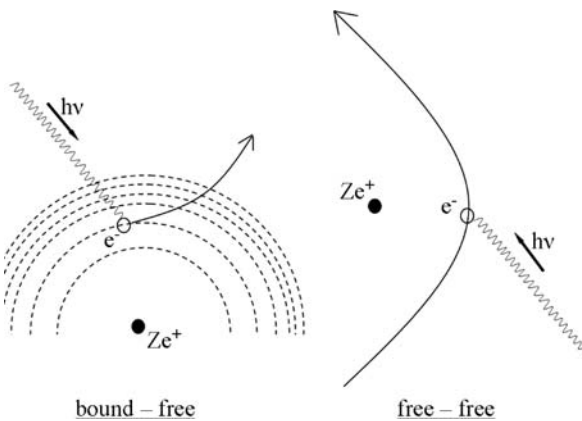
Fig. 8.1 Schematic illustration of the bound–free and free–free absorptions

The approximation of an hydrogenic atom has been made above, which is (partly) justified by the fact that elements are highly ionized in the stellar interiors. The absorption coefficient of a photon of frequency ν by an electron on a level n of an ion of charge Z_j is

$$a_{\mathrm{bf}}(\nu, j, n) = \frac{64\,\pi^4\, m_e\, e^{10}}{3^{3/2}\, c\, h^6}\ \frac{Z_j^4}{n^5\, \nu^3}\, g_{\mathrm{bf}}\,. \tag{8.19}$$

The factor g_{bf} is a dimensionless factor, called the Gaunt factor for bf absorption. It corrects the above semi-classical expression for quantum effects, in general $g_{\mathrm{bf}} \simeq 1$ and varies slowly with n and ν. When an atom has several bound electrons, the charge Z_j must be replaced by an effective charge, accounting for the screening effects of bound electrons (Sect. 9.4). We note that heavy elements (with high Z_j) are important absorbers and that absorption is stronger at longer wavelengths. At the edge frequency ν^*, the absorption goes like

$$a_{\mathrm{bf}}(\nu^*, j, n) \sim \frac{1}{n^5\, \nu^{*3}} \sim \frac{n^6}{n^5} \sim n \tag{8.20}$$

with (8.18). The absorption from the highly excited states is higher, contrarily to the first impression from (8.19). We thus have

$$a_{\mathrm{bf}}(\nu^*, j, n) \sim n \sim (h\nu^*)^{-\frac{1}{2}} \sim T^{-\frac{1}{2}}\,. \tag{8.21}$$

This means that the absorption coefficient for a given element at the edge frequency scales like $T^{-1/2}$. For an element of relative abundance X_j in mass fraction, the corresponding opacity is

$$\kappa_{\mathrm{bf}}(\nu, j, n) = a_{\mathrm{bf}}(\nu, j, n)\frac{\bar{n}_{\mathrm{e}}(j, n)\, X_j}{A_j\, m_{\mathrm{u}}}\,, \tag{8.22}$$

where $\bar{n}_{\mathrm{e}}(j, n)$ is the average number of bound electrons in the n shell of element j. It is estimated with the Saha–Boltzmann equation (7.23), assuming that the medium is highly ionized so that the ions will have at most one bound electron.

As frequency increases, the opacity coefficient decreases with ν^{-3} (8.19), but suddenly the energy is high enough to eject electrons from a deeper shell and the coefficient raises steeply to decline again in ν^{-3} until the next jump when the energy is high enough to eject an electron from a deeper shell. Then, the summation has to be made on the various elements j:

$$\kappa_{\mathrm{bf}}(\nu) = \sum_{j,n} a_{\mathrm{bf}}(j, n, \nu)\frac{X_j}{A_j\, m_{\mathrm{u}}}\,\bar{n}_{\mathrm{e}}(j, n). \tag{8.23}$$

Electron degeneracy, if present, decreases $\kappa_{\mathrm{bf}}(\nu)$, since many cells of the phase space of free electrons are occupied. Before taking the Rosseland average (3.22), one must sum up all the various absorption processes. For specific purpose, one may

take the mean Rosseland opacity for the bound–free transitions only. Let us examine how it scales with T. A dependence of the form $\kappa \sim \nu^\alpha$ in the mean Rosseland opacity (3.22) gives a dependence T^α [285], as obtained by integration of (3.22). Thus, the term ν^{-3} in (8.19) makes a dependence like T^{-3}. With account that the edge frequency scales like $T^{-1/2}$ (8.21), this gives a general dependence in $T^{-3.5}$. The mean opacity coefficient behaves roughly like [523], see also [610],

$$\kappa_{\rm bf} \simeq \kappa_{0,\rm bf}\, \varrho\, T^{-3.5} \quad \text{with} \quad \kappa_{0,\rm bf} \simeq 4.3 \times 10^{25} Z(1+X)\,, \tag{8.24}$$

with ϱ in g cm^{-3}, T in K and $\kappa_{\rm bf}$ in cm^2 g^{-1}. This is the Kramers law for bf transitions. We notice the dependence in the heavy element content Z, which makes $\kappa_{\rm bf}$ a major effect in stars of solar composition. It applies essentially for T above several 10^4 K depending on density (see Fig. 8.2).

Some factors of the order of unity are omitted, in particular the Gaunt factor, which is close to 1, and a so-called guillotine factor which accounts for the overestimate of the number of bound electrons given by Saha–Boltzmann relation at low T. Analytical expressions are no longer used for model calculations, but only for simple analytical scaling or estimates. Figure 8.2 shows the total opacity curves. On the right of the peak, we see the decrease approximately predicted by Kramers law for bound–free opacities.

8.3.1 Negative H Absorption

Absorption by the negative ion H$^-$ is a dominant feature of the continuous spectrum of the Sun. We have seen (Sect. 7.1.4) that negative H$^-$ ions may form according to the Saha equation (7.28). In view of the ionization potential of 0.747 eV for H$^-$, photons with $\lambda < 1.655\,\mu$ have enough energy to produce a bound–free transition from H$^-$ to H. The existence of H$^-$ absorption requires both neutral hydrogen and free electrons, which come from elements with low ionization potentials such as Na, K, Ca and Al (Sect. 7.1.4). Therefore, H$^-$ absorption is present only for a limited range of temperatures, from about 3000 (in order to have free e$^-$) to less than 10^4 K (in order to still have neutral H). The opacity behaves like [228]

$$\kappa_{\rm H^-} \approx 2.5 \times 10^{-31} \left(\frac{Z}{0.02}\right) \varrho^{\frac{1}{2}}\, T^9 \quad \text{cm}^2\,\text{g}^{-1}, \tag{8.25}$$

for $T \approx (3-6) \times 10^3$ K, $\varrho \approx (10^{-10} - 10^{-5})$ g cm^{-3} and $Z = 0.001 - 0.02$. The H$^-$ absorption increases fast with temperature up to about 10^4 K. The continuous absorption by H$^-$ is responsible for most continuous properties of the spectra of stars between 3000 and 7000 K. The steep growth of the opacity at low T (Fig. 8.2) is mainly due to this effect, in addition to the partial ionization of hydrogen and helium which increases the possibility of transitions for larger temperatures.
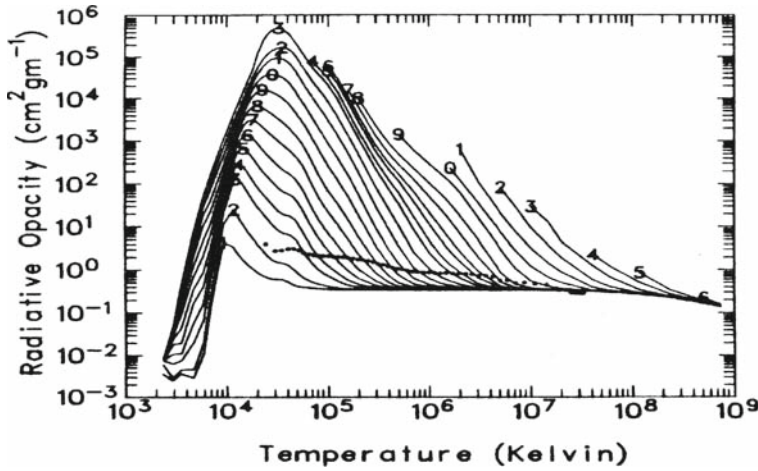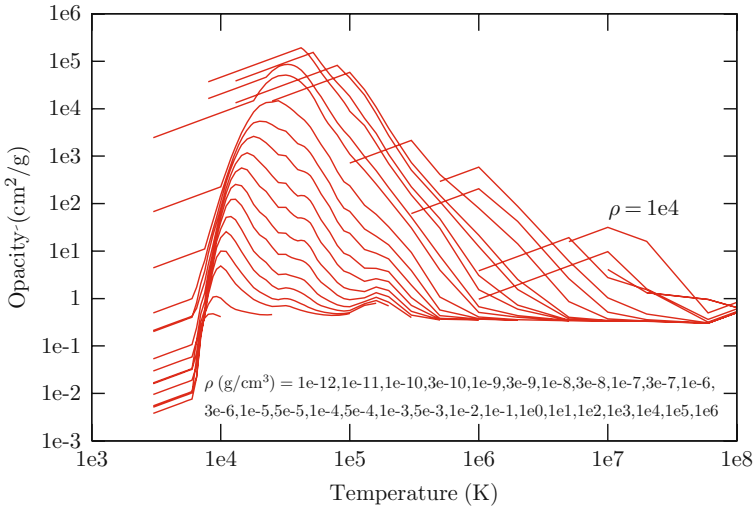
Fig. 8.2 Opacities with a difference of 25 years. Top: opacities from A.N. Cox in 1983 [144] as a function of T and ϱ for $X = 0.70$ and $Z = 0.02$. Curves nb. 3, 1, 9, 6 on the right of the peak correspond to $\varrho = 10^4, 10^2, 1.0, 10^{-2}$ g cm^{-3}. Curve 3 at the max. is for 10^{-3} g cm^{-3}. Curves 1, 7, 3 and 1 on the left of the peak correspond to $\varrho = 10^{-4}, 10^{-6}, 10^{-8}, 10^{-10}$ g cm^{-3}. Bottom: opacities in 2008 provided by A.N. Cox and A.T. Boothroyd from OPAL [493] for the new solar abundances [20], Appendix A.3. The *straight lines* on the left of each curve indicate where usual stellar conditions end. Courtesy by A.N. Cox

8.4   **Hyperbolic Transitions or Free–Free Opacity**

A free electron of velocity v moving in the Coulomb field of an ion of charge $Z_j\,e$ can absorb (ff absorption) or emit (Bremsstrahlung) a photon of frequency ν (Fig. 8.1). In the hydrogenic approximation, the absorption coefficient for ff absorption for an ion and a free electron is by volume unity

$$a_{\text{ff}}(\nu, j, v) = \frac{4\pi\,e^6}{3^{\frac{3}{2}}\,chm_{\text{e}}^2}\,\frac{Z_j^2}{v}\,\frac{g_{\text{ff}}}{\nu^3}\,, \tag{8.26}$$

where g_{ff} is the Gaunt factor (~ 1) for the process. This absorption is continuous, without jumps and has no frequency limit. This coefficient must first be integrated over the Maxwell–Boltzmann distribution (C.62) expressed in term of velocities

$$\kappa_{\text{ff}}(\nu\,j) = \frac{X_j}{A_j m_{\text{u}}}\int_0^\infty a_{\text{ff}}(\nu, j, v)\,dn_{\text{e}}(v), \tag{8.27}$$

where $dn_{\text{e}}(v)$ is the concentration of free electrons with velocities between v and $v+dv$. Then one must sum up over the various elements j,

$$\kappa_{\text{ff}}(\nu) = \sum_j \int_0^\infty \kappa_{\text{ff}}(\nu\,j)\,\frac{X_j}{A_j m_{\text{u}}}\,dn_e(v). \tag{8.28}$$

In (8.26), one has a dependence on $1/(v\,\nu^3)$. In thermal equilibrium v scales like $T^{1/2}$. As noted in Sect. 8.3, a dependence on ν^{-3} leads to a scaling with T^{-3}, making thus an overall dependence on $T^{-3.5}$, when account is given to the velocity. In addition the process depends on the electron density, which according to (7.42) yields a term $\varrho\,(1+X)$ and the abundances of hydrogen and helium lead to a factor $(X+Y)$. The mean Rosseland opacity (3.22) for the free–free absorption only is also roughly given by a Kramers law [523], see also [610],

$$\kappa_{\text{ff}} \simeq \kappa_{0,\text{ff}}\,\varrho\,T^{-3.5} \quad\text{with}\quad \kappa_{0,\text{ff}} \simeq 3.7 \times 10^{22}\,(X+Y)\,(1+X), \tag{8.29}$$

where κ_{ff} is in $\text{cm}^2\,\text{g}^{-1}$. The T and ϱ dependences are the same as for bound–free opacity, thus ff transitions produce the same slope of κ as a function of T (cf. Fig. 8.2). The coefficient $\kappa_{0,\text{ff}}$ is smaller than $\kappa_{0,\text{bf}}$ (8.24) for standard composition, so that bf transitions dominate over ff effects. However, the free–free opacity is essentially independent of metallicity Z and thus it dominates over bound–free opacity in low-Z stars.

In case of partial degeneracy, the distribution dn_{e} to be considered is the Fermi–Dirac rather than the Maxwell–Boltzmann distribution. Degeneracy limits the ff transitions, because the final stages of low energies are occupied. When electron concentration is high, screening effects (Sect. 9.4) play a role. Thus, the complete theory contains more effects, including also a Gaunt factor and a guillotine effect as mentioned for bf opacities.

8.5   Electronic Conduction

Due to their slow motions and high cross-sections, electrons and ions usually trans-
port little energy compared to photons. However, in degenerate media like the cores
of red giants and the white dwarfs, heat conduction by electrons, a current process
at terrestrial densities, becomes dominant. During MS evolution of solar-type stars,
conduction is marginal (cf. Fig. 8.3).

8.5.1   Electron Conduction in Non-degenerate Gas

In a non-degenerate gas, the ions of mass $A m_u$ and electrons of mass m_e have aver-
age quadratic velocities (C.63),

$$\sqrt{v^2}_i = \left(\frac{3kT}{A m_u} \right)^{\frac{1}{2}}, \quad \sqrt{v^2}_e = \left(\frac{3kT}{m_e} \right)^{\frac{1}{2}}. \tag{8.30}$$

The electrons are faster than the ions in a ratio $(A m_u / m_e)^{1/2} = 43 \sqrt{A}$. Thus, the
electron gas is made of fast particles with respect to the slower ion gas. If there is
a T gradient, the electrons move faster from regions of higher T toward regions of
lower T than the opposite. The ions also move faster in the same direction, but with
a smaller velocity difference. Electric neutrality prevents a net flux of charges, but
not a net energy flux.
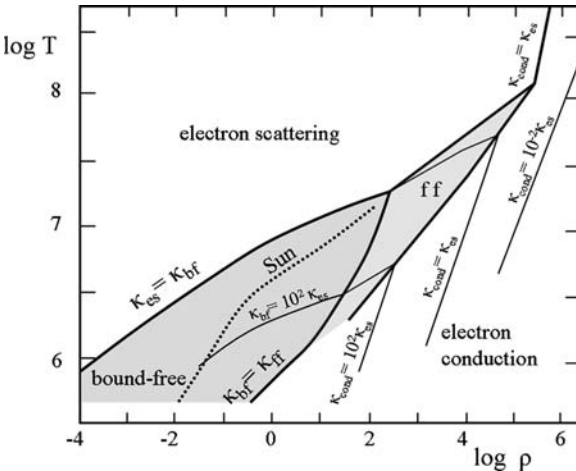
Fig. 8.3 Indications of the dominant opacity sources in the $\log T$ vs. $\log \varrho$ diagram. The location of
the solar internal structure is indicated by a *thick dotted line*. The electron conduction is expressed
in terms of the electron scattering opacity κ_{es}

Let us call n_+ the number of particles crossing a surface from left to right. This number is the same as the number n_- of particles from right to left. The energy flux is not necessarily zero, because the average energy on one side is different from that on the other side. For the radiative flux, we had an expression $F = -C_{\text{rad}}\,dT/dr$ (3.17), with $C_{\text{rad}} = 4ac\,T^3/(3\,\kappa\varrho)$. Similarly one writes for electron conduction

$$F_{\text{cond}} = -C_{\text{cond}}\frac{dT}{dr} \quad \text{with} \quad C_{\text{cond}} \equiv \frac{4ac\,T^3}{3\,\kappa_{\text{cond}}\,\varrho}, \tag{8.31}$$

which defines the conductive opacity κ_{cond}. For the two modes of energy transport, one sums up the heat fluxes

$$F_{\text{tot}} = F_{\text{rad}} + F_{\text{cond}} \equiv -\frac{4ac\,T^3}{3\,\kappa_{\text{tot}}\,\varrho}\frac{dT}{dr}. \tag{8.32}$$

Thus the addition law for the κ is

$$\frac{1}{\kappa_{\text{tot}}} = \frac{1}{\kappa_{\text{rad}}} + \frac{1}{\kappa_{\text{cond}}}. \tag{8.33}$$

The conductive flux can be estimated as follows:

$$F_{\text{cond}} \approx -n_e\overline{v}\ell\frac{dE_{\text{cin}}}{dr}, \tag{8.34}$$

with n_e the electron number per cm^3, for $\overline{v}$ we take the mean quadratic velocity (8.30), ℓ is the mean free path of the electrons and E_{cin} is their mean kinetic energy. This gives an energy transported by units of surface and time. In the non-degenerate case, one has $E_{\text{cin}} = (1/2)m_e\overline{v}^2 = (3/2)kT$, thus

$$F_{\text{cond}} \approx -n_e\overline{v}\ell\frac{3}{2}k\frac{dT}{dr} \quad \text{and} \quad C_{\text{cond}} \approx \frac{3}{2}kn_e\,\overline{v}\ell. \tag{8.35}$$

One needs to estimate the mean free path ℓ. If n_i is the number of ions per cm^3 and σ the cross–section for collisions between electrons and ions, one has $\ell = 1/(n_i\,\sigma)$. To estimate σ, one supposes that a collision occurs when the electron is close enough to the ion so that its potential energy in the electric field of the ion is equal to its kinetic energy:

$$\frac{1}{2}m_e\,\overline{v}^2 = \frac{Ze^2}{r_0}. \tag{8.36}$$

Thus the interaction radius is $r_0 = 2Ze^2/(m_e\overline{v}^2) = 2Ze^2/(3kT)$ and the cross-section is

$$\sigma = \pi r_0^2 = \frac{4\pi Z^2\,e^4}{9\,(kT)^2}. \tag{8.37}$$

The concentration is $n_i = \varrho/(Am_u)$, A being the mean atomic mass. Thus, one may express ℓ. For the electron concentration, one has $n_e = (1/2)(\varrho/m_u)(1+X)$ (cf. 7.42) and thus

$$C_{cond} \approx \frac{3}{2} k \frac{1}{2} \frac{\varrho}{m_u} (1+X) \left(\frac{3kT}{m_e}\right)^{1/2} \frac{1}{\frac{\varrho}{Am_u} \frac{4\pi Z^2 e^4}{9(kT)^2}} =$$

$$\frac{27\sqrt{3}}{16\pi} \frac{k^{7/2}}{m_e^{1/2} e^4} \frac{(1+X)}{Z^2/A} T^{5/2}. \tag{8.38}$$

The conductive opacity is [610]

$$\kappa_{cond} = \frac{4\,ac\,T^3}{3\,C_{cond}\,\varrho} \approx 5000 \frac{Z^2/A}{(1+X)\,(\varrho/10)} T_7^{1/2} \quad \text{in} \quad \frac{\text{cm}^2}{\text{g}}, \tag{8.39}$$

with $T_7 = T/10^7$. Despite its simplicity, this derivation is correct within a factor of 2. The coefficient C_{cond} increases rapidly with T. It decreases with Z, because the higher the Z, the shorter the mean free path. For MS stars, the mean free path of photons is much longer than that of electrons and electron conductivity is negligible (Fig. 8.3).

8.5.2   Electron Conduction in Degenerate Gas

Conduction by electrons dominates the heat transport in degenerate regions, the other processes becoming negligible with respect to it. In degenerate conditions, the mean velocity $\bar{v}$ of the electrons is much larger than the thermal velocity, because they occupy energy states up to the Fermi level. The electrons with p close to p_F provide the main contribution to the energy transport. The electron mean free path is also increased, because the electrons do not find available final states. Corresponding developments lead in the case of high degeneracy [610] to

$$\kappa_{cond} = 5.12\ 10^{-3} \frac{\sum Z_j^2 X_j \theta_j/A_j}{(1+X)^2} \frac{T_7^2}{(\varrho/10^5)^2} \frac{\text{cm}^2}{\text{g}}, \tag{8.40}$$

with $\theta_j \approx 0.85/Z_j^{1/3}$ and X_j the abundance of element j in mass fraction. For example, if $T > 10^7$ K and $\varrho = 10^5$ g cm^{-3}, one has according to (8.40) $\kappa_{cond} = 10^{-2}\,\kappa_{es}$, where κ_{es} is the electron scattering opacity. This means that the total opacity (8.33) is negligible, being as small as $10^{-2}\,\kappa_{es}$. Figure 8.3 shows the loci of equal opacities expressed in term of κ_{es}.

Many improvements in the calculations of conductive opacities have been brought by Itoh [268]. According to (8.31) and (8.33), the stellar regions where the conductive opacity is very low, i.e., where conduction is important, rapidly become isothermal.

8.6   Global View on Stellar Opacities

After summation over the various elements of the stellar medium, the total absorption coefficient at a given frequency is obtained by summing all coefficients for the various processes of absorption at frequency v,

$$\kappa_v = \left[\kappa_{\mathrm{bf}}(v) + \kappa_{\mathrm{ff}}(v) + \kappa_{\mathrm{bb}}(v) + \ldots\right]\left(1 - e^{-hv/kT}\right) + \kappa_{\mathrm{es}} + \ldots \qquad (8.41)$$

The atomic opacities are corrected by a term which accounts for the stimulated or induced emission, i.e., the process by which an electron on an energy level goes down to a lower energy level due to the income of a photon with the same energy as the energy difference between the two levels. The induced emission is correlated to the direction of the incident photons, thus the absorption at the considered frequency is reduced. The factor of reduction derived from the study of Einstein's coefficient is $(1 - e^{-hv/kT})$ [498]. The dots represent the other opacity sources, such as Compton diffusion, Raman and Rayleigh diffusion, molecular absorption, pair formation, etc., accounted for in the opacity tables. The induced emission does not act on scattering processes.

The terms depending on the frequency must be averaged with expression (3.22) to give the Rosseland mean opacity. This mean gives a particular high weight to the values of κ_v such that $hv/(kT) \simeq 4$.

8.6.1   Dependence on T and ϱ, Changes with Masses

The opacity is a function $\kappa = \kappa(\varrho, T, \mathrm{composition})$. Figure 8.2 shows two examples. Globally, the opacities show a big bump. At T equal to a few 10^3 K, the opacity is very low, since atomic and molecular matter has only bound–bound transitions. For $T \approx 3000$–8000 K, the opacity increases fast with little dependence on ϱ. This is mainly due to the hydrogen ionization, which forms ion H^- with an opacity described by (8.25). Bound–free transitions start developing and contribute to the opacity. Up to 1–2×10^4 K, depending on density, the opacity behaves globally like

$$\kappa \sim \varrho^\alpha T^\beta \quad \text{with} \quad \alpha \sim 0.3,\ \beta \sim 9\ . \qquad (8.42)$$

The maximum of opacity corresponds to the temperature where most H is ionized. For higher temperatures, the opacity, which is mainly due to heavy elements, decreases with increasing T because the elements lose their electrons and the possibilities of bf transitions decline. In this T regime, a rough approximation is the Kramers opacity law (8.24)

$$\kappa \sim \kappa_0\, \varrho\, T^{-3.5}\ . \qquad (8.43)$$
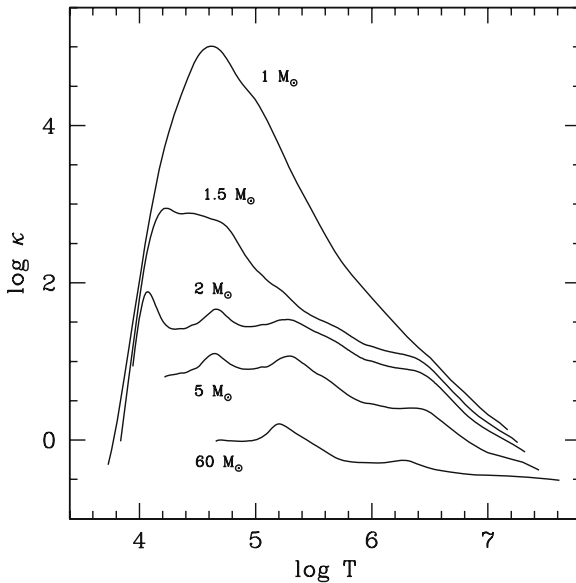
Fig. 8.4 The variation of the opacity as a function of T from surface to center in various stars on the ZAMS, the model of 1 $M_\odot$ corresponds to the present Sun

Some smaller bumps in the decreasing curve appear at higher T, they are due to bf transitions of some relatively important atoms, in particular Fe. These bumps are more visible in recent opacity data (see Figs. 8.2 bottom, 8.4 and 8.5), which include a detailed treatment of Fe lines. For high-enough T only electron scattering opacity is left. It decreases slightly for high T due to the transition from Thomson to Compton scattering according to expression (8.15).

There is an important property regarding density. In a medium with a very low ionization, each atom absorbs independently. The absorption by mass unit is essentially independent of ϱ. At the opposite, in a stage of partial ionization, the bf absorption depends on the possibilities of electrons to settle on atomic energy levels, this depends on the electronic concentration n_e. Therefore, the absorption coefficient in $cm^2\,g^{-1}$ depends on ϱ. These properties are also visible in Fig. 8.4 for stars where the densities are different.

Figure 8.3 shows the regions of the plane $\log T$ vs. $\log \varrho$ where the different opacity sources dominate. The boundaries of the domains are located where the considered opacities are equal. The location of the internal solar regions is indicated (bf opacity dominates). In the area corresponding to the degenerate medium (7.8), electron conduction dominates, this applies to the cores of red giants stars and to white dwarfs. Electron scattering dominates at high temperatures, in particular in massive stars.

Figure 8.4 shows the opacities as a function of T in stars of various masses. The low value due to electron scattering is visible in massive stars. For the 2 $M_\odot$ model and to a different extent for other models, one sees different bumps (see also Fig.
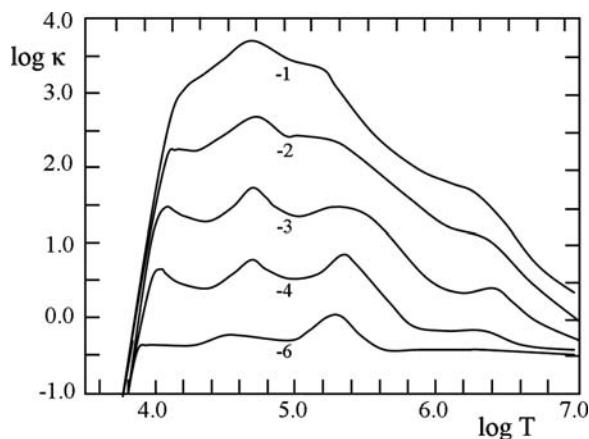
Fig. 8.5 Representation of the opacity as a function of $\log T$ for different values of $\log R$, where $R = \varrho/T_6^3$. From Rogers & Iglesias [493]

8.2 bottom): the one at $\log T \approx 4.0$ is a peak due to H^-, the bump near $\log T \approx 4.7$ is due to bound–free transitions of H^+, the bump near $\log T = 5.2 - 5.3$ is due to millions of Fe lines originating in the M shell of iron. The bump at $\log T \approx 6.3$ (and above) is also due to Fe, primarily to L shell bound–free transitions, with also minor contributions from Ni and CNO elements. One remarks that the major peak opacity in the outer solar layers is a factor of 10^5 larger than in a massive star, due to the difference of density. The opacity in the outer layers grows fast for stars between 2 and $1\,M_\odot$, producing a strong change of the luminosity as well as of the MS timescale (Sect. 25.2.2).

8.6.2 Opacity Tables

Detailed tables (OPAL) for the opacity and equation of state are currently developed by Forrest Rogers and Carlos Iglesias at Lawrence Livermore National Laboratory [493, 495]. Opacity calculations require the knowledge of the equation of state, the account for atomic physics, spectral line broadening and plasma collective effects. The atomic data are obtained from a parametric potential method. All the significant opacity effects are included as well as their interactions with degeneracy and collective electrostatic effects. Line broadening due to natural, Doppler and collisional effects are accounted for. Many physical effects acting specifically at $T < 10^4$ K or at high energies with $T > 10^9$ K are also included, as well as the effects of plasma coupling and degeneracy. Most recent progresses come mainly from improvements in the calculations of bound–bound absorption.

The OPAL library provides tables both for the equation of state and the opacity data. Various mixtures of 21 elements with temperatures $T > 6000$ K are considered.

The abundance of Ne accounts for all other heavier elements not specifically included. Various checks show that the errors resulting from this simplification are minor. The data for the equation of state are tabulated on a temperature–density grid and interpolation codes are available. As of 2007, the web address for the OPAL tables is http://www-phys.llnl.gov/Research/OPAL/.

In these tables, the opacities are given as a function $\log T$ for different values of $\log R$, where R is defined as $R = \varrho/T_6^3$, with $T_6 = T/10^6$. The interest of this representation is that within a star the ratio ϱ/T^3 is close to constant (cf. 3.101), so that the curves (see Fig. 8.5) using parameter R resemble those for stars of given masses in Fig. 8.4. Smaller interpolations have to be made when R values are used and this largely improves the accuracy of interpolated opacities.

Another major reference in opacity calculations is the "Opacity Project" (OP), which is an international collaboration to calculate the extensive atomic data required to estimate stellar envelope opacities and to compute Rosseland mean opacities [525]. Data from OP with codes for the calculation of mean opacities and radiative accelerations for any required chemical mixture, temperature and density are available on a 700-MB CD. The data from the OP and a suite of easy-to-use codes can be downloaded from: http://vizier.u-strasbg.fr/topbase/op.html.

Interesting comparisons between these two major opacity sources have been made by Rogers and Iglesias [493], see also [610]. The differences are small below $\log T = 5.6$, while above they can reach about 0.1 dex. Opacities for lower temperatures with account of molecular opacities and diffusion by dust grains are necessary for the study of cool stars, these have been calculated by Alexander & Ferguson [9].

Chapter 9
Nuclear Reactions and Neutrino Processes[*]

If the opacity determines the rate at which a star is radiating its energy, the nuclear reactions manage to compensate for the energy losses. Thus, the nuclear reactions do not fix the luminosity of a star, but they determine how long a star is able to live radiating such a luminosity. For the Sun, this lasts about 10 billions years. For ordinary stars where the law of perfect gas applies, the nuclear reactors are remarkably stable: the rate of nuclear reactions adjusts itself to maintain an exact energetic equilibrium. In degenerate media, however, this does not work and the nuclear reactors may oscillate, experience flashes or even explode.

Fusion nuclear reactions transform the original elements in nuclear ashes, which are new elements heavier than the initial ones. The stars realize in this way the synthesis of the chemical elements in the Universe. This is the process of stellar nucleosynthesis.

During the H- and He-burning phases, the energy goes out from the stars in the form of electromagnetic radiation. In later phases including supernova explosions, most of the energy goes out in the form of neutrinos and we also examine here these processes of energy losses.

9.1 Physics of the Nuclear Reactions

9.1.1 Reaction Energy

Let us consider a reaction of the form $a + X \rightarrow Y + b$. The reaction energy is given by the difference

$$Q = [M_a + M_X - (M_Y + M_b)]\, c^2 \tag{9.1}$$

i.e., the difference between the initial and the final masses, is expressed in MeV. The following equivalence applies between energy and atomic mass unit $m_u \longleftrightarrow$

---

[*]This chapter may form the matter of a basic introductory course.

931.494 MeV. The mass excess ΔM_{AZ} expressed in MeV is the difference between the mass of the nucleus and the sum of its components,

$$\Delta M_{AZ} = 931.494 \, (M_{AZ} - A) \quad \text{in MeV} , \tag{9.2}$$

$M_{A,Z}$ is the atomic mass of element (A,Z). ΔM_{AZ} is negative for a stable nucleus. With account of the conservation of the nucleon number, the energy Q becomes in MeV

$$Q = [\Delta M_a + \Delta M_X - (\Delta M_Y + \Delta M_b)] . \tag{9.3}$$

The average binding energy per nucleon $\Delta M_{AZ}/A$ is a fundamental property of nuclear physics with far reaching consequences in stellar evolution and element synthesis. Figure 9.1 illustrates the variation of the binding energy $|\Delta M_{AZ}/A|$ with the atomic mass number A. The curve first rapidly rises from hydrogen to more massive nuclei, because as A increases the short range nuclear forces pack the nucleons together in more bound systems. The most bound nucleus is ^{56}Fe. After this maximum, the binding energy slowly decreases for increasing A. This is due to the repulsive electrostatic force between protons, which is a long-range force which does not saturate as fast as the short-range strong nuclear forces.

The jump in the binding energy between low-mass elements, e.g., from ^{1}H to ^{4}He, makes their nuclear fusion to liberate a larger amount of energy per nucleon than the fusion of heavier elements, such as, for example, ^{12}C or ^{16}O. This contributes to the longer lifetimes of the first nuclear phases in stellar evolution, in particular of the H-burning phase. Exothermic fusion reactions are only possible up to ^{56}Fe. The heavier elements are not synthesized in this way, but by successive neutron captures (Sect. 28.5.3).
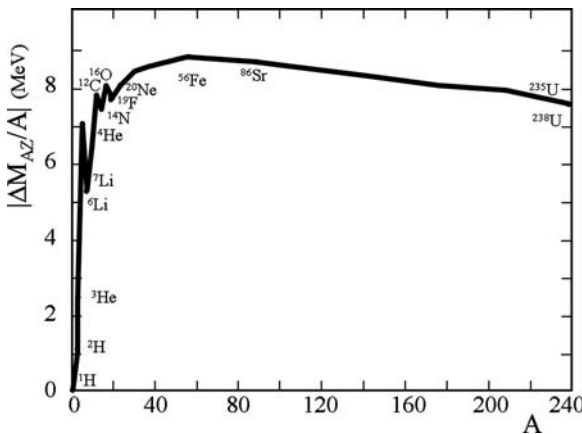
Fig. 9.1 Schematic illustration of the average binding energy $|\Delta M_{AZ}/A|$ per nucleon as a function of the atomic mass number A

9.2 Nuclear Reaction Rates

The nuclear reaction rates are mainly determined by the cross-sections σ of the particles, i.e., the effective surface of the particles for the considered interaction. The cross-section of a given reaction is the product of several terms (Sect. 9.3): the probability of geometrical encounter, the probability of barrier penetration, the probability that the compound nucleus decays into the considered channel, with an appropriate overall average on the velocity distribution of particles.

Let us first examine the global relations between the cross-sections and the nuclear reactions rates. We suppose that particles "X" are bombarded by particles "a" with a uniform flux as in lab experiments. The cross-section is defined by

$$\sigma \equiv \frac{\text{number of reactions of "X" due to "a" per second}}{\text{flux of incident particles "a"}}, \qquad (9.4)$$

with σ in cm^2. If the nuclei "X" have a uniform concentration n_X, the number of reactions by units of volume and time is the product of σn_X by the flux of incident particles. This flux is the number of particles "a" by cm^2 and by second passing near particle "X", i.e., $n_a v$ if the concentration of particles "a" is uniform and if v the relative velocity is the same for all particles. The reaction rate by volume unit is $r_{aX} = \sigma(v) v n_a n_X$, expressed in number of reactions per cm^3 and second. In general, one writes

$$r_{aX} = n_a n_X \int_0^\infty v \, \sigma(v) \phi(v) dv = n_a n_X < \sigma v >_{aX}, \qquad (9.5)$$

where $\phi(v)$ is the velocity distribution, normalized such that $\int_0^\infty \phi(v) dv = 1$ (Appendix C.6.2). This expression only applies if particles "a" and "X" are of a different kind. In this case, $n_a n_X$ is the number of interacting pairs of particles. If the particles are of the same sort, e.g., if particles "a" interact with other particles "a", the number of interacting pairs is $(1/2) n_a (n_a - 1) \cong (1/2) n_a^2$, since the interaction of two particles must be counted only once. Thus, a more general writing of (9.5) is

$$r_{aX} = \frac{n_a n_X \lambda_{aX}}{(1 + \delta_{aX})}, \quad \text{with} \quad \lambda_{aX} = < \sigma v >_{aX}, \qquad (9.6)$$

where δ_{aX} is Kronecker's symbol ($\delta_{aX} = 1$, if a=X; $\delta_{aX} = 0$, if a$\neq$X). λ_{aX} is the reaction rate by pair of particles. In thermodynamic equilibrium, the relative velocities v of particles of masses m_1 and m_2 with a reduced $m_{red} = m_1 m_2 / (m_1 + m_2)$ also follows the Maxwell–Boltzmann distribution (C.62)

$$\lambda_{aX} = 4\pi \left(\frac{m_{red}}{2\pi kT} \right)^{3/2} \int_0^\infty v^3 \sigma(v) \exp\left(-\frac{m_{red} v^2}{2kT} \right) dv . \qquad (9.7)$$

9.2.1   Particle Lifetimes and Energy Production Rates

The variation of the number of particles "X" in a volume unity due to interactions with particles "a" is $(-\partial n_X/\partial t)_a$. One defines the lifetime $\tau_a(X)$ of particles "X" bombarded by "a" as

$$\left(-\frac{\partial n_X}{\partial t}\right)_a \equiv \frac{n_X}{\tau_a(X)} , \qquad (9.8)$$

which means that in a time $\tau_a(X)$, the number of particles "X" is reduced by a factor e. According to (9.6), one also has $(-\partial n_X/\partial t)_a = (1+\delta_{aX})\, r_{aX}$ (if "a" = "X" each time there is a reaction, two particles disappear). The particle lifetime is

$$\tau_{aX} = \frac{n_X}{(1+\delta_{aX})\, r_{aX}} = \frac{1}{n_a\, \lambda_{aX}} = \frac{A_a\, m_u}{\rho\, X_a\, \lambda_{aX}} , \qquad (9.9)$$

where the partial concentration n_a is expressed in terms of the mass fraction X_a of the particle of atomic mass A_a, $n_a = \rho\, X_a/(A_a\, m_u)$. If an element "X" is destroyed by several reactions "i", the lifetime of element "X" is given by

$$\frac{1}{\tau(X)} = \sum_i \frac{1}{\tau_i(X)} , \qquad (9.10)$$

because the reactions rates add to each other. The energy production rate ε is the power produced by unit of mass (3.40),

$$\varepsilon = \frac{Q(\mathrm{erg})\, r_{aX}}{\varrho} = \frac{Q(\mathrm{erg})\, n_a n_X\, \lambda_{aX}}{\rho\,(1+\delta_{aX})} = \frac{Q\rho\, X_a X_X\, \lambda_{aX}}{A_a A_X\, m_u^2\,(1+\delta_{aX})} , \qquad (9.11)$$

where $Q(\mathrm{erg})$ is the energy in ergs liberated by one reaction (1 erg=1.6022 10^{-6} Mev, cf. Appendix A.1). X_a and X_X are the mass fractions of the elements of atomic mass A_a and A_X.

Analytical formulas were provided by Caughlan and Fowler [100]. In practice nowadays, one uses the tabulated values of $N_{AV}\,\lambda_{aX}$ ($= \lambda_{aX}/m_u$), where N_{AV} is the Avogadro number. The advantage of multiplying by N_{AV} is that the tabulated values are not too small numbers. The values $N_{AV}\,\lambda_{aX}$ are given in the NACRE Library, available at: http://pntpm.ulb.ac.be/nacre.htm. The reaction rates must be corrected by the effects of screening (cf. Sect. 9.4). There are other web sites providing nuclear reaction rates and cross sections such as http://www-phys.llnl.gov/Research/RRSN.

9.3   Nuclear Cross-Sections

Let us examine more closely the effects determining the nuclear cross-sections. For energies below 50 MeV, a typical reaction, which can occur through several channels, can be decomposed in three steps:

$$\underbrace{a + X}_{\text{channel a}} \longrightarrow C^* \longrightarrow \underbrace{Y + b}_{\text{channel b}} \; . \tag{9.12}$$
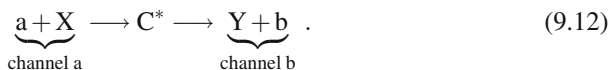
1. The interaction of "a" and "X": the wave associated to the incident particle interacts with the diffusion center of the target nucleus "X".
2. The penetration of the barrier of electrostatic potential $V(r)$ of the target nucleus, which leads to an unstable compound nucleus C^*. The potential barrier is

$$V(r) = \frac{Z_a Z_X e^2}{r} = \frac{1.44 \, Z_a Z_X}{r \, [\text{fermi}]} \quad \text{in MeV}, \tag{9.13}$$

for a front shock, with r the distance to the nucleus center. The distance r is expressed in fermi (10^{-13} cm). The nuclear potential is illustrated in Fig. 9.2. At short distance the potential well is attractive. Outside, the repulsive Coulomb force is acting. The typical nuclear radius, i.e., the distance from the center to the edge of the well is $r_{\text{nucl}} \approx 1.44 \times 10^{-13} A^{1/3}$ cm. At $T = 10^7$ K, the energy $kT = 0.86$ keV is much lower than the potential barrier given by (9.13). The penetration and nuclear interaction are only possible thanks to a quantum effect, the "tunnel–effect" which gives a certain transparency to the potential barrier as first shown by Atkinson & Houtermans [21].
3. The unstable compound nucleus disintegrates. The lifetime of this nucleus, although short, is long with respect to the crossing time of the nucleus at the speed of light ($\sim 10^{-21}$ s). The hypothesis, first expressed by Bohr, is that these three steps are independent and thus the disintegration of C^* does not depend on how it has been formed.
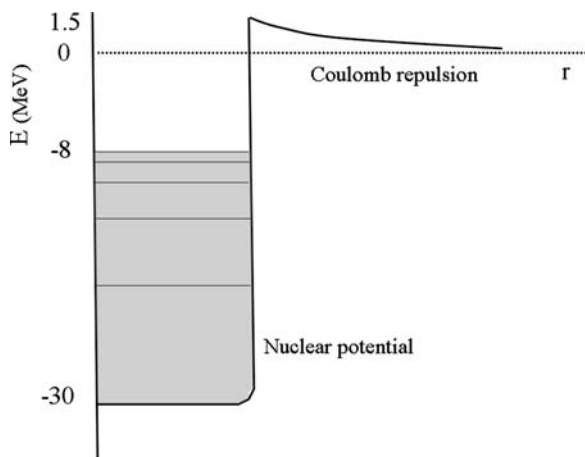
Fig. 9.2 Schematic representation of the nuclear potential well and of the Coulomb barrier in $1/r$. The *shaded area* represents the region occupied by the energy levels of the nucleus. The nucleus is bound with an energy of about -8 MeV. The height of the barrier potential is given by (9.13)

In high-energy reactions ($E \geq 100$ MeV) such as spallation reactions, the incoming particle interacts only with a few nucleons in the nucleus. These nucleons are ejected before the energy of the incident particle is distributed among the nucleons. In this case, the above scheme of three independent steps does not apply.

The width Γ of a nuclear energy level is related to its mean lifetime τ by

$$\Gamma = \hbar/\tau \,. \tag{9.14}$$

Γ is the sum of the partial widths associated with the various modes of formation and disintegration of the considered nucleus, $\Gamma = \Sigma_i \Gamma_i$. The ratio $\Gamma_i/\hbar$ is the probability by unit of time that the considered excited state of the nucleus C^* disintegrates through channel "i". One must distinguish the cross sections near and far from a resonance.

Close to a resonance: the cross sections have the following form given by the Breit–Wigner formula,

$$\sigma(a,b) = (2\ell+1)\,\pi\,\lambda'^2 \frac{\Gamma_a\,\Gamma_b}{(E - E_r)^2 + \left(\frac{\Gamma}{2}\right)^2} \,. \tag{9.15}$$

At low energies, Γ contains only a few terms and does not differ too much from the relevant Γ_i of the two channels a and b. $\lambda' = \lambda/(2\pi)$, ℓ is defined as follows. The momentum of incident particles is,

$$p = \frac{\hbar}{\lambda'} = k\hbar, \quad k: \text{integer} \quad \text{and} \quad \lambda' = \hbar\,(2\,m_{\text{red}}\,E)^{-1/2}, \tag{9.16}$$

where m_{red} is the reduced mass and E the relative energy of the particles. The angular momentum of the shock is

$$|\boldsymbol{J}| = |\boldsymbol{r} \times m\boldsymbol{v}| = b\,p = \frac{b\hbar}{\lambda'} \,, \tag{9.17}$$

where b is the impact parameter. The modulus J is quantified and one has $J = \ell\hbar$ so that $b = \ell\lambda'$ (see also [610]).

Far from a resonance: the cross section at weak energies can be written as

$$\sigma(a,b) = \frac{S(E)}{E}\,e^{-b/E^{1/2}} \quad \text{with} \quad b = 31.28\,Z_a\,Z_X\,A^{1/2} \text{ in } [(\text{keV})^{1/2}]. \tag{9.18}$$

A is here the reduced mass number $A = A_a\,A_X/(A_a + A_X) = m_{\text{red}}/m_u$, E is the relative energy of the particles $E = (1/2)\,m_{\text{red}}\,v^2$ with v the relative velocity. $S(E)$ is the "astrophysical cross-section factor" which expresses the probability of geometrical encounter with account of the various nuclear properties. Its theoretical value is often uncertain and one generally relies on experimental determinations (cf. Figs. 9.4 and 9.6). For a given reaction, the cross-section $\sigma(a,b)$ is measured in the lab at the lowest possible energies, typically ~ 100 keV. Then, $S(E)$ is calculated from
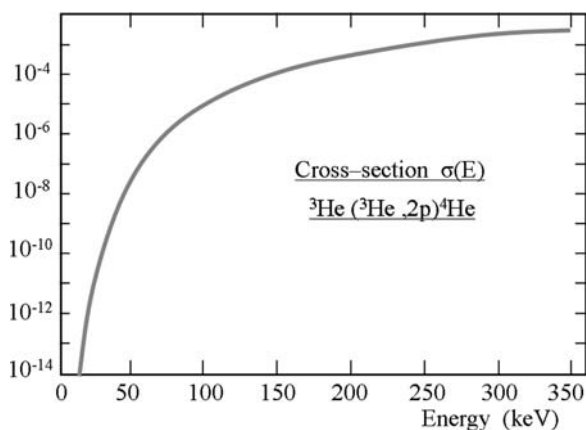
Fig. 9.3 Example of cross-section $\sigma(E)$ in barn (10^{-24} cm^2) as a function of the energy E for the reaction ^{3}He(^{3}He, 2p)^{4}He, the last step of the chain ppI for H burning. This reaction is the main energy source of the Sun. Adapted from Trautvetter [579]
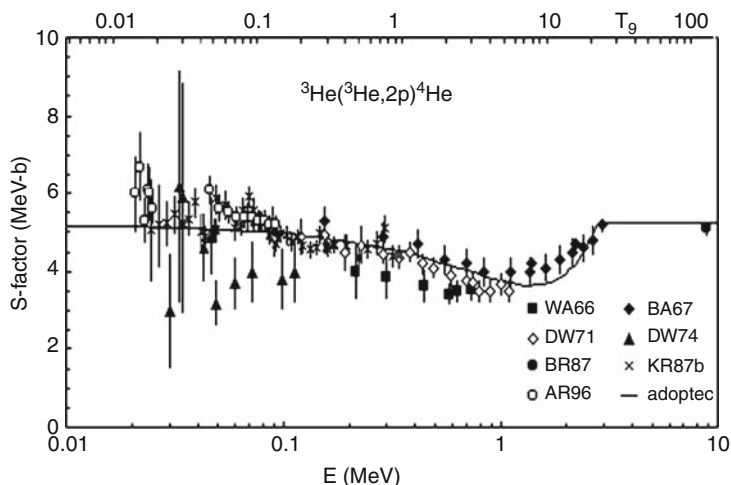
Fig. 9.4 Various empirical determinations of the factor S(E) as a function of energy for the reaction ^{3}He(^{3}He, 2p)^{4}He. The raise at low energies is due to the screening factor. From the Nacre Library, European Compilation of Reaction Rates for Astrophysics, with permission

(9.18). The extrapolation of the cross-section to low energies of 5–50 keV, typical of stellar conditions, is made with the S factor which varies much less than $\sigma(E)$. The possibility of unknown resonances may be a source of uncertainty.

Figures 9.3 and 9.4 show experimental results for the cross-section and $S(E)$ factor of the reaction ^{3}He(^{3}He, 2p)^{4}He as a function of energy. This important reaction is among the rare ones for which experimental determinations of the $S(E)$ factor are possible down to energies as low as that of the Gamov peak (Fig. 9.5) in the Sun ($E_0 = 22$ keV). The cross-section decreases by several orders of magnitude
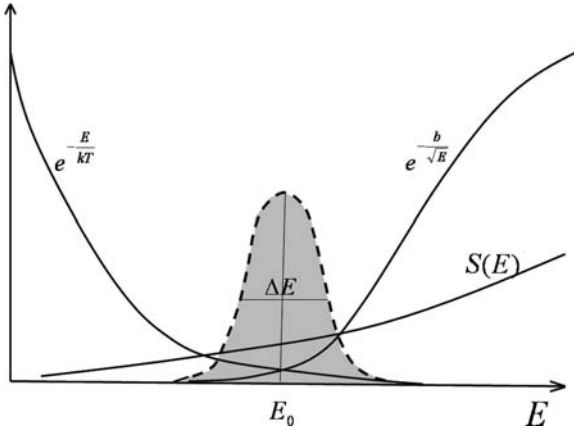
Fig. 9.5 Schematic representation of the various contributions to the reaction rate: on the *left*, the Maxwell distribution of the relative kinetic energies; on the *right*, the penetration factor of the potential barrier magnified by about 3 orders of magnitude. The Gamov peak is shown by the *gray* area, it is magnified by about 5 orders of magnitude. The astrophysical factor $S(E)$ varies slowly

below 100 keV (Fig. 9.3). This fast decrease is mainly due to the behavior of the penetration of the potential barrier with energy. The factor $S(E)$ for this reaction shows a rather weak dependence on energy. The recent determinations of $S(E)$ provide an empirical evidence for the screening effect (see Sect. 9.4), which makes a slight increase of $S(E)$ at low energies visible in Fig. 9.4.

9.3.1 The Rate of Non-resonant Reactions

Although nuclear rates are tabulated, it is useful to know what are the main effects shaping the global rates. Nuclear reactions occur in stars because the most energetic particles can go through the repulsive Coulomb barrier between positively charged nuclei. The energy of this barrier is expressed by (9.13), it is of the order of 1 Mev for hydrogen. For $T \sim 10^7$ K (for H burning) to a few 10^8 K (for heavier nuclei), the average relative kinetic energy of the particles is almost 3 orders of magnitude lower than the energy of the Coulomb barrier. This would prevent any nuclear fusion, but the tunnel effect permits the particles with the highest velocities to react.

The cross-section by pair of particles expressed by (9.7) is written as an average over the distribution of energies for a given reaction,

$$\lambda = <\sigma v> = \int_0^\infty \sigma(E)\, v(E)\, \psi(E) dE \;, \tag{9.19}$$

where the Maxwell–Boltzmann distribution $\psi(E)$ of energies is given by (C.61) with $\psi(E)dE = \phi(v)dv$. With $v = (2E/m_{\text{red}})^{1/2}$, (9.7) and (9.18) one has

$$< \sigma v > = \left(\frac{8}{m_{\text{red}}\pi}\right)^{1/2} \frac{1}{(kT)^{3/2}} \int_0^\infty S(E) \exp\left(-\frac{E}{kT} - \frac{b}{\sqrt{E}}\right) dE . \tag{9.20}$$

The result is largely dominated by the exponential term in (9.20). Figure 9.5 schematically shows the behavior of the various intervening terms.

- The Maxwell distribution of energies, which decreases fast with increasing energy, i.e., like $e^{-E/(kT)}$.
- The penetration factor due the tunnel effect, which grows up fast with growing energy, i.e., like $e^{-b/\sqrt{E}}$.
- The $S(E)$ factor which varies slowly in general.

The main contribution to the integral (9.20) comes from an energy range such that the exponential factor is maximum, i.e., where the product of the Maxwell energy distribution times the penetration factor is the largest. Most of the stellar nuclear reactions occur in the limited energy interval at the tail of Maxwell's distribution. The factor $S(E)$ can be considered as constant in this small energy interval, provided there is no resonance. Thus, a good approximation of $\lambda = < \sigma v >$ is obtained by replacing $S(E)$ by its value at energy E_0, called the Gamov energy, where the exponential is maximum,

$$< \sigma v > = \left(\frac{8}{m_{\text{red}}\pi}\right)^{1/2} \frac{S(E_0)}{(kT)^{3/2}} \int_0^\infty \exp\left(-\frac{E}{kT} - \frac{b}{\sqrt{E}}\right) dE . \tag{9.21}$$

Let us call

$$f(E) = \exp\left(-\frac{E}{kT} - \frac{b}{E^{1/2}}\right). \tag{9.22}$$

The energy of the Gamov peak is given by $d f(E)/dE = 0$, which leads to

$$E_0 = \left(\frac{bkT}{2}\right)^{\frac{2}{3}} = 1.220 \times (Z_a^2 Z_X^2 A T_6^2)^{1/3} \quad \text{keV} , \tag{9.23}$$

where A is the reduced mass number and $T_n = T/(10^n \text{ K})$. For $T_7 \sim 1$ in the case of light nuclei $E_0 = 10$–30 keV, while the average $kT \sim 1$–3 keV. The width of the energy domain contributing to the integral in (9.21) is only about 10 keV. This energy interval is very small with respect to the typical separation of stable nuclear energy levels. This is why the factor $S(E)$ can be considered as having little variation with energy in this interval.

The experimental measurements of cross-sections in the lab are aimed at obtaining information on $S(E)$ in the energy interval around the Gamov peak (cf. Fig. 9.6).

It is often not possible to obtain direct measurements of this factor at low energies, because the reaction rates are very low. The data obtained at higher energies
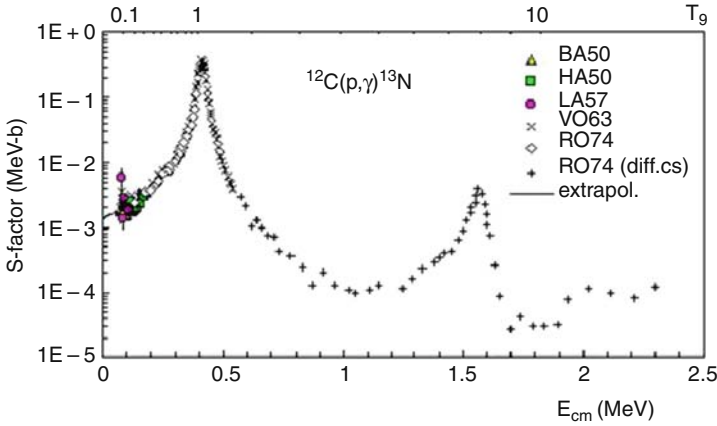
Fig. 9.6 Various empirical determinations of the factor S(E) as a function of energy for the reaction $^{12}C(p,\gamma)^{13}N$, which is one step of the CN cycle. There are broad resonances. From the Nacre Library, European Compilation of Reaction Rates for Astrophysics, with permission

have to be extrapolated. This is sometimes an uncertain operation where both experimental data and theoretical considerations intervene.

9.3.1.1 Approximate Reaction Rate

The resonant and non-resonant reactions rates follow some approximate relations, which we now examine. The maximum value of the term to be integrated in (9.21) is

$$f(E_0) = e^{-3E_0/(kT)} \equiv e^{-\tau}, \tag{9.24}$$

which is easily verified by using the above expression of E_0. This also defines the parameter τ,

$$\tau = -\frac{3E_0}{kT} = -\left(\frac{bkT}{2}\right)^{\frac{2}{3}} \frac{3}{kT} = 42.48 \left(\frac{Z_a^2 Z_X^2 A}{T_6}\right)^{\frac{1}{3}}. \tag{9.25}$$

To calculate the integral (9.21), one now proceeds numerically and the results are given as numerical tables. However, an analytical expression can be obtained by replacing the exponential term in (9.21) by a Gaussian curve centered in E_0, with a height $f(E_0)$ and a half-width ΔE, i.e., $f(E) \cong e^{-\tau} \exp(-(E-E_0)/\Delta E)^2$. At energy $E_0 + \Delta E$, the value of $f(E)$ is reduced by a factor e. Let us develop $f(E)$ around E_0 to the second order,

$$f(E) \cong f(E_0) + \underbrace{f'(E_0)(E-E_0)}_{=0} + \frac{f''(E_0)}{2}(E-E_0)^2. \tag{9.26}$$

If $f(E_0 + \Delta E)$ becomes negligible at energy $E_0 + \Delta E$, one gets

$$\Delta E \cong \left(\frac{-2f}{f''} \right)_{E_0}^{1/2} = \left(\frac{4}{3} E_0 kT \right)^{1/2} . \tag{9.27}$$

Thus, one can write the integral in (9.21)

$$\int_0^\infty f(E)\, dE \cong e^{-\tau} \int_0^\infty \exp\left(-\frac{E - E_0}{\Delta E} \right)^2 dE = \frac{1}{2} e^{-\tau} \sqrt{\pi}\, \Delta E . \tag{9.28}$$

The product $< \sigma v >$ becomes

$$< \sigma v > \cong \left(\frac{8}{\pi m_{\text{red}}} \right)^{1/2} \left(\frac{1}{kT} \right)^{3/2} S(E_0) \frac{\sqrt{\pi}}{2} e^{-\tau} \left(\frac{4}{3} E_0 kT \right)^{1/2} . \tag{9.29}$$

By expressing the energy E_0, one gets a dependence of the form $< \sigma v > \sim$ $S(E_0) e^{-\tau} \tau^2 / (A Z_a Z_X)$. If one writes $S(E_0)$ in barn×keV, with 1 barn $= 10^{-24}$ cm^2, one obtains numerically

$$< \sigma v > \cong \frac{7.21 \times 10^{-19}}{A Z_a Z_X} S(E_0)\, \tau^2 e^{-\tau} . \tag{9.30}$$

This makes a dependence with respect to T of the form

$$< \sigma v > \sim \frac{1}{T^{2/3}} e^{-\text{const}/(T^{1/3})} . \tag{9.31}$$

The reaction rate expressed in number of reactions in cm^{-3} s^{-1} is finally

$$r_{\text{aX}} = n_a n_X \frac{\lambda_{\text{aX}}}{(1 + \delta_{\text{aX}})} \cong \frac{2.62 \times 10^{29}\, \varrho^2 X_a X_X}{(1 + \delta_{\text{aX}})\, A Z_a Z_X A_a A_X} S(E_0)\, \tau^2 e^{-\tau} , \tag{9.32}$$

and the energy production rate is in erg g^{-1} s^{-1},

$$\varepsilon = \frac{r_{\text{aX}}\, Q(\text{erg})}{\varrho} \cong \text{fact.}\, \frac{Q \varrho X_a X_X}{(1 + \delta_{\text{aX}})\, T_6^{2/3}} \exp\left(\frac{-42.48\, (Z_a^2 Z_X^2 A)^{1/3}}{T_6^{1/3}} \right) . \tag{9.33}$$

The numerical factor comes from (9.32), from the Z_i, A_i of the elements and from $S(E)$. In practice, one adds to the above main term some correcting terms which account for the fact that $S(E)$ is not constant and that the Gamov peak has been approximated.

Often, for simple analytical estimates in a limited domain of T, one may use an expression of the form,

$$\varepsilon \approx \varepsilon_0 \varrho T^\nu \qquad \text{with} \qquad \nu \equiv \varepsilon_T \equiv \left(\frac{\partial \ln \varepsilon}{\partial \ln T} \right)_\varrho . \tag{9.34}$$

One may easily show from (9.30) that the exponent v, also called ε_T, can be expressed in terms of τ (9.25) by $v = (\tau - 2)/3$. Figure 25.3 illustrates the values of v in stars of different masses.

9.3.2   The Rate of Resonant Nuclear Reactions

Let us calculate the reaction rates when the main contribution to $<\sigma v>$ comes from a resonance in an energy interval around a value E_r where $\sigma(E_r)$ is large compared to neighbor values. If so, even the factor $S(E)$ varies a lot near the resonance. This situation happens mainly when the energy of the compound nucleus is close to the reaction energy E_r. The reaction rate is

$$r_{aX} = \frac{n_a n_X}{(1 + \delta_{aX})} \int_0^\infty v(E)\,\sigma(E)\,\frac{dn(E)}{n} \cong$$

$$\frac{n_a n_X}{(1 + \delta_{aX})}\, v(E_r)\, \frac{2}{\sqrt{\pi}}\, \frac{1}{(kT)^{3/2}}\, e^{-E_r/kT}\, E_r^{1/2} \int_0^\infty \sigma(E)\,dE \ . \qquad (9.35)$$

At the stellar energies, the possible resonances are narrow, thus $v(E)$ and $dn(E)/n$ have little variation over the energy interval of the resonance. Thus, their values can be estimated at the resonance energy E_r.

Let us examine the above integral. The maximum value, say h, of $\sigma(E)$ as illustrated in Fig. 9.7 is with the Breit–Wigner formula (9.15) for a frontal shock with a parameter of angular momentum $\ell = 0$:

$$h = \pi \lambda'^2 \frac{\Gamma_a \Gamma_b}{\Gamma^2/4} \quad \text{with} \quad \lambda' = \frac{\lambda}{2\pi} \ . \qquad (9.36)$$

We may consider the integral as the surface of the half of an ellipse. As illustrated by Fig. 9.7, the half-width of $\sigma(E)$ is $\Gamma/2$, thus the surface is surface $= \pi \Gamma h/2$ and the integral in (9.35) can be written

$$\int_0^\infty \sigma(E)\,dE = 2\pi^2 \lambda'^2 \frac{\Gamma_a \Gamma_b}{\Gamma} \ , \qquad (9.37)$$

where the indices "a" and "b" refer to the considered channels as in (9.12). The reaction rate (9.35) becomes, with m_{red} the reduced mass,

$$r_{aX} = \frac{n_a n_X}{(1 + \delta_{aX})} \left(\frac{2 E_r}{m_{red}}\right)^{1/2} \frac{2}{\sqrt{\pi}} \frac{E_r^{1/2}}{(kT)^{3/2}}\, e^{-E_r/kT}\; 2\pi^2 \lambda'^2 \frac{\Gamma_a \Gamma_b}{\Gamma} \ ,$$

$$= \frac{\varrho^2 X_a X_X \hbar^2}{A_a A_X m_u^2 (1 + \delta_{aX})} \left(\frac{2\pi}{A m_u kT}\right)^{3/2} \frac{\Gamma_a \Gamma_b}{\Gamma} \exp\left(\frac{-E_r}{kT}\right) \ . \qquad (9.38)$$
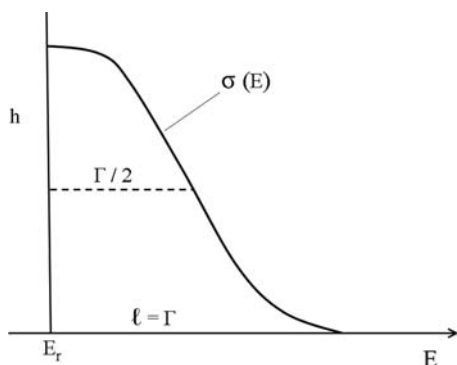
Fig. 9.7 Simplified representation of the resonance

If one expresses E_r and Γ, with the numerical factors one gets

$$r_{aX} = \frac{2.94 \times 10^{36}}{(1+\delta_{aX})}\,\varrho^2\,\frac{X_a X_X}{A_a A_X}\,\frac{1}{(A\,T_6)^{3/2}}\,\frac{\Gamma_a \Gamma_b}{\Gamma}\,\exp\left(-11.61\frac{E_r}{T_6}\right), \qquad (9.39)$$

with $T_6 \equiv T/(10^6\ \text{K})$. One sees that the functional form of the reaction rate and in particular its dependence with respect to T is very different from the case (9.32) where there is no resonance. As emphasized above (Sect. 9.2.1), the reaction rates are given in the form of electronic data tables.

9.4 Electron Screening

In a dense medium, each nucleus is surrounded by a cloud of free electrons, their global positive charge reduces the Coulomb repulsion between nuclei. This screening effect makes the penetration of the potential barrier easier. From Sect. 7.6.1, the potential near a nucleus of atomic mass number A_i is

$$\phi = \frac{Ze}{r}\,e^{-r/r_D} \quad \text{with} \quad r_D = \sqrt{\frac{kT}{4\pi e^2 n \chi}}, \qquad (9.40)$$

where $n = \varrho/(\mu\,m_u)$ is the mean concentration of the nuclei, χ is an effective charge $\chi = \mu\,\Sigma_i\,(X_i/A_i)\,Z_i\,(Z_i+1) \equiv \mu\,\zeta$. Quantity r_D is the Debye–Hückel radius. Thus, the potential energy of two nuclei "1" and "2" becomes

$$V(r) = \frac{Z_1 Z_2}{r}\,e^2\,e^{-r/r_D}, \qquad (9.41)$$

with e^2 expressed in CGS units (Gauss system), $e^2 = 23.0708 \times 10^{-20}\ \text{cm\,erg}$. As an example, for $T_6 = 10$, $\varrho = 10^2\ \text{g\,cm}^{-3}$, $\zeta = 1$ and $Z_1 \times Z_6 = 6$, one has $r_D/r_0 \simeq 10^2$,

where r_0 is the radius of the nucleus. For MS stars above $\sim 0.3\,M_\odot$, one has $r_D \gg r_0$. To the first order, the potential energy is

$$V(r) = \frac{Z_1 Z_2 e^2}{r} - \frac{Z_1 Z_2 e^2}{r_D} . \qquad (9.42)$$

The important term in (9.18), determined by the tunnel effect, is the energy difference $V(r) - E$ between the potential energy of the nuclei and the relative energy of the particles. This difference is

$$V(r) - E = \frac{Z_1 Z_2 e^2}{r} - \left(E + \frac{Z_1 Z_2 e^2}{r_D} \right) . \qquad (9.43)$$

It is like if the kinetic energy of the incident particle is increased by a quantity $V_0 = Z_1 Z_2 e^2 / r_D$. Thus, the true cross-section (with screening) is equal to that without screening for an energy higher by an amount V_0,

$$\sigma_{\text{screen}}(E) \simeq \sigma_{\text{no screen}}(E + V_0) . \qquad (9.44)$$

Let us calculate the product $< \sigma v >$,

$$< \sigma v >_{\text{screen}} = \int_0^\infty \psi(E) \, \sigma_{\text{screen}}(E) \, v(E) \, dE , \qquad (9.45)$$

where $\psi(E)$ is the Maxwell distribution of energies (C.61). Let us set $E' = E + V_0$, thus one has

$$< \sigma v >_{\text{screen}} = \int_{V_0}^\infty \psi(E' - V_0) \, v(E' - V_0) \, dE' \qquad (9.46)$$

$$\text{with }\ \psi(E' - V_0) \times v(E' - V_0) = \text{const}(E' - V_0) \, e^{-E'/kT} \, e^{V_0/kT}$$

$$\simeq \text{const}\, E' \, e^{-E'/kT} \, e^{V_0/kT} , \qquad (9.47)$$

because V_0 is weak with respect to E_0, the effective energy of the reaction. Thus, one can write

$$< \sigma v >_{\text{screen}} = < \sigma v >_{\text{no screen}} \ f, \quad \text{with} \quad f = e^{V_0/kT} , \qquad (9.48)$$

where f is the screening factor, numerically one has

$$\frac{V_0}{kT} = 0.188 \, Z_1 Z_2 \, \frac{(\zeta \varrho)^{1/2}}{T_6^{3/2}} , \qquad (9.49)$$

with $T_6 \equiv T/(10^6\,\text{K})$. This theory applies when $V_0/(kT) = Z_1 Z_2 e^2 / (r_D kT) \ll 1$, i.e., when V_0 is weak with respect to the effective energy. This is the "weak screening", the factor f although larger than 1.0 is still of the order of unity. This case applies to stellar densities $\varrho < 10^4$ g cm^{-3}.

For large densities $\varrho > 10^6$ g cm^{-3}, one generally has the case of "strong screening", which requires different approximations. The screening effect may become large and the reaction rate, which then depends essentially on the density, is increased by a large factor. In the extreme case of strong screening, one has the so-called "pycno–nuclear" reactions, where the potential barrier is almost washed out by the screening effect. However, if the medium is very dense and cold, it may crystallize. In this case, the reactions are inhibited by the fact that the nuclei are sticked to an electrostatic network and are prevented to experience collisions.

9.5   Neutrino Emission Processes

The cross-section of electron neutrinos of energies E_ν is given by

$$\sigma_\nu \approx 10^{-44} \left(\frac{E_\nu}{m_e c^2} \right)^2 \text{cm}^2 , \tag{9.50}$$

where m_e is the electron mass. For a nuclei concentration n, the corresponding mean free path is $\ell = 1/(n\sigma_\nu)$. For 1 MeV neutrinos, the mean free path in ordinary lead would be about 20 light-years! Over 10^9 neutrinos emitted in the solar center, barely one does not reach the surface. This means that the neutrinos emitted in a star by the various nuclear reactions, for example H burning (Table 25.1), escape directly. This is why their energies are not counted in the energy Q(MeV) of the nuclear reactions, but are indicated in parenthesis in the tables. Only during supernova explosions at densities of $\sim 10^{10}$ g cm^{-3}, significant energy and momentum can be transferred to the matter by neutrinos. This is an essential process for supernova explosions (Sect. 28.4.2).

The theory of weak interactions predict that for each electronic process emitting a photon, there is a probability $P(\nu_e \bar{\nu}_e)$ of emitting a pair of electron neutrino and antineutrino. The ratio of the probability to emit a neutrino pair to that of emitting a photon γ is

$$\frac{P(\nu_e \bar{\nu}_e)}{P\gamma} = \frac{\mathcal{G}}{\alpha^4} \left(\frac{E_\nu}{m_e c^2} \right)^4 \approx 3 \times 10^{-18} \left(\frac{E_\nu}{m_e c^2} \right)^4 , \tag{9.51}$$

where $\alpha = 1/137$ is the fine-structure constant and $\mathcal{G} \approx 10^{-5} (m_e/m_u)^2 = 3 \times 10^{-12}$ is the constant characterizing the ratio of weak to electromagnetic interactions. The above expression means that neutrinos emissions may occur in absence of nuclear reactions. Neutrinos emissions are equivalent to a loss of energy from the stellar interiors and one often speaks about *neutrino cooling*. This cooling occurs only at high enough T or ϱ. In practice, it is significant only after the end of He-burning for $T > 2 \times 10^8$ K and $\varrho > 10^3$ g cm^{-3} (present day models nevertheless include it in the He-burning phase).

Various processes of neutrino cooling, in addition to the ν emissions by nuclear reactions, occur in stellar interiors. The detailed calculations of the ν emissions processes are complex and based on the Weinberg–Salam theory of weak interactions with the assumption that there are only three types of neutrinos. Detailed analytical fitting formulas and numerical tables for the neutrino emission rates are given by Itoh et al. [269]. Here, we just give a few indications about the main effects of each process of neutrino emission.

9.5.1 Photo-neutrinos

The usual electron scattering or Thomson diffusion has a branching ratio given by (9.51) toward an emission of $\nu_e \bar{\nu}_e$

$$\gamma + e^- \longrightarrow \quad e^- + \gamma$$

$$\searrow \quad e^- + \nu_e \bar{\nu}_e \; .$$
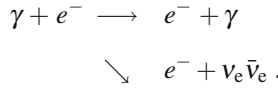
At thermodynamic equilibrium, the number of Thomson diffusions per cm^{-3} s^{-1} is $r_{e-\gamma} = n_e n_\gamma < \sigma_{es} v >$ (9.6), where n_e and n_γ are the concentrations of electrons and photons, σ_{es} is given by (8.11), the relative velocity v is equal to c. From Appendix C.1, at a given frequency ν one has $n_\gamma = (4\pi/c)(B_\nu(T)/h\nu)$. Integrating over the frequencies ν, the number of neutrinos per cm^{-3} s^{-1} is

$$r_{\nu_e \bar{\nu}_e} \approx \frac{4\pi}{c} \int_0^\infty \frac{B_\nu(T)}{h\nu} n_e \, \sigma_{es} \, c \, \frac{P(\nu_e \bar{\nu}_e)}{P\gamma} \, d\nu \; . \tag{9.52}$$

The term in $P(\nu_e \bar{\nu}_e)/P\gamma$ scales roughly like T^4, the term $(B_\nu(T)/h\nu)$ like T^3 and n_e like T. On the whole, this makes a strong dependence in temperature of the order of T^8. A rough approximation for the energy loss rate is

$$\varepsilon_{\text{photo}-\nu} \approx -5 \times 10^7 \, T_9^8 \quad \text{in erg g}^{-1}\text{s}^{-1} \; . \tag{9.53}$$

The rapid growth with T appears clearly in Fig. 9.8. The emission rate is generally independent of density, because $n_e \sim \varrho$ and $\varepsilon = Q(\text{erg})\, r/\varrho$ (9.11), except at very high ϱ where electron degeneracy reduces the number of free cells in the phase space, where the electrons can settle after the diffusion process (Fig. 9.8).

9.5.2 Pair Annihilation Neutrinos

Due to the Planck distribution of photons, exchange reactions between photons and pairs e^+e^- occur already below the threshold T of electron formation at 5.93×10^9 K corresponding to 0.51 MeV
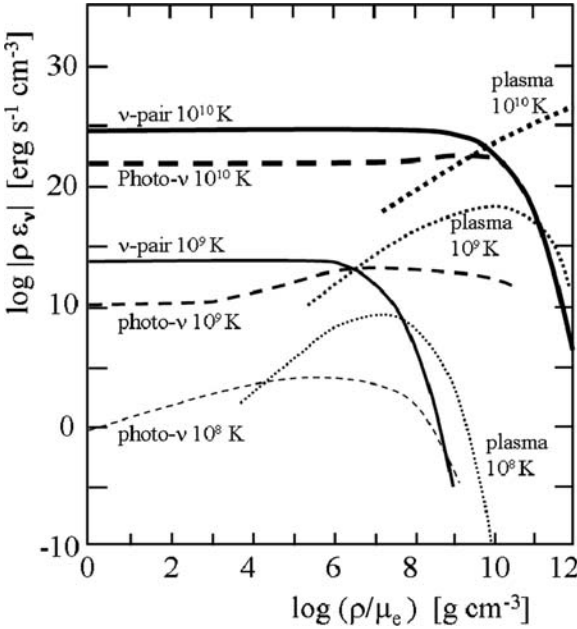
Fig. 9.8 Neutrino emission rates from pair annihilation, photo-neutrinos and plasma oscillations as functions of density for different temperatures. Each process is represented by lines of different types, thicker for higher T. For $T = 10^8$ K there is no pair annihilation process. Adapted from N. Itoh et al. [269]

$$\gamma + \gamma \rightleftharpoons e^- + e^+$$

$$\searrow \quad \nu_e \, \bar\nu_e \, .$$
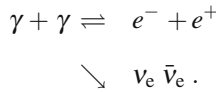
The branching ratio toward neutrino emission is given by (9.51). The energy loss rate is expressed as (9.11),

$$\varepsilon_{\nu-\text{pair}} \approx \frac{Q \, n_{e^+} n_{e^-} <\sigma v>_{e^+ e^-}}{\varrho} \frac{P(\nu_e \bar\nu_e)}{P\gamma} , \tag{9.54}$$

in erg g^{-1} s^{-1}. Here, the reaction energy is $Q = 2m_e c^2$, the cross-section $\pi r_0^2 = (3/8)\sigma_{es} = \pi(e^2/m_e c^2)^2$ (8.11), where r_0 is the classical radius of the electron. Thus, we have

$$\varepsilon_{\nu-\text{pair}} \approx \int_0^\infty \frac{n_{e^+} n_{e^-}}{\varrho} \pi r_0^2 \, v(E) \, 2m_e c^2 \frac{P(\nu_e \bar\nu_e)}{P\gamma} \, dE . \tag{9.55}$$

The number of electrons and positrons are the same and are given by the Fermi statistics (Appendix C.5), which gives for weak degeneracy according to (7.132) and (7.138)
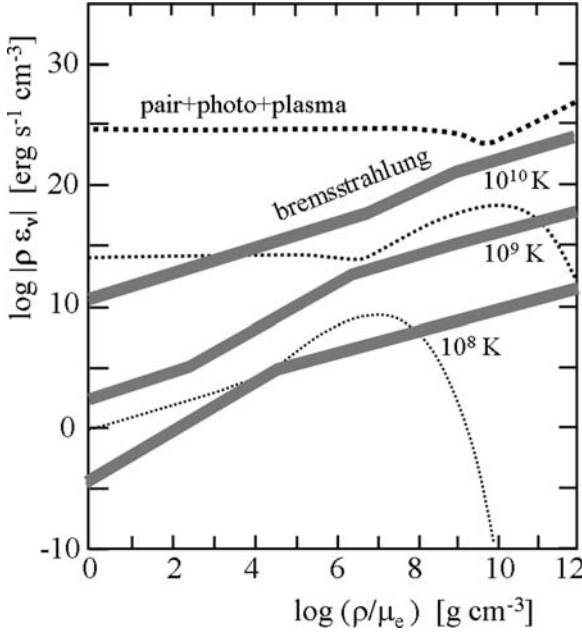
Fig. 9.9 The *thick lines* represent the emission rates for the bremsstrahlung process as a function of ϱ for $T = 10^{10}$, 10^9, 10^8 K; these lines apply to helium (*lower part* of the thick line), to carbon (*middle part*) and to iron (*upper part*). For comparison the corresponding sums of the pair, photo and plasma emission are represented. Adapted from N. Itoh et al. [269]

$$n_{e^-} = \frac{4\pi}{h^3}(2m_e kT)^{3/2} F_{1/2}(\psi) = \frac{2(2\pi m_e kT)^{3/2}}{h^3} e^{\psi} . \tag{9.56}$$

The degeneracy parameter ψ is related to the chemical potential μ by $\psi = \mu/(kT)$ (C.51). Here μ is given by (C.53)

$$\mu_i = \left(\frac{\partial U}{\partial N_i}\right)_{S,V} = -m_e c^2 . \tag{9.57}$$

Thus, the electron concentrations become

$$n_{e^-} = \frac{2(2\pi m_e kT)^{3/2}}{h^3} e^{-(m_e c^2)/(kT)} . \tag{9.58}$$

With these relations, the integral (9.55) leads to the following approximations

$$\varepsilon_{\nu-\text{pair}} \approx -\frac{4.9 \times 10^{18}}{\varrho} T_9^3 \, e^{\frac{-m_e c^2}{kT}} \quad \text{for } T_9 < 1 , \tag{9.59}$$

and

$$\varepsilon_{\nu-\text{pair}} \approx -\frac{4.5 \times 10^{15}}{\varrho} T_9^9 \quad \text{for } T_9 > 3 , \tag{9.60}$$

in erg g^{-1} s^{-1}, with $T_9 = T/(10^9 \text{ K})$. The reaction rate r in (nb cm^{-3} s^{-1}) is independent of the density and ε behaves like $1/\varrho$ (9.11). For the same reason as for photo-neutrinos, degeneracy reduces the emission (Fig. 9.8). The pair neutrino emission dominates over other processes at high T values and for not extreme densities (Fig. 9.11). It is the main process of ν emission for the advanced stages of massive stars.

9.5.3 Plasma, Bremsstrahlung, Recombination Neutrinos

Plasma-Neutrinos: An electromagnetic wave entering a sufficiently dense plasma generates collective oscillations of the electrons. In turn, these oscillations of a charged medium generate the emission of electromagnetic waves. *A plasmon* is the quantum of energy associated to these waves. They propagate in various directions and their sum has to be taken. According to (9.51), associated to each plasmon there is probability of emission of $\nu_e \bar{\nu}_e$.

The energy loss by plasma-neutrino dominates at high densities, in the degenerate domain of the plane $\log T$ vs. $\log \varrho$ (Fig. 9.11). The emission rate first increases with density (Fig. 9.8), because a higher ϱ favors collective plasma oscillations, in this regime at a given ϱ the ν emission rate increases with about T^4 because of the behavior of $P(\nu_e \bar{\nu}_e)/P\gamma$. Then, the curves go through a maximum and decline for higher densities, because the domains of a Coulomb liquid and then of ionic Coulomb crystal are entered (Sect. 7.6.4).

Bremsstrahlung Neutrinos: The process is the inverse of the hyperbolic or free–free transitions (Sect. 8.4). An electron slowed down in the Coulomb field of a charged nucleus emits electromagnetic radiation with a probability (9.51) of a pair $\nu_e \bar{\nu}_e$ emission (Fig. 9.10).

The emission rates behave like Z^2/A, where Z and A are the atomic number and the atomic mass, so that bremsstrahlung ν emission is more important for heavy elements. At high densities, the ν-emission goes like $\sim \varrho T^6$. Figure 9.9 compares the emission rates of bremsstrahlung neutrinos with the sum of photo-, pair-, plasma-
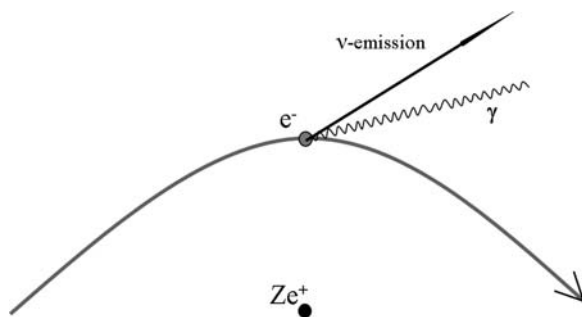
Fig. 9.10 Schematic illustration of the emission of bremsstrahlung neutrinos
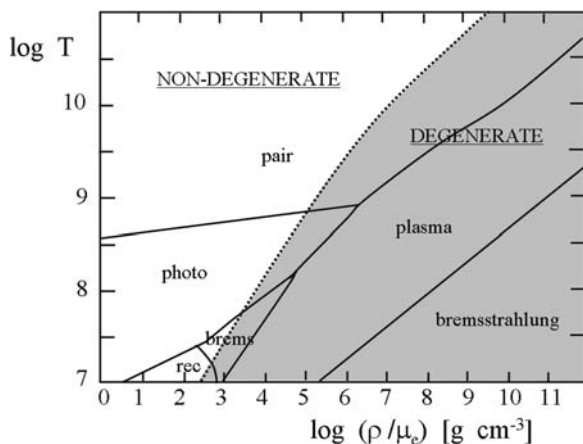
Fig. 9.11 The domains of the plane $\log T$ vs. $\log \varrho$ where the different processes of neutrino emissions dominate. The *dotted line* indicates the Fermi temperature T_F (see 7.146 and following remark), to the right of it (in the *gray* area) matter is degenerate. "rec" indicates neutrino from the recombination process. Adapted from N. Itoh et al. [269]

neutrinos. Bremsstrahlung neutrinos dominate at very high densities in a significant domain for C detonation and e capture (Fig. 26.10) and also in a small domain of moderate T and ϱ, however there the rates are so low that this is of no significance for evolution.

Recombination Neutrinos: A free electron in the continuum makes a transition to a bound atomic state, in a process which is the inverse of the photoionization or bound–free transitions (Sect. 8.3). Recombination neutrinos dominate at low T and ϱ (Fig. 9.11), i.e., for $T < 10^8$ K for pure ^{56}Fe, for $T < 2 \times 10^7$ K for pure ^{12}C, but they never dominate for helium or hydrogen. On the whole, the emission rates are very low and they have little significance.

There are other neutrino emission processes. The Urca process consists of an e^- capture by a nucleus with ν_e emission followed (e.g., after some convective transport) by a β decay with $\bar{\nu}_e$ emission. There are also synchrotron neutrinos: an electron moving in a strong field may emit a $\nu_e \bar{\nu}_e$ pair instead of a photon. However, only the photo-, pair-, plasma- and bremsstrahlung-neutrino processes play a significant role in stellar evolution.

Part III
Hydrodynamical Instabilities and Transport Processes

Chapter 10
Transport Processes: Diffusion and Advection

There does not seem to by anything in the Universe which stays for ever where it has been put once. This also applies to the elements synthesized in the stellar interiors. Classical evolution models assume that an element in a radiative zone, e.g., in the solar center, always stays exactly at the same place, i.e., for the next 10 billions years in the case of the Sun. Such an assumption ignores microscopic diffusion and the fact that stars, especially rotating stars, are subject to many instabilities which contribute to the transport of chemical elements and angular momentum. These processes considerably affect the course of evolution and nucleosynthesis.

We must distinguish between diffusion and advection:

Diffusion is a transport process which results from chaotic motions. It occurs in media with a gradient of one or several quantities, such as a chemical element, pressure, temperature, angular momentum, etc. In diffusion processes arising from hydrodynamical instabilities, only the quantities with a gradient are transported. This is the case of gradients of chemical composition and of angular momentum which are smoothed by diffusion.

Convection acts as a diffusion process, which mixes the elements with a very short timescale (dynamical timescale). Other diffusion processes generally have much longer timescales (thermal timescale). Diffusion may also act on a quantity homogeneously distributed in a medium where there is, for example, a T gradient. This is case of the microscopic or atomic diffusion, which is able to separate the nuclear species and create gradients of elements which were initially uniformly distributed.

An advection is a transport which results from the coherent displacement of relatively large volume elements, such as a stream or a current.

In many stellar models, advection is treated as a diffusion process, this is incorrect and leads to erroneous conclusions. The circulation of money in the world offers an interesting example of advective motions. If it would be a diffusion, the money would smoothly flow from the rich people to the poor ones. This does not seem to be the case, the flows of money is generally going the opposite way! This is typically an advection, i.e., a global transport of something. Treated as a diffusion, the transport of money would even have the wrong sign. Diffusion and advection do not obey to the same equations.

10.1   General Properties of Diffusion

There are several diffusion processes which work in stars: diffusion by shears in differentially rotating stars, microscopic or atomic diffusion which includes gravitational and radiative diffusions, diffusion by turbulence, magnetic diffusion, etc. These various processes obey some general properties.

10.1.1 Absence of Global Mass Flux

Let us consider a fluid with several different types of particles "i", which have a mass m_i, a concentration n_i and a velocity u_i. The mean velocity $\overline{\boldsymbol{u}}$ of the mixture is [40, 414]

$$\overline{\boldsymbol{u}} = \frac{\sum_i m_i n_i < \boldsymbol{u}_i >}{\sum_i m_i n_i} , \tag{10.1}$$

where $< \boldsymbol{u}_i >$ is the average velocity of particles of type "i". If $f_i(\boldsymbol{x}, \boldsymbol{p}, t)$ is the distribution function of the probability to find particles of type "i" at position $\boldsymbol{x}$, with momentum $\boldsymbol{p}$ and at time t, the average velocity $< \boldsymbol{u}_i >$ is given by

$$< \boldsymbol{u}_i > = \frac{1}{n_i} \int_{\text{ph}} f_i \boldsymbol{u}_i \, d\tau_{\text{ph}} \quad \text{with} \quad \int_{\text{ph}} f_i \, d\tau_{\text{ph}} = n_i , \tag{10.2}$$

where τ_{ph} is the phase space volume.

One might wonder why in (10.1), the weighting factor is the partial mass density and not the partial number density. This question is equivalent to ask whether the mean velocity of the mixture is zero when the net flux of the number of particles is zero (i.e., $\sum_i n_i < \boldsymbol{u}_i >= 0$) or when the net flux of the mass is zero (i.e., $\sum_i m_i n_i < \boldsymbol{u}_i >= 0$). Obviously, $\overline{\boldsymbol{u}} = 0$ when the net mass flux is zero, otherwise the center of gravity of the system would be moving.

The peculiar velocity of a given particle of the species "i" is defined as $\boldsymbol{v}_i = \boldsymbol{u}_i - \overline{\boldsymbol{u}}$. The mean value $\boldsymbol{v}_i$ for particles of species "i" is

$$< \boldsymbol{v}_i > = \frac{1}{n_i} \int_{\text{ph}} f_i \boldsymbol{v}_i \, d\tau_{\text{ph}} = < \boldsymbol{u}_i > -\overline{\boldsymbol{u}}. \tag{10.3}$$

This is the diffusion velocity of the particles of type "i" in the mixture. From (10.1), one has

$$\sum_i m_i n_i < \boldsymbol{v}_i >= 0. \tag{10.4}$$

This shows that there is no net mass flux associated to diffusion. The changes of chemical composition due to diffusion are to be added to those due to nuclear

reactions. Diffusion also modifies the mean molecular weight (and thus the hydro-static structure of the star), but does not induce any net mass flux in the medium.

10.1.2 Continuity Equation: Atomic Diffusion and Motion

Let us consider a mixture of several species of particles "i" with mass fractions X_i assumed to be small. This is the test particle approximation. The total density is ϱ. The elements "i" receive a net momentum which makes them move with an average total velocity $<u_i>=<v_i>+\overline{u}$, where $<v_i>$ is the average diffusion velocity of particles "i" with respect to the rest of the elements. The continuity equation applied to elements "i" writes

$$\frac{\partial\,(\varrho\,X_i)}{\partial t}+\boldsymbol{\nabla}\cdot(\varrho\,X_i<\boldsymbol{u_i}>)=0\,. \tag{10.5}$$

The gas globally also satisfies the equation of continuity (10.6), which is here

$$\frac{\partial\,\varrho}{\partial t}+\mathrm{div}(\varrho\,\overline{\boldsymbol{u}})=0\,. \tag{10.6}$$

Developing (10.5) with account of (10.6) gives

$$\varrho\,\frac{\partial X_i}{\partial t}+X_i\boldsymbol{\nabla}\cdot(\varrho<\boldsymbol{v_i}>)+\varrho\,(<\boldsymbol{v_i}>+\overline{\boldsymbol{u}})\cdot\boldsymbol{\nabla}X_i=0\,. \tag{10.7}$$

The change of the abundances X_i with time can be driven either by (1) a gradient of abundance X_i or by (2) a gradient of the product $\varrho<v_i>$. The first case is typical of hydrodynamic instabilities (Sect. 10.2). The second case is typical of atomic diffusion, where the product $\varrho<v_i>$ may be related, for example, to the P and T gradients in the medium. For an homogeneous composition, i.e., $\boldsymbol{\nabla}X_i=\mathbf{0}$, the timescale of the atomic diffusion is

$$t_{\mathrm{diff}}\approx\frac{\varrho}{|\boldsymbol{\nabla}\cdot(\varrho<\boldsymbol{v_i}>)|}\,. \tag{10.8}$$

If the density in the medium varies more than the velocity, one has

$$t_{\mathrm{diff}}\approx\frac{1}{<v_i>|\nabla\ln\varrho|}=\frac{H_\varrho}{<v_i>}\,, \tag{10.9}$$

where H_ϱ is the density-scale height (5.35). When a steady state is reached, the abundances X_i no longer change. From (10.7), one gets

$$\frac{\boldsymbol{\nabla}X_i}{X_i}=-\frac{\boldsymbol{\nabla}\cdot(\varrho<\boldsymbol{v_i}>)}{\varrho\,(<\boldsymbol{v_i}>+\overline{\boldsymbol{u}})}\,. \tag{10.10}$$

As shown by Vauclair [600], (10.10) says that the abundance gradients expected in case of diffusion are reduced by $(1 + \bar{u}/ < v_i >)$ if there is a global motion of velocity $\bar{u}$.

10.1.3 Fluxes of Particles, Velocities and Diffusion Coefficient

The properties of diffusion can be studied in the mean free path approximation: only the average properties of each species of particles are studied. Thus, we shall now omit the brackets indicating the average: $< v_i >$ is just noted v_i and this characterizes a mean particle of type "i".

We consider a binary (i.e., two components) mixture with a gradient of abundance X_i of the test elements "i" along the direction r. The other quantities are assumed constant in space. Let n_i be the number concentration and $v_{T,i}$ the thermal velocities of particles "i", supposed to be isotropically oriented. The flux (in number) of particles "i" entering into a fluid element at coordinate r coming from a nearby level $r - \delta r$ is

$$J_i^+ = \frac{1}{6} v_{T,i}(r - \delta r)\, n_i(r - \delta r) = -\frac{1}{6}\frac{\partial(v_{T,i}\, n_i)}{\partial r}\delta r, \qquad (10.11)$$

where the factor $1/6$ comes from the averaging of $\cos^2 \vartheta$, where ϑ is the angle of impact of the particles on a surface element perpendicular to the r axis (see Fig. B.1). As in the elementary kinetic theory of gases, one may also obtain this factor by considering a small cube in the fluid. A fraction $1/6$ of the particles with random motions at level $r - \delta r$ enters the cube by the considered side. The outgoing flux is similarly $J_i^- = -(1/6)\, v_{T,i}(r + \delta r)\, n_i(r + \delta r) = -(1/6)\, (\partial(v_{T,i} n_i)/\partial r)\delta r$. Summing the entering and outgoing fluxes, one gets the total flux (in number) in direction r,

$$J_i = J_i^+ + J_i^- = n_i v_i = -\frac{1}{3}\frac{\partial(v_{T,i}\, n_i)}{\partial r}\,\ell_i, \qquad (10.12)$$

where ℓ_i is the mean free path of particles "i". The sign minus indicates that the particles move in the direction opposite to the concentration gradient. The velocity v_i expresses the average diffusion velocity of particles "i", it is different from the thermal velocities $v_{T,i}$. The flux of particles can also be expressed as the mass of particles "i" per units of surface and time:

$$J_i(\text{mass}) = \varrho X_i v_i = -\frac{1}{3}\varrho\,\frac{\partial(v_{T,i}\, X_i)}{\partial r}\,\ell_i, \qquad (10.13)$$

where the total density ϱ of the gas is supposed constant in space and time. This shows that both a gradient of thermal velocity and of abundance may contribute to the diffusion of particles. The above relation provides a general expression of the diffusion velocity v_i.

Case of an abundance gradient: if we now consider a diffusion process due to a gradient of abundance only, which is equivalent to assume that the gradient of thermal velocities can be neglected, the diffusion velocity can be written from (10.13)

$$\boldsymbol{v_i} = -\frac{D_i}{X_i} \boldsymbol{\nabla} X_i \,, \tag{10.14}$$

with the diffusion coefficient D_i for particles i given by (10.13),

$$D_i = \frac{1}{3} \ell_i v_{\mathrm{T},i} \,. \tag{10.15}$$

One can also write from (10.13),

$$\boldsymbol{J_i} = D_i \varrho \, \boldsymbol{\nabla} X_i \,. \tag{10.16}$$

Another expression can be obtained from (10.12), such a relation is known as Fick's law. Depending on the physical process responsible for the diffusion, the diffusion coefficient may or may not depend on the chemical species considered. From (10.15), the diffusion timescale t_{diff} behaves like

$$t_{i,\,\mathrm{diff}} \sim \frac{\ell_i^2}{D_i} \,. \tag{10.17}$$

This timescale grows with the square of the size of the considered region.

Case of turbulent medium: forms (10.3)–(10.16) can be used to express the diffusion coefficient, atomic or arising from hydrodynamical instabilities, provided the appropriate expressions for ℓ and v_{T} are used. In a turbulent medium, the fluid elements have a distribution of velocities which is not of thermal origin. However, the resulting effects in presence of a gradient of abundance $\boldsymbol{\nabla} X_i$ are similar to those of thermal motions: the chemical gradient will be smoothed tending toward an homogeneous distribution. The effects of turbulence on the chemical distribution can be treated as a diffusion, where the turbulent velocities are represented to first order by the average velocity v_{turb} and the mean free path ℓ, both being taken the same for the various elements. One has

$$\boldsymbol{v}_{\mathrm{turb}} = -\frac{D_{\mathrm{turb}}}{X_i} \boldsymbol{\nabla} X_i \,. \tag{10.18}$$

The corresponding diffusion coefficient D_{turb} is given by

$$D_{\mathrm{turb}} \approx \frac{1}{3} \ell \, v_{\mathrm{turb}} \,. \tag{10.19}$$

The above expressions are applied to derive the diffusion coefficients due to hydrodynamical processes, such as shear instabilities. They can also be applied to

time-dependent convection, i.e., when the turnover time of convection is of the same order as the nuclear timescales (see Sect. 6.3).

Comparisons of coefficients: let us compare the diffusion coefficients for atomic and turbulent diffusions. For atomic process, the mean free path between collisions of a particle "i" is $\ell_i \sim 1/(\sigma_i n)$, where σ_i is the cross-section of particle "i" in the medium of concentration n (number density). In thermal equilibrium, the root-mean-square velocity is $v_{T,i} = (3kT/m_i)^{1/2}$, so that the diffusion coefficient behaves like [600]

$$D_i \approx \left(\frac{k}{3m_i} \right)^{1/2} \frac{T^{1/2}}{\sigma_i n} . \tag{10.20}$$

For neutral atoms, the cross-section is constant with T. For ionized atoms, where collisions are dominated by the balance between electrostatic and thermal forces, $\sigma_i \sim T^{-2}$ and the diffusion coefficient behaves like $D_i \sim T^{5/2}/n$. Since in stellar interiors, one generally has about $\varrho/T^3 \approx$ const (3.101), this implies that the atomic diffusion coefficients behave like $D_i \sim T^{-1/2}$. Thus atomic diffusion is weaker in deeper stellar interiors than in outer layers.

In general, atomic diffusion is much weaker than turbulent diffusion or diffusion processes arising from hydrodynamical instabilities. Typically, the coefficient of atomic diffusion of light elements is of the order of $D_i \sim 10^3$ cm^2 s^{-1} at the basis of the atmosphere in a 3 M$_\odot$ star [600] (see also Table 10.1). The corresponding diffusion timescale for the whole star would be $t_{\text{diff}} \sim (2.0R_\odot)^2/(10^3 \text{ cm}^2 \text{ s}^{-1}) \sim 1.94 \times 10^{19}$ s, i.e., 6.1×10^{11} yr. On the contrary, the diffusion coefficient due to shear turbulence are of the order of 10^8–10^{11} cm^2 s^{-1} [409], i.e., a factor 10^5–10^8 larger than the atomic diffusion, while the coefficient D for convection is of the order of 10^{16} cm^2 s^{-1}. The corresponding timescales are smaller by the same factors.

Table 10.1 Some typical values concerning atomic diffusion in a A-type star with $T_{\text{eff}} = 8500$ K. $\Delta M/M$ is the mass fraction up to the surface, D_{ip} is the diffusion coefficient given by (10.69), v is the diffusion velocity given by (10.85), $t_{\text{diff}} = H_P/v$ is expressed in years, otherwise the units are in CGS. From Alecian [6]

Parameter	Upper layers	Base of envelope
$T(K)$	19170	4.34×10^6
ϱ	1.09×10^{-08}	5.86×10^{-01}
n_e	$4.77 \times 10^{+15}$	$2.88 \times 10^{+23}$
n_p	$4.46 \times 10^{+15}$	$2.38 \times 10^{+23}$
R	$1.09 \times 10^{+11}$	$4.95 \times 10^{+10}$
$\Delta M/M$	5.17×10^{-11}	5.00×10^{-02}
g	$2.06 \times 10^{+04}$	$9.41 \times 10^{+04}$
H_P	$5.33 \times 10^{+07}$	$2.64 \times 10^{+09}$
D_{ip}	$3.01 \times 10^{+02}$	2.26×10^{-01}
v	6.19×10^{-05}	2.05×10^{-10}
$t_{\text{diff}}(\text{yr})$	$2.73 \times 10^{+04}$	$4.08 \times 10^{+11}$

This shows that in the presence of a fast hydrodynamical mixing process, such as turbulence, the atomic diffusion can generally be neglected, however, in the Sun both diffusion and meridional circulation have to be considered.

10.2   Diffusion by an Abundance Gradient

In a chemically inhomogeneous region, several hydrodynamical processes of mixing may be present. In many cases, the transport of the chemical elements and angular momentum can be treated as a diffusion process, with a coefficient D specific to the considered process. A noticeable exception is the transport of angular momentum by meridional circulation, which must not be treated as a diffusion (Sect. 10.5).

10.2.1   Equation of Diffusion

We consider here a diffusion process due to the motion of particles with a diffusion velocity v_i depending only on the abundance gradient according to expression (10.14). This expression satisfies condition (10.4),

$$\sum_i m_i n_i \boldsymbol{v}_i = -\varrho D \boldsymbol{\nabla} \left(\sum_i X_i \right) = \boldsymbol{0}, \tag{10.21}$$

because of $\sum_i X_i = 1$ and of the relation between the concentration n_i and the partial density ϱX_i is

$$n_i = \frac{\varrho X_i}{A_i m_{\mathrm{u}}}, \tag{10.22}$$

with A_i the atomic mass expressed in atomic mass units m_{u}. Let us consider a one-dimensional problem, where particles "i" may diffuse along the radial direction r. Thus, (10.14) writes

$$v_i = -\frac{D}{X_i} \frac{\partial X_i}{\partial r}. \tag{10.23}$$

The variation due to diffusion of the number of particles in the element of volume V and surface S is, due to conservation of the particle number,

$$\frac{\partial}{\partial t} \int_V n_i \, dV = -\int_S n_i \boldsymbol{v}_i \cdot \boldsymbol{dS}, \tag{10.24}$$

which expresses the continuity (1.1). From the Gauss theorem $\int_V \mathbf{\nabla} \cdot \mathbf{A}\, dV = \int_S \mathbf{A} \cdot d\mathbf{S}$ with (10.22) and (10.23), one obtains

$$\frac{\partial n_i}{\partial t} = -\frac{1}{r^2}\frac{\partial}{\partial r}(r^2 n_i v_i) = \frac{1}{r^2}\frac{\partial}{\partial r}\left(\varrho\, r^2 D\, \frac{\partial\left(\frac{n_i}{\varrho}\right)}{\partial r}\right). \tag{10.25}$$

Replacing n_i by its expression as a function of X_i gives

$$\frac{\partial}{\partial t}(\varrho\, X_i) = \frac{1}{r^2}\frac{\partial}{\partial r}\left(\varrho\, r^2 D\, \frac{\partial X_i}{\partial r}\right). \tag{10.26}$$

This equation can be written more generally by considering diffusion, with an appropriate coefficient D in any direction,

$$\frac{\partial}{\partial t}(\varrho\, X_i) = \mathbf{\nabla} \cdot (\varrho\, D\, \mathbf{\nabla} X_i). \tag{10.27}$$

Summing expressions (10.26) over all the chemical species i, one obtains

$$\frac{\partial \varrho}{\partial t} = \frac{1}{r^2}\frac{\partial}{\partial r}\left(\varrho\, r^2 D\, \frac{\partial}{\partial r}(1)\right) = 0. \tag{10.28}$$

This is consistent with matter conservation: the diffusions of the various elements compensate each other. In case of two species, this implies that every time a particle "1" of mass m_1 diffuses in a direction, there are (m_1/m_2) particles "2" diffusing in the opposite direction. The density can be taken out of the time derivative in (10.26) and the derivative is then considered at a Lagrangian mass coordinate M_r,

$$\varrho\, \frac{\partial X_i}{\partial t}\bigg|_{M_r} = \frac{1}{r^2}\frac{\partial}{\partial r}\left(\varrho\, r^2 D\, \frac{\partial X_i}{\partial r}\right). \tag{10.29}$$

In what precedes, we did not consider the possible presence of a general fluid motion. Thus, the Lagrangian derivatives d/dt and $\partial/\partial t$ are equivalent (see relations 1.18). If there is a motion with velocity $\mathbf{u}$, we must write the equation expressing the change of abundance X_i as (cf. Appendix B.1.2),

$$\varrho\, \frac{dX_i}{dt} = \varrho\, \frac{\partial X_i}{\partial t} + \varrho\, \mathbf{u} \cdot \mathbf{\nabla} X_i = \mathbf{\nabla} \cdot (\varrho\, D\, \mathbf{\nabla} X_i), \tag{10.30}$$

which provides a more general form of the diffusion equation. Expression (10.29) gives the change of composition due to one or more diffusion processes at a given level M_r in the star. There are a number of physical processes producing element diffusion, correspondingly the expressions of the diffusion coefficients are different in each case.

10.2.2 Boundary Conditions and Interpolations

The conditions at the stellar center and surface are

$$\frac{\partial X_i}{\partial r}\bigg|_{M_r=0} = \frac{\partial X_i}{\partial r}\bigg|_{M_r=M} = 0 , \tag{10.31}$$

where M is the total mass. The same conditions apply at any boundaries, if there is no abundance step. If there is some transport of the chemical elements in the adjacent region, it may be advantageous to use throughout the two domains a diffusion equation with the appropriate local coefficients.

Great care must be given in the interpolation, if any, of the diffusion coefficients. If at two mesh points $k-1$ and k, the coefficients are D_{k-1} and D_k, the meaningful average at a fraction f (counted from $k-1$) of the distance between the points $k-1$ and k is not $(1-f)D_{k-1}+fD_k$. The quantities to be added are the diffusion timescales, i.e., the inverse of the diffusion coefficients [414]. Thus, the appropriate average is [414]

$$D_f = \frac{D_{k-1}D_k}{fD_{k-1}+(1-f)D_k} . \tag{10.32}$$

Consistently, we see that the smallest diffusion coefficient governs the diffusion between two mesh points.

Various quantities may experience a diffusion process and a diffusion equation can be written for them depending on the physical processes at work. For example, if there is some diffusion of angular momentum, one may express the diffusion of the specific angular momentum $r^2\Omega$ [179],

$$\varrho\frac{d(r^2\Omega)}{dt} = \frac{1}{r^2}\frac{\partial}{\partial r}\left(\varrho r^4 D_\Omega \frac{\partial\Omega}{\partial r}\right) , \tag{10.33}$$

where Ω is the angular velocity and D_Ω the appropriate diffusion coefficient (Sect. 10.5.4). In stellar models, the values of the radii r change with time, however, the diffusion time steps are chosen sufficiently small so that r can be considered as constant during one diffusion time step. The same is true for the diffusion coefficient and other structural variables. The above equation (10.33) thus becomes

$$\varrho r^2\frac{d\Omega}{dt} = \frac{1}{r^2}\frac{\partial}{\partial r}\left(\varrho r^4 D_\Omega \frac{\partial\Omega}{\partial r}\right) , \tag{10.34}$$

or more generally

$$\varrho r^2\frac{d\Omega}{dt} = \nabla\cdot\left(\varrho r^2 D_\Omega \nabla\Omega\right) . \tag{10.35}$$

The boundary conditions at the center and at the surface are

$$\frac{\partial \Omega}{\partial r}\bigg|_{M_r=0} = \frac{\partial \Omega}{\partial r}\bigg|_{M_r=M} = 0. \tag{10.36}$$

At boundaries where there is no viscous coupling the same conditions apply. In general, the transport equation for the angular momentum may contain other terms expressing the advection of angular momentum by meridional circulation (Sect. 10.5) and the effects of magnetic braking (Sect. 21.3). These last two effects are not diffusion processes and they enter the equation of the variation of angular momentum with their own specific expressions.

The various methods for solving diffusion equations have been discussed in details [414]. The most robust method is the method of the implicit differences. The importance of correctly estimating the diffusion coefficients between mesh points is emphasized (see 10.32). The connection between radiative and convective regions must be treated with great care.

10.2.3 Caution About the Use of Concentrations

Often the equation of diffusion (10.26) for an element "i" is written as

$$\frac{d}{dt}(\varrho\, c_i) = \frac{1}{r^2}\frac{\partial}{\partial r}\left(\varrho\, r^2 D \frac{\partial c_i}{\partial r}\right), \tag{10.37}$$

with partial concentration c_i instead of mass fraction X_i, without indication on the precise meaning of c_i. Partial concentration in number is the ratio of the number of particles "i" to the total number per volume unity, i.e., $c_i = n_i/n$, where $n = \sum_i n_i$. Partial concentration in mass is equivalent to the mass fraction X_i. Let us consider the diffusion equation for the partial concentration in number. Replacing c_i in (10.37) by n_i/n and expressing n_i as a function of X_i with $X_i = c_i\,(A_i/\mu)$, one obtains

$$\frac{d}{dt}(\varrho\,\mu\, X_i) = \frac{1}{r^2}\frac{\partial}{\partial r}\left(\varrho\, r^2 D \frac{\partial}{\partial r}(\mu\, X_i)\right), \tag{10.38}$$

where $\mu = \varrho/(n m_u)$ is the mean molecular weight of the ions. The same remark as for (10.29) and (10.30) applies here about the use of partial or straight derivatives. This equation is identical to (10.26) only if μ is constant as a function time and position. Thus, (10.38) is equivalent to (10.26) only when it is applied to a minor constituent "i", the abundance of which does not influence μ significantly and when μ has no gradient. Evidently, in general (10.38) is not equivalent to (10.25) and (10.26).

The incorrect use of concentrations c_i (number fractions) can easily be seen. Let us write c_i as number fractions in (10.37),

$$\frac{d}{dt}\left(\varrho\, \frac{n_i}{n}\right) = -\frac{1}{r^2}\frac{\partial}{\partial r}\left(r^2 \varrho\, \frac{n_i}{n} w_i\right). \tag{10.39}$$

There, we have introduced a velocity $w_i = -D/(n_i/n) \ \partial (n_i/n)/\partial r$. This velocity is not a diffusion velocity, because $\sum_i m_i n_i w_i = -nDm_{\mathrm{u}}(\partial\mu/\partial r)$ is not equal to zero except where μ is constant. Relation (10.39), as it is written, expresses the change of $\varrho n_i/n = \mu \, n_i \, m_{\mathrm{u}}$ resulting from the transport of the quantity $(\varrho n_i/n)$ in an element of volume. However, physically this is not $\varrho n_i/n$ which diffuses, but the particles themselves. Thus, in general the use of the number fractions is not physically appropriate, as stressed by [414].

There are two conditions for (10.37) to be equivalent to (10.25) and (10.26): (1) the particles which diffuse must have a very small abundance, so small that their diffusion does not affect $\mu = \varrho/(nm_{\mathrm{u}})$; (2) μ must not vary in the region where the particles diffuse. If the first condition is verified for trace elements, the second is generally not true in stellar evolution.

10.3   Microscopic or Atomic Diffusion

Diffusion processes may also act in an initially chemically homogeneous medium. The thermal motions of ions and electrons produce global motions of some chemical species in presence of a gradient of some property, such as pressure or temperature. The differential microscopic effects of a force applied on the ions are able to separate them, leading to differences of their concentrations. Diffusion is responsible for the atmospheric properties of the chemically peculiar stars (CP) in the range of T_{eff} of about 7000–15000 K. Diffusion may also play a role in the inner radiative zone of solar-type stars, which have a long-enough lifetime to allow microscopic effects, such as gravitational settling, to be efficient.

A condition for significant microscopic diffusion is that no other efficient large-scale motions is present, such as convection, turbulent motions, meridional circulation, radiative winds, etc., which would largely overcome the effects of microscopic diffusion (Fig. 10.1). The importance of microscopic diffusion generally decreases with depth in stars as shown in Sect. 10.1.3.

10.3.1   Gravitational Settling

Let us consider a binary mixture, where the component "i" has a very low abundance, so that its contribution to the total density is negligible. This is the so-called test atom approximation. Let us also consider initial conditions with constant P, T and ϱ and suppose that there is an acceleration a_i acting on particles "i" only. These particles will reach a state of hydrostatic equilibrium characterized by the equality of the force acting on them by volume unity and the gradient of partial pressure of particles "i":
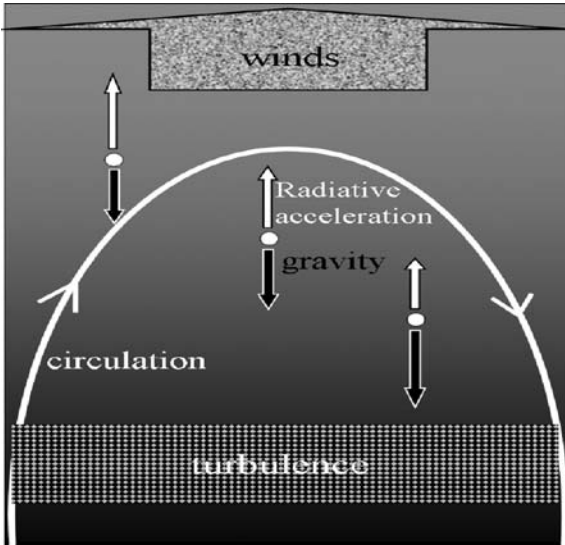
Fig. 10.1 The atomic diffusion results from the balance between the two following main forces: the ions are pushed upward by a radiative acceleration and downward by gravity. These two effects compete with each other. If hydrodynamical processes, such as convection, circulation and turbulence, are present, they are generally largely dominating over atomic diffusion. Adapted from G. Alecian [6]

$$\frac{\partial P_i}{\partial r} - \varrho \, X_i a_i = 0 \,. \tag{10.40}$$

The acceleration a_i is due to the forces $F_i = m_i a_i$ acting on particles "i" of mass $m_i = A_i m_u$. Such forces are the gravity force, the electric forces and other forces f_i',

$$F_i = -A_i m_u g + Z_i e E + f_i' \,, \tag{10.41}$$

where E is the electric field. If the law of perfect gas applies to the medium, the particles "i" obey the relation $P_i = (k/m_i) X_i \varrho \, T$ and one gets

$$\frac{1}{X_i} \frac{\partial X_i}{\partial r} - \frac{F_i}{kT} = 0 \,. \tag{10.42}$$

The first term multiplied by $-D$ gives the diffusion velocity due to a composition gradient (10.23). Thus, the diffusion velocity accounting for the acceleration a_i experienced by the particles can be written as

$$v_i = -D \left(\frac{1}{X_i} \frac{\partial X_i}{\partial r} - \frac{F_i}{kT} \right) \,. \tag{10.43}$$

The equilibrium state is the limit of the small perturbations due to diffusion [429], since at equilibrium (10.42) the diffusion velocity is zero. One may consider various sources of acceleration a_i.

An example is the pressure gradient always present in stars. It is a source of a particular acceleration for particles "i", if their mass $m_i = A_i m_u$ is different, typically larger, than the average mass $m = \mu m_u$ of the particles. The equation of the global hydrostatic equilibrium (1.5) can be written with the law of perfect gas,

$$\frac{1}{P}\frac{\partial P}{\partial r} = -\frac{mg}{kT}\,. \tag{10.44}$$

The net force on the test particles is the difference $F_i = -(m_i - m)g$, which gives

$$\frac{F_i}{kT} = -\frac{(m_i - m)}{m}\frac{mg}{kT} = \left(\frac{m_i}{m} - 1\right)\frac{1}{P}\frac{\partial P}{\partial r}\,, \tag{10.45}$$

$$\text{so that}\quad v_i = -D\left(\frac{1}{X_i}\frac{\partial X_i}{\partial r} + (m_i - m)\frac{g}{kT}\right)\,. \tag{10.46}$$

This gives the diffusion velocity due to both a gradient of concentration and gravitational settling: gravity produces a separation of the elements due to their different masses. As the pressure gradient is simply related to gravity, the above effect can also be written in terms of the pressure gradient. In general, there are also other forces at work in a diffusion process. The main problem of the atomic diffusion is to express the actions of the various forces on the different atomic particles in the medium.

If the initial distribution of elements "i" is homogeneous, and if the test particles are much more massive than the average particle, i.e., $m_i \gg m$, one can write the diffusion velocity due to gravitational settling as

$$v_i \approx -D\frac{m_i g}{kT}\,, \tag{10.47}$$

which is often used to obtain an order of magnitude of the velocity of atomic diffusion, since gravitational settling is a dominant process together with radiative diffusion. The velocity is negative since the heavy element "i" is sinking in the star. Some diffusion coefficients are given in Sect. 10.3.4.

10.3.2 Equations of Motion of Charged Particles

At the microscopic level, in addition to the effects of the pressure gradients and gravity g, the particle motions are influenced by the electrostatic force due to their electric charges, if the medium is ionized. The collisions between particles also influence their motions by transfer of momentum; this effect is equivalent to a friction. The hydrostatic equilibrium of particles "i" with mass fraction X_i, atomic mass number A_i, electric charge Z_i leads to [190]

$$\frac{\partial P_i}{\partial r} = -\varrho \, X_i \, g + \frac{\varrho \, X_i}{A_i \, m_\mathrm{u}} Z_i \, e \, E + \sum_{j \neq i} \mathcal{K}_{ij}(v_j - v_i) + \mathcal{K}_{ie}(v_e - v_i), \qquad (10.48)$$

where E is the local microscopic electric field produced by the particle displacements. ϱX_i is the partial density of particles "i" with a concentration $n_i = \varrho X_i / (A_i \, m_\mathrm{u})$. The coefficients $\mathcal{K}_{ij}$ and $\mathcal{K}_{ie}$ are the so-called resistance coefficients of particle "i" with other particles "j" and with the electrons, respectively. These coefficients in g cm^{-3} s^{-1} express the resistance force by volume unity produced by the differences of velocities between particles. These coefficients are tabulated by Paquette et al. for a number of cases [461].

Let us consider a mixture with two particle species "1" and "2". The first term on the right of (10.48) can be written as $+(\varrho X_i / \varrho)(\partial P / \partial r)$ with the help of the equation for the global hydrostatic equilibrium (1.5). We thus have two equations of hydrostatic equilibrium for the two kinds of particles,

$$\frac{\partial P_1}{\partial r} - \frac{(\varrho X_1)}{\varrho} \frac{\partial P}{\partial r} - \frac{\varrho X_1}{A_1 \, m_\mathrm{u}} Z_1 e E = \mathcal{K}_{12}(v_2 - v_1) + [\mathcal{K}_{1e}(v_e - v_1)], \qquad (10.49)$$

$$\frac{\partial P_2}{\partial r} - \frac{(\varrho X_2)}{\varrho} \frac{\partial P}{\partial r} - \frac{\varrho X_2}{A_2 \, m_\mathrm{u}} Z_2 e E = \mathcal{K}_{21}(v_1 - v_2) + [\mathcal{K}_{2e}(v_e - v_2)]. \qquad (10.50)$$

We also have two equations of continuity like (10.6)

$$\frac{\partial (\varrho X_1)}{\partial t} + \frac{1}{r^2} \frac{\partial}{\partial r}(r^2 \varrho X_1 v_1) = 0, \qquad (10.51)$$

$$\frac{\partial (\varrho X_2)}{\partial t} + \frac{1}{r^2} \frac{\partial}{\partial r}(r^2 \varrho X_2 v_2) = 0. \qquad (10.52)$$

The momentum conservation during the motions implies

$$n_1 A_1 m_\mathrm{u} v_1 + n_2 A_2 m_\mathrm{u} v_2 + [m_e n_e \, v_e] = 0 \longrightarrow X_1 v_1 + X_2 v_2 = 0. \qquad (10.53)$$

We can neglect the transfer of momentum by the electrons, owing to their small masses, thus we skip the term in square brackets in (10.53) and the collision terms in square brackets in (10.49) and (10.50). The concentration of electrons is given by the condition of electric neutrality $n_1 Z_1 + n_2 Z_2 = n_e$.

Thus, equations (10.49), (10.50), (10.51), (10.52) and (10.53) form a complete system for the five unknown quantities [190]:

– the abundances X_1 and X_2,
– the velocities v_1 and v_2,
– and the electric field E,

which can thus be determined. Below we derive the electric field and the diffusion velocities from this set of relations.

10.3.3 The Electric Field and the Diffusion Velocities

The resistance coefficients $\mathcal{K}_{12}$ and $\mathcal{K}_{21}$, which express the pressure gradients resulting from the velocity differences, are equal by symmetry, since there is momentum conservation in collisions without chemical transformation. We can thus add (10.49) and (10.50) and obtain an expression for the electric field,

$$eE = \frac{\frac{\partial}{\partial r}(P_1 + P_2) + g\varrho(X_1 + X_2)}{\frac{\varrho}{m_u}(Y_1 Z_1 + Y_2 Z_2)},\tag{10.54}$$

a product expressed as a force by volume unity (g s^{-2} cm^{-2}). We see that the electric field depends on the departures from the hydrostatic balance between the gravity acting on the partial densities and their partial pressure gradients. We call Y_i the ratio (cf. Sect. 25.1.2)

$$Y_i = \frac{X_i}{A_i}.\tag{10.55}$$

We divide (10.50) by the partial pressure P_2,

$$P_2 = n_2 kT = \frac{\varrho X_2}{A_2 m_u} kT,\tag{10.56}$$

and get

$$\frac{\partial \ln P_2}{\partial r} + \frac{A_2 m_u g}{kT} - \frac{Z_2}{kT}\left[\frac{\frac{\partial}{\partial r}(P_1 + P_2) + g\varrho(X_1 + X_2)}{\frac{\varrho}{m_u}(Y_1 Z_1 + Y_2 Z_2)}\right]$$
$$= -\mathcal{K}_{21}\frac{A_2 m_u}{\varrho X_2 kT} v_{21},\tag{10.57}$$

where $v_{21} = v_2 - v_1$. Further simplifications lead to

$$\frac{\partial \ln P_2}{\partial r} + \frac{m_u g}{kT}\left(A_2 - \frac{Z_2 A_1(1 + \frac{X_2}{X_1})}{Z_1 + Z_2\frac{Y_2}{Y_1}}\right)$$
$$- \frac{Z_2\left(1 + \frac{Y_2}{Y_1}\right)}{\left(Z_1 + Z_2\frac{Y_2}{Y_1}\right)}\frac{\partial \ln(P_1 + P_2)}{\partial r} = -\mathcal{K}_{21}\frac{m_u}{\varrho Y_2 kT} v_{21}.\tag{10.58}$$

This expression allows us to write the velocity difference v_{21}, however, we can further transform the above expression by calling P_{ion} the sum of the two partial pressures $P_{\mathrm{ion}} = P_1 + P_2$,

$$\frac{P_2}{P_{\mathrm{ion}}} = \frac{n_2}{n_1 + n_2} = \frac{Y_2}{Y_1 + Y_2} = \frac{Y_2}{Y_{\mathrm{ion}}} \quad \text{with} \quad Y_{\mathrm{ion}} = Y_1 + Y_2.\tag{10.59}$$

Thus, one has

$$\frac{\partial \ln P_2}{\partial r} = \frac{\partial \left(\ln \frac{Y_2}{Y_{\text{ion}}} \right)}{\partial r} + \frac{\partial \ln P_{\text{ion}}}{\partial r} . \tag{10.60}$$

The velocity difference v_{21} becomes

$$v_{21} = -\frac{Y_2 \varrho \, kT}{m_{\text{u}} \mathcal{K}_{21}} \times$$

$$\left[\frac{\partial \left(\ln \frac{Y_2}{Y_{\text{ion}}} \right)}{\partial r} + \frac{\partial \ln P_{\text{ion}}}{\partial r} \left(1 - \frac{Z_2 \left(1 + \frac{Y_2}{Y_1} \right)}{Z_1 + Z_2 \frac{Y_2}{Y_1}} \right) + \frac{m_{\text{u}} g}{kT} \left(A_2 - \frac{Z_2 A_1 \left(1 + \frac{X_2}{X_1} \right)}{Z_1 + Z_2 \frac{Y_2}{Y_1}} \right) \right] . \tag{10.61}$$

We write the term in front of the square bracket as

$$\frac{Y_2 \varrho \, kT}{m_{\text{u}} \mathcal{K}_{21}} = D_{12} \left(1 + \frac{Y_2}{Y_1} \right) , \tag{10.62}$$

in a way consistent with expression (10.23). This gives the following expression for the diffusion coefficient D_{12},

$$D_{12} = \frac{n_1 \, n_2 \, kT}{(n_1 + n_2)} \frac{1}{\mathcal{K}_{21}} = \frac{Y_2 \varrho \, kT}{m_{\text{u}} \mathcal{K}_{21}} \frac{Y_1}{Y_1 + Y_2} . \tag{10.63}$$

If we want to obtain the diffusion velocity of particles "2", we can use relation (10.53) for momentum conservation and get

$$v_{21} = v_2 - v_1 = v_2 \left(1 + \frac{X_2}{X_1} \right) . \tag{10.64}$$

This yields for the velocity of particles "2"

$$v_2 = \frac{1 + (Y_2/Y_1)}{1 + (X_2/X_1)} D_{12} \times$$

$$\left[-\frac{\partial \left(\ln \frac{Y_2}{Y_{\text{ion}}} \right)}{\partial r} + \frac{m_{\text{u}} g}{kT} \frac{A_1 Z_2 - A_2 Z_1}{Z_1 + Z_2 (Y_2/Y_1)} + \frac{Z_2 - Z_1}{Z_1 + Z_2 (Y_2/Y_1)} \frac{\partial \ln P_{\text{ion}}}{\partial r} \right] . \tag{10.65}$$

The velocity of particles "2" is thus determined as a function of three different gradients [190]:

- The first term in the bracket expresses the diffusion due to the gradient of abundance of the considered element. If element "2" is a test element, this term is equivalent to (10.23).
- The second term is the so-called gravitational term. It is proportional to the global pressure gradient and it also accounts for the (generally opposed) effect of the microscopic electric field E (10.54). For nuclei with $A_1/A_2 = Z_1/Z_2$, this term

vanishes. This is the case for the light elements where $A_i = 2Z_i$, such as ^{4}He, ^{12}C, ^{16}O, etc.

– The third term is proportional to the pressure gradient of the ions. It is generally not important.

Additional terms may be added to account for the effects of thermal diffusion (Sect. 10.3.5), radiative acceleration (Sect. 10.4.1) and possible magnetic fields (Sect. 10.4.3).

10.3.4 Diffusion Equation

The equation of diffusion of particles "2" can be written by combining the diffusion equation (10.29) with expression (10.23),

$$\varrho \left.\frac{\partial X_2}{\partial t}\right|_{M_r} = -\frac{1}{r^2}\frac{\partial}{\partial r}\left(\varrho\, r^2 X_2\, v_2\right), \tag{10.66}$$

where v_2 is given by (10.65). This equation is subject to the boundary conditions discussed in Sect. (10.2.2). Care has to be given to the interpolation of the diffusion coefficients (10.32) if there is also a diffusive transport in the adjacent zone [414].

At this stage, we do not yet have the expression for the diffusion coefficient D. The time evolution of the fluid is described by Boltzmann equation which gives the time variation of the distribution function $f_i(r, v_i, t)$ so that $f_i(r, v_i, t) dr^3 dv^3$ is the number of particles "i" in the volume element dr^3 centered on $\boldsymbol{r}$ and with a velocity in the volume dv^3 centered on $\boldsymbol{v}$. The Boltzmann equation is solved under certain hypotheses [6, 112, 193], such as binary interactions, elastic collisions, negligible electron mass, Debye–Hückel potential around the ions (7.104). The solution of Boltzmann equation provides the diffusion coefficient with account of particle collisions.

The diffusion coefficient depends on the kind of particles interactions: charged–charged, charged–neutral or neutral–neutral. The most important case for the stars is the first one, i.e., the interaction between ions. In this case, the diffusion coefficient for ions of type "1" and "2" is [6, 600], see also (B.53),

$$D = \frac{3}{16n}\frac{(2kT)^{5/2}}{(\pi m_{\mathrm{r}})^{1/2}}\frac{1}{Z_1^2 Z_2^2\, e^4\, \ln(1 + \xi_{12}^2)} \tag{10.67}$$

where $m_{\mathrm{r}} = A_1 A_2\, m_{\mathrm{u}}/(A_1 + A_2)$ is the reduced mass and $n = n_1 + n_2$, the total concentration of particles. ξ_{12} is given by

$$\xi_{12} = \frac{4kT}{Z_1 Z_2\, e^2}\, r_{\mathrm{D}}, \tag{10.68}$$

where r_{D} is the Debye–Hückel radius given by (7.99).

10.3.4.1   Diffusion of Ions With Protons

In the useful case of the diffusion of ions "i" with protons "p", the diffusion coefficient becomes [112],

$$D_{ip} = 2 \times 10^9 \frac{T^{5/2}}{n_p Z_i^2 \ln\left[1 + (2.73 \times 10^8 T^3)/(n_p Z_i^2)\right]} \,, \tag{10.69}$$

in cm^2 s^{-1}, where n_p is the proton concentration. The approximation is made that only collisions with an impact parameter shorter than the Debye–Hückel radius are considered (the potential is supposed Coulombian). For impact parameters larger than R_D, the interaction potential is assumed negligible. Further developments leading to diffusion coefficients with screened potentials for different ions have been performed by Paquette et al. [461].

For estimates of the orders of magnitude, the diffusion velocity of an element "i" with respect to hydrogen may be estimated by considering only the effect of gravity according to relation (10.47).

10.3.5   Effect of a Thermal Gradient

The presence of a temperature gradient also produces particle diffusion, because in this case there is a gradient of the thermal velocities, which by successive binary collisions may lead to a non-zero average diffusion velocity for each type of particles "i", even if there is no global motions.

Let us consider test particles "i" with a constant density. Their thermal velocities $v_{T,i}$ behave like $T^{1/2}$ and they vary with depth. If we consider a horizontal plane in the stellar medium, the probability of collision by surface unity on each side of the plane is according to (10.11, see also 9.4)

$$n_i v_i = \frac{1}{6} v_{T,i}(r+dr) n_i(r+dr) \frac{\sigma_i(r+dr)}{\sigma_i(r)}$$
$$- \frac{1}{6} v_{T,i}(r-dr) n_i(r-dr) \frac{\sigma_i(r-dr)}{\sigma(r)} . \tag{10.70}$$

Developing the product $v_{T,i}(r)\sigma_i(r)$ to the first order over a length ℓ_i, which is the mean free path for element "i", we get for a constant concentration n_i

$$v_i = \frac{1}{3} v_{T,i} \ell \frac{1}{v_{T,i}\sigma_i} \frac{\partial(\sigma_i v_{T,i})}{\partial r} . \tag{10.71}$$

The direction and size of the diffusion velocity depend on how the cross-section varies with T. Neutral atoms have a cross-section σ_i constant with T, thus only the dependence of $v_{T,i}$ on T intervenes, thus $[\partial(\sigma v_T)/\partial r]$ behaves like $\partial T/\partial r$. Thus

neutral atoms tend to move from the hot to the cool places. At the opposite, the ionized particles have $\sigma_i \sim T^{-2}$, and thus they tend to move toward the hottest stellar regions. Taking these dependences into account, one has

$$v_i = D \left(\alpha_{T,i} \frac{1}{T} \frac{dT}{dr} \right) . \qquad (10.72)$$

The dependences of v_T and σ would give a coefficient $\alpha_{T,i} = -1.5$ for ionized particles. However, the electric charges of the particles also influence the motions and this leads to [112]

$$\alpha_{T,i} = -2.65 \left(\frac{Z_i}{Z_j} \right)^2 , \qquad (10.73)$$

where Z_i/Z_j is the charge ratio of the considered ions, "i" being the test ion and "j" the basic constituent. The term in parentheses in (10.72) is to be added in the square bracket of (10.65) containing the different contributions to the diffusion velocity.

10.4   The Radiative Diffusion

Among the forces acting on ions, the radiative force is a major one in stars. Momentum is transferred from the photons to the ions, the amount of transfer depending on the opacity. Among the four main opacity processes (Sect. 8): bound–bound, bound–free, free–free and electron scattering, only the first two directly contribute to the radiative acceleration of atoms, because the photons are effectively absorbed. Gravitational and radiative accelerations dominate the effects of microscopic diffusion [6, 600].

10.4.1   Radiative Acceleration

Only the non-isotropic part of the radiation field (i.e., the flux) contributes to the transfer of momentum in the vertical direction. Let $F_\nu \, d\nu$ be the radiation flux between frequencies ν and $\nu + d\nu$. The radiative acceleration of the atoms B is determined by the gradient of radiation pressure on the atoms in the frequency interval $d\nu$,

$$g_{\text{rad,B}}(\nu) \, d\nu = -\frac{1}{\varrho_B} \frac{dP_{\text{rad,B}}(\nu)}{dr} \, d\nu , \qquad (10.74)$$

where $\varrho_B = n_B \, m_B$ is the partial density of atoms B. We now use (3.16) relating the pressure gradient to the flux in a specific frequency interval and the radiative acceleration becomes

$$g_{\text{rad, B}}(v)\,dv = \frac{\kappa_{\text{B}}(v)\,F_v}{c}\,dv, \tag{10.75}$$

where $\kappa_{\text{B}}(v)$ is the opacity of atoms B at frequency v. For radiative equilibrium in the case of an optically thick medium, the flux F_v is related (3.20) to the derivative of Planck's function by

$$F(v)\,dv = -\frac{4\pi}{3}\frac{1}{\kappa(v)\varrho}\frac{\partial B_v}{\partial T}\frac{dT}{dr}\,dv, \tag{10.76}$$

where we use the fact that B_v depends on r through the temperature $T(r)$. The opacity $\kappa(v)$ is the total opacity from all sources at frequency v. The radiative acceleration of the atoms B integrated over all frequencies becomes

$$g_{\text{rad, B}} = -\frac{4\pi}{3c}\frac{1}{n_{\text{B}}\,m_{\text{B}}}\int_0^\infty \frac{\kappa_{\text{B}}(v)}{\kappa(v)}\frac{\partial B_v}{\partial T}\frac{dT}{dr}\,dv. \tag{10.77}$$

The total opacity at frequency v can be separated into two terms,

$$\kappa(v) = \kappa_{\text{B}}(v) + \kappa_{\text{other}}(v), \tag{10.78}$$

where one distinguishes the opacity due to particles B only and the opacity due to all other atoms. There are two cases [600]:

- If the opacity $\kappa_{\text{B}}(v)$ of the particles B dominates, the two opacities cancel in the integral (10.77) and the radiative acceleration of particles B goes like $g_{\text{rad, B}} \sim 1/n_{\text{B}}$. Thus, the presence of more particles B reduces their individual acceleration, which means that the flux is saturated.
- If $\kappa_{\text{B}}(v)$ is negligible, there is no saturation effect and thus the opacity $\kappa_{\text{B}}(v)$ is proportional to n_{B} and thus the radiative acceleration of individual particles is constant.

For radiative equilibrium with energy conservation, the T gradient can be written simply with (3.17)

$$\frac{dT}{dr} = -\frac{3\,\kappa\varrho\,T_{\text{eff}}^4}{16\,T^3}\left(\frac{R}{r}\right)^2. \tag{10.79}$$

There, κ is the Rosseland mean opacity (Sect. 3.1.4). One uses $F(r)\,r^2 = F(R)R^2$ and $F(R) = \sigma\,T_{\text{eff}}^4$ (Sect. C.1). The Stefan–Boltzmann constant is $\sigma = ac/4$. The radiative acceleration becomes

$$g_{\text{rad, B}} = \frac{\pi\kappa\varrho\,T_{\text{eff}}^4}{4c}\left(\frac{R}{r}\right)^2\frac{1}{n_{\text{B}}m_{\text{B}}}\int_0^\infty \frac{\kappa_{\text{B}}(v)}{\kappa_{\text{B}}(v)+\kappa_{\text{other}}(v)}\frac{1}{T^3}\frac{\partial B_v}{\partial T}\,dv. \tag{10.80}$$

As such, the above expression applies whether the acceleration is due to spectral lines or to continuum absorption.

10.4.2 Acceleration by Spectral Lines

Each spectral lines of an atom B contributes to the radiative acceleration. The opacity coefficient $\kappa_B(\nu)$ is related to the cross-section by $\kappa_B(\nu) = \sigma_B(\nu) n_B / \varrho$ (Sect. 8.1.2). The cross-section for the atom B in the ionization stage "i" for the transition from level m to level n is (cf. 8.6)

$$\sigma_{B,i,m,n}(\nu) = \frac{\pi e^2}{m_e c} f_{B,i,m,n} \, \phi_{B,i,m,n} \,, \tag{10.81}$$

where $\phi_{B,i,m,n}$ (see 8.5) is the broadening function of the considered transition. One has to sum up over the contributions of the various transitions $m \to n$ and over the ionization stages,

$$\sigma_B(\nu) = \sum_{i,m} \sum_{n>m} \sigma_{B,i,m,n}(\nu) \,. \tag{10.82}$$

The recombination and de-excitation lines do not contribute to acceleration since they are isotropic processes.

The result of the integration (10.80) depends on the broadening function of the spectral lines. For an unsaturated Doppler line with a Gaussian profile, the broadening function is essentially independent of the ion concentration n_B. For saturated lines with a Lorentz profile, the broadening function varies like $n_B^{1/2}$, thus one has [600]

$$g_{\text{rad},B} \sim \frac{1}{n_B} \quad \text{for Doppler profile (unsaturated profile)} \,,$$

$$g_{\text{rad},B} \sim \frac{1}{n_B^{1/2}} \quad \text{for Lorentz profile (saturated line)} \,. \tag{10.83}$$

For elements with a low abundance, where the lines are not saturated, the most abundant ion of a given element generally has its resonant lines close to the maximum of the Planck function. In addition, if one assumes that the sum of the oscillator strengths $f_{B,i,m,n}$ from the level m considered to all upper levels n is equal to 1, one obtains according to Michaud et al. [418] the following expression of the radiative acceleration at level r with temperature T in a star of radius R and effective temperature T_{eff},

$$g_{\text{rad},B} = 1.7 \times 10^8 \, \frac{(T_{\text{eff}}/10^4)^4}{A_B \, (T/10^4)} \left(\frac{R}{r}\right)^2 \,, \tag{10.84}$$

in cm s^{-2}. A_B is the atomic mass number of the element considered, the above expression does not apply to noble gases. In (10.65) for the diffusion velocity, the radiative diffusion intervenes with $(A_2 \, m_u/(kT)) \, g_{\text{rad}}$, so when accounting also for the thermal diffusion (Sect. 10.3.5), we finally have the complete expression of the diffusion velocity:

$$v_2 = \frac{1+(Y_2/Y_1)}{1+(X_2/X_1)} D_{12} \times \left[-\frac{\partial (\ln \frac{Y_2}{Y_{\text{ion}}})}{\partial r} + \frac{m_u g}{kT} \frac{A_1 Z_2 - A_2 Z_1}{Z_1 + Z_2(Y_2/Y_1)} \right.$$

$$\left. + \frac{Z_2 - Z_1}{Z_1 + Z_2(Y_2/Y_1)} \frac{\partial \ln P_{\text{ion}}}{\partial r} + \alpha_{T,2} \frac{\partial \ln T}{\partial r} + \frac{A_2 m_u}{kT} g_{\text{rad},2} \right], \qquad (10.85)$$

where the last two terms are, respectively, the thermal diffusion and the radiative diffusion of the element "2". In general, the gravitational and radiative diffusions dominate the process. The OPAL and Opacity project (cf. Chap. 8) provide monochromatic opacities for various elements and allow the calculation of radiative accelerations [488].

10.4.3 Continuum Absorption, Redistribution, Magnetic Field

In a bound–free transition, the momentum of the absorbed photon is shared between the ion and the ejected electron [258]. Let us call f_{elec}, the fraction of the photon momentum embarked on the average by the electrons. This fraction is known only in a few simple cases, such as the state $1s$ and the states with $n = 2$ of the hydrogen atom. Amazingly, the value of f_{elec} can be larger than 1, when the energy of the incident photon is above some threshold. The reason is that the electron leaves the atom with a momentum higher than the momentum of the incident photon, which implies a recoil of the ion. For example, in the case of a $1s$ electronic configuration, the fraction f_{elec} is given by

$$f_{\text{elec}} = \frac{8}{5} \frac{h\nu - I_{1s}}{h\nu}, \qquad (10.86)$$

where I_{1s} is the ionization potential from level $1s$. This expression may lead to $f_{\text{elec}} > 1.0$. The above approximation is acceptable for hydrogenoid atoms, such as C, N, O, Ne, Mg, Si, S and Ar in stellar envelopes. For other ions, it cannot be used. A parametric expression for the optically thick case is given by Alecian [7]. On the whole, a proper account of radiative acceleration by bound–free absorption demands further studies of the atomic processes [488].

In the stellar medium, a given element is present under different ionic forms and there are continually reactions of ionization and recombination. This brings an additional difficulty in the calculation of the diffusion velocity. The problem is to know how the acceleration received by an atom in a given ionization stage is transmitted to the new ion if further ionizations or recombinations occur. With the assumption that after a recombination or ionization an ion keeps for some characteristic time a "memory" of its previous momentum, some methods to statistically treat the redistribution of the radiative and gravitational accelerations have been proposed [8, 429]. Another approach [214] considers that atoms in an ionization stage i with a low n number ($n \leq 2$) have a small ionization probability, thus the momentum

received by such atoms essentially remains for themselves. For atoms with $n > 2$, it is considered that the momentum is entirely transferred to the ionization stage $i + 1$. Recombination transfers no or very little momentum, since as a result of recombination the atom is generally in a high excitation state, which is quickly reionized again.

The magnetic field has two possible actions: the first effect, which has generally been neglected, is that the strong spectral lines which are saturated are separated into their Zeeman components by the magnetic field. This de-saturates the strong lines and may contribute to increase the radiative acceleration. In Ap stars with magnetic field of $\sim 10^4$ G [258], the Zeeman separation is for some elements (like Si) of the same order as the Doppler broadening. Thus, in this case the effect is small.

The second effect concerns the motion of the ions in the magnetic field. The charged particles have a spiral motion around the lines of the magnetic field. The component of the diffusion velocity parallel to the field is in principle not affected, while the diffusion perpendicular to the field lines is modified. The studies of diffusion with magnetic field [112] indicate a reduction of the diffusion velocity by a factor f according to S. Vauclair [600],

$$ f = \frac{1}{1 + \omega_i^2 \, t_{\text{coll},i}^2} \quad \text{with} \quad \omega_i = \frac{Z_i \, e \, H}{m_i} \, , \tag{10.87} $$

where ω_i is the Larmor frequency of the ion of charge Z_i, H is the magnetic field expressed in Gauss and $t_{\text{coll},i}$ is the average time interval between two collisions of the particles "i". The above expression shows that the magnetic field has negligible effects in dense stellar regions, because the collision timescale $t_{\text{coll},i}$ becomes very small.

10.4.4   Orders of Magnitude, Diffusion in A Stars

Table 10.1 gives some examples of the values characterizing the diffusion of light elements in the atmosphere and at the base of the envelope of an A-type star [6]. The diffusion velocities are generally very slow and the diffusion coefficients very small, even when compared to slow hydrodynamical processes such as meridional circulation (Chap. 11). One also notices from the table that the effects of diffusion strongly decrease with depth in stars in agreement with the remarks following Eq. (10.20).

Element diffusion is efficient in the envelopes of slowly rotating stars, with no significant convective zone and stellar winds. These conditions lead to the occurrence of chemically peculiar (CP) stars in the domain of A-type stars, as well as in white dwarfs. The radiative interior of solar-type and lower mass stars down to 0.4 $M_\odot$ are also subject to element diffusion due to their long lifetimes. The chemical consequences of this internal diffusion may be brought later to the surface by the convective envelopes.

A recent overview of the properties of the CP stars in relation with atomic diffusion is given in [640]. There are several groups of chemically peculiar A stars, which are in general slowly rotating:

- **The CP1 or Am stars** are at the surface deficient in Ca and C (by a factor of ~ 5) and in Sc (by an order of magnitude). They show excesses of Fe-peak elements and also of elements with higher atomic masses (factor of 3). They are generally binaries. The Am stars represent $\sim 13\%$ of A stars.
- **The CP2 or Ap stars** show excess of Si (up to a factor of 30), Cr (up to 10^3), Sr (up to 3×10^3) and Eu (up to 10^6). The Fe-peak elements are overabundant by a factor $10-10^2$. The binary frequency is low. They have magnetic fields and their relative frequency is about 5% .
- **The CP3 or Hg–Mn stars** or non-magnetic Ap stars show excesses of Hg (up to a factor 10^4) and Mn (up to 10^6). They have excesses often larger than 10^2 for Be, Ga, Y, Xe (up to 10^5), Eu, Gd, W, Pt, Pb and Bi. The binary frequency is normal and they represent $5-10\%$ of A stars.
- **The CP4 or He weak stars** are defined from the weakness of their HeI lines. They are generally hotter than the Am and Ap stars with $T_{\text{eff}} = 13000-15000$ K.

10.4.5   Atomic Diffusion in the Sun

The basic system of equations for treating atomic diffusion has been written and applied to the solar model [573], see also [514]. Recent works by Michaud and colleagues [419] show that atomic diffusion produces a relative reduction of the surface He content by 12% with respect to its initial value and an increase $\Delta Y = 0.013$ at the center. The original Z value at the surface is reduced by about 9%, while the relative Z increase at the center is about 14%. The abundance of Li at the surface of the hotter halo stars is likely reduced to 50% of its original value [416]. Similar estimates by Eggenberger [169] shows that the surface He content changes from $Y = 0.2766$ to 0.2440, i.e., a reduction by 11.8%, the surface metal content changes from $Z = 0.0192$ to $Z = 0.018$, i.e., a reduction by 6.3%. The central Z increases from $Z = 0.0192$ to $Z = 0.0206$, i.e., an increase by 7.3%. Taken at face, these results mean that the present observed solar abundances (Appendix A.3) are not the initial solar abundances.

The ages of the globular clusters are reduced by 10–12% when atomic diffusion is accounted for [591].

These various results show that for fine determinations of the properties of the Sun and halo stars, as well as for A-type stars, the account for microscopic diffusion is necessary. A recent review about the role of the atomic diffusion for the Sun, the MS stars up to 25,000 K, the age determination of globular clusters, the horizontal branch stars, the white dwarfs and neutron stars has been made by Michaud [417].

10.5 Transport of Angular Momentum in Stars

Not all transport processes can be treated as a diffusion, a typical case is the transport of angular momentum by the advection due to meridional circulation. We shall see here that the equation governing the transport of angular momentum contains also terms different from a diffusion equation, a point which requires a special care.

In a rotating star, the evolution of the angular velocity Ω has to be followed at each level r in the star, so that a full description of $\Omega(r, t)$ is available. The values of $\Omega(r, t)$ influence the mixing of elements and in turn the evolution of $\Omega(r, t)$ also depends on the distribution of the mean molecular weight μ. Thus, there is strong inter-connexion between the distributions of rotation and of the elements in stellar interiors.

10.5.1 Equation of Transport

Let us consider the situation illustrated in Fig. 10.2, where an element of volume limited by ABCD rotates around the vertical axis with an angular velocity $\Omega = \dot{\varphi}$. The mass of the volume element is $\varrho\, r^2 \sin\vartheta\, d\vartheta\, d\varphi\, dr$ and the component of the angular momentum $\boldsymbol{J}$ aligned with the rotational axis is

$$dJ = \varrho\, r^4 \sin^3\vartheta\, d\vartheta\, d\varphi\, dr\, \Omega\ , \tag{10.88}$$

the other components are zero. In Lagrangian coordinates, the derivative of the angular momentum of the moving fluid mass element is
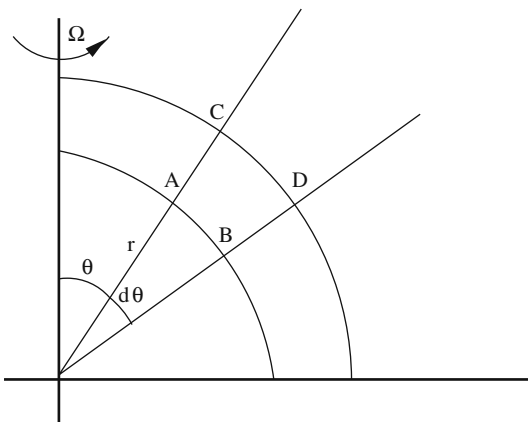
Fig. 10.2 The momentum of the small element ABCD rotating around the vertical axis is derived, r is the radial coordinate of point A and ϑ its colatitude

$$\varrho\, r^2 \sin \vartheta \, d\vartheta \, d\varphi \, dr \, \frac{d}{dt} (r^2 \sin^2 \theta \, \Omega)_{M_r}.\tag{10.89}$$

Let us express this derivative more explicitly. First, one can write

$$\varrho \frac{d}{dt} (r^2 \sin^2 \vartheta \, \Omega)_{M_r} = \frac{d}{dt} (\varrho\, r^2 \sin^2 \vartheta \, \Omega)_{M_r} - r^2 \sin^2 \vartheta \, \Omega \left. \frac{d\varrho}{dt} \right|_{M_r}. \tag{10.90}$$

The relation between the Lagrangian and Eulerian derivatives (Sect. 1.1.4) together with the previous expression gives

$$\varrho \frac{d}{dt} (r^2 \sin^2 \vartheta \, \Omega)_{M_r}$$

$$= \frac{\partial}{\partial t} (\varrho\, r^2 \sin^2 \vartheta \, \Omega)_r + \boldsymbol{U} \cdot \boldsymbol{\nabla} (\varrho\, r^2 \sin^2 \vartheta \, \Omega) - r^2 \sin^2 \vartheta \, \Omega \left. \frac{d\varrho}{dt} \right|_{M_r}, \tag{10.91}$$

where $\boldsymbol{U}$ is the velocity of the motion, if any one. Using

$$\left. \frac{d\varrho}{dt} \right|_{M_r} = \left. \frac{\partial \varrho}{\partial t} \right|_r + \boldsymbol{U} \cdot \boldsymbol{\nabla} \varrho, \tag{10.92}$$

and the continuity equation $(\partial \varrho / \partial t)\big|_r = -\boldsymbol{\nabla} (\varrho \cdot \boldsymbol{U})$ (1.1), one obtains

$$\left. \frac{d\varrho}{dt} \right|_{M_r} + \varrho\, \boldsymbol{\nabla} \cdot \boldsymbol{U} = 0, \tag{10.93}$$

which incorporated in (10.91) gives

$$\varrho \frac{d}{dt} (r^2 \sin^2 \vartheta \, \Omega)_{M_r} = \frac{\partial}{\partial t} (\varrho\, r^2 \sin^2 \vartheta \, \Omega)_r + \boldsymbol{\nabla} \cdot (\boldsymbol{U} \varrho\, r^2 \sin^2 \vartheta \, \Omega). \tag{10.94}$$

This expresses the derivative (10.89) of the angular momentum $\boldsymbol{J}$. This derivative is equal to the momentum $\mathcal{M}$ of forces applied to the volume element,

$$\frac{d\boldsymbol{J}}{dt} = \mathcal{M}. \tag{10.95}$$

Various types of momentum of force can be applied to a rotating fluid element. Below we consider the momentum of forces by shears due to internal differential rotation. Depending on the differential rotation, the shears could have vertical and horizontal components.

10.5.2   *Transport of Angular Momentum by Shears*

Let us first consider the important case of a vertical or radial shear and call η_{v} the dynamic viscosity (B.12) in the vertical direction. Due to the shear, some forces are applied on the surface of the volume element. The force by the surface unity described by the segment AB (Fig. 10.2) during its rotation around the vertical axis is equal to

$$\eta_{\mathrm{v}} \frac{dv_{\varphi}}{dr} = \eta_{\mathrm{v}} r \sin \vartheta \frac{d\Omega}{dr} \ . \tag{10.96}$$

The modulus of the viscous force applied on the surface described by AB is

$$F_{\mathrm{AB}} = \eta_{\mathrm{v}} r^{3} \sin^{2} \vartheta \frac{d\Omega}{dr} \, d\vartheta \, d\varphi \ . \tag{10.97}$$

The momentum of the force is $\mathcal{M} = r \times F_{\mathrm{AB}}$, so the contribution of the viscosity to the force momentum is

$$F_{\mathrm{AB}} \, r \sin \vartheta \, \sin \frac{\pi}{2} = \eta_{\mathrm{v}} r^{4} \sin^{3} \vartheta \frac{d\Omega}{dr} \, d\vartheta \, d\varphi \ . \tag{10.98}$$

For the volume element with section ABCD, the gain of force momentum over the distance dr is

$$\frac{\partial}{\partial r} \left(\eta_{\mathrm{v}} r^{4} \sin^{3} \vartheta \, d\vartheta \, d\varphi \frac{\partial \Omega}{\partial r} \right) dr. \tag{10.99}$$

Let us consider the case of a tangential shear, which occurs when $d\Omega/d\vartheta \neq 0$. The force by surface unity due to the tangential shear with an horizontal viscosity η_{h} is equal to $\eta_{\mathrm{h}} r \sin \vartheta \left[\partial \Omega/(r \partial \vartheta) \right]$, thus the force on the surface described by AC during its rotation is $\eta_{\mathrm{h}} r \sin^{2} \vartheta (\partial \Omega/\partial \vartheta) dr d\varphi$.

To obtain the momentum of the force, one has to multiply by $r \sin \vartheta$. The gain on the force momentum when passing from AC to BD is

$$\frac{\partial}{r \partial \vartheta} \left(\eta_{\mathrm{h}} r^{2} \sin^{3} \vartheta \, dr d\varphi \frac{\partial \Omega}{\partial \vartheta} \right) r d\vartheta \ . \tag{10.100}$$

We now write the equation for the change of angular momentum (10.95) by using (10.94), (10.99) and (10.100). We simplify by $dr d\vartheta \, d\varphi$ and get the equation for the transport of the angular momentum of the mass element

$$\varrho \, r^{2} \sin \vartheta \frac{d}{dt} (r^{2} \sin^{2} \vartheta \, \Omega)_{M_{r}}$$

$$= \frac{\partial}{\partial r} \left(\eta_{\mathrm{v}} r^{4} \sin^{3} \vartheta \frac{\partial \Omega}{\partial r} \right) + \frac{\partial}{\partial \vartheta} \left(\eta_{\mathrm{h}} r^{2} \sin^{3} \vartheta \frac{\partial \Omega}{\partial \vartheta} \right) \ . \tag{10.101}$$

We express the dynamic viscosity coefficients in terms of the kinematic coefficients $v_v = \eta_v/\varrho$ and $v_h = \eta_h/\varrho$. According to App. (B.4), the coefficient v of kinematic viscosity is also the diffusion coefficient D of the chemical elements. We divide the left- and right-hand side member of (10.101) by $r^2 \sin \vartheta$,

$$\varrho \frac{d}{dt}(r^2 \sin^2 \vartheta \, \Omega)_{M_r}$$

$$= \frac{\sin^2 \vartheta}{r^2} \frac{\partial}{\partial r}\left(\varrho D_v r^4 \frac{\partial \Omega}{\partial r}\right) + \frac{1}{\sin \vartheta} \frac{\partial}{\partial \vartheta}\left(\varrho D_h \sin^3 \vartheta \frac{\partial \Omega}{\partial \vartheta}\right). \quad (10.102)$$

We get the first member according to (10.94) and develop the divergence into spherical coordinates. We finally obtain the equation describing the transport of the angular momentum [632],

$$\varrho \frac{d}{dt}(r^2 \sin^2 \vartheta \, \Omega)_{M_r} = \frac{\partial}{\partial t}(\varrho \, r^2 \sin^2 \vartheta \, \Omega)_r + \nabla \cdot [U \varrho \, r^2 \sin^2 \vartheta \, \Omega]$$

$$= \frac{\partial}{\partial t}(\varrho \, r^2 \sin^2 \vartheta \, \Omega)_r + \frac{1}{r^2} \frac{\partial}{\partial r}(\varrho \, r^4 \sin^2 \vartheta \, U_r \Omega) + \frac{1}{r \sin \vartheta} \frac{\partial}{\partial \vartheta}(\varrho \, r^2 \sin^3 \vartheta \, U_\vartheta \Omega)$$

$$= \frac{\sin^2 \vartheta}{r^2} \frac{\partial}{\partial r}\left(\varrho D_v r^4 \frac{\partial \Omega}{\partial r}\right) + \frac{1}{\sin \vartheta} \frac{\partial}{\partial \vartheta}\left(\varrho D_h \sin^3 \vartheta \frac{\partial \Omega}{\partial \vartheta}\right). \quad (10.103)$$

There, U_r is the vertical component of the velocity and U_ϑ the horizontal component. During evolution, one should also account for the velocity $\dot{r}$ of contraction or expansion and replace $U_r \to U_r + \dot{r}$, while U_ϑ remains the same. No assumption has been made on the distribution of Ω in the star, thus the above equation is general. In the case of a shellular rotation law with $\Omega = \Omega(r)$, the above expression is simpler as described below.

10.5.3 Some Properties of Shellular Rotation

The assumption has been made by Zahn [632] that internal rotation depends essentially on the distance to the stellar center and little on latitude (Sect. 2.2). The reason is the strong horizontal turbulence (Sect. 12.1 which produces enough coupling to enforce an almost constant Ω on isobars. One writes

$$\Omega(r, \vartheta) = \overline{\Omega}(r) + \widehat{\Omega}(r, \vartheta), \quad (10.104)$$

with $\widehat{\Omega} \ll \overline{\Omega}$. As before, ϑ is the colatitude. The horizontal average $\overline{\Omega}$ is defined as the angular velocity of a shell rotating like a solid body and having the same angular momentum as the considered actual shell. One has

$$\overline{\Omega}(r) = \frac{\int_0^\pi \Omega(r, \vartheta) \sin^3 \vartheta \, d\vartheta}{\int_0^\pi \sin^3 \vartheta \, d\vartheta}. \quad (10.105)$$

The justification for this average is given by the way the mean angular momentum on a shell is defined (10.112). In general, a vector field on the sphere can be represented by spherical harmonics. If the field is axially symmetric, it can be expressed in spherical functions. Thus, one represents the meridional circulation by [386, 632]

$$ \boldsymbol{U} = \underbrace{\sum_{l>0} U_l(r)\, P_l(\cos\vartheta)\,\boldsymbol{e}_r}_{U_r} + \underbrace{\sum_{l>0} V_l(r)\, \frac{dP_l(\cos\vartheta)}{d\vartheta}\,\boldsymbol{e}_\vartheta}_{U_\vartheta}, \qquad (10.106) $$

where $\boldsymbol{e_r}$ and $\boldsymbol{e}_\vartheta$ are the unit vectors along the radial and colatitude directions. We consider only the radial component of the velocity, since it produces the chemical mixing and transports the angular momentum. We limit the development of the Legendre polynomials to the second order

$$ \boldsymbol{U} = U_2(r)\,P_2(\cos\vartheta)\,\boldsymbol{e}_r + V_2(r)\,\frac{dP_2(\cos\vartheta)}{d\vartheta}\,\boldsymbol{e}_\vartheta\,, \qquad (10.107) $$

with $P_2(\cos\vartheta) = \frac{1}{2}(3\cos^2\vartheta - 1)$. The reason why the zero-order polynomials are not present is because P_0 is a constant, which would not permit the velocity to vanish. The first as well as the odd higher order terms P_3, $P_5 \ldots$ are not symmetrical with respect to the equator and thus they are set to zero. It is interesting to note that only the $l = 2$ component of the circulation is able to advect a net amount of angular momentum; as shown by Spigel and Zahn [542] the higher order components do not make a vertical transport of angular momentum. The term in P_4 has been considered by Mathis & Zahn [386] in the context of the solar tachocline (cf. Sect. 16.6.3).

The application of the equation of continuity in the anelastic approximation gives the term V_2 [632]. In spherical coordinates, the continuity in a stationary situation implies ($\frac{\partial \varrho}{\partial t} \approx 0$ defines the anelastic approximation)

$$ \boldsymbol{\nabla}\cdot(\varrho\,\boldsymbol{U}) = \frac{1}{r^2}\frac{\partial}{\partial r}(r^2 \varrho\, U_r) + \frac{1}{r\sin\vartheta}\frac{\partial}{\partial\vartheta}\left(\varrho\sin\vartheta\, V_2\frac{dP_2(\cos\vartheta)}{d\vartheta}\right) = 0. \quad (10.108) $$

With $dP_2/d\vartheta = -3\cos\vartheta\,\sin\vartheta$, one has

$$ \frac{1}{r^2}\frac{\partial}{\partial r}(r^2 \varrho\, U_r) = -\frac{\varrho\, V_2}{r\sin\vartheta}\left(3\sin^3\vartheta - 6\sin\vartheta\cos^2\vartheta\right) $$

$$ = -\frac{\varrho\, V_2}{r}\left(3 - 9\cos^2\vartheta\right) = 6\frac{\varrho\, V_2}{r}P_2(\cos\vartheta). \qquad (10.109) $$

From (10.107), one obtains after simplification by $P_2(\cos\vartheta)$,

$$ \frac{1}{r}\frac{d}{dr}\left[\varrho\, r^2 U_2(r)\right] - 6\varrho\, V_2(r) = 0\,. \qquad (10.110) $$

This expression is useful, it provides $V_2(r)$ and the horizontal component of the meridional velocity $U_\vartheta = V_2(r) \frac{dP_2(\cos \vartheta)}{d\vartheta}$, once $U_2(r)$ is known. In the course of stellar evolution, we account for circulation velocities as well as for expansion or contraction and thus one must consider

$$U_r = U_2(r) P_2(\cos \vartheta) + \dot{r} . \tag{10.111}$$

The patterns of meridional circulation (Fig. 11.2) during stellar evolution are obtained from the components U_r and U_ϑ.

10.5.4 Transport in Shellular Rotation

We now use the previous expressions to derive the equation of transport of the angular momentum in the vertical direction for the case of shellular rotation. For that we multiply (10.103) by $\sin \vartheta \, d\vartheta$ and integrate it over ϑ from 0 to π. Let us examine the successive terms in (10.103) with account of (10.111):

First term:

$$\int_0^\pi \frac{\partial}{\partial t} (\varrho r^2 \sin^2 \vartheta \, \Omega)_r \sin \vartheta \, d\vartheta$$

$$= \frac{\partial}{\partial t} \varrho r^2 \int_0^\pi \Omega(r, \vartheta) \sin^3 \vartheta \, d\vartheta = \frac{\partial}{\partial t} \left(\varrho r^2 \overline{\Omega} \right)_r \int_0^\pi \sin^3 \vartheta \, d\vartheta . \tag{10.112}$$

This shows why $\overline{\Omega}$ is defined by expression (10.105). The possible variations of ϱ with ϑ are neglected.

Second term:

$$\int_0^\pi \frac{1}{r^2} \frac{\partial}{\partial r} \left(\varrho r^4 \sin^2 \vartheta \, (U_r + \dot{r}) \Omega(r, \vartheta) \right) \sin \vartheta \, d\vartheta. \tag{10.113}$$

Let us first consider the term with U_r since it contains $P_2(\cos \vartheta)$ and let us also retain only the term $\overline{\Omega}(r)$ in $\Omega(r, t)$, this gives

$$\frac{1}{r^2} \frac{\partial}{\partial r} \left(\varrho r^4 U_2(r) \overline{\Omega}(r) \right) \int_0^\pi \sin^3 \vartheta \, \frac{1}{2} (3 \cos^2 \vartheta - 1) \, d\vartheta \tag{10.114}$$

$$= \frac{1}{r^2} \frac{\partial}{\partial r} \left(\varrho r^4 U_2(r) \overline{\Omega}(r) \right) \left[\int_0^\pi \sin^3 \vartheta \, d\vartheta - \frac{3}{2} \int_0^\pi \sin^5 \vartheta \, d\vartheta \right] \tag{10.115}$$

$$= -\frac{1}{5} \frac{1}{r^2} \frac{\partial}{\partial r} \left(\varrho r^4 U_2(r) \overline{\Omega}(r) \right) \int_0^\pi \sin^3 \vartheta \, d\vartheta, \tag{10.116}$$

where we have accounted that $\int_0^\pi \sin^5 \vartheta \, d\vartheta = (4/5) \int_0^\pi \sin^3 \vartheta \, d\vartheta$. The expansion or contraction term in $\dot{r}$ becomes

$$\frac{1}{r^2}\frac{\partial}{\partial r}\left(\varrho\, r^4\overline{\Omega}(r)\right)\int_0^\pi \sin^3\vartheta\, d\vartheta\,, \tag{10.117}$$

which contrarily to the term in $U_2(r)$ does not contain a factor $(-1/5)$.

Third term:

$$\int_0^\pi \frac{1}{r\sin\vartheta}\frac{\partial}{\partial\vartheta}\left(\varrho\, r^2\sin^3\vartheta\, U_\vartheta\,\Omega(r,\vartheta)\right)\sin\vartheta d\vartheta$$

$$= \varrho r\overline{\Omega}(r)\int_0^\pi \frac{\partial}{\partial\vartheta}\left(U_\vartheta\sin^3\vartheta\right)d\vartheta$$

$$= -3\varrho r\overline{\Omega}(r)V_2(r)\int_0^\pi \frac{\partial}{\partial\vartheta}\left(\sin^4\vartheta\cos\vartheta\right)d\vartheta = 0, \tag{10.118}$$

where we have used (10.110).

Fourth term:

$$\int_0^\pi \frac{\sin^2\vartheta}{r^2}\frac{\partial}{\partial r}\left(\varrho\, D_\mathrm{h}\, r^4\frac{\partial\Omega(r,\vartheta)}{\partial r}\right)\sin\vartheta\, d\vartheta$$

$$= \frac{1}{r^2}\frac{\partial}{\partial r}\left(\varrho\, D_\mathrm{h}\, r^4\frac{\partial\overline{\Omega}}{\partial r}\right)\int_0^\pi \sin^3\vartheta\, d\vartheta, \tag{10.119}$$

where one assumes that the coefficient D_h does not depend on ϑ.

Fifth term:

$$\frac{\partial\Omega(r,\vartheta)}{\partial\vartheta} = \frac{\partial\overline{\Omega}(r)}{\partial\vartheta} = 0\,, \tag{10.120}$$

with the assumption of shellular rotation. The fifth term vanishes.

Collecting the five contributions to (10.103) and simplifying the equations by $\int_0^\pi = \sin^3\vartheta\, d\vartheta$, one obtains finally

$$\frac{\partial}{\partial t}(\varrho\, r^2\overline{\Omega})_r = \frac{1}{5r^2}\frac{\partial}{\partial r}\left(\varrho\, r^4\overline{\Omega}[U_2(r)-5\dot{r}]\right) + \frac{1}{r^2}\frac{\partial}{\partial r}\left(\varrho\, D_\mathrm{v}\, r^4\frac{\partial\overline{\Omega}}{\partial r}\right). \tag{10.121}$$

This is the Eulerian expression for the transport of angular momentum. We can make several remarks:

– The term in $\dot{r}$ is important [372] only in the pre-MS phases as well in inter-nuclear contraction phases. The characteristic time associated to the transport of Ω by the circulation is the Edington–Sweet timescale (11.79) $t_\mathrm{ES}\approx t_\mathrm{KH}\left(\Omega^2 R/g_s\right)^{-1}$,

where g_s is the gravity at the surface and t_{KH} the Kelvin–Helmholtz timescale (1.73). Clearly t_Ω is longer than t_{KH}. In evolutionary phases at the Kelvin–Helmholtz timescale, the term in $\dot{r}$ is the dominant one, while during the MS phase this is not the case.

– In regions where $U_2(r)$ is positive (in general this is the case in the inner radiative envelope of massive stars, where circulation is raising along the polar axis, Sect. 11.3), an expansion with $\dot{r} > 0$ opposes its effect to circulation. On the contrary, in the outer layers where in general $U_2(r)$ is negative, an expansion reinforces circulation.

– We see that from Fig. 11.3 that when $U_2(r)$ is positive, the advection transports the angular momentum toward the interior.

– If as in general Ω decreases toward the exterior, diffusive processes transport the angular momentum toward the exterior.

The term in $\dot{r}$ only appears in the Eulerian formulation (10.121). In the Lagrangian formulation, where one follows a fluid mass element, the equation for the transport of angular momentum is simply

$$\varrho \frac{\partial}{\partial t}(r^2 \overline{\Omega})_{M_r} = \frac{1}{5r^2} \frac{\partial}{\partial r}(\varrho \, r^4 \overline{\Omega} \, U_2(r)) + \frac{1}{r^2} \frac{\partial}{\partial r}\left(\varrho \, D_v \, r^4 \frac{\partial \overline{\Omega}}{\partial r}\right). \quad (10.122)$$

The effects of expansion or contraction are automatically included [372]. This equation is currently applied in stellar models for calculating the evolution of Ω. With account of the detailed expression of $U_2(r)$ for the meridional circulation (Sect. 11.4.1), which contains terms up to the third spatial derivative of $\Omega(r,t)$, the above equation is of the fourth order (see 11.82) and thus it requires great care to be solved numerically.

10.5.5   Boundary Conditions

Care has also to be given to the boundary conditions for the transport of angular momentum. As the order of the system is four, we need four boundary conditions at the edges of a radiative region. Let us call r_t and r_b the radii at the top and at the bottom of the zone. In stars with $M > 1.3$ M$_\odot$, r_t and r_b are, respectively, the stellar surface and the edge of the convective core. If there is no viscous momentum at the edges, one has

$$\frac{\partial \Omega}{\partial r} = 0 \quad \text{in } r = r_t, \, r = r_b \,. \quad (10.123)$$

These two conditions impose the continuity of the first derivative of Ω at the edges. It also applies at the stellar center for solar-type stars which have an inner radiative zone. The other two boundary conditions are provided by the equation of transport of the angular momentum (10.122) applied at the boundaries [556]. One has with (10.123)

$$\frac{1}{5} d[\varrho\, r^4\, \overline{\Omega}\, U_2] = \varrho\, \frac{d}{dt}[r^2\overline{\Omega}] r^2 dr \,. \tag{10.124}$$

By integrating this relation over the interior and exterior zones (if any one), one obtains the conditions at the bottom and the top,

$$\frac{1}{5}\varrho\, r^4\, \overline{\Omega}\, U_2 \bigg|_{r_b} = \frac{d}{dt}\left[\overline{\Omega} \int_0^{r_b} r^4 \varrho\, dr\right] \quad \text{in } r = r_b \,,$$

$$-\frac{1}{5}\varrho\, r^4\, \overline{\Omega}\, U_2 \bigg|_{r_t} = \frac{d}{dt}\left[\overline{\Omega} \int_{r_t}^R r^4 \varrho\, dr\right] + \mathcal{M}_\Omega \quad \text{in } r = r_t \,. \tag{10.125}$$

The radial components U_2 of the velocity at the surface and center are zero. $\mathcal{M}_\Omega$ represents the momentum of force applied at the stellar surface, typically by magnetic field in solar-type stars (Sect. 21.3) or by tidal effects in binary systems. If there is no convective core, $r_b \rightarrow 0$ and the first condition becomes $U_2(r=0)=0$. Similarly, if there is no convective envelope $r_t \rightarrow R$ and the second condition is $U_2(r=R)=0$. The solutions at the center and surface tend toward zero and present no divergence which would prevent these conditions to be applied ([556], see also 11.4).

Chapter 11
Meridional Circulation

The problem of meridional circulation has been studied for nearly a century since the time of Eddington [168] and it is still in progress today. This is probably one of the field of Astrophysics, where the developments have been the slowest ones! Physically, meridional circulation arises because the equipotentials, or surface levels, are closer to each other in the polar regions and more spaced in the equatorial regions due to the centrifugal force. The radiative flux is proportional to the effective gravity, i.e., to the distance between equipotentials. Thus, there is (in a simple picture) an excess of flux along the polar axis and a deficiency near the equatorial plane (Sect. 4.2.1). This thermal imbalance generates global circulation motions in the meridian plane.

There was for long a severe physical problem: the solutions for meridional circulation were not conserving the angular momentum. Thus the reality of the circulation was questioned [80] (see Rieutord [489]). Some solutions without circulation were envisaged [285, 499], while some authors proposed solutions which in fact did not respect the basic laws of physics! The problem was solved by Zahn [632], who showed that one must treat simultaneously the equation for energy conservation which expresses the thermal imbalance, the Poisson equation and the conservation of angular momentum. A self-consistent solution was found at last and this was a great step forward.

Several effects related to the first three derivatives of the angular velocity $\Omega(r)$ intervene in differentially rotating stars and make the behavior of meridional circulation rather complex in evolved stars. Today, there are still uncertain points regarding circulation, in particular the interactions with the horizontal turbulence and magnetic field. The amount of differential rotation on horizontal layers depends on these two effects and on the account of high order terms in the developments [198, 386] . The properties of circulation in fast rotating stars also need to be explored.

11.1 The Energy Conservation on an Isobar

We follow here the self-consistent solution proposed by Zahn [372, 632]. There are several significant progresses in the physics of the problem.

– A physically self-consistent solution, as mentioned above.
– A general equation of state is accounted for.
– A stationary situation is not necessarily assumed.
– The effects of the horizontal turbulence on the thermal flux are accounted for, as well as on the transport of chemical elements.
– The effects of a chemical gradient are treated. This is particularly relevant since mixing is important in regions with a chemical gradient.

The interaction of circulation and magnetic field is discussed in Sect. 13.6.

11.1.1 Thermal Imbalance

Meridional circulation derives from thermal imbalance (see Sect. 4.2.1). We start by developing [632] the equation of energy conservation (3.42, 3.43)

$$\rho T \frac{dS}{dt} = \boldsymbol{\nabla} \cdot (\chi \boldsymbol{\nabla} T) + \varrho \, \varepsilon - \boldsymbol{\nabla} \cdot \boldsymbol{F}_{\mathrm{h}} \tag{11.1}$$

where S is the entropy per unit of mass and χ the thermal conductivity (3.41). The term ε refers to the nuclear energy production rate only. We include the flux $\boldsymbol{F}_{\mathrm{h}}$ of thermal energy due to a the horizontal turbulence (Sect. 12.1), which transmits heat by viscous friction. This can be written as

$$\boldsymbol{F}_{\mathrm{h}} = -D_{\mathrm{h}} \varrho \, T \, \boldsymbol{\nabla}_{\mathrm{h}} S \simeq -D_{\mathrm{h}} \varrho \, C_P \, \boldsymbol{\nabla}_{\mathrm{h}} T \, , \tag{11.2}$$

where D_h is the diffusion coefficient characterizing the horizontal turbulence (Sect. 12.1) and $\boldsymbol{\nabla}_{\mathrm{h}}$ is the horizontal gradient. As usual, a diffusion coefficient is expressed in $\mathrm{cm}^2 \, \mathrm{s}^{-1}$ and the flux in $\mathrm{erg} \, \mathrm{cm}^{-2} \, \mathrm{s}^{-1}$. The coefficient D_h is large with respect to that of vertical diffusion, a fact responsible for shellular rotation and the one dimensionality of the chemical composition [632].

We have shown (Sect. 2.2.2) that in the case of shellular rotation it is advantageous to write the structure equations on isobars. Thus, to study the thermal disequilibrium on a level surface or isobar, we expand the structural quantities around their average on an isobar up to the second Legendre polynomials $P_2(\cos \vartheta)$, where ϑ is the colatitude,

$$T(P, \vartheta) = \overline{T}(P) + \widetilde{T}(P) \, P_2(\cos \vartheta), \tag{11.3}$$

$$T \, dS(P, \vartheta) = \overline{T} \, d\overline{S}(P) + \overline{T}(P) \, d\widetilde{S}(P) \, P_2(\cos \vartheta) \, . \tag{11.4}$$

A shellular rotation law $\overline{\Omega}(r)$ leads to fluctuations which have the above dependence in ϑ. However, taking the latitudinal dependence of $\Omega(r, \vartheta)$ into account would lead to higher order expansion in Legendre functions [386]. There, we may remark that there is no term $\widetilde{T} d\overline{S} P_2(\cos \vartheta)$ in the second expression, because $[T dS(P, \vartheta)]/d\vartheta = T\widetilde{S}[dP_2(\cos \vartheta)/d\vartheta]$. The temperature gradient is developed as follows

$$\nabla T = \nabla \overline{T} + \nabla \widetilde{T} \, P_2 \cos \vartheta + \widetilde{T} \, \nabla P_2 (\cos \vartheta)$$

$$= \varrho \left[\frac{d\overline{T}}{dP} + \frac{d\widetilde{T}}{dP} P_2 (\cos \vartheta) \right] \frac{\nabla P}{\varrho} + \widetilde{T} \, \nabla P_2 (\cos \vartheta) \, . \tag{11.5}$$

Let us consider the various terms in (11.1). To express the non-stationarity, we develop the left member as above

$$\varrho T \frac{dS}{dt} = \overline{\varrho} \, \overline{T} \frac{d\overline{S}}{dt} + \overline{\varrho} \, \overline{T} \frac{d\widetilde{S}}{dt} P_2 (\cos \vartheta) \, , \tag{11.6}$$

and note that the horizontal average in Lagrangian coordinates is the gravitational energy production (Sect. 3.3.2)

$$- \varepsilon_{\text{grav}} = \overline{T} \frac{d\overline{S}}{dt} = C_P \frac{d\overline{T}}{dt} - \frac{\delta}{\varrho} \frac{dP}{dt} \, . \tag{11.7}$$

We develop linearly the term $\nabla \cdot (\chi \nabla T)$

$$\nabla \cdot (\chi \nabla T) = \varrho \chi \left[\frac{d\overline{T}}{dP} + \frac{d\widetilde{T}}{dP} P_2 (\cos \vartheta) \right] \left[\nabla \cdot \left(\frac{\nabla P}{\varrho} \right) \right]$$

$$+ \nabla \left[\varrho \chi \left(\frac{d\overline{T}}{dP} + \frac{d\widetilde{T}}{dP} P_2 (\cos \vartheta) \right) \right] \cdot \frac{\nabla P}{\varrho}$$

$$+ \chi \widetilde{T} \nabla^2 P_2 (\cos \vartheta) + \nabla (\chi \widetilde{T}) \cdot \nabla P_2 (\cos \vartheta) \, . \tag{11.8}$$

Let us examine the term $\nabla \cdot \left(\frac{\nabla P}{\varrho} \right)$, i.e., the divergence of both gravity and centrifugal force. For the divergence of the centrifugal force, one has

$$\nabla \cdot \left(\frac{1}{2} \Omega^2 \nabla (r \sin \vartheta)^2 \right)$$

$$= \frac{1}{r^2} \frac{\partial}{\partial r} r^2 \Omega^2 r \sin^2 \vartheta + \frac{1}{r \sin \vartheta} \frac{\partial}{\partial \vartheta} \sin^2 \vartheta \Omega^2 r \cos \vartheta$$

$$= \sin^2 \vartheta \, r \frac{d\Omega^2}{dr} + 3 \sin^2 \vartheta \Omega^2 + 2 \cos^2 \vartheta \Omega^2 - \sin^2 \vartheta \Omega^2$$

$$= 2\Omega^2 + \frac{2}{3} r \frac{d\Omega^2}{dr} [1 - P_2 (\cos \vartheta)] \, . \tag{11.9}$$

We have use the fact that $\sin^2 \vartheta = \frac{2}{3} [1 - P_2 (\cos \vartheta)]$. By similarity with (2.6) in case of solid body or cylindrical rotation, we shall write here for the divergence of the centrifugal force,

$$\boldsymbol{\nabla}\left(\frac{1}{2}\,\Omega^2\,\boldsymbol{\nabla}(r\sin\vartheta)^2\right) = 2\,\overline{\Omega}^2 + 2\widetilde{\Omega}^2 P_2\,(\cos\vartheta)\;. \tag{11.10}$$

By comparing the expressions of the divergence (11.9) and (11.10), one gets the two following relations:

$$\overline{\Omega}^2 = \Omega^2 + \frac{1}{3}\,r\,\frac{d\Omega^2}{dr} \quad\text{and}\quad \widetilde{\Omega}^2 = -\frac{1}{3}\,r\,\frac{d\Omega^2}{dr}\;. \tag{11.11}$$

With Poisson's equation (Sect. 1.2.1), the divergence of the effective gravity becomes

$$\boldsymbol{\nabla}\cdot\left(\frac{\boldsymbol{\nabla}P}{\varrho}\right) = -4\,\pi\,G\varrho + 2\,\overline{\Omega}^2 + 2\,\widetilde{\Omega}^2\,P_2(\cos\vartheta)\;. \tag{11.12}$$

We now develop (11.1) putting the term $\overline{\varrho}\,\overline{\varepsilon}_{\mathrm{grav}}$ in the second member and the horizontal diffusion term on the left-hand side,

$$\overline{\varrho}\,\overline{T}\left[\frac{d\widetilde{S}}{dt} - D_{\mathrm{h}}\widetilde{S}\nabla^2\right]P_2(\cos\vartheta) = <\overline{\varrho\chi}\,\frac{d\overline{T}}{dP}\left(-4\,\pi\,G\overline{\varrho} + 2\,\overline{\Omega}^2\right)$$

$$+\overline{\varrho}\,\frac{d}{dP}\left(\overline{\varrho\chi}\,\frac{d\overline{T}}{dP}\right)\overline{g}^2 + \overline{\varrho}\,(\overline{\varepsilon} + \overline{\varepsilon}_{\mathrm{grav}}) >$$

$$+\left[\left(\widetilde{\varrho\chi}\,\frac{d\overline{T}}{dP} + \overline{\varrho\chi}\,\frac{d\widetilde{T}}{dP}\right)\left(-4\pi G\overline{\varrho} + 2\,\overline{\Omega}^2\right)\right]P_2(\cos\vartheta)$$

$$+\left[\overline{\varrho\chi}\,\frac{d\overline{T}}{dP}\left(-4\,\pi G\widetilde{\varrho} + 2\,\widetilde{\Omega}^2\right) + \overline{\varrho}\,\frac{d}{dP}\left(\overline{\varrho\chi}\,\frac{d\overline{T}}{dP}\right)2\overline{g}\,\widetilde{g}\right]P_2(\cos\vartheta)$$

$$+\left[\overline{\varrho}\,\frac{d}{dP}\left(\widetilde{\varrho\chi}\,\frac{d\overline{T}}{dP} + \overline{\varrho\chi}\,\frac{d\widetilde{T}}{dP}\right)\overline{g}^2 + \overline{\chi}\,\widetilde{T}\,\nabla^2\right]P_2(\cos\vartheta)$$

$$+\left[\widetilde{\varrho}\,\frac{d}{dP}\left(\overline{\varrho\chi}\,\frac{d\overline{T}}{dP}\right)\overline{g}^2 + \widetilde{\varrho\varepsilon}\right]P_2(\cos\vartheta)\;. \tag{11.13}$$

In this section, the quantity "g" always refers to the effective gravity, i.e., with account of the centrifugal force. The term in $\boldsymbol{\nabla}(\chi\widetilde{T})\cdot\boldsymbol{\nabla}P_2(\cos\vartheta)$ is zero since the two vectors are perpendicular. The term with $<>$ is also zero, which means that there is an average radiative equilibrium on a level surface including nuclear and gravitational energy production. However, this equilibrium is not satisfied locally at the different colatitudes. The zero of $<>$ implies

$$\overline{\varrho\chi}\,\frac{d\overline{T}}{dP}\left(-4\,\pi\,G\overline{\varrho} + 2\,\overline{\Omega}^2\right) + \overline{\varrho}(\overline{\varepsilon} + \overline{\varepsilon}_{\mathrm{grav}}) = -\overline{\varrho}\,\frac{d}{dP}\left(\overline{\varrho\chi}\,\frac{d\overline{T}}{dP}\right)\overline{g}^2\;. \tag{11.14}$$

Only the terms containing the fluctuations in $P_2(\cos\vartheta)$ are left in (11.13). One also has the following relation

$$\overline{\varrho\chi}\,\frac{d\overline{T}}{dP} = \frac{\int\!\int \overline{\chi}\,\boldsymbol{\nabla}T\cdot d\boldsymbol{\Sigma}}{\int\!\int \boldsymbol{g}\cdot d\boldsymbol{\Sigma}} = \frac{\int\!\int \overline{\chi}\,\boldsymbol{\nabla}T\cdot d\boldsymbol{\Sigma}}{\int\!\int\!\int (\nabla^2\Phi + 2\,\Omega^2)\,d\tau} = \frac{L}{4\,\pi G M_*(r)}\;. \qquad (11.15)$$

$M_*(r)$ is the reduced mass, i.e., the mass which would produce the same gravitational attraction if there would be no centrifugal force,

$$M_*(r) = M_r\left(1 - \frac{\Omega^2}{2\pi G\varrho_m}\right)\;, \qquad (11.16)$$

where ϱ_m is the mean density inside the considered level surface.

11.1.2   The Horizontal Thermal Balance

From the developed expressions of energy conservation, we can obtain some relations for the horizontal fluctuations of the various quantities. Let us examine the successive terms multiplied by $1/\overline{\varrho}$ in (11.13). The first terms after the brackets $<\,>$ leads to

$$\frac{1}{\overline{\varrho}}\left(\widetilde{\varrho\chi}\,\frac{d\overline{T}}{dP} + \overline{\varrho\chi}\,\frac{d\widetilde{T}}{dP}\right)\left(-4\pi G\overline{\varrho} + 2\,\overline{\Omega}^2\right)$$

$$= \frac{1}{\overline{\varrho}}\left[\overline{\varrho\chi}\,\frac{d\overline{T}}{dP}\left(\frac{\widetilde{\varrho\chi}}{\overline{\varrho\chi}} + \frac{d\widetilde{T}}{dT}\right)\left(-4\pi G\overline{\varrho} + 2\,\overline{\Omega}^2\right)\right]$$

$$= \frac{1}{\overline{\varrho}}\left[-\overline{\varrho}\,\frac{d}{dP}\left(\overline{\varrho\chi}\,\frac{d\overline{T}}{dP}\right)\overline{g}^2 - \overline{\varrho\varepsilon}\right]\left[\frac{\widetilde{\varrho\chi}}{\overline{\varrho\chi}} + \frac{d\widetilde{T}}{dT}\right]$$

$$= -\frac{L}{M_*}\left(1 - \frac{\overline{\Omega}^2}{2\pi G\overline{\varrho}}\right)\left[\frac{\widetilde{\varrho\chi}}{\overline{\varrho\chi}} + \frac{d\widetilde{T}}{dT}\right]\;. \qquad (11.17)$$

Then, the next terms in (11.13) gives

$$\frac{1}{\overline{\varrho}}\,\overline{\varrho\chi}\,\frac{d\overline{T}}{dP}\left(-4\pi G\widetilde{\varrho} + 2\widetilde{\Omega}^2\right)$$

$$= \frac{1}{\overline{\varrho}}\,\frac{L}{4\pi G M_*}\left[-4\pi G\widetilde{\varrho} + 2\widetilde{\Omega}^2\right] = \frac{L}{M_*}\left(-\frac{\widetilde{\varrho}}{\overline{\varrho}} + \frac{\widetilde{\Omega}^2}{2\pi G\overline{\varrho}}\right)\;. \qquad (11.18)$$

The following term (in $\overline{g}\widetilde{g}$) yields with the help of (11.15)

$$\frac{1}{\varrho}\left[\overline{\varrho}\frac{d}{dP}\left(\overline{\varrho\chi}\frac{d\overline{T}}{dP}\right)2\overline{g}\,\widetilde{g}\right] = \frac{2}{\varrho}\left[\overline{\varrho\chi}\frac{d\overline{T}}{dP}(4\pi G\overline{\varrho} - 2\overline{\Omega}^2) - \overline{\varrho}(\overline{\varepsilon} + \overline{\varepsilon}_{\mathrm{grav}})\right]\frac{\widetilde{g}}{\overline{g}}$$

$$= 2\left[\frac{L}{M_*}\left(1 - \frac{\overline{\Omega}^2}{2\pi G\overline{\varrho}}\right) - (\overline{\varepsilon} + \overline{\varepsilon}_{\mathrm{grav}})\right]\frac{\widetilde{g}}{\overline{g}}. \tag{11.19}$$

The next term (in $\overline{g}^2$) is developed as

$$\frac{d}{dP}\left(\widetilde{\varrho\chi}\frac{d\overline{T}}{dP} + \overline{\varrho\chi}\frac{d\widetilde{T}}{dP}\right)\overline{g}^2$$

$$= \overline{g}^2\widetilde{\varrho\chi}\frac{d}{dP}\left(\frac{d\overline{T}}{dP}\right)$$

$$+ \overline{g}^2\frac{d\overline{T}}{dP}\frac{d}{dP}(\widetilde{\varrho\chi}) + \overline{g}^2\overline{\varrho\chi}\frac{d}{dP}\left(\frac{d\widetilde{T}}{dP}\right) + \overline{g}^2\frac{d\widetilde{T}}{dP}\frac{d}{dP}(\overline{\varrho\chi})$$

$$= \frac{\overline{g}^2}{4\pi G}\frac{L}{M_*}\frac{d}{dP}\left(\frac{\widetilde{\varrho\chi}}{\overline{\varrho\chi}} + \frac{d\widetilde{T}}{d\overline{T}}\right) - (\overline{\varepsilon} + \overline{\varepsilon}_{\mathrm{grav}})\left(\frac{d\widetilde{T}}{d\overline{T}} + \frac{\widetilde{\varrho\chi}}{\overline{\varrho\chi}}\right)$$

$$+ \frac{L}{M_*}\left(1 - \frac{\overline{\Omega}^2}{2\pi G\overline{\varrho}}\right)\left(\frac{\widetilde{\varrho\chi}}{\overline{\varrho\chi}} + \frac{d\widetilde{T}}{d\overline{T}}\right). \tag{11.20}$$

The first and fourth terms in this expression cancel with two terms in (11.17). Let us now examine the term in ∇^2,

$$\frac{\overline{\chi}\widetilde{T}}{\overline{\varrho}}\nabla^2 P_2(\cos\vartheta) = \frac{\overline{\chi}\widetilde{T}}{\overline{\varrho}}\frac{1}{2}\frac{1}{r^2}\frac{1}{\sin\vartheta}\frac{\partial}{\partial\vartheta}\left[\sin\vartheta\frac{\partial}{\partial\vartheta}(3\cos^2\vartheta - 1)\right]$$

$$= -\frac{\overline{\chi}\widetilde{T}}{\overline{\varrho}}\frac{6}{2r^2}\left[2\cos^2\vartheta - \sin^2\vartheta\right] = -6\frac{\overline{\chi}\widetilde{T}}{\overline{\varrho}r^2}P_2(\cos\vartheta) \tag{11.21}$$

The next term was found by Urpin et al. [586], it is

$$\frac{\widetilde{\varrho}}{\overline{\varrho}}\frac{d}{dP}\left(\overline{\varrho\chi}\frac{d\overline{T}}{dP}\right)\overline{g}^2 = -\frac{\widetilde{\varrho}}{\overline{\varrho}}\frac{\overline{\varrho\chi}}{\overline{\varrho}}\frac{d\overline{T}}{dP}\left(-4\pi G\overline{\varrho} + 2\overline{\Omega}^2\right) - \frac{\widetilde{\varrho}}{\overline{\varrho}}(\overline{\varepsilon} + \overline{\varepsilon}_{\mathrm{grav}})$$

$$= \frac{\widetilde{\varrho}}{\overline{\varrho}}\frac{L}{M_*}\left(1 - \frac{\overline{\Omega}^2}{2\pi G\overline{\varrho}}\right) - \frac{\widetilde{\varrho}}{\overline{\varrho}}(\overline{\varepsilon} + \overline{\varepsilon}_{\mathrm{grav}}). \tag{11.22}$$

Collecting the various terms which depend on $P_2(\cos\vartheta)$ in (11.13), we can write the horizontal components of the equation of energy conservation,

$$\overline{T}\left[\frac{d\widetilde{S}}{dt}+D_{\mathrm{h}}\frac{6}{r^2}\widetilde{S}\right]$$

$$=2\left[\frac{L}{M_*}\left(1-\frac{\overline{\Omega}^2}{2\pi G\overline{\varrho}}\right)-(\overline{\varepsilon}+\overline{\varepsilon}_{\mathrm{grav}})\right]\frac{\widetilde{g}}{\overline{g}}+\frac{L}{M_*}\frac{\widetilde{\Omega^2}}{2\pi G\overline{\varrho}}$$

$$+\frac{\overline{g}^2}{4\pi G}\frac{L}{M_*}\frac{d}{dP}\left(\frac{d\widetilde{T}}{d\overline{T}}+\frac{\overline{\varrho}\widetilde{\chi}}{\varrho\chi}\right)-(\overline{\varepsilon}+\overline{\varepsilon}_{\mathrm{grav}})\left(\frac{d\widetilde{T}}{d\overline{T}}+\frac{\overline{\varrho}\widetilde{\chi}}{\varrho\chi}\right)$$

$$+\frac{\widetilde{\varrho}\,\overline{\varepsilon}}{\overline{\varrho}}-\frac{\widetilde{\varrho}(\overline{\varepsilon}+\overline{\varepsilon}_{\mathrm{grav}})}{\overline{\varrho}}-\frac{6\widetilde{\chi}\overline{T}}{r^2\overline{\varrho}}-\frac{L}{M_*}\frac{\overline{\Omega}^2}{2\pi G\overline{\varrho}}\frac{\widetilde{\varrho}}{\overline{\varrho}}\,. \tag{11.23}$$

The last term (in $\widetilde{\varrho}/\overline{\varrho}$) must not be neglected, although it is smaller by a factor $\overline{\Omega}^2/(2\pi G\overline{\varrho})$ than the other terms, because it may become large near the surface. Only the term with the large square parenthesis in the second member of (11.23) is present in a barotropic star (i.e., a star where surfaces of constant ϱ, P and gravity coincide). The new terms for baroclinic stars were first found by Zahn [632] and complemented in [372]. Below we shall replace the derivative (d/dP) by $-1/(\overline{\varrho}\overline{g})\,(d/dr)$ using the equation of hydrostatic equilibrium, g being the effective gravity.

The heat deposition by circulation currents is accounted for in the system of equations, while the heating due to viscous friction on meridional currents is considered as negligible. The horizontal heat transport by horizontal turbulence is important and is included here.

11.2 Some Properties of Baroclinic Stars

One needs to express the fluctuations of various quantities such as $\widetilde{\varrho}, \widetilde{g}, \widetilde{T}, \widetilde{\mu}$, etc. and the relations between them. In a star in solid body or cylindrical rotation, the centrifugal force can be derived from a potential. The pressure, temperature and density are constant on equipotentials (cf. Sect. 2.1.2). The star is barotropic. In differential rotation, this is no longer the case. The average structure can be described in terms of isobars, however the density and temperature vary on isobars (cf. Fig. 11.1). The stars are said baroclinic.

11.2.1 The Fluctuations of T, μ, ε and χ

To establish the relations between the fluctuations of the different quantities, let us introduce some new variables, namely
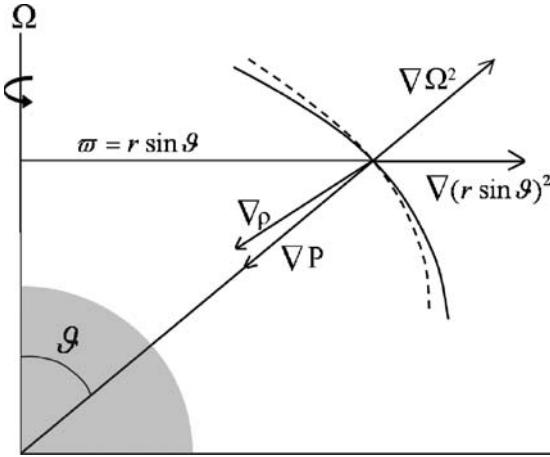
Fig. 11.1 In a star with shellular rotation, the surfaces of equal density (*dashed line*) and pressure (isobar, *continuous line*) do not coincide. The star is baroclinic. The gradient of density has a horizontal component (i.e. on the isobar) and the same for the T gradient. Adapted from Zahn [632]

$$\Theta = \frac{\widetilde{\varrho}}{\varrho} \quad \text{and} \quad \Lambda = \frac{\widetilde{\mu}}{\mu} \,. \tag{11.24}$$

From the general equation of state (7.169) at constant pressure, one has

$$\frac{\widetilde{\varrho}}{\varrho} = -\delta \frac{\widetilde{T}}{T} + \varphi \frac{\widetilde{\mu}}{\mu} \quad \text{or} \quad \varphi \Lambda - \delta \frac{\widetilde{T}}{T} = \Theta \,, \tag{11.25}$$

which relate the horizontal fluctuations of μ, T and ϱ on an isobar.

One writes a diffusion equation for X_i of the form (10.30), with account of circulation to obtain a constraint on Λ. We develop X_i up to the 2nd Legendre polynomial and account that the horizontal turbulence is much larger than the vertical one (Sect. 12.1). This gives [104]

$$\varrho \frac{\partial X_i'}{\partial t} + \varrho \, U_r \frac{\partial \overline{X}_i}{\partial r} = \frac{1}{r^2 \sin \vartheta} \frac{\partial}{\partial \theta} \left(D_\mathrm{h} \varrho \sin \vartheta \frac{\partial X_i'}{\partial \vartheta} \right) \,, \tag{11.26}$$

$$\text{with} \quad U_r = U_2(r) \, P_2(\cos \vartheta) \,, \quad X_i' = \widetilde{X}_i(r) \, P_2(\cos \vartheta) \,, \tag{11.27}$$

$\overline{X}_i$ being the average on the level surface. Such developments are necessary to express the parameter Λ in Sect. 11.3. We note another subtlety: in order to neglect D_v with respect to D_h, one also needs that $(\partial/\partial r)|D_\mathrm{v}|$ is small with respect to $(1/r)|D_\mathrm{h}|$ [386]. Here we identify the isobars with spherical shells, thus one must not consider too fast rotation velocities. We ignore the variations of ϱ and D_h with ϑ and the equation becomes,

$$\left(\frac{\partial \widetilde{X}_i}{\partial t} + U_2(r)\frac{\partial \overline{X}_i}{\partial r}\right) P_2(\cos\vartheta) = D_{\mathrm{h}}\widetilde{X}_i \nabla^2_\vartheta (P_2(\cos\vartheta)) . \tag{11.28}$$

With $\nabla^2_\vartheta [P_2(\cos\vartheta)] = -(6/r^2) P_2(\cos\vartheta)$, where $P_2(\cos\vartheta)$ is the second Legendre's polynomial, one obtains

$$\frac{\partial \widetilde{X}_i}{\partial t} + U_2(r)\frac{\partial \overline{X}_i}{\partial r} = -\frac{6}{r^2} D_{\mathrm{h}}\widetilde{X}_i . \tag{11.29}$$

The inverse of the mean molecular weight is a linear function of the mass fraction X_i (7.34) and one has likewise

$$\frac{\partial \widetilde{\mu}}{\partial t} + U_2(r)\frac{\partial \overline{\mu}}{\partial r} = -\frac{6}{r^2} D_{\mathrm{h}}\widetilde{\mu} . \tag{11.30}$$

For the relative fluctuations $\Lambda = \widetilde{\mu}/\mu$, one obtains

$$\frac{\partial \Lambda}{\partial t} = \frac{U_2(r)}{H_P}\nabla_\mu - \frac{6}{r^2} D_{\mathrm{h}}\Lambda , \tag{11.31}$$

with $\nabla_\mu = d\ln\overline{\mu}/d\ln P$ and H_P the pressure scale height (5.24). In a stationary situation, one has

$$\Lambda = \frac{r^2 U_2(r)\nabla_\mu}{6 H_P D_{\mathrm{h}}} . \tag{11.32}$$

This relates the horizontal fluctuations of μ to the vertical μ gradient for given horizontal turbulence and vertical velocity. We see that for a larger horizontal turbulence, the chemical fluctuations on an isobar are smaller, while a larger vertical velocity creates chemical inhomogeneities on the level surfaces.

There are several expressions for the coefficient of horizontal turbulence (see Sect. 12.1). For example, if it is proportional to the velocity of circulation like $D_{\mathrm{h}} \approx C_{\mathrm{h}} r U_2(r)$ [104], where C_{h} is of the order of unity, one gets

$$\Lambda \approx \frac{r\nabla_\mu}{6 C_{\mathrm{h}} H_P} . \tag{11.33}$$

If so, the amplitude of the horizontal fluctuations is a fraction of the vertical gradient of composition, in a way which does not depend on rotation to the first order. The reason is that, in this case, rotation increases the vertical and horizontal motions in the same way.

11.2.1.1   The Fluctuations of Radiative Conductivity and Nuclear Rates

The radiative conductivity χ and the nuclear energy generation rates ε also show horizontal fluctuations. We now develop horizontally the radiative conductivity χ and the nuclear energy generation rate,

$$\frac{\widetilde{\chi}}{\chi} = -\chi_T \frac{\widetilde{T}}{T} + \chi_\mu \frac{\widetilde{\mu}}{\mu} = -\chi_T \frac{\Theta}{\delta} + \Lambda \left(\chi_\mu + \frac{\varphi}{\delta} \chi_T \right) \tag{11.34}$$

$$\text{and} \quad \frac{M}{L} \frac{\widetilde{\varrho \varepsilon}}{\overline{\varrho}} = \frac{\overline{\varepsilon}}{\varepsilon_m} \left[\varepsilon_T \frac{\widetilde{T}}{T} + \varepsilon_\mu \frac{\widetilde{\mu}}{\mu} \right] + \frac{\overline{\varepsilon}}{\varepsilon_m} \frac{\widetilde{\varrho}}{\overline{\varrho}}$$

$$= \frac{\overline{\varepsilon}}{\varepsilon_m} \left[\Theta \left(1 - \frac{\varepsilon_T}{\delta} \right) + \Lambda \left(\frac{\varphi}{\delta} \varepsilon_T + \varepsilon_\mu \right) \right] , \tag{11.35}$$

where we have used (11.25). The quantity $\varepsilon_m(r) = L(r)/M(r)$ is the sum of nuclear and gravitational energy produced with radius r. The quantities with an index are logarithmic derivatives

$$\chi_T = \left(\frac{\partial \ln \chi}{\partial \ln T} \right)_{P,\mu} , \quad \chi_\mu = \left(\frac{\partial \ln \chi}{\partial \ln \mu} \right)_{P,T} , \tag{11.36}$$

$$\varepsilon_T = \left(\frac{\partial \ln \varepsilon}{\partial \ln T} \right)_{P,\mu} , \quad \varepsilon_\mu = \left(\frac{\partial \ln \varepsilon}{\partial \ln \mu} \right)_{P,T} . \tag{11.37}$$

11.2.2 The Baroclinic Equation

In shellular rotation, all quantities other than P vary in latitude on an isobar. We have found relations between the fluctuations of T, μ and the density fluctuations Θ. One needs now a relation between the density fluctuations and their physical cause, i.e., the amount of differential rotation. Following Zahn [632], one takes the *curl* of (2.1) for hydrostatic equilibrium

$$- \frac{1}{\varrho^2} \boldsymbol{\nabla} \varrho \times \boldsymbol{\nabla} P = -\frac{1}{\varrho} \boldsymbol{\nabla} \varrho \times \boldsymbol{g} = \frac{1}{2} \boldsymbol{\nabla} \Omega^2 \times \boldsymbol{\nabla} (r \sin \vartheta)^2 , \tag{11.38}$$

since $\boldsymbol{\nabla} \times \boldsymbol{\nabla} \Phi = 0$, which means that in $\boldsymbol{\nabla} \varrho \times \boldsymbol{g}$ the main vector components are parallel and do not contribute to the product ($\boldsymbol{g}$ is here the effective gravity). This is the *curl* of Euler's equation (1.4) where the meridian dynamical terms are neglected, this is the so-called "thermal wind equation" used in meteorology. It expresses the baroclinicity of the models. By dividing it by the norms of the vectors, it allows us to obtain the (small) angle between the vectors of effective gravity $\boldsymbol{g}$ and $\boldsymbol{\nabla} \varrho$. The above product depends on the gradient of Ω in the star. The gradient of the horizontal density component is $\widetilde{\varrho} \, dP_2(\cos \vartheta)/(r \, d\vartheta)$ and, to the first order, the first member is $\overline{g}(\widetilde{\varrho}/\overline{\varrho})(1/r)(dP_2(\cos \vartheta)/d\vartheta)\, \boldsymbol{e}_\varphi$. The vectorial product in the second member gives

$$\left[\frac{\partial \Omega^2}{\partial r} r \sin \vartheta \cos \vartheta - \frac{\partial \Omega^2}{\partial \vartheta} \sin^2 \vartheta \right] \boldsymbol{e}_\varphi , \tag{11.39}$$

where e_φ is the vector perpendicular to the meridional plane. We may identify the main terms in (11.38). Consistently in the shellular model, one may to the first order ignore the variation of Ω with ϑ. Thus, one has

$$\overline{g}\,\frac{\widetilde{\varrho}}{\overline{\varrho}}\,\frac{1}{r}\,\frac{dP_2(\cos\vartheta)}{d\vartheta} = -\frac{d\Omega^2}{dr}\,r\sin\vartheta\cos\vartheta\,, \qquad (11.40)$$

which then gives the baroclinic equation [632],

$$\Theta = \frac{\widetilde{\varrho}}{\overline{\varrho}} = \frac{1}{3}\,\frac{r^2}{\overline{g}}\,\frac{d\Omega^2}{dr}\,. \qquad (11.41)$$

With (11.11), one may write

$$\overline{\Omega}^2 = \Omega^2 + \frac{\overline{g}}{r}\,\Theta \quad\text{and}\quad \widetilde{\Omega}^2 = -\frac{\overline{g}}{r}\,\Theta\,, \qquad (11.42)$$

which relates the horizontal fluctuations of density to the deviations from the hypothesis of shellular rotation.

11.2.3 The Horizontal Fluctuations of Effective Gravity

In expression (11.23), essential for finding the circulation velocity, the relative fluctuations $\widetilde{g}/\overline{g}$ represent the main driving term. This is the ratio of the horizontal component of the effective gravity to the average effective gravity on an isobar. It is clear that this ratio is of the order of the centrifugal force to gravitational acceleration,

$$\frac{\widetilde{g}}{\overline{g}} \approx \left(\frac{\Omega^2\,r_0^3}{GM}\right)\,. \qquad (11.43)$$

where r_0 is a radius at colatitude $\vartheta \approx 54^o$, where $P_2(\cos\vartheta) = 0$.

We want now to develop the theory up to the second Legendre polynomial (cf. Zahn [632] and earlier works by Gratton [219], Sweet [555], Öpik [449]). The way is relatively long and the reader in a hurry may jump to (11.62). The density at any point of spherical coordinate (r,ϑ) can be represented in two ways, either by expressing the departure from spherical symmetry,

$$\varrho(r,\vartheta) = \varrho_0(r) + \widehat{\varrho}(r)P_2(\cos\vartheta)\,, \qquad (11.44)$$

or by expressing the departure from an isobar,

$$\varrho(P,\vartheta) = \overline{\varrho}(P) + \widetilde{\varrho}(P)\,P_2(\cos\vartheta)\,. \qquad (11.45)$$

The pressure itself, evidently constant on an isobar, can be written in terms of its deviations from the spherical symmetry,

$$P(r, \vartheta) = P_0(r) + \widehat{P}(r_0)P_2(\cos \vartheta) \,. \tag{11.46}$$

Let us call $\zeta(r)P_2(\cos \vartheta)$ the non-spherical change of the radial coordinate r on an isobar. The pressure at point $r_0 + \zeta(r)P_2(\cos \vartheta)$ can be obtained by developing (11.46) near r_0,

$$P[r_0 + \zeta(r)P_2(\cos \vartheta), \vartheta] = P_0(r_0) + \underbrace{\zeta \frac{dP_0}{dr} P_2(\cos \vartheta)}_{=0} + \widehat{P}(r_0)P_2(\cos \vartheta). \tag{11.47}$$

P being constant on an isobar, we get for ζ

$$\zeta = -\frac{\widehat{P}}{(dP_0/dr)} \,. \tag{11.48}$$

The other variables can be written the same way, for example,

$$\varrho[r_0 + \zeta(r)P_2(\cos \vartheta), \vartheta] = \varrho_0(r_0) + \zeta \frac{d\varrho_0}{dr} P_2(\cos \vartheta) + \widehat{\varrho}(r)P_2(\cos \vartheta)$$

$$= \overline{\varrho}(P) \underbrace{\left(-\frac{\widehat{P}}{dP_0} dr \frac{d\varrho_0}{dr} + \widehat{\varrho}(P) \right)}_{=\widetilde{\varrho}} P_2(\cos \vartheta) \,. \tag{11.49}$$

This yields the relation between the variations of density on the sphere and on the isobar,

$$\widetilde{\varrho}(P) = \widehat{\varrho} - \widehat{P} \frac{d\varrho_0}{dP_0} \,. \tag{11.50}$$

One sets $\varrho_0(r_0) = \overline{\varrho}(P)$, which defines the mean radius r_0 of an isobar; as a matter of fact it is the radius at $P_2(\cos \vartheta) = 0$, i.e., for $\sin^2 \vartheta = 2/3$. The approximation $d\varrho_0(r_0)/dP_0 = d\overline{\varrho}/dP$ is also made.

The baroclinic equation (11.41) becomes in terms of the variations with respect to the sphere (11.50) and with account of the equation of hydrostatic equilibrium $dP_0/dr = -\varrho_0 \overline{g}$,

$$g_0 \frac{\widehat{\varrho}}{\varrho_0} + \frac{\widehat{P}}{\varrho_0^2} \frac{d\varrho_0}{dr} = \frac{r^2}{3} \frac{d\Omega^2}{dr} \,, \tag{11.51}$$

which relates the pressure and density fluctuations. The equation of hydrostatic equilibrium (2.1) in the ϑ-direction provides another relation,

$$\left[\frac{1}{\varrho}\boldsymbol{\nabla}P\right]_\vartheta = -[\boldsymbol{\nabla}\varPhi]_\vartheta + \frac{1}{2}\Omega^2\left[\boldsymbol{\nabla}(r\sin\vartheta)^2\right]_\vartheta , \tag{11.52}$$

$$\frac{1}{\varrho_0}\frac{1}{r}\widehat{P}\frac{dP_2(\cos\vartheta)}{d\vartheta} = -\frac{1}{r}\widehat{\varPhi}\frac{dP_2(\cos\vartheta)}{d\vartheta} + \Omega^2 r\sin\vartheta\cos\vartheta , \tag{11.53}$$

where $\varPhi$ is the gravitational potential as defined in Sect. 2.1.2 (sometimes the potential is defined with a different sign [632]). After simplification by the terms in ϑ, this gives

$$\frac{\widehat{P}}{\varrho_0} = -\widehat{\varPhi} - \frac{1}{3}r^2\Omega^2 . \tag{11.54}$$

The elimination of $\widehat{P}$ between (11.51) and (11.54) gives

$$g_0\widehat{\varrho} - \frac{d\varrho_0}{dr}\widehat{\varPhi} = \frac{r^2}{3}\frac{d}{dr}(\varrho_0\Omega^2) . \tag{11.55}$$

$\widehat{\varPhi}$ represents the non-spherical part of the gravitational potential. In the Roche model (Sect. 2.1.3) where one assumes a central spherical potential, $\widehat{\varPhi}$ is equal to zero. This is what we do here to estimate $\widetilde{g}/\overline{g}$. Thus, the above two equations just express the non-spherical variations of pressure and density as functions of rotation. Further conditions on the non-spherical deviations of the gravitational potential can be found in literature [632], however these deviations are finally not retained in the study of meridional circulation. They should be accounted for only at a higher order level.

The gravity on an isobar, where $r = r_0 + \zeta P_2(\cos\vartheta)$, can be developed the same way as (11.47)

$$g(P,\vartheta) = g_0(r_0) + \zeta\frac{dg_0}{dr}P_2(\cos\vartheta) + \widehat{g}P_2(\cos\vartheta) . \tag{11.56}$$

If we identify this expression with $g(P,\vartheta) = \overline{g} + \widetilde{g}P_2(\cos\vartheta)$, we have $\widetilde{g} = (dg_0/dr)\zeta + \widehat{g}$. With $\zeta = \widehat{P}/(\varrho_0 g_0)$ according to (11.48) and hydrostatic equilibrium, one obtains the following relation between the deviations of gravity with respect to the sphere and to the equipotential,

$$\widetilde{g} = \frac{dg_0}{dr}\left(\frac{\widehat{P}}{\varrho_0 g_0}\right) + \widehat{g} . \tag{11.57}$$

The non-spherical component $\widehat{g}$ of the effective gravity, i.e., the centrifugal force, can be written as (ignoring a term $d\widehat{\varPhi}/dr$ on the right)

$$\widehat{g}(r) = \frac{2}{3}\Omega^2 r . \tag{11.58}$$

At the colatitude where $P_2(cos\vartheta) = 0$, the centrifugal acceleration is anyway included in $g_0(r_0)$. At the pole the contribution of the centrifugal force in g_0 and in $\widehat{g}P_2(\cos\vartheta)$ cancel each other, so consistently there is no effect of the centrifugal force. With (11.58), $\widetilde{g}$ becomes

$$\widetilde{g}(P) = \frac{dg_0}{dr}\left(\frac{\widehat{P}}{\varrho_0\,g_0}\right) + \frac{2}{3}\Omega^2 r\,. \tag{11.59}$$

Now, we use (11.54) to eliminate the horizontal variation of pressure $\widehat{P}$ and ignoring the perturbation $\widehat{\Phi}$. We have

$$\widetilde{g}(P) = -\frac{1}{3}\frac{dg_0}{dr}\left(\frac{r^2\Omega^2}{g_0}\right) + \frac{2}{3}\Omega^2 r \tag{11.60}$$

$$\text{and}\qquad \frac{\widetilde{g}}{\overline{g}} = \frac{1}{3}\Omega^2\frac{d}{dr}\left(\frac{r^2}{g_0}\right)\,. \tag{11.61}$$

The term g_0 also includes the centrifugal force, however, if in the above equation we retain only the first order term in Ω^2, we have to set $g_0 \approx GM/r_0^2$, so that the amplitude of the relative horizontal fluctuations of the effective gravity behaves as

$$\frac{\widetilde{g}}{\overline{g}} \approx \frac{4}{3}\left(\frac{\Omega^2 r_0^3}{GM}\right)\,, \tag{11.62}$$

where r_0 is the radius in $P_2(\cos\vartheta) = 0$. This expression of $\widetilde{g}/\overline{g}$ in terms of the ratio of the centrifugal force to gravity is necessary to find the velocity of meridional circulation with the help of (11.23). As anticipated above in (11.43), it is of the order of $\Omega^2 r_0^3/(GM)$!

11.3   The Velocity of Meridional Circulation

The velocity of meridional circulation is the main quantity characterizing this effect, it is developed into two components (10.107)

$$\boldsymbol{U} = U_2(r)\,P_2(\cos\vartheta)\,\boldsymbol{e}_r + V_2(r)\frac{dP_2(\cos\vartheta)}{d\vartheta}\,\boldsymbol{e}_\vartheta\,, \tag{11.63}$$

$U_2(r)$ is the amplitude of the radial component of the meridional circulation velocity, and $V_2(r)$ is the amplitude of the horizontal component with condition (10.110) relating the two components. The first member of the equation of energy conservation (11.13) or (11.23) leads to the velocity of the circulation driven by the thermal imbalance on a level surface. Accounting only for the first order terms in the horizontal fluctuations, one has

$$\overline{T}\frac{d\widetilde{S}}{dt} = \overline{T}\frac{\partial\widetilde{S}}{\partial t} + U_2(r)\overline{T}\frac{\partial\overline{S}}{\partial r} \ . \tag{11.64}$$

Indeed, the above term $\overline{T}\frac{\partial\widetilde{S}}{\partial t}$ should be more generally $\overline{T}\left[(\partial/\partial t)\widetilde{S} + \dot{r}\widetilde{S}\right]$. For slow evolutionary phase, the term in $\dot{r}$ is generally neglected. The various developments of the physical variables χ, ε, ϱ and g introduce in expression (11.23) terms depending:

– on Ω^2, either explicitly or through $\widetilde{g}/\overline{g}$ and Θ,
– on the horizontal variations of μ expressed by Λ.

If we separate these two types of contributions, we can write (11.23) as

$$\overline{T}\left[\frac{d\widetilde{S}}{dt} + D_{\mathrm{h}}\frac{6}{r^2}\widetilde{S}\right] = \frac{L}{M_*}\left(E_\Omega^* + E_\mu\right) \ . \tag{11.65}$$

There is an asterisk attached to E_Ω^* because this form will be further modified below. Let us call $f_\varepsilon = \overline{\varepsilon}/(\overline{\varepsilon} + \overline{\varepsilon}_{\mathrm{grav}})$, H_T the temperature scale height $H_T = -\overline{T}\,dr/d\overline{T}$, ϱ_m is average density inside mass coordinate M_r. The term depending on Ω is

$$
\begin{aligned}
E_\Omega^* = {} & 2\left[1 - \frac{\overline{\Omega^2}}{2\pi G\overline{\varrho}} - \frac{(\overline{\varepsilon} + \overline{\varepsilon}_{\mathrm{grav}})}{\varepsilon_m}\right]\frac{\widetilde{g}}{\overline{g}} \\[2mm]
& - \frac{\varrho_m}{\overline{\varrho}}\left\{\frac{r}{3}\frac{d}{dr}\left[H_T\frac{d}{dr}\left(\frac{\Theta}{\delta}\right) - \frac{\chi_T}{\delta}\Theta + \Theta\left(1 - \frac{1}{\delta}\right)\right] - \frac{2H_T\Theta}{r\delta} + \frac{2}{3}\Theta\right\} \\[2mm]
& - \frac{(\overline{\varepsilon} + \overline{\varepsilon}_{\mathrm{grav}})}{\varepsilon_m}\left\{H_T\frac{d}{dr}\left(\frac{\Theta}{\delta}\right) + \frac{\Theta}{\delta}(f_\varepsilon\varepsilon_T - \chi_T) + \Theta\left(2 - f_\varepsilon - \frac{1}{\delta}\right)\right\} \\[2mm]
& - \Theta\frac{\overline{\Omega^2}}{2\pi G\overline{\varrho}} \ .
\end{aligned}
\tag{11.66}
$$

The last term results from (11.22). In the case of uniform rotation, the quantity Θ defined by (11.41) is zero and only the first term in $\widetilde{g}/\overline{g}$ remains in E_Ω^*. This term is then positive, which means that the circulation (11.63) is going up along the polar axis and descending along the equatorial plane, a pattern which transports the angular momentum inward, as illustrated by the inner loop of Figs. 11.2 and 11.3. Close to the surface, the term $\overline{\Omega^2}/(2\pi G\overline{\varrho})$ becomes important and may change the sign of circulation as first pointed out by Gratton [219] and Öpik [449]. This produces an outer circulation cell turning in the opposite direction and which makes an outward transport of angular momentum. We call this outer cell the Gratton–Öpik circulation cell. It plays an important role in stellar evolution by pumping angular momentum in the interior and increasing the surface rotation. Conversely, the absence of this cell in low metallicity models [410] produces a high differential rotation during MS evolution, which favors a large mixing of chemical elements.
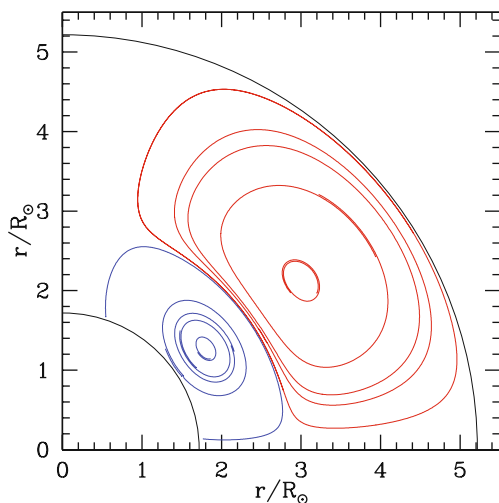
Fig. 11.2 Circulation currents in a 20 $M_\odot$ star in the middle of the H-burning phase. The initial rotation velocity is 300 km/s. The inner loop is raising along the polar axis, while the outer loop, the Gratton–Öpik circulation cell, is going up in the equatorial plane. Courtesy by G. Meynet
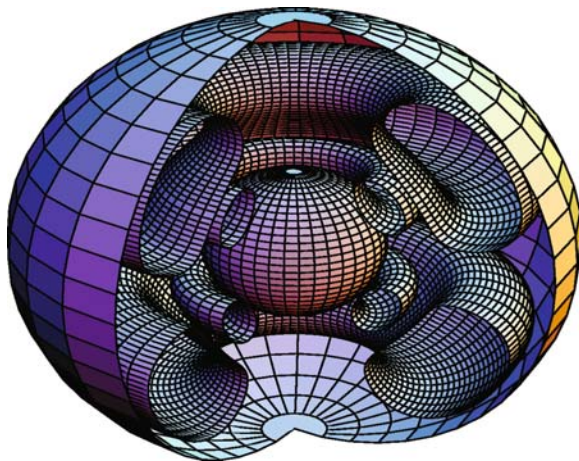
Fig. 11.3 Schematic structure with stream lines of meridional circulation in a rotating 20 $M_\odot$ model of 5.2 $R_\odot$ with $Y = 0.30$, $Z = 0.02$ and $v_{ini} = 300$ km s^{-1} at the beginning of the MS phase. The figure is made as a function of M_r. In the upper hemisphere on the right section, matter is turning counterclockwise along the outer stream line and clockwise along the inner one. The inner sphere is the convective core. It has a radius of 1.7 $R_\odot$. From Meynet & the author [410]

The term $-\varrho_m/\overline{\varrho}\{\ldots[\ldots]\}$ is positive, the dependence in $1/\overline{\varrho}$ makes it larger in the outer layers. It is generally the dominant one (apart from the term in $\widetilde{g}/\overline{g}$), due to the derivatives of Θ. The second and third terms in $-\varrho_m/\overline{\varrho}\{\ldots\}$ can be significant near the surface. Terms in $-\frac{\overline{\varepsilon}}{\varepsilon_m}$ are negligible in general, as well as the last one.

The term E_μ depending on the μ variations is given by

$$
E_\mu = \frac{\varrho_m}{\overline{\varrho}}\left\{\frac{r}{3}\frac{d}{dr}\left[H_T\frac{d}{dr}\left(\frac{\varphi}{\delta}\Lambda\right) - \left(\chi_\mu + \frac{\varphi}{\delta}\chi_T + \frac{\varphi}{\delta}\right)\Lambda\right] - \frac{2H_T}{r}\frac{\varphi}{\delta}\Lambda\right\}
$$

$$
+ \frac{\overline{\varepsilon}+\overline{\varepsilon}_{\mathrm{grav}}}{\varepsilon_m}\left\{H_T\frac{d}{dr}\left(\frac{\varphi\Lambda}{\delta}\right) + \Lambda\left(f_\varepsilon\varepsilon_\mu + f_\varepsilon\frac{\varphi}{\delta}\varepsilon_T - \chi_\mu - \frac{\varphi}{\delta}\chi_T - \frac{\varphi}{\delta}\right)\Lambda\right\}.
$$

$$\tag{11.67}$$

The term E_μ is different from zero only in regions where there is a μ gradient as shown by (11.32), it also implies the second and third derivatives of μ, which shows the need to accurately describe the μ profile in stellar interiors. E_μ is significant in regions surrounding the convective core, when there is one, and in the center of solar-type stars.

Let us now turn to the first member of (11.65) and express the entropy. In a medium of varying composition, the entropy of mixing must be taken into account (Appendix C.4). If we approximate the stellar matter by a mixture of H and He with a fixed abundance of heavy elements, the complete expression of the entropy may be written (C.47) as,

$$
dS = C_P\left[\frac{dT}{T} - \nabla_{\mathrm{ad}}\frac{dP}{P} + \Phi\frac{d\mu}{\mu}\right].
$$

$$\tag{11.68}$$

Let us consider the horizontal fluctuations of entropy determined by $\widetilde{S}$,

$$
\widetilde{S} = C_P\left[\frac{\widetilde{T}}{\overline{T}} + \Phi\frac{\widetilde{\mu}}{\overline{\mu}}\right] = C_P\left[\left(\frac{\varphi}{\delta} + \Phi\right)\Lambda - \frac{\Theta}{\delta}\right],
$$

$$\tag{11.69}$$

because there are no pressure fluctuations on the isobar; there we have used (11.24) and (11.25). From the expression of entropy (11.68), one can write the entropy gradient in terms of the various parameters ∇ (Sect. 3.3.5),

$$
\frac{\partial\overline{S}}{\partial r} = \frac{C_P}{H_P}\left(\nabla_{\mathrm{ad}} - \nabla - \Phi\nabla_\mu\right).
$$

$$\tag{11.70}$$

with $\nabla_\mu = (d\ln\overline{\mu}/d\ln P)$, (3.79). Now, we may write (11.65) with (11.69) and (11.70).

$$C_P \overline{T} \left(\frac{\varphi}{\delta} + \Phi \right) \frac{\partial \Lambda}{\partial t} - \frac{C_P}{\delta} \overline{T} \frac{\partial \Theta}{\partial t} + U_2(r) \frac{C_P}{H_P} \overline{T} \left(\nabla_{\mathrm{ad}} - \nabla - \Phi \nabla_\mu \right)$$

$$= \frac{L}{M_*} \left(E_\Omega^* + E_\mu \right) - \frac{6}{r^2} D_{\mathrm{h}} C_P \overline{T} \left(\frac{\varphi}{\delta} + \Phi \right) \Lambda + \frac{6}{r^2} D_{\mathrm{h}} C_P \overline{T} \frac{\Theta}{\delta} . \qquad (11.71)$$

Now, we eliminate $\partial \Lambda / \partial t$ with the help of (11.31) and get the final form of the equations expressing the energy conservation from (11.1) to (11.65),

$$-\frac{C_P}{\delta} \overline{T} \frac{\partial \Theta}{\partial t} + U_2(r) \frac{C_P}{H_P} \overline{T} \left(\nabla_{\mathrm{ad}} - \nabla + \frac{\varphi}{\delta} \nabla_\mu \right)$$

$$= \frac{L}{M_*} \left(E_\Omega^* + E_\mu \right) + \frac{6}{r^2} D_{\mathrm{h}} C_P \overline{T} \frac{\Theta}{\delta} = \frac{L}{M_*} \left(E_\Omega + E_\mu \right) . \qquad (11.72)$$

Care has to be given that one has not a term Φ as in (11.71), but $\varphi = (\partial \ln \varrho / \partial \ln \mu)_{P,T}$ in the first member. There E_Ω^* has been replaced by

$$E_\Omega = E_\Omega^* + \frac{2 H_T}{r} \frac{\varrho_m}{\varrho} \frac{D_{\mathrm{h}}}{K} \frac{\Theta}{\delta} . \qquad (11.73)$$

The velocity $U_2(r)$, which is the amplitude of the radial part of the circulation velocity (11.63), can be written as

$$U_2(r) = \frac{P}{\overline{\varrho g} C_P \overline{T} \left(\nabla_{\mathrm{ad}} - \nabla + \frac{\varphi}{\delta} \nabla_\mu \right)} \left[\frac{L(r)}{M_*(r)} \left(E_\Omega + E_\mu \right) + \frac{C_P}{\delta} \overline{T} \frac{\partial \Theta}{\partial t} \right] . \qquad (11.74)$$

This is the main expression characterizing the meridional circulation, also called the Eddington–Sweet circulation. The various quantities P, $\overline{T}$, $\overline{\varrho g}$, E_Ω, etc… are taken at the considered level r. The overlined terms mean the average density over the considered isobar, i.e., these are the values given by the equations of stellar structure for rotating stars (Sect. 4.1.3). The horizontal component V_2 is defined by (10.110) at each level. A positive value of $U_2(r)$ means a positive velocity, i.e., an upward current along the polar axis and an inward motion near the equatorial plane, as illustrated by the inner loop in Fig. 11.2. The system of the above equations coupled with the equations of transport of angular momentum can be solved, for example, by the Henyey method or by a generalization of the method of Newton [454]; the procedure needs care, because the system of equations is of the fourth order (see 11.81).

   Since the denominator of (11.74) contains the difference of the gradients of the Brunt–Väisälä frequency N^2, the question has arisen why there is not at the denominator of (11.74) a term N_Ω^2 as present in (6.49). Clearly, there is no such term here. The reason is that the difference of the ∇ terms arises from the density gradient, which does not explicitly depend on the Ω gradient.

11.4   Properties of Meridional Circulation

11.4.1   Simplified Expressions and Timescale

In a stationary situation, the term $\partial\Theta/\partial t$ in (11.74) is zero, one also has $\overline{\varepsilon}_{\mathrm{grav}} = 0$ and $f_\varepsilon = 1$. These simplifications apply to the MS evolution since the internal profile $\Omega(r)$ varies slowly. However, in later phases this hypothesis is not valid, since the characteristic timescale of the circulation is of the same order as the evolutionary timescale.

The case of uniform rotation. For uniform rotation, the term Θ is zero according to its definition (11.41), however E_μ depending on Λ is in general not equal to zero. One has $\Lambda = 0$ only in a region with an homogeneous composition. If so, only the driving term E_Ω is acting in the expression of the velocity $U_2(r)$ and one has

$$U_2(r) = \frac{2P}{\overline{\varrho g} C_P \overline{T} \left(\nabla_{\mathrm{ad}} - \nabla + \frac{\varphi}{\delta}\nabla_\mu\right)} \frac{L(r)}{M_*(r)} \left[1 - \frac{\overline{\Omega^2}}{2\pi G\overline{\varrho}} - \frac{(\overline{\varepsilon} + \overline{\varepsilon}_{\mathrm{grav}})}{\varepsilon_m}\right] \frac{\widetilde{g}}{g}. \tag{11.75}$$

In the case of a perfect gas, in regions without any significant energy production, this becomes with (11.62), (7.90) and (11.16)

$$U_2(r) = \frac{16}{15} \frac{L(r)\, r^2}{GM_r^2} \frac{1}{\left(\nabla_{\mathrm{ad}} - \nabla + \frac{\varphi}{\delta}\nabla_\mu\right)} \frac{\Omega^2 r^3}{GM_r}. \tag{11.76}$$

This relation is useful for estimates of order of magnitude. If radiation pressure is important, the above expression is modified with (3.98) and (7.90),

$$U_2(r) = \frac{16}{9} \frac{\beta}{(32/3) - 8\beta - \beta^2} \frac{L(r)\, r^2}{GM_r^2} \frac{1}{\left(\nabla_{\mathrm{ad}} - \nabla + \frac{\varphi}{\delta}\nabla_\mu\right)} \frac{\Omega^2 r^3}{GM_r}, \tag{11.77}$$

which essentially scales with β, the ratio of gas to total pressure.

The driving term. The driving term in the square brackets in the second member of (11.74) is E_Ω. If we keep only the main terms in E_Ω, the expressions (11.66) and (11.62) show that E_Ω behaves essentially like,

$$E_\Omega \simeq \frac{8}{3} \left[1 - \frac{\Omega^2}{2\pi G\overline{\varrho}}\right] \left(\frac{\Omega^2 r^3}{GM_r}\right). \tag{11.78}$$

Circulation timescale. The circulation timescale t_{circ}, also called the Eddington–Sweet timescale t_{ES}, is of the order of the stellar radius divided by $U_2(R)$,

$$t_{\mathrm{ES}} \approx \frac{R}{U_2(R)} \approx \frac{GM^2}{LR} \frac{GM}{\Omega^2 R^3} \approx \frac{t_{\mathrm{KH}}}{\Omega^2 R^3/(GM)}. \tag{11.79}$$

where t_{KH} is the Kelvin–Helmholtz timescale (1.73). Thus, the circulation timescale is of the order of t_{KH} divided by the ratio of the centrifugal force to gravity parameter $\Omega^2 R^3/(GM)$. Thus, in rotating stars, t_{ES} is some multiple of t_{KH}.

Examples of meridional velocities are given in Figs. 11.6 and 11.8. For a 20 $M_\odot$ star with an initial velocity of 300 km s^{-1}, $t_{ES} \approx 5 \times 10^5$ yr for $U_2 = 2 \times 10^{-2}$ cm. This is much shorter than the MS lifetime (9.3×10^6 yr). This means that the transport of angular momentum by circulation is efficient during the MS phase. The transport of chemical elements is less efficient, because it is reduced by the horizontal turbulence (Sect. 11.6.1).

The behavior of $U_2(r)$ at the center and surface. Let us examine the behavior of $U_2(r)$ at the center, when there is no convective core.

$U_2(r)$ must tend toward zero at the center, otherwise matter would escape from the stellar center! In (11.74), the term $P/[C_P \overline{T} \left(\nabla_{ad} - \nabla + (\varphi/\delta)\nabla_\mu\right]$ tends toward a finite value at the center, while $L/(Mg)$ behaves as $1/r$ and diverges. Looking for the barotropic term in E_Ω, we see that the term $\widetilde{g}/g$ given by (11.61) or (11.62) becomes a constant at the center. The term $\widetilde{g}/g$ is multiplied by $f = \left(1 - \overline{\Omega^2}/(2\pi G\overline{\varrho}) - (\overline{\varepsilon} + \overline{\varepsilon}_{grav})/(\varepsilon_m)\right)$. Near the center, the term in ε tends to 1. The term $\Omega^2/(2\pi G\overline{\varrho})$ tends to a small finite value. Thus, near the center, f tends to $-\Omega_c^2/(2\pi G\varrho_c)$, while it should normally tend to zero. Numerically, this is not a problem because $U_2(r)$, even very close to the center remains limited with a very large horizontal component. Therefore, Mathis and Zahn [391] suggest for consistency to use for the first bracket term in (11.66)

$$f = \left[1 - \frac{\overline{\Omega^2}}{2\pi G\overline{\varrho}} + \frac{\Omega_c^2}{2\pi G\varrho_c} - \frac{(\overline{\varepsilon} + \overline{\varepsilon}_{grav})}{\varepsilon_m}\right], \qquad (11.80)$$

so that $U_2(r)$ tends toward zero at the center in agreement with physical considerations. Near the surface, $U_2(r)$ tends to zero according to (11.77), since at the stellar surface radiation pressure dominates (Sect. 3.6).

Behavior at the edge of convective zones. Expressions of $U_2(r)$ not containing the term ∇_μ at the denominator would predict an infinite velocity at the edge of a radiative and semiconvective zone, with an inverted circulation in a semiconvective region. Here, the solution is continuous.

Expression (11.74) formally predicts an infinite velocity at the border of a convective core defined by Ledoux criterion (5.26). However, according to (11.70) this just mean that $\partial \overline{S}/\partial r$ is zero, but the energy equation is equilibrated [391] by the term $d\widetilde{S}/dt$ in (11.65). The velocity of meridional circulation is defined by the equation of angular momentum conservation (10.122). For example, in a stationary situation, this gives (11.83), and if $\partial\Omega/\partial r = 0$ at this edge, one gets $U_2(r) \to 0$.

The order of the overall problem. The expression of $U_2(r)$ (11.74) contains through E_Ω terms up to the second derivative of Θ. Since Θ depends on the derivative of Ω, this means that $U_2(r)$ depends on the third derivative of Ω. Now, through the equation of transport of angular momentum, the evolution of Ω depends on the derivative of $U_2(r)$. Thus, on the whole the time evolution of Ω depends on the fourth derivative of Ω, i.e.,

$$t_{\mathrm{ES}} \, \frac{\partial \Omega}{\partial t} \sim R^4 \, \frac{\partial^4 \Omega}{\partial r^4} \; . \tag{11.81}$$

This means that the differences of rotation brought about by circulation enter within a time δt over a distance δr into a radiative zone with

$$\delta r \sim t^{1/4} \; . \tag{11.82}$$

which means that the progression of the differences of Ω brought about by circulation needs much more time for larger regions.

11.4.2   T and μ Excesses and Circulation Patterns

The circulation patterns play a major role on how the angular momentum is transported and thus on the evolution of rotation. Due to the high order of the system, great care has to be given about simple reasoning concerning the T and μ excesses in relation with the patterns of meridional circulation. The derivatives of Ω and μ in E_Ω and E_μ greatly influence the circulation.

Solid body rotation. For solid body rotation and also at the beginning of evolution if there is no gradient of Ω, i.e., if Θ is zero (and Λ also), there is an excess of T along the polar axis (Fig. 11.4). $U_2(r)$ is positive and matter rises along the polar axis. The effects are essentially thermal. The velocity is determined by (11.75) or (11.76). This circulation pattern, if it persists, brings matter enriched in helium along the polar axis, making a positive μ excess in regions with T excesses. The hotter lifted material will cool and thus tends to sink. The typical velocity of such motions has been discussed for the semiconvection (see 6.34). The μ currents are opposed to the driving effect of circulation. They tend to inhibit circulation and are called μ barriers.

Figure 11.4 shows the variations $\widetilde{T} P_2(\cos \vartheta)$ of temperature in the model of a 20 $M_\odot$ at the beginning of the H-burning phase (Fig. 11.3). The star is rotating like a solid body and is thus barotropic. The T excess along the polar axis makes the inner cell to rise there. This is the classical case generally considered in literature. In the outer regions, due to the lower density the Gratton–Öpik term produces an inverse circulation (Sect. 11.5).

Differential rotation. As evolution proceeds, rotation becomes differential and the star baroclinic, thus expression (11.74) of the circulation velocity $U_2(r)$ also contains terms with the derivatives of Ω. These terms originate from the horizontal fluctuations of the radiative flux. In particular, the term with the third derivative of Ω arises from the thermal diffusion of the horizontal T fluctuations, which are themselves related to the Ω gradient by (11.25). The term with the second derivative of Ω arises from the fluctuations of the radiative conductivity. The density fluctuations lead to the first derivatives (11.41). When there is differential rotation, the patterns of circulation cannot be derived by the simple above-thermal reasoning, since the fluctuations of density are now defined by the baroclinic equation (11.41).
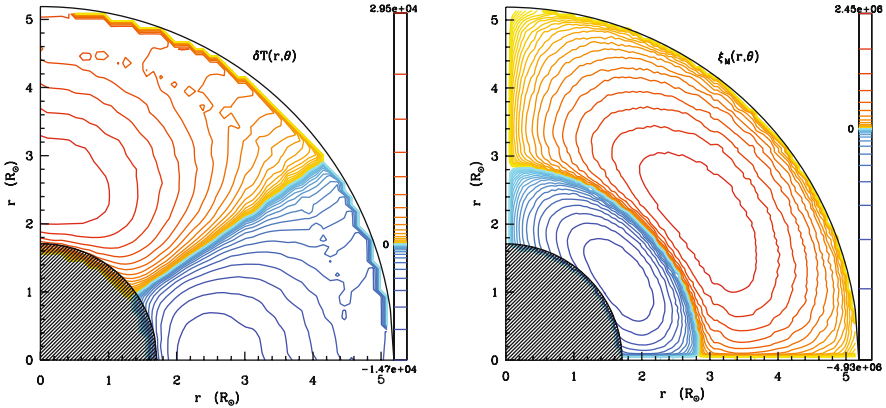
Fig. 11.4 *Left*: the fluctuations of temperature $\widetilde{T}P_2(\cos\vartheta)$ in a rotating 20 M$_\odot$ at the beginning of H burning at an age of 3.5×10^5 yr, as in Fig. 11.3. The initial velocity is 300 km s^{-1}, the composition is the standard one with $Z = 0.02$. The T excess (up to 2.95×10^4 K) is positive near the polar axis and negative (down to -1.47×10^4 K) close to the equatorial plane. *Right*: the circulation pattern in the same model, the inner circulation cell is turning clockwise, while the outer one (Gratton–Öpik cell) turns in the opposite direction. Courtesy T. Decressin [153]

Figure 11.5 shows the variations $\widetilde{T}P_2(\cos\vartheta)$ on the equipotential in a 5 M$_\odot$ star of low Z during MS evolution. The star is rotating differentially and is baroclinic. The amplitude of the fluctuations is rather large reaching $+1.8 \times 10^5$ K in the inner region closer to the polar axis and -9.1×10^4 K in the inner equatorial region. Despite the higher T near the polar axis, the density fluctuations make the matter of the large inner cell to rise in the equatorial plane and to descend along the polar axis. However, the circulation velocity is much smaller at lower Z (Fig. 11.9). The matter enriched in helium rising in the equatorial plane produces an excess of μ, while along the polar axis there is defect of μ. The outer circulation cell, due to the Gratton–Öpik effect, turns in the opposite way, i.e., is rising along the polar axis.

These examples show how different may be the circulation patterns in differentially rotating stars. In Fig. 11.5, the large inner cell takes angular momentum from the core and brings it outward, while this was the opposite in Fig. 11.4. Here, this makes the surface to rotate faster and the core slower.

The two effects of μ gradients. A gradient of the mean molecular weight μ influences the velocity of meridional circulation and in turn circulation modifies the μ gradient. A non-zero μ gradient acts in two ways:

1. A μ gradient has an effect due to the horizontal fluctuations of $\widetilde{\mu}$, which through Λ and its derivatives contribute to E_μ. As for Ω, $U_2(r)$ depends on the first four derivatives of μ and is thus very sensitive to the μ profile. In the simple barotropic case, the μ term is opposed to the main driving term, making the so-called μ currents studied by Mestel [400].
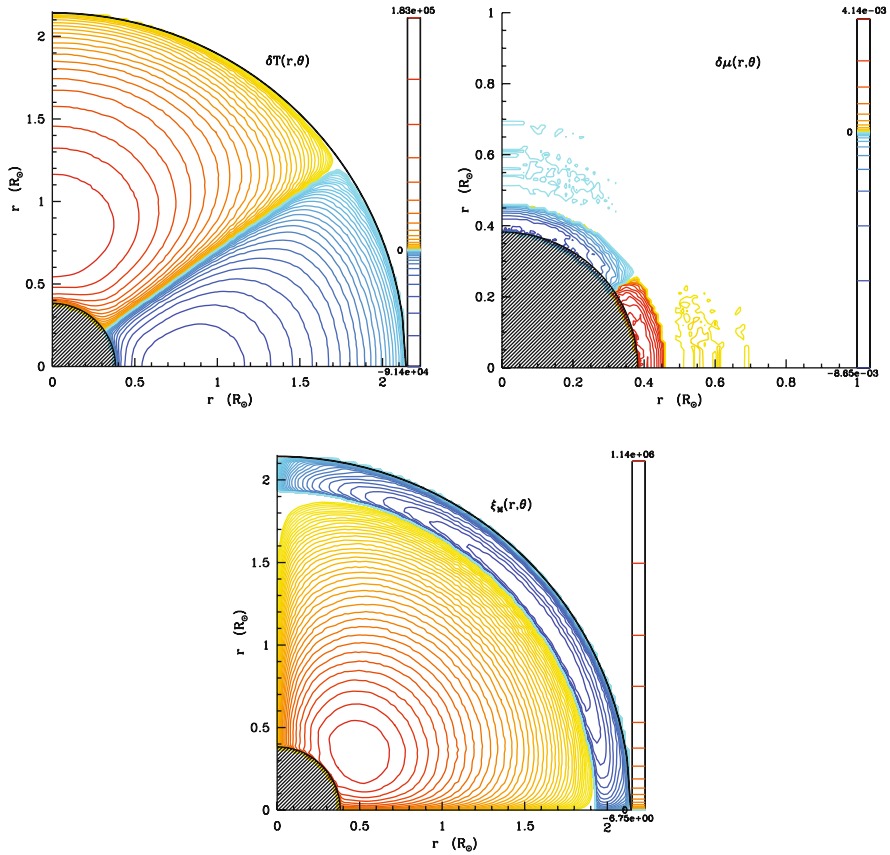
Fig. 11.5 The T excesses $\widetilde{T} P_2(\cos\vartheta)$, μ excesses $\widetilde{\mu} P_2(\cos\vartheta)$ and circulation currents in a 5 M$_\odot$ star with $Z = 0.0005$, $v_{ini} = 300$ km s^{-1}, an age of 3.45×10^7 yr and $X_c = 0.53$. The inner cell turns counterclockwise and the external clockwise. The T excesses $= +1.8 \times 10^5$ K in the interior close to the polar axis and -9.1×10^4 K in the inner equatorial region, they are smaller near the surface. μ excesses only occur close to the core, they are positive near the equator, consistently with the rotation of the inner cell. Courtesy T. Decressing [153]

2. The other way in which the μ gradient intervenes is through the term $\nabla\mu$ at the denominator of (11.74). Curiously this essential term was generally ignored. Its origin is interesting [372]. It comes from the horizontal fluctuations $\widetilde{S}$ of entropy in (11.65), which depend on $\widetilde{T}$ and $\widetilde{\mu}$ through the equation of state. The horizontal fluctuations of μ themselves depend on the vertical gradient $\nabla\mu$ through the transport of μ variations (11.31).

The result for the velocity (11.74) does not explicitly depend on D_h, apart from the additive term in the second member of (11.73). The role of the horizontal turbulence is essential because it prevents the fluctuations $\widetilde{\mu}$ to be large and allows a linear treatment. The meridional circulation is insensitive to the dependence of

entropy on the chemical composition expressed by the coefficient Φ. A term Φ is only remaining in the expression of $\overline{\varepsilon}_{\mathrm{grav}}$ derived from (3.67).

11.5   The Major Role of the Gratton–Öpik Term

The noticeable term $\left(1 - (\overline{\Omega^2}/2\pi G\overline{\varrho})\right)$ in (11.66) is the Gratton–Öpik term, which is important in the outer layers. The Gratton–Öpik term was often neglected in the expression of the velocity of the meridional circulation, because it is a term in Ω^2, which itself multiplies the term $\widetilde{g}/\overline{g}$. However, the omission is not justified, because the local density on an isobar $\overline{\varrho}$ may become very small and lead to a large $\overline{\Omega^2}/(2\pi G\overline{\varrho})$ ratio, making $U_2(r)$ to change sign. Let us recall that a positive $U_2(r)$ makes the circulation going up along the polar axis and descend in the equatorial plane, thus transporting angular momentum inward. A negative $U_2(r)$ makes an outward transport of angular momentum.

The sign and size of $U_2(r)$ drastically influence stellar evolution, because the transport of angular momentum influences the steepness of the Ω gradient, which in turn may produce shears favoring the mixing of the chemical elements. Also, depending on the internal transport of angular momentum, a rotating star may evacuate more or less angular momentum, thus influencing the final rotation at the time of supernova. The Gratton–Öpik term is an important effect in stellar evolution.

11.5.1   Departure from Solid Body and Initial Ω Convergence

Let us suppose that one starts calculating the evolution and transport of rotation from a model with a constant internal Ω. The terms in Θ and Λ, which both reduce $U_2(r)$, are absent and this drives a large positive circulation velocity. Figure 11.6 shows the evolution of $\Omega(r)$ and $U_2(r)$ in a 20 M$_\odot$ star with an initial velocity of 300 km s^{-1}. The circulation velocity is positive everywhere at the beginning and has its highest value of about 2×10^{-2} cm s^{-1}. This corresponds to a characteristic time of the Eddington–Sweet circulation $t_{\mathrm{ES}} \approx R/U_2(R) \approx 5.7 \times 10^5$ yr.

As a consequence of the circulation descending in the equatorial plane and bringing angular momentum inward, the angular velocity of the stellar core increases while it decreases in the envelope. In a time of 1–2% of the MS lifetime, the $\Omega(r)$ profile converges toward an equilibrium profile characterized by a moderate differential rotation (Fig. 11.6). Simultaneously, as differential rotation increases tending toward an equilibrium profile, the amplitude of $U_2(r)$ decreases and the value of $U_2(r)$ is negative in the outer layers. This is due to the Gratton–Öpik term, which is significant in low density regions and produces an inverse circulation. Thus there are two cells of meridional circulation as those illustrated in Figs. 11.4 and 11.3. As evolution proceeds, the higher derivatives of $\Omega(r)$ make the patterns more complex.
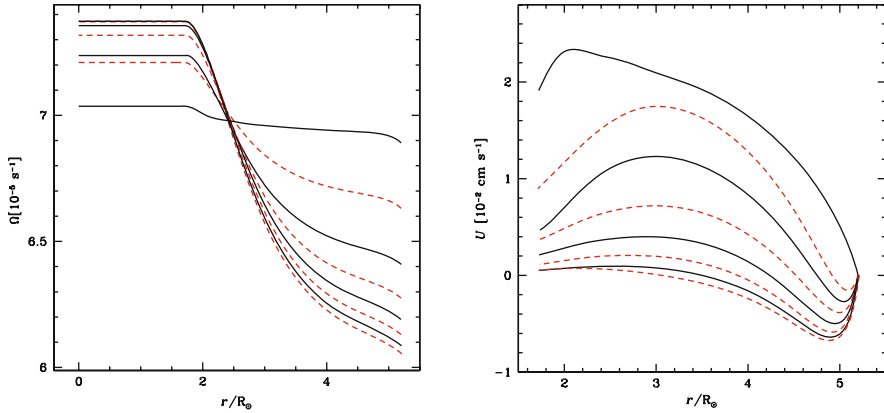
Fig. 11.6 *Left*: initial evolution of the angular velocity $\Omega(r)$ in a 20 $M_\odot$ star with $v_{\mathrm{ini}} = 300$ km s^{-1} (standard abundance). Starting from a nearly flat profile, the solutions rapidly converge toward an equilibrium profile of differential rotation. The time interval between two consecutive curves is 19200 years. *Right*: $U_2(r)$ the vertical component of the meridional circulation velocity. Time proceeds from top to bottom. From Meynet and the author [409]

11.5.2   Stationary Circulation in Equilibrium with Diffusion

If the internal distribution of rotation would be perfectly stationary, the transport of angular momentum would be negligible and $\varrho \frac{\partial}{\partial t}(r^2\overline{\Omega})_{M_r} = 0$ in (10.122). This would imply that $U_2(r)$ is given by

$$U_2(r) = -5D\frac{\partial \ln \overline{\Omega}}{\partial r} \ . \tag{11.83}$$

The transport of angular momentum by meridional circulation would just compensate diffusion. If Ω decreases outward, diffusion makes an outward transport of angular momentum and circulation compensates it by an inward transport. This can only be done by positive values of $U_2(r)$, even close to zero (Fig. 11.7). The comparison of the full and stationary solutions shows results which are too much different to allow the above simplification (11.83). This means that the real transport is far from stationary. The inner contraction and the outer expansion make the left-hand side of (10.122) different from zero. Although, (11.83) would be a simple way to estimate the circulation velocity, it is not advisable to apply it. In case of stellar winds, the loss of angular momentum at the surface also contributes to deviations from stationarity.

Since very small values of $U_2(r)$ are enough to make up for diffusion, one concludes that meridional circulation with its current values is much more efficient for the transport of the angular momentum than the current diffusion process by shear instability (Sect. 12.2).
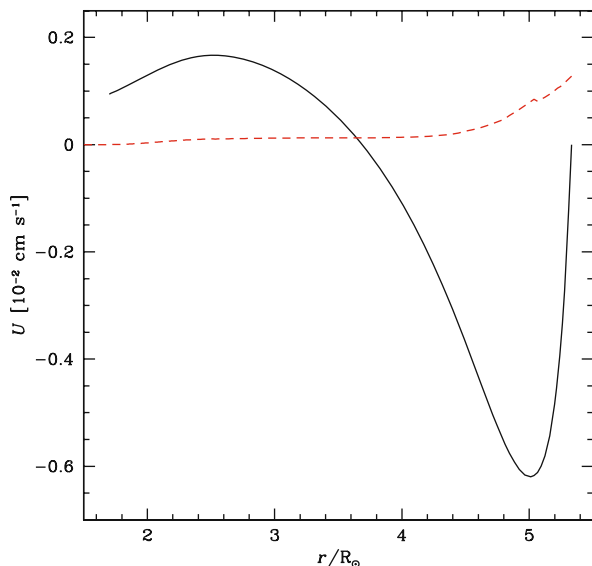
Fig. 11.7 Non-stationary (*continuous line*) and stationary (*broken line*) solutions for $U(r)$ the vertical component of the velocity of the meridional circulation (cf. 11.83) as a function of the distance to the center in a 20 $M_\odot$ model at the end of the initial convergence. From Meynet and the author [409]

11.5.3 The Gratton–Öpik Circulation and Evolution

11.5.3.1 During MS Evolution with Standard Composition

Figure 11.8 illustrate the evolution of $\Omega(r)$ and $U_2(r)$ during the MS phase of a rotating 20 $M_\odot$ star. One notices the growth of the differential rotation at the edge of the core, an effect which drives shear mixing of the chemical elements. There is a general decrease of $\Omega(r)$ during MS evolution, also for the core. This results from the mass loss by stellar winds, which remove matter with a ratio of angular momentum to mass higher than the stellar average. During most of the MS phase, the core does not rotate faster than by a factor of 2 with respect to the surface. Only at the very end of the MS phase, the fast contraction of central regions accelerates the core rotation. The transport of angular momentum is no longer governed by meridional circulation, but by the local conservation of the angular momentum. The reason is that the evolution becomes faster and there is not enough time for meridional circulation to act significantly.

The evolution of the vertical component $U_2(r)$ of the meridional circulation is shown in Fig. 11.8 right. The outer zone with negative $U_2(r)$, i.e., with circulation rising in the equatorial plane, progressively deepens during MS evolution. This is due the decrease of the density in the outer layers, which favors the Gratton–Öpik cell. The velocities become larger in the outer regions. In particular, at the very end
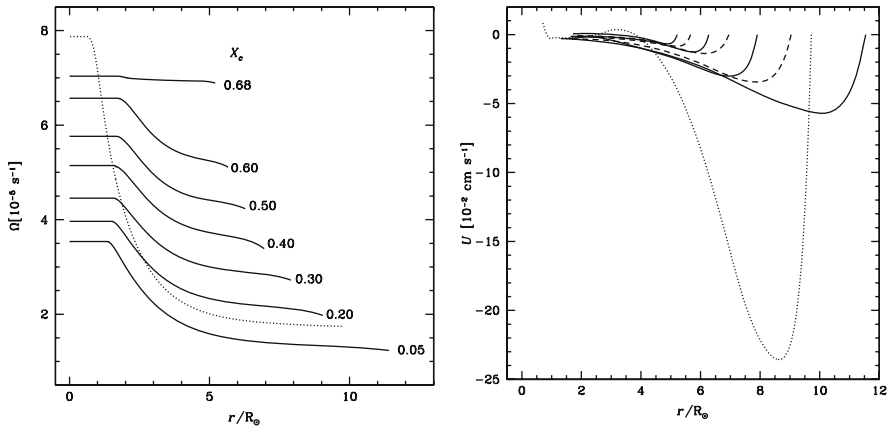
Fig. 11.8 *Left*: evolution of the angular velocity Ω as a function of the distance to the center in a 20 $M_\odot$ star with an initial velocity $v_{\text{ini}} = 300$ km s^{-1} and a standard composition with $Z = 0.020$. X_c is the hydrogen mass fraction at the center. The dotted line in both figures shows the profile when the He core contracts at the end of the H-burning phase. *Right*: the vertical component $U_2(r)$ of the velocity of meridional circulation at the same stages of the MS evolution. The negative component becomes more important at the end of the MS due to the decrease of density in the outer layers. From G. Meynet and the author [409]

of the MS phase, the velocities are about an order of magnitude larger than at the beginning. Close to the core, the velocities change from positive at the beginning of the MS phase to negative, always keeping very small values. This is mainly due to the term $\widetilde{g}/g$, which is small in the interior.

The deepening of the inverse circulation during evolution means that the difference between the stationary (11.83) and the non-stationary solutions (11.74) becomes larger and larger. This confirms that the stationary solutions must not be applied. Some authors treat meridional circulation as a diffusion process. This is not advisable, because the expressions of diffusion and advection are quite different in the equation of transport of angular momentum (10.122). In addition, since both positive and negative velocities $U_2(r)$ are present, the use of an always positive diffusion coefficient to represent meridional circulation is incorrect.

11.5.3.2   The Gratton–Öpik Cell at Very Low Metallicity

Meridional circulation is different at very low metallicity Z. The stars are more compact and thus the density remains relatively high in stellar envelopes, thus the ratio $\Omega^2/(2\pi G\overline{\varrho})$ is small, making the Gratton–Öpik term very weak. Figure 11.9 shows the evolution of $U_2(r)$ for a 20 $M_\odot$ star with $Z = 10^{-5}$. This is very different from the case at $Z = 0.02$ in Fig. 11.8. In the model at $Z = 10^{-5}$, large negative values of $U_2(r)$ are not present in the outer layers. There, $U_2(r)$ is equal to a few
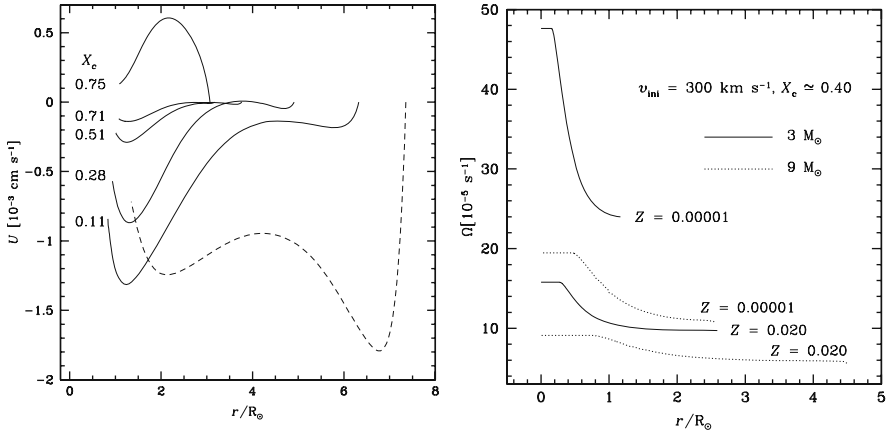
Fig. 11.9 *Left*: evolution of $U_2(r)$ the radial term of the vertical component of the velocity of meridional circulation for a model of 20 $M_\odot$ with $Z = 10^{-5}$ at various stages during the MS phase (continuous line). X_c is the hydrogen mass fraction at the center. The dashed line shows the values of $U(r)$ inside a 20 $M_\odot$ model at $Z = 0.004$ when $X_c = 0.28$. *Right*: variation of the angular velocity Ω as a function of the distance to the center in 3 and 9 $M_\odot$ star models with $v_{ini} = 300$ km s^{-1}, $Z = 0.020$ and $Z = 10^{-5}$ and $X_c \simeq 0.40$. From G. Meynet and the author [410]

-10^{-4} cm s^{-1} at the end of the MS phase, while it was 10^2–10^3 times more negative in the corresponding models at $Z = 0.02$, due to the low density in the envelope.

In the inner layers, the values of $U_2(r)$ are not very much different at $Z = 10^{-5}$ and in the case of $Z = 0.02$ (care about the different scale has to be given). Figure 11.9 also shows the curve for a model at $Z = 0.004$. In the interior, $U_2(r)$ is about the same as at $Z = 10^{-5}$ (this is true for all Z values). The external dip of $U_2(r)$ is about intermediate between that of models at $Z = 10^{-5}$ and $Z = 0.02$.

The small values of $U_2(r)$ in the external layers of models at $Z = 10^{-5}$, i.e., a lack of outward transport of angular momentum, favor a steep internal Ω gradient with a significant gradient up to the stellar surface. Figure 11.9 (right) shows that the gradient of Ω is generally much steeper at lower Z value than at standard Z. In turn, high gradients are responsible for strong chemical mixing making large surface enrichments in products of CNO burning. As a consequence, the various model properties (size of the core, lifetimes, chemical yields, final remnants) are largely influenced. This shows that meridional circulation is major ingredient of proper evolutionary models.

11.6   Meridional Circulation with Horizontal Turbulence

Meridional circulation transports both angular momentum and chemical elements. These two transports do not interact in the same way with the horizontal turbulence, which develops in differentially rotating stars. It enforces an almost constant

rotation on surface levels making Zahn's law of shellular rotation [632]. For now, we describe this horizontal turbulence by a diffusion coefficient D_h, the form of which is studied in Sect. 12.1.

The interaction of horizontal turbulence with meridional circulation considerably reduces the vertical transport of chemical elements. This is not the case for the transport of angular momentum. This is favorable in view of the observed absence of Li depletion in red giants of young clusters, while the simple theory of meridional circulation predicts a depletion [117]. Comparisons of solar models and observations [468] also suggest that circulation transports the angular momentum more efficiently than the chemicals elements.

11.6.1   Transport of the Elements

Remarkably, the combination of the transport of chemical elements by meridional circulation and horizontal turbulence is equivalent to a diffusion process [104]. Figure 11.10 illustrates this interaction. An upward advective fluid column (left) is moving up and brings elements "1" higher compared to a nearby column of fluid which does not move or moves more slowly. At each time step, the horizontal turbulence makes an average composition of the two columns in horizontal layers. Progressively, this makes a smooth vertical composition gradient connecting the two homogeneous parts "0" and "1" by half a Gaussian curve. Such a smooth composition gradient is the same as that produced by a diffusion coefficient. Below, we are searching the appropriate diffusion coefficient for this combined effect. Numerical experiments [113] confirm that the interaction of horizontal turbulence and advection makes a distribution like an error function.

Let us consider a stellar medium with large-scale circulation motions of velocity U and some diffusion processes characterized by a diffusion coefficient D, which is a tensor with vertical and horizontal components. The general equation of transport of the element "i" with mass fraction X_i is according to (10.30)

$$\varrho \frac{\partial X_i}{\partial t} + \varrho\, U \cdot \nabla X_i = \nabla \cdot (\varrho\, D\, \nabla X_i) \; . \tag{11.84}$$

Let us assume that the star does not depart much from spherical geometry and that ϱ and D are only functions of the radius r, both being constant over the layer considered. The diffusion tensor D is decomposed in a vertical term D_v and a horizontal one D_h with $D_v \ll D_h$. The abundance $X_i(r, \vartheta)$ is developed like (11.4) on a spherical shell,

$$X_i(r, \vartheta) = \overline{X}_i(r) + \widehat{X}_i(r, \vartheta) = \overline{X}_i(r) + \widetilde{X}_i(r)\, P_2\,(\cos \vartheta) \; . \tag{11.85}$$

The horizontal average of a function f is taken as the average over the stellar surface (2.23). The term $\cos \varepsilon$ appearing in the expression of the surface element

Advection   Horizontal diffusion
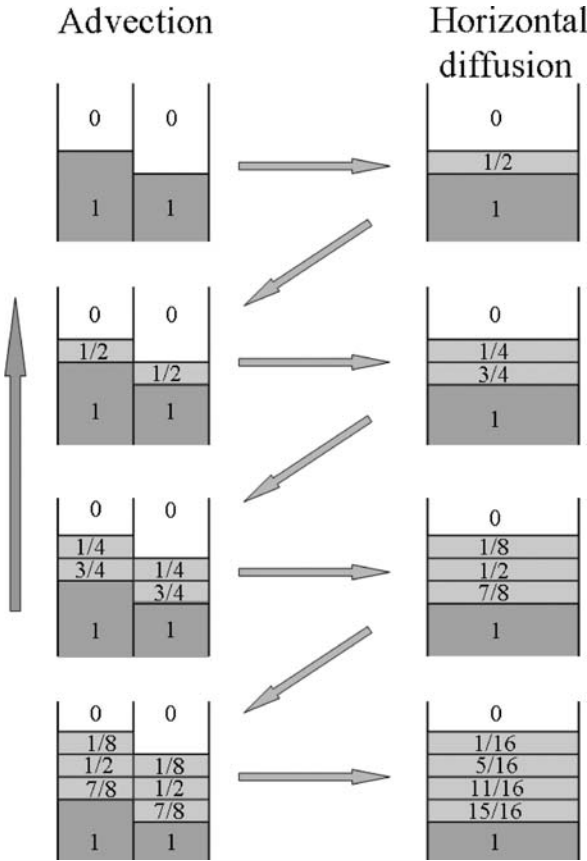
Fig. 11.10 Schematic illustration of the combination of the effects of circulation and horizontal turbulence. The very left column is moving up, at each time step the horizontal turbulence mixes the layers. This makes a distribution like the error function, showing that the combination of both motions acts as a diffusion as far as the mixing of elements is concerned. Adapted from slides by J.-P. Zahn

(2.23) is omitted and all functions are assumed axially symmetric, including the velocity $\boldsymbol{U}$,

$$< f > = \frac{1}{2} \int_0^\pi f \sin \vartheta \, d\vartheta \, , \tag{11.86}$$

With this development, (11.84) becomes

$$\varrho \frac{\partial \overline{X}_i}{\partial t} + \varrho \frac{\partial \widehat{X}_i}{\partial t} + \varrho U_r \frac{\partial \overline{X}_i}{\partial r} + \varrho \boldsymbol{U} \cdot \boldsymbol{\nabla} \widehat{X}_i = \boldsymbol{\nabla} \cdot \left(\varrho D \boldsymbol{\nabla} (\overline{X}_i + \widehat{X}_i) \right) \, . \tag{11.87}$$

where U_r is the radial component of the velocity, which is developed into Legendre polynomials (cf. 10.106)

$$U_r = \sum_{l>0} U_l(r) P_l(\cos \vartheta) \,. \tag{11.88}$$

The horizontal average of (11.87) is taken, neglecting $\partial \widehat{X}_i / \partial t$ with respect to $\partial \overline{X}_i / \partial t$. $< U_r >= 0$, thus the third term on the left may be neglected,

$$\varrho \frac{\partial \overline{X}_i}{\partial t} + \frac{1}{r^2} \frac{\partial}{\partial r} \left[r^2 \varrho < \widehat{X}_i U_r > \right] = \frac{1}{r^2} \frac{\partial}{\partial r} \left[\varrho r^2 D_v \frac{\partial \overline{X}_i}{\partial r} \right] \,. \tag{11.89}$$

There we have used the fact that $< \widehat{X}_i >= 0$ and we are left only with the vertical component D_v of the diffusion coefficient. The second term on the left results from

$$\frac{1}{r^2} \frac{\partial}{\partial r} \left[r^2 \varrho < \widehat{X}_i U_r > \right] = \varrho U_r \frac{\partial \widehat{X}_i}{\partial r} + \widehat{X}_i \underbrace{\frac{1}{r^2} \frac{\partial}{\partial r} (r^2 \varrho U_r)}_{=0} \,. \tag{11.90}$$

Here, the second term on the right is zero due to the equation of continuity, in which one assumes that ϱ is constant in the anelastic approximation. The second term on the left of (11.89) expresses the effect of the advection of the horizontal inhomogeneities on the change of the average composition with time. This is the term we want to evaluate. For that we need to know the horizontal distribution $\widehat{X}_i$ on a level surface. This distribution is the result of the advection by circulation and of the horizontal transport by diffusion. By assuming that the vertical change of the average abundance is larger than the changes of the horizontal fluctuations

$$\partial \overline{X}_i / \partial r \gg \left| \nabla \widehat{X}_i \right| \,, \tag{11.91}$$

one obtains an equation describing the horizontal transport by making the difference of expressions (11.87) – (11.89),

$$\varrho \frac{\partial \widehat{X}_i}{\partial t} + \varrho U_r \frac{\partial \overline{X}_i}{\partial r}$$

$$= \frac{1}{r^2} \frac{\partial}{\partial r} \left[r^2 \varrho D_v \frac{\partial \widehat{X}_i}{\partial r} \right] + \frac{1}{r^2 \sin \vartheta} \frac{\partial}{\partial \vartheta} \left[\varrho \sin \vartheta D_h \frac{\partial \widehat{X}_i}{\partial \vartheta} \right] \,. \tag{11.92}$$

This establishes a relation between the temporal variation of $\widehat{X}_i$, the advection of the mean composition and on the right the vertical and horizontal diffusion. We express the fact that the horizontal turbulence is much stronger than the vertical one by

$$D_h \gg D_v \frac{\ell_h^2}{\ell_v^2} \,, \tag{11.93}$$

where ℓ_h and ℓ_v are the distances over which the composition changes significantly. This means that the timescale for the horizontal diffusion is much shorter than for

the vertical diffusion. Expression (11.92) has an asymptotic solution, reached after a time $t \gg r^2/D_h$

$$\frac{r^2}{D_h} \frac{\partial \overline{X}_i}{\partial r} U_2 P_2(\cos \vartheta) = \frac{1}{\sin \vartheta} \frac{\partial}{\partial \vartheta} \left[\sin \vartheta \frac{\partial \widehat{X}_i}{\partial \vartheta} \right] . \tag{11.94}$$

The development (10.106) of the radial component U_r has been limited to the second Legendre polynomial. The second member becomes with (11.85)

$$\frac{\widetilde{X}_i}{\sin \vartheta} \frac{\partial}{\partial \vartheta} \left[\sin \vartheta \frac{\partial}{\partial \vartheta} P_2(\cos \vartheta) \right] = \frac{\widetilde{X}_i}{\sin \vartheta} \frac{\partial}{\partial \vartheta} (-3 \cos \vartheta \, \sin^2 \vartheta)$$

$$= \widetilde{X}_i \left(3 \sin^2 \vartheta - 6 \cos^2 \vartheta \right) = -6 \widetilde{X}_i P_2(\cos \vartheta) . \tag{11.95}$$

The asymptotic solution for the horizontal fluctuation is

$$\widetilde{X}_i = -\frac{r^2}{D_h} \frac{\partial \overline{X}_i}{\partial r} \frac{U_2}{6} . \tag{11.96}$$

One may now calculate the advection of the horizontal inhomogeneous distribution described by the term $< \widehat{X}_i(r, \vartheta) U_r >$ in (11.89),

$$< \widehat{X}_i(r, \vartheta) U_r >= \frac{1}{2} \int_0^\pi \widehat{X}_i(r, \vartheta) U_r \sin \vartheta d\vartheta$$

$$= -\frac{r^2}{D_h} \frac{\partial \overline{X}_i}{\partial r} \frac{U_2^2}{12} \int_0^\pi [P_2(\cos \vartheta)]^2 \sin \vartheta d\vartheta . \tag{11.97}$$

Thus, equation (11.89) for the horizontal average can be written

$$\varrho \frac{\partial \overline{X}_i}{\partial t} = \frac{1}{r^2} \frac{\partial}{\partial r} \left[\varrho \, r^2 \, (D_v + D_{eff}) \frac{\partial \overline{X}_i}{\partial r} \right] . \tag{11.98}$$

The coefficient D_{eff} is thus defined by

$$D_{eff} = \frac{r^2}{D_h} \frac{U_2^2}{12} \int_0^\pi [P_2(\cos \vartheta)]^2 \sin \vartheta d\vartheta , \tag{11.99}$$

with

$$\int_0^\pi [P_2(\cos \vartheta)]^2 \sin \vartheta d\vartheta = \frac{1}{4} \int_0^\pi \left[9 \cos^4 \vartheta + 1 - 6 \cos^2 \vartheta \right] \sin \vartheta d\vartheta$$

$$\frac{1}{4} \left[\frac{18}{5} + 2 - 4 \right] = \frac{2}{5} . \tag{11.100}$$

With the other numerical factor, the effective diffusion coefficient for circulation with horizontal turbulence becomes

$$D_{\text{eff}} = \frac{(rU_2)^2}{30 D_{\text{h}}} . \tag{11.101}$$

This expression was obtained by Chaboyer and Zahn [104]. It shows that the effects of meridional circulation and horizontal turbulence on the transport of the elements (only) is equivalent to a diffusion process.

The above development implies some conditions, namely (11.91), (11.93) and the condition for steady state necessary for the asymptotic solution (11.94). These conditions mean that D_{h} must be large enough compared to meridional circulation and vertical diffusion. In no case, one must put $D_{\text{h}} \to 0$ in (11.101). For the validity of the above results, one must have

$$D_{\text{h}} \gg |rU_2(r)| . \tag{11.102}$$

This means that

$$D_{\text{eff}} \ll \frac{rU_2(r)}{30} , \tag{11.103}$$

which shows that the effective diffusion by meridional circulation in presence of horizontal turbulence is much smaller than a coefficient of the order of $D \sim \frac{1}{3} U_2(r) r$, which would apply if circulation would be alone. This confirms that the horizontal turbulence strongly inhibits the transport of the chemical elements by meridional circulation.

11.6.2 Transport of the Angular Momentum

The transport of chemical elements is governed by (10.103), which contains both advection and diffusion terms. There is a major difference between the transport of chemical elements and the transport of angular momentum. For the chemical elements, both the advection and the diffusion operate on the same quantity, i.e., the abundance X_i. For rotation, the diffusive term acts on the derivative of the angular velocity Ω, while the advective term in (10.103) acts on the angular momentum $(r\sin\vartheta)^2\Omega$. The consequence is that the horizontal diffusion favors the horizontal uniformity of Ω, while meridional circulation transports some angular momentum.

The reasoning illustrated in Fig. 11.10 cannot be applied to the effects of advection and turbulence on the transport of the angular momentum. A fluid element shifted away from the rotation axis by horizontal motions tends to go back due to the local conservation of angular momentum (cf. Rayleigh–Taylor instability, Sect. 6.4.2). This suggests that the local conservation of angular momentum limits the effect of the horizontal motions for the transport of angular momentum. One might wonder whether the horizontal turbulence itself is not limited by this effect. This is

a possibility, however turbulence may also be present without a net flux of angular momentum: the outward moving turbulent elements being compensated by inward moving ones. This leads to the suggestion [104] that the horizontal turbulence does not greatly interfere with the advection of angular momentum, if strong it maintains a shellular distribution of the angular velocity (and of the chemical elements) as nicely shown by the numerical models of Charbonneau [113] in Fig. 12.1.

Chapter 12
Rotation-Driven Instabilities

Rotation, and especially differential rotation, generates a number of instabilities. We know this on the Earth with for example the west winds, the jet streams, the many effects of the Coriolis force. On the fast rotating surface of Jupiter, we observe turbulent waves at the interface of differentially rotating zones, the Red Spot is a long-living hurricane generated by rotation, etc.

The various rotational instabilities produce some mixing of the elements and transport angular momentum in stellar interiors. We examine the instabilities specifically generated by rotation. In addition, rotation also influences the other instabilities, such as convection, semiconvection, pulsations, gravity waves, stellar winds, etc.

12.1 Horizontal Turbulence

Horizontal turbulence is generally ignored in most stellar models. Nevertheless, it has major consequences as shown by the numerical examples of Sect. 12.1.5. Turbulent motions are created by differential rotation, which makes shear instabilities between layers of different velocities. In a stable radiative zone, the turbulence is likely much stronger [632] in the horizontal direction than in the vertical one. The reason is that in the vertical direction the stable thermal gradient opposes stronger forces to the fluid motions than horizontally.

The horizontal turbulence is characterized by a coefficient of horizontal kinematic viscosity ν_h, which as usual is also the coefficient D_h of horizontal diffusion of the elements (Appendix B.4). There are some indications in favor of the horizontal turbulence, the main one comes from the study of the tachocline by Spiegel and Zahn [542]. The tachocline is the transition zone between the rigid rotation in the radiative interior and the external convective envelope, where rotation varies with latitude (see Sect. 16.6.3). If the horizontal turbulence is strong, the tachocline is very thin [542] which is in agreement with helioseismic observations. Another indication in favor of the horizontal turbulence is that the vertical transport of the chemical elements by meridional circulation needs to be reduced, while this is not the case for the transport of angular momentum (Sect. 11.6.2). This is suggested by

the observations of the abundance of Li and other light elements in the Sun and in old open star clusters in relation with their rotational velocities [102, 103]. Also, the account for horizontal turbulence brings the mixing of CNO elements by meridional circulation to a level consistent with observations in massive stars [409].

The horizontal turbulence plays an important role in several respects:

– The strong coupling due to the horizontal turbulence maintains the angular velocity Ω almost constant on isobars, which makes the rotation shellular [632] (Fig. 12.1). This rotation law brings many simplifications into the equations of stellar structure.
– It reduces the transport of the elements by meridional circulation.
– It modifies the diffusion by shears and the heat transport by circulation.
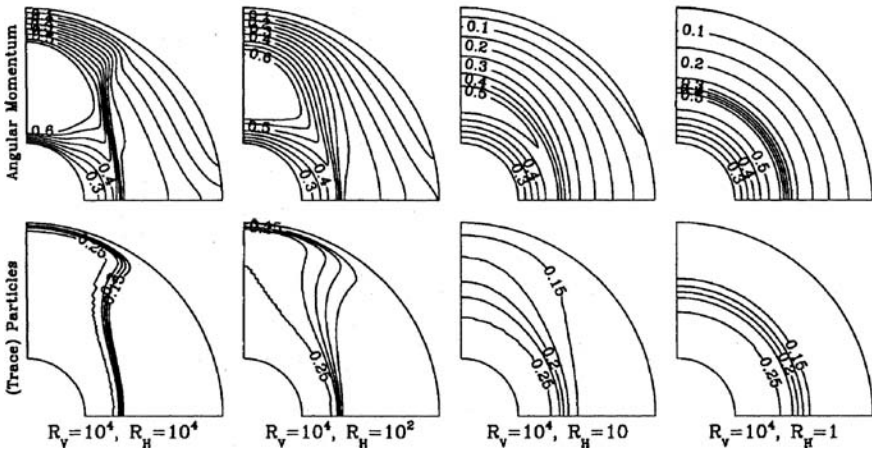
Fig. 12.1 Effects of anisotropy on the distribution of the angular velocity (*top row*) and of the chemical elements (*bottom row*). The various panels show the equilibrium situation for different values of the Reynolds numbers $R_H = UR/D_H$ from 10^4 to 1, where D_H is the coefficient of horizontal turbulence and UR expresses the vertical transport. The vertical Reynolds number $R_V = UR/D_V$ is fixed to 10^4, where D_V is the vertical diffusion. The two panels show the occurrence of 1D solutions for high horizontal turbulence. From Charbonneau [113]

The horizontal turbulence in rotating stars is a complex problem with many uncertainties. There are several approaches leading to different results for the coefficient of diffusion D_h.

12.1.1   The Horizontal Fluctuations of Ω

For the estimates of the viscosity or diffusion coefficient by horizontal turbulence, one needs first to know the amplitude Ω_2 of the horizontal fluctuations of the angular

velocity in latitude on the isobar. Following expression (B.79), one develops the angular velocity as follows

$$\Omega(r,\vartheta) = \overline{\Omega}(r) + \widehat{\Omega}(r,\vartheta) = \overline{\Omega}(r) + \Omega_2(r)\left(P_2(\vartheta) + \frac{1}{5}\right), \qquad (12.1)$$

The development of a physical variable in spherical functions does not usually contain the factor $1/5$. However, the above development of the angular velocity is the one appropriate in the Eq. (10.103) of conservation of the angular momentum. The factor $1/5$ is consistently derived in Appendix B.6.1 (see also 2.26).

In order to obtain an equation governing $\Omega_2(r)$, one takes the complete Eq. (10.103) in (r,ϑ) for the transport of the angular momentum and subtract (10.122) multiplied by $\sin^2\vartheta$ [632]. This gives

$$\frac{\partial}{\partial t}(\varrho\, r^2 \sin^2\vartheta\, \widehat{\Omega}) + \nabla\cdot(\varrho\, r^2 \sin^2\vartheta\, \overline{\Omega}\, U) + \frac{\sin^2\vartheta}{5r^2}\frac{\partial}{\partial r}(\varrho\, r^4 U_2\overline{\Omega})$$

$$= \frac{\sin^2\vartheta}{r^2}\frac{\partial}{\partial r}\left(\varrho\, D_{\mathrm{v}} r^4 \frac{\partial\widehat{\Omega}}{\partial r}\right) + \frac{1}{\sin\vartheta}\frac{\partial}{\partial\vartheta}\left(\varrho\, D_{\mathrm{h}}\sin^3\vartheta\,\frac{\partial\widehat{\Omega}}{\partial\vartheta}\right). \qquad (12.2)$$

The first term is the difference of the time derivatives in the two mentioned equations with account of (12.1). In the second term, one assumes that the contribution depending on $\widehat{\Omega}$ multiplied by the advection is negligible with respect to that with $\overline{\Omega}$. The two terms on the right-hand side are the differences of the corresponding terms with account of (12.1). D_{v} and D_{h} are the vertical and horizontal parts of the diffusion coefficients. The above expression governs the time variations of the horizontal fluctuations of Ω. The assumption of a large horizontal diffusion means that it dominates over the vertical diffusion, i.e., $D_{\mathrm{h}} \gg D_{\mathrm{v}}$. Thus, with (12.1) one has

$$\sin^2\vartheta\left(P_2(\cos\vartheta) + \frac{1}{5}\right)\frac{\partial}{\partial t}(\varrho\, r^2\Omega_2)$$

$$+ \frac{1}{r^2}\frac{d}{dr}(\varrho\, r^4\overline{\Omega}\, U_2\sin^2\vartheta P_2(\cos\vartheta)) + \frac{1}{r\sin\vartheta}\varrho\,\overline{\Omega} V_2\frac{d}{d\vartheta}\left(\sin^3\vartheta\frac{dP_2}{d\vartheta}\right)$$

$$+ \frac{\sin^2\vartheta}{5r^2}\frac{\partial}{\partial r}(\varrho\, r^4 U_2\overline{\Omega}) = \varrho\, D_{\mathrm{h}}\frac{1}{\sin\vartheta}\frac{d}{d\vartheta}\left(\sin^3\vartheta\frac{d\widehat{\Omega}}{d\vartheta}\right), \qquad (12.3)$$

where U_2 and V_2 are the vertical and horizontal components of the meridional circulation (11.63). We may use (10.110), derived from the equation of continuity, to express V_2 in term of U_2 and obtain

$$\sin^2\vartheta\left(P_2(\cos\vartheta)+\frac{1}{5}\right)\frac{\partial}{\partial t}\left(\varrho\,r^2\,\Omega_2\right)+\frac{1}{r^2}\frac{d}{dr}\left(\varrho\,r^4\,\overline{\Omega}\,U_2\right)\left[\sin^2\vartheta\left(P_2(\cos\vartheta)+\frac{1}{5}\right)\right]$$

$$+\frac{1}{6}\overline{\Omega}\frac{d}{dr}\left(\varrho\,r^2 U_2\right)\frac{1}{\sin\vartheta}\frac{d}{d\vartheta}\left(\sin^3\vartheta\frac{dP_2}{d\vartheta}\right)=\varrho\,D_{\rm h}\frac{1}{\sin\vartheta}\frac{d}{d\vartheta}\left(\sin^3\vartheta\frac{d\widehat{\Omega}}{d\vartheta}\right).$$

$$(12.4)$$

Let us examine in the third term on the left,

$$\frac{1}{\sin\vartheta}\frac{d}{d\vartheta}\left(\sin^3\vartheta\frac{dP_2}{d\vartheta}\right)=\frac{1}{\sin\vartheta}\frac{d}{d\vartheta}\left(-3\cos\vartheta\sin^4\vartheta\right)$$

$$=3\sin^4\vartheta-12\cos^2\vartheta\sin^2\vartheta=\sin^2\vartheta\left(3-15\cos^2\vartheta\right)$$

$$=-10\sin^2\vartheta\left[\left(\frac{3\cos^2\vartheta}{2}-\frac{1}{2}\right)+\frac{1}{5}\right]=-10\sin^2\vartheta\left[P_2(\cos\vartheta)+\frac{1}{5}\right].\,(12.5)$$

The terms $\sin^2\vartheta\left[P_2(\cos\vartheta)+(1/5)\right]$ can be simplified and (12.4) becomes

$$\frac{\partial}{\partial t}\left(\varrho\,r^2\,\Omega_2\right)+\frac{1}{r^2}\frac{d}{dr}\left(\varrho\,r^4\,\overline{\Omega}\,U_2\right)-\frac{10}{6}\overline{\Omega}\frac{d}{dr}\left(\varrho\,r^2 U_2\right)=-10\varrho\,D_{\rm h}\,\Omega_2.\quad(12.6)$$

This is the equation governing the evolution of the horizontal fluctuations Ω_2 of rotation as a function of circulation and horizontal turbulence. If one assumes a stationary situation between the homogenization due to the horizontal turbulence and meridional circulation, one gets

$$D_{\rm h}\,\Omega_2=-\frac{1}{10\varrho\,r^2}\frac{d}{dr}\left[\varrho\,r^4\overline{\Omega}\,U_2(r)\right]+\frac{1}{6}\frac{\overline{\Omega}}{\varrho}\frac{d}{dr}\left[\varrho\,r^2 U_2(r)\right]$$

$$=-\frac{\overline{\Omega}}{10\varrho}\frac{d}{dr}\left[\varrho\,r^2 U_2(r)\right]-\frac{U_2}{10}\frac{d}{dr}\left[r^2\overline{\Omega}\right]+\frac{1}{6}\frac{\overline{\Omega}}{\varrho}\frac{d}{dr}\left[\varrho\,r^2 U_2(r)\right]$$

$$=\frac{1}{15}\frac{\overline{\Omega}}{\varrho}\frac{d}{dr}\left[\varrho\,r^2 U_2(r)\right]-\frac{U_2}{10}\frac{d}{dr}\left[r^2\overline{\Omega}\right]$$

$$=\frac{1}{5}r\overline{\Omega}\,U_2\left[\frac{1}{3}\frac{d\ln(\varrho\,r^2 U_2)}{d\ln r}-\frac{1}{2}\frac{d\ln(r^2\overline{\Omega})}{d\ln r}\right].\qquad(12.7)$$

With relation(10.110) between the vertical and horizontal component of the meridional circulation, one can write

$$\frac{1}{3}\frac{d\ln(\varrho r^2 U_2)}{d\ln r}=\frac{1}{3\varrho r}\frac{d(\varrho\,r^2 U_2)}{dr}=2V_2.\qquad(12.8)$$

Thus, (12.7) becomes finally

$$\frac{\Omega_2(r)}{\overline{\Omega}(r)} = \frac{1}{5}\frac{r}{D_h}\left[2V_2(r) - \alpha U_2(r)\right], \quad \text{with } \alpha = \frac{1}{2}\frac{d\ln(r^2\overline{\Omega})}{d\ln r}\right). \qquad (12.9)$$

For uniform rotation, $\alpha = 1$. Expression (12.9) gives the relative amplitude of the horizontal fluctuations of the angular velocity $\Omega(r,\vartheta)$ in terms of the horizontal diffusion and meridional circulation. As expected, a large D_h reduces the horizontal differential rotation.

A large positive circulation with $U_2(r) > 0$, (i.e., clockwise circulation pattern in the upper right quadrant) would increase the horizontal differential rotation, because in general the term in V_2 dominates in (12.9), thus making Ω_2 larger. As the term $P_2(\cos\vartheta)$ is positive near the polar axis, this makes a faster rotation near the polar axis. Depending on the choice of D_h (see next subsections), the relative differential rotation $\Omega_2(r)/\overline{\Omega}(r)$ in the horizontal direction may amount to a fraction between $1/5$ and about 10^{-3}.

Let us note that equation (12.6) for the time evolution of Ω_2 can also be written in terms of U_2 and V_2

$$\frac{d}{dt}\left(\varrho\, r^2\Omega_2\right) - 2\varrho\,\overline{\Omega}r\left[2V_2(r) - \alpha U_2(r)\right] = -10\varrho\, D_h\Omega_2. \qquad (12.10)$$

Without the physically justified additive constant of $1/5$ in (12.1) as derived in (B.6.1), the simplifications leading to (12.6) and (12.10) would not have occurred.

12.1.2   A First Estimate of the Horizontal Turbulence

We may now estimate the coefficient D_h or v_h due to the horizontal turbulence. This first estimate was proposed by Zahn [632]. It is based on the property of (12.9), which shows that the amplitude Ω_2 of the horizontal variations of angular velocity remains small with respect to the average $\overline{\Omega}$ on the isobar as long as D_h is larger than $|2V_2 - \alpha U_2|$. Thus, one adopts as first estimate at a level r in the star

$$D_h(1) = v_h = \frac{1}{c_h}r|2V_2 - \alpha U_2| \qquad (12.11)$$

with $c_h < 1$. The parenthesis (1) indicates this is the first estimate. This ensures that Ω_2 is small with respect to $\overline{\Omega}$, i.e.,

$$\frac{\Omega_2(r)}{\overline{\Omega}(r)} = \frac{c_h}{5}. \qquad (12.12)$$

This first estimate (12.11) of D_h is not satisfactory for several reasons [352, 632]. First, it leads to the ratio (12.12), which indicates that the differential rotation on isobars is constant with depth in stars. Also, the ratio $\Omega_2/\overline{\Omega}$ shows no dependence on v_h, while such a dependence should normally be expected. In addition, this ratio is independent of the angular velocity, which is rather unlikely. Another difficulty

occurs for models of low Z, where D_h is of the same order as the coefficients for vertical diffusion due to shear turbulence [352], a situation which is not consistent with the hypothesis of a dominant horizontal turbulence, necessary for the validity of shellular rotation.

The above expression of D_h implies that the effective diffusion coefficient D_{eff} (11.101) of the chemical elements by the combined effects of meridional circulation and horizontal turbulence may be written as,

$$D_{eff} = \frac{(rU_2)^2}{30 D_h} = \frac{c_h}{30} \frac{rU_2^2}{|2V_2 - \alpha U_2|} \; . \tag{12.13}$$

The denominator is of the order of $|U_2|$, which means that the diffusion of the elements by meridional circulation in presence of horizontal turbulence is about 1–2 orders of magnitude smaller than $|rU_2|$, which implies a great reduction of the vertical transport. In case where the denominator vanishes, it is suggested [632] to express it by $(|2V_2 - \alpha U_2|^2 + U^2)^{1/2}$, in order to avoid any divergence.

These values of D_h (called below $D_h(1)$) and of D_{eff} in a model of $20 \, M_\odot$ at the very beginning of the MS phase are shown in Fig. 12.3. One notices the relatively large value of the horizontal turbulence, a factor of 3 below the thermal diffusivity K and above the vertical diffusion due to shears. The figure also shows the small value of D_{eff}, which illustrates the modest influence of meridional circulation on the mixing of chemical elements.

12.1.3   Turbulent Diffusion from Laboratory Experiment

Laboratory experiments provide another estimate of the coefficient of diffusion by turbulent transport in a differentially rotating medium [388, 486]. The experiment is the Couette–Taylor cylinder in which there is some fluid between an outer and an internal cylinder. One of the cylinders is made to rotate around the axis. The experiment shows the occurrence of turbulence when the angular velocity increases with the distance ϖ to the rotation axis, while the linear stability analysis of Sect. 6.4 predicts stability.

Experiments performed with the inner cylinder at rest show that, when the relative separation $\Delta\varpi/\varpi$ between the two cylinders (ϖ is the distance to the axis) is larger than $\sim 1/20$, turbulence appears as soon as the Reynolds number $\mathcal{R}e$ (Appendix B.5.1) is larger than some critical value of the order of 10^5. The Reynolds number in this case can be written as

$$Re \equiv \frac{\ell v}{\nu} \; \rightarrow \; \frac{\varpi \left(\varpi^2 \frac{d\Omega}{d\varpi}\right)}{\nu} \; . \tag{12.14}$$

This leads to an estimate of the turbulent viscosity of the form [486]

$$v = \beta \, \varpi^3 \left| \frac{d\Omega}{d\varpi} \right| \quad \text{with } \beta \approx (1.5 \pm 0.5) \times 10^{-5} . \tag{12.15}$$

The above results apply to strong differential rotation. It is not yet clear [388] whether this also applies to mild differential rotation, as in stellar interior. The above Eq. (12.15) becomes in spherical geometry, for a shear in latitude only (as usual ϑ is the colatitude),

$$v = \beta \, (r \sin \vartheta)^3 \left| \frac{d\Omega(r, \vartheta)}{r d\vartheta} \right| = \beta \, r^2 \sin \vartheta^3 \left| \frac{d\widehat{\Omega}(r, \vartheta)}{d\vartheta} \right|$$

$$= \beta r^2 \, |\Omega_2| \sin^3 \vartheta \left| \frac{dP_2}{d\vartheta} \right| , \tag{12.16}$$

where (12.1) is used. Taking the average over the sphere, one has

$$v_h = \frac{1}{2} \int_0^\pi \beta \, r^2 \, |\Omega_2(r)| \sin^3 \vartheta \left| \frac{d}{d\vartheta} P_2(\cos \vartheta) \right| \sin \vartheta d\vartheta$$

$$= \frac{1}{2} \beta \, r^2 \, |\Omega_2(r)| \int_0^\pi \sin^3 \vartheta \, |3(-\sin \vartheta) \cos \vartheta| \sin \vartheta \, d\vartheta$$

$$= \frac{3}{2} \beta \, r^2 \Omega_2(r) \left(\int_0^{\pi/2} \sin^5 \vartheta \cos \vartheta d\vartheta - \int_{\pi/2}^\pi \sin^5 \vartheta \cos \vartheta d\vartheta \right)$$

$$= \frac{3}{2} \beta \, r^2 \Omega_2(r) \left(\left[\frac{\sin^6 \vartheta}{6} \right]_0^{\pi/2} - \left[\frac{\sin^6 \vartheta}{6} \right]_{\pi/2}^\pi \right)$$

$$= \frac{3}{2} \beta \, r^2 \Omega_2(r) \left(\frac{1}{6} + \frac{1}{6} \right) . \tag{12.17}$$

Thus, finally one gets the coefficient of turbulent viscosity

$$v_h = \frac{1}{2} \beta \, r^2 \, |\Omega_2| . \tag{12.18}$$

One can now eliminate Ω_2 between this equation and (12.9) valid in the stationary limit. One gets for the diffusion and viscosity coefficients due to horizontal turbulence [388],

$$D_h(2) = v_h(2) = \left(\frac{\beta}{10} \right)^{1/2} (r^2 \overline{\Omega})^{1/2} \, [r \, |2 V_2 - \alpha U_2| \,]^{1/2} . \tag{12.19}$$

The parenthesis (2) indicates this is a second estimate of D_h. A diffusion coefficient can be written as $D = (1/3)\ell \, v$ (see Appendix B.4.3), thus the relevant velocity v considered here is the geometric mean of the rotation velocity $r\overline{\Omega}$ and of a velocity of the order of the velocity of meridional circulation.

12.1.4   What Sets the Timescale of Horizontal Turbulence ?

One may first remark that the above diffusion coefficient (12.18) by horizontal tur-
bulence derived from laboratory experiments is essentially the definition of the vis-
cosity or diffusion coefficient, if the characteristic timescale of the process is equal
to $1/(\beta\,\Omega_2)$, i.e.,

$$\nu_h \approx \frac{\ell^2}{t_{\text{diff}}}, \quad \text{with} \ \ t_{\text{diff}} \approx \frac{1}{\beta\,\Omega_2}\,, \tag{12.20}$$

with $\ell \sim r$. This relation means that only the degree of the differential rotation in ϑ
determines the importance of horizontal turbulence. This looks possible, however it
is not known whether this is always the case.

The Couette–Taylor experiment is made in a cylindrical geometry and the mo-
tions on an isobar are somehow different, as well known from meteorology. There
are various effects which may intervene in the turbulence: the differential rotation
due Ω_2, the vertical component U_2 of the circulation, the horizontal component V_2 of
the circulation and the effects of the Coriolis force which are of the order of $\Omega_2 V_2$.
If these last effects are dominant for the horizontal motions as is the case for terres-
trial atmospheric motions, the appropriate timescale for the horizontal diffusion is
not $(1/\beta\,\Omega_2)$, but

$$t_{\text{diff}} \approx \left(\frac{r}{\Omega_2 V_2}\right)^{1/2}. \tag{12.21}$$

With this timescale, we obtain a coefficient ν_h of the form,

$$\nu_h \approx A \left(r^3 \Omega_2 V_2\right)^{\frac{1}{2}}. \tag{12.22}$$

The amount of differential rotation Ω_2/Ω is given by (12.9). We may eliminate
Ω_2 between (12.22) and (12.9) and obtain another estimate of the coefficient of
viscosity due to the horizontal turbulence,

$$D_h(3) = \nu_h(3) = A\,r\left(r\overline{\Omega}(r)\,V_2\,[2V_2 - \alpha U_2]\right)^{\frac{1}{3}}. \tag{12.23}$$

The parenthesis (3) indicates this is the third estimate. Various considerations [352]
suggest a value of $A \leq 0.1$. We see that the above expression has the usual form
$\nu_h = (1/3)\,l \cdot v$ for a viscosity, where the appropriate velocity v is a geometric mean
of three velocities: – 1. A velocity $(2V_2 - \alpha U_2)$ as in Eq. (1) by Zahn ([632]), – 2.
The horizontal component V_2 of the meridional circulation. – 3. The average local
rotational velocity $r\overline{\Omega}(r)$. This rotational velocity is usually much larger than either
$U_2(r)$ or $V_2(r)$, typically by 6–8 orders of a magnitude in upper main sequence stars
rotating at the average velocity. This coefficient $D_h(3)$ gives a bit more weight to
the effect of the meridional circulation than coefficient $D_h(2)$. Nevertheless, these
two expressions of D_h lead to rather similar results, as shown below.

12.1.5 Consequences

12.1.5.1 Comparison of the Various Coefficients

We have three different expressions for the diffusion coefficient by horizontal turbulence in stars, which we presented to show how uncertain the situation is. One has

$$D_h(1) = \frac{1}{c_h} r \left| 2V_2 - \alpha U_2 \right| ,$$

$$D_h(2) = \left(\frac{\beta}{10} \right)^{1/2} \left(r^2 \overline{\Omega} \right)^{1/2} \left[r \left| 2V_2 - \alpha U_2 \right| \right]^{1/2} ,$$

$$D_h(3) = A r \left(r \overline{\Omega}(r) V_2 \left[2V_2 - \alpha U_2 \right] \right)^{\frac{1}{3}} . \tag{12.24}$$

In stellar models [352], one typically has $V_2 \sim (1/3)U_2$ and $|2V_2 - \alpha U_2| \sim V_2$. Thus the ratios of the coefficients behave like

$$\frac{D_h(2)}{D_h(1)} \approx c_h \left(\frac{\beta}{10} \right)^{1/2} \left(\frac{r\overline{\Omega}}{V_2} \right)^{1/2} , \quad \frac{D_h(3)}{D_h(1)} \approx A c_h \left(\frac{r\overline{\Omega}}{V_2} \right)^{1/3} . \tag{12.25}$$

The velocity $r\overline{\Omega}$ is $\sim 10^2$ km s^{-1}, while $V_2 \sim 10^{-2}$ cm s^{-1}. Thus, one has $D_h(2) > D_h(3) \gg D_h(1)$. Figure 12.2 shows these three coefficients during the MS evolution of 1.5 M$_\odot$ star with an initial rotation of 110 km s^{-1}. $D_h(2)$ and $D_h(3)$ are close to each other and about 4–5 orders of magnitude larger than $D_h(1)$. This is due to the account of the rotation velocity $\overline{\Omega} r$ instead of V_2 or U_2 in the diffusion coefficient.
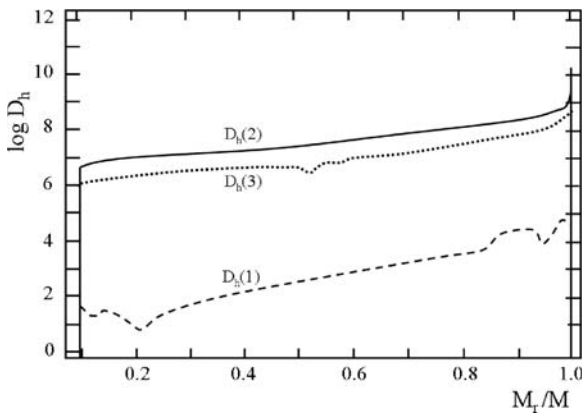
Fig. 12.2 The various coefficients $D_h(i)$ with $i = 1, 2, 3$ of horizontal turbulence in a 1.5 M$_\odot$ star at an age of 1.368×10^9 yr. A value $A = 0.08$ is taken in $D_h(3)$. The initial rotation was 110 km s^{-1}. Adapted from Mathis et al. [388]

Figure 12.3 compares $D_h(1)$ and $D_h(3)$ to the other diffusion coefficients of diffusion in a 20 $M_\odot$ star with an initial rotation velocity of 300 km s^{-1} at the beginning of MS evolution. There, the ratio $D_h(3)/D_h(1)$ is about a factor 40, i.e., less than in the previous example. The reason is that in an initial stellar model, which has an almost uniform rotation, the meridional circulation is much larger than during evolution, where it reaches an equilibrium (Sect. 11.4.2). During further MS evolution, the above ratio is about 10^2, for a velocity of 220 km s^{-1} and a vertical component of the meridional circulation $U_2 \sim (0.3 - 3) \times 10^{-1}$ cm s^{-1}.
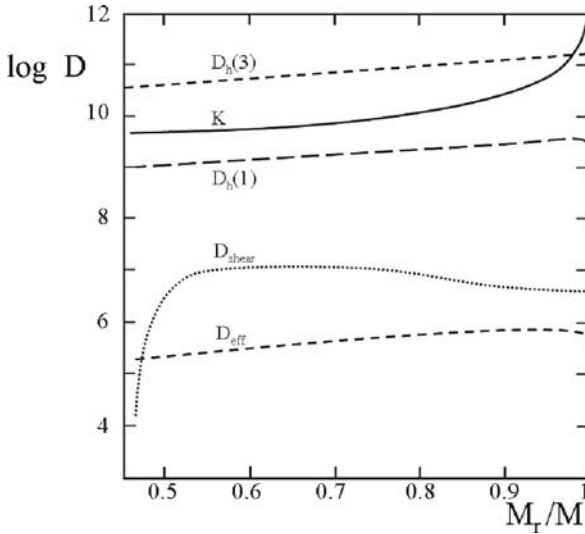
Fig. 12.3 The three diffusion coefficients in the interior of a star model of 20 $M_\odot$ at the beginning of the MS phase. The central H content is $X_c = 0.702$, while the initial one was $X_c = 0.705$. $D_h(2)$ is almost equal to $D_h(3)$. K is the thermal diffusivity (3.46). D_{shear} is the diffusion coefficient by shears (12.68) and D_{eff} is the diffusion coefficient (11.101) of elements by circulation with account of horizontal turbulence; these two coefficients are calculated here with $D_h(3)$. From the author [352]

Figure 12.3 shows that $D_h(3)$ and $D_h(2)$ become even larger than the thermal diffusivity, which is usually the most efficient diffusivity in stars. One also sees that the horizontal turbulence is orders of magnitude larger than D_{shear} the diffusion by shear turbulence or than D_{eff} the diffusion of the elements by meridional circulation, a remark also true for the model of 1.5 $M_\odot$ of Fig. 12.2.

12.1.5.2   The Differential Rotation in the Horizontal Direction

From the diffusion coefficients (12.24) and (12.9), the relative amount of differential rotation in the horizontal directions is given by

$$\text{For } D_\text{h}(2): \quad \frac{\Omega_2(r)}{\overline{\Omega}(r)} = \frac{1}{5}\left(\frac{10}{\beta}\right)^{1/2}\left(\frac{|2V_2 - \alpha U_2|}{r\overline{\Omega}}\right)^{1/2}$$

$$\text{For } D_\text{h}(3): \quad \frac{\Omega_2(r)}{\overline{\Omega}(r)} = \frac{1}{5A}\left(\frac{(2V_2 - \alpha U_2)^2}{r\overline{\Omega}V_2}\right)^{1/3}. \tag{12.26}$$

In both cases, the ratios are $\sim 10^{-3}$, meaning that the hypothesis of shellular rotation is verified. The relative horizontal fluctuations are smaller for higher rotation velocities. For $D_\text{h}(1)$, the above ratio is 1/5 (12.12).

12.1.5.3   Reduction of the Fluctuations of Abundances in Latitude

Another consequence of a higher horizontal turbulence is that according to (11.31) or (11.32), the horizontal fluctuations $\Lambda = \tilde{\mu}/\mu$ of the mean molecular weight are reduced. In turn, there is less opposition from the horizontal μ gradient to meridional circulation which is thus enhanced.

12.1.5.4   Change of D_eff Due to Horizontal Turbulence

The coefficient D_eff of diffusion of the chemical elements by meridional circulation (11.101) contains D_h at the denominator. Thus, a strong horizontal turbulence reduces the transport of chemical elements by meridional circulation (Sect. 11.6.1). The numerical results [388, 389] in the case of $1.5\,M_\odot$ models show that the D_eff obtained with $D_\text{h}(2)$ and $D_\text{h}(3)$ are almost equal, they are smaller by a factor $\sim 10^2 - 10^3$ with respect to D_eff obtained with $D_\text{h}(1)$, consistently with the above remark.

The horizontal turbulence also strongly influences the shear mixing (Sect. 12.3.2). On the whole, the increase of the shear turbulence in the outer layers is the dominant effect for the chemical enrichments. These are larger for a larger diffusion coefficient D_h (see below). The horizontal turbulence influences several other instabilities and it has thus a great importance.

The above approaches certainly are the infant steps in a domain, where certainly great progresses are needed. The future developments may come from both multi-dimensional studies and asteroseismology.

12.2   Shear Instabilities and Mixing

Astrophysical media have in general both velocity and density gradients. We have seen the Rayleigh–Taylor instability occurring when a denser fluid is supported by a lighter one (Sect. 6.4.2). The instability created in two superposed fluids flowing

with different horizontal velocities is known as the Kelvin–Helmholtz instability. The velocities gradient between the different layers may generate a shear instability, while the usual density stratification favors stability. The balance of the two effects needs to be studied in details: the criterion expressing the instability condition is known as the Richardson criterion, as discussed below. The heat losses and diffusion, which also influence the stability, add some complexity to the problem.

12.2.1 The Richardson Criterion

Following Chandrasekhar [110], let us consider two cells in a fluid at levels z and $z + \delta z$, with velocities V and $V + \delta V$, respectively (cf. Fig. 12.4). If there is some turbulent displacement, the work to be done against gravity to exchange the two cells is

$$\delta W = g \, \delta \varrho \, \delta z \quad \text{with } \delta \varrho = \left(\frac{d \varrho'}{dz} - \frac{d \varrho}{dz} \right) \delta z \,, \tag{12.27}$$

where $\delta \varrho$ is the density excess of the fluid element at the end of its displacement δz, ϱ' and ϱ refers to the internal and external densities. The above expression results from the fact that there are two cells, each with a density difference $(1/2) \, |\delta \varrho|$ on a trip $|\delta z|$. After the exchange, the two cells have the same average velocity $(1/2) \, (2V + \delta V)$. The kinetic energy δK possibly available to do the work against gravity is the difference between the initial and the final values of the kinetic energy,

$$\delta K = \frac{1}{2} \varrho \left[\left(V^2 + (V + \delta V)^2 \right) - 2 \left(V + \frac{\delta V}{2} \right)^2 \right] = \frac{1}{4} \varrho \, (\delta V)^2 \,. \tag{12.28}$$
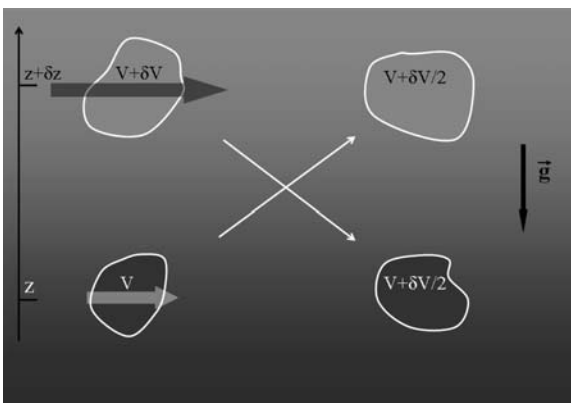
Fig. 12.4 Velocity exchanges during shear instability, as a result the velocities in the medium tend toward a local average. Adapted from Talon [556]

The instability develops if $\delta K > \delta W$ and one gets

$$\mathcal{R}i \equiv \frac{g}{\varrho} \frac{d\varrho/dz}{(dV/dz)^2} < \frac{1}{4} = \mathcal{R}i_{\mathrm{crit}} , \tag{12.29}$$

where $\mathcal{R}i_{\mathrm{crit}}$ is the critical Richardson number. The canonical value is $1/4$ as indicated above. However, instabilities may occur already for values of $\mathcal{R}i$ below about 1.0 [72, 89]. We further develop the above expression of the Richardson criterion. The relative density excess can be written with the help of the equation of state (cf. 5.20 and 5.23),

$$\frac{d(\delta \ln \varrho)}{dz} = \delta \left(\frac{d\ln T}{dz} - \frac{d\ln T_{\mathrm{int}}}{dz} \right) - \varphi \frac{d\ln \mu}{dz} = \frac{1}{H_P} \left[\delta(\nabla_{\mathrm{int}} - \nabla) + \varphi \nabla_\mu \right]. \tag{12.30}$$

where δ in front of the parenthesis is the thermodynamic coefficient (3.60). The Richardson criterion (12.29) for instability becomes

$$\mathcal{R}i \equiv \frac{N^2}{(dV/dz)^2} < \mathcal{R}i_{\mathrm{crit}}, \quad \text{and} \quad N^2 = \frac{g\,\delta}{H_P} \left(\nabla_{\mathrm{int}} - \nabla + \frac{\varphi}{\delta} \nabla_\mu \right), \tag{12.31}$$

where $N^2 = N_T^2 + N_\mu^2$ (5.25) is the Brunt–Väisälä frequency. For adiabatic convection, one has $\nabla_{\mathrm{int}} \to \nabla_{\mathrm{ad}}$. In a star with shellular rotation $\Omega(r)$, $dV/dr = r\sin\vartheta\,(d\Omega/dr)$, where ϑ is the co-latitude. Criterion (12.31) for instability becomes locally

$$N^2 < \mathcal{R}i_{\mathrm{crit}} \left(\sin\vartheta\, r \frac{\partial \Omega}{\partial r} \right)^2 . \tag{12.32}$$

In numerical models, one needs to consider the average gradient of Ω for the transports of angular momentum and chemical elements (12.39 and 12.41). In order the shear instability is not damped by viscous effects, the Reynolds criterion (12.69, see Appendix B.5.1) must also be satisfied.

12.2.1.1   Is There N_Ω^2 in Richardson's Criterion ?

The question has arisen [556] whether N^2 in the Richardson criterion in the form (12.31) should not contain, for a medium with rotation, first a term N_Ω^2 as is the case in the Solberg–Hoiland criterion (Sect. 6.4.3) and second whether the centrifugal force modifies the criterion. Above, one has considered the balance between the changes of potential and kinetic energy and there is no other mechanical energy. Thus, N^2 in (12.31) does not contain N_Ω^2. However, it is clear that in a rotating star the gravity in N^2 is the effective gravity (2.11), which also accounts for the centrifugal force.

12.2.2   Dynamical Shears

The above form of the Richardson criterion does not account for the thermal effects. Thus, it only applies when these are negligible, i.e., for Peclet numbers (B.66) much larger than 1.0. In this case, the instability is often called a dynamical shear instability, because it occurs on the local dynamical timescale $(\ell/g)^{1/2}$, where ℓ is the considered lengthscale. This dynamical instability rarely occurs in stellar models, because the Brunt–Väisälä frequency is generally high enough to prevent the dynamical shear instability. For rotating massive stars, the Ω gradient becomes steep enough to overcome the stable density stratification only in the advanced pre-supernova phases [251].

If the shear instability occurs according to (12.31), the following diffusion coefficient can be adopted (Appendix B.4.3),

$$D_{\text{shear}} = \frac{1}{3} v \ell \approx \frac{1}{3} r \Delta\Omega \, \Delta r \,, \tag{12.33}$$

where $\Delta\Omega$ is the variation of the angular velocity over the zone of vertical extension Δr, where the shear instability occurs according to (12.31). Numerical models [251] give $D_{\text{shear}} = 10^{12} - 10^{14}$ cm^2 s^{-1} in the pre-supernova stage of a star with an initial mass of 15 M$_\odot$ and inital velocity of 300 km s^{-1}. In this case, the dynamical shear modifies the distribution of the elements only over a very thin zone. The reason is that the instability occurs in regions with steep Ω gradients, which only concern very limited regions, where the μ gradients are also very steep. Thus, although the diffusion coefficient is quite large, the global effect is minor. Changing the critical Richardson number from $\mathcal{R}i_{\text{crit}} = 1/4$ to 1 makes practically no difference.

12.2.3   Thermal Effects at Constant μ

The density stratification, in particular in regions with a high μ gradient, is generally able to prevent the shear instability predicted by (12.31). However, the thermal diffusivity from a displaced fluid element weakens the stabilizing effect of the thermal stratification. This weakening is important: stellar models [409, 563] show that it leads to a significant mixing in the H-burning phase of intermediate and massive stars.

The radiative losses from an eddy have been calculated in Sect. 5.4.1, the difference between the internal and the external gradients is (5.67)

$$\nabla_{\text{int}} - \nabla = \frac{\Gamma}{\Gamma+1} \left(\nabla_{\text{ad}} - \nabla\right) \quad \text{and} \quad \Gamma = \frac{v\ell}{6K} = \frac{\nabla - \nabla_{\text{int}}}{\nabla_{\text{int}} - \nabla_{\text{ad}}} \,. \tag{12.34}$$

The density excess writes (12.30)

$$\frac{d(\delta \ln \varrho)}{dz} = \frac{1}{H_P} \left[\delta \left(\frac{\Gamma}{\Gamma + 1} \right) (\nabla_{ad} - \nabla) + \varphi \nabla_\mu \right] , \qquad (12.35)$$

and the Richardson criterion for instability becomes [348]

$$\left(\frac{\Gamma}{\Gamma + 1} \right) N_{T,ad}^2 + N_\mu^2 < \mathcal{R}i_{crit}(dV/dz)^2 , \qquad (12.36)$$

with $N_{T,ad}^2 = (g\,\delta/H_P)\,(\nabla_{ad} - \nabla)$ and $N_\mu^2 = (g\,\delta/H_P)\nabla_\mu$ (5.25). In the adiabatic case $\Gamma \to \infty$, one gets the usual criterion (12.31). In the non-adiabatic case with $\Gamma \ll 1$, if μ is constant one gets

$$\frac{g\delta(\nabla_{ad} - \nabla)}{H_P\,(dV/dz)^2} \frac{v\ell}{K} = \frac{N_{T,ad}^2}{(dV/dz)^2} \frac{v\ell}{K} < 6\,\mathcal{R}i_{crit} . \qquad (12.37)$$

The factor 6 comes from the spherical geometry adopted, it is absent in some derivations [632]. Expression (12.36) is to be considered in general, since the Peclet number $\mathcal{P}e = 6\Gamma$ in stars covers a wide range, from 10^{-3} to 10^2. The account for thermal diffusivity increases the domain of shear instability (Fig. 12.5). It operates at the thermal timescale.

In the simplified case with $\Gamma \ll 1$ and $\mu = $ constant (12.37), the coefficient for the vertical diffusion by shears is easily expressed. The turbulent diffusion is dominated by the largest eddies satisfying Richardson's criterion
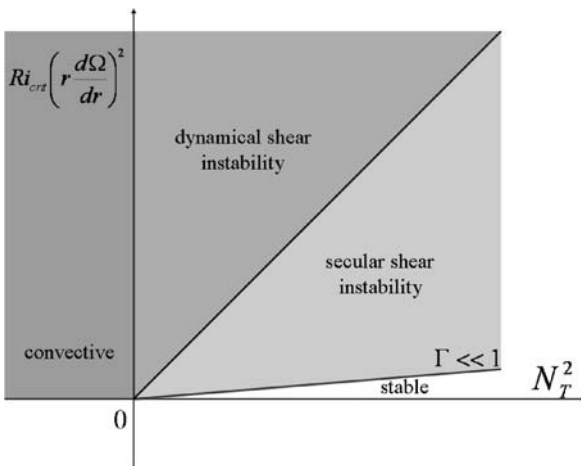
Fig. 12.5 The two terms of the Richardson criterion and the regions of instabilities in the case of medium with constant μ. In the adiabatic case ($\Gamma = \infty$), when $\mathcal{R}i_{crit}\,(dV/dz)^2$ is larger than N_T^2, the medium is shear unstable at the dynamical timescale (*middle gray area*). For large thermal diffusivity ($\Gamma \ll 1$), the instability domain is more extended due to the heat losses which reduce the T stratification (*light gray area*). The limit between the stable and the secular shear instability depends on the value of Γ

$$D_{\text{shear}}(r, \vartheta) = v_{\text{shear}}(r, \vartheta) = \frac{1}{3} v \ell = 2K\Gamma = 2 \mathcal{R}i_{\text{crit}} K \frac{(dV/dz)^2}{N_{T,\text{ad}}^2} . \qquad (12.38)$$

This is both the diffusion and the viscosity coefficients at a given location (r, ϑ) (Appendix B.4.3). However, formally the average on an isobar must be taken in a different way for D_{shear} and v_{shear}, because v_{shear} intervenes in the equation for the transport of angular momentum (10.122), while D_{shear} intervenes in the equation of the chemical transport (10.30).

Let us first consider the viscosity v_{shear} which applies to the transport of the angular momentum. In a star rotating with an angular velocity Ω (or $\overline{\Omega}$) at level r, one has $dV/dr = r \sin \vartheta (d\Omega/dr)$, where ϑ is the colatitude. In order to preserve the usual form (10.122) of the equation expressing the conservation of the angular momentum, one must define an average diffusion coefficient on the isobar,

$$v_{\text{shear}}(r) = \frac{\int_0^\pi v_{\text{shear}}(r, \vartheta) \sin^3 \vartheta d\vartheta}{\int_0^\pi \sin^3 \vartheta d\vartheta}$$

$$= \frac{2 \mathcal{R}i_{\text{crit}} K}{N_{T,\text{ad}}^2 \int_0^\pi \sin^3 \vartheta d\vartheta} \int_0^\pi \left(r \sin \vartheta \frac{d\Omega}{dr} \right)^2 \sin^3 \vartheta d\vartheta . \qquad (12.39)$$

Noting that the ratio $\int_0^\pi \sin^5 \vartheta d\vartheta / \left(\int_0^\pi \sin^3 \vartheta d\vartheta \right) = (4/5)$ and ignoring the horizontal fluctuations of Ω, we get for the diffusion coefficient by shears in the vertical direction with $\mathcal{R}i_{\text{crit}} = 1/4$,

$$v_{\text{shear}}(r) = \frac{2}{5} K \left(\frac{r}{N_T} \frac{d\Omega}{dr} \right)^2 . \qquad (12.40)$$

This coefficient was first found by Zahn [632]. Different geometries of the eddies may lead to different numerical factors in the above expression. This expression ignores the μ gradient and is thus only applicable in homogeneous zones, it does not account for the effects of horizontal turbulence. In order that the shear instability is not damped by viscous effects, we stress that the Reynolds criterion (12.69, see Appendix B.5.1) must also be satisfied.

For the diffusion coefficient D_{shear} of the elements, there is no term ϑ in the vertical diffusion equation and the average leads to $\int_0^\pi \sin^2 \vartheta d\vartheta / \left(\int_0^\pi d\vartheta \right) = (1/2)$, so that the average over the isobar is for $\mathcal{R}i_{\text{crit}} = 1/4$

$$D_{\text{shear}}(r) = \frac{1}{4} K \left(\frac{r}{N_T} \frac{d\Omega}{dr} \right)^2 . \qquad (12.41)$$

Even if the average of $D_{\text{shear}}(r, \vartheta)$ and $v_{\text{shear}}(r, \vartheta)$ over the isobar must be taken in a different way, the difference between the two expressions is rather academic, since there are other uncertain numerical factors.

Numerical simulations of shear instability [72] show a diffusion coefficient, which from the figures given by the authors behaves locally like

$$D_{\text{shear}}(r, \vartheta) \approx 6 \times 10^9 \frac{(dV/dz)^2}{N^2} ,\qquad (12.42)$$

where the notations are the same as in Fig. 12.4. These simulations confirm that $\mathcal{R}i$ (12.31) is the leading factor in the diffusion. This is similar to the diffusion coefficient (12.38) found above, although the hypotheses (adiabacy is assumed) and physical conditions of the numerical models, are different.

The corresponding timescale goes like $t_{\text{shear}} \sim R^2/v_{\text{shear}}$ according to (B.22). This means that for a star with a given Ω gradient, the timescale depends on $t_{\text{shear}} \sim R^2/K \sim t_{\text{KH}}$, i.e., the Kelvin–Helmholtz timescale (1.73).

12.2.4   The T Gradient in Shears

In radiative layers with shear transport, the thermal gradient ∇ is not necessarily equal to ∇_{rad}, since the turbulent eddies may also contribute to the transport. The luminosity due to the shear transport can be written

$$L_{\text{shear}} = 4\pi r^2 \varrho\, v\, \ell \frac{d(\delta q)}{dr} ,\qquad (12.43)$$

where v is the average vertical velocity of the turbulent eddies, ℓ their mean free path and δq is the difference in the heat content by mass unit between the turbulent eddies and the surrounding medium. Let us express $d(\delta q)$ with the help of $dT = -T\nabla dr/H_P$ (5.64),

$$d(\delta q) = C_P\, d(T_{\text{int}} - T) = C_P\,(dT_{\text{int}} - dT) = C_P T\,(\nabla_{\text{int}} - \nabla)\frac{dr}{-H_P}.\qquad (12.44)$$

Now, from the definition of the Peclet nummber (B.65), one has $v\ell = \mathcal{P}e\,K$ and thus the luminosity transported by the shear turbulence is,

$$L_{\text{shear}} = -\frac{4\pi r^2 \varrho}{H_P}\mathcal{P}e\,K C_P T\,(\nabla_{\text{int}} - \nabla) ,\qquad (12.45)$$

where ∇_{int} is the gradient in the turbulent eddies and ∇ the external gradient of the medium. The radiative luminosity is from (5.32),

$$L_{\text{rad}} = \frac{4\pi r^2 \varrho}{H_P} K C_P T \nabla ,\qquad (12.46)$$

and thus one has the following ratio of the two luminosities,

$$\frac{L_{\text{shear}}}{L_{\text{rad}}} = -\mathcal{P}e\,\frac{\nabla_{\text{int}} - \nabla}{\nabla} .\qquad (12.47)$$

This ratio is evidently positive since $\nabla > \nabla_{\text{int}}$. $\mathcal{P}e = 6\,\Gamma$ (Appendix B.5.3) and one may eliminate ∇_{int} with the first equation of (12.34) and obtain

$$\frac{L_{\text{shear}}}{L_{\text{rad}}} = -\frac{6\,\Gamma^2}{1+\Gamma}\,\frac{\nabla_{\text{ad}} - \nabla}{\nabla} \,. \tag{12.48}$$

The total luminosity L_r^{tot} is the sum of the luminosities transported by radiation and shear instabilities. Thus, one may define a fictitious gradient ∇_{rad} as the gradient that would be necessary for radiation to carry this total flux, in the same way as for convection in Sect. 5.1.3,

$$\nabla_{\text{rad}} = \frac{3\,\kappa\,\varrho\,H_P}{4\,ac\,T^4}\,\frac{L_r^{\text{tot}}}{4\,\pi\,r^2} = \nabla\left(1 - \frac{6\,\Gamma^2}{1+\Gamma}\,\frac{\nabla_{\text{ad}} - \nabla}{\nabla}\right) \,. \tag{12.49}$$

Thus, we get for the actual T gradient [364]

$$\nabla = \frac{\nabla_{\text{rad}} + \frac{6\,\Gamma^2}{1+\Gamma}\nabla_{\text{ad}}}{1 + \frac{6\,\Gamma^2}{1+\Gamma}} \,. \tag{12.50}$$

If the heat losses are very large, $\Gamma \to 0$ and $\nabla \to \nabla_{\text{rad}}$. At the opposite, for negligible heat losses, $\Gamma \gg 1$ and $\nabla \to \nabla_{\text{ad}}$. In real cases, depending on the value of Γ, ∇ lies somewhere between ∇_{rad} and ∇_{ad}. We see how to calculate Γ in the next subsection.

12.2.5 Thermal Effects and μ Gradient

Let us express the diffusion coefficient by shears in the general case where there are thermal losses and a μ gradient. The Richardson criterion for instability can also be written (12.36) with $\mathcal{R}i_{\text{crit}} = 1/4$,

$$\frac{g\delta}{(dV/dz)^2\,H_P}\left(\frac{\Gamma}{\Gamma+1}(\nabla_{\text{ad}} - \nabla) + \frac{\varphi}{\delta}\nabla_\mu\right) < \frac{1}{4} \,. \tag{12.51}$$

For the largest eddies at the edge of the shear instability, the efficiency Γ of the transport is from (12.36)

$$\Gamma = \frac{(1/4)(dV/dz)^2 - (g\varphi\nabla_\mu)/H_P}{(g\delta/H_P)\left[\nabla_{\text{ad}} - \nabla + (\varphi/\delta)\nabla_\mu\right] - (1/4)(dV/dz)^2} \,. \tag{12.52}$$

As in (12.38), diffusion is dominated by the largest eddies and one has

$$D_{\text{shear}} = \frac{1}{3}v\ell = 2K\Gamma \,, \tag{12.53}$$

with the above value of Γ. Eqs. (12.52) and (12.50) form a system of two equations with two unknown quantities ∇ and Γ [364]. Eliminating ∇ between these two equations, one obtains

$$(\Gamma + \Gamma^2)(\nabla_{\text{ad}} - \nabla_{\text{rad}})\frac{g\delta}{H_P}$$

$$+ (1 + \Gamma + 6\Gamma^2)(\Gamma + 1)\left[\frac{g\varphi\nabla_\mu}{H_P} - \frac{1}{4}\left(\frac{dV}{dz}\right)^2\right] = 0. \qquad (12.54)$$

This can be written in a more condensed form as

$$6B\Gamma^2 + (A + B)\Gamma + B = 0 \,,$$

$$\text{with } A = \frac{g\delta}{H_P}(\nabla_{\text{ad}} - \nabla_{\text{rad}}) \,, \quad B = \frac{g\varphi\nabla_\mu}{H_P} - \frac{1}{4}\left(\frac{dV}{dz}\right)^2 . \qquad (12.55)$$

A further simplification gives

$$f(\theta) = 6\,\theta\Gamma^2 + (1 + \theta)\Gamma + \theta = 0 \,,$$

$$\text{with } \theta = \frac{B}{A} = \frac{\frac{\varphi}{\delta}\nabla_\mu - \frac{1}{4}\frac{H_P}{g\delta}\left(\frac{dV}{dz}\right)^2}{\nabla_{\text{ad}} - \nabla_{\text{rad}}}. \qquad (12.56)$$

The two solutions of this second degree equation are given by

$$\Gamma = -\frac{1 + \theta}{12\,\theta} \pm \frac{\sqrt{(1 + \theta)^2 - 24\,\theta^2}}{12\,\theta}. \qquad (12.57)$$

Remarkably, the diffusion coefficient D_{shear} and the largest Γ corresponding to unstable motions depend only on a single number, the parameter θ (12.56). For shear instability in a radiative zone (i.e., with $A > 0$), the Richardson criterion is just,

$$f(\theta) < 0 \,. \qquad (12.58)$$

This relation expresses the Richardson criterion in a medium with a μ gradient and heat losses. The various solutions of this equation are functions of Γ (see details in [364]). For the case relevant to stellar interiors with $\Gamma \ll 1$, one has from (12.58) $\Gamma \approx -\theta/(1 + \theta) \approx -\theta$. This leads to the following local diffusion or viscosity coefficient

$$D_{\text{shear}} = 2K\frac{(1/4)\,(dV/dz)^2 - (g\varphi\nabla_\mu)/H_P}{(g\delta/H_P)(\nabla_{\text{ad}} - \nabla_{\text{rad}})} . \qquad (12.59)$$

Again, the average over $(dV/dz)^2$ should be taken differently for v_{shear} and D_{shear} as in (12.41) and (12.40). In absence of a μ gradient, one is brought back to (12.38).

The above criterion shows that diffusion due to shear turbulence occurs if

$$\frac{1}{4}\left(\frac{dV}{dz}\right)^2 > \frac{g\varphi\nabla_\mu}{H_P} , \qquad (12.60)$$

i.e., it is sufficient that the excess energy in the shear overcomes the stabilizing effect of the μ gradient. In absence of a μ gradient, any shear is unstable. However, in order the instabilities are not damped by viscous effects, the system must also satisfy the Reynolds criterion (12.69, see Appendix B.5.1). The stabilizing effect of the thermal structure does not intervene in the stability criterion, but only in the value of the diffusion coefficient (12.59).

If the above condition is applied to stellar interiors of differentially rotating models [408], it essentially kills the mixing in regions where there is a μ gradient and easily allows mixing in homogeneous regions where it has no effect! The observations of massive stars show evidences of a significant mixing (Sect. 27.4.2). Thus, the above expression of the Richardson criterion, although formally correct, gives too stringent conditions. Several solutions to this problem were proposed [349, 562]. Below, we examine the effect of the horizontal turbulence, which considerably reduces the inhibiting effect of the μ gradient on the shear instability.

12.3 Shear Mixing with Horizontal Turbulence

The vertical turbulence is generally too weak to drive vertical mixing, because of the stable density stratification particularly with high μ gradients. However, in the horizontal direction, the turbulence is not inhibited (Sect. 12.1) and it reduces the composition and temperature differences between the turbulent eddies and their surroundings (Fig. 12.6). Thus, the recall force of buoyancy is smaller and the shear instability is favored [562].

12.3.1 Richardson Criterion with Horizontal Turbulence

In calculating the density difference between a turbulent eddy and the surroundings, we have assumed (12.30) that there is no change of composition of the fluid elements. If one now assumes that the internal composition of an eddy varies during its motion due to the horizontal turbulence, the derivative of the density difference becomes

$$\frac{d(\delta\ln\varrho)}{dz} = \frac{1}{H_P}\left[\delta(\nabla_{\text{int}} - \nabla) - \varphi(\nabla_{\text{int},\mu} - \nabla_\mu)\right]. \qquad (12.61)$$

The difference of the internal and external μ gradients can be estimated in the same way as the difference of the T gradients (12.34). We make the substitution
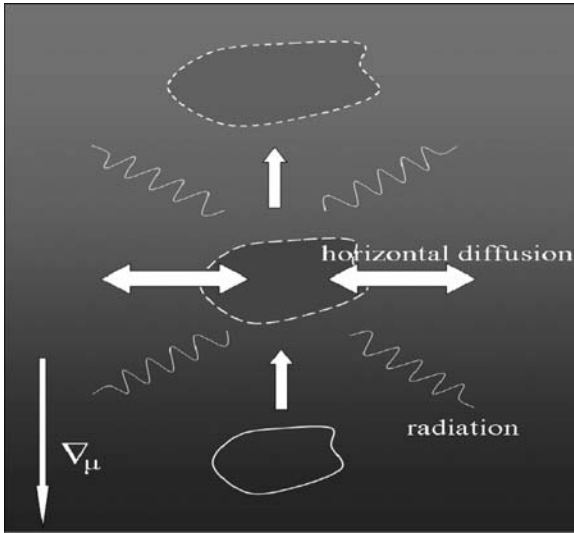
Fig. 12.6 Illustration of the role of the horizontal turbulence, which reduces the composition difference of the vertically moving eddies in a medium with a shear. Adapted from Talon & Zahn [562]

of ∇ by ∇_μ, of K by D_h and of ∇_{ad} by 0. One gets [562]

$$\nabla_{\mu,\mathrm{int}} - \nabla_\mu = -\frac{\Gamma_\mu}{\Gamma_\mu + 1}\nabla_\mu \quad \text{with } \Gamma_\mu = \frac{v\ell}{6D_h}, \tag{12.62}$$

where v and ℓ are the typical velocity and mean free path of the shear motions. D_h being larger than K, Γ_μ is smaller than Γ. With the density gradient (12.61) and Richardson's criterion (12.29), one gets

$$\left(\frac{\Gamma}{\Gamma+1}\right)N_{T,\mathrm{ad}}^2 + \left(\frac{\Gamma_\mu}{\Gamma_\mu+1}\right)N_\mu^2 < \mathcal{R}i_{\mathrm{crit}}\left(\frac{dV}{dz}\right)^2 \tag{12.63}$$

This expression of the criterion accounts for the reduction of the stabilizing effect both by the thermal diffusion through Γ and by the horizontal turbulence through Γ_μ which diminishes the effective μ gradient.

12.3.2   The Coefficient of Shear Diffusion with Turbulence

The turbulent eddies with the largest sizes $x = v\ell/6$ are those which give the largest contribution to the vertical transport. For these eddies, the equality in (12.63) is satisfied, which gives

$$\frac{x}{x+K+D_h} N_{T,\,ad}^2 + \frac{x}{x+D_h} N_\mu^2 = \mathcal{R}i_c \left(\frac{dV}{dz}\right)^2 . \tag{12.64}$$

In this expression, one has accounted that the horizontal turbulence carries some heat, so that D_h adds its effect to the thermal diffusivity K and one makes the replacement $K \rightarrow (K + D_h)$. This second-order equation allows one to express the coefficient for the vertical shear diffusion due to shear $D_{shear} = (1/3)v\ell = 2x$. In stars, this expression can be simplified, because the shear turbulence is moderate with $D_{shear} \ll K$, in addition $D_{shear} \ll D_h$,

$$\frac{x}{K+D_h} N_{T,\,ad}^2 + \frac{x}{D_h} N_\mu^2 = \mathcal{R}i_c \left(\frac{dV}{dz}\right)^2 . \tag{12.65}$$

This is now a first-order equation giving the local diffusion coefficient. In spherical coordinates at a colatitude ϑ [562], it is

$$v_{shear}(r, \vartheta) = D_{shear}(r, \vartheta) = 2x = \frac{2\,\mathcal{R}i_{crit} \left(r \sin\vartheta \frac{d\Omega}{dr}\right)^2}{[N_{T,\,ad}^2/(K+D_h)] + N_\mu^2/D_h}. \tag{12.66}$$

The different averages over the isobar as in (12.40) and (12.41) lead to the coefficients with $\mathcal{R}i_{crit} = 1/4$

$$D_{shear}(r) = \frac{(2/5)\,\mathcal{R}i_{crit} \left(r \sin\vartheta \frac{d\Omega}{dr}\right)^2}{[N_{T,\,ad}^2/(K+D_h)] + N_\mu^2/D_h} , \tag{12.67}$$

$$v_{shear}(r) = \frac{(1/4)\,\mathcal{R}i_{crit} \left(r \sin\vartheta \frac{d\Omega}{dr}\right)^2}{[N_{T,\,ad}^2/(K+D_h)] + N_\mu^2/D_h} . \tag{12.68}$$

These are the coefficients, noted indifferently v or D, but with the numerical coefficients, respectively, for the equations of transport of the angular momentum (10.122) and of the chemical elements (10.30). If the horizontal turbulence is weak with D_h not much larger than D_{shear}, this equation must not be used. In such a case (12.59) should be employed. The μ gradient in (12.66) does not intervene so drastically here in (12.59), because it is weakened by the effect of the horizontal turbulence.

   The above criterion (12.65) shows that there is always a scale small enough for the shear instability to be present and for the diffusion coefficients (12.66) to apply. However, at small scales the viscosity can damp the instabilities. This is expressed by the Reynolds criterion (Appendix B.5.1): for an instability to be present, one must have

$$\mathcal{R}e \equiv \frac{v\ell}{v} \geq \mathcal{R}e_{crit} , \tag{12.69}$$

with $\mathcal{R}e_{crit} \approx 10$ [562]. In intermediate and massive stars, the main viscosity to be considered in (12.69) is the radiative viscosity (B.52). Thus, the above condition (12.69) becomes

$$3 D_{\mathrm{shear}} \geq 10 \, v_{\mathrm{rad}} \, . \tag{12.70}$$

This condition, which expresses that turbulence is not damped, must be verified before applying the coefficients of shear diffusion (12.68).

Discussion. A strong horizontal turbulence generally favors the vertical diffusion by shears, because it kills the effects of the μ gradient. In a region with a negligible μ gradient, from (12.67) D_{shear} scales like

$$D_{\mathrm{shear}} \sim K + D_{\mathrm{h}} \, . \tag{12.71}$$

In general, in the course of evolution the high values of $D_{\mathrm{h}}(2)$ or $D_{\mathrm{h}}(3)$ are not too different from K. Thus, a high horizontal turbulence makes a moderate increase of D_{shear}.

In regions with a steep μ gradient (i.e., close to the convective core), the behavior is like

$$D_{\mathrm{shear}} \sim D_{\mathrm{h}} \, , \tag{12.72}$$

according to (12.67). Thus, a high horizontal turbulence increases the vertical transport by shears. This is well confirmed by numerical models [352, 388]. Thus, like for meridional circulation, the efficiency of shear mixing strongly depends on the horizontal turbulence.

12.4 Baroclinic Instabilities

For stars with solid or cylindrical rotation, the centrifugal force can be derived from a potential (Sect. 2.1.2). If so, the equipotentials and isobars coincide, the star is said barotropic: ϱ, P and T are constant on equipotentials.

For other cases of differential rotation, all quantities other than P vary with colatitude on an isobar. The star is said baroclinic. The relations between the fluctuations of the various quantities on isobars have been found in Sect. 11.2.2, they depend on the amount of differential rotation Ω_2 (Sect. 12.1.1). The small angle between the effective gravity and $\boldsymbol{\nabla}\varrho$ can be expressed with the baroclinic Eq. (11.38)

$$-\frac{1}{\varrho^2}\boldsymbol{\nabla}\varrho \times \boldsymbol{\nabla}P = -\frac{1}{\varrho}\boldsymbol{\nabla}\varrho \times \boldsymbol{g}_{\mathrm{eff}} = \frac{1}{2}\boldsymbol{\nabla}\Omega^2 \times \boldsymbol{\nabla}(r\sin\vartheta)^2 \, , \tag{12.73}$$

where $\boldsymbol{g}_{\mathrm{eff}}$ is the effective gravity. We see that the internal gradient of Ω determines the baroclinicity.

Various instabilities may appear in a baroclinic star. Let us consider various displacements in Fig. 12.7 and suppose them adiabatic. The lines of constant entropy (Appendix C.4) and of constant P are indicated. The displacement of a fluid element from points A to B is such that the density of the cell is higher than the surrounding
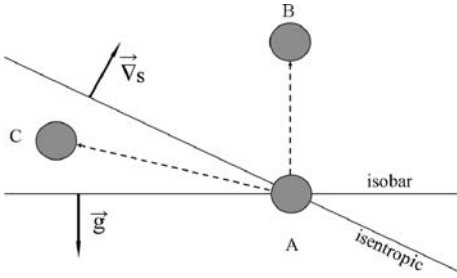
Fig. 12.7 Illustration of the baroclinic instability. The gravity is perpendicular to the isobar, the line of constant entropy is also shown. A displacement from A to B is stable, while from A to C it is unstable, i.e., the fluid element is not brought back

and the cell is brought back to its original position, which means stability with respect to perturbations.

The situation is different for a displacement from A to C. The fluid element is hotter than its surrounding and the buoyancy force further moves the cell away from its original position, which means that for such displacements some instabilities may occur for baroclinic stars. However this does not imply that all baroclinic stars are unstable, since we have not yet accounted for the non-adiabatic effects and for the conservation of the angular momentum which could restore stability.

12.4.1 The Goldreich–Schubert–Fricke or GSF Instability

The conditions for stability to axisymmetric perturbations in a rotating star were originally studied in the inviscid limit by Goldreich and Schubert [213]. They recovered the Rayleigh–Taylor criterion (6.50). The conditions that departures from cylindrical rotation are unstable were found

$$N_{\Omega}^2 < 0 \quad \text{and} \quad (\partial \Omega / \partial z) \neq 0 \, . \tag{12.74}$$

The proper account of a finite viscosity v together with thermal diffusivity K was given by Fricke [187] and Acheson [4], who found instability for each of the two conditions,

$$\frac{v}{K} N_{T,\,\mathrm{ad}}^2 + N_{\Omega}^2 < 0 \quad \text{or} \quad \left| \varpi \frac{\partial \Omega^2}{\partial z} \right| > \frac{v}{K} N_{T,\,\mathrm{ad}}^2 \, , \tag{12.75}$$

where the various quantities have the same meaning as in Sect. 6.4.3. ϖ is the distance to the rotation axis and z the vertical coordinate parallel to the rotation axis. Numerical simulations ([290]) show that the GSF instability takes the form of narrow finger-like vortices in the radial direction. The justifications of the above conditions are:

– The first inequality corresponds to the instability predicted by the Solberg–Hoiland criterion (6.53) with the density gradient (12.35) and the account for the term $\Gamma = v\ell/(6K) \sim v/K$. If $N_\Omega^2 < 0$, a displaced fluid element experiences a centrifugal force larger than in the surrounding medium and further moves away (Sect. 6.4.2), which produces an instability. Criterion (12.75) expresses that instability arises if the T gradient, with account for thermal and viscous diffusivities, is insufficient to compensate for the growth of the centrifugal force during an arbitrary small displacement.

– The second inequality expresses a baroclinic instability related to the differential rotation in the direction z (parallel to Ω). If a fluid element is displaced over a length δz in the z direction, so that $\partial\Omega/\partial z \cdot \delta z > 0$, then the angular velocity of the fluid element is larger than the local angular velocity and the excess of centrifugal force on this element leads to a further displacement and thus to instability. The stable situation is that described by the Taylor–Proudman theorem (Appendix B.1.7). The medium is more unstable when the angle between isobars and iso-angular momentum lines is larger.

It has often been concluded from the second criterion that only cylindrical rotation laws are stable (solid body rotation being one of which). This is not correct, since viscosity is never zero. In particular the horizontal turbulence produces a strong horizontal viscous coupling, with a large ratio v/K (cf. Fig. 12.2) which does not favor the GSF instability according to the above criteria (12.75). In addition, one must also account for the stabilizing effect of the μ gradient as shown below.

12.4.1.1 The μ Gradient and the GSF Instability

In the course of evolution, μ gradients develop in regions surrounding the convective core where the Ω gradients are also large. The μ gradients rapidly produce stabilizing effects and the above criterion (12.75) for the GSF instability becomes in this case [288, 556]

$$\frac{v}{K} N_{T,\,\mathrm{ad}}^2 + \frac{v}{K_\mu} N_\mu^2 + N_\Omega^2 < 0 \,. \tag{12.76}$$

There, K_μ is the molecular diffusivity (see Appendix B.4.1) which is of the same order as the viscosity v, thus the stabilizing effect of the μ gradient is not much reduced by molecular viscosity. The instability becomes a triple-diffusive instability. As soon as there is a significant μ gradient, it largely dominates and is able to stabilize the medium [288]. Thus, the GSF instability is not likely important in regions with $N_\Omega^2 < 0$ surrounding the stellar cores in advanced phases. The occurrence of horizontal turbulence, however, reduces the recall effect of the μ gradient and it might in some cases favor the GSF instability, as it does for shear instability.

12.4.2 The ABCD Instability

There is another instability: the so-called Axisymmetric-BaroClinic-Diffusive or ABCD instability [288, 556]. It is a baroclinic instability with account of the effects of angular momentum, heat diffusion and mean molecular weight, it is also a triple-diffusive instability. Let us consider Fig. 12.7. In a rotating medium, when the fluid element moves from A to C, it is brought back due to the conservation of angular momentum. However, in C the fluid eddy is hotter than the surrounding medium and, due to thermal diffusivity, it looses some energy. Thus, when back to A, the eddy is cooler and it overpasses its equilibrium position, as for semiconvection (Sect. 6.2): the oscillation amplitude grows. It is thus a different process than the GSF instability. The instability criterion is [288]

$$\frac{\nu}{K}\left(N_{T,\,\mathrm{ad}}^2 + N_\mu^2\right) + N_\Omega^2 < 0 \,, \tag{12.77}$$

which is the same as (12.76) except that the thermal diffusivity K is now replacing the molecular diffusivity K_μ. Since the Prandtl number $\mathcal{P}r = \nu/K$ is small (Appendix B.5.2), the stabilizing effect of the μ gradient is reduced, thus favoring the instability which develops in the indicated domain of Fig. 12.8. However, if horizontal turbulence is present, it constitutes the main source of viscosity with $\nu \approx D_\mathrm{h}$. In this case the ratio ν/K may be larger than 1.0 and the instability has difficulty to arise. Because the ABCD instability arises from an overstability, the horizontal turbulence or any other source of viscosity tends to kill it. We see from Fig. 12.8 that for large enough values of ν/K, the zone of the ABCD unstable zone
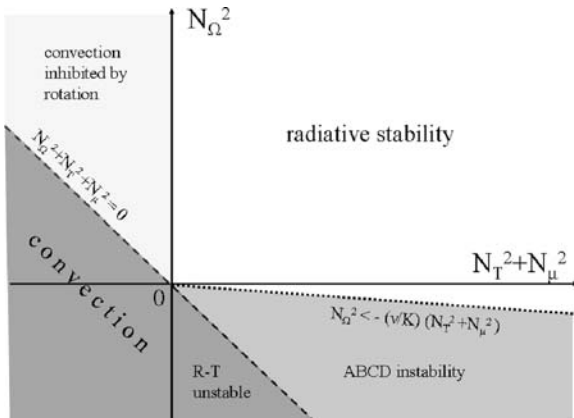
Fig. 12.8 Plot of the instability regions as a function of the Brunt– Väisälä frequency and of the Rayleigh–Taylor frequency N_Ω^2. According to the Solberg–Hoiland criterion (Sect. 6.4.3), for large enough N_Ω^2 convection is inhibited by rotation (6.53). Regions with negative values of N_Ω^2 are Rayleigh–Taylor(R–T) unstable. The ABCD instability develops in the indicated region, the upper limit of which depends on the Prandtl number ν/K, which is of the order of 10^{-6}. If horizontal turbulence is present, ν/K may be larger than 1.0

is smaller. If N_Ω^2 is very negative, the layers are subject to the Rayleigh–Taylor instability, which occurs at the dynamical timescale and would be much faster than the ABCD instability.

The real importance of the ABCD and GSF instabilities are difficult to appreciate and not well known at present, there are also some other possible instabilities. In models with horizontal turbulence, it seems justified to ignore the ABCD instability, while this is is not true for the GSF instability. The above criteria result from linear analysis and the growth rate of these instabilities are small and there is no estimate of their limiting amplitudes.

On the whole, the instabilities due to rotation play a role in stellar evolution. This is certainly the case for the horizontal turbulence and for the shear instabilities, while the role and importance of the baroclinic instabilities in evolution is still uncertain.

Chapter 13
Magnetic Field Instabilities and Transport Processes

Magnetic field is one of the last frontiers in astrophysics, often explored later than other effects. It plays a big role in some specific problems of stellar evolution. In star formation, the magnetic coupling between the central forming star and the surrounded disk allows the star to evacuate a lot of angular momentum and to keep a constant rotation rate despite its contraction. Magnetic fields are present in low-mass stars and in the convective envelopes of solar-type stars, where they are generated by a solar-type dynamo; the magnetic coupling of the very weak stellar winds nevertheless produces a strong braking of the axial rotation. Strong fossil fields are present in Ap stars. The magnetic field of neutron stars is an essential piece of the pulsar properties.

A big and still controversial question is whether a dynamo operates in radiative zones with differential rotation. A magnetic field would have great consequences on the evolution of rotation by exerting an efficient torque able to reduce the differential rotation or even to impose a nearly uniform rotation. There, we report on the present status of these difficult problems. There are a few books and extensive articles devoted to the magnetic field in astrophysics [110, 114, 287, 460].

13.1 The Equations of Magnetohydrodynamics (MHD)

The Maxwell equations are given in Appendix B.2, both in the MKSA and Gauss systems of units. Usually in astrophysics, the Gauss system is used (with reason or not?). We follow this practice and briefly give here the basic equations of MHD and some of their important properties for astrophysics.

13.1.1 The MHD Equations in Astrophysics

The magnetohydrodynamic (MHD) equations are an ensemble formed with the equations of electromagnetism (see Appendix B.2) and the equations of the fluid mechanics. Some properties are specific to astrophysics [480]:

– In a plasma, the particles experience the Lorentz force

$$\boldsymbol{F}_{\mathrm{L}} = q\boldsymbol{E} + \frac{1}{c}q\boldsymbol{v} \times \boldsymbol{B} \quad \text{or} \quad \boldsymbol{F}_{\mathrm{L}} = q\boldsymbol{E} + (1/c)\boldsymbol{j}\,dV \times \boldsymbol{B}\,, \qquad (13.1)$$

where q is the charge ($q > 0$ for a positive charge), $\boldsymbol{E}$ the electric field, $\boldsymbol{B}$ the magnetic induction, $\boldsymbol{v}$ the velocity of the charges. The current density $\boldsymbol{j}$ is the current $\boldsymbol{I}$ by volume unity, while the current is the charge crossing a cm^2 per second, dV is the volume element. The Lorentz force should be added on the right-hand side of the Navier–Stokes (13.8) and Euler equations (13.11). In the MKSA system, the Lorentz force writes $q\boldsymbol{E} + q\boldsymbol{v} \times \boldsymbol{B}$.

– The Ohm's law $\boldsymbol{E} = \boldsymbol{j}/\sigma$ (B.35) states that the electric field $\boldsymbol{E}$ in a conductor is proportional to the current. In a moving plasma, the total electric field becomes $\boldsymbol{E} + (1/c)\boldsymbol{v} \times \boldsymbol{B}$ in the Gauss system.

– At speeds much lower than c, the displacement current $\partial\boldsymbol{D}/\partial t$ can be neglected in Maxwell's equations (B.34).

– The permeability is about constant (except for ferro- and paramagnetic solids). One usually sets $\mu = 1$ in plasma astrophysics.

The Maxwell equations (Appendix B.2) become with the above specifications,

$$\boldsymbol{\nabla} \times \boldsymbol{E} = -\frac{1}{c}\frac{\partial\boldsymbol{B}}{\partial t}\,, \qquad \boldsymbol{E} = -\frac{1}{c}\boldsymbol{v} \times \boldsymbol{B} + \frac{\boldsymbol{j}}{\sigma}\,, \qquad (13.2)$$

$$\frac{4\pi}{c}\boldsymbol{j} = \boldsymbol{\nabla} \times \boldsymbol{B}\,, \qquad\qquad \boldsymbol{\nabla}\cdot\boldsymbol{B} = 0\,. \qquad (13.3)$$

In the Gauss system of units, the magnetic field is expressed in Gauss, 1 G corresponding in CGS units to $1\ \mathrm{g}^{1/2}\ \mathrm{cm}^{-1/2}\ \mathrm{s}^{-1}$. From (13.2) with the expressions of $\boldsymbol{E}$ and $\boldsymbol{j}$, we get the induction equation

$$\frac{\partial\boldsymbol{B}}{\partial t} = \boldsymbol{\nabla} \times (\boldsymbol{v} \times \boldsymbol{B}) - \boldsymbol{\nabla} \times (\eta\,\boldsymbol{\nabla} \times \boldsymbol{B}) \quad \text{with} \quad \eta = c^2/(4\pi\sigma)\,, \qquad (13.4)$$

the magnetic diffusivity ($\eta = 1/\sigma$ in the MKSA system). σ is the electrical conductivity. This equation expresses the effect of a velocity field on the magnetic field in the plasma in the presence of a magnetic diffusivity η. The microscopic plasma viscosity is given by (B.53). With the Maxwell equations, we get

$$\frac{\partial\boldsymbol{B}}{\partial t} = \boldsymbol{\nabla} \times (\boldsymbol{v} \times \boldsymbol{B}) + \eta\,\nabla^2\boldsymbol{B}\,. \qquad (13.5)$$

The first term on the right-hand side of (13.5) expresses the induction from the flow field and is a source term for creating the field $\boldsymbol{B}$. The second term expresses the resistive dissipation, it acts as a sink for the magnetic field due to the ohmic effect. This is the induction equation, which is basic in magnetohydrodynamics; it couples the electromagnetic properties to the dynamical ones, determining $\boldsymbol{B}$ when the velocity $\boldsymbol{v}$ is known. When $\boldsymbol{B}$ is obtained, $\boldsymbol{j}$ results from the first equation in (13.3) and $\boldsymbol{E}$ from the second in (13.2).

The ratio of the two terms on the right-hand side of (13.5) is the magnetic Reynolds number

$$\mathcal{R}m = \frac{\ell\,v}{\eta}\,, \tag{13.6}$$

where ℓ and v are typical length scale and velocity, respectively. There are two limiting cases:

– $\mathcal{R}m \gg 1$: The dissipation term in (13.5) is negligible. From (13.2), one gets $\boldsymbol{E} = -(1/c)\boldsymbol{v} \times \boldsymbol{B}$. This is the usual situation in astrophysics where length scales are large. In a sunspot with $\ell = 10^8$ cm, $v = 10^6$ cm s^{-1} and $\eta = 10^4$ cm^2 s^{-1}, one finds $\mathcal{R}m \approx 10^{10}$.

– $\mathcal{R}m \ll 1$: The dynamical term in (13.5) is negligible. One gets a diffusion equation

$$\frac{\partial \boldsymbol{B}}{\partial t} = \eta\,\nabla^2 \boldsymbol{B}\,, \tag{13.7}$$

where the diffusion timescale of the field is $\tau = \ell^2/\eta$.

Since $\mathcal{R}m$ is large in general, the diffusion timescale is also large, e.g., $\sim 3 \times 10^4$ yr for sunspots. This means that the rapid changes of sunspots are not due to dissipation. The dissipation timescale for the magnetic field over the entire Sun is of the order of 10^{10} yr, meaning that global magnetic fields in stars do not dissipate very much.

13.1.2   Equations of Stellar Structure with Magnetic Field

The Lorentz force acting on a unit volume with a current density $\boldsymbol{j}$ in a medium with a magnetic field $\boldsymbol{B}$ is $(1/c)\boldsymbol{j} \times \boldsymbol{B}$ (cf. 13.1). Thus, if we account for the Lorentz force with $\boldsymbol{j}$ expressed by the first of Eq. (13.3), we get for the Navier–Stokes equation (B.20),

$$\varrho\frac{d\boldsymbol{v}}{dt} = \varrho\left(\frac{\partial \boldsymbol{v}}{\partial t} + (\boldsymbol{v}\cdot\boldsymbol{\nabla})\boldsymbol{v}\right)$$

$$= -\boldsymbol{\nabla}P + \varrho\,\boldsymbol{g}_{\text{eff}} + \frac{1}{4\pi}(\boldsymbol{\nabla}\times\boldsymbol{B})\times\boldsymbol{B} + \varrho\,v\nabla^2\boldsymbol{v}\,, \tag{13.8}$$

where v is the coefficient of kinematic viscosity (Appendix B.4.1). The term containing the Lorentz force can be written by developing the vectorial product

$$\frac{1}{4\pi}(\boldsymbol{\nabla}\times\boldsymbol{B})\times\boldsymbol{B} = (\boldsymbol{B}\cdot\boldsymbol{\nabla})\frac{\boldsymbol{B}}{4\pi} - \boldsymbol{\nabla}\left(\frac{B^2}{8\pi}\right)\,. \tag{13.9}$$

The second term on the right-hand side has the same form as $-\nabla P$. Thus, $B^2/8\pi$ can be identified as the pressure due to the magnetic field,

$$P_B = \frac{B^2}{8\pi} .\tag{13.10}$$

This pressure acts in the direction from high to low magnetic fields. The first term on the right of (13.9) also represents a force, which is directed along the field line B and is proportional to the change of the direction B, i.e., it grows with the curvature of the field lines. It is a magnetic tension of magnitude $B^2/(4\pi)$. This tension tends to make the field lines shorter, like elastic bands, which would have in addition a higher tension when curvature is larger.

Expression (13.8) allows us to write the equivalent to the Euler equation with magnetic field, when viscosity is negligible,

$$\varrho \frac{d\boldsymbol{v}}{dt} = -\nabla P + \varrho\, \boldsymbol{g}_{\mathrm{eff}} + \frac{1}{4\pi}(\nabla \times \boldsymbol{B}) \times \boldsymbol{B} ,\tag{13.11}$$

or the equivalent to the equation of hydrostatic equilibrium,

$$\nabla P = \varrho\, \boldsymbol{g}_{\mathrm{eff}} + \frac{1}{c}\boldsymbol{j} \times \boldsymbol{B} .\tag{13.12}$$

If gravity is negligible, one has a state of magnetostatic balance $\nabla P = (1/c)\,\boldsymbol{j} \times \boldsymbol{B}$. If the gas pressure is negligible with respect to magnetic field, the equation further simplifies to

$$\boldsymbol{j} \times \boldsymbol{B} = 0 ,\tag{13.13}$$

which characterizes a so-called force-free field, where there is a balance between magnetic pressure and magnetic tension. This equation implies that $(4\pi/c)\,\boldsymbol{j} = \nabla \times \boldsymbol{B}$ is parallel to $\boldsymbol{B}$, which also gives $\nabla \times \boldsymbol{B} = \alpha\,\boldsymbol{B}$. If (13.13) is satisfied everywhere in a volume V and on its surface, the only solution is $\boldsymbol{B} = 0$. Thus, a force-free field which is non-zero in a given volume V must be anchored on the boundary of the volume [480], for example, by some current at the surface of the volume considered.

13.1.2.1   The System of Equations of Stellar Structure

The system of equations with magnetic field is formed by the Euler equation (13.11), with magnetic field rotation being included in the effective gravity g_{eff}. There are in addition the continuity equation (1.1) and the induction equation (13.5) which describes the evolution of the magnetic field. The system must be completed by an equation for the heat transport similar to (11.1), but in addition a term $\mathcal{M}$ due to the ohmic dissipation

$$\rho T \frac{dS}{dt} = \boldsymbol{\nabla} \cdot (\boldsymbol{\chi} \boldsymbol{\nabla} T) + \varrho\, \varepsilon + \boldsymbol{\nabla} \cdot \boldsymbol{F}_\mathrm{h} + \mathcal{M}\,, \tag{13.14}$$

with $\mathcal{M} = j^2/\sigma$ for an isotropic diffusivity η. This term may play a role for a meridional circulation driven by magnetic field. However, for the global heat transport, it is negligible. Similarly it is neglected in the current equation (3.40) of energy production. The method of solutions develops the equations in spherical harmonics [390], the magnetic field being expressed with its poloidal and toroidal components.

13.1.3 Alfvén Waves

If a local perturbation is applied to a magnetic field, the perturbation propagates as a wave along the field lines, in the same way as a wave propagates along a perturbed elastic band. The rigorous study of the magnetic field perturbations involves the induction equation (13.5), for example with $\eta = 0$, the equation of motion (13.8) with the Lorentz force and the continuity equation (1.1), where $\boldsymbol{B}$, $\boldsymbol{v}$ and ϱ have to be developed to the first order [110, 480]. Here, we derive the perturbation velocity in a straightforward way by scaling the inertial and magnetic terms in the Euler equation (13.11). We get

$$\varrho\, \frac{v}{t} \sim \frac{1}{R} \frac{B^2}{4\pi}\,, \tag{13.15}$$

with $t \sim R/v$, one can write

$$v^2 \sim \frac{B^2}{4\pi\varrho} \equiv v_\mathrm{A}^2\,. \tag{13.16}$$

v_A is defined as the Alfvén velocity, which is the velocity of a magnetic wave. In the same way as for the velocity of a perturbation propagating along a rope, the Alfvén velocity v_A is the square root of the ratio of the tension (13.9) and of the mass density, i.e.,

$$v_\mathrm{A} = \sqrt{\frac{\text{tension}}{\varrho}} = \frac{B}{\sqrt{4\pi\varrho}}\,. \tag{13.17}$$

The corresponding Alfvén frequency at radius r in spherical geometry is

$$\omega_\mathrm{A} = \frac{B}{r(4\pi\varrho)^{1/2}}\,. \tag{13.18}$$

The inverse $\tau_\mathrm{A} = 1/\omega_\mathrm{A}$ is the timescale characterizing magnetic equilibrium (in non-rotating stars). The Alfvén waves are transverse waves, i.e., the displacement is perpendicular to the propagation direction (like for a pinched elastic band). The velocity v_A is oriented in the direction of the magnetic field; for a direction making

an angle ϑ with $\boldsymbol{B}$, the velocity is $v_A \cos \vartheta$. There is another kind of waves, the magneto-acoustic waves which occur when the pressure is non-zero in the medium. Such waves combine the effects of Alfvén and sonic waves. The frequencies are generally much higher than for Alfvén waves. Magnetic diffusivity η produces some damping and the frequency changes during the propagation of magnetic waves.

13.1.4 Dynamos and the Solar Dynamo

A dynamo is a system where a flow field $\boldsymbol{v}$ can sustain by induction a field $\boldsymbol{B}$ against ohmic dissipation and where $\boldsymbol{B}$ is amplified by stretching the field lines [114]. The inductive term in the induction equation (13.5) can be written as (see also 13.46),

$$\frac{\partial \boldsymbol{B}}{\partial t} = (\boldsymbol{B} \cdot \boldsymbol{\nabla})\boldsymbol{v} - (\boldsymbol{v} \cdot \boldsymbol{\nabla})\boldsymbol{B} - \boldsymbol{B}(\boldsymbol{\nabla} \cdot \boldsymbol{v}) \, , \qquad (13.19)$$

where account has been given to $\boldsymbol{\nabla} \cdot \boldsymbol{B} = 0$. Depending on the velocity gradient, the first term on the right can produce an exponential growth of the field through the induction equation and build a dynamo. The velocity field at work in the solar dynamo is the solar differential rotation, both radially and latitudinally. A stellar dynamo requires that both the poloidal and toroidal components are sustained against ohmic dissipation. It requires the two following effects to generate each of the field components from the other one; if not, the field progressively vanishes by ohmic dissipation:

– The α effect: let us first consider a toroidal field, with field lines parallel to the equator. A small loop of a field line may appear and be essentially contained in a plane orthogonal to the equator. This loop generates a horizontal electrical current, which by Ampere's law creates a field with a poloidal component (a loop could also appear on a poloidal field and create a toroidal field).
– The ω effect: a poloidal field in a differentially rotating star is stretched horizontally, creating toroidal field components.

13.1.4.1 The Solar Dynamo

The action of the solar dynamo can be decomposed in the following steps where the α and ω effects intervene:

1. Near the minimum of solar activity, there is a weak axisymmetric dipole field (~ 1 G) emerging at high latitude and extending far out in the corona, the field lines cross the equatorial plane at a distance of a few solar radii and connect back to the opposite polar region.
2. The polar regions rotate every 34 days, while the equatorial regions do it in 25.5 days. The inner frozen-in field lines are stretched out in the east–west direction.

The winding-up of the field lines generates (ω effect) a strong toroidal field component (several 10^2 G at low latitudes), converting some of the kinetic energy of differential rotation into magnetic energy. These toroidal components have opposite directions in the two hemispheres.

3. The vertical convective motions create upward magnetic loops, with their planes still oriented in the toroidal direction. This further intensifies the field which locally reaches an intensity of a few kG. The loops of the field lines are twisted in the north–south direction by the Coriolis force, generating a poloidal field component (α effect). When the bunches of field lines erupt at the solar surface, as a result of magnetic buoyancy (Sect. 13.7.2), they produce bipolar active regions. The ordered toroidal field at the base of the convective zone may reach intensities of $\sim 10^4$–10^5 G before erupting.

4. The feet of the emerging loops migrate toward lower latitudes, from about 30–40° to 15°, maybe due to meridional circulation and magnetic diffusion. Magnetic reconnection of northern and southern loops, i.e., a sudden change of the field geometry closing the loops in a different way, is able to rebuild the poloidal field across the equator with a polarity opposite to the initial one. The reconnection liberates large closed loops feeding energy into the corona. The new poloidal field then retracts below the surface in equatorial regions reproducing again the geometry of the first step in the cycle.

The dynamo in a convective region derives its energy mostly from the energy flux of the star, thus there is plenty of energy to feed the dynamo. The main remaining questions about the solar cycle [114] regard the generation of the poloidal field component, the roles of meridional circulation and of small scale turbulence, etc.

13.1.5   Observed Fields and Limits

Magnetic fields are present in most kinds of stars, but with different intensities. T Tauri stars show magnetic fields in the range of 1–2.5 kG [225], brown dwarfs, M and K dwarfs also show such strong fields and evidences of large spots. The average poloidal field in the Sun is of the order of 1 G; however, there are fine structures with field intensities reaching locally a few kG. The field in solar-type stars originates from the convective dynamo in the envelope, which produces time–dependent fields responsible for the observed magnetic activity cycles. In fully convective stars ($M <$ 0.4 $M_\odot$), a different, possibly more turbulent, dynamo may be present.

Fields reaching several tens of kG are observed in Ap stars, which have globally organized fields, generally dipolar with an axis inclined with respect to the rotation axis. These fields are stable over decades, they are likely of fossil origin with some further evolution [63]. At the opposite, Am and HgMn stars show no evidence of magnetic fields [521].

Searches for magnetic fields in OB-type stars show in general no evidence of fields at the level of $\sim$100 G [392]. There are, however, a few exceptions, such as θ Ori C, an O7-type star with a field of 1–2 kG [166], and ω Ori (B2IIIe) with an

oblique poloidal field of 530 G [438]. Weak poloidal fields of a few 10^2 G have also been found in some B stars [242]. The origin of these fields, fossil or dynamo created, is still uncertain. It is unlikely that, if built in the convective core, the field can be advected by meridional circulation to the surface [116]. Thus, there must be either a dynamo process, different from the solar dynamo, or some transport mechanism.

Let us consider a straight flux tube of magnetic field of intensity B perpendicular to the stellar surface. If P_{ext} and P_{int} are, respectively, the pressures outside and inside the tube, the lateral pressure equilibrium or magnetostatic balance (13.12) implies

$$\frac{B^2}{8\pi} = P_{ext} - P_{int} \,. \tag{13.20}$$

The hydrostatic equilibrium for an atmosphere of given gravity g and constant opacity κ leads to the following estimate of the pressure at an optical depth $\tau = 2/3$, $P(\tau = 2/3) = (2/3)\,g/\kappa$ (see Eq. 24.18). Since P_{int} should be positive, the maximum possible field B_{eq} for magnetic equilibrium is [503],

$$B_{eq}\,(\tau = 2/3) = \left(\frac{16\pi}{3}\,\frac{g}{\kappa}\right)^{1/2}. \tag{13.21}$$

This expression gives the order of magnitude of the equilibrium field intensities. These are indicated in Table 13.1 for stars of various spectral types.

This applies to local field tubes as present in stars with an external convective zone. The observed field intensities are of the above order of magnitude; however, they are often up to a factor of 2 larger than the values in Table 13.1. The discrepancies seem to be due to the fact that the theoretical models for deriving the field intensities use the same gaseous pressure inside and outside the intense field tubes [503]. For an O star with $\log g = 4.0$ and electron scattering opacity, the equilibrium field would be about 200 G. The occurrence of convective envelopes in very luminous O stars (Sect. 5.5.1), especially if they rotate fast, could explain the presence of magnetic fields in some OB stars. It is clear that large-scale dipolar fields, as in Ap stars, are not following the above condition (13.21), since they are global stellar fields.

Table 13.1 The equilibrium field for stars of various spectral types. The stars are on the ZAMS, except the Sun

Spectral type	Field (kG)
M0	2.8
K0	1.5
Sun	1.3
G0	1.0
F2	0.6

13.2 Magnetic Braking of Rotating Stars

The convective dynamo operating in the external layers of solar-type stars creates a magnetic field, as seen above. As a consequence, the field may force the outer plasma resulting from the weak stellar winds to co-rotate with the star up to a large distance. This produces a loss of angular momentum from solar-type and lower mass stars, with many consequences for stellar evolution. There are also direct effects on the distributions of rotational velocities as a function of ages and masses, in particular

- The steep decrease of rotational velocities v near spectral type F3 ($M \sim 1.4\,M_\odot$), a limit below which Pop. I stars have a convective envelope.
- The decrease of v with the stellar age t according to a law $v \sim t^{-0.5}$, known as the Skumanich law [534] for solar-type stars.

Let us call r_A the radius up to which the outer material of the stellar wind co-rotates at angular velocity Ω with the star of mass M and radius R. The value of r_A is determined by the field strength B_0 at the surface. The star loses mass and let (dM/dt) be the total mass crossing the sphere of radius r_A by unit of time. The loss of angular momentum in a spherical shell [279] for a star of radius R and angular velocity Ω is for a radial and a dipolar field,

$$\frac{dJ}{dt} = \frac{2}{3}\frac{dM}{dt}R^2\Omega\left(\frac{r_A}{R}\right)^2_{\text{radial}},$$

$$\frac{dJ}{dt} = \frac{2}{3}\frac{dM}{dt}R^2\Omega\left(\frac{r_A}{R}\right)^1_{\text{dipole}}. \tag{13.22}$$

For other geometries, the exponent n is different [279]. Co-rotation of the stellar wind is present up to a radius r_A where the Alfvén velocity v_A (Sect. 13.1.3) is larger or equal to the wind velocity v. This means that up to this point the magnetic field dominates the dynamic of the wind. The wind velocity is currently a multiple k_{wind} of the local escape velocity. These two velocities are, respectively,

$$v_A = \frac{B_A}{(4\pi\varrho)^{\frac{1}{2}}} \quad \text{and} \quad v_{\text{wind}} = k_{\text{wind}}\left(\frac{2GM}{r_A}\right)^{\frac{1}{2}}, \tag{13.23}$$

where B_A is the field at r_A. The conservation of mass gives

$$\dot{M} = 4\pi\varrho\, r_A^2\, v_{\text{wind}}, \tag{13.24}$$

and the conservation of the magnetic flux, in the radial case, gives

$$B_0 R^2 = B_A r_A^2, \tag{13.25}$$

where B_0 is the field at the stellar surface $r = R$. By using (13.24), (13.23) and the equality $v_{\text{wind}} = v_A$ at the co–rotation radius r_A, one obtains $(\dot{M}\,v_{\text{wind}})^{1/2} = r_A B_A$.

Thus, expression (13.25) of the flux conservation is

$$B_0 R^2 = r_A \left(\dot{M} v_{\text{wind}} \right)^{1/2} . \tag{13.26}$$

From this, we get the ratio (r_A/R) in the radial case with (13.23)

$$\frac{r_A}{R} = \frac{B_0 R}{\dot{M}^{1/2} v_{\text{wind}}^{1/2}} = \frac{B_0 R}{\dot{M}^{1/2} k_{\text{wind}}^{1/2}} \frac{r_A^{1/4}}{(2GM)^{1/4}} , \tag{13.27}$$

also $v_A = v_{\text{wind}}$ with (13.25) and (13.24) leads to

$$\frac{B_0 R^2 v_{\text{wind}}^{1/2}}{r_A^{1/2} \dot{M}^{1/2}} = k_{\text{wind}} (2GM)^{1/2} , \text{ thus } r_A^{1/4} = \frac{B_0^{1/3} R^{2/3}}{(k_{\text{wind}} \dot{M})^{1/6} (2GM)^{1/2}} . \tag{13.28}$$

This inserted in (13.27) gives

$$\frac{r_A}{R} = \frac{1}{2^{\frac{1}{3}} G^{\frac{1}{3}}} \frac{B_0^{\frac{4}{3}}}{k_{\text{wind}}^{\frac{2}{3}}} \frac{R^{\frac{5}{3}}}{\dot{M}^{\frac{2}{3}} M^{\frac{1}{3}}} , \tag{13.29}$$

where the mass loss rate $\dot{M}$ is taken here as a positive quantity. In the dipole case, the magnetic flux conservation is $B_0 R^3 = B_r r_A^3$ and a similar analysis leads to a different dependence on r_A/R, so that one can write the rate (13.22) of loss of angular momentum as

$$\frac{dJ}{dt} = \frac{2}{3} \frac{dM}{dt} R^2 \Omega \left(\frac{r_A}{R} \right)_{\text{radial}}^n , \tag{13.30}$$

with $n = 2$ or $n = 3/7$ depending on whether the field is radial or dipolar. We need to know B_0 in (13.29). One assumes that the magnetic flux is proportional to some power a of the rotation rate Ω

$$B_0 = k_B \left(\frac{R}{R_\odot} \right)^{-2} \Omega^a . \tag{13.31}$$

With this assumption, the ratio r_A/R (13.29) becomes, for example, in the radial case

$$\left(\frac{r_A}{R} \right)_{\text{radial}} \sim k_{\text{wind}}^{-\frac{2}{3}} k_B^{\frac{4}{3}} \Omega^{\frac{4a}{3}} R^{-1} \dot{M}^{-\frac{2}{3}} M^{-\frac{1}{3}} , \tag{13.32}$$

and the loss of angular momentum (13.30)

$$\frac{dJ}{dt} = K_W \Omega^{1 + \frac{4an}{3}} R^{2-n} \dot{M}^{1 - \frac{2n}{3}} M^{-\frac{n}{3}} . \tag{13.33}$$

The various constants are grouped in the factor K_W. Mass loss implies a loss of angular momentum (both losses being expressed as positive quantities). The value of n

depends on the field geometry. A value of $n = 1.5$ is often adopted, it is between the radial and dipolar cases which respectively correspond to $n = 2$ and $n = 3/7$. If so, dJ/dt is independent from the mass loss rates. The value $n = 1.5$ reproduces Skumanich's observed law (13.42) for the decrease of the rotation velocities of solar-type stars with time [534].

The parameter a describes the dependence of the magnetic flux on the angular velocity Ω. A value $a = 1$, meaning that the magnetic flux grows linearly with Ω, is supported by magnetic field measurements of solar-type stars [501] up to velocities equal to 10 times the solar rotation velocity. Above, there are saturation effects (Sect. 13.2.1). The value of the parameter K_W is adjusted on observations. If the mass and radius in (13.33) are expressed in solar units, the mass loss rates are in units of $10^{-14} M_\odot$ yr^{-1} and Ω in s^{-1}, the value of K_W in (13.33) is 2.7×10^{47} g cm^2 [279]. Expression (13.33) receives some further developments below.

13.2.1   Saturation Effects

Comparisons of the above developments with observations of rotation velocities for stars of various masses and ages have led to further improvements. However, this brings more parameters in the theory, which allows one to reduce the discrepancies. Despite these reserves, two effects seem physically justified: the saturation effect and its mass dependence.

The observations of magnetic fields for solar-type stars support a linear dynamo (13.31) with $a = 1$ and a saturation for angular velocities $\Omega > 10\,\Omega_\odot$ [501]. Above this limit there is no further increase of the magnetic field. Other diagnostics, such as X-ray flux and stellar spots, also support a saturation effect in the field creation by stellar dynamos.

One may wonder whether the observed saturation results from the dynamo process itself or from effects in the signatures of the magnetic field. If the saturation lies in the dynamo, the effect should also be present for the loss of angular momentum by magnetic braking. This seems to be the case [35], because otherwise observations would show no fast rotators on the ZAMS. Thus, above a certain rotation limit Ω_{sat}, one sets $a = 0$ in the dynamo expression (13.31). We adopt the intermediate value $n = 1.5$ and the rate of angular momentum loss is expressed by the two equations

$$\frac{dJ}{dt} = -K_W \, \Omega^3 \left(\frac{R}{R_\odot}\right)^{\frac{1}{2}} \left(\frac{M}{M_\odot}\right)^{-\frac{1}{2}} \quad \text{for} \quad \Omega < \Omega_{sat}, \qquad (13.34)$$

$$\frac{dJ}{dt} = -K_W \, \Omega \, \Omega_{sat}^2 \left(\frac{R}{R_\odot}\right)^{\frac{1}{2}} \left(\frac{M}{M_\odot}\right)^{-\frac{1}{2}} \quad \text{for} \quad \Omega \geq \Omega_{sat}. \qquad (13.35)$$

The behavior of $\Omega(t)$ as a function of time is different for these two laws:

1. If we suppose that the mass, radius and moment of inertia do not change too fast with time, we get from (13.34) the Skumanich law $\Omega \sim t^{-1/2}$, implying that

faster rotators experience a greater velocity decrease. Thus, the ratio of $v \sin i$ between the fastest and slowest rotators declines with time.

2. Under the same assumptions we get from (13.35)

$$\Omega = \Omega_0 e^{-at} , \tag{13.36}$$

where a is a constant. This means that once Ω_{sat} is reached, all stars of a given mass spin down by the same factor over a given time, so that the ratio between the fastest and slowest rotators remains the same.

The value of K_{W} is adjusted by requiring that a 1 $M_\odot$ star reaches the age of the Sun with the observed solar rotation $\Omega_\odot = 2.9 \times 10^{-6}$ s^{-1}. This yields $K_{\text{W}} = 2.7 \times 10^{47}$ g cm^2, a value which may depend on the transport efficiency in the model. This calibration does neither depend on the disk lifetime nor on the initial rotation nor on Ω_{sat}, because at the age of the Sun all rotation histories have converged to the same velocities.

The value of Ω_{sat} influences the evolution of rotation during the end of the pre-MS phase and the early MS phase. A lower value of Ω_{sat} leads to several effects: (1) The braking is less efficient and thus the peak velocity when the star reaches the ZAMS is higher. (2) The star stays longer in the saturation regime. (3) The spin-down timescale is increased.

Thus, for a lower Ω_{sat}, the convergence of rotation velocities intervenes later. As an example, for $\Omega_{\text{sat}} = 14 \Omega_\odot$ the convergence occurs at 2×10^8 yr, while for $\Omega_{\text{sat}} = 10 \Omega_\odot$ it intervenes at 4×10^8 yr. The value of Ω_{sat} is best constrained by clusters with ages intermediate between those of the Pleiades ($\sim 1.1 \times 10^8$ yr) and of the Hyades (6×10^8 yr). A value of $\Omega_{\text{sat}} = 14 \Omega_\odot$ seems acceptable [60], in order to reproduce the distribution of the rotational velocities of the stars from 0.5 to 1.0 $M_\odot$ in the Hyades (Fig. 21.5).

13.2.2 Mass Dependence

The X-ray activity, measured by the ratio $L_{\text{X}}/L_{\text{bol}}$ of the X-ray to the bolometric luminosities of solar-type stars, is better related to the inverse of the Rossby number $\mathcal{R}o$ than to the rotation period P_{rot}. The Rossby number $\mathcal{R}o$ (cf. Appendix B.5.4) is the ratio of the inertia to the Coriolis forces. In a convective zone, $\mathcal{R}o$ scales like $P_{\text{rot}}/t_{\text{conv}}$, where t_{conv} is the turnover time of convection (5.49). This means that if the star has a thin outer convective zone, the chromospheric activity is enhanced, a fact which is consistent with the observed increase of $L_{\text{X}}/L_{\text{bol}}$ with mass. This luminosity ratio also shows a saturation effect and this suggests the possibility of a mass-dependent value of the saturation level Ω_{sat} [292],

$$\Omega_{\text{sat}}(\text{star}) = \Omega_{\text{sat}}(\odot) \frac{t_{\text{conv}}(\odot)}{t_{\text{conv}}(\text{star})} . \tag{13.37}$$

As said above, a value of $\Omega_{\text{sat}}(\odot)$ an order of magnitude larger than $\Omega_{\odot}$ is appropriate for solid body rotation; for differential rotation, a saturation value of about 5 $\Omega_{\odot}$ appears preferable [292]. Expression (13.37) leads to $\Omega_{\text{sat}} = 2.5, 6, 10$ and 15 $\Omega_{\odot}$ for models of 0.6, 0.8, 1.0 and 1.2 $M_{\odot}$, respectively. The increase of Ω_{sat} with mass results from the thinner external convective zones when mass increases in the range of solar-type stars.

If Ω_{sat} would be constant with mass, the predicted velocities would decrease with time for all masses, but they would keep higher for the higher masses. The reason is the mass dependence of (13.34) and (13.35), while the radius changes little with mass. Such a result would contradict observations, since cluster data show that rapid rotation disappears more quickly for the higher mass stars in the mass interval of 0.5–1.2 $M_{\odot}$.

The above mass-dependent Ω_{sat} (13.37), suggested by observations of X-ray activity, gives a better agreement with observations, better reproducing the faster decrease of rotation velocities with time for the higher mass stars in the considered interval (Fig. 21.5). (It has been suggested [533] that Ω_{sat} might decrease faster than suggested by (13.37) for masses lower than 0.4 $M_{\odot}$.)

13.2.3   Consequences

There are many consequences of the magnetic braking during star formation and the MS phase of solar-type stars. Let us consider the case of solid body rotation in the MS phase, where the stellar radius R and moment of inertia I do not change rapidly. The angular momentum is

$$J = I\Omega = I\frac{v}{R}, \tag{13.38}$$

where v is the rotational velocity at equator. Figure 13.1 illustrates the moment of inertia for stars of various masses and metallicities on the zero-age sequence. The angular momentum of stars of different masses is illustrated as a function of the angular velocity in Fig. 13.2. For stars of standard composition, the moment of inertia behaves with mass like

$$I \sim M^{2.25}. \tag{13.39}$$

From (13.33) and (13.38), we get for constant I and R

$$\frac{I}{R}\frac{dv}{dt} \sim \Omega^{1+(4an/3)}. \tag{13.40}$$

Since R is taken constant, the integration gives

$$v \sim t^{[-3/(4an)]}. \tag{13.41}$$
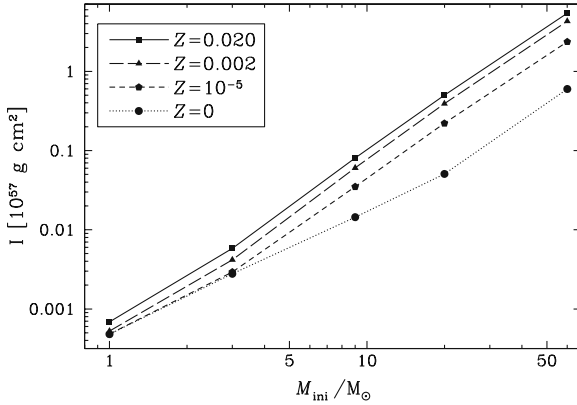
Fig. 13.1 The moment of inertia for stars of various masses and metallicities Z on the zero-age sequence. From S. Ekström et al. [176]
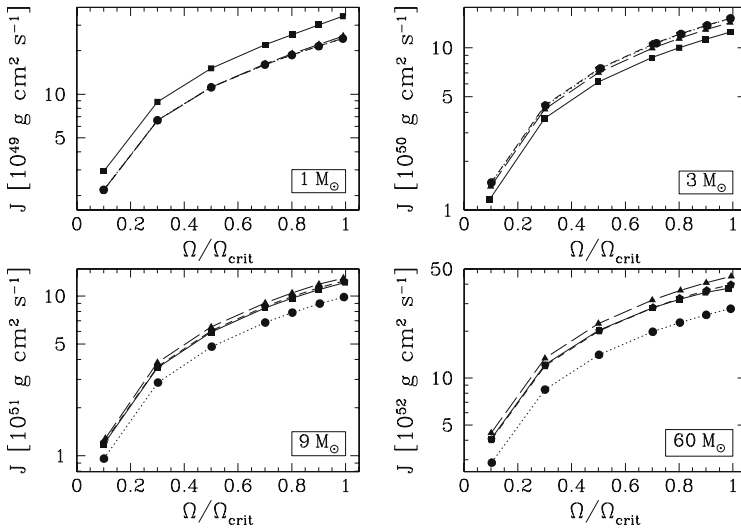
Fig. 13.2 The values of the angular momentum J of stars of different masses on the ZAMS with $Z = 0.02$ as a function of $\omega = \Omega/\Omega_{\text{crit}}$. The changes of the stellar radii with rotation are taken into account. Courtesy from S. Ekström

For $a = 1$ and $n = 1.5$, this gives the Skumanich law [534] for the decrease of the rotational velocities with time in solar-type stars:

$$v \sim t^{-0.5} . \tag{13.42}$$

Thus, for $n = 1.5$ the predicted braking is in agreement with observations for solar-type stars. Figure 21.4 shows the evolution of the rotation velocity as a function of age during the pre-MS and MS phases for a 1 $M_\odot$ star for various n. A curve

$\log v$ vs. $\log t$ intermediate between the curves for $n = 1$ and $n = 2$ reproduces well Skumanich's law (13.42) for ages larger than 10^8 yr. The evolution of the angular velocity is determined by

$$\frac{1}{\Omega}\frac{d\Omega}{dt} = \frac{1}{J}\frac{dJ}{dt} - \frac{1}{I}\frac{dI}{dt}. \tag{13.43}$$

Thus, both the magnetic braking and the decrease of the moment of inertia I during the MS phase determine the evolution of the rotation velocity of solar-type stars. One has also to account for the transport processes (e.g., meridional circulation), which redistribute the angular momentum.

The change of the parameters of magnetic braking have the following consequences on evolution:

1. Effects of n: larger n values increase the dependence of the loss of J on Ω. For larger n, the loss of angular momentum starts earlier during the pre-MS phase. For $n = 1.5$, the loss of J goes like Ω^3 (Fig. 21.4).
2. Effects of K_W: multiplying the value of K_W by a factor f reduces the value of the velocities by $f^{1/2}$ after the maximum of the curves in the diagram $\log v$ vs. $\log t$ (Fig. 21.4).

Magnetic braking has many consequences in the formation and evolution of solar-type stars (Sect. 21.3).

13.3 Magnetic Field Properties in Radiative Regions

Magnetic fields are also important in radiative regions, because they can efficiently contribute to the transport of angular momentum and affect the evolution (Fig. 13.3). The main effect of a magnetic field is to favor a strong internal coupling, which may lead to solid body rotation. This is for example expressed by the so-called Ferraro law of isorotation (Sect. 13.3.1).

Quite generally, there is a strong interaction between differential rotation and magnetic field. The coupling of different layers by the magnetic field only allows a very small degree of differential rotation, close to uniform rotation [401]. Even very weak poloidal fields are able to enforce solid body rotation, for the Sun the limit is around 0.03 G [402]. This is of interest for the internal solar rotation (Sect. 13.6). Also, the small shear of the poloidal field by differential rotation gives rise to an azimuthal field. Models in Sect. 13.6 confirm the nearly solid body rotation of stars with self-generated magnetic fields (Sect. 13.3.3).

Radiative equilibrium is broken on equipotentials of stars with a large-scale magnetic field (13.14) in the same way as it is broken in rotating stars. Thus, circulation currents are also driven in stars with a poloidal field, whether axisymmetric or not, with or without some toroidal field [430].

A critical aspect concerns the instabilities of the magnetic structures and their possible amplification by the winding-up of the lines by differential rotation. The magnetic instabilities may also directly transport the elements and the field they
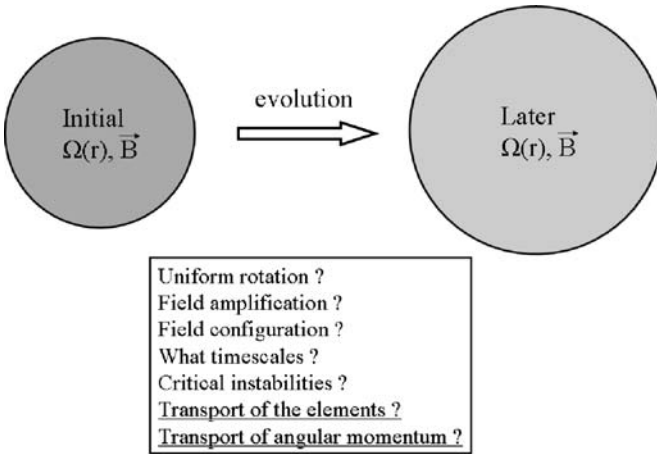
Fig. 13.3 Questions regarding the magnetic field and evolution

create may insure the internal coupling of the angular velocity in radiative regions (cf. Sect. 13.4).

13.3.1   The Ferraro Law of Isorotation

The law of isorotation was found by Ferraro [183, 184]. This law or theorem says the following: "The magnetic field of a star can only remain steady if it is symmetrical about the axis of rotation and each line of force lies wholly in a surface which is symmetrical about the axis and rotates with uniform angular velocity". To derive this law, we separate the magnetic field into poloidal and toroidal components [558] in spherical coordinates (r, ϑ, φ),

$$B = B_p + B_\varphi .\tag{13.44}$$

Several simplifications are made. The fluid is assumed to have no other motions than a rotation with velocity component $v_\varphi = r \sin \vartheta \, \Omega$ in the direction of the unity vector e_φ. It is incompressible which implies $\nabla \cdot v = 0$ and perfectly conducting ($\eta = 0$). The solution is stationary and axisymmetric. The induction equation (13.4) for the component B_φ becomes

$$\frac{\partial B_\varphi}{\partial t} = [\nabla \times (v \times B)] \cdot e_\varphi = [(\nabla \cdot B)v - (\nabla \cdot v) \cdot B] \cdot e_\varphi.\tag{13.45}$$

The operator ∇ acts as a derivative on the subsequent terms so that one has

$$\frac{\partial B_\varphi}{\partial t} = [v(\nabla \cdot B) + (B \cdot \nabla)v - B(\nabla \cdot v) - (v \cdot \nabla)B] \cdot e_\varphi.\tag{13.46}$$

The first and third terms are zero, because of the Maxwell equations (13.3) and because of the incompressibility. Accounting for the fact that the only motion is rotation with a velocity component $v_\varphi = r \sin \vartheta \, \Omega$, one gets

$$\frac{\partial B_\varphi}{\partial t} = [(\boldsymbol{B_p} \cdot \boldsymbol{\nabla}) v_\varphi \boldsymbol{e}_\varphi - (v_\varphi \boldsymbol{e}_\varphi \cdot \boldsymbol{\nabla}) \boldsymbol{B}] \cdot \boldsymbol{e}_\varphi = (\boldsymbol{B_p} \cdot \boldsymbol{\nabla}) v_\varphi \, . \qquad (13.47)$$

The second term in the bracket is zero, because there is no φ gradient of B_φ due to the axial symmetry. This equation shows that a toroidal field can be produced from a poloidal field in the presence of differential rotation. The stationarity imposes

$$(\boldsymbol{B_p} \cdot \boldsymbol{\nabla}) \Omega = 0 \, . \qquad (13.48)$$

This expression states that there is no gradient of Ω along a poloidal field line. Thus, the Ferraro theorem is that stationarity, together with the other mentioned conditions, imposes that the poloidal field lines have a constant Ω. Since the loop described by the poloidal field lines go from the center to the surface, it is a common extension to say that magnetic fields produce solid body rotation. In practice, this requires some time during which diffusion may adjust the fluid velocity to that of the field lines.

13.3.2   Field Amplification by Winding-Up

Differential rotation stretches the frozen-in field lines and after several rotation periods the field lines are wound-up with a strong toroidal component. The field lines become very close to each other, meaning that the field has been amplified. Some energy of the differential rotation is converted into magnetic energy. Let us assume [545] that the initial field is weak, i.e., the average Alfvén frequency $\overline{\omega}_A$ (13.17) is small compared to the rotation frequency Ω,

$$\overline{\omega}_A = \frac{\overline{B}}{R(4\pi\overline{\varrho})^{1/2}} \ll \Omega \, , \qquad (13.49)$$

where $\overline{B}$ and $\overline{\varrho}$ are the mean field and density, respectively, R is the radius. The above condition is verified for the Sun (if $\overline{B} < 10^6$ G) and for early-type stars.

Let us consider only the azimuthal motions due to rotation and ignore magnetic diffusivity in the induction equation (13.5) as well as the thermal effects. The initial poloidal field $\boldsymbol{B}_p$ is assumed axisymmetric around the rotation axis. The components $(B_r, B_\vartheta, 0)$ do not change with time, but a new toroidal component B_φ can be generated by the differential rotation. Equation $\boldsymbol{\nabla} \cdot \boldsymbol{B} = 0$ implies that $\boldsymbol{B} = \boldsymbol{\nabla} \times \boldsymbol{\psi}$, where $\boldsymbol{\psi}$ is a function called the stream function, the value of $\boldsymbol{\psi}$ is constant on a given field line. Thus, for an axisymmetric field the two components of $\boldsymbol{B}$ are

$$B_r = (\boldsymbol{\nabla} \times \boldsymbol{\psi})_r = \frac{1}{r^2 \sin \vartheta} \frac{\partial \psi}{\partial \vartheta} \, , \quad B_\vartheta = (\boldsymbol{\nabla} \times \boldsymbol{\psi})_\vartheta = -\frac{1}{r \sin \vartheta} \frac{\partial \psi}{\partial r} \, . \qquad (13.50)$$

The components of the induction equation (13.5) become then, since B_r and B_ϑ are constant and only $v_\varphi \neq 0$,

$$\frac{\partial B_r}{\partial t} = 0, \quad \frac{\partial B_\vartheta}{\partial t} = 0, \quad \frac{\partial B_\varphi}{\partial t} = r \sin \vartheta \; \boldsymbol{B}_p \cdot \boldsymbol{\nabla}\Omega \;. \tag{13.51}$$

The equation for the toroidal component can be integrated in time

$$B_\varphi = \underbrace{r \sin \vartheta \int_0^t |\nabla\Omega| \, dt}_{\text{nb. of differential revolutions}/2\pi} \left(\boldsymbol{B}_p \cdot \frac{\boldsymbol{\nabla}\Omega}{|\nabla\Omega|} \right) . \tag{13.52}$$

The initial field can be considerably amplified. Since the number of differential revolutions (i.e., the number of rotations due to differential rotation) can be huge, even a minute initial field can become large after a certain time [545]. A rough estimate of the minimum initial poloidal field is obtained by considering a field such that its Alfvén velocity (13.17) is equal to the velocity necessary for crossing the stellar radius during the star lifetime t_0, i.e., $v_A = R/t_0$. For the Sun, this gives an Alfvén velocity of 2.2×10^{-7} cm s^{-1} and an initial field of the order of 10^{-6} G. This is a rough estimate, since the growing field and the differential rotation would change with time. Nevertheless, it shows that the amplification of even a very small poloidal field may occur and influence star evolution. In general, the initial field may be larger than the above minimum.

13.3.3 Magnetic Field Evolution and Rotational Smoothing

The Alfvén waves at different points in the star oscillate independently with different frequencies [545]. The oscillating lines of the intense field become locally close to each other and interact. This process is called "phase mixing". As the length scale between the field lines becomes small, magnetic diffusion comes into play and has to be accounted for. Let us consider a differentially rotating star with a weak initial non-axisymmetric poloidal field $\boldsymbol{B}_p$, which we decompose into axisymmetric and non-axisymmetric parts such that

$$\boldsymbol{B}_p = \boldsymbol{B}_a + \boldsymbol{B}_{na}, \;\; \text{with} \;\; \frac{\partial \boldsymbol{B}_a}{\partial \varphi} = 0 \;\; \text{and} \;\; < \boldsymbol{B}_{na} >_\varphi = 0 \,, \tag{13.53}$$

where the last relation means that the azimuthal average of the non-axisymmetric part vanishes. A constant diffusivity η is assumed. The induction equation (13.5) is linear in the field and thus it applies to each of the two components in (13.53) which are winding up. The non-axisymmetric field has opposite polarities at latitudes differing by less than π, since the average $< \boldsymbol{B}_{na} >$ vanishes. Let us consider, at a given colatitude ϑ, two points with opposite polarity separated by a distance ℓ in the direction of the rotation gradient (e.g., vertically in the case of shellular rotation). The

two points will have the same φ after a time t such that,

$$t \approx \frac{\text{circonference}}{\text{diff. velocity}} \approx \frac{2\pi r}{q\Omega \ell}, \tag{13.54}$$

where $q = r|\nabla\Omega|/\Omega$ is a parameter of differential rotation, always counted positively. Its value is ≤ 2, otherwise the star would be Rayleigh–Taylor unstable (Sect. 6.4.2). The opposite polarities over a distance ℓ cancel each other by magnetic diffusion after a time of the order of $t_d \approx \ell^2/\eta$. This means that the non-axisymmetric component of the poloidal field has a relative decay given by

$$\frac{1}{B_{na}}\frac{\partial B_{na}}{\partial t} \approx -\frac{1}{t_d} \approx -\eta\left(\frac{t\Omega q}{2\pi r}\right)^2, \tag{13.55}$$

where (13.54) is used to express ℓ. The integration of (13.55) yields

$$\ln B_{na} \approx -\eta\left(\frac{\Omega q}{\pi r}\right)^2 \frac{t^3}{3} + \text{const}. \tag{13.56}$$

or

$$B_{na} = B_{na}(0)\, e^{-(t/t_\Omega)^3}, \quad \text{with} \quad t_\Omega \approx \left(\frac{12\pi^2 r^2}{\eta\,\Omega^2 q^2}\right)^{1/3}. \tag{13.57}$$

The timescale t_Ω is the rotational smoothing time, i.e., the timescale for the decrease of the non-axisymmetric component of the field. The index "0" indicates the initial values at time $t = 0$. The non-axisymmetric component decays exponentially. For an initial Sun rotating with $\Omega = 3\times 10^{-5}$, i.e., 10 times faster than the present Sun, with $\eta = 10^3$ and $q = 0.1$, one finds $t_\Omega \approx 10^3$ yr. The non-axisymmetric component of the field disappears very rapidly and the star evolves toward a stage of differential rotation with an axisymmetric magnetic field.

The above conclusion applies if the initial field is weak enough, so that the magnetic torque exerted by the field is insufficient to impose solid body rotation. The condition is that the initial Alfvén travel time $t_A(0) = 1/\omega_A(0)$ is longer than the smoothing time t_Ω [545],

$$\frac{r(4\pi\varrho)^{1/2}}{B_0} > \left(\frac{12\pi^2 r^2}{\eta\,\Omega^2 q^2}\right)^{1/3}. \tag{13.58}$$

This shows that the initial field B_0 must be smaller than B_1,

$$B(0) < B_1 = r(4\pi\varrho)^{1/2}\left(\frac{\eta\,\Omega^2 q^2}{12\pi^2 r^2}\right)^{1/3}. \tag{13.59}$$

After a time t_Ω, there remains only an axisymmetric poloidal field in the differentially rotating star. The magnetic coupling by this poloidal field keeps a constant rotation Ω on the magnetic surface (the magnetic coupling is achieved by the phase

mixing of different Alfvén waves, which damps out the differential motions on a magnetic surface, thus imposing $\Omega = $ const).

On the contrary, if the initial field $B(0)$ is larger than B_1 (13.59), the rotational smoothing does not happen and the field remains non-axisymmetric. The magnetic torque is able to suppress the differential rotation, leading to a state of uniform rotation. This is achieved by Alfvén waves traveling on the non-axisymmetric magnetic surfaces and by phase mixing. The differential motions on these surfaces are damped out and as they are non-axisymmetric, the only solution is a state of uniform rotation.

In conclusion, there are schematically two possibilities for the evolution of the field in rotating stars [545]:

– For initial fields smaller than B_1: the star tends toward a state of differential rotation with an axisymmetric poloidal field, Ω being constant on magnetic surfaces.
– For initial fields larger than B_1: the star tends toward solid body rotation with a non-axisymmetric field.

These are the main evolutionary scenarios for radiative stellar regions and they are confirmed by many numerical models [431, 432]. The further evolution of the field and rotation may also be influenced by magnetic instabilities.

13.4 The Tayler Instability and Possible Dynamo

Several magnetic instabilities may occur and produce displacements, influencing both rotation and magnetic field as well as contributing to the transport processes. There are various types of instabilities. A most important instability is the Tayler instability, which has the lowest threshold and a short timescale.

13.4.1 The Tayler Instability

The original result of Tayler [567] was that a purely toroidal field $B_\varphi(r, \vartheta)$, even very weak, in a stably stratified star is unstable on an Alfvén timescale $t_A = R/v_A$. The first magnetic instability to appear is a non-axisymmetric instability of type $m = 1$, which was further studied by Spruit [545, 546]. The instability is confined to horizontal surfaces, which avoid work against the stable stratification. This instability occurs under a wide range of conditions and is characterized by a low threshold and a very short growth time.

Let us consider an azimuthal field consisting of concentric loops around the rotation axis. The instability appears as low-azimuthal order displacement in a ring around the star (Fig. 13.4). The magnetic loops move apart from the rotation axis, like a disordered heap of tires. They move apart due to the magnetic pressure of the toroidal field loops, which press on each other: the pressure is released by sideways

Fig. 13.4 Unstable displacements with $m = 1$ of the azimuthal magnetic field in the polar region. The large arcs (*thin broken lines*) indicate the horizontal stellar surfaces. Adapted from Spruit [545]
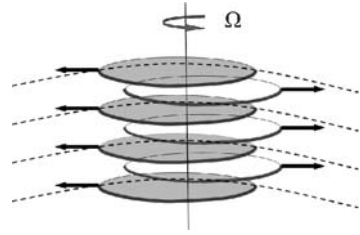
motions. This instability was first found in the case where thermal and magnetic diffusivities $K = \eta = 0$ and without rotation. Tayler's instability is always present in a sizable region around the poles. Detailed calculations of the instability were performed from wave perturbations of the form

$$\xi = \xi_0 \exp i\,(lr + m\varphi + nz - \sigma_B t) \;, \tag{13.60}$$

applied to the conservation equations, which provide a dispersion relation [4]. In a rotating star, the instability is also present [472]; however, the characteristic growth rate σ_B of the instability is, if $\omega_A \ll \Omega$,

$$\sigma_B = \frac{\omega_A^2}{\Omega} \;, \tag{13.61}$$

instead of the Alfvén frequency ω_A, because the growth rate of the instability is reduced by the Coriolis force [546]. One usually has the following ordering of the different relevant frequencies: (1) the Brunt–Väisälä frequency N which is the highest, (2) the rotation frequency Ω, (3) the Alfvén frequency ω_A or the reduced value ω_A^2/Ω, i.e.,

$$N \gg \Omega \gg \omega_A \;. \tag{13.62}$$

Typically in the Sun, one has $N \approx 10^{-3}$ s^{-1}, $\Omega = 3 \times 10^{-6}$ s^{-1} and a field of 1 kG would give an Alfvén frequency as low as $\omega_A = 4 \times 10^{-9}$ s^{-1}.

In the slow rotating case, if one has $\omega_A > \Omega$, the Tayler instability has little interest, since in such a case the star would first be unstable with respect to the Richardson criterion. Thus, the shear instability would develop rather than Tayler's instability. (This can be seen from ω_A/Ω given in (13.81) below. If $\omega_A/\Omega > 1$, one has $q\Omega/N > 1$, which apart from a numerical factor is equivalent to the Richardson condition (12.31) for instability.)

13.4.2   The Tayler–Spruit Dynamo and Questions

The question of a dynamo generated by the Tayler instability is a debated subject at the time of this writing with still many uncertainties. Owing to the enormous

potential consequences [172, 237, 369] of a possible dynamo in rotating radiative layers, we nevertheless present some of the basic current results, indicating the differences between authors. The reader should be cautious on this fast developing subject and well follow the up-to-date developments.

Spruit [545, 546] first made the interesting suggestion that a dynamo could operate in the radiative zone of a differentially rotating star thanks to Tayler's instability. Let us consider a star with a shellular rotation law $\Omega(r)$ with an initially weak poloidal magnetic field B_r, so that the magnetic forces are negligible. (Strong initial field leads to solid body rotation, Sect. 13.3.3.) The radial component is wound-up by differential rotation. After a few differential turns, an azimuthal field of component B_φ is present, its strength grows linearly in time (13.52) and the component B_φ dominates over B_r. At some stage, the field B_φ becomes unstable, due to Tayler's instability which is the first instability encountered. The instabilities mainly have horizontal components, but there is also a small vertical component of size l_r, limited by the action of buoyancy forces. This small radial component of the field is further wound-up by differential rotation, which then amplifies the toroidal component of the field up to a stage where dissipation effects would limit its amplitude. In this way, a strong toroidal field develops together with a limited radial field. The horizontal component enforces shellular rotation, while the vertical field component favors solid body rotation.

Numerical simulations by Braithwaite [62] and by Zahn et al. [634] confirm the existence of Tayler's instability. Braithwaite also finds the existence of a dynamo loop in agreement with Spruit's analytical developments. Zahn et al. do not find the dynamo loop proposed by Spruit and question what may close the loop.

13.4.3   Conditions for Instability

A dynamo at work in a radiative region derives its energy from the differential energy of rotation. The differential rotation itself results from several effects: (1) the change of the moment of inertia as evolution proceeds, (2) the spin-down due to some magnetic coupling and/or mass loss at the stellar surface, (3) the transport by meridional circulation.

Compared to the energy available for the solar dynamo driven by convection, the amount of energy available from differential rotation is limited. The energy density u_B of a magnetic field of intensity B is $u_B = B^2/(8\,\pi)$ (13.10). The Alfvén frequency (13.18) is in a spherical geometry $\omega_A = B/\left((4\,\pi\rho)^{\frac{1}{2}}\,r\right)$. Thus, the magnetic energy density u_B can be written as

$$u_B = \frac{1}{2}\,\rho\,r^2\omega_A^2\,. \tag{13.63}$$

In stable radiative layers, there is in principle no particular motions. However, if due to an instability some displacements of vertical amplitude $l_r/2$ occur around an average stable position, the restoring buoyancy force produces vertical oscillations around the equilibrium position with a frequency equal to the Brunt–Väisälä frequency N. The restoring oscillations will have an average density of kinetic energy $u_N = f_N \rho \, l_r^2 N^2$, where f_N is a geometrical factor of the order of unity. In order to be able to produce a vertical displacement, the magnetic field must be large enough to overcome the buoyancy effect. In terms of energy densities, this is $u_B > u_N$, otherwise the restoring force of gravity would counteract the magnetic instability at the dynamical timescale. From this, one obtains $l_r^2 < \frac{1}{2f_N} r^2 \frac{\omega_A^2}{N^2}$. If $f_N = \frac{1}{2}$, we have the condition found by Spruit ([546]; Eq. 6)

$$l_r < r \, \frac{\omega_A}{N} \, , \tag{13.64}$$

where r is the radius at the considered level in the star. Thus, the vertical length l_r of a magnetic instability is limited by the buoyancy force. At the opposite, if this radial scale is very small, the perturbation is quickly damped by the magnetic diffusivity characterized by a value η (in cm^2 s^{-1}). Thus, the radial amplitude must satisfy,

$$l_r^2 > \frac{\eta}{\sigma_B} = \frac{\eta \, \Omega}{\omega_A^2} \, , \tag{13.65}$$

where Ω is the angular velocity and σ_B is the characteristic frequency for the growth of the Tayler instability (13.61) when the Coriolis force is accounted for. The combination of the two limits (13.64) and (13.65) gives for the case of marginal stability,

$$\left(\frac{\omega_A}{\Omega} \right)^4 = \frac{N^2}{\Omega^2} \frac{\eta}{r^2 \, \Omega} \, . \tag{13.66}$$

This is the minimum value of ω_A, and thus of the magnetic field B, for the instability to occur under the condition $\omega_A \ll \Omega$. This equation relates the magnetic diffusivity η and the Alfvén frequency ω_A. It was derived by Spruit [545, 546] both from heuristic arguments as well as from the dispersion relation [4], which agrees up to a numerical factor of the order of unity. The term η is not only the magnetic diffusivity but it also has the physical meaning of a diffusion coefficient, because of the nature of the displacement (of maximum size l_r) produced by the instability. The instability is confined within a domain, limited on the large side by the stable stratification (13.64) and on the small scales by magnetic diffusion (13.65).

Zahn et al. [634] re-examined the problem by studying the dispersion relation as a function of a parameter $(\eta/K)N_T^2/N_\mu^2$ (cf. def. in 5.1.2) and find that a numerical factor called $[AS]$ multiplies the first member of (13.66). For $(\eta/K)N_T^2/N_\mu^2 = 0, 0.01, 0.1, 1, 10, \infty$, the factor is $[AS] = 4.92, 4.65, 3.48, 1.73, 1.09, 0.364$ at the optimal conditions for the onset of the instability (with account of a factor of 2 in their writing). This precises, but does not contradict the Spruit results, which were given

omitting numerical factors of the order of unity. Zahn et al. also critically review the heuristic arguments leading to an equation like (13.66).

An unstable vertical displacement of size ℓ from the azimuthal field of length scale r and intensity B_φ also feeds a radial field component B_r. The size of this field component is defined by the induction equation (13.5), which gives the following approximation over the time δt of the unstable displacement,

$$B_r \approx \delta B \approx \frac{1}{r} \frac{\ell}{\delta t} B_\varphi \, \delta t \, . \tag{13.67}$$

For the maximum displacement l_r, this gives

$$\frac{B_r}{B_\varphi} \approx \frac{l_r}{r} \, . \tag{13.68}$$

This provides an estimate of the ratio of the radial to azimuthal field components.

13.4.4 Thermal Diffusivity

Not only the magnetic diffusivity η plays a role in defining the amplitude of the instability but also the thermal diffusivity K (as also shown by the parameter $[AS]$ mentioned above, see also Spruit [546]). In a radiative region, the effects of the buoyancy force are opposed to the instability. However, these effects are reduced by the radiative losses as in the cases of semiconvection or shear instabilities (Sect. 12.2). The heat losses have also to be accounted for in the case of magnetic instabilities. For a fluid element displaced over a length l_r, the thermal fluctuations diffuse with a timescale $t_{\text{therm}} \approx l_r^2/K$, where K is the thermal diffusivity (3.46). Let us call t_B the typical timescale over which the magnetic instability develops. In a time t_B, the fluctuations are reduced by a factor f due to the thermal losses,

$$f = \frac{t_B}{t_{\text{therm}}} + 1 \, . \tag{13.69}$$

If $f \to 1$, as for $t_{\text{therm}} \gg t_B$, one has the adiabatic case. On the other hand, if $f \to \infty$, as for $t_{\text{therm}} \ll t_B$, the situation is highly non-adiabatic. This factor f is related to the usual Peclet number $\mathcal{P}e = t_{\text{therm}}/t_{\text{dyn}} \sim v \, l_r/K$ by $f = (1/\mathcal{P}e) + 1$ (cf. Appendix B.5.3), factors of the order of unity being omitted.

Instead of the Peclet number, one often considers (Sect. 5.4) a factor Γ, which is the ratio between the energy delivered by a fluid element to the energy lost during the displacement of the fluid element. For spherical fluid elements, one has $\Gamma = (1/6) \, \mathcal{P}e$ (Sect. 5.4.1). However, the fluid elements are likely not spherical in Tayler's instability. We should rather consider thin slabs of thickness l_r. If so, the relation between Γ and the Peclet number is $\Gamma = (1/2) \, \mathcal{P}e$ by a reasoning similar to that made in Sect. 5.4.1. Thus, the following relation is valid between the factor f and Γ,

$$\Gamma = \frac{1}{2}\frac{1}{(f-1)} \quad \text{or} \quad f = \frac{1+2\Gamma}{2\Gamma} . \tag{13.70}$$

In the adiabatic case, $f \to 1$ and $\Gamma \to \infty$; if non-adiabatic effects are important, f is large and Γ is small.

The general expression of the Brunt–Väisälä frequency for a displaced fluid element is given by (5.23) and (5.25). One also has relation (5.67) between the various T gradients, but we have a factor of 2 instead of 6 (12.50), due to the above-mentioned geometry,

$$\nabla = \frac{\nabla_{\text{rad}} + \frac{2\Gamma^2}{1+\Gamma}\nabla_{\text{ad}}}{1 + \frac{2\Gamma^2}{1+\Gamma}} . \tag{13.71}$$

Thus, in a radiative zone where there is some non-adiabatic motions of matter, the thermal gradient depends on the efficiency Γ. The actual gradient lies between the adiabatic and radiative gradients depending on Γ. If we write Γ in terms of f, we also have

$$\frac{\Gamma}{\Gamma+1} = \frac{1}{2f-1} . \tag{13.72}$$

Thus, we may also express the Brunt–Väisälä frequency in terms of f in agreement with (5.67)

$$N^2 = \frac{1}{2f-1}N^2_{T,\text{ad}} + N^2_\mu . \tag{13.73}$$

One can go a step further by writing Γ with the ratio η/K of the magnetic to thermal diffusivity. As seen after (13.69), one has $\Gamma = v\,l_r/(2K) \simeq (1/2)\,l_r^2/(t_{\text{dyn}}\,K)$, where l_r is the vertical length scale of the instability. Instabilities over smaller length scales are removed by magnetic diffusivity. We consider here the marginal case $l_r^2 = \eta\,t_{\text{dyn}}$, which implies that the vertical length scale is just the minimum scale to avoid magnetic diffusivity. We get

$$\Gamma = \frac{1}{2}\frac{\eta}{K} , \tag{13.74}$$

and $\Gamma/(\Gamma+1) = \eta/(\eta+2K)$. We see that the ratio η/K of the magnetic to thermal diffusivities determine the heat losses and one gets

$$N^2 = \frac{\frac{\eta}{K}}{\frac{\eta}{K}+2}\,N^2_{T,\text{ad}} + N^2_\mu , \tag{13.75}$$

where $N^2_{T,\text{ad}}$ and N^2_μ are defined in (5.60). This is the oscillation frequency of a fluid element displaced by the Tayler instability in a medium with account of both the magnetic and thermal diffusivities η and K [368]. In regions where the μ gradient is negligible, one is left only with $N^2_{T,\text{ad}}$ and one has, if $\eta/K \ll 1$,

$$N^2 \to \frac{1}{2}N^2_{T,\text{ad}}\frac{\eta}{K} . \tag{13.76}$$

This means that the minimum Alfvén frequency for Tayler instability as given by (13.66) leads to the condition (omitting the factor of 2), as originally found by Spruit [546]

$$\frac{\omega_A}{\Omega} > \left(\frac{N}{\Omega}\right)^{1/2} \left(\frac{\eta}{K}\right)^{1/4} \left(\frac{\eta}{r^2\Omega}\right)^{1/4}, \tag{13.77}$$

$$\text{or} \quad \frac{\omega_A}{\Omega} > \left(\frac{N}{\Omega}\right)^{1/2} \left(\frac{\eta}{K}\right)^{1/2} \left(\frac{K}{r^2\Omega}\right)^{1/4}, \tag{13.78}$$

under the general conditions $\omega_A \ll \Omega$ and $\eta/K \ll 1$, as mentioned above. If the above condition (13.78) is not satisfied, the differential rotation is insufficient to drive the dynamo and there is no magnetic field. The numerical factor [AS] given above may improve the accuracy of such expressions.

13.4.5 Solutions of the Dynamo Equations

The solutions originally developed by Spruit [546] applied to two limiting cases: case 0 when the μ gradient dominates over the thermal gradient and case 1 without μ gradient. More general solutions were found [368] with a proper account of μ gradient and non-adiabatic effects.

   We need an additional equation giving the field strength. On one hand, the field decays due to magnetic diffusivity, on the other hand it is amplified by differential rotation. In a steady equilibrium, the amplification and damping timescales τ_a and τ_d are equal. For shellular rotation, only the radial component contributes to the amplification by field line stretching. The amplification time of the instability is defined as "the timescale on which the radial field B_r is amplified into an azimuthal field of the same order as the already existing azimuthal field" [546]. According to the expression for the winding-up of field lines (13.52), one has the following value for the toroidal component of the field created by the dynamo,

$$B_\varphi \approx B_r r \left(-\frac{\partial \Omega}{\partial r}\right) \tau_a. \tag{13.79}$$

 We use the parameter q of differential rotation defined as $q = |-d\ln\Omega/d\ln r|$ (since Ω generally decreases with growing r, q would in general be positive anyway). Expressing the ratio B_r/B_φ by (13.68) with l_r given by (13.64), we get

$$\tau_a = \frac{N}{\omega_A \Omega q}, \tag{13.80}$$

Now, the equality of timescales τ_a and σ_B^{-1} leads to (this is the critical point!)

$$\frac{\omega_A}{\Omega} = q\frac{\Omega}{N}, \tag{13.81}$$

which fixes the Alfvén frequency and thus the magnetic field intensity as a function of structural variables [546]. At present, it is not clear whether another dynamo loop [634] may exist giving another condition than the above one. We may however remark that apart from the specific value of σ_B, the principles used in this derivation are very general. When account is taken of the expression of the Brunt–Väisälä (Eq. 13.75), this equation becomes

$$\left(\frac{\omega_A}{\Omega}\right)^2 = \frac{\Omega^2 q^2}{N_{T,\,\mathrm{ad}}^2 \frac{\eta/K}{\eta/K+2} + N_\mu^2}. \tag{13.82}$$

By eliminating N^2 between (13.66) and (13.82), we obtain a new expression for the magnetic diffusivity [368],

$$\eta = \frac{r^2 \Omega}{q^2} \left(\frac{\omega_A}{\Omega}\right)^6. \tag{13.83}$$

It varies with the power 6 of the magnetic field (there a numerical factor depending on the term $[AS]$ could be included, cf. Sect. 13.4.3). Equations (13.66) and (13.82) form a system of two equations for the two unknown quantities η and ω_A. Instead, one may also consider the system of equations formed by (13.82) and (13.83). Now, we introduce the general expression of η given by (13.83) in (13.82) and obtain a system of degree 8,

$$\left(\frac{\omega_A}{\Omega}\right)^2 \left[N_T^2 \frac{r^2 \Omega}{q^2 K}\left(\frac{\omega_A}{\Omega}\right)^6 + N_\mu^2 \left(\frac{r^2 \Omega}{q^2 K}\left(\frac{\omega_A}{\Omega}\right)^6 + 2\right)\right]$$
$$= \left(\frac{r^2 \Omega}{q^2 K}\left(\frac{\omega_A}{\Omega}\right)^6 + 2\right) \Omega^2 q^2. \tag{13.84}$$

Since the ratio (ω_A/Ω) always appears with a power of 2, we now define a new variable $x = (\omega_A/\Omega)^2$ and get [368] a system of degree 4,

$$\frac{r^2 \Omega}{q^2 K}\left(N_T^2 + N_\mu^2\right) x^4 - \frac{r^2 \Omega^3}{K} x^3 + 2N_\mu^2\, x - 2\Omega^2 q^2 = 0. \tag{13.85}$$

We have transformed our system of two equations of degree 4 with two unknown quantities η and ω_A into one equation of degree 4 with only one unknown quantity x. The solution provides the value of the Alfvén frequency ω_A and by (13.83) the value of η. The above equation applies to the general case where both ∇_μ and N_T are different from zero and where thermal losses may reduce the restoring buoyancy force. This equation can be solved numerically (Sect. 13.6). The solution and properties of (13.85) have been discussed [368]. Numerically, the positive uniquely defined solution of (ω_A/Ω) is easily obtained, e.g., by the Newton method.

The expression of N_T (5.25) contains the term ∇ given by (5.32), which contains the ratio η/K. If we would fully develop the above equation taking this additional dependence into account, we would get an equation of order 10. However, the

dependence in η/K introduced by ∇ in the expression of N^2 is of a higher order in η/K than the one in (13.75). Since η/K ranges between 10^{-2} and 10^{-7} according to numerical models [368] (Figs. 13.7 and 13.8), we may ignore these higher order terms.

There are various peculiar solutions of (13.85), which are interesting.

1. If $N_T = 0$, (13.82) leads to

$$x = \left(q \frac{\Omega}{N_\mu} \right)^2 , \tag{13.86}$$

which is just (13.81) when the term in the μ gradient dominates in the Brunt–Väisälä frequency. If so, the magnetic diffusivity becomes

$$\eta = r^2 \Omega q^4 \left(\frac{\Omega}{N_\mu} \right)^6 . \tag{13.87}$$

This relation shows that the mixing of chemical elements decreases strongly for larger μ gradients and grows fast for larger q values. This strong inverse dependence on the μ gradient limits the chemical mixing by the Tayler–Spruit instability in the regions above the convective core. The same solution is also found when the terms in x^4 and x^3 are negligible, while N_μ is different from zero.

2. We now consider the case $N_\mu = 0$. For that, we start with Eqs. (13.66) and (13.82) and assume that the ratio η/K is small (which is verified in stellar conditions, cf. Figs. 13.7 and 13.8). Developments like those leading to (13.85) give

$$\frac{r^2 \Omega}{q^2 K} N_T^2 x^4 + 2 N_\mu^2 x - 2 \Omega^2 q^2 = 0 . \tag{13.88}$$

This equation is similar to (13.85) for $N_\mu = 0$, except that the term in x^3 is absent. Now, if $N_\mu = 0$, the solution of (13.88) is easily obtained

$$\left(\frac{\omega_A}{\Omega} \right) = 2^{\frac{1}{8}} q^{\frac{1}{2}} \left(\frac{\Omega}{N_T} \right)^{\frac{1}{4}} \left(\frac{K}{r^2 \Omega} \right)^{\frac{1}{8}} = 2^{\frac{1}{8}} q^{\frac{1}{2}} \left(\frac{\Omega}{N_T} \right)^{\frac{1}{8}} \left(\frac{K}{r^2 N_T} \right)^{\frac{1}{8}} , \tag{13.89}$$

which then allows us to express η. In numerical models, it is preferable to solve the general equation (13.85).

Condition on the minimum differential rotation: The ratio ω_A/Ω given by the solution of (13.85) has to be equal or larger than the minimum value defined by (13.66). This leads to a condition on the minimum differential rotation for the dynamo to work [546]

$$q > \left(\frac{N}{\Omega} \right)^{7/4} \left(\frac{\eta}{r^2 N} \right)^{1/4} , \tag{13.90}$$

where N is given by (13.75) and η by (13.83). When N^2 is larger, as for example when there is a significant μ gradient, the differential rotation necessary for the dynamo to operate must also be larger. If the above condition is not fulfilled, there is no stationary solution and the dynamo does not operate. In practice, this often occurs in the outer stellar envelope.

There is a second condition. One needs to check that $\Omega > \omega_A$. If this is not realized, the present system of equations does not apply and one should consider the case of very slow rotation [369]. However, even the Sun with its low rotation has a value of $\omega_A/\Omega \ll 1$. Thus, for all cases of interest, this second condition is satisfied.

13.5   Transports of Angular Momentum by the Magnetic Field

The main effect of the magnetic field on stellar evolution is to favor an internal rotation tending toward solid body rotation and to ensure a strong coupling able to transfer the spin-up of the central regions to the outer layers, as evolution proceeds. Thus, the surface rotation velocities of stars with internal magnetic coupling keep faster during evolution (Fig. 13.6 left). This favors mass and angular momentum losses.

13.5.1   Viscous Coupling by the Field

The Alfvén frequency is obtained from (13.85) and η is given by (13.83). The azimuthal field component largely dominates over the radial one, thus one has the approximation

$$B_\varphi \approx (4\pi\rho)^{\frac{1}{2}}\, r\, \omega_A. \tag{13.91}$$

The radial component of the field is given by (13.68) with l_r given by the maximum length (13.64) used with N given by (13.75). If N_μ dominates, this gives

$$B_\varphi = (4\pi\rho)^{\frac{1}{2}} r\, q\frac{\Omega^2}{N_\mu} \quad \text{and} \quad \frac{B_r}{B_\varphi} = q\left(\frac{\Omega}{N_\mu}\right)^2. \tag{13.92}$$

Let us now turn toward the transport of angular momentum by the magnetic field. The momentum of force S by volume unity due to the magnetic field is obtained by writing the momentum of the Lorentz force (13.1). The current density $\boldsymbol{j}$ is given by the first of (13.3). Thus, one has

$$S = \boldsymbol{r} \times \boldsymbol{F}_L = \frac{1}{c}\boldsymbol{r} \times (\boldsymbol{j} \times \boldsymbol{B}) = \frac{1}{4\pi}\boldsymbol{r} \times ((\nabla \times \boldsymbol{B}) \times \boldsymbol{B}), \tag{13.93}$$

or in modulus

$$S \approx \frac{1}{4\,\pi}\, B_{\mathrm{r}} B_{\varphi} = \frac{1}{4\,\pi}\, \left(\frac{l_{\mathrm{r}}}{r}\right) B_{\varphi}^2 = \rho\, r^2 \left(\frac{\omega_{\mathrm{A}}^3}{N}\right), \tag{13.94}$$

where (13.68) and the maximum length (13.64) are used. The units of S are $\mathrm{g\ s^{-2}\ cm^{-1}}$, the same as for B^2 in the Gauss system. The kinematic viscosity v (in $\mathrm{cm^2\ s^{-1}}$) for the vertical transport of angular momentum can be expressed in terms of S (the viscosity of a fluid represents its ability to transport momentum from one place to another, B.48). According to Appendix B.4.1, one has

$$v = \frac{\eta}{\varrho} = \frac{1}{\varrho}\, F\, \frac{dr}{dv} = \frac{1}{\varrho}\, F\, \frac{dr}{r\,d\Omega} = \frac{1}{\varrho}\, F\, \frac{d\ln r}{\Omega\, d\ln\Omega}, \tag{13.95}$$

where F according to the definition of the viscosity is a force by surface unity, which also corresponds to a momentum of force by volume unity in $\mathrm{g\ s^{-2}\ cm^{-1}}$. Considering only positive quantities, with $q = |d\ln\Omega/d\ln r|$ and (13.94), one has

$$v = \frac{S}{\rho\, q\, \Omega} = \frac{\Omega\, r^2}{q} \left(\frac{\omega_{\mathrm{A}}}{\Omega}\right)^3 \left(\frac{\Omega}{N}\right). \tag{13.96}$$

This is the general expression of viscosity v with ω_{A} given by the solution of (13.85) and with N by (13.75). If N_{μ} dominates in (13.75), one has from (13.86)

$$v_0 = r^2\, \Omega\, q^2 \left(\frac{\Omega}{N_{\mu}}\right)^4. \tag{13.97}$$

The μ gradient, through its reduction of the field particularly in the vertical direction, also reduces the transport of angular momentum, but much less than for the chemical elements as given by (13.87). We recall that the diffusion coefficient of the chemical elements is determined by η, which is here the magnetic diffusivity.

We have the full set of expressions necessary to obtain the Alfvén frequency ω_{A} (13.85), the magnetic field (13.92), the magnetic diffusivity η (13.83) and the viscosity v (13.96) for the vertical transport of the angular momentum by the magnetic field. These expressions apply to the general case, where both the μ and T gradients and radiative losses play a role. In all cases, these general expressions also lead consistently to the approximate asymptotic expressions when N_{μ} or N_T dominates in (13.75) [368].

13.5.2 Horizontal Coupling of Rotation

In models without magnetic field, the horizontal turbulence enforces an almost constant rotation on isobars, which makes shellular rotation (Sect. 12.1). It is likely that a strong azimuthal field reduces or even suppresses the horizontal turbulence. We

define a horizontal diffusion or viscosity coefficient due to the magnetic field as the square of the typical length scale r divided by the typical timescale of the magnetic instability, i.e., σ_B^{-1} as given by (13.61),

$$D_{B_\mathrm{h}} = r^2\,\sigma_B = r^2\,(\omega_\mathrm{A}^2/\Omega) = \frac{B_\varphi^2}{4\pi\,\rho\,\Omega}, \qquad \text{for} \quad \Omega \gg \omega_\mathrm{A}\,. \qquad (13.98)$$

The interaction of turbulence and magnetic field is complex. We suggest, as a first guess, that if $D_{B_\mathrm{h}} > D_\mathrm{h}$ the magnetic coupling dominates over horizontal turbulence and reciprocally. The value of D_{B_h} is larger than 10^{11} cm^2 s^{-1} in a 15 $M_\odot$ model with an initial rotation of 300 km s^{-1}. This is equal or larger than the coefficient of horizontal turbulence (Sect. 12.2). Thus, magnetic field may dominate over the horizontal turbulence. The value of D_{B_h} is large enough to ensure horizontal coupling, so that the assumption of shellular rotation is still valid.

13.5.3 Check for Consistency

Let us make a check for consistency. The rate of magnetic energy production W_B per unit of time and volume must be equal to the rate W_ν of dissipation of rotational energy by the magnetic viscosity ν. We assume here that the whole energy dissipated is converted into magnetic energy, considering thermal dissipation as negligible. The differential motions are those of the shellular rotation $\Omega(r)$, so that the velocity difference at radius r is $dv = r\,d\Omega$. The amount of energy corresponding to a velocity difference dv during a time dt for an element of matter dm in a volume dV is

$$W_\nu = \frac{1}{2}\,dm\,(dv)^2 \frac{1}{dV}\frac{1}{dt} = \frac{1}{2}\varrho\,\nu\left(\frac{dv}{dr}\right)^2 = \frac{1}{2}\varrho\nu\Omega^2 q^2\,, \qquad (13.99)$$

because the viscous time dt over a distance dr is given by $dt = (dr)^2/\nu$ (Appendix B.4.1). We also use the parameter of differential rotation q (Sect. 13.4.5). This gives with the expression (13.96) for the kinematic viscosity,

$$W_\nu = \frac{1}{2}\varrho\,q\,r^2\frac{\Omega}{N}\,\omega_\mathrm{A}^3\,. \qquad (13.100)$$

With (13.82), which defines the field amplitude $(\omega_\mathrm{A}/\Omega) = \Omega\,q/N$, the dissipation rate of the differential energy of rotation finally becomes

$$W_\nu = \frac{1}{2}\varrho r^2 q^4 \Omega^3 \left(\frac{\Omega}{N}\right)^4\,. \qquad (13.101)$$

We now turn to the rate W_B of magnetic energy creation by units of volume and time. The magnetic energy density is $B^2/(8\pi)$ (13.10), it is produced within a characteristic time given by $\sigma_B^{-1} = (\omega_\mathrm{A}^2/\Omega)^{-1}$,

$$W_{\mathrm{B}} = \frac{B^2}{8\pi} \frac{\omega_{\mathrm{A}}^2}{\Omega} = \frac{1}{2} \varrho r^2 \frac{\omega_{\mathrm{A}}^4}{\Omega} \,, \tag{13.102}$$

where we have used (13.91) to express the magnetic field, because B_φ is the main field component. If we express $\omega_{\mathrm{A}}/\Omega$ (as recalled after 13.100), we get the same expression as (13.101), thus

$$W_v = W_{\mathrm{B}}. \tag{13.103}$$

The rate of magnetic energy creation in a volume element is equal to the rate of dissipation of differential rotation by the magnetic viscosity. This shows the consistency of the field expression for B_φ, of the transport coefficient v together with the energy conservation in the process of field creation.

Alternatively, if we impose the equality of the dissipation rates (13.100) and (13.102) and if we use the value of σ_{B}, the induction equation and the maximum l_r from (13.64), we get the condition $(\omega_{\mathrm{A}}/\Omega) = \Omega \, q/N$ which fixes the field amplitude.

13.6   Models with Magnetic Field and Circulation

The results below refer to the above dynamo model. The term $[AS]$ discussed in Sect. 13.4.3 as well as another way to close the dynamo loop may change the quantitative results. However, the coupling of rotation by the magnetic field characterized by the coefficient v is so incredibly efficient that even if the timescale of this coupling would be longer by, say, one or two orders of a magnitude, the main model consequences would be about the same! Thus, to this extent these conclusions are rather general.

There are complex interactions between the magnetic instability, which generates the field, and the thermal instability which drives the meridional circulation [368]. We can identify the following closed loop of effects:

– Differential rotation creates the magnetic field.
– Magnetic field tends to kill differential rotation.
– Smaller differential rotation enhances meridional circulation.
– Meridional circulation increases differential rotation.
– Differential rotation creates the magnetic field, etc …

Thus, the magnetic field tends to kill its source. The balance of these effects is subtle and needs to be calculated with time steps short enough with respect to the fastest process, i.e., the transport of angular momentum by the magnetic coupling expressed by v. For example, in a 15 $M_\odot$ model $v \sim 10^{10}$–10^{11} cm^2 g^{-1} in the significant part of the interior (Fig. 13.8 right), which implies that the time steps $\tau \approx (\Delta R)^2/v$ corresponding to shell masses of thickness ΔR are small. Models in
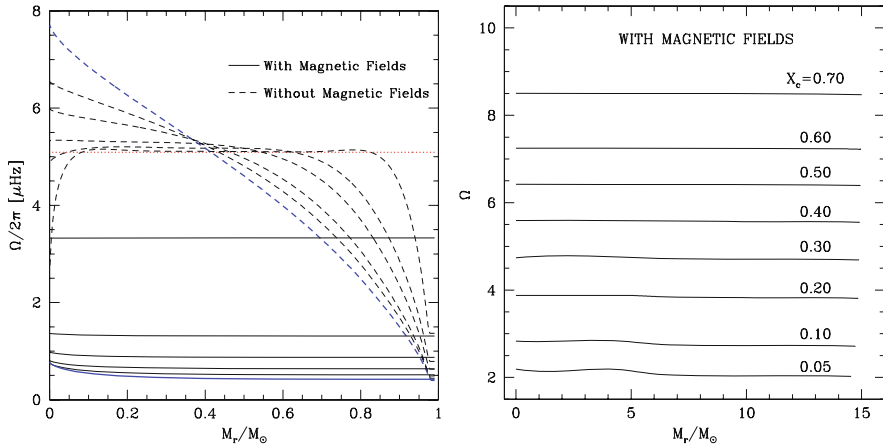
Fig. 13.5 *Left*: rotation profiles as a function of the Lagrangian mass in evolving solar models with and without magnetic field [172] (magnetic braking at the surface is accounted for). The dotted line indicates the initial profile. As evolution proceeds, the global profile for the case without magnetic field becomes steeper, while with magnetic field Ω is almost constant, its value goes down strongly in time due to braking at the stellar surface. *Right*: rotation profiles at various stages of evolution (labeled by the central H content X_c) of a 15 $M_\odot$ model with $X = 0.705, Z = 0.02$, an initial velocity of 300 km s^{-1} and magnetic field. The evolution of velocity in a model without field is shown in Fig. 11.8. From the author and G. Meynet [369]

Fig. 13.5 are calculated with time steps equal to 20 yr, which implies 6×10^5 models for covering the MS phase of a 15 $M_\odot$ star [369]. Even if the model structure does not change very much, the above requirement is necessary to have a proper description of the equilibrium between the thermal instability responsible for meridional circulation and the magnetic instability.

13.6.1   Evolution of Ω, B and the Diffusion Coefficients

13.6.1.1   The Evolution of Rotation

The presence of a magnetic field totally modifies the internal profile of the angular velocity $\Omega(r)$. With the magnetic field created by the Tayler–Spruit dynamo, the internal distribution of Ω soon tends toward a constant internal Ω profile. This is illustrated by Fig. 13.5 for 1 and 15 $M_\odot$ stars. For the 1 $M_\odot$ model with magnetic field, there is a strong decrease of the constant Ω during evolution due to the account of magnetic braking at the surface. In the case without Tayler–Spruit dynamo, the magnetic braking at the surface due to the solar dynamo has also been accounted for, which favors the formation of a rather strong Ω gradient as evolution proceeds. Remarkably, the internal magnetic field leads [172] to the constancy of Ω, as derived

from helioseismology [141]. Transport by gravity waves also produces a constant Ω in the Sun and helioseismology should hopefully discriminate between the two.

The results for the 15 $M_\odot$ model with magnetic field can be compared to those without a magnetic field (Fig. 11.8) which show significant Ω gradients due to the loss of angular momentum at the surface. In models with magnetic field, the Ω profile is not exactly constant, otherwise the differential rotation parameter q would be zero and the magnetic field would no longer be sustained. This can be seen near the center in both the 1 and 15 $M_\odot$ models at the end of their MS phase.

Figure 13.6 (left) shows the evolution of the rotation velocity at the stellar surface in 15 $M_\odot$ models with and without magnetic field. The strong internal coupling by the magnetic field makes the star to keep a higher rotational velocity v during the MS phase, because the outer layers tend to co-rotate with the convective core as it spins up due to the increase of the central density. Also, we see that the initial evolution of v on the ZAMS is quite different. With rotation only, an equilibrium distribution of $\Omega(r)$ is reached (Fig. 11.6), which lowers the surface velocity. With magnetic field, an initial distribution $\Omega(r) = $ const is already an equilibrium solution; thus, there is no significant initial adjustment of the surface velocity.
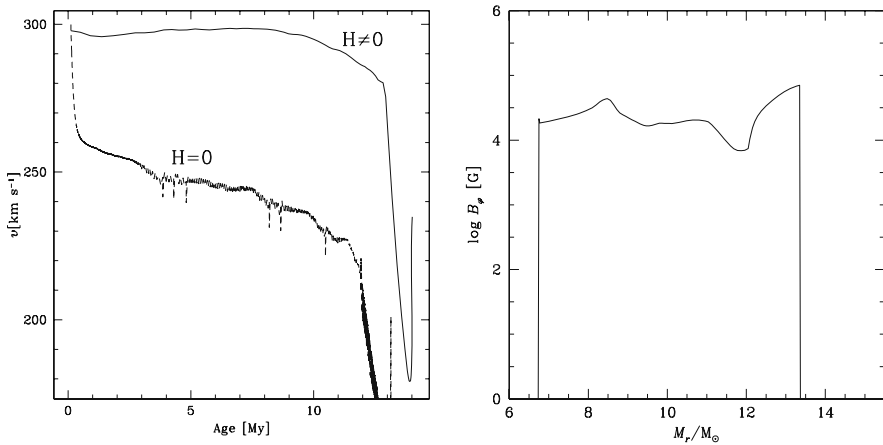

Fig. 13.6 *Left*: evolution of the equatorial velocity for models of a 15 $M_\odot$ with rotation only (*lower curve*) and for the model with rotation and magnetic field (*upper curve*). Same composition and initial velocity as in Fig. 13.5. *Right*: distribution of the azimuthal component of the magnetic field in the 15 $M_\odot$ when the central H content is $X_c = 0.60$. From the author and G. Meynet [369]

13.6.1.2 Evolution of the Magnetic Field

The magnetic field is present when differential rotation is large enough so that condition (13.90) is satisfied. For the 1 $M_\odot$ model at the solar age, the field due to Tayler–Spruit dynamo is present throughout the radiative zone of the Sun with an

azimuthal component of the order of a few 10^2 G. In the convective envelope, the solar dynamo is at work and creates fields which can reach locally high values (Sect. 13.1.4).

For the model of 15 $M_\odot$, the magnetic field is generally present from a location just above the convective core over a large fraction of the radiative envelope (Fig. 13.6, right). In the early main sequence phase when $X_c = 0.60$, the field is present from $M_r = 6.7\ M_\odot$ up to 13.4 $M_\odot$, where the differential rotation becomes insufficient for condition (13.90) to be satisfied. The average field intensity is about 2×10^4 G, which corresponds to $\omega_A/\Omega = 5 \times 10^{-4}$. As evolution proceeds, the region where the magnetic field is present becomes larger due to the recession of the convective core, the external limit does not change very much. As an example, when $X_c = 0.05$, the magnetic field is present from 4.4 up to 13.8 $M_\odot$. Thus, the Tayler–Spruit dynamo does not create a magnetic field at the surface of intermediate and massive stars, because, there, differential rotation is too small.

13.6.1.3   Diffusion Coefficients in Magnetic Models

The runs of the various diffusion coefficients are illustrated for models of 1 and 15 $M_\odot$ with magnetic field in Figs. 13.7 and 13.8. The diffusion coefficients are up to 8 orders of magnitude larger in the higher mass stars. In both models, the largest diffusion coefficient is the viscosity coefficient ν, which expresses the magnetic coupling and makes $\Omega \sim$ const. The values of ν are about 6 orders of magnitude larger than the diffusion coefficient η for the transport of the chemical elements.

In the solar model, the various coefficients of transport of the chemical elements are all very low. The timescale for diffusion by the magnetic instability $t \sim R^2/\eta$ is of the order of 1.5×10^{18} yr, which makes the effect negligible.

In the 15 $M_\odot$ model, the main contribution to the transport of chemical elements is due to the meridional circulation expressed by the coefficient D_{eff}, which is larger than the coefficients due to shear and magnetic instabilities. The velocity of circulation is higher ($U_2(r) \approx 10^{-2}$ cm s^{-1}) than in rotating models without magnetic field (cf. Fig. 11.6), because meridional circulation is generally faster when Ω is constant. The orders of magnitude and the relative ratios of the various diffusion coefficients remain about the same during the MS evolution. Figures 13.7 and 13.8 also show the very small values η/K, which justify the simplifications made in writing (13.85).

On the whole, the magnetic field is much more efficient than the circulation for the internal coupling of rotation, while the transport of the chemical elements is dominated by the meridional circulation, which is amplified by the nearly flat Ω profile created by the magnetic field. In a stationary state, by analogy with (11.83) one can define a velocity U_B for the vertical transport of the angular momentum by the magnetic field,
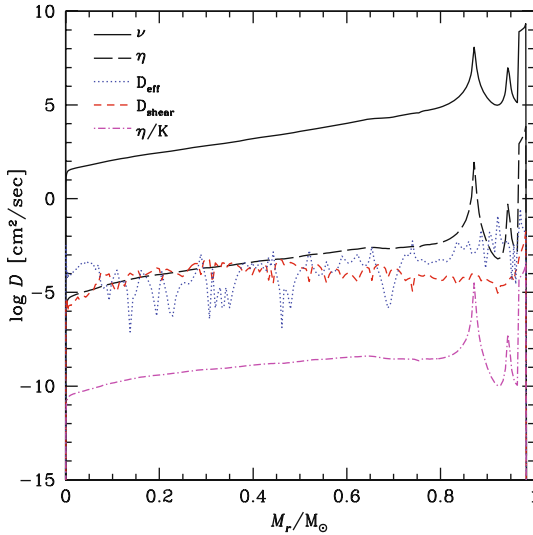
Fig. 13.7 The various diffusion coefficients in a solar model with rotation and magnetic field [172]. ν expresses the diffusion of angular momentum by magnetic field, η the transport of chemical elements by the magnetic instability, D_{eff} the transport of the elements by meridional circulation, D_{shear} the transport of the elements and angular momentum by shear turbulence, η/K the ratio of magnetic to thermal diffusivity
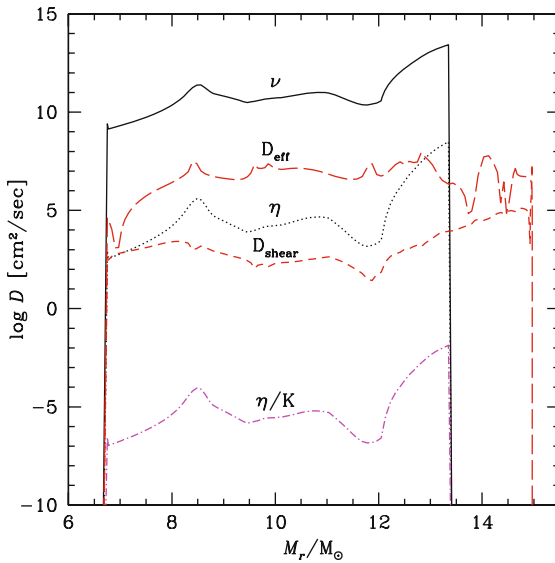

Fig. 13.8 The diffusion coefficients in the model of 15 $M_\odot$ with rotation and magnetic field as described in Fig. 13.5. The magnetic field is present in the region where ν is shown, there B_φ has an average intensity of 2×10^4 G. The various coefficients are defined in Fig. 13.7. From the author and G. Meynet [369]

$$U_{\mathrm{B}} = 5 \, \frac{v}{r} \, \left| \frac{\partial \ln \Omega}{\partial \ln r} \right| . \tag{13.104}$$

In general U_{B} is much larger than $U_2(r)$, confirming the dominant role of the magnetic field for the transport of angular momentum.

13.6.2 Evolutionary Consequences

Let us briefly list some general evolutionary consequences of the presence of a magnetic field in comparison with models without magnetic field:

– Magnetic field is able to account for the internal solid body rotation of the Sun in agreement with helioseismic observations [172]. There are however other possible solutions.
– Magnetic field enforces an almost solid body rotation. As a matter of fact, an equilibrium state is quickly reached with a very small amount of differential rotation just enough to sustain the dynamo. The strong internal coupling of rotation by the magnetic field transmits the central spin-up to the stellar surface, which thus rotates faster during evolution.
– As rotation velocities keep higher, the losses of mass and angular momentum by massive stars are favored. This leads to final stages with lower rotation; however, this also depends on the evolutionary tracks followed by the stars. This may be an advantage to account for the relatively low rotation period of young pulsars (Sect. 28.6.2); for the interpretation of the precursor models for γ-ray bursts (GRB), see Sect. 28.6.3.
– The higher velocity of meridional circulation in the models with magnetic field produces larger mixing than in a rotating model without magnetic field. The enrichment N/C reaches a factor of about 10 in a model of 15 $M_\odot$ with an initial velocity of 300 km s^{-1} (Fig. 13.9). There is even a significant helium enhancement at the surface [369]. These results may however more depend on the specific dynamo and field intensity at work.
– The larger mixing increases the convective core in intermediate and massive stars, which in turn increases the MS lifetimes (by about 20% in the example given).
– Some layering may appear with successive magnetic and non-magnetic regions, with possible steps in chemical composition (Sect. 6.2).

In the context of the uncertainties discussed in Sect. 13.4.2, a clear result is that it is meaningful to further study the magnetic field in view of the importance of its evolutionary effects revealed by the above models.
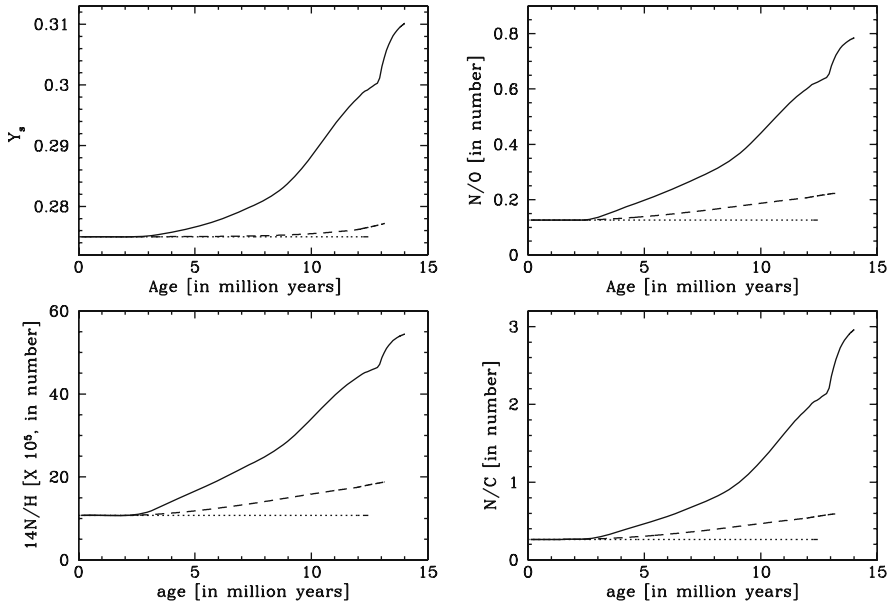
Fig. 13.9 Evolution of the surface helium content Y_s and of the ratios N/O, N/H and N/C (in mass fractions) for various 15 $M_\odot$ models: the dotted line applies to model without rotation, the short broken line to model with rotation (v_{ini}= 300 km s^{-1}) but without magnetic fields, the continuous line to model with rotation (v_{ini}= 300 km s^{-1}) and magnetic fields. From the author and G. Meynet [369]

13.7 Other Magnetic Instabilities

There are other magnetic instabilities, which could also occur and perhaps play a role. Below, we briefly discuss some of them in the case of weak fields, where the phase mixing (Sect. 13.3.2) does not intervene.

If the field is strong, phase mixing intervenes, the field is reduced on timescale set by magnetic diffusivity. It seems that the field decays toward a state of minimum energy characterized by uniform rotation [545, 547]. The stability of magnetic equilibrium reached in this case has often been questioned. However, the strong magnetic fields of Ap stars (up to 10^4 G) and of some white dwarfs (up to 10^7 G) do not change on timescales of decades. These stars are slow rotators and their field would change on the Alfvén timescale of the order of a year (for Ap stars) and of a day (for white dwarfs), if they were unstable. This is up to now the best argument in favor of the stability of strong fields [545], particularly for white dwarfs which likely do not have a central dynamo to sustain the field.

13.7.1 Magnetic Shear Instability and Transport

Let us consider a weak magnetic field in a differentially rotating star in radiative equilibrium. The field, supposed to be initially poloidal, may also become locally unstable due to the shear created by differential rotation. The basic physics of the instability is the following one [31]. Let us consider a fluid element displaced outward in a magnetic differentially rotating medium, where the angular velocity $\Omega(r)$ is considered to decrease outward. The displaced fluid element is submitted to two magnetic effects:

– The field is trying to enforce rigid rotation.
– The field is trying to return the fluid element back to its starting position by resisting the stretching imposed by the displacement.

This last effect is evidently stabilizing, while the first one favors the instability, because the field is trying to force the fluid element to rotate too fast for its radial location. An excess of angular momentum drives the fluid element outward and one has a situation analogous to that of the Rayleigh criterion (Sect. 6.4.2). This instability is symmetric with respect to the rotation axis.

The magnetic shear instability has been studied by several authors [4, 30, 31, 545]. The thermal stratification, and even more if there is a stratification by the μ gradient, may limit this instability to only cases of extreme differential rotation. Thus, this instability may essentially occur on horizontal surface, if there is some shear on these surfaces. This could happen for cylindrical rotation, but evidently not for shellular rotation.

As for the shear instability without magnetic field, the stabilizing effect of the thermal stratification is reduced by thermal diffusion (Sect. 12.2.3), in particular on small scales. Thus, the magnetic shear instability may be present when heat losses are important. The condition for the instability with respect to a small displacement was found to be [4, 545]

$$q > \frac{N_{T,\mathrm{ad}}^2}{2\Omega^2} \frac{\eta}{K} \quad \text{with} \quad q = -\frac{d\ln\Omega}{d\ln r} , \tag{13.105}$$

where $N_{T,\mathrm{ad}}^2$ is the adiabatic thermal part of the Brunt–Väisälä frequency (5.60) and K the radiative diffusivity (3.46). An amazing conclusion is that the instability criterion is independent of the strength of the field [31]. This is because the magnetic tension due to the stretching of the field lines is responsible for both the stabilizing (the return of the fluid element to its initial position) and destabilizing effects (the enforcing of uniform rotation).

One may understand the above condition in the following simplified way, without forgetting that it was originally found by a more complex development. If one considers an equilibrium situation between the forces tending to reset the fluid element to its original position and those tending to drive it farther out, accounting that the two magnetic effects cancel each other, one is left with an equilibrium between *the excess of centrifugal force* and the buoyancy force acting on the fluid element.

The situation is similar to that considered for obtaining the Solberg–Hoiland and GSF instability criteria (Sect. 12.4.1),

$$N_T^2 + N_\Omega^2 > 0 ,$$ (13.106)

in the equatorial plane and for no μ gradient. The contribution from only the differential rotation to N_Ω^2 becomes,

$$N_\Omega^2 \rightarrow 2\Omega^2 \frac{d\ln\Omega}{d\ln r} .$$ (13.107)

We transform N_T^2 to $N_{T,\mathrm{ad}}^2$ according to (5.68). We account that the efficiency of the transport Γ is very small and that it can be identified, with a geometrical factor of the order of unity, to the ratio η/K according to (13.74) and thus we obtain,

$$q > \frac{N_T^2}{2\Omega^2} = \frac{\Gamma}{\Gamma+1} \frac{N_{T,\mathrm{ad}}^2}{2\Omega^2} \rightarrow \frac{N_{T,\mathrm{ad}}^2}{2\Omega^2} \frac{\eta}{K} .$$ (13.108)

This is identical to (13.105) and we thus understand the condition for magnetic shear instability. If the differential rotation is high enough for the above condition to be satisfied, the magnetic shear instability develops.

If the instability occurs, it produces some mild magnetic turbulence, which may contribute to transport the chemical elements and angular momentum. Thermal diffusion on small scales is destabilizing, thus the diffusion will be determined by the largest scales $\eta/K \approx v\ell/K$ for which the instability still occurs, as made in Sect. 12.2.3, see also [545]. This corresponds to the limit given by (13.108) and provides the following diffusion coefficient,

$$\eta = 2q\Omega^2 \frac{K}{N_{T,\mathrm{ad}}^2} .$$ (13.109)

The corresponding viscosity coefficient v is of the same order of magnitude, since the motions are rather slow with a turbulent energy of the order of the magnetic energy. If the shear instability dominates, the corresponding value of η can be taken for calculating the evolution of the magnetic field as well as for the transports of the elements and of the angular momentum. Some works however suggest a ratio v/η for this instability of the order of 0.1 [545]. The medium with magnetic shear is also subject to the processes of winding-up (Sect. 13.3.2) and of field diffusion or smoothing (Sect. 13.3.3).

The ratio η/K is in general very small, not necessarily as small as the ratio obtained for the Tayler–Spruit dynamo (Fig. 13.7). For the Sun, the ratio obtained from the typical microscopic plasma viscosity (B.56) is $\eta/K \approx 5 \times 10^{-5}$, with $\Omega \approx 3 \times 10^{-6}$ s^{-1} and a typical value $N \sim 10^{-3}$ s^{-1}, thus a value of q of the order of unity is necessary to generate the instability. Thus, it is only for extremely strong differential rotation that the magnetic shear instability would come into play.

Since the Tayler–Spruit dynamo needs a lower threshold to work, it creates a magnetic field which drastically reduces differential rotation, so that the occurrence of the shear instability is unlikely if Tayler's instability first sets in and drives the dynamo. Above, we have not accounted for the stratification in chemical composition. With account of the μ gradient, the problem becomes a triple-diffusive instability problem, where simultaneously the chemical, thermal and magnetic diffusions need to be considered [398]. A μ gradient exerts a recall force much stronger than thermal stratification, thus if present, it further contributes to inhibit the magnetic shear instability and to make it of little importance.

13.7.2 Magnetic Buoyancy

The simplest case of magnetic buoyancy, originally considered by Parker [459], is that of a horizontal tube of magnetic flux lying at some depth in the solar envelope, where the average surrounding field is negligible with respect to that inside the tube. The tube is assumed in pressure equilibrium with the surroundings, which implies motions slower than the sound velocity. The tube is also in thermal equilibrium due to the rapid heat transfer by convection or radiation. The presence of an additional magnetic pressure inside the tube implies a lower gas pressure and a lower gas density, since the temperature is the same inside and outside. The tube, which is lighter than the surroundings, tends to rise by the effect of magnetic buoyancy. This effect is contributing to the emergence in the sunspots of bunches of magnetic lines created by the solar dynamo (Sect. 13.1.4).

If P_{int}, P_{ext} and P_{magn} are, respectively, the internal, external and magnetic pressures, one has the magnetostatic balance (13.20) $P_{\text{ext}} = P_{\text{int}} + P_{\text{magn}}$ with $P_{\text{magn}} = B^2/(8\pi)$. The internal and external gas pressures are given by $P = [k/(\mu m_{\text{u}})]\varrho T$, so that the relation between the external and internal densities is, assuming the same internal and external T,

$$\varrho_{\text{ext}} = \varrho_{\text{int}} + \frac{\mu m_{\text{u}}}{kT}\frac{B^2}{8\pi} . \tag{13.110}$$

Thus, the buoyant force per volume unity is

$$\boldsymbol{F}_{\text{buoy}} = \frac{\mu m_{\text{u}}}{kT}\frac{B^2}{8\pi}(-\boldsymbol{g}) . \tag{13.111}$$

A magnetic tube with a field of 10^3 G located at a depth of 10^3 km, where $\varrho_{\text{ext}} \approx 0.8 \times 10^{-8}$ g cm^{-3} and $T \approx 1.5 \times 10^4$ K, has a density difference $(\varrho_{\text{ext}} - \varrho_{\text{int}}) \approx 0.04\,\varrho_{\text{ext}}$, which is equivalent to what an additional heating of 600 K would make [459]. This is comparable to the conditions for convection in the outer solar layers (5.50) and the tube normally starts rising.

The presence of a positive gradient of magnetic field in the direction of gravity may also lead to some gas motions. If the gradient is larger than some limit, the field

motions will reduce the gradient by a new buckling of the field lines. As above, the density stratification opposes its effect to the magnetic buoyancy, the stratification may result from the T and μ gradients. Let us consider a displacement over a vertical distance δr of a fluid element in a medium where there is a vertical gradient of the magnetic field. The fluid element will have a density deficit $\Delta \varrho < 0$ with respect to the surrounding medium ($\Delta \varrho$ is the difference between the internal and external ϱ). The magnetic buoyancy works if the outwards acceleration of the fluid element is stronger than the recall force by mass unit, i.e., according to (5.23),

$$-g\,\frac{\delta(\Delta \varrho)}{\varrho} = N^2\,\delta r\,, \tag{13.112}$$

where the notations are those of Sect. 5.1.2. The relative acceleration due to the magnetic field is directed outward, if the field increases inward. The density gradient resulting from the magnetic field can be expressed in terms of the magnetic pressure gradient,

$$-g\,\frac{\delta \varrho}{\varrho} = -\frac{g}{\Gamma_1}\,\delta \ln P_{\mathrm{B}} = -\frac{g}{\Gamma_1 P}\left(\frac{dP}{dr}\right)_{\mathrm{B}}\delta r\,. \tag{13.113}$$

Here, $\delta \varrho$ is the density difference of the fluid element resulting from an adiabatic displacement δr in the magnetic field gradient. The coefficient Γ_1 (7.57) depends on the equation of state; we assume that it is not influenced by the field, which is reasonable since the magnetic pressure is a small fraction of the gas pressure. Here, $(dP/dr)_{\mathrm{B}}$ represents the contribution to the gradient of pressure due to the magnetic field,

$$\left(\frac{dP}{dr}\right)_{\mathrm{B}} = \frac{1}{4\pi}\,B\,\frac{dB}{dr} = \frac{1}{4\pi}\,\frac{B^2}{r}\,\frac{d\ln B}{d\ln r}\,. \tag{13.114}$$

With the Alfvén frequency $\omega_{\mathrm{A}} = B/\left[r(4\pi\varrho)^{1/2}\right]$ from (13.18), one has

$$\left(\frac{dP}{dr}\right)_{\mathrm{B}} = p\,r\,\omega_{\mathrm{A}}^2\varrho, \quad \text{with} \quad p = \frac{d\ln B}{d\ln r}\,. \tag{13.115}$$

For a field decreasing outward, p is a negative quantity. The relative force (13.113) becomes

$$-g\,\frac{\delta \varrho}{\varrho} = -\frac{g}{\Gamma_1 P}\,p\,r\,\omega_{\mathrm{A}}^2\varrho\,\delta r = -\frac{p\,r\,\omega_{\mathrm{A}}^2}{\Gamma_1 H_P}\,\delta r\,, \tag{13.116}$$

where we have expressed the pressure scale height $H_P = -(dr/dP)P = P/(g\varrho)$. The fluid element continues its motion, if the outward acceleration (13.116) due to the magnetic field gradient is larger than the recall acceleration $N^2\delta r$ due to the stable stratification, i.e.,

$$- p\,\omega_{\mathrm{A}}^2 > \Gamma_1 N^2 \frac{H_P}{r} \, . \tag{13.117}$$

If there is only a thermal stratification, the Brunt–Väisälä frequency is just the component N_T^2 and if, like in (13.108), one expresses the efficiency Γ of the transport in terms of the ratio η/K (13.74) of the magnetic to thermal diffusivity, one gets $\Gamma \approx \eta/K$, with a geometrical factor of the order of unity. The above equation then becomes

$$- p\,\omega_{\mathrm{A}}^2 > \Gamma_1 N_{T,\mathrm{ad}}^2 \frac{\eta}{K} \frac{H_P}{r} , \tag{13.118}$$

It expresses that the magnetic field must be large enough with a steep outward decreasing field $(-p > 0)$ to overcome the recall effect of buoyancy in the radiatively stable layers. High heat losses (i.e., small η/K) reduce the recall force and thus favor the instability. More general expressions applicable down to the stellar centers and also accounting for differential rotation have been established [4, 545].

13.7.2.1 Magnetic Buoyancy vs. Tayler's Instability

It is interesting to compare the instability of the magnetic buoyancy to the Tayler instability. For a field gradient $-p \approx 1$, the critical Alfvén frequency, noted ω_{Ab}, for the buoyancy instability is

$$\omega_{\mathrm{Ab}} \approx \left(\frac{\eta\,H_P}{K\,r} \right)^{1/2} N \, . \tag{13.119}$$

This critical frequency can be compared to the critical frequency (13.77) for Tayler's instability, noted here ω_{AT}. The ratio of the two frequencies is

$$\frac{\omega_{\mathrm{Ab}}}{\omega_{\mathrm{AT}}} \approx \left(\frac{\eta}{K} \right)^{1/4} \left(\frac{H_P}{r} \right)^{1/2} \left(\frac{N}{\Omega} \right)^{1/2} \left(\frac{r^2\,\Omega}{\eta} \right)^{1/4} . \tag{13.120}$$

This ratio is slightly smaller for faster rotation. In general, $\omega_{\mathrm{Ab}}/\omega_{\mathrm{AT}} \gg 1$ for MS stars as well as for white dwarfs and neutron stars [545]. In the case of the Sun, one has $\omega_{\mathrm{Ab}}/\omega_{\mathrm{AT}} \approx 10^3$. This means that the magnetic buoyancy instability only appears for much larger fields than the fields built up by the Tayler instability.

13.7.2.2 General Remarks

Thus, the sequence of the events in the development of the magnetic field in a radiative zone is likely the following. The winding-up of a small field produces a toroidal field, which soon becomes unstable to Tayler instability. The vertical coupling imposed by Tayler–Spruit dynamo makes rotation almost uniform. The magnetic field is adjusted to the marginal condition, as in the numerical example of Sect. 13.6.1,

so that the very high field necessary for buoyancy is not reached. The same applies to the magnetic shear: Tayler's instability, which is first met, prevents the conditions for magnetic shear to appear in a radiative region in differential rotation.

The overall conclusion is that the Tayler instability and the Tayler–Spruit dynamo may dominate the evolution of the magnetic field in radiative stellar regions. The consequences for the evolution may be considerable, in particular a nearly solid body rotation coupled with an enhanced mixing of the elements is obtained in models which account for the Tayler–Spruit dynamo. The enhanced mixing results from the interaction of the magnetic field and meridional circulation (Sect. 13.6). However, there is still some caveat at present, since, if the Tayler instability is confirmed by the existing numerical magneto-hydrodynamical models, the Tayler–Spruit dynamo is supported by some of them and not by other ones (Sect. 13.4.2).

Chapter 14
Physics of Mass Loss by Stellar Winds

It is amazing that even before they are completely formed, massive stars already evaporate and lose mass. Then, during the Main Sequence and later phases, they continue to intensively evaporate so that when, for example, a $100 \, M_\odot$ star explodes as a supernova it is left with only about $10 \, M_\odot$. The mass loss results from the stellar winds driven by the strong radiation pressure of very luminous stars, which pushes the mass outside. The main transfer of momentum is due to the absorption of the stellar radiation by stellar lines. The AGB stars and red supergiants also experience strong mass loss, due mostly to the absorption and diffusion of radiation by dust and to pulsations. In massive stars and in the advanced evolution of intermediate mass stars, mass loss is a dominant effect influencing all the outputs of stellar evolution and nucleosynthesis.

The wind velocities of OB stars reach up to $3000 \, \mathrm{km \, s^{-1}}$ with mass loss rates up to $\dot{M} \sim 10^{-5} \, M_\odot \, \mathrm{yr}^{-1}$, much higher than $10^{-14} \, M_\odot \, \mathrm{yr}^{-1}$ the rate for the Sun. For a $60 \, M_\odot$ star with a MS lifetime of 3.5×10^6 yr, this means the loss of about $35 \, M_\odot$. In this chapter, we give a short insight into the physics of stellar winds. For a more complete approach, we refer the reader to the excellent book by H. Lamers and J. Cassinelli [301], to the reviews by R. Kudritzki and J. Puls [298] and by S. Owocki [452, 453].

14.1 Stellar Wind Properties

The continuum and line absorptions in stellar atmospheres transfer the radiation momentum to the stellar matter accelerating it outward. The momentum is mainly transferred by UV photons in resonance lines of Fe and CNO elements. Thus the radiatively driven stellar winds are efficient mainly in hot bright stars, like OB stars, and with enough heavy elements. One absorption by an ion may increase its velocity by a few $10 \, \mathrm{cm \, s^{-1}}$, thus millions of absorption are necessary to accelerate the ions to velocities of a few $10^3 \, \mathrm{km \, s^{-1}}$. Most of the ions receive little acceleration and they are embarked in the outward wind by electric coupling, thus the

momentum of the efficiently accelerated ions is shared with many ($\sim 10^5$) other ones. This means that the efficient ions must absorb tens or hundreds billions of photons.

The Doppler effect is saving the stellar winds! Without the Doppler shift, the already slightly accelerated ions in the wind could not be further accelerated because all the flux at the efficient absorption wavelengths λ_0, specific of a given ion, would have already been absorbed in the lower layers. However, during their acceleration the ions of velocity v absorb the photons at wavelengths $\lambda_0 + (v/c)$ with a different v at each level r in the wind. This allows the ions to "use" the photons in relatively broad wavelength bands, making line absorption an efficient process for the wind acceleration.

An ion which absorbs a fraction ΔL of the stellar luminosity L receives a force $\Delta L/c$. A force makes a change of the momentum $\boldsymbol{p} = m\boldsymbol{v}$ per unit of time. Thus, if the whole luminosity would be used to accelerate some mass ΔM per unit of time at a limiting external velocity v_∞, one would have the limiting mass loss rate $\dot{M} v_\infty = (L/c)$, assuming the photons are used only once. Due to multiple scattering, the observed $\dot{M} v_\infty/(L/c)$ ratios in WR stars may be of the order of 10 [1].

The ratio L/c^2 is a mass per unit of time, i.e., a mass loss rate, thus

$$\dot{M} = \frac{c}{v_\infty} \frac{L}{c^2} = N \frac{L}{c^2} \qquad \text{with } N = \frac{c}{v_\infty}. \tag{14.1}$$

L/c^2 is the mass defect by nuclear reaction by unit of time, but is also the mass loss rate due to the momentum L/c brought at velocity c. It can be interpreted [301] as the mass loss rate for one optically thick line, thus N is the number of effective lines producing the mass loss rate. Values of N around 10^2 give mass loss rates corresponding to the observed values for OB stars. All quantities in (14.1) are expressed in CGS units.

Another interesting limit of the mass loss rates is "the photon tiring limit". It is obtained by assuming that the power L of a star is entirely used to change the gravitational energy $-(3/2)GM^2/R$ (Sect. 24.5),

$$L \sim \frac{d}{dt}\left(\frac{3\,GM^2}{2R}\right) \Rightarrow \dot{M} \sim \frac{RL}{3\,GM}, \quad \text{num. } \dot{M} \approx 1.07 \times 10^{-8}\frac{RL}{M}\,\mathrm{M_\odot\,yr^{-1}}, \tag{14.2}$$

where R, L, M are in solar units. This expression is to be compared to the Reimers' formula (27.3), it can be written using the escape velocity v_{esc}

$$\dot{M} \sim \frac{L}{v_{\mathrm{esc}}^2} \sim \frac{c}{v_{\mathrm{esc}}} \frac{L}{c v_{\mathrm{esc}}}. \tag{14.3}$$

Since $v_\infty \sim v_{\mathrm{esc}}$ (14.20), the mass loss rate $\dot{M}$ in (14.2) is larger than in (14.1) by a factor $(c/v_{\mathrm{esc}}) \sim 10^3$).

14.2   Radiatively Line-Driven Winds

The main purpose of the theory of stellar winds is to provide an estimate of the mass loss rates as a function of the stellar properties, to describe the wind acceleration and identify the main driving effects of the winds.

14.2.1   Simplified Theory

The equations determining the mass flow outside the star are the equations of continuity (1.7) and momentum conservation (1.2) with account of radiation (Appendix 3.6.2). We solve them here in the simplest approximation [295]. We consider a star of mass M (M is taken as constant with r since the total mass in the wind is negligible) with transport in the radial direction from a point source in a stationary situation ($d/dt = 0$) and get

$$\dot{M} = 4\pi r^2 \varrho \, v = \text{const.} \,, \tag{14.4}$$

$$v \frac{dv}{dr} = -\frac{GM}{r^2} + \frac{1}{\varrho} \frac{dP}{dr} + g_{\text{rad}} \,. \tag{14.5}$$

The radiative acceleration $g_{\text{rad}} = g_{\text{rad,es}} + g_{\text{rad,L}}$ consists in an acceleration $g_{\text{rad,es}} = \kappa_{\text{es}} F/c$ (3.115) due to the continuous absorption by electron scattering and an acceleration $g_{\text{rad,L}}$ due to the spectral lines (Appendix C.1.1). This last term is here represented by $g_{\text{rad,es}}$ times a multiplication factor

$$g_{\text{rad,L}} = g_{\text{rad,es}} M(t) \,, \tag{14.6}$$

where $M(t)$ is called the force multiplier. It depends on the optical depth t, because the ratio of the line to electron scattering opacities varies with the optical depth (at a given T_{eff}). In a static medium, the optical depth τ is defined by $d\tau = -\kappa \varrho dr$ (24.17) integrated inward from the surface. In a moving medium, it is appropriate to define it as [97]

$$t = \kappa_{\text{es}} \varrho \, v_{\text{th}} \left| \frac{dr}{dv} \right| \,, \tag{14.7}$$

which is the optical depth for electron scattering through which the wind velocity changes by v_{th}, the thermal velocity at the surface, i.e., $v_{\text{th}} = (2\mathcal{R}T_{\text{eff}}/\mu)^{1/2}$ (C.63). At a given T_{eff}, the force multiplier is represented by

$$M(t) = k t^{-\alpha} \,, \tag{14.8}$$

where k and α are called the force multiplier parameters. k roughly expresses the number of lines with significant strength and α the slope of the line strength

Table 14.1 Force multiplier parameters from Pauldrach et al. [462] at $Z = 0.017$

T_{eff}	k	α
50000	0.124	0.640
40000	0.124	0.640
30000	0.170	0.590
20000	0.320	0.565

distribution as a function of optical depth. A value of $\alpha = 2/3$ is often considered as typical for O-type stars. Values from non-LTE atmosphere models are given in Table 14.1. This applies to stars on the MS. Empirical determinations by Lamers et al. [303] from the comparison of terminal and escape velocities (14.20) lead to the following (different) values of α:

$$\alpha = \quad 0.52, \quad 0.24, \quad 0.17, \quad 0.15$$
$$\text{for } T_{eff} = \geq 4.35, \quad 4.30, \quad 4.00, \quad 3.90$$

From (14.8), we see that at low t values, such as $t = 10^{-4}$ or 10^{-6} in the wind at $r \gg R$, the line opacities are 10^2–10^3 times larger than Thomson scattering. The force multiplier $M(t)$ also depends on the ionization of the medium, thus on the electron concentration n_e at a given T_{eff} [462], the effect is however limited and we omit it here (see Sect. 14.2.2). $M(t)$ depends linearly on metallicity Z. The momentum equation (14.5) becomes, with Γ (3.117) for electron scattering and ignoring the effect of the pressure gradient,

$$v \frac{dv}{dr} = -\frac{GM}{r^2}(1 - \Gamma) + \frac{\kappa_{es}L}{4\pi r^2 c} kt^{-\alpha} . \tag{14.9}$$

Now, with (14.4), t can be written as

$$t = \kappa_{es} \frac{\dot{M}}{4\pi r^2 v} v_{th} \frac{dr}{dv} , \tag{14.10}$$

(dv/dr) being positive in the accelerated wind. Equation (14.9) becomes

$$\underbrace{r^2 v \frac{dv}{dr}}_{D} = -GM(1 - \Gamma) + \underbrace{\frac{\kappa_{es}Lk}{4\pi c} \left(\frac{4\pi}{\dot{M} v_{th} \kappa_{es}}\right)^{\alpha}}_{C} \left(r^2 v \frac{dv}{dr}\right)^{\alpha} , \tag{14.11}$$

$$\text{or} \qquad CD^{\alpha} = D + GM(1 - \Gamma) . \tag{14.12}$$

Since C is a constant as well as $GM(1 - \Gamma)$, expression (14.12) can only be satisfied for various distance r if D is also a constant, thus

$$r^2 v \frac{dv}{dr} = D = \text{const.} \tag{14.13}$$

This is easily integrated, one has

$$-\frac{1}{2}\frac{dv^2}{d(1/r)} = D \qquad \longrightarrow \qquad v^2\Big|_{v(R)}^{v(r)} = -2D\frac{1}{r}\Big|_R^r .$$

(14.14)

Taking $v(R) \cong 0$, one obtains for the velocity at level r in the wind

$$v^2(r) = 2\frac{D}{R}\left(1-\frac{R}{r}\right) .$$

(14.15)

For $r \to \infty$, one has $v_\infty^2 = 2D/R$, thus the velocity can be written as

$$v = v_\infty \sqrt{1-\frac{R}{r}} .$$

(14.16)

Figure 14.1 shows the velocity law in the wind (14.29, $\beta = 0.5$ for the above law). The steep curves show that the maximum line acceleration g_L is close to the star at $r/R \leq 1.1$. We need to find the constant D. In expression (14.12), let us consider the two functions of D:

$$z = CD^\alpha \qquad \text{and} \qquad y = D + GM(1-\Gamma) .$$

(14.17)

The first one is a power law ($\alpha \sim 0.5$), the second a straight line. Depending on the values of C and $GM(1-\Gamma)$, the two curves may (a) intersect twice, (b) have a tangent point or (c) have no intersection. Equation (14.12) says $z = y$, if
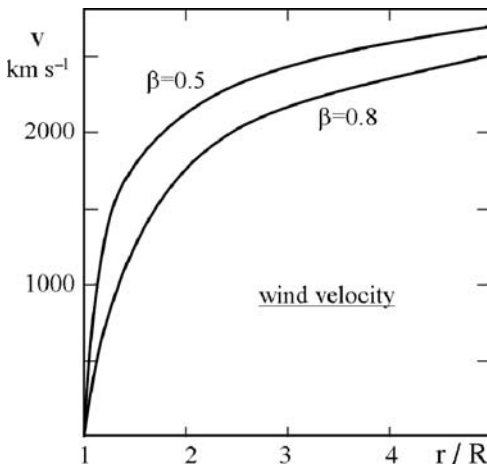
Fig. 14.1 The velocity in the wind as a function of r/R, with R the stellar radius for two cases of β in $v = v_\infty [1 - (R/r)]^\beta$ (14.29, see also 14.16). The terminal velocity $v_\infty = 3000$ km s^{-1} in both cases

in addition one wants the solution to be unique, then it is given by case (b). This means that not only the two functions are equal but also their first derivatives with respect to D,

$$\frac{dz}{dD} = \frac{dy}{dD} \quad \longrightarrow \quad C = \frac{D^{1-\alpha}}{\alpha}. \quad (14.18)$$

This value of C put in relation (14.12) gives

$$D = [\alpha/(1-\alpha)] \, GM(1-\Gamma) \quad (14.19)$$

and $\quad v_\infty = \left(\frac{\alpha}{1-\alpha} \frac{2GM(1-\Gamma)}{R}\right)^{1/2} = \left(\frac{\alpha}{1-\alpha}\right)^{1/2} v_{esc}. \quad (14.20)$

$v_{esc} = \{[2GM(1-\Gamma)]/R\}^{1/2}$ is here the escape velocity with account of radiation pressure on matter experiencing electron scattering. Now, we can get the mass loss rate $\dot{M}$ from the expression of C (14.11) with C given by (14.18) and D by (14.19),

$$\dot{M} = \frac{4\pi}{\kappa_{es} v_{th}} \left(\frac{k\,\alpha\,\kappa_{es}L}{4\pi c}\right)^{1/\alpha} \left(\frac{1-\alpha}{\alpha}\right)^{\frac{1-\alpha}{\alpha}} [GM(1-\Gamma)]^{\frac{\alpha-1}{\alpha}}. \quad (14.21)$$

The force multiplier parameter α appears in almost every term. The mass loss rates depend on L directly and also through the reduced mass $[GM(1-\Gamma)]$. From Table 4.1, we have between 10 and $120\,M_\odot$

$$L \sim [GM(1-\Gamma)]^{3.06} \quad \text{or} \quad GM(1-\Gamma) \sim L^{0.327}. \quad (14.22)$$

Thus, for $\alpha = 0.6$ one has the following behavior of the product giving $\dot{M}$:

$$L^{1/\alpha} [GM(1-\Gamma)]^{\frac{\alpha-1}{\alpha}} \sim L^{1.67}[L^{0.327}]^{-0.67} \sim L^{1.45}, \quad (14.23)$$

and for $\alpha = 0.5$

$$L^{1/\alpha} [GM(1-\Gamma)]^{\frac{\alpha-1}{\alpha}} \sim L^{2.00}[L^{0.327}]^{-1.00} \sim L^{1.67}. \quad (14.24)$$

This is close to the observational relations [148, 298], see Sect. 27.3.1,

$$\dot{M} \sim L^{1.6} \text{ for OV stars},$$

$$\dot{M} \sim L^{1.5} \text{ for OI stars}. \quad (14.25)$$

Expression (14.21) for the $\dot{M}$ rates contains the leading terms determining the mass loss rates, however, there are some additional effects.

14.2.2   Metallicity, Velocities and Other Effects

The successive developments of the theory of stellar winds have led to the considerations of several other effects (e.g., [297, 298, 301, 452, 462]):

Metallicity effects. The mass loss rates scale with metallicity Z like [148]

$$\dot{M} \sim Z^{\frac{1-\alpha}{\alpha-\delta}} . \tag{14.26}$$

With $\alpha = 0.6$ and $\delta = 0.05$ (see ionization effects below), one has $\dot{M} \sim Z^{0.73}$ close to the value derived by Vink et al. [605], who give

$$\dot{M} \sim Z^{0.69} \quad \text{for OB stars with } T_{\text{eff}} \geq 25000\,\text{K}, \tag{14.27}$$

$$\dot{M} \sim Z^{0.64} \quad \text{for B} - \text{supg with } T_{\text{eff}} \leq 25000\,\text{K}. \tag{14.28}$$

The dependence of the mass loss rates on metallicity is responsible for differences in the populations of massive stars in galaxies and also for differences in the chemical yields with metallicity. The terminal velocity v_∞ is found observationally to scale like $v_\infty \sim Z^{0.13}$ [323].

Finite disk effects and velocities. The above simple model accounts only for radiation in the radial direction, like if the star were a point source. Close to the stellar surface, a given ion does not receive the momentum corresponding to the stellar luminosity only from the internal radial direction, but this momentum comes from various directions. Therefore, the overall momentum was overestimated as well as the $\dot{M}$ rates (14.21), which should be multiplied by a factor $(1 + \alpha)^{1/\alpha}$ to account for the finite disk effect [462]. $\dot{M}$ reduction by 0.2 and 0.6 dex are found at 10^6 and 10^3 L$_\odot$ [301].

Noticeably, the terminal wind velocity v_∞ is larger due to the finite disk corrections, because according to (14.6), (14.7) and (14.8), the line acceleration g_L scales like $g_L \sim r^{-2}t^{-\alpha} \sim r^{-2}\left[\varrho\left(dr/dv\right)\right]^{-\alpha}$. The $\dot{M}$ rates being smaller, the optical depth t is smaller as well as the density, this makes a larger g_L leading to larger final velocities with $v_\infty \cong (2-3)\, v_{\text{esc}}$, instead of ~ 1.23 given by (14.20) with $\alpha = 0.6$. At the same time, the velocity profile as a function of r in the wind is smoother. Instead of (14.16), it becomes

$$v = v_\infty \left(1 - \frac{R}{r}\right)^\beta , \tag{14.29}$$

with an exponent $\beta = 0.8$ rather than 0.5 (Fig. 14.1).

Ionization effects. The force multiplier $M(t)$ also depends on the ionization in the wind, which itself depends on T_{eff} and on n_e the electron concentration. Thus, an additional term is included in the force multiplier

$$M(t) = kt^{-\alpha} \left(\frac{n_e}{W}\right)^\delta , \tag{14.30}$$

with n_e in units of 10^{-11} cm^{-3}. W is a dilution factor. The parameter δ is 0.02, 0.09, 0.07, 0.07 for the T_{eff} values of Table 14.1. Thus, the ionization effect brings another multiplication factor

$$\left(\frac{n_e}{W}\right)^{\delta/\alpha} \tag{14.31}$$

on the right-hand side of the mass loss rate formula (14.21), while it does not affect the terminal velocity (14.20). The account for $\delta \neq 0$ reduces the wind acceleration, however, owing to the small value of the exponent δ, the effect is not large.

Rapid changes of ionization near 20000 and 10000 K lead to variations of the force multipliers k and α leading to rapid changes of $\dot{M}$ and of v_∞/v_{esc} with T_{eff}. Such transitions, the abruptness of which is still a matter of discussion, are called bi-stability limits [303].

Gas pressure effects. We have ignored the effect of the gradient of gas pressure in (14.5). This is justified because in external layers the gas pressure is generally negligible as well as its gradient. The changes brought by this effect are inferior to 10% [452].

Multiple scattering. The photons absorbed and re-emitted at a lower frequency or scattered in a spectral line cannot be again absorbed in the same line at another r in the wind, however, under some conditions they could be absorbed by other lines at lower frequencies depositing some momentum. In a dense medium like in the thick wind of WR stars, multiple scattering may enhance the transferred wind momentum by a factor of 6 with respect to single scattering, while in OB stars it amounts to a factor of ~ 2. The back-scattered photons contribute to the heating of the atmosphere, thus producing a blanketing effect from the wind.

In evolutionary models, one uses mass loss rates based on fits of observational relations or given by analytical expressions derived from grids of stellar wind models [604, 605] for different M, L, T_{eff} and Z. Account of clumping in the wind has reduced $\dot{M}$ in the above parameterizations. Indeed, there is a variety of instabilities which can produce fluctuations in the wind [452]. There has been some debates whether the mass loss rates should be further reduced due to clumping. This does not seem to be the case.

14.3   Kudritzki's Wind Momentum–Luminosity Relation

There is an important relation between the mechanical wind momentum $\dot{M}v_\infty$ of the mass outflow and the luminosity L of hot stars predicted by the theory of radiative winds. It was found and studied in a series of works by Kudritzki and coworkers [297, 298, 481]. Such a relation is established for O-type stars in the Galaxy and in the Magellanic Clouds, as well as for A- and B-type supergiants in the Galaxy [298] (Fig. 14.2). The WLR provides a new way to obtain absolute luminosities from spectroscopic observations. The potentialities of the wind momentum–luminosity relation (WLR) for the determination of extragalactic distances were considered as great [298].
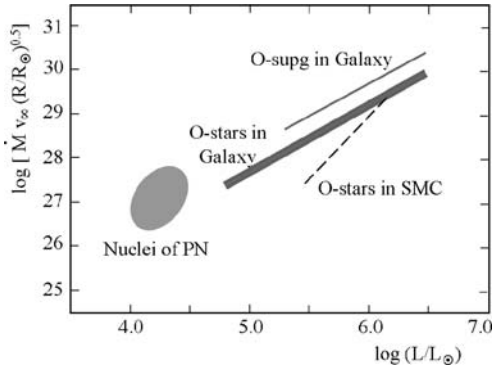
Fig. 14.2 The wind-momentum relation for galactic O stars (class V,III), supergiants and central stars in planetary nebulae (PN), the relation for O stars in the SMC is also shown. Adapted from R.P. Kudritzki and J. Puls [298]

As seen above (Sect. 14.2.1), the mass loss rates and the terminal velocities behave as

$$\dot{M} \sim L^{\frac{1}{\alpha}}[M(1-\Gamma)]^{1-\frac{1}{\alpha}} , \qquad (14.32)$$

$$v_\infty \sim \left[\frac{GM(1-\Gamma)}{R}\right]^{0.5} , \qquad (14.33)$$

with Γ the Eddington factor for κ_{es} the electron scattering opacity. The product of the above two terms is

$$\dot{M}v_\infty \propto \frac{1}{R^{0.5}}L^{\frac{1}{\alpha}}[M(1-\Gamma)]^{\frac{3}{2}-\frac{1}{\alpha}} . \qquad (14.34)$$

Thus, with a value $\alpha = 2/3$, which is close to that for O stars, one obtains the wind–momentum relation

$$\dot{M}v_\infty R^{0.5} \sim L^{\frac{3}{2}} . \qquad (14.35)$$

Thus, the determinations of the terminal velocities from the blue edge of the absorption part of the P-Cygni profiles, with mass loss rate determinations from Hα line emissions, together with spectroscopic estimates of the radii, provide independent luminosity determinations. Figure 14.2 shows some small differences in the relation for supergiants and for different metallicities, which can be corrected after proper calibrations.

14.3.1   Rotation and the WLR Relation

The effects of axial rotation on the wind momentum–luminosity relation have been investigated [351]. Despite the fact that the mass loss rates may grow a lot with

rotation (Sect. 14.4), the effects on the wind–momentum relation are small on the average due to some compensating effects in the various terms involved. The relation becomes for stars with a rotation velocity v

$$\dot{M} v_\infty R^{0.5} \sim L^{\frac{3}{2}} f_\Omega \qquad (14.36)$$

with $f_\Omega < 1.01$ up to $v/v_{\mathrm{crit},1} = 0.65$, and $f_\Omega = 1.045$, 1.10 for $v_{\mathrm{crit},1} = 0.8$ and 0.9, respectively, $v_{\mathrm{crit},1}$ being the usual critical velocity (4.34). Different orientation angles between the rotation axis and the line of sight produce some limited scatter ($< 10\%$).

14.4 Rotation Effects on Stellar Winds

The interactions of rotation and stellar winds have many far-reaching consequences [350]: (1) rotation introduces anisotropies in the stellar winds, because the effective gravity is changing with latitude and because of the von Zeipel theorem (Sect. 4.2.2) the polar regions are hotter than the equatorial ones, a effect now observed (Sect. 18.40); (2) the global mass loss rates are increased by rotation; (3) the anisotropies of the stellar winds allow a star with strong polar winds to lose lots of mass without losing to much angular momentum; on the contrary, equatorial mass loss removes a lot of angular momentum; (4) the winds may also affect the patterns of meridional circulation, however, these effects have not yet been investigated thoroughly enough so far.

14.4.1 Latitudinal Variations

We are applying the results from the section on stellar winds as well as from Chap. 4.2 on radiative transfer in rotating stars. At the surface of a rotating star, we are considering the local radiative flux $F(\vartheta)$ and the mass flux $\Delta\dot{M}(\vartheta)/\Delta\sigma$ at a given colatitude ϑ rather than the luminosity L and the total mass loss rates $\dot{M}$ as in (14.21) above. Thus, divided by surface unity (14.21) can be written as

$$\frac{\Delta\dot{M}(\vartheta)}{\Delta\sigma} \sim \left(\frac{1}{T_{\mathrm{eff}}(\vartheta)}\right)^{1/2} (k\alpha)^{1/\alpha} \left(\frac{1-\alpha}{\alpha}\right)^{\frac{1-\alpha}{\alpha}} F^{1/\alpha}(\vartheta)\, g_{\mathrm{tot}}^{(\alpha-1)/\alpha}(\vartheta), \quad (14.37)$$

where we only keep the terms which vary with colatitude ϑ. The term in T_{eff} comes from the thermal velocity, which also varies with latitude (this term was absent in [350]); from (4.23), $T_{\mathrm{eff}} \sim (g_{\mathrm{eff}})^{1/4}$. k and α are the force multiplier parameters (Table 14.1), which here may vary with ϑ. With the expressions of the radiative flux (4.21), of the total gravity (4.27) with (4.30) and of T_{eff} (4.23), we get

$$\frac{\Delta \dot{M}(\vartheta)}{\Delta \sigma} \sim A \frac{1}{\left(\frac{L(P)}{4\pi(ac/4)GM_\star}\right)^{1/8} g_{\text{eff}}^{1/8}} \left[\frac{L(P)}{4\pi GM_\star(P)}\right]^{\frac{1}{\alpha}} \frac{g_{\text{eff}}}{[1-\Gamma(\Omega,\vartheta)]^{\frac{1}{\alpha}-1}}$$

$$\text{with} \quad A = (k\alpha)^{\frac{1}{\alpha}} \left(\frac{1-\alpha}{\alpha}\right)^{\frac{1-\alpha}{\alpha}}, \tag{14.38}$$

with $M_\star$ given by (4.22). This can further be written as

$$\frac{\Delta \dot{M}(\vartheta)}{\Delta \sigma} \sim A \, (ac/4)^{1/8} \left[\frac{L(P)}{4\pi GM_\star(P)}\right]^{\frac{1}{\alpha}-\frac{1}{8}} \frac{g_{\text{eff}}^{1-\frac{1}{8}}}{[1-\Gamma(\Omega,\vartheta)]^{\frac{1}{\alpha}-1}} . \tag{14.39}$$

The above expression predicts anisotropic stellar winds. We can identify the following two effects [350]:

- g_{eff} effect: due to the higher gravity at the poles of rotating stars, the polar mass flux is enhanced, while the equatorial flux is smaller.
- κ effect: when the opacities are not only due to electron scattering, the higher opacities at lower T_{eff} lead to higher k and smaller α at the equator and thus favor equatorial ejections. The term A increases by a factor of 3 from $T_{\text{eff}} = 50000$ to 20000 K (Table 14.1). The two terms in square brackets also lead to higher rotational enhancements of the mass loss for lower values of α, an effect particularly important in the equatorial regions of B stars. Bi-stability limits may also occur over the stellar surface between the poles and equator.

In all cases, the proximity to $\Gamma = 1$ leads to enhanced rotational winds. Care must be given that in the theory of radiatively driven winds, the total opacity at a given optical depth is expressed with the force multipliers in terms of the electron scattering opacity κ_{es}. This means that in $\Gamma_\Omega(\vartheta)$ (4.29) the opacity to be considered here is κ_{es}, the electron scattering opacity!

Figure 14.3 shows 3D representations of the distributions of the mass loss rates around a very bright star similar to η Carinae. In the figure on the left, a $T_{\text{eff}} = 30000$ K is assumed, the star is hot enough for the electron scattering opacity to dominate from pole to equator. Thus, the distribution of the mass loss rates with ϑ is shaped only by the g_{eff} effect, which produces the peanut shape of the distribution of the mass loss rates by stellar winds. Such peanut-shaped nebulae are observed around several Luminous Blue Variables [444], such as η Carinae and AG Carinae. The occurrence of polar jets together with an equatorial ejection is a characteristic of B[e] stars [637]. Also, a polar wind enhancement is observed in some Be stars [396]. In the figure on the right, a $T_{\text{eff}} = 25000$ K is assumed. Thus, in the cooler equatorial regions the opacity is higher, i.e., the force multiplier parameter α is lower. This provokes an equatorial enhancement of the stellar winds (κ effect) forming a kind of a disk in addition to the peanut shape of the g_{eff} effect, which is always present. The fate of the matter in the wind is determined, like in the spherical case, by the velocities and densities which for rotating stars depend on ϑ. Collective effects
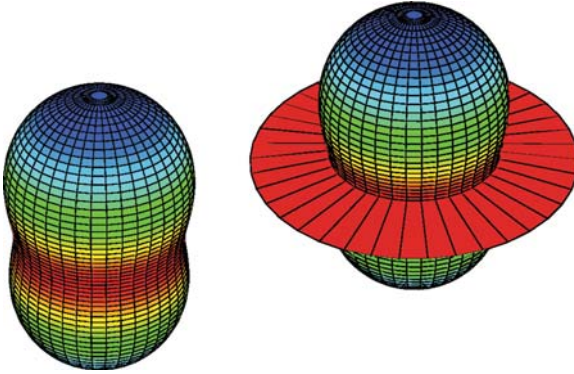
Fig. 14.3 *Left*: the mass fluxes around a rotating star of $100\,\mathrm{M}_\odot$ with $10^{6.5}\,\mathrm{L}_\odot$ and a ratio of the angular velocity to the break-up angular velocity $\omega = 0.80$, assuming a polar $T_{\mathrm{eff}} = 30000$ K. *Right*: the same star but with a polar $T_{\mathrm{eff}} = 25000$ K; here the opacity jump in the equatorial regions also provokes a ring ejection (κ effect). From the author and V. Desjacques [356]

in wind acceleration [452] such as due to pulsations, running waves, convective plumes, etc., may also intervene.

14.4.1.1   Wind Density and Velocity in Rotating Stars

The velocity in the wind behaves like (14.29) with v_∞ given by (14.20). In a rotating star, these quantities have to be considered locally at a colatitude ϑ. In particular v_∞ is modified by the account of the centrifugal force (4.30),

$$v_\infty = \left(\frac{\alpha}{1-\alpha} \frac{2GM[1-\Gamma(\Omega,\vartheta)]}{R} \right)^{1/2} \left[1 - \frac{\Omega^2 R(\vartheta)^3}{GM} \sin^2 \vartheta \right]^{1/2}. \quad (14.40)$$

For v_∞ given by the above expression, one has to assume that the ejected particles keep their angular momentum. The value of the terminal velocity is much higher at the pole than at the equator, due to the change of the centrifugal force. The effect is further enhanced if α is larger at the pole than at the equator. The wind density is given by the continuity equation (14.4). It decreases with distance like $\sim r^{-2}$. At some distance r of the surface, under the assumption of no collective effects in the wind, the density is given by the local mass flux (14.39) divided by the local velocity

$$\varrho(r,\vartheta) = \frac{1}{v(r,\vartheta)} \frac{\Delta \dot{M}(\vartheta)}{\Delta \sigma}. \quad (14.41)$$

For constant α, the wind is denser at the pole than at the equator. For higher k and lower α at the equator, the wind density is larger at the equator than at the pole [350].

14.4.2 Mass Loss and Rotation

It is useful to know how the total mass loss rates integrated over all directions depend on the rotation velocities and on the proximity of the $\Omega\Gamma$ limit. If $\Sigma(\omega)$ is the total surface, we have from (14.39)

$$\frac{\dot{M}}{\Sigma(\omega)} \sim A \left[\frac{L(P)}{4\pi GM_\star}\right]^{\frac{1}{\alpha}-\frac{1}{8}} \overline{\left(\frac{g_{\text{eff}}^{7/8}}{(1-\Gamma(\Omega,\vartheta))^{\frac{1}{\alpha}-1}}\right)}, \qquad (14.42)$$

where the bar indicates the mean value. We approximate the mean of the ratio by the ratio of the means and consider appropriate means for α and $\Gamma(\Omega,\vartheta)$ (for κ_{es}, these are constant with ϑ). From (11.15), g_{eff} is

$$\overline{g_{\text{eff}}} = \frac{\int\int g_{\text{eff}}\cdot d\sigma}{\Sigma(\omega)} = \frac{4\pi GM_\star}{\Sigma(\omega)}, \qquad (14.43)$$

after integration over the stellar surface which is an isobar. This leads to the following expression for the total mass loss rate from the star:

$$\dot{M} \sim \frac{A\,L(P)^{\frac{1}{\alpha}-\frac{1}{8}}\,\Sigma^{1/8}}{(4\pi GM)^{\frac{1}{\alpha}-\frac{7}{8}}\left[1-\frac{\Omega^2}{2\pi G\rho_{\text{m}}}\right]^{\frac{1}{\alpha}-\frac{7}{8}}(1-\Gamma(\Omega))^{\frac{1}{\alpha}-1}}. \qquad (14.44)$$

From (4.29), one has $\Gamma_\Omega = \Gamma/\{1-[\Omega^2/(2\pi G\rho_{\text{m}})]\}$, where Γ is the Eddington ratio corresponding to electron scattering opacity. This relation expresses how the total mass loss rate from a star depends on mass, luminosity, Eddington factor and rotation. We ignore the small difference introduced by the change of total surface with rotation, owing to the small power.

Let us consider a rotating star with angular velocity Ω and a non-rotating star of the same mass M at the same location in the HR diagram. The ratio of their mass loss rates can be written as

$$\frac{\dot{M}(\Omega)}{\dot{M}(0)} = \frac{(1-\Gamma)^{\frac{1}{\alpha}-1}}{\left[1-\frac{\Omega^2}{2\pi G\rho_{\text{m}}}\right]^{\frac{1}{\alpha}-\frac{7}{8}}[1-\Gamma(\Omega)]^{\frac{1}{\alpha}-1}}. \qquad (14.45)$$

If $\Omega = 0$, this ratio is equal to 1. It can also be expressed in terms of $v/v_{\text{crit},1}$, the ratio of the rotational velocity v to the critical velocity (4.34), since we have $\frac{\Omega^2}{2\pi G\rho_{\text{m}}} \simeq \frac{4}{9}\frac{v^2}{v_{\text{crit},1}^2}$ over a large range of values (see 4.38 and following remarks). For a star with a small Eddington factor Γ, it simplifies to

$$\frac{\dot{M}(\Omega)}{\dot{M}(0)} \simeq \frac{1}{\left[1 - \frac{4}{9}\left(\frac{v}{v_{\text{crit},1}}\right)^2\right]^{\frac{1}{\alpha} - \frac{7}{8}}} . \tag{14.46}$$

This equation shows that the effects of rotation on the $\dot{M}$ rates remain moderate in general. However, for stars close to the Eddington limit, rotation may drastically increase the mass loss rates, in particular for low values of α, i.e., for stars with log $T_{\text{eff}} \leq 4.30$. In cases where $\Gamma > 0.639$, a moderate rotation may make the denominator of (14.45) to vanish, indicating large mass loss.

Table 14.2 shows some numerical results based on (14.44) for different initial stellar masses at the end of the Main Sequence (MS) phase in the Geneva models at Z = 0.02 [513]. The values are given for the empirical force multipliers α [303], which span a large range of values as mentioned in Sect. 14.2.1. The ratio $\dot{M}(\Omega)/\dot{M}(0)$ has a maximum value of about 1.60 for hot stars with a small Γ. The amplification of the mass loss rates is larger for stars with higher Γ and/or lower T_{eff}. The indication "crit" means that the combination of the radiation pressure and rotation makes the surface layers unbound before the usual critical velocity $v_{\text{crit},1}$ (4.34) is reached. A very high mass loss is likely to result, determined by the evolution of M, R and rotation velocity. For $\Gamma > 0.639$, the critical velocity $v_{\text{crit},2}$ applies (Fig. 4.3). This is the regime of the $\Omega\Gamma$ limit, which concerns objects like the LBV stars.

Table 14.2 Γ at the end of the MS for various initial masses and ratios $\dot{M}(\Omega)/\dot{M}(0)$ of the $\dot{M}$ rates for a star at break-up rotation to that of a non-rotating star of the same mass and luminosity at log $T_{\text{eff}} \geq 4.35$, at log $T_{\text{eff}} = 4.30$, 4.00 and 3.90. The empirical force multipliers α by Lamers et al. ([303]) are used

M_{ini}	Γ	$\frac{\dot{M}(\Omega)}{\dot{M}(0)}$ $\alpha = 0.52$	$\frac{\dot{M}(\Omega)}{\dot{M}(0)}$ $\alpha = 0.24$	$\frac{\dot{M}(\Omega)}{\dot{M}(0)}$ $\alpha = 0.17$	$\frac{\dot{M}(\Omega)}{\dot{M}(0)}$ $\alpha = 0.15$
120	0.903	crit	crit	crit	crit
85	0.691	crit	crit	crit	crit
60	0.527	4.00	101.8	1196	3731
40	0.356	2.26	14.4	58.5	112.1
25	0.214	1.86	7.43	21.3	34.5
20	0.156	1.77	6.21	16.1	25.0
15	0.097	1.69	5.33	12.8	19.1
12	0.063	1.66	4.95	11.4	16.7
9	0.034	1.63	4.67	10.4	15.0

The anisotropies are likely to play a great role in the evolution of rotating stars. They are beautifully confirmed by observations. Polar mass loss allows the fast rotating hot stars to lose lots of mass without losing too much angular momentum, thus these stars keep high rotation velocities. This effect has been advocated to explain how the precursors of gamma-ray bursts may have lost a lot of mass and at the same time kept a very high rotation [413].

Part IV
Acoustic and Gravity Waves. Helio- and Asteroseismology

Chapter 15
Radial Pulsations of Stars

Variable stars have always fascinated mankind, showing non-immutable objects on the celestial sphere thought to be the domain of gods. Indeed, oscillatory phenomena are frequent in natural systems: the level of the sea shows tidal oscillations and waves, the blowing winds produce oscillating noise, the clouds form waves on the side of mountains, some geysers are periodic, etc. Stars do not escape to this rule of Nature.

What makes the beautifully self-controlled stellar nuclear reactors oscillating periodically, like is the case for the famous Cepheids? This question was answered by Eddington in 1926 [168]. If at an appropriate depth, neither too superficial nor too deep, in a stellar envelope, the opacity increases with temperature T (contrarily to the general behavior of the opacity), a small compression induces a higher T, thus a higher opacity. More heat is retained and as it cannot easily go out due to the higher opacity, it produces an expansion which goes beyond the equilibrium point. Then, T becoming lower, the opacity declines, the energy goes out and gravity recalls the system backward, which again produces a compression, etc. In this way the star engine is working cyclically.

There are several kinds of pulsations. They may be radial, meaning that the star inflates and contracts with purely radial motions, keeping the spherical symmetry during a pulsation cycle. Radial pulsations can produce large changes of radius and luminosity. Pulsations may be non-radial, with motions also having a horizontal component. The amplitudes of non-radial oscillations are generally small. Stellar pulsations offer tools for a better understanding of the internal stellar physics. Cepheids are standard candles for the calibration of the distances in the Universe. Some fundamental references about the theory of radial pulsations are Ledoux & Walraven [317], Ledoux [319], Cox [146], Gautschy & Saio [203]; see also Bono et al. [56].

15.1 Thermodynamics of the Pulsations

There is a similarity between the thermodynamics of an engine and of a star. In an engine, there are some driving and damping effects which tend respectively to in-

crease or reduce the work production. Some basic conditions have to be fulfilled for an engine or a star to produce work to the outside or to sustain pulsations against dissipation effects. Let us consider a mass element in the stellar gas. The First Principle says that the energy $\delta Q^{\swarrow}$ provided to the system goes into the increase of the internal energy δU and into the work $\delta \mathcal{T}^{\nearrow}$ provided to the outside, i.e., $\delta Q^{\swarrow} = \delta U + \delta \mathcal{T}^{\nearrow}$. This also applies over a pulsation cycle,

$$\oint \delta Q^{\swarrow} = \underbrace{\oint \delta U}_{=0} + \oint \delta \mathcal{T}^{\nearrow} . \tag{15.1}$$

At the end of a cycle, the internal energy is back to its initial value. The work toward the exterior is positive (i.e., the pulsation is sustained) if the mass element is absorbing some heat from the pulsation cycle. Let us consider the entropy δS of the mass element, $\delta S = \delta Q^{\swarrow}/T$. It is a function of the state of the medium, so that over a cycle, one has

$$\oint \frac{\delta Q^{\swarrow}}{T} = 0 . \tag{15.2}$$

This shows that a medium keeping T constant during a cycle cannot produce any work since $\oint \delta Q^{\swarrow} = 0$. Let us suppose that the temperature $T(t)$ at a time t is equal to an average T_0 plus a small fluctuation $\Delta T(t)$,

$$T(t) = T_0 + \Delta T(t) . \tag{15.3}$$

The entropy over a cycle can be written to the first order

$$0 = \oint \frac{\delta Q^{\swarrow}}{T} = \oint \frac{\delta Q^{\swarrow}}{T_0 + \Delta T} \approx \oint \frac{\delta Q^{\swarrow}}{T_0} \left(1 - \frac{\Delta T}{T_0} \right) \tag{15.4}$$

or

$$\oint \delta Q^{\swarrow} \approx \oint \delta Q^{\swarrow} \frac{\Delta T}{T_0}, \tag{15.5}$$

which is also the work provided to the outside,

$$\delta \mathcal{T}^{\nearrow} \approx \oint \frac{\Delta T}{T_0} \delta Q^{\swarrow} . \tag{15.6}$$

In order a positive work $\delta \mathcal{T}^{\nearrow} > 0$ to be produced, $\delta Q^{\swarrow}$ and ΔT must have the same sign, i.e., the heat must be provided when the temperature is high and released when the temperature is low,

$$\delta Q^{\swarrow} > 0 \quad \text{with} \quad \Delta T > 0 \quad \text{and/or} \quad \delta Q^{\swarrow} < 0 \quad \text{with} \quad \Delta T < 0. \tag{15.7}$$

It may be sufficient that only the first or the second condition is satisfied. In a pulsating star, some regions may absorb heat and other parts lose it. The condition

for pulsation is that the total work over the star is positive,

$$\text{Total work} \approx \oint \frac{\Delta T}{T_0} \delta Q^{\checkmark} \, dM_r > 0 \, . \tag{15.8}$$

In stars, two possible mechanisms able to be the driving engine of pulsations have been identified:

– *The ε mechanism*. During compression by a pulsation, T increases so the rate ε of nuclear energy production is also increased, cf. (9.34). This satisfies the first part of condition (15.7). Then the system expands, goes beyond its equilibrium point and comes back under the recall force of gravitation.
– *The κ mechanism*. Normally in a non-pulsating star, a compression produces an increase of ϱ and T so the opacity κ decreases. The medium becomes more transparent (e.g., 8.43) and the energy escapes faster. This means $\delta Q^{\checkmark} < 0$ with $\Delta T > 0$, i.e., the opposite of the first condition of (15.7). Thus, there is no pulsation in general.

If, however, κ increases with T, as it occurs in a region of partial hydrogen and helium ionization, or as due to the increase of the opacity by the H$^-$ ion (cf. Sect. 8.6.1), a compression makes T higher, thus a higher κ. This means that at higher T, more heat is retained, i.e., $\delta Q^{\checkmark} > 0$ and the first of conditions (15.7) is satisfied. The second is also satisfied, because the retained energy makes an expansion, T and κ decrease, thus the energy escapes more easily from the star, i.e., one has $\delta Q^{\checkmark} < 0$ for $\Delta T < 0$. The star is pulsating.

These mechanisms will appear in the study of the non-adiabatic pulsations. The κ mechanism is the dominant instability mechanism of pulsating stars. The Cepheids are the best example with pulsations driven by the zone of partial second ionization of helium, see also Sect. 15.4. The ε mechanism is in general not working in stars, because the damping dominates, however, it is possible that Wolf-Rayet stars are unstable, due to both the ε and κ mechanisms [145, 342]. Let us note that the damping is not the viscous damping, but the "radiative damping": radiation escapes from the compressed hot layers, this removes energy from the pulsations and tends to damp them.

15.2   Linear Analysis of Radial Oscillations

There are several ways to study the radial stellar instabilities. Here, we examine the linear theory with developments which may be used for both numerical models and analytical studies. Oscillations of small amplitudes around an equilibrium situation are considered. A linear theory does not provide the amplitudes which are determined by non-linear effects. However, it allows us to determine the pulsation periods and the various overtones. If the non-adiabatic effects are accounted for, it is also possible to determine whether a star is stable or not, the linear theory showing which are the driving and damping regions.

Generally, the pulsation properties are mainly determined by the envelope, which harbors the non-adiabatic effects and also determines the pulsation period, since the sound speed (C.27) is lower there. We start from the four basic equations (1.12), (1.4), (3.17) and (3.40) of stellar structure expressed in Lagrangian form,

$$\frac{\partial r}{\partial M_r} = \frac{1}{4\pi r^2 \varrho}, \qquad\qquad \frac{\partial P}{\partial M_r} = -\frac{1}{4\pi r^2}\left(\frac{GM_r}{r^2} + \frac{\partial^2 r}{\partial t^2}\right), \quad (15.9)$$

$$\frac{\partial T}{\partial M_r} = -\frac{3\,\kappa}{4\,acT^3}\frac{L_r}{16\,\pi^2 r^4}, \qquad\qquad \frac{\partial L_r}{\partial M_r} = \varepsilon + \varepsilon_{\mathrm{grav}}. \qquad (15.10)$$

The acceleration term is included in the second equation, but not rotation, otherwise spherical symmetry would be broken. We consider the case of radiative transfer. Convection introduces, in some cases, an additional complexity. We comment on it below (Sect. 15.2.1). The heat $\varepsilon_{\mathrm{grav}}$ brought by contraction or removed by expansion is expressed by (3.64). We consider here stellar envelopes and thus ignore the nuclear term ε.

Let us consider small Lagrangian perturbations around the equilibrium values, denoted with a subscript "$_0$". For a given mass element, one has

$$r(M_r,t) = r_0(M_r) + \delta r(M_r,t)$$

$$P(M_r,t) = p_0(M_r) + \delta P(M_r,t)$$

$$T(M_r,t) = t_0(M_r) + \delta T(M_r,t)$$

$$L(M_r,t) = \ell_0(M_r) + \delta L(M_r,t). \qquad (15.11)$$

This may be written as

$$r(M_r,t) = r_0(M_r)\left[1 + \frac{\delta r(M_r,t)}{r_0(M_r)}\right] = \left[1 + r'(M_r,t)\right], \qquad (15.12)$$

which defines $r'(M_r,t)$. The same for P, T and L,

$$P(M_r,t) = p_0(M_r)\left[1 + p'(M_r,t)\right],$$

$$T(M_r,t) = t_0(M_r)\left[1 + t'(M_r,t)\right],$$

$$L(M_r,t) = \ell_0(M_r)\left[1 + \ell'(M_r,t)\right]. \qquad (15.13)$$

Now, we introduce these last expressions in the equilibrium Eq. (15.10) keeping only the first-order terms. In the first equation, the first and the second members become, respectively,

$$\frac{\partial r}{\partial M_r} = \frac{\partial [r_0(1+r')]}{\partial M_r} = (1+r')\frac{\partial r_0}{\partial M_r} + r_0\frac{\partial r'}{\partial M_r} \, , \qquad (15.14)$$

$$\frac{1}{4\pi r_0^2 \varrho_0 (1+r')^2(1+\varrho')} \approx \frac{\partial r}{\partial M_r} (1-2r'-\varrho') \, . \qquad (15.15)$$

It remains with account of the corresponding equilibrium equation

$$r_0\frac{\partial r'}{\partial M_r} = \frac{\partial r_0}{\partial M_r} (-3r'-\varrho') \, . \qquad (15.16)$$

We want to eliminate the fluctuations of density ϱ' with the equation of state (3.60), in order to only have the four dependent variables r, P, T and L_r,

$$\varrho' = \frac{\delta \varrho}{\varrho_0} = \alpha\frac{\delta P}{P_0} - \delta\frac{\delta T}{T} \, , \qquad (15.17)$$

$$\varrho' = \alpha p' - \delta t' \, , \qquad (15.18)$$

where α and δ are given by (3.60), the variations of μ due to ionization are accounted for by α and δ. Finally, one has

$$\frac{\partial r'}{\partial M_r} = -\frac{1}{4\pi r_0^3\varrho_0} (3r' + \alpha p' - \delta t') \, . \qquad (15.19)$$

In the second equation for the motions, the first and second members give, respectively,

$$\frac{\partial P}{\partial M_r} = \frac{\partial [p_0(1+p')]}{\partial M_r} = (1+p')\frac{\partial p_0}{\partial M_r} + p_0\frac{\partial p'}{\partial M_r} \, , \qquad (15.20)$$

$$-\frac{1}{4\pi r^2}\left(\frac{GM_r}{r^2} + \frac{\partial^2 r}{\partial t^2}\right) = -\frac{GM_r}{4\pi r_0^4(1+r')^4} - \frac{1}{4\pi r_0^2(1+r')^2}\frac{\partial^2 r_0(1+r')}{\partial t^2}$$

$$= -\frac{1}{4\pi r_0}\sigma_0^2 (1-4r') - \frac{1}{4\pi r_0}(1 - \underbrace{2r'}_{2nd\ order})\frac{\partial^2 r'}{\partial t^2} + \dots$$

$$\qquad (15.21)$$

The last term leads to a second order and we ignore it. We define

$$\sigma_0^2 = \frac{GM_r}{r_0^3} \, , \qquad (15.22)$$

σ_0 is a frequency, it is the fundamental frequency, which is of the order of the inverse of the dynamical timescale (1.28). We are left with

$$\frac{\partial p_0}{\partial M_r} + p' \frac{\partial p_0}{\partial M_r} + p_0 \frac{\partial p'}{\partial M_r} = -\frac{1}{4\pi r_0} \sigma_0^2 (1 - 4r') - \frac{1}{4\pi r_0} \frac{\partial^2 r'}{\partial t^2} . \qquad (15.23)$$

The first terms on the left and the right cancel each other and we have with account that $(\partial p_0 / \partial M_r) = -\sigma_0^2/(4\pi r_0)$,

$$\frac{\partial p'}{\partial M_r} = \frac{1}{4\pi r_0 p_0} \left[\sigma_0^2 (4r' + p') - \frac{\partial^2 r'}{\partial t^2} \right] . \qquad (15.24)$$

In the third equation for heat transfer, we have for the first member,

$$\frac{\partial T}{\partial M_r} = \frac{\partial t_0 (1 + t')}{\partial M_r} = \frac{\partial t_0}{\partial M_r} + t_0 \frac{\partial t'}{\partial M_r} + t' \frac{\partial t_0}{\partial M_r} . \qquad (15.25)$$

Now, in the second member we express the perturbation of the opacity,

$$\kappa = \kappa_0 (1 + \kappa') \quad \text{with } \kappa' = \frac{\delta \kappa}{\kappa} . \qquad (15.26)$$

We write the opacity as follows,

$$\kappa = \kappa_0 P^{\kappa_P} T^{\kappa_T} , \qquad (15.27)$$

where the logarithmic derivatives κ_P and κ_T are exponents slowly variable with temperature and density. We have also,

$$\ln \kappa = \kappa_P \ln P + \kappa_T \ln T ,$$

$$d \ln \kappa = \kappa_P d \ln P + \kappa_T d \ln T ,$$

$$\kappa' = \kappa_P p' + \kappa_T t' . \qquad (15.28)$$

The second member of the equation of transfer gives

$$-\frac{3\kappa}{4acT^3} \frac{L_r}{16\pi^2 r^4} = -\frac{3\kappa_(1 + \kappa') [\ell_0 (1 + \ell')]}{4ac\, 16\pi^2 t_0^3 (1 + t')^3 r_0^4 (1 + r')^4}$$

$$= -\frac{3\kappa_0 \ell_0 (1 + \kappa' + \ell') (1 - 3t') (1 - 4r')}{4ac\, 16\pi^2 t_0^3 r_0^4} . \qquad (15.29)$$

Now, the perturbed equation of transfer becomes

$$\frac{\partial t_0}{\partial M_r} + t_0 \frac{\partial t'}{\partial M_r} + t' \frac{\partial t_0}{\partial M_r} = -\underbrace{\frac{3\kappa_0 \ell_0}{4ac\, 16\pi^2 t_0^3 r_0^4}}_{\frac{\partial t_0}{\partial M_r}} \left(1 + \ell' + \kappa_P p' + \kappa_T t' - 4r' - 3t'\right) .$$

The first terms on the left and the right cancel each other and the perturbed equation of transfer is finally

$$\frac{\partial t'}{\partial M_r} = \frac{1}{t_0}\left(\frac{\partial t_0}{\partial M_r}\right)\left[\ell' - 4r' + \kappa_P p' + t'(\kappa_T - 4)\right] . \tag{15.30}$$

The fourth equation, i.e., for energy production, becomes similar with account that the nuclear energy production is zero in stellar envelopes and the form (3.64) for ε_{grav}

$$\frac{\partial \ell_0}{\partial M_r} + \ell' \frac{\partial \ell_0}{\partial M_r} + \ell_0 \frac{\partial \ell'}{\partial M_r} = -C_P \frac{\partial t_0 (1 + t')}{\partial t} + \frac{\delta}{\varrho_0 (1 + \varrho')} \frac{\partial p_0 (1 + p')}{\partial t}$$

$$= -C_P \frac{\partial t_0}{\partial t} - C_P t_0 \frac{\partial t'}{\partial t} + \frac{\delta}{\varrho_0 (1 + \varrho')} \frac{\partial p_0}{\partial t} + \frac{\delta}{\varrho_0 (1 + \varrho')} p_0 \frac{\partial p'}{\partial t} . \tag{15.31}$$

The first and second terms on the left are zero at equilibrium, since there is no energy production in the envelope. The first and third terms on the right are zero at equilibrium, since the equilibrium quantities do not vary in time. The term ϱ' in the last term on the right can also be ignored, since it would introduce a second-order term. Finally, we have

$$\frac{\partial \ell'}{\partial M_r} = -\frac{p_0 \delta}{\ell_0 \varrho_0}\left[C\frac{\partial t'}{\partial t} - \frac{\partial p'}{\partial t}\right] , \tag{15.32}$$

with

$$C = \frac{C_P t_0 \varrho_0}{p_0 \delta} . \tag{15.33}$$

Equations (15.19), (15.24), (15.30) and (15.32) are the four linear homogeneous differential equations for the four unknowns r', p', t', ℓ' as functions of M_r. The coefficients are those from the equilibrium models.

The quantities $r', \ldots$ or $\delta r(M_r, t), \ldots$ in (15.11) are developed as,

$$\delta r(M_r, t) = \delta r(M_r) e^{i\omega t} = \delta r(M_r) e^{-\omega_I t} e^{i\omega_R t} . \tag{15.34}$$

ω is in general complex, ω_R and ω_I represent the real and imaginary parts of the frequency. In a non-adiabatic study, if ω_I is positive, the amplitude is decreasing, if negative it is increasing. One also has $\frac{\partial}{\partial t} = i\omega$. When the above four differential equations are completed by appropriate boundary conditions (Sect. 15.2.2), the solutions r', p', t', ℓ' as functions of M_r can be determined. However, solutions of the equations with their boundary conditions only exist for some specific values ω_n^2, with $n = 0, 1, 2, 3 \ldots$. The ω_n are ordered by increasing values of n. The value ω_0, the shortest frequency defines the fundamental mode, while $\omega_1, \omega_2, \ldots$ are the first, the second overtone, etc. To these various modes, the corresponding solutions are $r'_0(M_r), r'_1(M_r), r'_2(M_r), \ldots$ with similar notations for the other variables $p'(M_r)$, $t'(M_r)$ and $\ell'(M_r)$.

Figure 15.1 shows the behavior of $\delta L/L = \ell'$ in a Cepheid model of 7 M$_\odot$ in relation with the opacity and the cumulated work provided be the pulsation (i.e., the sum of the work, with its sign from the interior to the surface). We see that in the region where the opacity grows with depth, i.e., $\kappa_T > 0$ and $\kappa_P > 0$ the work is
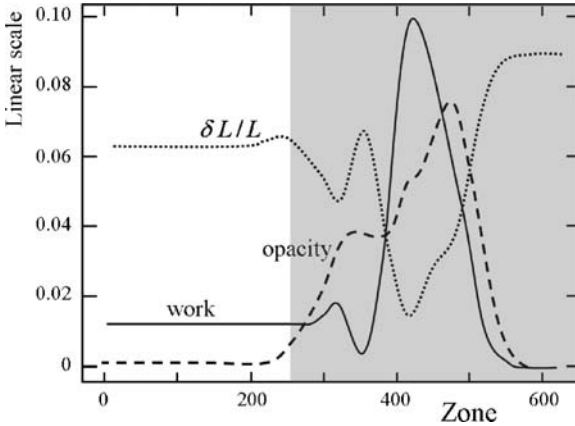
Fig. 15.1 The relative excess of luminosity $\delta L/L$, the cumulative work and the opacity in a Cepheid model of 7 $M_\odot$ as a function of the zoning of the outer layers. The stellar surface is on the left, the white area is the atmosphere with optical depth $< 2/3$, the gray area is the optically thick envelope. The cumulative work is the sum of the work, positive or negative, from the inner zone (600) up to the surface. As the integrated work up to the surface is positive, the star is unstable. Adapted from Schaller [512]

positive. There, some luminosity is subtracted from the emergent flux to feed the pulsation. The cumulated work at the surface (on the left of the figure) is positive, i.e., the integral work from the interior to the surface is positive and thus the star is unstable. If there would only be the κ mechanism at work, we would expect the work to grow, starting from the interior, only in regions above the maximum of κ, i.e., where κ decreases outward. However, there is also the effect of the partial ionization on the adiabatic exponents Γ_i to be accounted for (cf. Fig. 7.4). There is a minimum of Γ_3 deep in the zone 550 and this has a destabilizing effect which makes the driving zone to start a bit deeper than as given by the location of the maximum of the opacity. Figure 15.4 below further shows in a simplified model which effects contribute to stability and instability.

The above equations can be solved numerically by finite differences and by application of the Henyey method. It is preferable [96] to first discretize the equations in finite differences and then to linearize them. These equations are used for a simple analytical model below (Sect. 15.3).

15.2.1 Convection

Convection in cores and envelopes introduces an additional difficulty. The first and simplest approach is to assume that convection does not vary with pulsation. In fact, this means that at all times the convective flux would be the same as in the equilibrium model. A second approach is to develop to the first order the expressions

for the convective flux, assuming that convection adapts instantaneously to the new state created by pulsation.

The first approach is acceptable if the turnover time of convective motions (5.49) is much longer than the pulsation period P, while the second is acceptable in the opposite case,

$$t_{\text{turnover}} \gg P \qquad \text{constant convection,}$$
$$t_{\text{turnover}} \ll P \qquad \text{convection adapts itself.}$$

For the solar envelope as well as for the convective cores of massive stars, one rather has the second case. In the first case, there is almost no effect of convection. In the second case, the instability is moderately favored [59]. However, often the reality corresponds to an intermediate situation, with turnover times of the same order as the pulsation periods (e.g., for red giants) and thus appropriate developments have to be made [196, 222].

15.2.2 Boundary Conditions and Eigenvalue Problem

Four boundary conditions are needed and various degrees of refinement are possible, often leading to an increased complexity. The solutions are evidently not insensitive to the boundary conditions and great care has to be taken. We summarize a basic choice of boundary conditions. At the outer boundary, a first condition can be obtained by assuming

$$\frac{\partial p'}{\partial M_r} = 0 \,, \tag{15.35}$$

at the base of the atmosphere, which means that no force is applied at the surface. However, if there is mass loss and running wave in the atmosphere, this condition does not apply. Running waves produce a considerable damping of the pulsation.

A second condition at the surface is obtained by assuming that the photosphere (with given mass and pressure at its basis) is floating above the inner pulsating layers. A relation connecting ℓ', r', t' at the surface is easily obtained by linearizing the temperature-optical depth $T(\tau)$ relation (24.19; see for example[34]).

In the center, the conditions are

$$r' = 0 \quad \text{and} \quad \ell' = 0 \,, \tag{15.36}$$

which imply no displacement and light fluctuations (some of the early models had only one condition in the deep interior, e.g., a condition of adiabacy like, $C(\partial t'/\partial t) - (\partial p'/\partial t) = 0$; if so, the problem is not completely defined and a continuous range of solutions for ω is possible). Through the boundary conditions, the proper frequencies are a property of the whole star. Nevertheless, the outer layers

play a dominant role since they harbor the non-adiabatic effects and also determine the pulsation period, since the sound speed is smaller there.

Now, we have four Eqs. (15.19), (15.24), (15.30) and (15.32) with four boundary equations, the problem is in principle determined for any value of ω. The point is that the equations are linear and homogeneous, so that the scaling of the solutions is not yet fixed. A scaling must be adopted and one usually takes $r' = \delta r/r = 1$ at the stellar surface as a normalization. This makes one more, i.e., five constraints, to be satisfied by the system of four equations. The consequence is that the system only accepts solutions for some specific values of the frequency, called eigenfunctions ω_n^2 with $n = 0, 1, 2, 3 \ldots$ as mentioned above. Practically, if the integration of the system of equations is started from a couple of boundary conditions, it will match the other couple of boundary conditions only for some values ω_n of the frequency. For each ω_n, corresponding to the fundamental or to the overtones, there are specific solutions, $r'_n(r)$, $p'_n(M_r)$, $t'_n(M_r)$ and $\ell'_n(M_r)$, called eigenfunctions. The fundamental oscillation with a frequency ω_0 has no node between the center and the surface. The first overtone has one node between the center and the surface, the second overtone has two, etc.

Physically, the eigenvalue problem appears because the star may have stationary oscillations only for some suitable oscillation frequencies which permit an integer number of half wavelength to be fitted within the stellar resonant cavity. The real part ω^R of the frequency determines the period $P_n = 2\pi/\left|\omega_n^R\right|$ and the imaginary part ω^I gives the damping or the driving of the pulsation. Mathematically, the problem is a so-called Sturm–Liouville problem. In practice the choice of a good numerical method for finding the eigenfunctions is essential [96, 512].

Figure 15.2 illustrates the eigenfunctions r'_0, r'_1 and r'_2 for a β Cephei variable star, an about 11 $M_\odot$ star in the MS stage. The pulsation amplitudes are large at the surface (where they are normalized to unity) and very small in the deep layers, particularly in the interior with respect to the nodes of the overtones. The square of the amplitudes at some point in the star vary like the inverse of the density, consistently with an even distribution of the pulsation energy in the star. The higher overtones with more internal modes have shorter oscillation periods, since the wavelengths are shorter. The values of the periods and period ratios of the modes are discussed in term of the pulsation constant Q_n associated to each mode (Sect. 15.5.1).

Since the basic equations (15.10) contain all the physics of the problem, it is also possible to study the pulsations by integrating numerically these equations which include the hydrodynamic term $\partial^2 r/\partial t^2$. The procedure is started from an equilibrium solution, which is perturbed in some way, and the evolution of the system is followed with very short time steps, i.e, small fractions of the expected pulsation period. Similar boundary conditions as those mentioned above can be adopted. After some transient harmonics have dissipated, the system either converges toward the initial equilibrium and is thus stable or stationary oscillations progressively emerge with some limiting amplitudes since the non-linear effects are accounted for by the full set of equations.
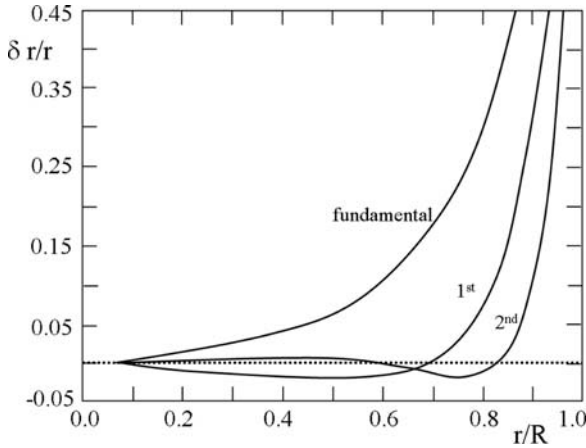
Fig. 15.2 The perturbations of radius for the fundamental mode, the first and second overtones as functions of radius in α Vir, a 11 $M_\odot$ Main Sequence star. Each mode is normalized to 1.0 at the surface. Adapted from A.N.Cox [144]

15.3   Baker's One-Zone Analytical Model

The previous developments form a basis for numerical models, which allow us to study the stability of a particular stellar model. It is, however, useful to have an analytical model for understanding the essential physical effects of pulsation. The one-zone model by Baker [32] is a clever approach, which was the starting point of further developments [146].

   The coefficients of the four Eqs. (15.19), (15.24), (15.30) and (15.32) are time independent, thus time and space variables can be separated. The one-zone model keeps the time dependence, but in order to get rid of the space dependence of the coefficients and variables, it considers only one single thin spherical layer of mass m located somewhere in the star (cf. Fig. 15.3). The equilibrium state of the thin shell is defined by r_0, p_0, t_0, ℓ_0. The fluctuations r', p', t' are considered as constant through the shell,

$$\frac{\partial r'}{\partial M_r} = \frac{\partial p'}{\partial M_r} = \frac{\partial t'}{\partial M_r} = 0 \,. \tag{15.37}$$

The same equation for ℓ' would mean adiabacy and thus no driving or damping of the pulsation, thus an essential property would be lost. Therefore, we need to calculate the gain or loss of luminosity through the shell. We assume that there is a luminosity fluctuation ℓ'_L at the lower limit of the shell and ℓ'_U at the upper limit. The average and gradient of ℓ' are thus

$$\ell' = \frac{\ell'_U + \ell'_L}{2} \quad \text{and} \quad \frac{\partial \ell'}{\partial M_r} = \frac{\ell'_U - \ell'_L}{m} \,. \tag{15.38}$$
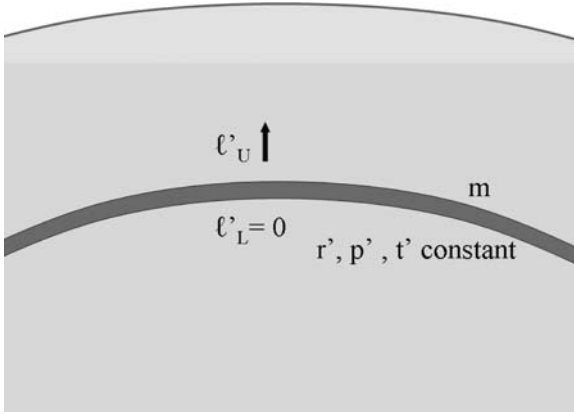
Fig. 15.3 Schematic representation of the one-zone model

We then assume that there is no fluctuation at the bottom of the shell. Thus, the variations of the emerging flux result only from effects in the shell, the interactions of the shell with the surroundings are ignored. We have

$$\ell'_L = 0 \quad \text{and thus} \quad \frac{\partial \ell'}{\partial M_r} = \frac{\ell'_U}{m} = \frac{2\ell'}{m} \,. \tag{15.39}$$

We keep the essential properties of the interaction of the gas layer with the radiation passing through it. The gas modulates with a certain frequency the constant flux entering at the bottom ($\ell'_L = 0$) and produces a variable flux at the top. This happens because radiative energy may be removed from the flux and fed into mechanical pulsation energy, alternatively radiative energy may be radiated away at the expense of the mechanical oscillation energy. Thus, we have either a driving of the pulsation or a radiative damping. The oscillation frequency is a characteristic of the physical conditions of the system. With conditions (15.37) and (15.39), the four equations (15.19), (15.24), (15.30) and (15.32) become

$$3r' + \alpha p' - \delta t' = 0 \,, \tag{15.40}$$

$$\frac{\partial^2 r'}{\partial t^2} = \sigma_0^2 (4r' + p') \,, \tag{15.41}$$

$$\ell' - 4r' + \kappa_P p' + (\kappa_T - 4)t' = 0 \,, \tag{15.42}$$

$$C\frac{\partial t'}{\partial t} - \frac{\partial p'}{\partial t} = -\mathcal{K}\sigma_0 \ell' \,, \tag{15.43}$$

$$\text{with} \quad \mathcal{K} = \frac{2}{m\sigma_0} \frac{\ell_0 \varrho_0}{P_0 \delta} \,. \tag{15.44}$$

The various quantities are taken at the level considered. With (3.76) to express $P_0\delta$, we see that $\mathcal{K}$ scales as the ratio of the luminosity L_0 by the product of the heat content of the shell times the frequency σ_0. Thus $\mathcal{K} \approx \ell_0/(\sigma_0 E_{\text{th}})$ is the ratio of

the luminosity to the heat content E_{th} of the shell times the pulsation period (cf. also 15.76). As some of this content may be radiated away during one pulsation cycle, $\mathcal{K}$ plays an essential role for the non-adiabatic effects. If $\mathcal{K} = 0$, we have $C(\partial t'/\partial t) - (\partial p'/\partial t) = 0$ which implies adiabacy according to (3.63). If so, the mechanical and thermal parts of the pulsations would essentially be uncoupled.

Now we combine the four equations into a single one, without making yet the hypothesis of adiabacy. First, ℓ' is eliminated between the third and the fourth equation,

$$C\frac{\partial t'}{\partial t} - \frac{\partial p'}{\partial t} = -4\mathcal{K}\sigma_0 r' + \mathcal{K}\sigma_0 \kappa_P p' + \mathcal{K}\sigma_0(\kappa_T - 4)t'. \tag{15.45}$$

The first equation gives

$$t' = \frac{3r' + \alpha p'}{\delta}, \tag{15.46}$$

which allows one to eliminate t',

$$\frac{3C}{\delta}\frac{\partial r'}{\partial t} - \frac{C\alpha}{\delta}\frac{\partial p'}{\partial t} - \frac{\partial p'}{\partial t}$$

$$= -4\mathcal{K}\sigma_0 r' + \mathcal{K}\sigma_0 \kappa_P p' + + \mathcal{K}\sigma_0(\kappa_T - 4)\frac{3r'}{\delta} + \mathcal{K}\sigma_0(\kappa_T - 4)\frac{\alpha p'}{\delta}. \tag{15.47}$$

Now, p' is eliminated with the second equation,

$$\frac{3C}{\delta}\frac{\partial r'}{\partial t} + \left(\frac{C\alpha}{\delta} - 1\right)\frac{1}{\sigma_0^2}\frac{\partial^3 r'}{\partial t^3} - 4\left(\frac{C\alpha}{\delta} - 1\right)\frac{\partial r'}{\partial t} = -4\mathcal{K}\sigma_0 r'$$

$$+ \mathcal{K}\sigma_0 \kappa_P \frac{1}{\sigma_0^2}\frac{\partial^2 r'}{\partial t^2} + \mathcal{K}\sigma_0(\kappa_T - 4)\frac{3r'}{\delta} - \mathcal{K}\sigma_0 \kappa_P 4r'$$

$$+ \mathcal{K}\sigma_0(\kappa_T - 4)\frac{\alpha}{\delta}\frac{1}{\sigma_0^2}\frac{\partial^2 r'}{\partial t^2} - \mathcal{K}\sigma_0(\kappa_T - 4)\frac{\alpha}{\delta}4r'. \tag{15.48}$$

This is a third-order equation of the form,

$$\frac{\partial^3 r'}{\partial t^3} + \mathcal{K}\sigma_0 A\frac{\partial^2 r'}{\partial t^2} + \sigma_0^2 B\frac{\partial r'}{\partial t} + \mathcal{K}\sigma_0^3 Dr' = 0, \tag{15.49}$$

with

$$A = -\frac{\alpha(\kappa_T - 4) + \kappa_P \delta}{\alpha C - \delta}, \quad B = \frac{3C - 4(\alpha C - \delta)}{\alpha C - \delta}$$

$$\text{and} \quad D = \frac{(4\alpha - 3)(\kappa_T - 4) + 4\delta(\kappa_P + 1)}{\alpha C - \delta}. \tag{15.50}$$

From the definition of C (15.33), from (3.76) and (7.57), we have

$$C = \frac{\Gamma_2}{\Gamma_2 - 1} = \frac{1}{\nabla_{\mathrm{ad}}} \quad \text{and} \quad \Gamma_2 = \frac{C}{C - 1} . \tag{15.51}$$

One also has from (7.58)

$$C = \frac{\Gamma_1}{\Gamma_3 - 1} , \tag{15.52}$$

and with (7.66), we can eliminate $\Gamma_3 - 1$ and obtain,

$$\Gamma_1 = \frac{C}{\alpha C - \delta} \quad \text{and} \quad \Gamma_3 - 1 = \frac{1}{\alpha C - \delta} . \tag{15.53}$$

This means that the coefficients A, B, D can be expressed in terms of Γ_i, α, δ and κ_P, κ_T.

We now suppose that the relative fluctuations r' of the radius have the following form

$$r'(M_r) = \xi(M_r) e^{st} . \tag{15.54}$$

This expression introduced in the differential equation (15.49) leads to

$$s^3 + \mathcal{K} \sigma_0 A s^2 + \sigma_0^2 B s + \mathcal{K} \sigma_0^3 D = 0 . \tag{15.55}$$

This cubic equation defines the complex frequencies s of the pulsations of the model. This is the eigenvalue equation for the one-zone model. We now examine the solutions and constraints resulting from this relation, both for the adiabatic and non-adiabatic pulsations.

15.3.1 Adiabatic Pulsations

Let us consider the case where the pulsations do not exchange heat with their surroundings. As a consequence, one cannot say whether the pulsations are sustained or damped, i.e., whether the star is stable or not. Nevertheless, a pulsation period can be determined, which is always very close to the period obtained in the non-adiabatic case (see Sect. 15.4.2). From (3.64), $dq = 0$ implies $C_P(\partial T/\partial t) - (\delta/\varrho)(\partial P/\partial t) = 0$ and thus with (15.33), this gives

$$C \frac{\partial t'}{\partial t} - \frac{\partial p'}{\partial t} = 0. \tag{15.56}$$

Following the steps from (15.45) (15.46) (15.47) (15.48) and (15.49), we have

$$\mathcal{K} \sigma_0 A s^2 + \mathcal{K} \sigma_0^3 D = 0 \quad \text{and} \quad s^2 + \sigma_0^2 B = 0 . \tag{15.57}$$

The adiabatic solution for s is

$$s_{ad} = \pm i \sqrt{B} \, \sigma_0 \,, \tag{15.58}$$

with B given by (15.50) with relations (15.51) (15.52) and (15.53), we get

$$B = \frac{3 \frac{\Gamma_2}{\Gamma_2 - 1} - 4 \frac{1}{\Gamma_3 - 1}}{\frac{1}{\Gamma_3 - 1}} = 3 \frac{\Gamma_2}{\Gamma_2 - 1} (\Gamma_3 - 1) - 4 = 3\Gamma_1 - 4 \,, \tag{15.59}$$

and s_{ad} becomes

$$s_{ad} = \pm i \sqrt{3\Gamma_1 - 4} \, \sigma_0 \,. \tag{15.60}$$

There are two possibilities for s_{ad}:

- If $\Gamma_1 > 4/3$: the solutions for r' (15.54) are sinusoidal, without damping since this is the adiabatic case.
- If $\Gamma_1 < 4/3$: r' grows exponentially and we have a dynamical instability, consistently with the result (1.69) from the Virial theorem.

The above expression (15.60) of the pulsation frequency also shows that the ionization in the envelope, which decreases Γ_1, contributes to increase the pulsation period. The above expression leads to the well-known period-luminosity-color relation for Cepheids discussed in Sect. 15.5.1.

15.4   Non-adiabatic Effects in Pulsations

Non-adiabatic effects produce the driving and the damping of pulsations. Their study allows us to understand the physical effects playing a role in stellar pulsations. Large uncertainties still concern the interactions of pulsations with processes such as convection and stellar winds.

15.4.1   The κ and γ Mechanisms

Equation (15.55) with $\mathcal{K} \neq 0$ determines the stability. For the star to be stable, the three roots s_1, s_2, s_3 of the equation must have negative real parts, so that the amplitude of the oscillations decrease in time according to (15.54). As shown below, the conditions for negative roots are [32]

$$\sigma_0^2 B > 0 \,, \tag{15.61}$$

$$\mathcal{K} \sigma_0^3 D > 0 \,, \tag{15.62}$$

$$\mathcal{K} \sigma_0^3 (AB - D) > 0 \,. \tag{15.63}$$

This results from the properties of the solutions of a polynomial equation of the form

$$s^3 + a_1 s^2 + a_2 s + a_3 = 0 .$$ (15.64)

The three solutions s_1, s_2, s_3 of a cubic equation follow the properties [69],

$$s_1 + s_2 + s_3 = -a_1 ,$$ (15.65)

$$s_1 s_2 s_3 = -a_3 ,$$ (15.66)

$$s_1 s_2 + s_1 s_3 + s_2 s_3 = a_2 .$$ (15.67)

- Condition (15.61) results from the fact that the sum of the products in (15.67) must be positive, thus a_2 has to be positive. This gives condition (15.61), which implies $\Gamma_1 > 4/3$, which is the condition for dynamic stability, as mentioned just above. If not satisfied, the star implodes or explodes on the dynamical timescale.
- Condition (15.62) results from the fact that the product (15.66) must be negative, if the three roots are negative. Thus a_3 is positive, which gives condition (15.62). It expresses the secular stability (i.e., over a time of the order of the Kelvin–Helmholtz timescale) of the system discussed in Sect. 15.4.3.
- Condition (15.63) expresses the pulsational stability. The reason and meaning of this condition are derived later (see 15.75). Let us just verify here that it is self-consistent. This condition implies that the difference $a_1 a_2 - a_3 > 0$. Since a_2 and a_3 are both positive, the previous inequality necessarily implies that a_1 is positive, which is consistent with condition (15.65) if the three roots are negative. One also verifies that $a_1 a_2 - a_3 > 0$ gives

$$- s_1^2 s_2 - s_1^2 s_3 - s_1 s_2 s_3 - s_1 s_2^2 - s_1 s_2 s_3 - s_2^2 s_3 - s_1 s_3^2 - s_2 s_3^2 > 0$$ (15.68)

a relation which is evidently satisfied if all roots are negative.

Let us examine the pulsation stability. One can express (15.63) more explicitly with (15.50). After simplification of identical terms, one has

$$AB - D = -3C\kappa_P\delta - 4\delta\alpha C - 3\kappa_T\delta + 12\delta + 4\delta^2$$

$$= 3C\delta\left[-\kappa_P - \frac{\kappa_T}{C} + \frac{-4(\alpha C - \delta) + 12}{3C}\right] > 0 .$$ (15.69)

With (15.51) to (15.53), this gives finally the stability condition

$$-\left(\frac{\kappa_T}{C} + \kappa_P\right) - \frac{4}{3\Gamma_1} + \frac{4}{C} > 0 .$$ (15.70)

The instabilities, when present, are vibrational instabilities, i.e., the star pulsates periodically. The examination of this relation shows the factors which favor the stability and instabilities:

- *The κ mechanism.* The first term in (15.70) shows the major influence of the opacity on pulsations. Positive values of κ_T and κ_P imply a higher opacity in the contracted stage of a pulsating star. More energy is retained and converted into mechanical energy. This produces pulsation driving at the expense of the radiative flux. In the expansion phase, the release of energy would be increased. This is just the κ mechanism (Sect. 15.1).
- *The partial ionization.* In current stellar envelopes, one has Kramers' opacity, thus $\kappa_P = 1$ and $\kappa_T = -4.5$ with $C = 1/\nabla_{\mathrm{ad}} = 5/2$. Thus, $-\left(\frac{\kappa_T}{C} + \kappa_P\right) = 4/5$ and this favors stability. However, if C becomes large as in a ionization zone (cf. Fig. 7.1 for ∇_{ad}), the function $-(\kappa_T/C + \kappa_P)$ may be negative and has a destabilizing effect. Simultaneously, if C becomes very large, it also reduces the positive term $4/C$ and this also favors the instability. These destabilizing effects of a large C are sometimes called the γ effect.
- *Spherical geometry.* The term $-4/(3\Gamma_1)$ is always destabilizing, it is absent in a plane parallel geometry. In view of the definition (7.57) of Γ_1, this term expresses the change of density during compression. In plane parallel geometry, the radiation would "see" the same column density of gas at all stages during a pulsation cycle. In spherical geometry, compression increases the column density radiation has to go through. Thus, more energy is retained at compression in spherical geometry and this is destabilizing.
- *Radiative damping.* The term $4/C$ is always stabilizing. It is due to the radiative damping which removes heat and acts like a viscous drag on the pulsations. One can realize the physical meaning of this term from the fact that $1/C = \nabla_{\mathrm{ad}}$ expresses the change of T during compression. In an isothermal medium $C \to \infty$, this term would be zero as there is no radiative energy loss by pulsations. As seen above, a large C reduces this stabilizing effect.

In Fig. 15.4, the three terms of relation (15.70) are represented as well as their sum. The term $-(\kappa_T/C + \kappa_P)$ is stabilizing in the outer layers and destabilizing in the deeper envelope. If there would only be the dominant term κ_T, the destabilizing region would essentially cover the left zone of the κ peak (cf. Fig. 15.1), where this term is positive. However, in regions deeper than the opacity peak $(\Gamma_3 - 1) \to 0$, $C \to \infty$ according to (15.52) and the role of κ_T, which would favor stability there, vanishes. With κ_P still positive, this effect shifts the instability zone to deeper layers, as already seen in Fig. 15.1. The geometrical term $-4/(3\Gamma_1)$ is always destabilizing, while the radiative damping is stabilizing as seen above.

15.4.1.1   Ionization Effects

The value of C (15.51) and (15.52), which varies a lot during ionization, plays a great role in the stellar stability. The value of C affects the coefficients A, B, D. Partial ionization by increasing C favors the instability, but it also has another effect: surprisingly, it limits the amplitude of the pulsations.

Let us consider a star in which the pulsations become large enough so that a significant mass shell is fully ionized in the contracted stage and recombined in the
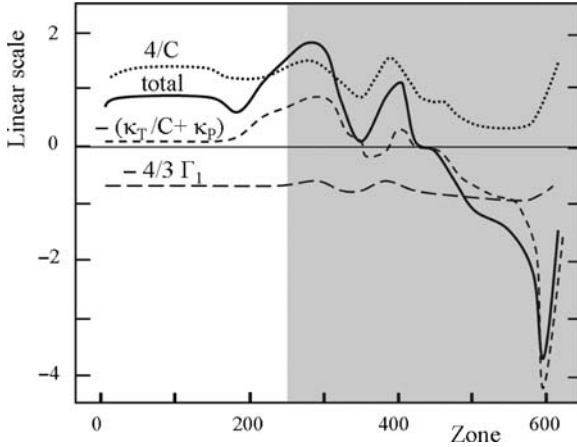
Fig. 15.4 The three terms of condition (15.70) for stability in a Cepheid model of 7 $M_\odot$ and their sum. The stellar surface is on the left, the white area is the atmosphere with optical depth $< 2/3$, the gray area is the optically thick envelope. Adapted from Schaller [512]

expanded stage. This would imply that C is small in these two leading phases, and we have seen that a small C favors stability. Thus, ionization, apart from having a destabilizing role, may also become an effect which may limit the growth of linear pulsations when the amplitudes become large. In addition, non-adiabatic effects, which lead to a heat leakage from pulsations, also limit the pulsation amplitudes.

15.4.1.2   A Straightforward Approach

The effects controlling the instability can also be understood in a rather direct approach. One has from the expression of ℓ' given by (15.42),

$$\ell' = 4r' - \kappa_P p' - (\kappa_T - 4)t' . \tag{15.71}$$

Using the adiabatic approximations to express p' and t' as functions of ϱ', we have $t' = (\Gamma_3 - 1)\varrho'$ and $p' = \Gamma_1 \varrho'$, we get, ignoring the displacement term,

$$\ell' \approx (4 - \kappa_T)(\Gamma_3 - 1)\varrho' - \kappa_P \Gamma_1 \varrho' = \left[(4 - \kappa_T)(\Gamma_3 - 1) - \kappa_\varrho \right] \varrho' . \tag{15.72}$$

Let us consider a compression phase, thus ϱ' is positive. For Kramers' opacity with $\kappa_T = -3.5$ and $\kappa_\varrho = 1$, one has a positive ℓ', meaning that more luminosity is leaving the shell than entering into it. Thus, no mechanical energy is available for pulsation driving and the star is stable, this is the general case. Thus, positive values of $(-\kappa_T)$ and $(-\kappa_\varrho)$ contribute to the stability, in agreement with (15.70). Conversely, if $(-\kappa_T)$ and $(-\kappa_\varrho)$ are negative, less luminosity is going out, more is retained in the shell and exerts pulsation driving. The destabilizing effect of partial ionization is also present through the term $(\Gamma_3 - 1)$, the γ effect.

15.4.2 The Damping Timescale of Pulsations

We can gain further insight in expanding the solutions of (15.55) as functions of the coefficient $\mathcal{K}$ (15.44), which determines the non-adiabatic effects,

$$s = s_0 + s_1 \mathcal{K} + s_2 \mathcal{K}^2 + \ldots . \tag{15.73}$$

We have the roots $s_0 = \pm i\sqrt{B}\,\sigma_0$ (15.60) for the adiabatic case with $\mathcal{K} = 0$. Inserting (15.73) in the cubic, we get keeping only the first-order term in $\mathcal{K}$,

$$3s_0^2 s_1 + \sigma_0^2 B s_1 + \sigma_0^3 D + \sigma_0 A s_0^2 = 0 ,$$

$$s_1 \left(-3\sigma_0^2 B + \sigma_0^2 B \right) = -\sigma_0^3 D + \sigma_0^3 AB , \tag{15.74}$$

where the above expression of s_0^2 is used. This yields

$$s_1 = -\frac{\sigma_0}{2B} \left(AB - D \right) . \tag{15.75}$$

If $AB - D > 0$, which is our condition (15.63), we have $s_1 < 0$ which implies a decreasing amplitude in time and thus stability with respect to pulsation. This justifies the above interpretation of this condition. $AB - D > 0$ implies the stability condition (15.70), provided the dynamic stability with $B > 0$ is also satisfied. If not, the amplitudes increase with time.

From the representation of the pulsation (15.54) and (15.73), it is clear that the damping time τ_d of the pulsation is of the order of $(s_1 \mathcal{K})$, i.e.,

$$\tau_d \approx \frac{1}{\mathcal{K}\sigma_0} \approx \frac{mp_0}{\ell_0 \varrho_0} \approx \frac{mkt_0}{\mu m_u \ell_0} \approx \frac{E_{th}}{\ell_0}, \tag{15.76}$$

where we used (15.44) and the law of perfect gas. There, E_{th} is the thermal content of the layer of mass m. Thus, the damping time is the thermal diffusion timescale, i.e., the time needed for the luminosity to radiate all the heat content of the layer. For the whole star, this is the Kelvin–Helmholtz timescale (Sect. 3.2.4). A similar timescale intervenes for the growth of pulsations due to the non-adiabatic effects.

The second-order term s_2 in (15.73), which we do not calculate here, would be imaginary. This indicates that there is only a second-order correction to be brought to the adiabatic frequency calculated above (15.60). Thus, as there is no first-order correction, the adiabatic frequency is a good approximation.

The timescale characterizing the non-adiabatic effects for the whole star is given by τ_d (15.76). The relative importance of non-adiabacy for a single layer during one pulsation cycle is given by the ratio (P/τ_d) of the pulsation period to the damping time. If the period is short, the non-adiabatic effects are small. Since $\tau_d \approx E_{th}/\ell_0$, this means that the non-adiabatic effects will be small when the heat content of the layer is high. Thus, the deep layers have in general little driving or damping effects for the κ mechanism, so these effects are determined by the outer layers.

15.4.3 Secular Instability: Conditions on Opacities and Nuclear Reactions

For now, we have the adiabatic solution s_{ad} or s_0, the pulsational solutions with s_1. There is also a so-called secular solution s_S to (15.55). It is obtained if s is small, i.e., if the timescale of the perturbation is long. The cubic becomes in this case

$$Bs + \mathcal{K}\sigma_0 D = 0 \tag{15.77}$$

and the solution is

$$s_S = -\frac{\mathcal{K}\sigma_0 D}{B} = -\frac{\mathcal{K}\sigma_0 D}{3\Gamma_1 - 4} . \tag{15.78}$$

If $D > 0$ for $\Gamma_1 > 4/3$, the root is real and negative, which implies stability. From (15.78), the timescale of the instability is also

$$\tau_S \approx \frac{1}{\mathcal{K}\sigma_0} \approx \tau_d \tag{15.79}$$

as for the damping time seen above (15.76), i.e., the timescale for the whole star is the Kelvin–Helmholtz time.

What is this secular instability ? It is a disequilibrium between the luminosity available from below at some level and the ability of the opacity to let this flux go out. If radiation cannot escape, there is an expansion at the timescale τ_S, or a gravitational contraction in the opposite case. The process is very slow with respect to current pulsations, while it is fast with respect to the nuclear timescale. This is why it is called a secular instability. It was already studied by Jeans [274] and by Ledoux [319]. The criterion for stability (for $\Gamma_1 > 4/3$) is just $D > 0$, i.e.,

$$(4\alpha - 3)(\kappa_T - 4) + 4\delta(\kappa_P + 1) > 0 . \tag{15.80}$$

For a perfect gas with $\alpha = \delta = 1$, the stability condition becomes

$$\kappa_T + 4\kappa_P > 0 . \tag{15.81}$$

For the Kramers law with $\kappa_T = -4.5$ and $\kappa_P = 1$, the stability condition is not verified. This is normal, since we have not included the energy production. A radiative envelope deprived of energy source contracts at its Kelvin–Helmholtz time.

15.4.3.1 Why Are the Main Nuclear Burning Phases Stable ?

The best known secular instability at the Kelvin–Helmholtz timescale is the fast evolution toward the red giants at the end of the MS phase. It is interesting to see that it can find a consistent explanation in this context. The complete form of the criterion including the energy production rate ε in the equations lead to the following

stability condition [319] for a perfect gas,

$$\kappa_T + 4\,\kappa_P > -3\,\varepsilon_\varrho - \varepsilon_T \,, \tag{15.82}$$

$$\text{with}\quad \varepsilon_\varrho = \left(\frac{\partial \ln \varepsilon}{\partial \ln \varrho}\right)_T \quad \text{and}\quad \varepsilon_T = \left(\frac{\partial \ln \varepsilon}{\partial \ln T}\right)_\varrho . \tag{15.83}$$

This criterion shows that for stability there must be some condition on the dependence on (ϱ, T) of the opacity with respect to the (ϱ, T) dependence of the production rate. For a given opacity, the positive sensitivity of the nuclear reactions to ϱ and T must be strong enough to ensure secular stability. Conversely, for given nuclear reactions, the growth of the opacity with density and temperature must be as large as possible. For Kramers opacity and nuclear reactions with $\varepsilon_\varrho = 1$ and $\varepsilon_T \geq 4$, the above condition shows that the secular stability is largely ensured. This is why stars are secularly stable in current nuclear phases.

In a stage where gravitational contraction dominates, the rate of energy production ε_g is given by (20.6) for a mono-atomic perfect gas. Assuming homologous contraction with $\dot{r}/r = -(1/3)\dot{\varrho}/\varrho$, one gets

$$\varepsilon_{\text{grav}} = \frac{1}{5}\,c_P\,T\,\frac{\dot{\varrho}}{\varrho} . \tag{15.84}$$

Here, $\varepsilon_\varrho = -1$ and $\varepsilon_T = 1$, one sees that the criterion (15.83) is not verified and the star is secularly unstable. In addition, if due to low T in the outer envelope, the gas is neutral, then $\kappa_P \approx 0$ according to Sect. 8.6.1 and this also favors the instability. This is quite consistent, when a star starts contracting it cannot get out of the instability until nuclear reactions take over with their strong dependence on T.

15.5   Relations to Observations: Cepheids

There are many kinds of variable stars: the main categories are shown in Fig. 15.5. Their properties have been reviewed for example by Gautschy and Saio [203, 204]. Some stars in this astrophysical zoo show radial oscillations like the Cepheids, other ones have non-radial oscillations like the slowly pulsating variables (SPB) and the solar-like variables. As an illustration, we discuss here some properties of the Cepheids. The non-radial oscillations of solar-like variables are extensively discussed in the context of Chap. 16.

15.5.1   The Period-Luminosity-Color Relations

There is a fundamental relation between the periods and average densities of pulsating stars, which leads to the period-luminosity-color (PLC) relations and in turn to
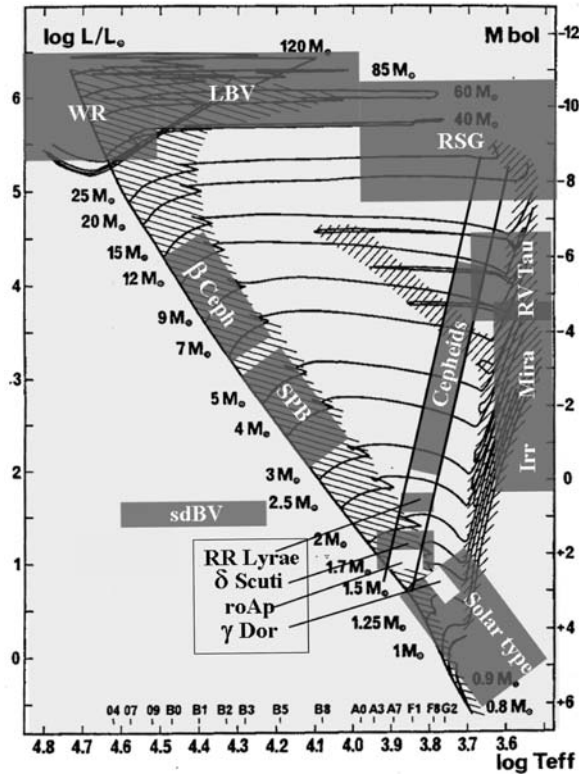
Fig. 15.5 HR diagram with the principal categories of variable stars according to current literature superposed on evolutionary tracks of the Geneva group [513]. These are the Wolf Rayet stars (WR), luminous blue variables (LBV), red supergiants (RSG), β Cephei (β Ceph), Cepheids (Cepheids), slowly pulsating B stars (SPB), RV Tauri (RV Tau), Miras, irregular (Irr), blue variable subdwarfs (sdBV), RR Lyrae, δ Scuti, roAp, γ Doradus (γ Dor) and the solar-like stars studied in asteroseismology. The variable white dwarfs are not represented

the famous period-luminosity (PL) relation for Cepheids, which is of major use for the distance calibration in the Universe.

Apart from second-order effects, the non-adiabatic periods are the same as the adiabatic values (Sect. 15.4.2), thus one can safely use the adiabatic relations. From (15.22) and (15.60), the fundamental period of pulsation P_0 is

$$P_0 = \frac{2\pi}{|s|} = \frac{2\pi}{\sqrt{(3\Gamma_1 - 4)\frac{GM_r}{r_0^3}}} \, . \tag{15.85}$$

For the entire star of radius R, mass M and mean density $\overline{\varrho}$ we get

$$P_0 = \frac{2\pi}{\sqrt{(3\Gamma_1 - 4)G\overline{\varrho}\,(4\pi/3)}} = \left(\frac{3\pi}{(3\Gamma_1 - 4)G\overline{\varrho}}\right)^{1/2} \, . \tag{15.86}$$

This is a fundamental relation, which shows that the stellar pulsation periods (and the dynamical time 1.28) vary like the inverse of the mean density. For the Sun with a mean density of 1.4 g cm^{-3}, the period is of the order of 55 minutes, for a red giant it may reach a hundred days and for a white dwarf it is about 1 s. A decrease of Γ_1, as due for example to radiation pressure, produces a slight increase of the periods. More generally, it may be noted that a relation of the timescale with $\bar{\varrho}^{-1/2}$ exists for all kinds of configurations in gravitational equilibrium, from the Universe as a whole to a planet.

The relation between period and mean density is often written as

$$P = Q \left(\frac{\bar{\varrho}}{\varrho_\odot} \right)^{-1/2} , \qquad (15.87)$$

where Q is called the pulsation constant. Q evidently depends on the overtone considered: one writes Q_0 for the fundamental mode, Q_1 for the first overtone, Q_2 for the second, and so on (when we write Q, this applies to any pulsation mode). Table 15.1 gives some typical values of the pulsation constant.

Table 15.1 Examples of pulsation constants Q

Type of stars	Q values (days)
polytrope $n = 0$	0.116
polytrope $n = 1.5$	0.071
polytrope $n = 3$	0.0383
Cepheids	0.035–0.050
β Cepheids:	
Q_0	0.0375
Q_1	0.027
Q_2	0.022

Sources: Polytropes from Ledoux and Walraven [317]. Cepheids from Saio and Gautschy [504]. β Cepheids from Lesh & Aizenman [324].

The typical period ratio of the first overtone to the fundamental mode is $P_1/P_0 = 0.755$, for the second overtone to the fundamental mode $P_2/P_0 = 0.605$ and for the third overtone to the fundamental mode $P_3/P_0 = 0.506$ for a typical MS model of 1.6 $M_\odot$. These fractions are evidently not $1/2, 1/3, 1/4$ because the sound wave traveling through the star spends relatively more time between the surface and the first node, since the sound speed scales like $\sqrt{T}$ (C.27).

The pulsation periods of any harmonics scale with mass and radius like

$$P \sim Q \frac{R^{3/2}}{M^{1/2}} . \qquad (15.88)$$

One can eliminate the mass M with the mass–luminosity relation (3.30) and the radius R with (C.15),

$$M \sim L^{1/\alpha} \quad \text{and} \quad R^{3/2} \sim \left(\frac{L}{T_{\text{eff}}^4}\right)^{3/4}, \tag{15.89}$$

which gives

$$P \sim \frac{Q L^{-(1/2\alpha)} L^{3/4}}{T_{\text{eff}}^3}. \tag{15.90}$$

In the mass domain of the Cepheids from about 3 to 12 $M_\odot$, one typically has $\alpha = 3.3$ and thus

$$\log P_0 \approx \log Q_0 - 3 \log T_{\text{eff}} + 0.60 \log \frac{L}{L_\odot} + \text{const}, \tag{15.91}$$

or

$$\log \frac{L}{L_\odot} = 1.67 \log P_0 + 5 \log T_{\text{eff}} - 1.67 \log Q_0 + \text{const}'. \tag{15.92}$$

The periods are given in days, if the constant Q is expressed in days. This is the period-luminosity-color (PLC) relation characterizing radially pulsating stars. It depends on the value of Q for the corresponding mode of pulsation and on the stellar structure considered. Caution must be given to the fact that Q varies through the HR diagram, even for the Cepheids (see Fig. 15.7 right), the above relation is only a rough approximation. If we take a typical value of $Q_0 = 0.0383$, appropriate to a polytrope of index $n = 3$ (which provides a simplified stellar model, cf. Sect. 24.5.1), we can draw iso-period lines over the whole HR diagram, as illustrated in Fig. 15.6 for a fundamental pulsation mode with the assumption of a constant Q_0. The range of densities is such that the periods extend from about 1 h for the Sun to a few hundreds of days for the most luminous red supergiants. This figure is useful to anticipate the order of magnitude of the pulsation periods of stars to be observed.

15.5.2 *Physics of the Instability Strip*

The Cepheids occur in a so-called "instability strip", i.e., a relatively narrow band in the HR diagram crossed by the stars with a mass between about 3 and 12 $M_\odot$ as illustrated in Fig. 15.5. Cepheids pulsate in the fundamental mode (Q_0) with periods from about 2 to 50 days. Let us discuss the reasons why pulsating stars are present in a narrow range of T_{eff}. One can schematically distinguish three zones in the stellar envelope:

– The outer zone near the stellar surface has a very low density. Even if it covers a significant radius, this zone has very small mass and heat content. The luminosity
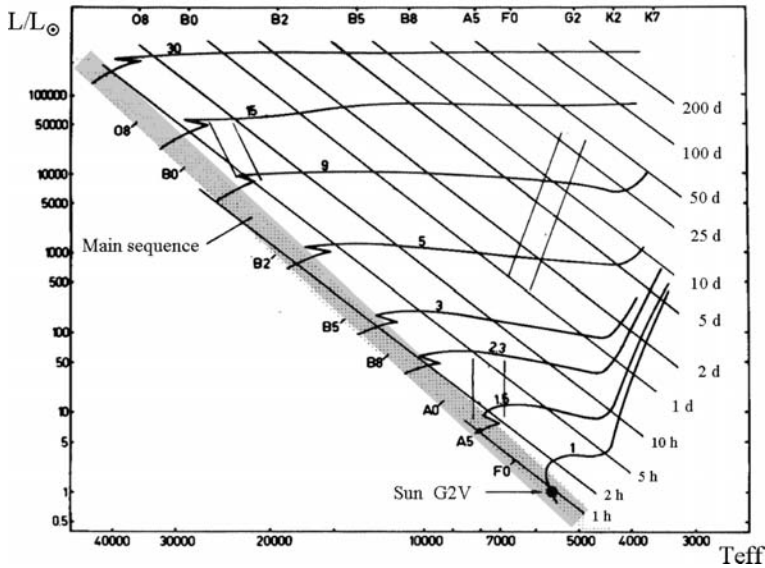
Fig. 15.6 HR diagram with lines of constant period in the fundamental mode for a pulsation constant $Q_0 = 0.0383$. The periods are given in days (label "d") or in hours (label "h"). The spectral types are given along the Main Sequence and at the top of the figure for the giants and supergiants. The number along each track indicates the corresponding mass. The location of the Sun is indicated, as well as the location of Cepheids, δ Scuti variables and β Cephei, see also Fig. 15.5. Courtesy from G. Burki [78]

perturbations ℓ' only have negligible energy exchanges there and thus they remain essentially constant, despite this zone may be formally non-adiabatic.

– At moderate depths, there is an intermediate non-adiabatic zone with significant mass and heat contents, so that this zone may produce a large driving or damping of the pulsation.
– At large depths, the heat content is so large that the exchange of energy with the pulsation has no effect on its heat content and the pulsation may be regarded as adiabatic.

The instability strip is determined mainly by the location in depth of the intermediate zone. Let us consider, as an example, a $7\,M_\odot$ star moving horizontally from the left to the right in the HR diagram due to its internal evolution. At $T_{\text{eff}} \geq 8000\,\text{K}$, the regions of partial ionization of H, He are in the outermost zone, the partial ionization of $He^+ \rightarrow He^{++}$ ($T \approx 4 \times 10^4$ K) being the leading effect. Elements hydrogen and helium are fully ionized in the intermediate zone, so that a Kramers-like opacity dominates. Coefficients κ_T and κ_P are negative and the star is stable.

As further evolution reduces T_{eff}, the He^+ region first and then the He and H partial ionization regions enter the intermediate non-adiabatic zone. The adiabatic exponents Γ_i decrease and the opacity regime may have positive κ_T and κ_p, two reasons making the star unstable.

A further decrease of T_{eff} brings the zones of partial ionizations in the deep adiabatic zone, where the destabilizing factors have little influence. Thus we understand that it is only over a limited range of T_{eff} values that the stars are unstable: this is the origin of the instability strip. This strip covers a broad range of magnitudes.

In practice, most Cepheids occur in the part of the blue loops where the evolution is the slowest, this is generally the blue extremity of the loops. Thus, most Cepheids are present at the luminosity where the extremity of the blue loops lie in the strip. As shown by Fig. 15.5, different kinds of variable stars, in addition to the Cepheids, occupy various parts of the instability strip, which extends down to the white dwarf sequence.

It is rather straightforward to derive the luminosity–T_{eff} relation in the instability strip [147]. The non-adiabatic zone driving the instability lies at a depth Δm in mass below the surface, where the ratio E_{th}/P of the thermal content of the upper layers to the period P is of the same order as the luminosity L (cf. Sect. 15.4.2),

$$\frac{c_V \overline{T} \Delta m}{P} \sim L . \tag{15.93}$$

The pressure at the base of the layer of thickness Δm is a fraction $\Delta m/M$ of the central pressure (1.20). In addition, one easily finds the pressure (cf. 24.23) at some level within a hydrostatic envelope of perfect gas with a Kramers opacity of the form $\kappa = \kappa_0 \varrho\, T^{-3.5}$. Equaling these two estimates of the pressure at the depth Δm gives, ignoring the numerical coefficients,

$$\frac{GM \Delta m}{R^4} \sim \left(ac\, \frac{k}{\mu m_{\text{u}} \kappa_0} \right)^{1/2} \left(\frac{M}{L} \right)^{1/2} T^{4.25} . \tag{15.94}$$

This provides the following scaling for Δm,

$$\Delta m \sim \frac{R^4}{M} \left(\frac{M}{L} \right)^{1/2} T^{4.25} . \tag{15.95}$$

With (15.93) and (15.88), Δm also scales like

$$\Delta m \sim LP = QL \frac{R^{3/2}}{M^{1/2}} . \tag{15.96}$$

Here, T is a constant corresponding to the ionization temperature considered, i.e., about 4×10^4 K for He$^+$. For a constant Q, we get from the two expressions of Δm the following relation for stars in the instability strip,

$$L \sim R^{5/3} , \tag{15.97}$$

independently of M. Since by definition $L = 4\pi R^2 \sigma T_{\text{eff}}^4$, the scaling with $R^{5/3}$ implies that $T_{\text{eff}}^4 \sim R^{-1/3}$, so that

$$R \sim T_{\text{eff}}^{-12} \quad \text{and} \quad L \sim R^{5/3} \sim T_{\text{eff}}^{-20} . \tag{15.98}$$

There is little change of T_{eff} of Cepheids with their average luminosity; this explains why the instability strip is almost vertical in the HR diagram. The above simple developments give a relation for the instability strip,

$$\log T_{\text{eff}} = -0.05 \log \frac{L}{L_{\odot}} + \text{const}'' . \tag{15.99}$$

This slope is remarkably close to that obtained from numerical models, which give for the blue edge of the instability strip a relation $\log T_{\text{eff}} = -0.036 \log \frac{L}{L_{\odot}} + 3.925$ [504]. The theoretical width of the strip is about 0.05 dex in T_{eff}, the observational width being slightly larger, of the order of 0.08 dex in effective temperature [507].

15.5.3 The Period–Luminosity Relation

Since we have the PLC relation (15.92) and also a relation $L - T_{\text{eff}}$ for the instability strip (15.99), one can eliminate T_{eff} from the two and get a period– luminosity (PL) relation for the Cepheids:

$$\log \frac{L}{L_{\odot}} = 1.34 \log P_0 - 1.34 \log Q_0 + \text{const}''' . \tag{15.100}$$

The relation obtained from numerical models is [504]

$$\log \frac{L}{L_{\odot}} = 1.270 \log P + 2.570 , \tag{15.101}$$

for the blue edge, while for the red edge the slope is 1.244 and the constant 2.326. It is satisfactory that the simple analytical developments give a slope close to that from numerical models. These relations are illustrated in Fig. 15.7 left. At a given luminosity, the period at the red edge is about 25% longer than at the blue edge, because the average density is lower. The average observed PL relation for galactic Cepheids is [507]

$$M_V = -(3.087 \pm 0.085) \log P - (0.914 \pm 0.098) . \tag{15.102}$$

This corresponds to a slope of 1.235 in the $\log L$ vs. $\log P$ diagram, in relatively good agreement with the theoretical values. This relation plays a considerable role in the calibration of the extragalactic distance scale. The numerical models of Fig. 15.7 (left) present no metallicity effect in the PL relation over the range of the metallicities from the SMC to the Galaxy ($Z = 0.004$ to $Z = 0.020$). While several works claimed there is no observable Z effect in the PL relation, recent results by Sandage and Tammann [507] show significant differences with Z in the observed PL relations, so that a specific empirical PL relation has to be used for each metallicity. The extreme case is that of the Cepheids of Population II, the W Virginis stars, which
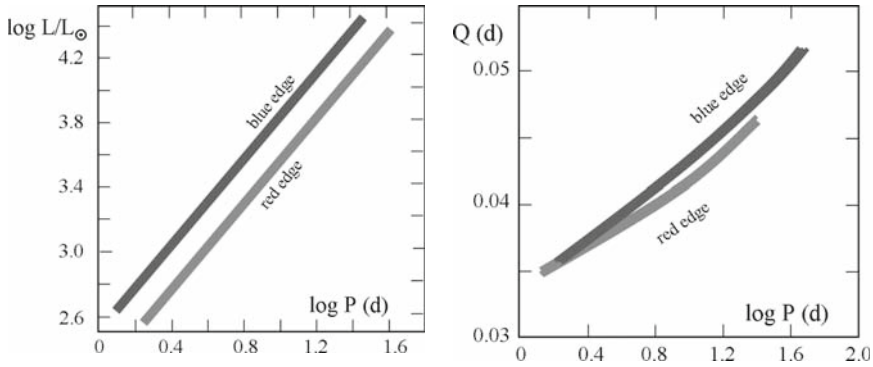
Fig. 15.7 *Left*: period-luminosity relation for the blue and red edges from numerical models of composition $X = 0.70$ with $Z = 0.02$–0.04. *Right*: the pulsation constant Q_0 for the Cepheids as a function of the periods, for the blue and red edge (same symbols as on the *left* and same composition). Adapted from Saio & Gautschy [504]

are old low-mass stars with $M < 1\,M_\odot$. A Cepheid and a W Virginis at the same location in the HR diagram have the same radius, however, their mean densities are very different. The much lower density of the W Virginis stars leads to a period about a factor 3.5 longer at a given luminosity.

We have considered the Q_0 values as constant. However, the Q values in general depend on the stellar structure and the Cepheids of different luminosities have slightly different structures, thus the Q_0 values also depend on the luminosity or period of the Cepheids. Figure 15.7 (right) shows these effects: Q_0 increases with periods with a small difference between Cepheids at the blue or red edge. The maximum difference reaches about 50% which is far from negligible for the period-luminosity relation. The physical reason for the variation rests on the behavior of the ratio of the sound speed $c_S \sim \sqrt{T}$ in the outer layers to the average sound speed in the star: at higher luminosity (and longer periods), the Cepheids have a larger thin envelope with low temperature so that the above ratio is smaller. Therefore, the pulsation constants Q_0 are larger for more luminous Cepheids.

15.5.4 Light Curves

There is a great variety of Cepheid light curves with different bumps, in particular there are systematic differences according to the luminosity. The amplitudes around the mean luminosity vary a lot, from a few percents to 1 magnitude. Also, at a given location in the HR diagram the amplitudes are not necessarily the same. Figure 15.8 shows the typical variations of magnitude, velocity, radius and $T_{\rm eff}$ of a Cepheid. The velocity curve is the mirror image of the brightness curve with the same degree of skewness, the peak in luminosity corresponds to the largest expansion velocity. The variation of radius is such that its derivative gives the velocity curve. The maximum
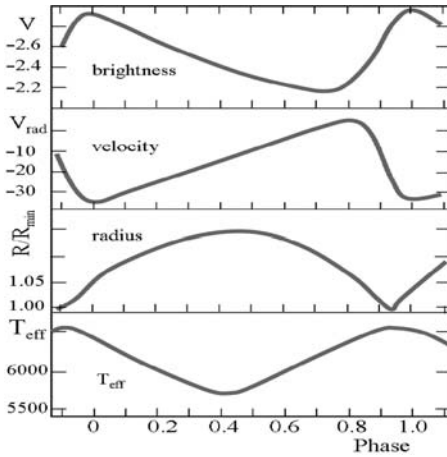
Fig. 15.8 Schematic representation of the variations of *V* magnitude, radial velocity, radius with respect to the minimum radius and effective temperature of a classical Cepheid (δ Ceph) over one period. Adapted from J.P. Cox [146]

of brightness occurs slightly after the minimum radius, i.e., at the point with the average velocity on the steep descending part of the velocity curve. This is the so-called phase lag. It is the variation of T_{eff} which essentially determines the brightness variations, because of the dependence in T_{eff}^4 of the luminosity. T_{eff} is maximum, as a result of gas compression, when the radius is minimum. Thus, globally there is a correspondence between the minimum radius and the maximum luminosity. However, in details the star reaches its maximum luminosity when the opaque layers associated to the zone of partial ionization are the thinnest and the lag is due to the most external location of the H-ionization shell slightly after the minimum radius.

The non-linear effects which determine the amplitude of the pulsation are not yet fully explored. The same is true for the large differences of amplitudes between Cepheids in the Galaxy and the Magellanic Clouds and the amplitude differences from star to star. There is also a long-standing mass-discrepancy problem, in the sense that the masses derived from the pulsation theory are lower than those inferred from the evolutionary theory. Improved opacities have reduced the problem [203], however not totally.

Cepheids are slowly rotating stars, however, some of them may have had fast rotation during the MS phase. For such cases, rotation has two indirect effects on the properties of Cepheids. First, rotation during the MS phases increases the mass of the stellar cores and makes the stars more luminous when they are in the Cepheid instability strip. The radius is also increased, the mean density lower and the period longer. Thus, rotation produces a shift both in luminosity and in period. There is a second effect of rotation: rotational mixing produces a self-enrichment of the surface layers in helium. This may influence the driving and damping of the pulsation with possibly some consequences for the amplitudes of the pulsations. On the whole, we can say that the consequences for the Cepheids of the various rotational instabilities and mixing processes are far from being well explored.

Chapter 16
Nonradial Stellar Oscillations

Nonradial pulsations do not necessarily have great effects on the course of stellar evolution, except possibly for the transport of angular momentum (Chap. 17). However like seismic oscillations due to earthquakes, they provide tests of the interior structure of the oscillating body. The study and observations of nonradial oscillations of the Sun have led to the magnificent development of helioseismology, which provides information on the inner structure and temperature of the Sun with an accuracy better than 1% as well as on the interior solar rotation. The same techniques applied to stars with observations on big telescopes or satellites, like COROT and MOST, have opened the promising and already successful field of asteroseismology.

16.1 Basic Equations of Nonradial Oscillations

The amplitudes of nonradial oscillations generally are small. Thus, the equations describing the oscillations can be obtained by linear developments of the equations of stellar structure [131, 317, 585]. The unperturbed star is in a state of spherical hydrostatic equilibrium; the effects of rotation and magnetic field are ignored in a first approach. As usual in stellar pulsations, radiative damping is the main damping effect.

16.1.1 Starting Equations

For convenience, we write here the basic equations to be perturbed, namely the continuity equation (B.3), the equation of motion (B.4) and the energy equation (3.34):

$$\frac{\partial \rho}{\partial t} + \mathrm{div}(\rho\, \boldsymbol{v}) = 0 \,, \tag{16.1}$$

$$\rho \frac{d\boldsymbol{v}}{dt} = \rho \left[\frac{\partial \boldsymbol{v}}{\partial t} + (\boldsymbol{v} \cdot \boldsymbol{\nabla})\boldsymbol{v} \right] = -\boldsymbol{\nabla}P + \rho\, \boldsymbol{g} \,, \tag{16.2}$$

$$\varrho \frac{dq}{dt} = \varrho \, \varepsilon - \boldsymbol{\nabla} \cdot \boldsymbol{F} \, . \tag{16.3}$$

The gravity $\boldsymbol{g} = (-g, 0, 0)$ is given by $\boldsymbol{g} = -\boldsymbol{\nabla} \Phi$, with $g = \frac{\partial \Phi}{\partial r}$ (1.35). The gravitational potential satisfies the Poisson equation (1.44):

$$\Delta \, \Phi = 4 \pi \, G \varrho \, . \tag{16.4}$$

The derivative (dq/dt) of the heat brought or removed by unit of mass is according to (C.22)

$$\frac{dq}{dt} = \frac{1}{\varrho \, (\Gamma_3 - 1)} \left(\frac{dP}{dt} - \frac{\Gamma_1 \, P}{\varrho} \frac{d\varrho}{dt} \right) \, . \tag{16.5}$$

At equilibrium, the star model is static. The time derivatives and the velocities disappear from the equations. The continuity equation is identically zero and the equation of motion reduces to the equation of hydrostatic equilibrium. The equilibrium quantities are indicated by a zero subscript. One has for hydrostatic equilibrium, Poisson's and energy equations, respectively,

$$\boldsymbol{\nabla} P_0 = \varrho_0 \, \boldsymbol{g}_0 = -\varrho_0 \, \boldsymbol{\nabla} \Phi_0 \, , \tag{16.6}$$

$$\Delta \, \Phi_0 = 4 \pi \, G \varrho_0 \quad \text{and} \quad \epsilon_0 - \frac{1}{\varrho_0} \boldsymbol{\nabla} \cdot \boldsymbol{F}_0 = 0 \, . \tag{16.7}$$

For spherical symmetry, these are the usual 1D equations.

16.1.2   Perturbations of the Equations

We consider small displacements $\boldsymbol{\xi}$ around the equilibrium position $\boldsymbol{r}_0$, with the indicated components in spherical coordinates:

$$\boldsymbol{\xi} = \boldsymbol{r} - \boldsymbol{r}_0 = \left(\xi_r, \xi_\vartheta, \xi_\varphi \right) \, . \tag{16.8}$$

In the Eulerian description (Sect. 1.1.4), the perturbed quantities are considered at a given location $\boldsymbol{r}$; they are developed as an example for pressure:

$$P(\boldsymbol{r}, t) = P_0(\boldsymbol{r}) + P'(\boldsymbol{r}_0, t) \, . \tag{16.9}$$

It is often useful to define a frame which follows the motion of the perturbed fluid element. This is the Lagrangian coordinate system, in which the perturbed quantities are developed like:

$$P(\boldsymbol{r}, t) = P_0(\boldsymbol{r}_0) + \delta P(\boldsymbol{r}_0, t) \, . \tag{16.10}$$

To the first order, the Lagrangian and Eulerian perturbations are related by

$$\delta P(\boldsymbol{r},t) \approx \delta P(\boldsymbol{r}_0,t) = P'(\boldsymbol{r}_0,t) + P_0(\boldsymbol{r}) - P_0(\boldsymbol{r}_0)$$

$$= P'(\boldsymbol{r}_0,t) + \boldsymbol{\xi} \cdot \boldsymbol{\nabla} P_0(\boldsymbol{r}), \quad \text{with} \quad \delta \boldsymbol{r} \equiv \boldsymbol{\xi}. \tag{16.11}$$

To this approximation, $\boldsymbol{\nabla} P_0(\boldsymbol{r}) \approx \boldsymbol{\nabla} P_0(\boldsymbol{r}_0)$ and $P'(\boldsymbol{r},t) \approx P'(\boldsymbol{r}_0,t)$. The linear equations for the perturbations are obtained by applying expressions of the form (16.9) to the basic Eqs. (16.1) (16.2) (16.3) and (16.4) and subtracting the equilibrium equations. The terms of higher order in P', ϱ' or $\boldsymbol{v}(\partial\boldsymbol{\xi}/\partial t)$, etc. are neglected. The continuity Eq. (16.1) gives in the Eulerian form

$$\frac{\partial \varrho'}{\partial t} + \mathrm{div}(\varrho_0 \boldsymbol{v}) = 0 \quad \text{or} \quad \varrho' + \boldsymbol{\nabla} \cdot (\varrho_0 \boldsymbol{\xi}) = 0. \tag{16.12}$$

The Lagrangian form is by application of (16.11)

$$\delta\varrho + \varrho_0 \boldsymbol{\nabla} \cdot \boldsymbol{\xi} = 0. \tag{16.13}$$

The equation of motion (16.2) gives

$$\varrho_0 \frac{d^2\boldsymbol{\xi}}{dt^2} = \varrho_0 \frac{\partial^2\boldsymbol{\xi}}{\partial t^2} = \varrho_0 \frac{\partial\boldsymbol{v}}{\partial t} = -\boldsymbol{\nabla} P' + \varrho_0 \boldsymbol{g}' + \varrho' \boldsymbol{g}_0. \tag{16.14}$$

If there is no general fluid motion, the partial derivatives are also straight derivatives. One has $\boldsymbol{g}' = -\boldsymbol{\nabla}\Phi'$. Φ' satisfies the perturbed Poisson equation

$$\nabla^2 \Phi' = 4\pi G \varrho'. \tag{16.15}$$

Because dq is a quantity by unit of mass, the Lagrangian perturbation of (16.3) is simply

$$\varrho_0 \frac{\partial \delta q}{\partial t} = \delta(\varrho\epsilon - \boldsymbol{\nabla} \cdot \boldsymbol{F}) = (\varrho\epsilon - \boldsymbol{\nabla} \cdot \boldsymbol{F})', \tag{16.16}$$

because the divergence of $(\varrho\epsilon - \boldsymbol{\nabla} \cdot \boldsymbol{F})_0$ at equilibrium is zero. The first member is given by the perturbation of (16.5):

$$\frac{\partial \delta q}{dt} = \frac{1}{\varrho(\Gamma_3 - 1)} \left(\frac{\partial \delta P}{\partial t} - \frac{\Gamma_1 P_0}{\varrho_0} \frac{\partial \delta \varrho}{\partial t} \right). \tag{16.17}$$

There, Γ_1 and Γ_3 are considered at the equilibrium stage, since they are slowly varying functions. For adiabatic motions, one has $\delta q = 0$, which gives $\partial\delta P/\partial t = (\Gamma_1 P_0/\varrho_0)\partial\varrho/\partial t$. After integration, it is

$$\delta P = \frac{\Gamma_1 P_0}{\varrho_0} \delta\varrho. \tag{16.18}$$

16.1.3 Separation in Vertical and Horizontal Components

The equations governing the perturbations are of the form

$$[A] \frac{\partial y}{\partial t} = B(y) , \tag{16.19}$$

where the vector y contains the perturbed variables $(P', \varrho', \xi, \ldots)$, $[A]$ is a matrix and B a linear operator. The coefficients $[A]$ and B of this equation are independent of time. The solutions are of the form

$$y(r,t) = \hat{y}(r) \exp(-i\omega t) . \tag{16.20}$$

Thus, one has $(\partial/\partial t) \to -i\omega$, where ω is the cyclic frequency related to the observed frequency ν and oscillation period P by

$$\omega = 2\pi\nu = \frac{2\pi}{P} . \tag{16.21}$$

The solutions are written in the complex form, where the physical solution is the real part. Equation (16.19) becomes

$$-i\omega[A] \cdot \hat{y} = B(\hat{y}) , \tag{16.22}$$

which defines the amplitude $\hat{y}$. The equilibrium state is spherically symmetric; thus in the linear approximation the displacement ξ can be decomposed into its radial and horizontal components:

$$\delta r = \xi = (\xi_r, \xi_h) , \tag{16.23}$$

where the component "h" lies in the local horizontal plane defined by the unity vectors e_ϑ and e_φ in spherical coordinates. Let us consider the effects of this decomposition on the equations of the perturbations. The perturbed continuity equation (16.12) becomes

$$\varrho' = -\frac{1}{r^2} \frac{\partial}{\partial r}(\varrho_0 r^2 \xi_r) - \varrho_0 \nabla_h \cdot \xi_h . \tag{16.24}$$

The dependence in ϑ and φ in the derivatives of the above equations only appears through the term ∇_h^2. There, the index "h" represents both components in ϑ and φ, for example, $\nabla_h \Phi = (1/r)\left(0, \dfrac{\partial \Phi}{\partial \vartheta}, \dfrac{1}{\sin\vartheta} \dfrac{\partial \Phi}{\partial \varphi}\right)$. The frequency ω is absent because it appears on both sides of the continuity equation (16.12) (in the second term, ω comes from $v = \partial\xi/\partial t$). We can obtain from (16.14) an equation of motion for both the radial and horizontal components:

$$\varrho_0 \frac{\partial^2 \xi_r}{\partial t^2} + \frac{\partial P'}{\partial r} + \varrho_0 \frac{\partial \Phi'}{\partial r} + \varrho' g_0 = 0 , \tag{16.25}$$

$$\varrho_0 \frac{\partial^2 \xi_h}{\partial t^2} + \nabla_h P' + \varrho_0 \nabla_h \Phi' = 0 \,. \tag{16.26}$$

The horizontal divergence of (16.26) becomes

$$\varrho_0 \frac{\partial^2}{\partial t^2} \nabla_h \cdot \xi_h + \nabla_h^2 P' + \varrho_0 \nabla_h^2 \Phi' = 0 \,. \tag{16.27}$$

From (16.24), one can express $\nabla_h \xi_h$,

$$\nabla_h \xi_h = -\frac{\varrho'}{\varrho_0} - \frac{1}{r^2 \varrho_0} \frac{\partial}{\partial r} (\varrho \, r^2 \xi_r) \,, \tag{16.28}$$

and eliminate it in (16.27), taking into account that ϱ_0 is the equilibrium value and that its time derivative is zero:

$$-\frac{\partial^2}{\partial t^2} \left(\varrho' + \frac{1}{r^2} \frac{\partial}{\partial r} (\varrho_0 \, r^2 \xi_r) \right) + \nabla_h^2 P' + \varrho_0 \nabla_h^2 \Phi' = 0 \,. \tag{16.29}$$

The perturbed Poisson equation (16.15) is, if we distinguish the vertical and horizontal parts,

$$\frac{1}{r^2} \frac{\partial}{\partial r} \left(r^2 \frac{\partial \Phi'}{\partial r} \right) + \nabla_h^2 \Phi' = 4 \pi G \varrho' \,. \tag{16.30}$$

In order to solve these equations together with the energy equation, one needs an appropriate representation of the horizontal solutions.

16.1.4 Decomposition in Spherical Harmonics

Any function of one variable can be represented as Fourier series by summation of sinus terms. In a similar way, any variations of a quantity over the surface of a sphere can be represented by spherical harmonics. This applies as well to the atomic model, the fluctuations of the cosmic microwave background, the terrestrial and stellar oscillations, etc.

In spherical coordinates r, ϑ, φ, where as usual ϑ is the colatitude and φ the longitude, the variations of the perturbations in ϑ and φ can be expressed as a function $f(\vartheta, \varphi)$ if the function f is an eigenfunction of the horizontal Laplace operator [131]

$$\nabla_h^2 f = -\frac{1}{r^2} \Lambda f \,, \text{ or explicitly}$$

$$\frac{1}{\sin^2 \vartheta} \left[\sin \vartheta \frac{\partial}{\partial \vartheta} \left(\sin \vartheta \frac{\partial f}{\partial \vartheta} \right) + \frac{\partial^2 f}{\partial \varphi^2} \right] = -\Lambda f \,, \tag{16.31}$$

where Λ is a constant and the factor $1/r^2$ has been simplified. The coefficients of this equation depend only on ϑ; the solution f can be separated as a product of the two variables ϑ and φ:

$$f(\vartheta, \varphi) = f_1(\vartheta) f_2(\varphi) . \tag{16.32}$$

Inserting this representation of $f(\vartheta, \varphi)$ in (16.31), we see that $f_2(\varphi)$ must satisfy an equation of the form

$$\frac{d^2 f_2}{d\varphi^2} = \alpha f_2 , \tag{16.33}$$

where α is a constant. The solution of this equation is

$$f_2(\varphi) = e^{\pm \alpha^{1/2} \varphi} , \quad \text{with } \alpha^{1/2} = im . \tag{16.34}$$

This is because the solutions for f_2 have to be continuous and periodic with $f_2(0) = f_2(2\pi)$, i.e., with m being an integer. The introduction of these expressions in (16.31) with $x = \cos \vartheta$ gives $\sin \vartheta \, d\vartheta = -dx$ and $\sin \vartheta (\partial/\partial \vartheta) = -(1-x^2)(d/dx)$. The derivative with respect to φ gives $(d^2/d\varphi^2) = -m^2$. Thus (16.31) leads to the following equation for f_1:

$$\frac{d}{dx}\left((1-x^2) \frac{d f_1}{dx} \right) + \left(\Lambda - \frac{m^2}{1-x^2} \right) f_1 = 0 . \tag{16.35}$$

If $\Lambda = \ell(\ell+1)$, where ℓ are integers, this is the so-called general Legendre equation [3, 230]. Its solutions in the interval $(-1, 1)$ are non-singular only if $0 \le m \le \ell$. The solution of (16.35) is

$$f_1(\vartheta) = P_\ell^m(\cos \vartheta), \tag{16.36}$$

where the $P_\ell^m(\cos \vartheta)$ are the associate Legendre polynomials. Since the integer m multiplies the coordinate φ, it is called the azimuthal order; ℓ is the degree of the polynomial. The P_ℓ^m are defined as

$$P_\ell^m = (-1)^m (1-x^2)^{m/2} \frac{d^m}{dx^m} (P_\ell(x))$$

$$= \frac{(-1)^m}{2^\ell \, \ell!} (1-x^2)^{m/2} \frac{d^{\ell+m}}{dx^{\ell+m}} (x^2-1)^\ell . \tag{16.37}$$

There, $P_\ell(x)$ are the (ordinary) Legendre polynomials. The associate Legendre polynomials P_ℓ^m usually appear in spherical geometry for expressing the horizontal part of the solution of the Laplace's equation $\nabla^2 \Psi = -\Lambda \Psi$. Equation (16.31) is of that form, which explains this type of solution here. The Legendre and the associate Legendre polynomials satisfy various relations [3], which are often useful.

For the complete solution of the Laplace equation (16.31), one has to account for (16.32) and (16.34); thus the function $f(\vartheta,\varphi)$ is finally

$$f(\vartheta,\varphi) = (-1)^m c_{\ell m} P_\ell^m(\cos\vartheta) e^{im\varphi} \equiv Y_\ell^m(\vartheta,\varphi) . \qquad (16.38)$$

There, the horizontal solution of the Laplace solution is $Y_\ell^m(\vartheta,\varphi)$, which is called the spherical harmonics of degree ℓ and order m. The constant $c_{\ell m}$ is a normalization constant, chosen in such a way that the integral of $|Y_{\ell m}|^2$ over a sphere of radius unity is equal to 1. This normalization (which uses a property called the orthogonality of the associate Legendre polynomials [230]) imposes that the constant $c_{\ell m}$ be given by

$$c_{\ell m}^2 = \frac{(2\ell+1)(\ell-m)!}{4\pi(\ell+m)!}. \qquad (16.39)$$

With these solutions, the horizontal component of the Laplace operator (16.31) becomes simply

$$\nabla_h^2 f = -\frac{\ell(\ell+1)}{r^2} f . \qquad (16.40)$$

If locally the perturbation is approximated by a plane wave satisfying (C.28), by putting this solution in (16.40), we get the following identification:

$$\frac{\ell(\ell+1)}{r^2} = k_h^2 , \qquad (16.41)$$

where k_h is the wave number in the horizontal direction. The operator ∇_h expresses the horizontal dependence in the perturbed equations (16.27), (16.28), (16.29) and (16.30); consequently the spherical harmonics $Y_\ell^m(\vartheta,\varphi)$ describes the horizontal behavior, while the radial and temporal variations are of the forms given by (16.20). Thus, we can write the variables in the perturbed equations (16.29) and (16.30) by using both (16.20) and (16.38):

$$\xi_r(r,\vartheta,\varphi,t) = \sqrt{4\pi}\, \widetilde{\xi}_r(r)\, Y_\ell^m(\vartheta,\varphi)\, e^{-i\omega t},$$

$$P'(r,\vartheta,\varphi,t) = \sqrt{4\pi}\, \widetilde{P}(r)\, Y_\ell^m(\vartheta,\varphi)\, e^{-i\omega t},$$

$$\varrho'(r,\vartheta,\varphi,t) = \sqrt{4\pi}\, \widetilde{\varrho}(r)\, Y_\ell^m(\vartheta,\varphi)\, e^{-i\omega t},$$

$$\Phi'(r,\vartheta,\varphi,t) = \sqrt{4\pi}\, \widetilde{\Phi}(r)\, Y_\ell^m(\vartheta,\varphi)\, e^{-i\omega t}. \qquad (16.42)$$

The factor $\sqrt{4\pi}$ comes from the normalization over the sphere. If one introduces this writing in the perturbed equations (16.26), (16.29) and (16.30), one gets after simplification and with (16.40)

$$-\omega^2 \varrho_0 \, \widetilde{\xi}_r = -\frac{d\widetilde{P}'}{dr} - \varrho_0 \frac{d\widetilde{\Phi}'}{dr} - \widetilde{\varrho}' g_0 \,, \tag{16.43}$$

$$\omega^2 \left(\widetilde{\varrho}' + \frac{1}{r^2} \frac{d}{dr}(\varrho_0 \, r^2 \widetilde{\xi}_r) \right) = \frac{\ell(\ell+1)}{r^2} \left(\widetilde{P}' + \varrho_0 \, \widetilde{\Phi}' \right) \,, \tag{16.44}$$

$$\frac{1}{r^2} \frac{d}{dr} \left(r^2 \frac{d\widetilde{\Phi}'}{dr} \right) - \frac{\ell(\ell+1)}{r^2} \widetilde{\Phi}' = 4\pi G \widetilde{\varrho}' \,. \tag{16.45}$$

One can also express Eq. (16.17) for the heat exchanges in this way. Care has to be given because (16.17) is in Lagrangian variables. However, expression (16.11) ensures that the Lagrangian and Eulerian perturbations can be developed in the same way. In (16.11), ∇P_0 has only a vertical component. One has

$$\delta\widetilde{P} - \frac{\Gamma_1 P_0}{\varrho_0} \delta\widetilde{\varrho} = \varrho_0 \, (\Gamma_3 - 1) \, \delta\widetilde{q} \,. \tag{16.46}$$

Equations (16.43) (16.44), (16.45) and (16.46) form the basic set expressing the variations with depth of $\widetilde{\xi}_r$, $\widetilde{P}'(r)$, etc. which describe the amplitudes of the nonradial oscillations. The solutions for the nonradial oscillations are thus obtained from a system of differential equations, which only have a radial dependence. There is no exact analytical solutions to this system; even numerically it is generally treated in the adiabatic approximation.

These equations do not contain the azimuthal order m. This results from the spherical symmetry of the equilibrium state. Rotation is not included here and there is no preferential choice of polar axis for the coordinate system, which would be implied by the presence of an m value in the equations.

The horizontal component ξ_h can be obtained from (16.26) by using (16.42); one has

$$-\varrho \, \omega^2 \xi_h + \sqrt{4\pi} \left(\widetilde{P}'(r) + \varrho \, \widetilde{\Phi}'(r) \right) \left(\frac{\partial Y_\ell^m}{r \partial \vartheta} + \frac{1}{r\sin\vartheta} \frac{\partial Y_\ell^m}{\partial \varphi} \right) e^{-i\omega t} = 0, \tag{16.47}$$

which gives

$$\xi_h = \sqrt{4\pi} \, \widetilde{\xi}_h(r) \left(\frac{\partial Y_\ell^m}{\partial \vartheta} \boldsymbol{e}_\vartheta + \frac{1}{\sin\vartheta} \frac{\partial Y_\ell^m}{\partial \varphi} \boldsymbol{e}_\varphi \right) e^{-i\omega t}, \tag{16.48}$$

where $\boldsymbol{e}_\vartheta$ and $\boldsymbol{e}_\varphi$ are the vector units. There $\widetilde{\xi}_h(r)$ is given by

$$\widetilde{\xi}_h(r) = \frac{1}{r\,\omega^2} \left(\frac{\widetilde{P}'}{\varrho_0} + \widetilde{\Phi}'(r) \right) \,. \tag{16.49}$$

According to the decomposition of the displacement vector one has with (16.23) and (16.42),

$$\delta \boldsymbol{r} = \sqrt{4\pi}\,\mathcal{R}\left\{\left[\tilde{\xi}_{\mathrm{r}}Y_{\ell}^{m}\boldsymbol{e}_{\mathrm{r}} + \tilde{\xi}_{h}\left(\frac{\partial Y_{\ell}^{m}}{\partial \vartheta}\boldsymbol{e}_{\vartheta} + \frac{1}{\sin\vartheta}\frac{\partial Y_{\ell}^{m}}{\partial \varphi}\boldsymbol{e}_{\varphi}\right)\right]e^{-i\omega t}\right\}, \quad (16.50)$$

There, $\mathcal{R}$ means that the real part of the bracket $\{\dots\}$ is taken.

16.2   Nonradial Adiabatic Oscillations

This is an important case, which allows one to treat stellar oscillations with a good accuracy [131]. The amplitudes of the nonradial oscillations being small, the radiative damping is usually not significant. However, we note that for the transport of angular momentum by gravity waves (Chap. 17), dissipation plays a role. Below we omit the indication "$\sim$" and the index "0" for the equilibrium quantities, but keep the prime for the amplitudes of the perturbations. The adiabatic nature of the oscillations is expressed by $\delta q = 0$.

16.2.1   Basic Equations

Equations (16.43), (16.44), (16.45) and (16.46) form the basic set which we now simplify. We write (16.46) making use of (16.11) to obtain the Eulerian expressions:

$$P' + \xi_r\frac{dP}{dr} = \frac{\Gamma_1 P}{\varrho}\left(\varrho' + \xi_r\frac{d\varrho}{dr}\right),$$

$$\text{i.e.,}\quad \varrho' = \frac{\varrho}{\Gamma_1 P}P' + \varrho\,\xi_r\left(\frac{1}{\Gamma_1 P}\frac{dP}{dr} - \frac{1}{\varrho}\frac{d\varrho}{dr}\right). \quad (16.51)$$

We might wonder whether the parenthesis on the right is equal to zero. The answer is no. It is true that the heat transfer δq of a given mass fluid element (Lagrangian coordinates) is equal to zero, but this is not true for the Eulerian form. With (16.51), we can eliminate ϱ' from (16.43) and get directly

$$\frac{dP'}{dr} = \frac{1}{\Gamma_1 P}\frac{dP}{dr}P' + \varrho\,\xi_r\left(\omega^2 - N_{\mathrm{ad}}^2\right) - \varrho\frac{d\Phi'}{dr}, \quad (16.52)$$

where N_{ad}^2 is the square of the adiabatic Brunt–Väisälä frequency (5.61):

$$N_{\mathrm{ad}}^2 = g\left(\frac{1}{\Gamma_1 P}\frac{dP}{dr} - \frac{1}{\varrho}\frac{d\varrho}{dr}\right). \quad (16.53)$$

Eliminating ϱ' from (16.44), we have

$$\frac{\varrho}{\Gamma_1 P}P' + \varrho\,\xi_r\left(\frac{1}{\Gamma_1 P}\frac{dP}{dr} - \frac{1}{\varrho}\frac{d\varrho}{dr}\right) + \varrho\,\frac{d\xi_r}{dr} + \xi_r\frac{d\varrho}{dr} + \frac{2}{r}\varrho\,\xi_r$$

$$= \frac{\ell(\ell+1)}{\omega^2 r^2}P' + \frac{\varrho\,\ell(\ell+1)}{\omega^2 r^2}\Phi', \tag{16.54}$$

which gives

$$\frac{d\xi_r}{dr} = -\left(\frac{2}{r} + \frac{1}{\Gamma_1 P}\frac{dP}{dr}\right)\xi_r + \frac{1}{\varrho}\left[\frac{\ell(\ell+1)}{\omega^2 r^2} - \frac{1}{c_S^2}\right]P' + \frac{\ell(\ell+1)}{\omega^2 r^2}\Phi'. \tag{16.55}$$

where c_S is the sound velocity (C.26). One defines a frequency S_ℓ by

$$S_\ell^2 = \frac{\ell(\ell+1)\,c_S^2}{r^2}. \tag{16.56}$$

S_ℓ is the Lamb frequency. Its inverse is the time for a sonic wave to travel over the distance $r/\sqrt{\ell(\ell+1)}$. With (16.55), it gives

$$\frac{d\xi_r}{dr} = -\left(\frac{2}{r} + \frac{1}{\Gamma_1 P}\frac{dP}{dr}\right)\xi_r + \frac{1}{\varrho\,c_S^2}\left[\frac{S_\ell^2}{\omega^2} - 1\right]P' + \frac{\ell(\ell+1)}{\omega^2 r^2}\Phi'. \tag{16.57}$$

Eliminating ϱ', we get for (16.45)

$$\frac{1}{r^2}\frac{d}{dr}\left(r^2\frac{d\Phi'}{dr}\right) = 4\pi G\left(\frac{P'}{c_S^2} + \frac{\varrho\,\xi_r}{g}N_{\mathrm{ad}}^2\right) + \frac{\ell(\ell+1)}{r^2}\Phi'. \tag{16.58}$$

Equations (16.52), (16.53), (16.57) and (16.58) form a system of four differential equations for the four variables ξ_r, P', Φ' and $d\Phi'/dr$ in the adiabatic case. If we would ignore the variations of the potential Φ', this would be a second-order system of equations. The coefficients are real and thus ω^2 is also real, which implies that ω is either purely real (oscillatory motions without damping) or purely imaginary (dynamical instability). This rather schematic situation is a consequence of the adiabatic assumption.

Four boundary conditions are needed. They may be obtained from a detailed expansion of the equations at the center and at the surface [585]. In a simple way, they can also be understood from geometrical and physical considerations [131]. Near the center, the conditions, which result from the regularity of the solutions, are as follows:

$$\text{if } r \to 0 \qquad \xi_r \approx \ell\,\xi_h, \quad \text{and} \quad \frac{d\Phi'}{dr} \approx \frac{\ell}{r}\Phi'. \tag{16.59}$$

The first condition expresses the fact that at the center both the vertical and horizontal oscillation amplitudes vanish simultaneously, the horizontal amplitude being a factor of about ℓ smaller than the vertical amplitude. The second condition says

that as a function of r, close to the center, the perturbations of the potential start from zero and grow with r^ℓ, implying that for very small r the nonradial distortion tends toward zero.

At the stellar surface, the perturbed potential Φ' and its derivative must be continuous. The external solution is of the form $\Phi' = A r^{-(\ell+1)}$, which vanishes at infinity and which is much smaller for higher number ℓ. This implies that at the surface $r = R$, one has

$$\frac{d\Phi'}{dr} + \frac{\ell+1}{r} \Phi' = 0 . \tag{16.60}$$

The other condition at the stellar surface $r = R$ is that the outer boundary is free (cf. Sect. 15.2.2), with no forces acting on the perturbations coming from the interior. This means that the Lagrangian pressure perturbations at the surface are zero. Thus, one has according to (16.11)

$$\delta P = P' + \frac{dP}{dr} \xi_r = 0 . \tag{16.61}$$

The propagation of the acoustic waves in the stellar atmosphere is further discussed in Sect. 16.3.3. The system of equations (16.52), (16.53), (16.57) and (16.58) is solved by numerical techniques for models of the Sun and solar-type stars. Some results are shown in Sect. 16.5.

16.2.2   Some Properties of the Equations

In Eqs. (16.52) and (16.57), the unknown quantities ξ_r and P' appear linearly; thus they can be multiplied by a constant quantity without modifying the equations. The system is said homogeneous and the solutions are obtained only within a constant multiplying factor. This factor would be fixed by the driving of the oscillations and by the damping effects, which would introduce non-linear terms into the equations.

The solutions give the variations of the amplitudes $\xi_r(r)$, $P'(r)$ with radius r; the variations $\varrho'(r)$, $T'(r)$ are also obtained from (16.51) and the equation of state. The temporal variations of the solutions are expressed by (16.42). Solutions only exist for some values of the frequency ω_n, which are called eigenvalues. They correspond to the stationary oscillation modes, i.e., when an integer or another specific number of wavelengths is taking place within the resonant cavity at the considered frequency (Sect. 16.2.5). Mathematically, this is expressed by the fact that the solution of the Legendre equation only exists for values of some integer numbers and such problems are known as a Sturm–Liouville problem (see also Sect. 15.2.2).

The coefficients of the equations depend on the run of four variables ϱ, P, g and Γ_1, of which only two are independent. If the density distribution $\varrho(r)$ is given, in a spherical star the gravity is defined everywhere and in turn the pressure is obtained by integration of the equation of hydrostatic equilibrium from the stellar surface.

Thus, only $\varrho(r)$ and Γ_1 define the oscillation frequencies and the relative amplitudes of the variables. Other pairs of variables may be chosen. For example, in the pair (ϱ, Γ_1) one may replace ϱ by c_S and get a function of (c_S, Γ_1), since the sound speed depends on (P, ϱ, Γ_1) (C.26). In stars where the law of perfect gas applies, the sound speed behaves like $c_S \sim \sqrt{T/\mu}$. The adiabatic exponent Γ_1 is close to $5/3$ except in the ionization zones (see Fig. 7.4), where it depends on the chemical composition. This implies that the solutions mainly depend on the run of c_S through the star.

It is interesting to compare the horizontal and radial amplitudes of the oscillations at the stellar surface. Expression (16.49) determines the horizontal amplitude, while the requirement (16.61) of null pressure perturbation at the surface gives the vertical amplitude. The ratio is

$$\frac{\xi_h}{\xi_r} = - \left(\frac{1}{r\omega^2 \varrho} \frac{dP}{dr} \right)_R = \frac{g}{R\omega^2} \approx \left(\frac{v_0}{\omega} \right)^2 , \qquad (16.62)$$

where v_0 is the fundamental frequency of pulsation (cf. Sect. 15.5.1). Thus, the ratio of the horizontal to the vertical amplitude is of the order of the square of the ratio of the fundamental frequency of the star (see 15.85) to the considered oscillation frequency. This means that the 5 min oscillation has relatively small horizontal amplitude with respect to vertical amplitude. At the same time, the radial amplitude relatively decreases for large ℓ.

The kinetic energy of an oscillation is by definition

$$E_{\text{kin}} = \frac{4\pi}{2} \int_0^R < |\boldsymbol{v}|^2 > \varrho \, r^2 dr , \qquad (16.63)$$

where $\boldsymbol{v}$ is the displacement velocity. The square average velocity is

$$< |\boldsymbol{v}|^2 > = \frac{< |\boldsymbol{\delta r}|^2 >}{\omega^2} , \qquad (16.64)$$

where $\boldsymbol{\delta r}$ is given by (16.50). This means that the kinetic energy of the oscillations depends on the square of the radial and horizontal amplitudes.

16.2.3 Simplification to a Second-Order Equation

One can bring some further simplifications in the system of equations of Sect. 16.2.1 without losing the physical essence of the problem. In addition to the adiabatic assumption, we now assume that the perturbations of the gravitational potential are negligible, a hypothesis which is known as Cowling approximation. It rests on the fact that in many cases the perturbations of the potential are negligible with respect to those of the local density. This is particularly the case when the spherical harmonic degree ℓ, which is the number of nodes at the stellar surface (cf. Sect. 16.2.5), is large, also when the radial order n (i.e., the number of nodes present in

the vertical direction) is high. In both cases, the spherical deviations from spherical symmetry cancel each other so that the resulting effects on the potential are negligible. Cowling's assumption reduces the number of equations from four to two, which considerably simplifies the discussion.

Introducing the pressure scale height H_P in (16.52) and (16.57), we have

$$\frac{dP'}{dr} = -\frac{1}{\Gamma_1 H_P} P' + \varrho \, \xi_r \left(\omega^2 - N_{\mathrm{ad}}^2 \right) , \tag{16.65}$$

$$\frac{d\xi_r}{dr} = -\left(\frac{2}{r} - \frac{1}{\Gamma_1 H_P} \right) \xi_r + \frac{1}{\varrho} \left[\frac{\ell(\ell+1)}{\omega^2 r^2} - \frac{1}{c_S^2} \right] P' . \tag{16.66}$$

These two equations are the more general forms of the adiabatic Cowling approximation. The pressure scale height is generally large with respect to the vertical wavelength of the oscillations, particularly for high radial modes. This is however not true at the stellar surface. The physics of the oscillation at the stellar surface is evidently important and this will be discussed in Sect. 16.3.3. The term $2/r$ is small, except near the center, with respect to the wavelength of the oscillation. Thus, we may make the corresponding simplifications, subject to the limitations indicated. This forms the basis of the so-called asymptotic theory of nonradial oscillations:

$$\frac{dP'}{dr} = \varrho \, \xi_r \left(\omega^2 - N_{\mathrm{ad}}^2 \right) , \tag{16.67}$$

$$\frac{d\xi_r}{dr} = \frac{1}{\varrho} \left[\frac{\ell(\ell+1)}{\omega^2 r^2} - \frac{1}{c_S^2} \right] P' . \tag{16.68}$$

We take P' from the second equation and introduce it in the first one and also neglect the derivatives of the quantities at equilibrium; we get a second-order equation for the vertical perturbations:

$$\frac{d^2 \xi_r}{dr^2} = \frac{\omega^2}{c_S^2} \left(1 - \frac{N^2}{\omega^2} \right) \left(\frac{S_\ell^2}{\omega^2} - 1 \right) \xi_r , \tag{16.69}$$

where S_ℓ is the Lamb frequency (16.56). There, a term $(d\xi_r/dr)(1/\varrho)(d\varrho/dr)$ has been neglected. When ξ_r is obtained, the horizontal amplitude is given by (16.49). The other variables P', ϱ', T' are obtained by (16.68), (16.51) and the equation of state (7.63), respectively.

The oscillation properties depend on the Brunt–Väisälä and Lamb frequencies, $N(r)$ and S_ℓ. The previous equation can be written as

$$\frac{d^2 \xi_r}{dr^2} = -K(r) \, \xi(r),$$

$$\text{with} \quad K(r) = \frac{\omega^2}{c_S^2} \left(\frac{N_{\mathrm{ad}}^2}{\omega^2} - 1 \right) \left(\frac{S_\ell^2}{\omega^2} - 1 \right) . \tag{16.70}$$

The sign of K determines the types of solution for ξ_r. One has the following possibilities:

– **K positive $\implies \xi_r$ is oscillating.** This occurs when

1) $|\omega|$ is greater than both $|N_{\mathrm{ad}}|$ and $|S_\ell|$ or
2) $|\omega|$ is smaller than both $|N|$ and $|S_\ell|$.

The oscillations are trapped in the zone limited by the points where $K(r) = 0$, which defines the turning points of the waves. Conditions (1) and (2) define very different types of oscillations.

Condition (1) defines high-frequency oscillations. These are acoustic or p mode oscillations, moving at the sound speed and where the restoring force is pressure (see Sect. 16.3). These modes are discussed in Sect. 16.3.

Condition (2) defines lower frequency oscillations. These are gravity or g modes, characterized by the Brunt–Väisälä, where the restoring force is gravity (see Sect. 5.1).

– **K negative $\implies \xi_r$ varies exponentially.** This occurs when

3) $|N_{\mathrm{ad}}| < |\omega| < |S_\ell|$ or
4) $|N_{\mathrm{ad}}| > |\omega| > |S_\ell|$.

These conditions fix the regions where the modes oscillate or vary exponentially. The exponential variation is generally a decline, unless there is a dynamical instability.

16.2.4 Domains of the Acoustic and Gravity Modes

Let us consider a small horizontal iron plate oscillating in a swimming pool. For oscillations frequencies lower than a limit ω_{ac}, the water is simply pushed upward and downward before equilibrium is restored by gravity forces. Gravity waves are generated; their basic frequency is the Brunt–Väisälä frequency N_{ad}. At the opposite, for oscillation frequencies above ω_{ac}, the medium is compressed by the plate motions before it has time to move; thus acoustic waves propagate. The cutoff frequency ω_{ac} will be further derived in Sect. 16.3.3; however a simple argument also provides it. In a stratified medium with a scale height H_P, if the timescale of the displacement of a cell in the middle of the layer is longer than the time taken by a sound wave to go back and forth through the medium, a gravity wave is produced. If the timescale is shorter than the travel time of the sound, one has an acoustic wave. Thus, the cutoff frequency separating the two cases is for a medium of perfect gas

$$\omega_{\mathrm{ac}} = \frac{c_{\mathrm{S}}}{2H_P} = \left(\frac{\gamma_{\mathrm{g}}\mathcal{R}T}{\mu}\right)^{1/2}\frac{\mu g}{2\mathcal{R}T} = \frac{g}{2}\left(\frac{\gamma_{\mathrm{g}}\mu}{\mathcal{R}T}\right)^{1/2} = \frac{\gamma_{\mathrm{g}}g}{2c_{\mathrm{S}}}, \qquad (16.71)$$

where $\mathcal{R}$ is the gas constant. Near the stellar surface, as T decreases rapidly, the cutoff frequency rises fast. This fast growth constitutes the limit of acoustic waves near the surface. In the atmosphere of the Sun, $\omega_{ac} \approx 0.03 \text{ s}^{-1}$, which corresponds to a period $P = 1/\nu = 2\pi/\omega \approx 200$ s.

Let us now examine the behavior of the other key frequencies which determine the nature of the waves.

- The Brunt–Väisälä N_{ad} (Sect. 5.1). Figure 16.1 shows its behavior in a solar model. At the very center, the gravity tends toward zero, which makes $N_{ad} \to 0$. N_{ad}^2 is then positive, as expected in a radiative zone. Slightly away from the center, N_{ad} reaches its highest value due to the μ gradient near the center. Then, N_{ad} decreases because the μ gradient vanishes and also because the gravity decreases. Indeed for the law of perfect gas, one can write $N_{ad}^2 = (g^2\varrho/P)(\nabla_{ad} - \nabla + \nabla_\mu)$. As r increases, g^2 decreases while (ϱ/P) does not change very much; thus N_{ad}^2 slightly decreases outward. It sharply becomes zero at the edge of radiative zone to become negative in the outer solar convective envelope.
- The Lamb frequency S_ℓ. It is defined by (16.56) and scales like $\sqrt{T/(\mu r^2)}$ and thus it continuously decreases outward as shown in Fig. 16.1. The acoustic wave with a given spherical harmonic degree ℓ must lie above the corresponding curve S_ℓ in Fig. 16.1. For $\ell = 1$, we see that the S_ℓ curve in Fig. 16.1 is partly below that of N_{ad}; this means that the wave of the corresponding frequencies have their inner turning point at the surface $N_{ad} = 0$.

The corresponding domains are illustrated in Fig. 16.1. According to condition (1) in Sect. 16.2.3, the acoustic modes occur mainly in the convective envelope of the Sun and over a part of the inner radiative region, depending on the ℓ value (with
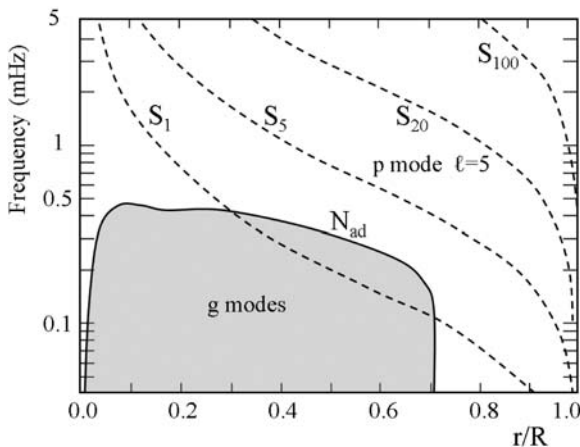
Fig. 16.1 Variations of the Brunt–Väisälä N_{ad} and of the Lamb $S_\ell(r)$ frequencies for various values of ℓ as a function of the radius in the solar model. The g-mode trapping region is indicated by a gray area. The outer convection extends from this zone to the surface. The trapping regions are also limited by the acoustic cutoff frequency (cf. Fig. 16.8). Adapted from J. Christensen-Dalsgaard [131]
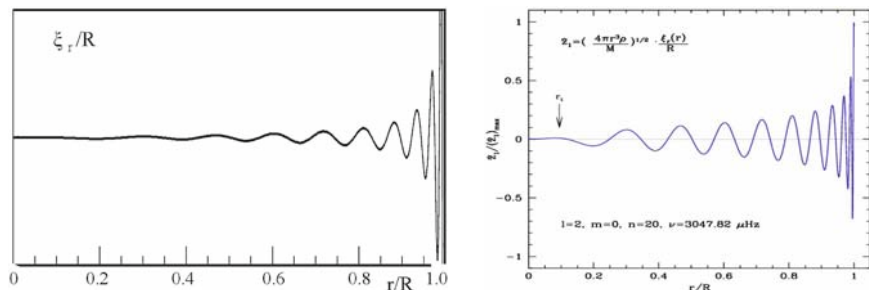
Fig. 16.2 *Left*: the relative amplitude ξ_r/R as a function of the radius in a solar model, $n = 20$ and $\ell = 2$. The amplitude decreases fast with depth. *Right*: oscillation amplitude for the case $n = 20$ and $\ell = 2$, but with a normalization by the square root of the inner density. Courtesy of P. Eggenberger [169]

variable amplitudes, cf. Fig. 16.2). Near the surface, the rise of ω_{ac} constitutes the limit, as shown in Fig. 16.8.

Figure 16.1 shows where according to condition (2) the g modes can propagate. The corresponding zone lies where N_{ad}^2 is positive, i.e., in the radiative interior of the Sun. The domain of g modes is also limited by the Lamb frequency, depending on the ℓ number. However, except for $\ell = 1, 2$ this makes no change, as it can be seen in Fig. 16.1.

16.2.5   The Degree ℓ and Radial Order n

Here we examine in more detail the significance of the various quantum numbers appearing in the above developments. The spherical harmonic degree ℓ appears in the system of equations (16.52) and (16.57) or in the second-order equation (16.70), and thus it directly influences the solutions for ξ_r and the other variables. From the properties of the Legendre polynomials and the study of their zeros, one learns that the degree ℓ is the number of nodes on the surface, i.e., the locations where the amplitudes are zero. This can also be seen in a simple way by the local identification (16.41) of the nonradial component with a plane wave at the stellar surface R:

$$k_h = \frac{2\pi}{\lambda_h} = \frac{\sqrt{\ell(\ell+1)}}{R} \ . \tag{16.72}$$

For large ℓ, this gives

$$\ell \, \lambda_h \approx 2\pi R \ , \tag{16.73}$$

which shows that there are about ℓ wavelengths λ_h of frequency ω over the stellar circumference.

The equations (16.52) and (16.57) or (16.70) subject to the boundary conditions (16.59) and (16.61) admit solutions only for some specific frequencies ω_n of "eigenmodes" corresponding to stationary waves. In a resonant cavity, interferences can be constructive or destructive. Stationary waves survive only for constructive interferences, which occur for some frequencies such that there is a specific number of half-wavelengths $\lambda/2$ in the cavity. In principle, for a liquid in a basin, one should have a node at the two extremities, i.e. there should be an integer number of half-wavelengths in the cavity. In a gas, the situation is different, because there is no steady wall at the reflexion point. Beyond this point, the wave becomes evanescent with an amplitude decreasing exponentially. Thus at a reflexion point, the wave must match an exponential decline over a distance more or less of $(1/4)\lambda$ as shown in Fig. 16.3. This means that only oscillations with a number $(n/2+1/4)\lambda$ in the cavity can be resonant. Therefore the integration of the wave number radially for a stationary wave must satisfy the condition

$$\int_0^R k_r \, dr = \left(\frac{n}{2}+\frac{1}{4}\right) 2\pi = \left(n+\frac{1}{2}\right)\pi . \tag{16.74}$$

This will be further studied in the asymptotic theory (Sect. 16.4.1). Number n is the number of zero along the stellar radius without counting the center and the surface. The value $n = 0$ corresponds to the fundamental radial mode, for which the period P_0 is the travel time of the sound wave from the surface to the center and return,

$$P_0 = 2 \int_0^R \frac{dr}{c_S} . \tag{16.75}$$
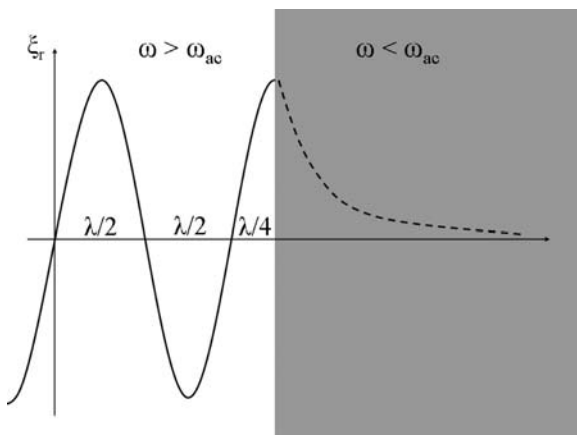
Fig. 16.3 Schematic representation of the boundary of a propagation zone of p modes. There is an integer number of $\lambda/2$, plus a fraction of $\sim (1/4)\lambda$ in the cavity. At the boundary, the stationary waves match an exponential decrease

This period is of the order of the dynamical timescale of the star (1.28).

The amplitude of a stationary wave for a nonradial p-mode oscillation is illustrated as a function of the radius in the Sun by Fig. 16.2, left. As the density increases with depth the oscillation amplitude declines. Figure 16.2, right, shows the same with a weighting by the square root of the inner density at the considered point, in agreement with the behavior of the energy of an oscillation mode.

The number m, which appears in the spherical harmonics (16.38), is absent in non-rotating star, since there is no particular axis of symmetry. It only appears in rotating stars (cf. Sect. 16.6); it is called the azimuthal number and corresponds to the number of nodal lines which cross the equator. In summary, the n, ℓ, m numbers represent

– **n**: the radial order, which is the number of nodal lines ($v = 0$) along the stellar radius, without counting the center and the surface.
– **ℓ**: the degree ℓ is the number of nodal lines on the surface of the star.
– **m**: the azimuthal order, i.e., the number of nodal lines crossing the equator.

A few didactic examples of oscillations in the acoustic modes for a solar-type star are given in Figs. 16.4 and 16.5 for different values of ℓ and m.

ℓ=2, m=1   ℓ=2, m=2

ℓ=5, m=5   ℓ=10, m=5
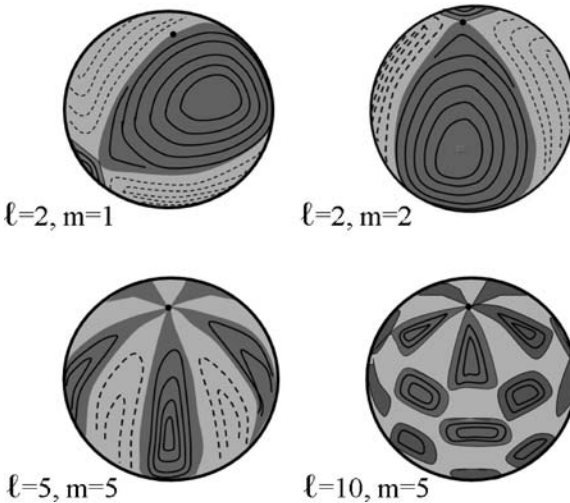
Fig. 16.4 Schematic illustration of some acoustic modes of different spherical harmonic degrees ℓ and azimuthal numbers m. Number ℓ gives the number of nodal lines (places where $v = 0$) and m the number of nodal lines crossing the equator. The darker areas moves upward while the clearer ones moves downward. The black dots show the point where the rotation axis crosses the surface

$$\ell = 10, m = 6$$
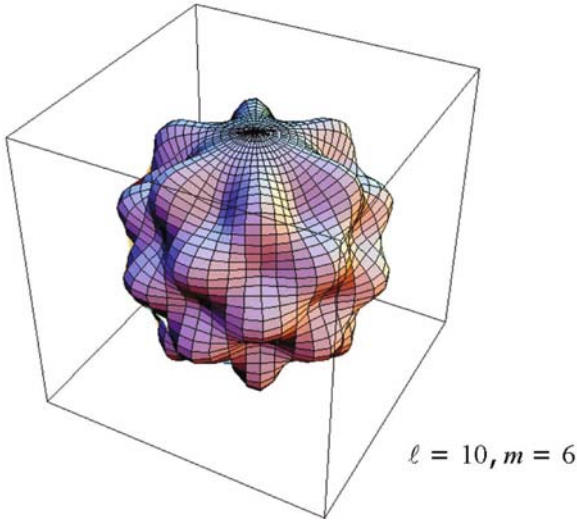
Fig. 16.5 Schematic illustration of the oscillation acoustic modes of a solar-type star with $\ell = 10$ and $m = 6$. The amplitudes are strongly exaggerated. Courtesy from P. Eggenberger [169]

16.3   Properties of Acoustic or p Modes

The p modes are present between the surface and a inner point called the turning point r_t where the wave frequency is equal to the Lamb frequency. Thus p modes occur in the outer convective envelope of the Sun and in a part of the radiative interior, as illustrated in Fig. 16.1.

16.3.1   Inner Turning Points of p Modes

Expressions (16.70) together with (16.56) define the inner turning point:

$$\frac{c_S^2(r_t)}{r_t^2} = \frac{\omega^2}{\ell(\ell+1)} \ . \tag{16.76}$$

Taking into account that for such modes $\omega \gg N$, $K(r)$ simplifies to

$$K(r) = \frac{1}{c_S^2} \left(\omega^2 - S_\ell^2\right) \ . \tag{16.77}$$

As S_ℓ depends on c_S, we see that the p modes are entirely determined by the sound velocity. Thus, these observed oscillations are stationary acoustic waves,
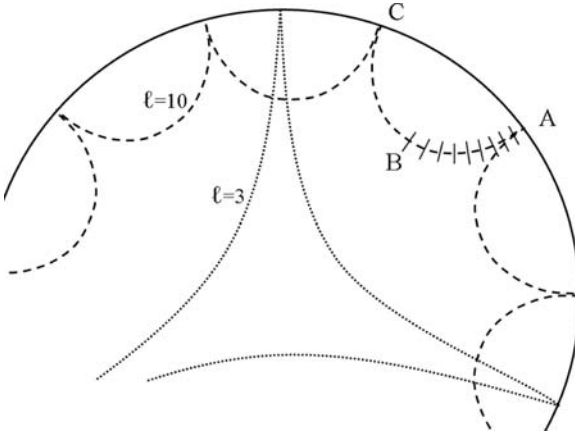
Fig. 16.6 Schematic illustration of mode propagation for $\ell = 10$ and $\ell = 3$. A wave front propagating from A progressively deviates more and more from the radial direction, as the sound speed becomes higher with depth. It reaches its turning point in B before turning back to C. The modes of lower ℓ have a deeper turning point for a given oscillation frequency

where the recall force is the internal pressure. Equation (16.77) can be obtained directly from the dispersion relation for a plane wave (C.29),

$$\omega^2 = c_S^2 \, |\boldsymbol{k}|^2 \, , \tag{16.78}$$

with $|\boldsymbol{k}|^2 = k_r^2 + k_h^2$ when separated into its radial and horizontal components. With (16.78) and the expression of k_h given by (16.41), one has

$$\frac{\omega^2}{c_S^2} = k_r^2 + \frac{\ell(\ell+1)}{r^2} \, , \tag{16.79}$$

which is equivalent to $k_r^2 = \frac{1}{c_S^2} \left(\omega^2 - S_\ell^2 \right)$. This means that one can identify $k_r^2 = K(r)$ and Eq. (16.77) is recovered. This identification is also evident from (16.70) if we develop ξ_r as $e^{ik_r r}$. It confirms that these modes are acoustic waves. Consistently at the inner turning point one has $k_r^2 = 0$, which means that there is no inward propagation.

The propagation of nonradial waves can be illustrated by analogy with the refraction in optics. Let us consider a beam reaching the surface of water with some incidence angle. As the refraction index in water is higher than in air, the beams travels in water with a smaller deviation from vertical than in air. Conversely, when a beam enters a medium with a lower refraction index (i.e., where the travel speed is higher), the deviation from vertical increases.

Similarly, the inward traveling acoustic waves meet higher and higher sound speed, which goes like $\sqrt{T/\mu}$. Thus, if there is a nonradial component, the waves are refracted and they deviate more and more from the local vertical direction, until they reach their turning point, for example at point B in Fig. 16.6. This turning point
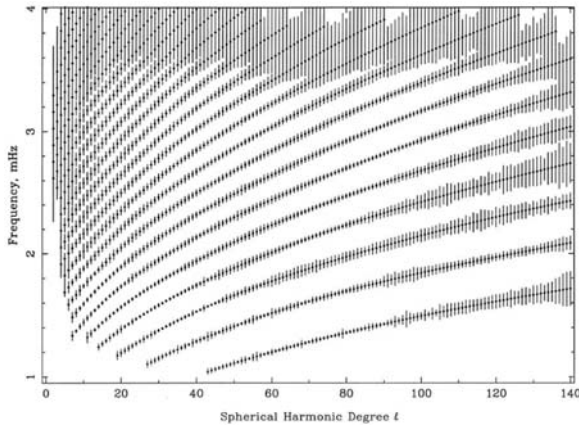
Fig. 16.7 The solar p modes observed at Big Bear Solar Observatory from K.G. Libbrecht and M.F. Woodard [325, 327]. Each parabolic line corresponds to a fix number n; the lowest line is for $n = 1$. The small vertical line show the $1\,\sigma$ error bar enlarged by a factor 10^3. With permission

for a given ℓ value is defined by condition (16.76); there, one has $k_r = 0$ and there is no further radial propagation. The location r_t of the turning point depends on both ℓ and on the considered frequency ω. Expression (16.76) and Fig. 16.6 show that the turning points are much deeper for lower ℓ values at a given frequency. Thus, each oscillation of a given ω and ℓ has its own resonant cavity.

16.3.2   Properties of the Solar Cavity: Parabolic Relations

Helioseismological analyses have permitted very accurate determinations of oscillations frequencies, in particular at Big Bear Solar Observatory [326]. There are remarkable relations in the plot of the various observed frequencies ν as a function of the spherical harmonic degree ℓ. Indeed, ℓ is not an "observation". What is observed is the horizontal length scale of the oscillation on the solar disk, to which a wave number k_h can be associated by (16.41) and thus an ℓ value. Figure 16.7 shows such a relation, ℓ is represented as a continuous function, but only integer values are present.

Numerical models of oscillations based on the equations of Sect. (16.2) provide solutions which allow us to very closely reproduce the observed parabolic relations of Fig. 16.7. This agreement was decisive in the identification of the nature of the solar oscillations.

Several properties of the solar resonant cavity, for example the change of the penetration depth of the acoustic mode as a function of ℓ and the parabolic relations between the frequencies and the horizontal wavelength (or k_h or ℓ), can be reproduced by a relatively simple analytical model [322]. The approximations made here apply for large ℓ values as observable in helioseismology and not for low ℓ values as

in asteroseismology (Sect. 16.4). The resonant cavity lies between the surface (more exactly the location where the acoustic frequency strongly rises, cf. Sect. 16.3.3) and the inner layer where the cyclic wave frequency ω is equal to the Lamb frequency. From (16.76) and (16.41), the inner turning point r_t is given by

$$c_S(r_t) = \left(\frac{\omega}{k_h}\right) , \tag{16.80}$$

for given values of ω and k_h. Let us make the approximation that the T gradient is constant and equal to the adiabatic gradient and that the equation of state is that of a perfect gas. At a depth δz below the surface (z increasing with depth), one has

$$T = \left(\frac{dT}{dr}\right)_{ad} \delta z \quad \text{with} \quad \left(\frac{dT}{dr}\right)_{ad} = \frac{T}{P}\nabla_{ad}\frac{dP}{dz} = \mu\frac{\gamma_g - 1}{\gamma_g \mathcal{R}} g = \frac{g}{c_P}, \tag{16.81}$$

where we have used (3.77). The gravity is the average value within the considered depth. At depth δz, the sound speed is given by Appendix (C.3):

$$c_S^2 = \frac{\gamma_g \mathcal{R} T}{\mu} = \gamma_g (c_P - c_V) \left(\frac{g}{c_P}\right) \delta z = (\gamma_g - 1)\, g\, \delta z . \tag{16.82}$$

Now, with (16.81) the depth of the cavity for a wave of frequency ω and horizontal number k_h becomes

$$\delta z = \frac{\omega^2}{(\gamma_g - 1)\, g\, k_h^2} . \tag{16.83}$$

The larger the k_h, i.e., the shorter the horizontal wavelength, the smaller the penetration δ of the considered mode, as illustrated in Fig. 16.6.

The period of the nonradial modes must satisfy condition (16.74), which imposes that the resonant cavity contains an odd number of $\lambda/4$ (Fig. 16.3):

$$(2n+1)\frac{\pi}{2} = \int_{r_t}^{R} k_r dr = \omega \int_{r_t}^{R} \frac{dr}{c_S} = \frac{\omega}{[(\gamma_g - 1)g]^{1/2}}\int_{r_t}^{R}\frac{dr}{\delta z^{1/2}} , \tag{16.84}$$

where we have used (16.80) and (16.82). Now, the integration of δz in the vertical direction gives

$$(2n+1)\frac{\pi}{2} = \frac{\omega}{[(\gamma_g - 1)g]^{1/2}}\, 2\,\delta z^{1/2} = \frac{2\,\omega^2}{(\gamma_g - 1)\, g\, k_h} , \tag{16.85}$$

with (16.83), where we also call δz the depth down to the return point. This gives for the mode with radial number n and horizontal number k_h,

$$\omega_n^2 = \frac{\left(n+\frac{1}{2}\right)\pi(\gamma_g - 1)g k_h}{2} \approx \left(n+\frac{1}{2}\right)g k_h = \left(n+\frac{1}{2}\right)g\frac{\sqrt{\ell(\ell+1)}}{r} , \tag{16.86}$$

where we make the approximation $\pi(\gamma_g - 1)/2 \approx 1$. This corresponds to the relations illustrated in Fig. 16.7. At large degree ℓ, these relations are close to parabolic $\omega^2 \sim \ell$. To each ℓ value correspond a certain k_h and a certain horizontal wavelength λ_h. For example, $\ell = 10, 100, 200$ correspond to $k_h \approx (0.014, 0.14, 0.29) \times 10^{-6}$ m^{-1} and $\lambda_h = 4.49 \times 10^5, 4.49 \times 10^4, 2.2 \times 10^4$ km, respectively. The power in the oscillations is essentially concentrated between 2 and 4 mHz and ℓ between 40 and 100. The space between the ridges decreases with increasing n values, as is evident from the expression of the spacing of the frequencies with n:

$$\frac{d\omega}{dn} = \frac{gk_h}{2\,\omega} = \frac{\omega}{2n+1} \,, \tag{16.87}$$

which behaves like $1/\sqrt{n}$ for large n.

The depth δz to which a given mode (n, ℓ) is going depends on both parameters. From (16.83) and (16.86) without the approximation, we get

$$\delta z = \frac{\left(n + \frac{1}{2}\right)\pi}{2\,k_h} = \frac{\left(n + \frac{1}{2}\right)\lambda_h}{4} = \frac{\left(n + \frac{1}{2}\right)\pi r}{2\sqrt{\ell(\ell+1)}} \,. \tag{16.88}$$

This shows that modes of higher n and lower ℓ provide deeper tests of the stellar conditions. This last expression provides an estimate of the depth reached by each mode in Fig. 16.7.

The observed surface variations in velocity and radiation are the summing up of 10^7 nonradial waves. The major solar oscillations correspond to $\ell = 10^2$–10^3, while the n values are mainly between 2 and 15.

Since g is the mean gravity over the propagation domain of the wave, the above development is not valid for too deep turning points. Thus, they apply only to modes confined not too far from the solar surface, i.e., for high ℓ values as observed in helioseismology. For asteroseismology, only small ℓ values are observable and different approximations have to be made (Sect. 16.4).

16.3.3   Behavior of p Modes at the Surface

In Eqs. (16.65) and (16.66), the pressure scale height and radius r were considered as large with respect to the oscillation wavelengths. Near the surface, H_P is small and the terms in H_P^{-1} can no longer be neglected. We assume that the law of perfect gas applies in the outer layers of solar-type stars with a constant μ. The atmosphere is considered to be isothermal and the effects of ionization are neglected, which are rather rough simplifications. The equation of hydrostatic equilibrium can be written as

$$\frac{dP}{dr} = -g\varrho = -\frac{P}{H_P} \tag{16.89}$$

from (1.5) and (5.24). The law of perfect gas with constant T implies that P varies like ϱ. Thus, the pressure and density-scale heights are the same and can be represented by

$$H = H_\varrho = \frac{P}{\varrho\, g} = \frac{kT}{g\mu m_{\mathrm{u}}} \,. \tag{16.90}$$

The extent of the atmosphere is negligible with respect to the radius; thus g can be taken as a constant. With a constant T we also have a constant H or H_P. The integration of the equation of hydrostatic equilibrium gives

$$P(h) = P(0)\, e^{-h/H}, \quad \text{and} \quad \varrho(h) = \varrho(0)\, e^{-h/H}, \tag{16.91}$$

with $h = r - R$ being positive above the photospheric radius R and negative below it.

In general, the perturbations, as in the case of convection, are non-adiabatic in the outer stellar layers. However, consistently with the assumption of a constant T, we also consider that the perturbations do not lose energy in the surrounding medium and we thus apply the adiabatic equations (16.65) and (16.66). We use (16.91) and ignore the term $2/r$, which is small and constant in the atmosphere; one has

$$\frac{dP'}{dh} = -\frac{1}{\Gamma_1 H} P' + \varrho(0) e^{-h/H} \left(\omega^2 - N_{\mathrm{ad}}^2\right) \xi_r, \tag{16.92}$$

$$\frac{d\xi_r}{dh} = \frac{1}{\Gamma_1 H}\xi_r + \frac{1}{\varrho(0) e^{-h/H} c_{\mathrm{S}}^2} \left(\frac{S_\ell^2}{\omega^2} - 1\right) P',$$

$$= \frac{1}{\Gamma_1 H}\xi_r + \frac{1}{\Gamma_1 P(0)} \left(\frac{k_h^2 c_{\mathrm{S}}^2}{\omega^2} - 1\right) e^{h/H} P'. \tag{16.93}$$

Since P and ϱ are expressed by (16.91), the sound velocity (C.26) in the atmosphere becomes $c_{\mathrm{S}}^2 = \Gamma_1 P(0)/\varrho(0)$ and the Brunt–Väisälä frequency (16.53)

$$N_{\mathrm{ad}}^2 = g \left(\frac{1}{\Gamma_1 P}\frac{dP}{dr} - \frac{1}{\varrho}\frac{d\varrho}{dr}\right) = g \left(-\frac{1}{\Gamma_1 H} + \frac{1}{H}\right). \tag{16.94}$$

Consistently with the hypothesis of constant T, which implies a similar behavior of $P(h)$ and $\varrho(h)$, we have

$$\Gamma_1 = 1, \quad N_{\mathrm{ad}}^2 = 0 \quad \text{and} \quad c_{\mathrm{S}}^2 = P_0/\varrho_0. \tag{16.95}$$

The above relations (16.92) and (16.93) simplify to

$$\frac{dP'}{dh} = \varrho(0) e^{-h/H} \omega^2 \xi_r - \frac{P'}{H}, \tag{16.96}$$

$$\frac{d\xi_r}{dh} = \frac{\xi_r}{H} + \frac{1}{P(0)} \left(\frac{k_h^2 c_{\mathrm{S}}^2}{\omega^2} - 1\right) e^{h/H} P'. \tag{16.97}$$

In the first of these two equations, we see that the gradient of the pressure perturbation is composed of two terms:

- The first one is the effect of the oscillatory displacement on the pressure gradient; this was the only term considered in the simple model of adiabatic oscillation (16.67).
- The second term is the effect of the pressure perturbation on the gradient of pressure perturbation. Indeed, this effect was already accounted for in expressing $P(r,t)$ by (16.91); thus the exponential decline of the perturbation of pressure is already present in the first term of (16.96). Therefore, to be coherent, we must not include the term responsible for the exponential decrease of P' a second time. Therefore we keep the equation for P' in the form given by (16.67).

From the second expression, we can express P' and introduce it in Eq. (16.67); we get

$$P(0)\frac{d^2\xi_r}{dr^2} - \frac{P(0)}{H}\frac{d\xi_r}{dh} - \varrho(0)\,\omega^2\left(\frac{k_h^2 c_S^2}{\omega^2} - 1\right)\xi_r = 0. \tag{16.98}$$

With the acoustic cutoff frequency $\omega_{ac} = c_S/(2H)$ defined above (16.71) and (16.95), the previous equation can be written:

$$\frac{d^2\xi_r}{dr^2} - \frac{1}{H}\frac{d\xi_r}{dh} + \frac{1}{H^2}\left(\frac{\omega^2}{4\,\omega_{ac}^2} - k_h^2 H^2\right)\xi_r = 0, \tag{16.99}$$

which is the equation of a harmonic oscillator with damping. We search a solution of the form $\xi_r = e^{ah/H}$, which introduced in (16.99) gives

$$a^2 - a + \left(\frac{\omega^2}{4\,\omega_{ac}^2} - k_h^2 H^2\right) = 0. \tag{16.100}$$

This second-degree equation has for solution

$$a_{\pm} = \frac{1}{2} \pm \frac{1}{2}\sqrt{1 - \frac{\omega^2}{\omega_{ac}^2} + 4k_h^2 H^2}. \tag{16.101}$$

The general solution is a combination of the above two solutions:

$$\xi_r = c_+ e^{h/(2H)\left(1 + \sqrt{1 - \frac{\omega^2}{\omega_{ac}^2} + 4k_h^2 H^2}\right)} + c_- e^{h/(2H)\left(1 - \sqrt{1 - \frac{\omega^2}{\omega_{ac}^2} + 4k_h^2 H^2}\right)}, \tag{16.102}$$

and c_+ and c_- are constants which are not fixed in this linear approximation. The term under the square root determines the nature of the perturbation:

- If $\left(1 - \frac{\omega^2}{\omega_{ac}^2} + 4k_h^2 H^2\right) > 0$, the solution is real and we have an exponential motion. The perturbation leads to an exponential displacement of the matter in the atmosphere.

– If $\left(1 - \frac{\omega^2}{\omega_{ac}^2} + 4k_h^2 H^2\right) < 0$, the solution is complex. The perturbation leads to a
wave propagating through the medium.

The critical solution separating the two regimes is given by

$$4k_h^2 H^2 = \frac{\omega^2}{\omega_{ac}^2} - 1 \quad \text{or} \quad k_h^2 = \frac{\omega^2 - \omega_{ac}^2}{c_S^2} , \qquad (16.103)$$

where (16.71) has been used. This is the dispersion relation of the horizontal components of the waves on a spherical surface corresponding to the adopted representation (16.42). Let us note that the complete dispersion relation accounting also for the vertical propagation would be

$$k_r^2 + k_h^2 = \frac{\omega^2 - \omega_{ac}^2}{c_S^2} . \qquad (16.104)$$

In order to have propagation, the left member of (16.104) must be positive; thus the propagation of acoustic waves only occurs for $\omega > \omega_{ac}$, the minimum frequency of propagating waves. This property is quite consistent with the above definition of ω_{ac} (16.71). At frequencies lower than ω_{ac}, there is no acoustic wave, but a matter displacement. These displacements may produce shocks and energy losses, which contribute to the heating of the chromosphere.

Apart from the term with the square root, the solution (16.102) contains exponential terms of the form $e^{h/(2H)}$ which grow exponentially toward the exterior. This is a consequence of the exponential decrease in density, because the energy density of the oscillation, which behaves like $\varrho\,\xi_r^2$, remains about constant in the zone where the oscillation propagates on account of (16.102) and (16.96). Outside this zone, when $\omega < \omega_{ac}$, the perturbation amplitude decreases exponentially, as described by solution c_- which is the only one present in this case.

Near the center, $\omega_{ac} \to 0$ because the gravity tends toward zero (cf. 16.71). The growth of the gravity in the center makes ω_{ac} to first increase steeply, before decreasing slowly as the gravity outward diminishes, while the changes of T remain limited. In the external layers, the rapid decrease of T makes ω_{ac} to rise fast near the surface. This forms the reflexion surface for a wide range of p modes with frequencies below 5 mHz (3 min). This frequency limit corresponds to the minimum of temperature of about 4500 K at the border of the photosphere and the chromosphere. Figure 16.8 shows the propagation domain of p modes with $\ell = 2$. Toward the exterior, this domain is limited by the acoustic cutoff frequency ω_{ac}, while toward the interior the Lamb frequency is the limit (see Sect. 16.2.3).

The oscillations with periods shorter than 3 min can go further outside. Beyond the photospheric minimum, the temperature rises again in the chromosphere before reaching up to 3×10^6 K in the solar corona; thus ω_{ac} decreases again and allows a chromospheric resonant cavity for p modes. The transit from the inner to the outer cavity is possible for oscillations with frequencies higher than 3 mHz.
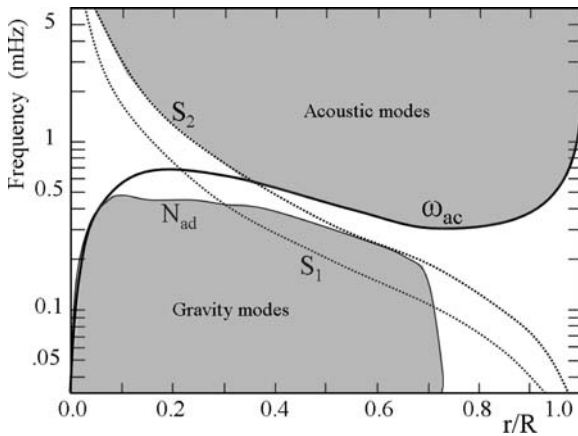
Fig. 16.8 The acoustic cutoff frequency ω_{ac} is represented by a thick line as a function of the solar radius in the present solar model. The Lamb frequencies for $\ell = 1, 2$ and the adiabatic Brunt–Väisälä frequency N are also shown. The zone of propagation of g and p modes with $\ell = 2$ are indicated by gray areas. The zone of p modes is limited near the surface by ω_{ac} and by the Lamb frequency of the corresponding ℓ in the interior (see also Fig. 16.1). For $\ell = 1, 2$, the g modes are also limited by S_1 and S_2. Adapted from P. Eggenberger [169]

16.3.4   Excitation and Damping

The energy density of a mode is concentrated in the region where it propagates. Outside this region, the oscillations decrease exponentially. In particular, the main oscillation of 5 min is evanescent in the photosphere, because the acoustic cutoff frequency ω_{ac} is higher than this value. This means that this oscillation is observed with a reduced amplitude.

The source of the excitation of the acoustic modes is likely the convective motions in the envelope of solar-type stars. Instabilities in the regions of partial ionization of hydrogen and helium may also favor the driving. The modes with small k_h and high periods go deeply and experience some radiative damping. The modes which overcome the temperature minimum in the photosphere develop large amplitudes and experience damping by shocks.

The mechanisms of excitation and damping are studied observationally by analyzing the temporal variations of the power spectrum of the oscillations. The results show that the modes with small ℓ decline exponentially with characteristic times of a few days. They are also re-excited on a similar timescale. Therefore, a given oscillation mode maintains its coherence a few days, then it vanishes and the same mode is re-excited with a different phase.

16.4   The Asymptotic Theory of p Modes

The previous developments show the different oscillation modes and their trapping in various regions. The equations are the basis for numerical solutions to be compared with helioseismic and asteroseismic observations. Further developments can be made to obtain analytical expressions, which provide a most useful basis for analyzing the observations.

In Sect. 16.2.3, the two equations (16.52) and (16.57) were combined with some heavy simplifications into one single second-order differential equation for the perturbation ξ_r, which allowed us to get the essence of the problem. However, the simplifications made at the stellar surface, in particular ignoring the terms in H_P^{-1}, do not give a turning point at the surface and thus one cannot directly determine the eigenfrequencies. More accurate second-order differential equations can be derived [131, 585]; we develop one of these in Sect. 17.1.2 for the transport by gravity waves. For values $n \gg \ell$, they have an asymptotic behavior which leads to most useful relations between the frequencies and the quantum numbers. Indeed, various elaborate developments are possible by also including the effects of sphericity and perturbations of the potential [216]. The main problems generally occur at the reflexion points, because the reflexion within a gaseous stratified medium is a complex process.

16.4.1   The Frequencies of p Modes

We adopt here a simple approach, which provides the main quantitative results for the p modes in the asymptotic limit of low ℓ values ($\ell \leq 3$ as observed in asteroseismology). A complete theory with an appropriate treatment of the surface conditions leads to a relation of the form (16.74) with just the factor $1/2$ on the right-hand side replaced by a phase constant α, which depends on both a contribution of $1/(4\lambda)$ coming from the inner turning point r_t and another contribution from the outer turning point (near R).
We have from (16.74) and (16.77), because the p modes have high frequencies,

$$\int_{r_t}^{R} k_r \, dr = \int_{r_t}^{R} K_r \, dr = \int_{r_t}^{R} \left(\omega^2 - S_\ell^2\right)^{1/2} \frac{dr}{c_S} = (n+\alpha)\,\pi\,. \qquad (16.105)$$

With the Lamb frequency (16.56), this can also be written as

$$\int_{r_t}^{R} \left(1 - \frac{\ell(\ell+1)c_S^2}{\omega^2 \, r^2}\right)^{1/2} \frac{dr}{c_S} = \frac{(n+\alpha)\,\pi}{\omega}\,. \qquad (16.106)$$

This is the Duvall relation [161, 167]; it was first discovered from the analysis of the frequencies of the solar oscillations, then confirmed by the asymptotic theory. It relates the frequency ω to the numbers n and ℓ. With a few developments, this

relation leads to interesting results supported by both observations and numerical models. We see that r_t is a function of $w \equiv \omega/\sqrt{\ell(\ell+1)}$. Thus, the Duvall relation can be written as

$$F\left(\frac{\omega}{\sqrt{\ell(\ell+1)}}\right) = \frac{(n+\alpha)\pi}{\omega}, \qquad (16.107)$$

with

$$F(w) = \int_{r_t}^{R} \left(1 - \frac{c_S^2}{w^2 r^2}\right)^{1/2} \frac{dr}{c_S}. \qquad (16.108)$$

We decompose the above integral in various segments as follows:

$$F(w) = \int_{0}^{R} \frac{dr}{c_S} - \int_{0}^{r_t} \frac{dr}{c_S} + \int_{r_t}^{R} \left[\left(1 - \frac{c_S^2}{w^2 r^2}\right)^{1/2} - 1\right] \frac{dr}{c_S}. \qquad (16.109)$$

In the case of asteroseismic observations, only the low-degree modes with $\ell \leq 3$ can be detected; thus the associated inner turning point is very close to the center of the star. The sound speed does not vary much near the center and it can be taken equal to the central value $c_S(0)$; this means that the second integral on the right-hand side can be simplified as

$$\int_{0}^{r_t} \frac{dr}{c_S} = \frac{r_t}{c_S(0)} \approx \frac{\sqrt{\ell(\ell+1)}}{\omega} = \frac{1}{w}, \qquad (16.110)$$

where we have used (16.79). The integrand in the third integral on the right-hand side of (16.109) is small everywhere, except close to r_t (where the parenthesis with power $1/2$ vanishes). The sound velocity c_S is also approximated by its central value. Making the transformation $u^2 = c_S^2(0)/(r^2 w^2)$, we get

$$\int_{r_t}^{R} \left[\left(1 - \frac{c_S^2}{w^2 r^2}\right)^{1/2} - 1\right] \frac{dr}{c_S} \approx \frac{1}{w} \int_{0}^{1} \left(1 - (1-u^2)^{1/2}\right) \frac{du}{u^2}, \qquad (16.111)$$

since we have $dr/c_S(0) = -(1/w)(du/u^2)$. For $r = r_t$, one has $u = 1$, while for $r = R$ we consider that $r \to \infty$, so that $u = 0$. Now, we have

$$\int_{0}^{1} \frac{du}{u^2} = -\frac{1}{u}\Big|_{0}^{1} = -1 + \infty, \qquad (16.112)$$

$$\int_{0}^{1} (1-u^2)^{1/2} \frac{du}{u^2} = -\frac{\sqrt{1-u^2}}{u}\Big|_{0}^{1} - \arcsin u\Big|_{0}^{1} = +\infty - \frac{\pi}{2}. \qquad (16.113)$$

Thus, one has

$$F(w) \approx \int_{0}^{R} \frac{dr}{c_S} - \frac{\pi}{2w} \quad \text{or} \quad \int_{0}^{R} \frac{dr}{c_S} - \frac{\sqrt{\ell(\ell+1)}\pi}{2\omega} \approx \frac{(n+\alpha)\pi}{\omega}, \qquad (16.114)$$

and finally

$$\omega = \frac{\left(n+(\sqrt{\ell(\ell+1)}/2)+\alpha\right)\pi}{\int_0^R \frac{dr}{c_S}} \, . \tag{16.115}$$

The various approximations made introduce a small difference with a more detailed analysis of the central regions, which show that the frequencies are very well described by (16.115) if $\sqrt{\ell(\ell+1)}$ is replaced by $\ell+(1/2)$ [565], which in all cases represents a very small difference. As ω is the cyclic frequency, we write the frequency ν of an oscillation of numbers n and ℓ as

$$\nu_{n\ell} = \frac{\omega_{n\ell}}{2\pi} \approx \left(n+\frac{\ell}{2}+\frac{1}{4}+\alpha\right)\Delta\nu, \tag{16.116}$$

with

$$\Delta\nu = \left(2\int_0^R \frac{dr}{c_S}\right)^{-1}. \tag{16.117}$$

$\int_0^R \frac{dr}{c_S}$ is the travel time of the sound from the center to the surface. Expression (16.115) implies

$$\nu_{n+1,\ell} - \nu_{n,\ell} \approx \Delta\nu, \tag{16.118}$$

$$\nu_{n,\ell+2} \approx \nu_{n+1,\ell}. \tag{16.119}$$

The first of these relations means that for the same ℓ, the frequencies of the modes with successive n are equally spaced (commas are put here for clarification, as a rule there are none). The second relation shows that increasing n by 1 leads to about the same frequency as a change of ℓ by 2. As this last relation is only an approximation, it means that each observed frequency is in fact composed of two contributions separated by a very small frequency interval, called the small separation $\delta\nu_{n\ell}$ (see definition in 16.122). The double components of the peaks due to this degeneracy are visible in Fig. 16.9, showing the observed frequencies of the velocity spectrum of the Sun. The double peaks are shown with more details in Fig. 16.10.

The present approximations apply only for very low ℓ values as observable in asteroseismology. In helioseismology, one makes different approximations (Sect. 16.3.2) because oscillations of large ℓ are observable. Indeed, when looking carefully to the frequency spacing in Fig. 16.7, one notices that for very low ℓ values the above approximations (16.119) are verified. This is no longer the case for the high ℓ values.
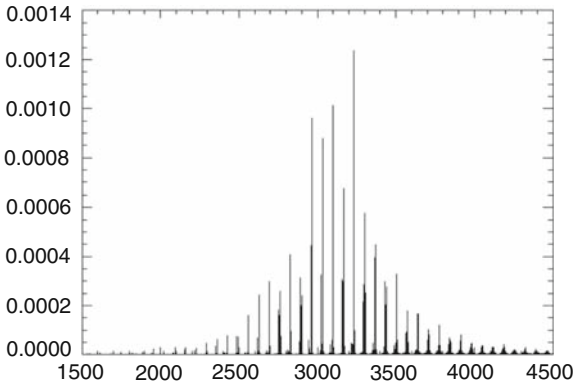
Fig. 16.9 The power spectrum of solar p modes from GOLF on the SOHO satellite (ESA and NASA) with very high signal to noise ratio. The frequency on the horizontal axis is given in μHz. The vertical scale represents the power in each mode in a linear scale. The doubling of the peaks is generally visible. Courtesy of S. Turck-Chièze
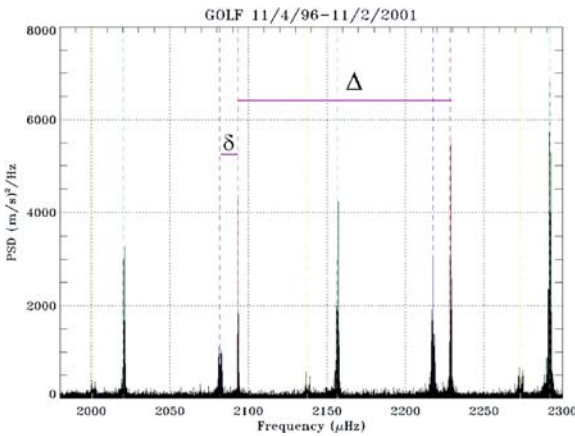
Fig. 16.10 Details from the solar power spectrum from GOLF illustrating the definitions of the large separation $\Delta \nu$ (noted Δ) and of the small separation $\delta \nu_{02}$ (noted δ). Figure from the GOLF experiment on the SOHO satellite of ESA and NASA; see [195]. Courtesy of S. Turck-Chieze

16.4.2 Second-Order Effects

The developments of (16.106) on account of higher order terms lead to [565]

$$\nu_{n\ell} \approx \left(n + \frac{\ell}{2} + \frac{1}{4} + \alpha \right) \Delta \nu - [A\,\ell(\ell+1) - \delta]\,\frac{\Delta\nu^2}{\nu_{n\ell}}, \qquad (16.120)$$

where

$$A = \frac{1}{4\pi^2 \Delta \nu} \left(\frac{c_S(R)}{R} - \int_0^R \frac{dc_S}{dr} \frac{dr}{r} \right) .$$ (16.121)

The second term in (16.120) gives rise to the small separation $\delta \nu_{n\ell}$; it comes from the fact that modes of different ℓ values penetrate down to different turning points. $\delta \nu_{n\ell}$ is the difference of frequencies differing by minus one for n and by plus two for ℓ:

$$\delta \nu_{n\ell} = \nu_{n\ell} - \nu_{n-1\ell+2}$$

$$\approx - [A\ell(\ell+1) - \delta] \frac{\Delta \nu^2}{\nu_{n\ell}} + [A(\ell+2)(\ell+3) - \delta] \frac{\Delta \nu^2}{\nu_{n-1\ell+2}} .$$ (16.122)

The definitions of the small and large separations are illustrated in Fig. 16.10. By neglecting the term in (c_S/R) and ignoring higher order terms, we get

$$\delta \nu_{n\ell} \approx -(4\ell+6) \frac{\Delta \nu}{4\pi^2 \nu_{n\ell}} \int_0^R \frac{dc_S}{dr} \frac{dr}{r} .$$ (16.123)

The small separation $\delta \nu_{n\ell}$, consistently with what is said above, depends mainly on the conditions close to the stellar center. It depends on the gradient of the sound speed weighted by dr/r, a weighting which heavily favors the central regions. Physically, this results from the fact that over most of its trip through the star the wave is essentially radial ($k_r \gg k_h$). The wave number k_h becomes important with respect to k_r only near the center due to the form of k_h given by (16.41). Thus, the same is true for the ℓ number and this explains that differences in ℓ have large effects in the central regions. The sound speed depends on $\sqrt{T/\mu}$ (C.27). Near the stellar center, T does not vary very much with r, while the variations of μ may be large due to the nuclear reactions. This means that the small separation is very sensitive to the mixing processes which may affect the distribution of the elements near the stellar center.

The parameter α depends on the phase change of the wave during its reflexion at the stellar surface, which itself depends on the outer structure. However, the depth where this reflexion occurs varies with frequency $\nu_{n\ell}$ (with a lower limit given by the acoustic cutoff frequency). Thus, α also varies with ν and this implies that the values of $\delta \nu_{n\ell}$ are changing with frequency. This leads to observable effects in a diagram showing the large and small spacing as a function of frequency (Fig. 16.13, right, and 16.14, right).

The observed and computed frequencies are often represented in terms of a small set of parameters appearing in the asymptotic developments. The mean large separation is given by (16.117), while an average small separation is defined as a mean over a few n numbers by

$$< \delta \nu_{n\ell} >_n \cong (4\ell+6) D_0 ,$$ (16.124)

with

$$D_0 \cong -\frac{1}{4\pi^2(n_0+\ell/2)} \int_0^R \frac{dc_S}{dr}\frac{dr}{r} \; .$$ (16.125)

The mean small separation $\delta v_{0,2}$ is given as an average of the separations between the modes $\ell = 2$ and $\ell = 0$ around a reference radial mode n_0, generally $n_0 = 21$ which corresponds to the central radial mode in the solar spectrum (Fig. 16.13). For example, in the case of α Cen A, one uses modes satisfying $15 \leq n+\ell/2 < 26$ for $\ell = 0,1,2$ to determine the average. The adopted criterion should be the same for the models and for the observations to analyze. One can also notice that A and $\delta v_{n\ell}$ are related. In practice, relation (16.120) is often written as

$$v_{n\ell} \cong \left(n+\frac{\ell}{2}+\frac{1}{4}+\epsilon\right)\Delta v - \frac{\ell(\ell+1)}{6}\delta v_{02}\,,$$ (16.126)

which allows one to determine the values of the mean large and small separations by adjustment of this simpler expression to the observed p-mode frequencies.

16.5   Helioseismology and Asteroseismology

The observations of the solar p modes, which have their turning points at different depths in the Sun, provide an invaluable information on the inner structure of the Sun. This is the domain of helioseismology.

For stars, the determination of the large and small separations provides a pair of new constraints, in addition to those already obtained from the HR diagram, which allow one to make accurate determinations of stellar parameters. This is the domain of asteroseismology.

16.5.1   Helioseismic Observations

Several major teams are performing helioseismology. The GOLF (Global Oscillations at Low Frequencies) experiment on the SOHO space mission (ESA and NASA) provides information on the internal structure of the Sun by measuring the spectrum of global velocity oscillations in the frequency range 10^{-7}– 10^{-2} Hz with emphasis on the low-order long-period waves which penetrate the solar core. The GONG (Global Oscillation Network Group) is a community-based program to study the internal structure and dynamics of the Sun. GONG has developed a six-station network of high-precision velocity imagers located around the Earth to obtain continuous observations of the Sun's "five-min" oscillations. The BiSON (Birmingham Solar Oscillations Network) also has six observatories around the world, which measure an average velocity over the solar surface (the Sun is observed like a star).

The experiment is sensitive to oscillations with long horizontal wavelength, which goes deep into the solar core.

Small individual elements at the solar surface can be analyzed. At a given point of the solar surface, the velocity field and brightness present almost sinusoidal variations (apart from irregularities and variable amplitudes) with a dominant period of about 5 min (3.3 mHz). These oscillations are the sum of $\sim 10^7$ individual acoustic oscillation modes. The fluctuations of both brightness and velocity provide detailed power spectrum of the solar p modes (Figs. 16.7 and 16.9). The key argument for this identification was the relation between the observed frequencies and wavenumber (Fig. 16.7), which is accounted for by relation (16.86). The values of the large and small separations for the Sun from the GOLF experiment on SOHO are $\Delta\nu = 134.9\,\mu\text{Hz}$ and $\delta\nu_{02} = 9.1\,\mu\text{Hz}$.

Comparison between theory and observations of the numerous solar modes can be made in a diagram like Fig. 16.7. There is another method, the inversion method which takes advantage that the p modes of various ℓ reach different depths according to [133, 215]. This allows one to reconstruct the internal profile of the sound velocity $c_S(r)$ as a function of the radius in the Sun. This profile mainly depends on the ratio $\sqrt{T/\mu}$. Figure 16.11, left, shows the theoretical profile of the sound velocity in the present solar model. Before the revision of the CNO abundances [20], the differences between observations and theory were very small. This has played a
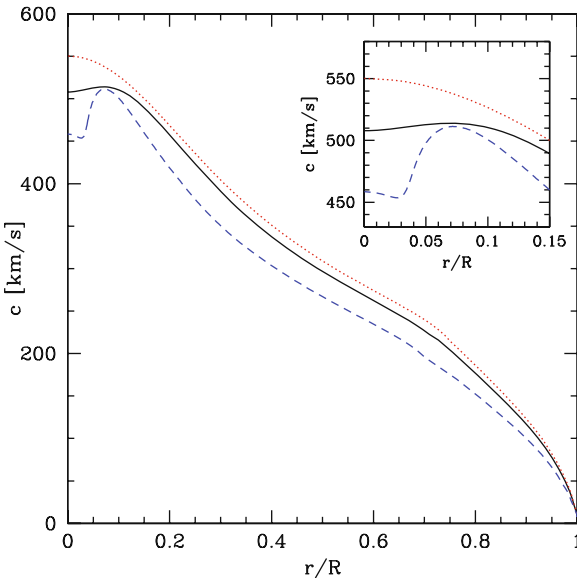
Fig. 16.11 The variations of the sound speed as a function of radius in models of a $1\,\text{M}_\odot$ star at an age of 0.4, 4.57 and 9.8 Gyr indicated by the dotted, continuous and dashed lines, respectively. The initial composition is $X = 0.718$, $Y = 0.268$, $Z = 0.014$. From P. Eggenberger [169]
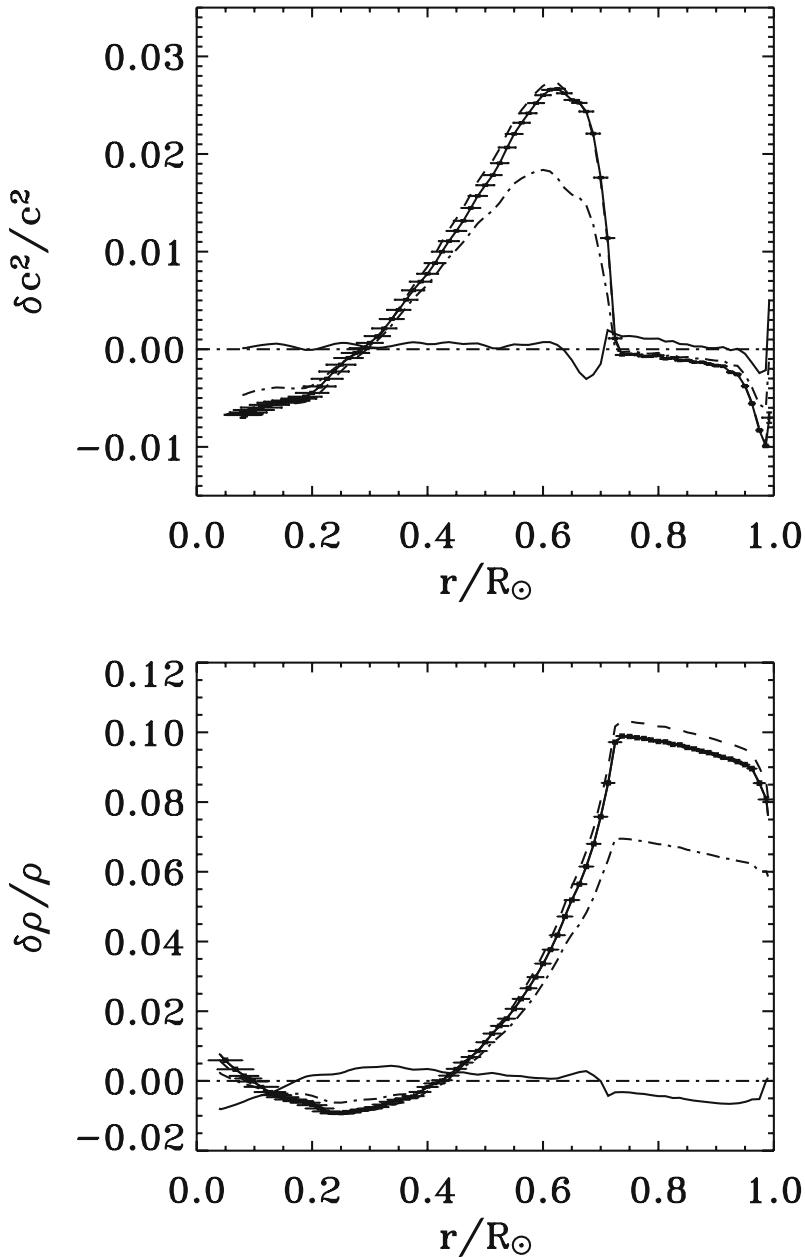
Fig. 16.12 *Upper*: the relative differences (squared) of the sound speed between the helioseismic observations with GOLF and MDI aboard SOHO (ESA and NASA) for three solar models with slightly different Z/X ratios. The full line with error bars is that based on new CN (*lower*); CNO abundances from Asplund [19]. The continuous line close to horizontal is not a physical model, but a so-called seismic model adjusted on observational constraints. The other *curves* correspond to different equations of state [152, 494, 495]. *Lower*: the equivalent in terms of density differences [582, 583]. Courtesy of S. Turck-Chièze

great role in the solution of the solar neutrino problem. The solar model was so closely constrained by helioseismology [38] that the quality of the modeling could no longer be taken as responsible for the too small solar neutrino flux. The solution came from the neutrino physics (Sect. 25.3.3).

The new CNO abundances [20] have altered the agreement of helioseismological observations and models [25]. Figure 16.12, upper part, presents the differences between the helioseismic results and the new solar model. These differences can also be expressed in terms of density (Fig. 16.12, lower part). It has been suggested that an increase of the neon abundance by a factor of 3 up to $\log(\mathrm{Ne}) = 8.29$ on the scale in which $\log N(\mathrm{H}) = 12$ would be able to restore the agreement, for the basis of the convective zone, but not for the core [26]. However, the discrepancy between models with new abundances and observations as well its possible solutions is still the matter of debates.

16.5.2 Asteroseismic Observations

For stars, only oscillation modes with $\ell \leq 2$ are observable from integrated light fluctuations; the brightness amplitudes of an individual p mode are about $\Delta L/L \approx 10^{-6}$. This means that such small light variations are observable only from space missions, such as MOST, COROT and KEPLER. The relative amplitudes are larger for radial velocities than for brightness measurements and oscillation modes with $\ell \leq 3$ can be observed by Doppler shifts in integrated light. The amplitude of a single p mode is usually smaller than about $20\,\mathrm{cm\,s^{-1}}$, and thus the Doppler shifts are very small $\Delta\lambda/\lambda \sim 6 \times 10^{-10}$. Rotating stars are difficult to observe; photometric observations may allow one to observe rotating and faint stars; however the necessary integration time would be very long.

The main source of the mode excitation is convection. Thus stars having a vigorous outer convective zone should present active p modes. Estimates of the amplitude of p modes suggest that velocity amplitudes are larger for stars of lower stellar gravity [70, 132]. Thus, stars more massive than the Sun, but with still a sufficient outer convective zone, or stars away from the zero-age sequence should have larger velocity amplitudes.

The first unambiguous detection of individual p-mode frequencies for a star was obtained for α Centauri A [57], with CORALIE, a ground-based spectrograph. A number of observations have been obtained with the HARPS spectrograph (High-Accuracy Radial Velocity Planetary Searcher) on the 3.6 m ESO telescope, an accuracy of a few tens of cm s^{-1} is currently obtained.

A series $v(t)$ of velocity observations distributed in time from $t = 0$ to $t = T$ contains many modes with different frequencies and amplitudes. The Fourier transform of $v(t)$ is

$$\widetilde{v}(\omega) = \int_0^T v(t)\, e^{i\omega t}\, dt. \qquad (16.127)$$
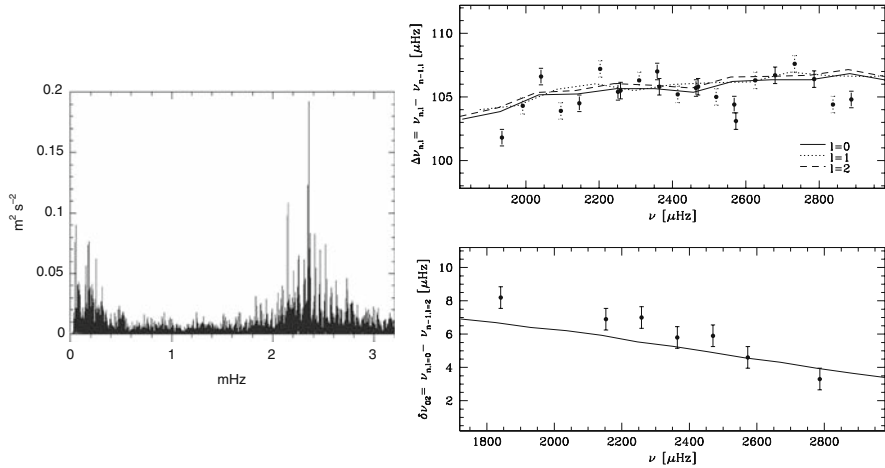
Fig. 16.13 *Left*: power spectrum of α Cen A, from F. Bouchy and F. Carrier [57]. *Right*: the large and small separations vs. frequency for α Cen A, comparison of the theoretical curves with the observations indicated by *dots* with error bars. From P. Eggenberger et al. [171]

The power spectrum $P(\omega)$ is

$$P(\omega) = |\widetilde{v}(\omega)|^2 . \tag{16.128}$$

It gives the distribution of amplitudes as a function of the frequencies (cf. Fig. 16.13, left). Various sources of noise, the total time of observation, the presence of gaps, the time sampling and the stochastic excitation of modes may produce artificial peaks in the power spectrum. This needs to be very critically analyzed, for example by autocorrelation techniques (Fig. 16.14, left) and by application of iterative processes to disentangle the astrophysically meaningful peaks from the aliases and noise [169].

The values of the large and small separations vary with frequency (Fig. 16.13, right) and this may give further information on the internal structure. This is also predicted by the asymptotic expressions given in Sect. 16.4.2 and also shown with more details by numerical calculations as illustrated in the figure. This confirms the need to define average values of the mean and large separations as mentioned above (16.125). In the case of α Cen A, the mean large and small separations are, respectively, $\Delta\nu = 105.5 \pm 0.1\,\mu\text{Hz}$ and $\delta\nu_{02} = 5.6 \pm 0.7\,\mu\text{Hz}$.

The identification of the individual frequencies of the modes is usually made with the help of a so-called echelle diagram (Fig. 16.14, right). This is a plot of the frequencies of the peaks as a function of the frequencies modulo the value of the large separation. According to (16.117), the frequencies of the p modes of a same degree ℓ are separated (to the first order) by an integer number n of large separations. Thus, the modes of a same degree ℓ describe a vertical line in an echelle diagram, which greatly facilitates the identification. Such a diagram is illustrated in Fig. 16.14
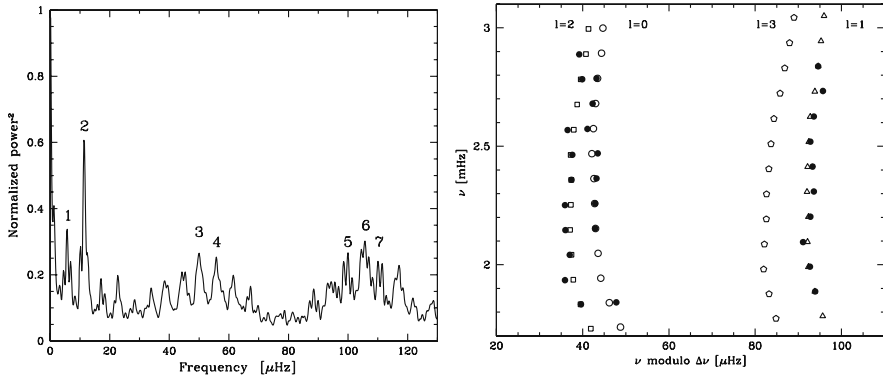
Fig. 16.14 *Left*: autocorrelation of the power spectrum of α Cen A. Peak nb. 1 at 5.5 μHz is due to the small separation $\delta\nu_{02}$ between modes $\ell = 0$ and $\ell = 2$. Peak 2 at 11.57 μHz ($= 1/24$ h) is the daily alias. Peaks 3 and 4 are due to correlations between modes of $\ell = 0, 1, 2$, so that the frequency separation between peaks 3 and 4 corresponds to $\delta\nu_{02}$. Peak 6 at 105.5 μHz indicates the value of the average separation. Peaks 5 and 7 result from correlations between radial and $\ell = 2$ modes. The other smaller peaks are due to correlations between modes and daily aliases From F. Bouchy and F. Carrier [57]. *Right*: echelle diagram of α Cen A. *Open symbols* refer to theoretical frequencies; various symbols are used for different ℓ, while *filled circles* give the observed frequencies [57]. From P. Eggenberger et al. [171]

for α Cen A. An excellent agreement between observations and numerical solutions of the perturbation equations is noticeable. Other stars with different evolutionary stages and heavy element contents have been observed.

16.5.3   The Asteroseismic Diagram

The large and small separations $\Delta\nu$ and $\delta\nu_{0,2}$ are two additional parameters, which combined with $(L, T_{\rm eff})$ obtained from the HR diagram help to further constrain the stellar parameters, $M, R, L, T_{\rm eff}, X, Y, Z$, age, $\alpha = \ell/H_P$. In the case of binary stars or of stars in open clusters, the constraints on the models are even stronger because of the additional information available. Close comparisons may enable us to further check and improve the physics of stellar models.

The theoretical values of $\Delta\nu$ and $\delta_{0,2}$ can be obtained either by numerical integration of the equations (which is preferable) or by the asymptotic developments (Sect. 16.4.1). For $\Delta\nu$, the differences between the two approaches for different ages and masses are small: the values from asymptotic theory are typically larger by about 5% than from the numerical models. For $\delta\nu_{0,2}$ the situation is less satisfactory. The asymptotic theory well predicts the trends with age and masses; however the values are about 20% larger for stars younger than the Sun and much smaller for larger ages [169].
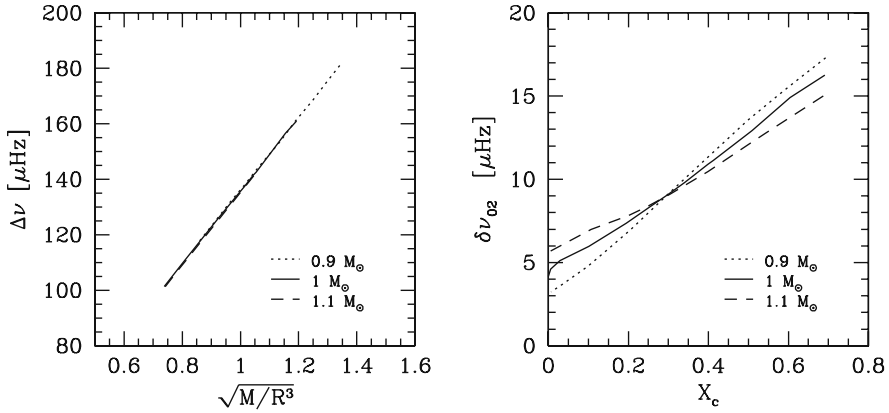
Fig. 16.15 *Left*: the mean large separation as a function of the square root of M/R^3, with M and R expressed in solar units for star of different masses. *Right*: the small separation $\delta_{0,2}$ defined in Sect. 16.5.3 as a function of the central H content in mass fraction. Solar model with an initial $X = 0.718$, $Y = .268$, $Z = 0.014$ and $\ell/H_P = 1.6$. From numerical models by P. Eggenberger [169]

Figure 16.15, left, shows that the large separation grows very closely with the square root of the average density. This is a direct consequence of the fact that the travel time R/c_S of the sound through the star, or the dynamical timescale (1.28), goes like the square root of the inverse of the average density. Figure 16.15, right, shows that when the central H content X_c decreases, i.e., when the age increases, the small separation declines. According to (16.123), the value of the small separation is mainly determined by the derivative of the sound speed in the central layers. From Fig. 16.11, we see that a positive gradient is progressively created in the center during evolution. This results from the higher mean molecular weight built in central regions by nuclear reactions. This positive gradient tends to cancel the negative contribution of the outer regions and thus produces a smaller value of the small separation as evolution proceeds. A higher mass (near $1\,M_\odot$) makes the initial value of the small separation slightly smaller, since the central T gradient is slightly flatter due to lower T sensitivity of the ppI chain as T increases.

Figure 16.16 shows the changes of the mean large and small separations with masses and ages. The behavior observed is just the consequence of Fig. 16.15. $\Delta\nu$ decreases with age and with increasing masses, since in both cases the average density decreases. The small separation decreases since X_c decreases. The curves are more differentiated than in Fig. 16.15, since the evolutionary timescales of the various models are very different.

A 2D diagram (Fig. 16.17) where the mean small separation $\delta\nu_{02}$ is plotted vs. the large separation $\Delta\nu$, or vs. D_0, as a function of masses and ages can be constructed as first shown by J. Christensen-Dalsgaard [130, 584]. This remarkable diagram, often called the asteroseismic diagram, permits a clear separation of masses and ages. It offers a beautiful complement to the HR diagram. To a couple of values
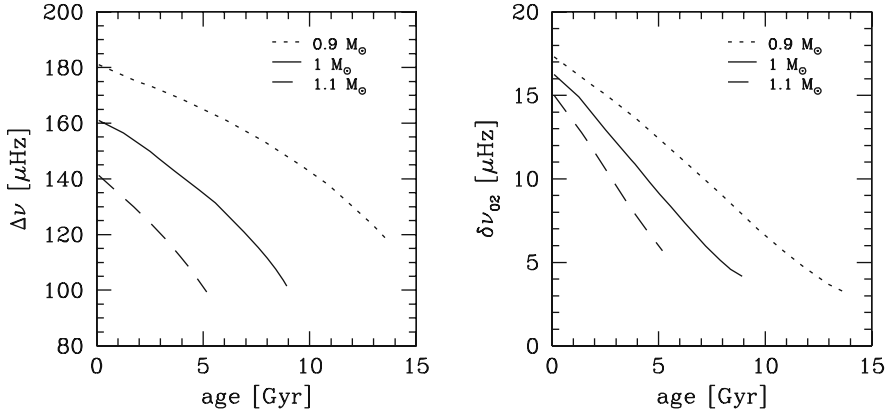
Fig. 16.16 The variations of the mean large and small separations as functions of the ages for different masses. From numerical models by P. Eggenberger [169]

$(\delta\nu_{02}, \Delta\nu)$, a couple (M, X_c) may be assigned, which is different from the couple (L, T_{eff}) or (L, R) obtained from the HR diagram. The combination of the data from the HR and asteroseismic diagrams opens new perspectives of access to the stellar parameters and provides new checks of the models.
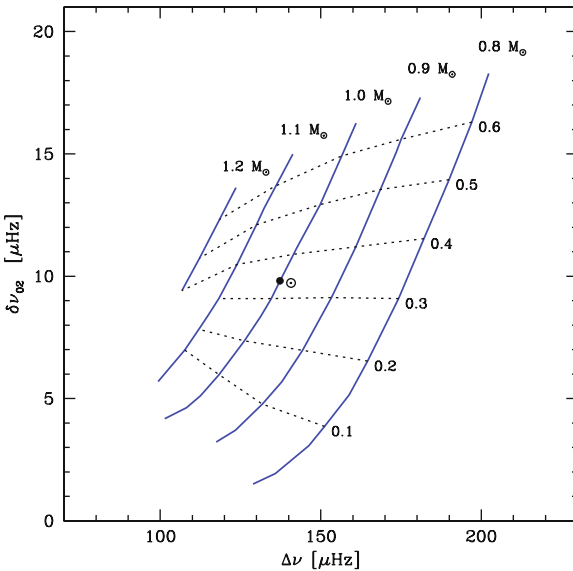
Fig. 16.17 Asteroseismic diagram for solar-type stars with solar composition $X = 0.718$, $Z = 0.014$ during their MS evolution. The evolution of different masses are indicated by continuous lines. The *dotted lines* show the loci with the same central H content X_c. The model with $1.2\,M_\odot$ is followed up to the appearance of a convective core. The solar observations are indicated. From P. Eggenberger [169]

16.5.4   Effects of X, Z and Mixing Length on the Large and Small Separations

Changes of the contents of hydrogen X and heavy elements Z (in mass fraction) produce shifts for both the HR and asteroseismic diagrams. Care has to be given to composition effects. As an example, for a constant Z, a shift from $X = 0.699$ to 0.675 reduces the large separation by 5 and 18 µHz, respectively, at the beginning and at the end of the MS evolution for a $1\,M_\odot$ star. For the small separation, these reductions are 0 and 1.2 µHz [169]. These effects are easily understood. A decrease in X makes the model less opaque; it is hotter (by $\sim +0.01$ dex in $T_{\rm eff}$) and brighter (by $\sim +0.07$ in L). Thus, in both the HR and asteroseismic diagrams, a decrease in X behaves like a slight increase of the stellar mass, which makes a decrease in $\Delta \nu$. For $\delta \nu_{02}$, an increase in the mass reduces the small separation, as shown in Fig. 16.16.

A change in metallicity Z significantly affects the two diagrams. As an example, a shift from $Z = 0.017$ to 0.028 makes the $1\,M_\odot$ star more opaque; it reduces $T_{\rm eff}$ by ~ 0.01 dex and the luminosity L by ~ 0.07, like a small mass reduction. Consistently with the trends with mass, this produces an increase of $\Delta \nu$ (by ~ 7 and 27 µHz at the beginning and end of the MS). As to the small separation, the effect is zero at the beginning of the MS and there is an increase by 2 µHz at the end of the MS.

Let us consider the case of Pop. II stars. The noticeable relation between the large separation and density (Fig. 16.15) is only slightly sensitive to Z: stars of lower Z have slightly lower $\Delta \nu$, by 5–10% for a large change from solar composition to $[Fe/H] = -2$ [169]. The relation between $\delta \nu_{02}$ and the central hydrogen content $X_{\rm c}$ is however more sensitive to Z. For the above change of $[Fe/H]$, $\delta \nu_{02}$ increases by ~ 3 µHz.

The choice of the mixing-length ratio $\alpha = \ell/H_P$ (5.40) also influences the asteroseismic diagram. An increase in α increases the heat transport in the outer layers and thus makes the stellar surface hotter and with a smaller radius. This increases the mean density and therefore enlarges $\Delta \nu$ (a 20% increase in α above $\alpha = 1.6$ makes $\Delta \nu$ about 5% larger). At the opposite, the mean small separation is almost unaffected by a change α. This is consistent since α influences the outer stellar layers, while $\delta \nu_{02}$ is sensitive to central conditions. Often the data from the HR and asteroseimic diagrams are complementary. The situation is even much better in binary system, like α Cen A and B [171], where one can assume the same initial composition for both components.

16.6   Rotational Effects: Splitting and Internal Mixing

There are two types of rotational effects on the nonradial oscillations:

– Rotational splitting: in the absence of rotation, there is no preferred axis and the modes of different m values are degenerate, i.e., $\omega_{n\ell m}$ behaves as $\omega_{n\ell}$. With

rotation, the modes of different m are split into $2\ell+1$ frequency components. The rotational splitting is a powerful source of information on the internal rotation of the Sun.

– Effects of mixing: the internal mixing modifies the stellar structure and therefore the oscillation frequencies.

16.6.1 The Rotational Splitting: First Approach

A stationary oscillation results from two waves propagating in opposite directions. On the surface of a star rotating with an angular velocity Ω, one wave is brought by the medium with a velocity $\boldsymbol{v} = \boldsymbol{\Omega} \times \boldsymbol{R}$ and the other wave is brought with a velocity $-\boldsymbol{v}$ and it thus experiences an opposite Doppler shift. This produces a splitting of the frequencies of the nonradial modes.

Let us consider a star rotating with angular velocity Ω and a wave with m nodes traveling in the direction opposite to rotation (retrograde wave) as illustrated in the left side of Fig. 16.18. We call ω the frequency in the rotating frame and ω_n the frequency as seen by a distant observer (inertial frame). In the retrograde case, the wave seen by the distant observer looks squeezed with respect to its shape in the rotating frame. This means that the frequency ω_n is higher than ω and it behaves like

$$\omega_n = \omega + m\Omega, \qquad (16.129)$$

with $m > 0$. Ω is multiplied by m because in one tour at angular velocity Ω the rotational shift is distributed over m oscillation wavelengths. For example, if $\omega = \Omega$,
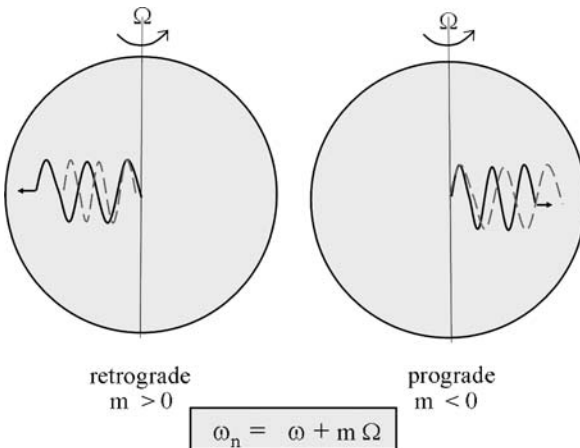
Fig. 16.18 Schematic illustration of retrograde and prograde waves. The wave in the rotating frames are shown in *black* and the waves as seen by the distant observer are in *gray*. It looks squeezed in the retrograde case and stretched in the prograde one

for $m = 1$ the frequency looks doubled for the distant observer; for $m = 10$, one has $\omega_n = 11\,\omega$, because there are now 11 periods seen by the distant observer during one original period. Conversely, for a wave traveling in the direction of rotation (prograde wave), the period looks stretched as seen by the distant observer, i.e., with a lower frequency, which implies that m is negative. The two opposite waves lead to opposite Doppler shifts, which produce a splitting of the observed frequencies in the distant frame. This is the first approximation of the splitting.

More generally, let us call $\delta\omega_{n\ell m}$ the change of the frequency due to rotation. This change can be written as a weighted function of the angular velocity in depth:

$$\omega_n = \omega + \delta\omega_{n\ell m} , \tag{16.130}$$

with

$$\delta\omega_{n\ell m} = m\beta_{n\ell} \int_o^R K_{n\ell}(r)\Omega(r)dr . \tag{16.131}$$

The weighting function $K_{n\ell}$ is called the rotational kernel. In the approximation above, one just has $\delta\omega_{n\ell m} = m\Omega$. Account has to be given, however, to the fact that Ω may vary with depth. To the first order, the weighting function of $\Omega(r)$ is simply the sound-travel time in the star, because the time during which the wave is brought forward or backward in the direction e_φ by the local rotation is proportional to the time the wave is spending in the considered layers. Thus, an approximation of the splitting is

$$\delta\omega_{n\ell m} \approx m \frac{\int_{r_t}^R \Omega(r)\frac{dr}{c_S}}{\int_{r_t}^R \frac{dr}{c_S}} . \tag{16.132}$$

For each mode, most of the contribution to the integral comes from the superficial layers, where the sound speed is lower. However, as the modes of different $n\,\ell$ reach different inner turning points, there is also some contributions from the deeper layers and this provides information (with different accuracies) on the inner rotation.

16.6.2   Further Steps

Further developments are needed to take into account the properties of the wave of numbers (n, ℓ) in relation with $\Omega(r)$. The frequency shift due to rotation may also depend on the motions due to the Coriolis force. Detailed developments are given in Appendix B (B.6.2). They lead to the following expressions for the rotational kernel in (16.131):

$$K_{n\ell} = \frac{\left(\xi_r^2 + \ell(\ell+1)\xi_h^2 - 2\xi_r\xi_h - \xi_h^2\right)r^2\varrho_0}{\int_0^R \left(\xi_r^2 + \ell(\ell+1)\xi_h^2 - 2\xi_r\xi_h - \xi_h^2\right)r^2\varrho_0 dr} , \tag{16.133}$$

$$\beta_{n\ell} = \frac{\int_0^R \left(\xi_r^2 + \ell(\ell+1)\xi_h^2 - 2\xi_r\xi_h - \xi_h^2 \right) r^2 \varrho_0 dr}{\int_0^R \left(\xi_r^2 + \ell(\ell+1)\xi_h^2 \right) r^2 \varrho_0 dr} . \tag{16.134}$$

This definition implies that the kernel $K_{n\ell}$ satisfies

$$\int_0^R K_{n\ell}(r)dr = 1 . \tag{16.135}$$

The kernel acts as a weighting function of $\Omega(r)$ according to depth. The sound speed being higher in deeper regions, it is clear from (16.132) that the weighting is much weaker in the deep interior than near the surface. The kernels also depend on the amplitudes ξ_r and ξ_h. In the case of solid body rotation, one gets

$$\delta\omega_{n\ell m} = m\beta_{n\ell}\Omega . \tag{16.136}$$

The coefficient $\beta_{n\ell}$ is in general close to 1 (between 0.97 and 1.00), since the term $\xi_r^2 + \ell(\ell+1)\xi_h^2$ generally dominates, especially for large ℓ values. This is also suggested by the comparison with the zero-order approximation (16.129). If one wants in addition to account for a possible dependence of Ω on ϑ, one uses expression (B.97) and develops $\Omega(r,\vartheta)$ as powers of $\cos\vartheta$, which is acceptable since the variations of rotation with the colatitude in the Sun are limited (Fig. 16.20).

Figure 16.19 shows an example of splitting for a $1.5\,\mathrm{M}_\odot$ star. In the non-rotating case, the spherical symmetry results in a unique peak in the power spectrum at the frequency of the $\ell = 2$ mode with $m = 0$. For the rotating model, the m degeneracy is lifted and four additional peaks appear in the power spectrum for the same mode $\ell = 2$, but for azimuthal order $m = \pm 1$ and ± 2. The asteroseismic observations do not yet allow us to measure the rotational splitting of stars. However, the rotational splitting can be indirectly detected by the increase of the scatter of individual nonradial modes it produces, as in the case of the F9V star β Vir [170].

The aim of the studies of the splitting is to derive the distribution of $\Omega(r)$ from the observations of the various $\delta\omega_{n\ell m}$. This is done by the inversion techniques applied to relation (16.131); such methods are also applied to the derivation of the sound speed in the solar interior (Fig. 16.12). The fact that the various waves reach turning points at different depths is used; thus the observed splitting provides information, weighted by the kernels, on $\Omega(r)$ at different depths. The different inversion techniques to extract $\Omega(r,\vartheta)$ from the splitting have been compared by Christensen-Dalsgaard et al. [133].

16.6.3   The Tachocline and Inner Solar Rotation

Figure 16.20 shows the variations of $\Omega(r,\vartheta)$ in the Sun as a function of depth from the GOLF experiment aboard SOHO. We see that rotation is faster at the equator with a period of 25 days and slower with a period of 33 days at high latitudes.
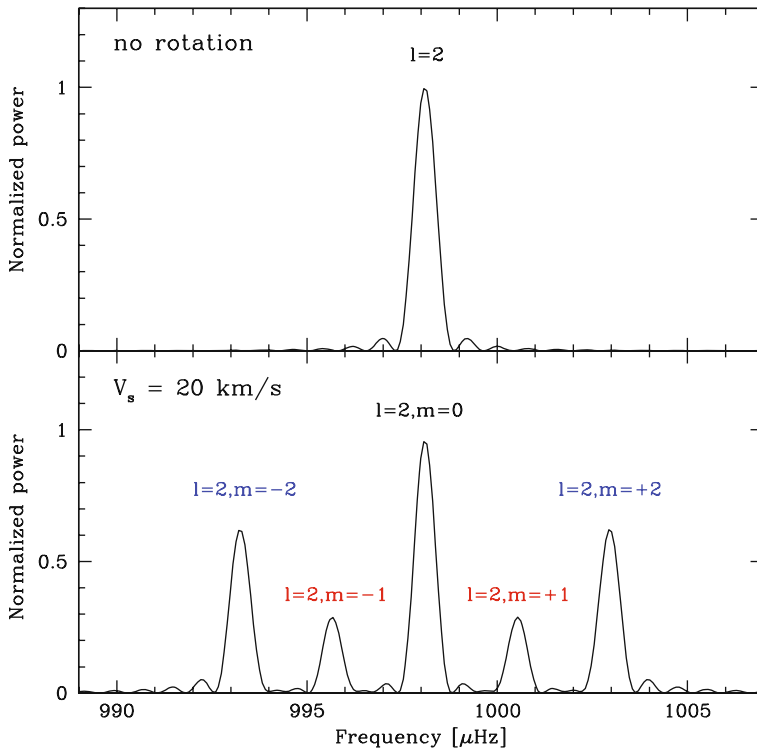
Fig. 16.19 Illustration of the rotational splitting: the power spectrum of an $\ell = 2$ mode for a $1.5\,M_\odot$ star without rotation and with a solid body rotation of $20\,\mathrm{km\,s^{-1}}$. From P. Eggenberger [169]

The helioseismological results at the solar surface are in agreement with data from sunspot observations. In the outer convective envelope down to the bottom of the convective zone at $r/R_\odot = 0.713$ [28, 131], there is the above-mentioned gradient of Ω in latitude. The various curves converge at about 30% of the radius from the surface, in a thin transition region which is called the tachocline (see below). Over most of the interior, $\Omega(r)$ is almost constant, the inner Sun turning like a solid body. There are three major problems in the solar rotation curve:

– The thinness of the tachocline.
– The flatness of $\Omega(r)$ in the radiative zone.
– The possible increase of $\Omega(r)$ in the center.

The helioseismic data show that the region over which the different curves converge is limited to less than 5% of the radius. Most of the tachocline lies in the radiative region below the convective envelope, the upper third being in the subadiabatic overshooting region below the convective envelope [115]. As shown by Spiegel and Zahn [542], one would normally expect the tachocline to extend deeper than observed (by $\sim 15\%$ of $R_\odot$), due to radiative and shear diffusion over the age of the Sun. The proposed solution [542] is that a strong horizontal turbulent diffusion (cf.
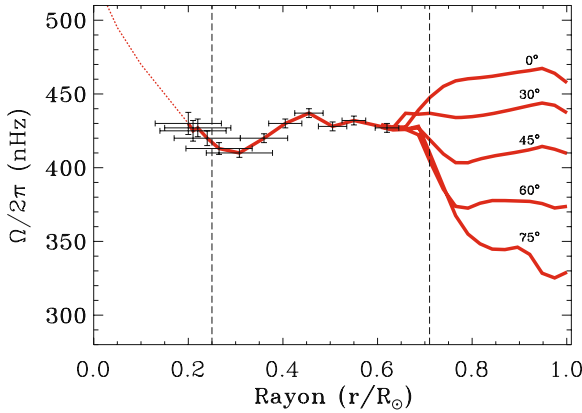
Fig. 16.20 The internal value of the angular velocity Ω as a function of solar radius in the Sun from the acoustic modes in helioseismic observations. In the outer layers, the *curves* are different according to the latitude (zero degree corresponds to the equator). The data are obtained from the inversion technique on modes $\ell \leq 25$ using a series of 2088 days. Below 0.2 R$_\odot$ the *dotted curve* indicates the result suggested by gravity modes using the GOLF experiment on SOHO (ESA and NASA); this part is however still uncertain. Data from [200, 583]. Courtesy of S. Turck–Chièze

Sect. 12.1) maintains a thin tachocline, because the horizontal turbulence prevents the extension of the shear zone in depth. Some debate exists whether a large-scale magnetic field in the radiative zone would not be responsible for the confinement of the transition shear zone. However, a recent work by Brun and Zahn [75] shows that a fossil magnetic field cannot inhibit the inward spread of the tachocline. While this favors the explanation in terms of horizontal turbulence, this does not prevent the existence of a dynamo in or near the tachocline able to generate strong fields of the order of 100 kG, which by magnetic buoyancy could rise through the envelope and produce spots at the solar surface. A limited extension of the tachocline (where strong mixing occurs) is also necessary to explain why ^{9}Be is not destroyed, while a fraction of ^{7}Li is destroyed in the Sun with respect to the meteoritic composition [73].

The second major question posed by solar rotation is why the radiative interior rotates uniformly. It is clear that as a result of increasing central density and transport processes, the Sun could have some non-uniform rotation. Thus, a mechanism is necessary to explain the solid body rotation. In Sect. 13.6.2, we have seen that a magnetic field can produce the necessary coupling to enforce solid body rotation in the Sun. Even very low fields would do it. Explanations are also proposed in terms of transport by gravity waves [559]. The question is still open [217, 559]. The answer may come from the behavior of $\Omega(r)$ in the solar center, since both effects may act in a different way.

The situation concerning the central solar rotation is still uncertain. In the deep interior, recent observations [200, 201, 583] suggest the detection of g modes from 10 year observations of Doppler velocity from the GOLF experiment aboard SOHO. The period corresponds to the prediction of the asymptotic theory for gravity mode

of angular degree $\ell = 1$. These observations tend to favor a rotation rate faster in the core than in the rest of the radiative zone.

16.6.4 Structural Effects of Rotation

The internal mixing by rotational effects influences the stellar structure and in turn the asteroseismic frequencies. The large separation $\Delta \nu$ experiences little change since the average stellar density is about the same. For an initial velocity of 100 km s^{-1} for a solar model, the relative increase in $\Delta \nu$ is smaller than 1% (1 μHz at 2 Gyr and 2.5%, i.e., 3.5 μHz at 8 Gyr [169]). The physical reason for the frequency increase is the slightly smaller radius of the solar models calculated with rotational mixing.

The rotational effects on the structure are relatively much more important for the small separation. The rotational mixing leads to more hydrogen in the center and this gives larger small separations $\delta \nu_{02}$. Figure 16.21 illustrates the effects as a function of frequency for a solar model at ages 2 Gyr and 8 Gyr. At 2 Gyr, the effects are essentially negligible. However, at greater ages, $\delta \nu_{02}$ experiences a relatively large increase, i.e., by about 50% at 8 Gyr for an initial velocity in the range of 30–100 km s^{-1}. The effects of rotational mixing evidently grow with age, because mixing has more time to influence the distribution of the elements.

The amplitude of the effects depends very much on the strength of the horizontal turbulence. A higher turbulence gives a larger effect, since mixing by shear turbu-
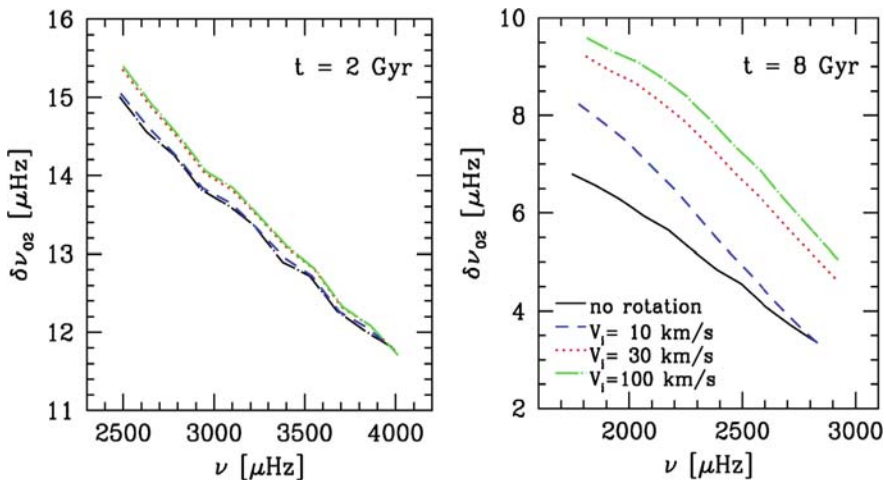
Fig. 16.21 The small separation $\delta \nu_{02}$ vs. frequency at two different stages with an age of 2 Gyr and 8 Gyr for a 1 M$_\odot$ solar model. The models are computed for different initial rotation velocities as indicated. The coefficient of horizontal turbulence is $D_h(3)$ (cf. Sect. 12.1.5). From P. Eggenberger [169]

lence is then stronger (Sect. 12.3.2). This brings more hydrogen to the center, which leads to a larger δv_{02}. Different coefficients $D_h(i)$ with $i = 1, 2$ and 3 of horizontal turbulence are considered in Sect. 12.3.2; the rotational effects predicted by $D_h(1)$ are smaller than those presented in Fig. 16.21. Coefficients $D_h(2)$ and $D_h(3)$ give the same results.

Helioseismology and asteroseismology have provided extraordinary useful information and new constraints on the stellar parameters, independently on the HR diagram. The rotational splitting gives access to the inner solar rotation which is challenging the hydrodynamic theories. The detailed analysis of the small separation may further enlighten the mixing processes in stars.

Chapter 17
Transport by Gravity Waves

A stone thrown into the water generates waves which propagate making nice circles on the water surface away from the impact point. These are surface gravity waves, because the water displaced by the stone is recalled back by gravity.

In stars, gravity waves are typically produced by the "convective pistons" injecting energy into a radiatively stable adjacent region. Due to the piston motions, the fluid elements at some depth are slightly moved up or down into regions of different densities. Gravity tends to bring the displaced fluid elements back to their initial positions; the elements go beyond their original equilibrium positions and oscillate. This induces other displacements and thus waves propagate within the medium. The frequencies of gravity waves or g-mode oscillations are low by contrast with acoustic waves, which have high frequencies and where the recall force is the ambient pressure.

The main effect of gravity waves in star evolution lies in their capacity to transport angular momentum and influence rotation; the transport of chemical elements by gravity waves is only a second-order effect. There are still many uncertainties, in particular regarding wave excitation, the Coriolis force and the interaction of the waves with the horizontal turbulence.

17.1 The Propagation of Gravity Waves

17.1.1 Properties of Gravity Waves

A first approach comes from the study of the criteria for convection (Sect. 5.1), where we have examined the vertical displacement of a fluid element in a stable stratified medium with gravity. Let us now consider a displacement $\boldsymbol{\xi}$ in a direction making an angle ϑ with respect to the vertical axis $\boldsymbol{r}$ (Fig. 17.1). With the same notations as in (5.1), the equation of motion is

$$\varrho_{\mathrm{int}} \frac{d^2 r}{dt^2} + g \left(\varrho_{\mathrm{int}} - \varrho_{\mathrm{ext}} \right) \cos \vartheta = 0 . \tag{17.1}$$
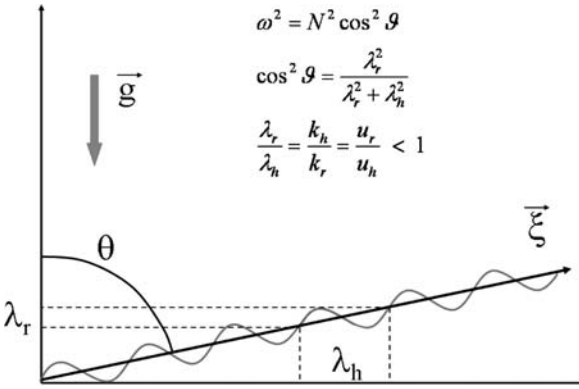
Fig. 17.1 Schematic illustration of the propagation of a gravity wave

This leads to an oscillation frequency ω for the fluid element given by

$$\omega^2 = N^2 \cos^2 \vartheta \, , \tag{17.2}$$

with the Brunt–Väisälä frequency N (5.5 or 5.23, the adiabatic value being generally taken since the oscillations are small). If T decreases faster than given by ∇_{ad}, N is imaginary and the medium is unstable to convection. Gravity waves and convection are the stable and unstable response to the same recall force. Gravity waves propagate only at frequencies $\omega < N$ with $N^2 > 0$. Gravity waves have a characteristic frequency ω, while acoustic waves have a characteristic velocity.

The wave numbers are defined by an equation of the form (C.28) for plane waves. The vertical and horizontal components are k_r and $k_h = \sqrt{k_\vartheta^2 + k_\varphi^2}$, where r, ϑ, φ are the spherical coordinates. The fluid element oscillates with frequency N for $k_h = 2\pi/\lambda_h \rightarrow \infty$, i.e., for negligible horizontal wavelength. For larger horizontal wavelength, the frequency is lower. A gravity wave has some constant frequency ω and its horizontal wavenumber k_h, in plane geometry, is conserved. In spherical geometry, $k_h^2 = \ell(\ell + 1)/r^2$ and the degree ℓ is the conserved quantity. Relation (17.2) leads to a dispersion relation

$$\omega^2 = N^2 \cos^2 \vartheta = N^2 \frac{k_h^2}{k_h^2 + k_r^2} \, , \quad \text{one also has} \quad \frac{k_h}{k_r} = \frac{u_r}{u_h} \, , \tag{17.3}$$

where u_r and u_h are the velocity components. The fluid element is moving perpendicularly to the direction of propagation. Equation (17.3) can be written as

$$k_r^2 = k_h^2 \left(\frac{N^2}{\omega^2} - 1 \right) . \tag{17.4}$$

Another approach is the study of nonradial oscillations (Sect. 16.2.3). From (16.70), we have gravity waves for $K(r) > 0$ with ω^2 smaller than both N^2 and S_ℓ^2, where S_ℓ

is the Lamb frequency (16.56). Thus, one has in spherical geometry,

$$K(r) = \frac{\omega^2}{c_S^2}\left(\frac{N^2}{\omega^2} - 1\right)\left(\frac{S_\ell^2}{\omega^2} - 1\right) \rightarrow \frac{1}{\omega^2}\left(N^2 - \omega^2\right)\frac{\ell(\ell+1)}{r^2}. \qquad (17.5)$$

From Sect. 16.3.1 one can identify $K(r)$ with k_r^2, this gives

$$k_r^2 = \frac{\ell(\ell+1)}{r^2}\left(\frac{N^2}{\omega^2} - 1\right) = \left(\frac{N^2}{\omega^2} - 1\right)k_h^2, \qquad (17.6)$$

where we have used (16.41). One takes $N^2 = N_{ad}^2$ in general. This is consistent with (17.4). We see the anisotropic nature of the internal gravity waves, even more than $N^2/\omega^2 \gg 1$, the horizontal wavelengths being much longer than the vertical ones. Also, one notices that k_r^2 increases with decreasing ω, this means that the frequency ω of the waves decreases with increasing order n.

The solutions for g modes are found by numerical integration of Eqs. (16.65) and (16.66) in the adiabatic case. Let us note that, as for p modes, an asymptotic theory can be developed for g modes. In the case of g modes with low degree ℓ and high order n, one has in terms of the periods P [565],

$$P_{n\ell} = \frac{P_0\ (n + (\ell/2) + \delta)}{\ell(\ell+1)} \quad \text{with} \quad P_0 = 2\pi^2\left(\int_{r_1}^{r_2}\frac{N}{r}dr\right)^{-1}. \qquad (17.7)$$

N is real only in a radiative zone, thus the integration is limited by the boundaries r_2 and r_1 of this zone. It is not surprising that for the g modes the fundamental period depends on the inverse of the Brunt–Väisälä frequency. In agreement with (17.6) larger n leads to longer periods. For g modes the periods are equally spaced, while for p modes it was the frequencies. In a convective region, the g modes are evanescent and their amplitudes decrease exponentially like $\xi_r \sim \varrho^{-1/2}r^{-(\ell+3/2)}$ [322], so that the amplitude of a g mode with $\ell = 30$ going through the solar convective envelope is reduced by a factor of 10^{-5}. As mentioned in Sect. 16.6.3, Garcia, Turck-Chièze and colleagues appear to have recently detected them from 10 years of GOLF observations.

17.1.2 Propagation Equation

One can write the basic equations of nonradial oscillations [318] in the Cowling adiabatic approximation starting from (16.65) to (16.66), with the variables $u = r^2\xi_r$ and $y = P'/\varrho$

$$\frac{du}{dr} + \frac{1}{\Gamma_1 P}\frac{dP}{dr}u = \left[\frac{\ell(\ell+1)}{\omega^2} - \frac{\varrho\,r^2}{\Gamma_1 P}\right]y, \qquad (17.8)$$

$$\frac{dy}{dr} + y\mathcal{A} = \frac{1}{r^2}\left(\omega^2 + \mathcal{A}g\right)u \quad\text{with}\quad \mathcal{A} \equiv \frac{1}{\varrho}\frac{d\varrho}{dr} - \frac{1}{\Gamma_1 P}\frac{dP}{dr}. \tag{17.9}$$

With account of the meaning of Γ_1 (7.57), one has $N^2 = -g\mathcal{A}$. We easily check that these equations are the same as (16.65) and (16.66). With u and y, the first equation then becomes

$$r^2\frac{d\xi_r}{dr} = -2r\xi_r - \frac{1}{\Gamma_1 P}\frac{dP}{dr}r^2\xi_r + \left[\frac{\ell(\ell+1)}{\omega^2} - \frac{\varrho r^2}{\Gamma_1 P}\right]\frac{P'}{\varrho}. \tag{17.10}$$

After division by r^2, using the definitions of H_P (5.24) and of S_ℓ^2 (16.56), expression (16.66) is recovered. Equation (17.9) becomes,

$$\frac{1}{\varrho}\frac{dP'}{dr} \underbrace{- \frac{P'}{\varrho^2}\frac{d\varrho}{dr} + \frac{P'}{\varrho^2}\frac{d\varrho}{dr}}_{=0} - \frac{P'}{\varrho}\frac{1}{\Gamma_1 P}\frac{dP}{dr} = \left(\omega^2 - N^2\right)\xi_r, \tag{17.11}$$

and (16.65) is recovered. We now eliminate y between (17.8) and (17.9) and account for the fact that ω^2 is small. We express y from the first equation and introduce it into the second one,

$$\frac{d^2 u}{dr^2} + \underbrace{\frac{1}{\Gamma_1 P}\frac{dP}{dr}\frac{du}{dr}}_{*} + u\frac{d}{dr}\left(\frac{1}{\Gamma_1 P}\frac{dP}{dr}\right) + \underbrace{\frac{du}{dr}\mathcal{A}}_{*} + \underbrace{\frac{1}{\Gamma_1 P}\frac{dP}{dr}u\mathcal{A}}_{**}$$

$$- \frac{1}{r^2}u\ell(\ell+1) + \underbrace{\omega^2 u\frac{\varrho}{\Gamma_1 P}}_{\to 0} - \frac{1}{r^2}\mathcal{A}gu\frac{\ell(\ell+1)}{\omega^2} + \underbrace{\frac{\mathcal{A}gu\varrho}{\Gamma_1 P}}_{**} = 0. \tag{17.12}$$

The sum of the two terms with one star gives $(1/\varrho)(d\varrho/dr)(du/dr)$ if we account for $\mathcal{A}$ as given by (17.9). The two terms with a double star cancel each other if we account for hydrostatic equilibrium and as indicated the term in ω^2 can be neglected. Thus, one is left with [318]

$$\frac{d^2 u}{dr^2} + \frac{1}{\varrho}\frac{d\varrho}{dr}\frac{du}{dr} + u\left[-\frac{\mathcal{A}g}{\omega^2}\frac{\ell(\ell+1)}{r^2} - \frac{\ell(\ell+1)}{r^2} + \frac{d}{dr}\left(\frac{1}{\Gamma_1 P}\frac{dP}{dr}\right)\right] = 0. \tag{17.13}$$

As seen in Sect. 16.2.2, the equations of nonradial oscillations lead to a Sturm–Liouville problem: solutions exist only for a discrete spectrum of values ω_n with $n \to \infty$. For $\mathcal{A} < 0$, the solutions correspond to gravity modes. As the last term in (17.13) is generally negative, the values of ω_n^2 are positive and correspond to oscillatory motions, while if $\mathcal{A} > 0$ one has a convection. If we would have eliminated u from (17.8) and have assumed large ω^2 values, we would have obtained a second-order equation corresponding to p modes.

In the context of the transport by gravity waves as originally developed by Press [479], this equation is further transformed by introducing a new variable $\Psi = \varrho^{1/2}u_r = \varrho^{1/2}r^2\xi_r$. One has then

$$\frac{d\Psi}{dr} = \varrho^{1/2}\frac{d(r^2\xi_r)}{dr} + r^2\xi_r\frac{d\varrho^{1/2}}{dr} \,, \tag{17.14}$$

$$\frac{d^2\Psi}{dr^2} = \varrho^{1/2}\frac{d^2(r^2\xi_r)}{dr^2} + 2\frac{d(r^2\xi_r)}{dr}\frac{d\varrho^{1/2}}{dr} + r^2\xi_r\frac{d^2\varrho^{1/2}}{dr^2} \,. \tag{17.15}$$

Expression (17.13) becomes, using the definition of k_h (16.41),

$$\frac{d^2\Psi}{dr^2} + \left(\frac{N^2}{\omega^2} - 1\right)k_h^2\Psi = \left[\frac{1}{\varrho^{1/2}}\frac{d^2\varrho^{1/2}}{dr^2} - \frac{d}{dr}\left(\frac{1}{\Gamma_1 P}\frac{dP}{dr}\right)\right]\Psi \,. \tag{17.16}$$

The second member is of the order of $1/H_P^2$ or $1/H_\varrho^2$, thus, if

$$k_r^2 = \left(\frac{N^2}{\omega^2} - 1\right)k_h^2 \gg H_P^{-2} \,, \tag{17.17}$$

it can be neglected. This is true as long as the vertical wavelength is much smaller than the pressure scale height. In this case, the propagation equation is just

$$\frac{d^2\Psi}{dr^2} + \left(\frac{N^2}{\omega^2} - 1\right)k_h^2\Psi = 0. \tag{17.18}$$

This is a useful and simple form of the wave equation. It can be solved by the WKBJ method [479]. This method, also used in the solution of the Schrödinger equation, assumes a solution of the form $e^{(i\Xi(r))}$, where $\Xi(r)$ varies fast with respect to other quantities at equilibrium, so that the wave number $d\Xi/dr$ is large which leads to some simplifications. For the details of the method, the reader is referred to Unno [585], see also [131]. The solution is expressed in terms of the velocity u_r in coordinates (r, ϑ, φ) [479],

$$u_r = Cr^{-3/2}\varrho^{-1/2}\left(\frac{N^2}{\omega^2} - 1\right)^{-1/4}P_\ell^m(\cos\vartheta)$$

$$\cos\left(\omega t - m(\varphi - \Omega t) - \int_r^{r_c}k_r dr\right) \,, \tag{17.19}$$

where C is a constant fixing the wave amplitude, r_c the radius of the base of the convective zone in solar-type stars, assuming that the convective envelope is the source of the gravity wave (for a massive star, other limits should be taken). This expression corresponds to a wave of frequency ω, degree ℓ and azimuthal order m. The other components of the velocity can be obtained from the continuity equation $\nabla \cdot \varrho \boldsymbol{u} = 0$, ignoring the time variations of ϱ (anelastic approximation). We recall that the wave and velocity are decomposed as $\boldsymbol{\xi}_{\ell,m}(\boldsymbol{r},t) = \xi_r Y_\ell^m(\vartheta,\varphi)e^{i\omega t}\boldsymbol{e}_r + \xi_h\nabla_h Y_\ell^m(\vartheta,\varphi)e^{i\omega t}$, with $\nabla_h = (1/r)[(\partial/\partial\vartheta)\boldsymbol{e}_\vartheta + (1/\sin\vartheta)(\partial/\partial\vartheta)\boldsymbol{e}_\varphi]$. If the terms in front of P_ℓ^m in (17.19) do not vary too much, one gets for the other velocity components

$$u_\vartheta = C \frac{rk_r}{\ell(\ell+1)} r^{-3/2} \varrho^{-1/2} \left(\frac{N^2}{\omega^2} - 1 \right)^{-1/4} \frac{d}{d\vartheta} \left[P_\ell^m(\cos\vartheta) \right]$$

$$\sin\left(\omega t - m(\varphi - \Omega t) - \int_r^{r_c} k_r dr \right), \qquad (17.20)$$

$$u_\varphi = Cm \frac{rk_r}{\ell(\ell+1)} r^{-3/2} \varrho^{-1/2} \left(\frac{N^2}{\omega^2} - 1 \right)^{-1/4} \frac{P_\ell^m(\cos\vartheta)}{\sin\vartheta}$$

$$\cos\left(\omega t - m(\varphi - \Omega t) - \int_r^{r_c} k_r dr \right) = m \frac{rk_r}{\ell(\ell+1)} \frac{u_r}{\sin\vartheta}. \qquad (17.21)$$

The ratio of the squares of the horizontal to the vertical velocity is (17.3)

$$\frac{u_\vartheta^2 + u_\varphi^2}{u_r^2} = \frac{k_r^2}{k_h^2} = \frac{N^2 - \omega^2}{\omega^2}. \qquad (17.22)$$

The vertical phase velocity is ω/k_r and the horizontal one $\omega r \sin\vartheta/m$. The group velocity in the radial direction is by definition,

$$v_g \equiv \frac{d\omega}{dk_r} = -\frac{(N^2 - \omega^2)^{1/2}}{k_h} \left(\frac{\omega}{N} \right)^2 = -\frac{(N^2 - \omega^2)}{N^2} \frac{\omega}{k_r}. \qquad (17.23)$$

This is the velocity at which the energy of a wave is transported. In solar-type stars, the kinetic energy is injected by waves from the convective envelope into the inner radiative layers (v_g has a sign minus). In massive stars, the convective core injects energy outward (v_g has a sign plus). In reality, the general solution is a stationary wave (cf. Sect. 17.3.2).

17.1.3 Non-adiabatic Effects

The non-adiabatic effects, in particular the thermal diffusion of the T fluctuations were neglected in the above derivation. Ideally, one should have used the non-adiabatic equations (16.43), (16.44), (16.45), (16.46) in the procedure leading to (17.18). This is not yet achieved, for now one follows the method by Press [479] and further improved by Zahn et al. [635], who accounted for the effect of the μ gradient on the wave propagation. Let us start from the linearized Euler equation for the perturbation (16.14) and from the equation of continuity (16.12) in Boussinesq approximation (i.e., $\partial\varrho/\partial t = 0$), which are respectively

$$\varrho_0 \frac{\partial \boldsymbol{v}}{\partial t} + \boldsymbol{\nabla} P' = \varrho' \boldsymbol{g} \quad \text{and} \quad \boldsymbol{\nabla} \cdot (\varrho_0 \boldsymbol{v}) = 0. \qquad (17.24)$$

One takes the Laplacian of the vertical component (along r) of the Euler equation,

$$\nabla^2 \left(\varrho_0 \frac{\partial v_r}{\partial t} \right) + \nabla^2 \left(\frac{\partial P'}{\partial r} \right) = -\nabla^2 \left(\varrho' g \right) , \tag{17.25}$$

where $(-g)$ is the component of gravity (1.3). Taking also the divergence of the Euler equation and using the continuity equation, we see that the first term vanishes and we obtain by deriving a second time $\nabla^2 (\partial P'/\partial r) = -g(\partial^2 \varrho'/\partial r^2)$

$$\frac{\partial}{\partial t} \nabla^2 (\varrho_0 v_r) = g \frac{\partial^2 \varrho'}{\partial r^2} - g\nabla^2 \varrho' = -g\nabla_h^2 \varrho' , \tag{17.26}$$

where the variations of g and ϱ_0 are ignored. Since $\nabla_h^2 \rightarrow k_h^2$ and using for the temporal derivative $\partial/\partial t \rightarrow -i\omega$, this equation becomes,

$$i\omega\nabla^2 (\varrho_0 v_r) = gk_h^2 \varrho' . \tag{17.27}$$

This equation of motion couples the vertical velocity and the density fluctuations for a given horizontal wave number.

In addition, we need an equation for the heat transport. We use (6.29), where the first term on the right expresses the heat advection, while the second term gives the heat diffusion, which we express with (3.45). This becomes

$$i\omega \frac{T'}{T} = (\nabla - \nabla_{\text{ad}}) \frac{v_r}{H_P} + \frac{K}{T} \nabla^2 T' . \tag{17.28}$$

To account for the effect of μ variations on the waves, we use the equation of state in the form,

$$\frac{\varrho'}{\varrho} = -\delta \frac{T'}{T} + \varphi \frac{\mu'}{\mu} , \tag{17.29}$$

where we consider the waves in local pressure equilibrium (anelastic approximation). The equation for the transport of μ corresponding to (17.28) is,

$$i\omega \frac{\mu'}{\mu} = \nabla_\mu \frac{v_r}{H_P} , \tag{17.30}$$

because there is, in principle, no diffusion of μ (or in other words the equivalent to ∇_{ad} for the μ exchanges is zero). This is only true if one neglects the effect of horizontal turbulence. There is no reason to omit the effect of D_h and in future works this should be accounted for. Ignoring it for the moment, the equation for the density perturbation becomes

$$i\omega \frac{\varrho'}{\varrho} = \frac{N_T^2 + N_\mu^2}{g} v_r - K\nabla^2 \left(\delta \frac{T'}{T} \right) , \tag{17.31}$$

where the variations of the mean quantities are neglected. The Brunt–Väisälä frequency is expressed here with (5.25). There, we use (17.29) and (17.30) to eliminate the T and μ fluctuations

$$i\omega \frac{\varrho'}{\varrho} = \frac{N^2}{g} v_r - K\nabla^2 \left(-\frac{\varrho'}{\varrho} + \frac{\varphi}{i\omega} \frac{\nabla_\mu}{H_P} v_r \right) ,$$

$$\left(i\omega - K\nabla^2 \right) \varrho' = \frac{N^2}{g} \varrho\, v_r - \frac{\varrho K}{i\omega} \nabla^2 \left(\frac{N_\mu^2}{g} v_r \right) . \tag{17.32}$$

We can express ϱ' with the equation of motion (17.27) and get for the first member and then for the full equation,

$$i\omega\varrho' - K\nabla^2\varrho' = \frac{\omega^2}{gk_h^2} \left(-\nabla^2(\varrho\, v_r) - \frac{i}{\omega} K\nabla^2(\nabla^2\varrho\, v_r) \right) ,$$

$$\nabla^2(\varrho\, v_r) + k_h^2 \frac{N^2}{\omega^2} \varrho\, v_r + \frac{iK}{\omega} \nabla^2 \left(\nabla^2 + k_h^2 \frac{N_\mu^2}{\omega^2} \right) \varrho\, v_r = 0 . \tag{17.33}$$

This is the wave equation in the anelastic approximation with account of non-adiabatic effects (leading to the damping terms in i) and of the effects of μ gradients. With $\nabla^2 \to k_r^2 + k_h^2$, it gives the following dispersion relation:

$$k_r^2 - k_h^2 \left(\frac{N^2}{\omega^2} - 1 \right) - i\frac{K}{\omega}(k_r^2 + k_h^2) \left[k_r^2 - k_h^2 \left(\frac{N_\mu^2}{\omega^2} - 1 \right) \right] = 0 . \tag{17.34}$$

This is a second-order equation for k_r^2, let us look for a solution in the quasi-adiabatic limit, i.e., with $k_r = A + BK + \cdots$, which gives in the linear approximation $k_r^2 = A^2 + 2ABK + \cdots$. One has

$$A^2 + 2BAK - k_h^2 \left(\frac{N^2}{\omega^2} - 1 \right) - i\frac{K}{\omega} \left(A^2 + 2BAK + k_h^2 \right)$$

$$\left[A^2 + 2BAK - k_h^2 \left(\frac{N_\mu^2}{\omega^2} - 1 \right) \right] = 0 . \tag{17.35}$$

By identifying the corresponding powers of K, we get $A^2 = k_h^2(N^2/\omega^2) - 1$ and for B,

$$B = \frac{i}{2\omega A}\left[A^4 - A^2 k_h^2\left(\frac{N_\mu^2}{\omega^2}-1\right) + k_h^2 A^2 - k_h^4\left(\frac{N_\mu^2}{\omega^2}-1\right)\right] = \frac{ik_h^3}{2\sqrt{N^2-\omega^2}}$$

$$\left[\left(\frac{N^2}{\omega^2}-1\right)^2 - \left(\frac{N^2}{\omega^2}-1\right)\left(\frac{N_\mu^2}{\omega^2}-1\right) + \left(\frac{N^2}{\omega^2}-1\right) - \left(\frac{N_\mu^2}{\omega^2}-1\right)\right]$$

$$= i\frac{k_h^3}{2\sqrt{N^2-\omega^2}}\left[\frac{N^2 N_T^2}{\omega^4}\right], \tag{17.36}$$

where we have used $N^4 - N^2 N_\mu^2 = N^2 N_T^2$. One has since the non-adiabatic term is small $k_r \approx A + BK$

$$k_r \approx \pm k_h\left(\frac{N^2}{\omega^2}-1\right)^{1/2} + i\frac{K}{2\omega}k_h^3\frac{NN_T^2}{\omega^3}\left(\frac{N^2}{N^2-\omega^2}\right)^{1/2}. \tag{17.37}$$

This provides the relation between the vertical and the horizontal wave numbers k_r and k_h like in (17.4). It also gives the damping factor of the waves.

Equation (17.33) can be compared to the wave equation (17.18) in spherical geometry, which does not account for the effects of radiative damping and of μ gradient. The suggestion by Press [479], followed by all authors, is to combine these two equations by adding to (17.18) (which accounts for the effects of variations of density and radius) the damping term from (17.33) obtained under the anelastic assumption. One gets with these approximations the following wave equation for $\Psi = \varrho^{1/2} u_r$:

$$\frac{d^2\Psi}{dr^2} + \left(\frac{N^2}{\omega^2}-1\right)\frac{\ell(\ell+1)}{r^2}\Psi + \frac{iK}{\omega}\nabla^2\left(\nabla^2 + k_h^2\frac{N_\mu^2}{\omega^2}\right)\Psi = 0. \tag{17.38}$$

If the damping term is not too large (which would make an evanescent solution), the solution of this equation is still given by (17.19) with account of the damping bringing an exponentially decreasing factor $e^{-\tau/2}$. The damping factor τ comes from (17.37), with the factor of 2 coming from the imaginary term of (17.37). At a level r, τ is

$$\tau(\omega,\ell,r) = [\ell(\ell+1)]^{3/2}\int_r^{r_c} K\frac{NN_T^2}{\omega^4}\left(\frac{N^2}{N^2-\omega^2}\right)^{1/2}\frac{dr}{r^3}. \tag{17.39}$$

The damping term τ is proportional to the thermal diffusivity and to the power -4 of the wave frequency ω. In case of differential rotation $\Omega(r)$, this leads to a different radiative damping for the prograde and retrograde waves, see Sect. 17.3.1 below. The weighting in r^{-3} arises from the spherical geometry. The damping in $e^{-\tau/2}$ applies to the three components $(u_r, u_\vartheta, u_\varphi)$ of the velocity. Figure 17.2 illustrates the damping factor in a solar model. The g modes of high ℓ are rapidly absorbed, while the low ℓ modes may transport angular momentum from the convective envelope down to the deep interior.
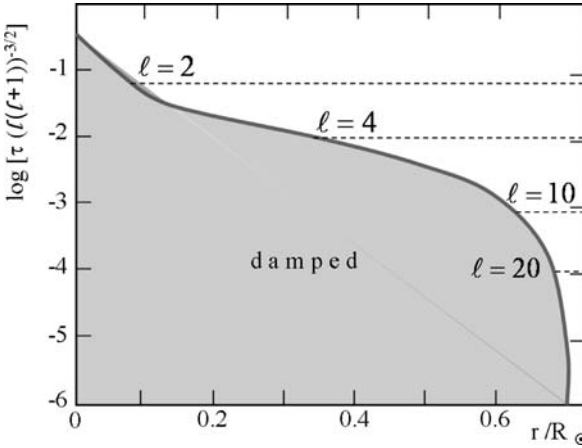
Fig. 17.2 The damping factor divided by $(\ell(\ell+1))^{3/2}$ at $\omega = 1\,\mu\mathrm{Hz}$ in the solar model. The depths where this damping term reaches a factor e are indicated. This term is the integral appearing in Eq. (17.39). Adapted from S. Talon [557]

17.2   Energy and Momentum Transport by Gravity Waves

The gravity waves propagate in radiative regions and transport some kinetic energy and angular momentum through the star [635]. Contrarily to early expectations, gravity waves likely do not significantly transport the chemical elements (Sect. 17.4.1).

Let us first evaluate in the adiabatic case the horizontal mean density of kinetic energy, using (17.22) to estimate the sum of the three components,

$$
\frac{1}{2}\varrho <u^2> = \frac{1}{4\pi} \int_0^{2\pi} \int_0^{\pi} \frac{1}{2}\varrho \left(u_r^2 + u_\vartheta^2 + u_\varphi^2 \right) \sin\vartheta\, d\vartheta\, d\varphi
$$

$$
= \frac{1}{2}\frac{N^2}{\omega^2}\frac{1}{4\pi} \int_0^{2\pi} \int_0^{\pi} \varrho u_r^2 \sin\vartheta\, d\vartheta\, d\varphi = \frac{1}{2}\frac{N^2}{\omega^2}\varrho <u_r^2> . \quad (17.40)
$$

This energy is transported with the group velocity v_{g} (17.23), so that the mean flux $\mathcal{F}_{\mathrm{kin}}$ of kinetic energy for a monochromatic wave is

$$
\mathcal{F}_{\mathrm{kin}}(\omega,\ell) = \frac{1}{2}\varrho <u^2> v_{\mathrm{g}} = -\frac{1}{2}\varrho <u^2> \frac{\left(N^2 - \omega^2\right)}{N^2}\frac{\omega}{k_r}
$$

$$
= -\frac{1}{2}\varrho <u^2> \left(\frac{\omega}{N}\right)^2 \frac{(N^2 - \omega^2)^{1/2}}{k_h} , \quad (17.41)
$$

in g s^{-3}. There, we use relation (17.4) between k_h and k_r, the appropriate sign has to be taken depending on the inward ($-$) or outward ($+$) propagation.

We now evaluate the flux of angular momentum transported by a wave of frequency ω. The density of angular momentum at a point (r,ϑ) is $\varrho\, r \sin\vartheta\, u_\varphi$ and the flux is obtained by multiplying it by the vertical velocity. The mean flux of angular momentum over a horizontal spherical surface is with (17.21)

$$\mathcal{F}_{\mathrm{ang}}(\omega,\ell,m) = \frac{1}{4\pi} \int_0^{2\pi} \int_0^{\pi} \varrho\, r \sin\vartheta\, u_\varphi u_r \sin\vartheta\, d\vartheta\, d\varphi$$

$$= -m \frac{r k_r}{\ell(\ell+1)} \frac{1}{4\pi} \int_0^{2\pi} \int_0^{\pi} \varrho\, u_r^2 \sin\vartheta\, d\vartheta\, d\varphi \,, \qquad (17.42)$$

where there is a simplification by $\sin\vartheta$ (same remark for the sign). From this expression and (17.41), we get the following general relation between the flux of angular momentum and of kinetic energy for given (ω,ℓ,m),

$$\mathcal{F}_{\mathrm{ang}}(\omega,\ell,m) = 2\frac{m}{\omega} \mathcal{F}_{\mathrm{kin}}(\omega,\ell,m) \,, \qquad (17.43)$$

in g s^{-2}. One defines an "angular momentum luminosity" $\mathcal{L}_{\mathrm{ang}}(\omega,\ell,m)$, i.e., the total change of angular momentum over the spherical surface at a level r per unit of time, as

$$\mathcal{L}_{\mathrm{ang}}(\omega,\ell,m,r) = 4\pi r^2 \mathcal{F}_{\mathrm{ang}}(\omega,\ell,m) \,, \qquad (17.44)$$

in g cm^2 s^{-2}. In the adiabatic limit, i.e., without the term with $e^{-\tau/2}$, the angular momentum luminosity would be conserved [635]. The total angular momentum is the sum on all waves (ω,ℓ,m) excited at the edge r_c of the convective zone, each wave being damped by the factor $e^{-\tau/2}$,

$$\mathcal{L}_{\mathrm{ang}}(r) = \sum_{\omega,\ell,m} \mathcal{L}_{\mathrm{ang}}(\omega,\ell,m,r_c) e^{-\tau(\omega,\ell,r)} \,, \qquad (17.45)$$

since the luminosity depends on u_r^2, the damping factor becomes $e^{-\tau}$. Figure 17.3 shows the angular momentum luminosity as a function of degree ℓ and frequency for a 1 M$_\odot$ star. The frequencies ω are smaller than the N value at the lower edge of the convective zone in agreement with Fig. 16.8. The ℓ values range from 1 to about 60, which corresponds to the characteristic length scale of convective motions, i.e., the mixing length. The various m modes are assumed to have the same excitation. One sees that $\mathcal{L}_{\mathrm{ang}}$ decreases for higher frequencies and that low ℓ values carry more angular momentum. Consistently with Fig. 17.2, these low ℓ waves are less absorbed.
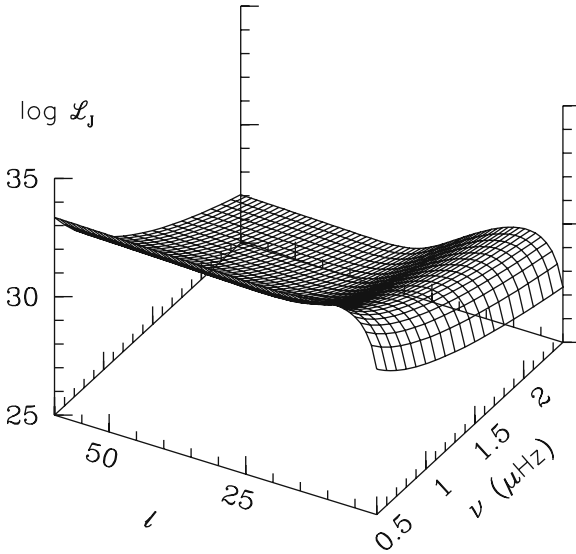
Fig. 17.3 The angular momentum luminosity $\mathcal{L}_{\text{ang}}$ in a 1 M$_\odot$ ZAMS model for various degrees ℓ as a function of the frequency $\nu = \omega/(2\pi)$ just at the inner edge of the convective envelope. The flux is here calculated with excitation by convective motions (Sect. 17.2.1). Courtesy from S. Talon [557]

The transport of angular momentum by gravity waves introduces an additional term in Eq. (10.122) for the transport of angular momentum, which expresses the change of angular momentum per volume and time units,

$$\varrho \, \frac{\partial}{\partial t}(r^2 \overline{\Omega})_{M_r}$$

$$= \frac{1}{5r^2} \frac{\partial}{\partial r}(\varrho \, r^4 \overline{\Omega} U_2(r)) + \frac{1}{r^2} \frac{\partial}{\partial r}\left(\varrho \, D_v \, r^4 \, \frac{\partial \overline{\Omega}}{\partial r}\right) \pm \frac{3}{8\pi} \frac{1}{r^2} \frac{\partial}{\partial r} \mathcal{L}_{\text{ang}}(r), \quad (17.46)$$

in g cm^{-1} s^{-2}. A sign plus in front of the angular momentum term corresponds to an inward traveling wave, a sign minus to an outward moving wave. As shown in Sect. 17.3.2, angular momentum may be deposited or extracted by gravity waves.

The above equation expresses average quantities weighted by $\sin^3 \vartheta$ (10.5.4). This gives a factor 4/3, included in the definition (10.105) of $\overline{\Omega}$. Moreover, the integration over $d\varphi$ has been simplified in (10.101), it would have given a factor 2π. Since $\mathcal{L}_{\text{ang}}(r)$ is the total angular luminosity over the stellar surface, we have to divide it by these factors 2π and 4/3 to be consistent, which explains the numerical factor $3/(8\pi)$ in the equation. This equation is subject to the boundary conditions (cf. Sect. 10.5.5) for solar-type stars

$$\frac{1}{5}\varrho\,r^4\,\Omega\,U_2\bigg|_{r_b} = \frac{d}{dt}\left[\Omega\int_0^{r_b}r^4\varrho\,dr\right] + \frac{3}{8\pi}\mathcal{L}_{ang}(r_b)\quad\text{at }r=r_b,$$

$$-\frac{1}{5}\varrho\,r^4\,\Omega\,U_2\bigg|_{r_t} = \frac{d}{dt}\left[\Omega\int_{r_t}^{R}r^4\varrho\,dr\right] + \mathcal{M}_\Omega - \frac{3}{8\pi}\mathcal{L}_{ang}(r_t)\quad\text{at }r=r_t,\quad(17.47)$$

where r_t and r_b refer to the top and bottom of the radiative zone.

17.2.1 Wave Excitation

Gravity waves are excited in convective regions, in which paradoxically they are evanescent. They are injected in a nearby radiative zone where they propagate. Two different processes of wave excitation have been investigated so far: by overshooting and by bulk convection. There are uncertainties in both processes [387]. We limit the presentation to the main points.

17.2.1.1   Excitation by Overshooting

Wave excitation is produced close to the edge of the convective region, because of the evanescence. Thus, overshooting fluid elements entering a radiative region may be quite efficient in producing gravity waves [199].

Let us start from the flux of kinetic energy (17.41) with a positive sign. The velocity u is the amplitude of the fluid velocity due to gravity waves to be distinguished from v the velocity of convective fluid elements. The turbulence in the convective region is assumed to follow the Kolmogorov spectrum with the typical relation between length scale λ and velocity,

$$\lambda \propto v^3\,,\tag{17.48}$$

for $\lambda < \ell_{conv}$, say the mixing length. The cyclic frequency of the waves generated by the convective motions is

$$\omega = 2\pi\nu = 2\pi\frac{v}{2\lambda} \sim \lambda^{-2/3}\,,\tag{17.49}$$

because a complete turnover time is in fact $2\lambda/v$. For the same reason, one has $k_h = \pi/\lambda$, assuming that λ characterizes the typical length scales in the convective zone. The matter density ϱ is continuous and the energy densities $(1/2)\varrho\,u^2 = (1/2)\varrho\,v_{conv}^2$ are the same at the edge of the convective zone, so that $u = v_{conv}$ for a given length scale λ.

The convective elements of frequency ω and length scale λ not only produce gravity waves with the same length scale, but their incoherent superposition also creates longer waves with $\lambda_h > \lambda$ at frequency ω [199]. Let us call n the number of

eddies which participate on average to one of these longer wavelengths λ_h. The velocity amplitudes of these incoherent randomly distributed oscillations are reduced by a factor $n^{1/2}$ with respect to the coherent case (alike the dispersion around the average of n variables with a Gaussian distribution),

$$u_{\text{incoh}} = \frac{1}{n^{1/2}} u_{\text{coh}} . \tag{17.50}$$

The overshooting motions are anisotropic with a strong vertical velocity component, but horizontally the sizes and velocities may be considered as isotropic with an average wavelength λ_h. In a horizontal surface area of size λ_h^2, there are many convective waves of horizontal size λ, thus

$$n \approx \left(\frac{\lambda_h}{\lambda} \right)^2 . \tag{17.51}$$

The excited waves have two horizontal components, say λ_x and λ_y, which are not necessarily equal so that a better approximation would be $n \approx (\lambda_x \lambda_y / \lambda)^2$. For a given λ_h, n is minimum when $\lambda_x = \lambda_y$, so that (17.50) is a maximum. The velocity of the waves generated by the incoherent convective motions is thus, for a frequency ω and a horizontal wavelength λ_h,

$$u(\omega, \lambda_h) = \frac{v}{n^{1/2}} = \left(\frac{\lambda}{\lambda_h} \right) v = \left(\frac{\lambda}{\lambda_h} \right) \frac{\omega \lambda}{\pi} . \tag{17.52}$$

With this expression of the velocity, the flux of kinetic energy (17.41) becomes

$$\mathcal{F}_{\text{kin}}(\omega, \lambda_h) = \frac{\varrho}{2\pi^3} \frac{(N^2 - \omega^2)^{1/2}}{N^2} \frac{\lambda^4 \omega^4}{\lambda_h} . \tag{17.53}$$

There, λ is unspecified and may be expressed in terms of the properties of the convective zone. From (17.48), one has

$$\lambda = \ell_{\text{conv}} \frac{v^3}{v_{\text{conv}}^3} , \tag{17.54}$$

while from (17.49), $v = \omega \lambda / \pi$ and thus with (17.54) one gets

$$\lambda^2 = \frac{\pi^3 v_{\text{conv}}^3}{\ell_{\text{conv}} \omega^3} . \tag{17.55}$$

With this expression for λ, the flux becomes [199]

$$\mathcal{F}_{\text{kin}}(\omega, \lambda_h) = \frac{\pi^3 \varrho}{2} \frac{(N^2 - \omega^2)^{1/2}}{N^2} \frac{1}{\lambda_h} \frac{v_{\text{conv}}^6}{\ell_{\text{conv}}^2 \omega^2} . \tag{17.56}$$

For given (ω, λ_h), the flux can be expressed in terms of the parameters of the convective zone. Since at the very edge of the zone $N^2 = 0$, the values of N^2, v_{conv} and ℓ_{conv} have to be taken at some "appropriate" distance of the edge (ideally, this "appropriate" distance should account for the evanescent character of the wave as well as for the gradient of N^2 and v_{conv}). The flux of angular momentum is then given by (17.43).

17.2.1.2 Excitation by Convective Motions

The excitation of gravity waves by the convective motions has been studied by Kumar and Quataert [299] and Kumar et al. [300]. They extend to g modes a model of generation of turbulent energy developed by Golreich et al. [212] to reproduce the energy spectrum of p modes. They consider that the wave excitation essentially results from the turbulent coupling of convective elements. They propose the following expression for the flux of kinetic energy just below the convective envelope of the Sun, as a function of (ℓ, ω) for solar-type stars, with the assumption of a Kolmogorov turbulence spectrum,

$$\mathcal{F}_{kin}(\omega, \ell, m) = \frac{\omega^2}{4\pi} \int_{conv.zone} \frac{\varrho^2}{r^2} \left[\left(\frac{\partial \xi_r}{\partial r} \right)^2 + \ell(\ell+1) \left(\frac{\partial \xi_h}{\partial r} \right)^2 \right]$$

$$\frac{v^3 L^4}{1 + (\omega \tau_L)^{15/2}} \times \exp \left[-h_\omega^2 \frac{\ell(\ell+1)}{2r^2} \right] dr, \qquad (17.57)$$

where ξ_r and ξ_h are the radial and horizontal displacements, both normalized to a unit energy flux at the bottom of the convective zone (the proper scaling being given by the other terms in the expression). In this equation, the term $\left(\frac{\partial \xi_h}{\partial r} \right)^2 \ell(\ell+1)$ has been arbitrarily introduced [299] by similarity with the term in ξ_r to account for the energy of the $\sqrt{\ell(\ell+1)}$ horizontal waves around the star. The convective velocity v is given by (5.45), L is the radial size of the largest turbulent eddies, $\tau_L \approx L/v$ is the turnover convective time, h_ω is the radial size of the largest eddy at level r with a frequency $\geq \omega$ ($h_\omega = L \times \min[1, (2\omega \tau_L)^{-3/2}]$). The flux of angular momentum is still given by (17.43). Only the waves up to the frequency N_{ad} in the lower part of the convective envelope can be excited. The highest frequencies up to this limit experience the strongest damping (17.39).

Figures 17.4 and 17.5 show the angular momentum luminosity as a function of $v = \omega/(2\pi)$ and ℓ at the inner edge of the convective envelope for various models. There are several common features. For larger masses between 1.1 and 1.45 $M_\odot$, the lower frequency waves are progressively absent for given values of ℓ. This is due to the higher temperatures and lower densities, which favor large values of the thermal diffusivity K. This increases the damping so that standing waves cannot exist. For increasing masses, $\mathcal{L}_{ang}$ becomes larger due to the higher luminosities, which make stronger convective motions and enhance the transport by nonradial
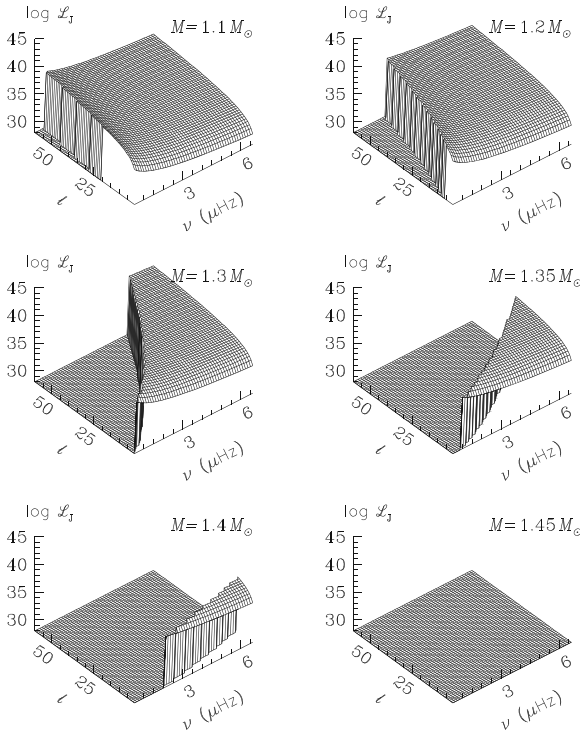
Fig. 17.4 Angular momentum luminosity for stars of various masses for the excitation by over-shooting according to R.J. Garcia Lopez and H.K. Spruit [199]. Picture from S. Talon and C. Charbonnel [559]

waves. The transport by the waves due to overshooting is stronger than the transport by the waves due to bulk convection, despite the fact that the waves are incoherent in the overshooting model.

As the mode excitation is concentrated at the limit of the convective zone, all the current uncertainties of the mixing-length theory concerning the velocity, the typical length scale, the frequency spectrum and the boundary location may intervene in these two estimates.

Some numerical 2D models of the generation and propagation of gravity waves have been made. In the case of overshooting, some 2D models [286] predict larger energy fluxes than the analytical models, while other ones [496] find smaller fluxes and show that convection does not continually drive standing g-mode frequencies. All numerical models suggest that the modes are excited over a broader range of frequencies and wavelengths. At present, it is not clear whether the differences are due to the analytical models or to the simplified nature of 2D models. The angular momentum transported by overshooting plumes appear [497] dominant over wave interactions in agreement with the results of Figs. 17.4 and 17.5.
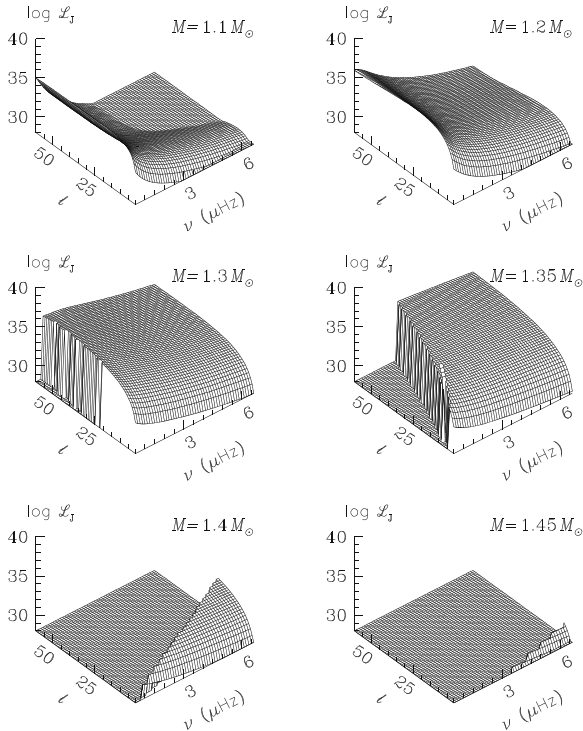
Fig. 17.5 Angular momentum luminosity for various stars with excitation by convective motions [212, 300]. Picture from S. Talon and C. Charbonnel [559]

17.3   Consequences of Transport by Gravity Waves

Some first results have already been obtained by S. Talon and C. Charbonnel regarding the internal solar rotation [561] and the distribution of lithium in MS stars [559]. This subject is likely promised to further developments regarding the waves generated in convective cores of massive stars, in the envelope of red giants and supergiants and their effects on evolution. The case of pre-supernovae may also be of interest (Sect. 28.4.2).

17.3.1   Shear Layer Oscillations "SLO"

Gravity waves deposit their angular momentum where they are damped. The damping of prograde $(m < 0)$ and retrograde $(m > 0)$ waves is not the same. Prograde waves have a smaller local frequency (Sect. 16.6) and therefore their damping factor τ (17.39) is higher. This means that prograde waves are dissipated closer to the

excitation zone than retrograde waves. These are dissipated further from the edge of the convective region and the same for angular momentum deposition.

Let us assume that the excitation by the convective envelope of solar-type stars produces prograde and retrograde waves of the same amplitudes. In solid body rotation (due to some high internal coupling), both waves are dissipated somewhere in the interior and their angular momentum is redistributed (solid body rotation means very strong coupling) and there is no effect on the angular momentum distribution.

We now consider the case of a differential rotation in solar-type stars, one has $\partial\Omega/\partial r < 0$ at the bottom of the convective zone due to magnetic braking at the stellar surface (Sect. 13.2). The prograde waves which move faster than the envelope bring angular momentum to the interior, while the retrograde waves which move slower extract angular momentum from below. The high-degree waves (with low frequencies) are very much damped. If prograde, these waves release their angular momentum just below the edge of the convective envelope, thus locally enhancing the value of $\Omega(r)$. If retrograde, these waves go slightly deeper into the radiative region, the angular momentum they are extracting leads to a local reduction of $\Omega(r)$. This makes first an outer positive (since damping is stronger) and then an inner negative peak of angular velocity (panels 1 and 2 of Fig. 17.6).

The shear turbulence comes into play and first diffuses the positive peak (from prograde waves) toward the convective envelope (panel 3). This occurs because the thermal diffusivity K of shear turbulence is larger toward the exterior. As a consequence, only the negative peak is left (panel 4). Then, the negative peak (from retrograde waves) also diffuses and merges with the convective envelope, while a
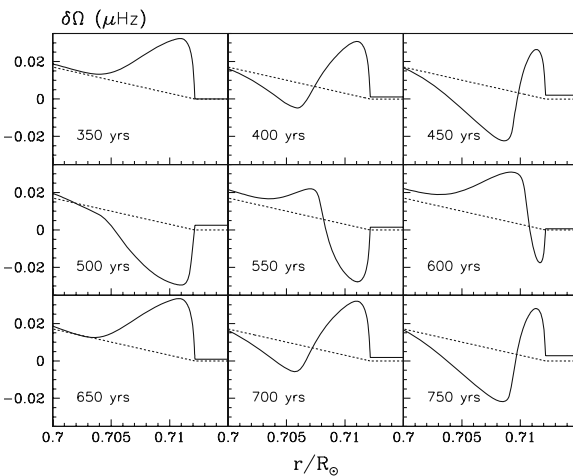
Fig. 17.6 Illustration of the oscillating shear layer (SLO) for a solar model. The lines show the difference of angular velocity with respect to the average in the considered zone at different ages. The dotted line shows the initial Ω profile. A peak from prograde waves forms first, followed by a negative peak from retrograde waves. The strong shear diffuses first the outer peak then the inner one and the cycles resumes. From S. Talon, P. Kumar and J.P. Zahn [561], with permission

new peak again forms at the same location as the previous one (panels 5, 6 and 7). It is followed by a new negative peak and the cycle resumes (panels 8 and 9). This dynamical situation is called a "shear layer oscillation" (SLO) by Talon and Charbonnel [560]. The timescale for one cycle is 300 yr for the Sun and about 2 yr for a $1.2 \, M_\odot$.

The behavior of the SLO depends on the relative importance of the turbulent viscosity (or diffusion) with respect to the wave flux [560]. For large viscosity, a stationary state may exist. For very low viscosity, the SLO likely would turn to chaotic motions, since the Reynolds number becomes very large. This last case seems less probable since the shear will unavoidably create a large viscosity.

17.3.2   The Solar Rotation Curve

The SLO acts as a filter on the internal gravity waves for the following reasons. The thermal diffusivity K was introduced in (17.28), if there is an additional source of diffusion by turbulence with a diffusion coefficient, like for the shear D_{shear} or the horizontal turbulence D_{h}, they should be added in (17.39),

$$\tau(\omega, \ell, r) = [\ell(\ell+1)]^{3/2}$$

$$\int_r^{r_{\mathrm{c}}} [K + D_{\mathrm{shear}} + D_{\mathrm{h}} + \cdots] \frac{N N_T^2}{\omega^4} \left(\frac{N^2}{N^2 - \omega^2} \right)^{1/2} \frac{dr}{r^3} . \qquad (17.58)$$

In the SLO, D_{shear} is important and enhances the damping. The current models do not account for D_{h} which may introduce some significant differences, because the horizontal turbulence is generally quite large.

With only the shear turbulence, the waves keep high enough amplitudes despite the filtering by the SLO to produce efficient angular momentum transport [560, 561]. This filtering is complex. It depends on the difference $\delta\Omega$ of rotation rates at the base of the convection zone and of the SLO,

$$\delta\Omega = \Omega_{\mathrm{c}} - \Omega_{\mathrm{SLO}} , \qquad (17.59)$$

which is negative due to the magnetic torque at the surface of solar-type stars. The waves traveling inward through the SLO meet first a "rapid" and then a "slow" layer. The rapid layer increases the damping of prograde modes (since their frequencies are decreased as seen in the rotating fluid), the damping is smaller for retrograde modes. The slow layer has an opposite and slightly smaller effect. The net effect of this asymmetric filtering is a larger reduction of the amplitudes of prograde modes with respect to those of retrograde modes.

Let us now turn to the deposition of angular momentum in the deep interior. The low-degree waves with high frequencies suffer much less damping and may go throughout the radiative region. Indeed, (17.39) shows that the damping factor τ behaves like $\ell(\ell+1)^{3/2}$. The gravity waves reach their maximum depth when $\omega(r, m)$

becomes equal to N (Fig. 16.8). Retrograde waves may go deeper and reach the central region, which contains little angular momentum and is thus rapidly spun down (Fig. 17.7), because it contains very little angular momentum. The waves which are reflected back then continue to loose angular momentum. High-frequency waves may be reflected up to several thousands of times before being fully damped (these contribute little to the transport). On the whole, the transport by gravity waves of various frequencies tends to reduce the difference of rotation between the envelope and the interior. Figure 17.7 shows an example of evolution of the internal distribution $\Omega(r)$ in a $1.0\,M_\odot$ model, with account of gravity waves, meridional circulation and shear turbulence. One sees the progressive flattening of the rotation profile in the radiative region starting from the central regions. The outer regions take a longer time to slow down since they contain more angular momentum. In the solar model, it is only at the present age of the Sun that the full radiative interior rotates almost like a solid body. This timescale for reaching solid body rotation is much longer than the timescale of 10^7 yr which was initially considered in studies including only gravity wave effects. One may wonder whether the inclusion of horizontal turbulence would not further increase this timescale, possibly making the transport by gravity waves inefficient.

From helioseismic data (Fig. 16.20), the central solar regions seem to rotate faster than the bulk of radiative interior. The question arises whether gravity waves predict a slower or a faster rotating core in the Sun. This may be a test whether the flat internal rotation curve is due to transport by gravity waves or by magnetic field (Sect. 13.6.2). At present, there are many uncertainties both in the observations and models so that any firm conclusion is premature.
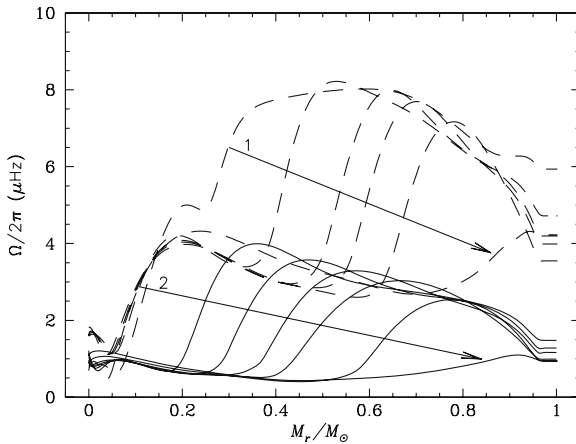
Fig. 17.7 Evolution of the distribution of the angular velocity as a function of time in a $1.0\,M_\odot$ model starting from the ZAMS. Account is given to gravity waves, meridional circulation and shear turbulence. The curves with *dotted lines* (package 1) correspond to ages 0.2, 0.21, 0.22, 0.23, 0.35 0.27 Gyr, the curves with *continuous lines* (package 2) correspond to 0.5, 0.7, 1.0, 1.5, 3.0 and 4.6 Gyr. Courtesy from S.Talon and C. Charbonnel [558, 560]

17.3.3   Waves and the Lithium Dip

The lithium dip [53, 606] is a property of the Li abundances of stars in the mass range of 1–1.5 $M_\odot$. In a domain of about 300 K centered at $T_{eff} = 6650$ K, the Li abundances are lower by a factor up to about 2.5 dex (Fig. 17.8) (this T_{eff} corresponds to about 1.42 $M_\odot$ in the Hyades cluster). The Li dip is present in clusters with ages larger than 10^8 yr, like the Hyades (6×10^8 yr); in younger cluster the Li dip is absent or much smaller.

   The full interpretation is interesting [559] because it needs several of the physical effects we have considered: convection, magnetic torque, shear mixing, meridional circulation and internal gravity waves. Starting from the hot side, we may distinguish the following domains of T_{eff} and associated effects (with the corresponding mass in the Hyades):

– $T_{eff} \geq$ 6900 K (1.48 $M_\odot$): the external convective zone is absent or very thin, thus there is no dynamo and no external coupling (slowing down) by a magnetic field. The gradient of Ω (cf. Fig. 11.8) is small and shear mixing negligible, just compensating microscopic diffusion.
– 6900 K $\geq T_{eff} \geq$ 6650 K (1.42 $M_\odot$): the outer magnetic torque becomes more important as a result of the increasing size of the convective envelopes. The torque creates an Ω gradient and the resulting shear mixing produces a diffusion of the elements and this leads to a destruction of Li when it is brought deep enough.
– 6650 K $\geq T_{eff} \geq$ 6200 K (1.28 $M_\odot$): the convective envelope becomes deeper, the magnetic torque, the Ω gradient and the mixing stronger. This would, if no other effect, further destroy the lithium. The fact the observations show that it is not the case implies something else. The suggestion [560] is that the convective zone is large enough to generate gravity waves, which transport the angular momentum
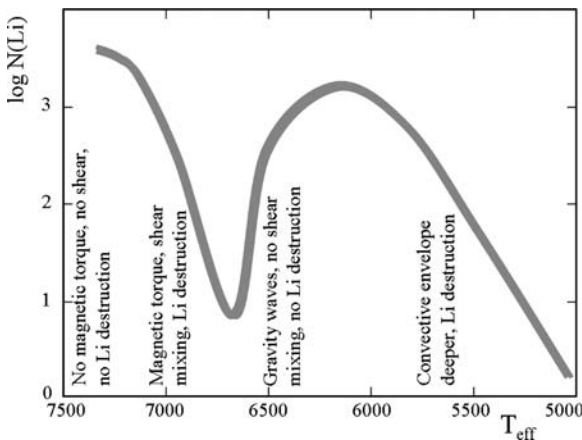
Fig. 17.8 Schematic illustration of the Li dip of the Hyades [52] with the main effects shaping the Li abundances

and thus reduces differential rotation and shear mixing. Thus, there is possibly less Li diffusion into the interior and Li is less destroyed.

– 6200 K $\geq T_{\mathrm{eff}}$: there, the larger and larger outer convective zones for lower T_{eff} go deep enough to bring Li below the critical $T = 2.5 \times 10^6$ K where it is destroyed. This explains the reduction of the Li abundance for stars below about 1.28 $M_\odot$.

Figure 17.8 illustrates the Li dip in the Hyades cluster and the various effects considered as responsible for this remarkable feature. On the whole, the interpretation of Li dip may offer a magnificent synthesis of the various physical effects intervening in the envelope of solar-type stars.

17.4 Transport by Gravity Waves and Open Questions

17.4.1 Particles Diffusion by Gravity Waves

The back and forth motions of a wave do not transport the chemical elements. There may be however some diffusion processes generated by the waves [199, 479, 558]. Let us consider a stellar medium permeated by gravity waves with $\omega \ll N$, the waves travel nearly horizontally (Fig. 17.1). As the horizontal wavelength is much larger than the vertical one, one also has $u_h \gg u_r$ (Fig. 17.1). The sinusoidal variation of u_h introduces locally a shear. The average shear rate is given by the ratio of u_h over the vertical wavelength

$$\left(\frac{\partial u_h}{\partial r} \right)^2 \approx k_r^2 u_h^2 \,. \tag{17.60}$$

In order for the Richardson criterion (12.31) to be valid, the flow must be steady. This condition is verified if the shear rate $k_r u_h$ is larger than the wave frequency ω [199]. With (17.60), the Richardson criterion becomes

$$\mathcal{R}i \equiv \frac{N^2}{(dV/dz)^2} = \frac{N^2}{(k_r u_h)^2} < \mathcal{R}i_{\mathrm{crit}} \,, \tag{17.61}$$

As in Sect. 12.2.3, we take the thermal diffusivity into account, assuming that the Peclet number $\mathcal{P}e = v\ell/K = 6\Gamma$ (B.66) is very small, thus

$$\frac{N^2}{(k_r u_h)^2} \frac{\ell v}{K} < \frac{1}{4} \,, \tag{17.62}$$

where we take the critical Richardson number equal to $1/4$. ℓ and v are the characteristic vertical distance and velocity, respectively. The diffusion coefficient due to the shear of gravity waves is [199]

$$D_{\text{wave shear}} = \frac{1}{3} v \ell = \frac{1}{12} K \frac{(k_r u_h)^2}{N^2} . \tag{17.63}$$

This diffusion coefficient is similar to (12.38), except that the shear rate is different. For a F star at middle of the Li gap ($\sim 1.42 \, M_\odot$), $D_{\text{wave shear}} = 6 \times 10^5$ cm^2 s^{-1} in the external layer where Li is burning [199]. This leads to a Li depletion in 7×10^7 yr. For more massive stars, the wave frequencies are larger than the shear rate and the above development becomes uncertain. Garcia Lopez and Spruit [199] have a numerical factor $1/4$ instead of $1/12$ in their diffusion coefficient and they point out that their coefficient should still be increased by a factor of 15 in order to account for the Li gap.

This suggests that shear from gravity waves, which applies to star with $M \leq 1.5$, is marginally significant. However, we note that its consequences have not yet been fully explored. Other processes of mixing by waves have been envisaged [428, 479, 516, 558]; however, their efficiency is uncertain.

17.4.2   Open Questions and Further Developments

There are several areas where the transport of angular momentum by gravity waves may need further developments [387].

- The description of the excitation of gravity waves by convective motions is still insufficient. In its present form, expression (17.57) was simply derived by analogy with the excitation of p modes by a convective zone. Other terms than those in $\left(\frac{\partial \xi_r}{\partial r} \right)^2$ and $\left(\frac{\partial \xi_h}{\partial r} \right)^2$ should likely intervene.
- The level of excitation by overshooting is higher than by the bulk of convective motions. A unified description of both effects should be developed.
- Figure 17.9 illustrates the different types of waves as a function of frequency. Above ω_{ac} there are acoustic waves, the gravity waves driven by buoyancy occur below the Brunt–Väisälä frequency N. For lower frequencies, we find the inertial waves for which the recall force is Coriolis force. The domains of gravity and inertial waves coincide over a range of frequencies, which may depend on stellar mass. This is the domain of the gravito-inertial waves, for which further theoretical developments are needed [387].

If we retain only the inertial and Coriolis terms in the equation of motion (B.26), we get

$$\frac{d\boldsymbol{v}}{dt} = -2 \boldsymbol{\Omega} \times \boldsymbol{v} . \tag{17.64}$$

For a wave of the form $e^{\omega t}$, with $d/dt \to \omega$, considering the modulus of this equation, we get at colatitude ϑ

$$\cos \vartheta = \frac{\omega}{2\Omega} . \tag{17.65}$$
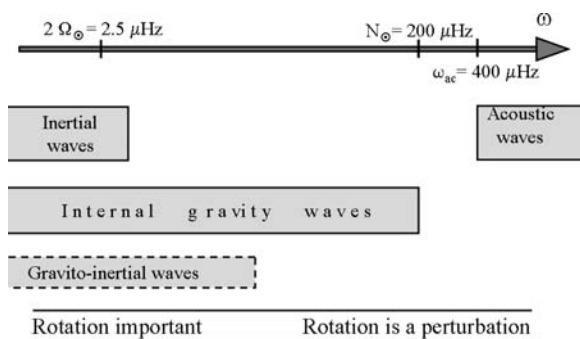
Fig. 17.9 The various types of waves in their frequency domains. The angular velocity, the Brunt-Väisälä frequency and the acoustic cutoff frequency at the base of the convective zone are indicated. Adapted from Mathis [387]

For a wave of frequency ω in a star rotating with angular velocity Ω, this is the maximum colatitude for inertial wave propagation. At a given frequency, for larger Ω one has $cos^2 \vartheta \rightarrow 0$ and the waves only exist near the equator.

The study of the propagation of gravito-inertial waves has been made by Kumar et al. [300] and the effects on the transport of angular momentum have been recently studied by Mathis [387]. The main conclusion is that gravito-inertial waves are confined in the equatorial region (this confinement being even stronger for retrograde than prograde waves) and that their contribution to the transport of angular momentum is reduced.

A problem for the gravity waves may be their interaction with horizontal turbulence. A first effect could result from the horizontal turbulence in (17.30). A second effect could be due to the account of D_h in the expression of the damping factor (17.58). As D_h is likely an order of magnitude larger than the thermal diffusivity K, the horizontal turbulence may increase the damping factor. In extreme cases, the strong horizontal turbulence could make the waves evanescent in the radiative zone.

Part V
Star Formation

Chapter 18
Pre-stellar Phase*

Let us consider a cloud in the blue sky of the Earth. Why does this cloud not pack together to form a small star in the air? The answer lies in the Jeans criterion, which says that in order a cloud, interstellar or whatever, to gravitationally contract and form a star, its self-gravity must win over the internal pressure forces which resist to contraction.

If an interstellar cloud starts collapsing, its gravity becomes stronger and stronger. However, remarkably the pressure in the cloud does not vary, since the temperature remains constant because the dust grains are able to radiate the whole potential energy liberated by contraction. This means that smaller parts of the cloud can further contract on their own. This is the process of fragmentation leading to the formation of star clusters and associations.

18.1 Overview and Signatures of Star Formation

The star formation process represents a density jump by a factor of about 10^{23}. The typical density of the interstellar medium is about 10^{-23} g cm^{-3}, while the average solar density is 1.4 g cm^{-3}. Major changes in the matter properties occur during such a density change. It is meaningful to distinguish three phases in star formation:

- **The pre-stellar phase:** it covers the contraction and fragmentation phases of an interstellar cloud under its gravitation. This phase is essentially isothermal due to the efficient cooling by dust grains.
- **The proto-stellar phase:** it concerns the evolution of the fragment up to the stage where the growth of internal pressure in the central core stops the fast contraction and fragmentation. The central core reaches hydrostatic equilibrium and evolves nearly adiabatically.
- **The pre-main sequence phase:** it is the phase of the evolution of the central object from the Hayashi line up to the zero-age main sequence (ZAMS).

---

*This chapter may form the matter of a basic introductory course.

The physical conditions, timescales and observational properties are different in these three phases.

Figure 18.1 shows the timescales and some properties of stars reaching a mass M at the end of the star formation process. Up to an age of $(1–2) \times 10^5$ yr, most stars experience accretion and are surrounded by a rotating accretion disk. Protostars are generally still embedded in a cocoon. The low-mass protostars show strong collimated jets, while massive protostars excite an ultra-compact HII region (UCHII) which further expand.

Massive stars show large bipolar outflows, thus a fraction of the infalling mass returns to the interstellar medium. The disks around massive protostars dissipate rapidly as a result of their high luminosities, which also further produce extended HII regions. Massive stars are still embedded in their accreting material, when they experiences H ignition. For lower mass stars, the disks last for a large part of the pre-MS phase.

The range of sizes and masses of the star-forming clouds is quite large:

- Small star-forming zones: with sizes of about 10 pc and masses of a few 10^2 $M_\odot$ (cf. Taurus region).
- Large star-forming regions: of the order of 100 pc and 10^4 $M_\odot$ (cf. the Orion region which contains about 10 O-type stars).
- Giant HII regions (GHII): they are equivalent to 100 times Orion, with masses up to a few 10^6 $M_\odot$. The 30 Dor nebula in the Large Magellanic Cloud is a magnificent example.
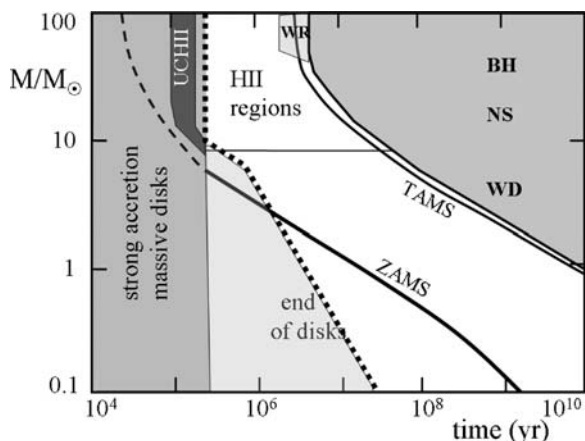
Fig. 18.1 Timescales and properties of stars reaching a final mass M during their formation. The time zero is counted since the formation of a hydrostatic core. Initially, accretion and massive disks maintain the star inside a cocoon. For intermediate masses, the disks survive up to the beginning of the MS phase, while for lower masses the disks disappear before the end of the pre-MS phase. For massive stars, the accretion phase and disks (if any) are present even after the star has reached the ZAMS. TAMS indicates the end of the MS phase, WR means Wolf–Rayet stars. BH, NS and WD mean black holes, neutron stars and white dwarfs. Adapted from Yorke [627]

– Starbursts: they are equivalent to upto 10^4–10^5 times Orion and mostly result from interactions of galaxies.

Observations of star formation in the Galaxy and in external galaxies are performed by various techniques, which provide different signatures:

– Large molecular clouds are observable in radio emission. The main molecule H_2 has no easy observable line. However, the molecule CO has an important line at $\lambda = 2.6$ mm, which permits the radio cartography of cold molecular clouds. A number ratio $CO/H_2 \simeq 6 \times 10^{-5}$ is usually adopted to estimate the cloud mass. Likely this ratio changes with the content in heavy elements of the region or galaxy studied.
– The grains in contracting clouds are a strong IR source, as well as the grains heated by the radiation of newly formed O stars.
– Dark clouds are observable in visible light: the Coal Sack as well as dark regions in Cygnus are beautiful examples. The Bok globules are dark spots visible on the bright background illuminated by young stars.
– Nebular emission lines in HII regions are a signature of recent star formation proportional to the number of ionizing O-type stars.
– The broad resonance UV lines, as observed by the Hubble Space Telescope, with often P-Cygni profiles, are a signature of massive star formation visible in the integrated spectrum of galaxies.
– The emission lines of WR stars, discernible in the integrated spectra of galaxies, provide a signature of star formation in the distant universe.

18.2   The Beginning of Cloud Contraction

The onset of the collapse of an interstellar cloud depends on the initial conditions, in particular on the temperature T and density ϱ in the cloud. In general, these conditions are not the same in a large cloud, which may give birth to a star cluster, or in a cloud fragment which will form a star. Turbulence and magnetic field also influence the collapse (Sect. 18.3).

18.2.1   The Jeans Criterion

An interstellar cloud starts contracting, when gravity forces overcome the forces due to the gradient of internal pressure, the cloud becomes gravitationally unstable. The Jeans criterion determines the conditions for the onset of contraction. Let us consider an isothermal sphere of mass M, radius R and average temperature T. Let P_{equ} be the ambient pressure with which the cloud is in equilibrium. The Virial theorem (Sect. 1.3) states that

$$2E_{\rm c} + \Omega = 2C_{\rm v}MT - q\frac{GM^2}{R} = 4\pi P_{\rm equ}R^3 \ , \tag{18.1}$$

where $E_{\rm c}$ is the kinetic energy, Ω the potential energy, $C_{\rm v}$ the specific heat by unit of mass at constant volume. For a monatomic and perfect gas of mean molecular weight μ, $C_{\rm v} = c_{\rm v} = (3/2)k/(\mu m_{\rm u})$. The density distribution in the initial configuration is not necessarily constant. For a polytrope (Sect. 24.5) of index n, one has $\Omega = -[3/(5 - n)](GM/R^2)$, so that $q = 3/(5 - n)$. For a constant density, $n = 0$ and $q = 3/5$, while for a more centrally condensed object, q is larger. The equilibrium pressure at the surface of a cloud varies with its parameters M, T and R,

$$P_{\rm equ} = \frac{c_{\rm v}MT}{2\pi R^3} - \frac{qGM^2}{4\pi R^4} \ . \tag{18.2}$$

The behavior of $P_{\rm equ}$ as a function of radius is sketched in Fig. 18.2. For small values of R, the negative term in R^{-4} dominates, while for larger R the positive contribution in R^{-3} is winning. $P_{\rm equ}$ reaches a maximum at $R_{\rm J}$, then it decreases $\to 0$ as R further increases. For fixed values of M, T and q, the derivative $dP/dR = 0$ defines the value $R_{\rm J}$ of the radius of the maximum pressure that the cloud in equilibrium can sustain,

$$R_{\rm J} = \frac{4}{9}q\,\frac{\mu m_{\rm u}}{k}\,\frac{GM_{\rm J}}{T} \ . \tag{18.3}$$

The stability depends on the value of the actual radius R with respect to $R_{\rm J}$.

– For $R < R_{\rm J}$: a reduction of radius R produces a reduction of $P_{\rm equ}$. Thus, if the cloud was initially in equilibrium with its surrounding medium, after a small decrease of R the sustainable pressure becomes smaller than the actual pressure
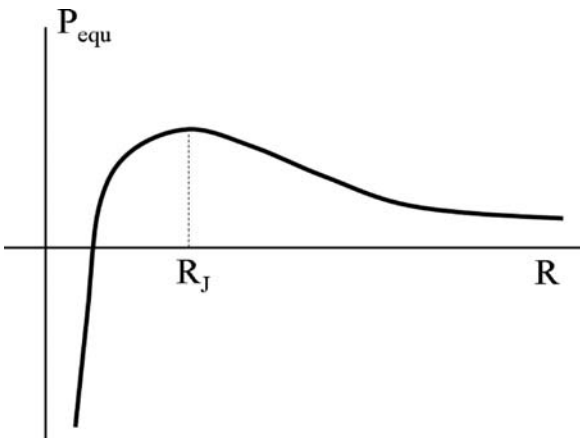
Fig. 18.2 Schematic variation of the equilibrium pressure $P_{\rm equ}$ as a function of radius R for a spherical body of mass M and temperature T in equilibrium

and the cloud starts contracting. This leads to a smaller value of R, which in turn makes a further reduction of the sustainable pressure, etc. The situation is unstable and the cloud collapses.

– For $R > R_J$: an increase of R makes a reduction of P_{equ}. If the cloud was initially in equilibrium with the ambient medium, the external pressure is now too strong and the cloud contracts recovering its initial size.

The critical radius R_J can be expressed as a function of the average T and ϱ in the cloud. Writing the mass M of the cloud at the critical limit $M_J = (4\pi/3)\varrho R_J^3$, one eliminates M_J from (18.3) and gets

$$R_J = \left(\frac{27}{16q\pi} \frac{kT}{\mu m_u G\varrho} \right)^{\frac{1}{2}} . \tag{18.4}$$

For given T and ϱ, configurations with a radius smaller than R_J starts collapsing. With radius (18.4), we can write the mass M_J, called the Jeans mass, above which a cloud of given T and ϱ becomes gravitationally unstable,

$$M_J = \frac{27}{16} \left(\frac{3}{\pi q^3} \right)^{\frac{1}{2}} \left(\frac{k}{\mu m_u G} \right)^{\frac{3}{2}} T^{\frac{3}{2}} \left(\frac{1}{\varrho} \right)^{\frac{1}{2}} . \tag{18.5}$$

The higher the temperature, the larger the mass for initiating the collapse, since gravitation has to overcome a larger internal gas pressure. At a given T, a higher density favors collapse. We also see that if the initial cloud has a more peaked density distribution, i.e., a larger q, the Jeans mass M_J would be smaller for the same average T and ϱ. This means that the collapse is initiated more easily. Numerically, for a homogeneous density $q = 3/5$ and with the first two terms on the right of (18.5), one gets a coefficient 3.548 (i.e., about $2\sqrt{\pi}$, which is also found sometimes!). For neutral atomic gas with solar composition, with a mean molecular weight $\mu = 0.77$, we get

$$M_J = 1.16 \times 10^5 \, M_\odot \left(\frac{T}{100} \right)^{\frac{3}{2}} \left(\frac{\varrho}{10^{-24}} \right)^{-\frac{1}{2}} , \tag{18.6}$$

where T is in K and ϱ is in g cm^{-3}. Thus, the masses of collapsing clouds are rather large: for dense clouds with $T = 10$ K and $\varrho = 10^{-22}$ g cm^{-3}, $M_J \approx 367$ $M_\odot$. Since only clouds with masses much larger than current stellar masses can start contraction, we see that a process of *fragmentation* is necessary to form stars. The Jeans mass is a fundamental parameter determining the beginning of cloud collapse, either for galaxy or star formation.

18.2.2 *Various Expressions of the Jeans Criterion*

Several accurate and inaccurate expressions of the Jeans mass are found in literature:

1. If one ignores the external pressure in (18.1), the Jeans radius in Eq. (18.3) is a factor of 2 smaller. The numerical coefficient in the expression of the Jeans mass (18.5) would be $27/(\sqrt{2} \cdot 4)$ instead of $27/16$. However, this solution is physically less satisfactory.

2. Let us derive the Jeans criterion by simple considerations on the free-fall timescale t_{ff} (Sect. 18.2.4) and on the sound-crossing timescale t_{cs}, which are

$$t_{\mathrm{ff}} \approx \frac{1}{\sqrt{G\varrho}} \quad \text{and} \quad t_{\mathrm{cs}} \approx c_{\mathrm{s}}/\lambda \, , \tag{18.7}$$

for a medium of density ϱ, size λ and sound velocity c_{s}. The time t_{cs} is the propagation time of acoustic waves in the medium, as such it also characterizes the action of pressure forces. One has two cases:

- If $t_{\mathrm{cs}} < t_{\mathrm{ff}}$: pressure forces are acting faster than dynamical perturbations, thus the system is in hydrostatic equilibrium.
- If $t_{\mathrm{cs}} > t_{\mathrm{ff}}$: gravitational collapse occurs faster than pressure adjustments and there is little opposite effect from thermal pressure.

In view of (18.7), contraction occurs if the size of the collapsing region is smaller than the Jeans length λ_{J} defined by $t_{\mathrm{cs}} = t_{\mathrm{ff}}$, i.e.,

$$\lambda_{\mathrm{J}} \approx \left(\frac{1}{G\varrho}\right)^{\frac{1}{2}} c_{\mathrm{s}} \, . \tag{18.8}$$

This expression of the Jeans length is approximate (cf. 18.16).

3. The Jeans length can also be obtained from the linear perturbations of a 1D infinite medium. One starts from the continuity, Euler and Poisson equations (Sect. 1.1) and considers small perturbations p_1, ϱ_1, $\boldsymbol{v}$ and $\boldsymbol{g}_1$ around a non-perturbed solution with $P = \text{const.}$ and $\varrho = \text{const.}$ and zero velocity v. The three equations become to the first order,

$$\frac{\partial \varrho_1}{\partial t} + \varrho \boldsymbol{\nabla} \cdot \boldsymbol{v}_1 = 0, \quad \frac{\partial \boldsymbol{v}_1}{\partial t} = -\left(\frac{\partial p}{\partial \varrho}\right)_{\mathrm{ad}} \frac{\boldsymbol{\nabla}\varrho_1}{\varrho} + \boldsymbol{g}_1, \tag{18.9}$$

$$\boldsymbol{\nabla} \cdot \boldsymbol{g}_1 = -4\pi G\varrho_1 \, . \tag{18.10}$$

The perturbations are adiabatic and the sound velocity is given by (C.26) $c_{\mathrm{S}}^2 = (\partial p/\partial \varrho)_{\mathrm{ad}}$. We take the divergence of the perturbed Euler equation

$$\boldsymbol{\nabla} \cdot \frac{\partial \boldsymbol{v}_1}{\partial t} = -\frac{c_{\mathrm{S}}^2}{\varrho} \nabla^2 \varrho_1 + \boldsymbol{\nabla} \cdot \boldsymbol{g}_1 \, . \tag{18.11}$$

As the spatial and time variations of the perturbations are not correlated, we have $\mathbf{\nabla} \cdot (\partial \mathbf{v}_1 / \partial t) = (\partial / \partial t)(\mathbf{\nabla} \cdot \mathbf{v}_1)$ and with (18.10)

$$\frac{\partial^2 \varrho_1}{\partial t^2} = c_S^2 \, \nabla^2 \varrho_1 + 4 \pi G \varrho \, \varrho_1 \, . \tag{18.12}$$

This equation admits as a solution a plane wave of the form

$$\varrho_1 = A \, e^{i(kx - \omega t)} \, , \tag{18.13}$$

and the resulting dispersion equation is

$$\omega^2 = k^2 \, c_S^2 - 4 \pi G \varrho \, . \tag{18.14}$$

For $k < k_J$, with

$$k_J = \left(\frac{4 \pi G \varrho}{c_S^2} \right)^{\frac{1}{2}} \, , \tag{18.15}$$

the frequency is imaginary, i.e., there is an exponential decay or growth of the perturbation wave, for example, the density grows exponentially. This occurs for characteristic lengths larger than the Jeans wavelength

$$\lambda_J = \frac{2 \pi}{k_J} = \left(\frac{\pi}{G \varrho} \right)^{\frac{1}{2}} c_S \, , \tag{18.16}$$

which is to be compared to (18.8). Some authors [47] take for the Jeans mass, the mass in a sphere of radius $\lambda_J/2$ (case 1), others authors [229] take $M_J = \varrho \, \lambda_J^3$ (case 2). In the first case, one has

$$M_J = \frac{4 \pi}{3} \varrho \left(\frac{\lambda_J}{2} \right)^3 = \frac{\pi^{\frac{5}{2}}}{6} G^{-\frac{3}{2}} \varrho^{-\frac{1}{2}} c_S^3 \, , \tag{18.17}$$

while in case 2, one has a factor of $\pi^{3/2}$. The sound velocity is $c_s = \sqrt{\gamma \frac{k}{\mu \, m_u} T}$ (C.27), where γ is the ratio of the specific heats, $\gamma = c_P/c_V$. For the isothermal sound speed, γ equals unity (e.g., 18.45) and we get for case 1,

$$M_J = \frac{\pi^{\frac{5}{2}}}{6} \left(\frac{k}{\mu m_u G} \right)^{\frac{3}{2}} T^{\frac{3}{2}} \left(\frac{1}{\varrho} \right)^{\frac{1}{2}} \, . \tag{18.18}$$

The numerical coefficient in (18.18) is 2.916 in case 1, instead of 5.568 in case 2. These values are to be compared to 3.548 in (18.5). The differences between the various numerical factors are not too critical in view of the uncertainties concerning the velocities. We prefer expression (18.5) since it does not impose an infinite medium and allows some external pressure, which is not the case for the derivation of (18.16) from linear perturbations.

18.2.3 Initializing the Cloud Collapse

Over a large interval of densities from $\varrho \approx 10^{-23}$ to $\varrho \approx 10^{-13}$ g cm^{-3}, the collapsing cloud remains isothermal (Sect. 18.4). An interstellar cloud with an actual mass $M < M_J$ will not start gravitational contraction, unless some external effect compresses the gas. If this happens, the increase of density ϱ produces a decrease of M_J and thus the actual cloud mass M may happen to be larger than the corresponding theoretical value M_J. When this occurs, collapse is initiated. Several mechanisms are able to produce the necessary density increase to initiate cloud contraction.

– **Contagious star formation:** if star formation starts in a galaxy rich in gas, the process of star formation may propagate through the galaxy like a forest fire. Shocks due to the ionization fronts around newborn massive stars hit the neighboring gas clouds and produce density enhancements. Shocks are also produced by supernova explosions. The large association of Scorpius-Centaurus is a magnificent example of sequential star formation. One observes from one side of the association to the other an age sequence, the oldest cluster with an age of a few 10^7 yr is the most scattered, then there is a young dense cluster with an age of a few 10^6 yr and finally the youngest objects of about 10^5 yr are compact IR sources.
– **Density wave in spiral galaxies**: the density waves associated to the arms of spiral galaxies produce a local compression of the gas, which initiates star formation. This is why young clusters are in spiral arms.
– **Galaxy interactions:** the collisions and interactions of galaxies produce gas compression and are responsible for intense star formation in starburst galaxies. On the average, observations in the distant universe show that star formation was on the average more active in the past.
– **Cloud collision:** Cloud–cloud collisions were the first mechanism proposed for star formation; however, this process plays a modest role.

18.2.4 The Timescale

The dynamical timescale or free-fall timescale t_{ff} characterizes the changes of mechanical equilibrium in a gravitational configuration. This timescale is generally much shorter than the thermal timescale. It plays an essential role in star formation and characterizes any dynamical event, for example the core collapse in supernova explosions. To derive t_{ff}, we start from (1.14)

$$\frac{\ddot{r}}{4\pi r^2} = -\frac{dP}{dM_r} - \frac{GM_r}{4\pi r^4} \, . \tag{18.19}$$

If the cloud is isothermal (Sect. 18.4), there is no pressure gradient and the equation becomes simply

$$\ddot{r} = -\frac{GM_r}{r^2} \ .$$ (18.20)

We suppose that the whole mass M of the cloud participates to the collapse and the integration of this equation (after multiplying it by $\dot{r}$) gives

$$\frac{1}{2}\left(\dot{r}^2 - \dot{r}_i^2\right) = GM\left(\frac{1}{r} - \frac{1}{r_i}\right) \ .$$ (18.21)

Two sets of initial conditions are particularly interesting:

18.2.4.1   Timescale for the Growth of Density

We consider a cloud with an infinite extension and no initial motion, i.e., at $t = 0$, one has $r_i = \infty$ and $\dot{r}_i = 0$. By expressing the mass in terms of the mean density $\overline{\varrho}$ and radius r at the time considered, we get from (18.21) $\dot{r}^2 = (8\pi G\overline{\varrho}\, r^2)/3$. This gives

$$\frac{1}{r}\frac{dr}{dt} = -\left(\frac{8\pi G\overline{\varrho}}{3}\right)^{\frac{1}{2}} \ .$$ (18.22)

For contraction, we choose the sign minus. Since the mass remains constant, we have $3\,(dr/r) = -(d\varrho/\varrho)$. The characteristic time $t_{\rm ff}$ of the free fall is

$$t_{\rm ff} \equiv \overline{\varrho}\,\frac{dt}{d\varrho} = +\frac{1}{\sqrt{24\pi G\varrho}}, \quad \text{numerically} \quad t_{\rm ff} = \frac{446\,\text{sec}}{\varrho^{\frac{1}{2}}}, $$ (18.23)

where $\overline{\varrho}$ is expressed in CGS units. During $t_{\rm ff}$, $\overline{\varrho}$ increases by a factor e.

18.2.4.2   Free-Fall Time as a Function of the Initial Density

We now consider a sphere of finite radius at rest, i.e., at $t = 0$, $\dot{r}_i = 0$ and $r = r_i$. We want to express the collapse time as a function of the average density $\overline{\varrho}(r_i)$ in the initial configuration of radius r_i. From (18.21), we get

$$v = -\left[2GM\left(\frac{1}{r} - \frac{1}{r_i}\right)\right]^{\frac{1}{2}} \ .$$ (18.24)

The sign minus applies to the collapse. The temporal dependence of v is related to that of $r = r(t)$. Let us make the substitution $r/r_i = cos^2\zeta$, which gives $dr = -2r_i \cos\zeta \sin\zeta d\zeta$ and one has

$$2\,r_i\cos\zeta\,\sin\zeta\,d\zeta = \left(\frac{2\,GM}{r_i}\right)^{\frac{1}{2}}\left(\frac{r_i}{r}-1\right)^{\frac{1}{2}}dt\,. \tag{18.25}$$

The second parenthesis on the right is $\sin\zeta/\cos\zeta$, thus one has $2\cos^2\zeta\,d\zeta = \left((2\,GM)/r_i^3\right)^{\frac{1}{2}}dt$ and by integration,

$$\zeta + \frac{1}{2}\sin 2\zeta = \left(\frac{2\,GM}{r_i^3}\right)^{\frac{1}{2}}t\,. \tag{18.26}$$

The initial conditions $r = r_i$ for $t = 0$ also implies $\zeta = 0$. The time $t_{\rm ff}$ for the complete collapse is given by the condition $r \to 0$, which demands $\zeta \to \pi/2$ according to the definition of ζ. Thus, we get

$$\frac{\pi}{2} = \left(\frac{2\,GM}{r_i^3}\right)^{\frac{1}{2}}t_{\rm ff} = \left(\frac{8\,\pi}{3}\,G\,\overline{\varrho}(r_i)\right)^{\frac{1}{2}}t_{\rm ff}\,, \tag{18.27}$$

and finally

$$t_{\rm ff} = \left(\frac{3\,\pi}{32\,G\,\overline{\varrho}(r_i)}\right)^{\frac{1}{2}}\,. \tag{18.28}$$

The complete timescale for the spherical collapse only depends on the initial density $\overline{\varrho}(r_i)$ of the configuration. For an initial density of, say, 10^{-20} g cm^{-3}, the above free-fall time would be 6.7×10^5 yr. This timescale characterizes the phase of isothermal collapse.

18.3   The Role of Magnetic Field and Turbulence

18.3.1   Magnetic Fields

Observations indicate that the interstellar clouds are often in a stage of equilibrium. If all clouds with masses higher than the Jeans mass would collapse, the resulting star formation rate (SFR) would be much larger than the current estimate of ~ 1 star kpc^{-2} yr^{-1} in the galactic plane. This suggests that the gravity of the clouds is balanced by various effects, such as magnetic field and turbulence. As to rotation, it is negligible for the cloud support, but it is important during the contraction of protostars (Chap. 21).

Magnetic fields of intensity B contribute to the cloud support and may be an obstacle to rapid star formation, especially more than contrarily to turbulence, magnetic fields are not easily dissipated. Current values of the fields in the interstellar medium are below about $10\,\mu$G (the fields are usually higher in denser regions and they become stronger during the collapse of protostars). The energy density of the magnetic field is

$$u_{\mathrm{B}} = \frac{B^2}{8\,\pi}, \tag{18.29}$$

in CGS units, we recall that 1 Gauss is equivalent to $1\,\mathrm{g}^{1/2}\,\mathrm{cm}^{-1/2}\,\mathrm{s}^{-1}$. The average energy density associated to gravitational energy in a homogeneous cloud of mass M and radius R is

$$u_{\mathrm{G}} = \frac{3}{5}\frac{GM^2}{R\left(\frac{4}{3}\pi R^3\right)} = \frac{9}{20\,\pi}\frac{GM^2}{R^4}. \tag{18.30}$$

If the two energy densities are of the same order, the mass M_{B} above which gravitation dominates over the magnetic field is

$$M_{\mathrm{B}} = \left(\frac{5}{18\,G}\right)^{\frac{1}{2}} B\,R^2. \tag{18.31}$$

With the above remark, the product of the units effectively is a mass. This can also be expressed in term of the magnetic flux $\Phi = \pi B R^2$

$$M_{\mathrm{B}} = \left(\frac{5}{18\,\pi^2}\right)^{\frac{1}{2}}\frac{\Phi}{\sqrt{G}} = 0.17\,\frac{\Phi}{\sqrt{G}}. \tag{18.32}$$

The original derivation, which accounts for the density structure [433], gives a not too different numerical factor, i.e., 0.13 instead of 0.17, if so one has

$$M_{\mathrm{B}} \approx 9.08 \times 10^2 \left(\frac{B}{30\,\mu\mathrm{G}}\right)\left(\frac{R}{2\,\mathrm{pc}}\right)^2 \mathrm{M}_\odot. \tag{18.33}$$

Two cases can be distinguished depending on whether the actual cloud mass M is larger than M_{B} or not:

1. If $M > M_{\mathrm{B}}$: the magnetic field is insufficient to prevent cloud collapse. The timescale of the collapse is not much increased with respect to t_{ff}. This case, which corresponds to large clouds, is likely leading to a high rate of star formation, with a large cluster or an association as the result. But, as discussed below, turbulence also plays a role.
2. If $M < M_{\mathrm{B}}$: the cloud is supported by the magnetic field, but it progressively diffuses out of the cloud. In a dense cloud, the fraction of the ionized gas is about 10^{-7} (see Sect. 18.4). The magnetic field is attached to the ions, while the neutral gas is not directly driven by the field. There is a viscous coupling between neutral and charged particles due to their collisions. However, over a timescale of the order of 10^7 yr the neutral and charged particles, not submitted to the same forces, diffuse apart. This process is called ambipolar diffusion: the diffusion of the field lines occurs mainly in two caps around the points where the axis of the field crosses the cloud surface. Ambipolar diffusion allows the clouds to finally

contract when the field has diffused out. This process may produce scarce stellar groups.

Magnetic fields may play a role at the very beginning of cloud collapse; however, some recent works (see below) suggest that the effects of interstellar turbulence are larger during cloud collapse and fragmentation. At further stages, magnetic fields again play a leading role in the coupling (disk locking) between the accretion disk and protostar (Sect. 21.2). Magnetic braking of rotation by stellar winds is a leading effect in formation and evolution of solar-type stars (cf. Sect. 21.3).

18.3.2   The Major Role of Turbulence in Star Formation

An additional pressure in a cloud results from internal turbulent motions. They contribute to the cloud support and may inhibit collapse. Let us suppose that in addition to thermal pressure, there is also locally a support by turbulent motions with an average velocity v_{turb} and by a magnetic field characterized by an Alfvén velocity $v_A = B/(\sqrt{4\pi\varrho})$ (Sect. 13.1.3). The corresponding crossing time of pressure effects is no longer $t_{cs} = c_s/\lambda$ as in Sect. 18.2.2, but

$$t_{cs} \approx \frac{\left(c_S^2 + v_{turb}^2 + v_A^2\right)^{\frac{1}{2}}}{\lambda}. \tag{18.34}$$

Thus, the corresponding Jeans mass behaves like

$$M_J \approx \frac{\left(c_S^2 + v_{turb}^2 + v_A^2\right)^{\frac{3}{2}}}{G^{\frac{3}{2}}\varrho^{\frac{1}{2}}}, \tag{18.35}$$

with an appropriate numerical coefficient of the order of 3 (Sect. 18.2.2). The internal support being larger, the Jeans mass is larger and this may explain why interstellar clouds have a relatively long survival time.

Observations and models suggest [334] that the above simple picture of an additional isotropic turbulent pressure must be revised since turbulence is highly supersonic, making shocks and high-density fluctuations. If so, star formation is controlled primarily by turbulence rather than by magnetic fields, also the observed strength of the magnetic field in molecular clouds is generally insufficient to prevent cloud collapse. Being highly supersonic, the turbulence does not act as an isotropic pressure, but the flow consists of a sequence of shocks and shocklets, which produce large local density fluctuations. Thus, the gas in a cloud will gravo-turbulently fragment and form contracting clumps and sub-clumps finally leading to star formation. A contracting cloud will have an inhomogeneous density structure with probably the most massive and dense sub-clumps at the center of the forming cluster. On the whole, turbulence is a major agent controlling stellar birth.

The broadening of the lines is a measure of the velocity dispersion in the clouds. The widths of the radio emission lines from interstellar clouds show that large turbulent motions are present, with supersonic turbulent velocities up to about 2 km s^{-1} (thermal velocities are about 0.3 km s^{-1}). The non-thermal component σ_{NT} of the dispersion velocity correlates with the size ℓ of the clouds

$$\sigma_{NT} = \sigma_0 \left(\frac{\ell}{\sigma_0}\right)^n . \tag{18.36}$$

This relation is known as Larson's law [314], typical values are $\sigma_0 = 1$ km s^{-1} for $\ell = 1$ pc and $n = 0.5$. Turbulence varies in the interstellar medium and this may explain the differences in star formation.

Model calculations show that without a continuous energy input, interstellar turbulence dissipates rapidly, in a time equal to the crossing time of the cloud at the average turbulent velocity. In a molecular cloud, this is less than a free-fall timescale. The evidence of self-similar structures in molecular clouds suggests that interstellar turbulence is driven on large scales of the order of hundred parsecs, i.e., larger than the cloud size. The main source of large-scale turbulence appears to be the momentum and energy input from supernovae explosions and galactic rotation. In regions of active star formation, there is also a mechanical input from Wolf–Rayet stars.

18.4 Isothermal Collapse and Cloud Fragmentation

The collapse of interstellar clouds and fragmentation are determined by the thermal properties of the gas and dust, which form the interstellar matter. In this respect, the differences between the thermal properties at solar and zero metallicity are enormous and lead to very different star formation (cf. Chap. 23).

18.4.1 Dust Grains and Cooling

The energy equilibrium of interstellar clouds is governed by heating and cooling processes. In absence of contraction, heating mainly comes from cosmic rays, which dissociate and ionize H_2 molecules. The resulting free electrons collide with dust grains and molecules providing some heating, they also dissociate and ionize other molecules. Thus, there is always a small fraction ($\sim 10^{-7}$) of ionized gas within an interstellar cloud. UV radiation from stars also liberates electrons, which contribute to heating the gas and dust.

There are several processes of cooling:

– **Atomic transitions:** atoms of hydrogen and helium as well as H_2 molecules are themselves not significant radiation emitters in the interstellar medium. Some cooling results mainly from minor components, which are heated by inelastic collisions with H and He. Collisions with CII ions excite their fine structure levels, which come back to equilibrium by emitting far-IR and radio radiation.
– **Molecular transitions:** CO molecules are a cooling agent. The molecular clouds are generally optically thick in the lowest rotational transitions of the CO molecules, thus the CO emission originates mainly from the cloud surface. From $T = 10$ to $50\,\mathrm{K}$, the CO emission grows by a factor of about 10^2, since higher rotational levels are excited.
– **Radiation by dust grains:** solid dust grains, formed by heavy elements, represent about 2% of the mass in the interstellar medium. Grains are responsible for the interstellar reddening. Their sizes range from about 0.005 to 0.25 μm, with a distribution of the grain radii r_g of the form $r_g^{-3.5}$ [548]. Grains are heated by stellar radiation and by collisions with atoms and molecules. The collisions transfer energy from the gas to the grains and provoke vibrations of their lattice structure, which emits IR radiation. The cooling by grains behave with the concentration n_H of H atoms and temperature of the dust like [548]

$$\Lambda_{\text{dust}} = 1.0 \times 10^{-10} \left(\frac{n_H}{10^3}\right) \left(\frac{T_{\text{dust}}}{10\,\mathrm{K}}\right)^6 \quad \mathrm{eV\,cm^{-3}\,s^{-1}}. \qquad (18.37)$$

We may compare the three types of cooling. For example, at $T = 10$ K and $n_H = 10^3$, the cooling by CII ions, CO molecules and grains is, respectively, 3×10^{-13}, 1×10^{-13} and 1×10^{-10} eV cm^{-3} s^{-1}. In addition, cooling by dust grains increases so fast with T_{dust} that it is largely the dominant cooling process during the collapse (at very low Z this no longer true, Sect. 23.1.1).

The thermal adjustment time of the cloud is $t_{\text{therm}} = c_v T / (< dU/dt >) \approx 100$ yr at solar metallicity. This is much shorter than the free-fall time and it enables the cloud to fast radiate the potential energy liberated by cloud collapse. Thus, the collapse is isothermal, this lasts until a density of about 10^{-14} g cm^{-3} is reached (about the average density of the Solar System up to Pluto). Isothermal changes are an essential property, they permit collapse and fragmentation (they also greatly simplify the numerical simulations).

18.4.2   The Initial Cloud Structure and its Evolution

In the above derivation of the Jeans mass, we have assumed constant ϱ and T. While constant T is a valuable assumption, this is not the case for density. We examine in more detail the structure of contracting clouds, which is critical for fragmentation and also for the accretion rates (Sect. 20.3).

The gravitational collapse of clouds is non-homologous, i.e., central regions collapse faster than external ones. Non-homology starts during the isothermal phase. As a result of contraction and fragmentation, clouds acquire a density law of the form $\varrho \sim r^{-2}$, which is little dependent on the initial conditions. Let us consider a spherical contracting cloud which goes through a sequence of decreasing radii $r_1, r_2, r_3, \ldots$. Inside a radius r_i, the mass M_{r_i} is always proportional to r_i, since according to (18.3), one has

$$r_i = \frac{4}{9} q \frac{\mu m_u}{k} \frac{G M_{r_i}}{T}. \tag{18.38}$$

After the stage with radius r_i, contraction leads to a smaller radius r_{i+1} with always the same proportionality factor between mass and radius since T and μ do not change, thus $M_{r_i} \sim r_i$. Denser and denser regions form in the interior of the cloud on shorter and shorter timescales. The contracting cloud progressively reaches a density structure of the form

$$\varrho(r) = \frac{M_r}{\frac{4}{3}\pi r^3} = \frac{27}{16\pi q} \frac{k}{\mu m_u} \frac{T}{G r^2}. \tag{18.39}$$

With the isothermal sound velocity $c_s = \sqrt{(k/\mu m_u)T}$ (Appendix C.3), this becomes

$$\varrho(r) = f \frac{c_s^2}{\pi G r^2}, \tag{18.40}$$

where $f = 27/(16q)$. This density distribution of the form $\varrho \sim r^{-2}$ for the outer parts of the cloud is confirmed by numerical models of isothermal collapse (Fig. 18.3), it is also the distribution in the outer layers of an isothermal polytrope (Sect. 24.5). The envelopes during cloud collapse are well described by the so-called "singular isothermal sphere" which behaves like [528]

$$\varrho = \frac{c_s^2}{2\pi G r^2} \quad \text{with} \quad M(r) = \frac{2 c_s^2}{G} r, \tag{18.41}$$

and is illustrated in Fig. 18.3. This asymptotic envelope solution does not apply to the center, since it would predict an infinite density. It is self-similar, i.e., it behaves the same at all scales and has no preferred scale length. This distribution leads to the "standard accretion rate" given by (19.24) (the accretion rate is determined by the ratio of the mass inside some radius divided by the corresponding free-fall time). Evidently, the free-fall time is shorter in the inner denser regions, thus the collapse proceeds inside-out.

Interesting physical solutions for an isothermal cloud are provided by the so-called Bonnor–Ebert spheres. These are isothermal polytropes (Sect. 24.5) in hydrostatic equilibrium truncated at some level, where they are in equilibrium with the external medium of pressure P_{ext}. Some density distributions of Bonnor–Ebert spheres are illustrated in Fig. 18.3. The density profiles are in r^{-2} in the outer layers
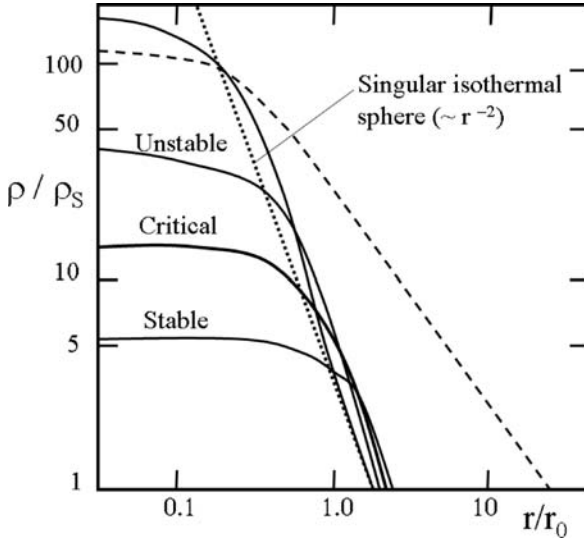
Fig. 18.3 Examples of density profiles as a function of the radius in Bonnor–Ebert spheres, i.e., truncated isothermal polytrope in a medium with an ambient pressure P_{ext}. The quantity ϱ_s is the surface density. The surface is at about $2\,r_0$, defined as $r_0 = c_s^2 (2\pi G P_{ext})^{-1/2}$. Distributions more concentrated than the critical one are unstable and collapse, those less concentrated are stable. The singular solution (*dotted line*) is the limiting curve with $\varrho \sim r^{-2}$ and an infinite central density [528]. The *broken line* illustrates the distribution in infalling regions above the shock, with $\varrho \sim r^{-3/2}$ (18.44). Adapted from McLaughlin & Pudritz [395]

and become flatter toward the center, a fact in agreement with current mapping of dust clouds. We have seen (Sect. 18.2.1) that a larger central condensation (factor q) favors gravitational instability. The same applies to Bonnor–Ebert spheres. Configurations more centrally condensed than a critical one (Fig. 18.3) are unstable, while less-concentrated configurations are gravitationally stable. We can make a simple estimate of the mass in a Bonnor–Ebert sphere as follows. The thermal pressure at the edge behaves like

$$P_{ext} = \frac{k}{\mu m_u}\varrho T = \varrho\, c_s^2 \ . \tag{18.42}$$

Introducing this behavior in the expression of the Jeans mass, we get for the critical mass of a Bonnor–Ebert sphere

$$M_{BE} \sim \frac{c_s^3}{G^{\frac{3}{2}}\varrho^{\frac{1}{2}}} \sim f\,\frac{c_s^4}{P_{ext}^{\frac{1}{2}}G^{\frac{3}{2}}} \ . \tag{18.43}$$

Detailed calculations give a factor $f = 1.18$. The critical Bonnor–Ebert sphere has a ratio of central to surface density of 14.3. The asymptotic extreme case is the

singular isothermal sphere (18.41), which well reproduces the density distribution in the outer layers of a collapsing cloud. The density profiles of Bonnor–Ebert spheres represent the various stages of a collapsing cloud. This is a better model than a succession of homogeneous spheres.

In the case of cluster formation, the central density remains moderate and a central density peak does not form. In star formation, central density gets higher, thermal pressure becomes significant and a hydrostatic core forms at the center, encompassing a few percent of the stellar mass. The matter infalling on the core forms an accretion shock. The infalling material follows simple laws, which are easily understood. The accretion rate behaves like $\dot{M}_{\text{accr}} = 4\pi r^2 \varrho v$, where the velocity v is about the free-fall velocity,

$$v(r) \sim r^{-\frac{1}{2}} \quad \text{and} \quad \varrho(r) \sim \frac{\dot{M}_{\text{accr}}}{r^2 v} \sim \frac{\dot{M}_{\text{accr}}}{r^{\frac{3}{2}}} . \tag{18.44}$$

Such laws apply in infalling regions above the shock, they are confirmed by numerical models [395].

18.4.3 The Hierarchical Fragmentation

The Jeans mass M_J in the local interstellar medium is orders of magnitude larger than current stellar masses (Sect. 18.2.1). Fragmentation of interstellar cloud is thus necessary to form stars (Fig. 18.4). Fragmentation is also in agreement with the fact that stars form in groups in the Galaxy. In a collapsing cloud with average density ϱ, regions with locally a higher density ϱ' collapse faster than the rest of the cloud.
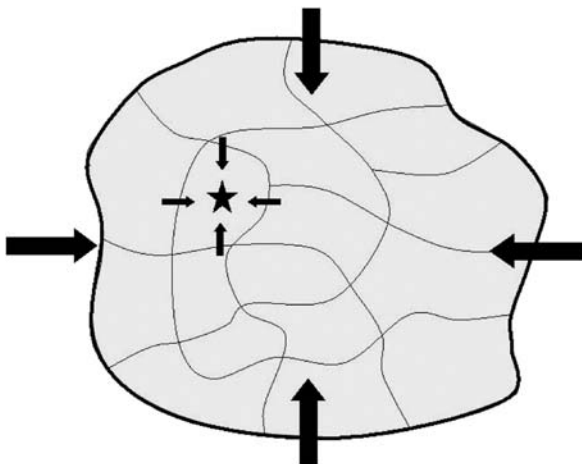
Fig. 18.4 Schematic representation of a cloud contraction and fragmentation

This is evident [254] since denser regions collapse with a timescale $t'_{\mathrm{ff}} \sim (G\varrho')^{-1/2}$, which is shorter than $t_{\mathrm{ff}} \sim (G\varrho)^{-1/2}$. In turn, the same argument applies to regions of higher densities, which pursue their own collapse faster in a succession of fragments of smaller and smaller scales. This process is known as "hierarchical fragmentation" [254].

The Jeans mass behaves as $M_{\mathrm{J}} \sim T^{3/2} (1/\varrho)^{1/2}$. If T would increase during collapse, M_{J} would grow and thus no smaller cloud fragment could collapse. We note that in an adiabatic transformation, the pressure behaves like $P \sim \varrho^{\gamma}$, for a perfect gas one has $T \sim \varrho^{\gamma-1}$, thus the adiabatic index γ is

$$\gamma = 1 + \frac{d \ln T}{d \ln \varrho} \, . \tag{18.45}$$

The Jeans mass behaves with density like

$$M_{\mathrm{J}} \sim \varrho^{\frac{3}{2}\left(\gamma - \frac{4}{3}\right)} \, . \tag{18.46}$$

Only if $\gamma < 4/3$, M_{J} decreases during collapse and fragmentation is possible. If the gas is isothermal, according to (18.45) we have $\gamma = 1$ and thus collapse and fragmentation can go on. The accretion shock produced by the infalling gas produces both central heating and outgoing radiation. As the timescale of contraction behaves like $1/\sqrt{G\varrho}$ (18.23), the rhythm of contraction accelerates as density is getting higher.

At some stage, the medium becomes opaque and contraction ceases to be isothermal. At a density of about 10^{-14}–10^{-13} g cm^{-3} the protostar enters the phase of adiabatic contraction. Thus, $\gamma = 5/3$ and according to (18.46) the Jeans mass no longer decreases for higher densities: no smaller cloud fragment collapses and fragmentation comes to an end. The fact that the opacity sets a limit on the smallest fragment is known as the *opacity-limited fragmentation*.

Due to rotation the process of hierarchical fragmentation could not be as simple as suggested by the above scenario. During contraction, the fragments may acquire sufficient angular momentum to be centrifugally supported as they further contract. This could prevent or at least delay further contraction and fragmentation at smaller scales, so that only a few fragmentation steps could possibly occur. The longer survival of fragments would enable them to interact and perhaps coalesce.

18.4.4 The Opacity-Limited Fragmentation

Fragmentation goes on as long as the energy from the cloud contraction is radiated away. When this is no longer the case, the process stops. Let us estimate the size of the smallest fragment in the opacity-limited fragmentation. The gravitational energy

$|\Omega| \approx GM^2/R$ of a cloud of mass M, radius R and average density ϱ is liberated in a time of the order of $1/\sqrt{G\varrho}$. Thus, the gravitational power produced is

$$\dot{E}_{\text{grav}} \approx \frac{GM^2}{R} (G\varrho)^{\frac{1}{2}} = \left(\frac{3}{4\pi}\right)^{\frac{1}{2}} \frac{G^{\frac{3}{2}} M^{\frac{5}{2}}}{R^{\frac{5}{2}}}. \tag{18.47}$$

The radiated power is at most that of the black body

$$\dot{E}_{\text{rad}} = 4\pi f \sigma T^4 R^2 , \tag{18.48}$$

where σ is the Stefan constant and f is a numerical factor ≤ 1. The collapse is isothermal as long as $\dot{E}_{\text{rad}} \gg \dot{E}_{\text{grav}}$. Indeed, we notice from (18.47) that $\dot{E}_{\text{grav}}$ does not depend on the mass of the collapsing configuration, since for a succession of fragments always at the limit of Jeans mass, the fragment masses vary linearly with radius. On the contrary, the radiated energy $\dot{E}_{\text{rad}}$ grows with R^2, i.e., like M^2. Thus, large configurations are always able to radiate their energy. The transition toward adiabatic collapse occurs for a mass small enough, i.e., when $\dot{E}_{\text{rad}} \approx \dot{E}_{\text{grav}}$. This gives a limiting mass

$$M_{\text{lim}}^5 \approx \frac{64\pi^3}{3} \frac{\sigma^2 f^2 T^8 R^9}{G^3} . \tag{18.49}$$

By eliminating the radius with $R = (3/4\pi)^{1/3} (M_{\text{J}}/\varrho)^{1/3}$, we get

$$M_{\text{lim}}^5 \approx \frac{64\pi^3}{3} \frac{\sigma^2 f^2 T^8}{G^3} \left(\frac{3}{4\pi}\right)^3 \left(\frac{M_{\text{lim}}}{\varrho}\right)^3 . \tag{18.50}$$

Fragmentation stops when the Jeans mass is equal to the mass limit, below which the contracting configuration is unable to radiate the gravitational power. The density at the Jeans limit (18.5) is

$$\frac{1}{\varrho} = \frac{M_{\text{lim}}^2}{3.548} \left(\frac{\mu m_{\text{u}} G}{k}\right)^3 \frac{1}{T^3} . \tag{18.51}$$

With this expression, we get for the lowest mass which can radiate the energy liberated by the collapse,

$$M_{\text{lim}} \approx \frac{(3.548)^{\frac{3}{2}}}{3^{\frac{1}{2}}} \frac{1}{G^{\frac{3}{2}} \sigma^{\frac{1}{2}}} \left(\frac{k}{\mu m_{\text{u}}}\right)^{\frac{9}{4}} f^{-\frac{1}{2}} T^{\frac{1}{4}} . \tag{18.52}$$

or numerically

$$M_{\text{lim}} \approx 0.018 \frac{T^{\frac{1}{4}}}{f^{\frac{1}{2}}} M_{\odot} . \tag{18.53}$$

This is an approximate estimate of the lowest mass which can form by cloud fragmentation. This important result leads to several remarks:

1. For $f \approx 1$ and $T \approx 10$ K, the smallest fragment is ~ 0.03 $M_\odot$. Thus the *minimum stellar mass* resulting from contraction and fragmentation of interstellar clouds is of the order of 10^{-2} $M_\odot$.
2. This minimum stellar mass is lower than the mass $M_H = 0.08$ $M_\odot$, above which nuclear fusion of hydrogen is active. Stars with masses between M_{lim} and M_H are brown dwarfs (Sect. 26.4.1).
3. For regions of lower metallicities Z, dust grains are less abundant, thus contracting clouds radiate less energy, i.e., f is likely smaller and M_{lim} larger. Thus, we might wonder whether very low-mass stars, such as brown dwarfs, also form at lower Z (as shown in Sect. 23.1.3, although the fragmentation process does not occur at $Z = 0$, very small hydrostatic cores nevertheless initially form, these small initial cores then lead to stars of different final masses depending on the amount of matter further accreted).
4. Objects with $M < 0.01$ $M_\odot$, such as giant planets, do not result from fragmentation, but from the process of *accumulation*. In a protostellar disk, small condensations of rocks (in the core) and ice grow by collisions and accumulation of materials from the surrounding disk.
5. For objects near the limit $M \sim 0.01$ $M_\odot$ in multiple systems, the reality is likely more complex than the rather schematic distinction between the processes of fragmentation and accumulation.

18.4.5   *The Initial Stellar Mass Spectrum*

The initial mass spectrum or initial mass function, the so-called IMF, can be approximated by

$$\frac{dN}{dM} = A M^{-(1+x)}, \tag{18.54}$$

$$\text{or} \quad \xi(M) \equiv \Phi(M) \equiv \frac{dN}{d\ln M} = \frac{dN}{dM} M = A M^{-x}, \tag{18.55}$$

which is often called $\Phi(M)$ or $\xi(M)$. The original Salpeter's slope obtained from stellar counts in open clusters is $x = 1.35$. A classical study [508] gives $x = 0.4, 1.5, 1.7$–2.0 in the ranges $M = 0.1$–1 $M_\odot$, $M = 1$–10 $M_\odot$ and above 10 $M_\odot$, respectively. Recent works [293, 333] confirm a nearly flat slope from about 0.2 to 0.6 $M_\odot$ which turns into a power law above 1 $M_\odot$ up to high masses with a slope equal or steeper than the Salpeter's law. There is no convincing differences in the IMF due to metallicity Z, e.g., between the Galaxy and the Magellanic Clouds. Indications exist that some regions of intense star formation, like starbursts, may be relatively richer in massive stars; in that case, one often speaks about a "top heavy IMF".

The thermodynamic state of the gas, which determines the density distribution in the clouds, appears to critically influence the mass spectrum and the range of stellar masses produced [273]. Studies of cloud collapse [54] suggest that there are two different regimes for mass accretion onto protostars.

1. If the gas dominates the gravitational potential, as is the case initially, the motions of the stars and of the gas are the same. There is no large systematic motion differences between the two components and the accretion on a protostar is determined by the local gravitational potential of the protostar.
2. Later when stars dominate the gravitational potential, they virialize and have different motions from the gas, i.e., with larger relative velocities. The accretion in this case results mainly from the sweeping of the interstellar gas by the fast moving stars (the so-called Bondi–Hoyle accretion). The accretion is less dependent on the local gravitational potential. These two regimes of accretion may lead to different IMF slopes: $(1+x) = -1.5$ in the first case, which applies mainly to the low-mass stars and -2.5 in the second, which concern mostly the massive stars.

Among other results from numerical simulations, we note the following:

– The IMF is also shaped by chaotic interactions between protostars [39]. This allows bursts of star formation to occur locally.
– Brown dwarfs and other stars could be formed from dynamical ejection of small fragments from unstable multiple systems.
– Star–disk encounters may form binaries, while stellar encounters rather destroy multiple systems.
– Close binaries may result from hardening of initially wider systems through successive encounters.

At present, the relative importance of fragmentation, collisions and accretion in shaping the different parts of the IMF is still uncertain.

Chapter 19
The Protostellar Phase and Accretion Disks[*]

At some stage in the collapse of a cloud fragment, the density is high enough ($\sim 10^{-14}$ g cm^{-3}) for the fragment to become opaque, thus it keeps for itself the energy liberated by contraction. The fragment enters an adiabatic contraction phase. The temperature and pressure in the central region start increasing. This is the beginning of the protostellar phase. Matter from the surrounding cloud falls onto the central core, the mass of which is growing. This is the process of accretion.

Contraction and mass accretion continue to proceed at about the free-fall timescale (about 10^6 yr). After different internal re-adjustments, the star becomes optically visible. This is the end of the protostellar phase. In the old models evolving at constant mass during the pre-MS phase, the star becomes visible at the top of the Hayashi line. In the scenario with continuing accretion, the stars are lying on the birthline and they are not yet visible due to the optically thick infalling material. In that sense, they are protostars. However, the stars on the birthline are mostly in hydrostatic equilibrium and their evolution can be treated as for pre-main sequence stars, thus they will be discussed in Chap. 20.

19.1 Accretion Disks

Accretion disks are a major characteristic of star formation. They provide observable signatures of protostars and allow the contracting matter to dissipate angular momentum to make the accretion possible (the excess of angular momentum amounts to a factor of 10^6 in the interstellar medium, Sect. 21.1). Disks show the major role of axial rotation in star formation.

19.1.1 Observations of Disks

The sub-millimetric and IR observations of star-forming regions suggest [11] an evolutionary sequence with schematically four successive classes from 0 to III.

---

[*]This chapter may form the matter of a basic introductory course.

These classes are based on the spectral distribution and on the amount of mass in the circumstellar disk (cf. Fig. 19.1).

- **Class 0, Young Accreting Protostars**: These objects show large far-IR and sub-millimetric emissions from molecular inflows with a temperature $T < 70$ K. These are very young protostars, with a massive and mostly spherical accretion of molecular gas and dust. The mass in the cloud is still large (> 0.5 $M_\odot$), the age is less than a few 10^4 yr (for a 1 $M_\odot$ star, ages counted since the formation of a small hydrostatic core).
- **Class I, Evolved Accreting Protostars**: These protostars show a strong IR emission (T from 70 to 600 K). They also have strong emission lines. The star, embedded in a massive accretion disk, is still not visible. Accretion is no longer spherically symmetric, jets or bipolar outflows are present. This class corresponds to the advanced stage of accretion. The ages are up to $(1–2)$ 10^5 yr.
- **Class II, Classical T Tauri Star**: The star is now visible as a classical T Tauri star with T from ~ 600 to 3000 K. It has entered the pre-MS phase. The disk with a mass of ~ 0.01 $M_\odot$ is still optically thick and produces a large IR excess. The age is typically 10^6 yr. T Tauri stars are considered to lead to stars with $M \leq 2$ $M_\odot$ on the ZAMS [381], while some authors put the limit up to 3 $M_\odot$.
- **Class III, Weak T Tauri Star**: The star is close to the main sequence, it shows weak emission lines. The disk is optically thin and produces only a small IR excess. The age is typically 10^7 yr.

There are several signatures of stellar disks: (1) IR continuum emission from the dust in the disk; (2) double spectral lines, in emission or in absorption, due to the Doppler shift produced by the disk rotation; (3) weak photospheric lines due to the "veiling" by the continuum flux of the outer regions; (4) strong collimated jets with aperture angles of only a few degree and velocities of several 10^2 km s^{-1} (for low and solar mass stars); (5) broad powerful polar outflows (for massive stars, Sect. 22.1.3); (6) some disks are directly visible on high-resolution images. On the basis of isochrones for pre-MS stars, the lifetimes of disks are estimated to be in the range of 10^6–10^7 yr.

19.1.2   Disk Formation

The existence of disks results from the rotation of the contracting clouds and from the evacuation of angular momentum in the process of gravitational contraction (Sect. 21.1). In the equatorial plane, the centrifugal force is opposed to accretion, while in the direction of the rotation axis the matter falls freely. Let us consider an interstellar cloud with a specific moment of inertia I and an angular rotation Ω. The specific angular momentum j is

$$j = I\Omega = I\frac{v}{r} \approx vr, \tag{19.1}$$
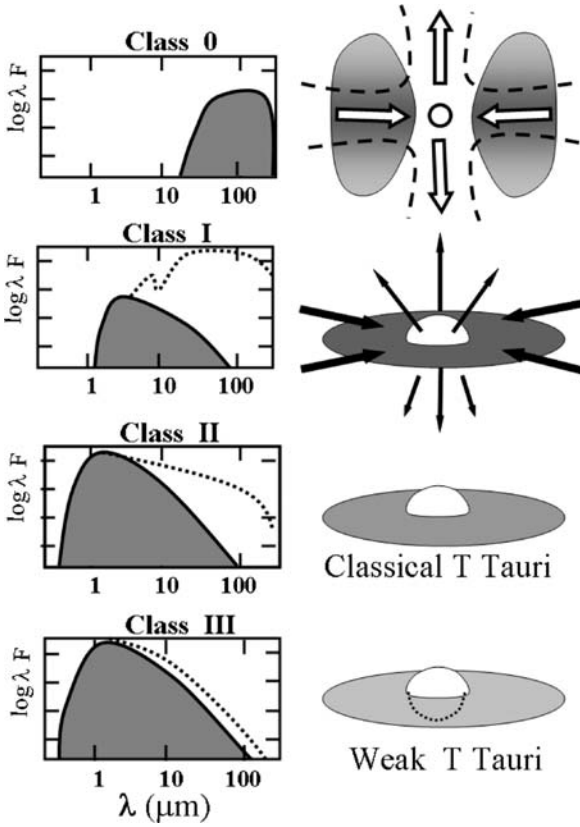
Fig. 19.1 The sequence of the various classes of accretion disks. On the left, a simplified representation of the stellar flux F is given (*shaded area*), the contribution of the disk is indicated by a *dotted line*. On the right a schematic representation of the object is given. Adapted from André [11]

where r is the radius. The matter falls until the centrifugal force is in equilibrium with gravity and imposes a circular orbit,

$$\frac{v^2}{r} = \frac{GM}{r^2} \quad \text{thus} \quad j^2 \approx GMr .\tag{19.2}$$

Matter falls from different directions, making an angle ϑ with the polar axis, and has a different angular momentum j_ϑ according to ϑ,

$$j_\vartheta = \Omega r^2 \sin^2 \vartheta .\tag{19.3}$$

The matter settles at equilibrium in the equatorial plane with a circular motion at a radius r_ϑ in the equatorial plane, such that

$$r_\vartheta \approx \frac{j_\vartheta^2}{GM} \, . \tag{19.4}$$

For $\vartheta = 0$, the angular momentum is negligible and the matter can reach the proto-
star. For $\vartheta = \pi/2$, j_ϑ is maximum and the matter sets in equilibrium in the equato-
rial plane at a radius r_ϑ (larger than the stellar radius). Material arriving from both
sides collide in the midplane and produce a flattened distribution of density [229],
which progressively forms a disk. The disk is therefore rotationally supported rather
than pressure supported.

19.1.3 Disk Properties and Evolution

We consider a disk constrained by the central gravitational potential of the protostar
to have a Keplerian rotation from its outer regions down to a place close to the
stellar surface. One also assumes that there is some transfer of angular momentum
between adjacent layers by some viscosity expressed by a coefficient ν (likely due
to turbulent viscosity). As the inner layers rotate faster, they transfer by viscous
coupling some angular momentum to the outer layers. Thus, the inner layers lose
angular momentum and sink into the potential well, while the outer layers gaining
angular momentum move outward. As some energy is lost by friction, the potential
energy of the system becomes progressively more negative and there is also a global
inward motion of the matter. Disk evolution is thus characterized by a release of
energy as a part of the matter of the disk is being accreted, while another part of the
matter (generally smaller) is spread to larger distances [229, 331].

Let us study the evolution of an accretion disk. We assume that the disk is ro-
tationally supported, with a decreasing angular velocity $\Omega(r)$ at a distance r from
the central star. The disk is supposed to be thin with a surface density σ. The mass
conservation of an annulus of matter between r and $r + \delta r$ implies that the net gain
per unit of time is the difference between what enters with a radial velocity v at level
r and gets out at $r + \delta r$,

$$\frac{\partial}{\partial t} (2\pi \sigma r \delta r) = 2\pi v(r,t)\sigma(r,t)\, r - 2\pi\, v(r+\delta r)\, \sigma(r+\delta r)\,(r+\delta r). \tag{19.5}$$

The limit for small δr expresses the continuity in the plane of the disk,

$$r\frac{\partial \sigma}{\partial t} + \frac{\partial}{\partial r}(r\sigma v) = 0\,. \tag{19.6}$$

The same reasoning applied to the conservation of the angular momentum $r^2\sigma\Omega$ by
surface unit yields

$$r\frac{\partial(r^2\sigma\Omega)}{\partial t} + \frac{\partial}{\partial r}(r\sigma v r^2 \Omega) = -\frac{1}{2\pi}\frac{\partial S}{\partial r}\,, \tag{19.7}$$

where S is the torque modulus of $\boldsymbol{S} = \boldsymbol{r} \times \boldsymbol{F}$, where $\boldsymbol{F}$ is the force. Here, the force, during a displacement with a velocity v in a direction $\boldsymbol{\varphi}$, is exerted by the viscosity v in a medium with a shear dv/dr (where the direction of r is perpendicular to the direction $\boldsymbol{\varphi}$). For a disk in circular rotation with angular velocity $\Omega(r)$, the force exerted by the viscosity is according to the definition (B. 48)

$$\boldsymbol{F} = -2\pi r\sigma v r \frac{d\Omega}{dr} \frac{\boldsymbol{\varphi}}{\varphi} ,\tag{19.8}$$

which is directed in the direction $-\boldsymbol{\varphi}$ opposite to the rotation motion. The torque produced by the viscous shear has a modulus

$$S = -2\pi r^2 \sigma v r \frac{d\Omega}{dr} ,\tag{19.9}$$

it is positive since $\frac{d\Omega}{dr} < 0$ (Keplerian rotation). One gets for (19.7),

$$\frac{\partial\left(r^2\sigma\Omega\right)}{\partial t} + \frac{1}{r}\frac{\partial}{\partial r}\left(\sigma v r^3 \Omega\right) = \frac{1}{r}\frac{\partial}{\partial r}\left(\sigma v r^3 \frac{d\Omega}{dr}\right) .\tag{19.10}$$

Developing the terms on the left and using (19.6), we get

$$\sigma v \frac{\partial}{\partial r}\left(r^2\Omega\right) = \frac{1}{r}\frac{\partial}{\partial r}\left(\sigma v r^3 \frac{d\Omega}{dr}\right) .\tag{19.11}$$

We may then use this relation to express the term $r\sigma v$ in (19.6) and obtain

$$\frac{\partial\sigma}{\partial t} = \frac{1}{r}\frac{\partial}{\partial r}\left[\left(\frac{d(\Omega r^2)}{dr}\right)^{-1}\frac{\partial}{\partial r}\left(-\sigma v r^3 \frac{d\Omega}{dr}\right)\right].\tag{19.12}$$

This is a diffusion equation for the material density in a thin accretion disk. As such, it is a general expression. We can simplify it for a spherical mass distribution with mass M at the interior of the disk. $\Omega(r)$ is given by $\Omega(r) = \left(GM/r^3\right)^{1/2}$. The diffusion equation (19.12) simplifies to [229]

$$\frac{\partial\sigma}{\partial t} = \frac{3}{r}\frac{\partial}{\partial r}\left[r^{\frac{1}{2}}\frac{\partial}{\partial r}\left(v\sigma r^{\frac{1}{2}}\right)\right] .\tag{19.13}$$

This describes the evolution of the disk density $\sigma(r)$ at each distance r in the disk of viscosity v as a function of time.

For a shear dv/dr (where r is perpendicular to the velocity), the energy W_v dissipated by units of time and volume by the viscosity v is $W_v = (1/2)\varrho v\left(dv/dr\right)^2$. In the accretion disk, the shear is $dv/dr = rd\Omega/dr$ and instead of the volume density ϱ, we have the surface density σ, so that the energy dissipated by units of time and surface in the disk is

$$W_\nu = \frac{1}{2}\nu\sigma\left(r\frac{d\Omega}{dr}\right)^2 . \qquad (19.14)$$

This energy is radiated away at the expense of the potential energy of the disk, which progressively moves to the interior. The exact solution of (19.13) depends on the expression of the viscosity. Simple analytical solutions for a constant viscosity show that, as time proceeds, the disk spreads toward both larger and smaller radii [331]. There is more and more mass at smaller radii and at the same time the disk expands outward to maintain angular momentum conservation. From (19.13), the disk evolution is characterized by a timescale $t_\nu \approx r^2/\nu$ (of the order of 10^5 yr).

A major uncertainty concerns the viscosity ν. Molecular viscosity is clearly insufficient and there must be other effects. A magnetic field may create a magnetic diffusivity coupling the adjacent stellar layers. Small-scale turbulent motions may also create a local coupling. Parametrizations of the form $\nu = \alpha c_s H$ are often considered, where c_s is the sound velocity and H an appropriate scale height for the density [630]. According to recent dynamical studies, the flow in the disk is turbulent [247] and the turbulent viscosity is compatible with $2 \times 10^{-4} < \alpha < 2 \times 10^{-2}$. In solar-type stars, effects of magnetic field are present, since they are needed to account for the disk locking, i.e., the magnetic coupling of the disk and star (Sect. 21.2).

Gravitational instabilities may also be present in massive disks at the beginning of the cloud collapse. If there is a large enough mass concentration, the instabilities may extract angular momentum from the inner regions and transfer it to the external layers.

19.1.4   Stationary Disks

During a part of their existence, disks may be considered as stationary, with constant rates of mass accretion. In such a state, some of their properties are independent of the viscosity [229]. Let us start from the conservation equations as above and impose a steady state. Mass conservation in the disk yields for the inward mass flow at level r

$$\dot{M} = -2\pi r\sigma v , \qquad (19.15)$$

where a positive radial velocity is directed outward. Equation (19.10) for mass conservation becomes after integration

$$\sigma v r^3\Omega = \left(\sigma\nu r^3\frac{d\Omega}{dr}\right)+C, \quad \text{or} \quad -\nu\sigma\frac{d\Omega}{dr} = -\sigma\Omega v+\frac{C}{r^3}, \qquad (19.16)$$

where C is a constant, which may be estimated as follows. From outside as r decreases, the Keplerian Ω increases up to some place $r_{\Omega\text{max}}$ defined by $d\Omega/dr = 0$ (which implies no shear), where $\Omega(r)$ reaches its maximum Ω_{max} and then goes

down to reach the value Ω at stellar surface $r = R$. One has

$$C = r^3 \, \sigma \, v \Omega_{max} = -\frac{r^2 \, \Omega_{max} \dot{M}}{2\pi} \, . \tag{19.17}$$

If $r_{\Omega max}$ is close to the protostellar radius R (which is verified for thin disks [229]), the angular velocity at $r_{\Omega max}$ is $\Omega_{max} = (GM/R^3)^{1/2}$ and C becomes

$$C = -\frac{\dot{M}(GMR)^{\frac{1}{2}}}{2\pi} \, . \tag{19.18}$$

With this value of C, $\Omega(r) = (GM/r^3)^{1/2}$ and (19.15), (19.16) become

$$v\sigma = \frac{\dot{M}}{3\pi} \left(1 - \frac{R^{\frac{1}{2}}}{r^{\frac{1}{2}}} \right) , \tag{19.19}$$

which show that in the external regions the surface density in a stationary disk varies like $1/v$. The rate (19.14) of energy dissipation by viscosity per unit of area and time becomes [331]

$$W_v(r) = \frac{1}{2} v\sigma \left(r\frac{d\Omega}{dr} \right)^2 = \frac{3}{8\pi} \frac{GM\dot{M}}{r^3} \left(1 - \frac{R^{\frac{1}{2}}}{r^{\frac{1}{2}}} \right). \tag{19.20}$$

In a stationary situation, the rate of energy dissipation is independent of v. The rate of energy released by the two faces of the accretion disk is

$$L_{diss} = 2 \times 2\pi \int_R^\infty W_v(r) r\, dr = \frac{1}{2} \frac{GM\dot{M}}{R} , \tag{19.21}$$

where R can be taken as the stellar radius (formally this should be the inner limit of the disk). It is interesting to notice that half of the potential energy available $(GM\dot{M})/R$ is radiated. Where is the rest of this energy? If the inner radius of the disk is very close to the star radius, there is almost no potential energy left at the inner disk. However, matter in the inner disk rotates in equilibrium on a circular orbit, where $v^2/r = GM/r^2$, so that its kinetic energy by unit of mass is half the potential energy $(1/2)v^2 = (1/2)GM/r$. Thus, the remaining half of the available energy lies in the kinetic energy of the matter at the inner boundary of the disk. This energy will be thermally dissipated during accretion at the stellar surface and most of this energy is likely re-radiated outward immediately (cf. Sect. 19.2.2).

If we also make the hypothesis that the disk is optically thick, it radiates like a black body and we can make (19.20) equal to $(ac/4)T^4(r)$, where $T(r)$ is the disk temperature at level r

$$T^4(r) = \frac{3GM\dot{M}}{2\pi ac\, r^3} \left(1 - \frac{R^{\frac{1}{2}}}{r^{\frac{1}{2}}} \right). \tag{19.22}$$

We get the distribution of the disk temperature $T(r)$, which is higher for higher accretion rates and larger stellar mass. The temperature steeply decreases toward the exterior of the disk. Formally this expression predicts $T = 0$ at the inner limit of the disk, this unphysical condition results from the simplified inner boundary conditions adopted, in particular the absence of shear. A better treatment of the disk boundaries may avoid this difficulty.

Expression (19.22) allows us to predict the energy distribution in the disk. The inner edge of the disk dominates the short wavelengths and the integrated spectrum shows a steep decrease at short wavelengths. At long wavelengths, the Planck emission of the various disk zones behaves as the square of the frequency and so does their summation over the disk. However in most cases, the disk is optically thin at long wavelengths, because the dust opacity declines rapidly at long wavelengths. This is, however, an interesting property, because if the disk becomes optically thin, its emission also depends on the mass present (while for optically thick regions the flux emitted depends only on the superficial T). The disk emission at a distance r depends on $T^4(r)$ (cf. 19.22) and is proportional to the column density $\sigma\, r^2$, i.e., to the local mass in the disk. This provides a possibility of estimating the disk mass [451]. Disk masses between $\sim 10^{-3}$ and $1\,M_\odot$ were found. Owing to the range of disk masses, a great variety of planetary systems seems possible.

Numerical simulations [628] of the formation of a $1\,M_\odot$ star show that within less than 10^5 yr a protostar of $0.45\,M_\odot$ forms within a radius of about $200\,R_\odot$ and has a large disk extending up to $500\,R_\odot$. The inner part of the disk around stars with an external convective zone ($M \leq 1.5\,M_\odot$) participates in the magnetic coupling of the star with the disk. This is the process of disk locking which plays an essential role in shaping the distribution of stellar rotation in solar-type stars (Sect. 21.2). The matter in the disk eventually reaches the star after dissipation of the angular momentum.

19.2   Accretion in Low and Intermediate Mass Stars

Ideally, the study of star formation should encompass simultaneously the three components of a forming star: the central core, the accretion disk and the parent cloud, since these three parts are highly interacting. The main parameter determining the evolution of the central body is the accretion rate $\dot{M}_{\text{accr}}$, which gives the amount of mass received by unit of time by the central-forming protostar. The mass accretion on the star comes from the disk, which is itself for some time replenished by the matter infalling from the cloud.

Observationally the accretion rates are estimated from IR fluxes by the relation (cf. 19.21),

$$\dot{M}_{\text{accr}} \simeq 2\,\frac{R L_{\text{IR}}}{GM} \ . \tag{19.23}$$

L_{IR} is the IR luminosity of the disk, R and M are the estimates of the radius and mass of the protostar, respectively. In practice, the disk luminosity has to be disentangled from the luminosity of the young star.

The estimates of $\dot{M}_{accr}$ range from a few 10^{-8} to a few 10^{-6} $M_{\odot}$ yr^{-1} for T Tauri stars and from about 10^{-6} to 10^{-4} $M_{\odot}$ yr^{-1} for Ae and Be Herbig stars. There is a correlation [82] between the observed accretion rates $\dot{M}_{accr}$ and the stellar masses M of the form $\dot{M}_{accr} \cong 10^{-8} (M/M_{\odot})^{1.95}$. It applies to classical T Tauri stars (with masses < 0.1–$1.5\,M_{\odot}$) and intermediate mass T Tauri stars (from 1.5 to about $2.0\,M_{\odot}$).

19.2.1 Theoretical Estimates of the Accretion Rates

The order of magnitude of $\dot{M}_{accr}$ is given by the ratio of the Jeans mass (18.17) and of the free-fall time (18.28) of the cloud

$$\dot{M}_{accr} \approx \frac{M_J}{t_{ff}} = \sqrt{\frac{32}{3} \frac{\pi^2}{6}} \frac{c_s^3}{G} \approx 5.4 \frac{c_s^3}{G} \,, \tag{19.24}$$

where $c_s = [(k/(\mu\, m_u))\, T]^{\frac{1}{2}}$ is the isothermal sound velocity (C.27). The above rate is higher than the accretion rate found for the collapse of the singular isothermal sphere (Sect. 18.4.2), where a numerical coefficient of 0.975 is obtained [528]. Different numerical models of cloud collapse typically lead to $\dot{M}_{accr} = (3-50)\,c_s^3/G$, i.e., from 5×10^{-6} to 10^{-4} $M_{\odot}$ yr^{-1}. For typical values $T = 10$–20 K, $c_s \approx 0.2$ km s^{-1} and $\dot{M}_{accr} \approx 10^{-5}$ $M_{\odot}$ yr^{-1}.

Interestingly enough, (19.24) suggests that the accretion rate is not directly determined by the star properties, but by the conditions in the parent cloud (which may depend on the already formed stars). It also shows that for a higher T in the cloud, there is a higher $\dot{M}_{accr}$. The reason is that a higher T allows a denser cloud to be in equilibrium. In turn, a denser cloud has a shorter free-fall time. Similarly any other support against gravity leads to higher accretion rates on the central object. If there is some magnetic pressure with an Alfvén velocity v_A and a turbulent velocity v_{turb}, $\dot{M}_{accr}$ becomes

$$\dot{M}_{accr} \approx \frac{(c_s^2 + v_A^2 + v_{turb}^2)^{3/2}}{G} \,. \tag{19.25}$$

Thus, strong turbulence in molecular clouds, as for example induced by previously born stars, and some magnetic support of the cloud lead to large accretion rates on the newly formed stars.

Various assumptions on the structure of molecular clouds (cf. Sect. 18.4.2) lead to different accretion rates and also to different behaviors of the rates with time. A critical question is to know how the accretion rates behave in time, since the history of $\dot{M}_{accr}$ determines the evolution of the protostar. The case of the singular isothermal sphere (Sect. 18.4.2, Fig. 18.3) leads to constant accretion rates of the form (19.24). An example of an initially peaked evolution of the accretion rate is
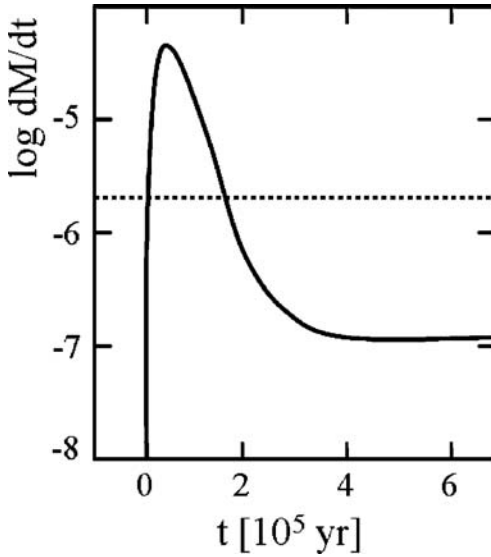
Fig. 19.2 Accretion rate as a function of time for a gravo-turbulent fragmentation from Schmeja and Klessen [518] predicting an initial peak in the accretion rate. The horizontal *dotted line* corresponds to (19.24) with a numerical coefficient 0.975

given in Fig. 19.2 which shows results of numerical simulations of accretion by a star embedded in a larger cloud, supposed to form a cluster. $\dot{M}_{\mathrm{accr}}$ fluctuates in a stochastic way, but the average rate can well be represented by a fitting formula [518]

$$\dot{M}_{\mathrm{accr}}(t) = \dot{M}_0 \frac{e}{\tau_0} t \, e^{-\frac{t}{\tau_0}} , \tag{19.26}$$

where $\dot{M}_0$ is the maximum accretion rate and τ_0 the age of this maximum. In the example illustrated in Fig. 19.2, the final mass of the star is $2.9\,\mathrm{M}_\odot$. Other forms of $\dot{M}_{\mathrm{accr}}$ growing with mass have been proposed [44].

19.2.2 Structure of the Protostar in the Accretion Phase

In the phase of strong accretion which leads to the formation of a hydrostatic core, the collapsing cloud has a structure [549] formed by shells with different properties, as illustrated in Fig. 19.3. The outer envelope contains most of the cloud volume. This region is optically thin and the collapse proceeds isothermally due to grain cooling (Sect. 18.4). As the local density is low, the infall velocity is small. For massive star formation, a reversal of the infall may occur due to the stellar radiation or the formation of an HII region (Chap. 22). Then, toward the interior there is a dust shell or envelope, which is optically thick due to dust grains. The outer edge
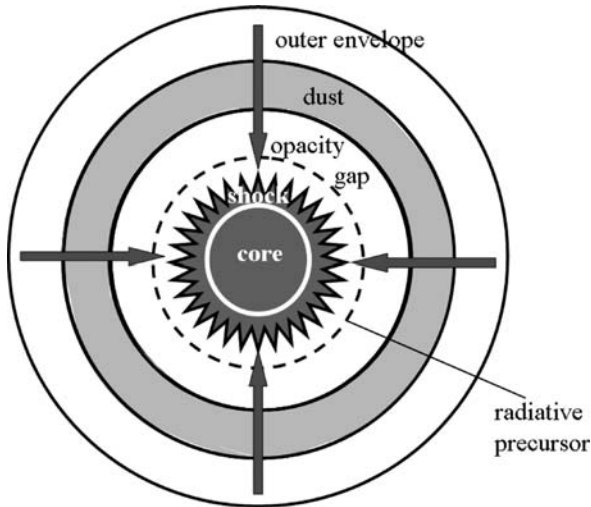
Fig. 19.3 Schematic structure of a protostar in the strong spherical accretion phase. The radii of the various shells are 10^{17} cm for the cloud boundary, 10^{14} cm for the outer edge of the dust layer, 10^{13} cm for the dust destruction front and 10^{11} cm for the accretion shock. Adapted from S.W. Stahler, F.H. Shu and R.E. Taam [549]

of the shell forms a kind of dust photosphere, the properties of which define the observable luminosity and T_{eff}. The interior limit of this shell is the dust destruction limit, where radiation is high enough to lead to the evaporation of the dust.

Inside the dust envelope, grains are destroyed and there is an opacity gap. There, the gas is essentially transparent and photons from the inner shock go freely through this region. At some depth, the increase of density and temperature makes the medium optically thick and one has a gas photosphere [549], making a radiative precursor to the future star. If the runs of ϱ and T are such that the medium is transparent down to the shock, the limit of the radiative precursor coincides with the shock layer.

At the accretion shock, the matter is brought to rest. If half of the potential energy of the infalling matter is dissipated in the disk (cf. 19.21) and the other half is radiated by the shock, the luminosity of the shock is

$$L = \frac{1}{2} \left(\frac{1}{2} v_{\text{ff}}^2 \dot{M}_{\text{accr}} \right) = \frac{GM}{2R} \dot{M}_{\text{accr}} , \qquad (19.27)$$

which is the same as (19.21). The decelerated matter settles into an optically thick hydrostatic core. The thermal adjustment of the core proceeds at its Kelvin–Helmholtz timescale. The core further increases in mass by accretion, until the reservoir is exhausted or until some reversal of the infall occurs. Most models of collapse ignore the effects of photons produced by the accretion shock. This is rather justified due to the low opacity in the outer part of the cloud, which allows radiation to escape freely. However, the dynamics of the dust shell is also influenced by radiation

transfer. The half of the potential energy is deposited in the boundary layers [185]. Most of this deposited energy is also directly re-radiated away and only a tiny fraction α enters the star. Locally, this is equivalent to an energy production rate ε_{accr}, produced by the accreted matter ΔM within the interval of time Δt

$$\varepsilon_{accr} \approx \frac{\Delta L}{\Delta M} \approx \alpha \frac{G\dot{M}_{accr}}{2R} \approx 3\alpha \left(\frac{R_\odot}{R}\right) \left(\frac{\dot{M}_{accr}}{10^{-7}}\right) \;\; \text{erg g}^{-1}\text{s}^{-1}, \quad (19.28)$$

with $\dot{M}_{accr}$ in $M_\odot$ yr^{-1}. This energy production rate is to be added to the other energy sources (for example deuterium burning) in the considered layers. It contributes to inflate the outer stellar radius, which in turn by decreasing the stellar temperature slows down the deuterium burning. The value of α is small, maybe a few percent [530]. If it would be large, a full treatment of the heat transfer should be made.

19.3   The Phase of Adiabatic Contraction

The evolution of the conditions in the core of the protostar of $1\,M_\odot$ is illustrated in Fig. 19.4. The part of the track before point A corresponds to the phase of isothermal collapse (the initial decrease is due to the fact that at very low density the atomic cooling is less efficient). The collapse is evidently non-homologous, since the free-fall timescale is shorter in central regions. As density increases beyond point A, the opacity gets higher and the radiation does not escape freely from the core. Thus, in first approximation the core follows an adiabatic evolution. Initially,
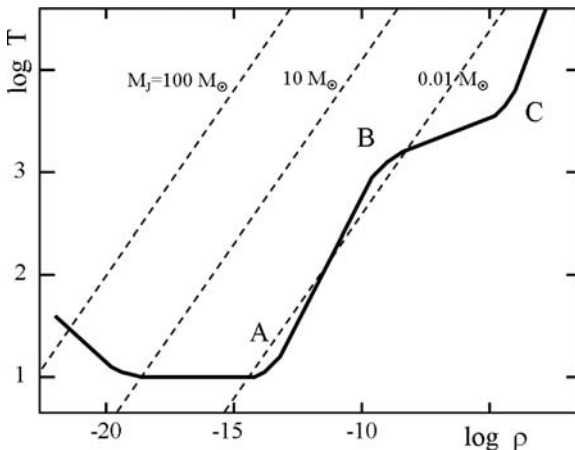
Fig. 19.4 Evolution of temperature and density at the center of a forming star evolving at a constant mass of $1\,M_\odot$ [576]. Point A marks the end of the isothermal phase. A–B is the adiabatic phase of molecular gas. B–C is the transition from molecular to neutral gas and from neutral to ionized gas. C marks the beginning of the adiabatic phase of ionized gas. Adapted from P. Bodenheimer [51]

the collapsing core consists mainly of molecular hydrogen. The H_2 molecule has 5 degrees of liberty. For an adiabatic change, the pressure P behaves as $P \sim \varrho^\gamma$ with $\gamma = (5+2)/5 = 1.40$ and T and ϱ of the perfect gas behave like

$$\varrho \sim \frac{P}{T} \sim \frac{\varrho^{1.40}}{T} \quad \text{and thus} \quad T \sim \varrho^{0.40} . \tag{19.29}$$

This is illustrated by the segment A–B in Fig. 19.4. Near $T = 2000\,\mathrm{K}$, the molecular dissociation $H_2 \rightarrow H + H$ absorbs a lot of energy and increases the specific heat accordingly. This makes the tracks flatter in segment B – C. Above about $T = 3000\,\mathrm{K}$, the ionization $H \rightarrow H^+ + e^-$ does the same. This maintains a relatively flat track up to C favoring core collapse. In point C, the evolution is adiabatic again. The gas is now ionized and the ratio of specific heats is $\gamma = 5/3$. In a similar way as above (19.29), this leads to a relation of the form

$$T \sim \varrho^{\frac{2}{3}} , \tag{19.30}$$

which produces the relatively steep slope above point C in Fig. 19.4. The adiabatic approximation becomes less acceptable as evolution further proceeds. Numerical models of this phase show progressively a considerable increase of the emitted radiation. The evolution of a $1\,M_\odot$ star is illustrated in Fig. 19.5. The starting point is at the end of the phase of isothermal collapse, when T is still $\sim 10\,\mathrm{K}$. The initial properties depend on the cloud model. As seen above, there is a variety of possible structures, with different density laws (Sect. 18.4.2). However, the properties
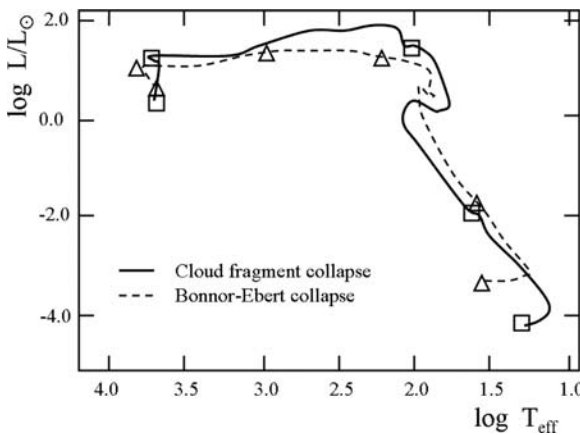
Fig. 19.5 Evolution in the plane $\log(L/L_\odot)$ vs. $\log T_{\mathrm{eff}}$ [623] during the formation by accretion of a star of $1\,M_\odot$ from the end of the isothermal collapse up to the top of the Hayashi line. Two cases of accretion are considered. (1) The accretion rates result from the modelization of the dynamical evolution of a molecular cloud. (2) The accretion rates result from the collapse of a Bonnor–Ebert sphere. The squares and triangles indicate the following ages on the two tracks: 1, 10, 100, 350 Kyr. The last square corresponds to 1 Myr, the last two triangles correspond to 0.5 and 1 Myr. Adapted from G. Wuchterl and R.S. Klessen [623]

of the star in the pre-MS phase are essentially independent of the uncertain initial conditions.

19.3.1 Evolution of the Central Object

In Fig. 19.5, two cases of stellar collapse leading to the formation of a star of $1\,M_\odot$ are compared. One case (thick line) represents the evolution of a 3D dynamical model of a cloud fragment, in which the accretion rates on the small protostellar core are derived from the surrounding cluster model. The collapse of a Bonnor–Ebert sphere, i.e., an isothermal sphere in hydrostatic equilibrium with a finite radius (Sect. 18.4.2), is also illustrated (dashed line). The two cases are not very different.

Let us describe the evolution of the cloud fragment from the end of the isothermal collapse to the Hayashi line, it can be divided into three parts:

Fast initial luminosity increase: L increases up to about $20\,L_\odot$ with $T_{\text{eff}} < 100$ K. The growth of central density and pressure allows a hydrostatic core to form. The free-falling inner envelope is characterized by density and velocity laws of the form (18.44)

$$\varrho \sim r^{-3/2} \quad \text{and} \quad v \sim r^{-1/2}, \tag{19.31}$$

while the outer parts of the cloud keep a density law $\varrho \sim r^{-2}$ (Sect. 18.4.2). The accreting matter on the core forms a shock, where the energy (19.27) of the infalling matter is dissipated. A stationary situation is produced (Fig. 19.3) with a growing core on which accretion goes on. The energy liberated evaporates the dust in an inner shell around the core, this reduces the opacity locally and thus radiation goes out. The photons arriving in the external dust envelope are absorbed and re-radiated in the IR and radio wavelengths.

Main accretion phase: As a result of the accretion, which peaks at $10^{-5}\,M_\odot$ yr^{-1}, the contracting star has reached a high luminosity during the early protostellar phase. The ongoing accretion leads to a surface temperature of 2000 K, with a luminosity up to $100\,L_\odot$ in about 10^5 yr. The higher density in the cloud model compared to the Bonnor–Ebert sphere leads to a higher accretion rate and thus to a higher average luminosity. This illustrates the fact that the accretion depends on the environment in the cloud.

End of the accretion: As accretion proceeds, the envelope becomes more transparent and T_{eff} increases. The star keeps its high luminosity and reaches a location close to the top of the Hayashi line (see next section) in the HR diagram in 10^6 yr. Until this stage, the timescale is of the order of the free-fall time. When accretion ceases, the star becomes visible and its luminosity decreases at about constant T_{eff}. This last part corresponds to the Hayashi phase at the beginning of the pre-MS evolutionary phase. The two models shown in Fig. 19.5 converge, which confirms that at the end of the protostellar phase the models are independent of the initial cloud structure.

19.4   Properties at the End of the Protostellar Phase

At the end of the phase of rapid and adiabatic contraction, the star is in the region of the red giants (Figs. 19.5 and 20.1) in a place in the HR diagram called the Hayashi line (Sect. 20.2). Noticeably, the properties of stars at the end of adiabatic contraction can be understood from simple considerations. The total energy present in a star of mass M and radius R is

$$E_{\text{tot}} = E_{\text{cin}} + \Omega + E_{\text{ion}} + \Delta \cong 0 , \qquad (19.32)$$

where E_{cin} is the kinetic energy of stellar particles, Ω is the potential energy, E_{ion} is the energy which was necessary to ionize the gas and Δ is the energy already lost by radiation. The star is barely bound and its total energy $E_{\text{tot}} \simeq 0$, with $E_{\text{tot}} \ll E_{\text{cin}}$ and $E_{\text{tot}} \ll |\Omega|$. As the star is in equilibrium, it must satisfy the Virial theorem $2E_{\text{cin}} + \Omega = 0$. Thus (19.32) becomes

$$\frac{\Omega}{2} + E_{\text{ion}} + \Delta \cong 0 . \qquad (19.33)$$

The potential energy is $\Omega = -q\,GM^2/R$ where q depends on the density distribution; for a polytrope of index n, $q = 3/(5-n)$ (24.71). The energy E_{ion} contains the dissociation energy of the molecular hydrogen and the ionization energy of H and He, which are the main constituents of the cloud:

$$\text{H}_2 \overset{4.48\,\text{eV}}{\rightarrow} 2\text{H} \overset{2 \times 13.6\,\text{eV}}{\rightarrow} 2\text{p} + 2\text{e}^- , \qquad (19.34)$$

$$\text{He} \overset{24.6\,\text{eV}}{\rightarrow} \text{He}^+ + \text{e}^- \overset{54.4\,\text{eV}}{\rightarrow} \text{He}^{++} + 2\text{e}^- . \qquad (19.35)$$
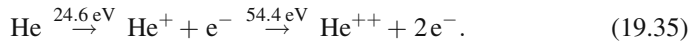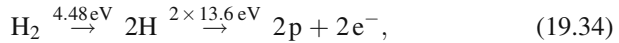
Thus, the ionization energy present in a star containing $N(\text{H})$ hydrogen and $N(\text{He})$ helium particles is

$$E_{\text{ion}} = 4.48N(\text{H}_2) + 13.6N(\text{H}) + (24.6 + 54.4)N(\text{He}) \ [\text{eV}]$$

$$= 15.84N(\text{H}) + 79N(\text{He}) \ [\text{eV}]$$

$$= 1.602 \times 10^{-12}(15.84X + 19.75Y)\frac{M}{m_{\text{u}}} \ [\text{erg}] = \chi\frac{M}{m_{\text{u}}} \ [\text{erg}] , \ (19.36)$$

where X and Y are, respectively, the hydrogen and helium mass fractions. If one assumes [231] that the amount Δ of energy radiated during the first phases is negligible, one gets

$$R \cong \frac{3}{2(5-n)}\frac{m_{\text{u}}G}{\chi}M. \qquad (19.37)$$

If the star is homogeneous in density, $n = 0$. For a fully convective star, the polytropic index (24.61) is $n = 3/2$. Numerically, for a star with a composition, say $X = 0.72$ and $Y = 0.28$, we get

$$\frac{R}{R_\odot} \cong 50.4 \, \frac{M}{M_\odot} \, . \tag{19.38}$$

This is a much larger radius than for a star on the MS. This result comes mainly from the hypothesis $\Delta \cong 0$, i.e., that the star has lost no energy, which implies that the star has not gone deep into its potential well. In reality this is not exactly the case. The star has radiated a lot; however, only during a short timescale of the order of t_{ff}. This makes the radius of the numerical models (Fig. 19.5) smaller than (19.38). The linear relation between mass and radius implies a fast decreasing average density for larger masses.

The average internal temperature $\overline{T}$ of the star can be estimated by (1.26). It is $\sim 4 \times 10^4$ K, while at the center it is a few 10^5 K. This is lower than the temperature $T = 2 \times 10^6$ K for the fusion of deuterium, which thus ignites slightly later in the evolution. We also see that the internal $\overline{T}$ of objects entering this phase (the Hayashi phase, Sect. 20.2.1) is independent of the stellar mass. As matter becomes partly ionized, the opacity gets higher making progressively the star fully convective. The luminosity of fully convective stars is given by (24.60). This means that for a given mass the large radius implies a relatively lower luminosity.

There are some differences between the numerical models (Sect. 19.3.1) and the above simple analytical model. The numerical model of a $1 \, M_\odot$ at an age of 10^6 yr is about twice brighter and 500 K hotter than the analytical model. These differences are due to the simplifications made in the analytical model, in particular the hypothesis that the star has lost no energy by radiation. Nevertheless, the analytical model has the virtue to enlighten the fundamental properties of stars at the beginning of the Hayashi line. Also, there is a small radiative core in the last models of Fig. 19.5. The reason is the higher T in the numerical model, the lower resulting opacity favoring the early recession of convection.

Chapter 20
The Pre-main Sequence Phase and the Birthlines[*]

In the pre-MS phase, the stars are in a stage of hydrostatic equilibrium; the evolution becomes much slower proceeding at the Kelvin–Helmholtz timescale, which is about 30 million years for the Sun. In addition to contraction, the nuclear deuterium burning produces an energy which significantly influences the evolution of solar and lower mass stars and produces an inflation of the radius. The accretion of matter from the parent cloud may continue for some time, if so the rate of mass accretion is a key parameter determining the properties of pre-MS stars. This phase of evolution leads the stars to the main sequence phase, where they experience nuclear fusion reactions of hydrogen into helium.

20.1 General Properties of Non-adiabatic Contraction

The pre- and protostellar phases were treated as adiabatic, because despite the growing luminosity, the total loss of energy was limited due to the short timescales. When evolution becomes slower, the adiabatic approximation is no longer valid. For a $1\,M_\odot$ star, the fast adiabatic phase ends at an age of $\sim 10^6$ yr, when the internal temperature $T \approx 10^5$ K and the density $\varrho \simeq 10^{-2}$ g cm^{-3}. Henceforth, the rhythm of contraction is much slower, because the whole star, supported by gas pressure, is now about in hydrostatic equilibrium.

20.1.1 The Kelvin–Helmholtz Timescale

For a star in equilibrium, the Virial theorem (Sect. 1.3) indicates that the increase $\Delta U = [1/(3\gamma - 3)]\,(-\Delta\Omega)$ of the specific internal energy is related to the difference of the specific potential energy $\Delta\Omega$. The radiated energy $\Delta U_{\rm rad}$ is the difference

---

[*]This chapter may form the matter of a basic introductory course.

between what is liberated by gravitational contraction and the increase ΔU of internal energy:

$$\Delta U_{\text{rad}} = (-\Delta\Omega) - \Delta U = \frac{3\gamma - 4}{3\gamma - 3}(-\Delta\Omega). \tag{20.1}$$

For an ionized gas $\gamma = 5/3$, half of the energy is used for heating the gas, while the other half is radiated away. For an average luminosity $\overline{L}$ over a timescale t_{KH}, one has $\Delta U_{\text{rad}} = \overline{L}t_{\text{KH}}$; thus we get

$$t_{\text{KH}} = \frac{\Delta U_{\text{rad}}}{\overline{L}} = \frac{3\gamma - 4}{3\gamma - 3}q\frac{GM^2}{R\overline{L}} \simeq \frac{GM^2}{R\overline{L}}, \tag{20.2}$$

with a numerical coefficient of the order of unity, (i.e., $3/10$ for constant density and $3/4$ for a typical density distribution with a polytropic index $n = 3$, Sect. 24.5). Numerically, this becomes for a coefficient equal to 1

$$t_{\text{KH}} = 3.1 \times 10^7 \text{yr} \left(\frac{M}{\text{M}_\odot}\right)^2 \left(\frac{R}{\text{R}_\odot}\right)^{-1} \left(\frac{L}{\text{L}_\odot}\right)^{-1}. \tag{20.3}$$

This is the Kelvin–Helmholtz timescale, expressing the time during which a star can radiate a luminosity $\overline{L}$ from the potential energy only. Currently the ratio of t_{KH} to the MS lifetime is of the order of $t_{\text{KH}}/t_{\text{MS}} = 10^{-2}$ (0.005 for a solar-type star and 0.02 for a massive star). For a mass–luminosity relation of the form $L \sim M^3$ and a mass–radius relation $R \sim M^{0.7}$ valid over the upper MS, one has $t_{\text{KH}} \sim M^{-1.7}$. We recall that t_{KH} is also the timescale for the stellar thermal adjustments (Sect. 3.2.4).

20.2   Pre-MS Evolution at Constant Mass

For long, it was considered that when the star reaches the Hayashi phase at the end of the adiabatic phase, the whole stellar mass has been assembled and that the star then evolves keeping a constant mass. Now, more refined scenarios are considered as discussed in further sections.

20.2.1   The Hayashi Line

The Hayashi line is an important concept in stellar evolution. It is the location of fully convective stars in the HR diagram. This locus is nearly vertical (combined effect of convective transport and opacity) and depends on the mass of the star. This is close to the location of post-MS red giants, since red giants have very extended convective envelope. Stars on the Hayashi line have large radii (Sect. 19.4). The main properties of the Hayashi line are as follows:

– The Hayashi line is at about constant $T_{\text{eff}} \approx 3500$ K (Figs. 20.1 and 20.2). This results from the high opacity below $T \simeq 7000$ K, due mainly to the photo-ionization of ion H^-. At low T, the opacity κ behaves like $\kappa \sim \varrho^{0.5} T^9$ (8.25). Thus, if T grows, κ grows even faster, which in turn reduces T. This produces a feedback maintaining T about constant.

– The Hayashi line is the lower T_{eff} limit of convective stars in the HR diagram, i.e., it applies to fully convective stars. To the right of it, there are no stable stars. If for a star model of given M and L, one would reduce T_{eff} below the value of the Hayashi line and make a larger radius, say R', the integration of the equation for mass conservation from the stellar center up to R' would give a mass superior to M, since the density distribution of a convective body is anyhow fixed by the polytropic index n (Sect. 24.5), i.e., for a fixed density distribution, a larger stellar radius would lead to a larger mass. Therefore, there is no star in equilibrium to the right of the Hayashi line.

– The location of the Hayashi line also depends on the mixing-length ratio ℓ/H_P for convection, since this ratio influences the stellar radius. An increase of ℓ/H_P from 1.0 to 1.5 shifts $\log T_{\text{eff}}$ by +0.06 dex, since a more efficient energy transport, as resulting from a larger ℓ, produces a smaller stellar radius.

– The T_{eff} of the Hayashi line also depends on metallicity Z and in particular on the abundances of metals with a low ionization potential, since they provide free electrons making ions H^- which contribute a lot to the opacity at low T. A lower Z reduces the opacity and thus increases the luminosity. To provide more energy, contraction is enhanced; the radius becomes smaller and so the T_{eff} of the Hayashi branch is higher.

– The initial model at the top of the Hayashi branch can be taken as a polytrope with index $n = 1.5$ (or even $n = 1$ with an analytical solution, Sect. 24.5). Stellar contraction makes a higher density, which in turn increases the opacity and thus the luminosity decreases: the star goes down the Hayashi line (Fig. 20.1).

– The Hayashi line terminates at a minimum luminosity and thereafter the star moves toward higher T_{eff} being made of a growing radiative core and an external convective envelope. The minimum luminosity is proportional to some power of the mass.

– When a star after the main sequence phase becomes a red giant, it evolves back toward low T_{eff}, it will actually settle down on a new Hayashi line according to the radiative core to convective envelope ratio.

20.2.2 Gravitational Energy Production and D Burning

During contraction, the rate of gravitational energy production is given by $\varepsilon_{\text{grav}} = -C_p \dot{T} + (\delta/\varrho)\dot{P}$ (Sect. 3.3.2). With $\nabla_{\text{ad}} = P\delta/(C_p \varrho T)$, this gives

$$\varepsilon_{\text{grav}} = C_p T \left(\nabla_{\text{ad}} \frac{\dot{P}}{P} - \frac{\dot{T}}{T} \right) . \tag{20.4}$$

From homology relations for stellar contraction (Sect. 3.4), we have $\dot{P}/P = -4\dot{R}/R$ and $\dot{\varrho}/\varrho = -3\dot{R}/R$ and with (3.86) we get

$$\varepsilon_{\text{grav}} = C_p T \left(-4\nabla_{\text{ad}} + \frac{4\alpha - 3}{\delta} \right) \frac{\dot{R}}{R} . \tag{20.5}$$

For a perfect and monatomic gas with $\alpha = 1$, $\delta = 1$, $C_P = c_p$ and $\nabla_{\text{ad}} = 2/5$, this is

$$\varepsilon_{\text{grav}} = -\frac{3}{5} c_p T \frac{\dot{R}}{R} . \tag{20.6}$$

Contraction ($\dot{R} < 0$) produces stellar energy. The energy production is not much concentrated near the stellar center, as for nuclear burning.

Figure 20.1 shows the pre-MS evolution at constant mass for 1 and 3 $M_\odot$ models. The Hayashi phase lasts about 2×10^7 yr for a 1 $M_\odot$ star and 10^6 yr for a 3 $M_\odot$ star. The radius decreases considerably during this phase, but the fusion of deuterium (noted D or ^{2}H) slows down the contraction. Figures 20.1 and 20.2 show that D early ignites on the Hayashi line for low-mass stars. D burning occurs at central temperature T_c between 1 and 2×10^6 K for stars from 1 to 60 $M_\odot$ (Table 20.1);
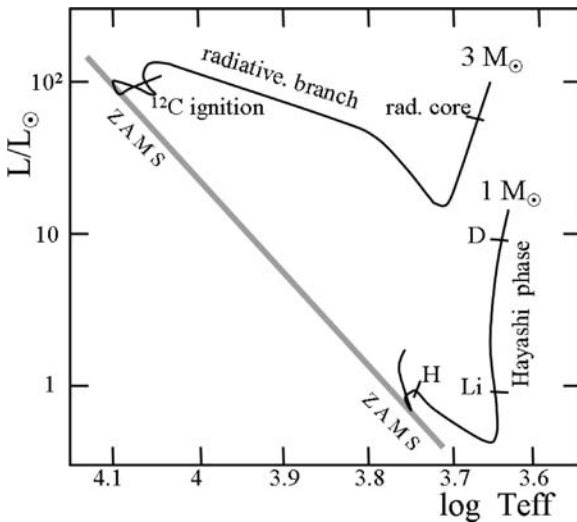
Fig. 20.1 Pre-MS evolutionary tracks for evolution at constant mass for 1.0 and 3.0 $M_\odot$. The places where the ignition of deuterium, lithium and hydrogen starts for the 1 $M_\odot$ model are indicated, as well as the ignition of deuterium and ^{12}C for the 3 $M_\odot$ model. Adapted from L. Siess [529]
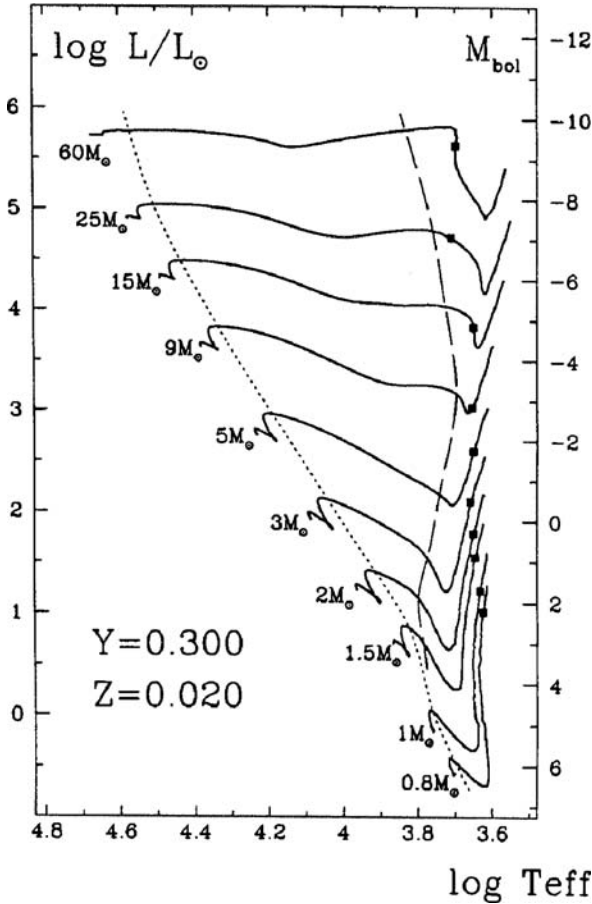
Fig. 20.2 Pre-MS tracks for evolution at constant mass. The squares on the tracks show the location of D ignition. The *long-broken line* represents the end of the convective envelope, *the dotted line* the appearance of convective cores (which rapidly disappear for lower masses). From P. Bernasconi and the author [44]

it starts at higher T in more massive stars because their average density is lower. D burning plays a great role during pre-MS evolution: by contributing to the luminosity, driving convection and inflating the stellar radius. The main reactions for deuterium burning are

$$D(p, \gamma)\,{}^3He \qquad D(D, p)\,{}^3H(, e^- v)\,{}^3He \qquad D(D, n)\,{}^3He. \qquad (20.7)$$
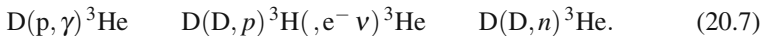
Table 20.1 The pre-MS lifetimes for constant mass evolution (t_{KH} is of the same order), its ratio to the H-burning phase and the temperature when 1% of the deuterium is burnt

Mass	$t_{\text{pre-MS}}$ in units of 10^6 yr	$\dfrac{t_{\text{pre-MS}}}{t_H}$	T(D burning) in units of 10^6 K
60	0.028	0.0082	1.93
15	0.117	0.0101	1.39
5	1.15	0.0122	1.17
2	23.4	0.0209	1.22
1.5	35.4	0.0131	1.16
1	38.9	0.0039	1.09
0.6	90.0*		1.09*
0.2	200.0*		0.85*

* Values from [548]

The first one is the most important by a factor 100 with respect to the other two at the relevant T; its energy generation rate is approximated by [456]

$$\varepsilon_D = 4.2 \times 10^7 \left[\frac{D}{H}\right] \left(\frac{\varrho}{1\,\text{g cm}^{-3}}\right) \left(\frac{T}{10^6\,\text{K}}\right)^n \text{erg g}^{-1}\text{s}^{-1}, \qquad (20.8)$$

with $n = 11.7$. $[D/H] = 2 \times 10^{-5}$ is the typical number ratio of hydrogen to deuterium. The high T sensitivity implies that during D burning the temperature does not change much and thus D burning has an efficient thermostatic effect, keeping T almost constant. The second and the third reactions are of nearly equal importance (they are often ignored in literature). In the stellar context, the β-disintegration of tritium can be regarded as instantaneous, since its half-lifetime is $t_{1/2} = 12.26$ yr, while the survival time of ^{2}H is much larger in pre-MS stars. D burning can contribute up to 90% of the stellar luminosity in pre-MS stars, the rest being produced by contraction. In low-M stars, D burning can nearly stop for a while the star contraction on the Hayashi line. After 3×10^5 yr, D is exhausted in a $1\,M_\odot$ model (10^5 yr for $3\,M_\odot$); the star continues its contraction down the Hayashi line. The importance of D burning is lower for higher masses, which are dominated by contraction. For $M > 4.5\,M_\odot$, D burning starts in regions which are already radiative due to the fast recession of the external convective zone, while below this mass limit it completely burns in the fully convective interior.

After D burning, nuclear burning of lithium occurs for $T > 2.5 \times 10^6$ K; the reaction is very sensitive to temperature (like T^{20}):

$$^7\text{Li} + ^1\text{H} \rightarrow ^4\text{He} + ^4\text{He} . \qquad (20.9)$$

Li burning occurs at smaller ages for larger masses: 10^9, 2.0×10^7, 1.4×10^6 and 2.4×10^5 yr for 0.06, 0.4, 1 and $3\,M_\odot$, respectively (Sect. 20.7). Beryllium Be burns for $T > 3.2 \times 10^6$ K and boron B for $T > 4 \times 10^6$ K. The minimum masses for Li, Be and B-burning are 0.055, 0.085 and $0.08\,M_\odot$ [106]. The fusion of these rare elements is not energetically significant; however they make the Li and Be abundances to change during pre-MS evolution. Thus, a high Li abundance is a distinctive signature of pre-MS stars (Sect. 20.7).

20.2.3 *From the Hayashi Line to the ZAMS*

Moving down on the Hayashi line, the star becomes more transparent, as H and He are ionized over a larger region. This reduces the radiative gradient ($\nabla_{rad} \sim \kappa L$) and convection disappears, first in the center, where a radiative core forms and then from almost the whole star. This produces an internal mass reorganization with steeper density gradients, corresponding to change of polytropic index n from 1.5–3 to 3–3.6. This transition occurs near the minimum of surface luminosity. The ages then are, respectively, 2×10^6 and 1.5×10^5 yr for 1 and $3\,M_\odot$.

Contraction is non-homologous, being faster in the center. A part of the released gravitational energy is used to expand the external layers, while the rest is radiated. Thus, the dip in luminosity is followed by a fast growth of the stellar radius and the luminosity. This effect is particularly visible for the higher mass models, where radiation pressure is large (Fig. 20.2). Convection completely disappears at the location indicated by a broken line. The star settles in the HR diagram on a slightly oblique long leftward ascending branch, which is the locus of radiative stars with a polytropic index $n \approx 3$. For masses lower than about $1.5\,M_\odot$, a proper radiative branch is absent, since these stars maintain a convective envelope during the whole contraction to the zero-age main sequence (ZAMS).

The start of H burning is preceded by a short phase of rather intense C-burning, during which carbon is brought to equilibrium (the cosmic C abundance is much larger than that of CNO equilibrium). Only a part of the CN cycle (Fig. 25.1) is operating at this stage, namely the reactions

$$^{12}C(p,\gamma)^{13}N(,\beta^+\nu)^{13}C(p,\gamma)^{14}N. \tag{20.10}$$
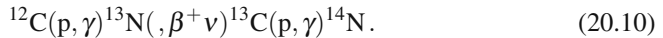
The above chain converts ^{12}C to ^{14}N and thus brings CN elements to equilibrium. The energy production rate ε by $^{12}C(p,\gamma)^{13}N$ goes like T^{19}, which favors the appearance of a convective core (the release of gravitational energy is also playing a role in massive stars). The resulting central expansion pumps energy and reduces L and T_{eff}; a knee on the tracks is resulting (Fig. 20.2). We may distinguish two mass domains:

– Stars with mass above about $1.3\,M_\odot$: when ^{12}C is brought to equilibrium, T is not yet high enough to make the full CN cycle operating. The core shrinks again and contraction operates until T is high enough. This produces a second knee in the tracks. Then, the growth of the central T allows the CNO cycle to operate.
– Below $1.3\,M_\odot$: the exhaustion of central ^{12}C makes the convective core to disappear; it is not revived by the pp chains, due to their low T-dependence, these chains stop contraction and the star sets on the ZAMS.

Various criteria have been proposed to fix precisely the time when a contracting star sets on the ZAMS, for example, the minimum stellar radius, the local maximum core radius, the minimum luminosity, a central H depletion of 1%. Some criteria cannot be applied to the whole range of masses. Moreover, they do not exactly coincide and thus do not lead to similar values for the pre-MS lifetimes. For example, the fourth criterion leads to much longer pre-MS lifetimes, in particular for very

massive stars. The first three generally give comparable values. It seems advisable to take the first one, because it is clearly defined. The pre-MS lifetimes from the top of the Hayashi line to the ZAMS are given in Table 20.1 with this definition. They are of the order of the Kelvin–Helmholtz timescale given by (20.2). They are very short for the most massive stars (i.e., of the order of a few 10^4 yr) due to their high luminosities.

20.3 Pre-MS Evolution with Mass Accretion

The above models assume that the whole stellar mass is already assembled at the end of the adiabatic phase. This is not necessarily the case. We shall thus examine the evolution of an initially small accreting core in hydrostatic equilibrium from the end of the adiabatic phase to the ZAMS. In many models [456], it is considered that stars are accreting at a constant rate $\dot{M}_{accr}$, typically of 10^{-5} $M_\odot$ yr^{-1} for solar-type stars. The accretion continues for some time, then the evolution proceeds at constant mass. At the end of accretion, the star experiences a period of relaxation and thermal re-adjustment and it joins a track very close to the track with its actual constant mass in the HR diagram. In some models, a transition period with decreasing mass accretion rates is considered (Sect. 20.7), but it does not make great changes.

20.3.1 The Birthline and Its Timescales

We define *the birthline* as the track described in the HR diagram by stars accreting mass at a "substantial rate". Since accretion stops when the star leaves the birthline, it is also in general the place where the star first becomes visible. What is a "substantial rate" of mass accretion? For solar-type stars, it is typically of the order of 10^{-5} $M_\odot$ yr^{-1} (Fig. 20.5). A more physical definition may be given: accretion dominates if $\dot{M}_{accr}$ is large enough so that

$$t_{accr} = \frac{M}{\dot{M}_{accr}} \ll t_{KH} = \frac{GM^2}{R^2 L} . \tag{20.11}$$

The star does not have the time to adjust thermally. Being not in thermal equilibrium, the star occupies a particular location in the HR diagram: the birthline, where evolution is dominated by accretion.

If the timescales are such that $t_{accr} \gg t_{KH}$, the star has the time to adjust thermally and the evolution proceeds in thermal equilibrium, i.e., the star is on the ZAMS. There is a continuous set of birthlines for different values of $\dot{M}_{accr}$ (Fig. 20.5). The birthline forms the upper envelope of the individual further tracks. (Some authors define the birthline as the equilibrium position of fully convective D-burning stars in the HR diagram.)

For stars with $M \leq 4.5\, M_\odot$ (a limit between 2.5 and $9\, M_\odot$ depending on authors) $t_{\mathrm{accr}} < t_{\mathrm{KH}}$ for the above current accretion rates. This is due to the relatively long Kelvin–Helmholtz timescale (20.1). For larger masses, we have the opposite: $t_{\mathrm{accr}} > t_{\mathrm{KH}}$. The thermal equilibrium is rapidly realized and, even if the accretion is not terminated, these stars generally lie on the ZAMS or close to it (Sect. 22.2).

20.3.2   The Luminosity from D Burning

The higher luminosities of stars on the birthline are mainly due to the nuclear D burning, which inflates the stellar radius and increases the luminosity. The higher the accretion rates, the larger the stellar radii and luminosities. Without accretion, D burning would only temporary slow down contraction. In the presence of accretion, the continuously infalling D is transported by convection toward the interior, where it burns at $T = 1\text{--}1.8 \times 10^6$ K.

Convective transport in pre-MS stars is fast, but it should not be treated as instantaneous (as is often made), since the timescale for nuclear burning in the interior becomes shorter than the turnover time. This transport establishes a D-gradient in the interior. To properly describe this gradient, it is necessary to use a time-dependent convective mixing, e.g., a diffusion process. The diffusion coefficient $D_{\mathrm{conv}} = \frac{1}{3} \ell_{\mathrm{conv}} v_{\mathrm{conv}}$, where v_{conv} is given by the mixing-length theory (Sect. 5.2). Typically D_{conv} is of the order of 10^{16} cm^2 s^{-1}. As a result of transport and D burning, a situation close to equilibrium is reached, where the stellar luminosity is about equal to the energy liberated by the burning of the accreted deuterium [456]:

$$L_{\mathrm{D}} \approx \left[\frac{D}{H} \right] X\, Q_{\mathrm{D}} \dot{M}_{\mathrm{accr}} \approx 20\, \frac{\dot{M}_{\mathrm{accr}}}{10^{-7}\, M_\odot\, \mathrm{yr}^{-1}}\, L_\odot , \qquad (20.12)$$

with $X = 0.70$ and the energy available per reaction $Q_{\mathrm{D}} = 5.5$ MeV (Table 25.1). Indeed, for stars up to $4\, M_\odot$ where convection disappears, L_{D} is generally slightly larger than the outgoing luminosity, since the energy from deuterium is also used for expansion and heating.

20.4   Evolution on the Birthline

Let us follow the evolution of an accreting star on the birthline with an accretion rate of $10^{-5}\, M_\odot$ yr^{-1}. The initial age is equal to about $(M / < \dot{M} >)$ for an average initial rate $< \dot{M} >$. Apart from this choice of the initial age, the evolution on the birthline is independent of the initial conditions.

Up to 1.2 $M_\odot$: for brown dwarfs and low-mass stars between 0.01 and $0.4\, M_\odot$, the luminosity is so low and the Kelvin–Helmholtz time so long that even the moderate thermostatic support of D burning maintains the star in equilibrium, making

a sort of deuterium main sequence. Low-mass stars are fully convective at the end of the adiabatic phase, as a result of the high opacity, up to a limit of 2.5 $M_\odot$. Due to D burning, for masses larger than about 0.2 $M_\odot$ the stellar radius of the accreting star grows almost linearly with the increasing stellar mass (Fig. 20.3) up to a mass of about 1.2 $M_\odot$. The reason is that the central stellar temperature behaves like $T_c \sim M/R$. As T_c is essentially constant during D burning, a linear relation between mass and radius is established.

From 1.2 to 2.5 $M_\odot$: if accretion goes on, the star on the birthline remains fully convective up to a mass limit of about 2.5 $M_\odot$. Above it, a radiative core develops; convection remains in an outer zone up to about 4–4.5 $M_\odot$. After the linear part ending at 1.2 $M_\odot$, the radius slightly declines as mass is growing up to about 2.5–3 $M_\odot$ (Figs. 20.3 and 20.4).

From 2.5 to 4 $M_\odot$: stars more massive than about 2.5 $M_\odot$ form an off-center radiative barrier, where D burns in shell and no longer reaches the stellar center, which has switched to radiative equilibrium and carries on with gravitational contraction. The increase of central T and the resulting increase of transparency favor the growth of the radiative core (Fig. 20.4).

Table 20.2 shows the main parameters for a star evolving on the birthline with $\dot{M}$ from $(1-2) \times 10^{-5}$ $M_\odot$ yr^{-1} [44]. The corresponding birthline is illustrated by a dotted line of 10^{-5} $M_\odot$ yr^{-1} in Fig. 20.5. The energy produced in the outer layers by D burning makes a luminosity L_D (20.12) larger than the outgoing luminosity (Fig. 20.7). This defines a mass limit of 4–4.5 $M_\odot$ up to which radiative equilibrium is not fast enough to dissipate the energy of D burning; this limit also corresponds to about the mass where convection disappears in the envelope.

The energy of D burning produces a fast stellar inflation with almost a doubling of the stellar radius as shown in Figs. 20.3 and 20.4. Of course, the larger the
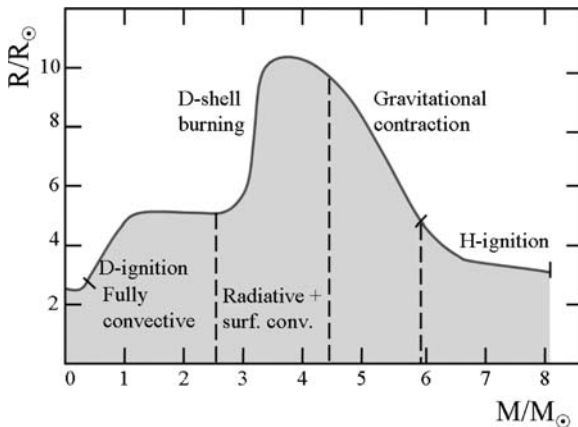
Fig. 20.3 Relation between the radius and mass of a star accreting at a rate $\dot{M}_{accr} = 10^{-5}$ $M_\odot$ yr^{-1}. Adapted from F. Palla and S.W. Stahler [456, 457]
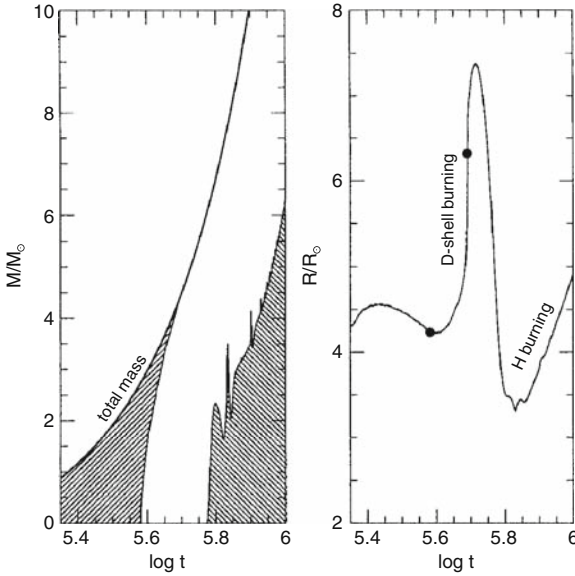
Fig. 20.4 *Left*: evolution of the convective zones (in *gray*) in a star with a growing mass. Initially the star is fully convective and then convection recedes from the center to finally disappear in the whole star. The star is then fully radiative and at higher masses a convective core appears. *Right*: corresponding evolution of the radius. From P. Bernasconi and the author [44]

Table 20.2 Properties of stars on the birthline at $Z = 0.02$ for accretion rates $(1 - 2) \times 10^{-5}$ M$_\odot$ yr^{-1}. The age, mass, luminosity, T_{eff}, radius and envelope mass fraction are given at various stages on the birthline. The slight variation of the mass loss rates is due to the account of the internal turbulent pressure in the cloud [44]

Age	$\dot{M}$	Mass	Log L	Log T_{eff}	R	M_{env}
yr	M$_\odot$ yr^{-1}	M$_\odot$	L$_\odot$	K	R$_\odot$	M_{env}/M
7.923×10^4	1.10×10^{-5}	0.801	0.731	3.632	4.223	1.000
8.826 10^4	1.11 10^{-5}	0.901	0.781	3.640	4.311	1.000
9.718 10^4	1.13 10^{-5}	1.000	0.813	3.647	4.331	1.000
1.192 10^5	1.16 10^{-5}	1.250	0.856	3.662	4.247	1.000
1.406 10^5	1.20 10^{-5}	1.500	0.875	3.673	4.126	1.000
1.815 10^5	1.26 10^{-5}	2.000	0.903	3.692	3.905	1.000
2.201 10^5	1.33 10^{-5}	2.500	0.922	3.708	3.708	0.750
2.568 10^5	1.40 10^{-5}	3.000	0.962	3.723	3.623	0.291
3.250 10^5	1.53 10^{-5}	4.001	1.236	3.760	4.189	0.022
3.875 10^5	1.66 10^{-5}	5.001	2.781	4.062	6.173	0.000
4.457 10^5	1.79 10^{-5}	6.006	3.238	4.278	3.864	0.000
4.994 10^5	1.92 10^{-5}	7.001	3.265	4.315	3.362	0.000
5.507 10^5	2.05 10^{-5}	8.013	3.468	4.365	3.374	0.000
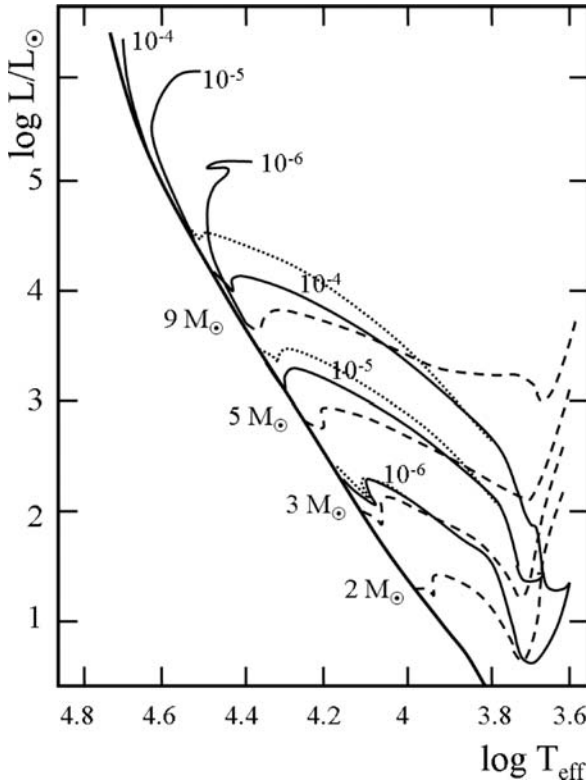
Fig. 20.5 The *dashed lines* show evolutionary tracks at constant mass (Fig. 20.2). The continuous lines show the birthlines for constant accretion rates $\dot{M}_{accr} = 10^{-6}, 10^{-5}, 10^{-4}$ M$_\odot$ yr^{-1}; these birthlines also extend to the *upper part* of the diagram in the MS stage. The *dotted lines* represent birthlines for accretion rates slightly growing with mass which may better fit observations for T Tauri stars (cf. Table 20.2; these three dotted birthlines correspond, respectively, to 0.1, 1.0 and 10.0 times the accretion rates considered in Table 20.2 and they start with accretion rates equal to $10^{-6}, 10^{-5}$ and 10^{-4} M$_\odot$ yr^{-1}, respectively. The *thick continuous line* is the ZAMS. Adapted from P. Norberg and the author [443]

accretion rate, the larger the radius inflation. From the expression of the central temperature as a function of mass and radius (1.26), one has $dR/R = dM/M - dT_c/T_c$. The temperature of the interior and of the D shell is not changing very much; thus the increase in the mass produces a corresponding fast increase in the radius. Thus, the birthline shows a steep increase in the luminosity in Fig. 20.8 due to the fact that the internal peak of luminosity has radiatively diffused toward the stellar surface. The phase of shell D burning, which inflates the radius, also delays the role of gravitational contraction as the main energy source.

Above 4 M$_\odot$: the radiated luminosity becomes greater than the accretion luminosity, i.e.

$$L_{\text{rad}} > \frac{GM\dot{M}}{R} \quad \Rightarrow \quad \frac{M}{\dot{M}} > \frac{GM^2}{L_{\text{rad}}R}, \qquad \text{i.e., } t_{\text{accr}} > t_{\text{KH}}. \qquad (20.13)$$

Thus, thermal relaxation intervenes fast enough and thermal equilibrium is achieved. Accretion may still proceed, but the rate of thermal adjustment is in general faster and the stars move toward the ZAMS. Evidently, the various mass limits depend very much on the accretion rates; those given here correspond to rates of the order of $10^{-5}\,M_\odot\,\text{yr}^{-1}$.

The end of the radius inflation for a star on the birthline occurs for masses of about $4.5\,M_\odot$; the convective envelope disappears at the same stage (cf. Fig. 20.4) and the star becomes fully radiative. The accretion still brings deuterium, but it stays at the stellar surface and escapes destruction. Thus, D has no effect anymore on the birthline and the energy only comes from contraction. The accreting star is fully radiative between about 4.5 and $6\,M_\odot$. It contracts slowly and this brings the accreting star on the ZAMS in the HR diagram (Fig. 20.5). There the CN cycle comes to equilibrium first (Sect. 20.2) and then hydrogen ignition occurs.

Higher accretion rates produce higher birthlines (Fig. 20.5). The accreting star effectively reaches the ZAMS near 4, 8 or $12\,M_\odot$ for constant accretion rate of 10^{-6}, 10^{-5} or $10^{-4}\,M_\odot\,\text{yr}^{-1}$, respectively. If the star continues to accrete mass when it has reached the ZAMS, it will move upward along the ZAMS since it is in thermal equilibrium due to the short Kelvin–Helmholtz timescale. Then, as H burning proceeds, the star starts moving leftward in the HR diagram at the nuclear timescale.

The birthline is an upper envelope (Fig. 20.8) of stellar tracks which leave the birthline and then evolve at constant mass. This can be shown easily. For radiative stars, one has the homology relation (Sect. 24.3)

$$\text{on the birthline :} \quad L \sim R^{-1/2} M^{11/2} \qquad (20.14)$$
$$\text{at constant mass :} \quad L \sim R^{-1/2}.$$

Thus, a star on the birthline with a growing mass becomes more luminous than a star which keeps its mass constant after leaving the birthline. Higher accretion rates shift the radius vs. mass relation toward higher radius for a given mass. Figure 20.5 also shows that growing accretion rates produce, for the same reasons, slightly steeper birthlines.

Comparisons of birthlines with various accretion rates and observations of Ae/Be Herbig and T Tauri stars are shown in Fig. 20.6. As the birthline is the upper envelope of pre-MS stars in the HR diagram, we see that in the range of 2–8 $M_\odot$ the rates should likely be about 1–3 times the rates of Table 20.2, i.e., of the order of 1–$6 \times 10^{-5}\,M_\odot\,\text{yr}^{-1}$. The comparison of birthlines and observations of pre-MS stars in the HR diagram may provide an indication of the accretion rates $\dot{M}_{\text{accr}}$, which is the leading parameter for pre-MS evolution.
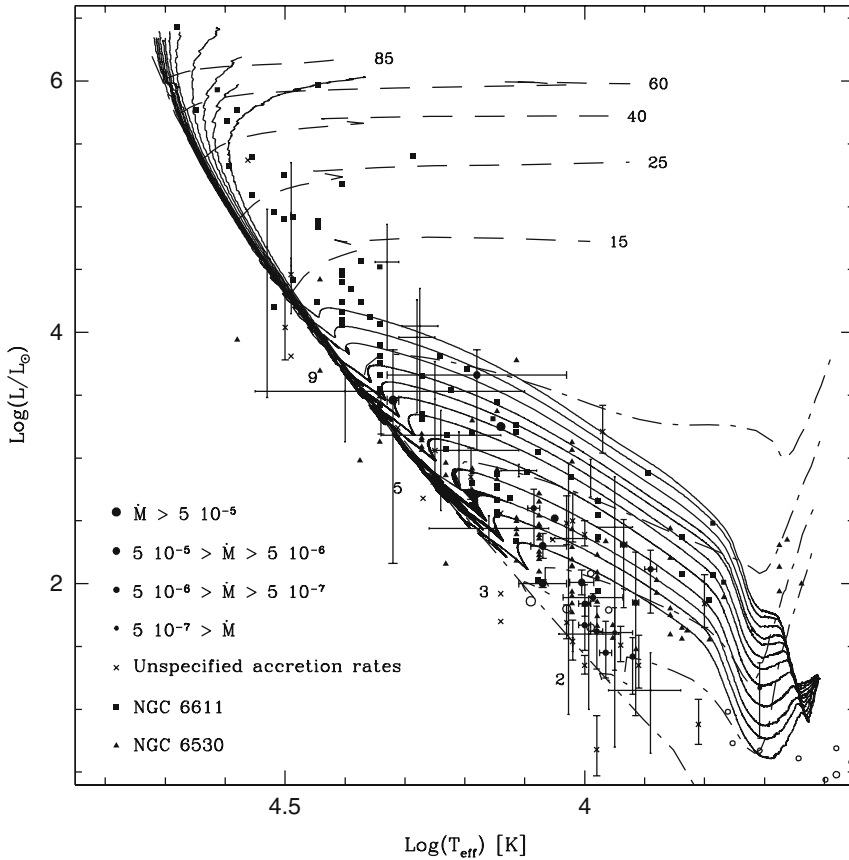
Fig. 20.6 Comparison of various birthlines with accretion rates equal from bottom to top to 0.1, 0.15, 0.2, 0.3, 0.5, 0.75, 1.0, 1.25, 1.75, 2.5, 3.5 and 5.0, the case illustrated by the data of Table 20.2. Pre-MS tracks at constant mass are indicated by *dot-dashed lines* and post-MS tracks of high masses by *dashed lines*. Numbers indicate the stellar masses. The observations are Ae/Be Herbig and T Tauri stars with different values of $\dot{M}_{accr}$ and sources. From P. Norberg and the author [443]

20.5   Evolution from the Birthline to the ZAMS

At some stage, accretion comes to an end or becomes negligible, because for example the cloud fragment has delivered most of its mass to the central body. When this occurs, maybe after some transition with a decreasing accretion rate, the stars leave the birthline. They follow tracks which finally join the track of the same constant mass (after some re-adjustments of the internal thermal equilibrium if it is not yet achieved, i.e., for $M \leq 4\,M_\odot$). Figure 20.8 shows a grid of star models of different final masses. During the first part of their evolution, the stars are accreting with rates of about $10^{-5}\,M_\odot\,yr^{-1}$ and they are on the birthline (Table 20.2). When accretion stops, they leave the birthline on a track with a lower luminosity as shown above.
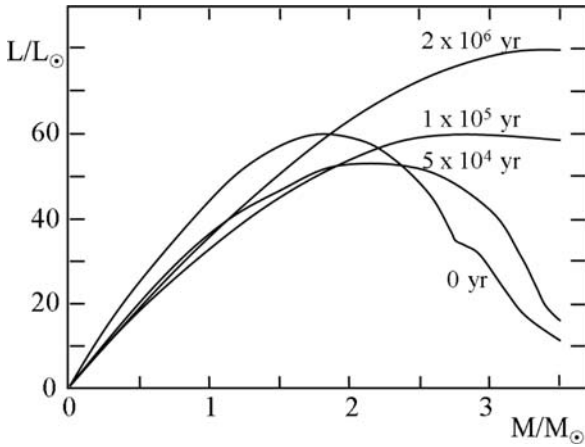
Fig. 20.7 Evolution of the internal luminosity of a $3.5\,M_\odot$ star after it has left the birthline. The time is counted since the birthline. There is an outward shift of the luminosity peak as the star tends to thermal equilibrium. During these phases, the surface luminosity grows strongly. Adapted from F. Palla and S.W. Stahler [456]

Stars of different masses leave the birthline in a different way. Stars with $M < 2.3$ $M_\odot$, which are fully convective, leave the birthline descending vertically on the Hayashi line (Fig. 20.8), because they burn fast the deuterium present, which is no longer replenished after the star has left the birthline. Contraction provides the main energy source and the stellar radius declines. A radiative core appears a little before the star reaches its minimum luminosity. Convection recedes toward the surface and the star settles on a radiative track. A convective envelope only remains in stars with $M < 1.5\,M_\odot$. After the minimum luminosity, the rise in brightness is very steep due to the readjustment of the internal L profile: the maximum which was deep in the star radiatively diffuses toward the surface (Fig. 20.7). For stars with $M \geq 1.2\,M_\odot$, CN burning starts slightly before the ZAMS and brings CN elements to their equilibrium values. Finally, H burning starts via the pp chains ($M \leq 1.2\,M_\odot$) or via the CNO cycle ($M > 1.2\,M_\odot$).

When they leave the birthline, stars with mass between 2.5 and $4\,M_\odot$ have a radiative core which grows until the star is fully radiative. Thus, these stars have no Hayashi phase: when they become visible, their $T_{\rm eff}$ are much higher than for evolution at constant mass: a $5\,M_\odot$ star appears with a $T_{\rm eff} \simeq 11500$ K (Fig. 20.8) instead of 4000 K at constant mass. The tracks show first a steep increase in luminosity, rather similar to that occurring for stars on the birthline for the above reasons. Non-homologous contraction supplies most of the energy: the interior, deprived of other energy source, contracts, while the outer layers expand due to the shift of the luminosity maximum toward the surface. The stars then join the tracks with constant mass and follow about the same evolution. A convective core forms when CN burning starts before the ZAMS.
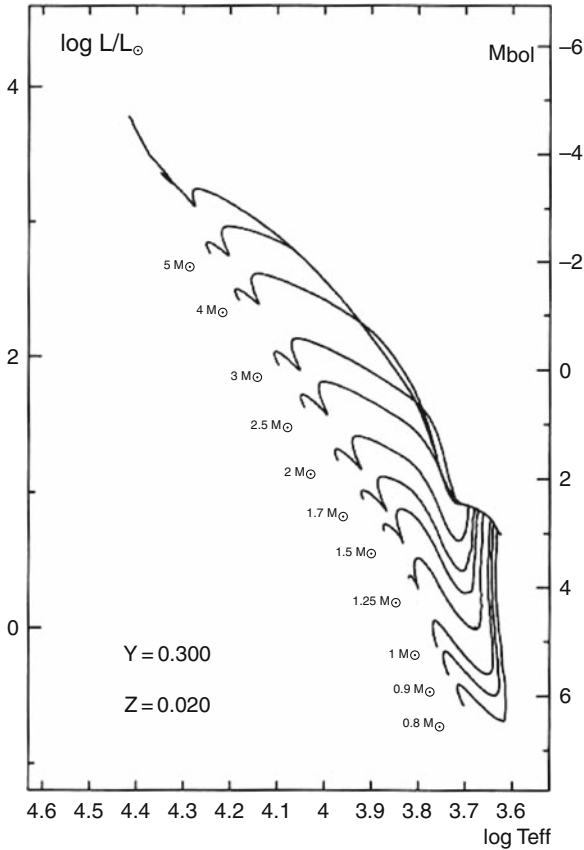
Fig. 20.8 Pre-MS tracks at solar composition with accretion from a cloud with thermal and turbulent support (cf. Table 20.2). The stellar masses on the ZAMS are indicated. The birthline is indicated by a thick line which forms the upper envelope of the various tracks. From Bernasconi [43]

Stars with mass above about $4.5\,M_\odot$ are fully radiative when they leave the birthline and they adjust rapidly on the corresponding tracks with constant mass, following the above $L \sim R^{-1/2}$ relation. The part of the radiative track, where they are observable, is short (Fig. 20.8).

Stars with mass above $\sim 6\,M_\odot$ already have a convective core when they leave the birthline. They contract for a short time before the ignition of the CNO cycle; then contraction stops. Stars with $M \geq 8\,M_\odot$ are studied in Chap. 22.

In the above accretion scenario, when they become visible the stars generally have smaller radii and luminosities (by a factor of about 10 and 100, respectively) than if they would appear at the top of the Hayashi line (Sect. 19.4). Compared to the tracks at constant mass of Fig. 20.2, the visible part of the tracks with accretion covers a much smaller area of the HR diagram, since stars on the birthline are still

embedded in their parent material. The comparison (Fig. 20.6) of the birthline and observations of T Tauri stars and Ae/Be Herbig stars supports the above scenario.

The various mass limits given above depend on metallicity Z and accretion rates. As an example, at $Z = 0.001$ the core remains fully convective up to a mass of $2\,M_\odot$ instead of $2.5\,M_\odot$. The convective envelope disappears at about $3.1\,M_\odot$ instead of about $4.5\,M_\odot$; the star joins the ZAMS near $6.5\,M_\odot$ instead of $7.5\,M_\odot$. There is a global shift of the domain to lower masses at lower Z, because due to lower opacities the stars are brighter and hotter; they behave like slightly more massive stars with solar Z.

20.6   Lifetimes, Ages and Isochrones

There are various possible definitions of the ages of T Tauri stars ($\leq 2\,M_\odot$), of Ae/Be stars ($\geq 2\,M_\odot$) and forming stars.

– We may define the zero age when the stars first become optically visible, i.e., when the phase of heavy accretion is over and the star leaves the birthline. Let us call $t_{\text{pre-MS}}$ the age defined in this way. This is often the age definition in the context of accretion models [456].
– Another possibility is to define an age t_{form} as the lifetime since the end of the isothermal collapse, i.e., from the starting point in Fig. 19.5. Such models are in their infancy and such ages are rarely available. The total formation time t_{form} could be estimated as the sum of the initial accretion time $t_{\text{ini.accr}} = M_{\text{ini}}/ < \dot{M}_{\text{ini.accr}} >$, where M_{ini} is the mass at the beginning of the birthline phase (typically a few tens of $M_\odot$) and $< \dot{M}_{\text{ini.accr}} >$ an appropriate average of the initial accretion rates, plus the time t_{birthl} spent on the birthline, plus the age $t_{\text{pre-MS}}$ after the birthline:

$$t_{\text{form}} = \frac{M_{\text{ini}}}{< \dot{M}_{\text{ini.accr}} >} + t_{\text{birthl}} + t_{\text{pre-MS}} \cdot \tag{20.15}$$

– In general for MS stars and post-MS stars, the ages are counted since the ZAMS. The relative error is small since the formation time is of the order of 1% of the H-burning lifetime.

Table 20.3 compares these to the lifetimes t_{classic} of models with constant mass (Sect. 20.2). Below $2\,M_\odot$, t_{form} and $t_{\text{pre-MS}}$ are nearly identical, since the pre-MS phase starts nearly on the Hayashi line. For larger masses more time is spent on the birthline and thus the pre-MS phase is shorter. For stars with mass close to $7\,M_\odot$, $t_{\text{pre-MS}}$ tends toward zero, since there the birthline joins the ZAMS. The differences of t_{form} and $t_{\text{pre-MS}}$ with respect to t_{classic} are also small up to about $1.2\,M_\odot$, since in both scenarios the stars have a long way to reach the ZAMS.

It is striking that above about $1.5\,M_\odot$ (and up to about $7\,M_\odot$) the total formation time t_{form} in the accretion scenario is shorter than the classical time. This is surprising at first, because during a part of its evolution on the birthline the accreting

Table 20.3 The lifetimes t_{form} and $t_{\text{pre-MS}}$ up to the ZAMS for the models with the accretion rates of Table 20.2 compared to the lifetime t_{classic} of models at constant mass (Sect. 20.2). An average rate $< \dot{M}_{\text{ini.accr}} >= 10^{-5}$ M$_\odot$ yr^{-1} is assumed before the birthline. The columns give the final masses, the total lifetimes t_{form}, the pre-MS lifetimes $t_{\text{pre-MS}}$ and the ratios with respect to the classic timescales of models at constant mass

Final mass M$_\odot$	t_{form} yr	$t_{\text{pre-MS}}$ yr	$\dfrac{t_{\text{form}}}{t_{\text{classic}}}$	$\dfrac{t_{\text{pre-MS}}}{t_{\text{classic}}}$
0.8	7.154×10^7	7.147×10^7	1.045	1.044
1.0	3.821×10^7	3.805×10^7	0.982	0.978
1.5	3.095×10^7	3.081×10^7	0.874	0.870
2.0	1.172×10^7	1.153×10^7	0.501	0.493
3.0	2.683×10^6	2.423×10^6	0.371	0.335
4.0	1.414×10^6	0.881×10^6	0.557	0.347
5.0	0.799×10^6	0.412×10^6	0.694	0.358

star has a lower luminosity than for constant mass evolution. However, it is a general property [529] that accreting stars have a higher central temperature and are younger than non-accreting stars. An accreting star goes through a succession of structures, which are more non-homologous than in the case of constant mass, i.e., contraction is faster in the center, where T becomes higher (the star is younger at the same central T). Also, not all the deuterium is burnt in the accretion scheme, while it is exhausted in the case of constant mass, which are fully convective initially and this makes more energy available. For $M > 7$ M$_\odot$, the ratio $t_{\text{form}}/t_{\text{classic}}$ very much depends on the accretion rates (Sect. 22.2).
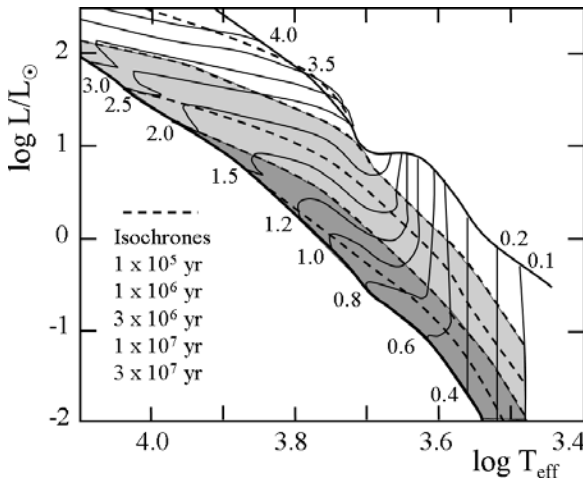
Fig. 20.9 Isochrones of various ages for pre-MS models with constant accretion rates of 10^{-5} M$_\odot$ yr^{-1}. Light gray shading shows the location of stars between 10^6 and 10^7 yr; dark area is for stars above 10^7 yr. The ages indicated here are $t_{\text{pre-MS}}$ (from the birthline). Adapted from S.W. Stahler and F. Palla [548]

Figure 20.9 provides an example of isochrones with various pre-MS ages $t_{\text{pre-MS}}$ from 10^5 to 3×10^7 yr. A few properties may be quoted:

- The smaller the $t_{\text{pre-MS}}$, the farther the isochrone from the ZAMS.
- Isochrones with larger $t_{\text{pre-MS}}$ reach the ZAMS at lower luminosities.
- For the age estimates, the values derived from accretion tracks are a factor of about 2–3 smaller for ages lower than 5×10^5 yr (with respect to tracks at constant mass), while above 10^6 yr the differences are negligible.

The comparison of HR diagrams of very young clusters and isochrones gives some insight into their history of star formation. However, the results are valid only if the models correspond well to the reality.

20.7   Lithium Depletion in Pre-MS Stars

Light elements are fragile. If the models have an external convective zone which extends deep enough to reach $T = 2.5 \times 10^6$ K, the abundance of ^{7}Li at the stellar surface starts decreasing. The surface abundance of lithium depends critically on the depth of the external convective zone. The initial abundance of lithium is very low; the number ratio $N(\text{Li})/N(\text{H})$ is 1.3×10^{-9} in the interstellar medium, i.e., $\log N(\text{Li}) = 3.1$ in a scale where $\log N(\text{H}) = 12.0$. In the Sun, the lithium abundance is about a factor 10^2 lower than in the interstellar medium, being $\log N(\text{Li}) = 1.1$. Lithium is observable, thanks to a faint line Li I 6708 Å, which allows lithium abundances to provide a test on the model structure for both pre-MS and MS stars.

20.7.1   Model Predictions

Pre-MS stars start contracting with a central T lower than 2.5×10^6 K; thus there is no Li depletion at the beginning of the birthline for all masses. Surface depletion appears during pre-MS evolution for $M < 1.2\ \text{M}_\odot$ when they reach the dip in luminosity at the bottom of their descending tracks. There, contraction makes the internal T high enough to destroy lithium. This is about the stage where a radiative core develops at the stellar center for $M > 0.4\ \text{M}_\odot$. If the bottom of the receding convective zone is above the critical level for Li burning, the surface abundance of lithium is not affected. This happens in stars with masses (on the ZAMS) above $1.2\ \text{M}_\odot$, while in stars with $M < 0.8 - 0.9\ \text{M}_\odot$, the external convective zone is deep enough to largely destroy lithium before the star reaches the ZAMS (Fig. 20.10).

For $1\ \text{M}_\odot$, after a fast depletion by ~ 10, there is a kind of a plateau (Fig. 20.10). The Li depletion goes on slowly during the whole MS phase due to internal mixing, so that the total decrease with respect to the initial Li abundance reaches a factor of 100 at the solar age. For the $0.8\ \text{M}_\odot$, the initial fast destruction is larger due to a deeper convective zone; it also reaches a plateau. For $0.6\ \text{M}_\odot$, the destruction
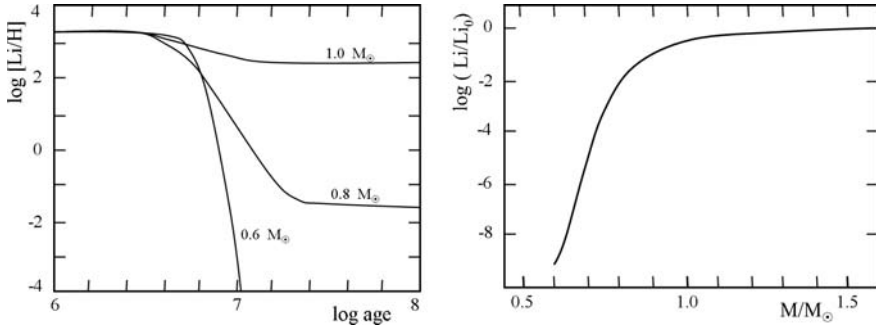
Fig. 20.10 *Left*: the evolution of the ^{7}Li abundance as a function of log (age) for different masses. The Li abundance is expressed as a number ratio with respect to hydrogen. The value of log H in the Sun is 12.0. The initial value adopted for the number ratio $N(\text{Li})/N(\text{H})$ is 2×10^{-9}. Adapted from L.T.S. Mendes, F. D'Antona and I. Mazzitelli [397]. *Right*: the abundance of lithium ^{7}Li as a function of stellar masses on the ZAMS relatively to the initial abundance Li$_0$. Adapted from L. Siess [529]

is complete in about 10^7 yr. The Li depletion becomes larger as the pre-MS stars approach the ZAMS. Figure 20.11 shows the region of the HR diagram of solar and lower mass stars where lithium depletion is expected from theoretical models [548]; this provides a test about the depth of the outer convective zone in pre-MS models.

Deuterium, more fragile than Li, is destroyed in stars below about $1.2\,M_\odot$ during their initial fully convective phase, while above that limit, due to the absence of a
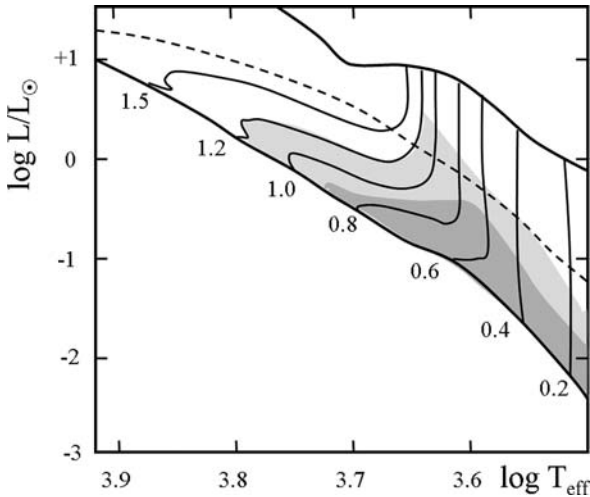
Fig. 20.11 Pre-MS evolutionary tracks for various stellar masses in $M_\odot$. The *upper and lower thick lines* are, respectively, the birthline and the ZAMS; the *broken line* is an isochrone of 10^6 yr. In the *white area* between the *two thick lines*, there is no Li depletion; in the *light shaded area*, the depletion is down to 10% of the initial value; in the *dark shaded area* depletion is between 10% of the initial value and complete depletion. Adapted from S.W. Stahler and F. Palla [548]

deep convective zone, deuterium keeps its initial abundance in case of accretion. The depth of the external convective zone is very sensitive to the physical inputs of the models, such as metallicity, opacity, convection, overshooting, rotation, extra mixing and residual accretion. Stars with a higher metallicity Z have a stronger Li depletion, because the opacity is higher and thus their external convective regions are deeper. Conversely lower Z stars have less Li depletion.

20.7.2   *Li and D in T Tauri Stars and Residual Accretion*

A residual accretion rate $\dot{M}_{accr}$ during the pre-MS phase affects the tracks in the HR diagram and the Li abundances; however for $\dot{M}_{accr} < 10^{-7} M_\odot \, \text{yr}^{-1}$ there is little effect for solar-type stars. Figure 20.12 compares three different cases of evolution of mass accretion with time [529], all starting from $0.5 \, M_\odot$ and finishing with $1.2 \, M_\odot$ to a case of constant mass evolution with $1.2 \, M_\odot$. The higher the initial accretion, the earlier the accreting star joins the track of constant mass. In the two cases where the initial accretion is not negligible, the accretion produces a small increase in stellar radius, before contraction takes over. The higher the initial accretion, the earlier the formation of a radiative core. The mass and age estimates from the location in the HR diagram are little affected by residual accretion.

The abundances of Li and D offer tests whether there is a continuing accretion during the pre-MS phase. Above $1.5 \, M_\odot$, no differences in the Li abundances are expected. Around $1 \, M_\odot$, surprisingly the abundance of Li is *decreased* by a factor of 4 in models with a residual accretion, due to the faster increase of the central T in accreting models, because of a more efficient contraction [529]. The best signature of late accretion (after the birthline) would be the presence of D on stars more massive than $1.2 \, M_\odot$ (but below about $4 \, M_\odot$, since these stars have no or only a very thin convective zone, cf. Fig. 20.4, and T is below 10^6 K so that D is not destroyed). Below $1.2 \, M_\odot$, D is anyway completely destroyed in convective envelopes.

Observations of lithium in T Tauri stars also provide [380] interesting constraints on models. For $L \geq 0.9 \, L_\odot$, the mean observed value of Li abundance is in agreement with the cosmic value of $\log N(\text{Li}) = 3.1$, with a marginal trend to have less depletion than predicted. For masses lower than the Sun, models tend to predict too much lithium depletion.

On the whole, it is still uncertain whether there is a significant pre-MS accretion after the birthline, either in the form of continuous matter infall or as Jupiter-like objects [612]. Li depletion in pre-MS stars seems related to rotation, in the sense that fast rotators near $1 \, M_\odot$ generally show less Li depletion than slow rotators. This might be an effect of rotation on the limit of the convective zone (Solberg–Hoiland criterion, Sect. 6.4.3).
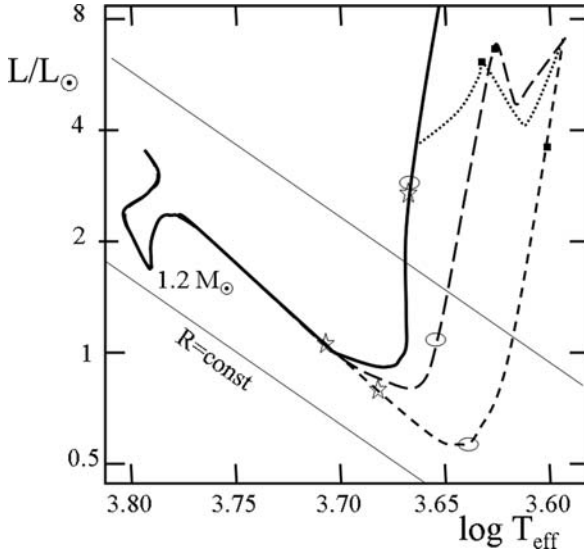
Fig. 20.12 The continuous *thick line* shows a pre-MS evolution for a constant $1.2\,M_\odot$ star. The three other tracks start at the top of the Hayashi line with $M = 0.5\,M_\odot$. The *dotted line* shows a fast initial accretion; the star reaching its final mass in 10^6 yr. The *long-broken* track is for a decreasing accretion rate. The *short-broken line* shows the track for a negligible accretion until 10^6 yr and a large after that. The *black squares* indicate the return to radius contraction as the main energy source, after some expansion due to D burning. The ellipses mark the beginning of a radiative core; this is about the point where Li is burning. The *stars* indicate the end of accretion. At point marked $1.2\,M_\odot$, the star reaches the ZAMS. Loci of constant radius are indicated. Adapted from Siess [529]

20.7.3 Li Depletion in Low-Mass Stars and Brown Dwarfs

The fact that the low-mass stars with masses $\leq 0.5\,M_\odot$ keep a constant $T_{\rm eff}$ during their descending tracks in the HR diagram (Fig. 20.11) leads to interesting developments [46] allowing us to obtain the radius, age and luminosity as a function of Li depletion. These stars are fully convective during Li burning; thus they have a polytropic structure of index $n = 1.5$ (Sect. 24.5). For such a structure the central density ϱ_c is proportional to the average density; as usual the central T behaves like GM/R (1.26); numerically

$$\varrho_c = 8.44 \left(\frac{M}{M_\odot}\right)\left(\frac{R_\odot}{R}\right)^3 {\rm g\,cm}^{-3}\,, \qquad (20.16)$$

$$T_c = 7.41 \times 10^6 \left(\frac{\mu_{\rm eff}}{0.6}\right)\left(\frac{M}{M_\odot}\right)\left(\frac{R_\odot}{R}\right) {\rm K}\,, \qquad (20.17)$$

where $\mu_{\rm eff} \leq \mu$, because partial degeneracy produces free electrons and thus the effective mean molecular weight is lower than that for perfect gas (however, for

simplification here we take $\mu_{\mathrm{eff}} \approx \mu$). Except during the initial D burning, gravitational contraction powers the stellar luminosity; thus by deriving the potential energy of the polytrope with $n = 3/2$ (Sect. 24.5) with respect to radius R and remembering that half of the change of potential energy is radiated, one gets

$$L = 4\pi R^2 \sigma T_{\mathrm{eff}}^4 = -\frac{3}{7}\frac{GM^2}{R^2}\frac{dR}{dt} . \tag{20.18}$$

We may integrate this equation from $t = 0$ with $R = \infty$ to the present radius R at time t. This time differs from the time $t_{\mathrm{pre\text{-}MS}}$ counted since the star has left the birthline. However, in low-mass stars, Li depletion occurs long after (≥ 10 Myr) the birthline; thus the times t_{form} and t_{preMS} are not too different (Table 20.3). One has

$$R = \left(\frac{3G}{28\pi\sigma}\right)^{\frac{1}{3}}\frac{M^{\frac{2}{3}}}{T_{\mathrm{eff}}^{\frac{4}{3}}}\frac{1}{t^{\frac{1}{3}}} , \tag{20.19}$$

numerically [46]

$$\frac{R}{R_\odot} = 0.850\left(\frac{M}{0.1\,M_\odot}\right)^{\frac{2}{3}}\left(\frac{3000\,\mathrm{K}}{T_{\mathrm{eff}}}\right)^{\frac{4}{3}}\left(\frac{10^6\,\mathrm{yr}}{t}\right)^{\frac{1}{3}} . \tag{20.20}$$

Equation (20.18) can be integrated keeping L constant; one has with (20.19)

$$L = \frac{3}{7}\frac{GM^2}{R}\frac{1}{t} = \left(\frac{3}{7}\right)^{\frac{2}{3}}(4\pi\sigma G^2)^{\frac{1}{3}}M^{\frac{4}{3}}T_{\mathrm{eff}}^{\frac{4}{3}}t^{-\frac{2}{3}} . \tag{20.21}$$

Numerically

$$\frac{L}{L_\odot} = 5.25 \times 10^{-2}\left(\frac{M}{0.1\,M_\odot}\right)^{\frac{4}{3}}\left(\frac{T_{\mathrm{eff}}}{3000\,\mathrm{K}}\right)^{\frac{4}{3}}\left(\frac{10^6\,\mathrm{yr}}{t}\right)^{\frac{2}{3}} . \tag{20.22}$$

These equations show how R and L decrease with time when the star goes down the Hayashi track. The lithium depletion can be considered as achieved when the timescale t_{Li} for the nuclear destruction of lithium (cf. 9.9) by $^7\mathrm{Li}(\mathrm{p},\alpha)^4\mathrm{He}$ is equal to the characteristic time t_{contr} of the star contraction:

$$t_{\mathrm{Li}} = \frac{\mu m_{\mathrm{u}}}{X\varrho <\sigma v>_{\mathrm{p,Li}}} \quad \mathrm{and} \quad t_{\mathrm{contr}} = -\frac{R}{dR/dt} , \tag{20.23}$$

where X is the H mass fraction. The equality of these two times gives a relation between the central temperature T_{c} and (M, T_{eff}) the time of depletion. One may eliminate T_{c} by (20.17) and obtain the dependence of the radius at the depletion time $R_{\mathrm{depl}} \sim T_{\mathrm{eff}}^{-1/6} M^{7/8} \mu^{3/4}$ (Fig. 20.13), as well as the scaling of the Li depletion time [46]:

$$t_{\mathrm{Li}} \sim T_{\mathrm{eff}}^{-7/2} M^{-5/8} . \tag{20.24}$$
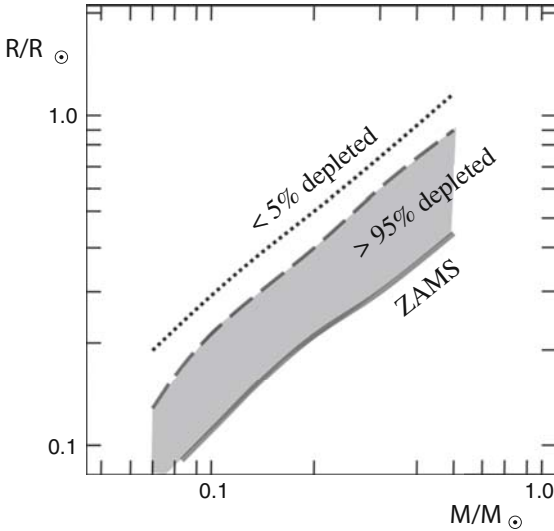
Fig. 20.13 Lines of constant Li depletion as a function of radius and mass. The lines of 5 and 95% depletion are shown. Adapted from L. Bildsten et al. [46]

The age is 50 Myr for 0.1 $M_\odot$, $T_{eff} = 3000$ K, $\mu = 0.6$ and a depletion factor of 2 (Fig. 20.14). Expression (20.24) applies to fully convective stars when degeneracy is unimportant (from 0.2 to 0.5 $M_\odot$). Degeneracy introduces correction terms in this equation [46], but the behavior is about the same: $t_{Li} \sim T_{eff}^{-3.51} M^{-0.715}$. If T_{eff} can be estimated and mass inferred from a grid of models, the observation of Li depletion provides with (20.24) or Fig. 20.15 an age estimate for clusters with an accuracy better than 25%.

The lithium abundance is also a constraint on the models. In Fig. 20.13, models predict that at a given mass, a contracting star above a certain radius limit should show no or little Li depletion. Below another limit, Li should be depleted. The two lines are close to each other, because of the high T-sensitivity of the Li-burning reaction. Since Li burns at a nearly constant T, the relation $T_c \sim M/R$ (20.17) imposes that the radii at these limits behave almost linearly with masses. The depletion times as a function of stellar masses are shown in Fig. 20.14 [105]. The two lines for depletion by factors 2 and 100 are close to each other for the same reasons as above. The lowest mass for Li burning is 0.06 $M_\odot$ at solar composition. For masses larger than this minimum mass, the depletion time decreases fast.

20.7.4 Li Dating from Brown Dwarfs and Low-M Stars

In very low mass stars and brown dwarfs, Li depletion takes a long time to be established, despite the fact that the stars are fully convective all the way. A radiative core appears in the course of pre-MS evolution only for $M > 0.4$ $M_\odot$. Figure 20.15
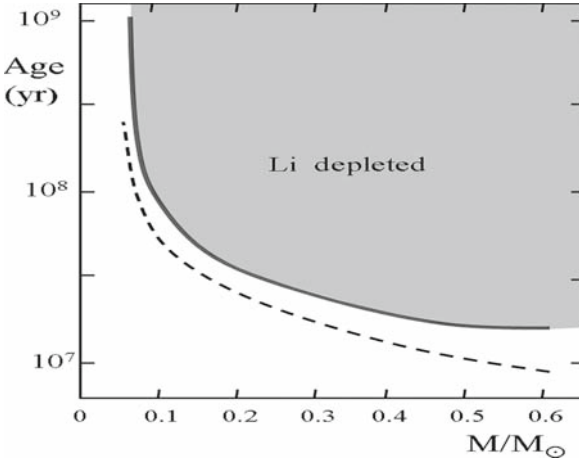
Fig. 20.14 The age of Li depletion as a function of stellar masses. The continuous *curve* corresponds to a depletion by a factor of 100, the *broken line* to a depletion by a factor of 2. Adapted from G. Chabrier, I. Baraffe and B. Plez [105]

provides a lithium diagnostic diagram for stars close to the brown dwarf limit [37]. The luminosities decrease with age as discussed above. The region of masses and ages of complete Li depletion is indicated (shaded area). For stars with masses and ages lower than this limit, there is not enough time for depletion.

If the luminosity L of the transition from depleted to unaltered Li can be determined observationally in a star cluster, an estimate of the cluster age is possible as well as of the mass where the transition occurs. The age estimate can also be expressed analytically. In the range of 0.2–$0.5\,M_\odot$, one can write (from 20.22) the stellar mass as a function of age and of L and T_{eff}. Putting this expression of the mass in (20.24), one obtains the time t_{Li} at which a star with parameters L and T_{eff} is depleted to a certain level $\ln(X_0/X)_{\text{Li}}$, where X_0 and X are, respectively, the initial and present Li abundances. The method has been successfully applied for stars close to the brown dwarfs limit (Fig. 20.15). There, degeneracy effects intervene and the depletion time becomes insensitive to T_{eff}, which is a great advantage since T_{eff} estimates for such stars are uncertain. The time t_{Li} behaves as [46]

$$t_{\text{Li}} = 58.3 \left(\frac{10^{-2.5} L_\odot}{L} \right)^{0.922} \left(\frac{0.6}{\mu} \right)^{2.52} \left(\frac{\ln(\frac{X_0}{X})_{\text{Li}}}{\ln 2} \right)^{0.0769} \text{Myr} . \quad (20.25)$$

The above expression, which applies in the interval $-3.50 < \log(L/L_\odot) < -2.32$, gives age estimates in agreement with numerical models (Fig. 20.15). The above method of "lithium dating", based on either numerical or analytical methods, has been applied [37, 46] to some very low mass stars and brown dwarfs in the Pleiades where there is no evidence of Li lines anymore. The Li dating implies an age of the Pleiades of about 120 Myr [77], which is 30% longer than the age derived from
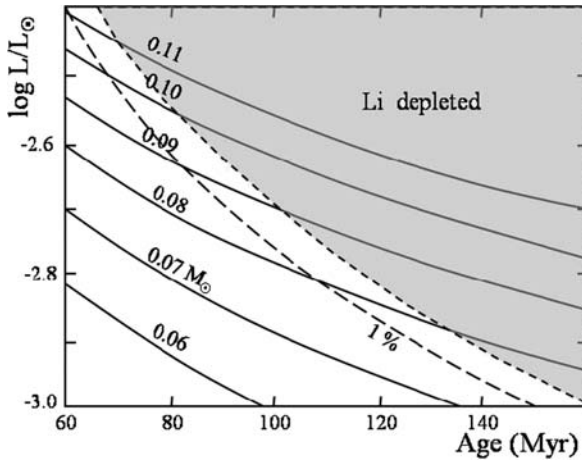
Fig. 20.15 A lithium diagnostic diagram: the evolution of the luminosity of stars near the brown dwarf limit as a function of age. The region where lithium is fully depleted is indicated by a gray area. The locus where lithium is depleted to 1% of the initial level is indicated by a *long-broken line*. The brown dwarf limit is at about 0.08 M$_\odot$. Adapted from G. Basri, G.W. Marcy and J.R. Graham [37]

MS turnoff of models without convective overshoot or rotation. However, the above age from Li dating is in good agreement with the age of models where the size of the convective core of upper MS stars is increased by some effect, like rotation or overshooting (Sect. 27.3.5).

Chapter 21
Rotation in Star Formation

If the stars would not exist, it would be easy to demonstrate it must be the case! The fact is that the internal motions present in an interstellar cloud lead the fragments to rotate faster and faster as they are contracting. Thus, they quickly reach break-up velocities preventing further contraction and fragmentation.

In order to form stars, the specific angular momentum has to be reduced by a factor of 10^5–10^6. Thus, an essential question in star formation is how the forming stars dissipate their excessive angular momentum. The magnetic field, which makes some coupling between the star and the surrounding matter, appears as a key factor in the process.

21.1 Steps in the Loss of Angular Momentum

From the interstellar clouds to the Sun, huge amounts of angular momentum have to be dissipated as shown in Table 21.1. We may distinguish three successive steps, with different physical effects (Fig. 21.1), in the evolution of the angular momentum from the interstellar medium to MS stars.

Table 21.1 The specific angular momentum j in various objects [385]

Object	j (cm^{-2} s^{-1})
Dense molecular cores	10^{21-22}
Wide binaries	10^{19-20}
Pre-MS stars (T Tauri)	10^{16-17}
Sun	10^{15}
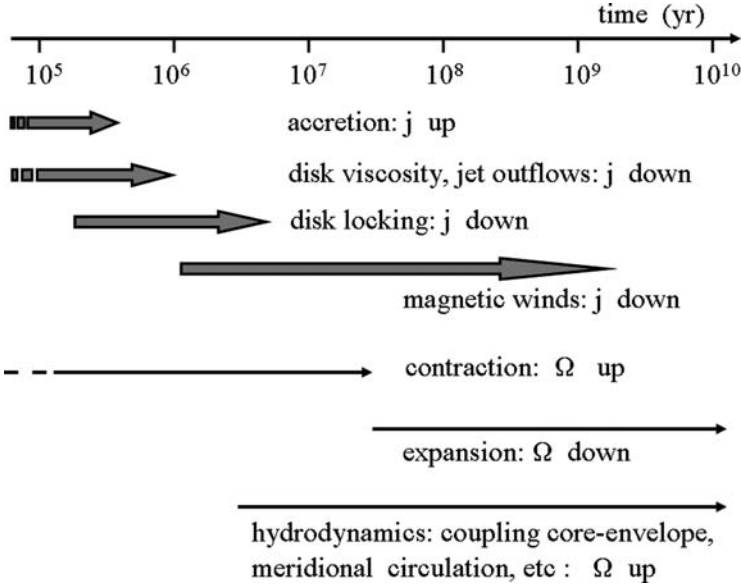
Fig. 21.1 Various effects influence stellar rotation as a function of time for a 1 M$_\odot$ star. The *thick arrows* show the effects changing the specific stellar angular momentum j, while the *thin arrows* show the effects conserving the angular momentum, but changing the angular velocity Ω at the stellar surface. Only two hydrodynamical processes are mentioned. Adapted from R.D. Mathieu [385]

21.1.1   From Interstellar Clouds to T Tauri Stars

Radio observations show velocity differences between the various parts of dense interstellar clouds. As a result, the net total angular momentum of the cloud differs from zero. The axial rotation observed for T Tauri stars ($M \leq 2$ M$_\odot$) results from this initial angular momentum. The problem is that the initial specific angular momentum j_{intst} of the interstellar matter is about 10^5 larger than the resulting specific momentum in T Tauri stars (cf. Table 21.1).

The typical velocity gradient ∇v in a dense cloud is about 1 km s^{-1} pc^{-1}. Thus, the specific angular momentum is $j_{\text{intst}} = \nabla v \, d^2$, where d is the size of the cloud, say 0.1 pc. This leads to $j_{\text{intst}} \approx 10^{21}$ cm^2 s^{-1} for a dense cloud. The specific angular momentum of a T Tauri star of rotation period P and radius R is $j_{\text{T Tau}} = k^2 R^2 (2 \pi/P)$. The value of k^2 is smaller than 2/5, appropriate for a homogeneous sphere (for a fully convective star with a polytropic index $n = 1.5$ (Sect. 24.5), $k^2 = 0.20$, while for a fully radiative star with polytropic index $n \approx 3$, one has $k^2 = 0.05$). For a rotation period of 10 days and a radius of 2 R$_\odot$, we get $j_{\text{T Tau}} \approx 10^{16}$ cm^2 s^{-1} for a T Tauri star (Table 21.1). This represents a decrease of j by a factor of about 10^5. Binary formation and tidal interactions between protostars, which transfer angular momentum from axial to orbital motion, as well as the bipolar outflows (cf. Sect. 22.1.3) and the magnetic coupling of the contracting object with its accretion disk are solutions used by Nature to solve the angular momentum problem.

21.1.2   From T Tauri Stars to the ZAMS

T Tauri stars have large spots at their surface, which modulate the emitted flux; this provides accurate rotation periods. The period distribution for T Tauri stars in the Orion Nebula is shown in Fig. 21.2. T Tauri stars with masses above $0.4\,M_\odot$ have an important peak of periods at about 8 days. The corresponding velocities are $v \sin i = 10$–$30\,\mathrm{km\,s^{-1}}$ and these stars rotate in general at less than 20% of their break-up velocity; a few ones reach 50%. If the T Tauri stars would keep their angular momentum during their evolution to the ZAMS, they would rotate with velocities of at least $200\,\mathrm{km\,s^{-1}}$ when arriving on the ZAMS, due to the large decrease in their moment of inertia as they contract (Fig. 21.3). In addition, the accretion of matter by T Tauri stars at a rate of $10^{-7}\,M_\odot\,\mathrm{yr^{-1}}$ would also produce a similar enhancement of the rotation velocity. This is not observed. For example, half of the stars in the Pleiades with masses between 0.6 and $1.0\,M_\odot$ have a rotation velocity lower than $10\,\mathrm{km\,s^{-1}}$ [482].

The main mechanism invoked to remove the angular momentum during the pre-MS contraction of T Tauri stars is the magnetic interaction with their accretion disk. Calculations indicate that fields of about 10^3 G can ensure the coupling of the star with its accretion disk. Thus, the assumption is generally made in stellar modeling that the rotational velocity v of a star remains constant up to an age fixed by the disk lifetime. Despite contraction and accretion, the star does not spin up and the angular momentum is not conserved by this process called disk locking. The disk lifetime is generally taken as a parameter adjusted on observations.
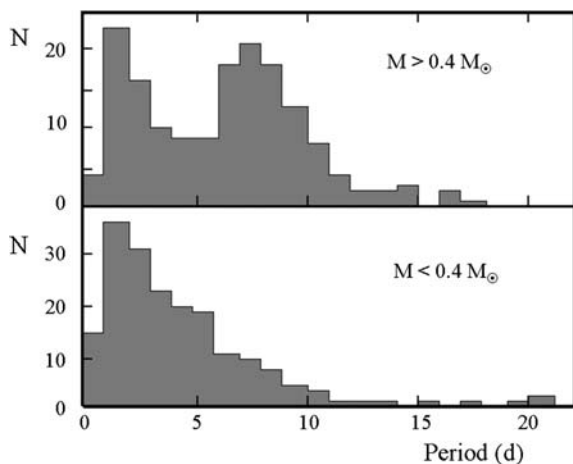
Fig. 21.2 Distribution of the number N of T Tauri stars as a function of the rotation periods for stars in the core of the Orion Nebula. The stars with mass above and below $0.4\,M_\odot$ are considered separately. Adapted from R.D. Mathieu [385]
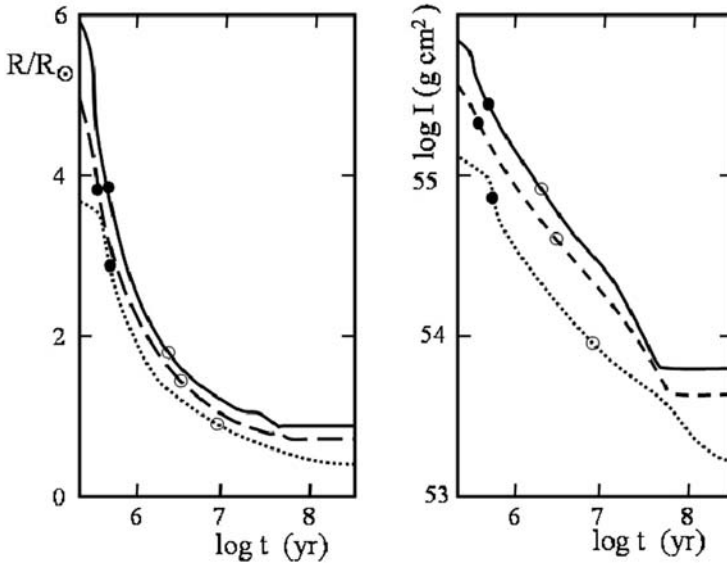
Fig. 21.3 Evolution of the stellar radius $R/R_{\odot}$ (*left*) and the log of the moment of inertia I (*right*) for stars of $1\,M_{\odot}$ (*continuous line*), $0.8\,M_{\odot}$ (*broken line*) and $0.5\,M_{\odot}$ (*dotted line*) as a function of age. The *black dots* indicate the stage at which the star leaves the birthline with $\dot{M}_{accr} = 10^{-5}\,M_{\odot}$ yr^{-1}. The *open dots* show the start of a radiative core. Adapted from J. Bouvier et al. [60]

21.1.3 End of Pre-MS Phase and Early Main Sequence

Another major observation to be explained is the break in rotational velocities near spectral type F3 ($\sim 1.4\,M_{\odot}$) on the MS. The velocities steeply decline from about $150\,\mathrm{km\,s^{-1}}$ in earlier spectral types to $10\,\mathrm{km\,s^{-1}}$ or less in later types. This transition occurs near the limit below which stars have a convective envelope.

There is another observation to be accounted for: the fraction of rapid rotators among solar-type stars decreases with age. An example is given by the three clusters: α Persei ($\sim 5.2 \times 10^7$ yr), Pleiades ($\sim 1.1 \times 10^8$ yr) and Hyades ($\sim 6 \times 10^8$ yr). In the α Persei cluster, half of the stars have $v \sin i \geq 50\,\mathrm{km\,s^{-1}}$; this fraction is 15% in the Pleiades and 0% in the Hyades.

Here, the main braking effect is the magnetic coupling of the star with its winds (Sects. 13.2 and 21.3). The convective envelopes in stars with $M \leq 1.4\,M_{\odot}$ allow stellar dynamos to operate and to create a magnetic field. The magnetic coupling constrains the wind to co-rotate with the star out to a large distance. Despite the very low mass loss rates, this process removes a considerable amount of stellar angular momentum during the end of the pre-MS phase as well as in the MS phase. The magnetic coupling is able to slow down the fast-rotating stars in a few 10^8 yr.

As illustrated in Fig. 21.1, the change of the moment of inertia due to contraction in pre-MS phase or expansion during MS-phase, as well as the various internal hydrodynamic processes like convection, meridional circulation, shear mixing and

horizontal turbulence in radiative zones, also contributes to the evolution of the rotation velocities.

21.2 Disk Locking and Magnetospheric Accretion

The braking by the magnetic coupling of the star and the wind (Sect. 21.3) is not sufficient, during the relatively short pre-MS lifetimes, to reduce rotation enough to account for the rotation velocities of stars on the ZAMS. A faster and more efficient process is needed. Disk locking, i.e., the magnetic coupling of the star and the accretion disk, is the most likely possibility.

There are many observational evidences of disks around pre-MS stars (Sect. 19.1). Disks have a major role in the dissipation of angular momentum, thanks to two effects. First, the viscous friction of their layers in differential rotation dissipates some rotational energy in the form of IR radiation (Sect. 19.1.3). Second, the convective dynamo in solar-type and lower mass stars creates a magnetic field which produces a coupling of the star with its surrounding disk. Observations of magnetic fields in T Tauri stars based on measurements of Zeeman broadening of photospheric lines give field values of the order of 1–2.5 kG [225], sufficient to maintain star–disk coupling.

Let us consider a star of mass M, radius R and a dipolar magnetic field of intensity B_0 at the surface. Around this star, there is an accretion disk on which the accretion rate is $\dot{M}_{\mathrm{accr}}$. The infalling material is exerting a torque on the disk. The ionization fraction in the disk is assumed sufficient to couple the stellar magnetic field to the disk. Let us find the radius r in the disk, where there is an equilibrium between the pressure (or energy densities) u_{B} and u_{infall} of the magnetic field and of the infalling material. These energy densities are

$$u_{\mathrm{B}} = \frac{B_{\mathrm{r}}^2}{8\,\pi} \quad \text{and} \quad u_{\mathrm{infall}} = \frac{1}{2}\dot{M}_{\mathrm{accr}}v_{\mathrm{infall}}^2 \frac{\Delta t}{\Delta V}\,, \tag{21.1}$$

where B_{r} is the magnetic field at distance r from the stellar center and Δt is the interval of time necessary for the infalling material at velocity v_{infall} to travel over a distance Δr. The element of volume is $\Delta V = 4\pi r^2 \Delta r$, with $\Delta r/\Delta t = v_{\mathrm{infall}}$. The equality $u_{\mathrm{B}} = u_{\mathrm{infall}}$ yields

$$B_{\mathrm{r}}^2 = \frac{\dot{M}_{\mathrm{accr}}\,v_{\mathrm{infall}}}{r^2}\,. \tag{21.2}$$

For the infall velocity, we take the free-fall velocity $v_{\mathrm{ff}} = (2GM/r)^{1/2}$, which is the maximum infall velocity. The magnetic field is assumed dipolar and at radius r in the equatorial plane it is

$$B_{\mathrm{r}} = B_0 \left(\frac{R}{r}\right)^3\,, \tag{21.3}$$

where B_0 is the field at the stellar surface $r = R$. Thus, (21.2) becomes

$$\left(\frac{R}{r}\right)^{12} = 2\,GM\,\frac{\dot{M}_{accr}^2}{B_0^4\,r^5}\,. \tag{21.4}$$

This allows us to define the so-called truncation radius r_T where the energy densities of the magnetic field and of the infalling matter are equal:

$$\frac{r_T}{R} = \frac{B_0^{\frac{4}{7}}\,R^{\frac{5}{7}}}{\dot{M}_{accr}^{\frac{2}{7}}(2GM)^{\frac{1}{7}}}\,. \tag{21.5}$$

Numerically, this is [229]

$$\frac{r_T}{R} = 3.7\left(\frac{B_0}{1\,\text{kG}}\right)^{\frac{4}{7}}\left(\frac{\dot{M}_{accr}}{10^{-7}\text{M}_\odot\text{yr}^{-1}}\right)^{-\frac{2}{7}}\left(\frac{M}{0.5\,\text{M}_\odot}\right)^{-\frac{1}{7}}\left(\frac{R}{2\,\text{R}_\odot}\right)^{\frac{5}{7}}\,. \tag{21.6}$$

Inside radius r_T the infalling matter is dominated by magnetic field: the matter is forced to move along the field lines down to the magnetic poles. Outside, matter infalls with little interaction with field. The numerical factor in (21.6) depends on the accretion properties. Current estimates give a ratio r_T/R between 2 and 10. Heavy accretion reduces the truncation radius, while a strong magnetic field increases it.

There has been some debate on how differential rotation in the disk winds up the field lines and whether the truncation radius coincides with the co-rotation radius, which is the radius where the Keplerian angular velocity is equal to the angular velocity of the star (at inner disk limit). If this is the case, there is no winding up of the magnetic field lines. However, it is more likely [229] that magnetic field lines penetrate the inner disk and are wound up, until some field reconnection releases the accumulated magnetic energy. This may be the source of X-ray flares, of time-varying magnetospheric accretion and spectral variations, as observed in T Tauri stars.

Magnetic fields of about 1 kG are able to produce the coupling of the star and disk, so that the rotation of the T Tauri star is locked to that of the disk with a rotation period unaffected by the stellar contraction. Thus, for stellar ages t smaller than the typical disk lifetime τ_{disk}, the stellar Ω is

$$\Omega\,(t \leq \tau_{disk}) \cong \Omega_0\,, \tag{21.7}$$

where Ω_0 is the angular velocity at the beginning of disk locking. The star keeps a constant Ω until $t = \tau_{disk}$. During this time, the stellar moment of inertia strongly decreases (Fig. 21.3), thus the star looses a considerable amount of angular momentum, as suggested in Table 21.1. Short disk lifetimes ($\tau_{disk} \leq 10^6$ yr) produce fast rotation on the ZAMS, while long disk lifetimes ($\tau_{disk} \geq 10^7$ yr) produce slow rotators.

21.2.1   Observational Evidences

The rotation periods of accreting T Tauri (classical T Tauri) stars are peaked around 8 days (Fig. 21.2); this is about twice longer than for the non-accreting T Tauri stars (weak line T Tauri). This was interpreted [60] as a result of disk locking: accreting stars are locked to their disk, while non-accreting stars are free to spin up as they contract. Some doubts about the disk-locking process have been emitted, due to the absence of direct correlation between the rotation periods and the IR signatures of disks. However, the relation between disks and slow rotation may not be as simple as supposed. For example, during pre-MS evolution, rotation may (1) vary from rapid to slow, due to the decrease of accretion and (2) then it may vary from slow to fast rotation at the end of disk locking. Some studies confirm that pre-MS stars evolve at constant rotation velocities during their first 3–5 Myr [483].

As shown in Fig. 21.2, there is a bimodal distribution of the rotation periods for T Tauri stars with masses larger than $0.4\,M_\odot$ ($M \leq 2\,M_\odot$). The long-period peak near 8 days is attributed to the slowly rotating disk-locked stars. If so, the initial conditions for constructing stellar models of pre-MS stars with rotation are well defined. The group of short-period stars might represent the stars which have spun up after the end of the disk-locking phase. Stars with masses below $0.4\,M_\odot$ have only short periods (Fig. 21.2).

T Tauri stars, whatever their masses (up to $\sim 2\,M_\odot$), have a broad distribution of rotation velocities as is the case for young stars on the ZAMS. Thus, the spread in rotation velocities is already established [385] when the stars have 10^6 yr. The disk lifetime τ_{disk} is still uncertain. Some cluster data [483] show a spin-up of rotation only for ages above 8×10^6 yr, while most estimates [60] suggest a median lifetime of disks of 3×10^6 yr.

21.3   Magnetic Braking and Rotation in Clusters

The theoretical relations expressing the magnetic braking have been developed in Sect. 13.2. Magnetic braking in the pre-MS and MS phases essentially determines the evolution of stellar rotation in solar-type stars, acting on a much longer timescale than disk locking.

21.3.1   Predicted Magnetic Braking

The rate of loss of angular momentum is expressed by (13.33), which depends on some parameters

– A parameter n defined in (13.22), which is equal to 2 for a radial and 1 for a
  dipolar field. Comparisons with observations support $n = 1.5$ (caution: this n
  here is not the polytropic index).
– A parameter a defined in (13.31), which expresses how the magnetic field grows
  with the angular velocity. A value $a = 1$ corresponds to the linear dynamo. Fac-
  tors $n = 1.5$ and $a = 1$ well reproduce the Skumanich's law for the decrease of
  rotational velocities with ages $v \sim t^{-0.5}$ (13.42).
– A multiplying factor K_W, which is the product of several other factors. A value
  $K_W = 2.7 \times 10^{47}$ g cm^2 is determined from observations.

Models of the evolution of rotation velocities for a 1 M$_\odot$ star are illustrated in
Fig. 21.4 for various values of n. The assumption of solid body rotation is made.
Several interesting features appear:

1. In the case with no loss of angular momentum J: during the pre-MS phase the
   decrease of I is faster than the decrease of R (Fig. 21.3). Thus, to keep J constant,
   the rotation velocity grows fast (13.38).
2. During the MS-phase, the increases of I and R nearly compensate each other in
   (13.38), so that v is about constant if J is constant.
3. The timescale of magnetic braking is longer than the evolutionary timescale
   which determines the change of structure and moment of inertia. Thus, the fast
   decrease of I leads to a growth of v during the pre-MS phase (Fig. 13.38), even
   in the presence of magnetic braking.
4. Figure 21.4 applies to solid body rotation. If the angular momentum is conserved
   in shells in radiative zones and as a whole in convective regions, the maximum of
   v reached at the end of the pre-MS phase is about 50 km s^{-1}, instead of 150 km
   s^{-1}. This is due to the smaller moment of inertia and the lower angular momen-
   tum available in the convective envelope compared to the case of solid rotation.
   The reality likely lies between these two extreme cases. In addition for a 1 M$_\odot$
   star, the mass of the convective envelope decreases and contracts during the pre-
   MS phase; this contributes to maintain a significant rotation velocity.
5. A curve intermediate between those for $n = 1$ and $n = 2$ behaves like (13.42)
   for ages larger than 10^8 yr. Larger n values make the star to lose more angular
   momentum. Figure 21.4 shows that for larger n, the loss of angular momentum
   starts earlier during the pre-MS phase. For $n = 1.5$, the loss of J goes like Ω^3.
6. Larger K_W reduce the rotation velocities (Sect. 13.2.3).
7. Whatever the initial angular momentum at the beginning of the pre-MS, the stars
   reach the same rotation velocities after about 10^8 yr. This occurs for solid body
   rotation as well as for conservation of J in shell, because in both cases if the initial
   rotation is larger, the loss of J is also larger. Therefore, the predicted velocities v
   are decreasing functions of age. The scatter should be smaller and smaller after
   10^8 yr.

There are several indications (Sect. 13.2.1) that the growth of the magnetic field
with Ω saturates for values larger than a limit Ω_{sat} an order of magnitude larger than
the solar value $\Omega_\odot$. The value of Ω_{sat} seems to grow with stellar mass as suggested
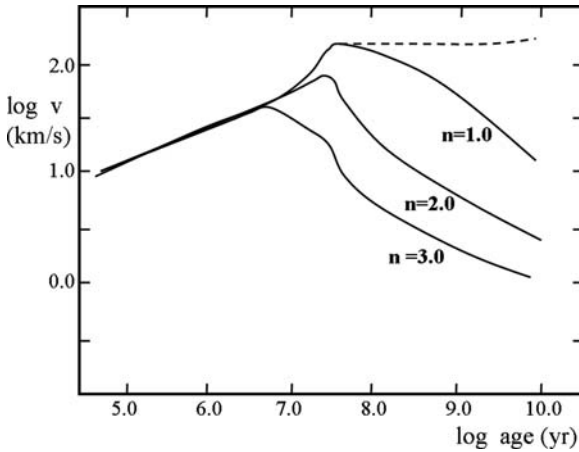
Fig. 21.4 Evolution of the rotational velocity as a function of time for a $1\,M_\odot$ star under the assumption of solid body rotation. Various values of n are considered. The pre-MS phase extends up to about 10^7 yr. The *broken line* shows the evolution without any loss of angular momentum. Adapted from S.D. Kawaler [279]

by (13.37). Such a behavior is consistent with the fast velocity decrease of the higher mass stars in this range which still have an external convective zone ($M < 1.4\,M_\odot$).

As shown in Fig. 21.1, the evolution of rotation also depends on the mechanisms of transport of angular momentum in stellar interiors. According to the internal coupling adopted, different disk lifetimes and different parameters for the magnetic braking are found. Moreover the stars are likely not in solid body rotation as often assumed. Comparisons between models and observations indicate that there is some moderate coupling between the radiative core and the convective envelope, the coupling transferring some of the central spin-up to the envelope.

21.3.2   Comparisons with Rotation Velocities in Clusters

The Pleiades and Hyades are the best studied clusters and they offer us a picture of the evolution of rotation at ages of 110 and 600 Myr, respectively (Fig. 21.5). Observations of rotation are available down to $0.1\,M_\odot$. The Pleiades represent the best case of rotational velocities of stars close to the ZAMS (a star with a mass of $0.7\,M_\odot$ is just reaching the ZAMS in this cluster). The following features can be noticed [550] in the Pleiades: a large spread of rotation velocities over the whole mass range, a big group of very slow rotators, a group of fast rotators (about 1/3 break-up), a bimodal distribution of velocities between 0.6 and about $1\,M_\odot$ and the M dwarfs with $M \leq 0.3\ M_\odot$ have less spread in rotation.

For the Hyades, the rotation velocities are much reduced compared to those in the Pleiades, except for the M dwarfs where the reduction is moderate. Other clusters in
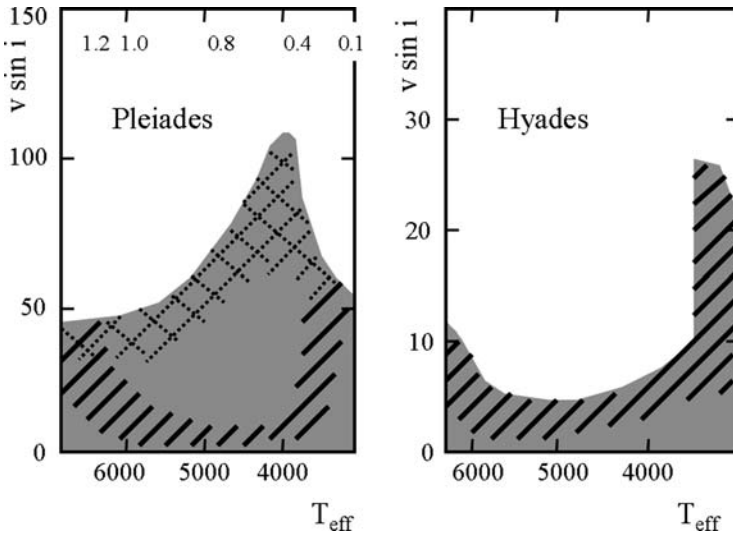
Fig. 21.5 Distributions of the rotational velocities in the Pleiades and Hyades as a function of T_{eff}. The *heavy shaded areas* indicate where most stars are lying; the *lighter shaded area* shows the location of a significant fraction of Pleiades stars. The *gray areas* indicate regions where stars may be present. The scale at the *top* of the *left* diagram is an indicative mass scale. Adapted from J. R. Stauffer [550]

the same range of ages confirm the picture provided by the Hyades and Pleiades. The interpretation of the observations (Fig. 21.5) is consistent with the various effects considered above and in Sect. 13.2.

– **Disk locking:** this process is necessary to account for the very slow rotation of a large fraction of solar-type and lower mass stars as in the Pleiades. Magnetic braking alone does not produce enough loss of angular momentum during the pre-MS phase to account for the high number of very slow rotators. Moreover, if it would do so, it would kill stellar rotation during the MS evolution phase, which is not the case.

– **Magnetic braking:** the general decrease of rotation with ages from the Pleiades to the Hyades is interpreted as resulting from the magnetic braking due to stellar winds.

– **Saturation effect:** as seen in Sect. 13.2.1, the saturation effect is supported by X-ray observations of magnetic activity. It allows us to account for the survival of some relatively fast rotators on the ZAMS, like in the Pleiades.

– **Mass dependence:** the limited decrease of rotation between the M dwarfs of the Pleiades and of the Hyades is likely due to the fact that most M stars have a rotational velocity above the saturation velocity, which is very low for such masses (cf. 13.37 and subsequent remarks).

– **Core-envelope partial coupling:** there are evidences that the angular momentum of the radiative core of slow rotators contribute to sustain the rotation of convective envelopes over a timescale of 100–200 Myr [482].

   The role of binarity with respect to rotation is uncertain. The formation of binaries in the pre-stellar phase may absorb a lot of angular momentum initially present (Table 21.1) and may thus contribute to reduce rotation. However, the presence of a companion around a forming star may also destroy or truncate the circumstellar disk and thus reduce the role of disk locking, thus favoring higher rotation in binaries. However in some cases, binarity may also extend the disk lifetime and thus favor slow rotators [14]. No clear theoretical picture is emerging about the effect of binarity on the initial rotation velocities. Observations show rather similar distributions of rotation velocities in single and double stars [61].

   Figure 21.6 shows quantitative comparisons [36] between cluster observations and models of 0.6 and $1.0\,M_\odot$ with and without disk locking. In all models, magnetic braking has been included with the saturation effect and mass dependence. Differential rotation is present, with some mixing processes treated as a diffusion. To make a long story short, models starting from the T Tauri stage with rotation periods of 4 and 16 days, respectively, corresponding to the lowest and highest periods observed are considered. The various observational constraints at different ages (in particular the occurrence of groups of low and fast rotations in the Pleiades) can only be satisfied if the models with small periods (fast rotation) have disks and the
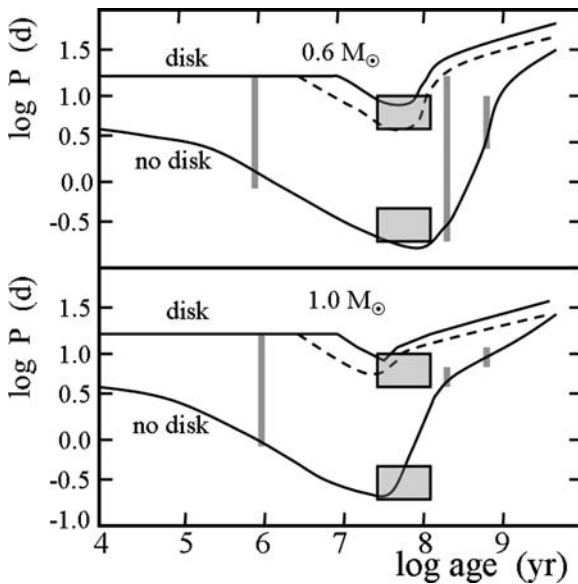
Fig. 21.6 Evolution of the rotation periods as a function of time for 0.6 and $1.0\,M_\odot$ models. In each diagram, the *upper continuous line* applies to a starting period of 16 days, a disk is present with a lifetime of 10^7 yr (*continuous line*) and with 3×10^6 yr (*broken line*); the *lower curve* applies to a starting period of 4 days, no disk is present. The *lower and upper boxes* represent the observed period for the fast and slow rotators in α Per and the Pleiades. The *gray bar* at 10^6 yr represents the observed range of periods in T Tauri stars. The *gray bars* at 2.5×10^8 and 6×10^8 yr represent data in NGC 3532 and the Hyades for the corresponding masses. Adapted from S. Barnes, S. Sofia & M. Pinsonneault [36]

models with high periods (low rotation) have no disks. The last part of the evolution of the period with age of the fast rotators in Fig. 21.6 obeys the Skumanich relationship, which as mentioned in Sect. 13.2.1 tends to reduce the velocity dispersion at high ages. As a last remark, the evolution of the fast sequence is better explained if the moment of inertia of only the outer zone is participating, while the whole star participates in the spin-down of the slow sequence. This may suggest that the degree of coupling depends on rotation.

The models with disk locking and a disk lifetime of 3×10^6 yr (dashed line) and 10^7 yr (upper continuous curve) in Fig. 21.6 are able to reproduce the slowest rotators in the young clusters. As mentioned above, these models have differential rotation. For solid body rotation, the disk lifetimes obtained from such comparisons would be of the order of 10–20 Myr. This is much longer than the order of million(s) years suggested by IR evidences of disks in pre-MS stars.

We remark that it may be a little embarrassing to need different processes with various parameters to account for the evolution of rotation velocities in solar-type and lower mass stars. However, this may just be the result of the richness of the physical processes acting in the evolution of these stars. Asteroseismological observations of pre-MS stars may provide decisive constraints.

Chapter 22
The Formation of Massive Stars

"How do massive stars form?" is still a major question. Some authors have considered that massive stars cannot form by mass accretion like intermediate or low-mass stars, because the radiation pressure of the very luminous protostars would repel the infalling matter and prevent the accretion. Thus, various scenarios have been explored, like the coalescence of protostars.

The interesting point is that if accretion is strong enough of the order of 10^{-3} $M_\odot$ yr^{-1}, the momentum of the infalling matter may overcome the radiation momentum of massive stars and accretion becomes possible. In addition, the accreting matter, especially if it forms a disk, protects itself against rapid grain destruction and ionization. Massive protostars show bipolar outflows indicating that a part of the infalling matter is re-directed in ejections around the polar axes. It is remarkable that the rates of bipolar ejection are related to the stellar luminosities over 6 orders of magnitude. There is an excellent review by H. Zinnecker and H.W. Yorke [639] on massive star formation.

22.1 The Various Scenarios for Massive Star Formation

Several competing scenarios for the formation of massive stars have been proposed over recent years. Some observations [126] favor the accretion scenario, as for lower mass stars. However, there are still uncertainties and the reality may be complex, with situations in dense clusters where both accretions and collisions play a role.

22.1.1 The Classical or Constant Mass Scenario

This is the case, studied since the 1960s, of the pre-MS evolution at constant mass, characterized by horizontal blueward evolutionary tracks in the HR diagram, from the Hayashi line to the ZAMS as shown in Fig. 20.2. The timescale is the Kelvin–Helmholtz timescale $t_{\mathrm{KH}} \approx GM^2/(RL)$, which corresponds to $\sim 1\%$ of the MS

lifetime. For example, for a 30 M$_\odot$ star, $t_{KH} = 3 \times 10^4$ yr. The evidences of disks make this scenario difficult to support.

However, we note that the constant mass scenario is an asymptotic limit of the accretion scenarios; it corresponds to the case of an extremely intense and fast initial accretion, which then declines steeply. Thus, the case of constant mass, although oversimplified, is an interesting limit (which might not be too far from the reality). As such, it remains a valuable comparison basis. Some timescales of constant mass pre-MS evolution are given in Table 20.1.

22.1.2   The Collision or Coalescence Scenario

Protostars are moving within interstellar clouds which later form a cluster. Thus, collisions of intermediate mass protostars have been suggested as a possible formation mechanism for massive stars [55]. Often in literature, the coalescence scenario has been supported with the argument that the accretion scenario is not possible for massive stars, because the high-radiation field of massive stars may reverse the infall. We stress that the coalescence may well be important, however not for the above negative reason. If the coalescence scenarios applies, it is due to positive reasons, because the collision probability in dense clusters is high. A nice feature of the coalescence scenario is that it considers the internal cluster dynamics as part of the game.

Observations: there are several arguments in favor of this scenario:

– Most massive stars do not form in isolation, but in the central regions of rich young clusters.
– There seems to be a relation between the mass of the most massive star in a cluster and the cluster mean density [568].
– There is a mass segregation in young clusters, with the most massive stars in the cluster center (even in very young not dynamically relaxed clusters). Also, the intermediate mass stars show some mass segregation. (We note that the process of cloud fragmentation, occurring according to the Jeans criterion, would produce the smallest stellar masses in the cluster center, if the gas is isothermal with a higher density in the cloud center.)
– The frequency of binaries, and in particular the occurrence of many short-period SB2 systems (e.g., with periods ≤ 5 d), is often high among OB stars [202]. This feature is in agreement with the collision theory, which predicts a high frequency of tight binaries among massive stars due to tidal captures and star–disk encounters [638].

Theory: for stellar collisions, as well as for particle collisions, the average timescale t_{coll} between two successive collisions behave like $(1/t_{coll}) \approx \sigma\, n\, v$, where σ is the cross-section, n the concentration of stars and v the average velocity. The full expression is [55]

$$\frac{1}{t_{\text{coll}}} = 16\sqrt{\pi}\,v_{\text{disp}}\,nR^2\left(1 + \frac{GM}{2R\,v_{\text{disp}}^2}\right), \tag{22.1}$$

where v_{disp} is the dispersion velocity in the cluster, M the stellar mass and R the stellar radius. The last term corresponds to the so-called gravitational focusing. In order to get a collision time $\leq 10^5$ yr, one needs a concentration $n \geq 10^8$ stars pc^{-3}, which is extremely high. The mean observed concentration in the Orion Nebula is $n \approx 10^3$ stars pc^{-3}, the maximum value is $n \approx 2 \times 10^4$ stars pc^{-3} in the core of the Nebula. These two values of the concentrations give, respectively, collision timescales of 10^{10} yr and of 7×10^8 yr. On this basis, the collision process would appear inefficient, at least there.

The claim has been made [54] that a cluster during its collapse would go through a transitory phase with a much higher density, maybe up to a factor of the order of 10^4 larger than the average present cluster density. The argument is that the gas accretion onto stars makes a cluster to shrink and to reach Virial equilibrium at a much smaller radius. If so, stellar mergers might dominate the mass buildup after a few crossing times, i.e., after about 4×10^5 yr. The formation of binaries may be favored in dense cores. A possible process is the so-called tidal capture, in which tidal interaction during a grazing encounter dissipates a lot of kinetic energy. This process may work for nearly equal mass protostars, while the encounter of a massive star with a lower mass object may destroy the smaller object with the formation of a disk. The disk would favor [54] subsequent captures due to the larger cross-section and due to the binding energy of the disk.

On the whole, collisions likely have a role in the formation of massive stars; however it is not necessarily a dominant role. Also, the alleged transitory high-
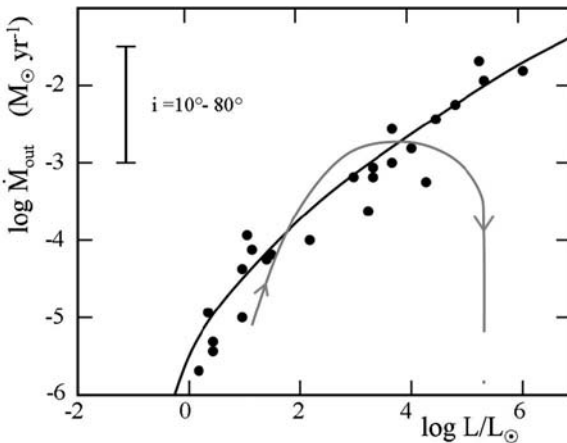
Fig. 22.1 The outflow rates as a function of the bolometric luminosity of the central object (Churchwell-Henning relation). An average inclination angle $i = 57.3$ degrees is assumed to derive the velocities. The error bar shows the uncertainty for $i = 10$–$80°$. Adapted from Henning et al. [241]. The gray line shows the approximate track for one star described by the expression (19.26) with $\dot{M}_0 = 2 \times 10^{-3}$ M$_\odot$ yr^{-1} and $\tau_0 = 8000$ yr (Sect. 22.4.1)

density stage is very uncertain. Also, the non-simultaneity of the gas accretion on each star certainly leads to less extreme transitory densities. Another major difficulty of the collision scenario is that it does not provide bipolar outflows as observed (Fig. 22.1).

22.1.3 The Accretion Scenario

The formation of massive stars by mass accretion is a most interesting possibility [41, 44, 443, 627]. The accretion scenario has often been criticized with the argument that the high radiation pressure of massive stars would reverse the accretion. However, if the momentum in the accretion flow is larger than the radiation momentum, accretion is possible (Sect. 22.3). Models confirm this possibility [630]. A constant accretion rate $\dot{M}_{accr}$ of about 10^{-5} $M_\odot$ yr^{-1} would require 10^7 yr to form a 100 $M_\odot$ star, while observations in young clusters suggest a formation age of $\sim 10^5$ yr. Thus, high values of $\dot{M}_{accr}$ are needed at least during a part of the formation time. As shown by (19.25), high accretion rates are possible if the contracting clumps in an interstellar cloud are dense enough. Supersonic turbulence, which creates shocks and high-density fluctuations in contracting clouds, may thus produce locally the high-density conditions necessary for initiating the formation of massive stars.

The modern view about massive star formation [518] is that, first, large quantities of dense gas are needed and the entire cloud must be gravitationally unstable to build up a clusters of stars. A massive cloud of, say more than 10^3 $M_\odot$, with a density $\varrho \geq 10^{19}$ g cm^{-3} is likely dominated by self-gravity and shows internal supersonic motions. Because of gravo-turbulent fragmentation with shocks, the density structure is highly inhomogeneous with clumps and sub-clumps leading to star formation. The most massive and densest sub-clumps in the turbulent structure will likely be at the cluster center and form the most massive stars. If so, there may already be a certain degree of mass segregation at the birth of the cluster.

There are several observations, which give support to the accretion scenario for massive stars with high values of $\dot{M}_{accr}$.

– **Turbulence:** the widths of molecular lines show non-thermal velocity components up to $v = 2.5$ km s^{-1}, i.e., larger than the thermal velocities ($v \leq 0.5$ km s^{-1} km s^{-1} in star-forming cores [95]). Non-thermal motions are larger in more massive cores (~ 5–100 $M_\odot$) as shown by relation (18.36). In general, massive cores are denser, have steeper density profiles and higher pressures than low-mass cores. The inhomogeneous cloud structure, with dense clumps and sub-clumps resulting from shocks in the turbulent supersonic environment, may largely permit locally accretion rates of about 10^{-3} $M_\odot$ yr^{-1}. Models suggest [394] that massive stars form in these high-density and turbulent regions in about 10^5 yr.
– **Luminosity and spectra:** IR observations at 2 μm of the high-mass star-forming region Orion KL Nebula [437] give $T_{eff} \approx 4500$ K with a luminosity above 4×10^4 $L_\odot$. The observations are consistent with

$$L \approx \frac{GM\dot{M}_{\text{accr}}}{2R} \quad \text{and} \quad T_{\text{eff}} \approx \left(\frac{GM\dot{M}_{\text{accr}}}{8\pi\sigma R^3} \right)^{\frac{1}{4}}, \tag{22.2}$$

produced by an accretion disk around a massive star of 10–25 $M_\odot$ with $\dot{M}_{\text{accr}} \approx 10^{-2}$ $M_\odot$ yr^{-1}. This very high accretion rate is compatible with the velocity dispersion observed in the core of the Orion KL molecular cloud. In general, the spectral distributions and fluxes emitted by hot cores are in agreement with disks having $\dot{M}_{\text{accr}} \approx 10^{-2}$ $M_\odot$ yr^{-1}.

– **Massive outflows:** massive molecular outflows are detected in more than half of the regions of massive star formation, thanks to far-IR and CO observations [135]. IR imaging at 2.2 μm with the VLT also provides direct evidence [126] of disk and outflows (Fig. 22.2). The outflow rates based on expansion velocities are in the range of 10^{-2}–10^{-4} $M_\odot$ yr^{-1} for massive objects [136], while the masses in the outflows are between 10 $M_\odot$ and a few 10^2 $M_\odot$. The ages of the outflows are typically a few 10^4 yr. Unlike for low-mass stars, the massive outflows are poorly collimated, with opening angle of a few tens of degrees. The outflows likely result from the infall from the disk; a fraction of the matter is accreted by the star and the rest is diverted into the bipolar outflows. The detailed mechanism, by which large masses are accelerated to supersonic speeds, is not clarified. Radiative heating and possibly magnetic field may be the main energy sources driving the outflows [328].

Remarkably, the outflow rates $\dot{M}_{\text{out}}$ well correlate [135, 136, 241] with the luminosities of the central objects over six decades of luminosity as illustrated in Fig. 22.1. To the first order, this relation, which may be called the Churchwell-Henning relation, is of the form $\dot{M}_{\text{out}} \sim L^{0.7}$, where L is the bolometric luminosity (Sect. 22.4.2). The mass-luminosity relation in the range of 2–85 $M_\odot$ is of the form
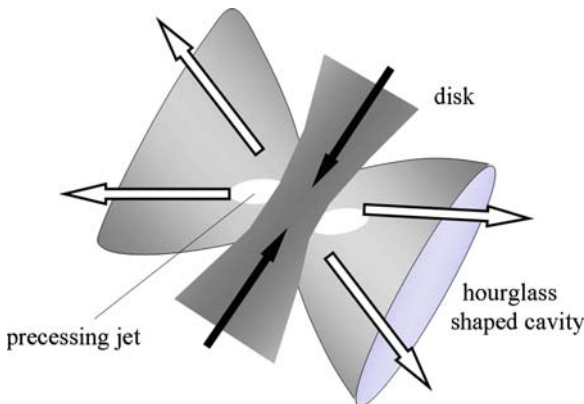
Fig. 22.2 Schematic picture of a protostellar disk with massive bipolar outflows. The central protostar is obscured by a large slowly rotating disk with a diameter of 20 000 AU and a mass of 100 $M_\odot$. A fraction of the infalling material is accelerated into bipolar precessing jets. The high-velocity wind forms an hourglass cavity in the ambient medium. Adapted from Chini [126]

$L \sim M^{2.2}$, so that one has about $\dot{M}_{\text{out}} \sim M^{1.54}$. A polynomial fit of the observations gives a more precise relation:

$$\log\left(\frac{\dot{M}_{\text{out}}}{M_\odot \, \text{yr}^{-1}}\right) = -5.28 + \log\frac{L}{L_\odot}\left(0.752 - 0.0278\log\frac{L}{L_\odot}\right) . \quad (22.3)$$

The outflow rates are related to the infall rate, since a fraction f (for example $f = 1/3$) of the infalling matter is accreted and a fraction $(1 - f)$ is ejected in the outflows. The relation between the values of $\dot{M}_{\text{out}}$ and the luminosities supports the idea of large accretion rates for massive stars giving an average rate of the form $\dot{M}_{\text{accr}} = [f/(1-f)]\dot{M}_{\text{out}}$, at least during the period during which the accretion rates are high (Sect. 22.4.1).

The ultra-compact (UC HII) regions represent an early stage in the evolution of star-forming zones, occurring when the heavy accretion phase has come to an end. About 10^3 UC HII regions are known. Their size is less than 0.1 pc and the mass content of the ionized region is small ($\sim 10^{-2}$ M$_\odot$). The newly formed star produces a small bounded ionization region, which is progressively extending in its parent surrounding cloud. IR observations suggest an inner cavity without dust, with $T \approx 300$ K at the inner face of the dust shell. Some "hypercompact" HII regions, likely representing an early stage of UCHII, have been detected.

Direct evidence for disks: some massive cores which are sources of bipolar outflows also show evidence for rotating disks and collimated jets. Observations from NH$_3$ lines with the VLA show [636] some flattened structures, perpendicular to the bipolar outflows. Blue shifted lines on one side and red shifted lines on the other side of an elongated structure, as well a velocity gradient along it, confirm the disk evidence in some cases.

A young massive object of about 20 M$_\odot$ (from its IR brightness) has been found [126] in M17 (Omega Nebula). It is surrounded by a large rotating disk extending up to about 20 000 AU and containing more than 100 M$_\odot$ of gas and dust (Fig. 22.2). A part of the material from the infalling disk is ejected perpendicularly to the disk in the form of bipolar jets. This object shows that a disk can survive in a dense cluster avoiding both disruption by tidal forces and evaporation by ionizing radiation from the protostar. Up to now, the number of disks identified is small. This may result from several factors: high-mass stars are deeply embedded in clouds; their lifetimes are very short or the new HII region evaporates the disk.

The available observations indicate that high-mass stars, at least up to 10^5 L$_\odot$, may form through an accretion process, with a certain similarity to low-mass stars. Thus, there are compelling evidences of accretion disks around massive stars in formation. Massive outflows are present up to very high masses (cf. Fig. 22.1) and may support their formation by accretion. However, some caution is still necessary, since there are no complete models including the system "cloud + disk + star" with all rotational effects and reproducing the outflows.

22.2   Timescales for Accreting Stars

We now examine several conditions on the timescales for accretion by massive stars. Let us recall that for a 1 $M_\odot$ star, the free-fall timescale t_{ff} is much smaller than the Kelvin–Helmholtz timescale t_{KH}, i.e., $t_{ff} < 10^6$ yr and $t_{KH} = 3 \times 10^7$ yr. The ratio of these two timescales is changing with stellar mass. From (18.28) and (20.2) one has

$$\frac{t_{ff}}{t_{KH}} \approx \frac{1}{\sqrt{G \varrho_{ini}}} \frac{RL}{GM^2}. \tag{22.4}$$

The initial density ϱ_{ini} is the density when the contracting cloud is at the Jeans limit; thus

$$\varrho_{ini} \sim \frac{M_J}{R_J^3} \sim M_J^{-2}, \tag{22.5}$$

since $M_J \sim R_J$ (18.3). If the whole initial mass collapses $M = M_J$, we get

$$\frac{t_{ff}}{t_{KH}} \sim \frac{RL}{G^{\frac{3}{2}} M} \sim \frac{M^\beta M^\alpha}{M} \sim M^{\alpha+\beta-1}, \tag{22.6}$$

where we use a mass–luminosity relation $L \sim M^\alpha$ and a mass–radius relation $M \sim R^\beta$. With $\alpha = 3$ and $\beta = 0.7$, typical values for the upper MS, we get $t_{ff}/t_{KH} \sim M^{2.7}$. Whatever the exact value of the exponent, the ratio t_{ff}/t_{KH} increases with mass. Schematically, we may have the two following situations:

- If $t_{ff} < t_{KH}$, the star has finished its main accretion phase before thermal equilibrium of the contracting star is achieved. This is why for lower mass stars, when accretion is finished, there is a long pre-MS track during which the star contracts at the Kelvin–Helmholtz timescale.
- If $t_{ff} > t_{KH}$, the contracting star has reached thermal equilibrium and is on the ZAMS before mass accretion is terminated (Fig. 20.5).

The value of the mass where both timescales are equal depends on the mass–radius relation for stars on the birthline, which in turn depends very much on the accretion rates. From Fig. 20.5, we see that for accretion rates $\dot{M}_{accr}$ between 10^{-6} and 10^{-4} $M_\odot$ yr^{-1}, the mass where the star sets on the ZAMS lies between 3 and 10 $M_\odot$. For $\dot{M}_{accr} = 10^{-5}$ $M_\odot$ yr^{-1}, in Fig. 20.5 it is about 6 $M_\odot$. Thus, for such a case, one has

$$\text{for M} < 6 \ M_\odot : \ t_{ff} < t_{KH} \implies \text{BIRTHLINE}$$
$$\text{for M} \geq 6 \ M_\odot : \ t_{ff} > t_{KH} \implies \text{ZAMS}$$

A limit of this order of magnitude agrees with the observations of Ae-, Be-Herbig stars (Fig. 20.6). However, the history $\dot{M}_{accr}(t)$ of the accretion rates leading to the formation of massive stars is certainly very different from a constant $\dot{M}_{accr}$, with
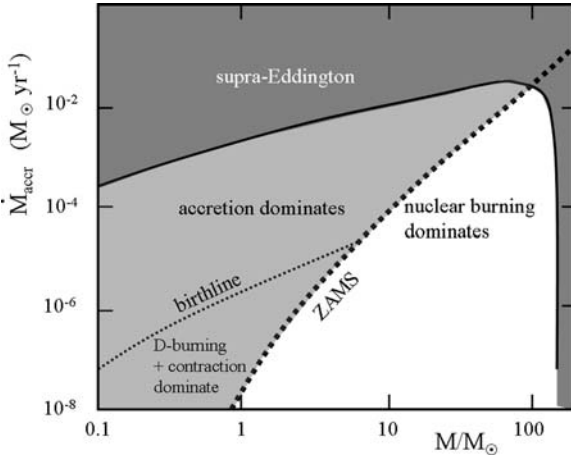
Fig. 22.3 Domains of accretion rates vs. masses. The heavy *dotted line* shows for stars on the ZAMS the place where the accretion luminosity is equal to the stellar luminosity. The *thin dotted* line shows the place where the accretion luminosity is equal to the contraction+D burning luminosity on the birthline. The *darker domain* shows the region where the accretion rate is such that the sum of the stellar and accretion luminosity is larger than the Eddington luminosity, assuming electron scattering opacity. Adapted from H.W. Yorke [627]

much higher values of the order of 10^{-2} or 10^{-3} $M_{\odot}$ yr^{-1} at some moments; in this case the tracks join the ZAMS at a different mass value (Sect. 22.4).

Different domains of accretion are shown in Fig. 22.3. The darker area indicates the supra-Eddington region, because of accretion (top) or of the high stellar luminosity (right). Above the thick dotted line, accretion luminosity dominates for stars on the ZAMS, below it the nuclear luminosity dominates. The thin dotted line shows the same for a star on the birthline, above it accretion dominates, below it contraction and D burning dominate. Thus, depending on its mass and accretion rate, a star may be in different regimes, with different sources powering its luminosity.

22.3   Limits on the Accretion Rates

Let us consider first a spherical inflow on a star of mass M and luminosity L. There are both upper and lower limits of the accretion rates (Fig. 22.4).

22.3.1   The Upper Limit on Accretion

A star may accrete matter if the inward acceleration of gravity $\boldsymbol{g}_{grav}$ is larger than the outward acceleration $\boldsymbol{g}_{rad}$ due to the radiation of the protostar. At any level r in the accretion flow, one must have
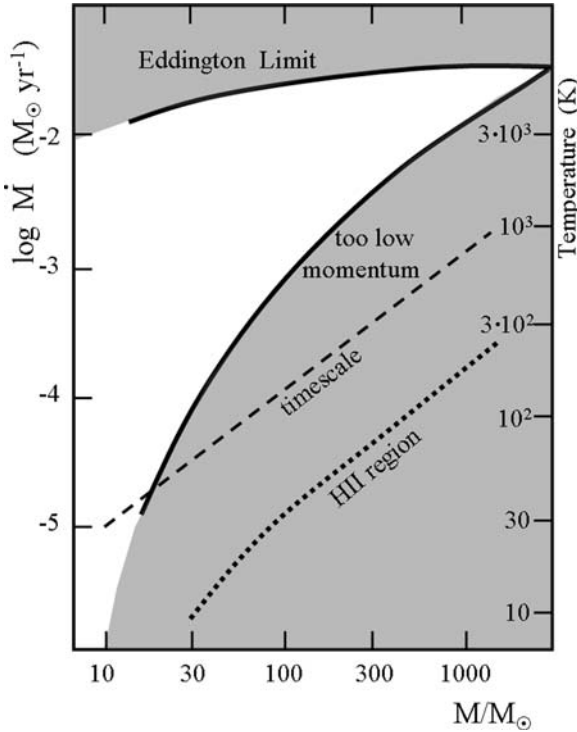
Fig. 22.4 Various limits on the accretion rates as a function of the protostellar mass. The white area is the region where accretion is permitted. The *upper limit* indicates where the inflow rate becomes supra-Eddington for electron scattering opacity. The limit below which the momentum in the inflow is smaller than the momentum of the radiation field is indicated (Sect. 22.3.3). Below the limit labeled "timescale" the formation timescale would be longer than 10^6 yr. Below the limit noted "HII region" an HII region expands beyond the dust destruction radius and prevents accretion. Adapted from M.G. Wolfire and J.P. Cassinelli [616]

$$\mathbf{g}_{\text{grav}} = -\frac{GM}{r^2}\frac{\mathbf{r}}{r} > \mathbf{g}_{\text{rad}} = -\frac{1}{\varrho}\frac{dP_{\text{rad}}}{dr}\frac{\mathbf{r}}{r} = \frac{\kappa(r)F_{\text{r}}}{c}\frac{\mathbf{r}}{r} , \qquad (22.7)$$

where F_{r} is the radiative flux and $\kappa(r)$ the total opacity at level r in the inflow. The above condition becomes

$$L_{\text{tot}} < \frac{4\pi c\,GM}{\kappa(r)} \equiv L_{\text{Edd}} \quad \text{with} \quad L_{\text{tot}} = L + L_{\text{accr}} , \qquad (22.8)$$

where the total luminosity L_{tot} is the sum of the intrinsic stellar luminosity L and of the accretion luminosity $L_{\text{accr}}(1/2)(GM\dot{M}_{\text{accr}}/r)$ deposited at the shock level. Here the Eddington luminosity is that calculated with the total opacity at level r in the inflow. The above condition becomes

$$L + \frac{GM\dot{M}_{accr}}{2r} < \frac{4\pi c GM}{\kappa(r)} . \tag{22.9}$$

This yields a maximum accretion rate $\dot{M}_{max}$,

$$\dot{M}_{max} = \frac{8\pi c r}{\kappa(r)} - \frac{2Lr}{GM} = \frac{8\pi c r}{\kappa(r)} \left(1 - \frac{L}{L_{Edd}}\right) , \tag{22.10}$$

r being the level where most energy is deposited. Above 100 $M_\odot$, the intrinsic stellar luminosity tends toward L_{Edd}; thus the maximum possible accretion rate goes down (Fig. 22.3). If the shock occurs at some larger distance r of the star, the maximum permitted accretion rate is larger, because the infalling matter does not fall deep into the potential well. Above the heavy dotted line in Fig. 22.3, the accretion luminosity is larger than the intrinsic stellar luminosity, if so we may ignore the stellar luminosity and have

$$\dot{M}_{max} \approx \frac{8\pi c r}{\kappa(r)} . \tag{22.11}$$

This maximum accretion rate is illustrated by the upper line in Fig. 22.4 (there, the addition of the stellar luminosity to the accretion luminosity is not made, otherwise the curve would turn down as in Fig. 22.3). For massive stars of about 100 $M_\odot$, accretion rates up to 3×10^{-2} $M_\odot$ yr^{-1} are possible. This figure applies to electron scattering opacity. For dust opacity, which is larger by typically 1–2 orders of a magnitude (cf. Sect. 22.3.2), the maximum possible accretion rate is smaller. However, account has also to be given that the appropriate r is larger. The maximum possible accretion rate is a critical limit, certainly influencing the upper mass limit of the IMF. Full model including the details of the disk, the shock and dust opacities is necessary for accurate modeling. On the right side of Fig. 22.4 a T scale is indicated. This is the temperature necessary to have the thermal hydrostatic support of the initial cloud. According to (19.24), $\dot{M}_{accr} \approx c_s^3/G$. With the isothermal sound velocity $c_s = [kT/(\mu m_u)]^{\frac{1}{2}}$ (Appendix C.3), we get

$$T \approx \frac{\mu m_u}{k} \left(G\dot{M}_{accr}\right)^{\frac{2}{3}} , \tag{22.12}$$

 for the necessary temperature to support the initial cloud. Actually, this is an upper bound of the cloud temperature, since other sources of support such as magnetic field and especially turbulence are present in regions of massive star formation. Higher T gives higher $\dot{M}_{accr}$, because more thermal support in the cloud permits a denser cloud to be in equilibrium; thus its free-fall time is shorter.

22.3.2   Conditions on Dust Opacity

The value of the dust opacity in an accretion flow plays a critical role in massive star formation, since it is the largest opacity source, much larger than the electron scattering opacity (Fig. 22.5). The shock is at some distance r of the protostar where the dust is the main opacity source with values $\kappa = 10$–100 cm^2 g^{-1}. A high opacity reduces $\dot{M}_{max}$. The above condition (22.8) for a star of mass M and luminosity L can also be expressed as a condition on the maximum opacity which permits accretion for a given star. Numerically this is [627]

$$\kappa < 3.9 \left(\frac{M}{30 \, M_\odot} \right) \left(\frac{L_{tot}}{10^5 \, L_\odot} \right)^{-1} \text{cm}^2 \text{ g}^{-1} . \tag{22.13}$$

Since a MS star of 30 $M_\odot$ has about a luminosity of 10^5 $L_\odot$, this condition is rather severe in view of the values in Fig. 22.5. The need to reduce the opacities in order to form massive stars is also found in models of spherical accretion [616]: a dust-to-gas ratio reduced by a factor of 4 appears necessary, as well as an absence of the largest graphite grains in the size distribution. At some radius r_{sub}, dust sublimates ($T_{sub} \approx 1800$ K). If the inflow is not stopped above this level, it will reach the star since below r_{sub} the opacity is much lower. On the contrary, if the inflow is stopped before r_{sub}, accretion is terminated and the star has reached its final mass.

The maximum mass limit depends critically on T_{sub}, which defines the inner boundary of the dust shell or cocoon. Except for a narrow region close to this inner boundary, the radiation field in the cocoon is re-radiated dust emission from the in-
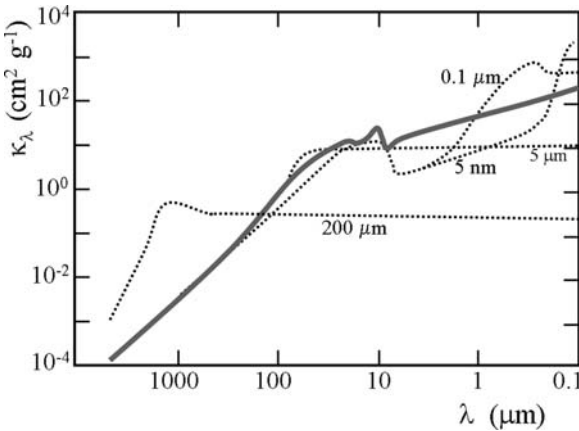
Fig. 22.5 Extinction coefficients for a mixture of dust and gas with a dust-to-gas mass ratio of 0.01. The *thick line* represents the dust models of Preibisch et al. [478] for dust grains of carbon and ice-coated silicates, which well reproduce the IR and far-IR spectra of protostellar sources. The *other lines* represent the coefficients for silicate grains of various radii. Grains currently have diameter distributions between 0.005 and 0.25 μm. Adapted from H.W. Yorke [627]

ner part of the cocoon. The temperature of this radiation field is thus close to T_{sub}. The lower the T_{sub}, the cooler the radiation field; thus the maximum of radiation is shifted to longer wavelengths, where the opacity is lower. As the radiative acceleration is proportional to the product $\kappa(r)\, F_r$ of the opacity by the flux, the lower the T_{sub}, the higher the upper limiting mass of the IMF. Models of spherical accretion suggest that the maximum mass–luminosity ratio behaves like [616]

$$\frac{L}{M} \sim T_{sub}^{-3} \, . \tag{22.14}$$

There are some effects which may alleviate the opacity problem:

– As a result of a high enough accretion, a photosphere may form with a T_{eff} lower than that of the stellar core. If so, the radiation from a massive protostar is shifted from UV to IR and the relevant opacity for accretion becomes smaller (Fig. 22.5).
– The distribution of the grain sizes could be modified by the young protostar, with some destruction of dust and a lowered dust-to-gas ratio.
– Coagulation of grains leading to higher grain radii may lead to a reduction of the opacity in dense regions such as the accretion disk.
– The accretion of optically thick blobs of mass M_{blob} and radius R_{blob} is also a way to reduce the opacity [627], which becomes

$$\kappa \sim \frac{\pi R_{blob}^2}{M_{blob}} \, . \tag{22.15}$$

The formation of stars by collision or coalescence (cf. Sect. 22.1.2) is an extreme case of such a process.
– In rotating models with an accretion disk, the problem of dust opacity is less severe (Sect. 22.3.4).

22.3.3 The Lower Limit on Accretion Rates

As shown in Fig. 22.4, there are also lower limits on the accretion rates. The most stringent one is due to a condition on the momentum: The outward momentum of the radiation field must be smaller than the momentum of the infalling matter. The momentum of the radiation is mostly deposited in a thin layer at the inner edge of the dust envelope. The momentum of a photon is $p = h\nu/c$; thus, for a star of luminosity L, the momentum is $p = (L/c)\Delta t$, where Δt is the unit of time. The momentum by unit of time and surface (i.e., the flux of momentum) is

$$F_{rad.\,mom.} = \frac{p}{4\,\pi r^2\,\Delta t} = \frac{L}{4\pi r^2\, c} \, . \tag{22.16}$$

The momentum of an element of gas of density ϱ and velocity v is $p = mv = \varrho\,\Delta V v$, where ΔV is the element of volume of thickness $\Delta \ell$. The flux of gas momentum is

$$F_{\text{gas mom.}} = \frac{\varrho \, \Delta V \, v}{4 \, \pi r^2 \, \Delta t} = \varrho \frac{\Delta \ell}{\Delta t} \, v = \varrho \, v^2 \; . \tag{22.17}$$

The mass conservation implies $\dot{M}_{\text{accr}} = 4\pi \, r^2 \varrho \, v$. The condition that the inward gas momentum must be larger than the outward radiation momentum becomes

$$\dot{M}_{\text{accr}} > \frac{L}{c \, v} \; . \tag{22.18}$$

The velocity v is estimated at the inner edge of the cocoon, where the momentum is deposited. For v we take the free-fall velocity $v_{\text{ff}} = (2 \, GM/r)^{\frac{1}{2}}$. This yields the condition

$$\dot{M}_{\text{accr}} > \frac{L}{c \, (2GM/r)^{\frac{1}{2}}} \; . \tag{22.19}$$

The value of r is also that of the inner edge of the cocoon, where the dust sublimates ($T_{\text{sub}} \approx 1800$ K).

Figure 22.4 shows this limit according to models of spherical accretion [616]. For example, accretion at rates of $\sim 10^{-5}$ M$_\odot$ yr^{-1} onto a 30 M$_\odot$ star is not possible. There are two other less severe limits. The limit, noted "timescale" in Fig. 22.4, is the limit below which the formation time would be longer than 10^6 yr, a value which is rather extreme. Below the limit noted "HII", an HII region forms and extends beyond the point of dust sublimation. This limit is not severe at least in Pop. I stars; however it may play a role in zero metallicity stars (Sect. 23.5.2).

22.3.4 *The Role of Rotation*

In the presence of rotation, the geometry of the accretion flow is not spherically symmetric and the formation of massive stars with lower accretion rates appears possible [436, 629]. Contracting clouds have a too large angular momentum to be directly accreted by the central protostar (Sect. 19.1). The infalling matter forms a large thick disk, which may extend up to several thousands of AU in agreement with the observations schematically represented in Fig. 22.2. Angular momentum is dissipated within the disk by the turbulent viscosity between the differentially rotating layers. The energy from rotation is partly radiated by the disk (the high density in the disk might favor for some time the growth of dust grains, lowering the opacity). Progressively, a fraction of the matter flows toward the inner disk. Then, from the disk to the star, the inflowing matter is not easily stopped by radiation, since dust is evaporated (cf. Fig. 22.6). A part of the infalling matter goes onto the central protostar while the rest is ejected as bipolar flows through a broad cavity, where radiation also escapes preferentially (Fig. 22.6). The infalling matter from the parent cloud forms shock fronts at the surface of the disk. Inside the radius r_{sub} of dust sublimation, located at $T_{\text{sub}} \sim 1800$ ($\kappa \approx 20$ cm^2 g^{-1}), dust is destroyed and the
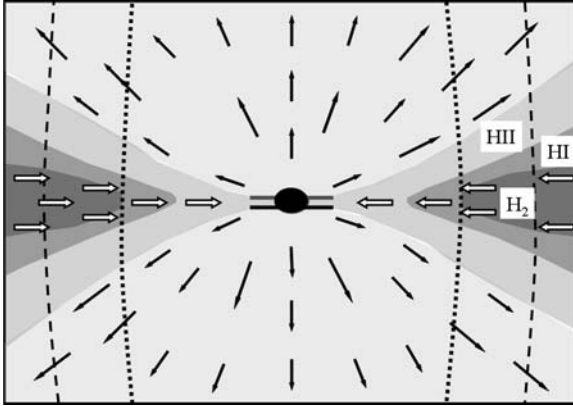
Fig. 22.6 The inner part of the accretion disk, corresponding to the central part of Fig. 22.2. Radiation and bipolar outflows produce evacuated low-density regions symmetrical around the rotation axis (vertical in the figure). These polar cavities are separated from the inner part of the accretion disk by HII and HI regions, with an ionization front at the interface of the two. In the inner part of the disk, molecular gas and dust may survive during the disk lifetime of about 10^5 yr. The *dotted line* shows r_{sub} the radius at which dust sublimates; the external *broken line* shows r_{esc} the radius beyond which the dust has an escape velocity below 10 km s^{-1}, allowing the gas to leave the disk when it photoevaporates. Adapted from H.W. Yorke [627]

effective opacity is lower. The radiation from the protostar and disk easily escapes in the lower density cavities and has little effect on the infalling matter within the optically thick disk. Such a protostellar system produces a spectrum which varies considerably according to the viewing angle, up to a factor 30 in bolometric luminosity (this is sometimes called the "flashlight" effect [629]). On the whole, rotation lowers the minimum accretion rate necessary to overcome radiation effects.

The polar outflows only have a small direct effect on the accretion disk; however radiation progressively photoevaporates the inner edges of the disk. Molecular gas and dust are surviving in the center of the disk outside a radius r_{sub} where the dust sublimates, molecules and dust are protected from destruction by the surrounding layers. Around the disk, there is an HI region; an ionization front separates this neutral region from the HII region. At some distance r_{esc}, the escape velocity is low enough so that the material which is photoevaporated escapes outward. Models yield [627] $r_{sub} = 25\,(M/30\,\mathrm{M_\odot})^{1.6}$ AU and $r_{esc} = 130\,(M/30\,\mathrm{M_\odot})$ AU. The radiative acceleration, the advance of the ionization front and the UV radiation from the ambient cluster lead to the progressive photoevaporation of the disk, which has a lifetime $< 10^5$ yr. The growth of the ionized bipolar cavity will at some stage inhibit further accretion from the parent cloud.

The present models do not account for the anisotropy of the radiation around a rotating protostar. Due to von Zeipel theorem (Sect. 4.2.2), T_{eff} is higher at the pole than at the equator. This anisotropy favors both the mass accretion from the disk in the equatorial plane and the outflow in the polar regions.

22.4   Accretion Models for Massive Star Formation

Ideally, a theoretical model treating simultaneously the cloud, the disk, the bipolar outflows and the protostar is necessary to determine the accretion rates $\dot{M}_{\mathrm{accr}}$ on the protostellar core, as well as the angular momentum of the infalling matter. For low and intermediate mass stars, the history of the accretion rate is not as critical as for massive stars, because the accretion timescale is shorter than the Kelvin–Helmholtz timescale. Thus, the accretion is completed rather early in the formation phase, especially for the lower mass stars. At the opposite for massive stars, the time evolution of $\dot{M}_{\mathrm{accr}}(t)$ most critically determines the evolution and its timescales.

22.4.1   Formation with Initially Peaked Accretion

Collapse models of slowly rotating massive molecular clumps show [630] that the treatment of the radiation transfer influences all results. A frequency-dependent opacity or a gray opacity does not give the same accretion rates (Fig. 22.7). For some values of initial parameters, a disk appears, which leads to an anisotropic distribution of radiation with a stronger flux at the poles, the anisotropy being more pronounced at short wavelengths. The more intense UV flux at the poles creates lower density polar cavities, with a reversal of the infall by the radiative force on the dust. The polar cavities are encased by shock fronts at the edge of the disk (Fig. 22.6), while the star still accretes material from the disk in the equatorial plane.
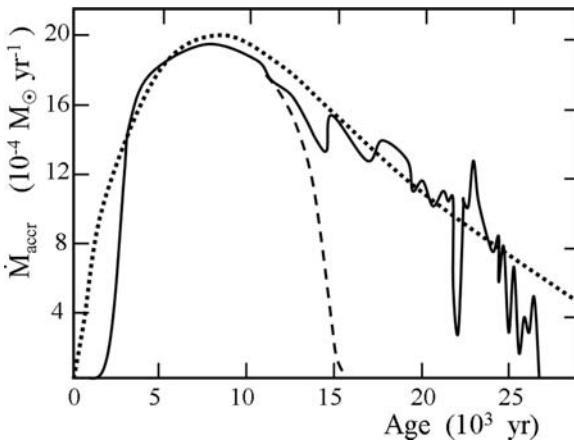
Fig. 22.7 Time evolution of the accretion rate in a model of a cloud clump collapse. The mass of the clump is 60 $M_\odot$ and the mass of the star after about 25000 yr is about 33 $M_\odot$. The *continuous line* refers to a model where a frequency-dependent opacity is considered, while the *dashed line* shows a gray case. Adapted from H.W. Yorke and S.R. Sonnhalter [630]. The *dotted line* shows the fitting formula (19.26) of S. Schmeja and S.R. Klessen [518] for $\dot{M}_0 = 2 \times 10^{-3}$ $M_\odot$ yr^{-1} and $\tau_0 = 8000$ yr

Initially during about 10^4 yr, the luminosity rises very rapidly due to the accretion energy deposited in the shock. However, after such a timescale, the accretion is no longer the dominant luminosity source, which is then due to stellar contraction. Figure 22.7 shows the time evolution of the accretion rates in a 60 $M_\odot$ clump leading to the formation of a 33 $M_\odot$ within 2.5×10^4 yr. $\dot{M}_{\mathrm{accr}}(t)$ grows sharply in 8000 yr and then declines progressively. The corresponding track (noted YS) in the HR diagram (Fig. 22.8) rises very steeply keeping at $T_{\mathrm{eff}} \approx 5000$ K. The photospheric radius at optical depth ≈ 1 is quite large as long as the accretion rate is high. Then, as accretion declines, the star becomes hotter and crosses the HR diagram: When accretion is over, the photospheric radius coincides with the star radius. Disks appear to be short-lived structures, with timescales less or equal to the accretion time. On the whole, numerical models show that massive stars can form through an accretion disk.
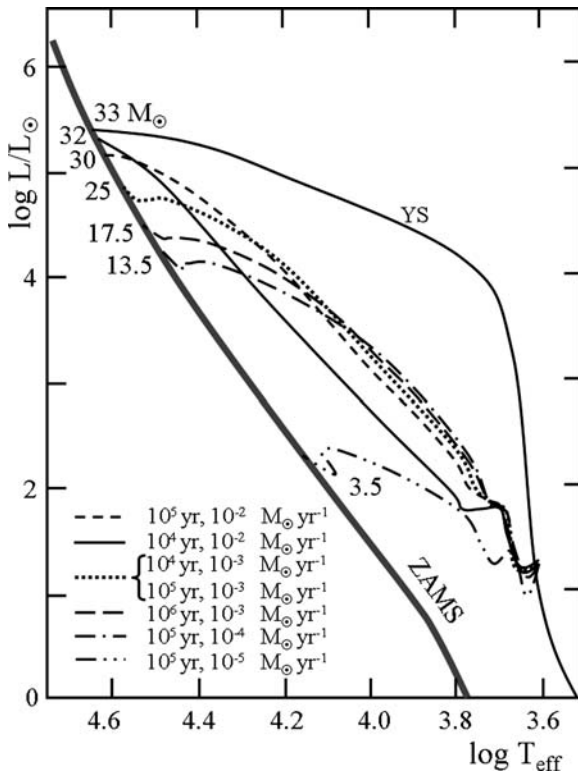
Fig. 22.8 Birthlines of massive stars for various accretion rates parametrized by (19.26) $\dot{M}(t) = \dot{M}_0 \frac{e}{\tau_0} t e^{-\frac{t}{\tau_0}}$ of S. Schmeja and S.R. Klessen [518]. The values of τ_0 and $\dot{M}_0$ in $M_\odot$ yr^{-1} are indicated, as well as the final masses on the ZAMS. These tracks do not account for the optically thick infalling matter. The track YS is from H.W. Yorke and C. Sonnhalter [630]; it accounts for the radiative transfer in the accretion flow and for the accretion luminosity. $L = 10^4$ $L_\odot$ is reached in 10^4 yr. From C. Peter [464]

Interestingly enough, the rates $\dot{M}_{accr}(t)$ from the above-mentioned numerical models have a behavior in time very similar to that illustrated in Fig. 19.2 and expressed by (19.26). The rates from the numerical models in Fig. 22.7 can be well fitted by a curve with a maximum accretion rate of $\dot{M}_0 = 2 \times 10^{-3}$ M$_\odot$ yr^{-1} and an age $\tau_0 = 8000$ yr with a cutoff at 25 000 yr. Noticeably, such a time sequence of $\dot{M}_{accr}(t)$ is in agreement with the sequence of events illustrated in Fig. 19.1, where $\dot{M}_{accr}$ shows an early peak.

Figure 22.8 shows [464] the HR diagram of the accreting stellar cores for a family of birthlines with accretion rates based on expression (19.26) for various choices of the maximum accretion rate $\dot{M}_0$ and of the age τ_0 of this maximum. Figure 22.9 shows the same birthlines when the accretion luminosity $L = G\dot{M}M/(2R)$ is added to the luminosity of the stellar cores. Figures 22.10 and 22.11 show the corresponding mass–luminosity and mass–radius relations, where the luminosity is the internal luminosity of the accreting stellar core and R is the radius of this core. We discuss these figures simultaneously and notice the following properties:

1. In Fig. 22.8, the core birthlines of stellar cores represent an extension toward high masses of the birthlines for intermediate stellar masses (Fig. 20.3). The higher the maximum accretion rate $\dot{M}_0$, the larger the final stellar masses. Very large timescales, like $\tau_0 = 10^6$ yr, lead to smaller masses on the ZAMS, since the star reaches the ZAMS before accretion is completed.
2. In Fig. 22.8, more massive stars arrive on the ZAMS at a shorter age than smaller final masses. Thus, if $\dot{M}_{accr}(t)$ is high at the beginning (19.26), *the most massive stars form faster*. The 30 M$_\odot$ star forms in about 10^4 yr, the 25 M$_\odot$ in 30 000 yr, the 13.5 M$_\odot$ in 1.5×10^5 yr. This behavior is opposite to that obtained from accretion rates growing with time.
3. The birthline by Yorke and Sonnhalter [630] noted "YS" in Fig. 22.8 results from numerical models of clump collapse. The account of the accretion luminosity in addition to the intrinsic luminosity and of the radiative transfer (with the optically thick inflow) produces larger luminosities and radii than those of the protostellar cores. The account of the accretion luminosity makes a fast initial growth of L. The differences between the track "YS" and the core tracks in Fig. 22.8 are mostly due to these two effects. Because of the disk, the radiation of the accreting star is highly anisotropic (Fig. 22.6): real objects may lie between the photospheric and the stellar core birthline depending on the angle of view.
4. The evolution of the model with $\tau_0 = 10^4$ yr and $\dot{M}_0 = 10^{-3}$ M$_\odot$ yr^{-1} in Fig. 22.9 is rather similar to the track by Yorke and Sonnhalter in Fig. 22.8. Also the timescales are comparable, both reach the knee where the star starts crossing the HR diagram almost horizontally in about 10^4 yr and reach the ZAMS in about 2.5×10^4 yr. This shows the capacity of these simple accretion models to reproduce a more complex physics and to explore a range of parameters.
5. At low accretion rates (e.g., 10^{-5} M$_\odot$ yr^{-1}), an increase of $\dot{M}_{accr}$ shifts the birthline of stellar cores toward higher luminosities (cf. Sect. 20.3). This is not the case for the very high rates (e.g., 10^{-3} M$_\odot$ yr^{-1}) considered here. There, higher accretion rates reduce the luminosities of a large part of the birthlines (Fig. 22.8). This is because fast-accreting stars are initially much out of equilibrium as

illustrated in Fig. 22.10, where we see that rapidly growing stars are underluminous with respect to the ZAMS for a large part of the track.

6. Stars on the birthline up to a mass of 2.5 $M_\odot$ are overluminous with respect to stars on the ZAMS, due to contraction and D burning. Then, they are strongly underluminous: The internal contraction produces a huge internal bump of luminosity of the kind illustrated in Fig. 20.7, which finally emerges at the stellar surface when the star reaches thermal equilibrium near the ZAMS. The rise in luminosity is large (Fig. 22.10) and governed by the Kelvin–Helmholtz timescale.

7. Figure 22.11 shows the mass–radius relations for stellar cores on various birthlines. These curves are similar to those for the formation of low and intermediate mass stars in Figs. 20.3 and 20.4 with a shift of the peak of radius toward higher masses. Up to a peak accretion rate of 10^{-3} $M_\odot$ yr s^{-1} (thick dotted line), the radius at the peak value increases with the maximum accretion rate, then the peak radius decreases especially if the accretion is rapid (τ_0 small). The accretion timescale is so short that the thermal inflation of the radius does not have the time to occur before the star is completed (and then it has a short Kelvin–Helmholtz timescale permitting it to settle on the ZAMS).

The above results well illustrate that the pre-MS evolution of massive stars is different from that of solar-type stars (Sect. 20.4), being essentially determined by the history of the accretion rate, since the Kelvin–Helmholtz is very short. An initial peak or bump in the accretion rates produces birthlines which join the ZAMS at very high luminosities; the birthlines are initially close to the Hayashi line before turning
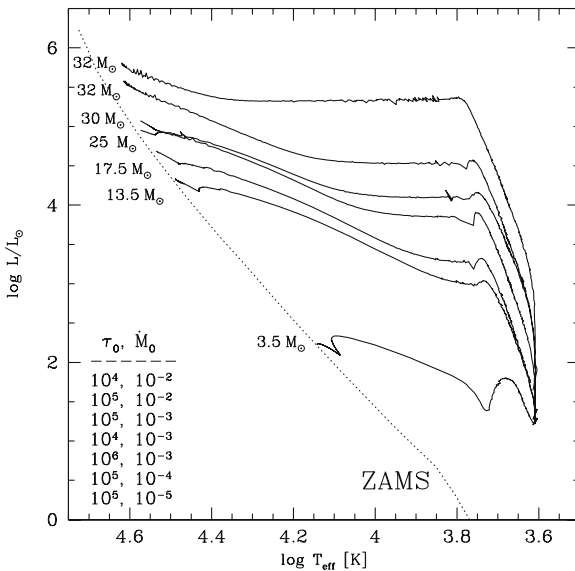
Fig. 22.9 Birthlines calculated with the accretion rates given by (19.26) as in Fig. 22.8. The values of the parameters τ_0 and $\dot{M}_0$ are indicated from the top to the bottom. The difference with Fig. 22.8 is that the luminosity here also accounts for the accretion luminosity L_{accr}. From C. Peter [464]
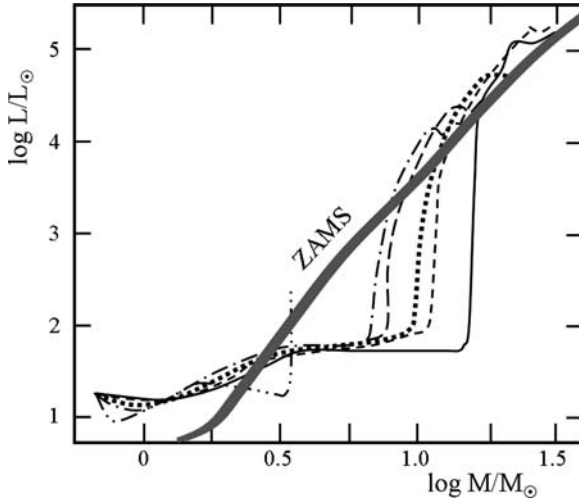
Fig. 22.10 Relation between luminosities and masses for stars on the various birthlines calculated with (19.26). The notation of the lines are the same as in Fig. 22.8. The *thick continuous line* shows the relation for stars on the ZAMS [464]
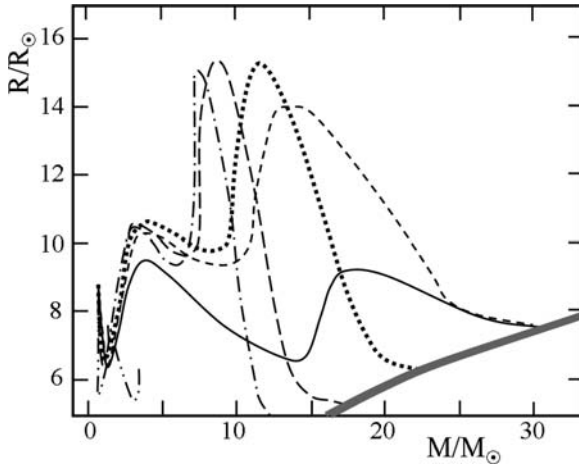
Fig. 22.11 Relation between radius and masses for stars on the various birthlines calculated with (19.26). The notation of the lines is the same as in Fig. 22.8. The *thick continuous line* shows the relation for the ZAMS [464]

almost horizontally toward the ZAMS. For initially peaked accretion rates, the most massive stars have smaller ages, of the order of 25 000 yr for a 30 $M_\odot$ star on the ZAMS. Finally, we notice that such an evolution and age are not very different from that of the classical pre-MS tracks at constant mass (Table 20.1).

Some models with accretion rates growing with time or with the mass already accreted have also been computed [42, 394, 443]; they differ from models of cloud

collapse [518] and imply that the more massive stars would form later than less massive stars.

22.4.2   The Churchwell–Henning Relation

It is interesting to superpose to the outflow rates in Fig. 22.1 the accretion rates given by expression (19.26) for $\dot{M}_0 = 2 \times 10^{-3}$ M$_\odot$ yr^{-1} and $\tau_0 = 8000$ yr corresponding to the numerical models [630] described in Fig. 22.7. This is shown by the gray line in Fig. 22.1. The adjustment of the two curves depends on the ratio of the accretion to the outflow rates. They are likely of the same order and for simplicity let us assume that the inflow and outflow rates are equal; however different ratios may be considered. The important result of Fig. 22.1 is that *the Churchwell–Henning relation appears to correspond to the upper envelope of an individual stellar path in the diagram of the accretion rates vs. the luminosity* as illustrated in Fig. 22.7. We note the following properties.

– The individual stellar path is close to the envelope over three to four decades in luminosity.
– For a large fraction of its formation time, an accreting star lies close to the Churchwell–Henning relation, i.e., for about 1.5×10^4 yr (over a total accretion time of 2.5×10^4 yr) in the case of the 33 M$_\odot$ star model [630].
– The star leaves the Churchwell–Henning relation, when the accretion rates fall down, i.e., when the star has almost reached its final stellar mass.
– There should be evidence of less active bipolar outflows below the Churchwell–Henning relation.

The Churchwell–Henning relation is a most valuable indication about the outflow and accretion rates near their maximum intensity, i.e., during a significant part of the accretion time.

Chapter 23
The Formation of First Stars in the Universe: Pop. III and Pop. II.5 Stars

The formation and evolution of the first stars is linked to great astrophysical and cosmological problems such as the reionization of the Universe, the search for $Z = 0$ stars, the chemistry of the most metal-deficient stars, the nature of the first supernovae, the γ-ray bursts (GRBs). The initial mass function (IMF) of the first stars and their mass limits are among major questions.

The differences between the formation at $Z_{\odot}$ and $Z = 0$ come mainly from the absence of dust in the interstellar gas. There is thus no cooling by collisions between dust grains and H_2 molecules, thus T in the interstellar medium is a few 10^2 K instead of 10–20 K, which has major consequences:

1. The collapse and fragmentation at very low Z are difficult, leading to large and rare fragments, at least below $Z \approx 10^{-3.5} \, Z_{\odot}$.
2. The hotter pre-stellar clouds can sustain a higher pressure and thus are more compact. In turn, the accretion rates which scale like $\dot{M}_{\mathrm{accr}} \sim c_{\mathrm{s}}^3/G$ are much higher than at solar Z, since the sound speed $c_{\mathrm{s}} \sim \sqrt{T}$.
3. At the same time, the radiation pressure of the star has less effect on the infalling matter, since there is no dust and the gas opacity is lower. This reduces the feedback from the protostar on the infalling material.

These effects suggest that the first stars were in general more massive ($\geq 10^2$ $M_{\odot}$) than at solar Z. This is true in an unperturbed medium. However, in regions (still at $Z = 0$) which have been ionized by shocks from supernovae or from the assembly of galactic material, deuteride HD is present producing an efficient cooling of the gas down to the CMB radiation at redshifts $z = 10 - 20$, i.e., a few 10 K. This leads to the formation of stellar masses of ~ 10 $M_{\odot}$, i.e., an order of magnitude less than for Pop. III and an order of magnitude more than for Pop. II and I. This second population at $Z = 0$ is called Pop. II.5 and it may contain much more stars than Pop. III [221, 275].

23.1   The Pre- and Protostellar Phases at $Z = 0$

The cosmological context is determined by the growth of density fluctuations, the evolution of the Jeans mass and the cooling processes at redshifts $z \leq 10^3$. Cold dark matter models suggest [211] that the first protogalaxies have a mass of the order of 10^4 M$_\odot$ and form at a redshift of $z \sim 40$. However, these very first protogalaxies are unlikely to form stars, because molecular H$_2$, which is the main cooling component (Sect. 23.1.1), has a very low abundance and thus cooling is very inefficient. More massive protogalaxies forming at $z \sim 30$ with mass 10^5–10^6 M$_\odot$ and temperatures of the order of $T = 10^2$–10^3 K are likely the first star-forming entities. The large optical depth to electron scattering observed by WMAP is currently interpreted as supporting massive star formation at redshifts above $z = 15$ [67].

23.1.1   Molecular H$_2$ and Gas Cooling

As for Pop. I stars, cooling is also necessary for cloud collapse and fragmentation to proceed (Sect. 18.4.3). While at solar Z, dust grains are the main cooling agents, the dominant coolant in the unperturbed medium at $Z = 0$ is molecular hydrogen H$_2$ (in medium having experienced strong ionizing shocks, molecule HD is the main coolant, Sect, 23.6.1). If heavy elements are present, H$_2$ would form mainly on dust grains. At $Z = 0$, the grain channel of H$_2$ formation is absent. H$_2$ cannot form by the simplest reaction H + H $\rightarrow$ H$_2$+ γ which is forbidden. At hydrogen concentrations $n_{\rm H}$ below 10^8 cm^{-3}, the two reaction chains operate:

$$\mathrm{H} + \mathrm{e}^- \rightarrow \mathrm{H}^- + \gamma \quad \text{and} \quad \mathrm{H}^- + \mathrm{H} \rightarrow \mathrm{H}_2 + \mathrm{e}^-,$$
$$\mathrm{H} + \mathrm{H}^+ \rightarrow \mathrm{H}_2^+ + \gamma \quad \text{and} \quad \mathrm{H}_2^+ + \mathrm{H} \rightarrow \mathrm{H}_2 + \mathrm{H}^+.$$
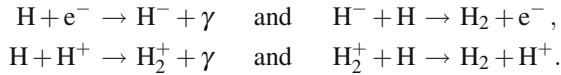
The formation of H$_2$ requires free electrons and protons, which are rare, but not totally absent after the cosmological phase of recombination. However, when a protogalaxy forms, the recombination rate increases, and free e$^-$ and H$^+$ disappear. A brief slot of conditions remains where H$_2$ can form [439] reaching a mass fraction of 10^{-3}–10^{-4} in protogalaxies. At concentrations above $n_{\rm H} = 10^8$ cm^{-3}, the following three-body reactions,

$$\mathrm{H} + \mathrm{H} + \mathrm{H} \rightarrow \mathrm{H}_2 + \mathrm{H} \quad \text{and} \quad \mathrm{H} + \mathrm{H} + \mathrm{H}_2 \rightarrow \mathrm{H}_2 + \mathrm{H}_2, \quad (23.1)$$
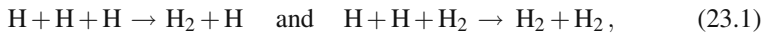
can significantly contribute to the formation of H$_2$ molecules. The cooling rate $\Lambda_{\rm H_2}$ by H$_2$ behaves [211] approximately like

$$\Lambda_{\rm H_2} \sim n_{\rm H_2}^\gamma T^\alpha \quad (23.2)$$

with $\alpha \approx 3$–5, the exponent (higher at lower T from about 10^2–10^4 K), and $n_{\rm H_2}$ the concentration of H$_2$ molecules. For concentrations below $n_{\rm H_2} = 10^4$ cm^{-3}, radiative

de-excitation dominates and $\gamma = 2$, while above this concentration collisional de-excitations dominate and $\gamma = 1$.

At solar Z, the cooling rate by dust grains is so high that the cooling time t_{cool} is much shorter than the free-fall timescale. Thus, the collapse proceeds isothermally over 10 orders of magnitude in density (Sect. 18.4). The lack of efficient cooling drastically affects the evolution of a cloud at $Z = 0$. Initially at relatively low T, the cooling rate Λ_{H_2} is negligible and the first stages of the collapse proceed nearly adiabatically. The gas reaches a temperature $T = 10^3$ K. The increase of T and n_{H_2} due to contraction then leads to a steep growth of the cooling rate Λ_{H_2}. Thus, the cooling time decreases until it becomes about equal to the free-fall timescale. The collapse is no longer adiabatic. As it further proceeds, the increase of density makes the H_2 cooling dominant over heating. The question is now whether this cooling is sufficient to drive cloud fragmentation at $Z = 0$.

23.1.2 Fragmentation of Metal-Free Clouds

At solar Z, the decrease of the Jeans mass during the isothermal collapse leads to cloud fragmentation (Sect. 18.4.3), with denser clumps collapsing faster in the hierarchical fragmentation, which ends when the gas becomes optically thick. Is there an efficient fragmentation at $Z = 0$? In this context, we may recall that even at solar Z, due to angular momentum problems, fragmentation may not be as efficient as ideally supposed.

At $Z = 0$, fragmentation is likely inefficient, because on one side the cooling processes in protogalaxies are much weaker and on the other side the thermal energy content is higher than at solar Z. The large thermal pressure creates a peaked density distribution in the protogalactic cloud at $Z = 0$. This gives fast contraction at the center, which may lead to the formation of one or several stars, before the rest of the protogalactic cloud has the time to fragment. These first stars will then produce a positive feedback: the shock from supernovae may enable the formation of HD molecules favoring Pop. II.5 star formation (Sect. 23.6). There is also some negative feedback: UV radiation may photodissociate H_2 and HD molecules inhibiting further formation. The development of an ionization front is also able to overrun the dynamics of the halo and to expel the gas [611]. These massive first stars are perhaps at the origin of the massive black holes in the center of active galactic nuclei.

When the metallicity of gas clouds is enriched up to a limit of about $Z = 10^{-5}$, the usual scenario of star formation applies (Sect. 18). In particular, cooling by ionized carbon or neutral oxygen [68] is efficient and can lead to the formation of low-mass stars as soon as C and O have abundances up to about 10^{-3} solar. This is not inconsistent with the finding of a few low-mass stars with $M \approx 0.8$ M$_\odot$ and an iron content of $\sim 5 \times 10^{-5}$ solar.

At $Z = 0$, rotation may have a positive effect for star formation unlike what happens at solar Z. Rotation by delaying the collapse of the central parts of a protogalactic cloud may give time [64] to other fragments for collapsing and possibly

merging into some more clumps. Turbulence and magnetic fields are likely of negligible importance for the first star generation, due to the absence of driving and dynamo.

On the whole, clumps rarely form at $Z = 0$, but when they form stellar contraction leads t_{cool} to decrease down to t_{ff} (Sect. 23.1.1). As cooling becomes important, the gas evolves from $T \approx 10^3$ K to $T \approx 200$ K and a concentration of H atoms $n_H \approx 10^4$ cm^{-3}. These T and n values appear in many simulations to correspond to a preferred stage of the gas [65, 67]. The Jeans mass at this stage is about 10^3 M$_\odot$. The facts that the Jeans mass of protostellar clumps is so high and that further fragmentation is unlikely suggest that the stars which form at $Z = 0$ are massive with mass likely ≥ 100 M$_\odot$. At densities higher than 10^4 cm^{-3}, H$_2$ cooling increases with density less than before, i.e., like n instead of n^2 (23.2). Eventually heating starts dominating again and will continue to do so for the rest of the evolution. Thus, the minimum fragments which may form in this whole process of contraction are those corresponding to these particular values of $n_H \approx 10^4$ cm^{-3} and $T \approx 200$ K. This sequence of events at $Z = 0$ is determined by the physics of cooling as it emerges from recent simulations [2, 65, 66].

23.1.3   Formation of an Adiabatic Core

Contraction continues in the cloud fragment, whether there is only one or a few of them and the internal density increases. Figure 23.1 illustrates the sequence of events occurring [491] in models of a collapsing cloud at $Z = 0$, including the thermal pressure and the pressure ionization effects, as well as the effects of radiative forces. Model calculations start at $T = 270$ K, $n_H = 2.6 \times 10^6$ cm^{-3} and a fraction of H$_2$ molecules of 5×10^{-4}. At the beginning, a self-similar density profile of the form $\varrho \sim r^{-2.2}$ develops in the outer parts of the cloud fragment (up to stage 5 in Fig. 23.1); this slope is close to the one found above (Sect. 18.4.2). When concentration n_H becomes higher than 10^8 cm^{-3}, the three-body reactions (23.1) convert most of H into H$_2$; this occurs between stages 1 and 3. The cooling rate thus increases, which favors contraction (stages 3–5). Radiative transfer becomes more complex since the cloud becomes optically thick in the vibration and rotation lines of the H$_2$ molecules at concentration $n_H \approx 10^{13}$ cm^{-3}. Cooling still occurs through the wings of H$_2$ lines which are optically thin and also from the continuum radiation which becomes dominant above $T = 1800$ K. Above $T = 1550$ K, H$_2$ starts to dissociate slowly after stage 3 (panel d), which takes a considerable energy and prevents fast increases in T and pressure P after the end of the self-similar phase. For $T \geq 2350$ K (stage 4), central regions become almost adiabatic. Even when $T = 15000$ K, the H$_2$ fraction in the center is 0.05. Molecules H$_2$ fully disappear at $T = 20000$ K with $n_H = 10^{23}$ cm^{-3}, their thermostatic action is then absent: T and P increase fast and the central collapse is halted.

A small hydrostatic core forms with a mass of about 0.005 M$_\odot$ in which matter soon becomes fully ionized. This core mass is essentially independent of the initial conditions chosen in the simulations. In panel (b) of Fig. 23.1, in the last models
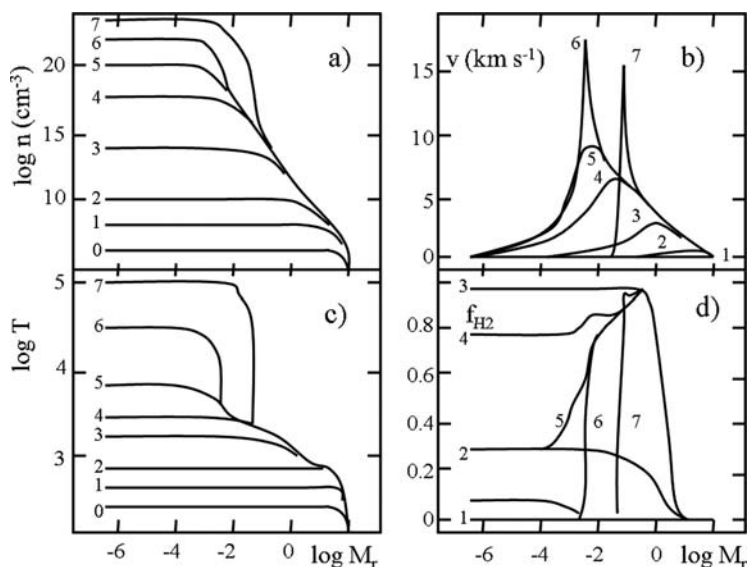
Fig. 23.1 Evolution of the structure of a cloud fragment of $10\,M_\odot$ at eight stages of the collapse. The models are labeled from 0 to 7. The panels show (**a**) the concentration n, (**b**) the infall velocity, (**c**) T and (**d**) the fraction f_{H2} of the H nuclei which are inside H_2 molecules. The horizontal axis expresses the enclosed mass in solar units within the cloud. The age zero is at model 0 with $T = 270$ K, the age is 720000 yr in model 1, 739000 yr in model 2, 739990 yr in model 3, 739999.6 yr in model 4 where H_2 is dissociating, then the successive models are within a fraction of year. A core has formed in model 6. Adapted from E. Ripamonti et al. [491]

the infall velocity is zero within the core. Outside the small core, the gas is still collapsing in almost free fall. A shock develops at the edge of the core, which exerts a compression on the central regions and the core temperature and density reach, respectively, 10^5 K and 0.3 g cm^{-3}. The shock progressively moves outward as matter is continuously accreted.

Interestingly enough, the opacity-limited fragmentation at $Z = 0$ leads to about the same lower stellar mass limit as at solar Z. This mass value is evidently not the final mass for most of the stars, since matter accretion from the cloud fragment determines the further evolution. As mentioned in Sect. 18.4.5, if for some reason accretion would be stopped, for example if the core is ejected by a dynamical interaction, some small stars like brown dwarfs could directly result from these small initial cores.

23.1.4   Accretion on the Core

The accretion rate $\dot{M}_{accr}$ and its evolution are the key parameters for $Z = 0$ stars, as is the case at higher Z (Sect. 20.3). After the formation of a small core, there are still

large amounts of H_2 in the outer regions external to the front shock at the edge of the core. A large H_2 shell is visible at stage 7 in panel (d) of Fig. 23.1; it is surrounded by a cloud of atomic hydrogen, which contains most of the cloud mass. Accretion of mass with the velocity and density of model 6 in Fig. 23.1 proceeds on the central core at rates of 10^{-2}–10^{-3} $M_{\odot}$ yr $^{-1}$, higher than the rates of intermediate mass stars at solar Z. The reason is straightforward: the accretion rate $\dot{M}_{accr}$ scales like the mass M of the gas cloud divided by the free-fall time

$$\dot{M}_{accr} \sim \frac{M}{t_{ff}} . \tag{23.3}$$

The free-fall time (18.23) behaves like $t_{ff} \sim \bar{\varrho}^{-1/2}$, where $\bar{\varrho}$ is the mean density. The initial mass, before fragmentation, is necessarily close to the Jeans mass which behaves like (18.5) $M_J \sim \left(T^3/\bar{\varrho}\right)^{1/2}$, thus the accretion rate scales like

$$\dot{M}_{accr} \sim M_J \varrho^{\frac{1}{2}} \sim T^{\frac{3}{2}} . \tag{23.4}$$

Since the temperature of the primordial gas is typically in the range of 200–1000 K instead of about 10–20 K at solar Z, the accretion rates are about 2–3 orders of magnitude higher than at solar Z. In numerical simulations [67], the accretion rates decrease from initial values of a few 10^{-2} $M_{\odot}$ yr^{-1} in the first years of collapse down to a few 10^{-3} $M_{\odot}$ yr^{-1} at an age of 10^5 yr. With such rates, a star of 200 $M_{\odot}$ forms in 10^5 yr. The above values are representative of existing simulations. Clouds initially in equilibrium with higher T and ϱ would have higher accretion rates.

While the formation of the small core is independent of the initial conditions in the cloud, this is not true for the further accretion rates, since they depend much on the T conditions in the cloud fragment. The accretion rate is also influenced by the radiation field of the central regions, which may reduce it. This effect is much less important at $Z = 0$, due to the absence of dust, than at solar metallicity. Other effects like the rotation of the contracting fragment, the mechanisms of transport of angular momentum and the formation of a disk may also play a role in the growth of the stellar mass. For now, the simulations of the evolution of the central accreting object generally assume a given accretion rate and do not calculate the cloud hydrodynamics, which is studied in other models.

23.2   The Mass–Radius Relation of $Z = 0$ Stars

After the formation of a protostellar core of about 0.005 $M_{\odot}$, the evolution becomes non-adiabatic and proceeds in a slower way determined by both the Kelvin–Helmholtz and accretion timescales t_{KH} and t_{accr}. The evolution can be treated as that of a hydrostatic core with an increasing mass determined by the accretion rate. The accretion of matter produces a shock, which is inside an optically thick ionized region. The outer edge of this ionized region almost coincides with the photospheric
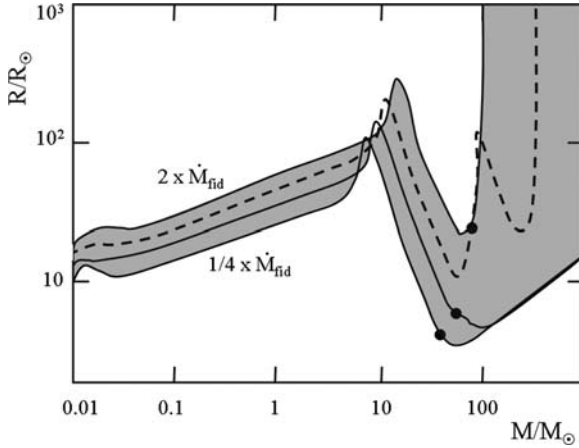
Fig. 23.2 Mass–radius relations for Z=0 stars on the birthline for different accretion rates 2, 1, (1/2) and (1/4) $\dot{M}_{\rm ref}$ (*gray* zone), where the reference value $\dot{M}_{\rm ref} = 4.4 \times 10^{-3}$ M$_\odot$ yr^{-1} (*dashed line*). The beginning of the H burning through the CN cycle is indicated by *black dots*. Adapted from K. Omukai and F. Palla [448]

radius. The radiation field has little effect until the core mass reaches a value as large as about 10^2 M$_\odot$.

The mass–radius relation M vs. R of these accreting protostars evolving on the birthline also presents the main effects appearing in the formation at solar composition (Sect. 20.4). In Fig. 23.2, the evolution is shown for four different values of $\dot{M}_{\rm accr}$ around a reference value of 4.4×10^{-3} M$_\odot$ yr^{-1}. This value of $\dot{M}_{\rm accr}$ corresponds to an ambient temperature of 1700 K. However, the evolution is soon independent of the initial conditions adopted in the starting model, except for the accretion rates.

Three phases can be distinguished [448] if accretion continues up to large masses at $Z = 0$. Let us consider the first two in this section.

1. **Adiabatic accretion phase up to about 10 M$_\odot$:** For such relatively small masses, the Kelvin–Helmholtz timescale $t_{\rm KH}$ is longer than the accretion timescale $t_{\rm accr}$ (20.3.1), thus the star has no time to thermally adjust. The radiative cooling is small. As a result, there is a gradual increase in the radius of the form $R \sim M^{0.27} \dot{M}_{\rm accr}^{0.41}$ [448] as illustrated on the left part of Fig. 23.2. Consistently, the growth of the mass leads to an increase of the temperature like $T \sim M/R \sim M^{0.73}$, which reduces the opacity and produces a steep increase of the peak interior luminosity when the mass is about 5 M$_\odot$ (Fig. 23.3). The arrival of the luminosity wave at the surface leads to an inflation of the star near 10 M$_\odot$. D burning does not play a big role.

2. **Kelvin–Helmholtz contraction phase from 10 to about 60 M$_\odot$:** Radiative equilibrium is achieved and the opacity in this hot medium is $\kappa_{\rm es}$ due to electron scattering, which implies $L \sim M^3$ (24.55). Thus the Kelvin–Helmholtz timescale $t_{\rm KH}$ behaves like
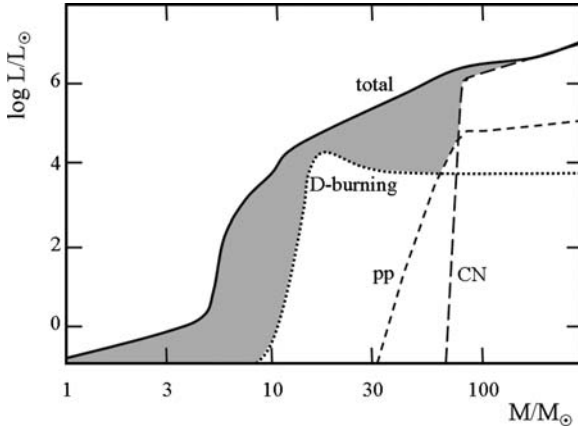
Fig. 23.3 Evolution as a function of the growing mass on the birthline at $Z = 0$ of the maximum of the interior luminosity (*continuous line*), of the contribution of D burning (*dotted line*), of the pp chain (*short-dashed line*) and of the CN cycle (*long-dashed line*). This refers to the reference accretion rate of 4.4×10^{-3} M$_\odot$ yr^{-1}. The difference between the total and nuclear luminosities is due to gravitational contraction (*gray area*). Adapted from K. Omukai and F. Palla [448]

$$t_{KH} = \frac{GM^2}{RL} \sim \frac{1}{MR} . \tag{23.5}$$

The radius being large at the end of the previous phase near $10\,M_\odot$, one has $t_{KH} < t_{accr}$. This favors prompt thermal adjustments and fast radiative losses, which make the core to shrink. Thus, in the part of the birthline (like it was for $M > 4.5\,M_\odot$ at solar Z), R decreases and a stage is reached where $t_{KH} \approx t_{accr}$, which gives

$$R \sim \frac{\dot{M}_{accr}\, M}{L} \sim \frac{\dot{M}_{accr}}{M^2} . \tag{23.6}$$

This implies a fast decrease of the radius as mass is growing (Fig. 23.2) and the star is evolving toward the ZAMS. During this contraction, the L/M ratio increases considerably. Various sources contribute to the stellar luminosity (Fig. 23.3). Deuterium ignites off-center when the mass is above $10\,M_\odot$ and soon the luminosity from D burning settles at a nearly constant level determined by the accretion rate. On the whole, D burning does not play an important role. Then, the pp chain enters in significant activity around $50\,M_\odot$; however, the rate of nuclear production is insufficient to compensate for the outgoing luminosity and thus to halt collapse. Contraction stops only when the hydrogen burning by the CN cycle starts (Fig. 23.3). This happens when the CN mass fraction, resulting from a short phase of triple α burning, is about 10^{-9} at a central temperature of about 10^8 K. This brings us to the third phase which concerns the very massive stars on the birthline.

23.3   Evolution of the Largest Masses at $Z = 0$

Let us follow the evolution of the very massive stars on the birthline. The fast global contraction stops soon after H ignition by the CN cycle. As shown in Fig. 23.2, this happens in the range of masses above about $60 \, M_\odot$ according to the rate of mass accretion. The further evolution of the continuously accreting objects is different depending on whether the accretion rate $\dot{M}_{accr}$ is smaller or larger than some reference rate of $\dot{M}_{ref} = 4.4 \times 10^{-3} \, M_\odot \, \mathrm{yr}^{-1}$ [448]; the reason is shown here (Sect. 23.3.1).

   At moderate accretion rates: For rates equal or lower to $\dot{M}_{ref}/2$, the models relax rapidly to the ZAMS (Fig. 23.4) which is reached at about 50–$60 \, M_\odot$. For rates lower than this limit, models with different $\dot{M}_{accr}$ follow a single mass–radius relation (Fig. 23.2) above $100 \, M_\odot$, which is characterized by a slow radius increase. The energy is entirely supplied by the CN cycle (Fig. 23.3). As mass is growing, the convective core occupies an increasing mass fraction, up to about 90% or more. Above $100 \, M_\odot$, the zero-metallicity stars obey a single mass–luminosity relation of the form

$$\frac{L}{L_\odot} = 1.6 \times 10^6 \left(\frac{M}{100 \, M_\odot} \right)^{1.35} . \tag{23.7}$$

The exponent of the M–L relation is small due to the high radiation pressure (Sect. 24.3.1). The luminosity largely remains below the Eddington limit. Thus, if the local reservoir of matter is sufficient, the accretion may continue to proceed without experiencing significant opposition from the stellar radiation pressure. The mass of the newly formed stars in this mass domain is set by the amount of circumstellar material available, which could be accreted during the stellar lifetime. The upper limit could be as high as $600 \, M_\odot$ [448]. However, a detailed study of the ionization zone around these hot stars is needed to see whether an HII region can reverse the infalling gas. This appears not to impose a severe mass limit [447], see Sect. 23.5.

   At high accretion rates: For accretion rates equal to or larger than $\dot{M}_{ref}$, the total luminosity which is the sum of the accretion and interior luminosities reaches the Eddington limit before hydrogen ignition. The strong radiation force provokes a fast expansion of the outer layers. The star does not set on the mass–radius and mass–luminosity relations (23.7), which characterize the moderately accreting stars as seen above. The expansion makes the temperature in the outer layers to decrease and thus the opacity to increase, which in turn accelerates the expansion. This results in a stripping of the surface layers, since the core radius reaches the photospheric radius (Fig. 23.4). Likely, there is even a reversal of the accretion in these supra-Eddington conditions. Thus, the accretion is over and the star relaxes on the ZAMS (Fig. 23.4) with a mass of about $300 \, M_\odot$ for an accretion rate $\dot{M}_{ref}$; for twice this rate, this mass would be about $90 \, M_\odot$. Thus, the upper mass limit is set by the accretion rate. The limit is lower for higher accretion rates, since the Eddington luminosity, with the corresponding radius inflation, is reached at a lower mass.
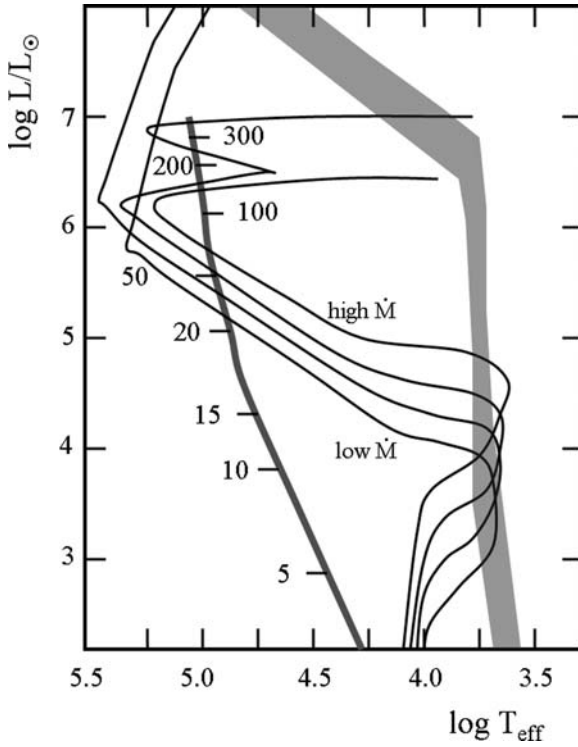
Fig. 23.4 The birthlines of primordial stellar cores for four different accretion rates equal to $1/4$, $1/2$, 1.0 and 2.0 times $\dot{M}_{\text{ref}} = 4.4 \times 10^{-3}$ $M_\odot$ yr^{-1}. The luminosities are in solar units. The temperatures T_{eff} are those of the accreting cores. The *gray area* shows the location of the stars if their photospheric temperature is represented. The ZAMS from non-accreting models is indicated by a thick line with masses in solar units. Adapted from K. Omukai and F. Palla [448]

It is unlikely that the accretion rates remain constant. The rates are determined by the evolution of primordial collapsing clumps. Models for such clumps evolution at $Z = 0$ [2] lead to rates close to $\dot{M}_{\text{ref}}$ up to 95 $M_\odot$, then they become smaller. If this happens, the star avoids the phase of fast expansion and settles on the ZAMS.

23.3.1   Critical Accretion for Massive Stars at $Z = 0$

Indeed, a critical accretion rate separates the above two kinds of evolution: (1) settling on the ZAMS given by (23.7) or (2) fast inflation stopping accretion. This critical accretion can be derived in a simple way, by equaling the total luminosity of the star (interior and accretion luminosities) to the Eddington luminosity. Accretion rates higher than this limit are not possible. The critical rate $\dot{M}_{\text{crit}}$ is defined by

$$L_{\text{tot}} = L_{\text{ZAMS}} + \frac{GM\dot{M}_{\text{crit}}}{R_{\text{ZAMS}}} = L_{\text{Edd}} . \tag{23.8}$$

The critical accretion rate is

$$\dot{M}_{\text{crit}} = \frac{4\pi c R_{\text{ZAMS}}}{\kappa_{\text{es}}} \left(1 - \frac{L_{\text{ZAMS}}}{L_{\text{Edd}}} \right) . \tag{23.9}$$

For the stellar masses of interest, one gets an estimate $\dot{M}_{\text{crit}} \approx 4 \times 10^{-3}$ $M_{\odot}$ yr^{-1} [448] for typical values of radius and luminosity. This critical rate is close to the reference value chosen above. Indeed, this is quite consistent, since rates of the order of $\dot{M}_{\text{ref}}$ or above lead to fast inflation bringing a halt to the accretion, since their total luminosity becomes supra-Eddington already during the Kelvin–Helmholtz contraction. On the contrary, stars with accretion rates lower than $\dot{M}_{\text{ref}}$ have a total luminosity which remains below L_{Edd}, at least until they reach the ZAMS, where their further evolution is determined by accretion or mass loss and internal evolution.

23.4   The HR Diagram of Accreting Stars at $Z = 0$

Figure 23.4 shows the HR diagram with the birthlines for the four different values of $\dot{M}_{\text{accr}}$ considered in the mass–radius relation (Fig. 23.2). ZAMS models of non-accreting metal-free stars are also shown. There are differences of T_{eff} between (1) the non-accreting models on the ZAMS, which are calculated with standard atmospheric boundary conditions; (2) the stellar cores, calculated without their optically thick atmosphere due to accretion, this produces objects of higher temperature when they reach the corresponding ZAMS; and (3) the photospheric radius located at optical depth $\tau \approx 2/3$ in the accreting wind. These differences are illustrated in Fig. 23.4.

We well recognize the upward evolution in the HR diagram of the growing cores during their adiabatic phase up to masses of about 10–20 $M_{\odot}$. Then, in the phase of fast contraction, the stellar cores cross the HR diagram and move to their own ZAMS located to the left of the usual ZAMS. The accreting models have an optically thick envelope at $\tau \approx 1$ in the accreting wind. Initially, over a large range of L, these photospheric T_{eff} (gray area in Fig. 23.4) are about constant near 6000 K; this is due to the strong growth of the H^{-}-bound–free opacity with temperature. The increase of the stellar mass leads to an increase of L, which produces the ionization of the medium, and electron scattering becomes the main opacity source in the accreting envelope. This strongly increases the previously low photospheric temperature, which becomes close to that of the stellar core. The two tracks of the core and envelope join at the top of the HR diagram.

23.4.1   The Case of Non-zero Metallicities

Pollution by heavy elements occurs very fast in the early evolution of a galaxy and soon some pre-stellar clumps in a galaxy reach metallicities Z of the order of 10^{-4}

$Z_\odot$. For such Z values, the evolution in the adiabatic and contraction phases shows some differences with respect to the case with $Z = 0$. Due to the higher CN abundance, the H burning starts at a lower T compared to the case of $Z = 0$, thus the contraction phase stops earlier leading to a larger stellar radius on the ZAMS. As a consequence the critical accretion rate $\dot{M}_{crit}$ (23.9) is 1.4 times larger at $Z = 10^{-6}$ than at $Z = 0$ and a factor of 2 at $Z = 10^{-4}$ [448]. Thus, the star may keep accreting at high rates with less chances to reach the Eddington luminosity and to experience violent expansion. Thus by increasing the value of $\dot{M}_{crit}$, a non-zero metal abundance contributes to favor the formation of very massive stars. When the metallicity is above a limit of the order of $Z \approx 10^{-4}$, star formation behaves more as for solar composition (Sect. 18).

23.4.2 The Role of Rotation

In the presence of rotation, the infalling gas is accreted onto a disk and a part of the disk material is further accreted onto the protostar, while the rest is evacuated in bipolar outflows. Thus, the growth of the stellar mass is mainly determined by the disk properties. However, apart from determining the accretion, the disk has relatively limited effects on the evolution of the protostar [564]. The star on the birthline evolves through the same sequence of an adiabatic phase, followed by a fast contraction phase ending to the ZAMS.

The main difference concerns the photosphere. Due to the disk, the gas density is reduced in the regions close to the protostar and out of the disk plane. The small optical depth of these regions makes the photosphere smaller and hotter than in the spherical case. This produces a rapid increase in the ionizing and far-UV luminosity, which may increase the radiative feedback on the infalling gas and reduce the accretion. At the opposite, the anisotropy of the stellar radiation field due to von Zeipel's relation (Sect. 4.2.2) will lead to a reduction of T_{eff} in the equatorial plane favoring accretion.

In view of the accumulating evidences of faster initial rotation velocities at lower Z (Chap. 29), the problems of rotation in the formation of $Z = 0$ and very low-Z stars are gaining importance.

23.5 The Upper Mass Limit at $Z = 0$

The value of the maximum stellar mass in the first stellar generation has far-reaching consequences, as it determines the reionization of the Universe, the type of the first supernovae and the initial galactic enrichments.

23.5.1 Main Effects

Different effects may influence the maximum scale of stellar mass according to the range of metallicities Z considered:

– Limit due to radiation pressure: At high enough metallicities, the reversal of the infall by radiation pressure on dust grains is the main effect limiting stellar masses. This process is important when the dust opacity becomes large, say at least larger than electron scattering opacities. For a current dust opacity of $30 \, \mathrm{cm^2}$ g^{-1}, the dust opacity is sufficient to reverse the infall for Z above 2×10^{-4}. This is the prevailing effect limiting the formation of massive stars in the Galaxy at present (Sect. 22).
– Limit due to the formation of an HII zone: The formation of HII region prevents further accretion, due to the steep gradients of temperature and pressure created at the outer edge of the HII region. This is a process present at all metallicities; however, at solar Z the radiation force on dust grains sets a more stringent upper mass limit.
– Limit due to the fragment mass: For metallicity above $Z \approx 10^{-5}$, fragmentation forms a mass spectrum rich in low-mass stars as is the case at solar Z. Thus, above $Z \approx 10^{-5}$ fragmentation is a dominant effect limiting and shaping the mass spectrum, together with the infall reversal by dust grains. On the contrary as seen above, the limit due to the fragment mass is not stringent at $Z = 0$. At very low metallicities $Z < 10^{-5}$, large fragments may form up to about $10^3 \, \mathrm{M_\odot}$. Thus, it is likely that the maximum mass is determined by the amount of mass which may be accreted in the process of star formation.

Among the effects which may inhibit accretion at very low Z, the formation of an HII ionization zone could be important and this is what we examine.

23.5.2 HII Region in a Free-Falling Envelope

The accretion rate onto a protostar is significantly reduced, if the protostar is able to transfer enough momentum to the infalling gas. The opacity due to H_2 lines is at most 5% of the electron scattering opacity and thus the stellar L should be much larger than the current Eddington luminosity for this effect to operate. However, the formation of an HII region around stellar cores with $T \sim 10^5$ K may prevent further accretion, because of the ability of its high T and pressure to halt the infall. A condition is that the photosphere vanishes or becomes itself ionized. From Fig. 23.4 this is the case for the largest stellar masses when they settle on the ZAMS, for not too high $\dot{M}_{\mathrm{accr}}$.

The ionization of the gas represents a lot of thermal energy. The HII region expands up to such a large radius that the hot ionized gas in the external parts of the HII region is no longer bound, thus there can be no further accretion. Let us examine the formation of an HII region in a free-falling envelope at $Z = 0$ [447]. In spherically

symmetric infall with the free-fall velocity u and accretion rate $\dot{M}_{\text{accr}}$ around a star of mass M, we have

$$u = -\left(\frac{2GM}{r}\right)^{\frac{1}{2}} \quad \text{and} \quad \dot{M}_{\text{accr}} = -4\pi r^2 \varrho u , \tag{23.10}$$

with $u < 0$ for inward motions. This gives a density profile

$$\varrho = \frac{\dot{M}_{\text{accr}}}{4\pi(2GM)^{\frac{1}{2}}} r^{-\frac{3}{2}} . \tag{23.11}$$

The number Q of ionizing photons emitted by a unit of time is for a gas in photoionization equilibrium between the interior radius R_{int} and the outer radius R_{HII} of the HII region [447]

$$Q = \int_{R_{\text{int}}}^{R_{\text{HII}}} \alpha_{\text{rec}} n(H^+) n(e) \, dV . \tag{23.12}$$

Here, $n(H^+)$ and $n(e)$ are the concentrations of H^+ ions and electrons; one assumes that the gas is composed only of ionized hydrogen, so that $n(H^+) = n(e) = \varrho/m_{\text{p}}$, where m_{p} is the proton mass. The term α_{rec} is the effective hydrogen recombination coefficient ($\alpha_{\text{rec}} = 2.6 \times 10^{-13}$ cm^3 s^{-1} at 10^4 K) in the so-called on-the-spot approximation, where it is assumed that the whole radiation with energy above the ionization energy is absorbed, while below it the medium is supposed to be transparent. The flux of photons entering the HII region is ignored. We can integrate (23.12) with the density profile (23.11) and obtain

$$Q = \frac{\alpha_{\text{rec}} \dot{M}_{\text{accr}}^2}{8\pi G m_{\text{p}}^2 M} \int_{R_{\text{int}}}^{R_{\text{HII}}} \frac{dr}{r} = \frac{\alpha_{\text{rec}} \dot{M}_{\text{accr}}^2}{8\pi G m_{\text{p}}^2 M} \ln\left(\frac{R_{\text{HII}}}{R_{\text{int}}}\right) . \tag{23.13}$$

This gives an exponential growth of the outer radius of the HII zone if the number of emitted photons $Q > Q^{\text{ff}}$

$$R_{\text{HII}} = R_{\text{int}} \, e^{\left(Q/Q_{\text{crit}}^{\text{ff}}\right)} , \tag{23.14}$$

with

$$Q_{\text{crit}}^{\text{ff}} = \frac{\alpha_{\text{rec}} \dot{M}_{\text{accr}}^2}{8\pi G m_{\text{p}}^2 M} = 1.0 \times 10^{51} \left(\frac{10^2 \, M_\odot}{M}\right) \left(\frac{\dot{M}}{10^{-3} M_\odot \text{yr}^{-1}}\right)^2 , \tag{23.15}$$

which is expressed in s^{-1}. This function is represented by the hatched area in Fig. 23.5 for two values of $\dot{M}_{\text{accr}}$. The limit $Q_{\text{crit}}^{\text{ff}}$, which decreases with mass, crosses the stellar emission rate Q at $\sim 300 \, M_\odot$ for $\dot{M}_{\text{accr}} = 10^{-3} \, M_\odot \, \text{yr}^{-1}$. Thus stars above about this limit cannot form because of the development of an ionized region with high T and pressure. For $\dot{M}_{\text{accr}} = 3.2 \times 10^{-3} \, M_\odot \, \text{yr}^{-1}$, the mass limit is $\sim 900 \, M_\odot$.
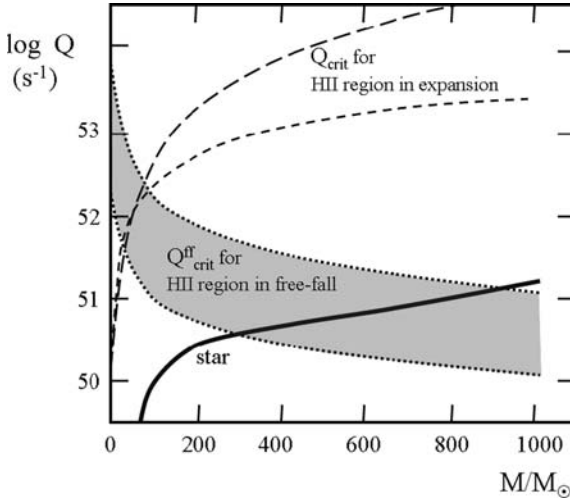
Fig. 23.5 The *continuous thick line* gives the number of ionizing photons Q emitted by $Z = 0$ stars as a function of mass. If the number of emitted ionizing photons from a star is higher than Q_{crit}^{ff}, an HII region in free-fall grows fast and the high P and T prevent star formation. The lower limit of the *gray zone* applies to $M_{accr} = 10^{-3}$ M$_\odot$ yr^{-1}, the upper one to a rate 3.2 times larger. The two *upper dashed lines* show the limits Q_{crit} above which an expanding HII region has a photon emissivity which can halt the collapse (Sect. 23.5.3). The upper line (*long dashed*) does not account for the additional effect of electron scattering, while the lower line (*short dashed*) accounts for it. Adapted from K. Omukai and S. Inutsuka [447]

The mass limit for star formation at $Z = 0$ very much depends on the accretion rate and is thus uncertain. A value of about 300 M$_\odot$ may be a reasonable guess.

23.5.3 Radiation Effect on an HII Region

The gas is also subject to momentum transfer by the stellar ionizing radiation. This effect modifies the density profile in the HII region and resisting the gravity may prevent the collapse. Let us write the radiative force in the HII region by unit of mass [447], supposing a medium of pure hydrogen,

$$f_{rad} = \frac{h\,\nu_{ion}}{c}\,\alpha_{rec}\,\frac{n(H^+)\,n(e)}{\varrho}\,, \qquad (23.16)$$

where as in (23.12) the term $\alpha_{rec}n(H^+)\,n(e)$ is the number of efficient photons per cm^3 and per second. We take $h\,\nu_{ion} = 13.6$ eV, the ionization potential of H, as the mean energy of ionizing photons. We now define a radius R_H, called the Haehnelt radius [226], such that the radiative acceleration is

$$f_{rad} \equiv 4\pi G R_H \varrho\,. \qquad (23.17)$$

If we compare the above radiative acceleration with $g = G 4 \pi \varrho \, r^3/(3 r^2)$, the gravity for a sphere of matter with an average density ϱ around the source, one finds that the radiative acceleration dominates gravity for $r < 3 R_H$. From (23.16) and (23.17), we get with $n(H^+) = \varrho/m_p$

$$R_H = \frac{\alpha_{rec} \, h \, \nu_{ion}}{4 \pi \, c \, G m_p^2} \, . \tag{23.18}$$

Numerically $R_H \approx 26$ pc. The momentum equation of the gas for a steady flow within the HII region can be written with an account of the radiative acceleration

$$u \frac{du}{dr} = -\frac{GM}{r^2} + 4 \pi G R_H \varrho \, , \tag{23.19}$$

where the thermal pressure is neglected, owing to the fact that the flows are supersonic or at least close to sonic (this assumption should probably be released in future). If the velocity is uniform in the HII region, we get from (23.19) a distribution of density of the form $\varrho = M/(4 \pi R_H r^2)$. This r dependence of the density is similar to that of the singular isothermal sphere (Sect. 18.4.2) and steeper than (23.11) for a free-falling region. This is not surprising since here the HII region is supported by a constant radiative force by unit of mass. The critical number Q_{crit} of ionizing photons per unit of time for an HII region around a star, where gravity is balanced by the radiative acceleration, can be written with (23.12) and the above $\rho(r)$:

$$Q_{crit} = \frac{\alpha_{rec} M^2}{4 \pi m_p^2 R_H^2} \int_{R_{int}}^{R_{HII}} \frac{dr}{r^2} \approx \frac{c}{h \nu} \frac{GM^2}{R_H} \frac{1}{R_{int}} \, , \tag{23.20}$$

where the last expression is obtained by writing one term R_H with (23.18) and by making the assumption that $R_{HII} \gg R_{int}$. Numerically, this is

$$Q_{crit} \approx 0.64 \times 10^{53} \left(\frac{10 R_\odot}{R_{int}} \right) \left(\frac{M}{100 \, M_\odot} \right)^2 \quad s^{-1} \, . \tag{23.21}$$

This is the maximum emissivity (long-dashed line in Fig. 23.5) permitting accretion ($R_{int} = 10 \, R_\odot$ is assumed). We see that actual ionizing photon emissivity of $Z = 0$ stars is much lower than the critical limit calculated above. This means that the radiation in an HII region does not prevent the formation of massive stars, even as high as $10^3 \, M_\odot$.

Very massive stars are close to the Eddington limit and thus the radiation force due to electron scattering in the ionized region has also to be accounted for. This can easily be made [447] by using the fact that this is equivalent in the present context to a reduction of the gravity. We write $G_{eff} = G(1 - \Gamma)$, which by (23.18) leads to $R_{H,eff} = R_H/(1 - \Gamma)$ and finally to

$$Q_{crit,eff} \approx \frac{c}{h \nu} \frac{GM^2}{R_H} \frac{1}{R_{int}} (1 - \Gamma)^2 \, . \tag{23.22}$$

This relation is represented by the short-dashed line in Fig. 23.5. Although this limit is more constraining than (23.21), it does not really put a limit to the mass spectrum. The physical reason for the difference between (23.22) and (23.15) for the free-fall case is that in the present case, due to radiative term in (23.19), the infall velocity is lower than free-fall (this might justify the introduction of a pressure term in (23.19)). The radiative term makes the density law steeper and in turn the critical number of ionizing photon to produce an expansion of the HII zone is higher.

The global conclusion is that the formation of an HII region does not impose a stringent upper mass limit of $Z=0$ stars. This limit is much higher than at $Z_\odot$, likely reaching a few 10^2 $M_\odot$. However, this applies to stars formed in an unperturbed environment without shocks, otherwise the formation of HD molecules may lower the limiting mass (see below).

23.6   The Pop. II.5 Stars

In shocked and ionized regions left over from the first stars, the formation of deuteride HD is possible making more cooling than the H_2 molecules. These regions, still at $Z = 0$, reach lower T and experience more fragmentation, thus leading to masses of ~ 10 $M_\odot$ forming the Pop. II.5 stars.

23.6.1   HD Formation and Gas Cooling

The basic reactions creating HD in the ionized primordial gas are [197, 275]

$$e^- + H \rightarrow H^- + h\nu, \quad H^- + H \rightarrow H_2 + e^-, \quad D^+ + H_2 \rightarrow HD + H^+. \quad (23.23)$$
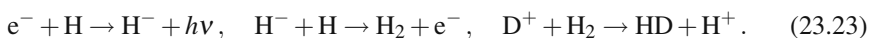
The conditions for this synthesis to occur is the existence of an ionized medium (e.g., to make e^- and D^+ and other ions) which then cools down. This may be achieved in a variety of conditions, in particular in fossil HII regions, resulting from the first supernovae or from the ionized regions made by the very luminous first stars, as well as from shocks in the galaxy formation.

Figure 23.6 illustrates the evolution of the abundances of the elements involved in the formation of HD as a function of T in the primordial gas at $Z = 0$ compressed and heated by the shock of a supernova. One sees the regular decline of the abundance of D^+ at $T < 8000$ K. Despite it, deuteride HD is created [275]. We also note the formation of D and H_2 at low T. HD can be photodissociated by UV photons, those emitted by the post-shock gas are insufficient to destroy the HD formed; however the situation may be different in an environment rich in massive $Z = 0$ stars.

HD molecules experience easier collisional excitation and have more frequent transitions than H_2, thus they make more efficient cooling. Instead of the typical $T \approx 200$ K seen above for H_2 (Sect. 23.1.2), the gas with HD molecules cools down
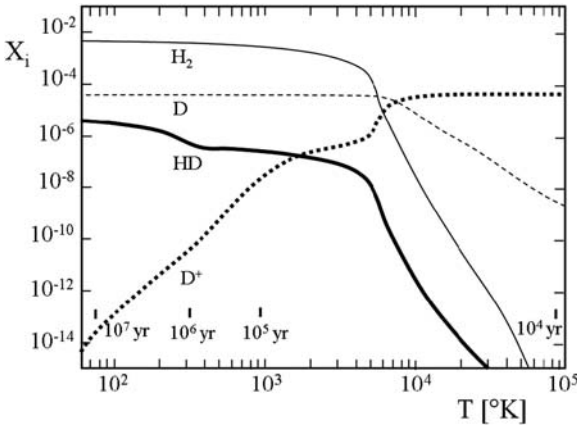
Fig. 23.6 The abundance of HD, H_2, D and D^+ as a function of T (with an approximate age scale) in the $Z = 0$ gas shocked by a supernova at redshift $z = 20$ (a velocity $v = 100\,\mathrm{km\,s^{-1}}$ is assumed in the shock, sufficient to produce about complete ionization). Adapted from J.L. Johnson and V. Bromm [275]

to a few 10 K, i.e., at the local T at redshift z of the cosmic microwave background (CMB), i.e.,

$$T(z)_{\mathrm{CMB}} = 2.7(1+z)\ \mathrm{K}. \tag{23.24}$$

The condition is that the abundance of deuteride HD is more than a minimum value of the order of 10^{-8} in mass fraction.

23.6.2 The Masses of the Pop. II.5 Stars

Let us estimate the typical mass of a Pop. II.5 star formed from the primordial gas shocked by a supernova [275]. One assumes that the HD abundance is sufficient for the gas to cool down to the CMB temperature at the redshift considered and that the gas cloud just before forming the star is a Bonnor–Ebert sphere (i.e., a truncated isothermal polytrope, Sect. 18.4.2). The mass of a Bonnor-Ebert sphere behaves like (18.43), i.e., $M_{\mathrm{BE}} \sim c_s^3/(G^{\frac{3}{2}}\varrho^{\frac{1}{2}})$,

$$\text{num. [456]:} \quad M_{\mathrm{BE}} \approx 700\,\mathrm{M}_\odot \left(\frac{T}{200\,K}\right)^{3/2} \left(\frac{n}{10^4\ \mathrm{cm}^{-3}}\right)^{-1/2}. \tag{23.25}$$

Here, T and n are the temperature and concentration of the post-shock gas at the time of star formation. If the strong shock has an isobaric evolution, the above T and n are related to the values T_{sh} and n_{sh} just after the shock by $n\,T = T_{\mathrm{sh}}\,n_{\mathrm{sh}}$. Let us write the concentration after the shock n_{sh} as $n_{\mathrm{sh}} = x n_0$, where n_0 is the pre-shock

concentration and x a numerical factor. Assuming that most of the kinetic energy of the gas with velocity v_{sh} at the time of the shock is converted into thermal energy, one has

$$k T_{sh} \approx m_H v_{sh}^2. \tag{23.26}$$

Expression (18.43) becomes in terms of T_{sh}, n_{sh}, with (23.26) and (23.24)

$$M_{BE} \sim T^{3/2} n^{-1/2} \sim T^{3/2} \frac{T^{1/2}}{T_{sh}^{1/2} n_{sh}^{1/2}} \sim (1+z)^2 (xn_0)^{-1/2} v_{sh}^{-1}, \tag{23.27}$$

$$\text{num. [275]} \quad M_{BE} \approx 4\,M_\odot \left(\frac{1+z}{21}\right)^2 \left(\frac{xn_0}{10^2 \text{ cm}^{-3}}\right)^{-1/2} \left(\frac{v_{sh}}{200\,\text{km s}^{-1}}\right)^{-1}. \tag{23.28}$$

The evolution of the baryonic matter in the Universe obeys the conservation law $\varrho R^3 = \text{const.}$ where R is the scale factor of the metric, which implies a concentration varying like

$$n_0 = n_1 \left(\frac{R_1}{R_0}\right)^3 = n_1 (1+z)^3, \quad \text{num.[275]} \quad n_0 = 0.3 \left(\frac{1+z}{21}\right)^3. \tag{23.29}$$

If one assumes that 30% of the mass in the Bonnor-Ebert cloud (23.28) is finally incorporated into the star, the typical stellar mass is [275]

$$M_{\text{Pop.II.5}}(z) \approx 20\,M_\odot \left(\frac{1+z}{21}\right)^{1/2} \frac{1}{x^{1/2}} \left(\frac{v_{sh}}{200\,\text{km s}^{-1}}\right)^{-1}. \tag{23.30}$$

This mass depends on the redshift z, since one has assumed that HD molecules are able to cool the contracting cloud down T_{CMB}. The earlier these Pop. II.5 stars form, the more massive they are on the average. The more intense the shock (higher v and x), the lower the masses. This suggests that the masses of the Pop. II.5 stars (with $Z = 0$) formed in a gas cloud which has gone through an ionized phase is about an order of magnitude smaller than the Pop. III stars ($Z = 0$) formed in a medium which has not experienced an ionizing shock. At $z = 10$, for $v_{sh} = 100, 200$ and $400\,\text{km s}^{-1}$, the typical mass (23.30) is 30, 14 and $4\,M_\odot$. Shocks may also be produced in dark matter galactic halos with $M > 10^8\,M_\odot$ during the assembly of the first dwarf galaxies. The Pop. II.5 stars formed in these conditions have a typical mass of $10\,M_\odot$ [275], i.e., of the same order as above.

In the above estimates, the effects of a possibly strong UV background have been neglected. If present, this would photodissociate the deuteride HD molecules (and H_2), thus preventing an efficient HD cooling. Thus, in regions of previous star formation, the UV emission and absorption should be accounted for a detailed modeling of the formation of Pop. II.5 stars.

As a summary, the first stars formed at $Z = 0$ in an unionized gas and cooling only through H_2 emission have masses of the order of $100\,M_\odot$ or more. After this first generation, the stars formed, still at $Z = 0$, in the gas ionized by the first stars have
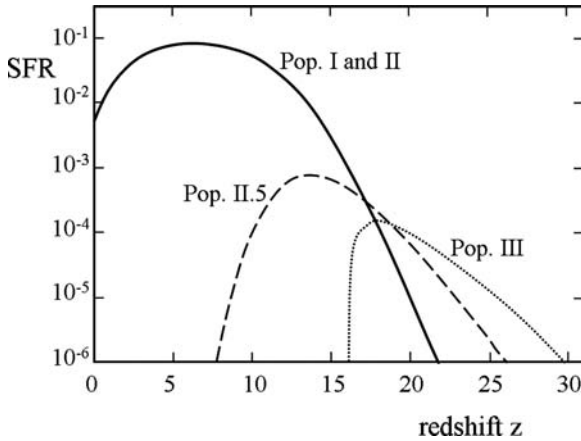
Fig. 23.7 The star formation rate in $M_\odot$ yr^{-1} Mpc^{-3} of Pop. III, Pop. II.5 and Pop. I/II as function of redshift. Adapted from T.H. Greif and V. Bromm [221]

masses of $\sim 10\,M_\odot$. Then, for metallicities Z higher than a few 10^{-4} star formation proceeds with the usual IMF of Pop. II and I peaking near $1\,M_\odot$. Figure 23.7 shows the possible star formation rates of these various populations [221]. The Pop. III stars are less important, representing about 10% by mass of $Z = 0$ star formation.

The question arises whether the account of the cooling by the HD molecules also modifies the formation of Pop. III stars born in an unperturbed environment. The answer is [490] that once the collapse has started HD cooling has a negligible importance. However, in an earlier stage of gas fragmentation for mass scale of $\sim 3 \times 10^5\,M_\odot$ HD cooling may lower T down to 50–100 K instead of 200 K, thus influencing the further star formation [490]. This may make the distinction of Pop. III and II.5 as in Fig. 23.7 a bit too schematic. On the whole, the conclusion is that a relatively broad spectrum of masses is not excluded for $Z = 0$ stars.

Part VI
Main-Sequence and Post-MS Evolution

Chapter 24
Solutions of the Equations and Simple Models*

Science is based on quantitative results. In astrophysics, these are obtained from observations and models. The key to progress is the close comparison of the two.

As the equations of stellar evolution have in general no analytical solutions, one solves them numerically, especially more than opacities and nuclear reaction rates are given as data tables. The numerical models or simulations of stellar evolution made great advances since the 1960s, thanks to the development of computers.

Many properties found by the numerical models can be derived analytically in a simplified and approximate way. Often, the analytical developments were made *after* the numerical models. The knowledge of the analytical relations is enlightening for the physical understanding of the astrophysical processes; this is why when possible we present them.

24.1 Hydrostatic and Hydrodynamic Models

Hydrostatic models apply when evolution is slow with respect to the dynamical timescale (1.28).

24.1.1 Hydrostatic Models and Vogt–Russel Theorem

We collect here the basic equations of equilibrium in Eulerian and Lagrangian forms (Table 24.1). These are the equations of hydrostatic equilibrium (1.6), of continuity (1.12), of energy equilibrium (3.40) and of energy transport, either radiative (3.17) or convective (5.57). In the interiors, convection is present if $\nabla_{\mathrm{rad}} > \nabla_{\mathrm{ad}}$ (Sect. 5.3), otherwise the transfer is radiative. The equation of state, opacities and nuclear reactions are expressed by the functions

$$\varrho = \varrho\,(P,T,X_i), \quad \kappa = \kappa(P,T,X_i), \quad \varepsilon = \varepsilon(P,T,X_i)\,, \tag{24.1}$$

---

*This chapter may form the matter of a basic introductory course.

Table 24.1 Basic equations in Eulerian and Lagrangian forms

	$\dfrac{dP}{dr}$	$=$	$-\dfrac{GM_r}{r^2}\varrho$	$\dfrac{dP}{dM_r}$	$=$	$-\dfrac{GM_r}{4\pi r^4}$
	$\dfrac{dM_r}{dr}$	$=$	$4\pi r^2 \varrho$	$\dfrac{dr}{dM_r}$	$=$	$\dfrac{1}{4\pi\varrho\, r^2}$
	$\dfrac{dL_r}{dr}$	$=$	$4\pi r^2 \varrho\,(\varepsilon + \varepsilon_{\text{grav}} - \varepsilon_v)$	$\dfrac{dL_r}{dM_r}$	$=$	$(\varepsilon + \varepsilon_{\text{grav}} - \varepsilon_v)$
rad :	$\dfrac{dT}{dr}$	$=$	$-\dfrac{3\kappa\varrho}{4acT^3}\dfrac{L_r}{4\pi r^2}$	$\dfrac{dT}{dM_r}$	$=$	$-\dfrac{GM_r T}{4\pi r^4 P}\nabla_{\text{rad}}$
conv :	$\dfrac{dT}{dr}$	$=$	$\dfrac{\Gamma_2 - 1}{\Gamma_2}\dfrac{T}{P}\dfrac{dP}{dr}$	$\dfrac{dT}{dM_r}$	$=$	$-\dfrac{GM_r T}{4\pi r^4 P}\nabla_{\text{ad}}$

generally given by numerical tables for different abundances X_i. We have a system of four first-order differential equations with four unknowns M_r, P, T, L_r as a function of r (Eulerian case), if $\varepsilon_{\text{grav}} = 0$. If not, $\varepsilon_{\text{grav}}$ has to be evaluated from the time derivative (3.64) with respect to previous models.

The chemical composition of the model needs to be specified; it normally results from previous evolution (Sect. 25.1.2). The simplest case is chemically homogeneous models, typically with hydrogen, helium and heavy element mass fractions $X = 0.70, Y = 0.28$ and $Z = 0.02$ (standard composition). The homogeneous composition is that of stars at the beginning of H burning on the zero-age main sequence (ZAMS) (only a few light elements are modified in pre-MS evolution, Sect. 20.7). The "best" initial solar composition is $X = 0.720, Y = 0.266$ and $Z = 0.014$ (Sect. 7.2; Appendix A.3). The four equations need boundary conditions. A zero-order approximation, e.g., in Eulerian form at $r = R$, is (see also Sect. 24.1.3)

$$L_r = L \quad M_r = M \quad P \approx 0 \quad T \approx 0. \tag{24.2}$$

We have four conditions with 3 free parameters R, L and M. Let us suppose that we integrate the four equations starting from the surface. When the center is reached, i.e., at $r = 0$, one should normally also have $L_r = 0$ and $M_r = 0$. This is not automatically the case for an arbitrary choice of R, L and M at the surface. This means that for a given M the other two surface parameters have to be adjusted until the integration leads simultaneously to $r = 0$, $L_r = 0$ and $M_r = 0$ when the center is reached. The two additional conditions at the center reduce the number of free parameters at the surface from three to one. Usually, one chooses the stellar mass M.

This leads to the Vogt–Russel theorem: The properties of a star of a given composition and in equilibrium are entirely determined by its mass M. The theorem is generally applied to chemically homogeneous stars; however we stress that this is not a necessity. There have been a number of rather academic discussions as to whether the Vogt–Russel theorem always applies. Indeed, there are cases where a minute change of composition may produce major changes of the overall parameters (such as the evolution from red supergiants to WR stars). However, thermal equilibrium is generally not satisfied in these cases. The Vogt–Russel theorem implies the existence of relations such as $L = L(M, \text{composition})$ and $R = R(M, \text{composition})$.

24.1.2 Hydrodynamic Equations

In a radially pulsating star or in rapid evolutionary phases (as in the protostellar phase or in the pre-supernova stage), the departures from hydrostatic equilibrium, i.e., the terms with $\ddot{r}$, are significant and Eq. (1.14) must be used. The time t appears as an independent variable in addition to M_r in the Lagrangian form, which is always used here. One introduces the velocity v as a new variable and the full set of equations becomes

$$\frac{\partial v}{\partial t} = -4\pi r^2 \frac{\partial P}{\partial M_r} - \frac{GM_r}{r^2} \, , \tag{24.3}$$

$$v = \frac{\partial r}{\partial t} \, , \tag{24.4}$$

$$\frac{\partial r}{\partial M_r} = \frac{1}{4\pi r^2 \varrho} \, , \tag{24.5}$$

$$\frac{\partial U}{\partial t} = -\frac{\partial L_r}{\partial M_r} + \varepsilon - \varepsilon_v - 4\pi P \frac{\partial (vr^2)}{\partial M_r} \, , \tag{24.6}$$

$$\text{rad}: \quad \nabla_{\text{rad}} = -\frac{3\kappa\varrho\, L_r P}{16ac\pi r^2 T^4} \frac{1}{(\partial P/\partial r)} \, , \tag{24.7}$$

$$\text{conv}: \quad \nabla_{\text{ad}} = \frac{\Gamma_2 - 1}{\Gamma_2} \, . \tag{24.8}$$

The derivative $(\partial/\partial M_r)$ is taken at a fixed t and $(\partial/\partial t)$ at a fixed M_r. The first equation is Euler's equation. The equation of energy equilibrium (24.6) requires some explanations. The expression of $\varepsilon_{\text{grav}}$ is (3.64)

$$\varepsilon_{\text{grav}} = -\frac{\partial U}{\partial t} - P \frac{\partial V}{\partial t} = -\frac{\partial U}{\partial t} + \frac{P}{\varrho^2} \left(\frac{\partial \varrho}{\partial t} \right)_{M_r} \, , \tag{24.9}$$

where U is the specific internal energy $U = aT^4/\varrho + (3/2)(kT/(\mu m_\text{u}) + \dots$. The continuity equation (1.1) gives

$$\frac{\partial \varrho}{\partial t}\bigg|_r = -\frac{1}{r^2} \frac{\partial (\varrho r^2 v)}{\partial r}\bigg|_t \, , \tag{24.10}$$

which is now used in

$$\frac{\partial \varrho}{\partial t}\bigg|_{M_r} = \frac{\partial \varrho}{\partial r}\bigg|_t \frac{\partial r}{\partial t}\bigg|_{M_r} + \frac{\partial \varrho}{\partial t}\bigg|_r = \frac{\partial \varrho}{\partial r}\bigg|_t v - \frac{1}{r^2} \frac{\partial (\varrho r^2 v)}{\partial r}\bigg|_t$$

$$= \frac{\partial \varrho}{\partial r}\bigg|_t v - v \frac{\partial \varrho}{\partial r}\bigg|_t - \frac{1}{r^2}\varrho \frac{\partial (r^2 v)}{\partial r}\bigg|_t = -\frac{1}{r^2}\varrho \frac{(\partial r^2 v)}{\partial r}\bigg|_t \, . \tag{24.11}$$

Thus, $\varepsilon_{\text{grav}}$ becomes

$$\varepsilon_{grav} = -\frac{\partial U}{\partial t} - 4\pi P \frac{\partial (r^2 v)}{\partial M_r}\bigg|_t . \tag{24.12}$$

The equation for L_r becomes (24.6) accounting also for ε_v. The two equations (24.7) and (24.8) are unmodified (Sect. 5.3). If the convective turnover time is not much shorter than the evolutionary timescale, time-dependent convection has to be applied (Sect. 6.3). The numerical solution of these equations requires great care in the process of discretization [404].

24.1.3   Boundary Conditions at the Center and Surface

Let us consider the Lagrangian form of hydrostatic equations. At the center, some equations diverge (e.g., the hydrostatic equilibrium). Thus, care has to be given. Near the center the density behaves like $\varrho(r) = \varrho_c + (d\varrho/dr)_c r$; because of the central symmetry one has $(d\varrho/dr)_c = 0$. Thus, the boundary condition for the continuity equation is $r = (3/(4\pi\varrho_c))^{1/3} M_r^{1/3}$. Similarly, one has for the energy equilibrium $L_r = (\varepsilon + \varepsilon_{grav})_c M_r$. The hydrostatic equilibrium gives, after integration,

$$\frac{dP}{dM_r} = -\frac{GM_r}{4\pi r^4} = -\frac{GM_r^{-1/3}}{4\pi}\left(\frac{4\pi\varrho_c}{3}\right)^{4/3}, \tag{24.13}$$

and

$$P - P_c = -\frac{3G}{8\pi}\left(\frac{4\pi\varrho_c}{3}\right)^{4/3} M_r^{2/3}. \tag{24.14}$$

Similarly, by expressing r and L_r in terms of M_r, and taking the opacity, density and energy production rates at the center, radiative and convective equilibria give respectively,

$$T^4 - T_c^4 = -\frac{1}{2ac}\left(\frac{3}{4\pi}\right)^{2/3} \kappa_c \left(\varepsilon + \varepsilon_{grav} - \varepsilon_v\right)_c \varrho_c^{4/3} M_r^{2/3}, \tag{24.15}$$

$$\ln T - \ln T_c = -\left(\frac{\pi}{6}\right)^{1/3} \left(\frac{G\nabla_{ad}\varrho^{4/3}}{P}\right)_c M_r^{2/3}. \tag{24.16}$$

In the hydrodynamic case, one evidently has $v = 0$ at the center.

Different codes handle the surface conditions in different ways. A good method to deal with the boundary conditions is the following one. One starts from the surface with the three parameters M, L and R. Let us introduce the optical depth τ as the independent variable in the atmosphere:

$$d\tau = -\kappa\varrho dr . \tag{24.17}$$

The equation of hydrostatic equilibrium becomes

$$\frac{dP}{dr} = -\varrho g \quad \Rightarrow \quad \frac{dP}{d\tau} = \frac{g}{\kappa(P,T)}. \tag{24.18}$$

This first-order differential equation is integrated in the atmosphere. Gravity g is constant. For the opacity, one uses a mean opacity, in general the Rosseland mean (3.22) although it is not very satisfactory in the atmosphere. The opacity is a function of (P,T). The temperature at a depth τ is given by the $T(\tau)$ relation, which for the gray case (κ constant) is [421]

$$T^4(\tau) = \frac{3}{4} T_{\text{eff}}^4 \left(\tau + \frac{2}{3}\right), \quad \text{for} \quad \tau = 0, \ T^4 = T_0^4 = \frac{T_{\text{eff}}^4}{2}. \tag{24.19}$$

It results from the transfer equation (3.8) applied to the gray case. This relation allows (24.18) to be solved: One starts from $\tau = 0$; with T as given above, the gaseous pressure is set to zero and the total $P = P_{\text{rad}} = (1/3)aT_0^4$. The integration is performed down to $\tau = 2/3$, where according to (24.19) one has $T = T_{\text{eff}}$, $P = P(\tau = 2/3)$ and $r = R$; the stellar radius R is by definition the radius at $\tau = 2/3$. For constant κ, one has from (24.18) $P(\tau = 2/3) = (2/3)GM/(R^2\kappa)$. The other quantities are $L_r = L$ and $M_r = M$. This means that, for a given mass M and composition, one has the values

$$\text{at } \tau = \frac{2}{3}: \quad L, \ T_{\text{eff}}, \ R, \ P(\tau = 2/3), \tag{24.20}$$

which may then be used as boundary conditions for the inward integration. The mass being given, these are not four boundary conditions, but only two, i.e., L and R, because T_{eff} and $P(\tau = 2/3)$ are derived from the first two.[1] Detailed ionization equilibrium, thermodynamic functions and non-adiabatic convection have to be treated in detail in the outer layers. There, the mass fraction M_r varies too slowly and is not an appropriate independent variable. Thus, one often takes $\ln P$ as the independent variable in the outer layers, as it varies significantly there.

24.1.4 Analytical Solutions in the Outer Layers

There are interesting approximations for the structure of both radiative and convective stellar envelopes. They evidently do not replace accurate numerical models, but they show us interesting properties. Let us divide the equation of hydrostatic equilibrium by the equation of radiative transfer in Eulerian coordinates (Table 24.1). We get after simplification by $r^2\varrho$

---

[1] In some codes, these two conditions (L,R) are replaced by analytical expressions relating P and T at some depth to L and R [285]. This allows one to avoid performing the outer integration at each step in a sequence of evolutionary models, because these relations are likely valid over 0.01–0.02 dex in L and R.

$$\frac{dP}{dT} = \frac{4\,ac}{3}\, 4\pi G \frac{M}{L}\frac{T^3}{\kappa} \, . \tag{24.21}$$

In the envelope, both M and L are about constant. Taking for κ the Kramers opacity law (8.43) and eliminating the density with (7.31), we get

$$\frac{dP}{dT} = \left(\frac{4\,ac}{3}\,\frac{k}{\mu m_{\mathrm{u}}}\,\frac{4\pi G}{\kappa_0}\,\frac{M}{L}\right)\frac{T^{7.5}}{P} \, . \tag{24.22}$$

The parenthesis containing only constant terms, we have

$$P = \left(\frac{1}{4.25}\,\frac{4\,ac}{3}\,\frac{k}{\mu m_{\mathrm{u}}}\,\frac{4\pi G M}{\kappa_0 L}\right)^{1/2} T^{4.25} \, . \tag{24.23}$$

The additive constant is zero, if for $P = 0$ one has $T = 0$. However, this is not necessarily the case and other boundary conditions (Sect. 24.1.3) may be taken. This applies to a radiative envelope. For an adiabatic convective envelope $\nabla_{\mathrm{ad}} = 2/5$ and we get according to the definition of $\nabla = d\ln T/d\ln P$ (3.75) for the same boundary conditions

$$P = f\,T^{2.5} \, , \tag{24.24}$$

where f is some constant. In a radiative zone T increases more slowly with pressure than in a convective zone, i.e., ∇ (here 0.235) $< \nabla_{\mathrm{ad}} = 0.4$.

It is interesting to examine how T varies with radius r. First in a radiative zone, deriving (24.23) and expressing the T gradient, we get

$$\frac{dT}{dr} = -\frac{1}{4.25\,T^{3.25}}\left(\frac{1}{4.25}\,\frac{4\,ac}{3}\,\frac{k}{\mu m_{\mathrm{u}}}\,\frac{4\pi G M}{\kappa_0 L}\right)^{-1/2}\frac{GM_r}{r^2}\varrho \, . \tag{24.25}$$

Eliminating ϱ with the law of perfect gas, we obtain with (24.23)

$$\frac{dT}{dr} = -\frac{1}{4.25}\,\frac{\mu m_{\mathrm{u}}}{k}\,\frac{GM}{r^2} \, . \tag{24.26}$$

This is easily integrated inward from (R, T_{eff}) to (r, T) and one obtains

$$T(r) - T_{\mathrm{eff}} = \frac{1}{4.25}\,\frac{\mu m_{\mathrm{u}}\,GM}{k}\left(\frac{1}{r} - \frac{1}{R}\right) \, . \tag{24.27}$$

The temperature in the outer layers varies like $\sim 1/r$. This is also true for a convective envelope. With (24.24) instead of (24.23), one obtains the same $(T - T_{\mathrm{eff}})$ relation except that the factor $1/4.25$ is replaced by $1/2.5$.

Expression (24.27) shows an important property: T_{eff} appears as an additive term to $T(r)$ for a given star. Thus, when at some depth T reaches values of 10^6 K or more, the fact that at the surface $T_{\mathrm{eff}} = 5800$ or 6000 K, as an example, makes no significant difference for $T(r)$ in the interior. This shows a general property of stellar

structure: The outer boundary conditions only have very little effects on the internal structure. In other words, for a star of given mass and composition, different surface conditions rapidly converge toward the same values in the stellar interior.

24.2 The Henyey Method

The first stellar models in the 1960s used a method, called the (U,V) plane method [523], where an outward integration from the center and an inward integration from the surface were made with the appropriate boundary conditions. The two solutions had to match somewhere in the interior, which requires some procedure to adjust the two surface conditions L and R.

The Henyey method [243, 285] has revolutionized stellar evolution (in mathematics, it is known as a relaxation method). A monument should be built to Henyey for his contribution, since most results of stellar evolution are indebted to it. The method can be applied to other systems of differential equations. The spherical star is divided in m concentric mass shells from the surface to the center. The point M_1 is at $\tau = 2/3$. The method is also applicable to rotating stars if the equations are written as in Sect. 2.

$$M_r = M \quad M_1 \quad M_2 \quad M_3 \qquad\qquad\qquad M_{m-1} \quad M_m$$

surface   center

For a MS model, one needs about 400 shells, for an AGB star several 10^3. In M_1, we have the two boundary conditions, which are in functional forms:

$$\mathcal{R}_1(r_1, P_1, T_1) = 0, \qquad \mathcal{R}_2(r_1, P_1, T_1) = 0. \tag{24.28}$$

These two equations might just be $r_1=R$ and $L_1=L$ or a more elaborate form (Sect. 24.1.3). The four differential equations (hydrostatic case) are replaced by four finite differences, as an example,

$$\frac{dr}{dM_r} = \frac{1}{4\pi r^2} \quad \Rightarrow \quad \frac{r_1 - r_2}{M_1 - M_2} = \frac{1}{4\pi} \frac{1}{r_{1+(1/2)}^2 \varrho_{1+(1/2)}}. \tag{24.29}$$

The variables with index $1+(1/2)$ are taken at an intermediate point, i.e., $r_{1+(1/2)} = (r_1 + r_2)/2$. This relation can be written in functional form:

$$G_1^1(r_1, P_1, T_1, r_2, P_2, T_2) = 0, \tag{24.30}$$

where the upper index is the interval number and the lower index (1–4) refers to the number of the differential equation in Table 24.1. The dependence with respect to P and T comes from ϱ. In a similar way, one has

$$G_2^1 = 0, \quad G_3^1 = 0, \quad G_4^1 = 0. \tag{24.31}$$

With (24.30), these are four algebraic equations and so on down to $j = m - 2$:

$$G_1^j = 0, \quad G_2^j = 0, \quad G_3^j = 0, \quad G_4^j = 0. \tag{24.32}$$

Near the center, the last interval is between M_{m-1} and M_m; see Sect. 24.1.3. As an example, $r = (3/(4\pi\varrho_c))^{1/3} M_r^{1/3}$ becomes $\frac{4\pi}{3}\varrho_{(m-1+1/2)}r_{m-1}^3 = M_{m-1}$, which is written as $Z_1(r_{m-1}, T_{m-1}, P_{m-1}, T_m, P_m) = 0$. On the whole,

$$Z - 1 = 0, \quad Z_2 = 0, \quad Z_3 = 0, \quad Z_4 = 0. \tag{24.33}$$

Let us suppose that one knows an approximate solution of the system, e.g., the model of the previous time step, r_j, P_j, L_j, T_j, with $j = 1, 2, 3, \ldots, m$. With this approximate solution, the equilibrium equations are not satisfied:

$$\mathcal{R}_i \neq 0, \quad G_i^j \neq 0, \quad Z_i \neq 0 \quad i = 1, \ldots, 4, \;\; j = 1, \ldots, m - 2. \tag{24.34}$$

Let us search new values $P_j + \delta P_j$, $r_j + \delta r_j$, $T_j + \delta T_j$ and $L_j + \delta L_j$, so that the algebraic equations (24.34) are satisfied, i.e.,

$$\mathcal{R}_i + \delta\mathcal{R}_i = 0, \quad G_i^j + \delta G_i^j = 0, \quad Z_i + \delta Z_i = 0. \tag{24.35}$$

The corrections $\delta P_j, \delta r_j$, etc. are small and relations (24.35) are linearized:

$$\mathcal{R}_i + \frac{\partial \mathcal{R}_i}{\partial P_1}\delta P_1 + \frac{\partial \mathcal{R}_i}{\partial T_1}\delta T_1 + \frac{\partial \mathcal{R}_i}{\partial r_1}\delta r_1 + \frac{\partial \mathcal{R}_i}{\partial L_1}\delta L_1 = 0, \quad i = 1, 2,$$

$$G_i^1 + \frac{\partial G_i^1}{\partial P_1}\delta P_1 + \frac{\partial G_i^1}{\partial r_1}\delta r_1 + \ldots\ldots \frac{\partial G_i^1}{\partial P_2}\delta P_2 + \frac{\partial G_i^1}{\partial r_2}\delta r_2 + \ldots\ldots = 0,$$

$$G_i^2 + \frac{\partial G_i^2}{\partial P_2}\delta P_2 + \frac{\partial G_i^2}{\partial r_2}\delta r_2 + \ldots\ldots \frac{\partial G_i^2}{\partial P_3}\delta P_3 + \frac{\partial G_i^2}{\partial r_3}\delta r_3 + \ldots\ldots = 0,$$

$$\ldots\ldots\ldots$$

$$G_i^{m-2} + \frac{\partial G_i^{m-2}}{\partial P_{m-2}}\delta P_{m-2} + \ldots\ldots\ldots \frac{\partial G_i^{m-2}}{\partial P_{m-1}}\delta P_{m-1} + \ldots\ldots\ldots = 0,$$

$$Z_i + \frac{\partial Z_i}{\partial P_{m-1}}\delta P_{m-1} + \ldots\ldots\ldots \frac{\partial Z_i}{\partial P_m}\delta P_m + \frac{\partial Z_i}{\partial T_m}\delta T_m = 0, \tag{24.36}$$

where $i = 1, 2, 3, 4$ in all equations except the two in $\mathcal{R}_i$. The dots represent the non-explicitly written derivatives. In each line one has the corresponding derivatives with respect to (P, T, r, L). In the last line, there are no derivatives with respect to r_m and L_m, because in the center $\delta r_m = 0$ and $\delta L_m = 0$. The above expressions represent a total of $2 + 4(m - 2) + 4$ equations for

$$\delta P_j, \; \delta r_j, \; \delta T_j, \; \delta L_j \quad \text{with} \quad j = 1, \ldots, m - 1 \quad \text{and} \quad \delta T_m, \delta P_m, \tag{24.37}$$

i.e., a total of $2 + 4(m - 1)$ unknowns. The system is thus determined.
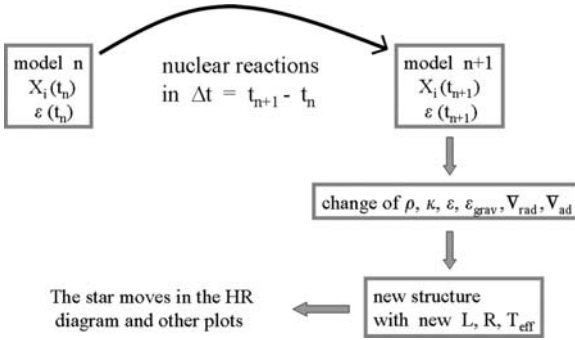
Fig. 24.1 Steps in stellar evolution

To solve this system of several hundreds or thousands of equations, advantage is taken that the non-zero terms are only close to the diagonal of the matrix and the equations are treated by successive blocks. If the equations of stellar structure were linear, one single iteration of the above process would be sufficient. As they are non-linear, the solutions after the first iteration,

$$P_j^1 = P_j + \delta P_j, \quad T_j^1 = T_j + \delta T_j, \quad L_j^1 = L_j + \delta L_j, \quad r_j^1 = r_j + \delta r_j, \tag{24.38}$$

are still not perfect. A second iteration has to be performed by the application of the above method to $P_j^1, r_j^1, T_j^1, L_j^1$. Then, further iterations are performed until all corrections are smaller than a prescribed value (e.g., 10^{-8}). Generally, 6–15 iterations are performed depending on the evolutionary stage. To favor the convergence of the method, only a fraction of the correction is generally applied in the first two iterations, for example $P_j^1 = P_j + \alpha \, \delta P_j$, with e.g., $\alpha = 1/4$ and $1/2$ in the first and second iterations. Finally, the above matrix of the $\mathcal{R}_i$, G_i^j and Z_i requires the calculation either analytically or numerically of many derivatives, such as $(\partial \ln \varrho / \partial \ln T)_P \equiv \varrho_T$ and similarly defined quantities $\varrho_P, \varepsilon_T, \varepsilon_P, \kappa_T, \kappa_P, \delta_T, \delta_P, (\nabla_{\text{ad}})_P$ and $(\nabla_{\text{ad}})_T$.

This concerns the solution of the structure equations for a given mass and composition at a time t_n. We need to know the composition and properties at time t_{n+1}. From a model of given structure and composition (mass fractions X_i), the nuclear reactions during the interval Δt change the composition. This modifies the physics and leads to a new structure (Fig. 24.1), which has to be again searched by the Henyey method. An example of the equations of composition changes is given for the ppI chain in Sect. 25.1.2. In a new structure, all the stellar parameters are modified and the star moves in the HR diagram.

24.3   Homology Transformations: Relations *M–L–R*

Homology transformations are scaling relations between physically nearby models. Historically, this was for deriving the properties of a new model from those of a nearby model without doing new lengthy calculations. Nowadays, these

transformations are still useful to get simple analytical relations between stellar parameters. As an example, let us consider two stars of nearby masses M and M' and compositions given by mean molecular weights μ and μ' with radii R and R',

$$M' = C_M M \text{ and } R' = C_R R, \text{ with } C_M, C_R \approx 1, \tag{24.39}$$

where C_M and C_R are constant. It is an "homology transformation", if these relations are also valid in the interior, i.e., if one has for any r

$$M'_r = C_M M_r, \quad r' = C_R r, \quad P' = C_P P, \quad T' = C_T T, \quad L'_r = C_L L_r. \tag{24.40}$$

Of course, the closer the models, the better these relations. Homology transformations are applicable to homogeneous models; they can also be used with special care for inhomogeneous models of similar structures. In general, one considers simple laws for the equation of state, opacities and nuclear reactions:

$$\varrho = \frac{\mu m_u}{k}\frac{P}{T}, \quad \kappa = \kappa_0 \varrho T^{-3.5}, \quad \varepsilon = \varepsilon_0 \varrho T^\nu. \tag{24.41}$$

The change of composition modifies the terms μ, κ_0 and ε_0 in (24.41):

$$\mu' = C_\mu \mu, \quad \kappa'_0 = C_\kappa \kappa_0, \quad \varepsilon'_0 = C_\varepsilon \varepsilon_0. \tag{24.42}$$

Let us make some applications to homogeneous stars with a composition specified by μ. The two models M and M' must satisfy the basic equilibrium relations. For example, the equation of hydrostatic equilibrium applied to the two models, i.e., $dP/dr = -(GM_r/r^2)\varrho$ and $dP'/dr' = -(GM'_{r'}/r'^2)\varrho'$, leads to the following relations between C_P, C_R etc.:

$$C_P = \frac{C_M^2}{C_R^4}, \tag{24.43}$$

in agreement with (1.20). With (24.41), we get $C_M/C_R^3 = C_\mu C_P/C_T$ and with the expression of C_P one obtains

$$C_T = C_\mu \frac{C_M}{C_R}, \tag{24.44}$$

consistently with (1.26). The energetic equilibrium now gives

$$C_L = C_\varepsilon \frac{C_M^2}{C_R^3} C_T^\nu = C_\varepsilon C_\mu^\nu C_M^{\nu+2} C_R^{-\nu-3}. \tag{24.45}$$

Let us first consider the case of radiative transfer; one gets

$$C_L = C_\kappa^{-1} C_M^{-2} C_R^7 C_T^{7.5} = C_\kappa^{-1} C_\mu^{7.5} C_M^{5.5} C_R^{-0.5}. \tag{24.46}$$

Equations (24.45) and (24.46) are two relations $L = L(M, R, \mu)$. One can eliminate R from them and get a relation $L = L(M, \mu)$:

$$C_L = C_\varepsilon^{-\frac{1}{2\nu+5}} \, C_\kappa^{-\frac{2\nu+6}{2\nu+5}} \, C_\mu^{\frac{14\nu+45}{2\nu+5}} \, C_M^{\frac{10\nu+31}{2\nu+5}} \,. \tag{24.47}$$

For $\nu = 4$ (ppI chain) and for $\nu = 17$ (CNO reactions), it gives [147] the following relations, respectively (not writing the C_L, etc.,)

$$L \sim \varepsilon_0^{-0.08} \, \kappa_0^{-1.08} \, \mu^{7.8} M^{5.5} \quad \text{and} \quad L \sim \varepsilon_0^{-0.02} \, \kappa_0^{-1.03} \, \mu^{7.3} M^{5.2}. \tag{24.48}$$

If one eliminates L from (24.45) and (24.46), one gets for the above ν values

$$R \sim (\kappa_0 \varepsilon_0)^{0.15} \, \mu^{-0.54} M^{0.08} \quad \text{and} \quad R \sim (\kappa_0 \varepsilon_0)^{0.51} \, \mu^{0.49} M^{0.69} \,. \tag{24.49}$$

The scaling of $T_{\text{eff}} \sim \left(L/R^2\right)^{1/4}$ gives for the two cases

$$T_{\text{eff}} \sim \kappa_0^{-0.35} \epsilon_0^{-0.10} \mu^{2.2} M^{1.33} \quad \text{and} \quad T_{\text{eff}} \sim \kappa_0^{-0.28} \epsilon_0^{-0.03} \mu^{1.6} M^{0.94}. \tag{24.50}$$

We note the following points:

– L increases fast with mass. An exponent of 5 applies near 1 $M_\odot$ (Sect. 25.2.2). For massive stars, the exponent is smaller due to electron scattering opacity and radiation pressure. On the average, one has (see next section)

$$L \sim M^3. \tag{24.51}$$

L also increases strongly with μ; it behaves like κ^{-1} (cf. 3.30). Remarkably an increase of the nuclear rate ε_0 does not produce a luminosity increase, due to the feedback which makes MS stars stable (Sect. 3.2.1).
– The radius has little sensitivity to the mass for solar-type stars. It has a weak dependence on μ. For upper MS stars, R increases like (Sect. 25.2.2)

$$R \sim M^{0.7} \,. \tag{24.52}$$

– For a given mass, stars of higher μ are hotter and much brighter.
    One can eliminate M between the relations for L and T_{eff} and obtain a relation $L = L(\mu, T_{\text{eff}})$, which represents the zero-age sequences of models of different μ. One gets for $\nu = 17$

$$L \sim \kappa_0^{0.53} \epsilon_0^{0.15} \mu^{-1.55} T_{\text{eff}}^{5.53} \,. \tag{24.53}$$

Homology relations apply if the hypothesis of small differences between the models is satisfied. If not, relations from numerical models are better used.

24.3.1 Other Effects: Electron Scattering, P_{rad}, Convection

Electron scattering: we examine the differences in the basic M–L and M–R relations due to various effects. Let us first consider a massive homogeneous star with electron scattering opacity (8.12); the opacity is constant inside the star, i.e., $\kappa = \kappa_0$. The equation of radiative transfer gives instead of (24.46)

$$C_L = C_\kappa^{-1} C_R^4 C_T^4 C_M^{-1} = C_\kappa^{-1} C_\mu^4 C_M^3 \,. \tag{24.54}$$

$$\text{i.e.,} \qquad L \sim \frac{\mu^4 M^3}{\kappa_0} \,, \tag{24.55}$$

which is similar to (3.25) and (3.30), also obtained for a constant opacity.

    Radiation pressure: if one accounts for the radiation pressure, the equation of state reads $\varrho = (\mu m_u/k)(\beta P/T)$ (3.98) and one gets instead of (24.44) $C_T = C_\mu C_\beta C_M/C_R$ and the following M–L relation:

$$L \sim \frac{\mu^4 \beta^4 M^3}{\kappa_0} \,. \tag{24.56}$$

We have seen in Fig. 3.5 that β decreases with increasing mass. Thus for larger masses, L increases less fast than M^3. For high radiation pressure, $\beta \sim M^{-1/2}$ (3.108) and thus the luminosity behaves in the extreme case like

$$L \sim \frac{\mu^4 M}{\kappa_0} \,, \tag{24.57}$$

i.e., a linear relation. The M–L relation (24.45) becomes

$$C_L = C_\varepsilon C_\beta^\nu C_\mu^\nu C_M^{\nu+2} C_R^{-\nu-3}, \tag{24.58}$$

and eliminating L between this equation and (24.56), one obtains for $\nu = 17$,

$$R \sim (\varepsilon_0 \kappa_0)^{\frac{1}{\nu+3}} \mu^{\frac{\nu-4}{\nu+3}} \beta^{\frac{\nu-4}{\nu+3}} M^{\frac{\nu-1}{\nu+3}} = (\kappa_0 \varepsilon_0)^{0.05} \mu^{0.65} \beta^{0.65} M^{0.80} \,. \tag{24.59}$$

Convective stars: their T gradient is mostly given by ∇_{ad}, which is a minimum value of ∇_{rad}. Thus, expression (24.46)

$$L \sim \frac{\mu^{7.5} M^{5.5}}{\kappa_0 R^{0.5}} \tag{24.60}$$

gives a minimum L for convective stars.

    There are many other possibilities to obtain useful relations by a proper scaling of the basic equations.

24.4   The Helium and Generalized Main Sequences

The zero-age main sequence (ZAMS) is the location in the HR diagram of chemically homogeneous stars at the beginning of MS evolution. As stars evolve, they become inhomogeneous forming a He core. The core size represents various mass fractions depending on masses, ages, mass loss and mixing. We examine the stellar properties according to the He-core mass fraction.

24.4.1   The Helium Sequence

The first case we examine is that of helium stars, which approximately correspond to some Wolf–Rayet stars (type WNE, Sect. 27.5) and extreme horizontal branch stars. Figure 24.2 compares the ZAMS of models of standard composition $X = 0.70$, $Z = 0.02$ ($\mu = 0.617$) and of almost pure helium stars $Y = 0.98$ and $Z = 0.02$ ($\mu = 1.342$). One notices that for a given mass the helium-rich stars are much brighter and hotter, while their radii are smaller. The internal structure of He stars shows some important differences with normal MS stars. The He-burning reactions are much more sensitive to T with an exponent $\nu \sim 30$ in (24.41); thus the mass fractions of the convective cores are larger, e.g., 0.27 $M_\odot$ in a 1 $M_\odot$ He star, while it is zero in the Sun. The central and average densities are much higher in He stars. The ratio of the radiation to the total pressure is also larger in He stars, e.g., 1.5% in a 1 $M_\odot$ instead of 5×10^{-4} in the Sun (Fig. 3.3). A consequence is the larger Eddington ratio Γ in He stars and this sets the maximum stellar mass of He stars around 16 $M_\odot$ [342, 440] compared to about 10^2 $M_\odot$ in Pop. I stars.

These very large differences of internal structure make the homology relations between He stars and H-rich stars relatively poor. With the above dependence $L \sim \mu^{7.3}$ for a given mass, one finds that the He sequence should be brighter by ~ 2.5 dex; this is about in agreement with lower masses in Fig. 24.2. The shift is smaller for higher masses, because due to electron scattering opacity, the dependence on μ is weaker (24.56). The radii of stars on the He sequence are smaller by ~ 0.7 dex compared to normal MS stars.

24.4.2   Generalized Main Sequences

The generalized main sequences are a most useful concept introduced by R. Kippenhahn and colleagues [205, 285]. It enlightens the interpretation of the stellar positions in the HR diagram, with applications for horizontal branch stars, blue and red supergiants and Wolf–Rayet stars.

The generalized MS are formed by models consisting of a He core of mass fraction q and an envelope of mass fraction $1 - q$ with a standard composition. There is a discontinuity of composition at the edge of the core. The models are supposed
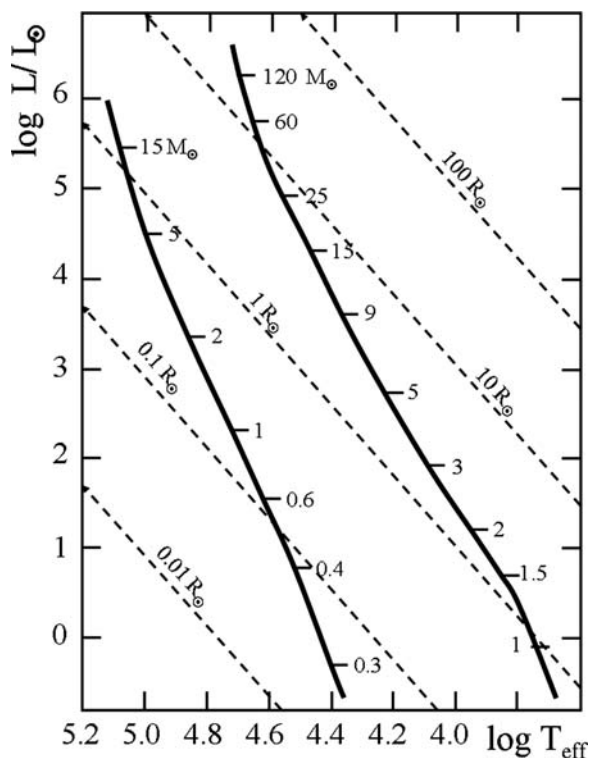
Fig. 24.2 On the *right*, the zero-age sequences with standard composition $X = 0.68$, $Z = 0.02$ and on the *left* with helium-rich $Y = 0.98$ and $Z = 0.02$. The masses along the sequences are indicated; the *broken lines* show loci of constant radii

in equilibrium, He is burning in the core and H is burning in a shell at the base of the envelope (when the envelope is thick enough). The models are described by two parameters: M the stellar mass and q.

Figure 24.3 shows some models in the range $\log L/L_\odot = 1.0$–5.0. For $q = 1$, one has the He sequence (Fig. 24.2). For smaller values of q, the H-rich envelope produces larger opacities and thus stellar inflation; the star is shifted to the right of the He sequence. For $q \leq 0.7$ or 0.8 (the lower limit is for higher mass stars), the stars inflate much more and have a lower T_{eff} and a convective envelope. They lie close to the Hayashi line (Sect. 20.2.1). When $q \leq 0.2$ (a limit depending on M, see Fig. 24.3), the models are shifted back to the blue and for $q = 0$ they are on the ZAMS.

Figure 24.3 shows how a model of a given M moves in the HR diagram when q is increasing during evolution as a result of nuclear burning and mass loss (if any). The luminosity and radius vary as a function of q. For $q \geq 0.2$, L increases. For $q \geq 0.6$ and up to $q = 1$, the L remains about constant. The reason [285] of this constancy is that the increase of the He-core luminosity when q increases above 0.6 is about compensated by a decrease of the H-shell luminosity, while for lower q
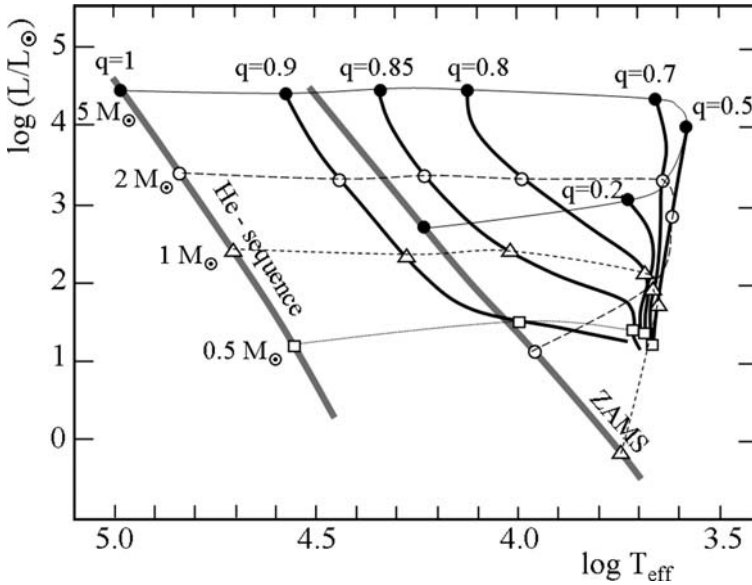
Fig. 24.3 Generalized MS in the HR diagram. Models of various total mass with He cores representing different mass fraction q are shown. *Thick lines* connect models with the same fraction q, *thin lines* connect models of the same total mass. The usual MS and He sequence are shown by *thick gray lines*. The envelope composition is $X = 0.68, Z = 0.02$. Adapted from P. Giannone et al. [205, 285]

values this compensation is not achieved and the stars have a luminosity determined by H burning. The change of the balance between H and He burning is verified (e.g., Fig. 26.2). Also, the opacity in models with higher q values is lower on the average, which favors higher luminosities.

24.5 Polytropic Models

With fast computers, polytropic models [109] have lost a part of their interest. However, they remain useful as simplified models. We briefly touch the subject, emphasizing interesting properties. A polytropic star (also said a polytrope) is a star in which one has

$$P = K\varrho^{\gamma} \quad \text{or} \quad P = K\varrho^{1+1/n} \quad \text{with} \quad n = \frac{1}{\gamma - 1} . \qquad (24.61)$$

γ or n are constants, n is called the polytropic index and K is another constant (this is not the thermal diffusivity 3.46). The equations of hydrostatic equilibrium and continuity (24.1) together with (24.61) form a complete system of equations which can be integrated giving relations such as $\varrho(r)$ and $P(r)$. $T(r)$ can be

obtained from the equation of state $\varrho(P,T)$. From hydrostatic equilibrium, we get $M_r = -r^2/(\varrho\,G)\,(dP/dr)$. Inserting M_r in the continuity equation, we get the Poisson equation in spherical coordinates:

$$\frac{1}{r^2}\frac{d}{dr}\left(\frac{r^2}{\varrho}\frac{dP}{dr}\right) + 4\pi G\varrho = 0\,, \tag{24.62}$$

or

$$\frac{\gamma}{\gamma-1}\frac{K}{r^2}\frac{d}{dr}\left(r^2\frac{d\varrho^{\gamma-1}}{dr}\right) + 4\pi G\varrho = 0\,. \tag{24.63}$$

There, we use (24.61) and the fact that $d\varrho^\gamma/dr = [\gamma/(\gamma-1)]\varrho\,(d\varrho^{\gamma-1}/dr)$. Let us introduce a dimensionless variable ϑ so that

$$\varrho \equiv \varrho_c\,\vartheta^n;\quad\text{thus}\quad P = P_c\,\vartheta^{n+1}\,. \tag{24.64}$$

With this new variable, (24.63) becomes

$$\varrho_c^{1/n}(n+1)\frac{K}{r^2}\frac{d}{dr}\left(r^2\frac{d\vartheta}{dr}\right) + 4\pi G\varrho_c\,\vartheta^n = 0\,,$$

or

$$\frac{1}{\xi^2}\frac{d}{d\xi}\left(\xi^2\frac{d\vartheta}{d\xi}\right) = -\vartheta^n\,. \tag{24.65}$$

This is the equation of Lane–Emden. The new space variable ξ is given by

$$\xi = \alpha r\quad\text{with}\quad \alpha^2 = \frac{4\pi G}{(n+1)K}\,\varrho_c^{(n-1)/n}\,. \tag{24.66}$$

In the center, one has $\xi = 0$ with $\vartheta = 1$ and $d\vartheta/d\xi = 0$. The first condition results from the definition (24.64) and the second from spherical symmetry. The surface is located in ξ_1 such that $\vartheta(\xi_1) = 0$. Analytical solutions exist for $n = 0$, 1 and 5:

$$\vartheta_0(\xi) = 1 - \frac{\xi^2}{6}\,,\quad \vartheta_1(\xi) = \frac{\sin\xi}{\xi}\,,\quad \vartheta_5(\xi) = \left(1 + \frac{\xi^2}{3}\right)^{-1/2}\,. \tag{24.67}$$

The radius remains finite for $n < 5$. For $n = 5$, $\vartheta_5 = 0$ only for $\xi = \infty$; however the decrease of the density is so steep that the total mass remains finite. Polytropic models have been extensively studied by Eddington [168] and Chandrasekhar [109], who provide numerical tables for other indices n.

The sequence of polytropes from $n = 0$ to $n = 5$ describes a sequence of increasing central condensations. One has

$n =$	0	1	1.5	2	3	4	4.5	5
$\varrho_c/\overline{\varrho} \approx$	1	3.3	6	11.4	54.2	622	6.2×10^3	∞

A few examples of the internal density distribution for different n indices are shown in Fig. 24.4. The polytrope of $n = 0$ is homogeneous in density, while that with $n = 5$ has an infinite central condensation.
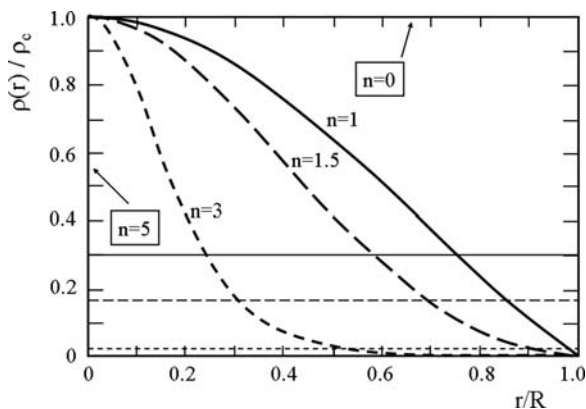
Fig. 24.4 Examples of polytropic distributions of density normalized in each case to the central density. A *horizontal line* indicates the average density for each model. The ratios $\varrho_c/\overline{\varrho}$ are given below. The case $n = 0$ lies on the upper horizontal axis. The case $n = 5$ lies on the left vertical axis and on the lower horizontal axis

24.5.1 Interesting Polytropes

There are some cases of particular interest. The first case is that of a star of perfect gas and radiation; it has an equation of state given by (3.100). For small internal variations of β, one has $\gamma = 4/3$, i.e., $n = 3$. As a matter of fact, real stars are not far from a polytrope of index $n = 3$. However, if it would exactly be $n = 3$, the star would be unstable (Sect. 1.3.1).

The second case is that of an internal adiabatic convective zone. There $\gamma = 5/3$, i.e., $n = 3/2$. Convective regions are polytropic with index $n = 1.5$, i.e., they have a relatively small density contrast. The equation of fully degenerate gas in the non-relativistic case (7.148) also has the same index $n = 3/2$. Thus, white dwarfs are essentially polytropes of index $n = 3/2$. An examination of the equation of state of gaseous, icy and rocky planets has shown us that they are close to polytropes with indices between $n = 1/3$ and $2/3$. These various applications confirm the interest of polytropes.

There are many properties of polytropes, e.g., one can express M_r, $g(r)$, $\overline{\varrho}_r/\varrho_c$, etc. as functions of ϑ and ξ [109]. The potential energy Ω of polytropes is particularly useful. Let us derive it. With the potential $\Phi(r) = -GM_r/r$ (Sect. 1.2.1) and (24.61) the equation of hydrostatic equilibrium is

$$\frac{1}{\varrho}dP = \frac{n+1}{n}K\varrho^{(1/n)-1}d\varrho = -d\Phi \; . \tag{24.68}$$

We integrate the terms in $d\varrho$ and $d\Phi$ from r to R; we then express P and get

$$-(n+1)\frac{P}{\varrho} = \Phi(r) - \Phi(R) \; , \tag{24.69}$$

at level r, where account is given that $P(R) = 0$. We integrate it again:

$$(n+1)\int_0^M \frac{P}{\varrho}\,dM_r = -\int_0^M \Phi\,dM_r + \Phi(R)\int_0^M dM_r \; , \tag{24.70}$$

and with (1.41) and (1.49), we get finally

$$\Omega = -\frac{3}{5-n}\frac{GM^2}{R} \; . \tag{24.71}$$

We see that for $n = 0$ (homogeneous), the factor q in (1.34) is $3/5$; for MS stars with $n \approx 3$ one has $q = 3/2$, while for $n = 5$ one has $q \to \infty$ because this polytrope is infinitely concentrated.

24.5.2 Isothermal Sphere

In this case, with the law of perfect gas one has $\gamma = 1$ in (24.61), i.e., $P = K''\varrho$ where K'' is some constant. One has to make other changes of variables in the Poisson equation (24.62). Let us introduce

$$\psi = -\ln\frac{\varrho}{\varrho_c}, \quad \text{i.e.,} \quad \varrho = \varrho_c e^{-\psi} \; . \tag{24.72}$$

Expression (24.61) becomes

$$\frac{1}{\xi^2}\frac{d}{d\xi}\left(\xi^2\frac{d\psi}{d\xi}\right) = e^{-\psi} \,, \text{with} \quad \xi = \alpha r \quad \text{and} \quad \alpha^2 = \frac{4\pi G\varrho_c}{K''} \; . \tag{24.73}$$

In the center, one has $\xi = 0$, $\varrho = \varrho_c$ and thus $\psi = 0$; the central spherical symmetry implies $d\psi/d\xi = 0$. Making the replacement $\xi \to 1/x$, the above equation becomes

$$x^4\frac{d}{dx}\left(\frac{d\psi}{dx}\right) = e^{-\psi} \; , \tag{24.74}$$

which admits $e^{-\psi} = 2x^2$ as a singular solution. For this solution, one has

$$e^{-\psi} = \frac{2}{\xi^2} \quad \text{and} \quad \varrho = \varrho_c\frac{2}{\alpha^2 r^2} = \frac{K''}{2\pi G}\frac{1}{r^2} \; . \tag{24.75}$$

As shown by Chandrasekhar [109], any solution of (24.73) tends for $\xi \to \infty$ toward the singular solution with $\varrho \sim 1/r^2$. The surface is obtained for $\psi \to \infty$, i.e., for $\xi \to \infty$. The mass of the isothermal polytrope is

$$M_r = 4\pi \int_0^R \varrho\, r^2 dr = 4\pi \varrho_c \int_0^\infty \frac{e^{-\psi}}{\alpha^3}\, \xi^2 d\xi \quad \to \quad \text{const} \int_0^\infty d\xi \,, \qquad (24.76)$$

which tends toward ∞ for $\xi \to \infty$, i.e., the mass of the isothermal polytrope is infinite (a finite self-gravitating sphere of perfect gas cannot be isothermal).

A density law in r^{-2} is often met in problems where the outer layers of a gravitational system may to first approximation be considered as isothermal, e.g., in the initial contraction of interstellar clouds (Sect. 18.4.2) or in the outer density structure of star clusters or galaxies.

On the whole, polytropes provide meaningful distributions of density consistent with hydrostatic equilibrium and continuity.

Chapter 25
Evolution in the H-Burning Phases[*]

The hydrogen-burning phase or main sequence (MS) phase is the longest phase of stellar evolution, in which stars spend 85–90% of their nuclear life. There are several reasons why this phase is the longest one: (1) fusion of H into He produces more nuclear energy per nucleon, (2) the stars are less luminous than in later phases, (3) convective cores, when present, are larger than in later phases, thus the nuclear reservoirs are larger. The He-burning phase lasts about 10–15% of the nuclear life, while the further stages up to the supernova only represent about 10^{-3} of the nuclear life. This means that the observed stars belong to these first two stages of nuclear evolution. The Sun is of major concern for us and we examine its properties in detail.

Many properties of stars in the final stages are shaped by the physics of the H-burning phase. For example, the size of the iron cores of massive stars and their fate as neutron stars or black holes depend on the core size in the MS stage. The distribution of the specific angular momentum which determines the possible evolution of massive stars at low Z toward gamma-ray bursts essentially depends on the evolution of rotation in MS stars.

Numerical models rapidly become obsolete. Thus, we try to pay more attention to the fundamental facts the models illustrate, rather than on their ephemeral numerical values.

25.1 Hydrogen Burning

H burning converts four protons into an α particle, with liberation of energy (Fig. 9.1) due to a relative mass defect of 0.0071. This is an order of magnitude more than in further nuclear phases. Stars in the H-burning phase are on the main sequence in the HR diagram. There are two major chains of reactions: the proton–proton (pp) chains dominating in stars with masses lower than about 1.2 $M_\odot$ and the CNO cycle which dominates above.

---

[*]This chapter may form the matter of a basic introductory course.

25.1.1 The pp Chains

There are three chains, called ppI, ppII and ppIII, turning hydrogen into helium (Table 25.1). The ppI chain is usually the dominant one, the relative importances of the last two increase with T. We give the reactions with the total energy produced and the energy in the form of neutrinos (escaping immediately). The energy participating in the radiative transfer is the difference of the two. The approximate reaction times (9.9) in the solar interior are indicated.

The first reaction is very slow, as shown by the timescale τ which indicates the approximate average time the particle has to wait before reacting in the solar interior (9.9). The slowness of this reaction results from the weak interaction process. In ppI, the first two reactions have to operate twice to produce two ^{3}He in order that the third reaction is possible. The cross-section and $S(E)$ factor of this reaction are given in Fig. 9.4. The total available energy (taking an average ν energy of 0.25 MeV for the first reaction) is thus $2 \times (1.192 + 5.493) + 12.859 = 26.23$ MeV for four nucleons, i.e., 6.56 MeV per nucleon. This corresponds to an energy per gram $E_{11} = 6.33 \times 10^{18}$ erg g^{-1} (cf. Appendix A.1). The neutrinos embark about 2% of the reaction energy.

From the ^{3}He produced in ppI, the first reaction in ppII produces ^{7}Be. This nucleus can either capture a free electron (reaction with little dependence on T) which leads to ^{7}Li and the ppII chain or ^{7}Be can capture a proton, which leads to ^{8}B unstable to positron decay in the ppIII chain, together with emission of an energetic neutrino. The result of this decay is ^{8}Be, which is highly unstable (with a lifetime of 10^{-16} s). The inverse of this reaction is the first step in the 3α reaction (Sect. 26.1). The amounts of energy liberated by the three pp chains are different because of different neutrino losses. The ppII chain produces about 25.66 MeV, the ppIII

Table 25.1 The pp chains, with energies and timescales in years, days or seconds. The maximum ν energies are given, the relevant average ν energies are, respectively, 0.25, 0.81 and 7.2 MeV for the three reactions concerned in this table

				Q		Approximate τ
ppI	^{1}H + ^{1}H	$\longrightarrow$	^{2}H + e$^+$ + ν_e	1.442 ($\nu < 0.420$)	MeV	7×10^9 yr
	^{2}H + ^{1}H	$\longrightarrow$	^{3}He + γ	5.493	MeV	1 s
	^{3}He + ^{3}He	$\longrightarrow$	^{4}He + 2^{1}H	12.859	MeV	1.5×10^5 yr
ppII	^{3}He + ^{4}He	$\longrightarrow$	^{7}Be + γ	1.587	MeV	9.5×10^5 yr
	^{7}Be + e$^-$	$\longrightarrow$	^{7}Li + ν_e	0.862 ($\nu < 0.862$ 90%) ($\nu < 0.383$ 10%)	MeV	1.4×10^2 d
	^{7}Li + ^{1}H	$\longrightarrow$	2^{4}He	17.347	MeV	1.3×10^3 s
ppIII	^{7}Be + ^{1}H	$\longrightarrow$	^{8}B + γ	0.135	MeV	1×10^2 yr
	^{8}B	$\longrightarrow$	^{8}Be + e$^+$ + ν_e	17.98 ($\nu < 14.02$)	MeV	0.8 s
	^{8}Be	$\longrightarrow$	2^{4}He	0.095	MeV	

chain about 19.20 MeV, meaning that, respectively, about 4 and 28% of the energy are lost as neutrinos. Chain ppI produces one ^{4}He, while ppII and ppIII produce two.

The timescales of the various steps are very different, from 1 s to several Gyr. The first and slowest reaction controls the chains. For the ppI chain, the zero-order approximation of the energy generation rate is of the form $\varepsilon = \varepsilon_0 \varrho X^2 T^\nu$ with $\nu \approx 4$–5 in solar-type stars (Fig. 25.3), X or X_1 being the H-mass fraction. A better approximation is to take the rate of the slowest reaction (here ^{1}H+^{1}H) and to associate to it the total energy of the chain. This implies equilibrium of the various steps. The rate of ppI is given by [194] $N_{AV}\lambda_{11} \approx \left(3.82 \times 10^{-15} e^{\left(-3.38/T_9^{1/3}\right)}\right)/T_9^{2/3}$, where $T_9 = T/(10^9 \text{ K})$. The total energy is 26.23 MeV, but one reaction produces only half of this energy, since two ppI reactions are necessary to form one helium. This gives $Q_{11} = 2.102 \times 10^{-5}$ erg. With account of (9.11, see also 25.5), one gets

$$\varepsilon_{\mathrm{ppI}} \approx 2.38 \times 10^4 \varrho X_1^2 \frac{e^{-3.38/T_9^{1/3}}}{T_9^{2/3}} f_{11} \quad \text{in erg g}^{-1}\text{s}^{-1}. \tag{25.1}$$

For stellar models, all relevant reactions have to be accounted for with data from the numerical tables (Sect. 9.2.1). In the Sun the contribution of ppI is ~ 84 and of ppII is 14%. The rest is mostly from the CNO cycle (see below).

25.1.2 Equations for Composition Changes

Let us consider at level M_r in a star an element i made from element h and transformed into element j: $h \rightarrow i \rightarrow \quad j$. The change of the mass fraction X_i of element i (labeled by the atomic mass number) at level M_r is

$$\frac{\partial X_i(M_r)}{\partial t} = \sum_h \frac{\varepsilon_{h \rightarrow i}}{E_{h \rightarrow i}} - \sum_j \frac{\varepsilon_{i \rightarrow j}}{E_{i \rightarrow j}}. \tag{25.2}$$

There, $\varepsilon_{h \rightarrow i}$ in erg g^{-1} s^{-1} is the nuclear energy generation rate by reactions leading to element i, similarly $\varepsilon_{i \rightarrow j}$ refers to reactions which destroy i. The quantities $E_{h \rightarrow i}$, $E_{i \rightarrow j}$ in erg g^{-1} are, respectively, the energies liberated by gram of element i produced by h and transformed into j. A ratio like $(\varepsilon_{h \rightarrow i}/E_{h \rightarrow i})$ is the change of mass fraction of the element considered by unit of time. Equation (25.2) applies to a radiative zone without mixing. For convection, an average of the abundances over the convective zone (cz) has to be made

$$\left(\frac{\partial X_i}{\partial t}\right)_{\mathrm{cz}} = \frac{\int_{\mathrm{cz}} \left(\sum_h \frac{\varepsilon_{h \rightarrow i}(M_r)}{E_{h \rightarrow i}} - \sum_j \frac{\varepsilon_{i \rightarrow j}(M_r)}{E_{i \rightarrow j}}\right) dM_r}{\int_{\mathrm{cz}} dM_r}. \tag{25.3}$$

Convective zones are homogeneous if the turnover time (5.49) is much shorter than the evolution timescale. If not, a diffusion scheme has to be employed (Sect. 6.3).

If there are several convective zones, the average is taken in each zone. As a didactical example, we shall write the equations of the composition changes for the elements in ppI, which show many interesting cases. Let us first consider the change of deuterium in mass fraction X_2 at a level M_r,

$$\frac{dX_2}{dt} = \frac{\varepsilon_{11}}{E_{11}} - \frac{\varepsilon_{12}}{E_{12}} , \qquad (25.4)$$

because ^{2}H is created by the first of the ppI chain (index ij refers to elements i and j) and destroyed by the second one (index 12). From (9.11), ε_{11} is

$$\varepsilon_{11} = \frac{Q_{11}(\mathrm{erg})\varrho\, X_1 X_1 \lambda_{11}}{A_1 A_1\, m_{\mathrm{u}}^2\ 2} f_{11}, \qquad (25.5)$$

where Q_{11} is the energy of the reaction "11" and f_{11} its screening factor. The factor of 2 results from the term $(1 + \delta_{aX})$ in (9.11). The energy E_{11} is

$$E_{11} = \frac{Q_{11}(\mathrm{erg})}{n\,m_{\mathrm{u}}} = \frac{Q_{11}(\mathrm{erg})}{2\,m_{\mathrm{u}}} , \qquad (25.6)$$

n is here the number of mass units of the element considered (here ^{2}H) transformed by the reaction (here "11"). With the division by m_{u}, one has the value per gram. Thus, the ratio ε_{11}/E_{11} becomes

$$\frac{\varepsilon_{11}}{E_{11}} = \frac{1}{(m_{\mathrm{u}}/2)} \frac{X_1}{A_1} \frac{X_1}{A_1} \frac{\varrho\,\lambda_{11}}{2} f_{11} = 2 Y_1 Y_1 \frac{[11]}{2} \quad \text{with } [11] \equiv \varrho\, N_{\mathrm{AV}} \lambda_{11} f_{11}, \qquad (25.7)$$

and $Y_i \equiv X_i/A_i$. The screening factor f_{11} is included in the bracket. One has $\varepsilon_{12}/E_{12} = 2 Y_1 Y_2 [12]$, so that the equation for the change of Y_2 is

$$\frac{dY_2}{dt} = Y_1^2 \frac{[11]}{2} - Y_1 Y_2 [12] . \qquad (25.8)$$

Let us consider the equation for the change of ^{3}He with mass fraction X_3

$$\frac{dX_3}{dt} = \frac{\varepsilon_{12}}{E_{12}} - \frac{\varepsilon_{33}}{E_{33}} , \qquad (25.9)$$

$$\text{with} \quad \frac{\varepsilon_{12}}{E_{12}} = \frac{Q_{12}\varrho\, Y_1 Y_2}{Q_{12} m_{\mathrm{u}}^2/(3\,m_{\mathrm{u}})} \lambda_{12} f_{12} = 3 Y_1 Y_2 [12], \qquad (25.10)$$

$$\text{and} \quad \frac{\varepsilon_{33}}{E_{33}} = \frac{Q_{33}\varrho\, Y_3 Y_3}{Q_{33} m_{\mathrm{u}}^2/(6\,m_{\mathrm{u}})} \frac{\lambda_{33}}{2} f_{33} \to 3 Y_3 Y_3 [33], \qquad (25.11)$$

$$\text{thus} \quad \frac{dY_3}{dt} = Y_1 Y_2 [12] - Y_3 Y_3 [33]. \qquad (25.12)$$

Great care has to be given to use the proper number "n" in (25.6). The factor of $n = 3$ in (25.10) occurs because there is one ^{3}He, i.e., 3 mass units created by the second reaction of ppI, while the factor of $n = 6$ in (25.11) occurs because the third

reaction in ppI destroys two ^{3}He. To complete the example, let us write the change of ^{4}He with mass fraction X_4,

$$\frac{dX_4}{dt} = \frac{\varepsilon_{33}}{E_{33}} = \frac{Q_{33}\varrho\,Y_3 Y_3}{Q_{33}m_u^2/(4\,m_u)}\frac{\lambda_{33}}{2}f_{33}, \quad \text{which gives} \quad \frac{dY_4}{dt} = Y_3^2\frac{[33]}{2}. \quad (25.13)$$

The factor $n = 4$ here is because the third reaction in ppI produces one ^{4}He. For hydrogen with mass fraction X_1, the equation is

$$\frac{dY_1}{dt} = -Y_1^2[11] - Y_1 Y_2[12] + Y_3^2[33]. \quad (25.14)$$

The system of equations (25.8, 25.12, 25.13 and 25.14) describes the changes of composition due to the chain ppI. It gives an example on how to express the changes of composition. Other systems of nuclear reactions are treated in the same way. A check of correctness of the system of equations can be made: the sum of the mass fractions must be equal to 1,

$$\sum_i X_i = 1 \quad \rightarrow \quad \sum_i \frac{dX_i}{dt} = 0 \quad \rightarrow \quad \sum_i A_i\frac{dY_i}{dt} = 0. \quad (25.15)$$

The above system for the ppI chain verifies this last equation and is thus correct. The mass fractions lost in the form of radiation are negligible and are not accounted for because atomic masses are taken as integers.

^{2}**H equilibrium:** When ^{2}H is created, it is immediately destroyed according to the timescales given in Table 25.1. The abundance of ^{2}H remains very low and changes only on timescales long with respect to the nuclear timescale. Thus, ^{2}H can be considered at equilibrium in (25.8), which gives

$$Y_2 = \frac{Y_1}{2}\frac{[11]}{[12]}. \quad (25.16)$$

Thus, the abundance Y_2 is determined by that of H and the ratio of the reaction rates. The system of equations simplifies to (25.14, 25.12 and 25.13) and Y_2 can be eliminated with (25.16). This is acceptable for a solar model because the nuclear lifetime of ^{2}H is a fraction $\sim 10^{-18}$ of the ^{1}H lifetime. The abundance ratio X_2/X_1, which is of the same order of magnitude, only changes slowly. Calculating the detailed evolution of ^{2}H in the Sun would impose too many time steps. The assumption of ^{2}H equilibrium does not always apply, e.g., in pre-MS evolution or in brown dwarfs Y_2 must be calculated explicitly. The evolution of isotope ^{3}He must be calculated explicitly.

Branching ratios: The branching ratios of the various chains are determined by the ratios of the reaction rates at the bifurcation, for example

$$\frac{\text{ppI}}{\text{ppII} + \text{ppIII}} = \frac{1}{2}\frac{[33]\,Y_3}{[34]\,Y_4} \quad \text{and} \quad \frac{\text{ppII}}{\text{ppIII}} = \frac{[e\,^7\text{Be}]\,Y_e}{[1\,^7\text{Be}]\,Y_1}. \quad (25.17)$$

The meaning of Y_e needs to be clarified. In general, $Y_i = X_i/A_i = n_i/(n\mu)$ (25.7). For electrons, this is $Y_e = n_e/(n\mu) = \frac{1}{2}(1+X)$ with (7.42). At the beginning of H burning in the Sun, ppI dominates over the other two chains. From $T_6 = T/(10^6) = 20$ to $T_6 = 23$, ppII would dominate and then ppIII. However, for $T_6 > 17$, the CNO cycle is more important.

25.1.3   The CNO Cycles

When $T_6 > 17$ for a standard composition, the H burning occurs mainly through the CNO cycles. CNO elements must be initially present, their sum $X_C + X_N + X_O$ does not change when the cycles operate, as easily verified from Table 25.2. However, the ratios of CNO elements, like X_N/X_C, are modified by the cycles. There is a basic cycle, the CN cycle (see Fig. 25.1), to which two ON loops are added, the relative importance of the ON loops increases for higher T. In addition, there is a rare loop from ^{18}O to ^{16}O through ^{19}F. The reactions of the CNO cycles are given in Table 25.2. As for the pp chains, the total energies are given and the ν energies must be subtracted for having the energy participating in the radiative energy transfer.

Figure 25.1 shows graphically the basic CN cycle and the loops. The astrophysical factor of the resonant reaction $^{12}C(p,\gamma)^{13}N$ is illustrated in Fig. 9.6. The net result of the cycle and of the loops is to convert four ^1H into one ^4He. From the indicated timescales, we see that the elements ^{13}N, ^{15}O, ^{17}F, ^{18}F are rapidly destroyed and can be set to equilibrium. This reduces the number of equations and allows one to adopt not too short time steps in evolutionary calculations. In the CN cycle, the slowest reaction is that which destroys ^{14}N, thus the CN cycle accumulates the elements in the form of ^{14}N. This is a major consequence of the CNO cycle. Some ^{12}C is also turned into ^{13}C so that the $^{12}C/^{13}C$ is decreased (Table 25.3). The energy
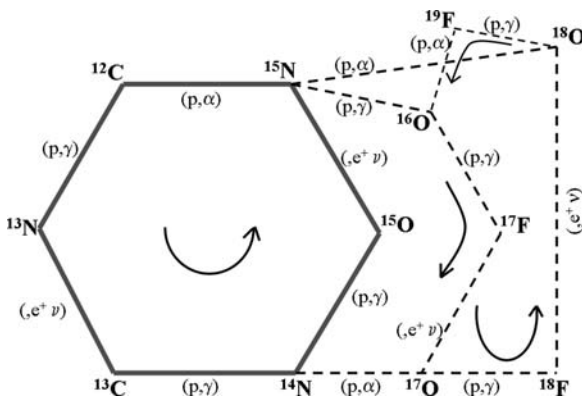
Fig. 25.1 Illustration of CN cycle (hexagon), the two ON loops and an additional branching with indication of the reactions. The whole forms the CNO cycles

Table 25.2 The CNO cycles with energies Q and approximate timescales at $T = 25 \times 10^6$ K. The maximum ν energies are given, the relevant average ν energies are, respectively, 0.70, 1.00, 0.94 and 0.37 MeV for the four reactions concerned

				Q		Approx. τ
CN	^{12}C + ^{1}H	$\longrightarrow$	^{13}N + γ	1.944	MeV	10^3 yr
	^{13}N	$\longrightarrow$	^{13}C + e$^+$ + ν_e	2.211 ($\nu < 1.20$)	MeV	420 s
	^{13}C + ^{1}H	$\longrightarrow$	^{14}N + γ	7.550	MeV	2.9×10^2 yr
	^{14}N + ^{1}H	$\longrightarrow$	^{15}O + γ	7.293	MeV	9.4×10^4 yr
	^{15}O	$\longrightarrow$	^{15}N + e$^+$ + ν_e	2.761 ($\nu < 1.73$)	MeV	120 s
	^{15}N + ^{1}H	$\longrightarrow$	^{12}C + α	4.966	MeV	3.7 yr
First ON	^{15}N + ^{1}H	$\longrightarrow$	^{16}O + γ	12.126	MeV	4.6×10^3 yr
	^{16}O + ^{1}H	$\longrightarrow$	^{17}F + γ	0.601	MeV	5.0×10^6 yr
	^{17}F	$\longrightarrow$	^{17}O + e$^+$ + ν_e	2.762 ($\nu < 1.74$)	MeV	66 s
	^{17}O + ^{1}H	$\longrightarrow$	^{14}N + α	1.193	MeV	3.1×10^6 yr
Second ON	^{17}O + ^{1}H	$\longrightarrow$	^{18}F + γ	5.609	MeV	4.2×10^3 yr
	^{18}F	$\longrightarrow$	^{18}O + e$^+$ + ν_e	1.656 ($\nu < 0.634$)	MeV	6.6×10^3 s
	^{18}O + ^{1}H	$\longrightarrow$	^{15}N + α	3.980	MeV	5 yr
Third ON	^{18}O + ^{1}H	$\longrightarrow$	^{19}F + γ	7.993	MeV	5×10^3 yr
	^{19}F + ^{1}H	$\longrightarrow$	^{16}O + α	8.115	MeV	5×10^2 yr

Table 25.3 Typical CNO abundance ratios (in mass fractions)

Ratios	Cosmic values	CNO equilibrium
^{12}C/^{14}N	~ 3.5	0.025
^{12}C/^{13}C	~ 62	3.3
^{16}O/^{14}N	~ 8.7	0.10

liberated by the CN cycle without the neutrinos is 25.03 MeV, i.e., 6.258 MeV per nucleon corresponding to an energy of 6.04×10^{18} erg g^{-1} (cf. Appendix A.1).

The branching ratio of the first ON loop with respect to the CN cycle is given by the ratio of the rates of ^{15}N(p,γ)^{12}C to ^{15}N(p,α)^{16}O which is of the order of the inverse ratio of the lifetimes of ^{15}N for the two reactions. Thus, the branching ratio between the first loop and the CN cycle is $\sim 10^{-3}$. The branching ratio between the second and the first loops is given by the ratio of the (p,γ) to (p,α) reactions upon ^{17}O, which is ~ 1 with some uncertainty [17]. ^{17}O is produced at $T_6 < 30$ and destroyed above.

The branching ratio of the loop going through ^{19}F is given by the ratio of the (p,γ) to (p,α) reactions upon ^{18}O, it is of the order of 10^{-3}. Thus, this rare loop is often omitted. Nevertheless, the rates indicate that some small accumulation of ^{19}F is produced. The main result of the three ON loops is to slowly convert (at a rate

increasing with T) some ^{16}O into ^{14}N, this conversion is much slower than for ^{12}C into ^{14}N.

As a result of CNO reactions, the abundances of all isotopes involved are changed with respect to their initial cosmic abundances, while the sum of their mass fractions is unchanged. Table 25.3 illustrates the differences of some important abundance ratios between the cosmic values and those of the cycles at equilibrium in a 20 M$_\odot$ star (see also Sect. 27.4).

The C/N and O/N ratios are reduced by about 2 orders of a magnitude at CNO equilibrium with respect to the cosmic values. During their evolution the intermediate and massive stars show almost all possible values between these two extremes. Values of C/N and O/N different from the cosmic values are a signature of surface enrichments.

The zero-order approximation of the energy generation rate is of the form $\varepsilon = \varepsilon_0 \varrho T^\nu$ with $\nu \approx 17$ at $T_6 = 25$ and $\nu \approx 13$ at $T_6 = 50$ (see 9.34 and remarks below). A better approximation is to take the rate [194] of the slowest reaction (here ^{14}N$+^1$H for the CN cycle) and to associate to it the total energy (25.03 MeV) of the cycle. This yields

$$\varepsilon_{\mathrm{CNO}} \approx 8.7 \times 10^{25} \varrho\, X_1 X_{\mathrm{CN}} \frac{e^{-15.228/T_9^{1/3}}}{T_9^{2/3}} f_{114} \quad \text{in erg g s}^{-1}. \qquad (25.18)$$

At the equilibrium of the CN cycle, $X_{\mathrm{CN}} \approx X_{12} + X_{14}$, while at full CNO equilibrium $X_{\mathrm{CN}} \approx X_{12} + X_{14} + X_{16}$, this last sum is of the order of $Z/2$ where Z is the metallicity. Of course, the detailed energy contributions of the various reactions have to be accounted for in accurate models.

25.1.4   Energy Production in MS Stars

Figure 25.2 illustrates the rates ε of the pp chains and of the CNO cycles as a function of T for standard composition. One notices the dominance of the CNO cycles at $T_6 > 17$ and the different slopes ν of the two rates.

Figure 25.3 shows the nuclear energy generation rates ε in the present Sun and in different stars on the ZAMS. These rates decrease very much away from the stellar centers. For each mass only a small mass range corresponding to the highest temperatures significantly contributes to the stellar luminosity. The changes of density also influence ε. We see how weak by unit of mass are the stellar energy production rates. In this context the typical order of magnitude of the energy liberated by the human body, i.e., ~ 1 W kg^{-1}, corresponds to 10^4 erg s^{-1} g^{-1}, i.e., much more than in stars!

Figure 25.3 shows the derivatives $\varepsilon_T = (\partial \ln \varepsilon / \partial \ln T)$, also called ν in expressions of the form $\varepsilon = \varepsilon_0 \varrho T^\nu$, as a function of T in the present Sun and in stars of different masses on the ZAMS. For the Sun, ν is just below 5 (often a value of 4 is adopted). For massive stars, a value of 17 is appropriate in a 2 M$_\odot$ star, while
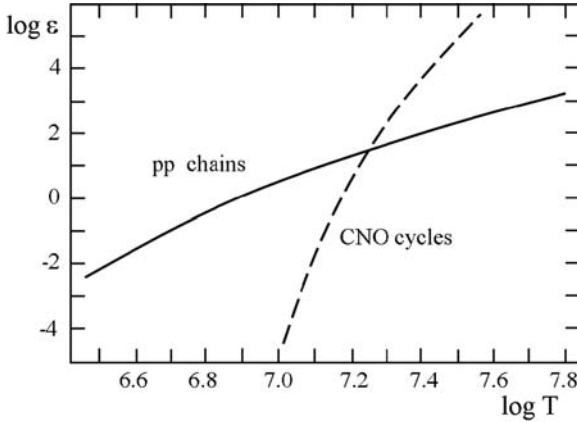
Fig. 25.2 Energy generation rates (erg g^{-1} s^{-1}) by the pp chains and by the CNO cycles as a function of T for $\varrho = 100$ g cm^{-3}, $X = 0.70$ and $X_{CNO} = 10^{-2}$

smaller values are appropriate for more massive stars ($v = 15$ for a 5 M$_\odot$ star and $v = 11$ for a 60 M$_\odot$ star).

The equations for the changes of the abundances X_i due to the pp chains and CNO cycles can be written according to the prescriptions of Sect. 25.1.2. A robust implicit method to solve these equations has been devised by Arnett and Truran [15]. There are two kinds of methods to integrate an equation like (25.2). For a time step from t_n to t_{n+1}, the simple explicit method uses the $\varepsilon(t_n)$ to get the new composition $X_i(t_{n+1})$. The more accurate implicit method proceeds by iterations. After a first application of the explicit method, the next iterations use the $\varepsilon(t_{n+1})$ to get the new compositions.

25.1.5   The NeNa and MgAl Cycles

There are two cycles of reactions not significant for energy production, but which change some isotopic ratios, working above $T_6 > 25$. These are the NeNa and MgAl cycles (Fig. 25.4). The NeNa chain starts from ^{20}Ne. The ^{20}Ne abundance is high enough not to be modified by the creation or destruction of the other much less-abundant isotopes (Appendix A.3). For these isotopes, the NeNA chain has the following effects for different $T_6 = T/(10^6\ K)$ [17]:

- ^{21}Ne: its abundance first increases with T up to a factor of ~ 6 at $T_6 = 35$, then if T further increases it declines by a factor of 10^2 at $T_6 = 60$.
- ^{22}Ne: it disappears for $T_6 < 30$ and recovers its initial value for $T_6 = 80$.
- ^{22}Na and ^{23}Na: the isotope 22 is generally negligible with respect to ^{23}Na. The abundance of ^{23}Na may increase by nearly an order of magnitude at H exhaustion in the range of $T_6 = 25$–60.
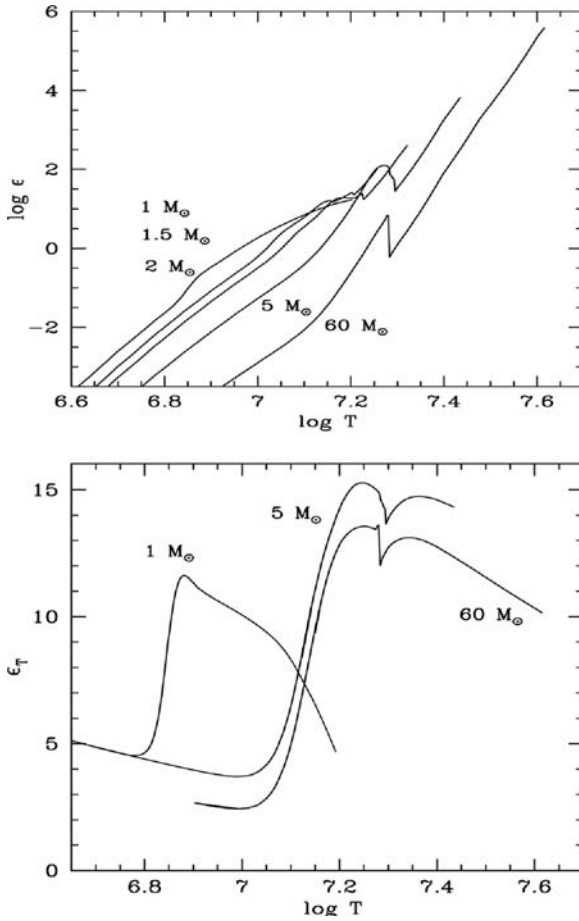
Fig. 25.3 *Top*: the log of the rates ε of nuclear energy generation in erg g^{-1} s^{-1} as a function of T in different stars on the ZAMS and for the present Sun. The kicks in the curves mark the edge of the convective cores. Outside of the cores, the CNO elements are not in equilibrium and this produces higher ε. *Bottom*: the exponent ν or ε_T as a function of T

The main effect of the NeNa cycle is to produce some Na enhancements, a fact supported by observations in red giants and supergiants (see below). The much smaller rate (factor 10^{-2}–10^{-3}) of ^{23}Na(p,γ)^{24}Mg with respect to ^{23}Na(p,α)^{20}Ne supports the view that the NeNa reactions form a cycle.

The MgAl cycle is, in principle, initiated by ^{24}Mg, the most abundant isotope of the cycle. However, the reaction rate of ^{24}Mg(p,γ)^{25}Al is very slow so that practically no ^{24}Mg is destroyed except at $T_6 > 60$. ^{25}Al rapidly disintegrates into ^{25}Mg. Then, a (p,γ) reaction leads to ^{26}Al, which exists in two forms, the long-lived (half-life $t_{1/2} = 7.1 \times 10^5$ yr) ground state ^{26}Al^g and the short-lived ($t_{1/2} = 6.35$ s) isomeric state ^{26}Al^m, the ground state being favored. These two states are generally
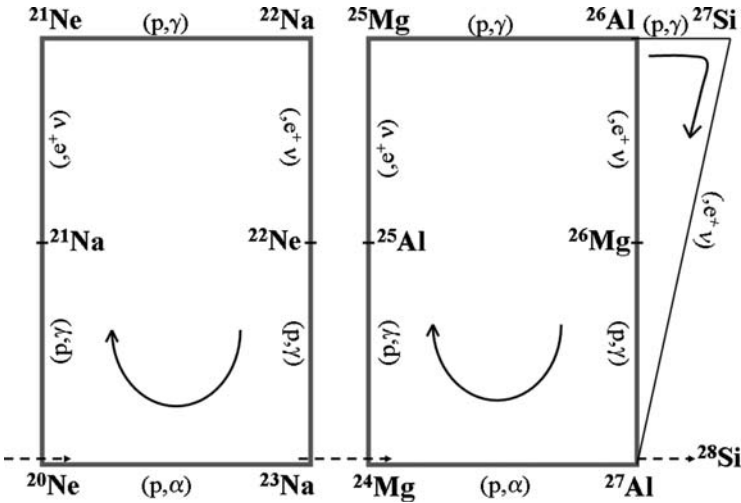
Fig. 25.4 The NeNa (*left*) and MgAl cycles (*right*)

treated as different elements. Reaction ^{25}Mg(p,γ)^{26}Al has the highest rate (at least larger by 3 orders of magnitude compared to the destruction of ^{24}Mg), thus the amount of radioactive ^{26}Al depends mainly on the initial quantity of ^{25}Mg. This reaction starts above $T_6 = 20$ and becomes very efficient to create ^{26}Al for $T_6 > 40$.

The resulting ^{26}Al^g is a most important isotope, since the e$^+$ disintegration of ^{26}Al^g and the subsequent annihilation of pairs e$^+$e$^-$ give rise to an observable γ line at 1.8 MeV. For $T < 40$, the destruction of ^{26}Al^g occurs mainly through β decay. Above $T_6 = 40$ (where lots of ^{26}Al^g is created), reaction ^{26}Al^g(p,γ)^{27}Si(,e$^+$v)^{27}Al comes into play in concurrence with the channel through ^{26}Mg. The rate of the (p,γ) destruction of ^{26}Al^g is uncertain, so that it affects the predictions of the γ-ray production as well as the ^{27}Al abundance. This abundance increases for $T_6 > 40$, up to an order of magnitude at $T_6 = 70$. However, the destruction rates of ^{27}Al by ^{27}Al(p,α)^{24}Mg and ^{27}Al(p,γ)^{28}Si are also uncertain, which may affect the cycling character of the MgAl cycle. Figure 26.18 shows the variety of conditions, in which H burning with the MgAl and NeNa cycles may occur.

25.1.5.1 Observational Consequences of the NeNa and MgAl Cycles

There are several astrophysical consequences of these two cycles, which we briefly mention. First, the 1.8 MeV γ-ray emission observed by satellites HEAO-3, SMM and INTEGRAL comes from the decay of ^{26}Al^g. The total amount of ^{26}Al^g in the Galaxy is estimated to be of the order of 1.5–3 M$_\odot$ and is mainly produced by massive OB stars. Measurements of isotopic ratios in meteorites and in dust grains likely of stellar origin indicate that ^{26}Al^g has decayed "in situ" starting from values compatible with stellar yields.

Globular cluster stars show two noticeable anticorrelations. The Na vs. O anti-correlation shows large [Na/Fe] excesses in stars with relative [O/Fe] deficiencies (the brackets indicate the excesses in log with respect to solar ratios). This anticorrelation results from the (p,γ) reaction on ^{16}O (cf. Fig. 25.1) which destroys ^{16}O (making ^{14}N), and from (p,γ) on ^{22}Ne in a partial NeNa cycle leading to ^{23}Na (at $T_6 > 20$). At $T_6 > 40$, ^{23}Na comes mainly from ^{20}Ne in the full NeNa cycle. There is also an anticorrelation MgAl, it results from the ^{24}Mg destruction and ^{27}Al production in the MgAl cycle. These anticorrelations seem to result [156] from enrichments by the winds of massive rotating stars in previous star generations. These winds had the composition of matter processed by the CNO, NeNa and MgAl cycles.

25.2   Basic Properties of MS Stars

We first examine some global properties of MS stars: their differences in structure and the change of their main parameters with mass and lifetimes.

25.2.1   Differences in Structure

High- and low-mass stars have very different internal structures (Fig. 25.5). Above about 1.2 M$_\odot$, the CNO cycles dominate the energy production (Fig. 25.2). The nuclear energy generation rate ε strongly depends on T, this dependence is expressed by ε_T or ν (Fig. 25.3). This means that the luminosity L is rapidly built near the center. In turn, the thermal gradient $\nabla_{\rm rad}$ (5.32) which depends on the ratio L_r/M_r is large. In stars with masses above ~ 1.2 M$_\odot$, $\nabla_{\rm rad}$ is larger than the adiabatic gradient $\nabla_{\rm ad}$ (about 2/5). Thus, when the CNO cycles dominate (at first it is just the CN cycle), the criterion for convective instability (5.54) is satisfied. This is why stars more massive than about 1.2 M$_\odot$ have a convective core. The size of the convective core determines the mass fraction which participates in the nuclear burning, the cores cover larger mass fractions in more massive stars. Stars with $M < 1.2$ M$_\odot$ burn hydrogen by the pp chains, with a milder dependence on T (Fig. 25.2) and thus show no convective cores, their deep interior being fully radiative.

The outer structures of low- and high-mass stars are also very different (Fig. 25.5). For $T_{\rm eff} < 7500$ K which corresponds to stellar masses $M < 1.4$ M$_\odot$, the opacities κ in the stellar envelopes are large as illustrated by Fig. 8.4, because hydrogen and other elements are partially ionized and provide numerous transitions. Larger κ values imply larger $\nabla_{\rm rad}$ (5.32) and thus convection. This is why stars with $M < 1.4$ M$_\odot$ have external convective envelopes, which extend deeper for lower masses. Details on the internal structure of a 1 M$_\odot$ are given below (Sect. 25.3). Below about 0.4 M$_\odot$, the opacities are large enough everywhere to make the stars fully convective.
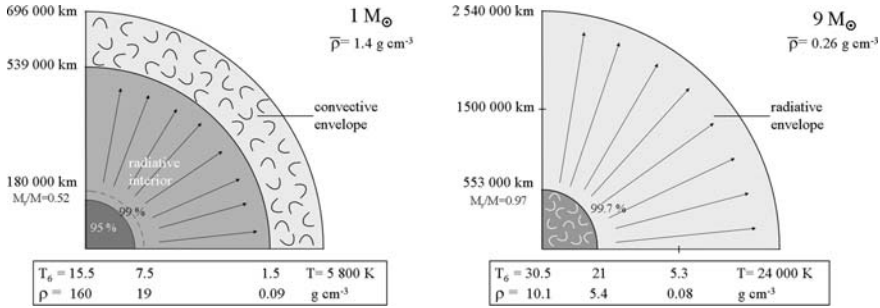
Fig. 25.5 Schematic structure of the Sun and a star of 9 $M_\odot$ on the main sequence with indications of T and ϱ. Cloudy regions indicate convection. The percentages indicate the fraction of the total energy produced

25.2.2 Main Parameters as a Function of Mass

Table 25.4 shows the main parameters as a function of mass for stars with a standard composition: luminosity L, $T_{\rm eff}$, gravity, radius R, mass fraction q_c of the convective core, mean density $\overline{\varrho}$, central density ϱ_c and central temperature T_c. These models are calculated with an overshooting parameter $d_{\rm over}/H_P = 0.2$ for $M \geq 1.5$ $M_\odot$; for 1.25 $M_\odot$ and below there is no overshooting included. The models starting H burning are chemically homogeneous: the stars are on the zero-age main sequence (ZAMS). Most global properties vary exponentially with mass, thus they are better represented in log scales. The main relation is evidently the M–L relation

$$L \sim M^\alpha . \qquad (25.19)$$

For a constant opacity, a value of $\alpha = 3$ is appropriate (24.55), this exponent is also an average for all stars. It gives a luminosity of 10^6 $L_\odot$ for a 100 $M_\odot$ star. Figure 25.6 shows the mass–luminosity relation, one notices the changes of the slope α as a function of mass (Table 25.5). These changes are due to the differences in opacities, nuclear rates and radiation pressure (Sect. 24.3). The change of α determines how the lifetimes vary with M (Sect. 25.2.3).

The stellar radii for main sequence stars increase only weakly with mass. A relation of the following form may be considered:

$$R \sim M^\beta . \qquad (25.20)$$

An exponent $\beta = 0.60$ characterizes this relation in the range of 1–120 $M_\odot$, $\beta = 0.56$ for the range 15–120 $M_\odot$, $\beta = 0.64$ for 1–15 $M_\odot$. In the interval 1–3 $M_\odot$, $\beta = 0.75$. These values are close to 0.7 as suggested by the homology relations for the upper MS stars (Sect. 24.3). Figure 25.7 illustrates the variations of the stellar radii as a function of the masses for different metallicities, one notices the much smaller radii for large masses at lower Z.

Table 25.4 Stellar parameters on the zero-age sequence for models of composition $X = 0.68$, $Y = 0.30$ and $Z = 0.02$ [120, 513]

$M/M_\odot$	$\log L/L_\odot$	$\log T_{\mathrm{eff}}$	$\log g$	$R/R_\odot$	q_c	$\overline{\varrho}$	$\log \varrho_c$	$\log T_c$
120	6.252	4.727	4.126	15.683	0.867	0.0438	0.171	7.638
85	6.006	4.705	4.134	13.075	0.822	0.0536	0.233	7.621
60	5.728	4.683	4.173	10.506	0.746	0.0729	0.332	7.611
40	5.373	4.640	4.180	8.510	0.664	0.0914	0.429	7.589
25	4.897	4.579	4.208	6.515	0.555	0.1273	0.577	7.564
20	4.650	4.544	4.218	5.760	0.508	0.1474	0.653	7.550
15	4.303	4.492	4.232	4.908	0.446	0.1787	0.762	7.529
12	4.013	4.448	4.249	4.305	0.408	0.2118	0.858	7.513
9	3.617	4.383	4.260	3.681	0.367	0.2542	0.988	7.488
7	3.257	4.321	4.263	3.235	0.342	0.2912	1.104	7.464
5	2.740	4.235	4.290	2.651	0.314	0.3780	1.290	7.433
4	2.385	4.173	4.300	2.344	0.294	0.4375	1.412	7.410
3	1.909	4.088	4.311	2.004	0.262	0.5250	1.570	7.377
2.50	1.600	4.031	4.313	1.826	0.235	0.5783	1.669	7.355
2.00	1.209	3.958	4.315	1.629	0.208	0.6516	1.780	7.323
1.70	0.916	3.901	4.309	1.512	0.186	0.6927	1.851	7.295
1.50	0.676	3.852	4.299	1.437	0.173	0.7119	1.881	7.265
1.25	0.325	3.808	4.395	1.175	0.031	1.085	1.928	7.213
1.00	−0.163	3.751	4.558	0.871	0.000	2.133	1.891	7.134
0.90	−0.313	3.729	4.574	0.811	0.000	2.378	1.917	7.108
0.80	−0.554	3.694	4.624	0.722	0.000	2.996	1.905	7.070
0.70	−0.821	3.654	4.673	0.638	0.000	3.793	1.893	7.030
0.60	−1.090	3.623	4.751	0.540	0.000	5.367	1.880	6.990
0.50	−1.370	3.595	4.840	0.445	0.000	7.986	1.869	6.953
0.40	−1.640	3.572	4.921	0.363	0.000	11.817	1.885	6.926
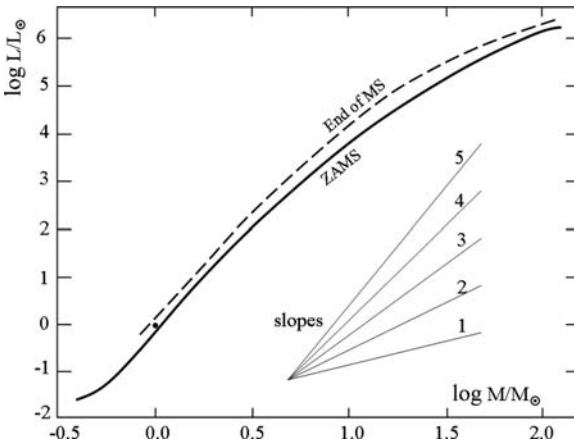
Fig. 25.6 The mass-luminosity relation for stars from 0.4 to 120 $M_\odot$ on the ZAMS and at the end of the MS phase for models with $X = 0.68$ and $Z = 0.02$. The dot shows the solar values. Some slopes are shown [513]

Table 25.5 The exponent α of the mass–luminosity relation

Mass in $M_\odot$	α
120–60	1.74
60–20	2.26
20–9	2.98
9–2	3.69
2–1	4.56
1–0.6	4.00
0.6–0.4	3.01
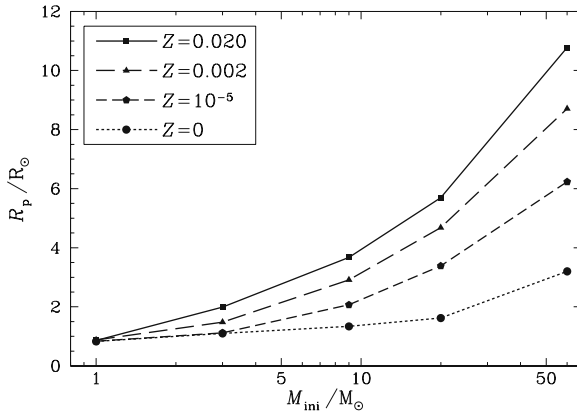
Fig. 25.7 The radii for models on the ZAMS vs. masses for different metallicities Z in the absence of rotation. R_p is here the stellar radius. From S. Ekström et al. [176]

The mass fraction of the convective core increases with mass (Table 25.4), because in high-mass stars the high ratio of radiation to gas pressure makes ∇_{ad} to decrease (Sect. 7.5). The mean density behaves like $\overline{\varrho} \sim M/R^3$, as $R \sim M^{0.6}$ it evidently decreases for massive stars. The central density behaves about in the same way; however, below 1.7 $M_\odot$ it keeps more or less constant. For very low stellar masses, the increasing electron degeneracy makes the average density to increase fast. The central temperature T_c increases continuously with mass because it varies like M/R (1.26).

25.2.3 Evolutionary Timescales

The lifetime of a star, alike the lifetime of a wood fire, is mainly determined by the amount of fuel available divided by the power emitted. For a star, the lifetime t_H of the H-burning phase is

$$t_H \approx \frac{\text{fuel available}}{\text{power}} \approx \frac{\Delta M c^2}{\overline{L}}, \tag{25.21}$$

where ΔM is the total mass defect, i.e., the total quantity of stellar matter annihilated in a star of average luminosity $\bar{L}$ during the MS phase. For the fusion reaction $4\,{}^1\text{H} \rightarrow {}^4\text{He}$, $4 \times 1.008\ m_\text{u}$ is turned into one He nucleus of mass $4.003\ m_\text{u}$, the mass difference Δm for one reaction is

$$
\begin{aligned}
4\ {}^1\text{H} &\rightarrow 4 \times 1.008\ m_\text{u} = & 4.032\ m_\text{u} \\
-\ {}^4\text{He} &\rightarrow & = -4.003\ m_\text{u} \\
\hline
\Delta m &= & 0.029\ m_\text{u}.
\end{aligned}
$$

The reaction involves four nucleons, the relative mass defect is $\Delta m/m = 0.029/4.032 = 0.0072$. The total mass defect ΔM for a star of mass M is $\Delta M = 0.0072 \times q_\text{c} \times M$ where q_c is the mass fraction of the convective core, or the region of efficient nuclear production for stars without radiative core. The lifetime of the H-burning phase is

$$
t_\text{H} \approx \frac{0.007\, q_\text{c}\, M\, c^2}{\bar{L}} . \tag{25.22}
$$

For the Sun, with $q_\text{c} \approx 0.1$ and $\bar{L} = L_\odot$, one gets $t_\text{H} \approx 3 \times 10^{17}\,\text{s} \approx 10^{10}$ yr, which is a correct order of magnitude (see Table 25.6). For other stellar masses, accounting for the mass–luminosity relation $L \sim M^\alpha$, one has

$$
t_\text{H} \sim \frac{M}{\bar{L}} \sim M^{1-\alpha} . \tag{25.23}
$$

For an average exponent $\alpha = 3$, this gives $t_\text{H} \sim M^{-2}$. From Table 25.5, in the range 1–2 $M_\odot$ one has $t_\text{H} \sim M^{-3.5}$ and in the range 60–120 $M_\odot$, $t_\text{H} \sim M^{-0.7}$. The MS lifetimes vary a lot near 1 $M_\odot$ and little for high-mass stars, even more if one accounts for the change of q_c.

Table 25.6 shows the MS lifetimes for the models of composition $X = 0.68$, $Y = 0.30$ and $Z = 0.02$ of Table 25.4, with an overshooting of 0.20 H_P well fitting

Table 25.6 The MS lifetimes t_H as a function of mass for $X = 0.68$ and $Z = 0.02$ with mass loss and an overshooting of 0.2 H_P [513]

Mass ($M_\odot$)	t_H(yr)	Mass ($M_\odot$)	t_H(yr)
120	2.561×10^6	4	1.647×10^8
85	2.823×10^6	3	3.525×10^8
60	3.447×10^6	2.5	5.849×10^8
40	4.303×10^6	2	1.116×10^9
25	6.408×10^6	1.7	1.827×10^9
20	8.141×10^6	1.5	2.695×10^9
15	1.158×10^7	1.25	3.948×10^9
12	1.600×10^7	1.00	9.845×10^9
9	2.639×10^7	0.90	1.550×10^{10}
7	4.319×10^7	0.80	2.503×10^{10}
5	9.446×10^7		

the observed cluster sequences. Massive stars evolve much faster than low-mass stars (factor up to 10^4), they are fast nuclear reactors and the main contributors to the chemical enrichments of galaxies. A star of 0.7 $M_\odot$ has a MS lifetime of about 35 Gyr, i.e., much longer than the age of the Universe, thus very low-mass stars have not evolved beyond the MS phase. Figure 25.5 shows the MS lifetime as a function of mass for two different Z values. The detailed numerical results depend on all physical assumptions in the star modeling.

25.3   Solar Properties and Evolution

A correct solar model must fit a number of constraints. First, the model must be constructed with the initial abundances which give the observed abundances of the Sun [20] at its present age when diffusion is accounted for (see Appendix A.3). Second, at the present age estimation of 4.57×10^9 yr, the solar model must have the observed luminosity and radius (A.2). The helium content Y of the Sun has still some uncertainty and Y is often adjusted so as to satisfy the luminosity and other constraints. The value of the mixing-length ratio ℓ/H_P used to treat non-adiabatic convection in external regions influences essentially the radius (and very little the luminosity). ℓ/H_P is adjusted in this way which gives a value of $\ell/H_P \approx 1.6$ with OPAL opacities.

Third, the solar model must fit the helioseismological constraints, in particular the small and large separations (Sect. 16.5). There were some difficulties recently. Before the revision of the solar abundances by Asplund and Grevesse [20], there was an excellent agreement between solar models and helioseismic data. This agreement was altered (Sect. 16.5.1) by the new abundances [25]; however, an increase of the neon abundance by a factor of 3 up to $\log(\mathrm{Ne}) = 8.29$, on the scale in which $\log N(\mathrm{H}) = 12$, might be able to restore agreement [26], but the point is debated. The helioseismic data also fix the location of the bottom of the convective zone of the Sun at $M_r/M = 0.713$–0.709 [28, 131, 169] as well as the thickness of the tachocline (Sect. 16.6.3).

25.3.1   Internal Structure

Figure 25.8 illustrates some internal properties of the present Sun as a function of the mass fraction M_r/M. At $M_r/M = 0.50, 0.90$, the radius is $r/R \approx 0.25, 0.50$. The limit $\nabla_{\mathrm{ad}} = \nabla_{\mathrm{rad}}$, which formally defines the bottom of the convective envelope (without overshooting) is at $M_r/M = 0.975$, which corresponds to $r/R = 0.709$ and $T = 2.21 \times 10^6$ K. Thus, 30% of the external radius contains only about 2.5% of the solar mass. T decreases smoothly away from the center and steeply in the very outer layers. For masses above 99.4% (i.e., 84.0% of R), T is above 10^6 K. Pressure and density vary the same way when normalized to their central values. The rate ε is the

highest at the center, rapidly building the luminosity according to $L(r) = \int_0^r \varepsilon \, dM_r$, 50% being produced in the central 8% of the mass. In the case of massive stars, the central growth of the luminosity is even steeper, due to the very strong dependence of ε on T (Fig. 25.2). Figure 25.8 shows the details in the outer 2% of the solar mass, in particular one notices the steep decrease of T in the superficial layers due to the strong opacity.
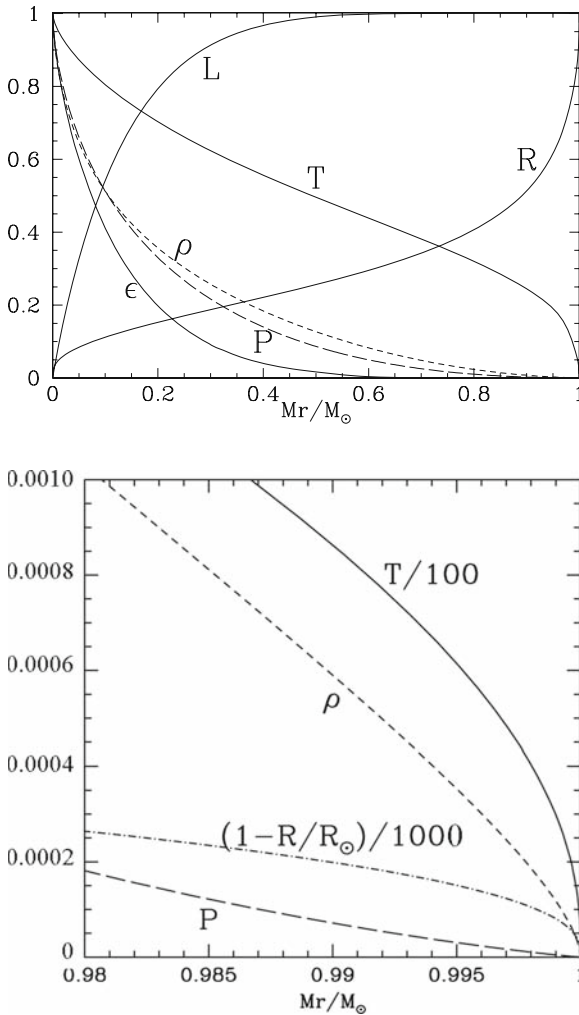
Fig. 25.8 Distribution of luminosity L, temperature T, density ϱ, pressure P, energy generation rate ε and radius R as functions of the mass fraction in the present Sun (best fit model for helioseismology). Each variable is normalized to its maximum value, i.e., $L = 3.8525 \times 10^{33}$ erg g^{-1} s^{-1}, $T = 1.5691 \times 10^7$ K, $\varrho = 1.5356 \times 10^2$ g cm^{-3}, $P = 2.3453 \times 10^{17}$ g cm^{-1} s^{-2}, $\varepsilon = 1.6982 \times 10$ erg g^{-1} s^{-1} and $R = 6.9645 \times 10^{10}$ cm. *Bottom figure*: details of the outer layers. T is divided by 10^2. For the radius the quantity $(1 - R/R_\odot)/1000$ is represented, i.e., a value 0.0002 corresponds to $R/R_\odot = 0.80$. Courtesy of P. Eggenberger

Figure 25.10 shows the evolution of internal structure of a 1 $M_\odot$ star. We see the broad region of nuclear energy production during the MS phase. Then, the main region of energy production migrates away from the center in a shell which narrows as evolution proceeds on the red giant branch.
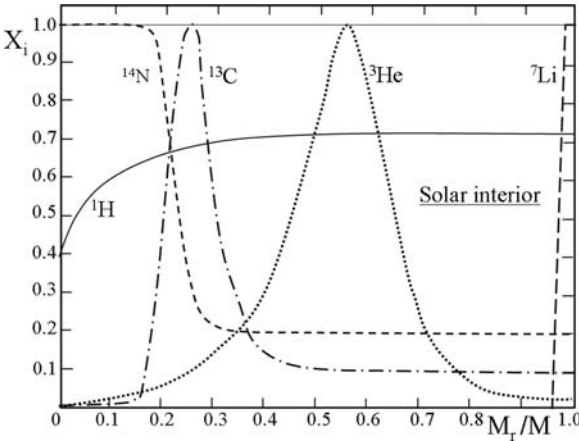
Fig. 25.9 Internal distribution of the abundance in mass fractions for some elements in the Sun. Except for H, the abundances are normalized to the maximum values reached in the Sun: $X(^{14}\mathrm{N}) = 3.34 \times 10^{-3}$ at the center, $X(^{13}\mathrm{C}) = 3.82 \times 10^{-4}$ at $M_r/M = 0.249$, $X(^{3}\mathrm{He}) = 3.448 \times 10^{-3}$ at $M_r/M = 0.550$, $X(^{7}\mathrm{Li}) = 7.37 \times 10^{-9}$ at the surface. ^{7}Li is destroyed for $T > 2.5 \times 10^6$ K, which corresponds to $M_r/M = 0.968$ and $r/R = 0.663$. From data by C. Charbonnel [119]
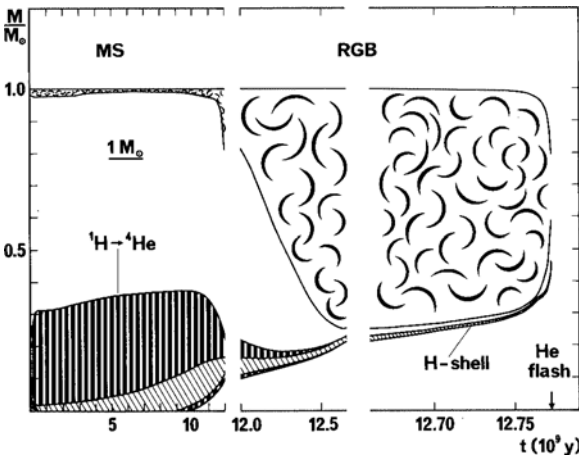
Fig. 25.10 Evolution of the internal structure of a 1 $M_\odot$ star with $X = 0.70$ and $Z = 0.02$ from the ZAMS to the He flash. The properties are represented according to the mass fraction as a function of time. Cloudy regions represent convective zones. Vertically hatched regions show the region where the nuclear energy generation rate ε is between 1 and 10 erg g^{-1} s^{-1} and diagonally hatched regions above 10 erg g^{-1} s^{-1}. From Maeder and Meynet [363]

The internal distribution of the elements in the Sun is illustrated in Fig. 25.9. The internal H profile shows a dip in the center with $X_c = 0.390$, because the nuclear rate ε is higher and has led to more fuel consumption. The H distribution joins smoothly a flat curve near the middle solar mass fraction (in stars with a convective core, the H profile is different, cf. Fig. 25.14). The distribution of ^{3}He shows a peak at $M_r/M = 0.55$ reaching $X(^3\text{He}) = 3.448 \times 10^{-3}$. There is a peak because close to the center ^{3}He is rapidly destroyed by the last reaction of the ppI chain, while in the outer layers it is not created by the second reaction. In the standard model, there is in principle no ^{3}He surface enrichment; however, mixing processes might have slightly enriched the surface with respect to the presolar abundances given by meteoritic data. In central regions, the basic CN cycle has already reached equilibrium and most of ^{12}C is turned to ^{14}N. In the transition region near $M_r/M = 0.25$, where CN equilibrium is partial, a bump of ^{13}C is formed. These new synthesized elements will appear at the surface in the red giant phase, when convective dredge-up brings them to surface. Below the radius where $T = 2.5 \times 10^6$ K, ^{7}Li is destroyed giving a very sharp profile.

25.3.2 The Evolution of the Sun

The evolution of the Sun in the HR diagram is illustrated in Fig. 25.11. It also shows all the various evolutionary phases discussed in other chapters. From the emergence of the Sun at the end of the protostellar stage (Chap. 19) characterized by the dynamical timescale ($\sim 10^6$ yr), the pre-main sequence proceeds at the Kelvin–Helmholtz timescale ($t_{\text{KH}} \sim 3 \times 10^7$ yr), first descending along the Hayashi branch and then joining the MS after a small hook due to the settling of the CN cycle to equilibrium. The H-burning or main sequence phase proceeds very slowly with a luminosity increase of about 7% per Gyr. The Sun with an age of 4.57 Gyr is presently near the middle of the MS phase, which ends at central H exhaustion at an age of 11.0052 Gyr.

After central H exhaustion, the nuclear H burning continues in a shell surrounding the extinct He core, which contracts making the pressure of degenerate electrons more important. The shell adds new He to the core and progressively migrates outward (Fig. 25.10). During these phases, the star leaves the MS phase and becomes a red giant. On the red giant branch, an outer convection zone develops and becomes deeper as the star becomes more luminous, at some stage its lower boundary penetrates the H-burning shell. This brings nuclear-processed materials to the surface, a process known as "dredge-up"; this is the first dredge-up. Being mostly convective ($\sim 70\%$ of the mass), the star lies close to the Hayashi branch (Sect. 20.2.1). The slow outward migration of the H-burning shell brings it to the chemical discontinuity let by the convective envelope at its deepest point. The decrease in the mean molecular weight μ makes a drop in luminosity, before L further increases again. This temporary slowing down of the brightening produces a small accumulation of stars in the sequence of old clusters in the HR diagram. In its further evolution, the

stellar luminosity essentially depends on the mass of the degenerate He core, a property which also applies to more massive stars in the advanced stages (Fig. 26.14). As the core grows, the rising of the luminosity on the red giant branch accelerates, as well as the radius inflation which reaches 10, then 100 and finally 234 $R_\odot$ at the tip of the red giant branch at an age of 13.210735 Gyr. About 0.3 $M_\odot$ is lost by stellar winds during the brightest part of this evolution.

At the point marked by a star at the top of the red giant branch, the so-called He flash occurs. The He-temperature ignition is reached in the core which is highly degenerate, with a central density of 1.02×10^6 g cm^{-3}. This produces a violent nuclear instability (Sect. 3.5). Due to strong neutrino cooling, the maximum T is at some distance of the center ($M_r/M \approx 0.1$), where degenerate He burning starts. Energy is radiated both toward the interior (where it is then evacuated by neutrinos) and the exterior. The high energy production by the flash drives a new temporary convective layer, which rapidly dies out without merging with the outer convective envelope. The He flash with its violent divergence of the nuclear energy production rate has for main effect to release the internal electron degeneracy in the core. At an age of 13.212520 Gyr, i.e., in about 1.8×10^6 yr, the star readjusts to non-degenerate central conditions. During these events, the central He content has decreased by about 5% from $Y_c = 0.986$ to 0.936. Then the star starts its non-degenerate phase of central He burning (point marked by a star at $\log L/L_\odot \approx 1.85$ in Fig. 25.11).
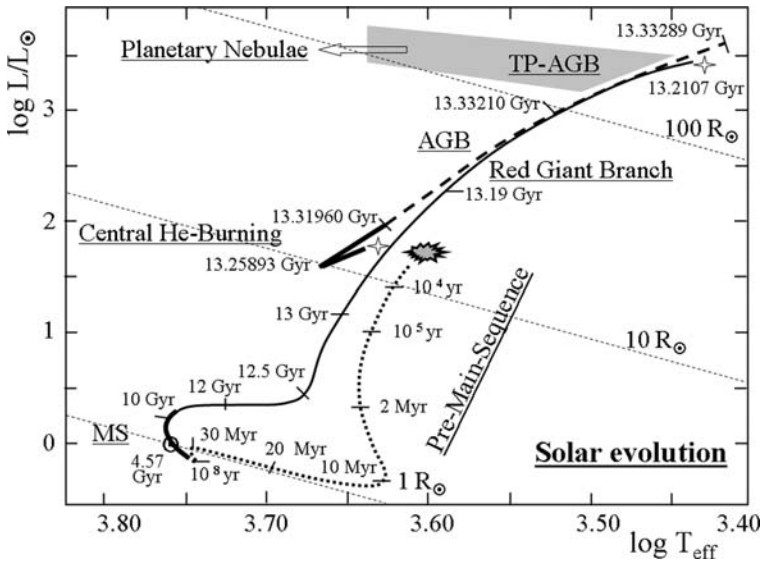
Fig. 25.11 HR diagram of the solar evolution with the best fit composition $X = 0.72$, $Y = 0.266$ and $Z = 0.014$ from the emergence of the dust cloud at the top of the Hayashi branch (taken here as zero age) to the evolution toward the planetary nebulae. Ages are indicated along the track (the composition being slightly different from that of Fig. 25.10, the timescales are also slightly different). The two 4-pike stars show the beginning and end of the He flash, which leads to the central He-burning sequence. From data by C. Charbonnel [119]
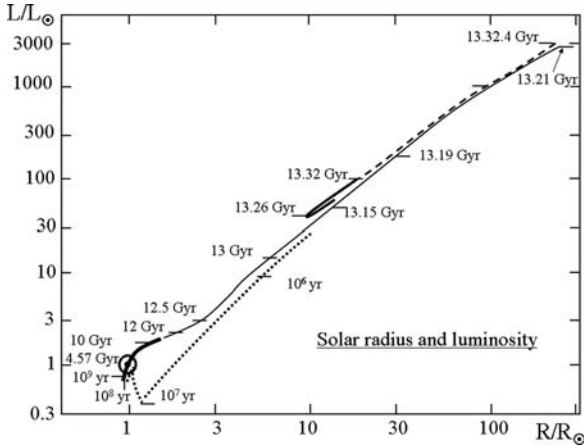
Fig. 25.12 The variations of luminosity and radius of the Sun through the ages. Same source [119] as in Fig. 25.11

The star enters a phase of non-degenerate He burning. The luminosity slightly decreases up to an age of 13.25893 Gyr where the central He content is $Y_c = 0.3620$ and He burning makes the star brightening again. For lower metallicity Z stars, this corresponds to the so-called horizontal branch (Sect. 26.5); at solar or higher Z, the corresponding accumulation of stars in the HR diagram is known as "the clump". The brightening and radius increase bring the star to the asymptotic giant branch (AGB), which joins asymptotically the red giant branch. This complex phase is studied in more detail in Sect. 26.6. Central He is exhausted at an age of 13.3196 Gyr. Most of the time between the end of central H burning and He ignition (2.314 Gyr) is spent in the H-shell burning on the red giant branch, while the duration of the quiet central He-burning lifetime is only 1.07×10^8 yr (plus 1.8×10^6 for the He flash). This is much shorter (by a factor of 10^2!) than the MS lifetime, this is due to the smaller nuclear energy available per nucleon, but even more because the star is much brighter than on the MS (Fig. 25.12).

After central He exhaustion, He burning goes on in a thin shell. As seen in Sect. 3.5.1, nuclear burning in very thin shells is unstable. This gives the so-called thermal pulses at the top of the AGB phase. This phase is called the TP-AGB phase (Sect. 26.6), while the early AGB phase is called E-AGB. The star gets a maximum radius of 312 $R_\odot$. It experiences increasing mass loss, the mass at the top of the TP-AGB phase is estimated to be about 0.6 $M_\odot$. During the last thermal pulses, the star in the post-AGB phase (Sect. 26.6.4) gets rid of its H-rich envelope and becomes a planetary nebula with a central white dwarf with a mass of about 0.55 $M_\odot$.

25.3.3   Solar Neutrinos

The so-called "solar neutrino problem" has been a severe problem for about 40 years [23], now it has found its solution in terms of neutrino physics, thanks in particular to the work of John Bahcall. At various steps of the pp chains, neutrinos are emitted

in the solar center. Due to their very small cross sections ($\sigma \sim 10^{-44}$ cm^2 at 1 MeV), they do not deposit their energy in the Sun, but escape in about 2 s. One can easily estimate the total solar neutrino flux. The solar luminosity is $L_\odot = 3.845 \times 10^{33}$ erg s^{-1} (Appendix A.2). The energy produced by the pp chain is 26.23 MeV (Table 25.1), i.e., 4.203×10^{-5} erg. This means that there are about

$$\frac{3.845 \times 10^{33} \text{ erg s}^{-1}}{4.203 \times 10^{-5} \text{ erg}} = 9.15 \times 10^{37} \text{ reactions s}^{-1}, \tag{25.24}$$

for the pp chains in the Sun. For each ppI reaction, there are two neutrinos emitted (since the first reaction has to work twice to make one ^{4}He nucleus), thus the rate of neutrino production is $L_\nu = 1.83 \times 10^{38}$ neutrinos s^{-1}, so the neutrino flux on the Earth is

$$F_\nu = \frac{1.83 \times 10^{38} \text{ neutrinos s}^{-1}}{4\pi(1.5 \times 10^{13})^2 \text{ cm}^2} = 6.47 \times 10^{10} \frac{\text{neutrinos}}{\text{cm}^2 \text{ s}}, \tag{25.25}$$

i.e., 60 billions of ν per second and per cm^2 (both in the day and night). The solar neutrino flux is counted in SNU (solar neutrino unit), which is defined as 1 SNU= 10^{-36} collisions per atom in the detector and per second. To get the energy spectrum of the solar neutrinos, the flux of each reaction producing neutrinos (see Table 25.7) has to be calculated.

In the Sun, about 84% of the He atoms formed are made by ppI, 14% by ppII while ppIII only occurs once in 5000. The CNO cycles contribute for about 1.6% to the energy. The pep neutrinos come from the reaction of two protons with an electron, this builds a ^{2}H nucleus. This reaction is not important energetically being 230 less probable than ppI; however, the pep neutrinos are significant. The hep neutrinos come from the fusion of ^{3}He with a proton forming an α particle. This reaction may produce neutrinos up to 18.77 MeV; however, the reaction is so rare, about 10^6 times less frequent than the one forming ^{7}Be, that it is negligible both energetically and for the neutrino production. The transformation of ^{7}Be into ^{7}Li produces neutrinos. Two energies are possible, 90% of them have an energy of 0.86 MeV, the rest 0.37 MeV. The neutrinos from ^{8}B may reach 14 MeV with an average of ~ 7.2 MeV, these are the most significant energetic neutrinos.

Table 25.7 Reactions producing neutrinos in the Sun

Reaction		Name	Energy
$p + p$	$\longrightarrow$ ^{2}H+e$^+$+ν_e	ppI	< 0.42 MeV
$p + e^- + p$	$\longrightarrow$ ^{2}H+ν_e	pep	1.44 MeV
^{3}He + p	$\longrightarrow$ ^{4}He+e$^+$+ν_e	hep	< 18.77 MeV
^{7}Be + e$^-$	$\longrightarrow$ ^{7}Li+ν_e	ppII	0.38, 0.86 MeV
^{8}B	$\longrightarrow$ ^{8}Be+e$^+$+ν_e	ppIII	< 14 MeV
^{13}N	$\longrightarrow$ ^{13}C+e$^+$+ν_e	CNO	< 1.20 MeV
^{15}O	$\longrightarrow$ ^{15}N+e$^+$+ν_e	CNO	< 1.73 MeV
^{17}F	$\longrightarrow$ ^{17}O+e$^+$+ν_e	CNO	< 1.74 MeV

The flux on Earth in ν number cm^{-2} s^{-1} of a given reaction, for example the ^{8}B disintegration, is given by an expression of the form

$$F_\nu(^8\mathrm{B}) = \frac{1}{4\pi d^2} \int_0^{M_\odot} \frac{\varepsilon_{17\mathrm{Be}}(M_r)\,dM_r}{Q_{17\mathrm{Be}}(erg)}\,, \tag{25.26}$$

where d is the distance from the Earth to the Sun. The various reactions have a different T sensitivity. For example, $F_\nu(^8\mathrm{B}) \sim T^{18}$, the other reactions have milder T dependence, for example, the pp neutrinos behave like $\varepsilon(\mathrm{ppI})$, i.e., $F_\nu(\mathrm{pp}) \sim T^4$. Thus, the half of the neutrinos from ^{8}B are emitted inside 0.05 R$_\odot$, for ppI this is 0.11 R$_\odot$. On the whole, the neutrinos are probes of central conditions. The energy spectrum of the solar neutrinos received on Earth is illustrated in Fig. 25.13. We see in agreement with (25.25) that the neutrino flux is of the order of 10^{11} ν per cm^2 per second. At high energies, only the neutrinos from ^{8}B in the ppIII chain are detectable.

Various experiments have been developed since 40 years, the Davis or chlorine experiment, Gallex, SuperKamiokande, Sudbury Neutrino Observatory (SNO) and more recently Amanda in the Antarctica. The "Solar Neutrino Problem" was the fact that the various experiments since the Davis experiment of 1967 observed only about $1/3 - 1/2$ of the neutrinos predicted by solar models (R. Davis got the Nobel Prize in 2002). Solutions were searched in terms of non-standard solar models; however, the solutions which could explain the observed neutrino deficiency were rejected by the very accurate constraints from helioseismology (Sect. 16.5). The explanation of the problem in terms of the neutrino physics succeeded [27]. The SNO experiment played a major role in this context. The experiment is located at a depth of 2.5 km in a mine at Sudbury, Ontario. The detector consists of 100 T of "heavy water – ^{2}H$_2$O" with 10^4 photomultipliers. The system is highly sensitive due to the large cross section of ^{2}H, it can detect the three types of neutrinos by the following reactions:
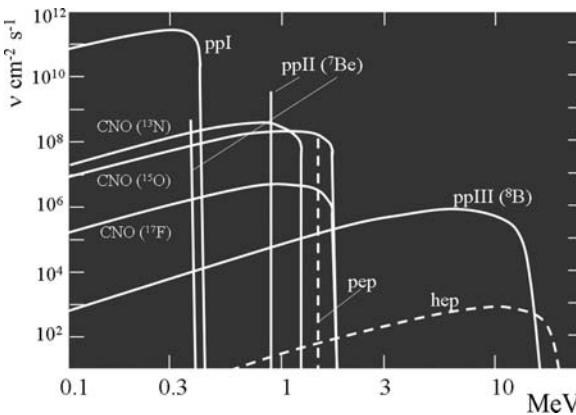
Fig. 25.13 The energy spectrum of the solar neutrinos (neutrino number per cm^2 and per second). Adapted from J. Bahcall, A.M. Serenelli and S. Basu [29]

$$\begin{aligned}
\nu_e + {}^2\text{H} &\longrightarrow p + p + e^-, \\
\nu_\mu + {}^2\text{H} &\longrightarrow p + n + \nu_\mu, \\
\nu_\tau + {}^2\text{H} &\longrightarrow p + n + \nu_\tau .
\end{aligned}$$

In addition the elastic diffusion $\nu_e + e^- \longrightarrow \nu_e + e^-$ of ν_e is observable, thanks to the Cerenkov emission of the electrons accelerated at relativistic speeds by neutrino collisions. The Cerenkov emission allows the SNO and SuperKamiokande experiments to have directional information on the neutrino source: the first neutrino picture of the Sun has been obtained. The results of the SNO experiment [5] show that experiment and theory are in full agreement now, if the three types of neutrinos are accounted for in the experiment, summed up and then compared to the predicted neutrino flux. The point is that the predicted neutrinos emitted by the Sun are all ν_e and the experiment implies that there are exchange reactions between the three types of neutrinos. This confirms an earlier suggestion of Mikheyev and Smirnov, following a work by Wolfenstein (see references in [24]), of interactions of the type

$$\nu_e \Longrightarrow \nu_\mu \Longrightarrow \nu_\tau . \tag{25.27}$$

The exchange occurs if the neutrino mass is between 10^{-4} and 10^{-2} eV. Several versions of the so-called MSW effect are existing with various exchange probabilities. The MSW effect leads to observable consequences [24].

– The energy spectrum of Cerenkov electrons: the energy spectrum of the neutrinos from ^{8}B is known (Fig. 25.13) and thus the energy spectrum of the Cerenkov electrons can be deduced. An excess is observed by SNO and SuperKamiokande for energies > 13 MeV in agreement with predictions.
– The day–night difference: the exchange rate depends on the medium crossed by the neutrinos. In the night there are more exchange reactions by the neutrinos reaching the detector through the Earth. An asymmetry $2(\text{night} - \text{day})/(\text{night} + \text{day}) \sim 0.07$ is observed consistently with the MSW effect [5]:
– A variation with the night zenithal angle: the predicted effect is small.
– The annual variations: nights are longer in winter, thus there is more interactions through the Earth. In addition in winter in the Northern hemisphere, the Earth is closer to the Sun leading to observable effects.

The observations support the MSW theory for now [5]. Neutrino astronomy, for the Sun and supernovae, is promising for major developments.

25.4   Evolution on the Main Sequence

25.4.1   Internal Properties, Tracks in the HR Diagram

During the MS phase, the fusion of hydrogen into helium progressively modifies the H and He profiles in the deep interior and thus the distribution of the mean molecular weight μ, while the composition of the outer layers does not change, in

principle. The average μ is thus increased and a higher luminosity is resulting. In this inhomogeneous body, the growth of the central L favors a global expansion of the outer layers, the associate cooling increases the opacity and makes T_{eff} to further decrease. This roughly explains the upward rightward displacement of the star in the HR diagram as it evolves (Fig. 25.16).

Figure 25.14 shows the internal profiles of hydrogen in models of 1 and 3 $M_\odot$. For the 1 $M_\odot$ star, as there is no convective mixing, the H profile just reflects the increase of the fusion rate ε near the center. At a given level, the change of the H-mass fraction is $\Delta X = \varepsilon \Delta t$. As ε is higher in the center, there is an increasing depletion in the center connected by a smooth curve to the unmodified surface composition. For the 3 $M_\odot$ star, the internal distribution of H during evolution is averaged in the convective core. Figure 25.14 shows the flat central H profile of a 3 $M_\odot$ star at two stages of its evolution. The differences of internal H distributions are reflected by the different shapes of the evolutionary tracks in the HR diagram (Fig. 25.17). Convective cores make the stars with $M \geq 1.25$ $M_\odot$ to evolve almost perpendicularly away from the ZAMS (zero-age main sequence), while in absence of central convection, the stars evolve first slightly upward the MS before deviating from it (Fig. 25.17).

At the beginning of the H-burning phase, stars are located on the ZAMS, where the composition is essentially homogeneous. As nuclear evolution proceeds, the stars leave the ZAMS with increasing L and R; the rightward tracks (Figs. 25.15 and 25.17) are characteristic of inhomogeneous evolution. In the case of homogeneous evolution, mixing processes are efficient enough to maintain the same composition from center to surface. The evolution is completely different: the star moves blueward in the HR diagram (Fig. 25.15), the MS lifetime is much longer since the
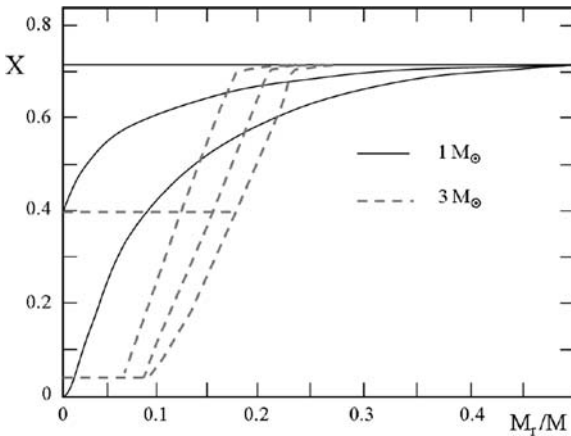
Fig. 25.14 Evolution of the distributions of hydrogen in stars of 1 and 3 $M_\odot$. Two stages of evolution are shown, at the middle and at the end of the H-burning phase. A convective core at 3 $M_\odot$ creates a flat H profile near the center. Three cases are shown for 3 $M_\odot$: no overshooting, overshooting with $d_{\text{over}}/H_P \approx 0.08$ and twice larger (from left to right). Adapted from the author [336]
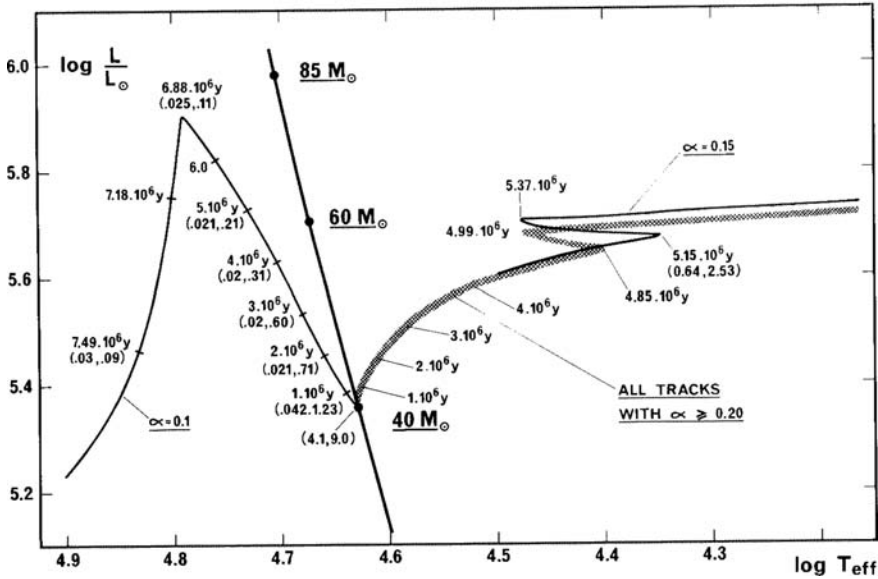
Fig. 25.15 HR diagram for 60 M$_\odot$ models evolving inhomogeneously with a rightward track and evolving homogeneously (blueward). The ages along the tracks are given, the C/N and O/N ratios (in mass fractions) at the surface are in parentheses. The α parameter is here a mixing parameter. From the author [344]

reservoir of nuclear fuel is much larger and the composition at the surface rapidly shows smaller C/N and O/N ratios typical of CNO equilibrium.

The reason for the homogeneous blueward evolution is accounted for by homology relations. From (24.49), the radius R has a weak dependence on μ, while the luminosity L depends strongly on μ (24.48). Thus, a star evolving homogeneously moves on a track of about constant R, which is less steep than the ZAMS (which follows a relation $L \sim T_{\rm eff}^{5.53}$, 24.53). As μ increases, the luminosity increases along this track of about constant R. If R would be strictly constant with μ, the homogeneous track would behave like $L \sim T_{\rm eff}^4$, which is not far from the track in Fig. 25.15.

Effects of overshooting and mixing: The overshooting from convective cores produces larger cores (Fig. 25.14). Thus the amount of nuclear fuel available is larger and the MS lifetimes are longer, e.g., by 18 and 36% in the examples of Fig. 25.16. The larger the overshooting, the more extended the MS track in the HR diagram. Observations support an overshooting of about 15–20% of a pressure scale height near 3 M$_\odot$ (Sect. 6.1.4), close to the intermediate case of Fig. 25.14. Other effects than core overshooting may contribute to the extension of the MS tracks, in particular, the various mixing processes due to rotation. The grid of models of Fig. 25.17 is performed with an average $d_{\rm over}/H_P \approx 0.20$, it reproduces well the observed cluster sequences. In this respect, the overshooting parameter derived from cluster sequences appears mostly as a fitting parameter covering all the physical effects which may extend the convective cores beyond $\nabla_{\rm rad} = \nabla_{\rm rad}$.
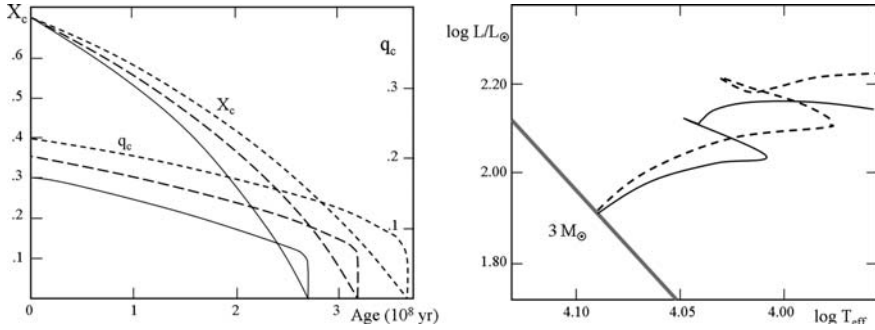
Fig. 25.16 *Left*: evolution of the core mass fraction for a 3 M$_\odot$ star with the three cases considered in Fig 25.14: no overshooting (continuous line), $d_{over}/H_P \approx 0.08$ and twice larger. The evolution of the central H content is also shown. *Right*: corresponding evolutionary tracks for the cases of no overshooting (continuous line) and of large overshooting. Adapted from the author [336]

25.5   The End of the Main Sequence

During the MS phase, H burning in the center progressively reduces the central H content (Fig. 25.16 left). The stars leave the ZAMS in the HR diagram and raise along their tracks, forming the long hatched band in Fig. 25.17. This phase ends when H is exhausted in the center ($X_c = 0$). For stars with a convective core ($M > 1.2$ M$_\odot$, the end of the MS phase occurs when H is exhausted in the core.

After that, the H burning migrates into a shell around the new He core, which then grows in mass due to the nuclear burning in the shell (Fig. 25.10). The He core, with T not high enough for He ignition, is deprived of nuclear energy source and becomes isothermal. There is a maximum mass fraction q_{SC} for an isothermal core of perfect gas, q_{SC} is the Schönberg–Chandrasekhar limit [520]. Above this limit, the core cannot sustain the upper layers and contracts. The star fast evolves toward the red giant branch.

25.5.1   The Schönberg–Chandrasekhar Limit

There is a maximum mass fraction permitted for an isothermal core of perfect gas. As P increases toward the center and T is constant, the density must provide the whole pressure and this becomes no longer possible. Above the limit, the isothermal core cannot sustain the pressure and collapses. This can be shown from the Virial theorem (1.54) applied to an isothermal core, with parameters labeled with an index 1. Let us call P_l the pressure at the core surface. With account for (1.48) the Virial theorem writes
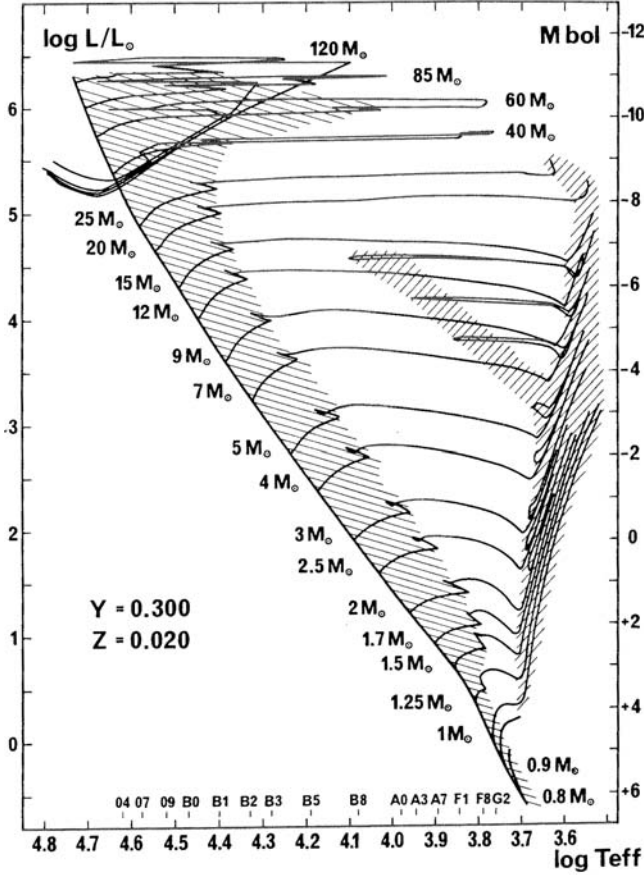
Fig. 25.17 Tracks in the HR diagram of models calculated with an overshooting parameter $d_{over}/H_P = 0.20$. At 1.25 $M_\odot$, a model without overshooting is used. The hatched areas indicate the slow phases of nuclear H burning (main sequence) and He burning (giants). Spectral types are indicated. The parts of the tracks descending to the left of the ZAMS for the most massive stars correspond to WR stars without hydrogen of types WNE and WC (Sect. 27.5). From G. Schaller et al. [513]

$$2E_{\text{cin},1} + \Omega_1 - 3P_1V_1 = 0,$$

$$\text{or} \quad 3(\Gamma_1 - 1)U_1 + \Omega_1 - 3P_1V_1 = 0. \tag{25.28}$$

One has $\Omega_1 = -q\,(GM_1^2/R_1)$. For a fully ionized perfect gas, one has $\Gamma_1 = 5/3$ and $U_1 = (3/2)\,[kT_1/(\mu_1 m_u)]\,M_1$. This gives for the pressure P_1 sustained by the core (see 18.2 in the derivation of the Jeans criterion in Sect. 18.2.1),

$$P_1 = \frac{3kT}{\mu_1 m_u}\frac{M_1}{4\pi R_1^3} - \frac{q\,GM_1^2}{4\pi R_1^4}. \tag{25.29}$$

This function has a maximum for $R_1 = (4/9)(\mu m_u q G M_1)/(k T_1)$. We adopt a structural factor $q = 3/2$ appropriate for MS stars (cf. Sect. 24.5.1). This value of R_1 introduced in (25.29) gives the maximum pressure sustainable by the isothermal core

$$P_{\max} \approx \frac{3^4}{2^7 \pi} \left(\frac{k T_1}{\mu_1 m_u} \right)^4 \frac{1}{G^3 M_1^2} \, . \tag{25.30}$$

For a given T, $P_{\max}$ is smaller if the core mass is larger. The core being isothermal, T_1 is also the central temperature $T_c \sim (1/3)(\overline{\mu} m_u/k)(q G M/R)$ (1.51), where $\overline{\mu}$ is the mean value for the whole star (M, R). $P_{\max}$ becomes

$$P_{\max} \approx \frac{3^4}{2^{11} \pi} \frac{G M^2}{R^4} \left(\frac{\overline{\mu}}{\mu_1} \right)^4 \left(\frac{M}{M_1} \right)^2 \, . \tag{25.31}$$

This pressure is to be compared to the actual pressure at the basis of the envelope $P_{\mathrm{env}} \approx a [3/(2\pi)](G M^2/R^4)$, i.e., a fraction "$a$" of the central pressure (1.20). A value of "a" $= 0.5$ is a reasonable estimate. For the core to be able to sustain the envelope, one must have $P_{\mathrm{env}} < P_{\max}$, which gives the condition

$$q_{\mathrm{SC}} = \frac{M_1}{M} < \left(\frac{3^3}{2^{10} a} \right)^{1/2} \left(\frac{\overline{\mu}}{\mu_1} \right)^2 \approx \frac{0.162}{\sqrt{a}} \left(\frac{\overline{\mu}}{\mu_1} \right)^2 \, . \tag{25.32}$$

This is the Schönberg–Chandrasekhar limit q_{SC}. If we take $a = 0.5$, the numerical factor in front of the term with μ becomes 0.230. In the core $\mu_1 \approx 4/3$, while in the envelope the mean molecular weight is ~ 0.61. $\overline{\mu}$ is some average over the star. Taking $\overline{\mu} = 0.9$, one gets $M_1/M \approx 0.10$ for the order of magnitude of the maximum permitted mass fraction. This is an appropriate order of magnitude for a star of about $2\,M_\odot$.

   If at the end of the MS, the He core is smaller than q_{SC}, H-shell burning proceeds increasing the core mass fraction until it reaches q_{SC}, then central contraction occurs. Upper main-sequence stars with masses greater than $\approx 1.8\,M_\odot$ have a core mass fraction bigger than q_{SC} at the end of the MS and when $X_c = 0$ they immediately experience central contraction, which is accompanied by an envelope inflation which brings the star to the red giant stage (Fig. 25.17, see also Sect. 26.2.1). Partial degeneracy slightly increases this mass fraction in solar-type stars.

25.5.2   Isochrones and Age Determinations

Isochrones (or time-lines) in the $\log L$ vs. $\log T_{\mathrm{eff}}$ diagram are obtained by connecting the points of the same ages on the tracks of various masses. The lines obtained in this way are the time lines or isochrones. In practice, a lot of intermediate tracks have to be calculated or interpolated (great care has to be given in the interpolations!). The isochrones in $\log L$ vs. $\log T_{\mathrm{eff}}$ have to be expressed in observables quantities, as for
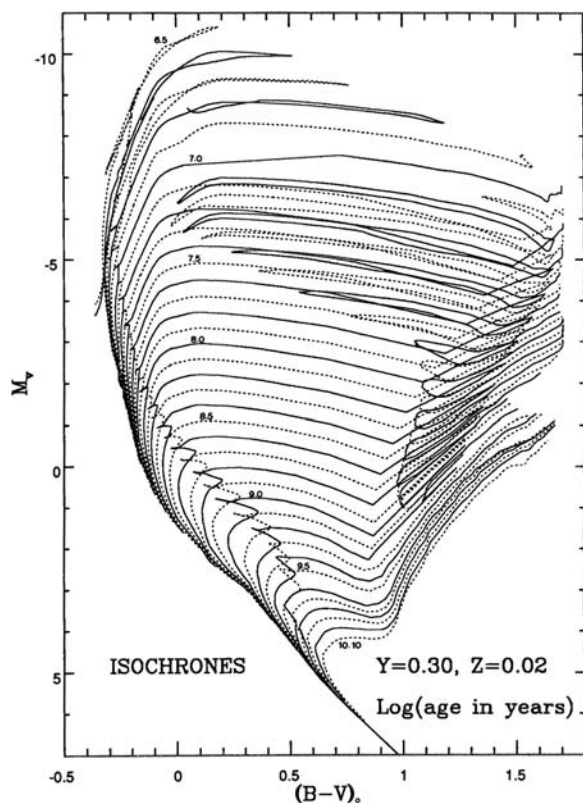
Fig. 25.18 Isochrones in the M_V vs. (B–V) diagram derived from tracks of Fig. 25.17, the logarithms of the ages are indicated. From Meynet et al. [415]

example M_V and $(B - V)$ (Fig. 25.18). For that, a reliable temperature calibration of the color index and a good scale of bolometric corrections are needed. There are extensive grids of evolutionary tracks and isochrones for broad ranges of masses and metallicities with appropriate He content Y made by the Padova Group [45, 208] and by the Geneva Group [121, 415, 435, 513] and these various works are actively pursued by the two groups (see also [598]).

In order to estimate the age of a star cluster, after proper account of interstellar reddening and distance modulus, the isochrone which best fits the observed sequence is searched. It provides the age estimate of the cluster, under the assumption that the stars in a cluster are coeval. This method has been extensively applied to open and globular clusters. The isochrones must be based on models with a composition corresponding to that of the considered cluster. In principle, the T_{eff} scale and the bolometric corrections must also be established for the cluster composition. For individual stars, the uncertainties of the age determinations are large, especially for stars close to the ZAMS. For ages of the order of 10^{10} yr or more as for globular clusters, the isochrones of different ages are so close to each other that the age

estimates are uneasy. Moreover, all uncertainties in the model physics and in the chemical composition of the cluster contribute to the age uncertainties.

Distributing stars on an isochrone according to the IMF allows one to make synthetic clusters. The comparison of the exact shapes of the real and synthetic clusters, as well as of the star distributions along the sequences, provides powerful tests of the models. Possible discrepancies may suggest some effects not accounted for in the model grids.

Chapter 26

Evolution in the He Burning and AGB Phases of Low and Intermediate Mass Stars with Rotation[*]

Helium forms the ashes of the H burning. At H exhaustion, the central temperature is not high enough to allow He to enter fusion reactions; a temperature above $T = 10^8$ K is necessary. The central stellar regions contract and heat until such a T is reached. The fusion of three nuclei of helium into carbon constitutes the entrance door to the further nucleosynthesis creating all the elements of the Mendeleiev table.

A number of remarkable types of objects are in the He-burning phase: the red giants, the red supergiants with radii up to 2000 $R_\odot$, the variable Cepheids, the AGB stars, most Wolf–Rayet stars, etc.

The models of the He-burning stars are very sensitive to the assumptions made as well as to the results of the previous phase. This led R. Kippenhahn to say that the evolution in the He-burning phase, in particular during the blue loops in the HR diagram, is a magnifying glass of all mistakes previously made in the modeling. The He-burning phase is the last stage of evolution observed before the stars become white dwarfs or explode as supernovae.

26.1 Helium Burning

To build elements heavier than ^{4}He, it would seem normal to first consider proton or α captures by helium nuclei; however the absence of stable nuclei of atomic mass $A = 5$ and 8 makes this kind of building problematic. In the early 1950s, nothing was supposed to halt the collapse at the end of H burning until supernova explosion intervenes at $T > 10^9$ K. It was the merit of Salpeter [506] to find that a Saha-like equilibrium $2\alpha \rightleftharpoons {}^8$Be allows a tiny concentration of ^{8}Be to exist (typically $X(^8\text{Be}) \approx 1.4 \times 10^{-8}$ at $T = 10^8$ K) and to capture an additional α particle, thus leading to ^{12}C formation. Hoyle [255] showed that the so-called triple-α reaction would not be fast enough at $T = 2 \times 10^8$ K to account for all the C, O and Ne observed in the Universe without a resonance of the reaction $^8\text{Be}(\alpha, \gamma)^{12}$C, which was effectively found subsequently. These discoveries opened the door for an evolution after the MS as well as for stellar nucleosynthesis.

---

[*]This chapter may form the matter of a basic introductory course.

Helium burning occurs at $T = (1 - 2) \times 10^8$ K in three steps:

1. There is first the formation of an unstable ^{8}Be nucleus:

$$^4\text{He} + ^4\text{He} \; \rightleftharpoons \; ^8\text{Be} + \gamma \quad (-92\,\text{keV})\,, \tag{26.1}$$
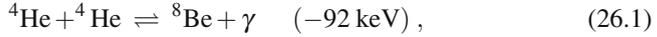
which is endothermic. The formed ^{8}Be has a lifetime of $\sim 2 \times 10^{-16}$ s, which is long with respect to the nuclear crossing time of 10^{-20} s.

2. During its short life, ^{8}Be may capture a α particle by a resonant reaction:

$$^8\text{Be} + ^4\text{He} \; \rightleftharpoons \; ^{12}\text{C}^* \quad (-286\,\text{keV})\,. \tag{26.2}$$
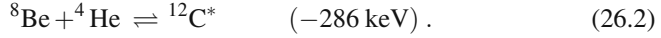
Most ^{12}C* is immediately destroyed by the inverse reaction.

3. The surviving ^{12}C* de-excites leading to stable ^{12}C:

$$^{12}\text{C}^* \rightarrow ^{12}\text{C} + \gamma \quad (7.656\,\text{MeV})\,. \tag{26.3}$$
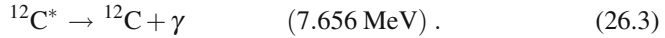
The total energy of the reaction, called the triple-α reaction, is $Q = 7.656 - (0.092 + 0.286) = 7.278$ MeV for 12 nucleons, which gives an average of 0.606 MeV per nucleon, i.e., 10.8 times less than for ppI. This corresponds to $E_{3\alpha} = 5.85 \times 10^{17}$ erg g^{-1} and contributes to make the He-burning phase relatively short. The rate of nuclear energy generation is

$$\varepsilon_{3\alpha} \approx 3.9 \times 10^{11} \frac{\varrho^2 Y^3}{T_8^3} e^{-\frac{42.94}{T_8}} f_{3\alpha} \quad \text{erg g}^{-1}\,\text{s}^{-1}\,, \tag{26.4}$$

where Y is the ^{4}He mass fraction and $f_{3\alpha}$ the screening factor. The nuclear rate ε has a strong dependence on T:

$$\varepsilon = \varepsilon_0 \varrho^2 Y^3 T^\nu, \quad \text{with } \nu \approx 19 \text{ at } T_8 = 2\,, \tag{26.5}$$

where ν varies between 40 and 19 from $T_8 = 1$ to 2. The triple collision creates a dependence in ϱ^2. The above reaction is accompanied by

$$^{12}\text{C}(\alpha, \gamma)^{16}\text{O} \; (7.162\,\text{MeV}) \qquad ^{16}\text{O}(\alpha, \gamma)^{20}\text{Ne} \; (4.730\,\text{MeV})\,. \tag{26.6}$$
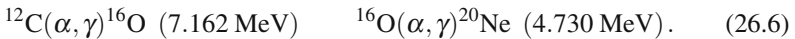
The first of this reaction is very important; it destroys a lot of ^{12}C and turns it into ^{16}O. In a remarkable sequel to the triple-α reaction, the energy of ^{12}C$ + \alpha$, which lies at 7.162 MeV, is close to a narrow resonance at 7.117 MeV of the ^{16}O nucleus, yet sufficiently far removed from it not to destroy all of the ^{12}C formed by the triple-α reaction. Still today, the exact rate of the ^{12}C$(\alpha, \gamma)^{16}$O contains some uncertainty. The value of this rate plays a great role for the amount of ^{16}O formed and for the size of the core in further evolutionary stages. The energy release of 7.162 MeV corresponds to 0.448 MeV per nucleon, i.e., to 4.32×10^{17} erg g^{-1}.

During the He-burning phase, the abundance of ^{12}C first increases and ^{16}O is negligible. Near the middle of the He phase, ^{12}C has a maximum because it is then significantly destroyed to produce ^{16}O, the abundance of which is then fast

increasing (Fig. 26.5). The amounts of C and O at the end of He burning are typically $X(^{12}C) \approx 0.19$ and $X(^{16}O) \approx 0.78$ in a 20 $M_\odot$ star. The amount of ^{16}O formed increases with T and thus with the stellar mass, since higher T are required when the electric charges of the particles are larger. The potential barrier for reaction $^{16}O(\alpha, \gamma)^{20}Ne$ is still higher and there is little neon formed ($X(^{20}Ne) \approx 0.0032$ at the end of He burning in a 20 $M_\odot$ star). The fraction of ^{20}Ne formed evidently increases with mass.

The above reactions are accompanied by some other ones, which are not important energetically, but have a nucleosynthetic importance, as they destroy ^{14}N which is the second most important product of CNO reactions:

$$^{14}N(\alpha, \gamma)^{18}F(, e^+ \nu_e)^{18}O(\alpha, \gamma)^{22}Ne \longrightarrow (\alpha, n)^{25}Mg \qquad (26.7)$$
$$\searrow (\alpha, \gamma)^{26}Mg, \qquad (26.8)$$

and

$$^{13}C(\alpha, n)^{16}O . \qquad (26.9)$$
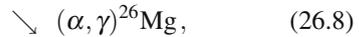
They also create new elements with many interesting consequences. Reaction $^{14}N(\alpha, \gamma)^{18}F$ is highly resonant and ^{14}N is rapidly destroyed at the beginning of He burning. Apart from a tiny fraction in the form of ^{18}O, ^{14}N is converted with the addition of two α into ^{22}Ne. The further evolution toward ^{25}Mg and ^{26}Mg is slower and occurs only in the most massive stars and in TP-AGB stars, where the neutron production leads to the synthesis of s-elements (Sect. 28.5.4). The reaction $^{13}C(\alpha,n)^{16}O$ occurs at the beginning of He burning and rapidly destroys the ^{13}C made in the H-burning phase. The processes of neutrino emission (Sect. 9.5) play a minor role during central He burning.

26.2 He Burning in Intermediate Mass Stars

We study the evolution of intermediate mass stars in the range of 2–9 $M_\odot$. Figure 25.17 shows the evolutionary tracks in the H- and He-burning phases for various masses. We examine the correspondence between the internal evolution and the tracks in the HR diagram for a 7 $M_\odot$ star (Fig. 26.1). The various steps [264, 285] are indicated by corresponding letters in the figures. Figure 26.2 shows the evolution of the structure of a 3 $M_\odot$ star.

26.2.1 From Main Sequence to Red Giants

A–B, Main sequence phase: this is the H-burning phase. The convective core decreases in mass letting behind it a zone of variable H and He contents. Only the inner part of the core produces a significant nuclear energy, but the available energy
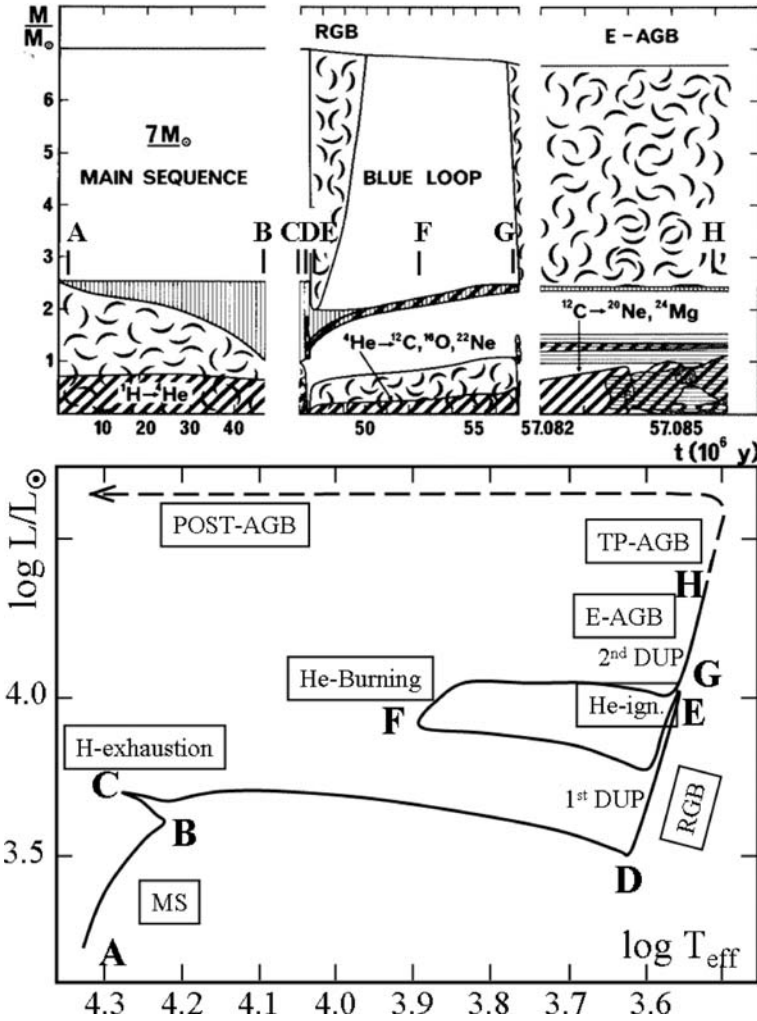
Fig. 26.1 *Upper part*: the evolution of the inner structure in the "Kippenhahn's way" for a star of 7 $M_\odot$ with $X = 0.70$ and $Z = 0.02$. The *horizontal scale* is the age from the ZAMS; the *vertical* is the mass. Cloudy regions are convective; hatched regions indicate where the nuclear energy rate is greater than 10^3 erg g^{-1} s^{-1}. Vertical hatching indicate variable H and He contents, horizontal hatching shows variable ^{12}C and ^{16}O. *White zones* are homogeneous. The models account for core overshooting in the H- and He-burning phases with $d_{over}/H_p = 0.25$. *Lower part*: track of the 7 $M_\odot$ in the HR diagram, with letters indicating the correspondence with the *upper part*. From the author and G. Meynet [363]
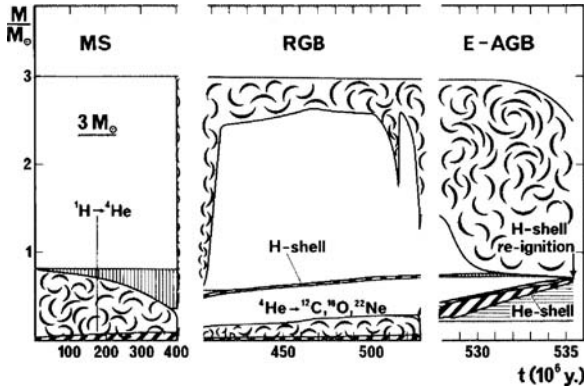
Fig. 26.2 Evolution of the inner structure for a star of 3 $M_\odot$, same remarks as for Fig. 26.1. From the author and G. Meynet [363]

reservoir is defined by the size of the convective core. This phase is the longest one; lifetimes are given in Table 25.6.

B–C, Overall contraction phase: in B, the central H content becomes very low with $X_c \approx 0.03$. To supply the energy, the core and the whole star contract. The decrease of the radius produces the hook from B to C in the HR diagram. In C, central hydrogen is exhausted, $X_c = 0$ and a He core is formed with a mass fraction of $\sim 10\%$ or more for larger masses.

C–D, Evolution toward the red giants: the transition from C to D occurs at the Kelvin–Helmholtz timescale, which is of the order of 1% of the MS lifetime. Thus, there are very few stars located in this region of the HR diagram, which is thus called the Hertzsprung gap. During this major transition an ensemble of effects intervenes.

(1) In C, the core deprived of nuclear sources becomes isothermal. Indeed from $dL_r/dM_r = 0$ we have with (3.17)

$$\varepsilon = 0 \implies L_r = 0; \quad \text{thus} \quad \frac{dT}{dr} = -\frac{3\,\kappa\varrho}{4\,acT^3}\frac{L_r}{4\pi r^2} \implies 0 . \quad (26.10)$$

There is a maximum mass fraction q_{SC} permitted for an isothermal core. This limiting fraction, known as the Schönberg–Chandrasekhar limit, is derived analytically in Sect. 25.5.1. If the actual core mass fraction in C is above q_{SC}, the core contracts at the Kelvin–Helmholtz timescale (1.73). This is typical of masses above 1.8 $M_\odot$ with a large isothermal core in C.

(2) Stars with $M < 1.8$ $M_\odot$ have a core mass fraction smaller than q_{SC} at the end of central H burning. Thus, these stars experience a phase of H burning in a relatively thick shell, progressively adding He to the isothermal core until it reaches the q_{SC} limit; then the core contracts. This phase of H burning in a thick shell (very short in Fig. 26.1) may, for the lower masses, last for a significant fraction of the H-burning phase. Some stars in clusters older than 10^9 yr are in this stage (e.g., cluster M 67).

(3) Core contraction does not stop before the nuclear energy generation takes over again (Sect. 15.4.3); thus it goes on until central He ignition. Remarkably, the core contraction also leads to a large expansion of the envelope so that the star becomes a red giant. This effect is often called the "mirror effect": An envelope expansion responds to a core contraction and reciprocally. The mirror effect has been discussed by several authors (e.g., [264, 285, 485, 554]) with different conclusions (see nb. 4 below).

Energy generation by contraction has a weak T dependence compared to nuclear reactions: ε_{nucl} goes like T^ν with high ν values, while $\varepsilon_{grav} \sim T$ (20.6). In Sect. 15.4.3 we see that nuclear energy generation rates with their high T sensitivity lead to stable situations for current opacity laws, in agreement with the heuristic analysis made in Sect. 3.2.1. On the contrary, the energy generation rate by contraction with its weak T dependence can never come out of an unstable situation.

(4) Breakdown of thermal equilibrium occurs in the envelope. Core contraction increases both ϱ and T with a law $\varrho \sim T^{1/3}$ and the initially high-energy production in the H-burning shell enhances the outgoing power. This favors a small envelope expansion and thus a small T decrease, which in turn makes an opacity increase in the envelope. Thus, a strange situation [485] is reached: Core contraction makes more L to be evacuated while the radiative transfer in the envelope can carry less luminosity. No thermal equilibrium is possible according to Sect. 15.4.3. At some stage, the breakdown of thermal equilibrium results in the envelope inflation at the Kelvin–Helmholtz timescale and leads to a red giant at point D (mirror effect).

(5) Shell-H burning and narrowing also characterize the transition from C to D. After H-core exhaustion the nuclear energy production goes on in the H-poor layers surrounding the core to form a thick H-burning shell. The strong energy production in the shell contributes to the inflation of the outer layers. Some authors consider the H shell as the main cause of radius inflation. It helps but is clearly not the main reason, because models in which ε is set to zero in the H shell also show the inflation to red giants [405]. During the second half of C–D, the shell narrows because (1) the inner shell layers are H exhausted and their He is added to the He core and (2) the envelope expansion lowers T and brings the nuclear reactions to an end. The lower L at point D results from both the weakening of the H-burning shell and the energy used in the envelope expansion. During further evolution the shell migrates outward increasing the He core.

(6) Close to point D, the lower T in the envelope produces a large increase in the opacity, now mainly due to ion H^- (Sect. 8.3.1), with electrons from the metals of low ionization potentials (Sect. 7.1.4). Convection reaches its deepest layer near point E, leading to the destruction of light fragile elements and to some surface enrichments (see D–E).

A high-density contrast forms between the core and the envelope, it increases in further phases. Apart from the outer layers, most of the envelope is adiabatic, which

makes a polytropic structure with $n = 3/2$. The star is (again) close to the Hayashi line (Sect. 20.2.1), with a T_{eff} nearly constant as L varies.

26.2.2   Evolution in the He-Burning Phase and Dredge-up

Let us further follow the evolution in the giant phase (Fig. 26.1) for stars which do not experience the He flash (cf. Sect. 25.3.2), i.e., for stellar masses above about 2.3 M$_\odot$.

D–E, Red giant branch, first dredge-up: the low T_{eff} resulting from envelope expansion produces very large opacities, which in turn favor convection. The external convective envelope becomes very deep and may cover 90% of the stellar radius (Fig. 5.8). The deep convective envelope reaches the layers processed by the CNO cycle and brings excesses of ^{14}N, ^{13}C and He to the surface together with a ^{12}C depletion. This is the first dredge-up. Figure 26.3 illustrates the predicted changes of the abundance ratios ^{14}N/^{12}C and ^{13}C/^{12}C along the red giant branch as functions of the luminosity for various stellar masses. The enrichment is first rapid and then there is a plateau, because the convective envelope does not get much deeper. More massive stars generally have stronger enrichments in the products of CNO burning, because the external convective envelopes reach deeper layers. The enrichments in ^{4}He are modest of the order of few percentage. The amplitude of ^{14}N and ^{13}C surface enrichments and the luminosity at which they appear on the red giant branch are powerful tests of the internal mixing.

Observations are in rough agreement with models for $M > 2.5$ M$_\odot$. However, there is a disagreement below this mass, in the sense that the observations show much more CNO-processed elements than predicted (e.g., ^{14}N and the ^{13}C/^{12}C ratio are too large [207, 220]). This suggests an additional mixing between the convective envelope and the H shell. Conservation of the angular momentum in red giant envelopes favors large differential rotation and shear mixing at the base of the envelope [118, 455]; however it does not seem sufficient to account for low-Z red giants.

Core contraction goes on until the temperature of central He ignition is reached. The energies from the core and the shell now contribute to increase the luminosity. The density profile of the star is more and more peaked at the center with an extended thin envelope.

E–F, He burning, blue loops: the temperature of He ignition depends on the density like ϱ^{-2}. Thus, He ignition occurs at a slightly lower central T for smaller masses, i.e., $T_{\text{c}} = 10^8$ K at 2 M$_\odot$ and 1.6×10^8 K at 20 M$_\odot$ (Fig. 26.9). The highly sensitive rate of ε produces a steep T gradient and a convective core appears within the central regions (Fig. 26.1) converting He into ^{12}C and ^{16}O. The contraction of the core is stopped and the core expands producing a decrease of L, surface convection recedes and the star leaves the Hayashi line. This is again the "mirror effect",
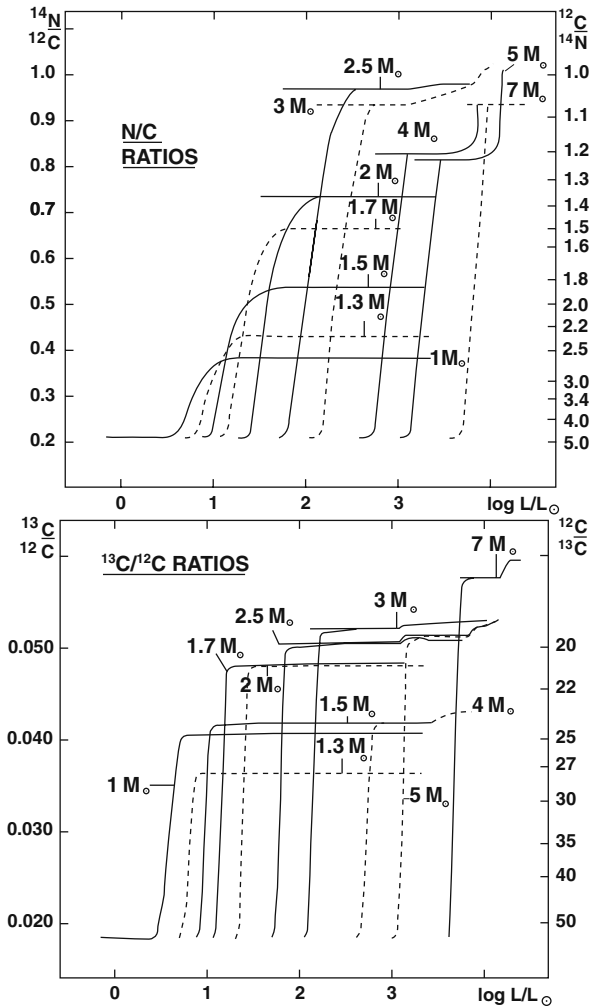
Fig. 26.3 *Top*: evolution of the surface ratio $X(^{14}N)/X(^{12}C)$ as a function of the luminosity on the red giant branch for different masses. *Bottom*: the same for $X(^{13}C)/X(^{12}C)$. From the author and G. Meynet [363]

but in the opposite way as between C and D. Core expansion produces envelope contraction, the stellar radius decreases and the star moves, first rapidly and then slowly toward point F, which is near the middle of the He phase. The core represents a much smaller mass fraction than during the MS phase. Overshooting for a given ratio d_{over}/H_P produces a smaller core increase than during the MS phase, because the pressure gradient is steeper. The H shell progressively looses its energetic importance and its outward migration slows down.
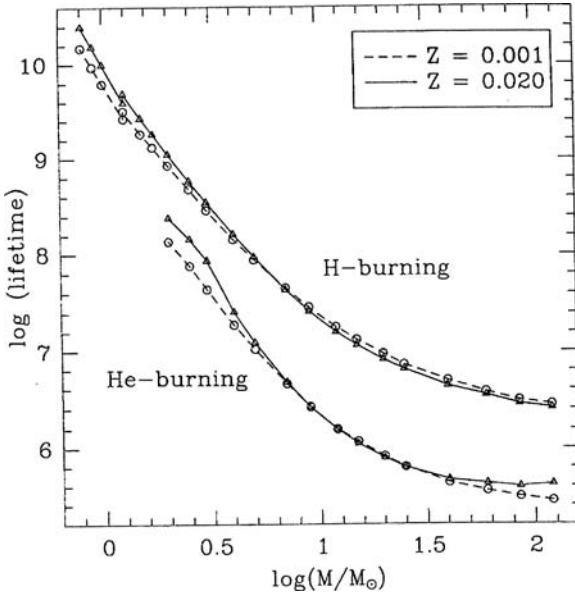
Fig. 26.4 The lifetimes (yr) for the H- and He-burning phases as a function of the mass on the ZAMS for $Z = 0.02$, $Y = 0.30$ and for $Z = 0.001$ and $Y = 0.243$, with an overshooting of $0.20\,H_P$ from the core. From G. Schaller et al. [513]

The duration of the He phase for the 7 $M_\odot$ model is 4.7×10^6 yr, i.e., 10% of the MS phase (this ratio is determined by L, the core sizes and the energy available per nucleon). Figure 25.17 indicates where most of the He-burning phase is spent, while Fig. 26.4 shows the lifetimes in the H- and He-burning phases for different masses for $Z = 0.02$ and $Z = 0.001$.

During its motion in the HR diagram from E to G, the star describes the blue loops, which are more extended for more massive stars (Fig. 25.17). The blue loops appear between about 3 and 12 $M_\odot$ (at standard composition); they are sensitive to most model ingredients (Sect. 26.2.4). During sufficiently extended blue loops, the stars cross the "Cepheid instability strip" (Sect. 15.5.2) where they pulsate radially and are observed as Cepheids. Most Cepheids occur in the slow part of the blue loop (near point F), if it lies within the instability strip. The blueward or redward evolution within the instability strip is responsible for the secular changes of some Cepheids. Cepheids no longer have the initial He and CNO compositions (Fig. 26.3), the He-surface mass fraction being a few percentage higher than the initial one.

F–G, End of central He burning: core He burning goes on after point F. When the central abundance Y_c of helium declines, the nuclear rate decreases ($\varepsilon \sim Y_c^3$) and central contraction again occurs. The mirror effect produces an expansion of the envelope and the star evolves to point G. In the second half of the He-burning phase, the reaction $^{12}C(\alpha, \gamma)^{16}O$ (with $\varepsilon \sim X(^4He)X(^{12}C)$) becomes dominant over
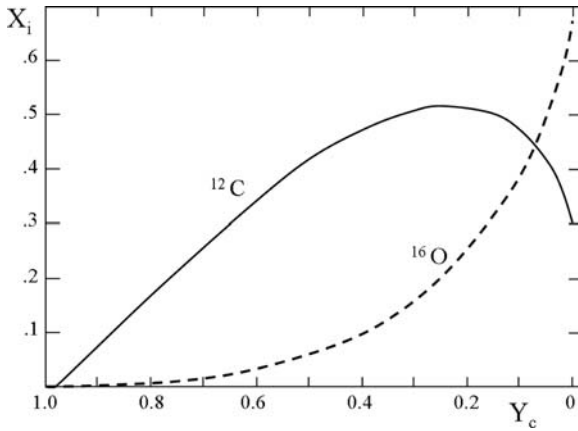
Fig. 26.5 Evolution of the carbon and oxygen abundances in the core of a 7 M$_\odot$ during the He-burning phase. The mass fraction of ^{12}C and ^{16}O is given as a function of the central helium content Y_c

^{4}He$(2\alpha, \gamma)^{12}$C, so that the core content in ^{12}C decreases (Fig. 26.5). At the end of He burning, the C and O abundances in the center of the 7 M$_\odot$ model are $X(^{12}$C$)=0.30$ and $X(^{16}$O$)=0.67$. The fraction of ^{16}O is higher in higher mass stars.

26.2.3 From AGB to the White Dwarfs

G–H, Upward the AGB phase: we briefly examine these stages; the complex physics of AGB stars is studied in Sect. 26.6. In point G, the He core is exhausted; the star is at the base of the so-called asymptotic giant branch (AGB), as also seen for the Sun (Fig. 25.11). A fraction of about 10% of the total mass has been removed by stellar winds. From the He-burning phase, the evolution depends much on the mass domain considered, the limits of the domains being influenced by rotation and overshooting. Below a limit called M_{up} (8.9 M$_\odot$ without overshooting), the central T is insufficient for the ignition of the ^{12}C$+^{12}$C reaction in the core. At this stage, the model consists of the three main regions: (1) a partly degenerate CO core. The energy from the nuclear reactions and core contraction is mainly evacuated by neutrinos, so that the photon luminosity is small in the core. The mass of the CO core determines the stellar properties. (2) An active He-burning shell produces a peak of luminosity equal to about twice the emergent luminosity; about half of the luminosity produced is used to expand the region above the He shell. The H shell is now extinct. (3) There is deep external convective envelope, which produces a second dredge-up (in stars with $M \geq 3.5$ M$_\odot$).

The 7 M$_\odot$ model in Fig. 26.1 has a central T high enough ($\sim 6 \times 10^8$ K) to ignite the ^{12}C$+^{12}$C reaction in the core (this behavior typical of larger masses is due to overshooting). However, C burning rapidly dies out and the star nevertheless evolves

like an AGB star (Fig. 26.9). Such objects near the upper limit of the AGB domain
are often called super-AGB stars (Sect. 26.6.4). Models with masses below M_{up} like
in Fig. 26.2 do not reach the T for C ignition. The CO core is surrounded by an
active He-burning shell, where reactions He $\longrightarrow$ C, O are increasing the CO-core
mass. The extinct H shell re-ignites, when it is almost reached by the He-burning
shell; this marks the end of the early AGB phase (E-AGB).

TP-AGB phase: Figure 26.6 shows the structure of the 3 $M_\odot$ model at the end of
the E-AGB phase. High degeneracy favors high electron conductivity (Fig. 8.3); this
leads to a nearly isothermal core. Strong neutrino emissions cool the center down,
so that the maximum T is reached near the outer edge of the CO core. The photon
luminosity is zero in the core and it raises to a maximum in the He-burning shell.
Outside the core, at the level of the He-burning shell there are very strong ϱ and T
gradients. Figure 26.6 also shows the various ε. There is a strong peak of energy
production in the He-burning shell (which also contracts). The temperature at the
base of the He shell increases with the mass of the CO core, so that the luminosity
produced by the He shell depends on the core mass (Fig. 26.14). The growth of
the core due to the He-shell burning makes the star rising on the AGB. The high
luminosity favors deep convection.
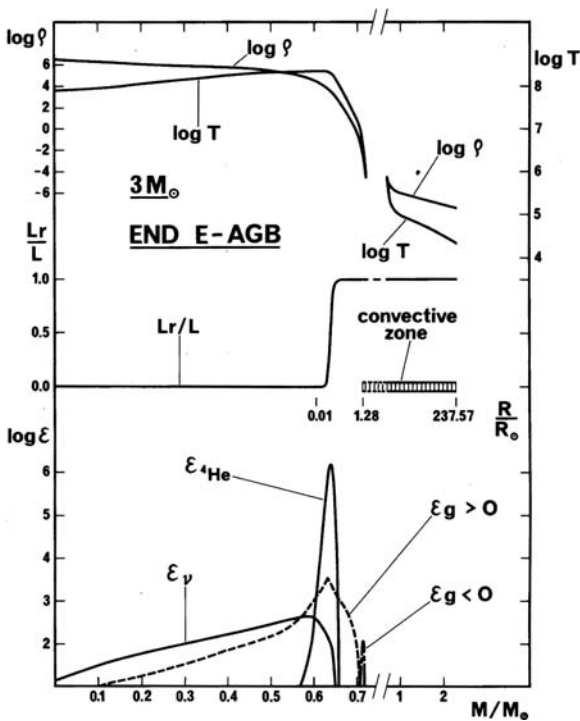
Fig. 26.6 Internal structure, luminosity and various ε rates in a 3 $M_\odot$ model at the end of the
E-AGB phase. From the author and G. Meynet [363]

During the end of its evolution, the star gets rid of its envelope revealing the central core, which becomes a white dwarf. The H- and He-burning shells are very thin and close to each other. Nuclear burning dominates in the H shell; however the thin He shell experiences instabilities (Sect. 3.5.1) with violent amplifications of He burning. This is the thermal pulse AGB phase (TP-AGB), during which the stars show cycles of strong luminosity changes with timescales of about 10^4–10^5 yr. The TP-AGB phase has major consequences: The mixing of the elements of the two shells produces the so-called *s*-elements by slow neutron capture on the existing elements of the Fe peak. The TP-AGB stars also become variables of the Mira type, with amplitudes up to 5 mag. and periods of 200–10^3 days. They experience strong mass loss and get rid of their envelopes. The last shell ejection makes a planetary nebula, which finally reveals a hot white dwarf.

26.2.4 The Blue Loops

The blue loops described in the HR diagram (Fig. 26.1) by stars in the range of 3–12 $M_\odot$ allow the stars to spend a fraction of their He-burning lifetime as Cepheids. We can easily understand which effects favor or inhibit the blue loops by using an interesting result by Kippenhahn and Weigert [285]: The blue extension of the loops mainly depends on the potential of the core $\Phi_c \sim M_c/R_c$. There is a critical value of the potential such that

$$\Phi_c < \Phi_{crit}(M) \;\Rightarrow\; \text{blue loops}\,,$$

$$\Phi_c > \Phi_{crit}(M) \;\Rightarrow\; \text{red giant}\,. \tag{26.11}$$

$\Phi_{crit}(M)$ increases with mass, being typically 0.83, 0.93 and 0.99 for 3, 5 and 7 $M_\odot$, respectively. Without entering extensive discussions, the consistency of expression (26.11) can be understood in the following way. The core potential grows with the core mass like $\Phi_c \sim M_c^{0.4}$. This means that any effect which increases the core mass and thus Φ_c also favors a redward evolution instead of a blue loop. (A red giant of a given mass has a very concentrated core, thus a high core potential, while a blue giant on the loops has a He core inflated by nuclear burning, thus a lower potential.) Thus, one has the following effects [363]:

– Core overshooting: it enlarges the core mass M_c; thus Φ_c and therefore overshooting reduce the size of the loops or may even suppress it.
– Rotation also reduces the blue loops because of the core extension due to internal mixing.
– Metallicity Z: in general a lower Z reduces the core size (since the opacity is lower, ∇_{rad} is also lower). This favors an extension of the blue loops.
– Mass loss by stellar winds, which is rather weak in the luminosity range of Cepheids, reduces the blue loops. The reason is that Φ_c remains the same, while $\Phi_{crit}(M)$ becomes smaller since the total mass M is smaller.

– A higher nuclear rate of $^{12}C(\alpha,\gamma)^{16}O$ increases the blue loops, because it requires a slightly lower T, which reduces the core mass.
– The overshooting below the convective envelopes in some cases may increase the extension of the blue loops, by slightly increasing the critical potential and decreasing the core mass.

26.3 Some Metallicity Effects in Evolution

It is a general rule that all stellar properties depend on metallicity Z.

1. Z effects on L and T_{eff}: the homology relations (24.48) and (24.50) give for stars on the ZAMS the dependence of L and T_{eff} on μ, κ_0 and ε_0 which all depend on Z. With a relation $Y = 0.24 + 2.4Z$ typical of the helium to metal enrichments in galaxies and with (7.41), one obtains [435] $\Delta \log \mu = \frac{4.5}{\ln 10} \mu \Delta Z$. A fitting of the opacity tables gives

$$\Delta \log \kappa_0 \approx 10 \Delta Z \quad \text{at } Z = 0.02, \tag{26.12}$$

and for the main reactions of the CN cycle

$$\Delta \log \varepsilon_0 = \left(\frac{1}{Z} - \frac{3.4}{X} \right) \frac{1}{\ln 10} \Delta Z . \tag{26.13}$$

With these relations, (24.48) and (24.50) give for $X = 0.70$ and $Z = 0.02$ with $\nu = 17$ (the various numbers represent the effects of μ, κ_0 and ε_0)

$$\frac{\Delta \log L}{\Delta \log Z} = 0.41 - 0.50 - 0.07 = -0.16 \tag{26.14}$$

$$\frac{\Delta \log T \text{eff}}{\Delta \log Z} = 0.09 - 0.16 - 0.09 = -0.16 . \tag{26.15}$$

The luminosity increases for decreasing Z mainly due to the lower opacity and the same for T_{eff}. These relations are approximate; nevertheless they allow us to understand the displacement of the ZAMS for models from $Z = 0.001$ to $Z = 0.04$ (Fig. 26.7). One notices some differences of the effects with mass: They are essentially due to the change in the opacity. For 20 $M_\odot$, electron scattering dominates and Z has no effect; however models of lower Z have a higher hydrogen content X and this increases the opacity making the stars less luminous. For $Z > 0.05$ (Fig. 26.7), higher Z makes L and T_{eff} larger again, because there the effects of μ dominate.

2. Effects on central T and ϱ: Fig. 26.7 (right) shows the effects of changes of Z on central conditions. At 3 $M_\odot$ a lower Z produces an increase in central density and temperature, because the star needs to supply more luminosity and since X_{CN} is lower (25.18), higher T and ϱ are needed. For 1 $M_\odot$, the ppI chain dominates and the last effect is small.
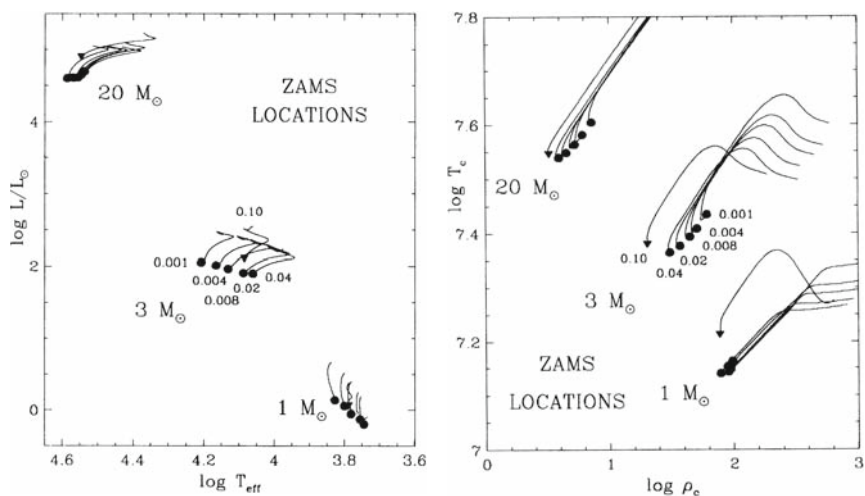
Fig. 26.7 *Left*: location in the HR diagram of ZAMS models of different Z and Y. *Right*: values of the central T and ϱ for the same models. A relation $Y = 0.24 + 2.4Z$ is adopted. From N. Mowlavi et al. [435]

3. The H-burning lifetimes of low-mass stars at $Z = 0.001$ are shorter than those at $Z = 0.020$ (Fig. 26.4). For high masses, the effect is opposite and small. In both cases, this is consistent with the above luminosity differences. For low and high masses, the He-burning lifetimes are longer at higher Z (Fig. 26.4), for low masses this results from the large He core and for high masses this comes from mass loss which reduces the stellar luminosity.

4. The Z effects depend on the masses. For $M \leq 2.3\ \mathrm{M_\odot}$, the He-burning stars form the horizontal branch at low Z (Sect. 26.5), while at solar Z the He-burning stars lie close to the red giant branch.

5. For intermediate mass stars, lower values of Z produce more extended blue loops as shown by comparison of Figs. 25.17 and 26.8, especially in the range of 2–5 $\mathrm{M_\odot}$. The physical reasons are given in Sect. 26.2.4.

6. At lower Z, the red giants, the AGB stars and the supergiants (for high masses) are bluer as a result of lower opacities, in particular due to less H^- as a result of less elements with a low ionization potential, such as Fe.

26.4   Central Evolution and Domains of Stellar Masses

While the HR diagram is useful for comparison of models and observations, it gives no insight into the physical effects determining the evolution and their end points. Stellar evolution being mainly determined by central conditions, we thus examine them and the different mass domains [127, 363]. The exact values of some limits are
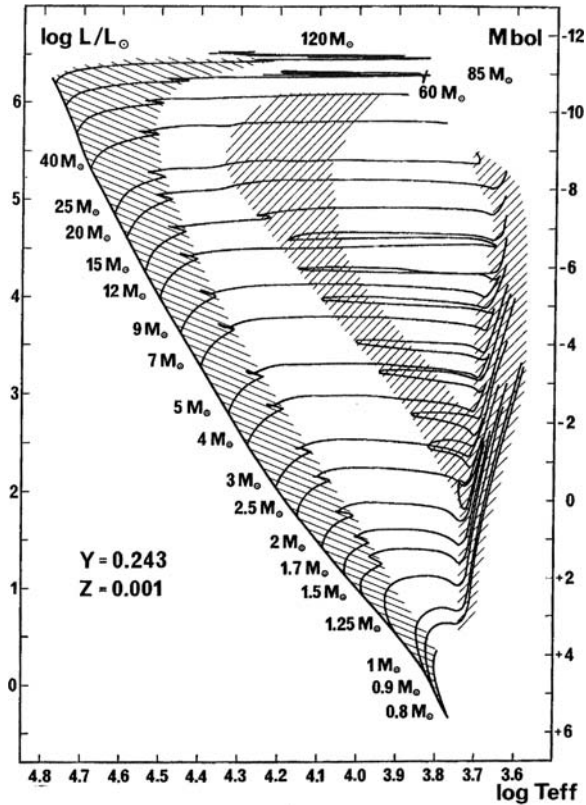
Fig. 26.8 Tracks in the HR diagram of models with composition $X = 0.756$ and $Z = 0.001$. Same remarks as for Fig. 25.17. From [513]

still uncertain, as they are affected by mixing processes, mass loss and metallicity effects (Table 26.1).

Figure 26.9 shows the evolution of various masses in the $\log T_c$ vs. $\log \varrho_c$ plot of central conditions. The general slope of the tracks is close to $1/3$ (3.87), with some exceptions: for low-mass stars degeneracy effects intervene, there is some cooling at the end of the H-burning phase for 1–5 $M_\odot$ and He ignition in the domain of 2–12 $M_\odot$ produces some expansion.

The critical point to consider for defining the mass domains is where the various nuclear phases occur with respect to the degeneracy limit (for $E_F > kT$ degeneracy dominates, Fig. 7.8). The degeneracy limit together with the limits for pair e^+e^- formation and for rapid electron capture (Fig. 26.10) determines the end points of stellar evolution.
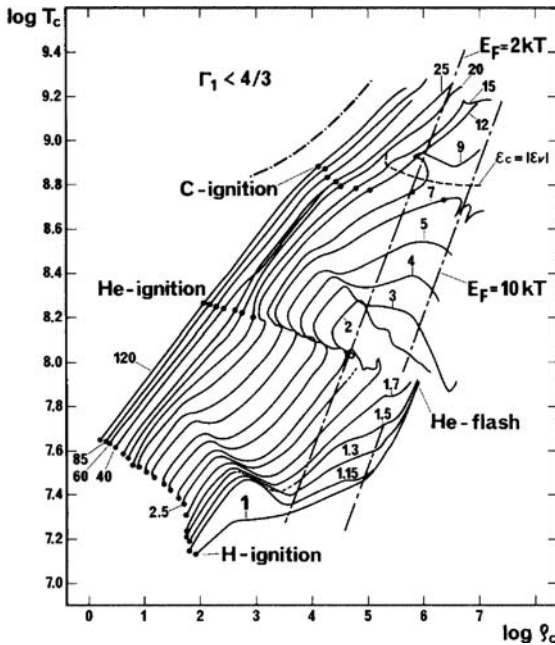
Fig. 26.9 Evolution of the central T and ϱ conditions for the models of Fig. 25.17 with an over-shooting of 0.25 H_P. The heavy dots indicate the variations nuclear ignitions. The pair instability domain e^+e^- (Sect. 7.8) is indicated by $\Gamma_1 < 4/3$. The lines where the Fermi energy E_F of the electrons is equal to 2 and 10 kT are shown. Above the line $\varepsilon_C = |\varepsilon_\nu|$, the neutrino losses are larger than the energy release by C burning. From the author and G. Meynet [363]
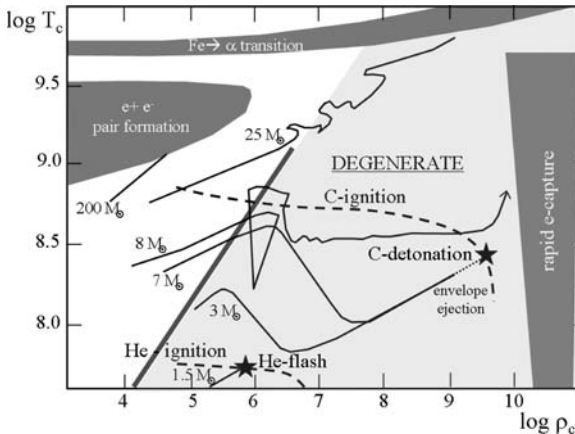
Fig. 26.10 Evolution of central conditions for different masses with indications of instability do-mains (Sect. 7.8), the Fe-α transition indicates the photodisintegration of Fe nuclei into α particles. The degenerate region is light gray. *Dashed lines* show the place where nuclear energy generation rates balance neutrino losses. Adapted from T.J. Mazurek and J.C. Wheeler [393]

Table 26.1 Indicative values of the mass limits for $X = 0.70$, $Z = 0.02$

Mass in $M_\odot$	No overshooting	Overshooting 0.25 H_P
	No mass loss	Mass loss
M_{min}	0.007 $M_\odot$	
M_H	0.08 $M_\odot$	
M_{HeF}	2.2 $M_\odot$	1.85 $M_\odot$
M_{UP}	8.9 $M_\odot$	6.6 $M_\odot$
M_{WD}	1.4 $M_\odot$	8.0 $M_\odot$
M_{EC}	10.2 $M_\odot$	8.0 $M_\odot$
M_{WR}		$\sim$30.0 $M_\odot$
M_{BH}	25 $M_\odot$	$\sim$ 50 $M_\odot$
$M_{e^+ e^-}$	100 $M_\odot$	120 $M_\odot$
M_{max}	$\sim$ 130 $M_\odot$	

26.4.1   The Mass Limits for Evolution

We distinguish the following important mass limits (Table 26.1).

M_{min}: there is a minimum mass in the opacity-limited fragmentation (Sect. 18.4.4) of about 0.007 $M_\odot$. Objects below this mass are in the domain of planets, likely formed by accumulation in protostellar disks.

M_H: this is the minimum mass for H burning. As central T increases with mass (Sect. 25.2.2), there is a mass $M_H \approx 0.08$ $M_\odot$ below which T is not high enough for H burning. Stars between M_{min} and M_H are brown dwarfs. Low-mass stars with $M > M_H$ have a stable MS phase. After central H exhaustion, they contract. If their mass is below a limit $M_{He} \approx 0.47$ $M_\odot$, their central T is insufficient for He ignition and the stars finish their life as He–H white dwarfs. However, this limit is academic since stars with $M < 0.9$ $M_\odot$ have a MS lifetime longer than the Hubble timescale.

M_{HeF}: this is the maximum initial mass for the He flash. Below $M_{HeF} \approx 2.3$ $M_\odot$ (values range from 1.7 to 2.5 $M_\odot$), after stable H burning the stellar interior becomes degenerate. The He core grows and heats up due to shell-H burning. When He ignites (core mass ≈ 0.5 $M_\odot$), fusion reactions in degenerate medium are unstable (Sect. 3.4) and produce the He flash at the top of the red giant branch (Sect. 25.3). The energy from the flash drives convection, increases T and lifts degeneracy. About 5% of the He in the core is burnt into C,O during the flash. Then, He burns in non-degenerate conditions on the horizontal branch (HB) for low Z values, for solar Z the HB is squeezed along the red giant branch. The star then becomes an AGB, then a planetary nebula and finally a He–C–O white dwarf.

M_{WD}: this is the maximum initial mass leading to the formation of a white dwarf (WD). It is ~ 8 $M_\odot$ from the observations of WDs in open clusters [607]. Stars in the interval M_{HeF} to M_{WD} have stable H- and He-burning phases. After central He exhaustion, contraction brings the C,O core into the degenerate domain (Fig. 26.9). The core cools first, then it is growing and heating due to He-shell burning. This evolution brings the star to a common track for the different M (core convergence,

cf. 3 and 7 M$_\odot$ in Fig. 26.10). The luminosity (mainly from the He shell) depends on the mass of the degenerate CO core (Fig. 26.14). Thus, stars of different M have the same properties when they have the same cores mass, which explains the convergence.

Stars with masses between M_{HeF} and M_{WD} are the intermediate mass stars. There is a competition between, in the center the T, ϱ evolution which tends to bring the star to C ignition (Fig. 26.10) and at the surface mass loss by stellar winds, which tends to remove the envelope. If the star first reaches the C-ignition limit, this is catastrophic, leading to an explosion with complete disruption of the star. At the opposite, if the mass loss rate in the TP-AGB phase is high enough to remove the envelope before C ignition, then the star experiences a planetary nebula event and finally becomes a white dwarf. Mass loss depends on the luminosity and other factors (pulsations, chemical composition, rotation, etc.) while central evolution goes on at its own pace; thus near M_{WD} it is difficult to bet on the winner of the competition. One generally rests on the observational determination (Fig. 26.21).

M_{UP}: this is the lower mass limit for C ignition leading to complete non-explosive C burning in the center. It corresponds to a core mass ≈ 1.06 M$_\odot$. The mass limit lies in the range of 6.6–8.9 M$_\odot$ depending on overshooting. With some (too) extreme overshooting, it is even down to 5.5 M$_\odot$ [208]. Due to heavy neutrino losses, the center is cooler than outer regions of the CO core; thus there is an off-center C ignition. Above M_{UP}, the off-center ignition rapidly proceeds down to the center so that C completely burns in the core (in a small domain of ~ 0.3 M$_\odot$ below M_{UP}, off-center C burning rapidly dies out letting mass loss to win the competition). The complete C burning event is explosive. The rate ε of energy liberated is larger than the thermal content divided by the free-fall time,

$$\varepsilon_{\text{C-explosion}} > \frac{C_P T}{t_{\text{ff}}} , \qquad (26.16)$$

so that this energy cannot be accommodated on the thermal timescale and it leads to an explosion on the dynamical timescale. One calls "detonation" an event with a supersonic shock wave and a "deflagration" a subsonic fusion front, both inducing some nucleosynthesis. Nomoto [441] has shown that degenerate C ignition produces a deflagration. The energy liberated is larger than the binding energy of the CO core, so that a complete disruption of the star results leading to a supernova explosion. This type of supernova is sometimes called SN I $1/2$. The existence of such explosions is doubtful and it depends on the respective values of M_{WD}, M_{UP} and M_{EC} (see below).

M_{EC}: this is the maximum initial mass for collapse by electron capture. Above it, further nuclear burning stages proceed in stable conditions. It lies between 8 and 10 M$_\odot$. The track of 8 M$_\odot$ in Fig. 26.10 illustrates the evolution of a star experiencing electron capture. After the phases of normal H and He burning, C ignition occurs in not too degenerate conditions (M_{EC} being above M_{UP}); degeneracy is temporarily lifted by a kind of C flash and then a stable C burning proceeds. Neutrino losses prevent the heating of the core, which strongly contracts and the star moves horizontally in Fig. 26.10. The core mass reaches the Chandrasekhar mass (the maximum

mass of a fully degenerate object, i.e., ~ 1.2 $M_\odot$, Sect. 7.7.5), it collapses and enters the region where the Fermi energy of the electrons is sufficient to induce fast capture by the heavy nuclei. It produces a supernova (SN II) event.

The limits M_{WD}, M_{UP} and M_{EC} are close to each other for standard composition. Their values depend on mass loss, Z and overshooting (Table 26.1). Let us discuss the various possibilities. 1. If one has (e.g., with some overshooting) $M_{UP} < M_{WD}$ and $M_{EC} < M_{WD}$, mass loss wins the competition against C deflagration and electron capture. Close to M_{WD}, one gets a ONeMg white dwarf. 2. If $M_{UP} < M_{WD} < M_{EC}$, there is some room for SN by electron capture above the WD limit (Fig. 26.10). 3. At the opposite if $M_{WD} < M_{UP} < M_{EC}$, there is C deflagration between M_{WD} and M_{UP} (SN I 1/2) and collapse by electron capture between M_{UP} and M_{EC}. In this last case, C burning is stable and then the resulting O+Ne+Mg core is degenerate and never reaches Ne ignition. The core has a mass reaching the Chandrasekhar's mass; it collapses and undergoes electron capture; the supernova explosion leads to a neutron star. A recent study of these limits taking into account different mass loss rates for metallicity $Z = 0.02$ suggests [474] a situation corresponding to the above case 2: CO white dwarfs form up to 7.0 $M_\odot$, ONe white dwarfs between 7.0 and 9.0 $M_\odot$, electron capture supernovae between 9.0 and 9.25 $M_\odot$ and core-collapse supernovae above 9.25 $M_\odot$.

Above M_{EC}, the stars go through all phases of stable nuclear burning (H, He, C, Ne, O and Si) and form an onion skin model with an iron core (Sect. 28.2.1), which then collapses into a supernova explosion. In the domain close to $M_{EC} \sim 10$–12 $M_\odot$, C burning is non-degenerate; however after that, degeneracy becomes high and the burnings of Ne, O and Si occur in the form of flashes. These are not destructive, leading to the formation of an onion skin model, which then explodes as a supernova.

$\underline{M_{WR}}$: this is the minimum initial mass for the formation of a Wolf–Rayet (WR) star, i.e., a bare core (Sect. 27.5). Above M_{WR}, mass loss is sufficient to remove the outer envelope in the course of evolution; the central regions still form the onion skin model. In the solar neighborhood, $M_{WR} \approx 25$ $M_\odot$. Depending on the mass lost, WR stars reveal the He, N core (WN stars) and in later stages the He, C, O core (WC stars).

$\underline{M_{BH}}$: the minimum mass for black-hole formation is still unknown. M_{BH} is mainly determined by the mass of the Fe core. Above about 2 $M_\odot$, Fe cores are too massive to form neutron stars; thus they form black holes. Without mass loss this corresponds to about an initial 25 $M_\odot$ star [617]. Mass loss and mixing may increase this value. Values in the range of 40–80 $M_\odot$ have been proposed from X-ray binaries and around 50 $M_\odot$ from pulsars in young associations.

$\underline{M_{e^+e^-}}$: this is the minimum mass for the formation of pair instability supernovae (PISN). For $T > 10^9$ K , equilibrium $\gamma + \gamma \leftrightarrow e^+ + e^-$ occurs (Fig. 26.9 and 26.10). The change in the equation of state lowers the adiabatic exponent $\Gamma_1 < 4/3$ and favors dynamical instability. When about 30% of the stellar mass have $\Gamma_1 < 4/3$, a PISN occurs leading to stellar destruction. Models with overshooting and mass loss [363] suggest that a 120 $M_\odot$ star is just at the limit where PISN may occur in Pop.

I stars (in the central Ne-burning phase). The occurrence of PISN seems favored at lower Z [312]. PISN have been suggested at $Z = 0$; however the absence of the "odd–even" effects in very metal deficient stars casts doubts on this possibility [101].

$\underline{M_{max}}$: the maximum stellar mass is determined by star formation (Sect. 22), with a value of M_{max} in the range of 100–150 $M_\odot$. Supermassive objects with $M > 4.1 \times 10^5$ $M_\odot$ have been suggested because they could be stabilized by general relativity effects; however their existence is hypothetical [13].

One generally calls in a rather schematic way "massive stars" those with masses above M_{WD} or M_{EC}; the "intermediate mass stars" are between M_{HeF} and M_{WD} and "low-mass stars" are below M_{HeF}.

26.4.2   Evolution of the Entropy per Baryon

The specific entropy is varying during evolution. The entropy of perfect gas for N particles in a given volume V is given by $S = Nk\ln(T^{3/2}V)$ (C.39). The entropy s per particle is

$$s = \frac{S}{N} = k\ln\left(T^{3/2}\frac{\mu m_u}{\varrho}\right) . \tag{26.17}$$

One can often neglect the variations of μ with respect to those of ϱ and T. The entropy is often expressed in units of s/k. During evolution, T behaves like $T \sim \varrho^{1/3}$ (Fig. 26.9); thus one has

$$s = k\ln\left(\frac{1}{\varrho^{1/2}}\right) + \text{const} . \tag{26.18}$$

Thus, the entropy per baryon decreases with increasing density during evolution. We recall that convection occurs in regions where the entropy decreases outward (Sect. 5.1.1). One can express $T^{3/2}/\varrho$ as a function of mass. Using $\varrho \sim M/R^3$ and $T \sim M/R$ (1.26), one gets

$$s = k\ln\left(M^{1/2}R^{3/2}\right) + \text{const}' . \tag{26.19}$$

Thus, the entropy per baryon is higher in more massive stars. The highest entropy is in the interstellar medium; star formation reduces s/k by 10–12. The evolution from the MS to the degenerate stages further reduces the entropy to zero (Appendix C.4.3). Therefore, the whole stellar evolution from star formation to condensed remnants appears as a process of internal entropy reduction together with an entropy injection in the surrounding medium.

26.5   The Horizontal Branch

The horizontal branch (HB) is formed by stars in the core He-burning phase, following the He flash for stars of initial masses $M \leq 2.3$ M$_\odot$. The main effect of the He flash is to lift the degeneracy; then after internal re-adjustments He burning proceeds in non-degenerate conditions on the HB. The horizontal branch is present only for metallicities Z lower than $Z \approx 0.004$. At solar Z, the low-mass stars burning helium lie very close to the red giant branch as shown for the solar case in Fig. 25.11; one generally speaks of the "clump" because of the resulting accumulation of stars in the HR diagram.

The HB stars have the same core mass, the reason being that the He flash occurs in degenerate cores of a given mass around 0.45–0.5 M$_\odot$. The distribution of stars along the HB in a globular cluster results from different ratios M_c/M of the core to the total mass. This is illustrated in Figs. 26.11 and 26.12. Stars with a high ratio M_c/M lie on the blue side of the HB, while those with smaller cores lie close to the red giant branch. The reason why the total masses at the end of the red giant are different is likely due to effects, such as rotation and instabilities, leading to different masses at the He flash.

The distribution of stars in the HR diagram according to $q = M_c/M$ is consistent with the generalized MS (Fig. 24.3). Stars with high q values lie close to the He sequence. Methods for constructing synthetic HB models avoiding the detailed computation of the He flash have been studied [526].

The HB crosses the instability strip for radial pulsations. The variable HB stars are the RR Lyrae. By simplicity, one often calls red HB stars those on the right side of the RR Lyrae strip in the HR diagram and blue HB stars those on the left side. The distribution of stars along the HB is a central question, because the HB observed in globular clusters presents very different morphologies. The distribution of stars along the HB depends on several parameters apart from the ratio $q = M_c/M$ mentioned above:

1. **The first parameter** is the content in heavy elements. For $Z \leq 10^{-3}$, the HB is more extended to the blue while red HB stars are rare or absent (Figs. 26.11 and 26.12). For higher Z, the red side is more populated (at solar Z, HB stars are confined to the red giant branch). There is an opacity effect, also the masses at the He flash are higher for higher Z (due to the lower central T), which makes larger HB masses [320, 321].
2. **The second parameter:** different HB morphologies for clusters of the same Z (particularly for low Z) indicate that there is a second parameter determining the HB properties. There are debates about this second parameter [99]. The clear point is that the age of the clusters is *one possible* second parameter [321], but not necessarily the only one. Larger ages make bluer HB in a way not too different from the effect of lower Z. The reason is that the mean mass at the He flash is smaller for larger ages [590].
3. **The third or nth parameter:** large differences in the helium abundances of many globular clusters have been found, e.g., ω Cen or NGC 2808 show, two
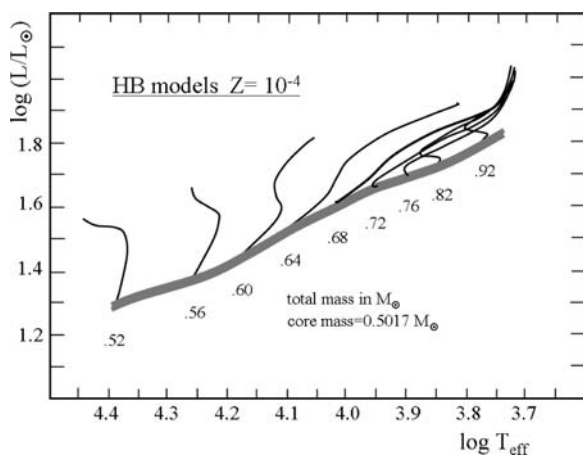
Fig. 26.11 Evolutionary tracks for horizontal branch stars with initial helium content $Y = 0.23$, $Z = 0.0001$, core mass 0.5017 $M_\odot$ and indicated total masses. Adapted from S. Yi, Y.-W. Lee and P. Demarque [625]
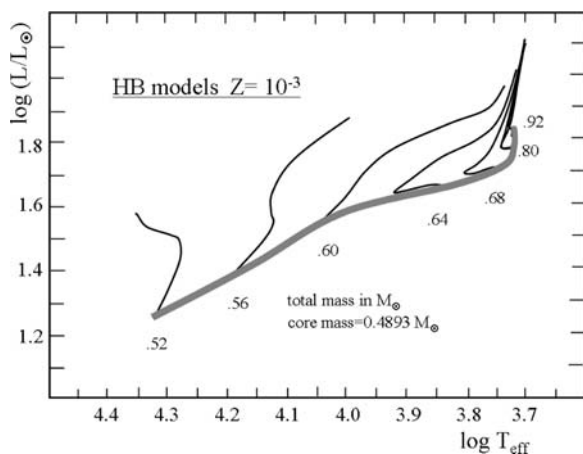
Fig. 26.12 Evolutionary tracks for horizontal branch stars with initial helium content $Y = 0.23$, $Z = 0.001$, core mass 0.4893 $M_\odot$ and indicated total masses. Adapted from S. Yi, Y.-W. Lee and P. Demarque [625]

main sequences, one with a He content $Y = 0.24$ and the other with $Y \approx 0.40$. Differences of He content rapidly make differences in the distribution of HB stars, He-rich stars being bluer because of their lower opacities. Cluster ω Cen shows hot extreme HB stars, likely associated to the very high initial He excesses in a fraction of the stars.

Most HB stars have rotation velocities < 10 km s^{-1}; however some blue HB stars have velocities up to 40 km s^{-1} [467]. Other clusters show larger velocities for red HB stars. The main effects of rotation result from previous phases, rotating

stars having larger cores, making the stars bluer. Rotating stars are also slightly overluminous and thus their mass loss on the red giant branch prior to the He flash was higher, leading to smaller total masses for a given core mass; this also makes HB stars bluer. However, the consequences of rotation have not been well examined. Differences in the CNO/Fe ratios and in the mass loss rates may also intervene.

On the HB, the He burning progressively makes a CO core, while H burning continues in a shell. The stars move away from the zero-age HB with different motions (Figs. 26.11 and 26.12). The post-HB stars move upward and for most of them redward in the HR diagram toward the AGB. In the figures, the HB stars with an initial ratio $q = M_c/M \geq 0.9$–0.95 move upward to the blue and will not join the AGB. These stars are often called "AGB manqué"; they become hot subdwarfs.

26.6 Evolution and Nucleosynthesis in AGB Stars

The AGB phase starts at the end of central He burning and ends at the ejection of the last shell forming a planetary nebulae and then a white dwarf (Fig. 26.1). AGB stars are important because they contribute to the light of galaxies and nucleosynthesis. The E-AGB (early) phase is marked by the He-burning shell and the growth of the CO core; it ends when the H shell re-ignites and then the TP-AGB phase starts showing thermal pulses (TP). There is an abundant literature on the AGB phase; see the reviews by Iben and Renzini [265], Busso et al. [81], Herwig [249] and van Winckel [597].

26.6.1 Structure and Instability of TP-AGB Stars

A number of particular events occur in the TP-AGB phase with major consequences. The structure at the beginning of this phase is schematically illustrated in Fig. 26.13. It consists of a degenerate CO core surrounded by two shells, one of He and the other of H, which burn alternatively. The mass M_{CO} of the core determines most properties of AGB stars. There is a huge convective envelope covering more than 99% of the stellar radius. The AGB radii extend from about 10^2 to 8×10^2 $R_\odot$, with $L = 2 \times 10^3$–5×10^4 $L_\odot$ and $T_{eff} = 2600$–3500 K. The neutrino luminosity from the degenerate core represents 10–15% of the photon luminosity. The atmosphere is very extended with a low gravity; it contains a broad range of molecules and dust grains. Heavy mass loss occurs particularly during the thermal pulses.

The stellar luminosity depends essentially on the mass of the CO core, the L vs. M_{CO} relation is illustrated in Fig. 26.14. This relation can be derived from homology relations [285]. It results from the fact that at the edge of the degenerate core the pressure gradient decreases by several orders of magnitude so that outer layers have practically no weight and the conditions in the shell are determined by the inner side.
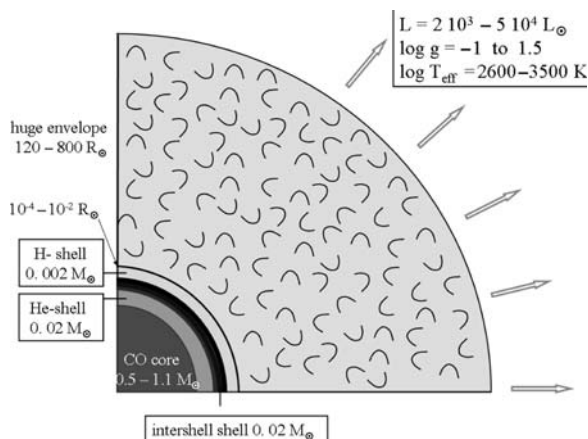
Fig. 26.13 Schematic representation of the internal structure of an AGB star with an initial 2.5 M$_\odot$ mass. Some domains of parameters are indicated
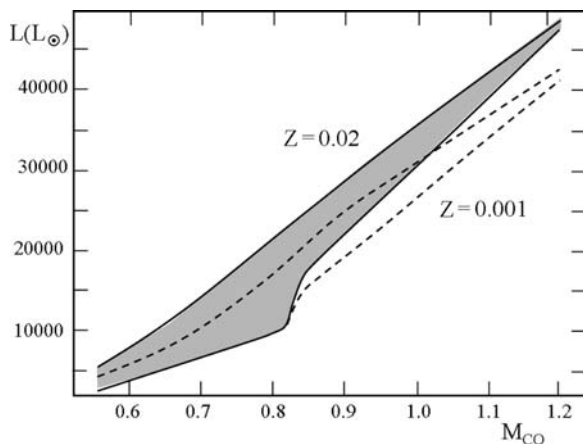
Fig. 26.14 Relation between the stellar luminosity and the mass of the CO core in TP-AGB stars. For each metallicity $Z = 0.02$ and $Z = 0.001$, the *broken line* shows the relation for the first pulse and the *upper continuous line* for the full amplitude pulse. Adapted from M. Groenewegen [223]

There is a difference between the luminosity at the first pulse and for full amplitude pulses, particularly for low core masses. Most properties depend on M_{CO}.

The two shells are very close to each other, being separated by a radiative intershell of $\sim 10^{-2}$ M$_\odot$ (low masses) to 10^{-3} M$_\odot$ (intermediate masses). Most of the time, the stellar luminosity is mainly produced by the re-ignited H-burning shell, while the He shell is inactive. H-shell burning progressively adds He to the intershell layer, increasing its mass. This enhances the density and temperature in the He shell up to a point where He-burning starts. This ignition is highly unstable, because the very thin He shell, even if it expands significantly, is too thin to change
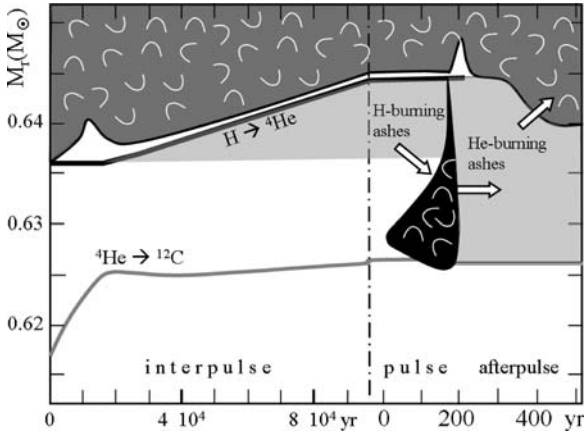
Fig. 26.15 Evolution in an AGB star with an initial 2.5 M$_\odot$. The *left side* shows an interpulse with H-shell burning. The *right side* shows the pulse with the He-burning convective tongue. In the afterpulse, dredge-up brings the nucleosynthetic products to the surface as indicated by the *arrows*. Adapted from N. Mowlavi [434]

its location r/R in the star and to alleviate the pressure exerted by the upper layers. Thus, the energy liberated makes T to increase, ε(He) grows a lot, T further increases and ε(He) amplifies exponentially (Sect. 3.5.1). This instability makes the thermal pulses.

Due to the strong energy liberation, the intershell region ceases to be radiative. Convection develops in and above the He-burning shell (Fig. 26.15). The "convective tongue" (in black) spreads out the new elements synthesized in the He-burning shell up to the H shell. At the same time, the expansion of the He shell finally succeeds in pushing the upper layers outward (this uses most of the energy from the pulse). The ensuing T and ϱ reductions bring the H-burning shell to extinction; the base of the convective envelope retreats upward. The convective tongue declines and the pulse dies out (Fig. 26.15); the He-burning shell is again extinct. The layers near the H-burning shell go down and are compressed again, leading to its reactivation. On a much longer timescale during the interpulse, energy accumulates again near the He-burning shell until the next thermal pulse.

Figure 26.16 shows the evolution of the parameters for a star of 2.5 M$_\odot$ during the thermal pulses. We see the growth of the C/O ratio at the surface due to the third dredge-up. If this change is accounted for in the opacity (and it must be), R increases considerably, T_{eff} is reduced and the mass loss rates are larger. The higher $\dot{M}$ leads to a shorter AGB lifetime and the star experiences a smaller number of pulses. As a consequence, the C/O ratio remains below a factor of 2 in agreement with AGB observations [153, 374]. The duration of the pulses is typically 250, 100 and 20 yr for AGB stars of initial mass 1, 3 and 6 M$_\odot$, while the interpulses last 2×10^5, 5×10^4 and 3×10^3 yr for these masses [191]. The growth of the degenerate CO core increases its gravitational potential, as well as the T and ϱ gradients at the edge and in the H-burning shell. This makes the thermal pulses more violent with larger
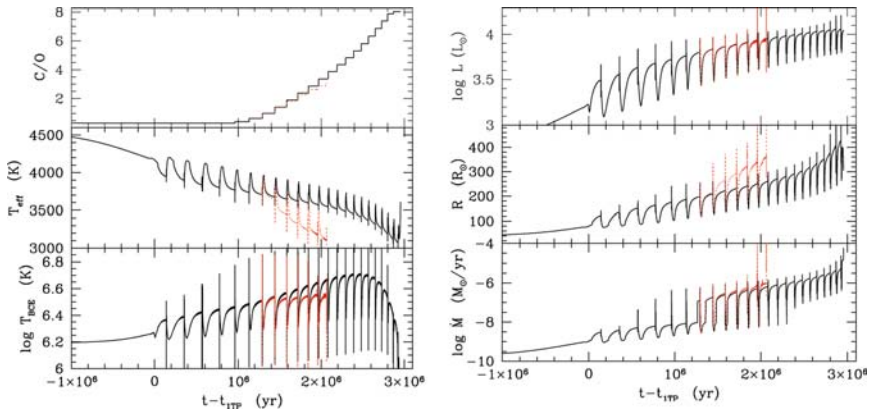
Fig. 26.16 The TP–AGB phase of a 2.5 $M_\odot$ star with $Z = 0.004$ with (*left*) the C/O ratio, T_{eff}, T at the base of the convective envelope, (*right*) L, R and $\dot{M}$. The thick continuous lines refer to local opacities corresponding to the local Z, the gray line takes into account of the change of C/O. From T. Decressin [153]

excursions in the HR diagram. The outer envelope comes deeper after the pulses and dredges up the new elements to the surface (as its mass decreases, the relative enrichments are larger). This means that the evolution has to be followed to the end of the TP-AGB for reliable nucleosynthetic yields of some elements to be obtained.

The evolution of the mass loss rates (in the range of 10^{-9} to a few 10^{-5} $M_\odot$ yr^{-1}) mimics the time evolution of the luminosity during the pulses and interpulses, since the expressions of the mass loss rates $\dot{M}$ depend much on the luminosity. Often the so-called Reimers' law is used for parametrizing the mass loss rates (Sect. 27.3.1). Other expressions for AGB stars [50] and pulsating winds [599, 615] have been derived.

Most AGB stars experience a phase of large amplitude radial pulsations, which enhance the $\dot{M}$ rates [599]. As the AGB stars progressively brighten (Fig. 26.14), mass loss also increases and finally almost only the core is left. The cycles of thermal pulses and interpulses are repeated (about 10–10^2 times) until the whole envelope is gone. Thus, the number of thermal pulses for a given mass depends on the mass loss rates. Figure 26.17 shows the evolution of the total and core masses. The core increases slightly after each pulse. At the end, the predicted masses of the white dwarf revealed by the planetary nebula should correspond to the observed masses of the white dwarfs, of the order of (0.55 ± 0.05) $M_\odot$ on the average (Sect. 26.6.4).

Analytical relations expressing the AGB properties (L variations, pulse and interpulse durations, etc.) as functions of the core mass have been made [223, 265]. They serve to construct the so-called synthetic models of AGB stars, where the AGB properties are parametrized with fitting formulae [377] .
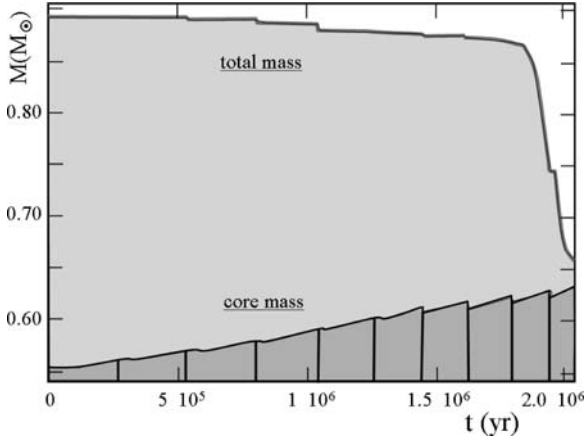
Fig. 26.17 Evolution of the total mass and of the core mass of a 0.9 $M_\odot$ with $Z = 5 \times 10^{-4}$. The mass loss rates are a few 10^{-9} $M_\odot$ yr^{-1} for the first pulses and reach a few 10^{-5} $M_\odot$ yr^{-1} in the last two pulses leading to a planetary nebulae. Adapted from M. Forestini [191]

26.6.2 Third Dredge-Up and TP-AGB Nucleosynthesis

Figure 26.15 shows that after the disappearance of the intershell convective zone, the external convective zone (CZ) may deepen again (this is a critical point depending on convective parameters and mixing). It reaches layers which were covered by the convective tongue and contains the products of He burning. The outer convective envelope, if it reaches these layers, brings the new synthesized elements to the surface: this is the third dredge-up. The efficiency of the third dredge-up is often measured by a parameter λ:

$$\lambda = \frac{\text{deepening of CZ after third dredge-up}}{\Delta M \text{ He core in interpulse phase}} = \frac{\Delta M_{TDU}}{\Delta M_{He}} , \qquad (26.20)$$

i.e., the ratio of the mass reduction of the H-exhausted core due to the third dredge-up to the mass increase of the H-exhausted core during the interpulse. For $\lambda = 0$ there is no dredge-up and for $\lambda = 1$ there is no net growth of the H-free core. It is remarkable that new elements appear immediately at the the surface. A proof is that technetium ^{99}Tc is observed in AGB stars [587]. This element is radioactive with a half-life of 2.1×10^5 yr, which is shorter than the stellar lifetime. Thus ^{99}Tc has been synthesized locally.

If the idea of the third dredge-up looks simple in principle, the models have difficulties to simulate this phase of mixing. First, the opacity in the intershell is electron scattering, i.e., a weak opacity which does not favor convection. In addition, there is a μ gradient, which does not favor the inward penetration of the convective envelope. Different choices of the convective parameters help the authors to get the third dredge-up, e.g., a larger mixing length. Also, overshoot below the envelope favors the third dredge-up [248], which is more efficient at lower Z. The degree

of overlap between successive convective tongues is uncertain and also depends on mixing (Sect. 26.7).

AGB stars make a rich nucleosynthesis in different sites [191, 434].

1. **H-burning shell:** temperature of H burning in AGB stars is higher than in MS stars (Fig. 26.18); it is between $T_6 = 40$ and 95, being higher for higher M and lower Z. At this T, the ON loops are working; however as the very thin H shell advances fast, the ON loops do not reach equilibrium, the same for the NeNa and MgAl cycles (Sect. 25.1.5). The CN cycle (which is at equilibrium) produces ^{4}He and ^{14}N with some ^{13}C, while the NeNa cycle produces mainly ^{23}Na and ^{22}Ne. The products of the MgAl cycle depend on T. For $T_6 = 55 - 75$, the radio-nuclide ^{26}Al^g is largely produced. The half-life $t_{1/2} = 7.1 \times 10^5$ yr of this isotope is shorter than the duration of the TP-AGB phase for stars with $M > 3$ M$_\odot$. Thus, it accumulates without being too much destroyed before being ejected. At higher T, less ^{26}Al^g is produced, because it is partially destroyed by proton captures (Fig. 25.4).

2. **He-burning in shell and in TP, s-elements:** during the interpulse, the energy production by the He shell is negligible with respect to that by the H shell. T at the base of the He shell is according to the masses between $T_8 = 1.2$ and 2.1. Some reactions nevertheless go on, like the destruction of ^{13}C by ^{13}C$(\alpha,n)^{16}$O in the He shell and intershell region.

   He burning during the thermal pulses occurs at $T_8 = 2.3$–3.9; thus it is orders of magnitude more powerful; in addition He is brought by convection into the most active burning layers. The main product is ^{12}C; it is transported by the convective tongue close to the H shell, where successive third dredges-up bring it to the stellar surface. For a C/O ratio > 1, the AGB star first observed as an M giant is turned into a C star. During the pulses, the H-burning products (^{4}He, ^{14}N, ^{13}C, etc.) sitting in the intershell are suddenly mixed into the He-burning tongue producing reactions such as

$$^{13}\text{C}(\alpha,\text{n})^{16}\text{O} \qquad ^{22}\text{Ne}(\alpha,\gamma)^{26}\text{Mg} \qquad ^{19}\text{C}(\alpha,\text{p})^{22}\text{Ne} \qquad ^{14}\text{N}(\alpha,\gamma)^{18}\text{O}$$
$$^{18}\text{O}(\alpha,\gamma)^{22}\text{Ne} \qquad ^{16}\text{O}(\alpha,\gamma)^{20}\text{Ne} \qquad ^{22}\text{Ne}(\alpha,\text{n})^{25}\text{Mg}$$
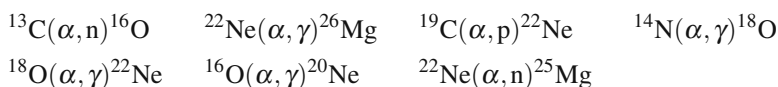
The injection of ^{13}C into the He-burning region leads to the production of neutrons. In the hottest pulses, neutron production by ^{22}Ne also occurs. Free neutrons lead to a most interesting nucleosynthesis in TP-AGB stars [81, 180]: a fraction of them is captured by elements of the Fe peak. In TP-AGB stars, the neutron flux is low enough so that the new nuclei formed by neutron capture have the time, if unstable, to β^- disintegrate before a new neutron is captured. This succession of n captures followed by β^- decays leads to heavy nuclei close to the valley of stability in the plane (N,Z). The heavy elements formed in this way (for example, Y, Sr, Zr, Ba, La, Nd, Tc and up to ^{208}Pb) are the "s-elements", formed by slow captures of neutrons, i.e., the neutron flux is low (the average time interval between two n captures by a nucleus is ~ 10 yr). The physics of the s-element synthesis is discussed in Sect. 28.5.4. About 70% of the heavy nuclei

beyond ^{56}Fe are s-elements produced by the s process, either in AGB stars or to a lesser extent in massive stars.

There is, however, a problem: there is not enough ^{13}C in the intershell to produce the observed amount of s-elements. Typically, the mass fractions and number ratios of ^{13}C and ^{56}Fe are

$$X(^{13}\text{C}) = 9 \times 10^{-5}, \quad X(^{56}\text{Fe}) = 6 \times 10^{-4} \quad \longrightarrow \quad \frac{n(^{13}\text{C})}{n(^{56}\text{Fe})} \approx 0.5 \to 1. \quad (26.21)$$

Thus, less than one neutron is available per ^{56}Fe seed. The rest is captured by (n,p) and (n,γ) reactions onto "poisons" for neutrons, such as ^{14}N and other elements in the range of ^{12}C to ^{30}Si. There is not enough neutrons to form the s-elements. Thus, more ^{13}C should be formed inside AGB stars.

Some of the neutrons from ^{13}C lead to the formation of protons: ^{14}N(n,p)^{14}C and ^{26}Al^g(n,p)^{26}Mg $\longrightarrow$ ^{18}O(p,α)^{15}N(α,γ)^{19}F. This leads to the formation of fluorine ^{19}F. These reactions are very sensitive to T, and ^{19}F is also destroyed by further reactions (n,γ) and (α,p). The amount of ^{13}C is also insufficient [434] to account for the observed fluorine.

3. **H diffusion**: some additional ^{13}C may originate [434] from partial mixing of protons of the H-burning shell into the intershell, which is enriched in ^{12}C by the previous convective tongue. This occurs just after the death of the convective tongue.

4. **Hot bottom burning**: in stars with initial masses $> 4 \, M_\odot$ (high-mass AGB stars), T at the basis of the convective envelope becomes above $T_6 = 50$ (Fig. 26.18), so that H burning and related reactions may occur. This H burning is called the hot bottom burning (HBB); the fusion layers are in contact with a huge reservoir of inactive matter and the reaction products immediately appear at the surface. Characteristic reactions are the building of ^{14}N, the destructions of ^{12}C (with ^{12}C/^{13}C $\approx$ 3), ^{15}N (with ^{14}N/^{15}N $\approx 10^4$) and ^{18}O. Also, fluorine is destroyed by ^{19}F(p,α)^{16}O. HBB may also be an efficient site for the production of ^{26}Al through the MgAl cycle.

The HBB by coupling fusion and convective mixing may also be a unique site for ^{7}Li production by the Cameron–Fowler process [84, 192]. The reaction ^{3}He(α,γ)^{7}Be of the ppII chain (Table 25.1) produces ^{7}Be. Normally, this element is rapidly destroyed by proton capture (leading to ^{8}B) and to a less extent by e^- capture (leading to ^{7}Li which would rapidly be destroyed). However, convection with a turnover time of a few 10^2 days has the time to evacuate ^{7}Be toward surface layers, where e^- captures which are little dependent on T turn it into ^{7}Li. The surface abundance of ^{7}Li may increase in a spectacular way, because of the relatively high abundance of ^{3}He. However, this enhancement only lasts as long as lithium is effectively produced, because the convective turnover brings it back to the bottom of the convective zone where it is rapidly destroyed. As mass loss is high in these stages, the HBB synthesis may lead to a significant galactic ^{7}Li enrichment.
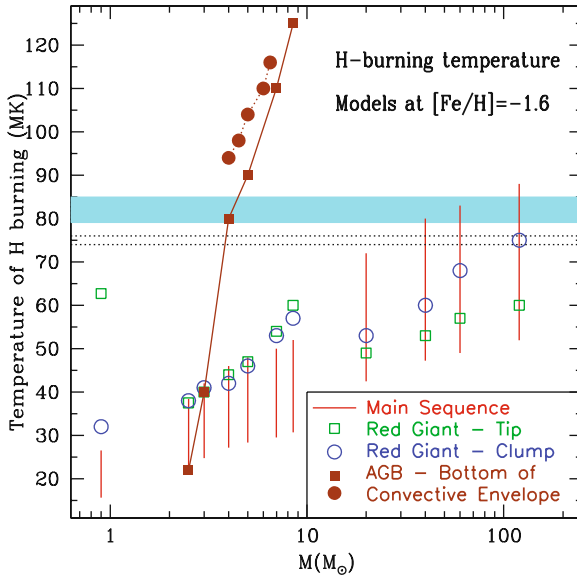
Fig. 26.18 The different T at which H can burn in stars: MS shell H burning, hot bottom burning, etc. The *dotted lines* show the minimum T for accounting for the observed O, Na, Mg, Al abundances in globular clusters. The thick gray line is the same for H burning in convective zones. Courtesy of C. Charbonnel

26.6.3 AGB Classification and Chemical Abundances

We now present, in a schematic and simplified way, some chemical properties of AGB stars related to the above nuclear evolution [81, 191, 192, 249, 376]. AGB stars form a complex zoo and the reader should be aware that if the overall qualitative agreement makes sense, the quantitative comparisons still make problems, particularly regarding the role of mixing. The critical point is the lack of ^{13}C for producing neutrons. From spectral classification, the following groups of AGB stars can be distinguished (Fig. 26.19). They form an evolutionary sequence consistent with the above scheme.

1. Most of the AGB stars belong to the spectral class M. They show ^{14}N excesses and ^{12}C deficiencies consistent with the first two dredges-up of the products of the CN cycle (C+N constant, low ^{12}C/^{13}C, O unchanged).
2. AGB stars of class S show excesses of N and s-elements correlated with ^{12}C excesses. This indicates that s-element synthesis occurs in a C-rich region. This is consistent with the third dredge-up bringing upward materials from the ^{12}C-rich intershell on which n captures have occurred during the thermal pulses (MS/S stars have intermediate properties between M and S stars). Among S stars, some show the radioactive Tc and some do not. Those without Tc seem to be normal

red giants while the other ones may have a surface polluted by a more evolved AGB companion in a binary system.

3. Carbon stars of type C are M stars in which C/O> 1. C stars are interpreted as S stars having experienced many times the third dredge-up, so that the envelope abundance of ^{12}C is sufficiently increased (SC stars have intermediate properties). C stars contain s-elements. C (and N) add opacity sources in the atmospheres of C stars [373]; this lowers T_{eff} and enhances the mass loss rates, thus reducing the number of pulses and the associated nucleosynthetic yields. (The new lower CNO abundances [20] make the formation of C stars easier).

4. J stars also have large C/O ratios; however their ^{12}C/^{13}C ratios are low (3–15). This seems to be the result of HBB in massive AGB stars, which destroys the ^{12}C brought by the third dredge-up.

5. Li in AGB stars. There is a wide distribution of ^{7}Li in AGB stars. The Li-rich stars seem explainable by the Cameron–Fowler process, since most of them also show excesses of s-elements. Those without s-elements may be initially very massive low-Z objects, in order to make HBB without having yet experienced the third dredge-up.
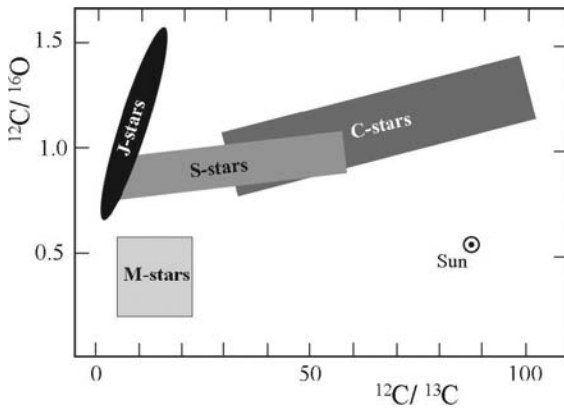
Fig. 26.19 Relation between ^{12}C/^{16}O and ^{12}C/^{13}C for the different spectral classes of AGB stars. The evolution goes (with shading becoming darker) from M stars → S stars → C stars → J stars. Adapted from V. Smith and D. Lambert [540]; see also M. Forestini [191]

The relation between abundance properties, the number and luminosity distributions of the various subgroups in galaxies of different Z is a major constraint. The remaining difficulties generally point in favor of more mixing. Artificial increases of the depth of the convective envelope enhance the third dredge-up, but there is a need for physically coherent transport processes. The uncertainties in the mass loss rates play a large role, in particular at the end the TP-AGB phase, where some "superwind" occurs.

26.6.4 Post-AGB Stars to Planetary Nebulae and White Dwarfs, Super-AGB Stars

Stars with initial masses up to about $M_{WD} \approx 8\,M_\odot$ lead to white dwarfs (WD). Most of the WD have masses equal to $0.55\,M_\odot$; thus mass loss plays an essential role in WD formation. The winds are enhanced by the high luminosities of AGB stars. The maximum luminosities L_{max} reached at the end of the AGB phase depend on the initial masses M_{ini}: $\log L_{max} \approx 3.5, 4.4$ and 4.8 for $M_{ini} = 1, 3$ and $8\,M_\odot$ [265]. The winds lead to the disappearance of the envelope and to the formation of a planetary nebula (PN) surrounding an initially hot white dwarf. Observations of mass, radius and expansion velocity ($v \sim 20$ km s^{-1}) of PNe indicate that the winds making the PNe are stronger than $10^{-5}\,M_\odot$ yr^{-1}, i.e., much more than predicted by (27.3) for the most massive AGB stars. Therefore, a short phase of "superwind" has been proposed [265] with rates of the order of 10^{-5}–$10^{-3}\,M_\odot$ yr^{-1} for about 10^3 yr. The stellar winds are enhanced by the luminosity peaks of the thermal pulses and by the Mira's pulsations; the associate shocks may contribute to the superwind. Also the ^{12}C enrichment in the late AGB phase could create dust grains leading to strong enhancements of the $\dot{M}$ rates. AGB stars in the superwind phase are obscured by an optically thick dusty circumstellar envelope and may be better observed in the IR.

When the remaining mass in the H-rich envelope becomes inferior to a limit of $\sim 10^{-2}\,M_\odot$, the central star starts departing from the AGB (let us call M_{eD} this limit [265]). The post-AGB star becomes hotter keeping about the same luminosity (Fig. 26.20) of about 10^3–$10^{4.5}\,L_\odot$; however the post-AGB stars are also often obscured by dusty ejecta. When $T_{eff} > 30000$ K, the star is able to ionize the ejecta and form a planetary nebula.

The minimum remaining mass M_{eR} of the envelope down to which the superwind is present is a critical parameter. If M_{eR} is large, the superwind stops early and the ejecta have the time to disperse before $T_{eff} \approx 30000$ K. In this case, there is no PN, a scenario which may occur in some cases. If M_{eR} is small, the star rapidly reaches the necessary T_{eff} for PN formation and the ejecta are ionized before they disperse. Since the youngest PNe have an age < 2000 yr, it is likely that $M_{eR} < M_{eD}$; this means that the superwind generally stops during the blueward motion away from the AGB in the HR diagram. For the low-mass post-AGB stars, the evolution is so slow that the ejecta have time to disperse and likely no PN forms.

After PN formation, the post-AGB star becomes the central star of a PN and further evolves to the blue keeping almost the same L up to $T_{eff} > 10^5$ K. Then, it starts fading. Figure 26.20 shows the tracks and timescales for different initial masses leading to WD. The evolution proceeds at a rate strongly depending on the remnant mass. The remnant evolves toward the He sequence (Fig. 24.2) and goes down on it. The star becomes a WD, with a further evolution governed by the cooling time of the non-degenerate gas of heavy nuclei, which supply the WD luminosity. Figure 26.21 shows the observational relations between the final and initial masses of low and intermediate mass stars, which is a test on the mass loss prescriptions in AGB stars.
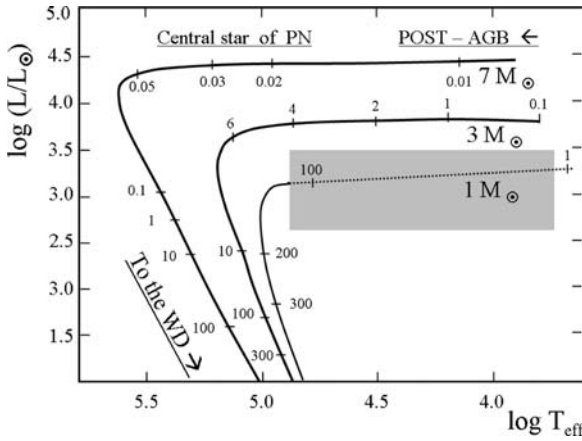
Fig. 26.20 Tracks in the HR diagram for different (initial) masses after the end of the AGB stage. The final masses (WD) are, respectively, 0.94, 0.605 and 0.524 $M_\odot$ for 7, 3 and 1 $M_\odot$ respectively. The ages after the AGB are given in units of 10^3 yr. The gray area covers several loops of a born-again AGB star resulting from late TP's on the hot side of the HR diagram. Adapted from T. Blöcker [50]
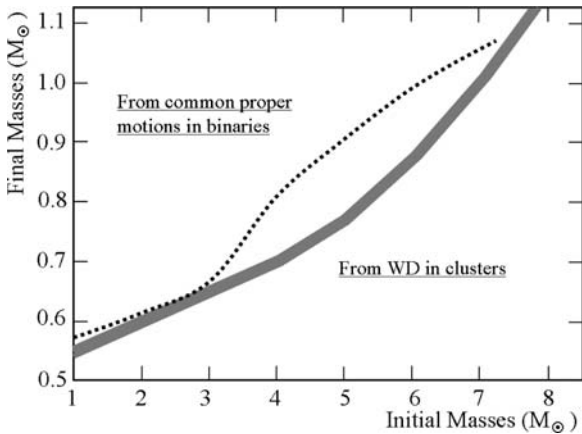
Fig. 26.21 Observational relation between initial and final masses based on white dwarfs in open clusters from V. Weidemann [607] and on WD with proper motions in binaries from S. Catalan [98]

It may happen, in a fraction of $\sim$ 10–20% of the cases, that a post-AGB star experiences a final, strong thermal pulse on the hot side of the HR diagram. If so, the ejected C from the intershell enhances the atmospheric opacity provoking expansion. C grains may form, further increasing the opacity. The central object of the PN then describes a loop from the hot to the AGB side of the HR diagram, becoming a so-called born-again AGB star. A few such late thermal pulses may occur producing several loops. In these objects, the thin H layer which was still remaining at the end of the AGB phase is likely mixed and burnt in the last pulse(s). For the born-again AGB stars, the evolution is so fast that it can be observed on human timescale and a

few candidates are known, in particular FG Sge and V4334 Sgr (Sakurai's object), which show strong light variations and appearance of s-elements within a few years. After the last pulse, nuclear burning in the He shell still goes on for a fraction of the interpulse before becoming extinct. This marks the end of the nuclear activity in the star. The evolution through the born-again stage is likely leading to H-poor O-type subdwarfs (SdO) and finally to WDs deprived of a thin superficial H layer. In general most WDs keep a thin superficial layer of H (white dwarfs of type DA).

Super-AGB stars: if the most massive stars leading to AGB stars do not loose enough mass, the central evolution proceeds up to C ignition. These super-AGB stars [249] with initial masses above M_{UP} might experience a C deflagration leading to the stellar disruption (Sect. 26.4.1). However, for stars close to M_{UP} the off-center burning may also rapidly die out, especially if mass loss is strong. In this case, a massive ONe-rich WD with $M \sim 1.1$ M$_\odot$ results. Recent studies of super-AGB and mass limits [474] suggest that, with current mass loss rates, stars with initial masses from 7 to 9 M$_\odot$ and $Z = 0.02$ become super-AGB stars and ONe white dwarfs.

For those stars where C ignites in the whole core, the catastrophe cannot be avoided by neutrino cooling. Such stars, if they exist, would explode from a kind of red supergiant with a H-rich envelope, making a SN II light curve. They would eject large amounts of radioactive Ni and Co like current supernovae of type I. These hypothetical supernovae explosions with characteristics of both SN II and SN I are said of type SN I 1/2 (Sect. 26.4.1).

26.7   Rotation and Mixing Effects in AGB stars

In order to produce the observed amount of s-elements, a sufficient quantity of ^{13}C ("a ^{13}C pocket") at the basis of the convective envelope is necessary, so that α captures on ^{13}C liberate neutrons which are then captured by elements of the Fe peak. Models currently have difficulties to produce the required amount of ^{13}C, although ad hoc adjustments of the convective parameters may reduce the problems. Self-consistent solutions are however preferable, rotationally induced mixing might improve the situation.

Figure 26.22 shows the chemical structure in a rotating 3 M$_\odot$ model of low Z at various stages of evolution with both effects of advection by meridional circulation and diffusion by shears [410]. Rotation makes a slightly larger CO core with a smoother He profile above it. The He-rich layers, which will later form the intershell, are strongly enriched in C and O by mixing. The ^{12}C from helium burning is brought by diffusion into the H-burning zone and partly converted into ^{14}N by the CNO cycle. This makes strong excesses of C, N and O, which diffuse into the outer convective envelope and contribute to the chemical yields. One then speaks about *primary nitrogen*, since N is not just the daughter of the initial CNO elements, but most of it results from the initial H and He.
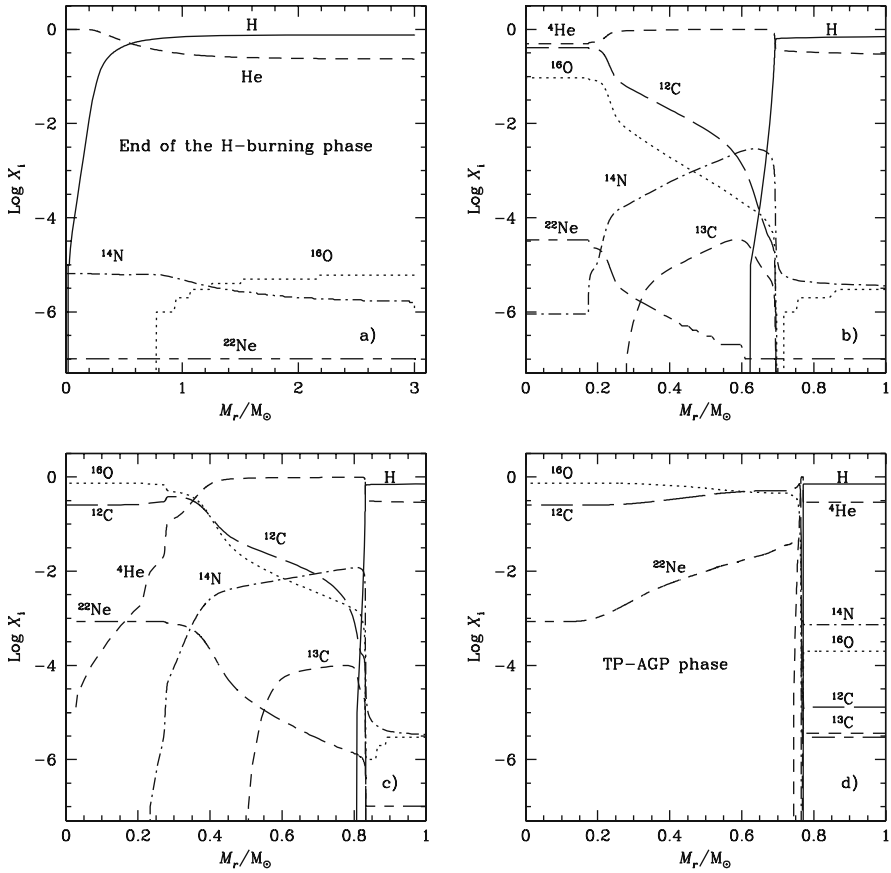
Fig. 26.22 Element abundances in a rotating 3 $M_\odot$ model at $Z = 10^{-5}$. The initial velocity on the ZAMS is 300 km s^{-1}, which corresponds to an average velocity during the MS of $\sim$230 km s^{-1}. Panel (**a**) shows the chemical structure at the end of the MS phase. Panels (**b**) and (**c**) at the middle and at the end of the core He-burning phase. The structure after the first five pulses along the TP-AGB branch is shown in panel (**d**). From G. Meynet and the author [410]

In rotating AGB stars with an initial $M > 4\,M_\odot$, the convective envelope reaches the intershell region bringing lots of C together with some N and O to the surface. Below 4 $M_\odot$, the convective envelope only reaches the level of the H/He discontinuity; thus only a small amount of C is brought to the surface; more C has been destroyed in the pre-AGB phase as a result of CNO processing and first dredge-up (Fig. 26.23) and the second dredge cannot compensate. In the 4 $M_\odot$ model, the two effects are just equal, as illustrated by Fig. 26.23. For $M > 4\,M_\odot$, the second dredge-up overcomes the previous destruction. In the upper right corner of Fig. 26.23, one sees the extreme C enrichment (4 dex) of a 7 $M_\odot$ star with $Z = 10^{-5}$, which has experienced a strong rotational mixing [410].
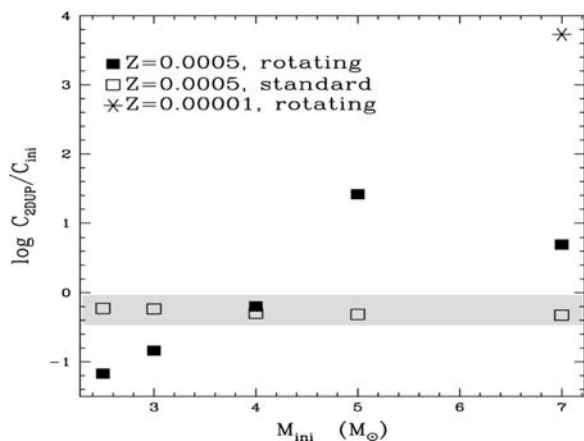
Fig. 26.23 Ratios of the carbon abundance (^{12}C in mass fraction) after the second dredge-up to the initial C content in AGB stars of different initial masses with and without rotation. From T. Decressin and C. Charbonnel [155]

Figure 26.24 shows some effects of rotation (black dots) and overshooting (open circles) on the properties of TP-AGB stars [155]. In rotating models, rotation is fully treated up to the TP-AGB phase and then with local angular momentum conservation. The following effects are found:

1. Rotation lowers the pulse strength and leads to large (cyclic?) variations of the peak luminosity from pulse to pulse. This is likely due to the continuous transport of the elements which broadens the He-rich buffer.
2. Rotation makes the interpulse durations shorter; the number of thermal pulses is higher. The He luminosity during the interpulse is increased due to the larger He layer; however the H luminosity still dominates.
3. There is no third dredge-up, as shown by the zero value of the λ parameter (26.20). Rotational mixing and convection are insufficient to allow the downward extension of the convective envelope after each TP (the μ gradient due to mixing inhibits the inward penetration of convection).
4. Local conservation being assumed, there is no transport of angular momentum: The envelope slows down and the contracting core accelerates, so that the resulting white dwarfs would rotate with velocities above 200 km s^{-1}, while the maximum observed velocities are < 60 km s^{-1} [280]. This shows the need of an efficient transport of angular momentum from center to surface, by instabilities, magnetic field or gravity waves [155].

From Fig. 26.24, we see that the overshooting brings an increase of the helium luminosity during the TP phase; the interpulse periods are initially larger and then decline. The third dredge-up is efficient as shown by the λ values of the successive pulses. Such models lead to the required conditions for producing the s-elements. Despite the rather ad hoc character of the overshooting parameters, this has the interest to show that a more efficient and deeper convective envelope is needed [249].
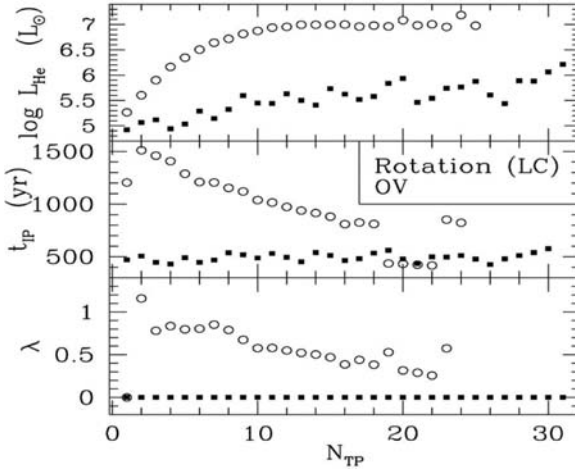
Fig. 26.24 Effects of rotation (*black dots*) on the properties of TP-AGB star of 7 $M_\odot$ with $Z = 10^{-5}$. Local conservation of angular momentum is assumed. Open circles show models with overshooting only. The tip of He luminosity L_{He} (pulse luminosity), the interpulse duration t_{IP} and λ (26.20) are shown as a function of the pulse number. From T. Decressin and C. Charbonnel [155]

26.8 Nucleosynthesis in AGB Stars

26.8.1 Nucleosynthesis in E-AGB stars

Figure 26.25 shows the average composition normalized to Fe for all layers outside the CO core at the end of the E-AGB phase for a 7 $M_\odot$ with an initial velocity $v_{ini} = 800$ km s^{-1} (close to the critical velocity) at $Z = 10^{-5}$. All layers outside the CO core are ejected in the late phases and contribute to the chemical enrichment (see Sect. 26.6.3). The model star, due to its low Z, has lost only 0.002 $M_\odot$ in previous phases. Figure 26.25 shows a major consequence of rotation in low-Z AGB star: there is an enhancement of ^{12}C, ^{13}C, ^{14}N, ^{16}O (together with ^{17}O and ^{18}O) and ^{19}F by a factor of $\sim 10^4$, of ^{22}Ne by 4×10^3, of ^{23}Na by 30 and of ^{26}Mg by 10. The enormous enhancements in CNO elements are due to the transport of ^{12}C from the He-burning core up to the H-burning shell, where a fraction is turned by the CNO cycles into ^{14}N (with some ^{13}C) together with some synthesis of other elements of the CNO and NeNa cycles. Nitrogen here is a primary element (Sect. 29.3.2). C and O are produced in the He-burning shell and dredged up. These elements reach the stellar surface during the second dredge-up, producing large enrichments. The surface metallicity Z reaches about 10^3 times the initial Z of the model (in a 60 $M_\odot$ model the factor is 10^6, cf. Fig. 29.9). Such a large production of C, N and O due to rotational mixing in AGB star (Fig. 26.25) only occurs for Z smaller than about 0.002. Above, rotational mixing is less efficient (Chap. 12). The C transported out from the CO core favors the formation of C stars already after the second dredge-up,
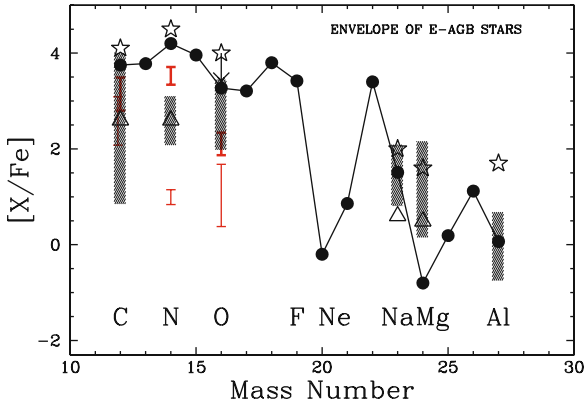
Fig. 26.25 Average chemical composition of the envelopes of E-AGB stars. The *continuous line* with *black circles* applies to a 7 $M_\odot$ model at $Z = 10^{-5}$([Fe/H] $= -3.6$) with an initial velocity $v_{ini} = 800$ km s^{-1}. The *vertical error bars* indicate the ranges of values for CNO elements in the models [410] with initial masses between 2 and 7 $M_\odot$ at $Z = 10^{-5}$; the *thick and thin bars* correspond to rotating ($v_{ini} = 300$ km s^{-1}) and non-rotating models. The observed abundances of extremely metal-poor stars are shown by hatched areas (observations by Plez and Cohen [473] with triangles, by Frebel et al. [186]) with stars). From G. Meynet et al. [407]

especially from massive low-Z AGB stars [155]. In massive AGB stars, a part of the C is then converted into N by hot bottom burning; this may together with further reactions also change the envelope composition in the course of its ejection.

The model abundances agree well with those observed in unevolved extremely metal-poor stars as shown in Fig. 26.25. This suggests that the ejected envelopes of fast-rotating AGB stars (and massive stars, see below) have substantially contributed to the early chemical enrichment of the Milky Way [407]. The non-rotating models cannot account for the high overabundances in nitrogen and oxygen, which can neither result from the yields of supernovae, because these would contain lots of other α elements.

The physical conditions in massive AGB stars and in high mass stars are not too different; the same nuclear reaction chains and mixing can occur leading to similar nucleosynthetic products. The lifetimes are different, but not too much: a 7 $M_\odot$ has a lifetime on the order of 40 Myr, an order of magnitude higher than a 60 $M_\odot$ star. Fast-rotating massive stars at low Z (Sect. 29.3.2) also produce large excesses of CNO and other elements. Most s-elements are likely produced by AGB stars; however a fraction (depending on Z) of them is also produced by massive stars; these are the s-elements of low-atomic mass number ($A \leq 90$), known as the light s-elements (ls), such as Sr, Y and Zr. By opposition, one distinguishes the heavy s-elements (hs), such as Ba, La and Ce, generally formed in AGB stars (there is a positive correlation between the (hs/ls) ratio and the total amount of s-elements present [596]). Other possible ways to distinguish between s-enrichments by massive stars and AGB envelopes may exist. Material from rotating massive stars is characterized

by lower $^{12}C/^{13}C$ ratios than AGB stars (there are also large differences predicted between non-rotating and rotating massive stars [124]). The AGB envelopes show very high overabundances of ^{17}O, ^{18}O, ^{19}F and ^{22}Ne, while the winds of massive rotating stars present weaker overabundances of these elements (compare Figs. 26.25 and 29.9 [407, 410]).

26.8.2 Nucleosynthesis in TP-AGB Stars

Rotating and non-rotating models enter the TP-AGB phase with very different internal chemical distributions as a result of the second dredge-up. In non-rotating TP-AGB models, the nucleosynthesis and the chemical yields depend a lot on the third dredge-up and on the hot bottom burning. This is not the case in the rotating star models, where the TP-AGB phase barely affects the chemical imprint of the previous phases, in particular of the second dredge-up [154]. The reason is that the rotating models due to their larger cores and higher luminosities are losing most of their envelope before the TP phase (this depends on mass and Z; the previous remark applies especially to AGB stars originating from low masses). As shown in Fig. 26.25, the main effect of rotation is to enhance the production of relatively light nuclides with $A < 23$.

During the TP-AGB phase, rotating models present a very large shear at the base of the convective envelope. Shear mixing diffuses protons into the ^{12}C-rich intershell layers. By successive p captures, this leads to the formation of ^{13}C and ^{14}N layers, which partly overlap each other. The α captures by ^{13}C during the interpulse phase should normally produce the desired s-elements; however the continuous diffusion of the abundant ^{14}N, which is a poison for neutrons due to the reaction $^{14}N(n,p)^{14}C$, strongly quenches the s-element production. Thus, shear mixing produces the desired ^{13}C pocket, but not the s-elements as shown by Siess et al. [531], who conclude that something may be missing in their treatment of rotation. Maybe magnetic field could reduce the shear mixing. This is an interesting possibility because it would also evacuate angular momentum from the future white dwarf as mentioned above. Finally some well-adjusted combinations of rotation and overshooting may increase the synthesis of the s-elements; however a full consistent theory of TP-AGB stars is still ahead of us.

Chapter 27
Massive Star Evolution with Mass Loss and Rotation[*]

Massive stars play a major role in the spectral and chemical evolution of galaxies.

– They are the main source of UV radiation and they power the far IR luminosity of galaxies through the heating of the dust.
– They are the progenitors of luminous blue variables (LBV), Wolf–Rayet stars, supernovae and black holes.
– They are the main nuclear reactors forming the heavy elements.
– They are observable at large distance in the Universe, either directly or by their signatures in the integrated spectrum of galaxies.
– The stellar winds and supernovae contribute almost equally to the injection of mechanical power and turbulence into the interstellar medium.

Massive stars have an initial mass larger than 8–9 $M_\odot$. After the H- and He-burning phases, they experience in non-degenerate conditions the further phases of nuclear burning, leading to the so-called onion skin model which explodes as a supernova. Their evolution in the H- and He- burning phases is heavily influenced by mass loss due to radiative stellar winds. These are able to remove most of the initial stellar mass, leaving only bare cores (Wolf–Rayet stars) deprived of their envelopes.

Massive stars are often fast rotators and experience rotational mixing which brings to the surface the elements synthesized in the core. Observations show large nitrogen and helium enrichments, particularly in low-Z stars. Rotation also enhances the mass loss rates by stellar winds and creates anisotropic winds, stronger at the poles than at the equator.

27.1 The Need for Both

The physics and evolution of massive stars are dominated by mass loss and by rotational mixing. At the origin of both effects, we find the large ratio T/ρ of temperature to density. This enhances the ratio of radiation to gas pressure, which goes

---

[*]This chapter may form the matter of a basic introductory course.
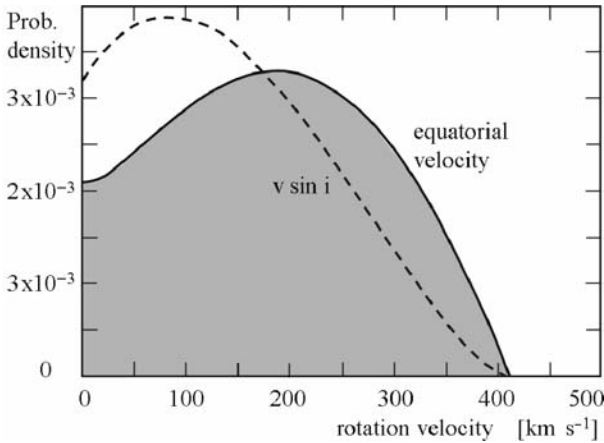
Fig. 27.1 Probability density by km s^{-1} of rotation velocities for 496 stars with types O9.5 to B8. Adapted from W. Huang and D.R.Gies [256]

like T^3/ρ and favors stellar winds (Sect. 3.6.1). A high T/ρ also enhances rotational mixing, since mixing by shear turbulence scales as the thermal diffusivity $K = 4acT^3/(3C_P \kappa \rho^2)$ (Sect. 12.2).

O, B and A stars have high rotational velocities v. Figure 27.1 shows the distribution of v for 496 OB-type stars [256]. The average velocity is 190 km s^{-1} after correction for the projection angle $\sin i$, see also Table 4.1. A velocity of 200 km s^{-1} corresponds to 52% of the break-up angular velocity for a 20 M$_\odot$ star (type BOV) in the middle of its MS phase. These velocity data account for gravity darkening (Sect. 4.2.2; [138, 578]). The velocities of O-type stars decrease by 30% or more during the MS phase due to mass loss and expansion, implying that the initial values are even larger.

Both mass loss and mixing influence the model outputs: tracks in the HR diagram, lifetimes, abundances, chemical yields and supernova progenitors. At a given v, the rotation effects are generally more important at lower metallicities. In addition, there are more fast rotators at lower Z [358, 378].

27.2   Evolution at Constant Mass

Although massive stars do not evolve at constant mass, it is useful to examine the evolution without mass loss. This provides a useful comparison point. Figure 27.2 shows the evolution of stars with 9, 15, 30, 60 and 120 M$_\odot$ at constant mass in the HR diagram. The MS band becomes wider for the most massive stars due to their larger convective cores. During the MS, the convective core recedes letting behind
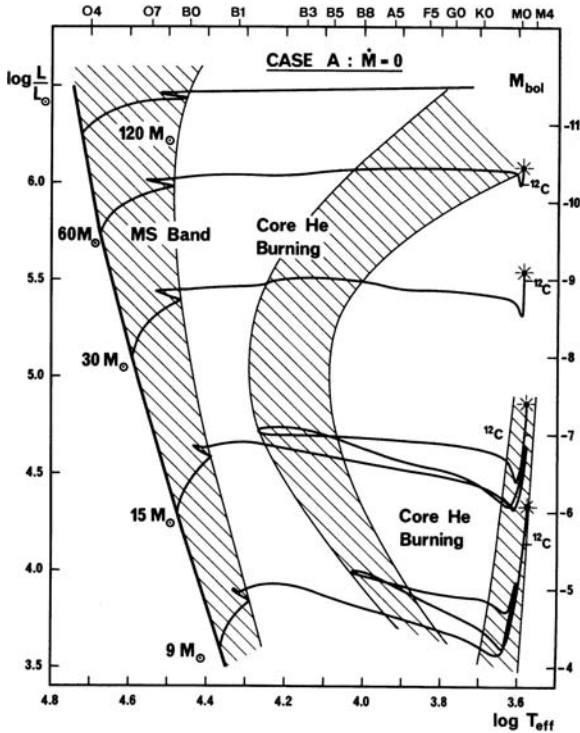
Fig. 27.2 Evolution of massive stars with $X = 0.70$ and $Z = 0.03$ at constant mass without over-shooting. The hatched areas show the phases of slow H and He burning. The "shiny dots" show the location of the pre-supernovae. The beginning of C burning after He exhaustion is indicated by ^{12}C. From the author [339]

it a zone of variable mean molecular weight μ (Fig. 27.3), forming a "sandwich" of radiative and convective zones. This region is subject to semiconvection [129].

The He-burning phase forms a "horn" in the HR diagram. Most of this phase is spent in the blue (except for the highest M), due to an intermediate convective zone above an active H-burning shell (Fig. 27.3). Convection homogenizes the composition and imposes a polytropic structure (Sect. 24.5) with a modest density contrast, this limits the growth of the radius, the star stays in the blue. Later, the He core grows and the H shell and the intermediate convective zone decline and the star evolves to the red.

Depending on mass, the stars reach the red-supergiant stage at the end of the He-burning phase or even later just before central ^{12}C ignition. Thus, there would be almost no red-supergiants predicted by models with constant masses. Later, a small C-burning core develops, the energy of which is evacuated by neutrinos. It is surrounded by a He-burning shell with a small convective zone. A huge convective envelope covers most of the stellar mass, bringing He and N to the stellar surface. Such stars end their life as supernovae exploding from red supergiant progenitors
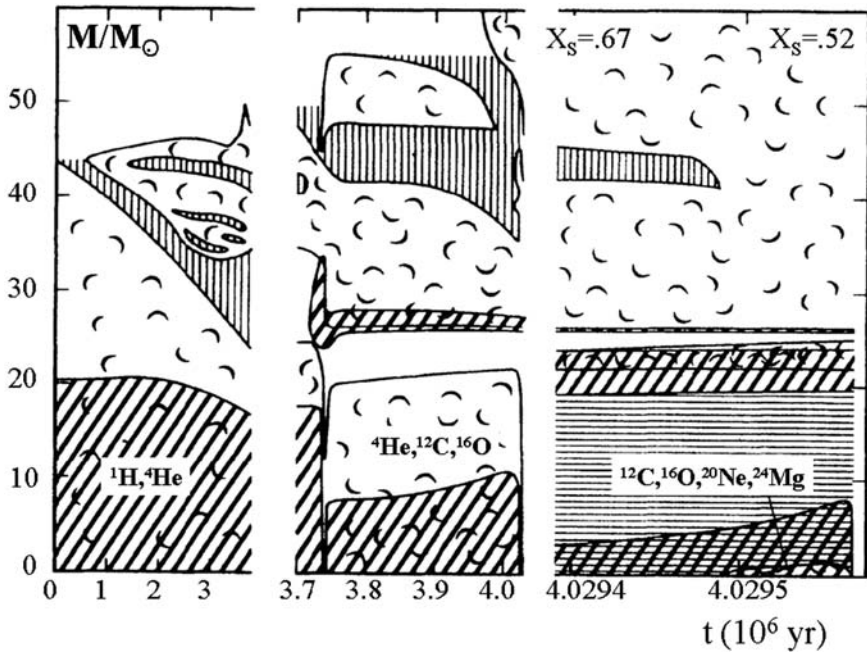
Fig. 27.3 Evolution of the structure (Kippenhahn's diagram) of a star of 60 $M_\odot$ with $X = 0.70$ and $Z = 0.03$ at constant mass as in Fig. 27.2. No overshooting is included. The H-, He- and C-burning phases are represented with different scales of time. Cloudy regions are convective, heavy diagonal hatching indicates where $\varepsilon > 10^3$ erg g^{-1} s^{-1}. Vertical hatching indicates variable H and He contents, horizontal hatching indicates variable C and O contents. From the author [338]

(likely SN IIp). The most massive stars $M \geq 120$ $M_\odot$ may explode from pair insta-
bility (Sect. 7.8).

27.3   Internal Evolution and the HR Diagram

27.3.1   Mass Loss Parametrizations

The basic physics of stellar winds is studied in Chap. 14. Owing to the many
uncertainties, stellar model makers often apply expressions of $\dot{M}$ derived from ob-
servations, which are also uncertain [301]. The situation is very moving, yester-
day's parametrizations may be obsolete tomorrow. Nevertheless, we show some
parametrizations to indicate the general trends. The mass loss rates increase with
L (27.2) and at a given L they strongly increase for lower T_{eff}. A good overview
of the $\dot{M}$ rates in the HR diagram was given by de Jager et al. [271]; a simple
parametrization of their data on the MS is

$$\log \dot{M} = -8.158 + 1.769 \log(L/L_\odot) - 1.676 \log T_{\text{eff}}. \tag{27.1}$$

The account for clumping effects in the wind has led to a reduction of the $\dot{M}$ by a factor 2 or 3 and questions arise about a further reduction. A clumping effect of the order of 3 as in [604, 605] seems now acceptable. For hot stars, parametrizations of the $\dot{M}$ rates are given by Kudritzki and Puls [298] and by Vink, de Koter and Lamers [604, 605] for different M, L, T_{eff} and metallicities Z. The low-Z O-type stars have $\dot{M}$ rates much fainter than the theoretical predictions. For O stars, $\dot{M}$ (taken > 0) behaves globally with L and Z as in (14.25) and (14.28), see also Mokiem et al. [425],

$$\dot{M} \sim L^{1.6} \qquad \text{and} \qquad \dot{M} \sim Z^{0.7}. \tag{27.2}$$

For red-supergiants and AGB stars, different parametrizations exist, such as the so-called Reimers' law [484] which has been very much used,

$$\dot{M} = 4 \times 10^{-13} \, \eta \, \frac{L}{gR} \quad \text{in } M_\odot \, \text{yr}^{-1}. \tag{27.3}$$

It means that a fraction η of the luminosity is used to modify the potential energy (see 14.2 and 14.3). This prescription has been completed by Blocker [50]. For pulsating winds in AGB stars, Vassiliadis and Wood [599] give

$$\log \dot{M}(M_\odot \, \text{yr}^{-1}) = -11.4 + 0.0125 \left[P(\text{days}) - 100 \left(\frac{M}{M_\odot} - 2.5 \right) \right] \tag{27.4}$$

$$\text{with } \log P = -2.07 + 1.94 \log \frac{R}{R_\odot} - 0.9 \log \frac{M}{M_\odot}, \tag{27.5}$$

in $M_\odot \, \text{yr}^{-1}$ with P the pulsation period in days (see also Willson [615]). Dust-enshrouded AGB stars and red supergiants have strong mass loss rates due to the high dust opacity, they can be represented by [595]

$$\log \dot{M} = -5.65 + 1.05 \log \left(\frac{L}{10^4 L_\odot} \right) - 6.3 \log \left(\frac{T_{\text{eff}}}{3500 \, \text{K}} \right), \tag{27.6}$$

with uncertainties ± 0.15, ± 0.14 and ± 1.2 for the three coefficients. The $\dot{M}$ rates in the Wolf–Rayet (WR) stages are very high, due (mostly) to their high L/M ratios (Fig. 27.15); instabilities may also contribute, as well as the optically thick radiation wind [446]. The $\dot{M}$ rates of WN and WC stars in terms of the luminosity in solar units, He content Y and metallicity Z are [445]

$$\log \dot{M} = -11.00 + 1.29 \log L + 1.73 \log Y + 0.47 \log Z, \tag{27.7}$$

with uncertainties $\pm 0.14, \pm 0.42$ and ± 0.09 for the last three numerical factors. The $\dot{M}$ rates in terms of the actual WR masses are [445],

$$\log \dot{M} = A + B \log \frac{M}{M_\odot} , \qquad (27.8)$$

with $A = -5.99$, $B = 1.06 \pm 0.22$ for H-rich WN stars, $A = -5.93$, $B = 1.13 \pm 0.26$ for WC stars. $A = -5.73$, $B = 0.88 \pm 0.14$ for all WR stars. Several parametrizations have been proposed, accounting for the reduction of the mass loss rates due to clumping effects in the wind and different effects including metallicity Z [150, 603]. However, $\dot{M}$ for WR stars does not only depend on Z but also on L/M or on the Eddington factor Γ, see [218].

The L dependence (27.2) implies that more massive stars lose a higher mass fraction during evolution. The determinations of the $\dot{M}$ rates are continuously revised. Therefore, we put the emphasis on the general results.

27.3.2 Mass Loss Effects in the HR Diagram

Figure 27.4 illustrates the effects of mass loss for a 30 $M_\odot$ star with a simple parametrization. The mass reduction makes the star less luminous, however it is overluminous for its actual mass, the MS band is more extended as the core mass fraction is larger (Fig. 24.3). In the expression of the MS lifetime $t_H \sim q_c M/L$, the quantities $(q_c \times M)$ and L are reduced by mass loss so that on the whole t_H does not change very much, increasing for current $\dot{M}$ rates, by about 5–10%.
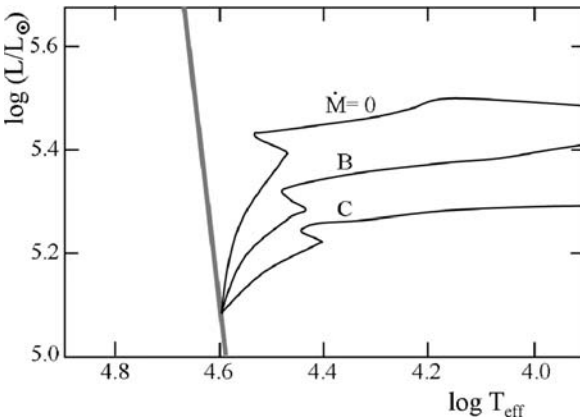
Fig. 27.4 MS tracks of a 30 $M_\odot$ star with $X = 0.70$ and $Z = 0.03$ without mass loss and with $\dot{M} = NL/c^2$ (14.1) in CGS units for $N = 70$ (B) and $N = 140$ (C)
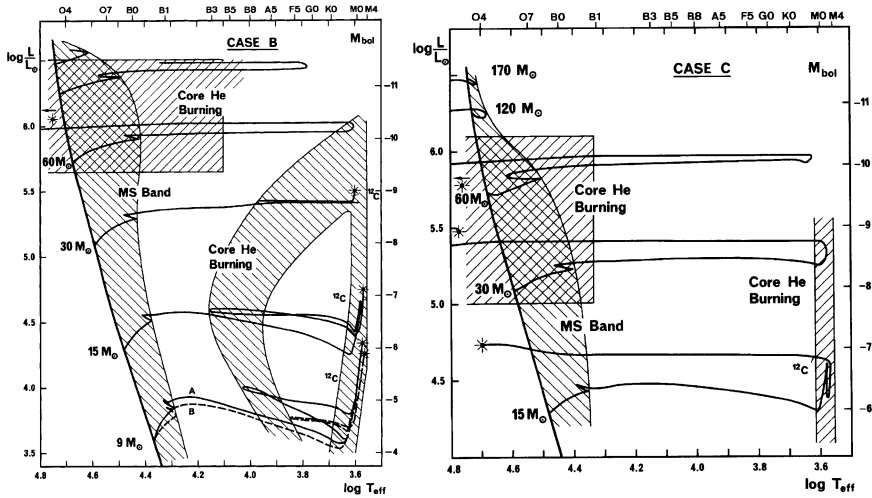
Fig. 27.5 Evolution of massive stars with mass loss and no overshooting for composition $X = 0.70$ and $Z = 0.03$ for two cases of mass loss rates with $\dot{M} = NL/c^2$ (14.1). *Left*: with $N \approx 70$. *Right*: with $N \approx 140$. From the author [339]

After the MS, the effects of mass loss on evolution are important. Figure 27.5 shows two cases (in case B: the final masses are 11.09, 12.49 and 24.80 $M_\odot$ for the initial masses 15, 30 and 60 $M_\odot$, respectively; in case C, the corresponding final masses are 3.50, 10.15 and 19.6 $M_\odot$). Mass loss as in case B produces a shift of the "horn" of the He-burning phase to the red, particularly for the brightest stars. This results from the decrease or absence (Fig. 27.6) of an intermediate convective zone. The disappearance of this zone results from the reduction of the envelope. There is a shift from B supergiants to A and F supergiants and there are more red supergiants than without mass loss. The blue loops of the 9 and 15 $M_\odot$ are smaller (Sect. 26.2.4). For the most massive stars ($\geq 60\ M_\odot$), the mass loss of the red supergiants removes the rest of the envelope. The star becomes a bare core, it evolves toward the He sequence (Fig. 24.2) and turns into a WR star.

For an extreme mass loss as in case C, the "horn" disappears. After the MS, the stars evolve quickly to the red supergiant stage, where they lose their envelope and become WR stars. Depending on $\dot{M}$, stars with $M > 60\ M_\odot$ make only a limited excursion to the red in the HR diagram up to the region of the luminous blue variables (LBV). In the extreme case, the stars lose enough mass on the MS to keep an almost homogeneous composition. Such stars turn to WR stars after the MS phase.

The evolution toward or away from the red supergiant is determined by several effects. 1. The increasing mass fraction of the He core (for $q \geq 0.5$) favors a blueward evolution toward the He sequence. 2. As mentioned above, an intermediate convective zone maintains the star in the blue side of the HR diagram. 3. A helium enrichment of the envelope lowers the opacity, reduces the radius and favors a blueward evolution. 4. A large luminosity over mass ratio contributes to the envelope expansion, however this effect is small.
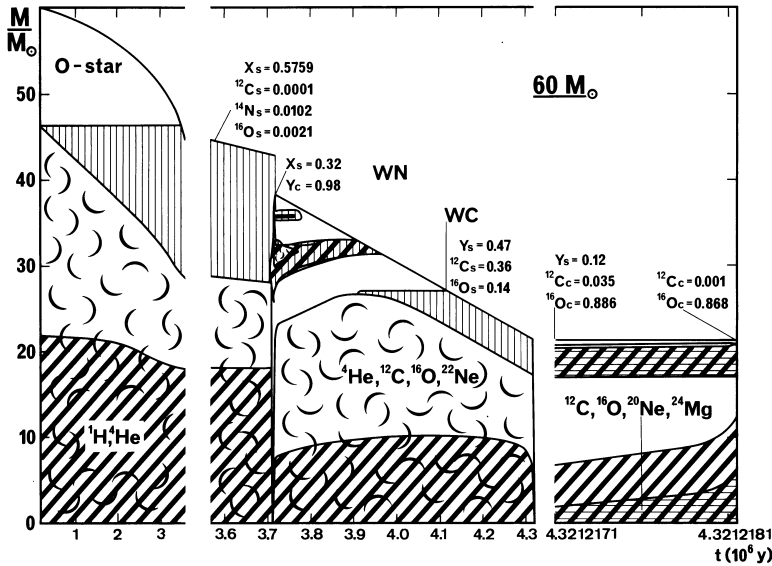
Fig. 27.6 Evolution of the internal structure of a 60 M$_\odot$ star ($X = 0.70$, $Z = 0.02$) up to central C exhaustion with mass loss rates [271] and a core overshooting of 0.25 H_P. Values of surface abundances in mass fractions are indicated with an index "s", while central abundances have an index "c". WN and WC indicate the Wolf–Rayet stages WN and WC. Same remarks as for Fig. 27.3. From the author [345]

An increasing mass loss first favors evolution toward the red supergiant (effect nb. 2), then further mass loss (effect nb. 1) increases the core mass fraction q bringing the star to the He sequence, at the same time mass loss reveals the inner layers which are He rich (effect nb. 3). The fraction q necessary to initiate a blueward evolution of massive stars of Pop. I away from the red-supergiant stage are about 65, 77 and 97% at 60, 30 and 15 M$_\odot$, respectively (cf. Fig. 24.3). Models with mass also better explain the upper limit of the distribution of massive stars in the HR diagram, an observed limit known as the Humphreys–Davidson limit [260, 261].

27.3.3   Internal Evolution with Mass Loss

Figure 27.6 illustrates the case of a 60 M$_\odot$ star. During the MS phase, the main difference is the absence of semiconvection, this is due to the luminosity reduction and loss of a part of the envelope. The surface is going down to deeper Lagrangian coordinates progressively revealing the internal layers. Near the end of the MS stage, the surface reaches layers which were in the core. The effects of the CNO cycle become visible at the surface: He enhancement, C (and O) decrease, while the N abundance increases a lot (Fig. 27.11).

After central H exhaustion, a H-burning shell develops. The shell is rapidly narrowing and joined by the stellar surface, where H disappears. There the composition is nearly pure He. The mass of the He core increases until the H-burning shell disappears. Then, mass loss removes He layers, thus making the core mass to decrease (at the same rate as the total M [305]). Before the core decreases, the evolution of the central conditions in the $\log T_c$ vs. $\log \varrho_c$ is the same as for constant mass evolution, despite the loss of the half of the stellar mass. But, as soon as the mass of the He core is reduced, the evolution becomes different with a lower T_c at a given density.

The ongoing mass loss reveals the products of central He burning at the surface: huge relative enhancements of C and O, while He diminishes regularly. The star is now a WC star. At the end of the He-burning phase, the core contracts until central C-ignition. All phases after He exhaustion have a total duration equal to a fraction $\sim 10^{-3}$ of the H-burning phase.

27.3.4 Effects of Rotation in the MS Phase

A rotating star is distorted and radiates anisotropically: hotter and brighter at the poles and cooler and fainter at the equator (Sect. 4.2.2). There is also a shift of luminosity which amounts up to $\Delta \log L = +0.5$ [371] for a fast rotating star seen pole-on and to -0.15 for a star seen equator-on. The average T_{eff} (Fig. 27.7 left) is defined by the total L and the total stellar surface. This T_{eff} corresponds to the value at $P_2(\cos \vartheta) = 0$, i.e., to a colatitude $\vartheta \approx 54^o$. The difference of the average T_{eff} is well visible for stars on the zero-age sequence, later it is masked by other effects.
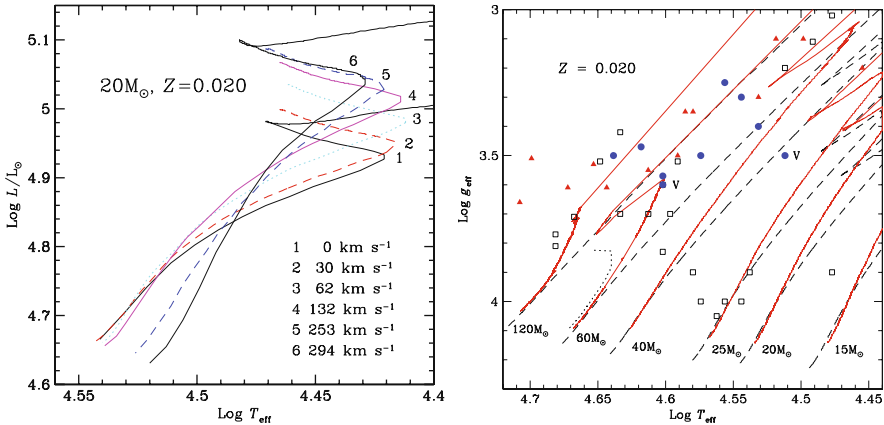
Fig. 27.7 *Left*: evolutionary tracks of a 20 M$_\odot$ star with $Z = 0.02$ with different initial velocities. *Right*: MS tracks in the plot of the effective gravity (including centrifugal force) vs. T_{eff}. The dashed and continuous lines are for zero rotation and for rotating models with initial $v = 300$ km s^{-1}. Observations by Herrero et al. [245, 246] are shown. From G. Meynet and the author [409]

As evolution proceeds, the increase of the central condensation produces some differential rotation, which leads to hydrodynamical effects, such as shear and horizontal turbulence (meridional circulation is also present in solid body rotating stars). The resulting mixing brings some He out of the convective core into the radiative envelope, slightly increasing its mean molecular weight. The higher resulting P and T in the interior favor a larger convective core. For a 20 $M_\odot$ mass with an average $\bar{v} = 200$ km s^{-1} during the MS phase, the relative core increase at the end of the MS phase is $\sim 20\%$. This increase makes a milder μ gradient than what overshooting would do. The larger core leads to a higher luminosity during subsequent evolution.

The He enhancement in the envelope lowers its opacity, which increases L and makes the star hotter, favoring a blueward track. Figure 27.7 (right) shows the tracks resulting from these various effects. Figure 27.8 (top) shows a global view of the tracks with and without rotation for stars with $M \geq 9$ $M_\odot$. Rotation enlarges the MS width for $M < 40$ $M_\odot$ and reduces it for larger masses. The enlargement results from the bigger He cores. For the highest masses this effect is dominated by the He enrichments. An extreme situation may occur for stars with $M \geq 60$ $M_\odot$ with high initial rotation: the convective core instead of shrinking expands during the MS phase and evolves to the blue in a quasi-homogeneous evolution to WR stars (Fig. 25.15).

Rotation by increasing the core makes the stars overluminous for their masses, which introduces some scatter in the M–L relation. Figure 27.7 (right) shows the MS evolutionary tracks in the $\log g_{\text{eff}}$ vs. $\log T_{\text{eff}}$ diagram. If a value of the mass of a rotating star is assigned from the g_{eff} and T_{eff} of non-rotating models (broken lines), a too high value of mass is obtained. This may be part of the origin of the mass discrepancy often found between the spectroscopic determinations and the values from evolutionary tracks.

27.3.5 Lifetimes and Age Estimates

The MS lifetimes are generally increased by rotation, from 15% at 120 $M_\odot$ to 25% at 9 $M_\odot$ [411]. This is due to the larger core and to the shear diffusion which continuously brings new H from the envelope into the core. An isochrone with rotation is almost identical to an isochrone without rotation with log age smaller by 0.1 dex [Fig. 27.8 (bottom)]. This means that ignoring the effect of rotation in the estimate of cluster ages leads to ages too small by about 25%. The spread in rotation and orientation angles introduces some scatter together with the effect of unsolved binaries.

The He-burning lifetimes depend on mass loss and mixing. For a 20 $M_\odot$ model at $Z = 0.02$, the ratio $t_{\text{He}}/t_{\text{H}}$ of the He- to the H-burning lifetimes passes from 0.11 to 0.08 for an initial rotation velocity passing from 0 to 300 km s^{-1}. For a 12 $M_\odot$, these values are 0.124 and 0.074 [411]. The effects are similar at lower Z. The
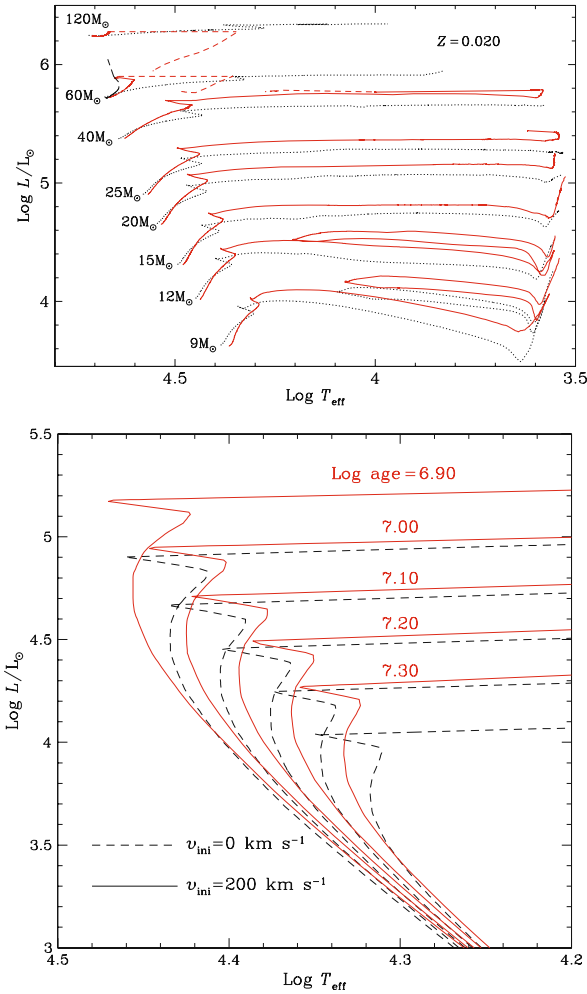
Fig. 27.8 *Top*: tracks at $Z = 0.02$ for non-rotating stars (*dotted lines*) and for stars with initial velocities of 300 km s^{-1} (*continuous lines*), corresponding to a MS average $\bar{v} = 160$–235 km s^{-1}. *Bottom*: isochrones of $\log(\text{age}) = 6.9$ to 7.3 for zero rotation (*dashed lines*) and for initial $v = 200$ km s^{-1} (*continuous lines*). The dashed line of $\log(\text{age}) = 6.9$ is close to the continuous line with $\log(\text{age})=7.0$. From G. Meynet and the author [409]

reasons for the shorter $t_{\text{He}}/t_{\text{H}}$ ratio are the higher luminosity and the longer MS lifetime in rotating models. However, extreme mass loss in the most massive stars ($M \geq 85$ M$_\odot$) leads to a lower luminosity in the advanced stages and increases their lifetimes.

27.3.6 He-Burning: Blue and Red Supergiants at Different Z

The upper luminosity limit of the red supergiants depends on metallicity. The higher Z, the lower the cutoff of the L distribution of red supergiants: in NGC 6822 ($Z = 0.005$) the upper limit is around $M_{bol} = -9.0$ ($M \sim 30$ M$_\odot$), while in M31 ($Z = 0.036$) it is around -7.5 ($M \sim 15$ M$_\odot$) [382]. This is an effect of the Z dependence of the mass loss rates (in the MS as well as in the red-supergiant stages): for higher Z, $\dot{M}$ values are higher and the stars more quickly become WR stars. Below about 25 M$_\odot$ at $Z = 0.02$, the He-burning phase is shared between the blue- and the red-supergiant stages. The stars are often close to a neutral state between a blue and a red location: minor structural changes can produce major differences of the radii. This is a limiting case of the Vogt–Russel theorem (Sect. 24.1.1).

An important question is the number ratio B/R of blue (Types B and A) to red (K and M) supergiants [311]. Figure 27.9 (left) shows the B/R ratio as a function of Z in the Milky Way and SMC. In the galactic interior, there is almost no red supergiants, this ratio is above 10; in the solar neighborhood it is about 3, and 0.6 in the SMC where there are lots of red supergiants (cf. also [384]). The red supergiants in Fig. 27.9 (left) are defined in a large spectral interval in order to encompass the changes of the mean types with Z: K5–K7 I in the SMC, M1 I in the LMC and M2 I in the Milky Way [383].

Figure 27.9 (right) shows that some bluewards shifts occur even at $Z = 0.02$ for certain rotational velocities. The blue shifts are influenced by mass loss, mixing and the intermediate convective zone (cf. Sect. 26.2.4). This is interesting in relation
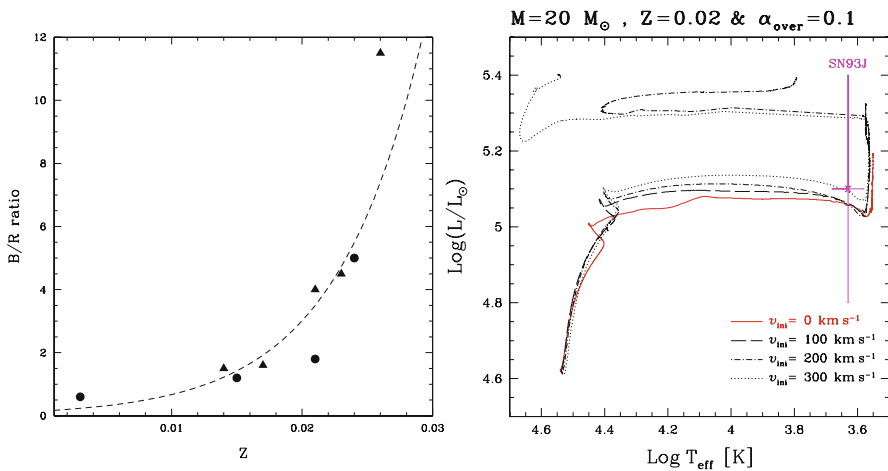
Fig. 27.9 *Left*: the blue to red-supergiant ratios B/R at different Z in clusters of $\log(\text{age}) = 6.8$–7.5. "B" includes B- and A-type supergiants, "R" the K and M supergiants. From P. Eggenberger et al. [173]. *Right*: evolutionary tracks for 20 M$_\odot$ stars at $Z = 0.02$ with different initial velocities. From Hirschi et al. [251]
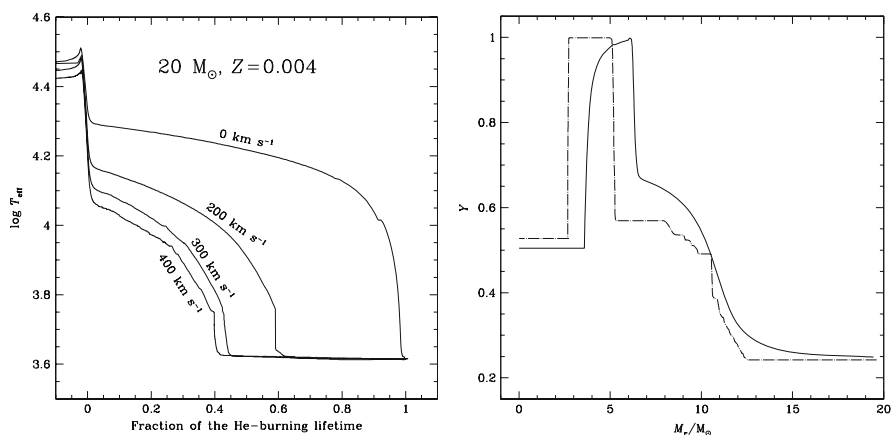
Fig. 27.10 *Left*: evolution of the T_{eff} as a fraction of the lifetime spent in the He-burning phase for different initial velocities. *Right*: distribution of He at the middle of the He-burning phase in a 20 $M_{\odot}$ model at $Z = 0.004$ with zero rotation (*dashed-dotted line*) and in a model with an initial velocity of 300 km s^{-1} (*continuous line*). From the author and G. Meynet [367]

with the B/R ratio at lower Z like in the Small Magellanic Cloud (SMC). There, the numerous red supergiants were difficult to explain for long, because models at low Z have little mass loss and they normally spend most of their He-burning phase in the blue [Fig. 27.10 (left)]. The B/R ratio decreases for higher rotation. A 20 $M_{\odot}$ rotating star spends about the half of its He-burning phase in the blue and the half in the red (this is the same at 15 $M_{\odot}$). The physical reason rests on the change of the internal He profile [Fig. 27.10 (right)]. Without rotation, there is a large intermediate convective zone, which keeps the star on the blue side. With rotation, the mild mixing increases the amount of He near the H-burning shell, reducing its efficiency. Thus, there is no intermediate convective zone keeping the star to the blue. These results are consistent with those about semiconvection in Sect. 6.2.1.

27.4   Evolution of the Chemical Abundances

The chemical abundances offer tests of stellar physics and evolution. Mass loss, mixing and mass exchange in binaries may affect surface compositions.

27.4.1   Steps in the Peeling-Off by Mass Loss

The removal of the outer layers by winds reveal the inner layers with a modified composition, in a nice illustration of the effects of the CNO cycles and He-burning reactions. In Fig. 27.11, ones sees five typical domains:
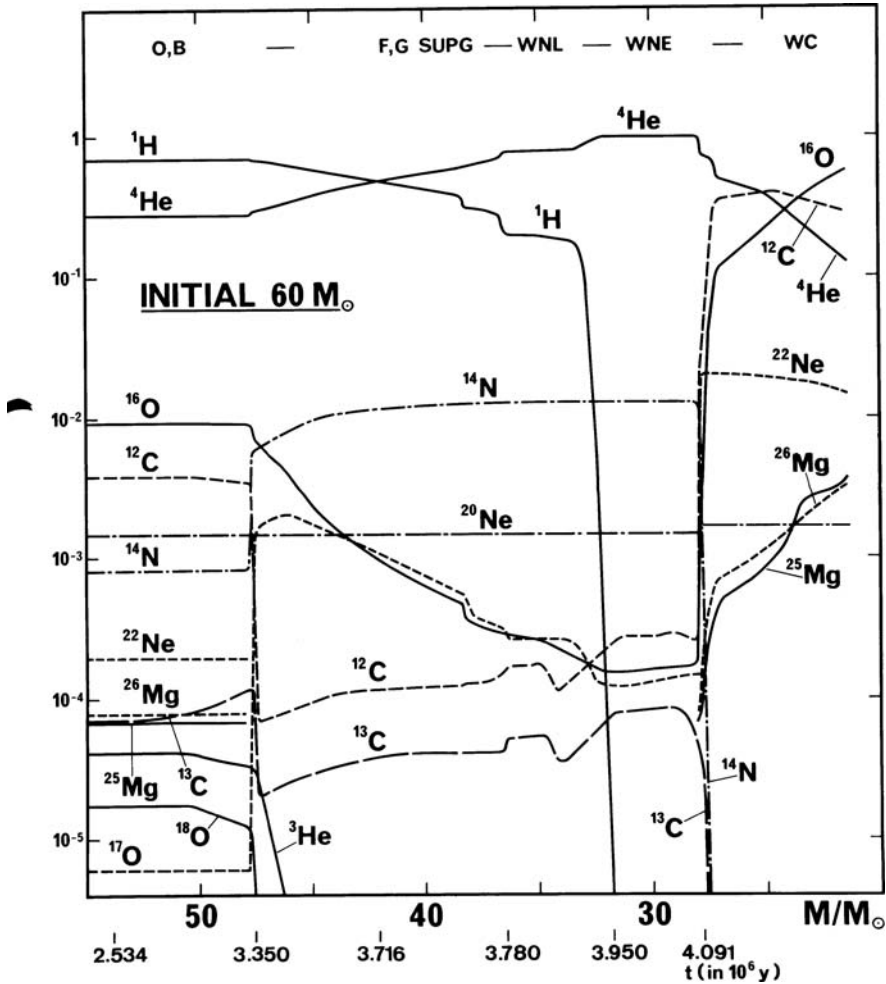
Fig. 27.11 Evolution of the surface abundances in mass fractions X_i for a 60 $M_\odot$ star ($X=0.70$, $Z=0.02$) as a function of the remaining mass and age. The age zero is on the ZAMS. Indications of the corresponding stages. From the author [345]

1. The initial abundances. For a 60 $M_\odot$ star at $Z = 0.02$, the CNO processed elements appear at the surface only at the very end of the MS phase. (Thus, mass loss does not account for the changes of surface composition observed in most OB stars, some additional effect is needed, Sect. 27.4.3).
2. Intermediate abundances due to partial CNO processing with possible dilution effects. This stage shows N enrichments, $^{13}C/^{12}C$ enhancements, C depletion and modest O depletion (Fig. 27.12). Such a composition is typical of LBV, blue, red-supergiants and late WN stars (WNL).
3. CNO equilibrium with H present. CNO equilibrium is reached before H exhaustion. The C/N and O/N ratios are reduced by two orders of a magnitude with respect to cosmic abundances (Fig. 27.11).

4. CNO equilibrium with H absent. The He mass fraction is 98%, the CNO ratios are the same as in (3). This stage corresponds to the early WN stars (WNE). The abundances are model independent, being determined mainly by nuclear cross-sections! The products of the NeNa and MgAl cycles (Sect. 25.1.5) appear mainly in massive stars at very low Z due to their higher central T and in the convective envelope of intermediate mass stars (Fig. 26.18).
5. Partial He burning. The products of He burning, i.e., ^{12}C, ^{16}O, ^{22}Ne are visible (Sect. 26.1). The changes are abrupt (rotation make them smoother). The abundances depend strongly on the models (mass loss, mixing, etc.). This stage corresponds to WC stars and to WO stars for O/C ratios > 1.

The above sequence results from a progression in the exposition of nuclear products. Of course, not all stars go through this whole sequence: the smaller the initial mass, the shorter the path. The changes of C/N (Fig. 27.12) are faster than those of O/N, because the ON loops need more time to reach equilibrium. In supergiants with initial $M \leq 60\ M_\odot$, the C/N and O/N ratios vary simultaneously, because when convective dredge-up bring CNO products to the surface, they have already reached equilibrium and convective dilution acts the same way on both elements. For $M > 60$ $M_\odot$, there is no dilution effect, thus C/N varies much faster than O/N.
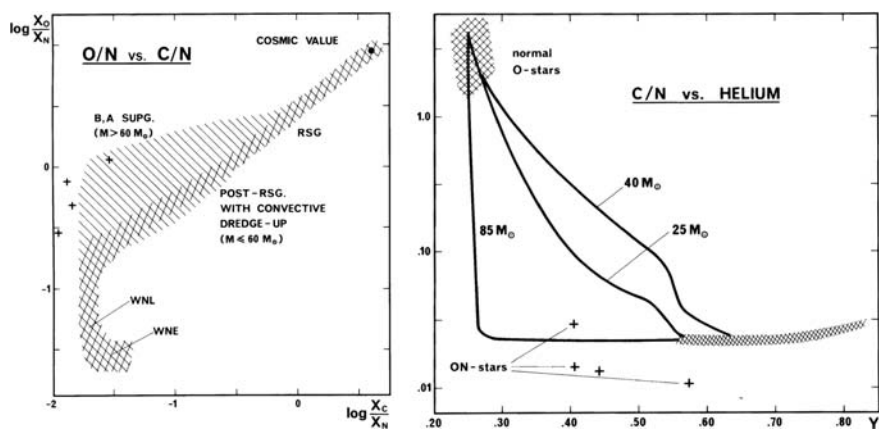
Fig. 27.12 *Left*: relation between the surface O/N and the C/N ratios for massive stars. *Right*: relation between the surface C/N and the He contents. Values are in mass fractions. Crosses represent ON stars. From the author [343]

27.4.2 Observed N/H Excesses

The amplitudes of the N enrichments at the end of the MS phase in massive stars are a reference point telling us the importance of mixing. The data at different Z are summarized in Table 27.1. In the Galaxy ($Z \approx 0.02$), the main data sources [244, 256, 257, 332, 535, 580, 601, 602] support significant excesses of He or of

Table 27.1 Values of the largest [N/H] excesses observed for different types of stars in the Galaxy, LMC and SMC. The average is equal to about the half of the indicated values. From the sources referred to in the text

Types of stars	[N/H] in Galaxy	[N/H] in LMC	[N/H] in SMC
O stars	0.8–1.0	–	1.5–1.7
B dwarfs $M < 20$ M$_\odot$	0.5	0.7–0.9	1.1
B giants, supg. $M < 20$ M$_\odot$	–	1.1–1.2	1.5
B giants, supg. $M > 20$ M$_\odot$	0.5–0.7	1.3	1.9

[N/H] (difference in log with respect to the corresponding local abundances). In the lowest mass range considered (6.6–8.2 M$_\odot$), small excesses of He/H are still present [332]. In the LMC ($Z \approx 0.008$), the excesses are larger [244, 262, 580]. In the SMC ($Z \approx 0.004$), still much larger N excesses are observed [58, 233, 234, 262, 580, 601].
  The various data show the following facts:

– On the average, Table 27.1 shows that the N enrichments are larger for larger masses.
– The table also shows that the N enrichments are larger at lower Z.
– Away from the ZAMS, but still in the main sequence, the He and N enrichments are larger [257] and they are even larger in the supergiant stages [601]. These various features are quite consistent with the predicted properties of rotational mixing.
– Correlations between N or He excesses and the observed $v \sin i$ have been made. Huang and Gies [256, 257] and Lyubimkov et al. [332] find a correlation of the He excesses with $v \sin i$ for B stars in the upper part of the MS band in agreement with model predictions. In other comparisons [263], most stars show an increase of the N/H ratio for larger $v \sin i$ compatible with model predictions, however, with a considerable scatter likely resulting from the large differences in the masses of the sample stars. Further studies [353] support a correlation of the N/H excesses with rotation, if the domains of masses and ages are not too extended. Binary interactions lead a fraction of about 20% of the stars to escape the general relation.

  To obtain a fine description of the effects of rotation, such as element mixing, transport of angular momentum or presence of a dynamo, it is necessary that the mass, age and Z domains are carefully distinguished and that the binaries are identified, since the enrichments depend on all these various properties. If $\log g$ is taken as an indicator of evolution, the rotational effect on the gravity should normally be accounted for.

27.4.3   Chemistry in Models with Rotation

Figure 27.13 (left) shows the predicted changes of the $\log(N/C)$ ratios with respect to the initial ratio. Without rotational mixing (dotted lines), there would be no enrichment until the red-supergiant stage. Rotation rapidly increases the N/C ratios on
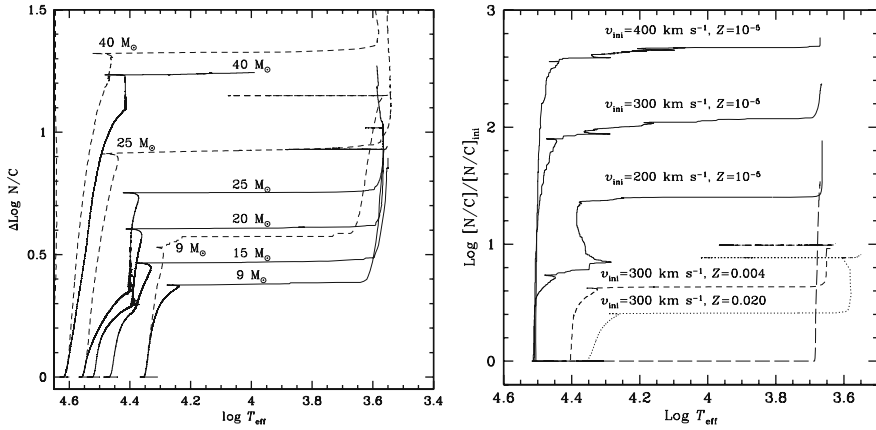
Fig. 27.13 *Left*: evolutionary tracks in the plot $\Delta \log(N/C)$ (change with respect to the initial N/C ratio) vs. $\log T_{\text{eff}}$ for various initial masses with $Z = 0.02$ with initial velocities 300 km s^{-1} (continuous lines). The dashed lines show the tracks with different model assumptions [409]. *Right*: excesses N/C in log scale for a 9 M$_\odot$ star at different metallicities and rotation velocities. The long-dashed line, at the bottom, corresponds to a non-rotating 9 M$_\odot$ stellar model at $Z = 10^{-5}$. From G. Meynet and the author [410, 411]

the main sequence, with a level depending on the velocities. This results from the steep Ω gradients which produce shear diffusion in the long-lived MS stars. The model results in Fig. 27.13 (left) predict N enrichments of the size of the observed effects in Table 27.1, they consistently predict larger N enrichments with increasing masses and ages.

N/C does not change too much during the first crossing of the HR diagram and again rises in the red stage. If the stars experience blue loops, they show on the blue side of the HR diagram high N/C ratios of about 5–30 typical of red supergiants. Thus, B supergiants at the same location in the HR diagram and with the same rotation may have different enrichments. As the $v \sin i$ converge toward low values during the red phase whatever their initial velocities, in the yellow and red phases stars of almost identical $v \sin i$ may exhibit different N/C enrichments.

Figure 27.13 (right) shows the N/C ratios in models of rotating stars with 9 M$_\odot$ for $Z = 0.02$, 0.004 and 10^{-5}. At $Z = 10^{-5}$ for the 9 M$_\odot$ model (and of other masses), there is a large N/C increase by one to two orders of magnitude [410]. This originates from the steep Ω gradients in rotating stars at low Z (Fig. 11.9), which drive a strong shear diffusion. Consistently with observations in Table 27.1, the lower Z models show larger N enhancements (in the SMC the N/C ratios are larger than for the $Z = 0.004$ model of Fig. 27.13 (right) and in better agreement with a somehow lower Z values).

At very low Z such as $Z = 10^{-5}$ for a given value of the rotation velocity, the enrichments are much larger (Fig. 27.13 (right), see also Fig. 26.25). At $Z < 10^{-3}$, the fast rotating stars of intermediate and high masses in the advanced red phases get very strong enrichments in CNO elements which significantly increase their Z values. As an example, a 7 M$_\odot$ with $Z = 10^{-5}$ gets in these phases X(CNO) =

$3.1 \cdot 10^{-3}$, i.e., 430 times the initial value. Thus, very low-Z stars may get higher Z near the end of their evolution (cf. Sect. 29.3.2). The reason is the diffusion of heavy elements out of the core, associated to the formation of primary nitrogen.

Models of rotating stars give results consistent with observations. Further careful comparisons in agreement with the remarks of Sect. 27.4.2 are still needed. Real differences may contain the germs of future progresses in our understanding.

27.4.4 Abundances and Massive Star Filiations

What are the evolutionary connections between the different kinds of massive stars? The answer comes from the comparisons of their properties in open star clusters and of their chemical abundances. Figure 27.4 indicates the possible filiations of massive stars of Pop. I. Globally, one has three main cases.

Above 60–40 M$_\odot$: always blue. The high mass loss rates remove enough mass so that stars lose their envelopes on the MS or in the blue supergiant stage as LBV. The stars never become red supergiants.

In the range 40–30 M$_\odot$: blue–red–blue. The stars only lose a fraction of their envelopes on the MS. They further evolve to the red-supergiant stage, where mass loss is sufficient to remove their envelope. Thus, they become bare cores and are observed as WR stars [338].

Below 25–30 M$_\odot$: blue–red. The stars still experience mass loss at all stages, however this is not sufficient to alter the global evolution in the blue or red locations. The mass loss and rotation may nevertheless still modify the lifetimes in the various phases and the chemical compositions.

TENTATIVE FILIATIONS:

Always blue

M> 90 M$_\odot$: O – Of – WNL – (WNE) – WCL – WCE – SN   (Hypernova ?)

M>60-90 M$_\odot$: O – Of/WNL ←→ LBV – WNL(H poor) – WCL-E– SN (SNIIn?)

M>40-60 M$_\odot$: O – BSG – LBV ←→ WNL – (WNE) – WCL-E –SN   (SNIb)
                                            – WCL-E – WO – SN (SNIc)

Blue – red - blue

M>30-40 M$_\odot$: O – BSG   –   RSG   –   WNE – WCE – SN   (SNIb)
                 OH/IR ←→ LBV ?

Blue – red

M>25-30 M$_\odot$: O – (BSG) – RSG – BSG ←→ RSG   SNIIL
                          BLUE LOOP

M>10-25 M$_\odot$: O – RSG – (Cepheid loop for M<15 M$_\odot$) – RSG – SN SNIIp

Fig. 27.14 Tentative filiations of massive stars in the solar neighborhood. A parenthesis indicates a brief stage, ⇔ indicates possible back and forth evolution between two stages. BSG and RSG mean, respectively, blue and red supergiants, the WR stars types WNL, WNE, WCL, WCE and WO are defined in Sect. 27.5, SN means supernova. The types of supernova explosions are suggested

Figure 27.14 shows with more details the possible evolutionary sequences for different intervals of initial masses in the solar neighborhood. The mass limits are uncertain and depend on the initial metallicity Z. At different Z, some sequences may be absent (Sect. 27.7). After central He exhaustion, the stellar envelopes have no longer the time to further evolve and their properties determine the nature of the supernova progenitors.

27.5 Wolf–Rayet Stars: the Daughters of O stars

27.5.1 WR Properties: the Zebras in the Zoo

Wolf–Rayet (WR) stars are identified with "bare cores" left over from the peeling of massive stars by stellar winds [302]. Their strong emission lines show highly non-solar chemical abundances, they have high mass loss rates and occur in young associations. There is about one WR star for 10^8 stars in the Galaxy. WR spectra show strong emission lines and fall into two sequences: 1. WN stars: the HeII and N lines dominate and 2. WC stars: the lines of HeII, C and O dominate. Reviews on the WR properties have been made by Abbott and Conti [1] and Crowther [149]. WR stars have the following properties:

Masses(actual):	~ 8–25 M$_\odot$ (up to 80 M$_\odot$ for H-rich WR stars).
Luminosities:	$\sim 10^5$–$10^{6.5}$ L$_\odot$.
Eddington factor:	~ 0.7 to ~ 1.0.
T_{eff}:	$\sim 3 \times 10^4$ to 1.5×10^5 K (Sect. 27.5.2).
$\dot{M}$:	$\sim 5 \times 10^{-6}$ to 10^{-4} M$_\odot$ yr^{-1}.
WN chemistry:	H, He, N (products of CNO burning).
WC chemistry:	He, C, O, no H (products of He burning).

The Eddington factors may approach unity [218, 305]. The late WN (WN9–WN6) stars, noted WNL, are generally more luminous and H-rich than the early WN (WN6–WN2), noted WNE, most of which have no H left. The late WC (WC9–WC6) stars are noted WCL, while the early WC (WC6–WC3) stars are noted WCE. The extreme WCE stars are the WO stars, which have higher O/C ratios. There are $\sim 4\%$ of transition WN/C stars, with intermediate characteristic between WN and and WC stars, i.e., simultaneously N and C enhancements. The mechanical power $L_w = (1/2)\dot{M}v_\infty^2$ emitted by WR stars represents a significant fraction of the photon luminosity L. With terminal velocities $v_\infty \sim 3000$ km s^{-1}, ratios L_w/L of 10–20% are feasible. Integrated over a WR lifetime of $\sim 5 \times 10^5$, L_w leads to an energy comparable to the mechanical energy produced by a supernova ($\sim 2 \times 10^{51}$ erg).

27.5.2 Optically Thick Winds. M–L–R–T_{eff} Relations

WR stars have a relatively simple structure once they have no hydrogen left at their surface, i.e., in the WNE and WC stages. Their physics is determined by their mass
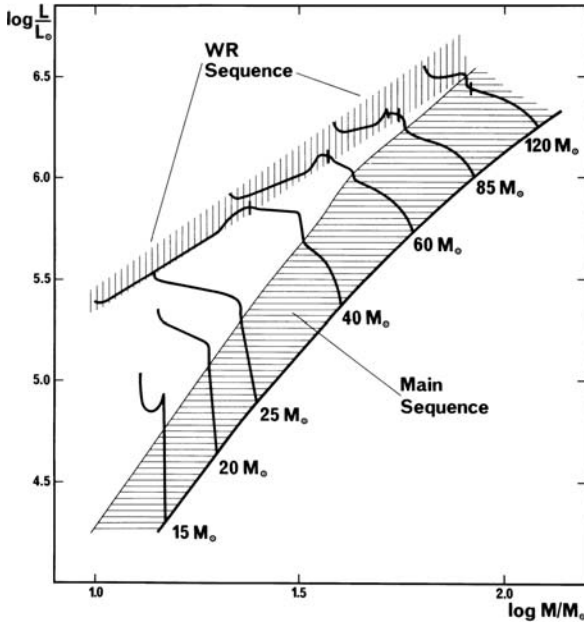
Fig. 27.15 Mass-luminosity relations for MS stars and WR stars (*hatched areas*). The evolutionary tracks are shown, the small slashes on the tracks indicate where the surface H content $X_s = 0.3$. From the author and G. Meynet [362]

and composition [305]. Thus, they generally obey simple relations between M, L, R and T_{eff} [305, 511]. WR stars are overluminous: for a given mass, they are about 1.5–3 magnitude brighter than an O star (Fig. 27.15). This is a consequence of their high He contents, this high luminosity is in agreement with homology relations (Sect. 24.3). The evolutionary tracks (Fig. 25.17) go first to higher luminosity as long as there is H left at the surface. When the He core starts decreasing due to mass loss, then the luminosity decreases. The mass–luminosity and luminosity–radius relations are [511]

$$\log \frac{L}{L_\odot} = 1.727 \log \frac{M}{M_\odot} + 3.495, \quad \log \frac{R}{R_\odot} = -1.845 + 0.338 \log \frac{L}{L_\odot}. \quad (27.9)$$

These relations can be specified for the various subtypes [305, 511], they are almost independent of the initial masses and mass loss rates.

Due to the high $\dot{M}$ rates, the winds of WR stars are optically thick. This means that the optical depth $\tau \approx 1$ (or 2/3) from where the emergent flux is coming is somewhere in the wind. Thus, the effective stellar radius $R_{2/3}$ is increased by the optically thick winds, which shift the emergent radiation toward longer wavelengths. A simple correction scheme to account for this effect has been proposed by de Loore et al. [329] and further developed [305, 513]. Let us call R the stellar radius. The optical depth at radius $R_{2/3}$ at $\tau = 2/3$ in the wind, where radiation is coming from, is

$$\tau = \int_{R_{2/3}}^{\infty} \kappa \varrho \, dr = \frac{2}{3}, \quad \text{with } \dot{M} = 4\pi r^2 \varrho \, v, \text{ and } v = v_\infty \left(1 - \frac{R}{r}\right)^{\beta}. \quad (27.10)$$

From (27.10) and (14.4), one gets for an exponent $\beta = 2$

$$\frac{\kappa \dot{M}}{4\pi v_\infty} \int_{R_{2/3}}^{\infty} \frac{dr}{r^2 \left(1 - \frac{R}{r}\right)^2} = \frac{2}{3}. \quad (27.11)$$

The opacity is assumed constant and the mass loss rates are isotropic. In the integral, let us write $x = R/r$, with $dr = -(r^2/R)dx$. For $r = R_{2/3}$ one has $x_{2/3} = R/R_{2/3}$ and for $r = \infty$ one has $x = 0$. The above expression becomes

$$R = -\frac{3 \kappa \dot{M}}{8\pi v_\infty} \int_{x_{2/3}}^{0} \frac{dx}{(1 - x)^2}. \quad (27.12)$$

The integral is

$$\int_{x_{2/3}}^{0} \frac{dx}{(1 - x)^2} = \frac{1}{1 - x}\Big|_{x_{2/3}}^{x=0} = 1 - \frac{1}{\left(1 - \frac{R}{R_{2/3}}\right)} = -\frac{R}{R_{2/3} - R}. \quad (27.13)$$

Thus, (27.12) becomes

$$R_{2/3} = R + \frac{3 \kappa \dot{M}}{8\pi v_\infty}, \quad \text{with } \dot{M} > 0. \quad (27.14)$$

The effective radius at $\tau = 2/3$ is equal to the stellar radius plus an additional term depending on $\dot{M}$ (27.10). For electron scattering opacity $\kappa_{es} = 0.20$, a mass loss rate of 5×10^{-5} $M_\odot$ yr^{-1} and a terminal velocity of 3000 km s^{-1}, the additional term in (27.14) is 3.79 $R_\odot$. The effective temperature at $\tau = 2/3$ is thus given by the usual relation $L = 4\pi R_{2/3}^2 \sigma T_{eff}^4$. The relation between the T_{eff} and the temperature $T_\star$ at $r = R$ is

$$\log T_\star = \log T_{eff} + \frac{1}{2} \log \frac{R_{2/3}}{R_{2/3} - \frac{3 \kappa \dot{M}}{8\pi v_\infty}}. \quad (27.15)$$

The optical depth of the wind of a typical WR wind is of the order of $\tau = 10$ [305]. We have considered κ as due to electron scattering only, however one may also account for the lines' opacities (Chap. 14) with the help of the force multiplier $M(t)$ (14.8). This has been done by Schaller et al. [513], as shown in Fig. 25.17, and in subsequent grids of massive stars quoted here.

Figure 27.16 shows the temperatures $T_\star$ and T_{eff} as a function of the actual masses for WC/WO stars, i.e., when there is no H left. $T_\star$ is about constant at $T = 10^5 - 1.5 \times 10^5$ K depending on $\dot{M}$. The values of T_{eff} are in the range of 15,000–40,000 K (WNE stars have the same $T_\star$, but a slightly higher T_{eff} due to their smaller $\dot{M}$). Figure 25.17 shows the location of WR stars in the HR diagram, the values of T_{eff}
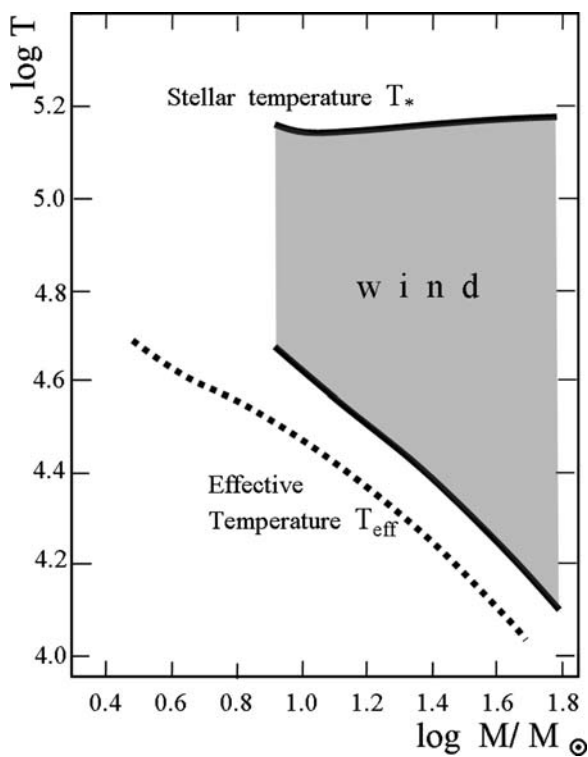
Fig. 27.16 Relations between the temperatures $T_\star$, T_{eff} and the actual masses of WC/WO stars for the $\dot{M}$ rates by de Jager et al. [271]. The dotted lines are for rates twice larger. Adapted from D. Schaerer and the author [511]

are given. The above distinction between $T_\star$ and T_{eff} is a rough simplification. Due to the T and ϱ structures of their atmospheres and winds, WR stars have complex spectral characteristics [509, 510].

27.6 WR Star Chemistry

27.6.1 Observations

Late WN stars (WNL) generally have H present, with an average value at the surface $X_s \approx 0.15$, while most early WN stars (WNE) have no H left [149]. In the Galaxy, some WNL stars with weak emission lines have $X_s \approx 0.50$. Other abundance ratios in mass fractions are N/He= $(0.035 - 1.4) \times 10^{-2}$, C/He= $(0.21 - 8) \times 10^{-4}$ and C/N= $(0.6 - 6) \times 10^{-2}$ [613]. These values are very different from the cosmic values (Appendix A.3) in agreement with Fig. 27.11. WN abundances are values of the CNO cycle at equilibrium, they are model independent, but a test of the nuclear cross-sections.

The transition WN/C stars show mass fractions of N $\sim$ 1% and C $\sim$ 5%, they represent $\sim$ 4–5% of the WR stars [140]. Without mixing, there would be no WN/C stars, because of the strong chemical discontinuity at the edge of the convective core in the He-burning phase (Fig. 27.11). A smooth chemical transition is needed to produce them in the process of peeling-off [307].

In WC stars, mass fractions of C between about 10 and 60% are observed, and about 5–10% for O [289, 538]. A trend was found by Smith and Hummer [538], in the sense of increasing C/He ratios from WCL to WCE stars. Further studies have cast doubts on this relation ([149, 289]). However, the point is not quite clearly settled in view of the uncertainties in the C and O abundances. Also C goes up and down during He burning and may give mixed results, thus a ratio like (C+O)/He should be preferred.

27.6.2 Mass Loss, Rotation and WR Chemistry

In WN stars, the equilibrium CNO abundances are independent of rotation. At the transition from WN to WC, mixing permits the simultaneous presence of ^{14}N, ^{12}C and ^{22}Ne. This corresponds to the transition WN/C stars. In the WC stage, rotation broadens the range of possible C/He and O/He ratios, permitting the products of He burning to appear at an earlier stage of nuclear processing with lower C/He and O/He ratios (Fig. 27.18).

Figure 27.17 (top) shows extreme cases of compositions in WC stars at high and low Z. At high Z, the $(C + O)/He$ ratios are very low, because due to heavy mass loss the nuclear products appear at an early stage of processing. At low Z, the (C+O)/He ratios are extremely high [Fig. 27.17 (bottom)], because the products of He burning appear (if they do it!) only very late in evolution. We note that if the mentioned trend found by Smith and Hummer [538] is confirmed, this would explain why WCL stars are found in high Z regions and WCE and WO stars in low-Z regions (Sect. 27.7) (Fig. 27.18).

Figure 27.17 (bottom) shows a fundamental diagram for WC stars, i.e., the (C+O)/He ratios as a function of L for WC stars of different M and Z. At low Z (low $\dot{M}$), only the most massive stars may become WC, thus their L are high. Their (C+O)/He ratios are high because the rare stars which enter the WC stage do it very late during central He burning. At higher Z, less massive stars may become WR stars, thus they have lower luminosities. As the $\dot{M}$ rates are higher, the products of He burning appear at an earlier stage of nuclear processing, i.e., with lower (C+O)/He ratios. These effects produce some interesting relations [539]:

– At a given L, the (C+O)/He ratios are higher in regions of lower Z.
– For a given (C+O)/He ratio, the WC stars in lower Z regions have much higher luminosities.

These model predictions need further observational confirmation [539]. This is also of interest for WO stars, which correspond to the most advanced stage of
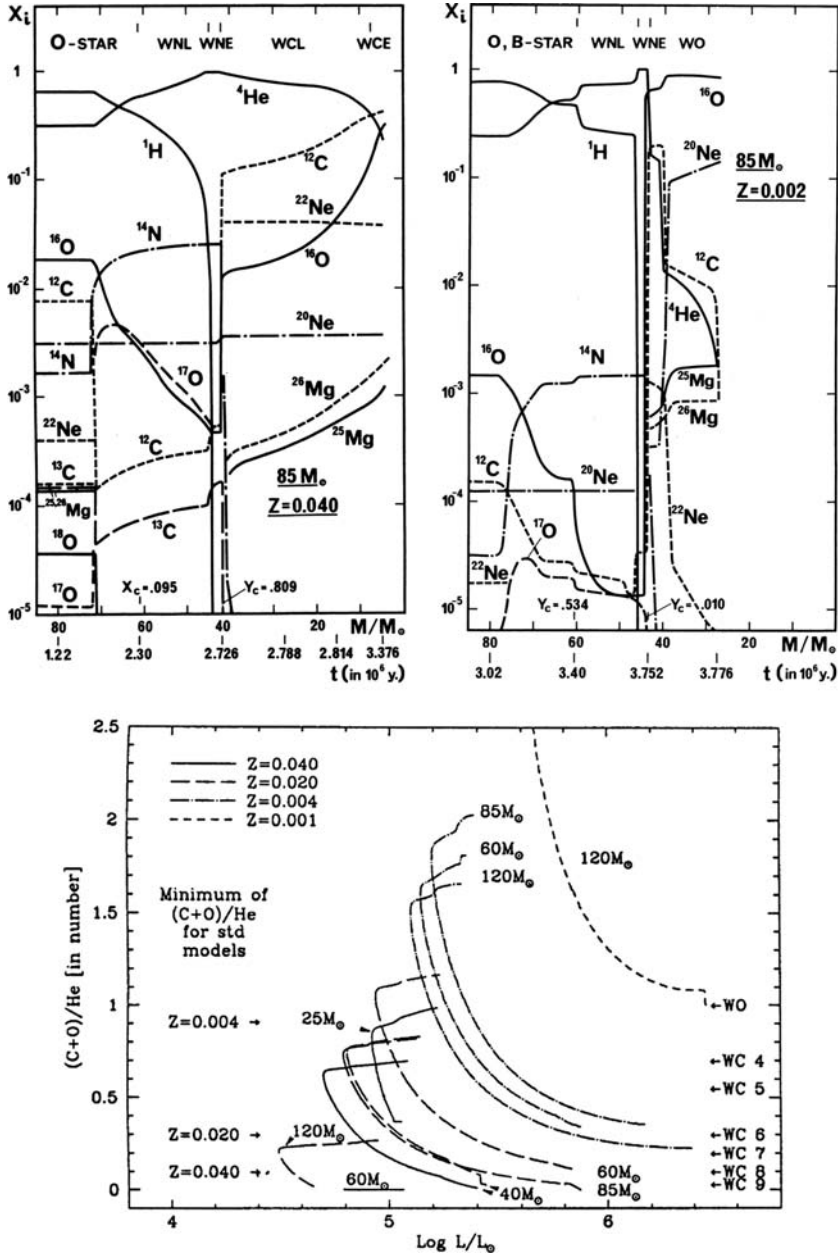
Fig. 27.17 *Top*: comparisons of extreme cases of evolution of surface abundances for very massive stars at $Z = 0.04$ and $Z = 0.002$ as a function of age and remaining mass. From the author [346]. *Bottom*: the (C+O)/He ratios in WC stars as a function of L for different Z and initial masses. The scale of WC subtypes by Smith and Hummer [538] is given. From the author and G. Meynet [365]
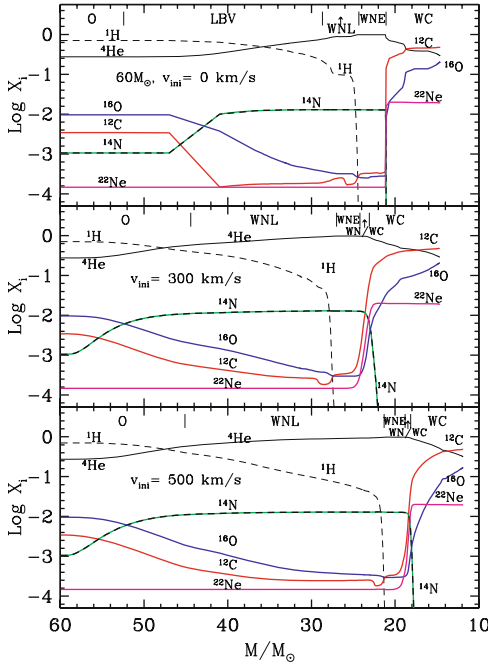
Fig. 27.18 Evolution of the surface abundance for 60 $M_\odot$ models at $Z = 0.02$ for three values of the initial velocities. From G. Meynet and the author [411]

evolution and are likely the progenitors of supernovae SN Ic, a small fraction of which leads to GRBs (Sect. 28.6.3).

27.6.3 ^{22}Ne in WC Stars

Let us now turn to ^{22}Ne in WC stars. Neon has three isotopes ^{20}Ne, ^{21}Ne and ^{22}Ne, with relative mass fractions 87.9% for ^{20}Ne, 0.3% for ^{21}Ne and 11.8% for ^{22}Ne (Appendix A.3). The destruction of ^{14}N in the He-burning phase by the reactions (26.9) leads to ^{22}Ne, which appears at the surface in the WC stage [341, 411]. The three isotopes cannot be separated spectroscopically. The models predict Ne enhancements by a factor of 20–30. However, the observations by Willis et al. [614], Smith and Houck [537], Ignace et al. [267] give excesses, respectively, of 3, 11 and 9.

Since, the abundance of the CNO elements have been reduced by a factor of ~ 2 and the Ne abundance has been revised upward [19], a new estimate has to be made. ^{22}Ne is the daughter of ^{14}N, which is itself the daughter of CNO elements. The sum of CNO elements is $X(\text{CNO}) = 0.00868$, which essentially becomes ^{14}N. Since two α particles are added to ^{14}N to form ^{22}Ne, the abundance of ^{22}Ne in WC stars should be

$$X(^{22}\text{Ne}) = \frac{22}{14} X(^{14}\text{N}) \quad \text{num.} \quad X(^{22}\text{Ne}) = 1.57 \times 0.00868 = 0.0136. \quad (27.16)$$

We get a sum of Ne isotopes of about $X(\text{Ne}) = 0.0154$ compared to $X(\text{Ne})_\odot = 0.0020$. This gives a relative Ne enhancement by a factor of 8 in agreement with observations quoted above.

The extreme WO model in Fig. 27.17 (top right) shows a small ^{20}Ne enhancement due to the $^{16}\text{O}(\alpha, \gamma)^{20}\text{Ne}$ reaction. The He processing is so much advanced that ^{22}Ne is destroyed making ^{25}Mg and ^{26}Mg by the reaction $^{22}\text{Ne}(\alpha,\text{n})^{25}\text{Mg}$ (26.9), with production of free neutrons and creation of s-elements (Sect. 28.5.4). This shows that WR stars may be the source of s-elements [476]. Up to now, there is no direct evidence that ^{22}Ne is destroyed in WC or WO stars of Pop. I stars as suggested by Fig. 27.17 (top right). The finding of some Mg excess and of s-elements from reaction $^{22}\text{Ne}(\alpha,\text{n})^{25}\text{Mg}$ would be a most interesting point.

WR stars may also be the source of some less abundant elements, such as ^{19}F (Table 25.2), the destruction rate is critical in this context [406]. Some radio-nuclides, such as ^{26}Al, ^{36}Cl, ^{41}Ca and ^{107}Pd can also be synthesized and ejected by WR stars [18]. These elements are also produced by AGB stars and it is important to discriminate between the two sources.

27.7 Number Ratios of WR Stars in Galaxies

27.7.1 Observed Number Ratios

There is a most striking property of massive star populations in galaxies: the relative frequencies of WR stars and red supergiants with respect to O type stars are very different from one galaxy to another one. The WR/O star number ratios may vary by a factor of 10, the same for WC/WN, while the ratios of red supergiants (RSG) to WR stars change by 2 orders of magnitude, as shown by Table 27.2.

Table 27.2 Number ratios of O stars, WR stars and red supergiants (RSG) in galaxies or galactic locations of different metallicity Z. Based on the data by the author and Conti [355] and by Massey [383]

Galaxy	Z	WR/O	WC/WN	RSG/WR
M31	0.036	0.24	0.90	0.06
Milky Way	0.018	0.10	0.88	~ 1
M33(inner)	0.020	0.06	0.58	0.2
M33(middle)	0.016	0.06	0.38	0.3
M33(outer)	0.007	0.06	0.20	1.4
LMC	0.008	0.04	0.20	2.0
NGC 6822	0.005	0.02	0.00	2.0
SMC	0.004	0.017	0.10	8.4
IC 1613	0.003	0.02	–	–

For the Milky Way, stars in the solar neighborhood with distance smaller than 3 kpc are considered. Table 27.2 shows that galaxies with higher Z have higher WR/O and WC/WN ratios and lower RSG/WR ratios. The galactic regions considered are large enough so that an average IMF and a constant star formation rate over the last 10^7 yr may be assumed (in a starburst, depending on the age the number ratios may be different).

27.7.2   Models with Mass Loss and Rotation

The explanation of the observed trends rests mainly on the fact that at higher Z the mass loss rates are higher (27.2), thus WR stars form more easily [359]. There is also more WC stars at higher Z, since they need more peeling-off. For the RSG numbers, a rough explanation is that, in the He-burning phase at low Z, the time not spent as a WR star is spent as a RSG. However, as shown in Sect. 27.3.6, the high number of RSG at low Z is also shaped by rotation effects on the inner structure.

Lifetimes t_{WR}: Figure 27.19 shows how the total WR lifetimes t_{WR} increase with mass and Z for models with rotation. Without rotation, the various curves would be lower by a factor of 2–3 [412]. Higher mass loss rates increase the WR lifetimes and lower the threshold above which WR stars are formed. Rotation acts in two ways, first by increasing the mass loss rates it favors the loss of the outer layers and second the rotational mixing of the elements brings He to the surface favoring the appearance of the He bare core. Thus, as far as WR formation is considered, rotation does on the whole about the same as mass loss, increasing t_{WR} and lowering the threshold mass. The integration over the initial mass function of
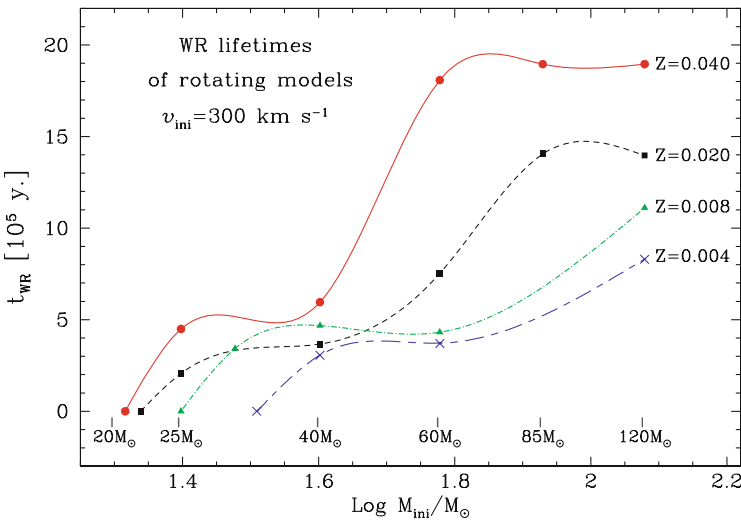
Fig. 27.19 Duration of the WR phases in units of 10^5 yr as a function of the initial masses for models with rotation [412]

the lifetimes t_{WR} and t_O (as O stars) is necessary to obtain the theoretical number ratios N_{WR}/N_O. Starbursts (regions of intense star formation) have to be treated with care as the various number ratios vary with the age and duration of the starburst [355].

WN subtypes and LBV: Figure 27.20 (left) gives an example of the variations of the WR subtypes with stellar masses. The duration of the WN phase (in particular of the WNL phase, with H present) depends on the internal H profile left in the star by the receding core. If, due to heavy mass loss and mixing, the WN stage is already entered during the MS phase, the WNL stage is considerably increased [412]. This is why the WNL phase is longer in more massive stars. The duration of the small WNE phase (He, N) generally decreases for higher M, because its duration is proportional to the mass between the H shell and the He core (which varies very little) and inversely proportional to the $\dot{M}$ rates.

If the stars go through the LBV stage, with very high mass loss rates of $\sim 10^{-3}$ $M_\odot$ yr^{-1}, the consequence is a drastic reduction of the WN phase (WNL in particular), the WNE phase does not change too much. This further implies an earlier entry into the WC phase. This scenario likely applies to stars with $M > 50$ $M_\odot$. As to the WC phase, which requires a lot of mass removal before being entered, its duration generally increases with the initial mass, as well as with mass loss rates and rotation.

Z effects: How do the WR subtypes vary with metallicity Z? The duration of the WNL phase increases for higher Z, due to higher mass loss. The duration of the WNE phase is generally smaller at lower Z, the reason is that the WNE masses are higher and so do the $\dot{M}$ rates. For the WC phase, the duration increases for higher Z. However, all lifetimes very much depend on the parameterizations of the mass loss rates in the various stages. Fig. 27.20 (right) shows the final stages as a function of the initial masses and Z.
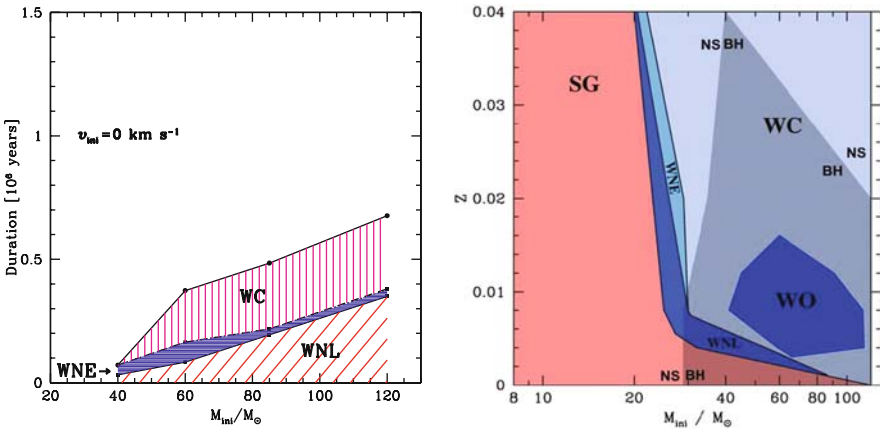
Fig. 27.20 *Left*: variations of the WR subphases as a function of the initial mass for models without rotation. From G. Meynet and the author [411, 412]. *Right*: the final stages at the time of the supernova explosion as a function of the initial masses and Z. The final stages as neutron stars (NS) and black holes (BH) are indicated. Courtesy from C. Georgy

WC subtypes: Observationally, the balance between the WCL and the WCE phases changes very much with metallicity: WCL stars are found at relatively high Z like in inner regions of the Milky Way, while low-Z galaxies like the Magellanic Clouds only have WCE stars and possibly some rare WO stars. At high Z with high $\dot{M}$, the products of He burning appear at an early stage of nuclear processing, thus with low (C+O)/He ratios. At low Z, this is the opposite. Thus, if WCL stars would have low (C+O)/He ratios and WCE stars high (C+O)/He ratios [538], the problem of the preferential location of WCL stars in high Z regions and of WCE stars in low-Z regions is solved [539]. This is not confirmed (Sect. 27.6), thus one should await better determinations, before supporting or not this interpretation.

Binaries and WR stars: Mass exchange in binary stars may also influence WR star formation [589]. Simulations of massive star populations including mass transfer in binaries improve some features, even if the agreement is far from complete [177]. Nevertheless, the main effect of binarity seems to concern more the enhancement of the mass loss rates than the mass transfer [470]. Models of WR+O binaries show that about 90% of the matter leaving the donor is then expelled by the rapid rotation of the mass receiving star, only $\sim 10\%$ being retained by the receiver.

On the observational side, thorough studies of the WR populations in the Galaxy [593, 594] and in the LMC and SMC by Foellmi et al. [188, 189, 424] set some limit to the role of binaries in the WR star formation, showing binary frequencies of, respectively, 24, 15 and 42%. Surprisingly, this is not more than among O stars in the Milky Way, where the frequency is 45% on the average [206]. The previous authors conclude that "binary evolution does not seem to have a particular influence on the formation of WR stars at low Z".

The problem needs a closer attention. Binary mass transfer is certainly one of the channels for forming WR stars due to the associated $\dot{M}$-enhancements. We may suspect that in the SMC the binary channel for forming WR stars is *relatively* important, despite the small number of WR stars present. The reason is that the fraction of binaries among O stars is very low in the SMC, i.e., of the order of 10% [379] while 42% of the WR stars are binaries. Thus, a large fraction of the rare WR stars at low Z may be due to the binary channel, as suggested long ago [340].

Finally, we would give a word of caution regarding number statistics. There are many models which fit *one* observation. However, the models must account for all observations, including the chemical abundances at various stages and metallicities.

27.8   Evolution of the Rotational Velocities

The evolution of rotation velocities of massive stars is sensitive to mass loss and transport of angular momentum by magnetic fields, convection and meridional circulation.

Figure 27.21 shows the evolution of the velocities v and of the ratio $\Omega/\Omega_{\text{crit}}$ as a function of age for models with $Z = 0.02$ as in Fig. 27.8. Due to the initial adjustment of meridional circulation (Sect. 11.5.1), an initial velocity of 300 km s^{-1}
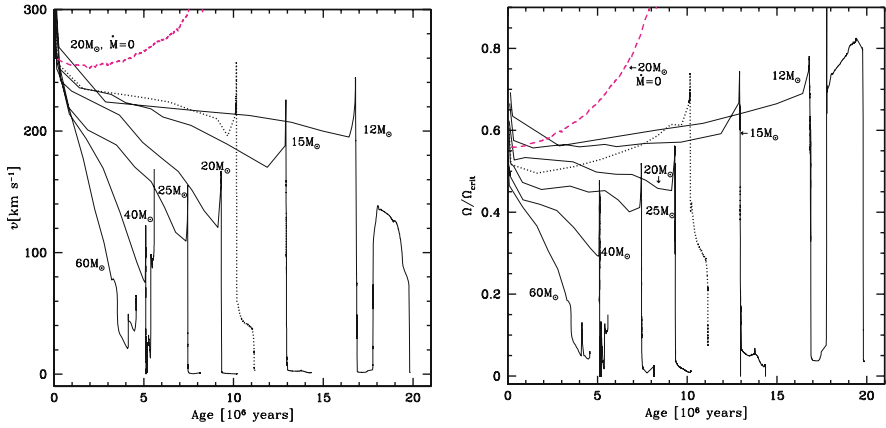
Fig. 27.21 *Left*: evolution of the rotational velocities as a function of time for the models of Fig. 27.8 with initial velocities of 300 km s^{-1}. The dotted line corresponds to a 20 M$_\odot$ model with $Z = 0.004$. The dashed line applies to a 20 M$_\odot$ model at $Z = 0.02$ without mass loss. *Right*: the same for the ratio $\Omega/\Omega_{\rm crit}$ of the angular velocity to the break-up velocity. From G. Meynet and the author [409]

very rapidly leads to $v = 200$ km s^{-1} or less (closely corresponding to the average of Fig. 27.1). Without mass loss (dashed line), v and $\Omega/\Omega_{\rm crit}$ go up fast and reach the critical value, because as the core contracts, it rotates faster and the transport by meridional circulation communicates a part of this fast rotation to the surface. The model of 20 M$_\odot$ at $Z = 0.02$ shows a moderate decrease of v, while the ratio $\Omega/\Omega_{\rm crit}$ remains almost constant during the MS phase. For the most massive stars which lose more mass and angular momentum, the decrease of rotation is large, because the matter removed from the surface embarks more angular momentum by mass unit than the stellar average. These stars end the MS phase with a low rotation. These results differ very much from the models [309, 310, 502] with solid body rotation, which reach the critical velocity even for low initial velocities.

At lower Z, mass loss is smaller and the removal of angular momentum during evolution is weaker. Thus, the rotation velocities and $\Omega/\Omega_{\rm crit}$ do not decrease or even grow fast [367]. Figure 27.21 shows an example (dotted line) for a 20 M$_\odot$ model at $Z = 0.004$. The increase of rotation at low Z is also reinforced by a more efficient outward transport of angular momentum due to the weaker Gratton–Öpik outer meridional circulation cell (Fig. 29.6). Due to these effects, the very low-Z stars are likely to reach critical velocities during their evolution (see Chap. 29).

At the end of the MS phase, there is a small peak of velocity in the contraction phase (Fig. 27.21). Then the stars move to the red-supergiant stage, v and $\Omega/\Omega_{\rm crit}$ decrease a lot (Fig. 27.22), because the evolution is too fast for meridional circulation (which works at a timescale (11.4.1) longer than the Kelvin–Helmholtz timescale) to ensure the internal coupling. The evolution of rotation, determined by the equations of Sect. 10.5.4, becomes nearly the same as given by local conservation of angular momentum. During the blue loops of a 12 M$_\odot$ model in Fig. 27.21,
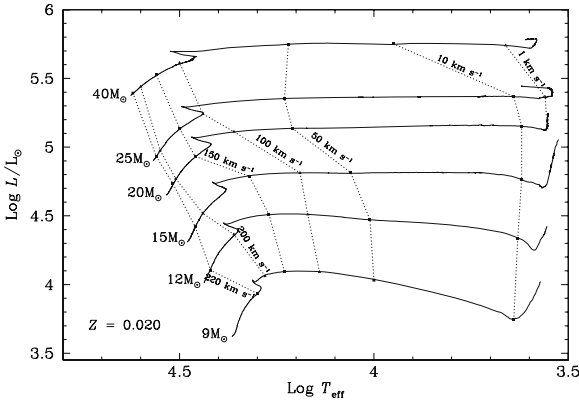
Fig. 27.22 Evolution of the rotational velocities along the evolutionary tracks up to the red giants or supergiants of Fig. 27.8 for initial velocities of 300 km s^{-1}. From G. Meynet and the author [409]

there is a strong increase of rotation, which may reach the critical value. This results from the stellar contraction which concentrates the angular momentum of the large convective envelope of the red giant into a thin outer mass layer [235].

Velocities (Fig. 27.1), T_{eff}, gravities and He contents have been determined for 500 B-type stars in clusters by Huang and Gies [256, 257]. The observed evolution of v is compatible with Fig. 27.21 (left) for the 9 and 12 M$_\odot$ models. The more massive stars in the sample up to 16 M$_\odot$ show a spin-down as predicted by the models. A few members of binary system show a marked spin-down in the advanced stages due to tidal interactions.

Comparisons of observed and predicted rotation velocities v have been made for post-MS stars from about 1 to 12 M$_\odot$ [160]. They support an evolution determined by local angular momentum conservation for yellow and red giants above 2 M$_\odot$. Below 1.5 M$_\odot$, there is a decline of v, consistent with the spinning-down due to magnetic braking (Sect. 13.2).

27.8.1   Rotation of LBV

The luminous blue variables (LBV) are most luminous OBA supergiants close to the Eddington limit, they have high mass loss rates and may experience violent outbursts [259–261]. For very high $\dot{M}$ rates (cf. [604, 605]), a rotating 120 M$_\odot$ model directly evolves to the blue and becomes a WR star avoiding the LBV stage. For more moderate rates of about $10^{-4.8}$ M$_\odot$ yr^{-1}, all models with initial $v < 650$ km s^{-1} evolve to the right in the region of LBV such as η Carinae.

In this last case, Fig. 27.23 illustrates the evolution of the rotational velocities of a 120 M$_\odot$ star for different initial velocities. Despite mass loss, the velocities increase during evolution due to the coupling by meridional circulation and they
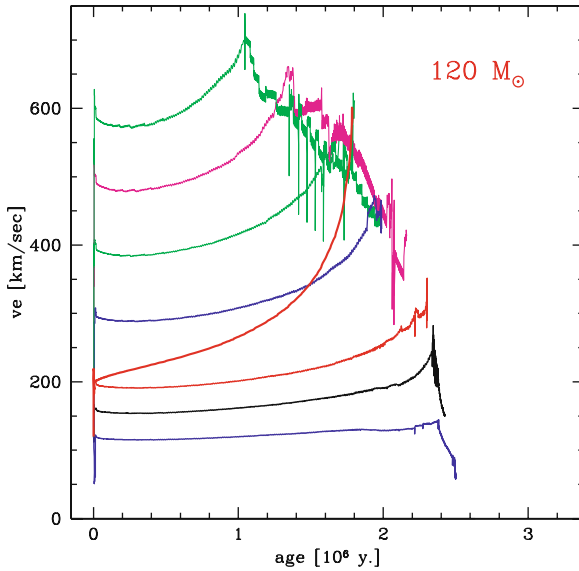
Fig. 27.23 Evolution of the rotational velocities for a 120 $M_\odot$ star at $Z = 0.02$ with different initial rotational velocities v_{ini}. The right envelope of the curves is the location where the stars reach their critical velocities. A model with solid body rotation with $v_{\mathrm{ini}} = 200$ km/s is also shown, it reaches the critical velocity faster

reach the critical velocity $v_{\mathrm{crit},2}$ at the $\Omega\Gamma$ limit (Sect. 4.4.4). In the figure, this limit describes the envelope to the right of the different tracks. The higher the initial velocity, the earlier the $\Omega\Gamma$ limit is reached. Solid body rotation, which is the extreme case of coupling, would lead the star more promptly to the $\Omega\Gamma$ limit as shown by the figure. Once they reach the limit, the star models lose the layers which progressively become unbound due to the growth of the radius. The stars keep on a common velocity–age track in Fig. 27.23 and stay at the $\Omega\Gamma$ limit, until their radius decreases when they become a WR star.

The Γ and the $\Omega\Gamma$ limits for rotating stars are an essential property of LBV stars, providing the conditions for the occurrence of their giant outbursts.

27.8.2   WR Star Rotation

There are few observations of the rotation of WR stars. Some information has been recently obtained from the co-rotating regions generating periodic variations in spectral lines [122]. The velocities are typically lower than about 50 km s^{-1} in very good agreement with model predictions. The evolution in the WR stages is fast and the transfer of angular momentum by meridional circulation is small, thus at this stage the evolution of rotation is dominated by the local conservation of angular

momentum unless there is a magnetic field. Most predicted periods are within a factor of 2–3 of a mean of about 10 days, the change of periods with time is smooth because v and R both decrease at the same pace [411]. At the opposite, the variations of v and Ω/Ω_c may be fast in some cases due to rapid changes of radius in particular when the star loses its last H layers.

At solar or higher Z, the expected velocities v are small with $v < 50$ km s^{-1} [411]. The reason is that a large part of the WNL phase occurs during the core H-burning phase, where the high mass loss has time to pump the whole internal angular momentum, so that when the star contracts to the WC stage there is almost no rotation left.

At lower Z, the predicted velocities of WR stars are higher than at $Z_\odot$, e.g., between 30 and 200 km s^{-1} at $Z = 0.004$. The variations of v and Ω/Ω_c are also greater and more rapid when the radius is changing. The break-up limit might be encountered during the WR phase. The reason is that, at low Z, the WR stage is not entered during the H-burning phase and despite mass loss the interior rotation is not killed. The relations with the rotation of pulsars and the conditions for Gamma-Ray Bursts are studied in Sect. 28.6. Much remains to be done on the evolution of rotation in the advanced stages.

Chapter 28
Advanced Evolutionary Stages and Pre-supernovae[*]

"My grand mother is a star" says H. Reeves. The understanding that all the heavy elements in our environment have been formed in the stellar nuclear cauldrons and then have been recycled in successive stellar generations is a major achievement, counting among the great discoveries of Science. This discovery was mainly due to Burbidge, Burbidge, Fowler and Hoyle [76].

Today, the abundances of the elements in the Universe keep the signatures of the conditions of temperature and density at which they have been formed in the stellar interiors billions years ago. Thus, if gold in the Universe is about 10 millions times less abundant than iron, this is because the nuclear cross-sections and physical conditions in supernovae have fixed this specific abundance ratio. By determining the chemical abundances in stars and studying the physical processes in the advanced nuclear stages of evolution, the astrophysicists are reconstructing the fantastic history of matter.

28.1 Nuclear Reactions in the Advanced Phases

We examine the main nuclear reactions leading to the onion skin model (Fig. 28.3) in the advanced phases of massive stars giving rise to supernovae.

28.1.1 C Burning

Carbon burning occurs at $T = (6 - 8) \times 10^8$ K in stars above $M_{up} \approx 7 - 9$ M$_\odot$ (Table 26.1). After He burning, the main ashes are ^{12}C and ^{16}O, the second one generally dominating. The element with the lowest potential barrier is ^{12}C, the reaction ^{12}C+^{12}C produces a compound nucleus ^{24}Mg which may disintegrate through several channels:

---

[*]This chapter may form the matter of a basic introductory course.

$$^{12}\text{C} + ^{12}\text{C} \longrightarrow \; ^{24}\text{Mg}^* \; \longrightarrow \; ^{24}\text{Mg} + \gamma \quad +13.931 \text{ MeV}$$
$$\longrightarrow \quad ^{20}\text{Ne} + \alpha \quad + 4.617 \text{ MeV}$$
$$\longrightarrow \quad ^{23}\text{Na} + \text{p} \quad + 2.240 \text{ MeV}$$
$$\longrightarrow \quad ^{23}\text{Mg} + \text{n} \quad - 2.599 \text{ MeV}$$
$$\longrightarrow \quad ^{16}\text{O} + 2\alpha \quad - 0.113 \text{ MeV}$$
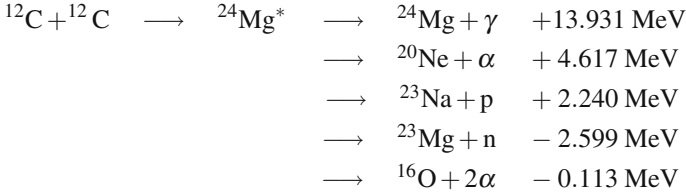
In stellar conditions, the α and p channels dominate. This is a general rule that particle channels, when energetically possible, tend to beat out the γ channel, which involves the electromagnetic interaction. The probability P_α and P_p of the α and p channels are given by $P_\alpha \approx P_p = (1 - P_n)/2$, where the probability for the neutron channel $P_n = 0.00011, 0.004, 0.054$ at $T_9 = 0.8, 1.2$ and 5, with $T_9 = T/[10^9$ K$]$. The rate of energy generation by $^{12}\text{C} + ^{12}\text{C}$ without screening behaves in first approximation like [617]

$$\varepsilon_{^{12}\text{C}} \approx 2.52 \times 10^8 \, Y_{12}^2 \, \varrho \, T_9^{27} \quad \text{in erg (g s)}^{-1}, \tag{28.1}$$

near $T_9 = 1$ and with $Y_{12} = (X_{12}/12)$. The energy liberated by C burning is $E_{12,12} = 4.0 \times 10^{17}$ erg g^{-1}, corresponding to 0.42 MeV per nucleon. This is about 6.6% of the energy produced per nucleon in the CNO reactions and 68% of that in the He burning. There are a number of other reactions, the main ones being

$$^{23}\text{Na}(\text{p},\alpha)^{20}\text{Ne} \tag{28.2}$$
$$^{23}\text{Na}(\text{p},\gamma)^{24}\text{Mg} \tag{28.3}$$
$$^{20}\text{Ne}(\alpha,\gamma)^{24}\text{Mg}(\alpha,\text{p})^{27}\text{Al} \tag{28.4}$$
$$^{16}\text{O}(\alpha,\gamma)^{20}\text{Ne}(\alpha,\gamma)^{24}\text{Mg}. \tag{28.5}$$
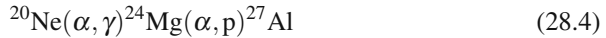
The first reactions convert almost all ^{23}Na to ^{20}Ne, letting only about 1% of ^{23}Na at the end of C burning in a $20\,\text{M}_\odot$ star of Pop. I. The main products resulting from the C destruction are ^{20}Ne and ^{24}Mg in a ratio of ~ 10. The most abundant element present is still ^{16}O continuously built and only slightly destroyed by $^{16}\text{O}(\alpha,\gamma)^{20}\text{Ne}$ during the He- and C-burning phases. Its abundance is about 85–90% at the end of the C-burning phase for a $20\,\text{M}_\odot$ star. There are many other reactions important for neutron production and capture and for the synthesis of minor elements [125]. The interesting particles and isotopes to be included at this stage are [16, 250]

$$\text{n, p, }\alpha, \; ^{12,13}\text{C}, \; ^{16}\text{O}, \; ^{20,21,22,23}\text{Ne}, \; ^{22,23,24}\text{Na}, \; ^{24,25,26}\text{Mg}, \; ^{25,26,27}\text{Al}. \tag{28.6}$$

Figures 28.1 and 28.2 show the internal abundances at the end of the main nuclear stages in an initial $20\,\text{M}_\odot$ star without and with rotation. One sees the changes due to central C burning, i.e., the destruction of ^{12}C and the production of ^{20}Ne and ^{24}Mg, a small amount of ^{16}O is turned into ^{20}Ne.
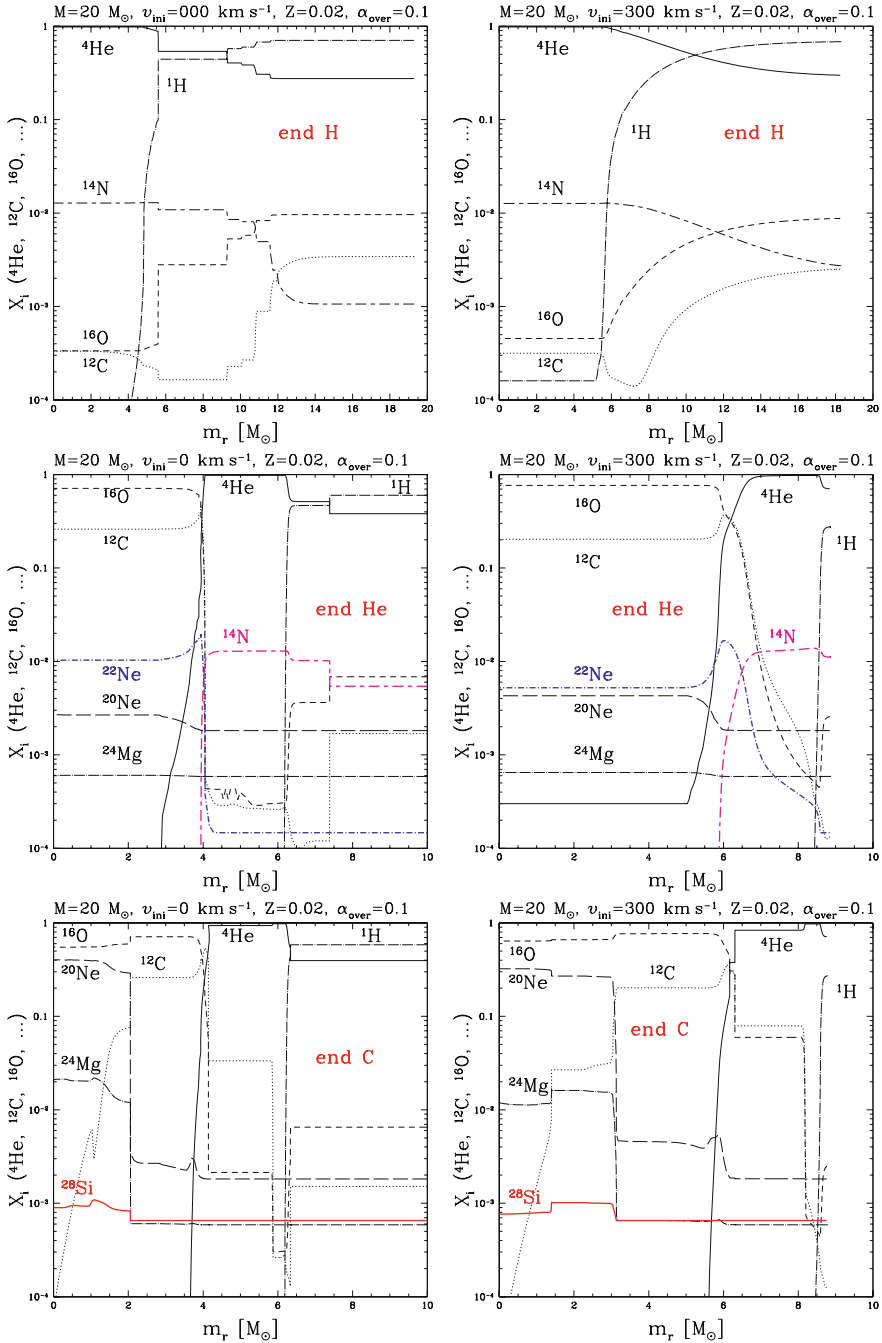
Fig. 28.1 Abundances in mass fraction as a function of mass at the end of central H (*top*), He (*middle*) and C (*bottom*) burnings for non-rotating (*left*) and rotating (*right*) 20 M$_\odot$ models with $X = 0.705$ and $Z = 0.02$. From R. Hirschi et al. [251]
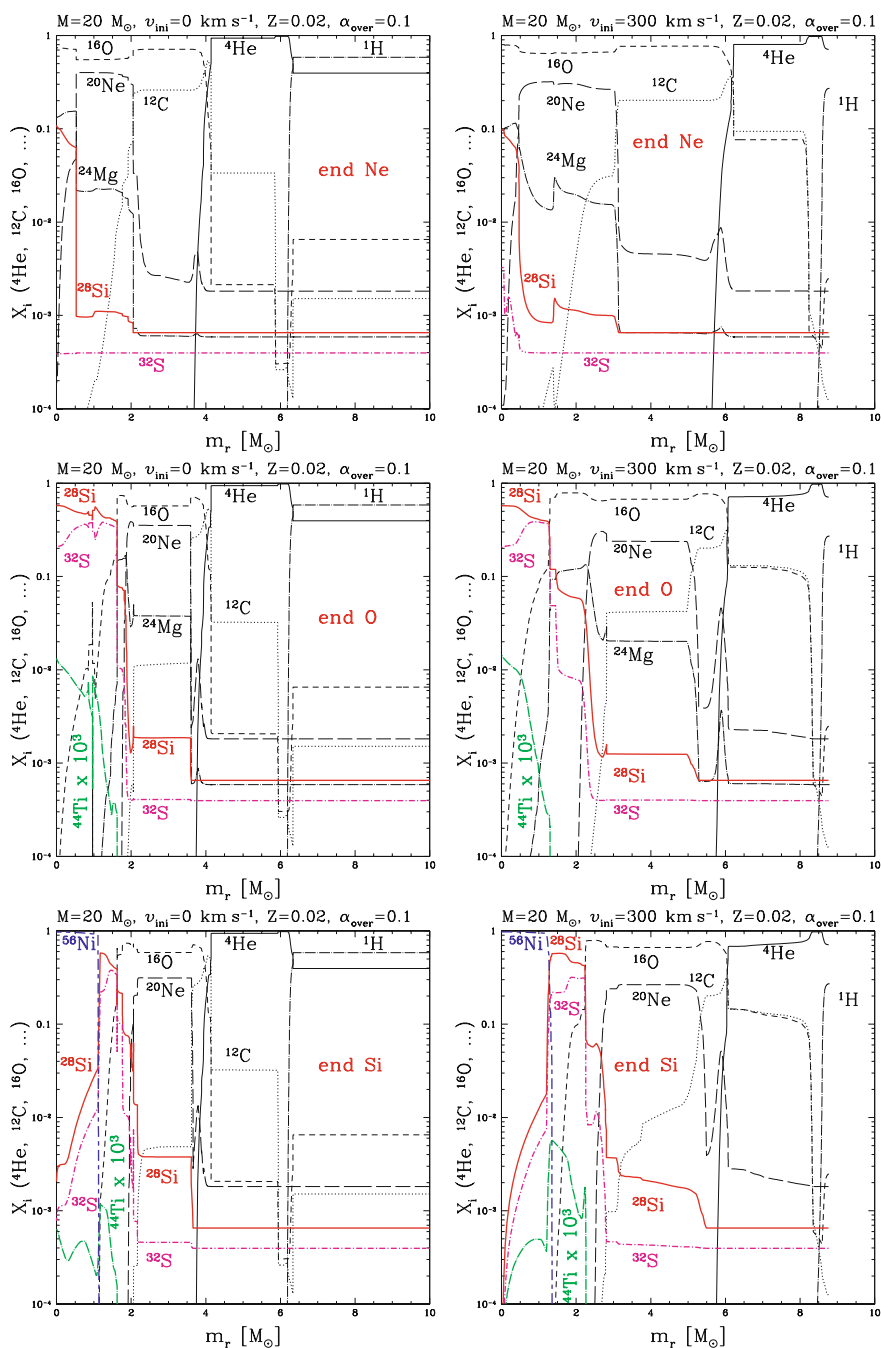
Fig. 28.2 Same as previous figure at the end of central Ne (*top*), O (*middle*) and Si (*bottom*) burnings. The abundance of ^{44}Ti (*dotted-long dashed line*) is enhanced by 10^3 for display purposes. From R. Hirschi et al. [251]

28.1.2 Ne Photodisintegration

The most abundant elements in the center after C burning are ^{16}O, ^{20}Ne and ^{24}Mg, with binding energies of respectively -7.16, -4.73, -9.32 MeV. One would expect ^{16}O to be the next element to enter fusion reactions. However, it is very stable because of its double magic number of protons and neutrons $Z = N = 8$. Thus, the less bound ^{20}Ne starts reacting first at $T \approx (1.2 - 1.5) \times 10^9$ K. A photodisintegration reaction occurs which liberates α particles captured by the remaining ^{20}Ne nuclei,

$$^{20}\text{Ne}(\gamma, \alpha)^{16}\text{O} \quad \text{and} \quad ^{20}\text{Ne}(\alpha, \gamma)^{24}\text{Mg} .$$
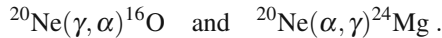
This happens when photons have enough energy for breaking the Ne nuclei, for example by α decay. Photodisintegration is the analogue for a nucleus of the photoionization for an atom; it is governed by an equation similar to the Saha equation (Sect. 7.1.2) with the appropriate nuclear partition functions. The rate of nuclear energy production can be approximated by [617]

$$\varepsilon_{20Ne} \approx 8.54 \times 10^{26}\, T_9^{12} \left(\frac{Y_{20}^2}{Y_{16}} \right) e^{-54.89/T_9} \quad \text{in erg g}^{-1}\,\text{s}^{-1} , \tag{28.7}$$

near $T_9 = 1.5$ and with Y_i defined in (25.7). The overall T dependence behaves like $\varepsilon_{20Ne} \sim T_9^{49}$. The energy E_{20} liberated per mass unit is $E_{20} = 1.10 \times 10^{17}$ erg g^{-1}, i.e., about 28% of the value for C burning. The reverse reaction ^{16}O$(\alpha, \gamma)^{20}$Ne was already operating during the He-burning phase, it continues to work and increase during the Ne photodisintegration so that at the end an equilibrium is nearly reached. Another important reaction is

$$^{24}\text{Mg}(\alpha, \gamma)^{28}\text{Si} .$$
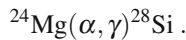
The main products at the end of Ne burning are ^{16}O, ^{24}Mg and ^{28}Si (Fig. 28.2). The ^{20}Ne $+ \gamma$ reaction is endothermic, however, the two main α captures make finally a positive energy production E_{20} as given above. These reactions are accompanied by a number of p, α and n captures not significant for the energy production, but for nucleosynthesis. The important isotopes to be added to those of the C burning are ^{27}Mg, ^{28}Al, ^{28,29,30}Si and ^{32}S.

28.1.3 O Burning

The fusion reaction ^{16}O$+^{16}$O occurs at about $T = 1.9 \times 10^9$ K, it produces the compound nucleus ^{32}S* which disintegrates through several channels, the main ones being

$$^{16}\text{O} + ^{16}\text{O} \longrightarrow ^{32}\text{S}^* \longrightarrow ^{32}\text{S} + \gamma \qquad +16.541 \text{ MeV}$$
$$\longrightarrow ^{28}\text{Si} + \alpha \qquad + 9.593 \text{ MeV}$$
$$\longrightarrow ^{31}\text{P} + \text{p} \qquad + 7.677 \text{ MeV}$$
$$\longrightarrow ^{31}\text{S} + \text{n} \qquad + 1.453 \text{ MeV}$$
$$\longrightarrow ^{24}\text{Mg} + 2\alpha \qquad - 0.392 \text{ MeV}$$
$$\longrightarrow ^{30}\text{P} + ^2\text{H} \qquad - 2.406 \text{ MeV} .$$
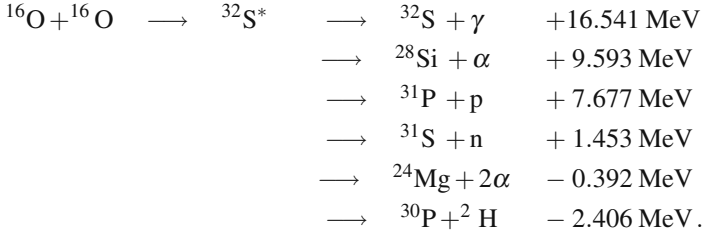
The typical probabilities of these reactions at the T indicated above are 34, 56, 5 and 5% for the α, p, n and ^{2}H channels. The rate of nuclear energy generation by $^{16}\text{O} + ^{16}\text{O}$ without screening behaves like [617]

$$\varepsilon_{16\text{O}} \approx 2.23 \times 10^7 \, Y_{16}^2 \varrho \left(\frac{T_9}{2} \right)^{33} \quad \text{in erg g}^{-1}\text{s}^{-1} , \tag{28.8}$$

near $T_9 = 2$. The energy liberated by $^{16}\text{O} + ^{16}\text{O}$ corresponds to $E_{16,16} = 5.00 \times 10^{17}$ erg g^{-1}, i.e., 0.52 MeV per nucleon close to that of C burning. The nuclei ^{31}P lead to various reactions (not very significant for the energy production) $^{31}\text{P}(\gamma,\text{p})^{30}\text{P}$, $^{31}\text{P}(\text{p},\gamma)^{32}\text{S}$, $^{31}\text{P}(\text{p},\alpha)^{28}\text{Si}(\alpha,\gamma)^{32}\text{S}$. A neutron excess η appears

$$\eta = \frac{n_\text{n} - n_\text{p}}{n_\text{n} + n_\text{p}} . \tag{28.9}$$

It is ~ 0.01, significant for production of elements by neutron captures. The main products of O burning are ^{28}Si and ^{32}S in a ratio of about 3 to 1 (Fig. 28.2). Some s-elements (Sect. 28.5.4) were formed by neutrons in the previous reactions and they are photodisintegrated into elements of the Fe group. Some limited groups in statistical equilibrium start forming, e.g.,

$$^{28}\text{Si}(\text{n}, \gamma)^{29}\text{Si and } ^{29}\text{Si}(\gamma,\text{n})^{28}\text{Si} ,$$
$$^{29}\text{Si}(\text{p}, \gamma)^{30}\text{P and } ^{30}\text{P}(\gamma,\text{p})^{29}\text{Si} .$$
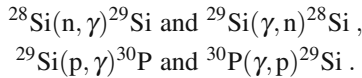
Further isotopes become relevant in this stage, namely ^{30,31,32,33}P, ^{31,33,34,35}S, ^{35,37}Cl, ^{36,37,38}Ar, ^{39}K, ^{40,42}Ca, ^{45}Sc and ^{44,46}Sc.

28.1.4 Silicon Burning

The fusion $^{28}\text{Si} + ^{28}\text{Si}$ does not occur, the high T necessary would photodisintegrate most isotopes. Thus, an ensemble of photodisintegrations occurs before, at about 3.3×10^9 K, in particular

$$^{28}\text{Si}(\gamma, \alpha)^{24}\text{Mg}(\gamma, \alpha)^{20}\text{Ne}(\gamma, \alpha)^{16}\text{O}(\gamma, \alpha)^{12}\text{C}(\gamma, 2\alpha)\alpha . \tag{28.10}$$
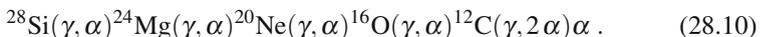
The liberated α particles form quasi-equilibrium reactions such as

$$^{28}\text{Si}(\alpha,\gamma)^{32}\text{S}(\gamma,\text{p})^{31}\text{P}(\gamma,\text{p})^{30}\text{Si}(\gamma,\text{n})^{29}\text{Si}(\gamma,\text{n})^{28}\text{Si} . \tag{28.11}$$
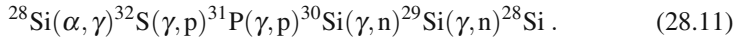
Quasi-equilibrium chains create elements of higher and higher atomic masses by capture of α from (28.10) onto heavier nuclei. The destruction and construction reactions progressively lead to a stage of statistical equilibrium (Sect. 28.5.2), in which the survivors are the most stable elements, i.e., the most bound ones near ^{56}Fe (Fig. 9.1). The approach to this stage over a limited range of isotopes is called a stage of quasi-equilibrium.

Two mains groups of quasi-equilibrium form, one around ^{28}Si up to ^{46}Sc and ^{48}Ti and the other one from ^{52}Cr up to ^{56}Fe [569, 570]. They are linked by reactions involving Ca, Sc, Ti isotopes, which are not in equilibrium until core collapse and form a bottleneck. The net main final result is the conversion of two ^{28}Si into one nucleus of the Fe group such as ^{56}Ni (Fig. 28.2).

The energy production is mainly determined by the α captures. A network with the multiple α elements between ^{28}Si and ^{56}Fe is sufficient to get the energy production [574]. The overall rate goes like $\varepsilon \sim T^{47}$ and the energy per unit of mass from two ^{28}Si nuclei turned to ^{56}Fe is $E_{28,28} = 1.9 \times 10^{17}$ erg g^{-1}. Beyond ^{56}Fe, there are no more fusion reactions, heavier elements are formed by neutron captures on the elements of the Fe group (Sect. 28.5.3).

28.2 The Advanced Phases with and Without Rotation

Models for the advanced phase have been studied by many authors, a few of them also consider the evolution with rotation [236, 237, 240, 251]. Table 28.1 summarizes the main parameters of a 15 M$_\odot$ during the advanced stages of evolution.

Table 28.1 The main parameters in the advanced evolution of a 15 M$_\odot$ star. From S.E. Woosley and Th. Janka [620]

Stage	Timescale	Fuel	Ashes	$T_c(10^9)$ K	ϱ_c g cm^{-3}	$L/L_\odot$ photons	$L_\nu/L_\odot$ neutrinos
H	1.1×10^7 yr	H	He	0.035	5.8	2.8×10^4	1.8×10^3
He	2.0×10^6 yr	He	C,O	0.18	1.4×10^3	4.4×10^4	1.9×10^3
C	2.0×10^3 yr	C	Ne,Mg	0.81	2.8×10^5	7.2×10^4	3.7×10^5
Ne	0.7 yr	Ne	O, Mg	1.6	1.2×10^7	7.5×10^4	1.4×10^8
O	2.6 yr	O,Mg	Si,S,Ar,Ca	1.9	8.8×10^6	7.5×10^4	9.1×10^8
Si	18 d	Si,S, Ar,Ca	Fe,Ni, Cr,Ti	3.3	4.8×10^7	7.5×10^4	1.3×10^{11}
Fe core collapse	~ 1 s	Fe,Ni, Cr,Ti	n star	~ 7.1	$> 7.3 \times 10^9$	7.5×10^4	$> 3.6 \times 10^{11}$
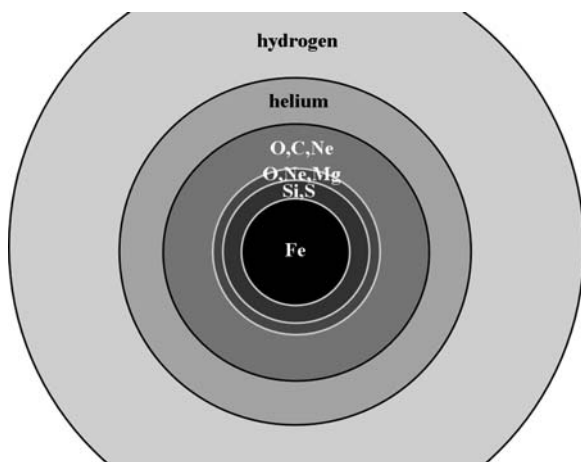
Fig. 28.3 Schematic representation of the onion skin model

The evolution accelerates, with shorter and shorter timescales due to the monstrous increase of the neutrino luminosity. The succession of nuclear reactions occurs at higher and higher central T and ϱ (except for a small expansion in the O-burning phase) in smaller and smaller cores (Table 28.3) forming a "onion skin model" (Fig. 28.3). The photon luminosity, the stellar radius and T_{eff} remain constant from the C-burning phase.

28.2.1 Toward the "Onion Skin" Model

Figures 28.1 and 28.2 show the evolution of the internal abundances of the elements in a rotating and a non-rotating star with an initial mass of $20\,M_\odot$, with an overshooting of $0.1H_P$ [251]. The figures show the models at the end of the main phases of nuclear burning. There are major changes in the center and limited changes in the He- and H-rich outer layers. Between the ends of the He- and C-burning phases, ^{12}C is destroyed and ^{20}Ne and ^{24}Mg are produced, a small amount of ^{16}O is also turned to ^{20}Ne. At the end of the Ne-burning phase, there are lots of ^{16}O, ^{24}Mg and ^{28}Si in the central regions. At the end of the O burning, ^{28}Si and ^{32}S dominate in the center. Changes have also occurred in the CO-rich shell: C has been mostly turned to Ne and Mg. At the end of the Si phase, ^{28}Si is replaced by ^{56}Ni in the center. The successive reactions lead to the so-called "onion skin" model with concentric layers rich in elements with atomic mass multiple of 4 (Fig. 28.3).

The main effect of rotation is that mixing enlarges the shells of the onion skin model internal to the He-rich layer. As a matter of fact, most of the differences due to rotation at the pre-supernova stage have an origin during the H- and He-burning phases. This starts in the H-burning phase with a larger He core and a smoother

internal chemical profile. At He exhaustion, rotation generally leads to a larger CO core, which keeps larger in further phases. In the final rotating model, the O shell contains about twice more mass than in the model without rotation, the Si and Ni cores are also larger. On the whole, rotation enhances the production of heavy elements. This statement applies to initial masses $< 30\,M_\odot$ with $Z = 0.02$; above, rotationally enhanced mass loss dominates and has opposite effects (Fig. 28.8).

28.2.2   Decoupling of Core and Envelope

The evolution of the envelope in equilibrium cannot occur at timescales shorter than the Kelvin–Helmholtz timescale t_{KH} (1.73), which is of the order of 10^5 yr for a $20\,M_\odot$ star. However, from the C-burning phase onward, T in the central regions is high enough for the energy to be evacuated mainly by the neutrinos with a luminosity L_ν. Thus, the core evolution proceeds with a timescale

$$t_{KH}(\nu) = \frac{(GM^2/R) + E_{nucl}}{L_\nu} \,, \qquad (28.12)$$

which becomes shorter and shorter due to the higher neutrino luminosity (Table 28.1). E_{nucl} is the total nuclear energy available in the considered phase ($E_{nucl} \approx 0$ in the contraction phases). As an example, the timescale for the contraction phase between the He exhaustion and C ignition is $t_{KH}(\nu) = (GM^2/R)/L_\nu \sim 10^3 - 10^4$ yr. The difference of timescales between the envelope and the core implies that the envelope can no longer adjust its thermal structure to the fast central evolution: at the surface, L and T_{eff} no longer change from the C-burning phase, the changes are generally small even from the end of the He-burning phase. The stars stay at the same place in the HR diagram until the supernova explosion.

28.2.3   Evolution of Central Conditions

Figure 28.4 shows the evolution of central conditions for initial 15 and $60\,M_\odot$ models with and without rotation. The evolution goes on with a slope $\sim 1/3$. The pressure of electron degeneracy dominates in the latest stages. For $M < 30\,M_\odot$ at $Z = 0.02$, rotation makes a higher central T and a lower ϱ due to the bigger cores, as for a slightly higher non-rotating mass. For the highest masses, the mass loss effects compensate those of mixing: central evolution is not much affected by rotation.

From the C-burning phase, the ν emission by pair e^+e^- annihilation (9.60) and the plasma process take away the whole energy produced by central nuclear reactions and contraction, while the photon luminosity comes from the shell burning. Within the core in the C-burning phase, one has an equilibrium

$$< \varepsilon_{12C} > \approx < \varepsilon_\nu > . \qquad (28.13)$$
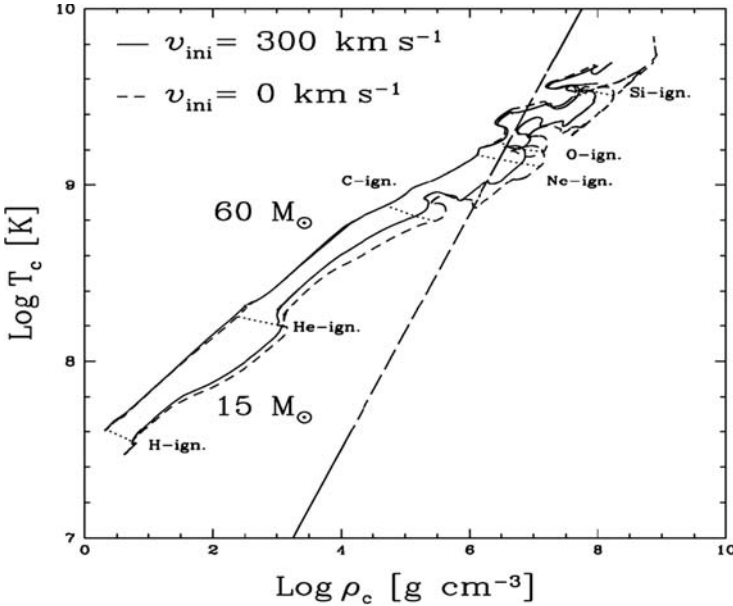
Fig. 28.4 Evolution of central conditions without and with rotation for $Z = 0.02$ models. The straight dashed line shows the electron degeneracy limit. From R. Hirschi et al. [251]

If we equal locally ε_{12C} given by (28.1) and $\varepsilon_{\nu\text{-pair}}$ given by (9.60) for $T_9 < 1$, with $Y_{12} = X_{12}/12$ for $X_{12} = 0.2$ and $\varrho = 10^5$ g cm^{-3}, we get

$$4.9 \times 10^{13} \, e^{-11.86/T_9} = 7 \times 10^9 \, T_9^{24} . \tag{28.14}$$

The solution gives $T \approx 7.4 \times 10^8$ K, i.e., a correct order of magnitude for the T of ^{12}C burning (Fig. 28.4). Figure 28.5 shows the rates ε at the end of the central C burning in a non-rotating 20 M$_\odot$. One sees the large central ν emission. At the level of the He-burning shell, neutrinos are no longer important. The He burning feeds the photon luminosity and produces some expansion ($\varepsilon_{\text{grav}} < 0$). The H-burning shell is almost extinct. For larger masses, the amount X_{12} at the end of the He burning is lower, which decreases ε_{12C}. The density is smaller which increases $\varepsilon_{\nu\text{-pair}}$ (9.60), thus C burning cannot compensate for ν losses and the core keeps contracting during the advanced stages. Rotation makes some differences: due to the hotter and larger core, X_{12} is lower at the end of the C phase in Fig. 28.1 and C burning can barely compensate for ν losses; the C-burning phase is thus shorter (Table 28.2).

Figure 28.6 shows the central evolution of the nuclear, neutrino and gravitational ε throughout the evolution of a 20 M$_\odot$ star. The gravitational energy production and the neutrino losses adjust closely to each other all the way, except for short periods of expansion in the O and Si burning phases, where nuclear energy production briefly dominates.
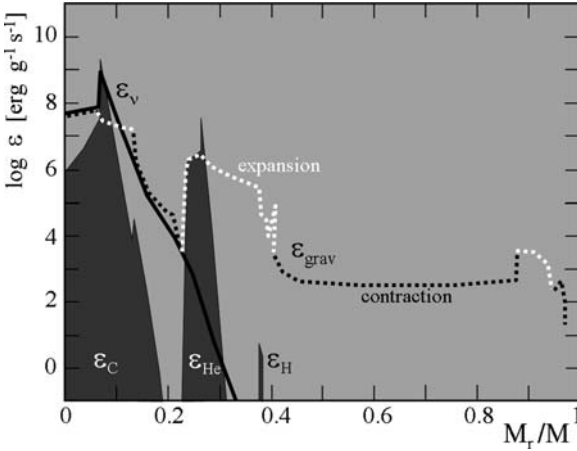
Fig. 28.5 Distribution of the energy production rates ε per unit of mass inside a $20\,M_\odot$ star ($Z =$ 0.02) at the end of the central C burning. The darker areas show the nuclear energy production, the thick continuous line gives the ν emission (*counted positive*) and the dotted line the gravitational energy, positive (*contraction*) in black, negative (*expansion*) in white. Adapted from Hirschi et al. [251]

Table 28.2 Lifetimes in years (exponent in parenthesis) of the advanced burning stages of massive stars at solar metallicity. Masses in $M_\odot$ and velocities v in km s^{-1} on the zero-age main sequence (ZAMS). From Hirschi et al. [251]

$M_{\rm ZAMS}$	15	15	20	20	40	40	60	60
$v_{\rm ZAMS}$	0	300	0	300	0	300	0	300
$t_{\rm H}$	1.13 (7)	1.43 (7)	7.95 (6)	1.01 (7)	4.56 (6)	5.53 (6)	3.62 (6)	4.30 (6)
$t_{\rm He}$	1.34 (6)	1.13 (6)	8.75 (5)	7.98 (5)	4.83 (5)	4.24 (5)	3.85 (5)	3.71 (5)
$t_{\rm C}$	3.92 (3)	1.56 (3)	9.56 (2)	2.82 (2)	4.17 (1)	8.53 (1)	5.19 (1)	5.32 (1)
$t_{\rm Ne}$	3.08	0.359	0.193	8.81 (-2)	4.45 (−2)	6.74 (−2)	4.04 (−2)	4.15 (−2)
$t_{\rm O}$	2.43	0.957	0.476	0.132	5.98 (−2)	0.176	5.71 (−2)	7.74 (−2)
$t_{\rm Si}$	2.14 (−2)	8.74 (−3)	9.52 (−3)	2.73 (−3)	1.93 (−3)	2.08 (−3)	1.95 (−3)	2.42 (−3)

28.2.4   Lifetimes and Core Masses, Rotation

One must distinguish the timescale $t_{\rm contr}$ for the core contraction between the end of the He-burning phase and C ignition and the timescale $t_{12\rm C}$ of the nuclear C-burning phase, the same for the other phases. The timescale $t_{\rm contr}$ is given by $t_{\rm KH}(\nu)$, it is 1040, 1840, 8500, 15200 and 56200 yr for 120, 60, 20, 15 and $9\,M_\odot$ stars, respectively [404]. The timescale $t_{12\rm C}$ can be estimated from the change of ^{12}C (Sect. 25.1.2)
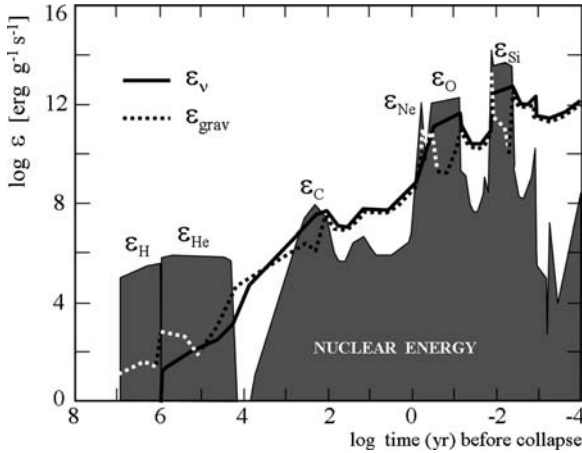
Fig. 28.6 Evolution of the rates of nuclear energy (*gray*), of neutrino emission (*continuous line*) and of gravitational energy (*dotted line*) for a 20 M$_\odot$ star with $Z = 0.02$. Same remark as for Fig. 28.5. Adapted from Hirschi et al. [251]

$$\frac{dX_{12}}{dt} = \frac{\varepsilon_{12C}}{E_{12,12}}, \quad \text{and thus} \quad t_{12C} \approx \left(\frac{dX_{12}}{dt}\right)^{-1}, \tag{28.15}$$

with the energy per gram $E_{12,12}$ given in Sect. 28.1.1. Let us take as above $X_{12} = 0.2$, $\varrho = 10^5$ g cm^{-3} and $T_9 = 0.8$, one gets $t_{12C} \approx 750$ yr, which is shorter than t_{contr}. This is a correct order of magnitude as shown in Table 28.2. With respect to the H-burning phase, the nuclear C-burning phase plus the previous contraction phase represent a fraction

$$\frac{t_{contr} + t_{12C}}{t_H} \sim 10^{-3} . \tag{28.16}$$

This ratio is the same if we include all nuclear phases after He exhaustion. A sensitive enough neutrino detector would see one massive star over 10^3 emitting more energy as neutrinos than as photons. Table 28.2 shows the lifetimes of the H, He, C, Ne, O and Si burning phases for different masses with and without rotation.

For a non-rotating 20 M$_\odot$ star, the C-burning phase lasts $\sim 10^3$ yr (50 yr for a 60 M$_\odot$ star). The more advanced phases are shorter: 70 days for Ne burning, 6 months for O burning and 3 days for Si burning. This results from the increasing ν emissions with T, from the decrease of the nuclear energy available (Fig. 9.1) and from the smaller cores (Table 28.3). With rotation, the lifetimes for stars with $M < 30$ M$_\odot$ are generally a factor of 2–3 smaller, for reasons given in the previous section. For higher masses, the effect is generally opposite, the higher mass loss in rotating stars leads to a lower T, thus a higher C content and a longer C phase.

28.3   Chemical Yields: *Z*, Mass Loss and Rotation Effects

Table 28.3 gives the initial masses, the final masses, the masses M_α of the He cores, $M_{\rm CO}$ of the CO cores, $M_{\rm Fe}$ of the iron cores and the remnant masses for models with mass loss with and without rotation for $Z = 0.02$. Often the nucleosynthesis and chemical yields are parametrized as a function of M_α or $M_{\rm CO}$, thus this table permits some correspondence with the initial masses. The core masses by various authors are different, especially more in the advanced stages, due to different $^{12}C(\alpha, \gamma)^{16}O$ reaction rates, overshooting, mass loss rates (or absence of mass loss). As stated above, the main model differences due to rotation generally already appear in the H- and He-burning phases.

The production of heavy elements with atomic mass number multiple of α is already determined at the end of the pre-supernova stage. The explosive nucleosynthesis during the supernova creates a lot of new elements with atomic masses between the successive α elements as well as elements beyond the Fe peak, produced by neutron captures (Sect. 28.5.3). However, the formation of these new elements only modifies by about 1% the abundances of the α elements in the onion skin layers, as shown by F. Thielemann [572]. Thus, the main yields are determined at the end of the pre-supernova stages, as for example in the bottom panels of Fig. 28.2 in the case of a $20\,M_\odot$ star. Both the stellar winds and the supernova explosion contribute to the injection of newly synthesized elements into the interstellar medium. These relative fractions are influenced by rotation, through mixing and mass loss.

Table 28.3 Final masses, masses of the He, CO, Fe cores and remnant masses as a function of the initial masses and rotation velocities. "A" next to 300 means that wind anisotropy was taken into account. From Hirschi et al. [252]

$M_{\rm ini}/M_\odot$	$v_{\rm ini}$ [km s^{-1}]	$M_{\rm final}$	M_α	$M_{\rm CO}$	$M_{\rm Fe}$	$M_{\rm remn}$
9	0	8.663	2.185	0.920	–	0.920
9	300	8.375	2.547	1.413	–	1.239
12	0	11.524	3.141	1.803	–	1.342
12	300	10.199	3.877	2.258	–	1.462
15	0	13.232	4.211	2.441	1.561	1.510
15	300	10.316	5.677	3.756	2.036	1.849
20	0	15.694	6.265	4.134	1.622	1.945
20	300	8.763	8.654	6.590	2.245	2.566
25	0	16.002	8.498	6.272	1.986	2.486
25	300	10.042	10.042	8.630	2.345	3.058
40	0	13.967	13.967	12.699	2.594	4.021
40	300A	12.646	12.646	11.989	2.212	3.853
60	0	14.524	14.524	13.891	2.580	4.303
60	300A	14.574	14.574	13.955	2.448	4.323
85	0	17.236	17.236	16.564	–	5.115
85	300A	12.314	12.314	11.666	–	3.776
120	0	16.254	16.254	15.591	–	4.819
120	300A	11.270	11.270	10.663	–	3.539

28.3.1   *Chemical Yields of* **α**-*Rich Nuclei*

The stellar nucleosynthetic production is an essential ingredient for the study of the chemical evolution of the galaxies. Care has to be given to the quantities to be used in this context [347, 575]. The quantities we consider here are the fractions $\Delta M_{ej}/M$ of the initial masses M ejected in various forms (these are the quantities called p_{im}^{tot} in Tinsley's formalism, while the "stellar yields" are formally the amount of mass ejected ΔM_{ej}).

Without mass loss, the fraction $\Delta M_{ej}/M$ of new elements produced continuously grows with M (Fig. 28.7 left). With mass loss, large amounts of new elements are ejected. This makes a big difference, because if they would have stayed in the star, these elements or a part of them would have been further transformed into heavier elements, thus contributing to the overall production (Fig. 28.7 right). Mass loss removes a lot of new He and C, thus increasing the yields in these elements and decreasing those of the new elements which would have been produced in absence of mass loss, in particular O and the other heavy elements multiple of α. In Fig. 28.7, one sees the changes of the various productions. Thus, metallicity Z by its effect on the opacity in the outer layers influences the $\dot{M}$ and in turn the advanced stages and their nucleosynthetic production [347].

Figure 28.8 shows the effects of rotation on the chemical yields at $Z = 0.02$. Below $30\,M_\odot$ (initial), the cores of rotating models are larger than for zero rotation, thus the production of α elements is enhanced, by a factor of 1.5–2.5 for C and O. The yields in heavy elements of a rotating star (with an initial velocity $300\,\mathrm{km\,s^{-1}}$) of $\sim 18\,M_\odot$ are like those of a non-rotating star of about $30\,M_\odot$. Above $30\,M_\odot$, the main effect of rotation is the enhancement of mass loss. This increases the products of H burning (He, N) injected into the interstellar medium. For ^{4}He, the wind contribution increases a lot with mass, it dominates for $M \geq 22\,M_\odot$ for rotating models
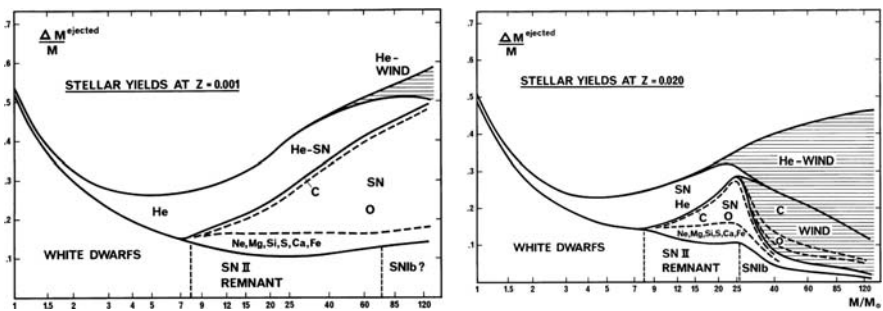
Fig. 28.7 The effects of mass loss on nucleosynthesis, with the mass fractions ejected as a function of the initial mass. The new He, the C, O and heavy elements are indicated, SN means ejected in supernovae. The remnant masses are also indicated in the lower part. The hatched areas indicate the wind contributions in new elements. $\dot{M}$ from de Jager et al. [271], a relation $\dot{M} \sim Z^{0.5}$ is assumed, $\dot{M}$ for WR stars from Langer [306]. *Left*: low-Z models with small mass loss. *Right*: models with $Z = 0.02$ and heavy mass loss. From the author [347]
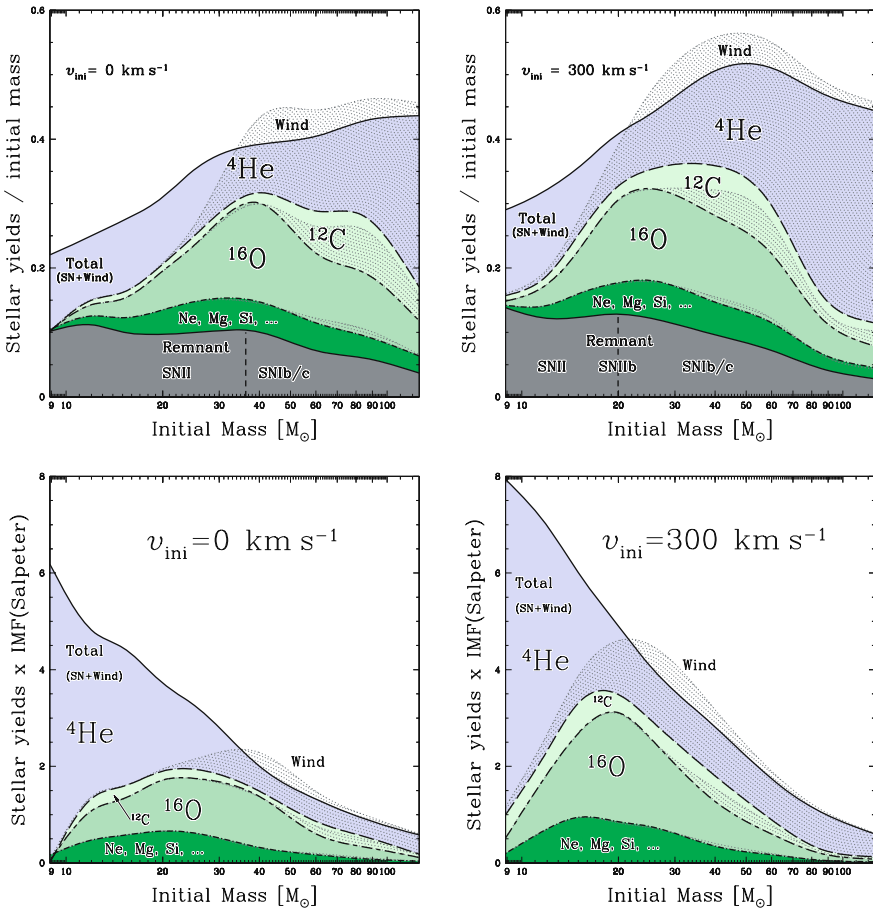
Fig. 28.8 Mass fractions ejected as a function of the initial masses for models with $X = 0.705$, $Z = 0.020$. The mass loss rates of all models are from Vink et al. [604, 605], de Jager et al. [271] and Nugis and Lamers [445] for WR stars. Anisotropic winds are accounted for $M > 40$ M$_\odot$. The wind contributions are shown with dotted areas. For ^{4}He, the wind contribution may be larger than the total yield, because some ^{4}He is destroyed in the supernova. Upper left: without rotation. Upper right: with rotation. Lower left and right: the same with convolution by a Salpeter's initial mass function $dN/dM \sim M^{-2.35}$. From R. Hirschi et al. [252]

($M \geq 35$ M$_\odot$ for zero rotation). The size of the cores is only slightly reduced by rotation, due to a compensation between extension by mixing and reduction by mass loss, thus the yields are about the same. When account is given to the weighting by the IMF, the production of oxygen and of α elements is globally enhanced by rotation, while the effect on the He production in massive stars remains limited.

28.4 Toward the Supernovae

Supernovae (SNe) are a subject in themselves (see book by Arnett [16]), with the physics of the explosions, the nucleosynthesis, the evolution of the lightcurves, the nature of the condensed remnants, the production of high-energy particles, etc. This is beyond the present scope. Here, we only consider a few points, in particular those directly related to previous evolution.

Supernovae (SNe) are stellar explosions during which a star may reach a luminosity of about 10^{10} L$_\odot$. The total luminous energy emitted is only $\sim 1\%$ of the mechanical energy released by a SN explosion ($\sim 10^{51}$ erg). In the form of neutrinos, the energy released is even 10^2 times larger ($\sim 10^{53}$ erg). Ten historical supernovae have been observed over the last 2000 yr. In our Galaxy, the rate of SN explosions is of the order of 1 every 30 yr. A part of the heavy elements synthesized during the evolution and explosion goes into the remnant (neutron star or black hole), another part is ejected at velocity $\geq 10^4$ km s^{-1}. Supernovae enrich the interstellar medium in the nucleosynthetic products; they also inject kinetic energy in the interstellar medium, compressing the medium and thus favoring new stellar births.

28.4.1 Supernova Types

At the origin, there were two main types of supernovae identified: Type I and type II. These types have been further refined and nowadays one may consider three main classes of supernovae, according to the occurrence mainly of HI, SiII and HeI lines in the spectra: SN Ia, SN II, SN Ib/Ic (Fig. 28.9) [581, 609]. Typical SN light curves are illustrated in Fig. 28.10.

SN Ia: they show SiII lines and no HI lines. They result from the explosion of a white dwarf (WD) in a binary system. The WD by mass accretion from the companion overcomes its Chandrasekhar limit (7.167), the ensuing collapse triggers C burning in degenerate conditions. The star is completely destroyed. SN Ia are observed in all types of galaxies, their light curves form a relatively homogeneous group, which makes them of great interest in cosmology. After a peak of about a month or more (Fig. 28.10), L decreases exponentially due to the radioactive ^{56}Co (Sect. 28.5.2).

SN II: their spectrum is dominated by H lines. They result from the core collapse of massive stars with $M > 8$ M$_\odot$ (Sect. 28.4.2). They are found in spiral arms and in regions of young stellar populations in galaxies. They form a heterogeneous group with various subgroups. The **SN IIP** show a plateau after the maximum of their light curve for a month or two (Fig. 28.10). They are interpreted as resulting from the core collapse of stars which have kept most of their envelope. The thermalization of the SN shock in the large envelope gives rise to the observed plateau. From observations in galaxies, the SN IIP have been shown recently to originate from the mass interval 7.5 (± 1) M$_\odot$ to 15 ($+3, -2$) M$_\odot$ [536]. The **SN IIL** show a continuous linear decline of luminosity after the maximum (Fig. 28.10). They have
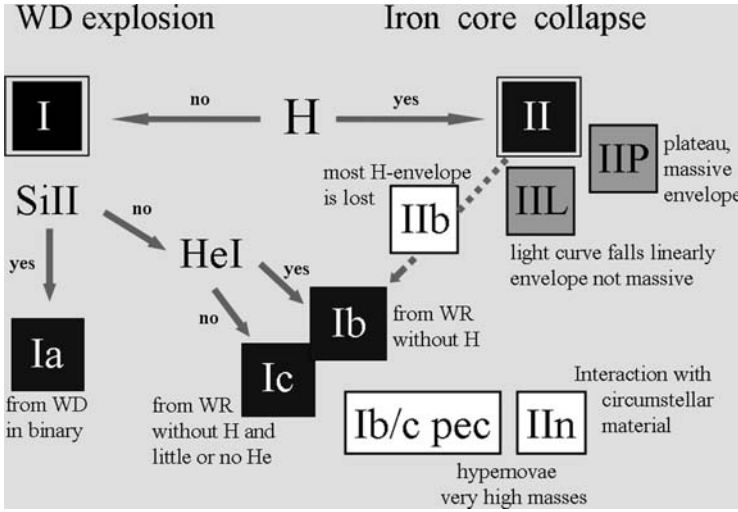
Fig. 28.9 Classification and main characteristics of supernovae. The main groups are in black squares. Adapted from M. Turatto [581]
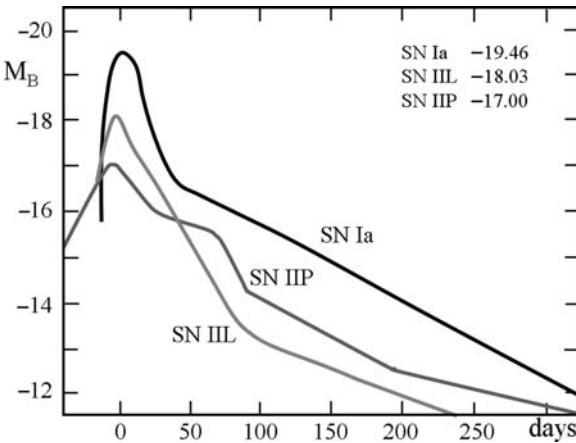
Fig. 28.10 Supernovae lightcurves (days after the maximum). Adapted from K.W. Weiler and R.A. Sramek [609]. The average maxima are from D. Richardson et al. [487]

lost some mass and kept a moderate envelope (~ 1–2 $M_\odot$), rich in H but insufficient to produce a plateau by the shock thermalization. The **SN IIb** show first a spectrum like SN II and later like SN Ib or c; they are interpreted as massive stars which have lost most of their envelope before the explosion. Evidence of interactions with the circumstellar gas is present in the spectra. The **SN IIn** show narrow emission lines on top of broad emission lines. The narrow lines are due to circumstellar outflows and SN IIn are interpreted as supernova explosions occurring in the course of heavy mass outflows.

The **SN Ib and SN Ic:** in the SN Ib there is no H and the He I lines dominate. They appear only in spiral galaxies and are associated with massive stars, more massive than the SN II progenitors. Type SN Ib likely results from the explosion of WR stars with no H present. The SN Ic have no H left and also no He I lines (or only very weak) in their spectra. They are likely resulting from WR stars which have lost all their H envelope and all or most of their He envelope. They are ~ 1.5 mag. fainter than SN Ia, due to the absence of envelope thermalizing the shock. The **hypernovae** are peculiar cases of SN Ib/c, very luminous and energetic, with extreme ejection velocities > 30000 km s^{-1}, maybe related to Gamma Ray Bursts (Sect. 28.6.3).

On the whole, it is remarkable to find among the supernovae a variety in the degrees of mass loss as we have seen in Chap. 27. Maybe in future some signatures due to rotation may be detected.

28.4.2   Core Collapse and Explosion

In general, one good reason is better than many ones. For core collapse, there are four good reasons for its occurrence:

1. As evolution proceeds from H to Si burning, there is less and less nuclear energy available (Fig. 9.1), thus core contraction must inexorably go on to compensate for the energy lost.
2. As central T and ϱ increase, the ν emissions (Sect. 9.5) remove more energy (Fig. 28.6), which can only be provided by core contraction.
3. At $T \approx 10^{10}$ K, $\varrho \approx 10^{10}$ g cm^{-3} (~ 1 MeV), the energetic photons are able to photodisintegrate the nuclei of the Fe peak,

$$^{56}\text{Fe} + \gamma \longrightarrow 13\,\alpha + 4n - 2.2\,\text{MeV/nucl}\,. \tag{28.17}$$

This reaction which makes the whole way back to α particles is endothermic and removes a lot of thermal energy, dramatically accelerating the collapse. The very large specific heats in this transition make the adiabatic exponent $\Gamma_1 < 4/3$ (Sects. 1.3.2, 7.4.1). Equilibrium is broken and the central regions collapse at the dynamical timescale.
4. When $\varrho > 10^{11}$ g cm^{-3}, the Fermi energy E_F of electrons is higher than the energy difference of 1.29 MeV between neutrons and protons and the inverse of the β decay of the neutron occurs:

$$\text{if } E_F(e^-) > (m_\text{n} - m_\text{p})c^2 \quad \text{then} \quad p + e^- \longrightarrow n + \nu_e\,. \tag{28.18}$$

This reaction initiates the collapse for stars between the limits M_{WD} and M_{EC} (Sect. 26.4.1) by electron captures. For more massive stars, the above process participates in the core collapse. The removal of the degenerate electrons, which were the source of the pressure, evidently precipitates the core collapse.

The potential energy liberated during the core collapse is of the order of 10^{53} erg. Most (99%) of this energy escapes in the form of neutrinos; the remaining 1% is released as kinetic energy of the order of 10^{51} erg. From that, 1% is again converted into luminous energy, giving rise to a supernova which is the most spectacular event in the sky, which finally represents only $\sim 10^{-4}$ of the total energy liberated.

All these reactions lead to the catastrophic implosion of the core. It collapses as in free fall, i.e., as if all sources of pressure were negligible. The dynamical timescale is $\tau_{ff} = 446 \, \mathrm{s}/\varrho^{\frac{1}{2}}$ for ϱ in g cm^{-3} (18.23). For $\varrho \approx 10^{10}$ g cm^{-3}, this leads to a timescale of $\sim 10^{-2}$ s characterizing the core collapse, ending a nuclear evolution of millions years.

28.4.2.1   The Explosion Mechanisms

The explosion mechanism is explained if one finds how the star converts 1% of the energy from the core collapse into the kinetic energy to eject the envelope. Several processes have been proposed:

– **The prompt bounce-shock mechanism:** the outer layers no longer supported by the pressure of degenerate electrons fall onto the dense neutron core of 0.6–0.8 $M_\odot$ resulting from the Fe-core collapse. A bounce occurs at a density of the order of the nuclear density ($\sim 10^{15}$ g cm^{-3}). The energy in the bounce is of the same order as the potential energy of the core, i.e., $\sim 7 \times 10^{51}$ erg, which is enough to provide the kinetic energy of the explosion. However, there is a strong damping of the shock by the neutrino emissions, as well by the photodisintegration of the outer layers of the Fe core. The shock may only propagate through a few 0.1 $M_\odot$ before being damped. Thus, this mechanism alone seems insufficient to drive supernova explosions [272], except perhaps in the lower mass range.

– **The delayed neutrino heating:** the potential energy liberated by the core collapse escapes the central regions as "thermal" neutrinos emitted by the various processes discussed in Sect. 9.5. At a density of 10^{11} g cm^{-3}, the optical depth for neutrinos is not negligible and a "neutrinosphere" temporarily forms where $\tau_\nu \sim 1$ (Fig. 28.11). The ν diffusion time t_{diff} out of the neutrinosphere is of the order of a few seconds, so that the ν luminosity is $L_\nu \approx |\Omega_{\mathrm{core}}|/t_{\mathrm{diff}} \approx 10^{53}$ erg s^{-1}, where Ω_{core} is the potential energy of the core. A small fraction of these neutrinos is captured at the level of the shock by reactions

$$\nu_e + n \rightarrow p + e^-, \quad \overline{\nu}_e + p \rightarrow n + e^+, \quad \nu_e + [A] \rightarrow \nu_e + [A], \text{ etc.,} \quad (28.19)$$
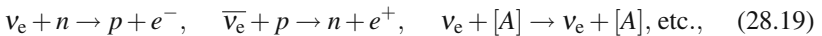
where $[A]$ represents heavy nuclei of atomic mass A. This mechanism coupled to the bounce seems able to reverse the collapse and produce the SN explosion only for stars with an initial mass below about 11 $M_\odot$. In more massive stars, the ν captures make the shock to stagnate but are insufficient to drive the explosion [272].

– **Rayleigh–Taylor Instability:** perturbations induced by neutrino-driven convection develop at the edge of the new neutron star, below the stagnating shock

where the v are captured. Rayleigh–Taylor instabilities also develop at other chemical interfaces and contribute to the ejection of metal-rich clumps, which emerge after about 300 s through the outer envelope and are ejected ballistically into the interstellar medium [282].

– **Core g-mode instability:** multi-dimensional hydrodynamic simulations of explosions show the excitation of g modes from the core that emit sufficient acoustic power to energize an anisotropic blast [79]. The core accretes on one side and explodes on the other side, thus the asymmetry starts in the very center. The explosion energies are larger for the more massive progenitors, with higher v fluxes. This acoustic powered mechanism is a bit delayed with respect to the neutrino emission and is still in the exploratory phase. The asymmetric explosion gives a kick to the pulsar or other remnants. [79].
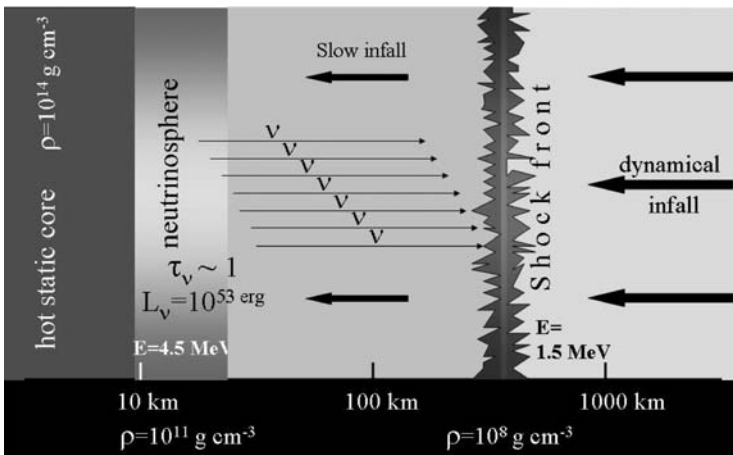
Fig. 28.11 Schematic illustration of the shock front, neutrinosphere and neutron core during core collapse

28.4.3 Final Masses and Remnants

Here, the "final masses" mean the mass at the time of the supernova explosion. The relation between the final and initial masses integrates all the effects of mass loss during evolution; it depends on the mass loss rates adopted and on the rotation (the mass lost between the C-burning phase and the SN explosion is usually supposed negligible). The relations with and without rotation are illustrated in Table 28.3. Generally the final masses with rotation are smaller. There are, however, exceptions as illustrated by the $60\,M_\odot$ model (in the zero rotation case, the star becomes an

LBV [411] and loses a lot of mass, while the rotating $60\,M_\odot$ star is turning early to a WR star and avoids the LBV zone in the HR diagram and its heavy mass loss).

Since the mass loss changes with metallicity Z, the relation between the initial and final masses also depends on Z. Figure 28.12 shows the relations for different initial Z. For $Z = 0.02$, most stars with initial masses between 20 and $120\,M_\odot$ finish their life with masses in the range of 10–$15\,M_\odot$ (see also Fig. 28.13). For $Z < 0.02$, the largest final masses originate from the range of 40–$60\,M_\odot$. The large differences between the initial and final masses beautifully illustrate the enormous effect of mass loss, enhanced or not by rotation. The details evidently depend on the $\dot{M}$ parametrizations.

Figure 28.13 shows different characteristic masses as a function of the initial masses [239] at standard composition: the mass after the mass loss by stellar winds, the mass M_α of the He core, the mass M_{CO} of the CO core and the mass of the remnants. Below $M_{WD} \approx 8\,M_\odot$, the remnant is a white dwarf. Above and up to $\sim 25\,M_\odot$, the remnant is a neutron star, a limit fixed by the maximum mass of a neutron star around 2–$2.5\,M_\odot$. The outer onion skin layers, slightly affected by the explosive nucleosynthesis, are all ejected. The final issue of WR stars is uncertain; it depends on the remaining masses, as illustrated by the various white dotted lines in Fig. 28.13 (see also Fig. 27.20 right). At masses above $\sim 25\,M_\odot$, the nature of the remnant depends on three effects: the fallback, mass loss and rotation. After the initial blast, a fraction of the inner layers can fall back onto the neutron star. If the remnant mass becomes higher than the maximum mass for a neutron star, the central core further collapses to become a black hole. The location of the cutoff
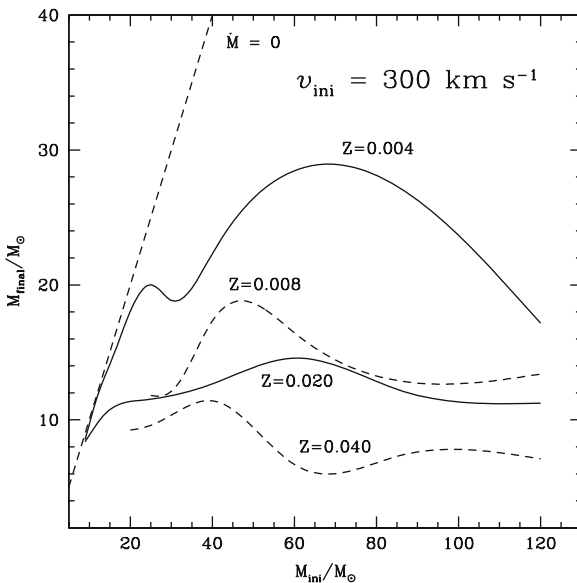
Fig. 28.12 Relation between the final and initial masses at different metallicities. From G. Meynet and the author [412]
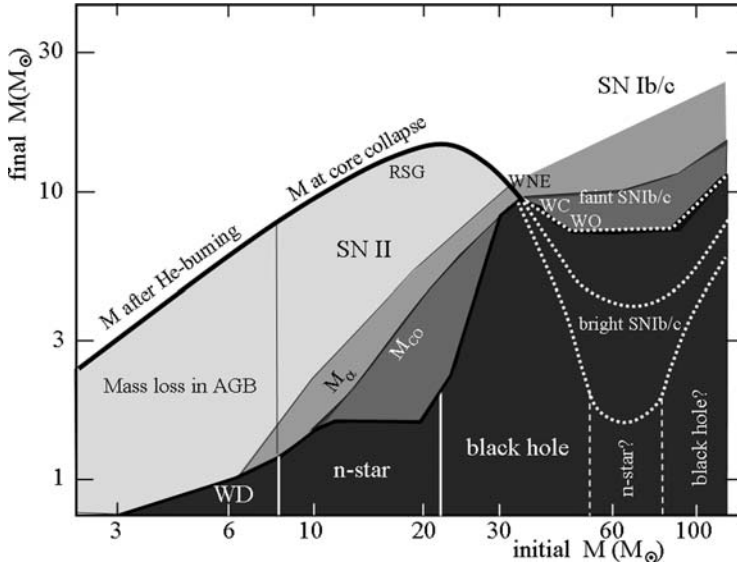
Fig. 28.13 The remnant masses (*black*), the mass of the CO core (*dark gray*), the mass of the He core (*medium gray*), the mass after He burning and at core collapse (*light gray*) as functions of the initial M. The differences with Table 28.3 result from different model assumptions. Adapted from A. Heger et al. [239]

mass between what is ejected and what is caught into the remnant is uncertain. The observations of the ratios of elements of the Fe peak produced in the deepest onion skin layers may provide some indication on the cutoff mass [442].

As mass loss and rotation in the H- and He-burning phase so much influence the evolution, it is often useful to determine the final fate of stars as a function of the mass M_α of the He core [238] (estimated at the end of the He-burning phase). This is shown in Table 28.4.

Table 28.4 The final fate of stars as a function of the mass M_α of the He core [238]. BH means black hole, PISN means pair instability supernova

$M_\alpha < \quad 9\,M_\odot$	SN II
$9\,M_\odot \leq M_\alpha < \quad 15\,M_\odot$	BH by fallback
$15\,M_\odot \leq M_\alpha < \quad 40\,M_\odot$	Direct BH formation
$40\,M_\odot \leq M_\alpha < \quad 64\,M_\odot$	Pulsational PISN and BH formation
$64\,M_\odot \leq M_\alpha < 133\,M_\odot$	PISN
$133\,M_\odot \leq M_\alpha$	Direct BH collapse

28.5 Explosive Synthesis

28.5.1 Elements with A < 56

The chemical yields obtained above (Fig. 28.8) are based on the structure of the onion skin layers just before the supernova explosion. However, the passage of the shock front through the onion skin layers induces an additional nucleosynthesis: the explosive nucleosynthesis, which creates new isotopes, but affects little the production of the α elements like C, O, Ne, Mg and Si [571]. In Fig. 28.14, we see that these elements multiple of α largely dominate.

The explosive nucleosynthesis creates the other elements on the lower curve up to ^{56}Fe (Fig. 28.14). In general, only the energetic production of the main reactions (Sect. 28.1) is accounted for in the hydrodynamical models of the explosion. The production of the other elements (which are in general not significant energetically)
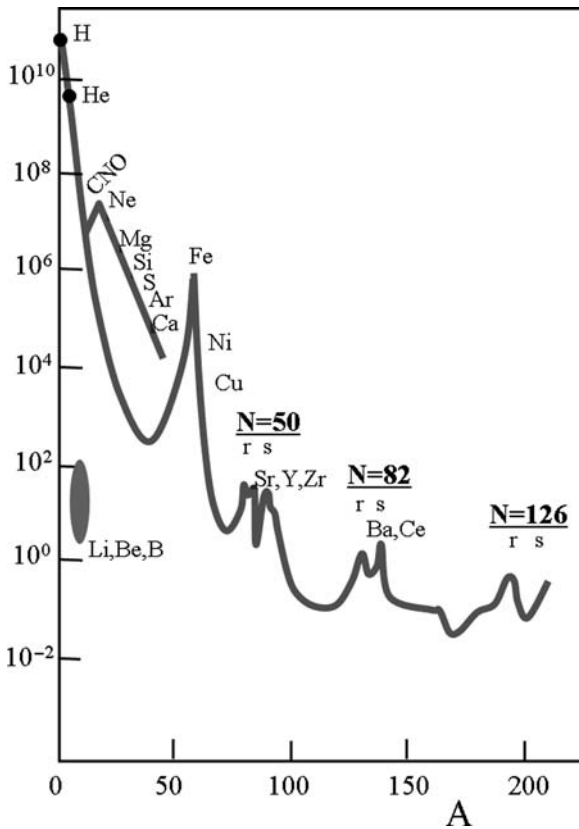
Fig. 28.14 Highly simplified distribution of the chemical abundances as a function of the atomic number. A few important elements are shown

is treated by "post-processing", i.e., the calculations of the detailed abundances of these elements are made with a nuclear network with equations of the form shown in Sect. 25.1.2:

$$\frac{dY_i}{dt} = Y_m Y_k [mk](\varrho, T) - Y_i Y_n [in](\varrho, T), \quad \frac{dY_m}{dt} = \ldots, \text{etc.} \tag{28.20}$$

for all reactions involved. The evolution of $\varrho(t)$ and $T(t)$, which defines the reaction rates $[mk]$ and $[in]$ are taken from the hydrodynamic models, as well as the neutron excess η.

Even more simply, the nuclear network has often been treated with $\varrho(t)$ and $T(t)$ given by

$$\varrho(t) = \varrho_0 e^{-t/(t_{expl})}, \quad T(t) = T_0 e^{-t/(3 t_{expl})}, \tag{28.21}$$

$$\text{with} \quad t_{expl} \approx \chi \, \tau_{ff} = \chi \, \frac{446 \sec}{\varrho^{\frac{1}{2}}}, \quad \text{with} \quad \chi \sim 1. \tag{28.22}$$

according to (18.23), with ϱ in g cm^{-3}. The factor $1/3$ between the variations of T and ϱ corresponds to $\Gamma_3 = 4/3$ for an adiabatic photon gas (Sect. 7.5). A choice of values ϱ_0, T_0, η leads to a certain distribution of the elements

$$(\varrho_0, T_0, \eta) \implies X_i\text{-distribution.} \tag{28.23}$$

Which triplet of values (ϱ_0, T_0, η) gives the observed distribution of elements in the domain of atomic masses A corresponding to the considered onion skin layer(s) is searched. Remarkably, the values of ϱ_0 and T_0 are slightly larger than the corresponding values of the onion skin layers, this is consistent with some additional heating from the shock. Another remarkable lesson is that the cosmic elements keep the signatures of the (ϱ, T) conditions of their nucleosynthesis.

There is another interesting property [572]. Among the α elements, the lighter ones result from the hydrostatic fusion and the quantities produced strongly depend on stellar masses, while the heavier elements are determined by the explosive nucleosynthesis and have little dependence on masses:

$$\underbrace{C, \ O, \ Ne, \ Mg, \ (Si),}_{\text{FROM HYDROSTATIC FUSION}} \qquad \text{amounts depend on M},$$

$$\underbrace{(Si), \ S, \ Ar, \ Ca, \ Fe,}_{\text{FROM EXPLOSIVE FUSION}} \qquad \text{amounts have little dependence on M}.$$

This is of great interest for the study of the chemical evolution of galaxies: the ratios of elements C to Mg bear the signature of the masses in which the elements have been produced. It is important to emphasize that the main enrichment in Fe comes from SN Ia (Sect. 28.4.1), thus not from massive stars, but from the low and

intermediate mass stars, which require at least a time of about 10^8 yr to reach the WD stage finally leading to the SN Ia.

28.5.2 The Fe Peak

Another group of elements is the iron peak elements. As illustrated in Fig. 28.14, these elements are quite abundant (see also Table A.1). We have seen in the reactions of Si melting (Sect. 28.1.4) that there are both destructions and buildings of elements by captures of α, p, n and γ particles by nuclei. A quasi-equilibrium is created, since the nuclear lifetimes are short with respect to the evolution of the system. This is not a perfect equilibrium because there is a net flux of particles toward higher atomic masses up to iron. Numerical simulations show that the nuclear evolution is dominated by large groups of nuclei in mutual equilibrium and that it is advantageous to take this property into account [458]. Let us examine the equilibrium of neutron captures and photodisintegrations

$$(A,Z) + \gamma \rightleftharpoons (A-1,Z) + \mathrm{n} . \tag{28.24}$$
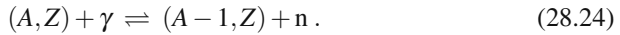
Such an equilibrium obeys to an equation analogous to Saha's equation (7.18)

$$\frac{n(A-1,Z)\,n_{\mathrm{n}}}{n(A,Z)} = 2\frac{U(A-1,Z)}{U(A,Z)}\frac{(2\pi\mu kT)^{3/2}}{h^3}e^{-\frac{Q_{\mathrm{n}}}{kT}} . \tag{28.25}$$

With, here, $\mu = \dfrac{(A-1)\times 1}{[(A-1)+1]}\dfrac{m_{\mathrm{u}}^2}{m_{\mathrm{u}}} = \dfrac{A-1}{A}m_{\mathrm{u}}$ and $\theta = \dfrac{(2\pi m_u kT)^{3/2}}{h^3}$,

$$\tag{28.26}$$

one gets $\dfrac{n(A-1,Z)\,n_{\mathrm{n}}}{n(A,Z)} = 2\dfrac{U(A-1,Z)}{U(A,Z)}\left(\dfrac{A-1}{A}\right)^{3/2}\theta\,e^{-\frac{Q_{\mathrm{n}}}{kT}} . \tag{28.27}$

$U(A,Z)$ is the nuclear partition function, m_u the atomic mass unit (Appendix A.1) and Q_{n} the binding energy of a neutron within nucleus (A,Z). In the same way, one has for reaction $(A-2,Z-1) + p \rightleftharpoons (A-1,Z) + \gamma$

$$\frac{n(A-2,Z-1)\,n_{\mathrm{p}}}{n(A-1,Z)} = 2\frac{U(A-2,Z-1)}{U(A-1,Z)}\left(\frac{A-2}{A-1}\right)^{3/2}\theta\,e^{-\frac{Q_{\mathrm{p}}}{kT}} , \tag{28.28}$$

where Q_{p} is the binding energy of the protons within nucleus $(A-1,Z)$. n_{n} and n_{p} are the concentrations of neutrons and protons, the mass of both are approximated by m_{u}. By multiplying the above two relations, one obtains

$$\frac{n(A-2,Z-1)\,n_{\mathrm{p}}n_{\mathrm{n}}}{n(A,Z)} = 2^2\frac{U(A-2,Z-1)}{U(A,Z)}\left(\frac{A-2}{A}\right)^{3/2}\theta^2\,e^{-\frac{Q_{\mathrm{n}}+Q_{\mathrm{p}}}{kT}} . \tag{28.29}$$

The properties of the intermediate nucleus $(A-1)$ disappear, except its binding energy. Similar equations can be written until the nucleus (A,Z) is related directly

to the concentration of neutrons and protons. By applying Z times the expression for p and $(A - Z - 1)$ times that for n, one gets

$$\frac{n_n \, n_p^Z \, n_n^{A-Z-1}}{n(A,Z)} = 2^{A-1} \frac{2}{U(A,Z)} \left(\frac{1}{A}\right)^{3/2} \theta^{A-1} e^{-Q(A,Z)/(kT)}, \tag{28.30}$$

where $Q(A,Z) = [Zm_p + (A - Z)m_n - m(A,Z)]c^2$ is the binding energy (counted positive) of the nucleus (A,Z). The partition function for the neutron is 2, since it has two states of spin. Thus, we get

$$n(A,Z) = U(A,Z) A^{3/2} \frac{n_p^Z \, n_n^{A-Z}}{2^A} \theta^{1-A} e^{Q(A,Z)/(kT)}. \tag{28.31}$$

The most stable elements (largest $Q(A,Z)$) survive, this is why the elements of the Fe peak are more abundant. The neutrons disintegrate (n$\rightarrow$ p+e$^-$+$\bar{\nu}$), which increases the ratio of protons to neutrons. On the other hand, electrons can be captured reducing the above ratio. However, the β disintegrations are slower than nuclear reactions and these effects are rather limited.

28.5.2.1 The Fe Photodisintegration

The above relations can be applied to the photodisintegration of ^{56}Fe which occurs for $T > 10^{10}$ K and $\varrho > 10^{10}$ g cm^{-3} and leads to α nuclei:

$$^{56}\text{Fe} + \gamma \rightleftharpoons 14\,^4\text{He} - Q. \tag{28.32}$$

With(28.31), one gets the concentrations $n(56)$ and $n(4)$

$$\frac{n(56)}{n(4)^{14}} = \frac{56^{3/2}}{4^{21}} \frac{U(56)}{U(4)^{14}} \frac{n_n^2}{n_p^2} \theta^{-13} e^{[Q(56)-14Q(4)]/(kT)}. \tag{28.33}$$

$Q(56)$ and $Q(4)$ are the binding energies of ^{56}Fe and ^{4}He, thus $Q(56) - Q(4)$ is the energy needed to dissociate ^{56}Fe into ^{4}He. Taking $n_n/n_p \approx 1$ (or 15/13 as in the ^{56}Fe nucleus) and using $n_i = \varrho X_i/(A_i m_u)$, we get the following approximation for the relation ϱ vs. T where $X(56)$ and $X(4)$ are equal:

$$X(4)^{13} \varrho^{13} \approx 10^{157.5} \left(\frac{T_9}{3}\right)^{19.5} 10^{-443/T_9}, \tag{28.34}$$

where $T_9 = T/10^9$. The limit where the half of the Fe nuclei have been broken is shown in Fig. 28.15. Other limits can be studied the same way, for example for the dissolution of α into n and p, or the limits between ^{56}Fe and ^{54}Fe.

The state of quasi-equilibrium in the physical conditions of supernovae leads mainly to ^{56}Ni, which is radioactive and disintegrate through
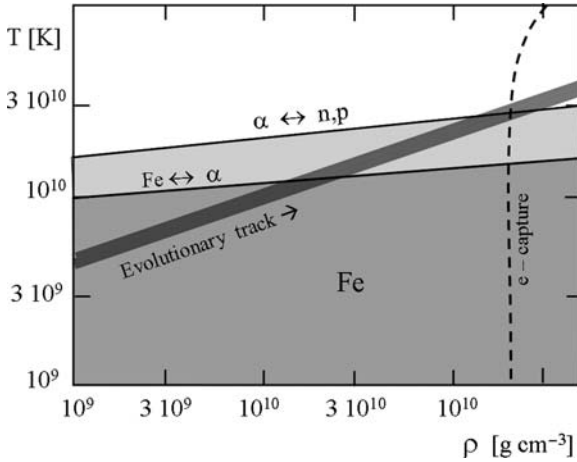
Fig. 28.15 Schematic evolutionary track of massive stars during core collapse with the lines where the half of the ^{56}Fe nuclei have broken to α and where the half of α have broken to n, p. Adapted from D.N. Schramm [522]

$$\underbrace{^{56}_{28}\mathrm{Ni}\,(e^-,\gamma)}_{t_{1/2}=6.1\,\mathrm{d}}\underbrace{^{56}_{27}\mathrm{Co}\,(e^-,\gamma)}_{t_{1/2}=78\,\mathrm{d}}{}^{56}_{26}\mathrm{Fe}\,. \tag{28.35}$$
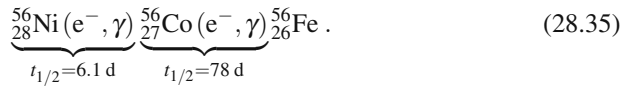
This sequence of disintegrations leads to ^{56}Fe, which is the most abundant element at high atomic mass. The γ rays of the second disintegration have been observed in SN1987A, they also powers the light curves of SN I and SN II after 1–2 months, giving a linear decrease of the brightness in magnitude scale as a function of time.

28.5.3 The Heavy Elements $A \geq 60$

The heavy elements beyond the iron peak can no longer be formed by fusion reactions [143, 403]. They form by neutron captures followed by β disintegrations, as an example

$$^{110}_{48}\mathrm{Cd} \to{}^{111}_{48}\mathrm{Cd} \to{}^{112}_{48}\mathrm{Cd} \to{}^{113}_{48}\mathrm{Cd} \to{}^{114}_{48}\mathrm{Cd} \to \underbrace{^{115}_{48}\mathrm{Cd}^*}_{} \longrightarrow \underbrace{^{116}_{48}\mathrm{Cd}}_{r-\mathrm{element}}\,.$$

$$\Downarrow \beta\ 54\,\mathrm{h}$$
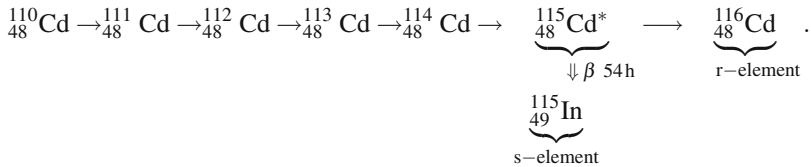
$$\underbrace{^{115}_{49}\mathrm{In}}_{s-\mathrm{element}}$$

If the neutron flux is low, the unstable $^{115}_{48}\mathrm{Cd}^*$ has time to disintegrate to indium $^{115}_{49}\mathrm{In}$ before a new neutron is captured. $^{115}_{49}\mathrm{In}$ is a s-element ("s"for slow) made when the neutron flux is low, i.e., in a slow process. On the contrary, if a new neutron is captured by $^{115}_{48}\mathrm{Cd}^*$ before it has time to disintegrate, the new element made,

here $^{116}_{48}$Cd, is said to be a r-element ("r" for rapid). Thus, if τ_β and τ_n are the characteristic times for β disintegration and between two successive n captures by the same nucleus, one has

$$\tau_\beta < \tau_n \quad \Longrightarrow \quad \text{s-elements,}$$
$$\tau_\beta > \tau_n \quad \Longrightarrow \quad \text{r-elements.}$$

τ_β depends on the nuclear species, while τ_n depends on the local neutron flux. s-elements represent about 70% of the elements formed by n captures. Some elements are produced by both processes, some by only one.

28.5.4 The s-Elements

The preferred sites are the AGB stars in the He-burning phase at $T \approx 3 \times 10^8$ K. The dominant neutron sources are

$$^{13}\text{C}(\alpha,\text{n})^{16}\text{O} \quad \text{for} \quad M < 3\,\text{M}_\odot$$
$$^{22}\text{Ne}(\alpha,\text{n})^{25}\text{Mg} \quad \text{for} \quad M \geq 3\,\text{M}_\odot$$
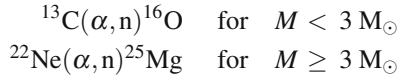
as discussed in Sect. 26.6.2. Neutrons are also produced by the second reaction in massive WR stars (Sect. 27.6), which form s-elements of lower A_i such as Sr, Y, Zr, while AGB stars form s-elements in the Ba peak preferentially (Fig. 28.14). A n capture is followed by a beta decay, which transforms a neutron into a proton, so that the stepwise path of the s-process in the plane (Z,N) remains close to the center of the stability valley (Fig. 28.16),

$$(Z,A)+\text{n} \longrightarrow (Z,A+1) \longrightarrow (Z+1,A+1)+e^- .$$
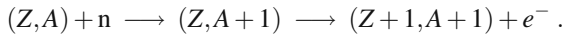
The typical value of the neutron concentration n_n for the s-process is about 10^7 cm^{-3} and $\tau_n \sim 10$ yr. For certain isotopes, there are various branching possibilities (e.g., ^{61}Ni in Fig. 28.16). In a medium with a neutron concentration $n_n(t)$, the variation of the abundance of an element "i" in the s-process can be written in terms of the concentrations (Sect. 25.1.2)

$$\frac{dn_i}{dt} = - <\sigma v>_i n_n(t)\,n_i(t) + <\sigma v>_{i-1} n_n(t)\,n_{i-1}(t) , \qquad (28.36)$$

where it is supposed that the β disintegration has the time to intervene. In an AGB star, $T \approx$ const. over long periods of time compared to nuclear timescales, thus $<\sigma v>$ is about constant and can be written as $<\sigma v>\approx \sigma(T)\,v_T$. The thermal velocities v_T vary with the mass of the nucleus, equipartition of energy being assumed. As the atomic numbers of heavy elements are high, one has $v_T(i) \sim v_T(i-1)$. Thus, one writes
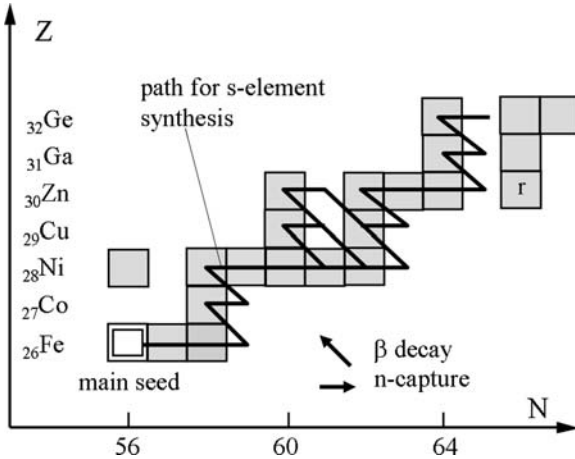
Fig. 28.16 The beginning of the path of s-elements in the Z, N plane of proton vs. neutron numbers. Adapted from F. Käppeler et al. [277]

$$\frac{dn_i}{dt} \approx v_T(i) \, n_\mathrm{n}(t) \left[-\sigma_i n_i(t) + \sigma_{i-1} n_{i-1}(t)\right] . \tag{28.37}$$

In stationary conditions, as during a nuclear phase, $dn_i/dt = 0$ and

$$\sigma_i n_i \approx \sigma_{i-1} n_{i-1} . \tag{28.38}$$

The products $\sigma_i n_i$ are constant. The elements with small cross-sections (such as for the magic Z and N numbers) have higher abundances, since they are less destroyed. Away from the seed element ^{56}Fe, there are less and less neutrons available since some of them have been captured before, especially at the "magic numbers" Z or $N = (2, 8, 20), 28, 50, 82, 126$. Thus, the products $\sigma_i n_i$ are about constant only over limited domain of atomic masses between two successive magic numbers. The observed abundances show different plateaux in a plot with the products $\sigma_i n_i$ vs. the atomic mass numbers. More complex solutions of (28.36) taking into account the decreasing value of n_n for heavier nuclei, the transitions between plateaux, etc., can be found. However, numerical models of the s-element synthesis are preferable.

28.5.5 The r-Elements

The r-elements are formed in supernovae SN II in very different conditions than the s-elements with neutron concentration $n_\mathrm{n} \approx 10^{19} - 10^{25}$ cm^{-3}, giving interval between two successive neutron captures $\tau_\mathrm{n} \approx 10^{-6}$ to 1 s. They are likely formed in the deep layers surrounding the collapsing core. There is no evidence of intermediate conditions for the synthesis between these and those of the s-process. At

high T and neutron flux, there is a quasi-equilibrium between neutron captures and photodisintegrations:

$$n + (Z, A) \rightleftharpoons (Z, A+1) + \gamma.$$
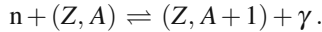
The neutron captures lead to a path of newly formed nuclei much outside the stability valley, the path shown as a thick gray line in Fig. 28.17 corresponds to a neutron energy of 2.4 MeV. On the r-process path, the new nuclei tend to accumulate at the magic Z and N numbers, where the cross-sections for further n captures are much smaller (the distribution of the elements on the r-process path could be calculated with statistical equilibrium, Sect. 28.5.2).

When the n irradiation is over, the elements on the r-process path (mainly on its intersection with the lines of magic Z and N) disintegrate by a cascade of several β decays which bring them to the stability valley,

$$(Z, A) \longrightarrow (Z+1, A) + e^- + \nu_e .$$
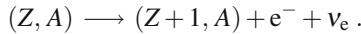
The farther a nucleus lies from the stability valley in Fig. 28.17, the faster its β disintegration occurs. The β disintegrations make shifts along a line $A = $ const., i.e., a diagonal going leftward and upward from the r-path to the stability valley. The elements accumulated at magic numbers on the r-process path arrive on the stability valley with a lower atomic mass number than the one of the s-process elements
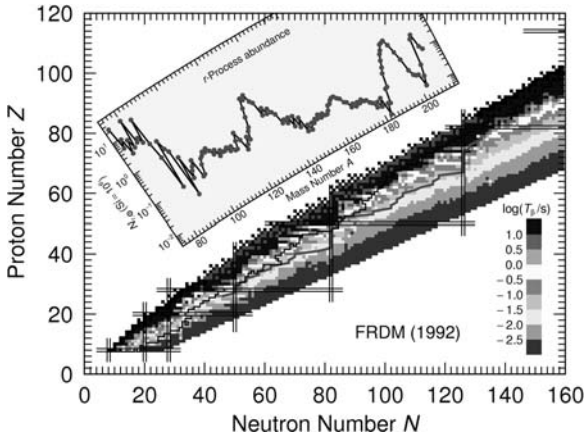
Fig. 28.17 Z vs. N plane of protons vs. neutron numbers. The valley of stability is formed by the black squares denoting β-stable nuclei. The gray region in the main graph shows calculated half-life with respect to β^- decay. The jagged black line gives the right-hand boundary of the region of known nuclei. The thick gray line shows the r-process path for typical stellar conditions. The solar r-process abundances shown in the insert are plotted vs. the mass number A, whose axis is curved slightly to follow the line of β-stability. A line perpendicular to the valley of β-stability and originating at a particular mass value crosses the A axis of the insert plot at right angles at this value and also passes through the point giving the abundance for this A value. The double lines show the magic numbers N and Z. Courtesy from P. Möller

with the same magic number (see also [426]). This is why in the distribution of the element abundances (Fig. 28.14) the peaks of r-elements are found at a lower atomic number than for the s-elements [291].

Fissions of heavy nuclei also occur forming lighter nuclei, fission determines the heaviest nuclei formed in the r-process. During the cascade of several β disintegrations, there is also some (γ, n) reactions, so that the nuclei which disintegrate are a bit shifted in atomic masses when they reach the stability valley. Thus, the products $\sigma_i n_i$ are scattered contrarily to the case of the s-elements. There is a big difference in the abundances of elements with odd and even (more stable) atomic numbers for the s-process, while it is not the case for the r-process.

The T and n_n conditions better reproducing the observed abundances of r-elements are $T \geq 10^9$ K, $n_n \approx 10^{20}$ cm^{-3} corresponding to $\tau_n \approx 1$ s [142]. Higher values of T and n_n are certainly reached during the SN explosion, however, the abundances keep mainly the signatures of the "freeze-out" time, i.e., when at the end of the synthesis process the timescale τ_n increases and becomes of the order of τ_β. The peaks of abundance are narrow and are the same in old halo stars as at solar abundances, this suggests a narrow range of stellar properties for the synthesis of the r-elements, not too different in the early galaxy as today [143]. Is this a property of the layers just surrounding the collapsing core and close to the cutoff mass?

The sum of the abundances of r-elements represents a mass fraction $\sum_i X_i \approx 10^{-7}$, which corresponds to $\sim 10^4$ M$_\odot$ of r-elements in the Galaxy. With ~ 3 SN per century, the Galaxy has experienced 10^8–10^9 SN, this makes an average of 10^{-4} to 10^{-5} M$_\odot$ of r-elements per SN, which is surprisingly small. Is there only a small fraction of the SNe producing r-elements? Plots of the abundances of chosen r-elements as a function of the Fe abundances show [143] more scatter in the early galactic evolution for the heavier r-elements (like Eu) than for the lighter r ones (like Ge). This may suggest that fewer r-process events produce the heavier r-elements. On the whole, many questions remain regarding the conditions and supernovae producing the r-elements at different stages of the galactic evolution.

28.5.5.1 The p-Elements

There are also p-elements with peaks at ^{92}Mo and ^{144}Sm, less abundant than the s- and r-elements by about one to two orders of magnitude. They are neutron poor and located on the other side of the stability valley with respect to r-elements. They may have several formation sites. Contrarily to simple expectations, the p-elements are probably not resulting from p-captures on Fe-peak elements, since conditions for p-captures are unlikely [477]. It is more probable that the p-elements are formed by (γ, n) reactions at $T = (2 - 3.3) \times 10^9$ K in the O/Ne layers during a SN explosion, on pre-existing s-elements (e.g., formed during He burning) [477].

28.6   Evolution of Rotation: Pulsars and GRBs

28.6.1   Distribution of the Specific Angular Momentum

The evolution of the internal stellar rotation is an interesting question pertaining to the rotation rates of pulsars as well as to the origin of the gamma ray bursts. It is determined by Eq. (10.122) accounting for all internal transport processes and by losses of mass and angular momentum at the surface (Sect. 14.4). After He exhaustion, the evolution is so fast that the angular velocity Ω is essentially determined by convection (supposed to maintain $\Omega = $ const.) and by the local conservation of the angular momentum, which imposes $\Omega(r)r^2 = $ const. for a mass element (at the equator), while the critical angular velocity Ω_{crit} behaves like $\Omega_{\mathrm{crit}}^2 r^3/(GM) \approx 1$. Thus, the local conservation leads to

$$\frac{\Omega(r)}{\Omega_{\mathrm{crit}}} \sim \frac{1}{r^{1/2}}. \tag{28.39}$$

Thus, as r decreases for a given mass element, its $\Omega(r)$ tends to get closer to the critical value. In the advanced phases, one generally ignores the transport processes other than convection, as they are acting on too long timescales. Even the dynamical shear (Sect. 12.2.2) has a limited action, owing to the very thin layers where it is present [251]. Figure 28.18 shows the evolution of the internal Ω profile in a $25\,M_\odot$ star from the ZAMS to the end of the core Si burning. During the MS, Ω decreases globally, because mass loss removes angular momentum, and meridional circulation makes an internal coupling. In the He phase, the contracting core spins faster, while the envelope slows down a lot in the red-supergiant phase before being lost. The central regions spin faster and faster as they contract, Ω nevertheless remains subcritical, reaching a value of $1\,\mathrm{s}^{-1}$ at the end of the Si phase.

We examine the evolution of $j(r) = (2/3)\Omega(r)r^2$ the specific angular momentum of a given shell mass of radius r. Pure contraction or expansion do not modify $j(r)$. Transport processes generally remove angular moment from the center to bring it into the outer layers. Convection, assumed to impose constant Ω, produces a tooth of $j(r)$: from the basis to the top of a convective zone $j(r)$ increases like r^2. At the edges of the convective zones, there are discontinuities of μ and Ω. Figure 28.19 shows the evolution of $j(r)$ from the ZAMS to core collapse. Most of the decrease of $j(r)$ occurs during the MS phase, as a result of mass loss and outward transport of angular momentum by circulation. The decrease of $j(r)$ in the He-burning phase is small. From there, the changes are small and mostly due to the teeth made by convection without a great difference in the mean curve [237]. From the end of the He burning to the end of the Si burning, the decrease of the total angular momentum is only 24%, while it was a factor of 5 between the ZAMS and the end of the He-burning phase in the example of Fig. 28.19. This shows the need for a careful treatment of rotation in the MS phase.
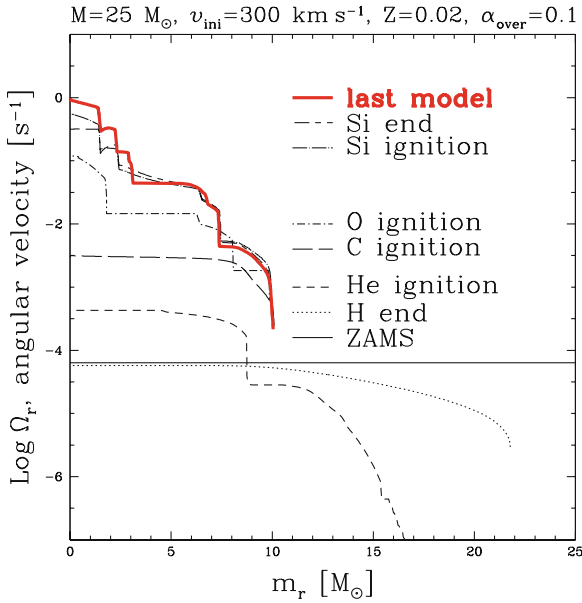
Fig. 28.18 Angular velocity as a function of the Lagrangian mass of a model with initially $25\,M_\odot$, $X = 0.705$, $Z = 0.02$ and $v = 300$ km s^{-1} at various stages up to the collapse (no magnetic fields). From Hirschi et al. [251]
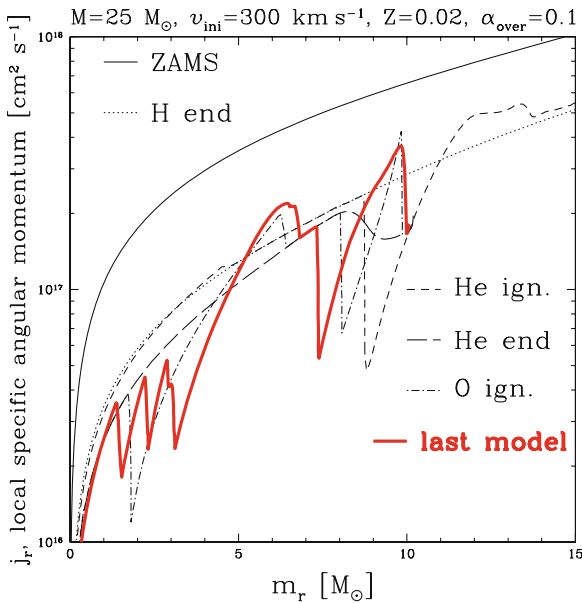
Fig. 28.19 Distribution of the specific angular momentum at various stages for the models of Fig. 28.18. From Hirschi et al. [251]

28.6.2   The Rotation of Pulsars

In the ATNF [22] catalogue of pulsars, there are about 20 pulsars with period $P <$ 100 ms (the shortest period is $P = 16$ ms and the second one is 33 ms for the Crab pulsar). The ages (as pulsars) are $< 10^5$ yr, they have slowed down slightly, but their periods at birth were likely ≥ 10 ms. From Fig. 28.18, the velocity at the end of Si burning is of the order of $\Omega \sim 1$ s^{-1} with a density of about 10^8 g cm^{-3} (Fig. 28.4). For a given element of mass with angular momentum conservation, the angular velocity varies like

$$\Omega \sim \frac{1}{r^2} \sim \varrho^{2/3} \,. \tag{28.40}$$

The neutron stars with a density above 10^{14} g cm^{-3} would spin with $P \sim 0.1$ ms. This is about two orders of magnitude faster than the most rapid pulsars. Thus, large amounts of angular momentum have to be lost somewhere, either during the core collapse or in the previous stages. The magnetic field, which enforces strong internal coupling, is a good candidate, because of its capacity to transport the fast rotation from the center to the outer layers (Sect. 13.5). Models [240] including the Tayler–Spruit dynamo (Sect. 13.4.2) indicate that internal magnetic fields reduce the final rotation rate of an iron collapsing core by a factor 30–50 compared to the non-magnetic case. Most of the reduction occurs in the H- and He-burning phase, because magnetic field is strong enough to impose solid rotation in these phases (cf. Sect. 13.6.1). For a 15 M$_\odot$ star in this grid, a period of 15 ms is predicted [240] for a pulsar at birth, close to the observed range.

28.6.3   GRBs: A Challenging Problem

Gamma ray bursts (GRB) are intense flashes of electromagnetic radiation with energies ~ 100 keV. They are the most energetic events ($\geq 10^{51}$ erg) in the Universe, they are isotropically distributed, every day one GRB occurs in the whole observable Universe. GRBs have been seen up to very high redshifts ($z > 6$). Their study gives information on stars in the early Universe. Observations indicate that long soft GRBs (a few s) are associated with the supernova explosion of massive stars (cf. Woosley and Bloom [619]). In a few cases, it has been possible to observe the type of the supernova: in four well-established cases [157], the SN was of type Ic, with no H and He lines. Such observations give support to the collapsar model proposed by Woosley [618], who suggests that the progenitor of the GRB is a massive WR star that collapses into a fast rotating black hole. Fast rotation allows part of the infalling matter to form a disk around the black hole, the disk acting as an efficient engine to extract gravitational energy. The specific angular momentum j needed is at least the value of the last stable orbit around a rotating black hole of mass M_{BH} [619]

$$j = \frac{2}{\sqrt{3}} \frac{GM_{BH}}{c} = 0.5 \times 10^{16} \frac{M_{BH}}{M_\odot} \quad \text{in cm}^2\text{s}^{-1}. \tag{28.41}$$

Such a high central angular momentum implies a high differential rotation in the progenitor. There are three components participating in the GRB. Part of the rotation energy powers strong relativistic polar jets and the GRB arises from interactions in these jets. The jets (1) are highly collimated, however, most of the energy in the explosion lies in the sub-relativistic ^{56}Ni-rich broad ejecta (2) (~ 1 radian) making the supernova. There is also a low-velocity component (3) which can fall back after the initial explosion [621]. The different proportions of these three components give a variety of GRBs and may perhaps vary with Z. The short duration of the GRBs points toward compact progenitors, i.e., stars that have lost their outer envelopes, like WR stars possibly of the WO subtype with little or no He left consistently with the SN Ic precursors (Sect. 27.5.1).

Only a very tiny fraction of supernovae or even of SN Ibc, and *a fortiori* of WR stars, leads to GRBs: the fraction of type Ibc supernovae leading to GRBs is between 0.5 and 4% [157]. Various observations of GRBs in galaxies point toward a very massive progenitor in a metal poor environment ($< (1/3) Z_\odot$). The understanding of GRB progenitors is challenging. On one hand, the star has to lose a large fraction of its initial mass to make a star with little helium left. On the other hand, the stellar core must keep a high specific angular momentum ($j > 10^{16}$ cm^{-2} s^{-1}) for the collapsar model to work. These two constraints are relatively contradictory, because the removal of a lot of mass often implies the loss of a lot of angular momentum.

28.6.4 Models for the GRB Progenitors

As indicated above, the formation of a collapsar requires at least three conditions:

- The central region must have retained a high specific angular momentum.
- The H and most of the He-rich envelope must have been thrown away in previous phases (extreme WC or WO star).
- The core size at the pre-supernova stage must be massive enough for forming a black hole ($M_{core} > 3$ M$_\odot$).

Models accounting for the effects of rotation but without magnetic fields have no difficulty in preserving enough angular momentum in their central regions [237, 252]. The conditions that the progenitor is a WO star is consistent with metal-poor environments [252, 539], see also Sect. 27.6.2. However, the mentioned models overestimate the frequency of GRBs. Binary mass transfer may bring large amounts of angular momentum, however, these amounts are about compensated by the tidal losses due to spin orbit coupling [469]. Models with magnetic fields have also been made [240]; the formation of a collapsar is difficult, the magnetic field extracting too much angular momentum.

A way to overcome this difficulty was proposed by Yoon and Langer [626] and Woosley and Heger [621, 622], who computed the evolution of fast rotating massive
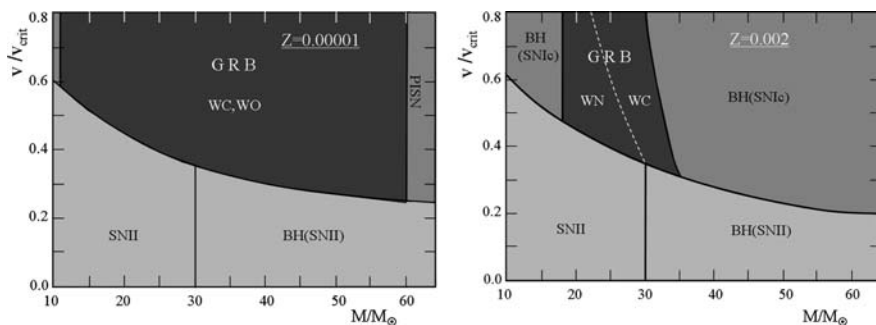
Fig. 28.20 Final fate of rotating massive stars as a function of the initial rotation velocity and mass. *Left*: for $Z = 10^{-5}$. *Right*: for $Z = 0.002$. Above the solid line, the models evolve quasi-homogeneously. The area of GRB progenitors is indicated by the nature of the WR stars. BH means black holes as a final stage, PISN means pair instability SN. Adapted from S.-C. Yoon et al. [626]

stars with magnetic fields which follow tracks of homogeneous evolution as in Fig. 25.15. These stars remain in the blue part of the HR diagram [344] and avoid the red-supergiant phase, thus they lose less angular momentum. They enter early into the WR phase due to the strong rotational mixing. The stars may keep a high rotation (but not sufficient, see below) when account is given to the weaker winds of WR stars at lower Z [150, 603].

The rarity of the GRB events is due to the fact that the GRB progenitors only occur for high initial stellar masses, for very high rotational velocities and for low metallicities $Z < 0.004$ [626]. Figure 28.20 show the final fate of the models as a function of the initial masses and velocities for two metallicities [626]. The relative frequency of GRBs increases with decreasing Z (and thus higher redshifts). A frequency of 5×10^{-3} for GRBs relatively to core-collapse SN (initial $M \geq 9\ M_\odot$) is predicted on the average in the Universe. The binary mass transfer may also lead to an homogeneous evolution, in which the mass transfer leads to high required rotation rate [85].

Thus, homogeneous evolution seems to permit rotating massive stars with magnetic field to keep enough angular momentum. However, there is still a problem: the above models have too much He to make a SN Ic (without H and He). A possible solution has been proposed in terms of the anisotropic winds (Sect. 14.4): the anisotropic winds permit the homogeneously evolving star with magnetic field to lose enough mass to make a WO star (thus giving a SN Ic) and to keep at the same time enough angular momentum to make a collapsar [413]. The velocity of the final WR star is about $20\,\mathrm{km\ s^{-1}}$ in the isotropic case and about $400\,\mathrm{km\ s^{-1}}$ in the anisotropic one, with an angular momentum $j = 5.6 \times 10^{16}\ \mathrm{cm^2\ s^{-1}}$ large enough to permit the collapsar model to work, while it is not the case with isotropic winds.

Many progresses should intervene in a near future, both on the observational side with more constraints on the progenitors and also on the theoretical side with a better magnetohydrodynamics in the models.

Chapter 29
Evolution of $Z = 0$ and Very Low Z Stars

The scientific curiosity, which is the quest for the understanding of our environment at small and large scales, is a honor of mankind. Among the deep questions, the study of the origin and history of our Universe is a major one as well as the search and studies of the zero-metallicity stars. These stars are the first ones born in the Universe after the Big Bang. Most of them no longer exist today. They have shaped the initial chemical evolution of the galaxies and their products have been recycled over and over.

The nucleosynthetic signatures of the ejecta of the first generations are present in the old most metal poor stars of the galactic halo. Some of these living fossils have been discovered recently, showing peculiar abundances with relative excesses of C, N, O elements over iron reaching factors up to 10^4 with respect to solar ratios. This shows that the first stars were evolving very differently and also had a different nucleosynthesis. At zero metallicity, everything is different: stellar opacities are much lower, the CNO cycles do not work initially, mass loss by radiative winds is very low. All these differences drastically modify the evolution and nucleosynthesis.

Star formation at $Z = 0$ (Chap. 23) leads to two populations: Pop. III and Pop. II.5 stars. Pop. III results from $Z = 0$ stars formed in an unperturbed environment, their masses are of the order of 10^2 M$_\odot$ or more (Sect. 23.5). Pop. II.5 stars are formed at $Z = 0$ from gas which has been shocked and ionized. This leads to the formation of deuteride HD molecules, which cool the gas and allow stellar formation with typical masses of the order of 10 M$_\odot$, an order of a magnitude larger than typical Pop. I and II stars. Pop. II.5 stars are likely to represent about 90% of the $Z = 0$ stars. There are suggestions [123, 358] that the first stars may have been fast rotators.

29.1 Basic Properties and Evolution of $Z = 0$ Stars

29.1.1 Differences in the Physics

We can directly infer a few physical consequences of $Z = 0$ on stellar models.

– There are no CNO cycles working initially. Only the pp chains are present. In high-mass stars they are insufficient to stop contraction until the 3α reactions start producing ^{12}C, then the CNO cycles may work.
– The opacities are generally lower (for low M), which makes a larger outgoing luminosity (3.25) and a smaller radius (24.49). In massive stars, dominated by electron scattering, the difference is small.
– Two effects are making the radius smaller at $Z = 0$: contraction and opacity (see Fig. 25.7).
– The central T and ϱ are higher due to the smaller radius (1.51).
– Convection is less efficient, because $\nabla_{\rm rad}$ (5.32) is smaller due to the lower κ and also due to the higher internal T.

While in standard evolution, the nuclear networks for H burning (pp+CNO) and He burning can be treated separately, since the reactions occur at very different T and ϱ values, this is no longer the case at $Z = 0$. A unique nuclear network with both H and He burnings must be built, since the two sets of reactions occur simultaneously.

Stellar winds are a big question. In many models at $Z = 0$ the mass loss rates are set to zero, owing to the fact that the $\dot{M}$-rates scale like $Z^{0.7}$ (27.2). The mass loss rates down to $Z = 10^{-4} Z_{\odot}$ have been studied by Kudritzki [296] with an appropriate distribution of line strengths. Using for $Z = 0$ the $\dot{M}$ rates for $10^{-4} Z_{\odot}$, Marigo et al. [375] found that radiative winds are unimportant except for stars with $M > 750\,{\rm M}_{\odot}$. In Sect. 29.2, we show that mass loss plays a role at very low Z only for the fast rotating stars.

29.1.2 The HR and $\log T_{\rm c}$ vs. $\log \varrho_{\rm c}$ Diagrams

Figure 29.1 shows the HR diagram for stars of 1–$100\,{\rm M}_{\odot}$ [377]. The low and intermediate mass stars at $Z = 0$ are hotter and more luminous compared to stars of standard composition (Fig. 25.17). Above $15\,{\rm M}_{\odot}$, there is almost no difference in L since the opacity is due to electron scattering, however, the radii are a factor of 4 smaller because the stars have contracted until He ignition (next section). The shift in $\log T_{\rm eff}$ of the ZAMS at $100\,{\rm M}_{\odot}$ amounts to 0.27 dex, at $5\,{\rm M}_{\odot}$ to 0.21 dex, at $1\,{\rm M}_{\odot}$ to 0.05 dex with respect to Pop. I stars. The MS lifetimes are shorter at $Z = 0$ for the low and intermediate masses compared to Table 25.6 at $Z = 0.02$: for a $1\,{\rm M}_{\odot}$ star it is 6.11 Gyr compared to 9.85 Gyr, at $2\,{\rm M}_{\odot}$ 0.635 Gyr compared to 1.12 Gyr, at $5\,{\rm M}_{\odot}$ 67.3 Myr compared to 94.5 Myr, at $15\,{\rm M}_{\odot}$ 11.3 Myr compared to 11.6 Myr. For higher mass stars, the differences are negligible. The ratio of the He to the H lifetimes is 1.6, 7, 10, and 9% at 1, 2, 5, 15 $M_{\odot}$ and above.

Figure 29.2 shows the evolution of central conditions [377], which shows the slope $T_{\rm c} \sim \varrho_{\rm c}^{1/3}$. Below about $15\,{\rm M}_{\odot}$ the pp chains supply energy while contraction still proceeds until the 3α reactions start and make enough ^{12}C for the CNO cycles
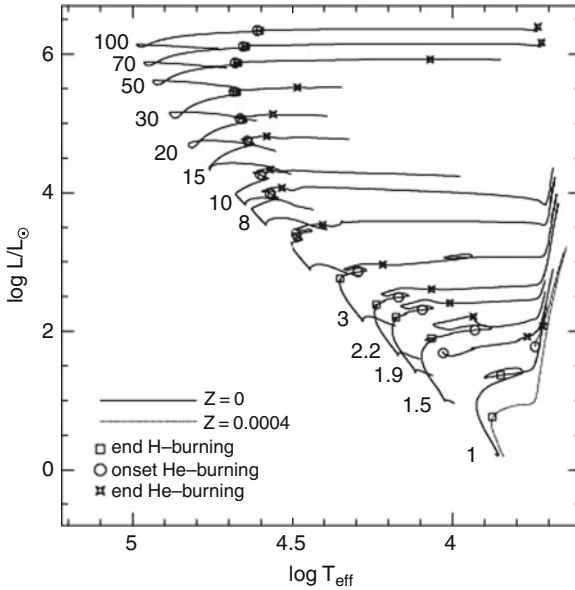
Fig. 29.1 Evolutionary tracks at $Z = 0$ up to the TP-AGB phase for intermediate mass stars and up to C ignition for massive stars. An overshooting with an extent of 0.5 H_P is applied for $M \geq 1.1$ M$_\odot$. The dotted line shows a 1 M$_\odot$ model at $Z = 0.004$. From P. Marigo, L. Girardi, C. Chiosi and P.R. Wood [377]

to work. Above 15 M$_\odot$, the pp chains have little effect and contraction proceeds until the 3α and CNO cycles start working.

29.1.3 Low-Mass Stars ($M < 3$ M$_\odot$)

H burning occurs with the pp chains. The central T is not high enough for He ignition. The radii on the ZAMS are not very different from those at higher Z (see case of 1 M$_\odot$ in Fig. 29.1). The tracks first go upward to the blue in the HR diagram, then they turn to the right when the central H content decline. During this phase, the central regions contract, become partially degenerate and heat up. The mild onset of the 3α reactions on line b) in Fig. 29.2 permits the CNO cycles to start. The CNO energy production, controlled by the 3α reactions, increases and the stellar cores expand (Fig. 29.2). Convection develops and brings H into the central degenerate regions, creating a small CNO flash. The 1 M$_\odot$ star makes a small loop before the end of the H-burning phase, while higher masses make the small loop during the He phase. After the core H-burning phase, the central regions contract a lot and the stars go up the red giant branch.

The central He ignition is marked by a large core expansion. Stars in the range of 1.5–3 M$_\odot$ make loops in the HR diagram phase during the He-burning phase. Then,
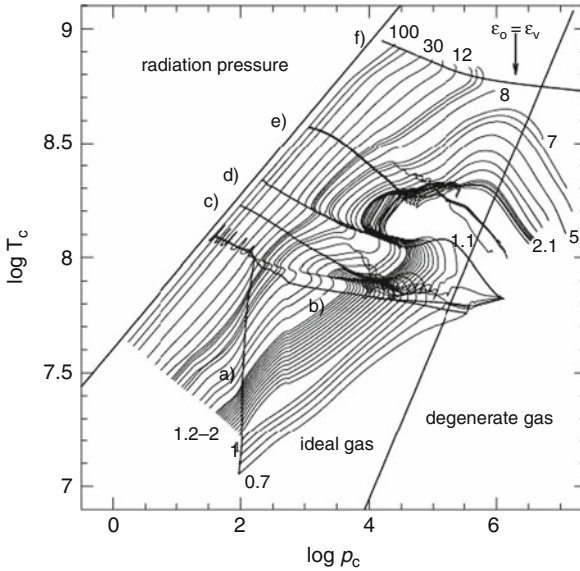
Fig. 29.2 Evolution of central conditions at $Z = 0$ (models of Fig. 29.1). The domains of different equations of state are indicated. Line (**a**) shows the onset of the pp reactions, (**b**) the onset of the 3α reaction which permits the CNO cycles to start, (**c**) the end of core H burning, (**d**) the central He ignition, (**e**) the end of the core He-burning phase and (**f**) the place where the neutrinos losses compensate for C burning. From P. Marigo, L. Girardi, C. Chiosi and P.R. Wood [377]

the cores contract again and the stars evolve to the red giant branch with a H-burning shell migrating outward. A He flash also occurs but at a luminosity lower by 1 dex than at standard composition.

29.1.4 Intermediate Mass Stars ($3 \, M_\odot < M < 10 \, M_\odot$)

As an example, we examine the case of a $5 \, M_\odot$ star at $Z = 0$ from the ZAMS to the end of the He-burning phase, described in details in Fig. 29.3 and Table 29.1. This evolution is a bit intricate and a bit of an academic problem, however, it is a nice illustration of the variety of possible star evolutions …

On the ZAMS, the pp chains partially stops the contraction. During most of the H burning (A–E), the star stays close to the ZAMS, since the ongoing contraction more or less compensates for the envelope expansion. The convective core disappears in the middle (point B) of the H-burning phase. The star becomes entirely radiative and partially degenerate in the center, which prevents central collapse. In C, the central $\varrho = 8.11 \times 10^2$ g cm^{-3} and $T = 8.4 \times 10^7$ K which permits the creation by the 3–α reaction of some very small amount of ^{12}C enabling the CNO cycles to ignite. A new convective core develops, which brings H to the center. The CNO cycles, controlled
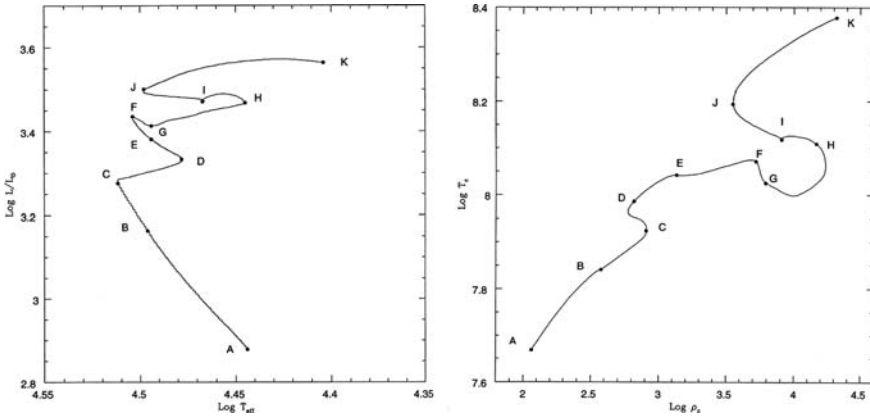
Fig. 29.3 *Left*: The detailed evolutionary track of a $5\,M_\odot$ star at $Z = 0$. Further information on the points A, B, C... is given in Table 29.1. *Right*: central evolution of the same model. From J.M. Feijoo [182]

Table 29.1 Evolution of a $5\,M_\odot$ star at $Z = 0$ with reference to Fig. 29.3. M_{cc} is the mass of the convective core, X_c, Y_c are the central values of the H and He abundances. From J.M Feijoo [182]

Age(in 10^6 yr)	Point	M_{cc}	X_c	Y_c	Central ^{12}C	Central ^{16}O
0.641	A	0.260	0.760	0.240	0.000	0.000
44.476	B	0.000	0.338	0.662	0.000	0.000
53.468	C	0.002	0.161	0.839	2×10^{-12}	0.000
63.477	D	0.111	0.016	0.984	8×10^{-11}	4×10^{-11}
64.029	E	0.000	0.000	1.000	6×10^{-9}	3×10^{-9}
64.128	F	0.000	0.000	0.999	5×10^{-4}	4×10^{-7}
64.193	G	0.000	0.000	0.999	6.6×10^{-4}	1×10^{-6}
65.149	H	0.024	0.000	0.997	0.002	3×10^{-6}
65.424	I	0.021	0.000	0.980	0.019	1.7×10^{-4}
68.463	J	0.084	0.000	0.593	0.333	0.073
71.285	K	0.000	0.000	0.000	0.202	0.798

by the 3α reaction, dominates the energy production. Around the core, there is a broad H-burning shell with active pp chains. The star evolves inhomogeneously and expands from C to D. In D, the central H content is low and to compensate for the energy deficit, the star contracts to E, where $X_c = 0$. It then further collapses to F. Noticeably, the star has two H-burning shells, an internal very peaked one due to the CNO cycles and a broader one due to the pp chains. From D to I, the evolution is fast ($\sim 10^6$ yr).

From F to G, the 3α reaction starts working, contraction slows down, the CNO H-burning shell amplifies and provokes a stellar expansion, which reduces T. From G to H, the central He burning amplifies and expansion goes on. In H, a small convective core appears and develops up to I and J, the central density decreases, which by the mirror effect produces an overall stellar contraction up to J. In J, one

is close to the middle of the He-burning phase, a lot of ^{12}C has been created and the ^{12}C$(\alpha, \gamma)^{16}$O becomes more significant. The core produces 38% of the luminosity, the peaked CNO shell 22% and the broad pp shell 40%. From J to K, the luminosity increases due to the higher μ. As He diminishes in the center, central contraction restarts, the envelope expands and the star evolves to the red. At He exhaustion in K, the central O content is about 80%. The further evolution up to C ignition leads the star to the red giant branch for a short time (Fig. 29.1).

29.1.5 High-Mass Stars ($M > 10\,M_\odot$)

The evolution is simpler (Figs. 29.1 and 29.2). The pp chain is insufficient to stop contraction which goes on until the 3α reaction starts and produces a mass fraction of ^{12}C of about 4×10^{-12}. The CNO cycles ignite and make a convective core. An almost "normal" MS phase in the HR diagram follows (Fig. 29.1), the 3α reaction controlling the CNO cycles. At the end of the MS phase, the central ^{12}C content is $\sim 10^{-9}$. Core He burning starts right away, there are also two H-burning shells, a thin CNO one and a broader pp shell. For a 20 $M_\odot$ star, the whole He-burning phase is in the blue, as a result of the constant mass and low Z, in a more pronounced way compared to Sect. 20.2. Only the most massive stars evolve to the red near the end of the He-burning phase. The central evolution is very linear in Fig. 29.2.

29.1.6 Other Properties: Mass Limits and CO Cores

The mass limit $M_{\rm HeF}$ for the He flash is $\sim 2.2\,M_\odot$ at $Z = 0.02$ (Sect. 26.4.1). $M_{\rm HeF}$ decreases with Z down to about $1.7\,M_\odot$ at $Z = 10^{-5}$, because lower Z stars have larger convective cores and thus from that point of view behave as more massive stars. At $Z = 0$, $M_{\rm HeF}$ further drops down to $\sim 1.1\,M_\odot$ for the above reason and because of the large shift of the tracks in the $\log T_{\rm c}$ vs. $\log \varrho_{\rm c}$ diagram (Fig. 29.2), which due to higher T just prevents the 1.1. $M_\odot$ star to enter the degenerate region.

The mass limit $M_{\rm UP}$ is the mass limit above which non-degenerate C-ignition occurs. It is $\approx 8.9\,M_\odot$ without overshooting and of $6.6\,M_\odot$ with moderate overshooting at $Z = 0.02$. $M_{\rm UP}$ decreases with decreasing Z down to about 5.9 $M_\odot$ at $Z = 10^{-5}$, due to the larger core masses at lower Z, as above. Surprisingly at $Z = 0$, $M_{\rm UP}$ raises again to about 8 $M_\odot$ [377], the reason is that when the pp chains dominate the convective cores are smaller, thus a higher total mass is necessary to be at the limit.

Figure 29.4 shows the masses of the He and CO cores as functions of the initial masses for three values of Z. While at standard Z, mass loss leads to WR stars and very low He- and CO-core masses, there is little differences for low Z and $Z = 0$ models. The masses of the CO core are indicative of what the nucleosynthesis might be if there is no rotation effects.
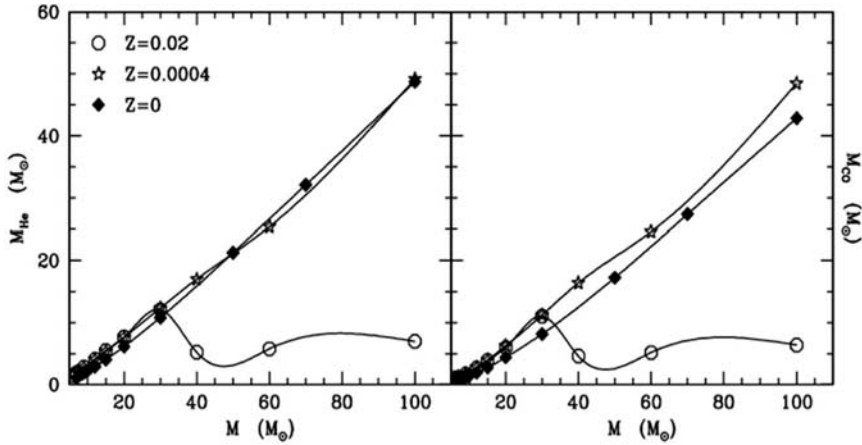
Fig. 29.4 Masses of the He and CO cores at C ignition in models with overshoot and various Z. From P. Marigo, L. Girardi, C. Chiosi and P.R. Wood [377]

29.2 Rotation Effects at Z = 0

29.2.1 HR Diagram and Lifetimes

In general, at a given ratio Ω/Ω_c of the critical angular velocity, the effects of rotation are larger at lower Z (Chap. 27), in addition there are more fast rotators at lower Z [358, 378]. We do not know the distribution of velocities at $Z = 0$, however, there are indications of extreme rotations at very low Z [123]. We emphasize that conclusions may be drawn only if a correct physics of transport by meridional circulation is accounted for.

Stellar models at $Z = 0$ with and without rotation are shown in Fig. 29.5 [175], see also Table 29.2. Mass loss rates from Kudritzki [296] for the lowest Z are used, with account for the rotational effects (14.45). If a model reaches the critical rotation, the unbound superficial layers are lost entering a disk which further dissipates. Rotation does not make big differences in the HR diagram (Fig. 29.5) despite the fact that the models reach critical velocities during the MS phase. The main difference is a drop of L when redward evolution starts, because some carbon diffuses from the core toward the H-burning shell, producing a sudden ignition of the CNO cycles driving convection in the H shell. This flash leads to a retraction of the convective core and a drop of L. Then, the star has a classical structure, with a He-burning core, a H-shell burning and an expanding envelope.

The rotating tracks end in a cooler part of the HRD than their non-rotating counterparts. The rotating 15 and 25 $M_\odot$ models end their life in the blue. The 85 $M_\odot$ experiences a blue loop after He burning. None of the models become a WR star. The MS lifetimes are increased by rotation from 12.8% for the 200 $M_\odot$ up to 24.5% for the 15 $M_\odot$ (Table 29.2). The lifetimes in the He-burning phase remain the same
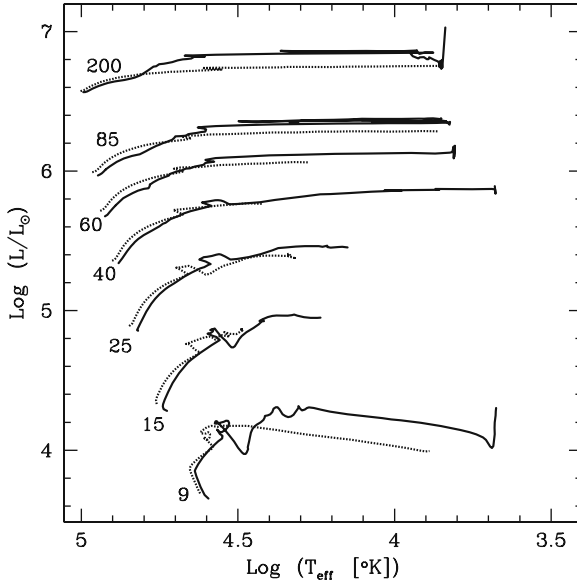
Fig. 29.5 Models with $X = 0.76$ and $Z = 0$ up to Si burning (C ignition for 9 and He exhaustion for 200 M$_\odot$). An overshooting with $d_{over} = 0.2 H_P$ is applied during the H- and He-burning phases. Models with rotation (continuous lines) and without (dotted lines). From S. Ekström et al. [175]

Table 29.2 Final M in M$_\odot$ after He exhaustion, initial v in km s^{-1}, lifetimes in the H- and He-burning phases in Myr, M_{CO} in M$_\odot$. The first column is for $v = 0$ and the second for the indicated v. From S. Ekström et al. [175]

Mass	v_{ini}	M_{fin}		t_H		t_{He}		M_{CO}	
9	0 500	9.00	9.00	19.50	23.90	1.99	2.58	1.13	1.20
15	0 800	15.00	14.96	10.60	13.20	0.83	0.98	2.92	2.71
25	0 800	25.00	24.75	6.64	7.88	0.56	0.50	5.39	6.30
40	0 800	40.00	37.99	4.60	5.41	0.36	0.41	14.52	13.53
60	0 800	59.99	57.59	3.60	4.20	0.30	0.31	25.11	30.58
85	0 800	84.94	74.57	3.05	3.52	0.31	0.28	34.50	43.92
200	0 800	199.95	183.56	2.27	2.56	0.23	0.24	95.69	95.97

except for 9 and 15 M$_\odot$, where there is an increase as a result of the drop in luminosity. The mass of the CO core at the end of central C burning are given in Table 29.2.

29.2.2 Evolution of the Rotation, Final Masses

At $Z = 0$, the existence of magnetic field is not likely, thus the main internal coupling process between the fast contracting core and surface is meridional circulation.

Figure 29.6 shows the internal profile of the vertical component $U_2(r)$ of the velocity of meridional circulation in $20\,M_\odot$ models of different Z. At $Z = 0.02$, there is a huge Gratton–Öpik cell (Sect. 11.5), which transports the angular momentum from the interior to the surface ($U_2(r) < 0$). At lower Z, the Gratton–Öpik cell is much less efficient and it is even absent at $Z = 0$ (Sect. 11.5.3). In Fig. 29.6, from $Z = 0.02$ to 0.002, 0.00001 and 0 the mean amplitudes $U_2(r)$ have the relative values: 1, 1/6, 1/25 and 1/100.

In $Z = 0.02$ models, the heavy mass loss pumps out a lot of angular momentum, so that despite the Gratton–Öpik cell the surface velocity generally decreases during the MS evolution of the most massive stars (Fig. 27.21). At $Z = 0$, mass loss is negligible and meridional circulation as well, there is however some transport by shears. The numerical models in Fig. 29.8 show that the internal transport of angular momentum is sufficient to bring the surface to critical rotation during MS evolution,
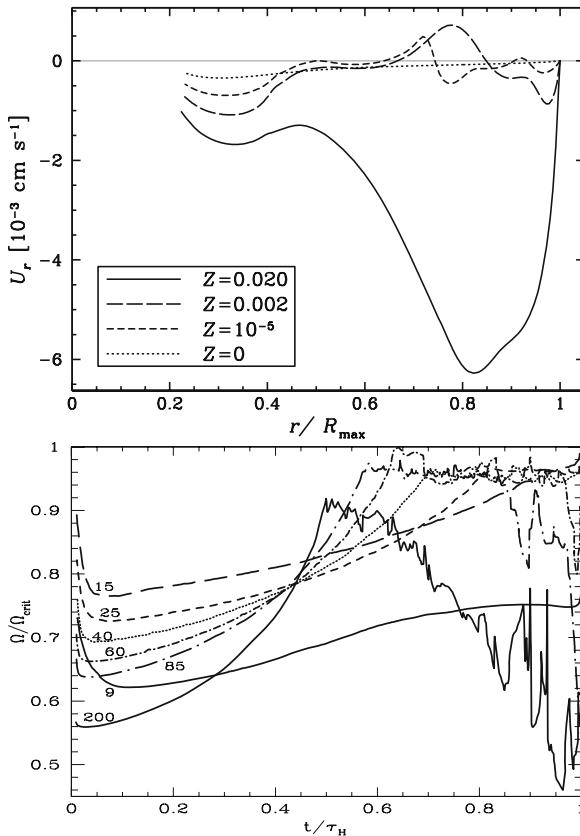
Fig. 29.6 *Top*: values of the velocity of meridional circulation $U_2(r)$ in $20\,M_\odot$ models of different Z. *Bottom*: evolution of the $\Omega/\Omega_{\mathrm{crit}}$ ratio during the MS phase of various masses at $Z = 0$. All the models start with $v_{\mathrm{eq}} = 800$ km s^{-1}, except the $9\,M_\odot$ which starts with 500 km s^{-1}. From G. Meynet, S. Ekström and A. Maeder [175]

provided the initial velocity is high enough ($\Omega/\Omega_c \geq 0.80$). The surface layers are no longer bound. Clearly, rotation does not provide enough momentum to bring the matter to infinity. Likely a "decretion disk" forms which further dissipates progressively. In this way the stars also experience some moderate mass loss, as shown by the final masses in Table 29.2. We shall see in the next section that for very low metallicities such as $Z = 10^{-8}$, rotating stars easily reach the critical velocity and stay there during a large fraction of the MS phase, so that the rotational mass loss is much larger than at $Z = 0$.

29.3 Rotation Effects in Very Low Z Models

The very old halo stars likely bear the signatures of very low Z rather than those of pure $Z = 0$ stars, because the initial galactic enrichments is fast. Thus, the properties of very low Z stars also deserve great attention. There is a remarkable interplay [410] between rotation, mass loss and chemical enrichments in low-Z stars (Fig. 29.7). Low Z implies small mass and angular momentum losses, it also implies a weak Gratton–Öpik circulation, which does not carry much angular momentum outward. This leads to higher internal Ω gradients, which in turn favor stronger mixing of the elements. The mixing is also faster due to the smaller radii (cf. 10.17). The high surface enrichments in heavy elements, particularly CNO elements, permits radiative winds and mass loss in the He-burning phase of massive and AGB stars. These stellar winds produce very peculiar chemical enrichments.
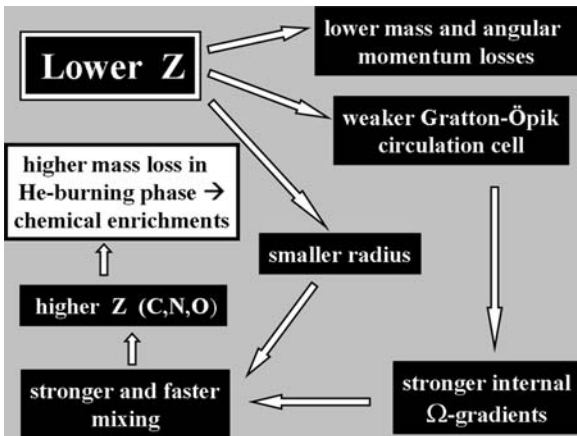
Fig. 29.7 Main effects of rotation and mass loss at very low Z

29.3.1   Rotational Mass Loss in the First Generations

In the Main Sequence Phase: at very low Z, mass loss by radiative winds is very low, thus very little angular momentum is lost. Simultaneously the Gratton–Öpik circulation cell is negligible. This favors internal mixing by shears (Sect. 11.5.3). The evolution of the surface velocities is influenced by these effects. Evidently, lower mass loss favor higher rotation velocities. The weaker Gratton–Öpik inverse circulation cell allows on one side the star to keep more angular momentum, on the other side it only weakly transmits the fast rotation of the contracting core to the surface. The net result is nevertheless that the lower Z stars have rotation velocities, which increase during the MS phase, easily reaching the critical values.

Figure 29.8 shows the evolution of the ratio Ω/Ω_{crit} at the surface of $60\,M_\odot$ MS models. At $Z = 10^{-8}$, the model with an initial $v = 800$ km s^{-1} reaches the break-up limit near the middle of the H-burning phase. The star stays at the break-up limit for the rest of its MS life, losing the unbound layers. The model ends its MS life with $57.6\,M_\odot$, having lost 4% of its initial mass. This is not large, because only the low density upper layers are ejected.

A model with the same initial velocity at $Z = 10^{-5}$ reaches the break-up limit early in the MS phase, because a given value of the initial velocity corresponds to a higher fraction of the critical velocity. This model ends its MS life with $53.8\,M_\odot$, having lost 10% of its initial mass. A model with an initial ratio $\Omega/\Omega_{crit} = 0.4$ just reaches the critical velocity at the very end of its MS phase, losing only $0.3\,M_\odot$. On the whole, during the MS phase of fast rotating stars at low Z there is some mass loss, not due to stellar winds, but due to the mechanical effect of the centrifugal force.

In the Post Main Sequence Phases: rotation favors the redward evolution in the HR diagram (Sect. 27.3.6). This is also true at very low Z. As an example, non-
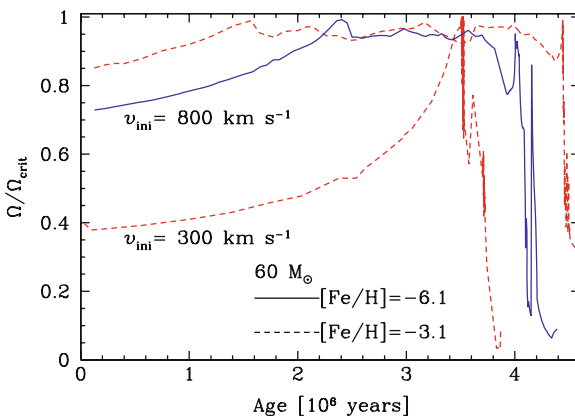
Fig. 29.8 Evolution of Ω/Ω_c at the surface of low-Z models of $60\,M_\odot$, with $[Fe/H] = -6.1$ and -3.1 corresponding to $Z \approx 10^{-8}$ and 10^{-5}, respectively. From G. Meynet, S. Ekström and A. Maeder [407]

rotating models of massive stars at $Z = 10^{-8}$ and 10^{-5} stay in the blue during their He phases, while fast rotating massive stars enter early in the red-supergiant stage, enhancing the mass loss. However, another important effect occurs. The strong mixing within an initially very low Z star brings lots of C N and O to the surface (see next section). The surface Z increases enormously by self-enrichment. As an example, a $60\,M_\odot$ star with an initial $Z = 10^{-8}$ (Fig. 29.8) with an initial $v = 800$ km s^{-1} reaches $Z \approx 0.01$ near the end of the He-burning phase, i.e., an increase of Z by a factor 10^6! For the same M and v but at $Z = 10^{-5}$, the relative Z enhancement is ~ 200. The high metallicities resulting from mixing favor mass loss, even with the scaling (27.2) possibly too weak for a red supergiant. Indeed, the C and O enrichments may favor dust formation, which could further increase the $\dot{M}$ rates. The remaining mass at the end of the He-burning phase is about $24\,M_\odot$ for the above example at $Z = 10^{-8}$ and $37.3\,M_\odot$ at $Z = 10^{-5}$. These examples show that fast rotating stars, even at very low Z, may lose a lot of mass with very peculiar abundances (see next section).

29.3.2 Enrichments by the Winds of the First Generations

Figure 29.9 compares the distributions of the elements in a $60\,M_\odot$ star at $Z = 10^{-8}$ with and without rotation in the blue- and red-supergiant stages. One notices many consequences of rotation:

– The decrease of the total mass resulting from the loss of the envelope.
– The high abundances of ^{14}N, ^{16}O and ^{12}C in the envelope making Z up to 0.01, while in the non-rotating model, these abundances are $< 10^{-8}$.
– In panels a) and b) of the rotating model, one sees the plateau made by a large convective zone associated to the H-burning shell. This convective zone results from the diffusion of C and O from the He-burning core, these products act as catalysts for the CNO cycles making the H-burning shell very active and thus convection develops. This enriches the convective zone in "primary N" (with also some primary ^{13}C). All these layers, extraordinarily rich in C, N and O are ejected in the wind. The case of N is the most interesting, since contrarily to C and O, it is not created in the onion skin layers of the pre-supernovae.
– Huge amounts of ^{4}He are also ejected into the interstellar medium.
– The masses of the CO cores are about the same. Often, rotation increases the size of the CO cores. This is not the case here, because of the large H-burning shell and its associated convective zone, which prevents the shell to migrate outward. In the model with rotation, the He processing goes further leading to more ^{16}O, ^{20}Ne, ^{24}Mg and less ^{12}C in the CO core compared to the case of no rotation. The final abundances of ^{25}Mg and ^{26}Mg are also higher, due to the destruction of ^{22}Ne by reactions (26.9). The neutrons from ^{22}Ne$(\alpha,n)^{25}$Mg captured by the elements of the Fe peak produce s-elements and possibly other isotopes.
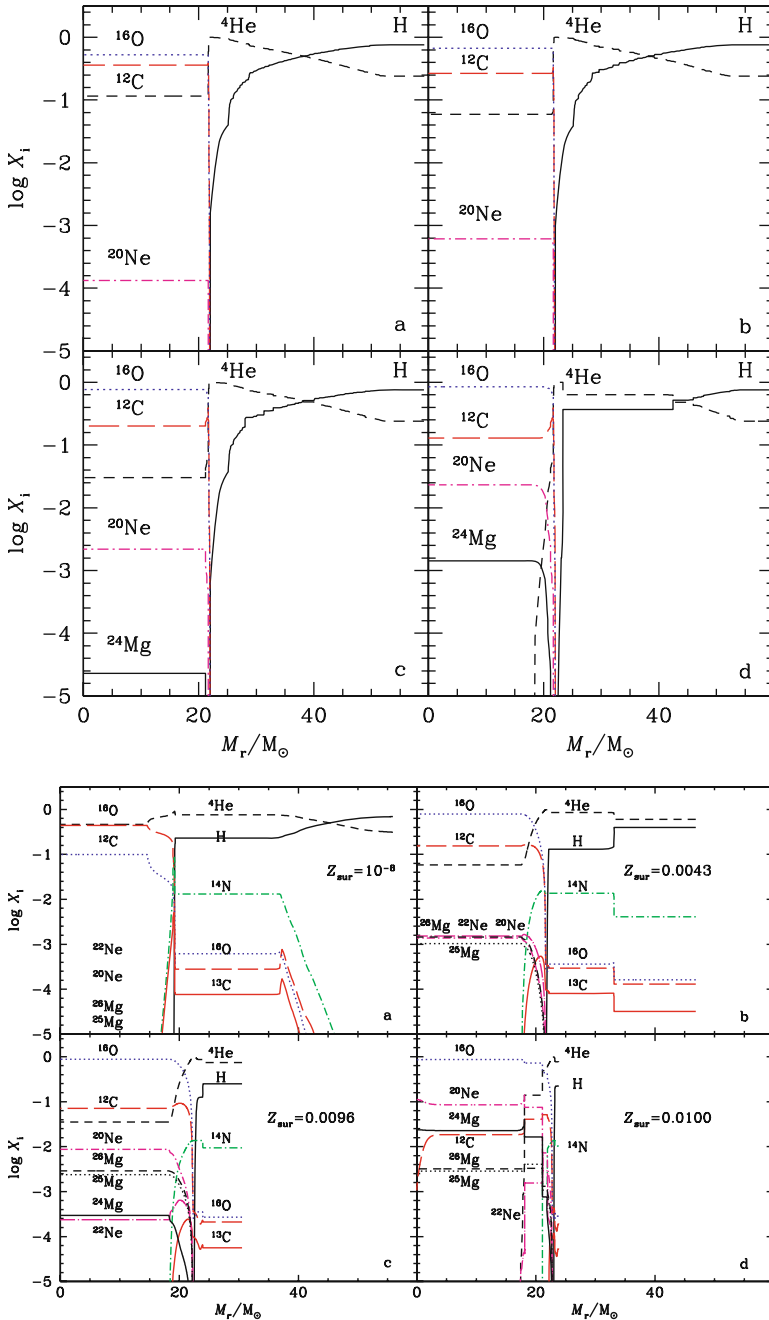
Fig. 29.9 *Top*: internal distribution of the elements in a 60 $M_\odot$ star with $Z = 10^{-8}$ without rotation at the end of He burning. ^{14}N is below 10^{-8}. Panels a,b,c,d: $Y_c = 0.12, 0.06, 0.03, 0.00$ with final $M = 59.73\ M_\odot$. *Bottom*: the same for an initial $\Omega = 0.73$ ($v = 800$ km s^{-1}) at similar Y_c. We see the decrease of the total M and the increase of Z at the surface. From G. Meynet, S. Ekström and A. Maeder [407]

Depending on M, Z and rotational velocity, the very low metallicity stars may produce primary N by diffusion of ^{12}C from the He-burning core into the H-burning shell, together with some C and O. Lots of these elements are ejected in the stellar winds and some at the time of the supernova explosion. Various cases have been considered [367, 407, 410], showing that primary N may be produced only below a metallicity of about $Z = 0.001$.

Figure 29.10 compares the abundances in the winds of the rotating model of Fig. 29.9 to various observed abundances ratios in C-rich extremely metal poor stars. A rotating model at $Z = 10^{-5}$ is also shown. The winds of low-Z stars reproduce the observed relative enhancements in CNO elements which reach a factor 10^4 as observed in these extreme stars. Also, the moderate excesses of Na, Mg and Al resulting from the NeNa and MgAl cycles (Sect. 25.1.5) are in agreement with the model predictions. The wind enrichments are mixed with the ejecta from the supernovae. The wind excesses are so large that the dilution with the SN yields does not significantly modify the relative excesses [407]. The AGB stars at low Z also produce similar excesses (Fig. 26.25). The predicted Ne abundance, high in the AGB yields and low in massive stars, may allow us to discriminate the two sources.

The low-Z massive rotating stars eject lots of He and this may be of some interest to account for the high initial He content [370, 471] in a fraction of the stars in some globular clusters, such as ω Cen. The injection from massive stars with low Z is also able to account for the O–Na and Mg–Al anticorrelations observed in globular clusters [153].

Mass loss in low-Z stars also influence their final fate as supernovae. Mass loss, either due to the fact that stars reach the critical velocity or due to stellar winds boosted by self-enrichment, leads to a reduction of the mass M_{CO} of the CO core. If M_{CO} becomes inferior to $64 \, M_\odot$ [238], no pair instability supernovae (PISN) exist
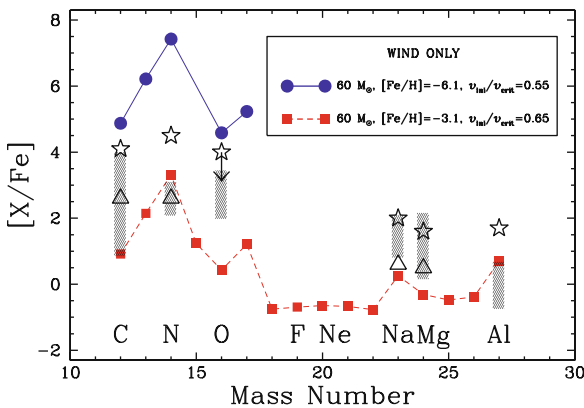
Fig. 29.10 Chemical composition $X_i/X(\text{Fe})$ (in log scale) of the winds of $60 \, M_\odot$ models (solid circles and squares) with different compositions ($Z = 10^{-8}$ and 10^{-5}) and rotation velocities. The values are normalized to the solar values, e.g., $[X_i/X(\text{Fe})]=0$ corresponds to the solar abundance ratio for element "i". The hatched areas, the stars and triangles represent various observations of C-rich very metal-deficient halo stars. From G. Meynet, S. Ekström and A. Maeder [407]

[238]. Up to now, there is no signatures of the yields of PISN in the chemical abundances of extremely low-Z stars [101].

Stellar evolution through the ages still contains many uncertainties, which give room for progresses in this beautiful field of science. The above points show how big the changes may be in stellar evolution brought by rotation.

Appendix A
Physical and Astronomical Constants

A.1 Physical Constants

Velocity of light	c	$= 2.99792458 \times 10^{10}$ cm s^{-1}
Gravitation constant	G	$= 6.67259 \times 10^{-8}$ dyne cm^2 g^{-2}
Planck constant	h	$= 6.62606876 \times 10^{-27}$ erg s
Elementary charge	e	$= 4.8032068 \times 10^{-10}$ E.S.U.
	e^2	$= 23.070796 \times 10^{-20}$ erg cm in E.S.U.
Mass of electron	m_e	$= 9.10938188 \times 10^{-28}$ g
		$= 0.510998902$ MeV
Mass of proton	m_p	$= 1.6726231 \times 10^{-24}$ g
		$= 938.27330$ MeV/c^2
Mass of ^{1}H atom	m_H	$= 1.6735344 \times 10^{-24}$ g
		$= 1.00783$ AMU
Mass of unit atomic weight (AMU)	m_u	$= 1.66053873 \times 10^{-24}$ g
		$= 931.494013$ MeV/c^2
Mass of neutron	m_n	$= 1.67492716 \times 10^{-24}$ g
		$= 939.565330$ MeV/c^2
Boltzmann constant	k	$= 1.3806503 \times 10^{-16}$ erg K^{-1}
		$= 8.617342 \times 10^{-5}$ eV K^{-1}
Avogadro number	N_{AV}	$= 6.02214199 \times 10^{23}$ mole^{-1}
Gas constant	$\mathcal{R}$	$= 8.314472 \times 10^7$ erg deg mole^{-1}
Stefan–Boltzmann constant $(ac/4)$	σ	$= 5.670400 \times 10^{-5}$ erg cm^{-2} K^{-4} s^{-1}
Proton–electron mass ratio	m_p/m_e	$= 1836.153$
Classical electron radius $(e^2/m_e c^2)$	r_e	$= 2.817940285 \times 10^{-13}$ cm
Thomson cross-section $(8\pi/3)r_e^2$	σ_e	$= 0.665245854 \times 10^{-24}$ cm^2
Energy of 1 eV		$= 1.602176462 \times 10^{-12}$ erg
Energy of 1 MeV		$= 1.602176462 \times 10^{-6}$ erg
Temperature associated to 1 keV	1 eV/k	$= 11604.506$ K
Rydberg constant $(\alpha^2 m_e c/2h)$	R_∞	$= 1.0973731568549 \times 10^5$ cm^{-1}

A.2 Some Astronomical Constants

Astronomical unit	AU	$= 1.49597870 \times 10^{13}$ cm
Parsec	pc	$= 3.085678 \times 10^{18}$ cm
		$= 3.26163$ light year
Solar mass	$M_\odot$	$= 1.9891 \times 10^{33}$ g
Solar radius	$R_\odot$	$= 6.9599 \times 10^{10}$ cm
Solar luminosity	$L_\odot$	$= 3.845 \times 10^{33}$ erg s^{-1}
Mean solar density	$\bar{\varrho}_\odot$	$= 1.409$ g cm^{-3}
Solar effective temperature	Teff$_\odot$	$= 5780$ K
Solar abs. bol. magnitude	$M_{\mathrm{bol},\odot}$	$= 4.72$
Solar constant		$= 1.373 \times 10^6$ erg cm^{-2} s^{-1}
		$= 1373$ W m^{-2}
Mass of the Earth	$M_\oplus$	$= 5.9737 \times 10^{27}$ g
Mass of Jupiter	M_J	$= (1/1047.7) \, M_\odot$

A.3 Initial Solar Abundances

Recent determinations of solar abundances yield $X = 0.7393$, $Y = 0.2485$ and $Z = 0.0122$ according to Asplund, Grevesse and Sauval [20]. The initial solar abundances are different because of microscopic diffusion of the elements during solar evolution. The initial X_i (mass fractions) giving the best fit to helioseismic data, also accounting for the neon value from Cunha et al. [151], are $X = 0.720$, $Y = 0.266$ and $Z = 0.014$ [169]. Table A.1 gives the initial X_i based on this fit and on Asplund et al. [20]. The elements not mentioned in the table represent a mass fraction 0.00148.

Table A.1 Initial solar abundances in mass fractions

^{1}H	0.7200000000	^{27}Al	0.0000493616
^{3}He	0.0000430936	^{28}Si	0.0005973605
^{4}He	0.2660000000	^{29}Si	0.0000665170
^{12}C	0.0022653054	^{30}Si	0.0000481417
^{13}C	0.0000363117	^{31}P	0.0000055375
^{14}N	0.0006562993	^{32}S	0.0003240687
^{15}N	0.0000023418	^{33}S	0.0000034809
^{16}O	0.0056906394	^{34}S	0.0000180401
^{17}O	0.0000038202	^{35}Cl	0.0000065406
^{18}O	0.0000128412	^{37}Cl	0.0000022086
^{19}F	0.0000005383	^{36}Ar	0.0000357510
^{20}Ne	0.0017866585	^{38}Ar	0.0000071074
^{21}Ne	0.0000056987	^{39}K	0.0000036558
^{22}Ne	0.0002396650	^{40}Ca	0.0000632558
^{23}Na	0.0000265373	^{42}Ca	0.0000004413
^{24}Mg	0.0004991580	^{45}Sc	0.0000000394
^{25}Mg	0.0000669308	^{44}Ti	0.0000000000
^{26}Mg	0.0000767465	^{46}Ti	0.0000028486
		^{56}Fe	0.0011364000

Appendix B
Complements on Mechanics and Electromagnetism

B.1 Equations of Motion and Continuity

We derive the general equations of motion and continuity. Although their form is very simple for spherical stars in hydrostatic equilibrium, the present general forms are useful when these simplifications do not apply.

B.1.1 Equations of Continuity and of Motion

Let us consider a volume element $dx\,dy\,dz$ with coordinates x, y, z. Let v_x be the component of the velocity at a point x through the face $dz\,dy$ and $v_x + \frac{\partial v_x}{\partial x}\,dx$ the velocity at point $x + dx$ through the face $dz\,dy$. The difference between the matter which goes out and which enters the volume element through the face $dz\,dy$ is

$$\frac{\partial}{\partial x}(\rho\,v_x)\,dx\,dy\,dz\,. \tag{B.1}$$

The net loss of matter in the volume element for all three components of velocity is $\mathrm{div}(\rho\,\boldsymbol{v})\,dx\,dy\,dz$; it can also be written as a change of density ρ:

$$-\frac{\partial\rho}{\partial t}\,dx\,dy\,dz \tag{B.2}$$

for any volume element. Thus, we get the equation of continuity

$$\frac{\partial\rho}{\partial t} + \mathrm{div}(\rho\,\boldsymbol{v}) = 0 \quad\text{or}\quad \frac{\partial\rho}{\partial t} + (\boldsymbol{v}\cdot\boldsymbol{\nabla})\rho = -\rho\,\mathrm{div}\,\boldsymbol{v}\,. \tag{B.3}$$

The equation of motion expresses that the acceleration $d\boldsymbol{v}/dt$ of a mass element in a given volume results from the forces exerted on it:

$$\rho\frac{d\boldsymbol{v}}{dt} = \rho\left[\frac{\partial\boldsymbol{v}}{\partial t} + (\boldsymbol{v}\cdot\boldsymbol{\nabla})\boldsymbol{v}\right] = \rho\,\boldsymbol{a} - \boldsymbol{\nabla}P + \dots, \tag{B.4}$$

where a is the acceleration exerted by the external forces F such as gravity or centrifugal force by unit of mass in the volume, P is the pressure and the dots represent the other possible forces. If all the external forces are negligible, we get the equation of Euler, which is non-linear in the velocity:

$$\left[\frac{\partial v}{\partial t} + (v \cdot \nabla)v\right] = -\frac{1}{\rho}\nabla P \,. \tag{B.5}$$

B.1.2 Remarks on Derivatives

The total variation of any quantity, for example, the total variation $d\rho$ of the density ρ, in a moving volume element is composed of two parts:

1. The variation during the time dt at a given point (x, y, z) is $(\partial \rho/\partial t)dt$.
2. The difference of density at time t between two points separated by dr traveling at velocity v by the volume element during time dt is

$$dx\frac{\partial \rho}{\partial x} + dy\frac{\partial \rho}{\partial y} + dz\frac{\partial \rho}{\partial z} = (dr \cdot \nabla)\,\rho. \tag{B.6}$$

The total variation $d\rho$ is thus $d\rho = \frac{\partial \rho}{\partial t}\,dt + (dr \cdot \nabla)\,\rho$, which gives

$$\frac{d\rho}{dt} = \frac{\partial \rho}{\partial t} + (v \cdot \nabla)\rho \,. \tag{B.7}$$

This is the total variation of the density for a moving fluid element. The term $(v \cdot \nabla)\rho$ is the *advection*, i.e., the projection of the density variation along the velocity; it represents the transport of matter. The derivative $\frac{d}{dt}$ is also written $\frac{D}{Dt}$ and called the total or hydrodynamical derivative.

B.1.3 Vectorial Operators in Spherical Coordinates

Spherical coordinates (r, ϑ, φ) are most appropriate for describing stars, ϑ being the colatitude. The unit vectors in these directions are e_r, e_ϑ and e_φ. The gradient of a scalar field Φ is

$$\nabla\Phi = \frac{\partial \Phi}{\partial r}\,e_r + \frac{1}{r}\frac{\partial \Phi}{\partial \vartheta}\,e_\vartheta + \frac{1}{r\sin\vartheta}\frac{\partial \Phi}{\partial \varphi}\,e_\varphi \,. \tag{B.8}$$

The divergence of a vector A of components $(A_r, A_\vartheta, A_\varphi)$ is

$$\nabla \cdot A = \frac{1}{r^2}\frac{\partial}{\partial r}(r^2 A_r) + \frac{1}{r\sin\vartheta}\frac{\partial}{\partial \vartheta}(\sin\vartheta A_\vartheta) + \frac{1}{r\sin\vartheta}\frac{\partial A_\varphi}{\partial \varphi} \,. \tag{B.9}$$

The Laplace operator $\Delta\Phi = \nabla^2\Phi$ of a scalar function Φ is

$$\Delta\Phi = \frac{1}{r^2}\frac{\partial}{\partial r}\left(r^2\frac{\partial\Phi}{\partial r}\right) + \frac{1}{r^2\sin\vartheta}\frac{\partial}{\partial\vartheta}\left(\sin\vartheta\frac{\partial\Phi}{\partial\vartheta}\right) + \frac{1}{r^2\sin^2\vartheta}\frac{\partial^2\Phi}{\partial\varphi^2}. \quad \text{(B.10)}$$

The rotational of a vector $\boldsymbol{B}$ is

$$\nabla\times\boldsymbol{B} = \frac{1}{r^2\sin\vartheta}\left[\frac{\partial}{\partial\vartheta}(r\sin\vartheta A_\varphi) - \frac{\partial}{\partial\varphi}(rA_\vartheta)\right]\boldsymbol{e}_r$$

$$+\frac{1}{r^2\sin\vartheta}\left\{\left[\frac{\partial}{\partial\varphi}A_r - \frac{\partial}{\partial r}(r\sin\vartheta A_\varphi)\right]r\boldsymbol{e}_\vartheta + \left[\frac{\partial}{\partial r}(rA_\vartheta) - \frac{\partial A_r}{\partial\vartheta}\right]r\sin\vartheta\,\boldsymbol{e}_\varphi\right\}.$$

$$\text{(B.11)}$$

B.1.4   Viscous Terms

The Euler equation does not account for the viscous forces, which we now consider. A small slab of area S floating on a viscous medium of density ρ and thickness d is opposing a force $\boldsymbol{F}$ to a displacement with velocity $\boldsymbol{v}$ in the plane defined by the slab. We define the tension τ in the plane of the slab

$$\tau \equiv \frac{F}{S} \equiv \frac{\eta\,v}{d}, \quad \text{(B.12)}$$

where η is the dynamic coefficient of viscosity in $\mathrm{g\,s^{-1}\,cm^{-1}}$ and $\eta = \rho\,v$ with v the kinematic coefficient of viscosity in $\mathrm{cm^2\,s^{-1}}$. If the x-axis is in the direction of motion and z is the vertical direction perpendicular to the slab, the tension along the x-axis by unit of slab surface is

$$\sigma_{xz} = \eta\,\frac{\partial v_x}{\partial z}. \quad \text{(B.13)}$$

The tension is symmetric $\sigma_{xz} = \sigma_{zx}$ for an isotropic medium. A fluid is said to be Newtonian if the tensions are linear and homogeneous functions of the velocity gradients; thus the linearity and symmetry imply the proportionality

$$\sigma_{xz} = \sigma_{zx} \propto \left(\frac{\partial v_x}{\partial z} + \frac{\partial v_z}{\partial x}\right), \quad \text{(B.14)}$$

the same for the other tensions. One adopts the general expression

$$\sigma_{ij} = \eta\left(\frac{\partial v_i}{\partial x_j} + \frac{\partial v_j}{\partial x_i}\right). \quad \text{(B.15)}$$

The meaning of σ_{xx} is that of a pressure on a surface perpendicular to the x-axis; it produces a change of velocity v_x from the constraints exerted on the surface $dy\,dz$. One has

$$\sigma_{xx} = 2\,\eta\,\frac{\partial v_x}{\partial x}. \tag{B.16}$$

One notices that $\sum \sigma_{ii} \neq 0$, for $i = 1\text{--}3$; thus the viscosity would make a pressure, which is not the case. Thus, one has to take

$$\sigma_{ij} = \eta\left(\frac{\partial v_i}{\partial x_j} + \frac{\partial v_j}{\partial x_i}\right) - \frac{2\eta}{3}\,\delta_{ij}\,\mathrm{div}\,\boldsymbol{v}\,. \tag{B.17}$$

The net viscous force on the volume element $dV = dx\,dy\,dz$ is the difference of the forces on the opposed faces of the volume element:

$$
\begin{aligned}
(f_{\mathrm{visc}})_x &= \left(\frac{\partial}{\partial x}\,\sigma_{xx}\,dx\right)dy\,dz + \left(\frac{\partial}{\partial y}\,\sigma_{xy}\,dy\right)dx\,dz \\
&\quad + \left(\frac{\partial}{\partial z}\,\sigma_{xz}\,dz\right)dy\,dx = \sum_{j=1}^{3}\frac{\partial}{\partial x_j}\,\sigma_{xj}\,dx\,dy\,dz \\
&= \left(\sum_j \frac{\partial}{\partial x_j}\,\eta\,\frac{\partial v_x}{\partial x_j} + \sum_j \frac{\partial}{\partial x_j}\,\eta\,\frac{\partial v_j}{\partial x}\right)dV - \frac{2}{3}\sum_j \frac{\partial(\eta\,\delta_{xj}\,\mathrm{div}\,\boldsymbol{v})}{\partial x_j} \\
&= \eta\,\nabla^2 v_x + \eta\,\frac{\partial^2 v_x}{\partial^2 x^2} + \eta\,\frac{\partial^2 v_y}{\partial y \partial x} + \eta\,\frac{\partial^2 v_z}{\partial z \partial x} - \frac{2}{3}\,\eta\,\frac{\partial}{\partial x}\left(\frac{\partial v_x}{\partial x} + \frac{\partial v_y}{\partial y} + \frac{\partial v_z}{\partial z}\right) \\
&= \eta\,\nabla^2 v_x + \left(\frac{\eta}{3}\right)\frac{\partial}{\partial x}\,\mathrm{div}\,\boldsymbol{v}\,. \tag{B.18}
\end{aligned}
$$

Sometimes, instead of the term $\eta/3$, a term $(\eta + \zeta)/3$ is written. ζ is said to be "the second viscosity"; it intervenes in the case of polyatomic gases submitted to fast oscillations. It accounts for the fact that the energy is transmitted more slowly to the vibration and rotation modes of molecules. This introduces additional viscous effects. The equation of motion (B.4) can now be written as

$$\rho\left[\frac{\partial \boldsymbol{v}}{\partial t} + (\boldsymbol{v}\cdot\boldsymbol{\nabla})\,\boldsymbol{v}\right] = \rho\,\boldsymbol{a} - \boldsymbol{\nabla}P + \eta\,\nabla^2 \boldsymbol{v} + \left(\frac{\eta}{3}\right)\boldsymbol{\nabla}\,(\mathrm{div}\,\boldsymbol{v})\,. \tag{B.19}$$

B.1.5 Navier–Stokes Equation

If the medium is incompressible, the density ρ is constant and from the continuity (B.3) $\mathrm{div}\,\boldsymbol{v} = 0$. Thus, the equation of motion becomes

$$\rho\left[\frac{\partial \boldsymbol{v}}{\partial t} + (\boldsymbol{v}\cdot\boldsymbol{\nabla})\,\boldsymbol{v}\right] = \rho\,\boldsymbol{a} - \boldsymbol{\nabla}P + \eta\,\nabla^2 \boldsymbol{v}, \tag{B.20}$$

which is the equation of Navier–Stokes. If we divide it by ρ, we get

$$\frac{d\boldsymbol{v}}{dt} = \frac{\partial \boldsymbol{v}}{\partial t} + (\boldsymbol{v} \cdot \boldsymbol{\nabla})\, \boldsymbol{v} = \boldsymbol{a} - \frac{1}{\rho}\,\nabla P + \nu \nabla^2 \boldsymbol{v}\,, \tag{B.21}$$

which is fundamental in fluid mechanics. The coefficient ν is the coefficient of kinematic viscosity, equal to $\nu = \eta/\varrho$. According to (B.21) the characteristic timescale of a viscous effect is of the order of

$$t_{\text{visc}} = \frac{R^2}{\nu}. \tag{B.22}$$

Some viscosity coefficients are given below (Sect. B.4.1). In astrophysical media, the main sources of viscosity are turbulent viscosity in turbulent media and radiative viscosity (B.52) in hot low-density media. If the external and viscous forces are negligible, we obtain the Euler equation (B.5).

   If the medium is compressible, as is the case for stellar media in general, the above equation still applies for motions with a small velocity v with respect to the sound velocity c_S. For a medium with a compressibility $\frac{\Delta \rho}{\rho} \sim \beta \, \frac{\Delta P}{P}$, ignoring the T effects one has for the sound speed (5.88)

$$c_S^2 \equiv \left(\frac{\partial P}{\partial \varrho}\right)_{\text{ad}} \sim \frac{P}{\varrho\,\beta}; \qquad \text{thus} \qquad \frac{\Delta \varrho}{\varrho} \sim \frac{\Delta P}{c_S^2 \varrho}\,. \tag{B.23}$$

The pressure behaves like $\Delta P \sim \frac{\text{force}}{\text{surface}} \sim \frac{\text{energy}}{\text{volume}} \sim \varrho\, v^2$. Thus, the relative density variations behave like $\frac{\Delta \varrho}{\varrho} \sim \frac{v^2}{c_S^2}$ and according to the equation of continuity, we neglect the term in div $\boldsymbol{v}$ in the equation of motion (B.19) if $M^2 = v^2/c_S^2 \ll 1$.

B.1.6 Equation of Motion with Rotation

The accelerations measured in a rotating frame (quantities with a prime) are related to those in an inertial frame (without a prime) by

$$\frac{d\boldsymbol{v}'}{dt} = \frac{d\boldsymbol{v}}{dt} - \boldsymbol{\Omega} \times (\boldsymbol{\Omega} \times \boldsymbol{r}') - \frac{d\boldsymbol{\Omega}}{dt} \times \boldsymbol{r}' - 2\,\boldsymbol{\Omega} \times \boldsymbol{v}'\,, \tag{B.24}$$

where the second and third terms on the right-hand side represent the centrifugal force (the third term is absent in a stationary situation). In a stationary rotating star, the centrifugal force at colatitude ϑ can also be written as $(1/2)\,\Omega^2 \boldsymbol{\nabla}(r \sin \vartheta)^2$. The last term is the Coriolis force.

   The term dv/dt or $\partial v/\partial t$ in the Navier–Stokes equation (B.20) or in the Euler equation (B.5) is the acceleration in the inertial system. To get the equations in the rotating frame, the change $(dv/dt) \rightarrow (dv'/dt)$ has to be made. The Navier–Stokes equation (B.20) becomes in the rotating frame

$$\frac{d\boldsymbol{v}'}{dt} = \frac{\partial \boldsymbol{v}'}{\partial t} + \left(\boldsymbol{v}' \cdot \nabla\right)\boldsymbol{v}'$$

$$= \boldsymbol{a} - \frac{1}{\varrho}\nabla P + v\nabla^2 \boldsymbol{v}' - \boldsymbol{\Omega} \times (\boldsymbol{\Omega} \times \boldsymbol{r}') - \frac{d\boldsymbol{\Omega}}{dt} \times \boldsymbol{r}' - 2\boldsymbol{\Omega} \times \boldsymbol{v}'. \quad \text{(B.25)}$$

The ratio of the inertial to Coriolis force is Rossby number (Sect. B.5.4). Viscosity acts locally.

B.1.7 Geostrophic Motions, Taylor–Proudman Theorem

If Ω is constant or has a cylindrical symmetry, the centrifugal acceleration can be derived from a potential, say V. One has (cf. Sect. 2.1.2) $-\nabla V = \Omega^2\boldsymbol{\varpi}$ and $V = -(1/2)\Omega^2\varpi^2$, where ϖ is the distance to the rotation axis. Equation (B.25) becomes for constant ϱ (with Ω also constant in time)

$$\frac{\partial \boldsymbol{v}'}{\partial t} + \left(\boldsymbol{v}' \cdot \nabla\right)\boldsymbol{v}' = -\nabla\left(\frac{P}{\varrho} - \frac{1}{2}\Omega^2\varpi^2 + \Phi\right) + v\nabla^2\boldsymbol{v}' - 2\boldsymbol{\Omega} \times \boldsymbol{v}'. \quad \text{(B.26)}$$

The fluid is incompressible; Φ is the gravitational potential (1.36). For a stationary state without viscosity, the equation becomes

$$2\boldsymbol{\Omega} \times \boldsymbol{v}' = -\nabla\left[\frac{P}{\varrho} - \frac{1}{2}\Omega^2\varpi^2 + \Phi\right]. \quad \text{(B.27)}$$

Fluid motions satisfying this equation are said to be geostrophic. This is typical of wind circulation on the Earth; the Coriolis force is perpendicular to the direction of the motion $\boldsymbol{v}'$. The generalized pressure term in square brackets is perpendicular to the direction of the motion, i.e., the wind blows parallel along the isobars and turns clockwise around high pressures in the northern hemisphere. Along a streamline, followed by a fluid element of velocity $\boldsymbol{v}'$, the generalized pressure term is constant. On the Earth, this equation applies in altitude where viscous effects are negligible. If we take the rotational of the above equation, we have

$$\nabla \times (\boldsymbol{\Omega} \times \boldsymbol{v}') = 0, \quad \text{(B.28)}$$

because the second member is a gradient. This equation becomes

$$\underbrace{(\boldsymbol{v}' \cdot \nabla)\boldsymbol{\Omega}}_{=0} - \underbrace{\boldsymbol{v}'(\nabla \cdot \boldsymbol{\Omega})}_{=0} - (\boldsymbol{\Omega} \cdot \nabla)\boldsymbol{v}' + \underbrace{\boldsymbol{\Omega}(\nabla \cdot \boldsymbol{v}')}_{=0} = 0. \quad \text{(B.29)}$$

If $\boldsymbol{\Omega}$ is constant as on Earth, $\nabla \cdot \boldsymbol{v}' = 0$ due to continuity, ϱ being constant. Thus one is left with

$$(\boldsymbol{\Omega} \cdot \nabla)\boldsymbol{v}' = 0. \quad \text{(B.30)}$$

 This is the Taylor–Proudman theorem, which says that the velocity cannot vary in the direction of the rotation axis. Thus, two particles on a line parallel to the rotation axis stay at the same distance from each other during rotation.

B.2 Maxwell Equations

Maxwell's equations are the general form of the equations of electromagnetism. Together with the equations of motion and continuity, they form the basic equations of magnetohydrodynamics. In the MKSA system, the Maxwell equations are

$$\nabla \times \boldsymbol{E} = -\frac{\partial \boldsymbol{B}}{\partial t} \qquad \nabla \cdot \boldsymbol{D} = \varrho_c, \qquad (B.31)$$

$$\nabla \times \boldsymbol{H} = \boldsymbol{j} + \frac{\partial \boldsymbol{D}}{\partial t} \qquad \nabla \cdot \boldsymbol{B} = 0 . \qquad (B.32)$$

For a low-density plasma $\boldsymbol{B} = \mu_0 \, \mu \, \boldsymbol{H}$, $\boldsymbol{D} = \epsilon_0 \, \epsilon \boldsymbol{E}$. $\boldsymbol{H}$ is the magnetic field, $\boldsymbol{B}$ the magnetic induction, often referred to as the magnetic field, μ the magnetic permeability, $\boldsymbol{E}$ the electric field, $\boldsymbol{D}$ the electric displacement, ϵ_0 the electrical permittivity of free space, ϱ_c the charge density and $\boldsymbol{j}$ the electric current density. In the Gauss system, used in astrophysics, Maxwell's equations are

$$\nabla \times \boldsymbol{E} = -\frac{1}{c}\frac{\partial \boldsymbol{B}}{\partial t} \qquad \nabla \cdot \boldsymbol{D} = 4\pi \varrho_c, \qquad (B.33)$$

$$\nabla \times \boldsymbol{H} = \frac{4\pi}{c}\boldsymbol{j} + \frac{1}{c}\frac{\partial \boldsymbol{D}}{\partial t} \qquad \nabla \cdot \boldsymbol{B} = 0 , \qquad (B.34)$$

with $\boldsymbol{B} = \mu \boldsymbol{H}$, $\boldsymbol{D} = \epsilon \boldsymbol{E}$ and the same definitions as above.

   The first law expresses that a variable magnetic field produces an electrical field (or a voltage); this is the Faraday law. The second law expresses that the electric charges are the source of the electric displacement (Gauss law). The third says that the motion of charged particles, i.e., a current, creates a magnetic field (Ampère law). The fourth indicates that there is no free magnetic particles. The current I through a surface S is the total charge q crossing this surface by unit of time, $I = dq/dt$. The current density $\boldsymbol{j} = (dI/dS)\,(\boldsymbol{v}/v)$ where dS is the surface element perpendicular to the motion of the charges and $\boldsymbol{j}$ is a vector in the direction of the motion of the positive charges of velocity $\boldsymbol{v}$. The Ohm law relates $\boldsymbol{E}$ and $\boldsymbol{j}$:

$$\boldsymbol{E} = \frac{\boldsymbol{j}}{\sigma} , \qquad (B.35)$$

where σ is the electrical conductivity, the inverse of the resistivity.

B.3　Statistical Mechanics: Pressure and Energy Density

Statistical mechanics provides a very useful relation between the energy density u and the pressure P exerted by a medium of particles of mass m and velocity v. The force $\boldsymbol{F} = d\boldsymbol{p}/dt$ on a surface results from the change of the particle momenta during collisions supposed to be elastic. The change of the momentum of a particle impacting a surface with an angle ϑ with respect to the normal is $\Delta p = 2\,p\cos\vartheta$. Let us call $N(\vartheta,p)d\vartheta dp$ the number of particles by units of time and surface with momentum and impact angle in the intervals $(p,p+dp)$ and $(\vartheta,\vartheta+d\vartheta)$. The pressure is (Fig. B.1)

$$dP = 2\,p\cos\vartheta\,N(\vartheta,p)d\vartheta dp. \tag{B.36}$$

We call $n(\vartheta,p)d\vartheta dp$ the concentration of particles with ϑ and p in the quoted limits and have the relation

$$N(\vartheta,p)\,d\vartheta\,dp = n(\vartheta,p)\,v\cos\vartheta\,d\vartheta\,dp\,, \tag{B.37}$$

since particles arriving tangentially to the plane do not contribute. Thus the pressure is

$$P = 2 \int_0^{\pi/2} \int_0^\infty p\cos^2\vartheta\,v\,n(\vartheta,p)\,d\vartheta\,dp\,. \tag{B.38}$$

For isotropic particle motions, let us call $n(p)\,dp$ the concentration of particles with a momentum between p and $p+dp$; we have

$$\frac{n(\vartheta,p)\,d\vartheta\,dp}{n(p)\,dp} = \frac{2\,\pi\,\sin\vartheta\,d\vartheta}{4\,\pi}\,. \tag{B.39}$$

This expression is introduced in (B.38). The integrations over ϑ and p are independent, which gives

$$P = \frac{1}{3} \int_0^\infty p\,v\,n(p)\,dp\,. \tag{B.40}$$

The density of kinetic energy of particles of mass m and momentum p is

$$u = \int_0^\infty n(p)\,E_{\text{cin}}(p)\,dp\,. \tag{B.41}$$

P and u may now be related for non-relativistic and relativistic particles.
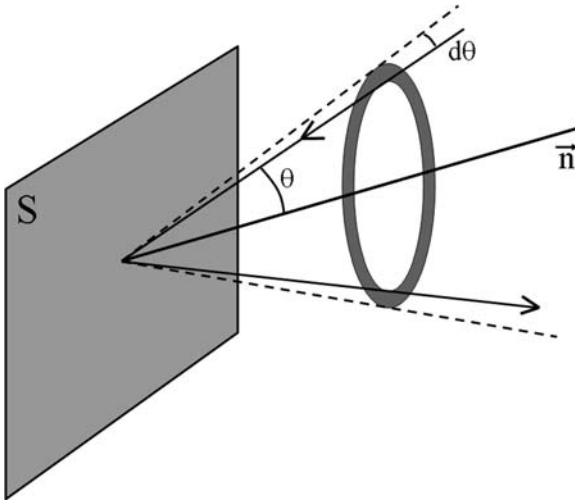
Fig. B.1 Elastic collision of particles with angles between ϑ and $\vartheta + d\vartheta$ with respect to the normal **n** to a surface S

B.3.1 Non-relativistic Particles

The kinetic energy and momentum are $E_{\mathrm{cin}} = p^2/(2m)$ and $p = mv$. The pressure becomes with (B.40)

$$P = \frac{1}{3} \int_0^\infty n(p)\, \frac{p^2}{m}\, dp = \frac{2}{3} \int_0^\infty n(p)\, E_{\mathrm{cin}}\, dp \,. \tag{B.42}$$

Thus, one has

$$P = \frac{2}{3} u \,. \tag{B.43}$$

Such a relation applies, for example, to a perfect gas, where $P = [k/(\mu\, m_{\mathrm{u}})]\varrho\, T$ and $u = (3/2)[k/(\mu\, m_{\mathrm{u}})]\varrho\, T$.

B.3.2 Relativistic Particles

In relativistic kinematics, the kinetic energy is

$$E_{\mathrm{cin}} = E - E_0 = mc^2 - m_0 c^2 = m_0 c^2 \left(\frac{1}{\sqrt{1-\beta^2}} - 1 \right), \tag{B.44}$$

with $\beta = v/c$ and m_0 the rest mass. For small β, this gives $E_{\mathrm{cin}} = \frac{1}{2}m_0 v^2$. The momentum is $p = mv = mc\beta$. By eliminating β between p and E_{cin} from (B.44),

one has for the total energy E

$$E^2 = p^2 c^2 + m_0^2 c^4 \,.\tag{B.45}$$

For photons or highly relativistic particles $E_{\text{cin}} \to pc$ and P (B.40) becomes

$$P = \frac{1}{3} \int_0^\infty n(p)\, pc\, dp = \frac{1}{3} \int_0^\infty n(p)\, E_{\text{cin}}\, dp \,,\tag{B.46}$$

which gives

$$P = \frac{1}{3} u \,.\tag{B.47}$$

In general, P/u lies between $1/3$ and $2/3$, the lower limit being reached for relativistic particles and the upper limit for non-relativistic particles. As an example, the factor $1/3$ applies to radiation pressure with $P_{\text{rad}} = (1/3)\, a T^4$ and radiative energy density $u_{\text{rad}} = a T^4$ (Sect. C.1).

B.4 Expressions of Viscosity, Conductivity and Diffusion

The equation of diffusion is derived in Sect. 10.2 for a general geometry. Here, we examine the expressions of viscosity, conductivity and diffusion coefficients. This is usually done in the context of the kinetic theory of gases, with a simple plane parallel geometry (the geometry influences the form of the equations, but not the various coefficients which depend on local conditions). Transfer of momentum gives rise to viscosity, transfer of heat to conductivity and transfer of particles to diffusion. Ideally, one should study the collisions of particles and then integrate over all parameters as we did above for pressure (Sect. B.3); however in the kinetic theory of gases, one considers particles with an average velocity $\bar{v}$ and a mean free path ℓ.

B.4.1 Viscosity from Turbulence, Radiation and Plasma

If a force $\boldsymbol{F}$ is applied tangentially on a slab at the surface of a horizontal layer of viscous liquid of vertical thickness z, a steady horizontal motion of the slab results with a velocity $\boldsymbol{v}$ in the direction of the applied force (Sect. B.1.4). The steady motion shows that due to viscosity the medium exerts an opposite equal horizontal force $-\boldsymbol{F}$. The dynamic viscosity η is defined by

$$F = \eta \frac{\partial v}{\partial z} \,,\tag{B.48}$$

where F is the modulus of the viscous force by surface unity. If n is the concentration of the particles of mean mass m, the number of particles crossing a surface unity by unity of time, due to random isotropic motions, is $(n/6)\,\bar{v}$ (see Sect. 10.1). The excess of momentum transported upward over a distance ℓ through a horizontal surface in the liquid is $(n/6)\,\bar{v}\,m(dv/dz)\,\ell$. This amount is to be counted twice, since a positive excess is transported by viscosity upward and a negative one downward; thus the total excess of momentum by units of time and surface is $(n/3)\,\bar{v}\,\ell\,m(\partial v/\partial z)$. Since $F = \partial \boldsymbol{p}/\partial t$, one has from the identification with (B.48)

$$\eta = \frac{n}{3}\,\bar{v}\,\ell\,m = \frac{1}{3}\,\varrho\,\bar{v}\,\ell\,, \tag{B.49}$$

which provides the coefficient of dynamic viscosity. The numerical factor depends on the particle interactions. The kinematic viscosity v is

$$v = \frac{\eta}{\varrho} = \frac{1}{3}\,\bar{v}\,\ell, \tag{B.50}$$

where v is expressed in $\mathrm{cm}^2\ \mathrm{s}^{-1}$ and η in $\mathrm{g}\ \mathrm{cm}^{-1}\ \mathrm{s}^{-1}$. These expressions apply to different physical cases, for example, it gives the viscosity coefficient of turbulent motions with an average velocity $\bar{v}$ and mean free path ℓ. Turbulent viscosity is generally much larger than the radiative and microscopic viscosities. The timescale for viscous adjustment is given by (B.22).

B.4.1.1   Radiative Viscosity

The photons also transport momentum in stars; thus a radiative viscosity can also be defined. If one applies the above expression (B.49) to photons, one has $v \to c$, $\ell \to 1/(\kappa\varrho)$, with $\varrho = u/c^2 = aT^4/c^2$; thus

$$\eta = \frac{1}{3}\frac{aT^4 c}{c^2 \kappa \varrho} = \frac{1}{3}\frac{aT^4}{c\kappa\varrho}\,. \tag{B.51}$$

A more refined development leads to [232] in $\mathrm{g}\ \mathrm{cm}^{-1}\ \mathrm{s}^{-1}$:

$$\eta = \frac{4}{15}\frac{aT^4}{c\kappa\varrho}\,, \tag{B.52}$$

which makes a small difference with respect to (B.51). In the Sun at $M_r/M = 0.5$, the radiative viscosity $v = 0.2\ \mathrm{cm}^2\ \mathrm{s}^{-1}$. At $M_r/M = 0.98$ in the Sun, $v = 1.9\ \mathrm{cm}^2\ \mathrm{s}^{-1}$. The associated timescale is $\sim 10^{14}$ yr.

B.4.1.2 Plasma or Molecular Viscosity and Resistivity

The dynamic viscosity $\eta = v\varrho$ of an ionized plasma with particles of atomic mass A_i and charge $Z_i e$ is [543] (see also 10.67)

$$\eta = 2.2 \times 10^{-15} \frac{T^{5/2} A_i^{5/2}}{Z_i^4 \ln \Lambda} \quad \mathrm{g\,cm^{-1}s^{-1}}. \tag{B.53}$$

Although it applies to a plasma, this viscosity is often called the molecular viscosity or the microscopic viscosity. Λ is the ratio of the Debye length (7.99) to the impact parameter in the plasma of electron concentration n_e:

$$\Lambda = 1.3 \times 10^4 \frac{T^{3/2}}{n_e^{1/2}} . \tag{B.54}$$

For a mixture of H and He with a mass fraction X of H, the viscosity is [515]

$$\eta \approx 2.2 \times 10^{-15} \frac{T^{5/2}}{\ln \Lambda} \frac{1 + 7X}{8} \quad \mathrm{g\,cm^{-1}s^{-1}} . \tag{B.55}$$

$\ln \Lambda \sim 4$ in the solar interior. The molecular viscosity at $M_r/M = 0.5$ in the Sun is 2.7 and $8.6\,\mathrm{cm^2\ s^{-1}}$ at $M_r/M = 0.98$. The magnetic diffusivity for a hydrogen plasma is

$$\eta \approx 5.2 \times 10^{11} \frac{\ln \Lambda}{T^{3/2}} \quad \mathrm{cm^2\ s^{-1}} . \tag{B.56}$$

These coefficients apply to the microscopic effects. For specific hydrodynamic and magnetic instabilities, the coefficients are different (e.g., Sect. 13.5.1).

B.4.2 Conductivity

Let us consider a medium with a gradient of temperature T along the vertical z-axis, T decreasing upward while z increases. The energy q transferred *by units of horizontal surface and time* is

$$\frac{\partial q}{\partial t} = -K' \frac{\partial T}{\partial z} , \tag{B.57}$$

where K' is a coefficient of conductivity expressed in erg $\mathrm{cm^{-1}\ s^{-1}\ K^{-1}}$. By the same reasoning as mentioned previously, the quantity of energy transported by the $(n/6)\,\overline{v}$ particles which move upward and by the same number which move downward is by units of surface and time,

$$- \frac{n}{3} \bar{v} C'_V \frac{\partial T}{\partial z} \ell \, ,$$ (B.58)

where C'_V is the specific heat at constant volume per particle, accounting for the fact that $n C'_V = \varrho \, C_V$, where C_V is, as usual, the specific heat by mass unity. Identifying the above two expressions, one gets

$$K' = \frac{1}{3} \varrho \, \bar{v} C_V \, \ell$$ (B.59)

for the coefficient of conductivity K' (different from K in $\text{cm}^2 \, \text{s}^{-1}$ in 3.45).

B.4.3 Diffusion Coefficient

The diffusion coefficient expresses the capacity of a medium to transport particles. Expressions of the diffusion coefficient have been derived in Sect. 10.1.3 and the equation of particle diffusion due to an abundance gradient is derived in Sect. 10.2.1. The general form of the diffusion coefficient for particles of average velocity $\bar{v}$ and mean free path ℓ is

$$D = \frac{1}{3} \bar{v} \ell \, .$$ (B.60)

From (B.50), one sees that the diffusion coefficient D and the coefficient ν of kinematic viscosity have similar expressions, although they have a different physical meaning.

B.5 Dimensionless Numbers

Several dimensionless numbers characterize the various regimes in hydrodynamics. The values of these numbers are in general very different in the astrophysical and terrestrial conditions.

B.5.1 Reynolds Number

In the Navier–Stokes equation (B.21), one may consider the ratio of the inertial term $(\partial v / \partial t)$ to the viscosity term to be

$$\frac{\text{inertial}}{\text{viscous}} \approx \frac{v/t}{\nu v / \ell^2} \approx \frac{\ell^2}{\nu t} \approx \frac{v \ell}{\nu} \, ,$$ (B.61)

where ℓ, v and t are typical lengthscale, velocity and timescale. The above ratio is the Reynolds number

$$\mathcal{Re} \equiv \frac{v\,\ell}{\nu}\,. \tag{B.62}$$

For $\mathcal{Re}$ numbers lower than a critical value $\mathcal{Re}_{\mathrm{crit}}$, viscosity effects dominate and turbulent motions are damped. For the flow in a tube, $\mathcal{Re}_{\mathrm{crit}} \approx 2300$. The value $\mathcal{Re}_{\mathrm{crit}}$ depends on the geometry and type of fluids. In stars, the scale ℓ is so large that turbulence generally easily sets in. The value of $\mathcal{Re}_{\mathrm{crit}}$ determines the timescale for which viscous dissipation takes more time than the growth of the turbulent instability. For $\mathcal{Re}$ larger than $\mathcal{Re}_{\mathrm{crit}}$, the spectrum of turbulence also extends to scales smaller than the critical one. For local conditions in stars a value of $\mathcal{Re}_{\mathrm{crit}} \approx 10$ is sometimes taken [562]. A magnetic Reynolds number can also be defined; see (13.6).

B.5.2 Prandtl Number

For a medium with heat conduction and motions, the ratio of the timescales for thermal adjustment $t_{\mathrm{therm}} \sim \ell^2/K$ (3.47) and for viscous adjustment $t_{\mathrm{visc}} \sim \ell^2/\nu$ (B.22) is the Prandtl number

$$\mathcal{Pr} = \frac{t_{\mathrm{therm}}}{t_{\mathrm{visc}}} = \frac{\ell^2}{K}\frac{\nu}{\ell^2} = \frac{\nu}{K}\,. \tag{B.63}$$

In stars at $T = 10^7$ K, it is $\sim 10^{-6}$, i.e., thermal adjustment is much faster than viscous adjustment. $\mathcal{Pr}$ is a property of the medium and not of the flow, contrary to the Reynolds number. For water or air, $\mathcal{Pr} \approx 1$. In stars, for radiative viscosity and transport one has from (B.52) and (3.46) the dimensionless ratio

$$\mathcal{Pr} = \frac{(\eta/\varrho)}{K} = \frac{4}{15}\frac{aT^4}{c\kappa\varrho^2}\frac{3\,\kappa C_P\varrho^2}{4\,acT^3} = \frac{C_P T}{5\,c^2}\,. \tag{B.64}$$

B.5.3 Peclet and Nusselt Numbers

The Peclet number is the ratio of the thermal to the dynamical timescales, generally taken as

$$\mathcal{Pe} = \frac{t_{\mathrm{therm}}}{t_{\mathrm{motion}}} = \frac{\ell^2}{K}\frac{v}{\ell} = \frac{v\ell}{K}\,. \tag{B.65}$$

If one accounts for the spherical geometry of the blob for calculating the radiative losses, one has a factor of 6 at the denominator (Sects. 5.4.2, B.5.3):

$$\frac{t_{\text{therm}}}{t_{\text{motion}}} = \frac{\ell^2}{6K}\frac{v}{\ell} = \frac{v\ell}{6K} \equiv \Gamma \ . \tag{B.66}$$

This is the way we defined Γ (see 5.66). Thus, $\Gamma = \mathcal{P}e/6$. Different geometries give different factors; the example of a radiative slab is given in Sect. 13.4.4. For large values of $\mathcal{P}e$, the moving eddies do not have the time to lose energy on their ways and the motions are adiabatic.

Nusselt number: $\mathcal{N}u$ is the ratio of the heat transferred in a moving fluid to that transferred by conduction. In stars, this is typically the ratio of the total (convective+radiative) to the radiative flux.

B.5.4 The Rossby Number

The Rossby number is the ratio of the absolute values of the inertial acceleration in the equation of Navier–Stokes to the Coriolis acceleration $\boldsymbol{a}_{\text{Cor}} = -2\boldsymbol{\Omega} \times \boldsymbol{v}$ (cf. B.24) for a medium rotating with an angular velocity Ω:

$$\mathcal{R}o = \frac{\text{inertial}}{\text{Coriolis}} = \frac{v^2/\ell}{2\Omega v \sin\varphi} = \frac{v}{2\Omega\ell\sin\varphi} \ , \tag{B.67}$$

where φ is the angle between the rotation axis and the direction of the fluid motion. At large scales, the Coriolis force tends to be relatively important.

B.6 More on the Physics of Rotation

B.6.1 The Angular Velocity in Spherical Functions

In a rotating star, the angular velocity $\Omega(r,\vartheta)$ is developed over the star in spherical harmonics in terms of the Legendre polynomials. However, the angular velocity is also developed in order to simplify the expression of the transport of the angular momentum (Sect. 10.5.4). In this case, as shown by Mathis (see also [386]), the proper functions of Ω for the angular momentum transport are not exactly spherical harmonics and they require a special attention. The development of $\Omega(r,\vartheta)$ in spherical harmonics is

$$\Omega(r,\vartheta) = \sum_{s=0}^{\infty} \Omega_s(r)P_s(\cos\vartheta) \ , \tag{B.68}$$

where $\Omega_s(r)$ is the radial component of each harmonics. The functions P_s are the Legendre polynomials,

$$P_0(x) = 1, \quad P_1(x) = x, \quad P_2 = \frac{1}{2}(3x^2 - 1),$$

$$P_3(x) = \frac{1}{2}(5x^3 - 3x), \quad P_4(x) = \frac{1}{8}(35x^4 - 30x^2 + 3)\dots. \qquad (B.69)$$

The Legendre polynomials obey, among other properties, to the following relations:

$$\int_{-1}^{1} P_m(x)P_n(x)dx = 0, \text{ for } m \neq n; \quad \int_{-1}^{1} (P_m(x))^2 dx = \frac{2}{2m+1}. \qquad (B.70)$$

On the other side, when we write $\Omega(r, \vartheta)$ and integrate it in expression (10.112) to get the angular momentum, we consider expression (10.104)

$$\Omega(r, \vartheta) = \overline{\Omega}(r) + \widehat{\Omega}(r, \vartheta), \qquad (B.71)$$

where $\overline{\Omega}$ is the mean angular velocity in the expression of the angular momentum and $\widehat{\Omega}$ expresses the corresponding differential rotation,

$$\overline{\Omega}(r) = \frac{\int_0^\pi \Omega(r, \vartheta)\sin^3 \vartheta\, d\vartheta}{\int_0^\pi \sin^3 \vartheta\, d\vartheta}. \qquad (B.72)$$

With (B.68), this becomes

$$\overline{\Omega}(r) = \frac{\int_0^\pi \sum_{s=0}^\infty \Omega_s(r)P_s(\cos \vartheta)\sin^3 \vartheta d\vartheta}{\int_0^\pi \sin^3 \vartheta d\vartheta} = \sum_{s=0}^\infty \Omega_s(r)\underbrace{\left(\frac{\int_0^\pi P_s(\cos \vartheta)\sin^3 \vartheta d\vartheta}{\int_0^\pi \sin^3 \vartheta d\vartheta}\right)}_{I_s}.$$

This defines I_s; its denominator is equal to $4/3$; thus

$$I_s = \frac{3}{4}\int_0^\pi \sin^2 \vartheta\, P_s(\cos \vartheta)\sin \vartheta\, d\vartheta. \qquad (B.73)$$

Let us express $\sin^2 \vartheta$ in terms of $P_2(\cos \vartheta)$; one has

$$P_2(\cos \vartheta) = 1 - \frac{3}{2}\sin^2 \vartheta; \quad \text{thus } \sin^2 \vartheta = \frac{2}{3}[1 - P_2(\cos \vartheta)]. \qquad (B.74)$$

I_s can be written as

$$I_s = \frac{3}{4}\int_0^\pi \frac{2}{3}[1 - P_2(\cos \vartheta)]P_s(\cos \vartheta)\sin \vartheta\, d\vartheta$$

$$= \frac{1}{2}\int_0^\pi [P_0(\cos \vartheta)P_s(\cos \vartheta) - P_2(\cos \vartheta)P_s(\cos \vartheta)]\sin \vartheta\, d\vartheta$$

$$= -\frac{1}{2}\int_1^{-1} P_0(x)P_s(x)\, dx + \frac{1}{2}\int_1^{-1} P_2(x)P_s(x)\, dx$$

$$= \frac{1}{2}\left[\frac{2}{2\times 0 + 1}\delta_{s,0} - \frac{2}{2\times 2 + 1}\delta_{s,2}\right] = \delta_{s,0} - \frac{1}{5}\delta_{s,2}, \qquad (B.75)$$

where $\delta_{s,i}$ is the Kronecker symbol. Thus, one has $I_0 = 1$ and $I_2 = -\frac{1}{5}$ while all the other components $I_s = 0$. We can write $\overline{\Omega}$ with (B.73),

$$\overline{\Omega}(r) = \sum_{s=0}^{\infty} \Omega_s(r) I_s = \sum_{s=0}^{\infty} \Omega_s(r) \left[\delta_{s,0} - \frac{1}{5} \delta_{s,2} \right] = \Omega_0(r) - \frac{1}{5} \Omega_2(r). \qquad \text{(B.76)}$$

We see that the average $\overline{\Omega}$ of the angular velocity on an isobar for the expression of the angular momentum is not equal to just the radial component of the first term of the development in spherical harmonics. One can also express the horizontal term $\widehat{\Omega}$ as

$$\widehat{\Omega}(r, \vartheta) = \Omega(r, \vartheta) - \overline{\Omega}(r) = \sum_{s=0}^{\infty} \Omega_s(r) P_s(\cos \vartheta) - \sum_{s=0}^{\infty} \Omega_s(r) I_s$$

$$= \Omega_0(r) + \sum_{s>0}^{\infty} \Omega_s(r) P_s(\cos \vartheta) - \Omega_0(r) - \sum_{s>0}^{\infty} \Omega_s(r) I_s$$

$$= \sum_{s>0}^{\infty} \Omega_s(r) \left[P_s(\cos \vartheta) - I_s \right] . \qquad \text{(B.77)}$$

The development of $\widehat{\Omega}(r, \vartheta)$ is

$$\widehat{\Omega}(r, \vartheta) = \Omega_2 \left[P_2(\cos \vartheta) + \frac{1}{5} \right] + \Omega_4 P_4(\cos \vartheta) + \Omega_6 P_6(\cos \vartheta) + \dots . \quad \text{(B.78)}$$

Thus, if we limit the development to the term in $P_2(\cos \vartheta)$, one has to take for the expression of the angular velocity in the angular momentum,

$$\widehat{\Omega}(r, \vartheta) = \overline{\Omega}(r) + \widehat{\Omega}(r, \vartheta) = \overline{\Omega}(r) + \Omega_2(r) \left[P_2(\cos \vartheta) + \frac{1}{5} \right] . \qquad \text{(B.79)}$$

The noticeable point is that there is a fraction $1/5$ to be added to $P_2(\cos \vartheta)$ multiplying $\Omega_2(r)$. For the other terms in the developments, there is no additive constant. This fraction $1/5$ only applies in the developments of $\Omega(r, \vartheta)$ for the angular momentum. Interestingly enough, this term $1/5$ is most useful in writing the equation for the time evolution of Ω_2 in (12.6).

Since all the terms I_s are equal to zero except for $s = 0$ and $s = 2$, this means from (B.73) that the only components of circulation able to carry angular momentum are the components in $P_0(\cos \vartheta)$ and in $P_2(\cos \vartheta)$. This is an argument to limit the development of the various functions to the second Legendre polynomial.

B.6.2 Rotational Splitting for Non-uniform Rotation

Some developments on the rotational splitting in helioseismology are given here in complement of Sect. 16.6.1 in order to account for the fact that Ω may be a function of r and ϑ and that the Coriolis force also influences the splitting [131, 227].

In the equation of motion (16.14), $\boldsymbol{\xi}$ is the perturbation displacement with respect to the fluid at rest and $\boldsymbol{v}$ the associated velocity. Now, we must consider the perturbation $\boldsymbol{\delta r}$ with respect to the fluid moving at a velocity $\boldsymbol{v_0}$, supposed to be small. One has the following relation between the material derivative of the displacement and the Lagrangian velocity perturbation:

$$\frac{d\boldsymbol{\delta r}}{dt} = \boldsymbol{\delta v} .\tag{B.80}$$

The material time derivative of the perturbation becomes with (1.17)

$$\frac{d\boldsymbol{\delta r}}{dt} = \frac{\partial \boldsymbol{\delta r}}{\partial t} + (\boldsymbol{v_0} \cdot \boldsymbol{\nabla})\,\boldsymbol{\delta r} .\tag{B.81}$$

The acceleration term in the left member of (16.14, see joined remarks) written for the velocity perturbation $\boldsymbol{\delta v}$ becomes with the above rule,

$$\frac{d^2\boldsymbol{\delta r}}{dt^2} = \frac{\partial^2\boldsymbol{\delta r}}{\partial t^2} + (\boldsymbol{v_0}\cdot\boldsymbol{\nabla})\frac{\partial\boldsymbol{\delta r}}{\partial t} + (\boldsymbol{v_0}\cdot\boldsymbol{\nabla})\frac{\partial\boldsymbol{\delta r}}{\partial t} + (\boldsymbol{v_0}\cdot\boldsymbol{\nabla})^2\boldsymbol{\delta r}.\tag{B.82}$$

For small velocities, we neglect the term in $\boldsymbol{v_0^2}$ and (16.14) becomes

$$\varrho_0\frac{\partial^2\boldsymbol{\delta r}}{\partial t^2} + 2\varrho_0\,(\boldsymbol{v_0}\cdot\boldsymbol{\nabla})\frac{\partial\boldsymbol{\delta r}}{\partial t} = -\boldsymbol{\nabla}P' + \varrho_0\,\boldsymbol{g}' + \varrho'\,\boldsymbol{g}_0 .\tag{B.83}$$

The oscillations around the equilibrium structure are of the form $e^{i\omega t}$; thus

$$-\omega^2\varrho_0\boldsymbol{\delta r} + 2i\omega\varrho_0(\boldsymbol{v_0}\cdot\boldsymbol{\nabla})\boldsymbol{\delta r} = -\boldsymbol{\nabla}P' + \varrho_0\,\boldsymbol{g}' + \varrho'\,\boldsymbol{g}_0 .\tag{B.84}$$

Formally these are the amplitudes. The two terms on the left correspond to a perturbed frequency, say ω', and we write their sum as

$$-\omega'^2\varrho_0\boldsymbol{\delta r} = -(\omega + \delta\omega)^2\varrho_0\boldsymbol{\delta r} \approx -(\omega^2 + 2\omega\delta\omega)\varrho_0\boldsymbol{\delta r} .\tag{B.85}$$

By comparison with (B.84), we identify $-\varrho_0\delta\omega\boldsymbol{\delta r} \longleftrightarrow i\varrho_0(\boldsymbol{v_0}\cdot\boldsymbol{\nabla})\boldsymbol{\delta r}$. Multiplying both sides of this expression by the complex conjugate $\boldsymbol{\delta r}^*$, one has

$$-\varrho_0\delta\omega|\boldsymbol{\delta r}|^2 = i\varrho_0\boldsymbol{\delta r}*(\boldsymbol{v_0}\cdot\boldsymbol{\nabla})\boldsymbol{\delta r} ,\tag{B.86}$$

so that by making the average over all layers, we get for the frequency shift due to the velocity field,

$$\delta\omega = -i\frac{\int_V \varrho_0 \boldsymbol{\delta r} * \cdot (\boldsymbol{v_0} \cdot \boldsymbol{\nabla}) \, \boldsymbol{\delta r} dV}{\int_V \varrho_0 \, |\boldsymbol{\delta r}|^2 \, dV} \, . \tag{B.87}$$

We evaluate this quantity for a motion of rotation with an angular velocity $\Omega(r, \vartheta)$, where as usual ϑ is the colatitude. The velocity is $\boldsymbol{v_0} = \Omega r \sin \vartheta \, \boldsymbol{e_\varphi}$. At a point of coordinates (r, ϑ, φ), the vector $\boldsymbol{\Omega}$ can be expressed by its components along the unity vectors $\boldsymbol{e_r}$ and $\boldsymbol{e_\vartheta}$ (Fig. B.2), $\boldsymbol{\Omega} = \Omega(\cos \vartheta \, \boldsymbol{e_r} - \sin \vartheta \boldsymbol{e_\vartheta})$, and one has

$$\boldsymbol{v_0} = \boldsymbol{\Omega} \times \boldsymbol{r}. \tag{B.88}$$

A quantity like $(\boldsymbol{v_0} \cdot \boldsymbol{\nabla}) \boldsymbol{F}$ is the gradient of $\boldsymbol{F}$ projected on the velocity $\boldsymbol{v_0}$; one has

$$(\boldsymbol{v_0} \cdot \boldsymbol{\nabla}) \boldsymbol{F} = \boldsymbol{e_F} (\boldsymbol{v_0} \cdot \boldsymbol{\nabla}) \, |F| + |F| \, (\boldsymbol{v_0} \cdot \boldsymbol{\nabla}) \, \boldsymbol{e_F} \, . \tag{B.89}$$

The gradient of the scalar $|F|$ is

$$(\boldsymbol{v_0} \cdot \boldsymbol{\nabla}) \, |F| = \Omega \, r \sin \vartheta \, \frac{1}{r \sin \vartheta} \frac{\partial \, |F|}{\partial \varphi} = i m \, |F| \, , \tag{B.90}$$

because for a perturbation the dependence on φ is given by $e^{(im\varphi)}$. The last term in (B.89) represents the change of the unit vector $\boldsymbol{e_F}$ along the velocity $\boldsymbol{v_0}$ produced by rotation. At some level in a rotating star the change of $\boldsymbol{e_F}$ is just produced by the rotation motion, which makes the unit vector $\boldsymbol{e_F}$, after a small displacement, to point in a slightly new direction. After one full axial rotation, the unit vector $\boldsymbol{e_F}$ is again the same. If $\boldsymbol{e_F}$ would coincide with $\boldsymbol{e_r}$, this projection would just be along $\boldsymbol{v_0}$ and we would have $(\boldsymbol{v_0} \cdot \boldsymbol{\nabla}) \boldsymbol{e_r} = \boldsymbol{e_{v_0}} = \boldsymbol{\Omega} \times \boldsymbol{e_r}$. More generally, one has

$$(\boldsymbol{v_0} \cdot \boldsymbol{\nabla}) \boldsymbol{e_F} = \boldsymbol{\Omega} \times \boldsymbol{e_F} \, , \tag{B.91}$$

and

$$(\boldsymbol{v_0} \cdot \boldsymbol{\nabla}) \boldsymbol{F} = i m \boldsymbol{F} + \boldsymbol{\Omega} \times \boldsymbol{F} \, . \tag{B.92}$$

According to the property of the cross-product and because $\boldsymbol{\Omega}$ has no component along $\boldsymbol{e_\varphi}$, one has

$$\boldsymbol{\Omega} \times \boldsymbol{F} = \Omega \left\{ - \sin \vartheta \, F_\varphi \boldsymbol{e_r} - \cos \vartheta \, F_\varphi \boldsymbol{e_\vartheta} + (\cos \vartheta \, F_\vartheta + \sin \vartheta \, F_r) \boldsymbol{e_\varphi} \right\} \, . \tag{B.93}$$

Now, we express the term in (B.87) using this last expression and (16.50) for $\boldsymbol{\delta r}$, in which we omit the tildas over the amplitudes ξ_r and ξ_h:

$$(\boldsymbol{v_0} \cdot \boldsymbol{\nabla}) \boldsymbol{\delta r} = i m \Omega \delta r + 2\sqrt{\pi} \Omega \left(-\xi_h \frac{\partial Y_\ell^m}{\partial \varphi} \boldsymbol{e_r} - \xi_h \cot \vartheta \frac{\partial Y_\ell^m}{\partial \varphi} \boldsymbol{e_\vartheta} \right)$$

$$2\sqrt{\pi} \Omega \left(\xi_r \sin \vartheta \, Y_\ell^m + \xi_h \cos \vartheta \frac{\partial Y_\ell^m}{\partial \vartheta} \right) \boldsymbol{e_\varphi} \, . \tag{B.94}$$

The numerator of (B.87) becomes then
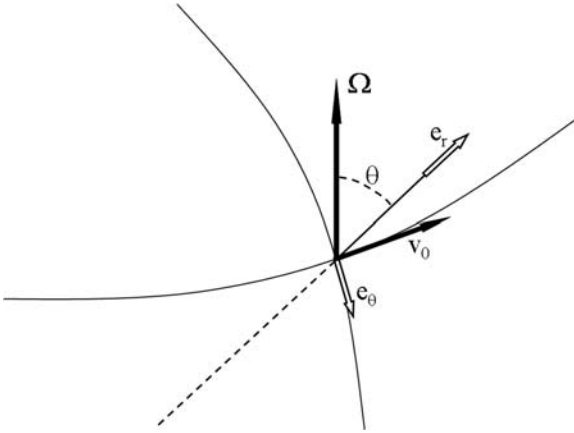
Fig. B.2 The various vectors in the spherical coordinate system

$$\int_V \varrho_0 \boldsymbol{\delta r} * \cdot (\boldsymbol{v_0} \cdot \boldsymbol{\nabla})\, \boldsymbol{\delta r} dV = im \int_V \varrho_0 \Omega \, |\boldsymbol{\delta r}|^2\, dV$$

$$+ 4\pi \int_V \varrho_0 \Omega \left\{ -\xi_r^* (Y_\ell^m)^* \xi_h \frac{\partial Y_\ell^m}{\partial \varphi} - |\xi_h|^2 \left(\frac{\partial Y_\ell^m}{\partial \vartheta} \right)^* \frac{\partial Y_\ell^m}{\partial \varphi} \cot \vartheta \right.$$

$$\left. + \xi_h^* \xi_r \left(\frac{\partial Y_\ell^m}{\partial \varphi} \right)^* Y_\ell^m + |\xi_h|^2 \left(\frac{\partial Y_\ell^m}{\partial \varphi} \right)^* \frac{\partial Y_\ell^m}{\partial \varphi} \cot \vartheta \right\} dV \,. \tag{B.95}$$

We use (16.38) for the spherical harmonics Y_ℓ^m. The derivatives with respect to φ give im for Y_ℓ^m, with a sign minus for the complex conjugate. Since in each term of the second integral, one has the product of Y_ℓ^m and its conjugate or the derivative of it, the exponential $e^{im\varphi}$ disappears. The integration in φ just gives a factor 2π. Thus, the previous expression can be written as

$$\int_V \varrho_0 \boldsymbol{\delta r}^* \cdot (\boldsymbol{v_0} \cdot \boldsymbol{\nabla})\, \boldsymbol{\delta r} dV = im 8\pi^2 c_{\ell m}^2 U_{n\ell m} \,, \tag{B.96}$$

with

$$U_{n\ell m} = \int_0^\pi \sin \vartheta d\vartheta \int_0^R \Omega \varrho_0 r^2 \left\{ |\xi_r|^2 P_\ell^m (\cos \vartheta)^2 \right.$$

$$- P_\ell^m (\cos \vartheta)^2 [\xi_r^* \xi_h + \xi_r \xi_h^*] + |\xi_h|^2 \left[\left(\frac{dP_\ell^m}{d\vartheta} \right)^2 + \frac{m^2}{\sin^2 \vartheta} P_\ell^m (\cos \vartheta)^2 \right]$$

$$\left. - 2 P_\ell^m (\cos \vartheta) \frac{dP_\ell^m}{d\vartheta} \cot \vartheta |\xi_h|^2 \right\} dr \,. \tag{B.97}$$

The denominator of (B.87) becomes

$$\int_V \varrho_0 |\boldsymbol{\delta r}|^2 \, dV = 8\pi^2 c_{\ell m}^2 D_{nlm} \,, \tag{B.98}$$

with

$$D_{n\ell m} = \int_0^\pi \sin\vartheta d\vartheta \int_0^R \varrho_0 r^2 \Big\{ |\xi_r|^2 \, P_\ell^m (\cos\vartheta)^2$$

$$|\xi_h|^2 \left[\left(\frac{dP_\ell^m}{d\vartheta} \right)^2 + \frac{m^2}{\sin^2\vartheta} P_\ell^m (\cos\vartheta)^2 \right] \Big\} dr \,. \tag{B.99}$$

The rotational perturbation (B.87) of the frequency can thus be written as

$$\delta\omega_{n\ell m} = m \frac{U_{n\ell m}}{D_{n\ell m}} \,. \tag{B.100}$$

From now on, we assume that Ω is only a function of r (for the general case see [131]). We use the orthogonality of the Legendre polynomials,

$$\int_1^1 P_k^m P_\ell^m dx = \frac{2(\ell+m)!}{(2\ell+1)(\ell-m)!} \delta_{k,\ell} \,, \tag{B.101}$$

where $\delta_{k,\ell}$ is here the Kronecker symbol. The last term in (B.97) gives

$$\int_0^\pi P_\ell^m(\cos\vartheta) \frac{dP_\ell^m}{d\vartheta} \frac{\cos\vartheta}{\sin\vartheta} \sin\vartheta d\vartheta = \int_1^{-1} x P_\ell^m(x) dP_\ell^m$$

$$= \underbrace{\frac{1}{2} x P_\ell^m(x)^2 \big|_{+1}^{-1}}_{=0} - \frac{1}{2} \int_1^{-1} P_\ell^m(x)^2 dx \,, \tag{B.102}$$

The second term is given by (B.101). We also note that

$$\int_0^\pi P_\ell^m \frac{d}{d\vartheta} \left(\sin\vartheta \frac{dP_\ell^m}{d\vartheta} \right) d\vartheta = \underbrace{P_\ell^m \sin\vartheta \frac{dP_\ell^m}{d\vartheta} \big|_0^\pi}_{=0} - \int_0^\pi \sin\vartheta \left(\frac{dP_\ell^m}{d\vartheta} \right)^2 d\vartheta \,. \tag{B.103}$$

This can be used to express the term in square bracket in (B.97),

$$\int_0^\pi \left[\left(\frac{dP_\ell^m}{d\vartheta} \right)^2 + \frac{m^2}{\sin^2\vartheta} P_\ell^m (\cos\vartheta)^2 \right] \sin\vartheta d\vartheta$$

$$= - \int_0^\pi P_\ell^m(\cos\vartheta) \left(\frac{d}{d\vartheta} \left(\sin\vartheta \frac{dP_\ell^m}{d\vartheta} \right) - \frac{m^2}{\sin\vartheta} P_\ell^m(\cos\vartheta) \right) d\vartheta$$

$$= \ell(\ell+1) \int_{-1}^{+1} P_\ell^m(x)^2 dx \,, \tag{B.104}$$

where one uses property (16.35) of the associate Legendre polynomial, writing $x = \cos\vartheta$ and $1/d\vartheta = -\sin\vartheta/dx$. The above relation is accounted for in (B.97) and (B.99). With (B.102) and (B.104), one finally gets for (B.100), also taking the orthogonality relation and after simplifying the numerical factors [131, 227],

$$\delta\omega_{n\ell m} = m\frac{\int_0^R \Omega(r)\left(\xi_r^2 + \ell(\ell+1)\xi_h^2 - 2\xi_r\xi_h - \xi_h^2\right)r^2\varrho_0 dr}{\int_0^R(\xi_r^2 + \ell(\ell+1)\xi_h^2)r^2\varrho_0\,dr}\ . \qquad \text{(B.105)}$$

This expression gives the rotational splitting for an oscillation mode $(n\ell m)$; it is the generalization of the expressions of Sect. (16.6.1).

Appendix C
Complements on Radiative Transfer and Thermodynamics

C.1 Radiation: Definitions

Here, we define some basic properties of the radiation field in stars. Let us consider a medium with a radiation beam at frequency v in a given direction s (Fig. C.1). The energy dU_v transmitted by a surface element $d\boldsymbol{\sigma}$ in a direction making an angle ϑ with the normal to $d\boldsymbol{\sigma}$, over the length ds centered on a solid angle $d\Omega$, during the time dt and in the frequency interval dv, is

$$dU_v \equiv I_v\, d\sigma \cos \vartheta\, dv d\Omega\, dt \;. \tag{C.1}$$

This defines the intensity I_v of a radiation beam.

Density of radiation energy: The density of radiation energy is the ratio of dU_v by the element of volume $dV = d\sigma \cos \vartheta\, c\, dt$ in which lies this energy in the interval of time dt. The density of monochromatic energy for the pencil of light considered is

$$du_v \equiv \frac{dU_v}{dv\, dV} = \frac{I_v}{c} d\Omega \;. \tag{C.2}$$

By integrating over all directions, one has

$$u_v \equiv \frac{1}{c} \int_\Omega I_v\, d\Omega \;. \tag{C.3}$$

The element of solid angle $d\Omega$ is (Fig. B.1) $d\Omega = 2\pi \sin \vartheta\, d\vartheta$. We may integrate I_v and u_v over the frequencies and write the integrated quantities without the index v, $u = 1/c \int_\Omega I\, d\Omega$. For an isotropic radiation I_0, one has

$$u_0 = \frac{4\pi}{c} I_0 \;. \tag{C.4}$$

Flux: The monochromatic flux, i.e., the energy crossing a surface in all directions by units of time, surface and frequency, is in a solid angle $d\Omega$
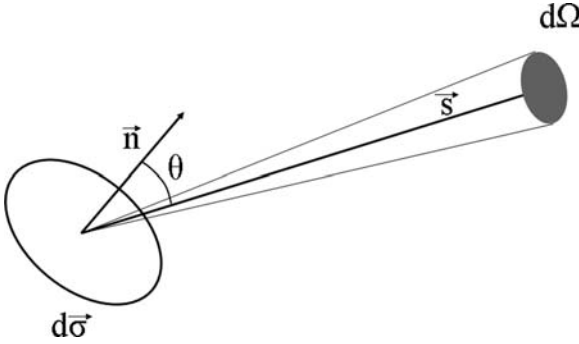
Fig. C.1 The geometrical parameters associated to a radiation beam

$$dF_\nu \equiv \frac{dU_\nu}{d\sigma\, dt\, d\nu} = I_\nu \cos\vartheta\, d\Omega$$

$$\text{which leads to}\quad F_\nu = \int_\Omega I_\nu \cos\vartheta\, d\Omega \ . \tag{C.5}$$

In the case of isotropy, the total flux F integrated over the whole solid angle around a given point is evidently zero. However, one may consider the outgoing flux F_ν^+. It is obtained by the integration of (C.5) over ϑ from 0 to $\pi/2$ (see Fig. B.1). The outgoing flux is thus

$$F_\nu^+ = \pi I_\nu \ . \tag{C.6}$$

We may also consider the total flux or the outgoing flux F^+ integrated over the frequencies, its units are W m^{-2} (MKSA) or erg s^{-1} cm^{-2} (CGS).

Luminosity: The monochromatic luminosity L_ν is the energy emitted by a star over all directions by units of time and frequency,

$$dL_\nu \equiv \frac{dU_\nu}{dt\, d\nu} = I_\nu \cos\vartheta\, d\Omega d\sigma,$$

$$\text{i.e.,}\quad L_\nu = \int_\Sigma \int_\Omega I_\nu \cos\vartheta\, d\Omega\, d\sigma = \int_\Sigma F_\nu^+\, d\sigma = 4\pi R^2\, F_\nu^+ , \tag{C.7}$$

where Σ is the total stellar surface. The same relation applies for L and F^+, the luminosity and flux integrated over the frequencies. One has for the outgoing flux, which at a level r in a star is generally noted as

$$F_r = \frac{L_r}{4\pi r^2} \ . \tag{C.8}$$

Radiation pressure : The radiation pressure is obtained from expression (B.38) applied to photons, with $v = c$, $p = h\nu/c$ and

$$n(\vartheta, p)\, d\vartheta\, dp = \frac{dU_\nu}{dV\, h\nu} = \frac{1}{c\, h\nu} I_\nu\, d\nu\, d\Omega\,. \tag{C.9}$$

The contribution to radiation pressure from the interval $(\nu, \nu + d\nu)$ is

$$P_\nu = \frac{2}{c} \int_0^{\pi/2} \int_0^\infty \cos^2 \vartheta\, I_\nu\, d\nu d\Omega\,. \tag{C.10}$$

We take into account the symmetry with respect to the surface S in Fig. B.1. The pressure is thus of the form

$$P_{\rm rad} = \frac{1}{c} \int_0^\pi I \cos^2 \vartheta\, d\Omega\,. \tag{C.11}$$

If the radiation is monochromatic with intensity I_ν, we have the radiation pressure $P_{\nu,\rm rad}$. The absence of index ν indicates the integrated value over the frequencies. For an isotropic radiation I_0, the radiation pressure becomes

$$P_{\rm rad} = \frac{4\pi}{c} \frac{I_0}{3}\,. \tag{C.12}$$

Black-body radiation: For a medium in equilibrium at constant temperature T in an isolated box, the intensity of the radiation is that of a black body given by Planck's law

$$I_\nu = B_\nu(T) = \frac{2h\nu^3}{c^2} \frac{1}{e^{\frac{h\nu}{kT}} - 1}\,;. \tag{C.13}$$

One may consider the monochromatic quantities (with index ν) or the integrated quantities. At thermal equilibrium, one has

– intensity $\quad\quad\quad\quad\quad : I = B(T) = \frac{\sigma}{\pi} T^4\,,$
– flux $\quad\quad\quad\quad\quad\quad\quad : F^+ = \pi I = \sigma T^4$ (but the total flux $F = 0$),
– energy density $\quad\quad\quad : u = \frac{4\pi I}{c} = \frac{4\sigma}{c} T^4 = a T^4\,,$
– radiation pressure $\quad\quad : P_{\rm rad} = \frac{1}{3} u = \frac{1}{3} a T^4\,. \tag{C.14}$

where σ is the Stefan's constant and $a = 4\sigma/c$ is the radiation constant.

Effective temperature: By definition, the effective temperature $T_{\rm eff}$ of a star of radius R and luminosity L is the temperature of a black body which for the same radius would have the same luminosity

$$L \equiv 4\pi R^2 \sigma T_{\rm eff}^4\,. \tag{C.15}$$

For the Sun, this expression leads to $T_{\rm eff} = 5770$ K.

C.1.1   The Quasi-Isotropic Case

In stellar interiors, the degree of anisotropy is very small (Sect. 3.1.2) and one may develop the intensity (monochromatic or integrated) like

$$I = I_0 + I_1 \cos \vartheta + I_2 \cos^2 \vartheta + \dots \tag{C.16}$$

One may introduce this in (3.8). Considering a small region of the star, we neglect the curvature effect (i.e., the derivative $\partial/\partial\vartheta$). The terms of the same order in $\cos \vartheta$ lead to $dI_{n-1}/dr = -\kappa\rho I_n$ for $n > 0$, because for $n = 0$ we also have the emission term j, which is isotropic. This implies

$$\frac{I_n}{I_{n-1}} \approx \frac{1}{\kappa\rho R} \sim \frac{\ell}{R}, \tag{C.17}$$

where ℓ is the mean free path (Sect. 3.1.2). In the Sun, the ratio $\ell/R \leq 10^{-10}$. This means that with this accuracy, one may develop (C.16) like $I = I_0 + I_1 \cos \vartheta$, with $I_1/I_0 \sim 10^{-10}$ on the average. In this case, we may calculate the energy density u, the emergent flux F^+, the radiation pressure P_{rad}, as well as the monochromatic quantities with (C.3), (C.5) and (C.11)

- energy density   : $u = \frac{4\pi I_0}{c} = \frac{4\sigma}{c}T^4 = aT^4$,
- total flux   : $F = \frac{4}{3}\pi I_1$,
- radiation pressure : $P_{\text{rad}} = \frac{1}{3}u = \frac{1}{3}aT^4$.

In the quasi-isotropic case, the energy density and radiation pressure depend only on the isotropic term I_0, while the total flux F depends on the anisotropic term I_1.

C.2   Expression of the Heat Changes $dq = dq(P, \varrho)$

It is useful in some cases, e.g., for stellar oscillations, to express the heat change dq as a function $dq = dq(P, \varrho)$ instead of the function $dq = dq(T, P)$ given in expression (3.63). Let us start from this last expression,

$$dq = C_P \, dT - \frac{\delta}{\varrho} \, dP \, . \tag{C.18}$$

With (7.63) for $\mu =$ const., we write this expression as a function of dP and $d\varrho$

$$dq = \left(C_P \frac{\alpha}{\delta} \frac{T}{P} - \frac{\delta}{\varrho} \right) dP - C_P \frac{T}{\delta} \frac{d\varrho}{\varrho} \, . \tag{C.19}$$

One has with (3.72), (7.70), (3.76) and (7.58),

$$C_P \frac{\alpha\, T}{\delta\, P} - \frac{\delta}{\varrho} = \frac{C_V\, \alpha\, T}{P\, \delta} = \frac{C_P\, T}{\Gamma_1 P\, \delta} = \frac{\Gamma_2}{\varrho\, \Gamma_1\, (\Gamma_2 - 1)} = \frac{1}{\varrho\, (\Gamma_3 - 1)} \,, \qquad (C.20)$$

with (7.68) and (7.58),

$$\frac{C_P\, T}{\varrho\, \delta} = \frac{P\, \Gamma_2}{\varrho^2\, (\Gamma_2 - 1)} = \frac{P\, \Gamma_1}{\varrho^2\, (\Gamma_3 - 1)} \,. \qquad (C.21)$$

With these last two expressions, we can now express (C.19) and obtain

$$dq = \frac{1}{\varrho\, (\Gamma_3 - 1)} \left(dP - \frac{\Gamma_1 P}{\varrho}\, d\varrho \right), \qquad (C.22)$$

which gives an expression of the heat brought or subtracted from the system as a function of the changes of pressure and density.

C.3   Adiabatic Acoustic Waves

The sound speed and acoustic waves appear in many chapters. Let us consider an homogeneous medium where gravity may be neglected with respect to the internal pressure. We consider some small displacement $\boldsymbol{\delta x}$ of the medium around equilibrium situation indicated by index "0". At this point in the medium, the various variables undergo a perturbation of the form $P = P_0 + P'$ (see Sect. 16.1). The equations of continuity (1.1) and motion (1.2) become to the first order in the velocity $\boldsymbol{v} = d\boldsymbol{\delta x}/dt$,

$$\frac{\partial \varrho'}{\partial t} + \boldsymbol{\nabla} \cdot (\varrho_0 \boldsymbol{v}) = 0 \quad \text{and} \quad \varrho_0 \frac{\partial^2 \boldsymbol{\delta x}}{\partial t^2} = -\boldsymbol{\nabla} P' \,. \qquad (C.23)$$

The divergence of the equation of motion gives

$$\varrho_0 \frac{\partial^2}{\partial t^2} (\boldsymbol{\nabla} \cdot \boldsymbol{\delta x}) = -\nabla^2 P' \,. \qquad (C.24)$$

The integration of the above perturbed equation of continuity in (C.23) yields $\varrho' + \boldsymbol{\nabla} \cdot (\varrho_0 \boldsymbol{\delta x}) = 0$, which allows us to write the above equation as

$$\frac{\partial^2 \varrho'}{\partial t^2} = \nabla^2 P' = \frac{\Gamma_1 P_0}{\varrho_0} \nabla^2 \varrho' \,. \qquad (C.25)$$

From (C.22), one has for *adiabatic perturbations* $P' = (\Gamma_1 P_0/\varrho_0)\varrho'$, thus

$$\frac{\partial^2 \varrho'}{\partial t^2} = c_S^2 \nabla^2 \varrho', \quad \text{with} \quad c_S^2 = \left(\frac{\Gamma_1 P_0}{\varrho_0} \right)_{\text{ad}} = \left(\frac{\partial P}{\partial \varrho} \right)_{\text{ad}} \,, \qquad (C.26)$$

where c_S is the speed of the perturbation with pressure as the recall force. This is the sound speed. For a perfect gas, it is

$$c_S = \sqrt{\gamma_g \frac{k}{\mu m_u} T} \, . \tag{C.27}$$

For the isothermal sound speed, $\gamma_g = 1$. Equation (C.26) is the classical equation for sound waves, it admits for plane waves a solution of the form,

$$\varrho' = A \exp i(\mathbf{k} \cdot \mathbf{r} - \sigma t), \tag{C.28}$$

where A is a constant. With (C.26), it leads to the dispersion relation

$$\sigma^2 = c_S^2 |\mathbf{k}|^2 \, , \tag{C.29}$$

which confirms that c_S is the velocity of the wave.

C.4   The Entropy of Radiation and Perfect Gas

Entropy is an important concept in Astrophysics. In cosmology, the constancy of the entropy of the universe after the inflation allows one to derive the main conservation laws. For stellar astrophysics, the evacuation of the entropy from stars dominates stellar evolution from their formation to the final remnants.

C.4.1   Entropy of Radiation

The entropy of radiation is very large in stars. Generally, as we will see, the main changes in the entropy of astrophysical media are due to the variations of the entropy of radiation. The first law of thermodynamics writes

$$dQ = dU + dw = dU + PdV, \tag{C.30}$$

where dQ is the heat provided to the system and dw the work provided by the system. The second law applies to irreversible transformations and says

$$dS = \frac{dQ}{T} \quad \text{with} \quad dS > 0 \tag{C.31}$$

for an isolated system. For a medium dominated by black-body radiation,

$$T\,dS = d(uV) + P\,dV = 4aT^3 V\,dT + \frac{4}{3}aT^4\,dV\,, \tag{C.32}$$

$$dS = d\left(\frac{4}{3}aT^3 V\right) \implies S = \frac{4}{3}aT^3 V\,. \tag{C.33}$$

The integration constant has been set to zero, implying that the entropy at $T = 0$ is zero. The entropy by volume unity is thus $s = (4/3)\,aT^3$.

Let us now search the relation between the entropy of radiation and the number of photons in a given volume. At equilibrium, one has $du_v = (4\pi I_v/c)/dv$ (cf. C.14), the number of photons with a wavelength between λ and $\lambda + d\lambda$ by volume unity is

$$dn_\gamma(\lambda) = \frac{8\pi}{\lambda^4}\frac{d\lambda}{e^{\frac{hc}{\lambda kT}} - 1}\,. \tag{C.34}$$

The total number of photons by volume unity is

$$n_\gamma = \int_0^\infty dn_\gamma = 0.37\,\frac{aT^3}{k}\quad\left[\frac{\text{photons}}{\text{cm}^3}\right]. \tag{C.35}$$

The entropy by volume unity can thus be written as

$$s = \frac{4}{3}aT^3 = \frac{4}{3}\frac{k}{0.37}n_\gamma = 3.604\,k n_\gamma\,. \tag{C.36}$$

In a medium dominated by radiation, the entropy by volume unity is proportional to the concentration of photons. Conservation of entropy in a given volume implies conservation of the photon number in this volume.

C.4.2 Entropy of a Mixture of Perfect Gas and Radiation

In a volume V with N gas particles, the total energy is $U = \frac{3}{2}NkT + aT^4 V$ and the pressure $P = \frac{N}{V}kT + \frac{1}{3}aT^4$. This gives

$$T\,dS = \frac{3}{2}NkdT + 4aT^3 V\,dT + aT^4\,dV + \frac{NkT}{V}dV + \frac{1}{3}aT^4\,dV, \tag{C.37}$$

which can be written as

$$dS = Nkd\left(\ln(T^{3/2}V)\right) + d\left(\frac{4}{3}aT^3 V\right)\,, \tag{C.38}$$

so that

$$S = \frac{4}{3}aT^3 V + Nk\ln(T^{3/2}V) = 3.604\,k n_\gamma V + Nk\ln(T^{3/2}V)\,. \tag{C.39}$$

The entropy is essentially proportional to the number of gas particles and to the photon number. Radiation evacuates entropy from stars to inject it into the outer medium. This reduces the internal entropy.

C.4.3 Degenerate Gases and Minimum Entropy

If we take the equation of state $P = K_1 \left(\rho / \mu_e \right)^{5/3}$ (7.148) of a fully degenerate gas in the non-relativistic case, the energy density is $u = (3/2)P$ and one has for the internal energy U in a volume V,

$$U = uV = \frac{3}{2} K_1 \left(\frac{\rho}{\mu_e} \right)^{\frac{5}{3}} \frac{\mu\, m_u}{\rho} = \frac{3}{2} K_1 \frac{\mu\, m_u}{\mu_e^{\frac{5}{3}}} \rho^{\frac{2}{3}} . \tag{C.40}$$

Thus, one has for $T\,dS$

$$T\,dS = dU + P\,dV = K_1 \frac{\mu\, m_u}{\mu_e^{\frac{5}{3}}} \frac{d\rho}{\rho^{\frac{1}{3}}} - P\frac{d\rho}{\rho^2} \mu\, m_u = 0 . \tag{C.41}$$

The fully degenerate medium corresponds to a minimum of entropy, which is consistent since this corresponds to a state of maximum order. For the case of relativistic degeneracy with $P = \frac{1}{3} u$ and $P = K_2 \left(\frac{\rho}{\mu_e} \right)^{\frac{4}{3}}$, similar developments lead to $T\,dS = 0$. Thus, consistently there is also no change of entropy in the relativistic fully degenerate gas.

The minimum of entropy: Conversely, we may also search what is the equation of state corresponding to a minimum of entropy. Let us do it first for a non-relativistic gas with $P = \frac{2}{3} u$,

$$T\,dS = dU + P\,dV = \frac{3}{2} d\,(PV) + P\,dV = \frac{3}{2} V\,dP + \frac{5}{2} P\,dV . \tag{C.42}$$

The condition $T\,dS = 0$ gives

$$\frac{dP}{P} = -\frac{5}{3} \frac{dV}{V} = \frac{5}{3} \frac{d\rho}{\rho}, \quad \text{i.e.,} \quad P \sim \rho^{\frac{5}{3}} . \tag{C.43}$$

This consistently shows that in the non-relativistic case a law of the form $P \sim \rho^{\frac{5}{3}}$ corresponds to an extremum of entropy. This applies to the degenerate gas and also to adiabatic changes of a perfect gas, as for adiabatic convection (5.58). Similarly in the relativistic case with $P = \frac{1}{3} u$, the condition $T\,dS = 0$ imposes a law of the form $P \sim \rho^{\frac{4}{3}}$.

C.4.4   The Entropy of Mixing

The effects of the changes of the mean molecular weight on the entropy are often ignored. This is appropriate when the changes of μ result from a change of T and P as is the case for ionization. There $\mu = \mu(\varrho, T)$ and the coefficients α and δ (3.60) express the changes of state. The same is true for the changes of the internal energy $U = U(\varrho, T)$. In this case, μ is not an independent variable.

However, a change ds of entropy may also result from a change of μ due to the transport of the chemical elements by some process. In such a case, the variations of entropy do not result from changes of T and ρ and the direct effects of the μ variations on the entropy have to be considered explicitly. In Sect. 3.3.3 in order to calculate $\varepsilon^{\mathrm{grav}}$, we have derived (3.67). This implies that the change ds of the entropy of mixing is

$$ds = \frac{C_P}{T} dT + \frac{1}{\varrho^2} \left(\frac{\partial \varrho}{\partial T} \right)_{P,\mu} dP + \frac{1}{T} \underbrace{\left[\left(\frac{\partial U}{\partial \mu} \right)_{\varrho,T} - \frac{P \varphi \delta}{\varrho \alpha \mu} \right]}_{\mathcal{A}} d\mu. \quad \text{(C.44)}$$

For a perfect mono-atomic gas with $U = (3/2)(\mathcal{R}T/\mu)$ and $\alpha = \delta = \varphi = 1$, one has $\mathcal{A} = -(5/2)(\mathcal{R}T)/\mu^2$ (cf. 3.68). It is useful to see what happens to $\mathcal{A}$ for a mixture of perfect gas and radiation. With U given by (7.73), one has

$$\left(\frac{\partial U}{\partial \mu} \right)_{\varrho,T} = -\frac{\mathcal{R}T}{\mu^2(\gamma_{\mathrm{g}} - 1)}. \quad \text{(C.45)}$$

With α, δ and φ given in Sect. 7.5, one has

$$\mathcal{A} = -\frac{\mathcal{R}T}{\mu^2(\gamma_{\mathrm{g}} - 1)} - \left(\frac{4}{\beta} - 3 \right) \frac{\mathcal{R}T}{\mu^2} = -\frac{\mathcal{R}T}{\mu^2} \left[\frac{1}{\gamma_{\mathrm{g}} - 1} + \left(\frac{4}{\beta} - 3 \right) \right]. \quad \text{(C.46)}$$

For a perfect mono-atomic gas with $\beta = 1$ and $\gamma_{\mathrm{g}} = 5/3$, one again finds $\mathcal{A} = -(5/2)(\mathcal{R}T)/\mu^2$. Here, we have obtained the general expression of entropy change, which allows us to account for the entropy changes due to the mixing of chemical elements.

C.4.4.1   Another Expression of the Entropy of Mixing

There are different ways in the literature to write the entropy of mixing, e.g.,

$$dS = C_P \left[\frac{dT}{T} - \nabla_{\mathrm{ad}} \frac{dP}{P} + \Phi \frac{d\mu}{\mu} \right]. \quad \text{(C.47)}$$

Comparing (C.44) and (C.47), we see that the terms in T are the same. With (3.76) and with δ (3.60), one can write the term in P in (C.47) as

$$-C_P \frac{\nabla_{ad}}{P} = -\frac{\delta}{\varrho T} = \frac{1}{\varrho^2} \left(\frac{\partial \varrho}{\partial T} \right)_{P,\mu} . \tag{C.48}$$

Thus, we verify that the terms in P are the same for a general equation of state. The terms in μ are also identical if one has

$$\Phi = \frac{\mathcal{A}\mu}{C_P T} . \tag{C.49}$$

Thus, the two expressions (C.44) and (C.47) are equivalent. In the case of a perfect gas, one simply has $\Phi = -1$.

C.5   Recalls on Fundamental Statistics

Let us consider a system of N identical particles, without interactions and in statistical equilibrium. Let N and the total energy E to be conserved. The number N_r of particles with an energy E_r is

$$N_r = \frac{g_r}{e^{-\psi + \frac{E_r}{kT}} + \alpha} , \qquad \alpha = 0 \text{ or } \pm 1, \tag{C.50}$$

where g_r is the number of internal degrees of freedom or of quantum states with energy E_r. There are three fundamental statistics with different hypotheses:

Boltzmann Statistics: $\alpha = 0$.
1.- Discernability of particles. 2.- The various complexions are equally probable. 3.- The macroscopic state is the one achieved by the largest number of complexions.

Bose–Einstein Statistics: $\alpha = -1$.
    1.- Uncertainty Principle. 2.- Undiscernability. 3.- Same probability for the microscopic states. 4.- The probability of a macroscopic state depends on the number of microscopic states which can make it. This statistic applies to particles with spin 0 or entire number (photons, π mesons, α particles, etc.)

Fermi–Dirac Statistics: $\alpha = +1$. The hypotheses are the same as for the Bose–Einstein statistics, with in addition the exclusion principle, which applies to particles with an half-integer spin (electrons, positrons, protons, neutrons, neutrinos, mesons, etc.). ψ is called the degeneracy parameter. If $\psi \ll -1$, $e^{-\psi}$ is very large and the Bose–Einstein and Fermi–Dirac statistics converge toward Boltzmann statistics; this occurs in low-density media. One has with μ being here the chemical potential (see next Section)

$$\psi = \frac{\mu}{kT}. \tag{C.51}$$

This intensive quantity is useful for the changes of states, as ionization, crystallization, neutronization, etc.

C.6 Thermodynamic Equilibrium

A system with only one kind of particles is defined by two of the variables P, T, V (instead of the specific volume V, one may have the specific density $\rho = 1/V$, also instead of T one may consider the specific entropy S). Often, a system contains several kinds of particles with numbers N_i. Due to a change of conditions, for example T, the ratios of the different N_i may change. Thus, the internal energy U is no longer a function of, for example, S and V, but it is $U = U(S, V, N_i)$, thus

$$dU = \left(\frac{\partial U}{\partial S}\right)_{V,N} dS + \left(\frac{\partial U}{\partial V}\right)_{S,N} dV + \sum_i \left(\frac{\partial U}{\partial N_i}\right)_{S,V} dN_i. \qquad (C.52)$$

The index N implies that all N_i are constant. The chemical potential of particles i expresses the change of U with the change of N_i

$$\mu_i = \left(\frac{\partial U}{\partial N_i}\right)_{S,V}. \qquad (C.53)$$

Thermal equilibrium means that T has reached an equilibrium value, while thermodynamic equilibrium means both thermal and chemical equilibrium. The condition of chemical equilibrium is that small changes of N_i do not change thermodynamical functions,

$$\sum_i \mu_i \, dN_i = 0. \qquad (C.54)$$

For example, in the absence of reactions the various dN_i are independent and for each species one has $\mu_i \, dN_i = 0$. Since $\mu_i \neq 0$, one has $dN_i = 0$. As to the photons, they interact with matter and their number is not fixed, thus $dN_i \neq 0$ and equilibrium demands $\mu_i = 0$.

C.6.1 Reactions with Changes of State

Let us consider a reaction written in the general form

$$\sum_i \nu_i A_i = 0, \qquad (C.55)$$

where A_i is here the symbol of element i (not its atomic mass) and ν_i is the stoichiometric coefficient. As an example, let us consider the ionization reaction

$$H^+ + e^- - H = 0, \quad \text{with} \quad \nu_H^+ = 1, \quad \nu_e = 1, \quad \nu_H = -1. \qquad (C.56)$$
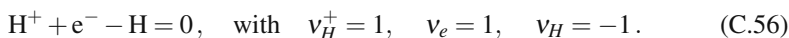
Each time ν_1 particles "1" are destroyed or produced, ν_i other particles "i" appear or disappear. The numbers of particles "1" and "i" are related by

$$dN_i = \frac{v_i}{v_1} dN_1 \ . \tag{C.57}$$

For an arbitrary change dN_1, the condition of chemical equilibrium becomes

$$\sum_i \mu_i \, dN_i = \frac{dN_1}{v_1} \sum_i v_i \, \mu_i = 0 \ . \tag{C.58}$$

Since dN_1 is anything, one has

$$\sum_i v_i \, \mu_i = 0 \ . \tag{C.59}$$

Since $\psi = \mu_i / kT$, the condition of chemical equilibrium also implies

$$\sum_i v_i \, \psi_i = 0 \ . \tag{C.60}$$

The sum of the products of the degeneracy parameters and stoichiometric coefficients is zero.

C.6.2 Maxwell–Boltzmann Distribution

The distribution of the velocities of particles of mass m under the assumption of a perfect gas is given by Maxwell–Boltzmann law, which gives the relative fraction of the particles with energies in the interval $E, E + dE$,

$$\psi(E) \, dE = \frac{dn(E)}{n} = \frac{2}{\pi^{1/2}} \frac{1}{(kT)^{3/2}} e^{-E/kT} E^{1/2} \, dE. \tag{C.61}$$

The relative number of particles with a velocity (whatever the direction) between v and $v + dv$ is given by

$$\phi(v) dv = \frac{dn}{n} = 4\pi v^2 \frac{m^{3/2}}{(2\pi kT)^{3/2}} e^{-\frac{mv^2}{2kT}} \, dv, \tag{C.62}$$

$$\text{with} \ \ v_{\text{peak}} = \sqrt{\frac{2kT}{m}} \ \ \text{and} \ \ \sqrt{\overline{v^2}} = \sqrt{\frac{3kT}{m}} \ , \tag{C.63}$$

with v_{peak} the most probable velocity and $\sqrt{\overline{v^2}}$ the root-mean-square velocity. One also has for the numerical coefficient $4\pi/(2\pi)^{3/2} = (2/\pi)^{1/2}$. One evidently has $\psi(E) \, dE = \phi(v) \, dv$ and the integrals over all velocities or energies are equal to unity,

$$\int_0^\infty \phi(v) \, dv = \int_0^\infty \psi(E) \, dE = 1 \ . \tag{C.64}$$

The Maxwell–Boltzmann distribution applies to stellar media satisfying the assumptions of a perfect gas.

References

1. D.C. Abbott, P.S. Conti: Ann. Rev. Astron. Astrophys. **25**, 113 (1987) 356, 703
2. T. Abel: Science **295**, 93 (2002) 574, 580
3. M. Abramowitz, I.A. Stegun: *Handbook of Mathematical Functions*, Dover Publ. 1043 p. (1965) 406
4. D.J. Acheson: Phil. Trans. Roy. Soc. London **289 A**, 459 (1978) 306, 331, 333, 349, 353
5. B. Aharmin, Q.R. Ahmad, S.N. Ahmed, R.C. Allen, T.C. Andersen: Phys. Rev. C **75**, 045502 (2007) 637
6. G. Alecian:*Transport Microscopique* in Cours de structure Interne, 5th session, ed. E. Schatzman, Obs. de Paris (1994) 220, 226, 231, 233, 237
7. G. Alecian: A&A **289**, 885 (1994) 236
8. G. Alecian, S. Vauclair: Fundam. in Cosmic Phys. **8**, 369 (1983) 236
9. D. Alexander, J. Ferguson: ApJ **267**, 337 (1994) 192
10. C.W. Allen: *Astrophysical Quantities*, Third Ed., Athlone Press (1991) 142
11. P. André: *Star Formation and the Physics of Young Stars*, Eds. J. Bouvier & J.P. Zahn, EAS Pub. Ser., **3**, 1 (2002) 497, 499
12. I. Appenzeller: A&A **5**, 355 (1970) 62
13. I. Appenzeller, W. Tscharnuter: A&A **25**, 125 (1973) 664
14. P.J. Armitage, C.J. Clarke: MNRAS **280**, 458 (1996) 549
15. D.A. Arnett, J.W. Truran: ApJ **157**, 339 (1969) 621
16. D.A. Arnett: *"Supernovae and Nucleosynthesis"*, Princeton Univ. Press. 598 p. (1996) 720, 734
17. M. Arnould, N. Mowlavi, A. Champagne: in *Stellar Evolution: What Should Be Done*, 32nd Liège Colloquium, p.17 (1995) 619, 621
18. M. Arnoud, S. Goriely, G. Meynet: A&A **453**, 653 (2006) 710
19. M. Asplund, N.Grevesse, A.J. Sauval, P. Allende, D. Kiselman: A&A **417**, 751 (2004) 435, 709
20. M. Asplund, N. Grevesse, A.J. Sauval: In *Element Stratification in Stars: 40 years of Atomic Diffusion*, Eds. G. Alecian, O. Richard, S. Vauclair, EAS Publ. Ser. **17**, p.21 (2005) 144, 184, 434, 436
21. R. d'E. Atkinson, F. Houtermans: Zeitschrift f. Physik, **54**, 656 (1929) 197
22. www.atnf.csiro.au/research/pulsar/psrcat 752
23. J.N. Bahcall: *Neutrinos Astrophysics*, Cambridge Univ. Press (1989)
24. J.N. Bahcall, P.I. Krastev, A.Y. Smirnov: Phys. Re. D **62**, 0930004 (2000) 637
25. J.N. Bahcall, S. Basu, M. Pinsonneault, A.M. Serenelli: ApJ **618**, 1049 (2005) 436, 629
26. J.N. Bahcall, S. Basu, A.M. Serenelli: ApJ **631**, 1281 (2005) 436, 629
27. J.N. Bahcall, M. Pinsonneault: Rev. Modern Phys. **64**, 885 (1992) 636
28. J.N. Bahcall, A.M. Serenelli, M. Pinsonneault: ApJ **614**, 464 (2004) 445, 629
29. J.N. Bahcall, A.M. Serenelli, S.Basu: ApJ Letters **621**, L85 (2005) 636
30. S.A. Balbus: ApJ **453**, 380 (1995) 349
31. S.A. Balbus, J.F. Hawley: ApJ **376**, 214 (1991) 349
32. N. Baker: *Stellar Evolution*, Eds. Stein & Cameron, Publisher, p.333 (1963) 381, 385
33. N. Baker, R. Kippenhahn: Zeitschrift f. Astrophys. **54**, 114 (1962) 146, 148
34. N. Baker, R. Kippenhahn: ApJ **142**, 868 (1965) 379

35. S. Barnes, S. Sofia: ApJ **462**, 746 (1996) 321
36. S. Barnes, S. Sofia, M. Pinsonneault: ApJ **548**, 1071 (2001) 549
37. G. Basri, G.W. Marcy, J.R. Graham: ApJ **458**, 600 (1996) 537, 538
38. S. Basu, M.H. Pinsonneault, J.N. Bahcall: ApJ **529**, 1084 (2000) 436
39. M.R. Bate, I.A. Bonnell, V. Bromm: MNRAS **339**, 577 (2003) 495
40. E. Battaner: *Astrophysical Fluid Dynamics*, Cambridge. Univ. Press. (1996) 216
41. M. Beech, R. Mitalas: ApJS **95**, 517 (1994) 554
42. R. Behrend, A. Maeder: A&A **373**, 190 (2001) 569
43. P.A. Bernasconi: A&A Suppl. Ser. **120**, 57 (1996) 528
44. P.A. Bernasconi, A. Maeder: A&A **307**, 829 (1996) 506, 517, 522, 523, 554
45. G. Bertelli, A. Bressan, C. Chiosi, F. Fagotto, E. Nasi: A&A Suppl. Ser. **106**, 275 (1994) 643
46. L. Bildsten, E.F. Brown, C.D. Matzener & G. Ushomirskyo: ApJ **482**, 442 (1997) 534, 535, 536, 537
47. J. Binney, S. Tremaine: *Galactic Dynamics*, Princeton Univ. Press. p. 291 (1987) 481
48. G.S. Bisnovatyi-Kogan: A&A **344**, 647 (1999) 104
49. S.I. Blinnikov, N.V. Dunina–Barkovskaya, D.K. Nadyozhin: ApJS **106**, 171 (1996); see also ApJS **118**, 603 (1998) 169
50. T. Blöcker: A&A **297**, 727 (1995) 670, 677, 689
51. P. Bodenheinmer: Rep. Prog. Phys. **35**, 1 (1972) 508
52. A.M. Boesgaard, K.G. Budge: ApJ **332**, 410 (1988) 469
53. A.M. Boesgaard, M.J. Tripicco: ApJ **301**, L49 (1986) 469
54. I.A. Bonnell: The Formation of Massive Stars through Stellar Collisions. In *Hot Star Workshop III: The Earliest Stages of Massive Star Birth*, ASP Conf. Ser. **267**, Ed. P.A. Crowther, p. 193 (2002) 495, 553
55. I.A. Bonnell, M.R. Bate, H. Zinnecker: MNRAS **298**, 93 (1998) 552
56. G. Bono, V. Castellani, M. Marconi: ApJ **529**, 293 (2000) 371
57. F. Bouchy, F. Carrier: A&A **390**, 205 (2002) 436, 437, 438
58. J.-C. Bouret, T. Lanz, J. Hillier, D.J. Heap, S.R. Hubeny et al.: ApJ **595**, 1182 (2003) 700
59. A. Boury, M. Gabriel, P. Ledoux: A&A **27**, 92 (1964) 379
60. J. Bouvier, M. Forestini, S. Allain: A&A **326**, 1023 (1997) 322, 542, 545
61. J. Bouvier, F. Rigaut, D. Nadeau: A&A **323**, 139 (1997) 549
62. J. Braithwaite: A&A **449**, 451 (2006) 332
63. J. Braithwaite, A. Nordlund: A&A **450**, 1077 (2006) 317
64. V. Bromm, P.S. Coppi, R.B. Larson: ApJ **527**, L5 (1999) 573
65. V. Bromm, P.S. Coppi, R.B. Larson: ApJ **564**, 23 (2002) 574
66. V. Bromm, A. Ferrara, P.S. Coppi, R.B. Larson: MNRAS **328**, 969 (2001) 574
67. V. Bromm, R.B. Larson: Ann. Rev. Astron. Astrophys. **42**, 79 (2004) 572, 574, 576
68. V. Bromm, A. Loeb: Nature **425**, 812 (2003) 573
69. I.N. Bronstein, K.A. Semendjaew: *Taschenbuch der Mathematik* Ed. Harri Deutsch, Zurich & Frankfurt, 584 p. (1966) 386
70. T.M. Brown, R.L. Gilliland: Ann. Rev. Astron. Astrophys. **32**, 37 (1994) 436
71. M.K. Browning, A.S. Brun, J. Toomre: ApJ **601**, 512 (2004) 130
72. W. Brüggen, W. Hillebrandt: MNRAS **320**, 73 (2001) 295, 298
73. A.S. Brun, H.M. Antia, S.M. Chitre, J.-P. Zahn: A&A **391**, 725 (2002) 446
74. A.S. Brun, M.S. Miesch, J. Toomre: ApJ **614**, 1073 (2004) 130
75. A.S. Brun, J.-P. Zahn: A&A **457**, 665 (2006) 446
76. E.M. Burbidge, G.R. Burbidge, W.A. Fowler, F. Hoyle: Rev. Mod. Phys. **29**, 547 (1957) 719
77. C.J. Burke, M.H. Pinsonneault: ApJ **604**, 272 (2004) 537
78. G. Burki: Orion, **37**, 124 (1979) 395
79. A. Burrows, L. Dessart, E. Livne, C.D. Ott, J. Murphy: ApJ **655**, 416 (2007) 738
80. F. Busse: Geophys. Astrophys. Fluid Dyn. **17**, 215 (1981) 249
81. M. Busso, R. Gallino, G.J. Wasserburg: Ann. Rev. Astron. Astrophys. **37**, 239 (1999) 667, 672, 674
82. N. Calvet, J. Muzerolle, C. Briceno et al.: AJ **128**, 1294 (2004) 505
83. M. Camenzind: Compact Objects in Astrophysics: White Dwarfs, Neutron Stars and Black Holes. Ed. M. Camenzind, Springer Verlag, 682 p. (2007) v, 170, 175

84. A.G.W. Cameron, W.A. Fowler: ApJ **164**, 111 (1971) 673
85. M. Cantiello, S.-C. Yoon, N. Langer, M. Livio: A&A **465**, L29 (2007) 754
86. V. Canuto: Ann. Rev. Astron. Atrophys. **13**, 335 (1975) 175
87. V.M. Canuto: ApJ **392**, 218 (1992) 114
88. V.M. Canuto: ApJ **416**, 331 (1993) 114
89. V.M. Canuto: A&A **384**, 1119 (2002) 295
90. V.M. Canuto, M. Dubovikov: ApJ **484**, L161 (1997) 114
91. V.M. Canuto, M. Dubovikov: ApJ **493**, 834 (1998) 114, 115, 116
92. V.M. Canuto, I. Goldmann, I. Mazzitelli: ApJ **473**, 550 (1996) 115
93. V.M. Canuto, I. Mazzitelli: ApJ **370**, 295 (1991) 115
94. A.C. Carciofi, A. Domiciano de Souza, A.M. Magalhaes, J.E. Bjorkman, F. Vakili: ApJ **676**, L41 (2008) 20, 74
95. P. Caselli, P.C. Myers: ApJ **446**, 665 (1995) 554
96. J.I. Castor: ApJ **166**, 109 (1971) 378, 380
97. J.I. Castor, D.C. Abbott, R.I. Klein: ApJ **195**, 157 (1975) 357
98. S. Catalan, J. Isern, E. Garcia-Berro, I. Ribas, C. Allende Priero, A.Z. Bonanos: A&A **477**, 213 (2008) 677
99. M. Catelan: ApJ **531**, 826 (2000) 665
100. G.R. Caughlan, W.A. Fowler: Atomic Data and Nuclear Data Tables **40** nb. 2, p. 83 (1988) 196
101. R. Cayrel, E. Depagne, M. Spite et al.: A&A **416**, 1117 (2004) 664, 769
102. B. Chaboyer, P. Demarque, M.H. Pinsonneault: ApJ **441**, 865 (1995) 284
103. B. Chaboyer, P. Demarque, M.H. Pinsonneault: ApJ **441**, 876 (1995) 284
104. B. Chaboyer, J.-P. Zahn: A&A **253**, 173 (1992) 256, 257, 277, 281, 282
105. G. Chabrier, I. Baraffe, B. Plez: ApJ **459**, L91 (1996) 536, 537
106. G. Chabrier, I. Baraffe: A&A **327**, 1039 (1997) 518
107. G. Chabrier, A.Y. Pothekin: Phys. Rev. E, **58**, 4941 (1998) 160, 169
108. S. Chandrasekhar: ApJ **74**, 81 (1939) 171
109. S. Chandrasekhar: *Stellar Structure*, Dover Ed. (1939) 607, 608, 609, 611
110. S. Chandrasekhar: *Hydrodynamic and Hydromagnetic Stability*, Oxford Univ. press, (1961) and Dover Ed. (1981) 294, 311, 315
111. S. Chandrasekhar: Rev. Modern Phys. **56**, 137 (1984) 8, 62
112. S. Chapman, T.G. Cowling: *The Mathematical Theory of non-uniform Gases*, Cambridge Univ. Press, 3rd Ed. (1970) 231, 232, 233, 237
113. P. Charbonneau: A&A **259**, 134 (1992) 277, 282, 284
114. P. Charbonneau: "*Dynamo Models of the Solar Cycle*", Living Rev. Solar Phys. **2**, 2 (2005) 311, 316, 317
115. P. Charbonneau, J. Christensen–Dalsgaard, J. Henning, R. Larsen, R.M. Schou et al.: ApJ **527**, 445 (1999) 445
116. P. Charbonneau, K. MacGregor: ApJ **559**, 1094 (2001) 318
117. P. Charbonneau, G. Michaud, C.R. Proffitt: ApJ **347**, 821 (1989) 277
118. C. Charbonnel: A&A **282**, 811 (1994) 651
119. C. Charbonnel: private comm. (2007) 631, 633, 634
120. C. Charbonnel, W. Daeppen, P. Bernasconi, A. Maeder, G. Meynet et al.: A&A Suppl. Ser. **135**, 405 (1999) 626
121. C. Charbonnel, G. Meynet, A. Maeder, D. Schaerer: A&AS **115**, 339 (1996) 643
122. A.N. Chené, N. St Louis: *Massive Stars as Cosmic Engines*, IAU Symp.250, Eds. F. Bresolin & J. Puls, p. 139 (2008) 716
123. C. Chiappini, S. Ekström, G. Meynet, R. Hirschi, A. Maeder: A&A **449**, 27 (2006) 755, 761
124. C. Chiappini, R. Hirschi, G. Meynet, , A. Maeder, F. Matteucci: astro-ph 0712.3434 (2008) 683
125. A. Chieffi, M. Limongi, O. Straniero: ApJ **502**, 737 (1998) 720
126. R. Chini, V. Hofmeister, S. Kimeswenger, M. Nielbock, D. Nurnberger et al.: ESO Messenger, **117**, 36 (2004) 551, 555, 556
127. C. Chiosi: *Nucleosynthesis and Chemical Evolution*, 16th Saas–Fee Course, Eds. B. Hauck et al., Geneva Observatory (1986) 658
128. C. Chiosi, C. Summa: Astroph. Sp. Sci. **8**, 478 (1970) 119

129. C. Chiosi, A. Maeder: Ann. Rev. Astron. Astrophys. **24**, 329 (1986) 687

130. J. Christensen–Dalsgaard, in *Space Research Prospects in Stellar Activity and Variability*, ed. F. Praderie, Publ. Observatoire de Paris, p. 11 (1984) 439

131. J. Christensen–Dalsgaard *Lecture Notes on Stellar Oscillations*, Institut for Fysik og Astronomi, Aarhus Universiteit, 5th Ed., 268 p. (2003) 401, 405, 409, 410, 415, 428, 445, 453, 629, 790, 793

132. J. Christensen–Dalsgaard, S. Frandsen: Solar Phys. **82**, 469 (1980) 436

133. J. Christensen–Dalsgaard, J. Schou, M.J. Thompson: MNRAS **242**, 353 (1990) 434, 444

134. E. Churchwell: ApJ **479**, L59 (1997)

135. E. Churchwell: *The Origin of Stars and Planetary Systems*. Eds. C. Lada & N. Kylafis, NATO Science Ser. **540**, Kluwer publ., p. 515 (1998) 555

136. E. Churchwell: Massive star formation: The role of bipolar outflows. In *Unsolved Problems in Stellar Evolution*, ed. M. Livio. Space Telescope Sci. Inst. Ser., vol **12**, p. 41 (2000) 555

137. G.W. Collins II: *The virial theorem in stellar astrophysics*, Tucson Arizona, Pachart publ. House, 143 p (1978) 13

138. G.W. Collins II: *Stellar Rotation*, IAU Symp 215, Eds. A. Maeder & P. Eenens, p. 1 (2004) 686

139. P.S. Conti, D. Ebbets: ApJ **213**, 438 (1977) 73

140. P.S. Conti, P. Massey: ApJ **337**, 251 (1989) 707

141. S. Couvidat, R.A. Garcia, S. Turck–Chièze et al.: ApJ **597**, L77 (2003) 344

142. J.J. Cowan, F.-K. Thielemann, J.W. Truran: Phys. Reports **208**, 267 (1991) 749

143. J.J. Cowan, F.-K. Thielemann: Physics Today, October 2004, **47** (2004) 745, 749

144. A.N. Cox: in *Astrophysical Processes in Upper Main Sequence Stars*. XIIIth Saas–Fee Course, Eds. B. Hauck & A. Maeder, Geneva Observatory, p.1 (1983) 184, 381

145. A.N. Cox, J.H. Cahn: ApJ **326**, 804 (1988) 373

146. J.P. Cox: *Theory of Stellar Pulsations*, Princeton Univ. Press, 380 p. (1980) 371, 381, 399

147. J.P. Cox, R.T. Giuli: *Principles of Stellar Structure*, Gordon and Breach, Science Publ. (1968). (See also A. Weiss et al. Extended Second Edition which covers the first 18 chapters of the original edition) 94, 98, 99, 100, 169, 177, 396, 603

148. P. Crowther: *Evolution of Massive Stars, Mass Loss and Winds*, Eds. M. Heydari–Malayeri et al., EAS Publ. Ser. **13**, 1 (2004) 360, 361

149. P. Crowther: Ann. Rev. Astron. Astrophys. **45**, 177 (2007) 703, 706, 707

150. P.A. Crowther, L. Dessart, D.J. Hillier, J.B. Abbott, A.W. Fullerton: A&A **392**, 653 (2002) 690, 754

151. K. Cunha, I. Hubeny, T. Lanz: ApJ **647**, L143 (2006) 144, 772

152. W. Daeppen, D. Mihalas, D.G. Hummer, B.W. Mihalas: ApJ **332**, 261 (1988) 435

153. T. Decressin: Thesis Univ. Geneva, 245 p. (2007) 270, 271, 669, 670, 768

154. T. Decressin, C. Charbonnel, L. Siess, A. Palacios: Mem. Soc. Astron. Italy, **75**, 682 (2005) 683

155. T. Decressin, C. Charbonnel: private comm. (2007) 680, 681, 682

156. T. Decressin, G. Meynet, C. Charbonnel, N. Prantzos, S. Ekström: A&A **464**, 1029 (2007) 624

157. M. Della Valle: AIP Conf. Proc. **836**, 367 (2006) 752, 753

158. P. Demarque, A. Sarajedini, X.J. Guo: ApJ **426**, 165 (1994) 117

159. P. Demarque, J.H. Woo, J.C. Kim, S.K. Yi: ApJ **155**, 667 (2004) 117

160. J.R. De Medeiros: in *Stellar Rotation*, IAU Symp 215, Eds. A. Maeder & P. Eenens, p. 144 (2004) 715

161. F.-L. Deubner, D.O. Gough: Ann. Rev. Astron. Astrophys. **22**, 593 (1984) 428

162. R.G. Deupree: *Stellar Rotation*, IAU Symp 215, Eds. A. Maeder & P. Eenens, p. 378 (2004) 130

163. M.P. Di Mauro, J. Christensen–Dalsgaard, H. Kjeldsen, T.R. Bedding, L. Paternò: A&A **404**, 341 (2003) 117

164. A. Domiciano de Souza, P. Kervella, S. Jankov, S. Abe, F. Vakili et al.: A&A **407**, L47 (2003) 74

165. A. Domiciano de Souza, P. Kervella, S. Jankov, F. Vakili, N. Ohishi et al.: A&A **442**, 567 (2005) 74

166. J.-F. Donati, G.A. Wade: A&A **341**, 216 (1999) 317

167. T.L. Duvall: Nature **300**, 242 (1982) 428

168. A. Eddington: *The Internal Constitution of Stars*. Dover Publ. (1926) 41, 58, 61, 63, 249, 371, 608

169. P. Eggenberger: Thesis Univ. Geneva (2006) 144, 238, 416, 419, 427, 434, 437, 438, 439, 440, 441, 445

170. P. Eggenberger, F. Carrier: New Astronomy **10**, 315 (2005) 444

171. P. Eggenberger, C. Charbonnel, S. Talon, G. Meynet, A. Maeder et al.: A&A **417**, 235 (2004) 437, 438, 441
172. P. Eggenberger, A. Maeder, G. Meynet: A&A **440**, L9 (2005) 332, 343, 346, 347
173. P. Eggenberger, G. Meynet, A. Maeder: A&A **386**, 576 (2002) 696
174. P. Eggleton et al.: A&A **23**, 35 (1973) 165, 169
175. S. Ekström, G. Meynet, C. Chiappini, R. Hirschi, A. Maeder: A&A **489**, 685 (2008) 761, 762, 763
176. S. Ekström, G. Meynet, A. Maeder, F. Barblan: A&A **478**, 467 (2008) 25, 27, 28, 75, 324, 627
177. J.J. Eldridge, R.G. Izzard, C.A. Tout: MNRAS **384**, 1109 (2008) 713
178. J.J. Eldridge, J. Vink: A&A **452**, 295 (2006)
179. A.S. Endal, S. Sofia: ApJ **220**, 279 (1978) 223
180. H. Falk: Ann. Rev. Astron. Astrophys. **43**, 435 (2005) 672
181. J. Faulkner, I.W. Roxburgh, P.A. Strittmatter : ApJ **151**, 203 (1968) 28
182. J.M. Feijoo: Diploma work, Geneva Observatory, 96 p. (1999) 759
183. V.C.A. Ferraro: MNRAS **97**, 459 (1937) 326
184. V.C.A. Ferraro, C. Plumpton: *An Introduction to Magneto–Fluid Mechanics*, Oxford Univ. Press, 254 p. (1966) 326
185. J. Frank, A. King, D. Raine: *Accretion power in astrophysics*, Cambridge Univ. Press (1985) 508
186. A. Frebel, W. Aoki, N. Christlieb, et al., Nature, **434**, 831 (2005) 682
187. K.J. Fricke: Zeitschrift f. Astrophys. **68**, 317 (1968) 306
188. C. Foellmi, A.F.J. Moffat, M.A. Guerrero: MNRAS **338**, 360 (2003) 713
189. C. Foellmi, A.F.J. Moffat, M.A. Guerrero: MNRAS **338**, 1025 (2003) 713
190. M. Forestini: *Principes fondamentaux de structure stellaire*, Gordon and Breach Science Publ. 413 p. (1999) 227, 228, 230
191. M. Forestini: Mém. d'Habilitation, Astrophysics Lab. Univ. Grenoble (2000) 669, 671, 672, 674, 675
192. M. Forestini, C. Charbonnel: A&A Suppl. Ser. **123**, 241 (1997) 673, 674
193. J.H. Fertziger, H.G. Kaper, *Mathematical Theory of Transport Processes in Gases*, Amsterdam, North Holland (1972) Bull. Acad. R. Belgique, Cl. Sci. 5 Ser. **60**, 866 (1974) 231
194. M.J. Harris, W.A. Fowler, G.R. Caughlan, B.A. Zimmerman: Ann. Rev. Astron. Astrophys. **21**, 165 (1983) 615, 620
195. A.H. Gabriel, J. Charra, G. Grec, J.-M. Robillot, T. Roca Cortés et al.: Solar Phys. **175**, 207 (1997) 431
196. M. Gabriel, R. Scuflaire, A. Noels, A. Boury: Bull. Acad. R. Belgique Cl. Sci. 5 Ser. **60**, 866 (1974) 379
197. D. Galli, F. Palla: Planet. Space Sci. **50**, 1197 (2002) 587
198. P. Garaud: MNRAS **335**, 707 (2002) 249
199. R.J. Garcia Lopez, H.K. Spruit: ApJ **377**, 268 (1991) 461, 462, 464, 470, 471
200. R.A. Garcia, T. Corbard, W.J. Chaplin, S. Couvidat, A. Eff-Darwich: Solar Phys. **220**, 269 (2004) 446
201. R.A. Garcia, S. Turck–Chièze, S.J. Jimenez-Reyes, J. Ballot, P.L. Palle et al.: *"Tracking solar gravity modes: the dynamics of the solar core"*, Science, **316**, 1591 (2007) 446
202. B. Garcia, J.C. Mermilliod: A&A **368**, 122 (2001) 552
203. A. Gautschy, H. Saio: Ann. Rev. Astron. Astrophys. **33**, 75 (1995) 371, 391, 399
204. A. Gautschy, H. Saio: Ann. Rev. Astron. Astrophys. **34**, 551 (1996) 391
205. P. Giannone, K. Kohl, A. Weigert: Z. f. Astrophys. **68**, 107 (1968) 605, 607
206. D. R. Gies: ApJ Suppl. **64**, 545 (1987) 713
207. K.K. Gilroy, J.A. Brown: ApJ **371**, 578 (1991) 651
208. L. Girardi, A. Bressan, G. Bertelli, C. Chiosi: A&A Suppl. Ser. **141**, 371 (2000) 643, 662
209. W. Glatzel: A&A **339**, L5 (1998) 77
210. W. Glatzel, M. Kiriakidis: MNRAS **263**, 375 (1993) 62
211. S. Glover: *"The Formation of the First Stars in the Universe"*. Space Sci. Rev. **117**, 445 (2005) 572
212. P. Goldreich, N. Murray, P. Kumar: ApJ **424**, 466 (1994) 463, 465
213. P. Goldreich, G. Schubert: ApJ **150**, 571 (1967) 306
214. J.-F. Gonzales, F. LeBlanc, M.-C. Artru, G. Michaud: A&A **297**, 223 (1995) 236
215. D.O. Gough: Solar Phys. **100**, 65 (1985) 434

216. D.O. Gough: *Astrophysical Fluid Dynamics*, Les Houches XLVII, Eds. J.-P. Zahn, J. Zinn–Justin, p. 399 (1993) 428
217. D.O. Gough, M.E. McIntyre: Nature **394**, 755 (1998) 446
218. G. Graefener, W.-R. Hamann: A&A **482**, 945 (2008) 690, 703
219. L. Gratton: Mem. Soc. Astron. Ital. **17**, 5 (1945) 259, 263
220. R.G. Gratton, C. Sneden, E. Carretta, A. Bragaglia: A&A **354**, 169 (2000) 651
221. T.H. Greif, V. Bromm: MNRAS **373**, 128 (2006) 571, 590
222. A. Grigahcene, M.-A. Dupret, M. Gabriel, R. Garrido, R. Scuflaire: A&A **434**, 1055 (2005) 379
223. M. Groenewegen: *On the Evolution and Properties of AGB Stars*, Thesis, Univ. Amsterdam, 222 p. (1993) 668, 670
224. S.A. Grossman, R.E. Taam: MNRAS **283**, 1165 (1996) 121
225. E. Guenther, H. Lehman: *The Tenth Cambridge Workshop on Cool Stars, Stellar System and the Sun*, Eds. R.A. Donahue & J.A. Bookbinder, ASP Conf. Ser. **154**, p. 1693 (1998) 317, 543
226. M.G. Haehnelt: MNRAS **273**, 249 (1995) 585
227. C.J. Hansen, J.P. Cox, H.M. van Horn: ApJ **217**, 151 (1977) 790, 794
228. C.J. Hansen, S.D. Kawaler: *Stellar Interiors, Physical Principles, Structure, and Evolution*, Springer Verlag, 445 p. (1999) 183
229. L. Hartmann: *Accretion Processes in Star Formation*, Cambridge Univ. Press, (1998) 481, 500, 501, 502
230. M. Harwit: *Astrophysical Concepts*, Springer Verlag, 714 p. (2006) 406, 407
231. C. Hayashi: Prog. Theor. Phys. Suppl. **70**, 35 (1981) 511
232. J. Hazlehurst, W.L.W. Sargent: ApJ **130**, 276 (1959) 783
233. S.R. Heap, T. Lanz: *Stellar Rotation*, IAU Symp. 215, Eds. A. Maeder and P. Eenens, ASP, P. 220 (2004) 700
234. S.R. Heap, T. Lanz, I. Hubeny: ApJ **638**, 409 (2006) 700
235. A. Heger, N. Langer: ApJ **324**, 210 (1998) 715
236. A. Heger, N. Langer: ApJ **544**, 1016 (2000) 725
237. A. Heger, N. Langer, S.E. Woosley: ApJ **528**, 368 (2000) 79, 332, 725, 750, 753
238. A. Heger, S.E. Woosley: ApJ **567**, 532 (2002) 740, 768, 769
239. A. Heger, S.E. Woosley, C.L. Fryer, N. Langer: *"From Twilight to Highlight: the Physics of SN*. Proc. of ESO, MPA, IMPE Workshop, ESO Astroph. Symp. Eds. W. Hillebrandt, B. Leibundgut, Springer Verlag, p.3 (2003) 739, 740
240. A. Heger, S.E. Woosley, H.C. Spruit: ApJ **626**, 350 (2005) 725, 752, 753
241. T. Henning, K. Schreyer, R. Launhardt, A. Burkert: A&A, **353**, 211 (2000) 553, 555
242. H.F. Henrichs, C. Neiner, V.C. Geers: *A Massive Star Odyssey: From Main Sequence to Supernova*, IAU 212, ed. K. van der Hucht et al. ASP, p. 202 (2003) 318
243. L.G. Henyey, J.E. Forbes, N.L. Gould: ApJ **139**, 306 (1964) 599
244. A. Herrero: *CNO in the Universe*, Eds. C. Charbonnel, D. Schaerer, G. Meynet, ASP Conf. Ser. **304**, 10 (2003) 699, 700
245. A. Herrero, R.P. Kudritzki, J.M. Vilchez, D. Kunze, K. Butler, S. Haser: A&A, **261**, 209 (1992) 693
246. A. Herrero, J. Puls, M.R. Villamariz: A&A **354**, 193 (2000) 693
247. F. Hersant, B. Dubrulle, J.M. Huré: A&A **429**, 531 (2005) 502
248. F. Herwig: A&A **360**, 952 (2000) 671
249. F. Herwig: Ann. Rev. Astron. Astrophys. **43**, 435 (2005) 667, 674, 678, 680
250. R. Hirschi: Thesis Univ. Geneva, 185 p. (2004) 720
251. R. Hirschi, G. Meynet, A. Maeder: A&A **425**, 649 (2004) 296, 696, 721, 722, 725, 726, 728, 729, 730, 750
252. R. Hirschi, G. Meynet, A. Maeder: A&A **433**, 1013 (2005) 731, 733, 753
253. E. Hofmeister, R. Kippenhahn, A. Weigert: Zeitschrift f. Astrophys. **59**, 215 (1964) 99, 100
254. F. Hoyle: ApJ **118**, 513 (1953) 492
255. F. Hoyle: ApJS **1**, 121 (1954) 645
256. W. Huang, D.R. Gies: ApJ **648**, 580 (2006) 686, 699, 700, 715
257. W. Huang, D.R. Gies: ApJ **648**, 591 (2006) 699, 700, 715
258. A. Hui-Bon-Hoa, *Abondances des Elements dans les Etoiles Chimiquement Particulières*, Thesis, Univ. Paris VII, 192 p. (1997) 236, 237

259. R.M. Humphreys: *The Fate of the Most Massive Stars*, ASP Conf. Ser. vol **332**, 14 (2005) 65, 715
260. R. Humphreys, K. Davidson: ApJ **232**, 409 (1979) 107, 692
261. R. Humphreys, K, Davidson: PASP **106**, 1025 (1994) 107, 692, 715
262. I. Hunter, P.L. Dufton, S.J. Smartt, R.S.I. Ryans, C.J. Evans et al.: A&A **466**, 277 (2007) 700
263. I. Hunter, I. Brott, D.J. Lennon, N. Langer, P.L. Dufton et al.: ApJ **676**, L29 (2008) 700
264. I. Iben: Ann. Rev. Astron. Astrophys. **5**, 571 (1967) 647, 650
265. I. Iben, A. Renzini: Ann. Rev. Astron. Astrophys, **21**, 271 (1983) 667, 670, 676
266. C.A. Iglesias, B.G. Wilson, F.J. Rogers, W.H. Goldstein: ApJ **445**, 855 (1995) 179
267. R. Ignace, J.P. Cassinelli, G. Tracy, E. Churchwell, H. Lamers: ApJ **669**, 600 (2007) 709
268. N. Itoh, H. Hayashi, Y. Kohyama: ApJ **418**, 405 (1993), see also **436**, 418 (1994) 188
269. N. Itoh, H. Hayashi, A. Nishikawa, Y. Kohyama: ApJ Suppl. Ser. **102**, 411 (1996) 208, 209, 210, 212
270. C. de Jager: A&A **138**, 246 (1984) 107
271. C. de Jager, H. Nieuwenhuijzen, K.A. van der Hucht: A&A Suppl. **72**, 259 (1988) 688, 692, 706, 732, 733
272. H.-Th. Janka, K. Langanke, A. Marek, G. Martinez-Pinedo, B. Muller: Phys. Report **442**, 38 (2007) 737
273. A.-K. Jappsen, R.S. Klessen, R.B. Larson, Y. Li, M.-M. Mac Low: A&A **435**, 611 (2005) 495
274. J.H. Jeans, *Astronomy and Cosmogony*, Cambridge Univ. Press. (1928) 390
275. J.L. Johnson, V. Bromm: MNRAS **366**, 247 (2006) 571, 587, 588, 589
276. M. Junker, A. D'Alessandro, S. Zavatarelli, C. Arpesella, E. Bellotti et al.: Phys. Rev. C **57**, 2700 (1998)
277. F. Käppeler, H. Beer, K. Wisshak: Rep. Prog. Phys. **52**, 945 (1989) 747
278. S. Kato: Publ. Astron. Soc. Japan **18**, 374 (1966) 119, 122
279. S.D. Kawaler: ApJ **333**, 236 (1988) 319, 321, 547
280. S.D. Kawaler: *Stellar Rotation*, IAU Symp. 215, Eds. A. Maeder, P. Eenens, ASP, p.561 (2004) 680
281. S.D. Kawaler, I. Novikov, G. Srinivasan: *Stellar Remnants*, Saas Fee Advanced Course 25, Eds. G. Meynet and D. Schaerer, Springer Verlag, 340 p. (1997) v, 170, 171, 175
282. K. Kifonidis, T. Plewa, H.-Th. Janka, E. Muller: A&A **408**, 621 (2003) 738
283. R. Kippenhahn, H.-C. Thomas: in *Stellar Rotation*, IAU Coll. 4, Ed. A. Slettebak, p.20 (1970) 31, 68
284. R. Kippenhahn, H.-C- Thomas, A. Weigert: Zeitschrift f. Astrophys. **61**, 241 (1995) 51
285. R. Kippenhahn, A. Weigert: *Stellar Structure and Evolution*, Springer Verlag (1990) 86, 98, 99, 122, 160
286. M. Kiraga, K. Stepien, K. Jahn: Acta Astron. **55**, 205 (2005) 464
287. J.G. Kirk, D.B. Melrose, E.R. Priest: *Plasma Astrophysics*, Saas-Fee Advanced Course 24, Ed. A.O. Benz, T.J.-L. Courvoisier, Springer Verlag, 324 p. (1994) 311
288. E. Knobloch, H.C. Spruit: A&A **125**, 59 (1983) 307, 308
289. L. Koesterke, W.-R. Hamann: A&A **299**, 503 (1995) 707
290. D.G. Korycansky: ApJ **381**, 515 (1991) 306
291. K.-L. Kratz, J.-P. Bitouzet, F.K. Thielemann, P. Moeller, B. Pfeiffer: ApJ **403**, 216 (1993) 749
292. A. Krishnamurthi, M.H. Pinsonneault, S. Barnes, S. Sofia: ApJ **480**, 303 (1997) 322, 323
293. P. Kroupa: MNRAS **322**, 231 (2001) 494
294. M.R. Krumholz, C.F. McKee, R.I. Klein: American Astron. Soc. **205**, 166.05 (2004)
295. R.P. Kudritzki: *Radiation in Moving Gaseous Media*, Saas–Fee Course, Eds. Y. Chmielewski, T. Lanz, Geneva Observatory, p.1 (1988) 357
296. R.P. Kudritzki: ApJ **577**, 389 (2002) 756, 761
297. R.P. Kudritzki, A. Pauldrach, J. Puls, D.C. Abbott: A&A, **219**, 205 (1989) 361, 362
298. R.P. Kudritzki, J. Puls: Ann. Rev. Astron. Astrophys. **38**, 613 (2000) 355, 360, 361, 362, 363, 689
299. P. Kumar, E.J. Quataert: ApJ **475**, L143 (1997) 463
300. P. Kumar, S. Talon, J.P. Zahn: ApJ **520**, 859 (1999) 463, 465, 472
301. H.J.G.L.M. Lamers, J.P. Cassinelli: *Introduction to Stellar Winds*, Cambridge Univ. Press, 438 p. (1999) 355, 356, 361, 688
302. H.J.G.L.M. Lamers, A. Maeder, W. Schmutz, J.P. Cassinelli: ApJ **368**, 538 (1991) 703
303. H.J.G.L.M. Lamers, T.P. Snow, D.M. Lindholm: ApJ **455**, 269 (1995) 358, 362, 368
304. K.R. Lang: *Astrophysical Formulae*, 3rd ed, Vol. 1, Springer Verlag, 614 p. (2006) 142
305. N. Langer: A&A **210**, 93 (1989) 693, 703, 704, 705

306. N. Langer: A&A **220**, 135 (1989) 732
307. N. Langer: A&A **248**, 531 (1991) 707
308. N. Langer: A&A **252**, 669 (1991) 120
309. N. Langer: *Luminous Blue Variables: Massive Stars in Transition*. Eds. Nota A., Lamers H. ASP Conf. Series **120**, p. 83 (1997) 64, 103, 104, 714
310. N. Langer: A&A **329**, 551 (1998) 714
311. N. Langer, A. Maeder: A&A **295**, 685 (1995) 696
312. N. Langer, C.A. Norman, A. de Koter, J. Vink, M. Cantiello, S.-C. Yoon: A&A **475**, L10 (2007) 664
313. N. Langer, D. Sugimoto, K.J. Fricke: A&A **126**, 207 (1983) 119, 121
314. R. Larson: MNRAS **194**, 809 (1981) 487
315. N.R. Lebovitz: Ann. Rev. Astron. Astrophys. **5**, 465 (1967) 19
316. P. Ledoux: ApJ **94**, 537 (1941) 62
317. P. Ledoux: Variable Stars, in *Handbuch der Physik* Bd. 51, Ed. S. Flugge, Springer Verlag, p. 605 (1958) 371, 393, 401
318. P. Ledoux: *Stellar Instability and Evolution*, IAU Symp. 59, Eds. P. Ledoux, A. Noels and A.W. Rodgers, Reidel Publ. Co. p. 135 (1974) 451, 452
319. P. Ledoux, Th. Walraven: Variable Stars, in *Handbuch der Physik* Bd. 51, ed. S. Flugge, Springer Verlag, p. 353 (1958) 371, 390, 391
320. Y.W. Lee, P. Demarque: ApJ Suppl. **73**, 709 (1990) 665
321. Y.W. Lee, P. Demarque, R. Zinn: ApJ **423**, 248 (1994) 665
322. J.W. Leibacher, R.F. Stein: Oscillations and Pulsations, in *The Sun as a Star*, Ed. S. Jordan, CNEAS and NASA Monograph Series, p. 263 (1981) 421, 451
323. C. Leitherer, C. Robert, L. Drissen: ApJ **401**, 596 (1992) 361
324. J.R. Lesh, M.L. Aizenman: A&A **34**, 203 (1974) 393
325. K.G. Libbrecht, M.F. Woodard: Nature, **345**, 779 (1990) 421
326. K.G. Libbrecht, M.F. Woodard, J.M. Kaufman: ApJS **74**, 1129 (1990) 421
327. K.G. Libbrecht: http://www.its.caltech.edu/ atomic/ (2006) 421
328. T. Lery, C. Combet, G. Murphy: Astroph. Space Sci. **293**, 263 (2004) 555
329. C. de Loore, P. Hellings, H. Lamers: *Wolf–Rayet Stars: observations, physics, evolution*, Eds. C. de Loore and A.J. Willis, Reidel. Publ. p.53 (1982) 704
330. C.C. Lovekhin, R.G. Deupree, C.I. Short: ApJ **643**, 460L (2006) 72
331. D. Lynden-Bell, J.E. Pringle: MNRAS **168**, 603 (1974) 500, 502, 503
332. L.S. Lyubimkov, S.I. Rostopochin, D.L. Lambert: MNRAS **351**, 745 (2004) 699, 700
333. K.L. Luhman, G.H. Rieke, E.T. Young, A.S. Cotera, H. Chen et al.: ApJ **540**, 1016 (2000) 494
334. M. Mac Low, R.S. Klessen: Rev. Modern Phys. **76**, 125 (2004) 486
335. A. Maeder: A&A **40**, 303 (1975) 110, 111
336. A. Maeder: A&A **47**, 389 (1976) 638, 640
337. A. Maeder: A&A **90**, 311 (1980) 106
338. A. Maeder: A&A **99**, 97 (1981) 688, 702
339. A. Maeder: A&A **102**, 401 (1981) 687, 691
340. A. Maeder: A&A **105**, 149 (1982) 713
341. A. Maeder: A&A **120**, 113 (1983) 709
342. A. Maeder: A&A **147**, 300 (1985) 373, 605
343. A. Maeder: A&A **173**, 247 (1987) 699
344. A. Maeder: A&A **178**, 159 (1987) 639, 754
345. A. Maeder: A&A **182**, 243 (1987) 692, 698
346. A. Maeder: A&A **242**,93 (1991) 708
347. A. Maeder: A&A **264**, 105 (1995) 732
348. A. Maeder: A&A **299**, 84 (1995) 297
349. A. Maeder: A&A **321**, 134 (1997) 122, 302
350. A. Maeder: A&A **347**, 185 (1999) 72, 76, 364, 365, 366
351. A. Maeder: A&A **373**, 122 (2001) 363
352. A. Maeder: A&A **399**, 263 (2003) 287, 288, 290, 291, 292, 305

353. A. Maeder: arXiv.0810.0657 (2008) 700
354. A. Maeder, P. Bouvier: A&A **50**, 309 (1976) 111
355. A. Maeder, P. Conti: Ann. Rev. Astron. Astrophys. **32**, 227 (1994) 710, 712
356. A. Maeder, V. Desjacques: A&A **372**, L9 (2001) 366
357. A. Maeder, C. Georgy, G. Meynet: A&A **479**, L37 (2008) 130, 132
358. A. Maeder, E. Grebel, J.C.Mermilliod: A&A **346**, 459 (1999) 78, 686, 755, 761
359. A. Maeder, J. Lequeux, M. Azzopardi: A&A **90**, L17 (1980) 711
360. A. Maeder, J.C. Mermilliod: A&A **93**, 136 (1981) 116
361. A. Maeder, J.C. Mermilliod: A&A **158**, 45 (1986) 117
362. A. Maeder, G. Meynet: A&A **182**, 243 (1987) 704
363. A. Maeder, G. Meynet: A&A **210**, 155 (1989) 117, 631, 648, 649, 652, 655, 656, 658, 660, 663
364. A. Maeder, G. Meynet: A&A **313**, 155 (1996) 300, 301
365. A. Maeder, G. Meynet: A&A **287**, 803 (1994) 708
366. A. Maeder, G. Meynet: A&A **361**, 159 (2000) 75, 77
367. A. Maeder, G. Meynet: A&A **373**, 555 (2001) 78, 697, 714, 768
368. A. Maeder, G. Meynet: A&A **422**, 225 (2004) 335, 336, 337, 338, 340, 342
369. A. Maeder, G. Meynet: A&A **440**, 1041 (2005) 332, 339, 343, 344, 346, 347, 348
370. A. Maeder, G. Meynet: A&A **448**, L37 (2006) 768
371. A. Maeder, E. Peytremann: A&A **7**, 120 (1970) 693
372. A. Maeder, J.-P. Zahn: A&A **334**, 1000 (1998) 245, 246, 249, 255, 271
373. P. Marigo: A&A **387**, 507 (2002) 675
374. P. Marigo: A&A **467**, 1139 (2002) 669
375. P. Marigo, C. Chiosi, R.P. Kudritzki: A&A **399**, 617 (2003) 756
376. P. Marigo, L. Girardi: A&A **469**, 239 (2007) 674
377. P. Marigo, L. Girardi, C. Chiosi, P.R. Wood: A&A **371**, 152 (2001) 670, 756, 757, 758, 760, 761
378. C. Martayan, M. Floquet, A.M. Huber, J. Gutierrez-Soto, J. Fabregat et al.: A&A **472**, 577 (2007) 686, 761
379. C. Martayan: *Massive Stars as Cosmic Engines*, IAU Symp.250, Eds. F. Bresolin & J. Puls, p. 571 (2008) 713
380. E.L. Martin, R. Rebolo, A. Magazzu, Ya.V. Pavlenko: A&A **282**, 503 (1994) 533
381. E.L. Martin: A&A **321**, 492 (1997) 498
382. P. Massey: ApJ **501**, 153 (1998) 696
383. P. Massey: Ann. Rev. Astron. Astrophys. **41**, 15 (2003) 696, 710
384. P. Massey, K.A.G. Olsen: ApJ **126**, 2867 (2003) 696
385. R.D. Mathieu: The Rotation of Low–Mass Pre–MS Stars. in *Stellar Rotation*, IAU Symp 215, Eds. by A. Maeder & P. Eenens, 113 (2004) 539, 540, 541, 545
386. S. Mathis, J.-P. Zahn: A&A **425**, 229 (2004) 29, 243, 249, 250, 256, 787
387. S. Mathis: *Effet du mélange interne sur l'évolution des étoiles: processus de transport dans les zones radiatives*, Thesis, Univ. of Paris XI, 287 pages (2006) 461, 471, 472
388. S. Mathis, A. Palacios, J.-P. Zahn: A&A **425**, 243 (2004) 288, 289, 291, 293, 305
389. S. Mathis, A. Palacios, J.-P. Zahn: A&A **462**, 1063 (2007) 293
390. S. Mathis, J.-P. Zahn: A&A **440**, 653 (2005) 315
391. S. Mathis, J.-P. Zahn: private comm. (2007) 268
392. G. Mathys: *Stellar Rotation*, IAU Symp 215, Eds. by A. Maeder & P. Eenens, p. 270 (2004) 317
393. T.J. Mazurek, J.C. Wheeler: Fundam. Cosmic Phys. **5**, 193 (1980) 660
394. C.F. McKee, J.C. Tan: ApJ **585**, 850 (2003) 554, 569
395. D.E. McLaughlin, R.E. Pudritz: ApJ **476**, 750 (1997) 490, 491
396. A. Meilland, Ph. Stee, M. Vannier, F. Millour, A. Domiciano de Souza et al.: A&A **464**, 59 (2007) 365
397. L.T.S. Mendes, F.D'Antona, I. Mazzitelli: A&A **341**, 174 (1999) 532
398. K. Menou, S.A. Balbus, H.C. Spruit: ApJ **607**, 564 (2004) 351
399. W.J. Merryfield: ApJ **444**, 318 (1995) 121
400. L. Mestel: Stellar Structure, in *Stars and Stellar Systems*, vol. 8, Eds. G.P. Kuiper and B.M. Middlehurst, Univ. Chicago Press, p. 465 (1965) 270

401. L. Mestel, R.J. Tayler, D. Moss: MNRAS **231**, 873 (1988) 325
402. L. Mestel, N.O. Weiss: MNRAS **226**, 123 (1987) 325
403. B.S. Meyer: Ann. Rev. Astron. Astrophys. **32**, 153 (1994) 745
404. G. Meynet: Thesis, Univ. of Geneva, (1989) 596, 729
405. G. Meynet: private communication (2007) 650
406. G.Meynet, M. Arnould: A&A **355**, 176 (2000) 710
407. G. Meynet, S. Ekström, A. Maeder: A&A **447**, 623 (2006) 682, 683, 765, 767, 768
408. G. Meynet, A. Maeder: A&A **321**, 465 (2000) 28, 30, 32, 33, 69, 302
409. G. Meynet, A. Maeder: A&A **361**, 101 (2000) 78, 220, 273, 274, 275, 284, 296, 693, 695, 701, 714, 715
410. G. Meynet, A. Maeder: A&A **390**, 561 (2002) 263, 264, 276, 678, 679, 682, 683, 701, 764, 768
411. G. Meynet, A. Maeder: A&A **404**, 975 (2003) 694, 701, 709, 712, 717, 739
412. G. Meynet, A. Maeder: A&A **429**, 581 (2005) 711, 712, 739
413. G. Meynet, A. Maeder: A&A **464**, L11 (2007) 368, 754
414. G. Meynet, A. Maeder, N. Mowlavi: A&A **416**, 1023 (2004) 125, 216, 223, 224, 225, 231
415. G. Meynet, J.-C. Mermilliod, A. Maeder: A&A Suppl. **98**, 477 (1993) 643
416. G. Michaud: *Evolution of Stars: The Photospheric Abundance Connection*, IAU Symp. 145, Eds. G. Michaud, A. Tutukov, Kluwer Acad. Publ. p. 111 (1991) 238
417. G. Michaud: *The A–Star Puzzle*, IAU Symp. 224, Cambridge Univ. Press, p. 173 (2004) 238
418. G. Michaud, Y. Charland, S. Vauclair, G. Vauclair : ApJ **210**, 447 (1976) 235
419. G. Michaud, O. Richard, J. Richer, D.A. VandenBerg: ApJ **606**, 452 (2004) 238
420. M.S. Miesch, A.S. Brun. J. Toomre: ApJ **641**, 618 (2006) 115
421. D. Mihalas: *Stellar Atmospheres*, W.H. Freeman and Co. 463 p. (1970) 597
422. J.A. Miralles, K.A. van Ripper: ApJS **105**, 407 (1996) 165
423. R. Mitalas: MNRAS **285**, 567 (1997) 8, 62
424. A. Moffat: *Massive Stars as Cosmic Engines*, IAU Symp.250, Eds. F. Bresolin & J. Puls, p. 119 (2008) 713
425. M.R. Mokiem, A. de Koter, J.S. Vink, J. Puls, C.J. Evans et al.: A&A **473**, 603 (2007) 689
426. P. Möller: Atomic Data Nucl. Data Tables **66**, 131 (1997) 749
427. J.D. Monnier, M. Zhao, E. Pedretti, N. Thureau, M. Ireland et al.: Science **317**, 342 (2007) 74
428. J. Montalban, E. Schatzman: A&A **354**, 943 (2000) 471
429. T. Montmerle, G. Michaud: ApJ Suppl. **31**, 489 (1976) 227, 236
430. D. Moss: MNRAS **226**, 281 (1987) 325
431. D. Moss: MNRAS **257**, 593 (1992) 330
432. D. Moss, L. Mestel, R.J. Tayler : MNRAS **245**, 550 (1990) 330
433. T. Ch. Mouschovias, L. Spitzer: ApJ **210**, 326 (1976) 485
434. N. Mowlavi: *The influence of binaries on stellar population studies*, Ed. D. Vanbeveren Kluwer, Dordrecht, p. 287 (2001) 669, 672, 673
435. N. Mowlavi, G. Meynet, A. Maeder, D. Schaerer, C. Charbonnel: A&A **335**, 573 (1998) 643, 657, 658
436. T. Nakano: ApJ **345**, 464 (1989) 563
437. T. Nakano, T. Hasegawa, J.I. Morino, T. Yamashita: ApJ **534**, 976 (2000) 554
438. C. Neiner, A.-M. Hubert, Y. Fremat, M. Floquet, S. Jankov et al.: A&A **409**, 275 (2003) 318
439. R. Nishi, H. Susa: ApJ **523**, L103 (1999) 572
440. A. Noels, C. Maserel: A&A **105**, 293 (1982) 605
441. K. Nomoto: *Stellar Nucleosynthesis*, Eds. C. Chiosi & A. Renzini, Reidel, Dordrecht, p. 238 (1984) 662
442. K. Nomoto, N. Tominaga, H. Umeda, C. Kobayashi, K. Maeda: Nuclear Phys. **777**, 421 (2007) 740
443. P. Norberg, A. Maeder: A&A **359**, 1025 (2000) 524, 526, 554, 569
444. A. Nota, Lecture Notes in Physics, **523**, 62 (1999) 365
445. T. Nugis, H. Lamers: A&A **360**, 227 (2000) 689, 690, 733
446. T. Nugis, H. Lamers: A&A **389**, 162 (2002) 689
447. K. Omukai, S. Inutsuka: MNRAS **332**, 59 (20032) 579, 583, 584, 585, 586
448. K. Omukai, F. Palla: ApJ **589**, 677 (2003) 577, 578, 579, 580, 581, 582
449. E.J. Öpik: MNRAS **111**, 278 (1951) 259, 263

450. J.R. Oppenheimer, G.M. Volkoff: Phys. Rev. **55**, 374 (1939). 172
451. M. Osterloh, S.V.W. Beckwith: ApJ **439**, 288 (1995) 504
452. S.P. Owocki: *Rotation and Mass Ejections: the Launching of Be–Star Disks*, in *Stellar Rotation*, IAU Symp 215, Eds. A. Maeder & P. Eenens, p 515 (2004) 78, 355, 361, 362, 366
453. S.P. Owocki: *Evolution of Massive Stars, Mass Loss and Winds*, Eds. M. Heydari–Malayeri et al., EAS Publ. Ser. **13**, 163 (2004) 355
454. A. Palacios: Thesis, Univ. of Toulouse, 130 p. (2002) 266
455. A. Palacios, C. Charbonnel, S. Talon, L. Siess: A&A **453**, 261 (2006) 129, 651
456. F. Palla: *Physics of Star Formation in Galaxies*, Saas–Fee Adv. Course, Eds. A. Maeder & G. Meynet, Springer Verlag, p. 9 (2002) 518, 520, 521, 522, 527, 529, 588
457. F. Palla, S.W. Stahler: ApJ **360**, L47 (1990) 522
458. S. Parete–Koon, W.R. Hix, C. Freiburghaus, F.-K. Thielemann: *Nuclei in the Cosmos IX*, Proc. Intnl. Conf. Nuclear Astrophys. p. 157 (2006) 743
459. E.N. Parker: ApJ **162**, 491 (1955) 351
460. E.N. Parker, *Cosmical Magnetic Fields: Their origin and their activity*, Oxford University press, 858 p. (1979) 311
461. C. Paquette, C. Pelletier, G. Fontaine, G. Michaud: ApJ suppl. **61**, 177 (1986) 228, 232
462. A. Pauldrach, J. Puls, R.P. Kudritzki: A&A **164**, 86 (1986) 358, 361
463. L.R. Penny: ApJ **463**, 737 (1996) 73
464. C. Peter: Diploma work, Geneva Observatory (2005) 566, 567, 568, 569
465. D.M. Peterson, C.A. Hummel, T.A. Pauls, J.T. Armstrong, J.A. Benson et al.: ApJ **636**, 1087 (2006) 20, 74
466. D.M. Peterson, C.A. Hummel, T.A. Pauls, J.T. Armstrong, J.A. Benson et al.: *The Power of Optical/IR Interferometry: Recent Scientific Results and 2nd Generation Instr.*, ESO Astroph. Symp., Springer Verlag, p. 43 (2008) 74
467. R.C. Peterson, R.T. Rood, D.A. Crocker: ApJ **453**, 214 (1995) 666
468. M.H. Pinsonneault, S.D. Kawaler, S. Sofia, P. Demarque: ApJ **338**, 424 (1989) 277
469. J. Petrovic, N. Langer, S.-C. Yoon, A. Heger: A&A **435**, 247 (2005) 753
470. J. Petrovic, N. Langer, K.A. van der Hucht: A&A **435**, 1013 (2005) 713
471. G. Piotto, S. Villanova, L.R. Bedin, et al.: ApJ, **621**, 777 (2005) 768
472. E. Pitts, R.J. Tayler: MNRAS **216**, 139 (1986) 331
473. B. Plez, J.G. Cohen, A&A **434**, 1117 (2005) 682
474. A.J.T. Poelarends, F. Herwig, N. Langer, A. Heger: ApJ **675**, 614 (2008) 663, 678
475. A.Y. Pothekin, G. Chabrier: Phys. Rev. E. **62**, 8554 (2000) 161
476. N. Prantzos, M. Hashimoto, K. Nomoto: A&A **234**, 211 (1990) 710
477. N. Prantzos, M. Hashimoto, M. Rayet, M. Arnould: A&A, **238**, 455 (1990) 749
478. Th. Preibisch, V. Ossenkopf, H.W. Yorke, Th. Henning: A&A **279**, 577 (1993) 561
479. W.H. Press: ApJ **245**, 286 (1981) 452, 453, 454, 457, 470, 471
480. E.R. Priest: *Plasma Astrophysics*, Saas–Fee Advanced Course 24, Eds. A.O. Benz, T. Courvoisier, Springer Verlag, p. 1 (1994) 311, 314, 315
481. J. Puls, R.P. Kudritzki, A. Herrero, A.W.A. Pauldrach, S.M. Haser et al.: A&A **305**, 171 (1996) 362
482. D. Queloz, S. Allain, J.C. Mermilliod, J. Bouvier, M. Mayor: A&A **335**, 183 (1998) 541, 548
483. L.K.M. Rebull, S.C. Wolff, S.E. Strom: AJ **127**, 1029 (2004) 545
484. D. Reimers: Mém. Soc. Roy. Sci. Liége, 6e Ser., **8**, 369 (1975) 689
485. A. Renzini, L. Greggio, C. Ritossa, L. Ferrario: ApJ **400**, 280 (1992) 650
486. D. Richard, J.P. Zahn: A&A **347**, 734 (1999) 288
487. D. Richardson, D. Branch, D. Casebeer, J. Millard, R.C. Thomas, E. Baron: AJ **123**, 745 (2002) 735
488. J. Richer, G. Michaud, F. Rogers, C. Iglesias, S. Turcotte, F. Leblanc: ApJ **492**, 833 (1998) 236
489. M. Rieutord: *Stellar Fluid Dynamics an Numerical Simulations: From the Sun to Neutron Stars*, Eds. M. Rieutord & M. Dubrulle, EAS Publ. Series, EDP Sciences, vol **21**, 275 (2006) 249
490. E. Ripamonti: MNRAS **376**, 709 (2007) 590
491. E. Ripamonti, F. Haardt, A. Ferrara, M. Colpi: MNRAS **334**, 401 (2002) 574, 575

492. F.J. Rogers, C.A. Iglesias: Science **263**, 50 (1994) 179
493. F.J. Rogers, C.A. Iglesias: Space Sci. Rev. **85**, 61 (1998) 177, 184, 191, 192
494. F.J. Rogers, A. Nayfonov: ApJ **576**, 1064 (2002) 435
495. F.J. Rogers, F.J. Swenson, C.A. Iglesias: ApJ **456**, 902 (1996) 191, 435
496. T.M. Rogers, G.A. Glatzmaier: MNRAS **364**, 1135 (2005) 464
497. T.M. Rogers, G.A. Glatzmaier: ApJ **653**, 756 (2006) 464
498. W.K. Rose: in *Advanced Stellar Astrophysics*, Cambridge Univ. Press, 477 p. (1998) 177, 189
499. I.W. Roxburgh: MNRAS **128**, 157 (1964) 249
500. I.W. Roxburgh: A&A **185**, 117 (1989) 112
501. S.H. Saar: *MHD Phenomena in Solar Atmospheres - Prototypes of Stellar Activity*, IAU Coll.
     153, Eds. Y. Uchida, T. Kosugi & H.S. Hudson, p. 367 (1996) 321
502. I.J. Sackmann, S.P.S. Anand: ApJ **162**, 105 (1970) 714
503. P.N. Safier: ApJ **510**, L127 (1999) 318
504. H. Saio, A. Gautschy: ApJ **498**, 369 (1998) 393, 397, 398
505. S. Sakashita, C. Hayashi: Prog. Theor. Phys. **22**, 830 (1959) 119
506. E.E. Salpeter: ApJ **115**, 326 (1952) 645
507. A. Sandage, G. Tamman: Ann. Rev. Astron. Astrophys. **44**, 93 (2006) 397
508. J. Scalo: Fund. Cosmic Phys. **11**, 1 (1986) 494
509. D. Schaerer, A. de Koter, W. Schmutz, A. Maeder: A&A **310**, 837 (1996) 706
510. D. Schaerer, A. de Koter, W. Schmutz, A. Maeder: A&A **312**, 475 (1996) 706
511. D. Schaerer, A. Maeder: A&A **263**, 129 (1992) 704, 706
512. G. Schaller: Thesis, Observatory of Geneva (1992) 378, 380, 388
513. G. Schaller, D. Schaerer, G. Meynet, A. Maeder: A&A Suppl. Ser. **96**, 269 (1992) 368, 392, 626, 628, 641
514. H. Schattl: A&A **395**, 85 (2002) 238
515. E. Schatzman: A&A **56**, 211 (1977) 784
516. E. Schatzman: "*Ondes internes*" in Cours d'Aussois (1993) 471
517. E. Schatzman: "*White Dwarfs*", Interscience Publ. New York (1958) 57
518. S. Schmeja, S.R. Klessen: A&A **419**, 405 (2004) 506, 554, 565, 566, 570
519. Th. Schmidt-Kaler: *Landolt-Börnstein, Numerical Data and Functional Relationships in Sci-
     ence and Technology*, vol. 2, p. 33 (1982) 73
520. M. Schönberg, S. Chandrasekar: ApJ **96**, 161 (1942) 640
521. S.L.S. Shorlin, G.A. Wade, J.F. Donati, J.D. Landstreet, P. Petit et al.: A&A **392**, 637 (2002) 317
522. D.N. Schramm: in *Advanced Stages in Stellar Evolution*, 7th Saas–Fee Course, Eds. P. Bou-
     vier, A. Maeder, 285 (1973) 745
523. M. Schwarzschild: *Structure and Evolution of Stars*, Princeton Univ. Press, (1958) 183, 185, 599
524. M. Schwarzschild, R. Härm: ApJ **128**, 348 (1958) 119
525. M.J. Seaton: MNRAS **362**, L1 (2005) 177, 192
526. A. Serenelli, A. Weiss: A&A **442**, 1041 (2005) 665
527. G. Shaviv, E.E. Salpeter: ApJ **184**, 191 (1973) 111
528. F. H. Shu: ApJ **214**, 488 (1977) 489, 490, 505
529. L. Siess: Thesis, Univ. Grenoble (1996) 516, 530, 532, 533, 534
530. L. Siess, M. Forestini, C. Bertout: A&A **326**, 1001 (1997) 508
531. L. Siess, S. Goriely, N. Langer: A&A **415**, 1089 (2004) 683
532. J. Silk: ApJ **438**, L41 (1995)
533. A. Sills, M.H. Pinsonneault, D.M. Terndrup: ApJ **534**, 335 (2000) 323
534. A. Skumanich: ApJ **171**, 565 (1972) 319, 321, 324
535. S. Smartt: A&A **391**, 979 (2002) 699
536. S. Smartt: *Massive Stars as Cosmic Engines*, IAU Symp.250, eds. F. Bresolin & J. Puls,
     p. 201 (2008) 734
537. J.-D.T. Smith, J.R. Houck: ApJ **622**, 1044 (2005) 709
538. L.F. Smith, D.G. Hummer: MNRAS **230**, 511 (1988) 707, 708, 713
539. L.F. Smith, A. Maeder: A&A **241**, 77 (1991) 707, 713, 753
540. V. Smith, D. Lambert: ApJ Suppl. Ser. **72**, 387 (1990) 675

541. S. Sofia, S.A. Barnes: Pre–Main Sequence Evolution of Rotating Stars in Relation with Observations in Young Clusters. in *Stellar Rotation*, IAU Symp 215, Eds. A. Maeder & P. Eenens, pp 419–428 (2004)

542. E. Spiegel, J.-P- Zahn: A&A **265**, 106 (1992) 243, 283, 445

543. L.J. Spitzer: *Physics of Fully Ionized Gases*, Wiley Publ. New York (1962) 784

544. H.C. Spruit: A&A **253**, 131 (1992) 120

545. H.C. Spruit: A&A **349**, 189 (1999) 327, 328, 329, 330, 331, 332, 333, 348, 349, 350, 353

546. H.C. Spruit: A&A **381**, 923 (2002) 330, 331, 332, 333, 334, 336, 337, 338

547. H.C. Spruit: arXiv astroph/0607164 (2006) 348

548. S.W. Stahler, F. Palla: *The Formation of Stars*, (Wiley Weinheim) (2004) 488, 518, 530, 532

549. S.W. Stahler, F.H. Shu, R.E. Taam: ApJ **241**, 637 (1980) 506, 507

550. J.R. Stauffer: Rotational Evolution of Intermediate and Low Mass Main Sequence Stars. in *Stellar Rotation*, IAU Symp 215, eds. A. Maeder & P. Eenens, p 127 (2004) 547, 548

551. W.F. Stellingwerf: ApJ **83**, 1184 (1978) 179

552. D.J. Stevenson: MNRAS **187**, 129 (1979) 120

553. R.B. Stothers: ApJ **383**, 820 (1986) 117

554. D. Sugimoto, M.Y. Fujimoto: ApJ **538**, 837 (2000) 650

555. P.A. Sweet: MNRAS **110**, 548 (1950) 259

556. S. Talon: Thesis, Univ. Paris VII, 187 p. (1997) 246, 247, 294, 295, 307, 308

557. S. Talon: *Stellar Fluid Dynamics and Numerical Simulations: From the Sun to Neutron Stars*, Eds. M. Rieutord, B. Dubrulle, EAS Publ. Ser. **21**, 105 (2006) 458, 460

558. S. Talon: *Aussois Lecture Notes*, arXiv0708.1499T (2007) 326, 468, 470, 471

559. S. Talon, C. Charbonnel: A&A, **405**, 1025 (2003) 446, 464, 465, 469

560. S. Talon, C. Charbonnel: A&A, **440**, 981 (2005) 467, 468, 469

561. S. Talon, P. Kumar, J.-P. Zahn: ApJ **574**, L175 (2002) 465, 466, 467

562. S. Talon, J.-P. Zahn: A&A **317**, 749 (1997) 302, 303, 304, 786

563. S. Talon, J.-P. Zahn, A. Maeder, G. Meynet: A&A **322**, 209 (1997) 296

564. J.C. Tan, C.F. McKee: ApJ **603**, 383 (2004) 582

565. M. Tassoul: ApJ Suppl. **43**, 469 (1980) 430, 431, 451

566. J.-L. Tassoul, J.P. Ostriker: A&A, **4**, 423 (1970) 78

567. R.J. Tayler: MNRAS **161**, 365 (1973) 330

568. L. Testi, F. Palla, T. Prusti, A. Natta, S. Maltagliati: A&A **320**, 159 (1997) 552

569. F.K. Thielemann, W.D. Arnett: ApJ **295**, 589 (1985) 725

570. F.K. Thielemann, W.D. Arnett: ApJ **295**, 604 (1985) 725

571. F.-K. Thielemann, M. Hashimoto, K. Nomoto: ApJ **349**, 222 (1990) 741

572. F.K. Thielemann, K. Nomoto, M. Hashimoto: ApJ **460**, 408 (1996) 731, 742

573. A. Thoul, J.N. Bahcall, A. Loeb: ApJ **421**, 828 (1994) 238

574. F.X. Timmes, R.D. Hoffman, S.E. Woosley: ApJS **129**, 377 (2000) 725

575. B. Tinsley: Fund. Cosmic Physics **5**, 287 (1980) 732

576. J.E. Tohline: Fund. Cosmic Phys. **8**, 1 (1982) 508

577. J. Toomre, A.S. Brun: *Stellar Rotation*, IAU Symp 215, Eds. A. Maeder & P. Eenens, p. 326 (2004) 129

578. R.H.D. Townsend, S.P. Owocki, I.D. Howarth: MNRAS **350**, 189 (2004) 686

579. H.-P. Trautvetter: *Nuclei in the Cosmos 2*, Proc. 2nd Intl. Conf. on Nucl. Astrophys., eds. F. Käppeler & K. Wisshak, Inst. of Physics Publ. p. 139 (1993) 199

580. C. Trundle, P.L. Dufton, I. Hunter, C.J. Evans, D. J. Lennon et al.: A&A **471**, 625 (2007) 699, 700

581. M. Turatto: *Supernovae and Gamma-Ray Bursters*, ed. K.W. Weiler, Lecture Notes in Physics, **598**, 21 (2003) 734, 735

582. S. Turck–Chièze, S. Couvidat, L. Piau, J. Ferguson, P. Lambert et al.: Phys. Rev. Lett. **93**, 211102-1 (2004) 435

583. S. Turck–Chièze, P. Lambert: Adv. Space Res. **40**, 907 (2007) 435, 446

584. R.K. Ulrich: ApJ **306**, L37 (1986) 439

585. W. Unno, Y. Osaki, H. Ando, H. Saio, H. Shibahashi: *Nonradial Oscillations of Stars*, Univ. of Tokyo Press, 420 p. (1989) 401, 410, 428, 453

586. V.A. Urpin, D.A. Shalybkov, H.C. Spruit: A&A **306**, 455 (1996) 254
587. S. Uttenthaler, J. Hron, T. Lebzelter, M. Busso, M. Schultheis et al.: A&A **463**, 251 (2007) 671
588. G.T. van Belle, D.R. Ciardi, T. ten Brummelaar, H.A. McAlister, S.T. Ridgway et al.: ApJ **637**, 494 (2006) 74
589. D. Vanbeveren, J. Van Bever, H. Belkus: ApJ **662**, L107 (2007) 713
590. D.A. VandenBerg: ApJS **51**, 29 (1983) 665
591. D.A. VandenBerg, O. Richard, G. Michaud, J. Richer: ApJ **571**, 487 (2003) 238
592. D.A. VandenBerg, P.B. Stetson: PASP **116**, 997 (2004) 117
593. K.A. Van der Hucht: New Astron. Rev. **45**, 135 (2001) 713
594. K.A. Van der Hucht: A&A **458**, 453 (2006) 713
595. J.Th. van Loon, M.-R.L. Cioni, A.A. Zijlstra, C. Loup: A&A **438**, 273 (2005) 689
596. H. Van Winckel, M. Reyniers: A&A **354**, 135 (2000) 682
597. H. Van Winckel: Ann. Rev. Astron. Astrophys. **41**, 391 (2003) 667
598. G.A. Vasquez, C. Leitherer, D. Schaerer, G. Meynet, A. Maeder: ApJ **663**, 995 (2007) 643
599. E. Vassiliadis, P. Wood: ApJ **413**, 641 (1993) 670, 689
600. S. Vauclair: *Astrophysical Processes in Upper Main Sequence Stars*, 13th Saas–Fee Course, p. 167 (1983) 218, 220, 231, 233, 234, 235, 237
601. K.A. Venn, N. Przybilla: *CNO in the Universe*, eds. C. Charbonnel, D. Schaerer, G. Meynet, ASP Conf. Ser. **304**, 20 (2003) 699, 700
602. M.R. Villamariz, A. Herrero: A&A **388**, 940 (2002) 699
603. J.S. Vink, A. de Koter: A&A **442**, 587 (2005) 690, 754
604. J.S. Vink, A. de Koter, H. Lamers: A&A **362**, 295 (2000) 362, 689, 715, 733
605. J.S. Vink, A. de Koter, H. Lamers: A&A **369**, 574 (2001) 361, 362, 689, 715, 733
606. G. Wallerstein, G.H. Herbig, P.S. Conti: ApJ **141**, 610 (1965) 469
607. V. Weidmann: A&A **363**, 647 (2000) 661, 677
608. A. Weigert: *L' évolution des étoiles*, Cours AVCP, eds. E. Joseph, A. Maeder, M. Mayor, Geneva Observatory (1969) 56, 58
609. K.W. Weiler, R.A. Sramek: Ann. Rev. Astron. Astrophys. **26**, 295 (1988) 734, 735
610. A. Weiss, W. Hillebrandt, H.-C. Thomas, H. Ritter: *Cox & Giuli's Principles of Stellar Structure, Extended Second Edition*, Cambridge Scientific Publ. (2004) 94, 98, 99, 100, 177, 180, 183, 185, 188
611. D. Wahlen, T. Abel, M.L. Norman: ApJ **610**, 14 (2004) 573
612. B.S. Wilden, B.F. Jones, D.N.C. Lin, D.R. Soderblom: AJ **124**, 2799 (2002) 533
613. A.J. Willis: in *Evolution of Stars: the Photospheric Abundance Connection*, IAU Symp. 145, eds. G. Michaud and A. Tutukov, Kluwer, p.195 (1991) 706
614. A.J. Willis, L. Dessart, P. Crowther: *Boulder-Munich II: Properties of Hot, Luminous Stars*, Ed. I. Howarth, ASP Conf. Ser. **131**, 66 (1998) 709
615. L.A. Willson: Ann. Rev. Astron. Astrophys. **38**, 573 (2000) 670, 689
616. M.G. Wolfire, J.P. Cassinelli: ApJ **319**, 850 (1987) 559, 561, 562, 563
617. S. Woosley: *Nucleosynthesis and Chemical Evolution*, 16th Saas–Fee Course, Eds. B. Hauck, A. Maeder, G. Meynet, Geneva Obs. (1986) 663, 720, 723, 724
618. S.E. Woosley: ApJ **405**, 273 (1993) 752
619. S.E. Woosley, J.S. Bloom: Ann. Rev. Astron. Astrophys. **44**, 507 (2006) 752
620. S.E. Woosley, H.-T. Janka: Nat. Phys. **1**, 147 (2005) 725
621. S.E. Woosley, A. Heger: AIP Conf. Proc. **836**, 398 (2006) 753
622. S.E. Woosley, A. Heger: ApJ **637**, 914 (2006) 753
623. G. Wuchterl, R.S. Klessen: ApJ **560**, L185 (2001) 509
624. D.R. Xiong, Q.L. Cheng, L. Deng: ApJS **108**, 529 1997 115
625. S. Yi, Y.-W. Lee, P. Demarque: ApJ **411**, L25 (1993) 666
626. S.-C. Yoon, N. Langer: A&A **464**, L11 (2005) 753, 754
627. H.W. Yorke: Theory of Formation of Massive Stars via Accretion. in *Star formation at High Angular Resolution*, IAU Symp. 221, Eds. M.G. Burton et al. p.141 (2004) 476, 554, 558, 561, 562, 564
628. H.W. Yorke, P. Bodenheimer, G. Laughlin: ApJ **411**, 274 (1993) 504
629. H.W. Yorke, P. Bodenheimer: ApJ **525**, 330 (1999) 563, 564
630. H.W. Yorke, C. Sonnhalter: ApJ **569**, 846 (2002) 502, 554, 565, 566, 567, 570

631. P.A. Young, C. Meakin, D. Arnett & C.L. Fryer: ApJ **629**, L101 (2005) 115, 116
632. J.-P. Zahn: A&A **265**, 115 (1992) 20, 29, 242, 243, 249, 250, 255, 256, 258, 259, 261, 277, 283, 284, 285
633. J.-P. Zahn: Space Sci. Rev. **66**, 285 (1994) 113
634. J.-P. Zahn, A.S. Brun, S. Mathis: A&A **474**, 145 (2007) 332, 333, 337
635. J.-P. Zahn, S. Talon, J. Matias: A&A **322**, 320 (1997) 454, 458, 459
636. Q. Zhang: Search for Disks and Outflows in High–Mass Protostellar Candidates: Implications for Formation Mechanism. in *Hot Star Workshop III: The Earliest Stages of Massive Star Birth*, ASP Conf. Ser. **267**, Ed. P.A. Crowther, p. 145 (2002) 556
637. F.J. Zickgraf: *Variable and Non-spherical Winds in Luminous Hot Stars*, IAU Coll. 169, Eds. B. Wolf et al., Springer Verlag, p. 40 (1999) 365
638. H. Zinnecker, M.R. Bate: Multiplicity of Massive Stars - A Clue to their Origin. in *Hot Star Workshop III: The Earliest Stages of Massive Star Birth*, ASP Conf. Ser. **267**, Ed. P.A. Crowther, p. 209 (2002) 552
639. H. Zinnecker, H.W. Yorke: Ann. Rev. Astron. Astrophys. **45**, 481 (2007) 551
640. J. Zverko, J. Ziznovsky, S.J. Adelman, W.W. Weiss: *The A–Star Puzzle*, IAU Symp. 224, Cambridge Univ. Press, 520 p. (2004) 238

Index

A&A LIBRARY

ASTRONOMY AND ASTROPHYSICS LIBRARY

Series Editors: G. Börner · A. Burkert · W. B. Burton · M. A. Dopita
A. Eckart · T. Encrenaz · E. K. Grebel · B. Leibundgut
A. Maeder · V. Trimble

ASTRONOMY AND ASTROPHYSICS LIBRARY

The Design and Construction of Large Optical Telescopes By P. Y. Bely

The Solar System 4th Edition
By T. Encrenaz, J.-P. Bibring, M. Blanc,
M. A. Barucci, F. Roques, Ph. Zarka

General Relativity, Astrophysics, and Cosmology By A. K. Raychaudhuri,
S. Banerji, and A. Banerjee

Stellar Interiors Physical Principles,
Structure, and Evolution 2nd Edition
By C. J. Hansen, S. D. Kawaler, and V. Trimble

Asymptotic Giant Branch Stars
By H. J. Habing and H. Olofsson

The Interstellar Medium
By J. Lequeux

Methods of Celestial Mechanics (2 volumes)
Volume I: Physical, Mathematical, and
Numerical Principles
Volume II: Application to Planetary System,
Geodynamics and Satellite Geodesy
By G. Beutler

Solar-Type Activity in Main-Sequence Stars
By R. E. Gershberg

Relativistic Astrophysics and Cosmology
A Primer By P. Hoyng

Magneto-Fluid Dynamics
Fundamentals and Case Studies
By P. Lorrain

Compact Objects in Astrophysics
White Dwarfs, Neutron Stars and Black Holes
By Max Camenzind

Special and General Relativity
With Applications to White Dwarfs, Neutron
Stars and Black Holes
By Norman K. Glendenning

Planetary Systems
Detection, Formation and Habitability of
Extrasolar Planets
By M. Ollivier, T. Encrenaz, F. Roques
F. Selsis and F. Casoli

The Sun from Space 2nd Edition
By Kenneth R. Lang

Tools of Radio Astronomy 5th Edition
By Thomas L. Wilson, Kristen Rohlfs and
Susanne Hüttemeister

Astronomical Optics and Elasticity Theory
Active Optics Methods
By Gérard René Lemaitre

**Physics, Formation and Evolution of
Rotating Stars** 1st Edition
By André Maeder